Murujuga Rock Art Monitoring Program:

Monitoring Studies Report 2024

Technical Report on Monitoring Studies completed from April 2023 to March 2024.

Prepared for
Murujuga Aboriginal Corporation
and
Department of Water and Environmental Regulation, Western Australia.

Preferred citation:

Curtin University (2024) *Murujuga Rock Art Monitoring Program: Monitoring Studies Report 2024*. Submitted to the Murujuga Aboriginal Corporation and the Department of Water and Environmental Regulation, Government of Western Australia. DWER Technical report COPP21065-REP-G-105, revision 2.

Doc No	Current Rev	Revision Date	Checked By	Approved By
COPP21065-REP-G-105	2	29/04/2025	B. Mullins	A. Baddeley

Revision history

Revision	Date	Revision Reason
A	13/05/2024	Preliminary for review
B	04/06/2024	Issued to DWER for peer review
C	27/08/2024	Updated following peer review
0	20/12/2024	Issued for use following close-out review
1	14/04/2025	Issued for final approval
2	29/04/2025	Data corrections to Appendix D Table D.1-51 and Figure D.1-49

Authors and contributors

Glen Aubrey, Adrian Baddeley, David Belton, Kasziem Bin-Sali, Katelyn Boase, Arne Bredin, Kimbra Bridges, Aaron Cavosie, Marco Coolen, Noel Cressie, Thomas Di Loreto, Katy Evans, John Fairweather, Ronald Fellows-Smith, Kliti Grice, Monica Gumulya, Toni Hannelly, Carmen Harris, Stephanie Hogg, Alex Holman, Peter Hopper, Laura Horan, Melanie Johnston-Hollitt, Andrew King, Pete Kinny, Katherine Landwehr, David Lynch, Dan Marrable, Alex Martin, Ryan Mead-Hunter, Abraj Mohomed, Benjamin Mullins, Rebecca O'Leary, Calvin Pang, Suman Rakshit, Will Rickard, Robert Ryan, Bettina Schaefer, Sebastian Stanley, Amy Stevens, Tommaso Tacchetto, Stefano Tenuta, Andrew Thorn, Taylor Tufto, Arun Veluchamy.

Acknowledgements

This work was supported by resources provided by the Pawsey Supercomputing Research Centre's Setonix Supercomputer (CFD and Spatial and Bioinformatics Modelling, https://doi.org/10.48569/18sb-8s43) and Nimbus Research Cloud (AQM data storage and processing, https://doi.org/10.48569/v0j3-qd51), with funding from the Australian Government and the Government of Western Australia.

The authors also gratefully acknowledge: (1) the West Australian Biogeochemistry Centre (UWA) and Dr Greg Skryzpek for provision of rainwater *pH* data, and (2) Dr Cameron McNaughton and Dr Leigh Crilley (WSP), Dr Frances Phillips and Prof David Griffith (U. Wollongong), Robyn Schofield (UoM), Prof Zoran Ristovski (QUT) for useful discussions on various topics within their respective research fields.

The data associated with this report is available on request from the Department of Water and Environmental Regulation.

The information contained in this report is copyright © 2021–2024 the Department of Water and Environmental Regulation (DWER) WA, except for prior art (background IP) of WSP, Curtin University and subcontractors. No part of the report may be reproduced or transmitted in any form by any means including, without limitation, electronic, photocopying, recording, or otherwise, without the prior written permission of DWER. No information embodied in the report which is not already in the public domain shall be communicated in any manner whatsoever to any third party without the prior written consent of DWER. While WSP, Curtin University and subcontractors consider that the information and opinions given in this work are sound, all parties must rely upon their own skill and judgement when making use of it. WSP, Curtin University and subcontractors do not make any representation or warranty, expressed or implied, as to the accuracy or completeness of the information contained in this report and assumes no responsibility for the accuracy or completeness of such information. WSP, Curtin University and subcontractors will not assume any liability to anyone for any loss or damage arising out of the provision of this report.

Executive summary

The Murujuga Rock Art Monitoring Program (**MRAMP**) is the most extensive scientific study to date to examine the impact of industrial air emissions on the rock art engravings of Murujuga, an area covering the Burrup Peninsula and Dampier Archipelago in Western Australia. This technical report contains the first two years of results from the research being undertaken to establish acceptable and unacceptable air pollutant exposure levels to protect the Murujuga rock art.

The extensive program of monitoring and the high spatial resolution of data collection, combined with rigorous laboratory investigation and innovative statistical techniques, have enabled the research team to establish important spatial patterns in rock porosity, microbiome and chemistry. The evidence for these patterns would have been unlikely to be statistically significant if a smaller number of study sites had been selected.

MRAMP will ultimately develop a series of Environmental Quality Criteria (**EQC**) as part of the Environmental Quality Management Framework (**EQMF**) for the ongoing management of the **Murujuga region**, with a focus on air quality. The EQC will consist of guideline (early warning) and standard (limit) levels for all key air pollutants (DWER, 2020). This management and monitoring framework will ensure the long-term protection of the rock art from anthropogenic emissions.

Research undertaken over the past two years has been based on the peer-reviewed *Murujuga Rock Art Monitoring Program: Monitoring Studies Data Collection and Analysis Plan* (**MSDCA Plan**) (Curtin University, 2022). This current report builds on the progress reported in the year one technical report, released in December 2023 (Curtin University, 2023). This report is not intended to be a stand-alone document; rather it is intended to be read in conjunction with the suite of published Murujuga Rock Art Strategy documents, including the:

- *Murujuga Rock Art Strategy* (DWER, 2020),
- *Murujuga Rock Art Monitoring Program: Conceptual Model* (DWER, 2021),
- *Murujuga Rock Art Monitoring Program: Monitoring Studies Data Collection and Analysis Plan* (Curtin University, 2022).

Further reports will be produced as the research studies are completed and as the project transitions to ongoing monitoring against EQC.

Three fieldwork campaigns were undertaken during the second year of studies between April 2023 and March 2024 inclusive, with seven campaigns to date. The second year of fieldwork comprised 18 weeks' duration in total. Fieldwork included monitoring 54 rock art panels across the five rock types found in the study area. All fieldwork on Murujuga, including rock sample collection, is approved by the Murujuga Aboriginal Corporation (**MAC**) Elders. To date, over 66,000 spectral/colour measurements of rock art condition have been recorded, along with over 2,000 surface elemental measurements using x-ray fluorescence (**pXRF**), and 6,000 surface electrochemical measurements (*pH*, *Eh*, Cl^-).

The 64 sample rocks and additional microbial samples collected in 2022 have been subject to ongoing analysis of their microstructure, organic chemistry and geochemistry, the bulk of which is now well advanced. Results of geological/geochemical analyses are presented in this report, with much of the organic geochemistry, microbial and air quality studies ongoing, as well as more

extensive statistical data synthesis.

Air Quality

Operation of 18 solar/passive air quality and weather monitoring stations and four mains-powered air quality monitors (**AQM**s) is ongoing. Eighteen months of monitoring data from passive and deposition instruments and up to six months of data from reference-grade powered instruments were analysed. The passive air quality data have shown important spatial trends which broadly support previous air quality modelling and monitoring. The real-time instruments are providing data which exhibit interesting diurnal and spatial variation. Evidence for trends in these data will be investigated.

Air quality data supports spatial trends in previous modelling (Ramboll Australia, 2022) for most chemical species, albeit with average levels slightly lower than the modelled values. The notable exception is ammonia (NH_3), which appears to be emitted into the airshed at a higher rate than predicted. Ozone (O_3), a secondary air pollutant, has been observed at higher levels relative to the Ramboll model (Ramboll Australia, 2022). Interesting spatial and diurnal trends in nitrogen dioxide (NO_2) are emerging from real-time and scanning instrument data. Moderate levels of formaldehyde (CH_2O) have also been observed, which is an intermediate product in the decomposition of methane (CH_4). There is not yet any suggestion that the levels of these latter two air pollutant species are significant with respect to rock art, however, sufficiently high concentrations of CH_2O or O_3 at ground level could be expected to impact the microbiome. Relatively high levels of black carbon (soot) have also been observed. Again, this requires further investigation due to suggestions it may contribute to delamination. Some black carbon is due to natural sources such as bushfires, however the majority appears to be anthropogenic.

High-resolution spatial mapping coupled with computational fluid dynamics (**CFD**) simulations suggest that pollutants may be channeled or concentrated in geographic features such as gorges, which frequently contain a particularly high concentration of engravings. It has also been observed experimentally, and predicted using CFD models, that due to frequent high wind speeds and point source emissions, air pollutants will often remain concentrated in narrow plumes, thereby exposing a relatively small strip of land to higher emissions. CFD simulations have been adapted to incorporate micro-scale processes involving the porous surface layer under moderate-high humidity conditions. This aids in understanding how gases such as NO_2 may react directly with moist pores in rock under nominally dry conditions, as appears to be the case from the chamber studies.

pH measurements

Measurements of *pH* from inert surfaces such as the deposition samplers and rainfall samplers clearly show that wet and dry deposition over the past two years has generally been neutral or slightly alkaline. *pH* measurements on rock surfaces are more challenging to interpret, due to the relatively small contribution from the rock surface and complex interactions which may occur on the rock prior to and during measurement. There is also the challenge of isolating relative contributions from deposited matter or organic acids formed by the microbiome. Measurements on the surface of bushfire-exposed rocks showed a clear (alkaline) signal which reverted to baseline over 9–12 months post exposure. Another important consideration in rock *pH* measurement is the contribution of clay minerals (e.g. dust) which are expected to be alkaline, as well as (neutral) sea spray. It is likely that a more extensive dataset of rock *pH* measurements, combined with a more

detailed analysis of deposition sampler data, will allow useful conclusions to be drawn from the rock *pH* measurements.

Porosity and patina formation

The porosity of the weathered rind (subsurface layer) of granophyre rock surfaces was found to be higher in a region centered around Dampier and extending to the main industrial precincts, and lower elsewhere. This pattern may represent anthropogenic impact and further investigation is required. Given that previous industrial emissions in the region of highest porosity were two-to-three times higher in the past, it appears that historic emissions from the former Dampier Power Station are likely to be the major contributor to elevated porosity. However, it is not yet known if industrial emissions have contributed to patina formation or altered patina formation rates. These questions are under active investigation.

The chamber studies have demonstrated a mechanism by which air pollutant exposure could increase porosity. This has been confirmed chemically (through analysis of leachate) and physically (through high resolution imaging of minerals before and after exposure).

Preliminary analysis of the microbiome dataset and correlation with geochemical data suggests that *Geodermatophilus* species are more abundant where porosity is elevated, and that *Chroococcidiopsidaceae* are more abundant when porosity is lower. This requires further investigation to determine whether these correlations indicate a causal connection or arise from opportunistic colonisation with respect to porosity. Furthermore, this analysis also suggests that surface manganese (a key component in desert varnish) is lower where porosity is elevated.

Microstructural and geochemical analysis indicated that the development of pores and the formation of patina are complex processes. While the action of NO_2 and SO_2 contribute to these processes, the historic “acidification” or “acid rain” hypothesis from the literature (Bednarik, 2007; Smith et al., 2022) is not supported by the current studies. Data from the MRAMP rainfall and dust deposition samplers show that the environment of Murujuga tends towards slightly alkaline/basic. This is also consistent with the results of thermodynamic modelling data, although care must be taken with this interpretation because the modelling assumes thermodynamic equilibrium, which is unlikely to be reached in the natural environment.

Field colour measurements

Spectral imaging of rock art is now producing high quality results after considerable work to optimise the method and error detection. However, questions remain over the utility of high resolution spectrophotometry versus more simplified photogrammetric approaches for ongoing monitoring.

Interim EQC

The project has developed guideline Interim EQC for three key air pollutants and a standard Interim EQC for one air pollutant. This enables the commencement of monitoring and reporting against these Interim EQC as part of the transition to longer term monitoring by MAC and DWER.

A clear path forward to develop (and refine) EQC from field and chamber observations has been established. These data will also be integrated with separate experiments to investigate microbiome sensitivity to air pollutants. The contribution of the microbiome and organic acids to rock-surface

processes is an important consideration which is under investigation.

Further work

The remaining components of the *Murujuga Rock Art Monitoring Program: Monitoring Studies Data Collection and Analysis Plan* (Curtin University, 2022) continue to be progressed as planned. Given the findings on porosity and confirmation of the mechanisms in the chamber studies, some additions to the methodology have been approved:

- Collection of additional rock samples from islands or regions not in the current study design to confirm the porosity gradient over the entire range of relevant rock types.
- Evaluation of a field permeameter as a non-invasive field-appropriate surrogate for porosity measurement. Results are promising, however more field data are needed. If successful, this method could be added to the monitoring plan to monitor porosity change over time.
- More comprehensive characterisation of bulk dust samples, and exploration of the role of dust in the *pH* and thermodynamics of the system, and in moderating *pH* from acid-gas species.
- Comprehensive consideration of the utility of rock surface *pH* and the potential for it to be included or excluded from ongoing monitoring under the EQMF.
- Investigation of the correlation between porosity and the two key microbiome genera.

Work will also progress to further synthesise and understand the rich data collected to date and additional monitoring and laboratory data as it becomes available to the statistical team. The chamber studies will be continued and more sophisticated models developed to refine no observed effect concentration (**NOEC**) or lowest observed effect concentration (**LOEC**) levels and in turn EQC. Investigation of the impacts of peak air pollutant levels (both from chamber and field data) will be a focus of further work.

Many opportunities exist for increased integration and analysis of combined datasets. These opportunities will be explored in the next reporting period. The project is on track to achieve the outcomes of delivering an ECQ and embedded ongoing monitoring strategy.

Contents

Executive Summary **ii**

1 Introduction **1**
1.1 Background . . . 1
1.2 Objectives of the MRAMP monitoring studies . . . 1
1.3 Scope of this report . . . 2
1.3.1 Inclusions . . . 2
1.3.2 Exclusions . . . 3
1.4 Abbreviations and definitions . . . 3
1.4.1 Abbreviations . . . 3
1.4.2 Chemical notation . . . 8
1.4.3 Glossary . . . 9
1.4.4 Site and sample numbering nomenclature . . . 14

2 Study methodologies, verification of competency, and quality assurance **17**
2.1 Elaboration of methodologies described in the MSDCA plan . . . 17
2.2 Personnel and verification of competency . . . 17
2.3 Quality assurance . . . 18
2.3.1 Air quality monitoring . . . 18
2.3.2 Fieldwork . . . 18
2.3.3 Laboratory analysis . . . 19

3 Monitoring studies undertaken in the field **21**
3.1 Field monitoring generally . . . 21
3.1.1 Location of field monitoring sites . . . 21
3.1.2 Summary of year one and two field campaigns . . . 21
3.2 Inorganic geochemistry fieldwork . . . 23
3.2.1 Objectives . . . 23
3.2.2 Methodology . . . 23
3.2.3 Fieldwork progress . . . 24
3.3 Surface change analysis (spectroscopy) fieldwork . . . 29
3.3.1 Objectives . . . 29
3.3.2 Methodology . . . 29

4 Laboratory analysis of field samples **31**
4.1 Organic geochemistry laboratory analysis . . . 31
4.1.1 Objectives . . . 31
4.1.2 Methodology . . . 31
4.1.3 Summary of previous work in year one . . . 31
4.1.4 Bulk sample analysis . . . 33
4.1.5 Gas chromatography - mass spectrometry analysis (GC-MS) . . . 34
4.2 Geology and inorganic geochemistry laboratory analysis . . . 40
4.2.1 Objectives . . . 40

4.2.2 Methodology . . . 40
4.2.3 Geological mapping . . . 40
4.2.4 X-ray diffraction . . . 42
4.2.5 Macro to microstructural characterisation: fresher rock and weathered rind . . . 42
4.2.6 Geochemical characterisation: weathered rind . . . 89
4.2.7 Macro to microstructural characterisation: patina . . . 97
4.2.8 Chemistry of the patina . . . 115
4.2.9 Discussion . . . 142
4.2.10 Thermodynamic modelling . . . 153
4.3 Microbiome laboratory analysis . . . 175
4.3.1 Objectives . . . 175
4.3.2 Methodology . . . 175
4.3.3 Work to date . . . 176
4.4 Chamber exposure (accelerated degradation) testing . . . 177
4.4.1 Objectives . . . 177
4.4.2 Methodology . . . 178
4.4.3 Work to date . . . 178

5 Air quality monitoring network establishment and operation 179
5.1 Objectives . . . 179
5.2 Methodology . . . 179
5.3 Solar/passive sites . . . 179
5.4 Powered air quality monitoring sites . . . 180
5.5 Environmental challenges for AQM equipment operations . . . 182
5.6 Monitoring equipment calibration and data visualisation . . . 183

6 Spatial mapping and surface modelling 185
6.1 Objectives . . . 185
6.2 Spatial mapping . . . 185
6.2.1 Scope of mapping . . . 185
6.2.2 Methodology . . . 186
6.2.3 Global navigation satellite system (GNSS) datum point . . . 186
6.2.4 Local RTK control survey . . . 187
6.2.5 Drone image processing . . . 190
6.2.6 Summary and issues . . . 191
6.2.7 Completed site summaries . . . 194
6.3 Computational fluid dynamics modelling . . . 194
6.3.1 Objectives . . . 194
6.3.2 Methodology . . . 194
6.3.3 Study of AQ11 . . . 195
6.3.4 Study of AQ07 and AQ08 . . . 200
6.3.5 Further work . . . 203

7 Statistical analysis of data from each component study 205
7.1 Chamber studies . . . 205

7.1.1 Background . . . 205
7.1.2 Experimental method . . . 206
7.1.3 Experiments conducted . . . 208
7.1.4 Statistical approach . . . 209
7.1.5 Statistical analysis and discussion . . . 211
7.1.6 Further work . . . 224
7.1.7 Discussion . . . 224
7.2 Field colour measurements . . . 227
7.2.1 Field campaigns and colour measurement . . . 227
7.2.2 JAZ instrument . . . 227
7.2.3 HDX instrument . . . 230
7.2.4 Statistical methodology for analysing percent reflectance . . . 231
7.2.5 Laboratory colour measurements using JAZ instrument . . . 232
7.2.6 Laboratory colour measurements using HDX instrument . . . 236
7.2.7 Campaign 7 and HDX instrument problems . . . 242
7.2.8 Analysis of the field colour measurements using the JAZ instrument . 242
7.2.9 Analysis of the field colour measurements using the HDX instrument . 243
7.2.10 Comparison between JAZ and HDX instrument for campaign 7 . . . 247
7.3 Industry data . . . 251
7.4 Inorganic geochemistry – *pH*, *Eh*, Cl^- . . . 253
7.4.1 Background . . . 253
7.4.2 *pH* observations . . . 253
7.4.3 Chloride ion (Cl^-) observations . . . 259
7.4.4 Oxidation-reduction potential (*ORP*) observations . . . 262
7.4.5 Multivariate association between *pH*, *ORP* and Cl^- . . . 265
7.4.6 Influence of bushfire emissions on rock surface *pH* . . . 269
7.5 Inorganic geochemistry – pXRF . . . 271
7.5.1 Background . . . 271
7.5.2 Multivariate analysis . . . 271
7.5.3 Ratios of pairs of elements . . . 281
7.6 Inorganic geochemistry – porosity . . . 285
7.6.1 Background . . . 285
7.6.2 Image processing . . . 286
7.6.3 Porosity curves . . . 289
7.6.4 Porosity index . . . 289
7.6.5 Spatial variation in porosity . . . 292
7.6.6 Significance test of elevated porosity . . . 294
7.7 Inorganic geochemistry – permeameter . . . 297
7.7.1 Background . . . 297
7.7.2 Measurement method . . . 298
7.7.3 Validation of technique . . . 298
7.7.4 Permeability observations . . . 299
7.8 Microbiome . . . 303
7.8.1 Background . . . 303
7.8.2 Statistical methodology . . . 303

7.8.3 Analysis of bacteria . . . 304
7.8.4 Analysis of fungi . . . 307
7.9 Organic geochemistry . . . 311
7.9.1 Background . . . 311
7.9.2 Exploratory data analysis of TOC and δ^{13}C . . . 312
7.9.3 Spatial smoothing of TOC and δ^{13}C observations . . . 315
7.10 Deposition sampler data . . . 319
7.10.1 Background . . . 319
7.10.2 Exploratory analysis of dry deposition sampler data . . . 319
7.10.3 Analysis of co-located sites . . . 328
7.10.4 Spatial smoothing of deposition sampler data . . . 331
7.10.5 Rainfall *pH* . . . 343
7.11 Passive samplers . . . 345
7.11.1 Background . . . 345
7.11.2 Exploratory data analysis of passive sampler data . . . 345
7.11.3 Correlations between different gases . . . 352
7.11.4 Residual variability . . . 357
7.11.5 Short-scale variability . . . 363
7.11.6 Spatial pattern of gas concentration . . . 369
7.12 Real time powered sites . . . 377
7.12.1 Gaseous species . . . 377
7.12.2 Particulates . . . 385
7.12.3 Scanning instruments . . . 389
7.13 Key findings from statistical analysis . . . 399
7.13.1 Chamber studies . . . 399
7.13.2 Field measurement of colour . . . 399
7.13.3 Industry data . . . 400
7.13.4 Inorganic geochemistry — *pH*, *Eh*, Cl^- . . . 400
7.13.5 Inorganic chemistry – pXRF . . . 401
7.13.6 Inorganic geochemistry – porosity . . . 401
7.13.7 Inorganic geochemistry – permeameter . . . 401
7.13.8 Microbiome . . . 401
7.13.9 Organic geochemistry . . . 402
7.13.10 Deposition sampler data . . . 402
7.13.11 Passive samplers . . . 402
7.13.12 Real time powered sites . . . 403

8 Associations between variables 405
8.1 Deposition versus passive samplers . . . 405
8.1.1 Background . . . 405
8.1.2 Comparison of “dry” deposition with passive samplers . . . 405
8.2 Microbiome versus other variables . . . 411
8.2.1 Background . . . 411
8.2.2 Association between microbiome and rock composition . . . 411
8.2.3 Association between bacteria and inorganic compound concentrations 413

8.2.4 Association between bacteria and rock porosity . . . 414
8.2.5 Association between bacteria, inorganic compound concentrations and rock porosity . . . 415
8.3 Ramboll model versus passive sampler data . . . 419
8.3.1 Background . . . 419
8.3.2 Data extraction and processing . . . 419
8.3.3 Comparison to Ramboll gas predictions . . . 420
8.4 Porosity versus explanatory variables . . . 427
8.4.1 Background . . . 427
8.4.2 Porosity after accounting for height above terrain . . . 427
8.5 Passive sampler data from MRAMP study and from industry . . . 433
8.6 Key findings from statistical comparative analysis . . . 435
8.6.1 Deposition samplers vs passive samplers . . . 435
8.6.2 Microbiome vs other component studies . . . 435
8.6.3 Ramboll predictions vs passive sampler observations . . . 435
8.6.4 Porosity versus explanatory variables . . . 436
8.6.5 Industry data and MRAMP data from passive samplers . . . 436

9 General summary 439
9.1 Summary . . . 439
9.2 Further work . . . 440
9.3 Conclusion . . . 441

APPENDICES 443

***A* Organic geochemistry – additional tables and figures 443**

***B* Geology and inorganic geochemistry – additional tables and figures 451**

***C* Microbiome 489**
C.1 Bacterial 16S rRNA amplicon sequencing processing . . . 489
C.1.1 16S rRNA sequence quality reports . . . 489
C.1.2 16S rarefication . . . 490
C.2 Fungal ITS amplicon sequencing processing . . . 493
C.2.1 ITS sequence quality reports . . . 493
C.2.2 ITS rarefication . . . 497
C.2.3 ITS additional analysis . . . 498
C.3 Microbiome sample log . . . 499

***D* Spatial mapping and surface modelling 517**
D.1 Spatial mapping site summaries . . . 517
D.2 CFD modelling process . . . 624
D.3 Geometry, sources and locations . . . 624
D.4 Mesh creation . . . 624
D.5 Simulation set-up and running . . . 624
D.5.1 Source terms . . . 625

D.5.2 Boundary conditions . . . 625
D.5.3 Running the simulations . . . 626
D.6 Post-processing . . . 627
D.7 Validation . . . 627

***E* Estimation of major historic emissions (Dampier power station) 631**

***F* Statistical methodology 635**
F.1 Spatial smoothing . . . 635
F.1.1 Executive summary . . . 635
F.1.2 Qualitative description of smoothing . . . 636
F.1.3 Mathematical definition . . . 639
F.1.4 Modifications . . . 644
F.1.5 Spatially weighted median . . . 647
F.1.6 Concordance between smoothed images . . . 649
F.1.7 Software . . . 650
F.2 Porosity analysis . . . 654
F.2.1 Problem statement . . . 654
F.2.2 Definition of porosity . . . 656
F.2.3 Identification of macroscopic surface . . . 656
F.2.4 Depth . . . 659
F.2.5 Estimating porosity as a function of depth . . . 661
F.2.6 Summary indices of porosity . . . 664
F.3 Monte Carlo tests . . . 665
F.3.1 Principle . . . 665
F.3.2 Monte Carlo test of spatially constant mean . . . 665

***G* Statistical analysis: additional results 671**
G.1 Porosity data . . . 671
G.1.1 Example outcomes for different rock samples . . . 671
G.1.2 Effect of greyscale threshold . . . 674
G.1.3 Spatial variation in porosity . . . 682
G.2 Porosity and rock height: further results and diagnostics . . . 689
G.2.1 Assessing initial evidence for a relationship . . . 689
G.2.2 Linear modelling . . . 690
G.2.3 Generalised linear modelling . . . 691
G.2.4 Beta regression modelling . . . 691
G.2.5 Significance tests . . . 695
G.3 Faulty field colour data . . . 696
G.3.1 Faults in JAZ data . . . 696
G.3.2 Faults in HDX data . . . 700
G.4 IVL passive samplers: further results and diagnostics . . . 702
G.4.1 Passive samplers — concordance . . . 702
G.4.2 Correlations between different gases . . . 703
G.4.3 Residual variability . . . 706
G.4.4 Analysis of co-located sites . . . 712

G.5 Ramboll predictions: further results and diagnostics 713

***H* Micro-photogrammetry** **719**
H.1 Imaging method 1 719
H.2 Imaging method 2 723
H.3 Preliminary processing – focus stacking with Helicon Focus 725
H.4 Photogrammetric model generation with Agisoft Metashape 726
H.5 DSLR method 726
H.6 Smartphone method 726
H.7 3D model analysis 732
H.8 Rectified images 733
H.9 Condition survey database 734

***I* Transition to a second spectrometer** **738**

REFERENCES **741**

List of Figures

Figure *3.1-1*: Map of field monitoring sites 22
Figure *4.1-1*: Ternary diagram of short (*n*-C_{14}-*n*-C_{20}), mid (*n*-C_{21}-*n*-C_{26}) and long chain n-alkanes (*n*-C_{27}-*n*-C_{33}) by rock type. 34
Figure *4.1-2*: GC-MS total ion chromatograms (TIC) of the saturated fraction from rock surface sample RS09_DOL S#191 and AQ03_GPH, representative of samples analysed. Observed ions ranged from m/z 50 to m/z 550. The highly raised baseline in AQ03_GPH is due to a large unresolved complex mixture of hydrocarbons (UCM) compared to the only slightly typical raised baseline in RS09_DOL S#191. 35
Figure *4.1-3*: GC-MS chromatograms of saturated fraction. Extracted ion m/z 57 of sample RS09_DOL S#191 and AQ03_GPH. 36
Figure *4.1-4*: GC-MS chromatograms of saturated fraction. Extracted ion m/z 191 of sample RS09_DOL S#191 and AQ03_GPH. 37
Figure *4.1-5*: GC-MS total ion chromatograms (TIC) of the aromatic fraction from rock surface sample RS09_DOL S#191 and AQ03_PH, representative of samples analysed. Observed ions ranged from m/z 50 to m/z 550. Unresolved complex mixture (UCM). 39
Figure *4.2-1*: Core-to-rind cross-section photograph of granophyre rock billet AQ11_GPH. The transition from the fresher rock to the weathered rind domain is indicated by a progressive colour variation to pale orange due to the alteration of minerals present within the fresher rock. A reddish patina is visible as a rim on the outermost part of the profile and a darker patina is localised at the bottom of topographic depressions. 47
Figure *4.2-2*: Plane-polarised (a), crossed-polarised (b) and crossed-polarised with γ-plate (c) photomicrograph of fine-grained spinifex texture in sample AQ06_GPH. Plagioclase phenocrysts characterised by sericite alteration are surrounded by a groundmass of quartz and microcline. Pale green chlorite (a) is widespread in the matrix. 48
Figure *4.2-3*: Photomicrograph of a portion of granophyre sample AQ17_GPH fresher rock displaying chlorite (green), tabular epidote (pale green) and bright orange stilpnomelane characterised by the typical acicular texture. . . . 49
Figure *4.2-4*: Plane-polarised (a), crossed-polarised (b) and crossed-polarised with γ-plate (c) photomicrograph of radial texture in sample AQ13_GPH. Pale green chlorite (a) forms coronae around the felsic intergrowth. High birefringent epidote (b) is associated with chlorite in the matrix. 50
Figure *4.2-5*: Plane-polarised photomicrograph of granophyre fresher rock (a) and weathering rind (b) from sample AQ06_GPH. From (a) to (b) the image shows the colour transition to pale orange and brown of large phenocrysts of albite and green chlorite as a consequence of their alteration. 51
Figure *4.2-6*: TIMA-BSE image of patina on granophyre sample AQ14_GPH. The image shows the detachment and internal delamination of the patina from the poorly weathered substrate as a result of sample preparation. 52

Figure *4.2-7*: EBSD phase map of weathered rind-fresher rock transition in granophyre sample AQ08_GPH. Microporosity is generated by the progressive disappearance of plagioclase and microcline, moving from the fresher rock (bottom of the image) towards the surface. 53
Figure *4.2-8*: BSE-SEM large area panorama of the transition region between fresher rock-weathered rind-patina from sample AQ08_GPH. The weathered rind is characterised by enhanced microporosity and the alteration of minerals present within the fresher rock. The red box indicates the location in the image of the close-up inset. 54
Figure *4.2-9*: (a) plane-polarised photomicrograph and (b) BSE-SEM image of albite in the weathering rind of sample AQ06_GPH. In (b), insets (i) and (ii) are shown in Figure *4.2-10*. (c) BSE-SEM image of dissolved albite. (d) Close-up image of the area indicated with a red box in (c). Albite is characterised by edge pits and irregular dissolution boundaries. The original portion of the mineral is now replaced by aggregates of clays such as kaolinite, illite and muscovite. 55
Figure *4.2-10*: BSE-SEM image of altered chlorite (i) and altered ilmenite (ii) from Figure *4.2-9*. 56
Figure *4.2-11*: (a) plane-polarised photomicrograph (b) TIMA-BSE (c) TIMA phase map showing the most abundant phases, and (d) distribution of clays and precursor minerals, shown in the legend as rock forming minerals, for the same portion of sample AQ06_GPH, displaying the transition from fresher rock to weathered rind domain. In (b), the red colour shows the region of the sample with epoxy resin, highlighting the enhanced porosity of the domain. In (d), clay minerals correspond to browner colours shown in (a). Clays include phases identified at the TIMA such as muscovite/illite, K-alt-chlorite, kaolinite and patina. 57
Figure *4.2-12*: TIMA modal analysis of the 31 granophyre samples comparing the average abundances of (a) major and (b) minor minerals between the fresher rock and weathered rind domains. 58
Figure *4.2-13*: Core-to-rind cross-section photograph of gabbro rock billet AQ15_GBR. The transition from the fresher rock to the weathered rind domain is indicated by a variation from green to dark orange due to the progressive alteration of precursor minerals within the fresher rock. A dark red patina is visible rimming the outermost part of the profile. 59
Figure *4.2-14*: Plane-polarised (a) and crossed-polarised (b) images of fresher rock part of gabbro from AQ15 study area. Larger tabular grains of augite are distinguishable by their highly birefringent colours. Enstatite is altered and replaced by fine-grained chlorite. In (a) the dark patchy mineral is epidote which replaces prismatic labradorite crystals. 60
Figure *4.2-15*: BSE-SE images of gabbro microstructures. (a) crystal of augite characterised by crystallographically controlled pigeonite exsolution. (b) prismatic labradorite with visible asymmetrical zoning. (c) and (d) secondary dendritic epidote forming at the expenses of labradorite. 61

Figure *4.2-16*: Crystallographic analysis of pigeonite exsolutions in augite. (a) electron forescattered image, (b) EBSD phase map and (c) pole figures of augite indicating the alignment of pigeonite exsolution along the 001 planes. . 62
Figure *4.2-17*: Plane-polarised (a) and cross-polarised (b) photomicrograph of the region of transition between fresher rock and weathered rind in gabbro from study area AQ15. The colour variation in (a) reflects alteration of augite crystals to dark-red alteration minerals. 63
Figure *4.2-18*: BSE-SEM large area panorama of the transition region between fresher rock-weathered rind-patina from sample AQ15_GBR. The weathered rind is characterised by enhanced microporosity and the alteration of precursor minerals present within the fresher rock. The red box indicates the location in the image of the close-up inset. 64
Figure *4.2-19*: Large area EBSD phase map showing a region of transition between fresher rock and weathered rind of samples RS16_GBR. The map indicates that porosity is mostly attributed to the alteration and dissolution of augite crystals and to a minor extent labradorite. Phase boundaries are highlighted by a ubiquitous gap between the crystals. 65
Figure *4.2-20*: Grain scale microstructural analysis of gabbro. BSE-SE images of labradorite (a) and augite (b-c) show in detail the patterns of dissolution occurring in the two main rock-forming minerals. (c) is the red box indicated in (b) whereas (d) is a close-up image of the green box in (c). Augite dissolved primarily along pigeonite exsolutions. In (d), variations in BSE grey tones indicate a process of chemical alteration internal to the pigeonite lamellae. 66
Figure *4.2-21*: (a) plane-polarised photomicrograph (b) TIMA-BSE (c) TIMA phase map showing the most abundant phases, and (d) distribution of clays and precursor minerals, shown in the legend as rock forming minerals, for the same portion of sample AQ15_GBR, displaying the transition from fresher rock to weathered rind domain. In (b), the red colour shows the region of the sample with epoxy resin, highlighting the enhanced porosity of the domain. In (d), clay minerals correspond to browner colours shown in (a). Clays include phases identified at the TIMA such as muscovite/illite, K-alt-chlorite, kaolinite and patina. 67
Figure *4.2-22*: Summary of TIMA modal analysis of gabbro samples that compares the abundances of (a) major and (b) minor minerals between the fresher rock and weathered rind domains. 68
Figure *4.2-23*: Plane polarised (a) and crossed-polarised (b) photomicrographs of fresher granite. A large anhedral quartz grain dominates the image and is surrounded by a fine-grained groundmass of felsic minerals. 69
Figure *4.2-24*: Cross-polarised panorama image with γ-plate inserted of sample AS02_GRT. Myrmekite of quartz and microcline are visible surrounding larger crystals of quartz. 70
Figure *4.2-25*: Plane-polarised (a) and crossed-polarised (b) photomicrographs of the weathered rind in granite. Dark-brown clays form surrounding quartz phenocrysts. 70

Figure *4.2-26*: BSE-SEM large area panorama of the transition between fresher rock-weathered rind-patina from sample AQ07_GRT. The weathered rind is characterised by enhanced microporosity and the alteration of precursor minerals present within the fresher rock. Brighter rims of chlorite and Fe-oxides form rims surrounding quartz. The red box indicates the location in the image of the close-up inset. 71

Figure *4.2-27*: BSE-SEM images of granite microstructures. (a, b) myrmekitic intergrowth between quartz and microcline. In the micro-texture, the dissolution of microcline forms empty spaces between the minerals. (c) larger albite crystals displaying asymmetric regions of dissolution enhanced at the contact with the surface (top of the image). In (d), the advanced stage of rock-forming mineral dissolution has cancelled the original texture of the rock leaving behind a chaotic microporous texture. 72

Figure *4.2-28*: (a) plane-polarised photomicrograph (b) TIMA-BSE (c) TIMA phase map showing the most abundant phases, and (d) distribution of clays and precursor minerals, shown in the legend as rock forming minerals, for the same portion of sample AQ07_GRT, displaying the transition from fresher rock to weathered rind domain. In (b), the red colour shows the region of the sample with epoxy resin, highlighting the enhanced porosity of the domain. In (d), clay minerals correspond to browner colours shown in (a). Clays include phases identified at the TIMA such as muscovite/illite, K-alt-chlorite, kaolinite and patina. 73

Figure *4.2-29*: Summary of TIMA modal analysis of granite samples that compares the abundances of (a) major and (b) minor minerals between the fresher rock and weathered rind domains. 74

Figure *4.2-30*: Plane-polarised (a) and crossed-polarised (b) photomicrographs of dolerite fresher rock. Prismatic crystals of augite are visible and highlighted by high birefringent colours in (b). (c) BSE-SEM image of augite aggregates displaying the internal chemical zonation and (d) secondary epidote replacing labradorite of the rock. 76

Figure *4.2-31*: Plane-polarised (a) and crossed-polarised (b) photomicrograph of the transition from the weathered rind to the fresher rock in dolerite. Despite the bright illumination, the section is quite opaque due the presence of fine-grained Fe-oxides and clays. 77

Figure *4.2-32*: BSE-SEM large area panorama of the transition from fresher rock to weathered rind to patina from sample AS01_DOL. The weathered rind is characterised by enhanced microporosity and the alteration of minerals present within the fresher rock. The red box indicates the location in the image of the close-up inset. Augite is characterised by bright Fe-rich rims. 78

Figure *4.2-33*: Grain scale microstructural characterisation of dolerite. (a) BSE-SEM image of altered labradorite crystal at the contact with the surface. Clays occur along the phase boundaries. (b) BSE-SEM image of partially dissolved augite. The crystal is surrounded by chlorite and a groundmass of finer grained labradorite. The brighter material is Fe-rich clays or oxides. 79

Figure *4.2-34*: (a) plane-polarised photomicrograph (b) TIMA-BSE (c) TIMA phase map showing the most abundant phases, and (d) distribution of clays and precursor minerals, shown in the legend as rock forming minerals, for the same portion of sample AS01_DOL, displaying the transition from fresher rock to weathered rind domain. In (b), the red colour shows the region of the sample with epoxy resin, highlighting the enhanced porosity of the domain. In (d), clay minerals correspond to browner colours shown in (a). Clays include phases identified at the TIMA such as muscovite/illite, K-alt-chlorite, kaolinite and patina. 80

Figure *4.2-35*: Summary of TIMA modal analysis of dolerite samples comparing the abundances of (a) major and (b) minor minerals between the fresher rock and weathered rind domains. 81

Figure *4.2-36*: (a) Plane-polarised photomicrograph of basalt from study area RS09. The matrix of the rock is dominated by fine-grained crystals of plagioclase, which surrounds anhedral augite grains. (b) BSE-SEM image of basalt. 83

Figure *4.2-37*: Plane-polarised (a) and crossed-polarised (b) photomicrograph of the region of transition from the fresher rock to the weathered rind in basalt from study area RS09. The colour variation of the domain is attributed by a distinct alteration of augite. 83

Figure *4.2-38*: Large area BSE image of the transition from the fresher rock to the weathered rind in sample AQ12_BAS. The weathered rind is characterised by dissolution of augite and the formation of porosity. Brighter particles indicate the localised formation of Fe-oxides. 85

Figure *4.2-39*: BSE-SEM image indicating the dissolution of augite and, to a lesser extent, plagioclase. 86

Figure *4.2-40*: (a) plane-polarised photomicrograph (b) TIMA-BSE (c) TIMA phase map showing the most abundant phases, and (d) distribution of clays and precursor minerals, shown in the legend as rock forming minerals, for the same portion of sample RS09_BAS, displaying the transition from fresher rock to weathered rind domain. In (b), the red colour shows the region of the sample with epoxy resin, highlighting the enhanced porosity of the domain. In (d), clay minerals correspond to browner colours shown in (a). Clays include phases identified at the TIMA such as muscovite/illite, K-alt-chlorite, kaolinite and patina. 87

Figure *4.2-41*: Summary of TIMA modal analysis of basalt samples that compares the abundances of (a) major and (b) minor minerals between the fresher rock and weathered rind domains. 88

Figure *4.2-42*: Large area EDS-SEM map of the transition from fresher rock to the weathered rind and patina from sample AQ08_GPH. In the maps, brighter colours indicate enrichment in the mapped element. 90

Figure *4.2-43*: Plane polarised photomicrograph (a) and potassium element map (b) of a chlorite crystal located at the transition between the weathered rind and fresher rock in sample AQ06_GPH. The brown colouration coincides with a localised enrichment in potassium. (c) and (d) represent the plane polarised light micrograph and K element map of an albite crystal at the weathered rind-patina interface of sample AQ06_GPH. Similarly, the altered regions of the mineral are characterised by higher K concentrations due to the illitisation of albite. 92

Figure *4.2-44*: Comparative chemistry for (a) albite, (b) microcline and (c,d) chlorite in granophyre. The plots indicate the average wt% of the considered element oxide between fresher rock (FR) and weathered rind (WR). Aside from those in RS04_GPH, feldspars of the weathered rind display a common depletion in Na. Across the domains, chlorite is depleted in Mg and enriched in K. 93

Figure *4.2-45*: EDS-TIMA map of sample AQ15_GBR. The maps show that the microstructural transition from the fresher rock to the weathered rind is accompanied by a thin section scale chemical variation. Colour intensity increases with element concentration. 95

Figure *4.2-46*: SEM-EDS map of gabbro acquired over altered augite (central grain) and labradorite (surrounding grains). The distribution of Mg, Fe, Na and Al are heterogeneous. Localised enrichments in Na may represent albite or other Na-rich alteration phases. 96

Figure *4.2-47*: A comparison of the average wt% FeO in augite rims in the fresher rock and weathered rind. The weathered rind is Fe-depleted relative to the fresher rock. 97

Figure *4.2-48*: Macro length-scale characterisation of patina. Images (a) and (c) are of unpolished cut surfaces of rock billets showing cross sections through AQ11_GPH and AQ15_GBR, respectively. Images (b) and (d) are top views of the billets shown in cross-section in images (a) and (c). 99

Figure *4.2-49*: SE-SEM images of patina from unpolished billets of granophyre (a,b,d,e,f,g,h) and gabbro (c). Features are shown at higher resolution in subsequent images. 100

Figure *4.2-50*: BSE-SEM images of patina in cross-section. (a) patina fills topographic lows and superficial fractures in sample AQ08_GPH. (b) patina fills micropores between quartz crystals that were part of a granophyric texture. (c) a thin film of patina (bright rim, around 5 μm thick) wraps around the edge of a fractured quartz grain that protrudes from the surface of granite sample AS02_GRT. In (d) a thicker patina ($\sim$300 μm) is found in a topographic depression of sample AQ15_GBR. Note the sub-parallel layering of the patina in the near-surface layers and a bright rim of Fe-oxides at the contact with the substrate. 102

Figure *4.2-51*: BSE-SEM images showing the development of patina within a rock fracture (a) and as a hanging patina within the weathered rind of granite (b). Samples AS02_GRT and AQ07_GRT, respectively. 103

Figure *4.2-52*: BSE-SEM images of fine-layered patina on top of altered granophyric intergrowths of quartz and microcline. The internal fine layering is defined by variation in grayscale brightness. At the contact with the substrate, the patina extends into the micropores of the rock. Internally, micro-to-nanoscale bright particles are visible. 104

Figure *4.2-53*: BSE-SEM images of stromatolitic patina type within gabbro AQ15_GBR. In (a) the patina has developed above a skeletal grain of augite, and is characterised by a sequence of superposed dome-like structures. (b) is a close-up image of (a), and shows an abrupt transition from a stromatolitic morphology to a fine-layered morphology. The top portion of the patina is characterised by an increase of microscale bright particles and a BSE-bright rim. 106

Figure *4.2-54*: BSE-SEM images of the massive patina type in sample AQ11_GPH. In (a) the patina is characterised by a broad undulose BSE-bright structure. The close-up image in (b) shows the lack of internal layering within the fine-grained material. Bright particles are disseminated throughout the microdeposit. Voids, fractures and channels are also visible. The channels are highlighted by bright rims. 107

Figure *4.2-55*: BSE-SEM image of gravelly patina type on top of a weathered portion of granophyric texture from sample EX05_GPH. In the image, the degree of consolidation decreases towards the top of the sequence. The BSE brightness increases with average atomic number of the material analysed.108

Figure *4.2-56*: BSE-SEM images showing variability within rock coatings. Images are from granophyre sample EX05_GPH. In (a) P-rich concretions fill the pores within the granophyre. Example shown by yellow arrow. (b) Close-up image of the quartz grain boundaries highlighted by a thin film of a different BSE-brighter material, shown by the red square in (a). The EDS spectrum of this region (not shown) indicates that the film is enriched in Al, P, S, and Ca. The BSE brightness increases with average atomic number of the material analysed. 109

Figure *4.2-57*: BSE-SEM large area panorama map of a portion of patina from sample AQ13_GPH. The patina is developed within a topographic depression defined by granophyre microstructures, and “hanging” from the walls of a pore cavity within the weathered rind. Notably, the “hanging” patina is connected to the superficial patina by a thin channel. This patina shows fine-layered and stromatolitic patina types. 110

Figure *4.2-58*: BSE-SEM large area panorama image of a patina formed on a topographic low of sample AQ15_GBR. The patina is largely characterised by stromatolitic-type textures developing on top of an extensively altered gabbro weathered rind. The substrate is characterised by large relict pyroxene and labradorite crystals. 111

Figure *4.2-59*: BSE-SEM large area panorama image of patina from sample AS01_DOL. Within the topographic low, the patina displays stromatolitic structures. In the top region the patina shows a more massive texture. 112

Figure *4.2-60*: BSE-SEM large area panorama image of patina from sample AQ11_GPH. The patina develops on a topographic low on top of an altered granophyre with thicker portions in proximity of deeper depressions of the substrate. Internally, the structure is dominantly of the massive type. Patina is also found “hanging” from the walls of the depression. 113
Figure *4.2-61*: BSE-SEM large area panorama image of patina from sample AQ07_GRT.114
Figure *4.2-62*: Compositional characterisation of patina microstructures. Large area EDS-SEM map of part of the patina on sample AQ13_GPH shown in Figure *4.2-57*. The distributions of Al, Fe, Mn, K and P are heterogeneous. Mn is mostly enriched in the outermost layers of the patina and Al is enriched in the regions in contact with the substrate. 117
Figure *4.2-63*: Compositional characterisation of patina microstructures. Large area EDS-SEM map of part of the patina showed in Figure *4.2-60* of the microstructural section from sample AQ11_GPH. Chemical heterogeneities are mostly observed for Al, Fe and Mn. By far, Mn is the more variable highlighting composite complex structures. Fe is enriched at the structural extremes of the patina forming a thin outermost rim on top of the sequence. P is widespread within the weathered rind. 118
Figure *4.2-64*: Compositional characterisation of patina. Large area EDS-SEM map of the patina on sample AQ15_GBR shown in Figure *4.2-58*. Fe and Mn are strongly heterogeneous. Al, Mg, Fe and P show systematic changes in abundance, shown by the color intensity, from the top to the bottom of the patina. 120
Figure *4.2-65*: Compositional scatterplots of EMP data for selected patina traverses. Element concentrations are expressed in wt% of oxides. 121
Figure *4.2-66*: ToF-SIMS map showing the distribution of selected positive ions for sample AQ08_GPH. Colour scales relate to the number of counts and are not quantitative. The elements are represented by their positive ions.125
Figure *4.2-67*: ToF-SIMS map showing the distribution of selected positive ions for sample AQ11_GPH, highlighting the compositional complexity. Colour scales relate to the number of counts and are not quantitative. The elements are represented by their positive ions. 126
Figure *4.2-68*: ToF-SIMS map showing the distribution of selected positive ions for sample AQ10_GPH, highlighting the compositional complexity. Colour scales relate to the number of counts and are not quantitative. The elements are represented by their positive ions. 127
Figure *4.2-69*: ToF-SIMS map showing the distribution of selected negative ions for sample AQ08_GPH, highlighting the compositional complexity. Colour scales relate to the number of counts and are not quantitative. The elements are represented by their negative ions. 128
Figure *4.2-70*: ToF-SIMS map showing the distribution of selected negative ions for sample AQ11_GPH, highlighting the compositional complexity. Colour scales relate to the number of counts and are not quantitative. The elements are represented by their negative ions. High counts of Cl and F hot spots are attributed to the resin. 129

Figure *4.2-71*: ToF-SIMS map showing the distribution of selected negative ions for sample AQ10_GPH, highlighting the compositional complexity. Colour scales relate to the number of counts and are not quantitative. The elements are represented by their negative ions. High counts of Cl and F hot spots are attributed to the resin. 130

Figure *4.2-72*: TEM nanoscale images of albite. (a) Location within the albite crystal selected for analysis. Albite is the mid-grey mineral that occupies most of the field of view. (b) Region of TEM lift out, showing that the rim of the albite grain has a higher BSE brightness than the interior. (c) Bright Field TEM image of the albite foil. Here, the large bright portion of the foil represents resin. The curved lines similar to the one highlighted by a yellow arrow are interpreted as local bending or linear defects (e.g. dislocations) of the crystal lattice. 131

Figure *4.2-73*: TEM HAADF image and STEM compositional maps of selected elements. Al, and to a lesser extent Na, decrease in abundance towards the top of the grain. Na and Cl form colocated nanoclusters in the outermost part of the grain. 132

Figure *4.2-74*: TEM observations of the patina lamellae. (a) HAADF image of the whole foil and (b) STEM-EDS map showing an overlap of Si, K, Mn and Fe. (c), (d), (e) and (f) show nanoscale structures of the patina. In (c) the fine layering is formed by bands of lighter material containing elongated clasts of clays. (d) close up image of clays within the patina. The flaky character of the clays is also visible. (e) Bright Field TEM image of the top portion of the patina below the protective Pt layer. In bright field, holes appear white revealing porosity within the patina. (f) high resolution STEM-HAADF image of a clay particle surrounded by a film of brighter material. Dark nanometre-sized holes are visible within the brighter matrix.134

Figure *4.2-75*: STEM Dark Field and STEM-EDS maps. Mn-rich bands are enriched in Na, K, Ca, Ti, Pb, Cr and S and depleted in Fe, Si and Al relative to the patina matrix. Ti-bearing nanoparticles are also shown. 135

Figure *4.2-76*: SE-SEM images showing the APT sample preparation procedure. (a, b) location of APT targets at the bottom of sample AQ15_GPH and top of AQ11_GPH, respectively. Images (c, d and e) displays the steps of wedge lift out, welding and needle shaping. (d) shows wedge precursor of needle M1 from sample AQ11_GPH. (e) shows needle M4 from sample AQ11_GPH. 136

Figure *4.2-77*: 3D reconstructions of atom probe specimens for AQ15_GBR. Each dot in the reconstruction represents one detected charged species, which may be a mono-atomic ion or a molecular species, and which is assigned to a particular element (e.g. Na, H_2O). For simplicity, not all inferred atoms are displayed. (a) Specimen M10. Left panel shows superimposed Mn, Fe, K and Na. Right hand panel shows the distributions of these elements individually. The same colour scheme is used for both panels. (b) Specimen M9. Upper left hand panel shows Mn and Fe. Lower left hand panel shows K, Na, Ti, H_2O. Right hand panel shows Si and a surface of constant HxO concentration, in yellow, that highlights the regions of high HxO content. HxO refers to all OH-bearing species. . . 138

Figure *4.2-78*: 3D reconstructions of atom probe specimens for AQ11_GPH. Each dot in the reconstruction represents one detected charged species, which may be a mono-atomic ion or a molecular species, and which is assigned to a particular element (e.g. Na, H_2O). For simplicity, not all inferred atoms are displayed. The maps show tubular heterogeneities of Fe and Al. K forms a cluster on the upper left hand side of the needle, which is collocated with an Fe- and Al-depleted surface. 139

Figure *4.2-79*: BSE-SEM images of stromatolitic patina within sample AS01_DOL where (b) is a close-up image of the area indicated by red box in (a). Element maps for Mn, Fe, C, and P are of the region shown in (b). Mn, C, and P show increased enrichment in a sponge-like part of the stromatolitic structure that is depleted in Fe. It is possible to speculate that the sponge-like, C-rich parts of the image form part of a biotically-mediated structure. The brightest C signal is from a pore filled with epoxy resin. . 148

Figure *4.2-80*: SEM-BSE images showing areas where patina overlies highly porous weathered rind substrate. As porosity increases, the area of patina:weathered rind contact decreases and the probability of flaking increases. Note the grain-scale features and complex void–mineral interfaces that support mineral dissolution rather than void formation by mechanical preparation.152

Figure *4.2-81*: Schematic illustration of the thermodynamic models presented here. (a) Equilibration of patina with atmosphere-equilibrated solutions (simulation set one). (b) Equilibration of weathered rind and fresher rock with atmosphere- and patina-equilibrated solutions (simulation set 2). Colours match the colours of the lines for the relevant simulations on Figs. *4.2-82–4.2-87*.158

Figure *4.2-82*: Selected total solute concentrations for simulation set one as a function of NO_2 or SO_2 concentration. (a) *pH*; (b) pe; (c) Fe^{3+}; (d) Mn^{+2}; (e) Si; (f) K. Concentrations are in moles per kg of water. 163

Figure *4.2-83*: Selected changes in mineral modes for simulation set one as a function of NO_2 or SO_2 concentration. (a) illite; (b) kaolinite; (c) hematite; (d) birnessite. 164

Figure *4.2-84*: Selected saturation indices for simulation set one as a function of NO_2 or SO_2 concentration. (a) Fe-oxides in NO_2-bearing solutions; (b) Fe-oxides in SO_2-bearing solutions; (c) Fe-oxides in NO_2- and SO_2-bearing solutions; (d) Mn-oxides in NO_2-bearing solutions; (e) Mn-oxides in SO_2-bearing solutions; (f) Mn-oxides in NO_2- and SO_2-bearing solutions. 165
Figure *4.2-85*: Selected total solution concentrations for simulation set 2 as a function of NO_2 concentration for patinated and unpatinated weathered rind and fresher rock. (a) *pH*, granophyre; (b) Na, granophyre; (c) K, granophyre; (d) Si, granophyre; (e) *pH*, gabbro; (f) Na, gabbro; (g) K, gabbro; (h) Si, gabbro. Concentrations on the y-axis are presented as natural logs for panels b–h. N^{+5} refers to the total concentration of species that include N with a valence of +5. 166
Figure *4.2-86*: Selected changes in mineral modes for simulation set 2 as a function of NO_2 concentration for patinated and unpatinated weathered rind and fresher rock. (a) albite, granophyre; (b) K-feldspar, granophyre; (c) illite, granopyhre; (d) kaolinite, granophyre; (e) albite, gabbro; (f) diopsite, gabbro; (g) anorthite, gabbro; (h) kaolinite, gabbro. 167
Figure *4.2-87*: Selected mineral saturation indices for simulation set 2 as a function of NO_2 concentration for patinated and unpatinated weathered rind and fresher rock. (a) K-feldspar, granophyre; (b) quartz, granophyre; (c) Mg-montmorillonite, granophyre; (d) K-montmorillonite, granophyre; (a) K-feldspar, gabbro; (b) quartz, gabbro; (c) Mg-montmorillonite, gabbro; (d) K-montmorillonite, gabbro. 168
Figure *5.3-1*: Passive AQM AQ14, showing contrast between weathering steel and patinated rock outcrops in the background. 181
Figure *5.4-1*: Powered AQM EX09, as installed on Mount Wongama. 182
Figure *6.3-1*: Real-time readings from AQ11 for PM5. Thick solid line is the median/50^{th} percentile, thin solid lines are 25^{th}/75^{th} percentile, and dashed lines 10^{th}/90^{th} for the period of available data. Purple dots represent the known point emission sources, as included in the Murujuga Airshed report (Ramboll Australia, 2022). 196
Figure *6.3-2*: Sample domains and scans used for AQ11 study. 197
Figure *6.3-3*: AQ11 AQM measurement vs site exposure 198
Figure *6.3-4*: Ground level concentration of idealised PM10 scalar, for different wind directions. 199
Figure *6.3-5*: AQ11 gorge effect on flow 200
Figure *6.3-6*: Region around AQ07/AQ08 modelled by CFD 201
Figure *6.3-7*: Flow through the quarry at AQ07/AQ08 202
Figure *6.3-8*: Streamlines mapped bi-directionally through AQ07 and AQ08, for a southerly wind direction. 203
Figure *6.3-9*: Comparison between modelled wind at AQ07 and AQ08. 203
Figure *7.1-1*: Design of chamber experiments: Idealised concentration profile of gas/pollutant in chamber against elapsed time of experiment. Solid line shows a single dose experiment which may be re-dosed daily for up to six days (dashed lines). 207

Figure *7.1-2*: Measured exposure profiles for (a) NOx and (b) SO_2. The solid black line is the smoothed estimate of exposure; grey shading is the pointwise 95% confidence interval for the true exposure. 209
Figure *7.1-3*: Measured exposure profile for NH_3. 210
Figure *7.1-4*: Boxplots of normalised cumulative response (after minus before exposure) against average dose NO_x, (a) broken down by rock type, and (b) for all rock types combined. Blue curve: smoothed mean response. Grey shading: pointwise 95% confidence intervals. GPHF is fine granophyre and GPHC is coarse granophyre. 213
Figure *7.1-5*: Boxplots of cumulative response (after minus before exposure) against average dose SO_2, (a) broken down by rock type, and (b) for all rock types combined. The blue curve is the smoothed conditional mean; grey shading is pointwise 95% confidence interval. 214
Figure *7.1-6*: Boxplots of cumulative response (after minus before exposure) against average dose NO_x plus SO_2, (a) broken down by rock type, and (b) for all rock types combined. The blue curve is the smoothed conditional mean; grey shading is pointwise 95% confidence interval. 215
Figure *7.1-7*: (a) Boxplots of change in Ca+Mg+Na+K concentration after exposure to HFO, broken down by rock type, and (b) histogram of change in Ca+Mg+Na+K concentration after exposure to HFO. The average HFO is 7174.744 $\mu g/m^3$ NOx and 1898.46 $\mu g/m^3$ SO_2. 216
Figure *7.1-8*: Boxplots of change in *pH* (after minus before exposure) against average dose NO_x, (a) broken down by rock type, (b) for all rock types combined. The blue curve is the smoothed conditional mean; grey shading is pointwise 95% confidence interval. 218
Figure *7.1-9*: Boxplots of *pH* change (after minus before exposure) against average dose SO_2, (a) broken down by rock type, (b) for all rock types combined. The blue curve is the smoothed conditional mean; grey shading is pointwise 95% confidence interval. 219
Figure *7.1-10*: Boxplots of *pH* (after minus before exposure) against average dose NO_x plus SO_2. (a) broken down by rock type, and (b) for all rock types combined. The blue curve is the smoothed conditional mean; grey shading is pointwise 95% confidence interval. 220
Figure *7.1-11*: (a) Boxplots of *pH* (after minus before exposure) against average dose HFO, broken down by rock type, and (b) histogram of *pH* (after minus before exposure) for average dose HFO. The average HFO is 7174.744 $\mu g/m^3$ NOx and 1898.46 $\mu g/m^3$ SO_2. 221
Figure *7.1-12*: (a) Boxplots of change in Ca+Mg+Na+K concentration after exposure to ammonia NH_3 broken down by rock type, and (b) histogram of change in Ca+Mg+Na+K concentration after exposure to NH_3. The average dose of NH_3 is 314.752 $\mu g/m^3$. 222
Figure *7.1-13*: (a) Boxplots of *pH* (after minus before exposure) for average dose NH_3 broken down by rock type, and (b) histogram of *pH* (after minus before exposure) for average dose NH_3. The average dose of NH_3 is 314.752 $\mu g/m^3$. 223

Figure *7.1-14*: SE-SEM images of the same regions of a plagioclase crystal. The images are taken before and after a full cycle of chamber studies. The red and yellow arrows point to physical changes induced by chemical alteration. In (a) corrugated surfaces and irregular boundaries are indicative of chemical weathering. In (b) a cluster of clay minerals likely formed by previous hydrolysis of plagioclase is also found dissolving after the experiments. In (c) red arrows indicate physical changes within pyroxene after chamber exposures. 225
Figure *7.2-1*: Screenshot of the interactive software to test the JAZ instrument data in the field 229
Figure *7.2-2*: Screenshot of the interactive software to aid use of the HDX instrument in the field; where (a) initial setup of the HDX and (b) field colour measurements. 232
Figure *7.2-3*: JAZ Test 2: observed percent reflectance versus wavelength (nm), the probe was in incubator and the JAZ in ambient conditions. The JAZ was recalibrated after each set of 10 readings per temperature increment. 234
Figure *7.2-4*: JAZ Test 3: observed percent reflectance versus wavelength (nm), the probe and JAZ inside incubator for the whole experiment. The JAZ instrument was recalibrated after each set of 10 readings per temperature increment. 235
Figure *7.2-5*: HDX Test 1: observed percent reflectance versus wavelength (nm). The HDX placed outside the incubator, probe applied to black glossy tile inside the incubator; and HDX calibrated once at the start. The blue colour variation in the plots is due to the differing number of replicates at different temperatures. 237
Figure *7.2-6*: HDX Test 2: observed percent reflectance versus wavelength (nm). The probe, HDX and light source placed inside the incubator. HDX calibrated once at the start of the experiment. The blue colour variation in the plots is due to the differing number of replicates at different temperatures. . . 238
Figure *7.2-7*: HDX Test 3: observed percent reflectance versus wavelength (nm). The calibration thin film and the probe applied to black glossy tile in incubator for entire experiment; and the HDX calibrated after each temperature increment. The blue colour variation in the plots is due to the differing number of replicates at different temperatures. 239
Figure *7.2-8*: HDX Test 4: observed percent reflectance versus wavelength (nm). The probe applied to black glossy tile in incubator for entire experiment; calibration thin film in ambient temperature for entire experiment; and the HDX calibrated at each temperature increment. The blue colour variation in the plots is due to the differing number of replicates at different temperatures. 240
Figure *7.2-9*: Predicted percent reflectance vs wavelength (nm) for HDX Test 3. The left panel has a smooth curve for each replicate for each temperature; and right panel has a smooth curve for each temperature over all replicates. 241
Figure *7.2-10*: Predicted percent reflectance vs wavelength (nm) for (a) AQ03_GPH, (b) AQ11_GPH, (c) AQ12_BAS and (d) EX06_GPH, with a different colour for each campaign. 244

Figure *7.2-11*: Art panel AQ08_GPH observed percent reflectance versus wavelength (nm), where each panel is a target number. . . . 245
Figure *7.2-12*: Art panel AQ11_GPH observed percent reflectance versus wavelength (nm), where red were the morning measurements and teal the afternoon measurements, each panel is a target number. . . . 246
Figure *7.2-13*: Art panel AQ12_BAS predicted percent reflectance versus wavelength (nm), with a smooth curve for each campaign measured by the JAZ and HDX instruments. . . . 248
Figure *7.2-14*: Art panel RS10_GBR2 predicted percent reflectance versus wavelength (nm), with a smooth curve for each campaign measured by the JAZ and HDX instruments. . . . 249
Figure *7.3-1*: Woodside IVL passive sample data for five sites. The colours show the season while shapes show individual months. . . . 252
Figure *7.4-1*: Boxplots of *pH* by campaign. . . . 254
Figure *7.4-2*: Boxplots of *pH* by rock type for each campaign. . . . 255
Figure *7.4-3*: Boxplots of observed *pH* minus campaign median *pH*, by rock type for each campaign. . . . 256
Figure *7.4-4*: Spatially smoothed *pH* values of campaigns 1 to 7 in panels a) to g), respectively. Colour map overlaid with contour lines. Blue line represents Karratha coastline; grey polygon is Legendre Island. . . . 257
Figure *7.4-5*: Spatially smoothed observed *pH* minus campaign median *pH* of campaigns 1 to 7 in panels a) to g), respectively. . . . 258
Figure *7.4-6*: Boxplots of Cl^- concentration by campaign. Note logarithmic scale. ISA (Ionic Strength Adjuster). . . . 259
Figure *7.4-7*: Boxplots of Cl^- concentration by rock type for different campaigns. Note logarithmic scale. ISA (Ionic Strength Adjuster). . . . 260
Figure *7.4-8*: Spatially smoothed chloride ion (Cl^-) concentration of campaigns 2 to 4 (a,b,c), campaign 5 with and without ISA (d,e), and campaigns 6 and 7 (f,g). Colour map overlaid with contour lines. . . . 261
Figure *7.4-9*: Boxplots of *ORP* by campaign. . . . 262
Figure *7.4-10*: Boxplots of *ORP* by rock type for different campaigns. . . . 263
Figure *7.4-11*: Spatially smoothed *ORP* from data from campaigns 2 (a) to 7 (f), respectively. Colour map overlaid with contour lines. . . . 264
Figure *7.4-12*: Campaign 2 pairwise scatterplots between *pH*, *ORP* and logarithm of chloride concentration. Where the panels above the diagonal show the correlation between two variables; panels on the diagonal show the histogram of each variable; panels below the diagonal show a scatterplot between two variables. . . . 265
Figure *7.4-13*: Campaign 3 pairwise scatterplots between *pH*, *ORP* and log of chloride concentration. Where the panels above the diagonal show the correlation between two variables; panels on the diagonal show the histogram of each variable; panels below the diagonal show a scatterplot between two variables. . . . 266

Figure *7.4-14*: Campaign 4 pairwise scatterplots between *pH*, *ORP* and log of chloride concentration. Where the panels above the diagonal show the correlation between two variables; panels on the diagonal show the histogram of each variable; panels below the diagonal show a scatterplot between two variables. . . . 266
Figure *7.4-15*: Campaign 5 pairwise scatterplots between *pH*, *ORP* and log of chloride concentration (with ISA). Where the panels above the diagonal show the correlation between two variables; panels on the diagonal show the histogram of each variable; panels below the diagonal show a scatterplot between two variables. . . . 267
Figure *7.4-16*: Campaign 5 pairwise scatterplots between *pH*, *ORP* and log of chloride concentration (without ISA). Where the panels above the diagonal show the correlation between two variables; panels on the diagonal show the histogram of each variable; panels below the diagonal show a scatterplot between two variables. . . . 267
Figure *7.4-17*: Campaign 6 pairwise scatterplots between *pH*, *ORP* and log of chloride concentration. Where the panels above the diagonal show the correlation between two variables; panels on the diagonal show the histogram of each variable; panels below the diagonal show a scatterplot between two variables. . . . 268
Figure *7.4-18*: Campaign 7 pairwise scatterplots between *pH*, *ORP* and log of chloride concentration. Where the panels above the diagonal show the correlation between two variables; panels on the diagonal show the histogram of each variable; panels below the diagonal show a scatterplot between two variables. . . . 268
Figure *7.4-19*: Boxplot of rock surface *pH* in bushfire exposed samples (red inset), shown with campaign 1-7 *pH* for comparison. . . . 269
Figure *7.5-1*: RDA biplot showing the relationship between chemical elements from the pXRF and rock types in campaign 1. Percentage in parentheses is the percentage of total variation explained by the RDA. . . . 273
Figure *7.5-2*: RDA biplot showing the relationship between pXRF chemical elements and rock types in campaign 2. . . . 274
Figure *7.5-3*: RDA biplot showing the relationship between pXRF chemical elements and rock types in campaign 3. . . . 275
Figure *7.5-4*: RDA biplot showing the relationship between pXRF chemical elements and rock types in campaign 4. . . . 276
Figure *7.5-5*: RDA biplot showing the relationship between pXRF chemical elements and rock types in campaign 5. . . . 277
Figure *7.5-6*: RDA biplot showing the relationship between pXRF chemical elements and rock types in campaign 6. . . . 278
Figure *7.5-7*: RDA biplot showing the relationship between pXRF chemical elements and rock types in campaign 7. . . . 279
Figure *7.5-8*: RDA biplot showing the relationship between pXRF chemical elements, rock types and the seven campaigns. . . . 280
Figure *7.5-9*: Boxplots of SiO_2:Ti by campaign. Note logarithmic scale. . . . 282

Figure *7.5-10*: Boxplots of SiO_2:Ti ratio by campaign after winsorization. Note logarithmic scale. . . . 283
Figure *7.5-11*: Spatial smoothing of SiO_2:Ti ratio in granophyre (GPH) of campaigns 1 (a) to 7 (g), respectively. The white colour polygons are the islands with zero granophyre samples. . . . 284
Figure *7.6-1*: Scanning electron microscope, back-scattered electron image of a thin section of granophyre sample from site AQ03. Surface at the top of image. The physical size of the image is about 10 mm wide by 7.5 mm high. Black area at top is exterior. Smaller, dark areas within sample are voids: one void is labelled in the figure. . . . 285
Figure *7.6-2*: Binary image obtained by thresholding the granophyre AQ03 image in Figure *7.6-1*. Binary value one (white) interpreted as rock; binary value zero (black) interpreted as void space. . . . 287
Figure *7.6-3*: Distance transform. (a) binary image; (b) distance transform of “top”. Granophyre from site AQ03, field four of four. . . . 288
Figure *7.6-4*: Estimation of porosity as a function of depth. (a) grey scale backscattered electron image microscope from Scanning electron microscope. (b) smoothed estimate of porosity as a function of depth. Granophyre, site AQ03, field 3 of 4. Porosity values are fractions between zero and one. 289
Figure *7.6-5*: Histogram of values of average porosity index for 99 granophyre rock samples at sites across Murujuga. Blue curve shows fitted gamma distribution. . . . 291
Figure *7.6-6*: Average porosity index of granophyre rock samples at sites across Murujuga. Perspective view showing porosity index values as vertical spikes. . . . 292
Figure *7.6-7*: Mean estimated porosity at each sample location. Perspective view showing mean porosity value at each location as a vertical spike. . . . 293
Figure *7.6-8*: Spatially smoothed (Nadaraya-Watson) average porosity (for depths from 0 to 3.1 mm) for morphological opening radius = 20 μm. . . . 293
Figure *7.6-9*: Results of pointwise Monte Carlo test of the null hypothesis of uniform porosity against the alternative of locally elevated porosity: (a) p-value of the test at each spatial location; (b) orange colour identifies locations where the test is statistically significant. . . . 295
Figure *7.7-1*: TinyPerm 3 and the Android device (NER website) . . . 297
Figure *7.7-2*: Boxplots of permeability measurements taken from eight sites before and after wet geochemistry sampling was conducted. Note logarithmic scale. . . . 299
Figure *7.7-3*: Histogram of 30 and 60 second permeability measurements at site EX06_GPH. Note logarithmic scale. . . . 300
Figure *7.7-4*: Permeability measurements for each rock type. Note logarithmic scale. 300
Figure *7.7-5*: Permeability measurements for all sites and the dolerite standard. Note logarithmic scale. . . . 301
Figure *7.7-6*: a) Spatial point data and b) spatial smoothing plots of winsorized permeability measurements, for granophyre. . . . 302

Figure *7.8-1*: Relative abundance of the 16S rRNA amplicon data grouped by sample type. Patina samples are grouped by which rock type they were sampled from. (a) relative abundance at Phylum level. (b) relative abundance at Genus level. Note that ”Unclas” is ”unclassified”. 304
Figure *7.8-2*: Spatially smoothed relative abundance (%) of selected taxa. 305
Figure *7.8-3*: Shannon diversity index of patina samples grouped by rock type, season and area. 306
Figure *7.8-4*: (a) NMDS ordination based on Bray-Curtis dissimilarity matrix of all samples grouped by sample type. (b) NMDS ordination based on Bray-Curtis dissimilarity matrix of patina samples grouped by rock type. 307
Figure *7.8-5*: Relative abundance of the ITS amplicon data grouped by sample type. Patina samples are grouped by rock type. (a) relative abundance at Phylum level. (b) relative abundance at Genus level. Note that ”Unclas” is ”unclassified”. 308
Figure *7.8-6*: Fungal ITS Shannon diversity index of patina samples grouped by rock type, season and area. 309
Figure *7.8-7*: NMDS ordination based on Bray-Curtis dissimilarity matrix of all samples grouped by sample type, stress = 0.20. 309
Figure *7.9-1*: Histograms of total organic carbon (TOC) and stable carbon isotopes (δ^{13}C) based on 64 observations. 312
Figure *7.9-2*: Boxplots of a) total organic carbon (TOC) and b) stable carbon isotope (δ^{13}C) for different rock types. Note logarithmic scale of TOC. 313
Figure *7.9-3*: Boxplots of (a) total organic carbon (TOC) and (b) stable carbon isotope (δ^{13}C) for different sites. Note logarithmic scale of TOC. 314
Figure *7.9-4*: Scatterplot of total organic carbon (TOC) against stable isotope ratio (δ^{13}C). Logarithmic scale for TOC. Pearson sample correlation coefficient 0.36. 315
Figure *7.9-5*: a) spatial plot of sampled TOC values at each site and b) spatially smoothed average TOC (logarithmic colour scale). 316
Figure *7.9-6*: a) spatial plot of sampled stable isotope (δ^{13}C) at each site and b) spatially smoothed average δ^{13}C. 317
Figure *7.10-1*: Boxplots of *pH* for the dry deposition samples by different sampling periods.320
Figure *7.10-2*: Boxplots of *pH* for the dry deposition samples by different sampling sites.320
Figure *7.10-3*: Boxplots of Ca^{2+}, K^{+}, and Mg^{2+} deposition rates for the dry deposition samples by different sampling periods. Note logarithmic scale. 321
Figure *7.10-4*: Boxplots of Ca^{2+}, K^{+}, and Mg^{2+} deposition rates for the dry deposition samples by different sampling sites. Note logarithmic scale. 322
Figure *7.10-5*: Boxplots of Cl^{-}, Na^{+}, and $SO_4{}^{2-}$ deposition rates for the dry deposition samples by different sampling periods. Note logarithmic scale. 323
Figure *7.10-6*: Boxplots of Cl^{-}, Na^{+}, and $SO_4{}^{2-}$ deposition rates by different sampling sites. Note logarithmic scale. 323
Figure *7.10-7*: Boxplots of $NH_4{}^{+}$, $NO_3{}^{-}$, and P deposition rates for the dry deposition samples by different sampling periods. Note logarithmic scale. 324
Figure *7.10-8*: Boxplots of $NH_4{}^{+}$, $NO_3{}^{-}$, and P deposition rates for the dry deposition samples by different sampling sites. Note logarithmic scale. 324

Figure *7.10-9*: Average *pH* and deposition rates by AQM. Data represent approximately 18 months of observation (8/02/2023 to 25/03/2024) except for EX02, EX09 and AQ01 (indicated by grey dots) where less than 12 months of data are available. . . . 326
Figure *7.10-10*: Median *pH* and deposition rates by AQM. Data from 8/02/2023 to 25/03/2024 that is approximately 18 months, apart from EX02 and EX09 and AQ01 where less than 12 months of data are available (grey points). . . . 327
Figure *7.10-11*: Boxplots of deposition rates of chemical species from dry deposition samples of co-located AQ07 and AQ08 sites. Note logarithmic scale. . 328
Figure *7.10-12*: Scatterplots of the AQ07 vs AQ08 values, for each chemical species. The black line is $y = x$. . . . 329
Figure *7.10-13*: Time series plots of deposition rates of chemical species, from dry deposition samples at co-located AQ07 and AQ08 sites, against collection date. Note logarithmic scale. Points were jittered to avoid overlap. . . . 331
Figure *7.10-14*: Spatially smoothed average *pH* for the dry deposition samples by different sampling periods. The blue line represents the Karratha coastline. The grey polygon is Legendre Island. . . . 333
Figure *7.10-15*: Spatially smoothed average Ca^{2+} deposition rate for the dry deposition samples by different sampling periods. . . . 334
Figure *7.10-16*: Spatially smoothed average K^{+} deposition rate for the dry deposition samples by different sampling periods. . . . 335
Figure *7.10-17*: Spatially smoothed average Mg^{2+} deposition rate for the dry deposition samples by different sampling periods. . . . 336
Figure *7.10-18*: Spatially smoothed average Na^{+} deposition rate for the dry deposition samples by different sampling periods. . . . 337
Figure *7.10-19*: Spatially smoothed average Cl^{-} deposition rate for the dry deposition samples by different sampling periods. . . . 338
Figure *7.10-20*: Spatially smoothed average $SO_4{}^{2-}$ deposition rate for the dry deposition samples by different sampling periods. . . . 339
Figure *7.10-21*: Spatially smoothed average $NH_4{}^{+}$ deposition rate for the dry deposition samples by different sampling periods. . . . 340
Figure *7.10-22*: Spatially smoothed average $NO_3{}^{-}$ deposition rate for the dry deposition samples by different sampling periods. . . . 341
Figure *7.10-23*: Spatially smoothed average P deposition rate for the dry deposition samples by different sampling periods. . . . 342
Figure *7.10-24*: Boxplots of *pH* by Dry, Wet, and Mist deposition samples (H_2O is distilled water). . . . 343
Figure *7.10-25*: Historical measurements of rainfall *pH* plotted against year of observation. The red dots are digitised from Bednarik (2007). Boxplots show recent data from Greg Skrypek, UWA. . . . 344
Figure *7.11-1*: Histograms of IVL sampler gas concentration observations across all stations and months. Separate gases are shown for each panel: (a) NO_2, (b) NH_3, (c) O_3, (d) SO_2 and (e) HNO_3. Panels (d) and (e) use logarithmic scale on horizontal axis. . . . 346

Figure *7.11-2*: Histograms of IVL sampler VOC measurements each VOC species. Panels: (a) benzene, (b) toluene, (c) n-octane, (d) ethylbenzene, (e) m-p-xylene, (f) o-xylene, and (g) n-nonane. Panels (c), (d), (e), and (f) use logarithmic scale on horizontal axis. 347
Figure *7.11-3*: Plots of IVL sampler gas concentration estimates against air quality station identifier, labelled by season (colour) and month (shape). Separate gases are shown for each panel: (a) NO_2, (b) NH_3, (c) O_3, (d) SO_2 and (e) HNO_3. In each panel, stations are ordered by their overall average concentration of NO_2. Note that panels (d) and (e) use logarithmic scales, due to the highly skewed distributions of the data for these plots. 349
Figure *7.11-4*: Plots of IVL sampler VOC measurements against air quality station for each VOC species, labelled by season (colour) and month (shape). AQM stations are ordered by increasing average NO_2 concentration. Panels: (a) benzene, (b) toluene, (c) n-octane, (d) ethylbenzene, (e) m-p-xylene, (f) o-xylene, and (g) n-nonane. Panels (c), (d), (e), and (f) are plotted on logarithmic scales. 351
Figure *7.11-5*: RDA biplot showing the relationship between gas measurements (NO_2, SO_2, NH_3, HNO_3, O_3) and month sin and cos. 356
Figure *7.11-6*: Paired variance versus paired mean for gas species (a) NO_2, (b) NH_3, (c) O_3, and (d) HNO_3. Where for example 1e-06 means 10^{-6}, or 0.000001.359
Figure *7.11-7*: SO_2 paired residual variance estimates against paired means (top) and paired residual variance by station and month (bottom). Right panels show stations by colour, while left panels show months by colour. Logarithmic scale is used for both mean and variance. 360
Figure *7.11-8*: Pairwise variance by pairwise mean for VOC species (a) benzene, (b) toluene, (c) n-octane, and (d) ethylbenzene. 361
Figure *7.11-9*: Pairwise variance by pairwise mean for VOC species (a) m-p-xylene, (b) o-xylene, and (c) n-nonane. 362
Figure *7.11-10*: Boxplots of passive sampler gas concentration measurements for stations AQ07 and AQ08 for gas species (a) NO_2, (b) NH_3, (c) O_3, (d) SO_2, and (e) HNO_3. 364
Figure *7.11-11*: Scatterplots of monthly sample mean gas concentration for station AQ07 versus station AQ08 for gas species (a) NO_2, (b) NH_3, (c) O_3, (d) SO_2, and HNO_3. Plots show the sample mean gas concentration for each sample period for each station. 365
Figure *7.11-12*: Boxplots comparing VOC measurements between stations AQ07 and AQ08 using a logarithmic scale for VOC species (a) benzene, (b) toluene, (c) n-octane, (d) ethylbenzene, (a) m-p-xylene, (b) o-xylene, and (c) n-nonane. 367
Figure *7.11-13*: Scatterplot of sample mean VOC concentration for station AQ07 versus station AQ08 using a logarithmic scale for VOC species (a) benzene, (b) toluene, (c) n-octane, (d) ethylbenzene, (a) m-p-xylene, (b) o-xylene, and (c) n-nonane. Plots show the sample mean gas concentration for each sample period. 368

Figure *7.11-14*: Spatially smoothed monthly average concentration of NO_2 by sampling period. Common colour map based on percentiles. 370
Figure *7.11-15*: Assessment of concordance between spatial patterns of NO_2 concentration in different months, estimated from spatially smoothed passive sampler data. (a) consensus ranks; (b) disagreement (standard deviation). . . . 371
Figure *7.11-16*: Spatially smoothed monthly average concentration of NH_3 by sampling period. Common colour map based on percentiles. 372
Figure *7.11-17*: Spatially smoothed monthly average concentration of O_3 by sampling period. Common colour map based on percentiles. 373
Figure *7.11-18*: Spatially smoothed monthly average concentration of SO_2 by sampling period. Common colour map based on percentiles. 374
Figure *7.11-19*: Spatially smoothed monthly average concentration of HNO_3 by sampling period. Common colour map based on percentiles. 375
Figure *7.12-1*: Time series plots for SO_2 concentration to date, for sites (a) AQ01, (b) EX02, (c) EX07 and (d) EX09. Data have been excluded where the validity is in question. 379
Figure *7.12-2*: Time series plots for SO_2 concentration over one week in February 2024, at sites (a) AQ01, (b) EX02 and (c) EX09. 380
Figure *7.12-3*: Time series plots for NO to date, where (a) AQ01, (b) EX02, (c) EX07 and (d) EX09. Data have been excluded where the validity is in question.381
Figure *7.12-4*: Time series data for NO_2, where (a) AQ01, (b) EX02, (c) EX07 and (d) EX09. Data have been excluded where the validity is in question. . . . 382
Figure *7.12-5*: Time series data for NH_3 for (a) AQ01, (b) EX02 and (c) EX07. Data have been excluded where the validity is in question. 383
Figure *7.12-6*: Time series plots for O_3 at (a) AQ01, (b) EX02, (c) EX07 and (d) EX09. 384
Figure *7.12-7*: Time series plot of $PM_{2.5}$ at EX07 since instrument commissioning. Data have been excluded where the validity is in question. 386
Figure *7.12-8*: Time series plot of PM_{10} at EX07 since instrument commissioning. Data have been excluded where the validity is in question. 387
Figure *7.12-9*: Time series plot of total suspended particulates (TSP) at EX07 since instrument commissioning. Data have been excluded where the validity is in question. 388
Figure *7.12-10*: Time series plot of black carbon (BC) and biomass-derived black carbon (BB) from Aethalometer instrument. Observations from September to October 2023 were obtained during initial startup and commissioning at the MAC office. Data from late November 2023 onward were obtained at the EX09 Mt Wongama site. 390
Figure *7.12-11*: Time series plot of CO_2 from Picarro instrument at EX09 since instrument commissioning. 392
Figure *7.12-12*: Time series plot of CH_4 from Picarro instrument at EX09 since instrument commissioning. 393
Figure *7.12-13*: Time series plot of C_2H_6 from Picarro instrument at EX09 since instrument commissioning. 394

Figure *7.12-14*: Differential slant column densities (dSCDs) from MAX-DOAS at 1° and 10° elevation angle. Note that the NO_2 and CH_2O have been divided by 10^{15} (one thousand trillion) to simplify the tick marks on the y-axis. . . . 396
Figure *7.12-15*: Differential slant column densities (dSCDs) from MAX-DOAS at 0° (W) and 180° (E). Note that the NO_2 and CH_2O have been divided by 10^{15} (one thousand trillion) to simplify the tick marks on the y-axis. 397
Figure *8.1-1*: Simplified 2D boxplots of dry bucket SO_4^{2-} and passive sampler SO_2 from each AQ and EX site. The points are the median SO_4^{2-} and the median SO_2, and the horizontal and vertical lines are are approximately 95% confidence intervals for the means. Note logarithmic scale in both axes. Data between May 2023 and December 2023. 407
Figure *8.1-2*: Simplified 2D boxplots of dry bucket NO_3^- and passive samples NO_2 from each AQ and EX site. The points are the median NO_3^- and the median NO_2, and the horizontal and vertical lines are approximately 95% confidence intervals for the means. Note logarithmic scale in both axes. Data between May 2023 and December 2023. 408
Figure *8.1-3*: Simplified 2D boxplot of dry bucket NH_4^+ and passive sampler NH_3 from each AQ and EX site. The points are the median NH_4^+ and the median NH_3, and the horizontal and vertical lines are approximately 95% confidence intervals for the means. Note logarithmic scale in both axes. Data between May 2023 and December 2023. 409
Figure *8.2-1*: Heatmap display of Spearman rank correlation between the pXRF elemental composition data and the abundance of the top 50 genera across patina samples. 412
Figure *8.2-2*: Heatmap display of Spearman rank correlation of the environmental data with the abundance of Fungi Genera across patina samples. 413
Figure *8.2-3*: RDA biplot showing the relationship between bacteria taxa, inorganic compound concentrations, porosity indices and site information. Percentage in parentheses is the percentage of total variation explained by the RDA. 416
Figure *8.3-1*: Gas concentrations measured by passive IVL samplers, and mean and maximum monthly Ramboll predictions, by station for each gas. Gases shown are (a) SO_2, (b) NO_2, (c) NH_3, (d) HNO_3 and (e) O_3. 421
Figure *8.3-2*: Passive IVL samplers by mean Ramboll predictions, coloured by month for each gas. Gases shown are (a) SO_2, (b) NO_2, (c) NH_3, (d) HNO_3 and (e) O_3. 422
Figure *8.3-3*: Passive IVL samplers by mean Ramboll predictions, coloured by AQM station for each gas. Gases shown are (a) SO_2, (b) NO_2, (c) NH_3, (d) HNO_3 and (e) O_3. 423
Figure *8.3-4*: Passive IVL samplers and mean Ramboll predictions averaged across all sample periods by station for each gas and overall maximum Ramboll prediction. Gases shown are (a) SO_2, (b) NO_2, (c) NH_3, (d) HNO_3 and (e) O_3. 425
Figure *8.3-5*: Passive IVL samplers by mean Ramboll predictions averaged across all sample periods by station for each gas. Gases shown are (a) SO_2, (b) NO_2, (c) NH_3, (d) HNO_3 and (e) O_3. 426

Figure *8.4-1*: Regression model for porosity index as a function of rock height above terrain. (a) observed average porosity ($+$) and predicted porosity (black line) versus rock height. Grey shading is pointwise 95% confidence interval for true relationship. (b) raw residuals ($\times$) versus rock height. Porosity index is average porosity at depths 0 to 1.3 mm, opening radius 20 μm. 429
Figure *8.4-2*: Spatial plot of raw residuals from the beta regression of porosity against rock height. 430
Figure *8.4-3*: Spatially smoothed average raw residual from the beta regression model of porosity against rock height. 431
Figure *8.4-4*: Pointwise Monte Carlo test of constant mean residual against a two-sided alternative. Beta regression of Porosity versus rock height. (a) p values for the pointwise test. (b) locations where the pointwise test result is statistically significant. 432
Figure *A-1*: Total lipid extract (TLE, mg) and saturated, aromatic and polar fraction (%) of rock surface samples. 444
Figure *A-2*: GC-MS total ion chromatograms (TIC) of the saturated fraction. Comparing rock surface sample RS01_GPH with fresher rock sample FR_RS01_GPH. Observed ions ranged from m/z 50 to m/z 550. Unresolved complex mixture (UCM). 445
Figure *A-3*: GC-MS total ion chromatograms (TIC) of saturated fraction. Comparing rock surface sample RS08_DOL, mixed samples RS08_DOL PI and PII with fresher rock sample FR_RS08_DOL. Observed ions ranged from m/z 50 to m/z 550. Unresolved complex mixture (UCM). 446
Figure *B-1*: SEM–EDS element distribution map of the region of the sample between the patina (top layer) and weathered rind (bottom layer) of sample AQ11_GPH, chemical heterogeneities are mostly observed for Al, Fe, Mn and P. Of these, Mn is by far the most variable, highlighting composite complex structures. Fe is enriched at the structural extremes of the patina forming a thin outermost rim on top of the sequence. P is widespread within the weathered rind. 451
Figure *B-2*: SEM-EDS element distribution map of the region of the sample between the patina (top) and weathered rind (bottom) of sample AQ15_GBR. In the image, Fe and Mn are strongly heterogeneous. Al, Mg, Fe and P show systematic changes in abundance from the top to the bottom of the patina. In the Fe map, higher concentrations highlight the framework of a ghost pyroxene crystal. In the patina, Co and P are also present. . . 452
Figure *B-3*: Microstructural-compositional link between stromatolitic patina and the Mn-Ba concentration relationship. Left panel shows BSE-SEM image of stromatolitic patina occurring in a portion of sample AQ15_GBR. Right panel shows the EMP concentration of MnO versus BaO along a bottom to top profile across the botryoidal structure. The graph indicates that higher concentrations of MnO coincide with high values of BaO. Concentration values are expressed in wt%. 453

Figure *B-4*: Microstructural-compositional link between patina and immediate substrate in sample AQ15_GBR. The profile across the BSE-SEM image of the patina obtained by EMP (left panel) indicates the variation in concentration of SiO_2, Al_2O_3 and MgO as a function of the position in the patina (right panel). Notably, there is a trend of depletion moving away from the weathered rind for the considered elements. Concentration values are expressed in wt% oxides. 453
Figure *B-5*: (top) BSE-SEM image of albite rims within sample EX03_GPH investigated by TEM. (bottom) SEM-EDS line analysis across the albite rim indicated in the image. The brighter rim of the grain in BSE coincides with an increase in C and a depletion in Si and Al. A faint depletion in Na is also visible. 454
Figure *C.1-1*: MultiQC report of the raw 16S rRNA V3–V4 forward sequences. 489
Figure *C.1-2*: MultiQC report of the raw 16S rRNA V3–V4 reverse sequences. 489
Figure *C.1-3*: MultiQC report of the trimmed 16S rRNA V3-V4 forward sequences. . . 490
Figure *C.1-4*: MultiQC report of the trimmed 16S rRNA V3-V4 reverse sequences. . . 490
Figure *C.1-5*: Post rarefication of the 16S rRNA samples to 11,000 reads per sample. 491
Figure *C.1-6*: Bacterial 16S alpha diversity grouped by sample type. a) Shannon diversity. b) Simpson diversity. c) ASVs observed 492
Figure *C.1-7*: Bacterial 16S NMDS ordination of patina samples, stress value 0.15. a) NMDS coloured based on rock type the patina was sampled from. b) NMDS coloured based on area the patina was sampled from. 492
Figure *C.2-1*: MultiQC report of the raw ITS forward sequences. 493
Figure *C.2-2*: MultiQC report of the raw ITS reverse sequences. 494
Figure *C.2-3*: MultiQC report of the trimmed ITS forward sequences. 495
Figure *C.2-4*: MultiQC report of the trimmed ITS reverse sequences. 496
Figure *C.2-5*: Post rarefication of the ITS samples to 10,000 reads per sample. . . . 497
Figure *C.2-6*: Fungal ITS alpha diversity grouped by sample type. a) Shannon diversity. b) Simpson diversity. c) ASVs observed 498
Figure *C.2-7*: Fungal ITS NMDS ordination of patina samples, stress value 0.21. a) NMDS coloured based on rock type the patina was sampled from. b) NMDS coloured based on area the patina was sampled from. 498
Figure *D.1-1*: Position uncertainties for AQ02: Top view (XY plane), side view (ZY plane) and front view (XZ plane) displays of all tie points, with colours representing uncertainty in the individual point position. The values are in metres, with a minimum uncertainty of 0.0051 metres and a maximum of 0.6867 metres. The median position uncertainty equals 0.0335 metres. 520
Figure *D.1-2*: Ortho-mosaic for AQ02. Plotted with control points and 100 x 100 m grid spacing. 521
Figure *D.1-3*: DEM for AQ02. Plotted with 100 x 100 m grid spacing. 521
Figure *D.1-4*: Position uncertainties for AQ03: Top view (XY plane), side view (ZY plane) and front view (XZ plane) displays of all tie points, with colours representing uncertainty in the individual point position. The values are in metres, with a minimum uncertainty of 0.0051 metres and a maximum of 0.6867 metres. The median position uncertainty equals 0.0335 metres. 524

Figure *D.1-5*: Ortho-mosaic for AQ03. Plotted with control points and 100 x 100 m grid spacing. 524
Figure *D.1-6*: DEM for AQ03. Plotted with 100 x 100 m grid spacing. 525
Figure *D.1-7*: Position uncertainties for AQ04: Top view (XY plane), side view (ZY plane) and front view (XZ plane) displays of all tie points, with colours representing uncertainty in the individual point position. The values are in metres, with a minimum uncertainty of 0.0051 metres and a maximum of 0.6867 metres. The median position uncertainty equals 0.0335 metres. 528
Figure *D.1-8*: Ortho-mosaic for AQ04. Plotted with control points and 100 x 100 m grid spacing. 529
Figure *D.1-9*: DEM for AQ04. Plotted with 100 x 100 m grid spacing. 529
Figure *D.1-10*: Position uncertainties for AQ05: Top view (XY plane), side view (ZY plane) and front view (XZ plane) displays of all tie points, with colours representing uncertainty in the individual point position. The values are in metres, with a minimum uncertainty of 0.0051 metres and a maximum of 0.6867 metres. The median position uncertainty equals 0.0335 metres. 532
Figure *D.1-11*: Ortho-mosaic for AQ05. Plotted with control points and 100 x 100 m grid spacing. 533
Figure *D.1-12*: DEM for AQ05. Plotted with 100 x 100 m grid spacing. 533
Figure *D.1-13*: Position uncertainties for AQ06: Top view (XY plane), side view (ZY plane) and front view (XZ plane) displays of all tie points, with colours representing uncertainty in the individual point position. The values are in metres, with a minimum uncertainty of 0.0051 metres and a maximum of 0.6867 metres. The median position uncertainty equals 0.0335 metres. 536
Figure *D.1-14*: Ortho-mosaic for AQ06. Plotted with control points and 100 x 100 m grid spacing. 537
Figure *D.1-15*: DEM for AQ06. Plotted with 100 x 100 m grid spacing. 537
Figure *D.1-16*: Position uncertainties for AQ07 and AQ08: Top view (XY plane), side view (ZY plane) and front view (XZ plane) displays of all tie points, with colours representing uncertainty in the individual point position. The values are in metres, with a minimum uncertainty of 0.0051 metres and a maximum of 0.6867 metres. The median position uncertainty equals 0.0335 metres. 540
Figure *D.1-17*: Ortho-mosaic for AQ07 and AQ08. Plotted with control points and 100 x 100 m grid spacing. 541
Figure *D.1-18*: DEM for AQ07 and AQ08. Plotted with 100 x 100 m grid spacing. . . . 541
Figure *D.1-19*: Position uncertainties for AQ09 (North): Top view (XY plane), side view (ZY plane) and front view (XZ plane) displays of all tie points, with colours representing uncertainty in the individual point position. The values are in metres, with a minimum uncertainty of 0.0051 metres and a maximum of 0.6867 metres. The median position uncertainty equals 0.0335 metres. 544
Figure *D.1-20*: Ortho-mosaic for AQ09 (North). Plotted with control points and 100 x 100 m grid spacing. 545
Figure *D.1-21*: DEM for AQ09 (North). Plotted with 100 x 100 m grid spacing. 545

Figure *D.1-22*: Position uncertainties for AQ09 (South): Top view (XY plane), side view (ZY plane) and front view (XZ plane) displays of all tie points, with colours representing uncertainty in the individual point position. The values are in metres, with a minimum uncertainty of 0.0051 metres and a maximum of 0.6867 metres. The median position uncertainty equals 0.0335 metres. 548
Figure *D.1-23*: Ortho-mosaic for AQ09 (South). Plotted with control points and 100 x 100 m grid spacing. 549
Figure *D.1-24*: DEM for AQ09 (South). Plotted with 100 x 100 m grid spacing. 549
Figure *D.1-25*: Position uncertainties for AQ10: Top view (XY plane), side view (ZY plane) and front view (XZ plane) displays of all tie points, with colours representing uncertainty in the individual point position. The values are in metres, with a minimum uncertainty of 0.0051 metres and a maximum of 0.6867 metres. The median position uncertainty equals 0.0335 metres. 552
Figure *D.1-26*: Ortho-mosaic for AQ10. Plotted with control points and 100 x 100 m grid spacing. 553
Figure *D.1-27*: DEM for AQ10. Plotted with 100 x 100 m grid spacing. 553
Figure *D.1-28*: Position uncertainties for AQ11: Top view (XY plane), side view (ZY plane) and front view (XZ plane) displays of all tie points, with colours representing uncertainty in the individual point position. The values are in metres, with a minimum uncertainty of 0.0051 metres and a maximum of 0.6867 metres. The median position uncertainty equals 0.0335 metres. 556
Figure *D.1-29*: Ortho-mosaic for AQ11. Plotted with control points and 100 x 100 m grid spacing. 557
Figure *D.1-30*: DEM for AQ11. Plotted with 100 x 100 m grid spacing. 557
Figure *D.1-31*: Position uncertainties for AQ12: Top view (XY plane), side view (ZY plane) and front view (XZ plane) displays of all tie points, with colours representing uncertainty in the individual point position. The values are in metres, with a minimum uncertainty of 0.0051 metres and a maximum of 0.6867 metres. The median position uncertainty equals 0.0335 metres. 560
Figure *D.1-32*: Ortho-mosaic for AQ12. Plotted with control points and 100 x 100 m grid spacing. 561
Figure *D.1-33*: DEM for AQ12. Plotted with 100 x 100 m grid spacing. 561
Figure *D.1-34*: Position uncertainties for AQ13: Top view (XY plane), side view (ZY plane) and front view (XZ plane) displays of all tie points, with colours representing uncertainty in the individual point position. The values are in metres, with a minimum uncertainty of 0.0051 metres and a maximum of 0.6867 metres. The median position uncertainty equals 0.0335 metres. 563
Figure *D.1-35*: Ortho-mosaic for AQ13. Plotted with control points and 100 x 100 m grid spacing. 565
Figure *D.1-36*: DEM for AQ13. Plotted with 100 x 100 m grid spacing. 565
Figure *D.1-37*: Position uncertainties for AQ14: Top view (XY plane), side view (ZY plane) and front view (XZ plane) displays of all tie points, with colours representing uncertainty in the individual point position. The values are in metres, with a minimum uncertainty of 0.0051 metres and a maximum of 0.6867 metres. The median position uncertainty equals 0.0335 metres. 568

Figure *D.1-38*: Ortho-mosaic for AQ14. Plotted with control points and 100 x 100 m grid spacing. 569
Figure *D.1-39*: DEM for AQ14. Plotted with 100 x 100 m grid spacing. 569
Figure *D.1-40*: Position uncertainties for AQ15 (Southwest): Top view (XY plane), side view (ZY plane) and front view (XZ plane) displays of all tie points, with colours representing uncertainty in the individual point position. The values are in metres, with a minimum uncertainty of 0.0051 metres and a maximum of 0.6867 metres. The median position uncertainty equals 0.0335 metres. 572
Figure *D.1-41*: Ortho-mosaic for AQ15 (Southwest). Plotted with control points and 100 x 100 m grid spacing. 573
Figure *D.1-42*: DEM for AQ15 (Southwest). Plotted with 100 x 100 m grid spacing. . . 573
Figure *D.1-43*: Position uncertainties for AQ15 and AQ16: Top view (XY plane), side view (ZY plane) and front view (XZ plane) displays of all tie points, with colours representing uncertainty in the individual point position. The values are in metres, with a minimum uncertainty of 0.0051 metres and a maximum of 0.6867 metres. The median position uncertainty equals 0.0335 metres. 577
Figure *D.1-44*: Ortho-mosaic for AQ15 and AQ16. Plotted with control points and 100 x 100 m grid spacing. 578
Figure *D.1-45*: DEM for AQ15 and AQ16. Plotted with 100 x 100 m grid spacing. . . . 578
Figure *D.1-46*: Position uncertainties for AQ17: Top view (XY plane), side view (ZY plane) and front view (XZ plane) displays of all tie points, with colours representing uncertainty in the individual point position. The values are in metres, with a minimum uncertainty of 0.0051 metres and a maximum of 0.6867 metres. The median position uncertainty equals 0.0335 metres. 581
Figure *D.1-47*: Ortho-mosaic for AQ17. Plotted with control points and 100 x 100 m grid spacing. 582
Figure *D.1-48*: DEM for AQ17. Plotted with 100 x 100 m grid spacing. 582
Figure *D.1-49*: Position uncertainties for AQ18: Top view (XY plane), side view (ZY plane) and front view (XZ plane) displays of all tie points, with colours representing uncertainty in the individual point position. The values are in metres, with a minimum uncertainty of 0.0047 metres and a maximum of 0.6218 metres. The median position uncertainty equals 0.0414 metres. 585
Figure *D.1-50*: Ortho-mosaic for AQ18. Plotted with control points and 100 x 100 m grid spacing. 586
Figure *D.1-51*: DEM for AQ18. Plotted with 100 x 100 m grid spacing. 586
Figure *D.1-52*: Position uncertainties for EX02 (Northeast): Top view (XY plane), side view (ZY plane) and front view (XZ plane) displays of all tie points, with colours representing uncertainty in the individual point position. The values are in metres, with a minimum uncertainty of 0.0051 metres and a maximum of 0.6867 metres. The median position uncertainty equals 0.0335 metres. 589
Figure *D.1-53*: Ortho-mosaic for EX02 (Northeast). Plotted with control points and 100 x 100 m grid spacing. 590

Figure *D.1-54*: DEM for EX02 (Northeast). Plotted with 100 x 100 m grid spacing. . . . 590
Figure *D.1-55*: Position uncertainties for EX02 (Southwest): Top view (XY plane), side view (ZY plane) and front view (XZ plane) displays of all tie points, with colours representing uncertainty in the individual point position. The values are in metres, with a minimum uncertainty of 0.0051 metres and a maximum of 0.6867 metres. The median position uncertainty equals 0.0335 metres. 592
Figure *D.1-56*: Ortho-mosaic for EX02 (Southwest). Plotted with control points and 100 x 100 m grid spacing. 594
Figure *D.1-57*: DEM for EX02 (Southwest). Plotted with 100 x 100 m grid spacing. . . 594
Figure *D.1-58*: Position uncertainties for EX03: Top view (XY plane), side view (ZY plane) and front view (XZ plane) displays of all tie points, with colours representing uncertainty in the individual point position. The values are in metres, with a minimum uncertainty of 0.0051 metres and a maximum of 0.6867 metres. The median position uncertainty equals 0.0335 metres. 596
Figure *D.1-59*: Ortho-mosaic for EX03. Plotted with control points and 100 x 100 m grid spacing. 598
Figure *D.1-60*: DEM for EX03. Plotted with 100 x 100 m grid spacing. 598
Figure *D.1-61*: Position uncertainties for EX04: Top view (XY plane), side view (ZY plane) and front view (XZ plane) displays of all tie points, with colours representing uncertainty in the individual point position. The values are in metres, with a minimum uncertainty of 0.0051 metres and a maximum of 0.6867 metres. The median position uncertainty equals 0.0335 metres. 601
Figure *D.1-62*: Ortho-mosaic for EX04. Plotted with control points and 100 x 100 m grid spacing. 602
Figure *D.1-63*: DEM for EX04. Plotted with 100 x 100 m grid spacing. 602
Figure *D.1-64*: Position uncertainties for EX05: Top view (XY plane), side view (ZY plane) and front view (XZ plane) displays of all tie points, with colours representing uncertainty in the individual point position. The values are in metres, with a minimum uncertainty of 0.0051 metres and a maximum of 0.6867 metres. The median position uncertainty equals 0.0335 metres. 605
Figure *D.1-65*: Ortho-mosaic for EX05. Plotted with control points and 100 x 100 m grid spacing. 606
Figure *D.1-66*: DEM for EX05. Plotted with 100 x 100 m grid spacing. 606
Figure *D.1-67*: Position uncertainties for EX06: Top view (XY plane), side view (ZY plane) and front view (XZ plane) displays of all tie points, with colours representing uncertainty in the individual point position. The values are in metres, with a minimum uncertainty of 0.0051 metres and a maximum of 0.6867 metres. The median position uncertainty equals 0.0335 metres. 609
Figure *D.1-68*: Ortho-mosaic for EX06. Plotted with control points and 100 x 100 m grid spacing. 609
Figure *D.1-69*: DEM for EX06. Plotted with 100 x 100 m grid spacing. 610

Figure *D.1-70*: Position uncertainties for EX07: Top view (XY plane), side view (ZY plane) and front view (XZ plane) displays of all tie points, with colours representing uncertainty in the individual point position. The values are in metres, with a minimum uncertainty of 0.0051 metres and a maximum of 0.6867 metres. The median position uncertainty equals 0.0335 metres. 613
Figure *D.1-71*: Ortho-mosaic for EX07. Plotted with control points and 100 x 100 m grid spacing. 614
Figure *D.1-72*: DEM for EX07. Plotted with 100 x 100 m grid spacing. 614
Figure *D.1-73*: Position uncertainties for EX08: Top view (XY plane), side view (ZY plane) and front view (XZ plane) displays of all tie points, with colours representing uncertainty in the individual point position. The values are in metres, with a minimum uncertainty of 0.0051 metres and a maximum of 0.6867 metres. The median position uncertainty equals 0.0335 metres. 616
Figure *D.1-74*: Ortho-mosaic for EX08. Plotted with control points and 100 x 100 m grid spacing. 618
Figure *D.1-75*: DEM for EX08. Plotted with 100 x 100 m grid spacing. 618
Figure *D.1-76*: Position uncertainties for EX09: Top view (XY plane), side view (ZY plane) and front view (XZ plane) displays of all tie points, with colours representing uncertainty in the individual point position. The values are in metres, with a minimum uncertainty of 0.0051 metres and a maximum of 0.6867 metres. The median position uncertainty equals 0.0335 metres. 622
Figure *D.1-77*: Ortho-mosaic for EX09. Plotted with control points and 100 x 100 m grid spacing. 623
Figure *D.1-78*: DEM for EX09. Plotted with 100 x 100 m grid spacing. 623
Figure *D.5-1*: Typical residual history for CFD simulation. 626
Figure *D.7-1*: Comparison of plume trajectories CFD and experiments of Chu and Goldberg (1974). 628
Figure *D.7-2*: Comparison of plume trajectories CFD and experiments of Fan (1967). 628
Figure *D.7-3*: Comparison of plume trajectories CFD and experiments of Slawson and Csanady (1971). 629
Figure *E-1*: Timeline of the Dampier power plant complex, categorised according to fuel type. 631
Figure *E-2*: Estimation of the NO_x emission rate out of the Dampier power plant complex: (a) Yearly emission rates, classified based on fuel usage; (b) maximum values of the NO_x emission rate using the 100% utilisation and growth models (mean values are indicated by black horizontal lines), compared against the Ramboll 2014 and 2030 models. 633
Figure *E-3*: Estimation of the SO_2 emission rate out of the Dampier power plant complex (see Figure *E-2* for details on captions). 634
Figure *F.1-1*: Spatial smoothing: (a) input data consisting of observations at scattered locations in space; (b) output colour image obtained by spatially smoothing the observations. Colour ribbon shows the representation of numerical values as colours, used in both panels. 635
Figure *F.1-2*: Spatial data: values of a variable observed at scattered locations. . . . 636

Figure *F.1-3*: Spatial smoothing by averaging within cells: (a) the spatial domain divided into a 5×5 grid of cells; (b) average values in each square. 637

Figure *F.1-4*: Spatial smoothing using a moving disc of fixed radius. Panels (a) and (b) show different positions of the disc centre. Panel (c) shows the result of smoothing. 637

Figure *F.1-5*: Effect of smoothing bandwidth. Spatial smoothing with Gaussian kernel, with bandwidth (a) $\sigma =$1 metre, (b) σ = 5 metres and (c) σ = 20 metres. Spatial domain is 200 metres wide. 638

Figure *F.1-6*: *Left:* observed versus predicted values. *Right:* leave-one-out residuals versus predicted values. 641

Figure *F.1-7*: Leave-one-out residuals plotted at their spatial locations 642

Figure *F.1-8*: Mean of squared residuals, as a function of smoothing bandwidth σ, for the data of Figure *F.1-2*. Optimal bandwidth value $\sigma =$5.46 metres indicated by dotted line. 643

Figure *F.1-9*: Logarithmic smoothing: (a) ratio of iron (Fe) to silica (SiO2) assayed by pXRF instrument on 123 rocks at 41 sites across Murujuga. Values are displayed on a logarithmic scale; (b) spatially smoothed ratio, displayed on logarithmic scale. 645

Figure *F.1-10*: Smoothing using the probability integral transformation. (a) ratio of iron (Fe) to silica (SiO2) assayed by pXRF instrument on 123 rocks at 41 sites across Murujuga. Values are displayed on the probability scale; (b) spatially smoothed ratio, displayed on probability scale. 646

Figure *F.1-11*: Spatially weighted median with bandwidth $\sigma = 5$. 648

Figure *F.1-12*: Spatially smoothed monthly average concentration of NO_2 by sampling period. Common colour map based on percentiles. 649

Figure *F.1-13*: Fractional rank of smoothed NO_2 concentration, for each month. 651

Figure *F.1-14*: Consensus rank for smoothed NO_2 concentration. 652

Figure *F.1-15*: Rank disagreement image for smoothed NO_2 concentration. 653

Figure *F.2-1*: Scanning electron microscope, backscattered electron image of thin section of sample rock - granophyre from site AQ03. Surface at top of image. Physical size of image is about 10 mm wide by 7.5 mm deep, image cut into four to provide multiple samples. 654

Figure *F.2-2*: Binary image obtained by thresholding Figure *F.2-1*. Binary value one (white) interpreted as rock; binary value zero (black) interpreted as void space. 655

Figure *F.2-3*: Connected component transform for granophyre from site AQ03, field 4 of 4: (a) binary input image (white = rock, black = void). (b) connected component transform of void. Each connected component of the void space is labelled by a different integer value. The integer values are graphically depicted as colours. 656

Figure *F.2-4*: Connected component transform applied to openings of different sizes for granophyre rock sample, site AQ09, field 4 of 4. (a) binary input image, opened by 10 μm, (b) connected component transform of void in (a). (c) binary input image, opened by 40 μm. (d) connected component transform of void in (c). Colours represent different connected sets (colours are repeated as needed). 658
Figure *F.2-5*: Distance transform. (a) binary image; (b) distance transform of "top". Granophyre, site AQ03, field 4 of 4. 660
Figure *F.2-6*: Illustrative example data for estimation of porosity curve. Indicator of void (one = void, zero = rock) is plotted against distance from rock surface, for a small sample of 50 pixels. 662
Figure *F.2-7*: Estimates of porosity calculated as the average void fraction in each band of distances, for the illustrative example in Figure *F.2-6*. 662
Figure *F.2-8*: Spline smoothing estimate of porosity as a function of depth, for the illustrative example in Figure *F.2-6*. 663
Figure *F.2-9*: Estimation of porosity as a function of depth. (a) grey scale back scattered electron image, scanning electron microscope. (b) smoothed estimate of porosity as a function of depth. Granophyre, site AQ03, field 3 of 4. . . 663
Figure *F.3-1*: Example data: values of porosity index obtained from rock samples at sites across Murujuga. 666
Figure *F.3-2*: Spatially smoothed (Nadaraya-Watson) porosity. 666
Figure *F.3-3*: Pointwise Monte Carlo p-values for the one-sided test of constant mean against the alternative of elevated local mean. Colour map for p-values is logarithmic. 667
Figure *F.3-4*: Orange colour indicates locations where a pointwise Monte Carlo test would reject the null hypothesis of constant mean against the alternative of elevated mean. 668
Figure *F.3-5*: Global test of uniformity. Histogram of test statistic values for the simulated data. Test statistic value for the observed data is shown as the red line. 669
Figure *G.1-1*: Back scattered electron images from scanning electron microscopy of thin sections from three different granophyre rock samples. Sample images from left to right, top to bottom are: (a) AQ08 cropped image 3, (b) AQ06 cropped image 2, and (c) AQ09 cropped image 4. 672
Figure *G.1-2*: Porosity curves for the three granophyre rock samples shown in Figure *G.1-1*. Curves computed using automatically selected bandwidth and without using morphological opening. Curves from left to right are for (a) AQ08 cropped image 3, (b) AQ06 cropped image 2, and (c) AQ09 cropped image 4 respectively. 673
Figure *G.1-3*: Estimated porosity curve for granophyre rock sample in panel (c) of *G.1-1*, , using morphological opening with radius 25 μm, and automatically-selected smoothing bandwidth. 674
Figure *G.1-4*: Backscattered electron image from scanning electron microscope of thin section from gabbro rock sample, site AQ08. This sample was used for initial threshold testing. 675

Figure *G.1-5*: Porosity curves for gabbro rock sample from site AQ08 (cropped image 1), showing the effects of different greyscale intensity thresholds. Thresholds (left to right) are: (a) 0.01, (b) 0.02, (c) 0.05, (d) 0.1, (e) 0.2, and (f) 0.5. 675

Figure *G.1-6*: Backscattered electron image from scanning electron microscope of thin sections from two gabbro rock sample images: (a) RS10 cropped image 3 (gabbro), and (b) AQ03 cropped image one (gabbro). 676

Figure *G.1-7*: Porosity curves computed from two sample images using different greyscale thresholds. Top and bottom rows are for the sample images (a) and (b) respectively in Figure *G.1-6*. Left column (a) and (d) uses threshold 0.02; middle column (b) and (e) uses threshold 0.05; right column (c) and (f) uses threshold 0.1. 677

Figure *G.1-8*: Porosity curves showing the effects of different bandwidths and morphological opening radii for sample image (b) in Figure *G.1-6*. The top row (panels (a)–(c)) has bandwidth adjustment of 0.5; middle row (panels (d)–(f)) bandwidth adjustment 1.0; bottom row (panels (g)–(i)) bandwidth adjustment of 2.0. Left column (panels (a), (d), (g)) uses morphological opening radius of 0, i.e. opening is not used; middle column (panels (b), (e), (h)) uses morphological opening radius 20 μm; right column (panels (c), (f), (i)) uses morphological opening radius 40 μm. 678

Figure *G.1-9*: Porosity indices by site. Indices shown are: (a) Average (depth $>$ 0), (b) Maximum (depth $>$ 0), and (c) Average (0 $<$ depth $<$ 3.1 mm). 681

Figure *G.1-10*: Plots of the Average Porosity index (over depths from 0 to 3.1 mm) from granophyre rock samples at sites across Murujuga. Each panel shows results for a different morphological opening radius: (a) 0 μm, (b) 10 μm, (c) 20 μm, and (d) 40 μm. 682

Figure *G.1-11*: Plots of the Maximum Porosity index (for all depths greater than 0 mm) from granophyre rock samples at sites across Murujuga. Each panel shows results for a different morphological opening radius: (a) radius = 0 μm, (b) radius = 10 μm, (c) radius = 20 μm, and (d) radius = 40 μm. . 683

Figure *G.1-12*: Spatially smoothed (Nadaraya-Watson) average of the average porosity index (over depths from 0 to 3.1 mm). Each panel shows results for a different morphological opening radius: (a) radius = 0 μm, (b) radius = 10 μm, (c) radius = 20 μm, and (d) radius = 40 μm. 684

Figure *G.1-13*: Spatially smoothed surface of maximum porosity index. Each panel shows results for a different morphological opening radius: (a) radius = 0 μm, (b) radius = 10 μm, (c) radius = 20 μm, and (d) radius = 40 μm. . 686

Figure *G.1-14*: Pointwise Monte Carlo test applied to the Average porosity (depth 0 to 3.1 mm) index data for morphology radius (a) 0 μm, (b) 10 μm, (c) 20 μm and (d) 40 μm. The top row shows the p-values calculated for the test. The bottom row shows points that are significant at the 0.05 level. 687

Figure *G.1-15*: Pointwise Monte Carlo test applied to the Maximum porosity (depth greater than 0) index data for morphology radius (a) 0 μm, (b) 10 μm, (c) 20 μm and (d) 40 μm. The top row shows the p-values calculated for the test. The bottom row shows points that are significant at the 0.05 level. 687

Figure *G.2-1*: Scatterplots of Average porosity index (depth 0 to 3.1 mm) versus rock height above surrounding terrain. Each panel shows the results for Average porosity calculated for a different opening radius as follows: (a) radius zero, (b) radius 10, (c) radius 20, (d) radius 25, (e) radius 40, and (f) radius 50. 690
Figure *G.2-2*: Distribution of Average porosity (depth 0 to 3.1 mm): (a) shows boxplot of average values categorised by opening radius, while (b) shows a histogram of average values categorised by opening radius. 692
Figure *G.2-3*: Residual diagnostic plots for the beta regression for Average porosity (0 - 3.1 mm) for opening radius 20 μm 694
Figure *G.3-1*: AQ09_GPH predicted % reflectance vs wavelength (nm). Where orange is campaign 1, blue campaign 2, pink campaign 3 and green campaign 4.697
Figure *G.3-2*: AQ11_GPH predicted % reflectance vs wavelength (nm). Where orange is campaign 1, blue campaign 2, pink campaign 3 and green campaign 4.697
Figure *G.3-3*: RS13_GBR (a) colour measurement (sample sensed photon count) and (b) predicted % reflectance vs wavelength (nm). There is a different colour for each replicate number. 698
Figure *G.3-4*: AQ03_GPH predicted % reflectance vs wavelength (nm). 699
Figure *G.3-5*: AQ03_GPH (a) target 5 (top row) and (b) target 10 (bottom row). Left panel is sample sensed photon count versus wavelength (nm); and right panel is observed % reflectance versus wavelength (nm). 701
Figure *G.4-1*: Consensus rank images for each gas, for the spatially smoothed passive sampler data. 702
Figure *G.4-2*: Rank disagreement (standard deviation) images for each gas, for the spatially smoothed passive sampler data. 703
Figure *G.4-3*: RDA biplot of gas measurements (NO_2, NH_3, HNO_3, O_3) versus northing and elevation. 704
Figure *G.4-4*: RDA biplot of gas measurements (NO_2, NH_3, HNO_3, O_3) versus month sin, month cos, northing and elevation. 705
Figure *G.4-5*: Paired NO_2 variance by mean plots (top row) and paired NO_2 variance by month (left panels) and by station (right panels). Logarithmic scale for vertical axes. Where for example 1e-05 means 10^{-5}, or 0.00001. . 706
Figure *G.4-6*: Paired NH_3 variance by mean plots (top row) and paired NH_3 variance by month (left panels) and by station (right panels). Logarithmic scale for vertical axes. 707
Figure *G.4-7*: Paired HNO_3 variance by mean plots (top row) and paired HNO_3 variance by month (left panels) and by station (right panels). Logarithmic scale for vertical axes. 708
Figure *G.4-8*: Paired O_3 variance by mean plots (top row) and paired O_3 variance by month (left panels) and by station (right panels). Logarithmic scale for vertical axes. 709
Figure *G.4-9*: Paired benzene variance by mean plots (top row) and paired benzene variance by month (left panels) and by station (right panels). Logarithmic scale for vertical axes and for mean value. 710

Figure *G.4-10*: Paired toluene variance by mean plots (top row) and paired toluene variance by month (left panels) and by station (right panels). Logarithmic scale for vertical axes and for mean value. 711
Figure *G.5-1*: Passive IVL Samplers and mean and maximum monthly Ramboll predictions for NO_2 showing each month. 713
Figure *G.5-2*: Passive IVL Samplers and mean and maximum monthly Ramboll predictions for NH_3 showing each month. 714
Figure *G.5-3*: Passive IVL Samplers and mean and maximum monthly Ramboll predictions for O_3 showing each month. 715
Figure *G.5-4*: Passive IVL Samplers and mean and maximum monthly Ramboll predictions for SO_2 showing each month. 716
Figure *G.5-5*: Passive IVL Samplers and mean and maximum monthly Ramboll predictions for HNO_3 showing each month. 717
Figure *H.0-1*: Two sites in the current research EX06_GPH and EX04_GBR that have been studied by CSIRO in 2015. The imaging scale is apparent. 720
Figure *H.1-1*: Camera configuration with objective partially obscured by ring light attached to the objective mount. When activated the ring light LED array provide a uniformly lit scene, removing all shadows created by the surface morphology. 721
Figure *H.1-2*: Imaging system mounted onto scanning frame and set on engraved surface at AQ11. 722
Figure *H.1-3*: Scanning frame mounted vertically at EX08. This orientation required considerable reprogramming to achieve uniform movements. 722
Figure *H.1-4*: The area to be scanned is defined by a 100 $\times$ 100 mm template that can be accurately realigned in subsequent scans. 723
Figure *H.3-1*: a) A focus stacked image from AQ11, b) compared to the most in-focus image from the primary set. Note how the left third of the primary image is now in focus on the stacked image. Image width 16 mm. 725
Figure *H.5-1*: A range of screen shots from the photogrammetric model. 727
Figure *H.5-2*: Detail of the surface with a 4 $\times$ 4 mm reference grid. 728
Figure *H.5-3*: This ribbon cross-section through the surface in Figure *H.5-1*. This view illustrates one way a detailed study of the surface profile can be made through appropriate mensuration software. 728
Figure *H.6-1*: An engraved rock showing gross spalling along the left side of the block. The engraved section on the right is also spalling but at a macro-scale that appears as lightening of the surface. It is this macro-spall area that is best studied with the macro-imaging technique. The area marked at right would make the ideal study area, having a deep groove that would reveal rounding and various surfaces including engraved channels. . . 730
Figure *H.6-2*: The rectified image of the reference area at AQ02. 731
Figure *H.6-3*: Detail of Figure *H.6-2*. Width of image 20 mm. 732
Figure *H.6-4*: Section view of the 3D model showing the well-developed contours achieved using the smartphone capturing 60 images in 15 minutes. . . 732
Figure *H.6-5*: Screenshot of the Photoshop Color Picker tool with various measurement systems including $L^*a^*b^*$. 733

Figure *H.8-1*: AQ09: image oriented post-processing to provide the best view of the engravings. The background has been removed in Metashape. 735
Figure *H.8-2*: Detail of the image above zoomed up to just before pixelation. This is not an extraordinary level of detail but has been achieved through 60+ general shots of the rock. 735
Figure *H.8-3*: AQ09_GPH constructed from 60+ images and processed through Metashape and Cloud Compare to arrive at a shadow free perpendicular view. On close inspection some shadows do remain as slightly darker areas. . . 736
Figure *H.8-4*: A single shot view of AQ09_GPH shows strong shadows and very low contrast in the engraving. 737

List of Tables

Table *1.4-1*: Analytical abbreviations and definitions. 4
Table *1.4-2*: Chemical terms. 8
Table *1.4-3*: Glossary. 9
Table *1.4-4*: Study site nomenclature. 15
Table *1.4-5*: Abbreviation codes for sample rock types. 15
Table *3.1-1*: Summary of field campaigns undertaken in the first two years of monitoring studies. 21
Table *3.2-1*: Number of *pH*, *Eh*, Cl^- and pXRF measurements on rock art panels taken for each campaign by site type. 25
Table *3.2-2*: Number of *pH*, *Eh*, Cl^- and pXRF measurements on sample rocks taken for each campaign by site type. 26
Table *3.2-3*: Number of *pH*, *Eh*, Cl^- and pXRF measurements taken on rock art panels for each campaign by rock type. Note: * indicates a repeat measurement on one rock art panel. 27
Table *3.2-4*: Number of *pH*, *Eh*, Cl^- and pXRF measurements taken on sample rocks for each campaign by rock type. 28
Table *4.1-1*: Overview of surface samples prepared from collected rock specimens. 32
Table *4.1-2*: Status of analyses in the rock surface and fresher rock samples. 33
Table *4.2-1*: Geological mapping status for MRAMP study sites. 41
Table *4.2-2*: Compilation of identified minerals among the analysed XRD granophyre samples. 43
Table *4.2-3*: Compilation of identified minerals among the analysed XRD gabbro samples. 45
Table *4.2-4*: Compilation of identified minerals among the analysed XRD granite samples. 46
Table *4.2-5*: Compilation of identified minerals among the analysed XRD dolerite samples. 46
Table *4.2-6*: Compilation of identified minerals among the analysed XRD basalt samples. 46
Table *4.2-7*: Compilation of median concentrations obtained by EMP analysis of patina. Values are expressed in wt%. Unanalysed components such as H_2O are measured by the difference between the total and 100%. BDL: below the detection limit of $\sim$0.05 wt%. 122
Table *4.2-8*: Bulk composition of the patina foil obtained by STEM-EDS. The values are background corrected and deconvolution has been applied for gallium (Ga) and plutonium (Pt). Ga is used for TEM specimen preparation and Pt is contained in the top protective layer. σ represents one standard deviation of the element concentration across the mapped area. 133
Table *4.2-9*: Bulk composition of the different patina specimens obtained from APT. Values are expressed in atom percent (at.%). σ is one standard deviation on the measured value. Specimen M4 is shown on Figure *4.2-76*(d). . . 140
Table *4.2-10*: Selected mineral phases and modes for the thermodynamic calculations. Assemblages are based on the XRD and TIMA results. Granophyre mineral modes are based on the minerals featured in Figure *4.2-12*. Gabbro mineral modes are based the minerals featured in Figure *4.2-22*. 157
Table *4.3-1*: Microbiome laboratory analysis work to date. 177

Table *6.2-1*: Coordinates and uncertainties of the datum point for the AQ and EX sites. Note CI represents the confidence interval (in meters) and is applied to the uncertainty (standard error). 188
Table *6.2-2*: Checks performed in field by repeat observations, or by checking against nearby SSM coordinates. Note that “Ell” is ellipsoidal height and ”Ortho” is orthometric height. 189
Table *6.2-3*: Phantom 4 Pro specifications and calibrated camera parameters. 192
Table *6.2-4*: Phantom 4 RTK specifications and calibrated camera parameters. . . . 192
Table *7.2-1*: Total number of valid, total number measured and percentage of valid rock art panels measured at each of the 7 campaigns. 243
Table *7.4-1*: Overall campaign data: start and end dates, days since last rain (before start of campaign), rain recorded during campaign, and median *pH*. . . 253
Table *7.10-1*: p-values of Shapiro-Wilk test for normality of each sample in AQ07 and AQ08. p-values of Levene’s test for homogeneity of variance across AQ07 and AQ08. p-values of the Wilcoxon rank-sum test which compares the distribution of two independent groups (AQ07 and AQ08). Bold figures indicate p-values which are statistically significant at the 5 % level. . . . 330
Table *7.11-1*: Overall summary statistics for passive sampler data. Mean, variance, standard deviation (SD) and ratio of standard deviation to mean, for assayed concentration of each analyte in μ g/m^3, using data from all AQM stations and sampling months. 348
Table *7.11-2*: Correlations between different gas species; annual average data. For each pair of gas species, the table entry shows the Spearman rank correlation ρ between the station average concentrations (averaged over all available IVL passive sampler assay results for each station) of the two gases. Statistically significant correlations are shown in bold type and annotated with one, two or three asterisks representing statistical significance at the 0.05, 0.01 and 0.001 level respectively. 354
Table *7.11-3*: Correlations between different gas species; monthly data. For each pair of gas species, the table entry shows the Spearman rank correlation ρ between the monthly mean concentrations of the two gases at each station for each month. Values marked with one, two or three asterisks indicate results that are statistically significant at the levels 0.05, 0.01 and 0.001 respectively. 355
Table *7.11-4*: Summary statistics for duplicate measurements from passive samplers. Overall mean, pooled estimate of residual variance, and ratio of residual standard deviation to overall mean, for each analyte. Mean measures are in μ g/m^3. 358
Table *7.11-5*: Calculation of raw estimates of the short-range mean square difference τ^2 between true values of gas concentrations at the sites AQ07 and AQ08. Columns give the number n of months for which paired data were available, the estimate of $\sigma^2 + \tau^2$ described in the text, and the resulting estimate of τ^2. Negative estimates are recorded as NA. 365

Table *8.1-1*: Pearson and Spearman rank correlation coefficients between corresponding measurements from the “dry” deposition samplers and passive samplers. Statistically significant correlations are shown in bold type, and annotated with one asterisk for $p < 0.05$, two asterisks for $p < 0.01$ and three asterisks for $p < 0.001$. 406
Table *8.2-1*: Spearman rank correlation ρ between bacterial taxa and MnO. Statistically significant correlations are shown in bold type and annotated with one, two or three asterisks representing statistical significance at the 0.05, 0.01 and 0.001 level respectively. 414
Table *8.2-2*: Spearman rank correlation ρ between each bacterial taxon and average porosity (0 to 3.1 mm depth). Statistically significant correlations are shown in bold type and annotated with one, two or three asterisks representing statistical significance at the 0.05, 0.01 and 0.001 level respectively. . . 415
Table *8.3-1*: Spearman rank correlation between the IVL measurements and monthly mean Ramboll predictions, for each gas species. 424
Table *8.3-2*: Spearman rank correlation between averaged IVL measurements and averaged monthly Ramboll predictions for each gas species. 426
Table *A-1*: List of Samples. 447
Table *B-1*: Summary of the plagioclase EMP analyses where WR refers to ‘weathered rock’ and FR refers to ‘fresher rock’ (part 1). 455
Table *B-2*: Summary of the standard deviation (SD) of the plagioclase EMP analysis of the minerals (part 1). 456
Table *B-3*: Summary of the plagioclase EMP analysis as annotated in Table *B-1* (part 2). 457
Table *B-4*: Summary of the SD of the plagioclase EMP analysis of the minerals (part 2). 458
Table *B-5*: Summary of the alkali K-feldspar EMP analysis as annotated in Table *B-1*.459
Table *B-6*: Summary of the SD of the alkali K-feldspar EMP analysis. 460
Table *B-7*: Summary of the clinopyroxene EMP analysis as annotated in Table *B-1*. 461
Table *B-8*: Summary of the SD of the clinopyroxene EMP analysis. 462
Table *B-9*: Summary of the orthopyroxene EMP analysis as annotated in Table *B-1*, includes the SD. 463
Table *B-10*: Summary of the chlorite EMP analysis as annotated in Table *B-1* (part 1). 464
Table *B-11*: Summary of the SD of the chlorite EMP analysis (part 1). 465
Table *B-12*: Summary of the chlorite EMP analysis as annotated in Table *B-1* (part 2). 466
Table *B-13*: Summary of the SD of the chlorite EMP analysis as annotated in Table *B-1* (part 2). 467
Table *B-14*: Summary of the epidote EMP analysis as annotated in Table *B-1* (part 1). 468
Table *B-15*: Summary of the SD of the epidote EMP analysis as annotated in Table *B-1* (part 1). 469
Table *B-16*: Summary of the epidote EMP analysis as annotated in Table *B-1* (part 2). 470
Table *B-17*: Summary of the SD of the epidote EMP analysis as annotated in Table *B-1* (part 2). 471
Table *B-18*: Summary of the amphibole EMP analysis as annotated in Table *B-1*, includes the SD. 473

Table *B-19*: Summary of the muscovite EMP analysis as annotated in Table *B-1*, includes the SD. . . . 474
Table *B-20*: Summary of the kaolinite EMP analysis of the mineral, includes the SD. 475
Table *B-21*: Summary of the clays EMP analysis as annotated in Table *B-1*, includes the SD. . . . 476
Table *B-22*: Summary of the AlPO EMP analysis as annotated in Table *B-1*, includes the SD. . . . 477
Table *B-23*: Summary of the apatite EMP analysis as annotated in Table *B-1*, includes the SD. . . . 478
Table *B-24*: Summary of the ilmenite EMP analysis as annotated in Table *B-1*, includes the SD. . . . 479
Table *B-25*: Summary of the oxide EMP analysis as annotated in Table *B-1*. . . . 480
Table *B-26*: Summary of the SD of oxides EMP analysis as annotated in Table *B-1*. 481
Table *B-27*: Summary of the stilpnomelane EMP analysis as annotated in Table *B-1*, includes the SD. . . . 482
Table *B-28*: The average (AVG) and standard deviation (SD) of the granophyre elemental analysis obtained by TIMA. . . . 483
Table *B-29*: Summary of the gabbro elemental analysis obtained by TIMA. . . . 484
Table *B-30*: Summary of the granite elemental analysis obtained by TIMA. . . . 485
Table *B-31*: Summary of the dolerite elemental analysis obtained by TIMA. . . . 486
Table *B-32*: Summary of the basalt elemental analysis obtained by TIMA. . . . 487
Table *C.3-1*: Sample Log. . . . 499
Table *D.1-1*: AQ02 site summary. . . . 518
Table *D.1-2*: AQ02 Position uncertainties (camera locations). . . . 518
Table *D.1-3*: AQ02 control points. Where “H” is horizontal and “V” is vertical. . . . 519
Table *D.1-4*: AQ03 site summary. . . . 522
Table *D.1-5*: AQ03 Position uncertainties (camera locations). . . . 522
Table *D.1-6*: AQ03 control points. . . . 523
Table *D.1-7*: AQ04 site summary. . . . 526
Table *D.1-8*: AQ04 Position uncertainties (camera locations). . . . 526
Table *D.1-9*: AQ04 control points. . . . 527
Table *D.1-10*: AQ05 site summary 530
Table *D.1-11*: AQ05 Position uncertainties (camera locations). . . . 530
Table *D.1-12*: AQ05 control points. . . . 531
Table *D.1-13*: AQ06 site summary. . . . 534
Table *D.1-14*: AQ06 Position uncertainties (camera locations). . . . 534
Table *D.1-15*: AQ06 control points. . . . 535
Table *D.1-16*: AQ07 and AQ08 site summary. . . . 538
Table *D.1-17*: AQ07 and AQ08 Position uncertainties (camera locations). . . . 538
Table *D.1-18*: AQ07 and AQ08 control points. . . . 539
Table *D.1-19*: AQ09 (North) site summary. . . . 542
Table *D.1-20*: AQ09 (North) Position uncertainties (camera locations). . . . 542
Table *D.1-21*: AQ09 (North) control points. . . . 543
Table *D.1-22*: AQ09 (South) site summary. . . . 546
Table *D.1-23*: AQ09 (South) Position uncertainties (camera locations). . . . 546

Table *D.1-24*: AQ09 (South) control points. . . . 547
Table *D.1-25*: AQ10 site summary. . . . 550
Table *D.1-26*: AQ10 Position uncertainties (camera locations). . . . 550
Table *D.1-27*: AQ10 control points. . . . 551
Table *D.1-28*: AQ11 site summary. . . . 554
Table *D.1-29*: AQ11 Position uncertainties (camera locations). . . . 554
Table *D.1-30*: AQ11 control points. . . . 555
Table *D.1-31*: AQ12 site summary. . . . 558
Table *D.1-32*: AQ12 Position uncertainties (camera locations). . . . 558
Table *D.1-33*: AQ12 control points. . . . 559
Table *D.1-34*: AQ13 site summary. . . . 562
Table *D.1-35*: AQ13 Position uncertainties (camera locations). . . . 562
Table *D.1-36*: AQ13 control points. . . . 564
Table *D.1-37*: AQ14 site summary. . . . 566
Table *D.1-38*: AQ14 Position uncertainties (camera locations). . . . 566
Table *D.1-39*: AQ14 control points. . . . 567
Table *D.1-40*: AQ15 (Southwest)site summary. . . . 570
Table *D.1-41*: AQ15 Position uncertainties (camera locations). . . . 570
Table *D.1-42*: AQ15 control points. . . . 571
Table *D.1-43*: AQ15 and AQ16 site summary. . . . 574
Table *D.1-44*: AQ15 and AQ16 Position uncertainties (camera locations). . . . 574
Table *D.1-45*: AQ15 and AQ16 control points. . . . 574
Table *D.1-46*: AQ17 site summary. . . . 579
Table *D.1-47*: AQ17 Position uncertainties (camera locations). . . . 579
Table *D.1-48*: AQ17 control points. . . . 580
Table *D.1-49*: AQ18 site summary. . . . 583
Table *D.1-50*: AQ18 Position uncertainties (camera locations). . . . 583
Table *D.1-51*: AQ18 control points. . . . 584
Table *D.1-52*: EX02 (Northeast) site summary. . . . 587
Table *D.1-53*: EX02 (Northeast) Position uncertainties (camera locations). . . . 587
Table *D.1-54*: EX02 (Northeast) control points. . . . 588
Table *D.1-55*: EX02 (Southwest) site summary. . . . 591
Table *D.1-56*: EX02 (Southwest) Position uncertainties (camera locations). . . . 591
Table *D.1-57*: EX02 (Southwest) control points. . . . 593
Table *D.1-58*: EX03 site summary. . . . 595
Table *D.1-59*: EX03 Position uncertainties (camera locations). . . . 595
Table *D.1-60*: EX03 control points. . . . 597
Table *D.1-61*: EX04 site summary. . . . 599
Table *D.1-62*: EX04 Position uncertainties (camera locations). . . . 599
Table *D.1-63*: EX04 control points. . . . 600
Table *D.1-64*: EX05 site summary. . . . 603
Table *D.1-65*: EX05 Position uncertainties (camera locations). . . . 603
Table *D.1-66*: EX05 control points. . . . 604
Table *D.1-67*: EX06 site summary. . . . 607
Table *D.1-68*: EX06 Position uncertainties (camera locations). . . . 607

Table *D.1-69*: EX06 control points. 608
Table *D.1-70*: EX07 site summary. 611
Table *D.1-71*: EX07 Position uncertainties (camera locations). 611
Table *D.1-72*: EX07 control points. 612
Table *D.1-73*: EX08 site summary. 615
Table *D.1-74*: EX08 Position uncertainties (camera locations). 615
Table *D.1-75*: EX08 control points. 617
Table *D.1-76*: EX09 site summary. 619
Table *D.1-77*: EX09 Position uncertainties (camera locations). 619
Table *D.1-78*: EX09 control points. 619
Table *D.5-1*: Conditions imposed on the simulation for emissions from stacks. 625
Table *D.5-2*: Boundary conditions for isothermal steady state flow (`simpleFoam`). . . . 626
Table *D.7-1*: Conditions for validation. 627
Table *G.1-1*: Site and images used to calculate porosity indices for each morphology opening radius. 680
Table *G.1-2*: Results of global Monte Carlo test of elevated spatial porosity using different porosity indices and morphological opening radii. A p-value of less than or equal to 0.05 indicates statistical significance. 688
Table *G.2-1*: Correlation between height and average porosity (to 3.1mm depth) by opening radius. The table shows the Pearson correlation and Spearman's rho with asterisks indicating statistical significance. 689
Table *G.2-2*: Beta regression models of porosity for different morphological openings. Model was applied to Averaged porosity (0 to 3.1 mm). Table shows the likelihood ratio test (LR test) p-value, pseudo R square, the mean and precision intercepts, and estimates and p-values for each coefficient. . 693
Table *G.2-3*: Results of global Monte Carlo test of constant mean residual, for each morphological opening radius. 695
Table *G.4-1*: Significance tests based on two-way ANOVA for gas measurements by station and month for stations AQ07 and AQ08. 712

1 Introduction

1.1 Background

The Murujuga Rock Art Monitoring Program (**MRAMP**) will develop a series of Environmental Quality Criteria (**EQC**), with a focus on air quality. These EQC will be incorporated into an Environmental Quality Management Framework (**EQMF**) for the ongoing management of the Murujuga region.

This document presents a summary of data collection, laboratory studies and analysis undertaken within the second year of scientific studies since approval of the Program's *Monitoring Studies Data Collection and Analysis Plan* (**MSDCA Plan**) in March 2022, the formal commencement of the first fieldwork campaign, and the *Murujuga Rock Art Monitoring Program: Monitoring studies report 2023* (Curtin University, 2023; hereafter referred to as "Year One Report") published December 2023 post peer review. This report is not intended to be a stand-alone document, rather it is intended to be read in conjunction with the *Murujuga Rock Art Monitoring Program: Conceptual Model*, MSDCA Plan and detailed methodology statements for component studies as referenced throughout.

The MSDCA Plan comprises a five-year scientific research program, and as such some components remain in progress with results not yet available. Likewise, statistical data analysis and integration of datasets is ongoing. Section 1.3 summarises the works completed and included or excluded from this report.

1.2 Objectives of the MRAMP monitoring studies

From Section 1.3 of the MSDCA Plan (Curtin University, 2022), the main research goals of the current phase of the MRAMP studies are to:

1. Measure accurately the colour and surface texture of rocks across the Murujuga region, establish baseline values for a long-term monitoring program, identify important differences in colour or surface texture which may be associated with accelerated (anthropogenic) weathering, and develop criteria for assessing weathering rates.
2. Identify and characterise the minerals, inorganic and organic chemicals, and microbes present on the rock surface and in the sub-layers, which are relevant to the appearance and integrity of the petroglyphs or may be involved in accelerating or preventing the degradation of the petroglyphs.
3. Determine which atmospheric pollutants are present in industrial (e.g. port, shipping and local industry) and natural emissions (e.g. marine aerosols, emissions from bushfires) on Murujuga, and which are capable of causing degradation of, or change in, the petroglyphs.
4. Under controlled laboratory conditions with small samples of rock, measure the effect of a known amount of pollutant chemical on the constituents of the rock surface and sub-layers.
5. Measure the concentration of atmospheric pollutants to which rocks are exposed across the Murujuga region.
6. Identify the weather conditions, environmental conditions and industrial output conditions which are likely to pose the greatest risk of degradation to petroglyphs.

7. Calculate the timescales over which changes are predicted to occur, and thresholds of pollutants giving rise to accelerated change.
8. Identify sentinel variables (“canary in the coal mine”) which can be observed in the field and which can serve as indicators (EQC) of increased risk of degradation.
9. Determine if soil monitoring will inform some processes or measurements on the rock surface.
10. To utilise world-leading statistical design, methodology, and analysis techniques.
11. Link all of the evidence in the studies above to reach rigorous scientific conclusions and provide a rigorous evidence base for the Conceptual Model, the EQMF, and the Monitoring Program as a whole.

The studies phase of the Program involves measuring and studying many things which will not be part of the final monitoring phase of the Program, but which must be understood to demonstrate links between the environmental variables and the impacts on the petroglyphs.

1.3 Scope of this report

This report summarises all work completed during the second year of the monitoring studies from April 2023 to March 2024. Works still in progress are reported as such and results will be forthcoming in subsequent reports and included in statistical analyses coincident with their completion.

1.3.1 Inclusions

Activities undertaken during the first two years of studies and reported on here are described in the following sections.

Fieldwork

Overall fieldwork:

- Seven fieldwork campaigns (three in the current year, four in the first year) were undertaken totalling approximately 28 weeks duration. Fieldwork involved monitoring 54 rock art panels and 64 sample rocks across the five rock types found in the study area.
- All available results from this work are presented in this document.

Spectrometry:

- Over 66,000 spectral/colour measurements of rock art condition are reported on and analysed in detail.

Field X-ray fluorescence:

- Over 2000 surface elemental measurements using portable X-ray fluorescence (**pXRF**) were collected and analysed.

Electrochemical measurements:

- Over 2500 surface electrochemical measurements (*pH*, *Eh*, Cl^-) were taken and are analysed in detail and examined for any correlation with air quality estimates.

AQM operation:

- The deployment of 18 solar/passive and four mains-powered air quality monitoring stations (**AQM**s) has been completed and these have been maintained throughout year two.

Laboratory analysis

- Detailed organic chemical characterisation of patina has been completed and the results are presented here. Detailed characterisation of some fractions of the current samples remain outstanding.
- Extensive investigation of the inorganic geochemistry of the 64 collected rock samples has been undertaken. Key findings on the composition of the patina and weathered rind are presented here. The porosity findings and historical weathering has formed the basis for the determination of some of the most sensitive response variables for the chamber studies.
- Initial (16S) DNA sequencing data from microbial samples are presented here. Correlations of microbial abundance with porosity and elements such as manganese (Mn) have been found and are presented here.
- The chamber studies approaches for both geochemical weathering and microbial toxicology tests have been finalised. A sufficient body of testing has been undertaken to permit the development of the first Interim EQC.

1.3.2 Exclusions

The MSDCA Plan encompasses a research program of several years' duration. As such, at the end of the second year of studies, some activities have not yet reached the point where sufficient data are available for meaningful analysis.

- Real-time (low-cost) air quality sensor data is not presented as the sensors are still undergoing calibration based on the IVL (Swedish Institute for Water and Air Pollution Research) laboratory passive sampler data and real-time (reference grade) instrument data. Furthermore, some of the reference grade instruments have experienced component failures or significant delays in the delivery of calibration gases, so some gaps in data exist.
- Passive sampler results are provided by the analytical laboratory one-to-three months after collection. Data presented includes the most recent results available.

1.4 Abbreviations and definitions

1.4.1 Abbreviations

The abbreviations listed in Table *1.4-1* are used throughout this report.

Table 1.4-1: Analytical abbreviations and definitions.

Abbreviations	Definition
2D	Two-dimensional
3D	Three-dimensional
AGRF	Australian Genome Research Facility
AHD	Australian Height Datum
ANOSIM	Analysis of similarity
ANOVA	Analysis of variance
APT	Atom probe tomography
AQI	Air quality index
AQM	Air quality monitoring / air quality monitoring station
ASV	Amplicon sequence variants
AUSPOS	Online GPS processing service
BDL	Below detection limit
BSE	Backscattered electron
BSE-SEM	Backscattered electron scanning electron microscopy
CASA	Civil Aviation Safety Authority
cDNA	Complementary DNA
CFD	Computational fluid dynamics
CIE	Commission Internationale de l'Éclairage (International Commission on Illumination)
CIELAB	The $L^*a^*b^*$ colour space defined by CIE. (Also CIELab or CIE $L^*a^*b^*$).
CSIRO	Commonwealth Scientific and Industrial Research Organisation
DBCA	Department of Biodiversity, Conservation and Attractions (Western Australia)
DEM	Digital elevation model
DNA	Deoxyribonucleic acid
DSM	Digital surface model
DWER	Department of Water and Environmental Regulation (Western Australia)
EA	Elemental analyser
EBSD	Electron backscatter diffraction
EDS	Energy dispersive X-ray spectroscopy
Eh	Oxidation reduction potential (*ORP*) relative to the potential of a Standard Hydrogen Electrode (SHE)
EMP	Electron microprobe
EQC	Environmental quality criteria

Abbreviations	Definition
EQMF	Environmental quality management framework
F	Faraday Constant (96,500 Coulombs)
fANOVA	Functional Analysis of Variance
FR	Fresher rock, which is the rock that does not show weathering alteration.
HAADF	High-angle-annular dark-field
HDX	Ocean HDX-UV-VIS spectrometer (Ocean Insight, Orlando, 2893 FL, USA), MRAMP portable spectrometer introduced for year two field observations.
HFO	Heavy fuel oil
ISA	Ionic strength adjuster
GC-irMS	Gas chromatography – isotope ratio mass spectrometry
GCxGC-TOFMS	Two dimensional gas chromatography - time of flight mass spectrometry
GC-MS	Gas chromatography – mass spectrometry
GC-TQ	Gas chromatography triple quadrupole
GNSS	Global navigation satellite systems
GSD	Ground sampling distance
ICP-AES	Inductively coupled plasma-atomic emission spectroscopy
ISO	International Organization for Standardization
ITS	Internal transcribed spacer (genomic marker)
IVL	Stiftelsen Institutet för Vatten- och Luftvårdsforskning (Swedish Institute for Water and Air Pollution Research)
JAZ	Portable spectrophotometer (Ocean Insight, Orlando, 2893 FL, USA). This instrument will continue to be used for the remainder of the study programme, in order to establish adequate cross validation between the JAZ and HDX instruments, and to serve as a backup instrument in the field. However the use of the JAZ instrument will be discontinued at the conclusion of the study when the ongoing Monitoring Program is established.
LAM-EDS	Large area map-EDS
LOD	Limit of detection
LOEC	Lowest observed effect concentration (LOEC)
MAC	Murujuga Aboriginal Corporation
MAG	Metagenome assembled genome
MGA2020	Map Grid of Australia 2020
MRAMP (the Program)	Murujuga Rock Art Monitoring Program
MSDCA Plan	Monitoring Studies Data Collection and Analysis Plan
NATA	National Association of Testing Authorities

Abbreviations	Definition
NMDS	Non-metric multidimensional scaling
NOTAM	Notices To Air Missions (aviation safety alert document system)
NOEC	No observed effect concentration (NOEC)
OH, HO or OH/HO Radical	Hydroxyl radical – short lived, highly reactive chemical species formed through a reaction between UV and H_2O.
ORP	Oxidation reduction potential (mV)
pe	Negative logarithm to base 10 of electron activity (dimensionless) $pe = F\ Eh / 2.3\ R\ T$
pH	Negative logarithm to base 10 of the hydrogen ion activity (dimensionless)
PM	Particulate matter
$PM_{2.5}$, PM_{10}	Particulate matter $<$ 2.5 and $<$ 10 microns (µm) aerodynamic diameter, respectively.
pXRF	Portable X-ray fluorescence
PY-GC-MS	Pyrolysis gas chromatography-mass spectrometry
QA/QC	Quality assurance and quality control
QTZ	Quartz fibre filter
R	Universal gas constant 8.314 J mol^{-1} K^{-1}
RDA	Redundancy analysis
RNA	Ribonucleic Acid
rRNA	Ribosomal RNA
RTK	Real time kinematic (processing)
SAB	Sabouraud agar
SEM	Scanning electron microscope / scanning electron microscopy
SE-SEM	Secondary electron SEM images
SEM-EDS	Scanning electron microscopy with energy dispersive X-ray spectroscopy
SI	Saturation index
SOA	Secondary organic aerosol
SSM	Standard survey marks
STEM	Scanning transmission electron microscopy
STEM-EDS	Scanning transmission electron microscopy with energy dispersive X-ray spectroscopy
T	Absolute temperature in Kelvin
TEM	Transmission electron microscopy

Abbreviations	Definition
TIC	Total ion chromatograms
TIMA	Tescan Integrated Mineral Analyser
TLE	Total lipid extract (mg)
TOC	Total organic carbon
ToF-SIMS	Time-of-flight-secondary ion mass spectrometry
TSA	Trypton soy agar
TSP	Total suspended particulates
UAV	Unmanned aerial vehicle
UCM	Unresolved complex mixture
UWA	University of Western Australia
VLOS	Visual line of sight
VOC	Volatile organic compound
vol.%	Percentage by volume of mineral, often estimated using percentage by area on a thin section
UV	Ultraviolet light
WR	Weathered rock
wt%	Percentage by weight
XRD	X-ray diffraction
XRF	X-ray fluorescence

1.4.2 Chemical notation

The following standard chemical notation has been used in this report.

Table 1.4-2: Chemical terms.

Term	Name	Term	Name
Al	Aluminium	Mn	Manganese
As	Arsenic	Ni	Nickel
Ba	Barium	Na	Sodium
Bi	Bismuth	NO	Nitric oxide
C	Carbon	NO_2	Nitrogen dioxide
Ca	Calcium	NO_x	Oxides of nitrogen (NO + NO_2)
Ce	Cerium	N_2O_5	Dinitrogen pentoxide
CH_2O	Formaldehyde	NH_3	Ammonia
Cl	Chlorine	O	Oxygen
Cl^-	Chloride ion	O_3	Ozone
Co	Cobalt	OH^-	Hydroxide
CO	Carbon monoxide	Os	Osmium
CO_2	Carbon dioxide	P	Phosphorous
Cr	Chromium	Pb	Lead
Cs	Caesium	Pt	Platinum
Cu	Copper	Pu	Plutonium
DCM:MeOH	Dichloromethane : methanol	Rb	Rubidium
Eu	Europium	Ru	Ruthenium
Fe	Iron	S	Sulphur
Ga	Gallium	Sc	Scandium
Fe_3O_4	Magnetite	Si	Silicon
Fe_2O_3	Hematite	SiO_2	Silica
H	Hydrogen	SO_2	Sulphur dioxide
Hg	Mercury	SO_x	Oxides of sulphur (SO_2 + SO_3)
H_2O	Water	Sr	Strontium
In	Indium	Th	Thorium
K	Potassium	Ti	Titanium
La	Lanthanum	U	Uranium
Li	Lithium	V	Vanadium
Mg	Magnesium	Y	Yttrium
N	Nitrogen	Zn	Zinc

1.4.3 Glossary

Table 1.4-3: Glossary.

Term	Definition
Airshed	A geographical region with a common flow of air or over which air pollutants are dispersed.
Anthropogenic	From human activity. In the context of this research anthropogenic includes human impact, including industrial, transport, tourism, site management, and all other impact that can be attributed to human activity. It can also be considered to include distal or global human activity which may impact the natural environment through changes in climate.
Barcoding gene	A gene that is shared by a group of organisms but differs in the genetic code between species because of evolutionary changes. Sequencing analysis of these genes in environmental samples can reveal evolutionary differences between the organisms within the group. This makes it possible to classify organisms that cannot be distinguished based on morphological features.
Biofilm	A biofilm growing on a surface typically comprises a syntrophic (feeding together) consortium of microbial cells that are embedded in a slimy extracellular matrix that is composed of extracellular polymeric substances (EPSs). The organisms that live close together can “communicate” with each other (share nutrients, exchange genes to make them immune to antibiotics etc.). In some cases a biofilm can comprise a single species of microbial cells, however it is not common in environmental contexts.
Biomarkers	Organic compounds produced from natural degradation of biochemicals produced by living organisms. The structure of a biomarker can sometimes be linked to a biochemical produced by a specific organism or group of organisms, while others are more general. They are known as “molecular fossils” as they can be used to infer the presence of certain organisms in ancient environments.
Bioweathering	The degradation of mineral/rock surfaces through biological mechanisms. Some examples include organic/inorganic acid production, physical alterations from hyphae growing into rock surfaces and metabolic processes resulting in the release of metals from the rock, and/or formation of new minerals.
Boxplot	The middle line (inside the box) is the median (50% of the data); the lower bound of the box is the lower quartile (first 25% of the data) and upper bound of the box is the third (75% of the data) quartile; “whiskers”(values at which the horizontal lines stop) are approximately 95% confidence interval; data points greater or lesser than the termination of the whiskers are outliers.
CAMx	Comprehensive air quality model, specially a multi-scale photochemical modelling system for gas and particulate air pollution.
Chemolithoautotrophic	Organisms that are able to utilise atmospheric carbon dioxide as a carbon source and utilise inorganic compounds as an energy source.

Term	Definition
Culturally Important Place / Culturally Important Site	A location that has been identified as having cultural significance to Traditional Owners and Custodians that may be due to the existence of archaeological, ethnographic, historic, natural or social values. This includes values that may or may not be tied to a specific feature or geographic point in the landscape. They may include tangible or intangible features that may be tied to specific points in the landscape or may apply to a broader area or landform unit.
Cumulative campaign	Cumulative values of a parameter during a MRAMP field measurement campaign, commencing on the first day of measurements until the final day of continuous (weekdays) measurement. Typically, 35 week duration.
Cumulative monthly	Cumulative values of a parameter during a calendar month.
Data cleaning	The process of correcting or removing incorrect, corrupted, incorrectly formatted, incorrectly duplicated, incomplete or spurious data values within a dataset.
Dispersion	The spreading out of emissions from a localised source (e.g. industry stack, wildfire) over a wide area due to the effect of wind.
Eh-pH	A parameter which indicates the stability of mineral or chemical systems based on the activity of hydrogen ions (*pH*) and electrons (*Eh*). These are often compared using an *Eh-pH* diagram (Pourbaix diagram).
End member	A pure chemical compound/mineral component entering into solid solution with other pure chemical compounds to form a series of minerals.
Endolithic lichens	Lichens that grow in rocks. Lichens were originally thought to occur through a symbiotic relationship of fungi and photosynthetic algae or cyanobacteria. It is currently understood that yeast and other bacterial species can also be present in the lichen consortium.
Environmental Quality Criteria (EQC)	EQC include both “Standard” and “Guideline” EQC (Environmental Protection Authority, 2016, 2017). The former represent limits above which sufficient evidence exists that impacts are likely to occur (to appropriate levels of confidence), whereas the latter represents EQC which are set to level where effects could theoretically occur - so as to ensure appropriate early warning such that emissions can be reduced before standards are reached. Both types of EQC may be “Interim” (preliminary), however it is expected that EQC will be finalised in 2025/2026 (subject to periodic review). EQC may monitor dose (e.g. air pollutants) or response (rock/art) parameters.
Environmental Quality Management Framework (EQMF)	A framework to guide the assessment and management of activities related to a particular environmental value.
Environmental Quality Objective	A specific management goal for a designated part of the environment that signals the level of environmental quality needed to protect the environmental value of an EQMF.
Environmental value	A beneficial use or an ecosystem health condition which requires protection from the effects of emissions or environmental harm.
Eukarya	Members of the domain Eukarya–calledeukaryotes–have membrane-bound organelles (including a nucleus containing genetic material) and are represented by five kingdoms: Plantae, Protista, Animalia, Chromista, and Fungi.

Term	Definition
Extracellular polymeric substances (EPS)	EPS consist of a variety of macromolecules that are secreted by bacteria in the environment to make biofilms.
Fermentation	The microbial enzymatic degradation of organic matter (e.g. carbohydrates) into short-chain fatty acids (notably acetic, propionic and butyric acids) that can lower the *pH* of the patina.
Fresher rock	Rock that does not show weathering alteration.
Gene transcription	The active expression of a gene that produces an RNA copy. This can be a structural component such as ribosomal RNA that makes up the ribosomes. Functional gene products are messenger RNA, which are translated into proteins within the ribosomes. Transcripts are indicative that the cell was alive and possibly active at the time of sampling since RNA is much more unstable and prone to degradation than DNA. DNA survives much longer in the environment.
Heterotrophs	Heterotrophic bacteria and fungi that derive energy from organic compounds.
Hypolithic	Microbial communities that colonise and grow below the rock surface where they are protected against UV damage and desiccation.
MAGs	Metagenome Assembled Genomes. This technique combines short environmental DNA sequences (metagenomes) to build genomes of key species present in the microbiome. Expressed genes (metatranscriptome) that are sequenced in parallel can be mapped against the assembled genomes to link these processes with the key species involved in patina formation and/or degradation.
Metabolic pathways	A metabolic pathway is a linked series of chemical reactions occurring within a cell. The reactants, products, and intermediates of an enzymatic reaction are known as metabolites, which are modified by a sequence of chemical reactions catalysed by enzymes. The genes involved in the individual enzymatic processes as part of the metabolic pathways and the active expression of these genes will be identified through respectively metagenomics and metatranscriptomics as defined below.
Metagenomics	The study of sequenced genetic material in environmental samples. Depending on sequence depth, this can reveal a holistic overview of the relative abundance of all microbial genes present. In our study this refers to microbial genes that encode for enzymes involved in processes leading to patina formation and/or degradation.
Metatranscriptomics	The study of microbial gene expression in environmental samples. Depending on sequence depth, this can reveal a holistic overview of the relative abundance of all actively expressed microbial genes present. In the MRAMP research this refers to actively expressed microbial genes that encode for enzymes involved in processes leading to patina formation and/or degradation. Owing to the short-lived survival of gene transcripts in the environment, their presence is indicative of an active role in these processes.
Microbial metabolites	Breakdown products or compounds that microbial communities use as energy sources, for growth and other cellular processes.
Microbiome	An integrated community of micro-organisms (bacteria, archaea, unicellular eukaryotes and fungi) occupying a particular habitat.
Microcolonial fungi	Colonies of fungi growing on rock surfaces. They are highly resistant against desiccation and ultraviolet damage.

Term	Definition
Mineral assemblages	Presence and abundance of mineral species in a given spatial region (either across the rock surface or from the rock surface to the “fresh(er)” rock below the outer weathered rind).
Mineral mode	Volume percentage of a mineral.
Murujuga	Traditional name for Burrup Peninsula and surrounding islands of the Dampier Archipelago.
Murujuga Rock Art Monitoring Program (MRAMP)	Overall program of work to be conducted to 2026. Includes initial studies to inform the design of the ongoing monitoring framework, as well as the development of EQC and the EQMF.
Ongoing monitoring	The ongoing monitoring refers to the longer-term monitoring program to be jointly run by MAC and DWER once the current program of works is complete (expected to commence from 2026). Also referred to as “long-term monitoring”.
Ordination	A group of statistical techniques for visualising and analysing multivariate data, which involve projecting high-dimensional data onto a two-dimensional graph so that similar data points are projected to similar positions in the graph.
Organic geochemistry	The study of organic compounds in the environment, including in rocks, sediments, soils, petroleum, aquatic environments and the atmosphere. Organic geochemistry studies the origin of organic compounds, their transportation processes, and the alteration they undergo in the environment, over time scales ranging from the present day to hundreds of millions of years ago.
Patina	In the Murujuga context the texture and colour of the rock surface is referred to as a patina. This is a deliberately broad definition, which encompasses the full spectrum of rock surface characterisation, including rock varnish or desert varnish. It also includes any other exposed, highly weathered rock surface and biota which may be present on the surface. The patina has been shown to form over a depletion zone, referred to as the crust or weathered rind. Weathered rind generally has a lighter appearance than both the patina and the underlying rock. An engraving is formed by breaking through the naturally formed patina to expose the lighter crust beneath. There may be cases were the engraving is deep enough to expose the underlying rock, which in this case may result in a darker engraved channel. There are many examples were a fully developed patina/varnish layer has regrown in engraved grooves. These examples are generally considered among the oldest petroglyphs for this reason.
Petroglyph	Literally “rock mark”, the term describes any cultural marking into a rock surface. The marks can be produced by a range of techniques, including pecking, pounding, incising, scratching or abrading, or a combination of two or more techniques. Techniques such as scratching can be very shallow (< 1 mm), while pecking can be from 1 mm to more than 100 mm deep. All petroglyphs at Murujuga are Culturally Important.
Photoautotrophs	Photoautotrophs are organisms that can make their own energy using light and carbon dioxide via the process of photosynthesis. Examples are cyanobacteria and green algae, known to colonise rock surfaces. Photoautotrophs are considered primary producers since their biomass can be consumed by heterotrophs (defined above) as a source of carbon and energy.
Photolysis	The process by which molecules are broken into small fragments by exposure to sunlight (typically UV radiation).

Term	Definition
Photospectrometry	An instrumental technique for measuring the chromatic reflectance of a surface by scanning at frequencies that cover the visible spectrum and beyond. Photospectrometry provides both a single value colour designation and spectral data that can indicate non-chromatic change. The technique has been applied to both the measurement of change and the characterisation of unknown minerals and compounds.
Primary producers	See definition of “photoautotrophs”.
p-value	A statistical measure used in evaluating the strength of evidence. First a “null hypothesis” is formulated. After data are obtained, the p-value is defined as the probability of obtaining data at least as extreme as the data that were obtained, where this probability is calculated under the assumption (for the sake of argument) that the null hypothesis is true. A small p-value is interpreted as evidence against the null hypothesis, because if the p-value is very small, then “either something very unlikely has happened, or the null hypothesis is false”. In this report, following standard conventions, a p-value < 0.05 is deemed ‘statistically significant’ evidence against the null hypothesis.
$p(d)$	Porosity function. The porosity (volume fraction occupied by voids, between zero and one) of rock at a depth of d microns below the outer surface. See Appendix *F*.2.5. Not established terminology.
Quartile	In statistical analysis of data or populations, the quartiles are three numbers which divide the population values or data values into four equal segments. The first quartile is a number that lies above one-quarter of the population and below three-quarters of the population. The second quartile is the median, lying above half of the population and below the other half of the population. The third quartile lies above three-quarters of the population and below one-quarter.
Secondary organic aerosol (SOA)	Solid or liquid organic molecules produced in the atmosphere by the reaction of smaller, gaseous organic molecules with oxygen (and often ozone and UV / OH radicals).
Stable isotopes	Atoms of the same element which contain a different number of neutrons in the nucleus. Most elements consist of more than one stable isotope, the ratios of which can be measured using specialised instrumentation. Stable isotope ratios in organic compounds are affected by the processes of formation and alteration, hence their measurement gives information on source and alteration history.
Weathered rind	The portion of the rock between the surface (patina) layer and the fresher inner rock. This layer is sufficiently close to the surface to have interacted with oxygen or other environmental conditions. The weathered rind is significantly thicker than the surface patina layer and has different colouration to the underlying fresher rock (core).

Term	Definition
Weathering	In the Murujuga context the concepts of weathering are differentiated as natural weathering and accelerated/anthropogenic weathering, which may be termed "degradation" to distinguish it from natural weathering. However, these effects may be difficult to decouple. • Natural Weathering: the alteration of a rock surface through natural agents such as the impacts of temperature cycles, microbial activity, and interactions with water and aerosols/gases released by the surrounding (natural) terrestrial and marine environments. Weathering may be subtractive (erosion) or additive (mineralisation or accretion). • Accelerated weathering: degradation due to anthropogenic activity over and above the rate of natural weathering.

1.4.4 Site and sample numbering nomenclature

Study sites

Study sites are generally identified with an alphanumeric code in the format:

AABB

where:

- AA is a two letter code indicating the type of study site as described in Table *1.4-4*.
- BB is a two digit sequential number derived from the study design outputs (MSDCA Plan Appendix I and Appendix II).

The exception to the standard nomenclature is study site "AQA1", which was added to the Program during the course of the first year of scientific studies and designates the MAC Office AQM.

Sample rocks

Sample rocks are identified with an alphanumeric code in the format:

AABB_CCC

where:

- AA is a two letter code indicating the type of study site as described in Table *1.4-5*.
- BB is a two digit sequential number derived from the study design outputs (MSDCA Plan Appendix I and Appendix II).
- CCC is the rock type as defined in Table *1.4-5*.

Rock art panels

Rock art panels are referred to in the same manner as the host rock. Where a study square includes more than one rock art panel on the same rock type a numeral will be added after the rock type to differentiate between the art panels (e.g. RS10_GPH1).

Table 1.4-4: Study site nomenclature.

Site code	Numbering	Count	Name	Descriptor
AQ	01 to 18	18	Air quality	Study squares where new MRAMP air quality monitors are installed. AQ01 is a mains powered station.
AQA	1	1	Air quality additional	Designation given to the location of the initial field prototype AQM installed at the MAC Office.
AS	01 to 02	2	Additional sample	Study squares providing targeted samples of rare rock types.
EX	01 to 09	9	Existing (AQM)	Study squares with existing industry/government air quality monitors, both solar/passive and mains powered. EX02 was a decommissioned mains powered monitoring station which has been replaced by MRAMP, EX07 is a mains powered industry monitoring station which contains additional equipment owned by MRAMP and operated on our behalf by an independent contractor, EX09 contains an industry solar/passive station and an MRAMP powered station.
RS	01 to 18	18	Representative sample	Study squares without AQMs, where field observations and sample collection occur to form a rigorous representative sample of the entire Murujuga region.
Total		**48**		

Table 1.4-5: Abbreviation codes for sample rock types.

Rock type code	Descriptor
BAS	Basalt
DOL	Dolerite
GBR	Gabbro
GBP	Polished gabbro
GPH	Granophyre
GPHC	Granophyre coarse crystal size
GPHF	Granophyre fine crystal size
GPHP	Polished granophyre
GRT	Granite

This page is intentionally blank.

2 Study methodologies, verification of competency, and quality assurance

2.1 Elaboration of methodologies described in the MSDCA plan

Full methods have been prepared as separate documents and provided to DWER. For the current report, the following methods are applicable:

- • COPP21065-PRO-G-102 Murujuga Rock Art Monitoring Program: Passive Air Quality Monitoring (AQM) Installation and Commissioning [Updated]
- COPP21065-PRO-G-103 Murujuga Rock Art Monitoring Program: Passive AQM Sample Collection, Maintenance and Context Observations [Updated]
- COPP21065-PRO-G-104 Murujuga Rock Art Monitoring Program: Powered Air Quality Monitor Installation and Commissioning [New]
- COPP21065-PRO-G-105 Murujuga Rock Art Monitoring Program: Unmanned Aerial Vehicle and Spatial Mapping [Unchanged]
- COPP21065-PRO-G-106 Murujuga Rock Art Monitoring Program: Inorganic Monitoring (pH and Portable X-Ray Fluorescence) [Unchanged]
- COPP21065-PRO-G-107 Murujuga Rock Art Monitoring Program: Microbiome Field Sample [Unchanged]
- COPP21065-PRO-G-110 Murujuga Rock Art Monitoring Program: Photospectrometric Colour Change Measurement [Unchanged]
- COPP21065-PRO-G-111 Murujuga Rock Art Monitoring Program: Field Permeameter [New]
- COPP21065-PRO-G-113 Murujuga Rock Art Monitoring Program: Organic Geochemistry of Rock Surfaces, Dust and Particulates [Updated]
- COPP21065-PRO-G-114 Murujuga Rock Art Monitoring Program: Inorganic Geochemistry Laboratory Analysis [Updated]
- COPP21065-PRO-G-117 Murujuga Rock Art Monitoring Program: Chamber Exposure Studies [Updated]
- COPP21065-PRO-G-118 Murujuga Rock Art Monitoring Program: Powered AQM Operations, Procedures and Observations [New]

2.2 Personnel and verification of competency

All personnel are appropriately trained and/or supervised in all methods relevant to their work prior to commencement of any task or activity.

In most cases this training, supervision and certification is undertaken by the lead researcher in each discipline or by the relevant facility/laboratory/instrument manager. Training for each discipline or activity is detailed in the relevant methods documents.

A key component of the project is to train the MAC Rangers in all relevant skills and methods required to undertake ongoing monitoring under the EQMF. After much consideration, it was decided that the desired approach was to create a series of five “Curtin Credentials” for this purpose. These are modelled on other Curtin University Credentials developed for Indigenous ranger training. Credentials represent a body of work approximately 1/5th of a typical university unit (subject) of study. The Credentials developed for MRAMP are:

- Passive Air Quality Monitoring
- Introduction to Workplace Health and Safety (under development)
- Realtime Air Quality Monitoring
- Rock Art Condition Monitoring (under development)
- Geology and Geochemistry for Rock Art Monitoring (under development).

2.3 Quality assurance

Extensive calibration, validation and quality assurance controls have been developed for all measurements and study components. These are detailed in the respective methodologies.

Some of the key protocols are summarised below.

2.3.1 Air quality monitoring

Passive sampler deployment occurs in duplicate at each AQM and utilises multiple field blanks as per best practice. Samples are analysed by IVL (Sweden) under International Organization for Standardization (**ISO**) certification (EN ISO IEC 17025:2017 *General Requirements for the Competence of Testing and Calibration Laboratories*) equivalent to the Australian National Association of Testing Authorities (**NATA**) certification standard.

Deposition samples are analysed by the NATA-accredited ChemCentre (who hold NATA accredited ISO/IEC 17025 (2017) certification for most analyses) following their chain of custody, documented blank, calibration and validation protocols for each method. Ultrapure water used in the methods has been obtained from the ChemCentre. Blank samples of ultrapure water are returned with each set of measurements.

Powered AQMs use a suite of real-time instruments meeting the requirements of relevant Australian Standard AS3580: *2023 Methods of Sampling and Analysis of Ambient Air* and United States Environmental Protection (USEPA) standards for ambient air monitoring. These are subject to zero and span calibrations at minimum four-weekly intervals, to ensure reliable results for research purposes. The data collected from these instruments with the co-located passive samplers will be used by the statistical team to develop robust region- and climate-specific calibration for the low power samplers in the passive AQMs.

2.3.2 Fieldwork

Spectrometry methods utilise thin films with known properties to undertake instrument calibrations at least once per rock art panel. The statisticians have developed a set of rigorous protocols and

criteria for quality assurance and quality control (**QA/QC**) checking of data. These protocols will be automated and applied in the field in real-time.

The pXRF instrument used for geological fieldwork contains an internal calibration standard and is calibrated each time it powers on. In addition, standard reference materials are measured twice per day and the results are recorded.

The equipment used for *pH*/*Eh*/Cl^- measurement is calibrated at least twice per day using known reference solutions. Ultrapure water is supplied by the ChemCentre and is the same water as used for AQM sample processing. Field blanks are tested twice per day and additional blanks are sent back to the ChemCentre each month for *pH* testing.

2.3.3 Laboratory analysis

All laboratory measurements utilise blanks and reference standards as per best practice. All instruments and equipment are serviced and calibrated according to manufacturer's protocols.

2.3.3.1 Quality assurance of SEM microanalysis data

Scanning electron microscopy (**SEM**) is an analytical technique used to obtain high-resolution images and elemental analyses of a sample's surface. QA/QC is an essential aspect of SEM microanalysis data analysis to ensure that the data obtained are reliable and accurate.

Protocol for the QA/QC of SEM microanalysis data:

- Instrument calibration
  The SEM instrument is calibrated regularly to ensure the accuracy of the data. Calibration includes the electron beam energy, beam current, and magnification. Instrumentation used in this study is regularly calibrated and analysis conditions are standardised.
- Sample preparation
  Proper sample preparation is crucial for obtaining accurate and reliable data. Samples are cleaned using ultrapure compressed air or water as appropriate to remove any surface contamination and handled with care to avoid any alteration. If appropriate, samples are prepared fixed in resin to ensure their integrity during the analysis process.
- Reproducibility
  To ensure the reproducibility of the data, multiple measurements of the same sample or replicate measurements of different samples under the same experimental conditions.
- Data analysis
  The SEM microanalysis data are analysed using appropriate statistical methods to identify significant differences between the samples. Data are also validated using complementary techniques such as Time-of-flight secondary ion mass spectrometry (**ToF-SIMS**), X-ray diffraction or XRF.
- Quality control
  To ensure the quality of the data, the SEM microanalysis data are checked for outliers, systematic errors, and other sources of variability. Data are reviewed by experts in the field to identify any potential issues or limitations.

In conclusion, the QA/QC steps listed above ensures the accuracy, reliability, and reproducibility of data produced by the SEM microanalysis process.

2.3.3.2 Quality assurance of time-of-flight secondary ion mass spectrometry data

Time-of-flight secondary ion mass spectrometry (**ToF-SIMS**) is an analytical technique used to investigate the surface chemistry and molecular structure of a sample. QA/QC is an essential aspect of ToF-SIMS data analysis to ensure that the data obtained are reliable, accurate and reproducible.

Some steps considered for the QA/QC of ToF-SIMS data:

- Instrument calibration
  To ensure the accuracy of the data, the ToF-SIMS instrument is calibrated regularly. Calibration includes the checking and optimising the mass accuracy, mass resolution, and primary ion intensity.
- Sample preparation
  Appropriate sample preparation is crucial for obtaining accurate and reliable ToF-SIMS data. Samples will be carefully cleaned to remove any surface contamination and will be stored under clean, dry conditions to minimise any atmospheric alteration.
- Reproducibility
  To ensure the reproducibility of the data, it is important to perform multiple measurements of the same sample or replicate measurements of different samples under the same experimental conditions.
- Data normalisation
  Normalisation is necessary to eliminate variations in signal intensity due to differences in sample conductivity, chamber vacuum, instrument sensitivity, and primary ion dose. Normalisation is achieved by dividing the signal by the total ion current.
- Data analysis
  The ToF-SIMS data is analysed using appropriate statistical methods to identify significant differences between the samples. The data is validated using complementary techniques, such as SEM, XRD and energy dispersive X-ray spectroscopy (**EDS**). Ions in the mass spectrum are identified using values from internationally recognised databases and peer reviewed literature.
- Quality control
  To ensure the quality of the data, the ToF-SIMS data is checked outliers, systematic errors, and other sources of variability. The data are reviewed by experts in the field to identify any potential issues or limitations.

3 Monitoring studies undertaken in the field

This section reports on the monitoring studies that were undertaken in the field in year two of the project. Section 3.1 provides general information about the field monitoring work. Section 3.2 covers the inorganic chemistry fieldwork. Section 3.3 reports on the colorimetry fieldwork. In year two, there was no microbiome collection fieldwork; this will resume in year three.

3.1 Field monitoring generally

3.1.1 Location of field monitoring sites

Figure *3.1-1* shows the location of field monitoring sites arising from the site selection process undertaken previously during development of the MSDCA Plan (Curtin University, 2022). All sites and artifacts included in the Program were approved by the Murujuga Aboriginal Corporation's Circle of Elders prior to commencement of the monitoring studies.

3.1.2 Summary of year one and two field campaigns

Table *3.1-1* outlines the seven fieldwork campaigns included in the first two years of monitoring studies. These dates were selected to correspond with wet, dry and shoulder seasons to create an understanding of the effect of seasonal changes. Historically, long-term peak rainfall has occurred in February and the lowest rainfall in October. However for the purposes of the project works the February-April campaigns are referred to as wet season campaigns, the June-July campaigns as shoulder season and the October-November campaigns as dry season. Note that this naming convention is purely for convenience and any analysis considers actual temperature and rainfall. Actual rainfall for the past two years has been lower during February compared to rainfall during the dry/shoulder seasons.

Table 3.1-1: Summary of field campaigns undertaken in the first two years of monitoring studies.

Campaign no.	Date	Inorganic geo-chemistry	Colour monitoring	Organic/ Microbiome	Veg. collection	Spatial mapping	Ad hoc (fire)
1	07 Mar - 08 Apr 2022	Y	Y	Y	Y	-	-
2	20 Jun - 29 Jul 2022	Y	Y	Y	Y	Y	-
3	03 Oct - 28 Oct 2022	Y	Y	-	-	Y	-
4	26 Feb - 21 Mar 2023	Y	Y	-	-	-	-
5	03 Jul - 21 Jul 2023	Y	Y	-	-	-	Y
6	23 Oct - 15 Nov 2023	Y	Y	-	-	-	-
7	27 Feb - 24 Mar 2024	Y	Y	-	-	-	-

Table *3.1-1* does not include installation and commissioning of AQMs or changeover of AQM samplers. This information is provided as part of the air quality monitoring discussion in Section 5.

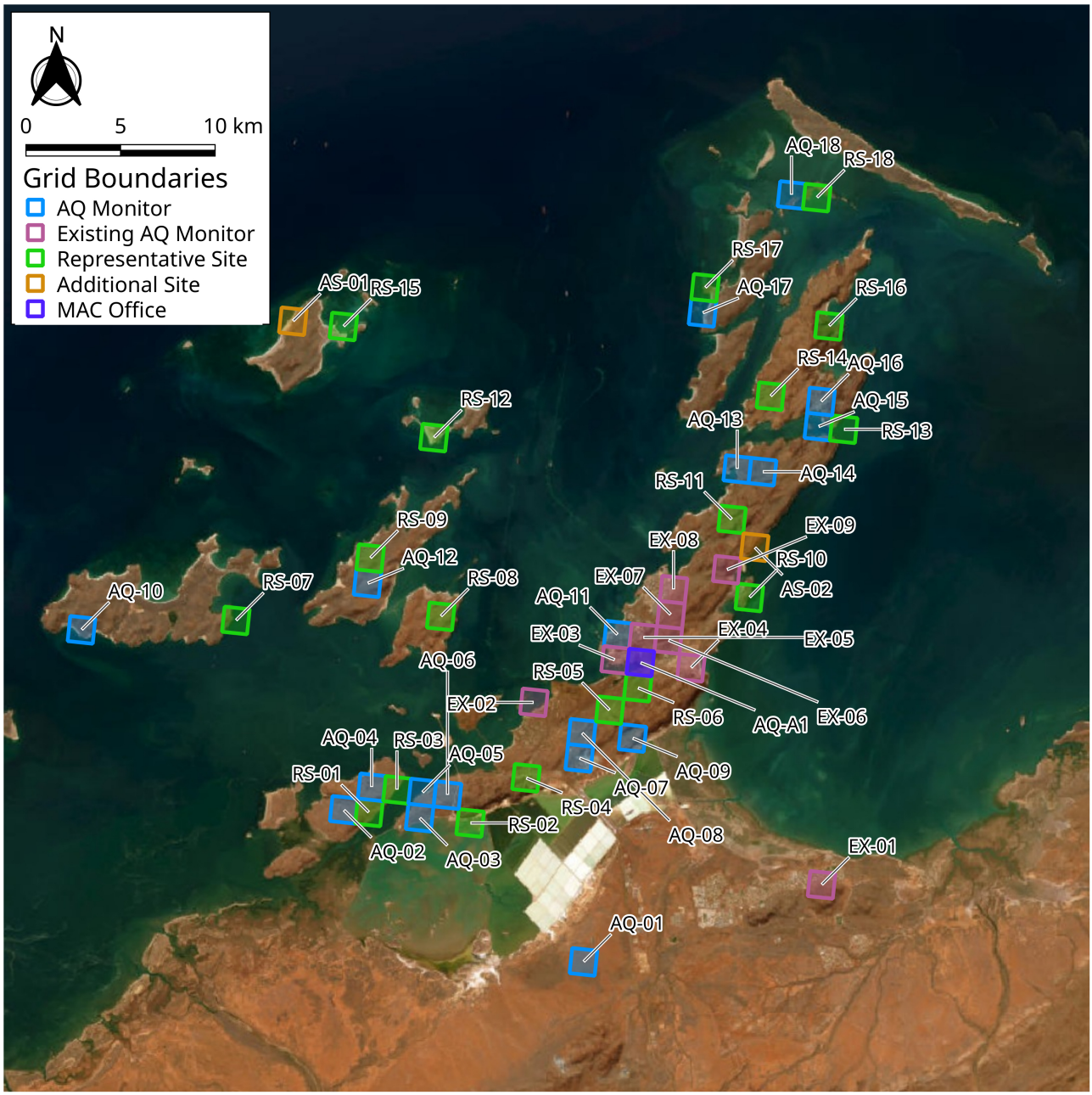

Figure 3.1-1: Map of field monitoring sites

3.2 Inorganic geochemistry fieldwork

3.2.1 Objectives

From Section 1.5 of the MSDCA Plan (Curtin University, 2022), the objectives of the inorganic geochemistry investigations are to:

1. Characterise the mineralogy and mineral compositions of the fresh rock, weathered rind, and patina for the granophyre, gabbro, dolerite, granite and basalt rock types from a range of settings including high and low exposure to industry emissions and differences in exposure to rain and wind.
2. Determine the mineralogy for these systems at thermodynamic equilibrium using thermodynamic calculations and use best practice approaches to estimate the timescales of change, based upon measured reaction rates, reaction mechanisms, and the results of other component studies (organic, microbiome, field observations, weathering experiments).
3. Compare the expected and observed mineralogy for sites with different exposure to anthropogenic emissions to (a) obtain proof-of-concept for the thermodynamic calculations; (b) investigate the presence of statistically significant differences among the sites and relate these to industry emissions.
4. Use the observations and calculations to identify components of the mineralogy that are most sensitive to industrial emissions and that can act as early indicators of change (EQC) and devise a monitoring strategy that will form part of the EQMF and ongoing monitoring Program.

3.2.2 Methodology

Inorganic geochemistry fieldwork in the field campaigns involved:

1. Performing an elemental surface analysis of the selected sample rocks (year one only prior to removal) and rock art panels using a portable X-ray fluorescence (**pXRF**) device.
2. Measuring the *Eh-pH* and chloride ion levels on the surface of the selected sample rocks.

During the second field campaign conducted in June-July 2022, sample rocks were removed from Murujuga and transported to Curtin University for in-depth destructive testing and analysis.

Further information on inorganic geochemistry field methodologies can be found in Section 3.2.4 of the MSDCA Plan (Curtin University, 2022) and the following component study methodology statements:

- COPP21065-PRO-G-106 Inorganic Monitoring (*pH* and Portable X-Ray Fluorometer)
- COPP21065-PRO-G-115 Sample Rock Collection

Variations from planned methodology

The Bruker Tracer 5G pXRF was selected as the desired instrument for the fieldwork due to the broad suite of elements it can measure. A Bruker Tracer 5G was purchased for use in campaigns 2 to 7. For the earlier campaign 1, an identical hire instrument was used. This instrument suffered an X-ray tube failure mid-campaign and was replaced by a second identical model instrument. Therefore, three instruments of the same model have been utilised across the campaigns. This

variable does not appear to have influenced results, however, has been noted and accounted for in analyses where possible. To avoid misunderstanding we emphasise that the analysis did not assume that the different individual instruments gave identical results. The analysis allowed for the possibility that the different individual instruments gave different results. The exploratory analysis did not find any evidence of a difference. The purchased Bruker Tracer 5G has remained reliable and been utilised for all year two measurements.

3.2.3 Fieldwork progress

Table *3.2-1* summarise the number of inorganic geochemistry observations taken during the 28 weeks of field campaigns.

Table 3.2-1: Number of pH, Eh, Cl^- and pXRF measurements on rock art panels taken for each campaign by site type.

Campaign no.	Site type	Number of measurements on rock art			
		pH	***ORP* (*Eh*)**	**Chloride**	**pXRF**
1	AQ	69	0	36	66
	AS	6	0	6	12
	EX	27	0	21	30
	RS	53	12	35	62
2	AQ	66	66	66	66
	AS	9	9	9	9
	EX	27	27	27	27
	RS	60	60	60	60
3	AQ	66	66	66	66
	AS	9	9	9	9
	EX	27	27	27	27
	RS	60	60	60	60
4	AQ	69	69	69	69
	AS	9	9	9	9
	EX	27	27	27	27
	RS	60	60	60	60
5	AQ	66	66	66	66
	AS	9	9	9	9
	EX	27	27	27	27
	RS	21	21	21	21
6	AQ	66	66	66	66
	AS	9	9	9	9
	EX	27	27	27	27
	RS	18	18	18	18
7	AQ	66	66	66	66
	AS	9	9	9	9
	EX	27	27	27	27
	RS	21	21	21	21

Table 3.2-2: Number of pH, Eh, Cl^- and pXRF measurements on sample rocks taken for each campaign by site type.

Campaign no.	Site type	Number of measurements on sample rocks			
		pH	***ORP* (*Eh*)**	**Chloride**	**pXRF**
1	AQ	66	2	36	63
	AS	6	0	6	12
	EX	24	0	24	30
	RS	81	10	49	87
2	AQ	63	63	63	63
	AS	9	9	9	9
	EX	27	27	27	27
	RS	87	87	87	87

*Table 3.2-3: Number of pH, Eh, Cl^- and pXRF measurements taken on rock art panels for each campaign by rock type. Note: * indicates a repeat measurement on one rock art panel.*

Campaign no.	Site type	Number of measurements on rock art			
		pH	***ORP* (*Eh*)**	**Chloride**	**pXRF**
1	BAS	11	2	9	12
	DOL	15	0	12	15
	GBR	39	3	20	36
	GPH	87	7	54	98
	GRT	3	0	3	9
2	BAS	12	12	12	12
	DOL	15	15	15	15
	GBR	39	39	39	39
	GPH	90	90	90	90
	GRT	6	6	6	6
3	BAS	12	12	12	12
	DOL	15	15	15	15
	GBR	39	39	39	39
	GPH	90	90	90	90
	GRT	6	6	6	6
4	BAS	12	12	12	12
	DOL	15	15	15	15
	GBR	39	39	39	39
	GPH*	93	93	93	93
	GRT	6	6	6	6
5	BAS	6	6	6	6
	DOL	12	12	12	12
	GBR	27	27	27	27
	GPH	72	72	72	72
	GRT	6	6	6	6
6	BAS	6	6	6	6
	DOL	12	12	12	12
	GBR	24	24	24	24
	GPH	72	72	72	72
	GRT	6	6	6	6
7	BAS	6	6	6	6
	DOL	9	9	9	9
	GBR	30	30	30	30
	GPH	72	72	72	72
	GRT	6	6	6	6

Table 3.2-4: Number of pH, Eh, Cl^- and pXRF measurements taken on sample rocks for each campaign by rock type.

Campaign no.	Site type	Number of measurements on sample rocks			
		pH	***ORP* (*Eh*)**	**Chloride**	**pXRF**
1	BAS	18	1	10	18
	DOL	21	0	21	21
	GBR	36	3	18	36
	GPH	87	8	60	93
	GRT	15	0	6	21
2	BAS	18	18	18	18
	DOL	24	24	24	24
	GBR	33	33	33	33
	GPH	93	93	93	93
	GRT	18	18	18	18

3.3 Surface change analysis (spectroscopy) fieldwork

3.3.1 Objectives

From Section 1.7 of the MSDCA Plan (Curtin University, 2022), the objectives of the spectroscopy investigations are to:

1. Accurately measure the colour, texture and elemental composition of selected rock surfaces across Murujuga.
2. Study the secondary reflectance characteristics to monitor chemical change, anticipating future colour change.
3. Capture the broad surface elemental distribution to understand colour change across whole surfaces to correlate with and inform spot measurements.
4. Establish baseline values for a long-term monitoring program.
5. Identify important differences or changes in colour, surface texture and elemental composition which may be associated with degradation of appearance or condition.
6. Develop deeper understanding of variation in elemental composition across the rock surface and its relationship to colour and texture.
7. Develop criteria for assessing degradation of appearance or condition.
8. Ensure that the study data provide information required by other component studies (such as the precise spatial location of each observation).

3.3.2 Methodology

Spectroscopy fieldwork in the field campaigns involved:

1. Spectroscopic measurement of 10 targets on each rock panel
2. In-field management of spectral files
3. Gathering of environmental and condition data at each site, including comprehensive photographic record of the site and its context.

Further information on spectroscopy field methodologies can be found in Section 3.2.3 of the MSDCA Plan (Curtin University, 2022) and the component study methodology statement:

- COPP21065-PRO-G-110 Photospectrometric Colour Change Measurement.

Variations from planned methodology

Sections 7.2.2 and 7.2.3 detail the extensive revisions and improvements incorporated in terms of equipment and methods in order to optimise the spectroscopy field methods.

The original study design assumed that the representative sample (RS) sites would only be visited in year one. However, the variability in the spectrometry, *pH* and other inorganics measurements required that the RS sites remain in the study for a longer period. The statistical team decided that

the RS sites would be stratified across campaigns so that each RS site would be measured at least once per year, DWER accepted this recommendation.

4 Laboratory analysis of field samples

This Section reports on laboratory analysis of samples collected in the field, and chamber experiments.

- Section 4.1 covers organic geochemistry.
- Section 4.2 covers geology and inorganic chemistry.
- Section 4.3 covers analysis of the microbiome.
- Section 4.4 reports on the chamber experiments.

4.1 Organic geochemistry laboratory analysis

4.1.1 Objectives

From Section 1.4 of the MSDCA Plan (Curtin University, 2022), the objectives of the organic geochemistry investigations are to:

1. Measure the molecular and stable isotopic composition of organics from all sources, including natural emissions (terrestrial vegetation, fire), anthropogenic emissions (shipping, traffic, industry) and organics present in the host rocks (including rock dust from iron ore transport), to produce a detailed characterisation of organic emissions in the Murujuga region. Including determination of the occurrence and magnitude of seasonal variations in emissions.
2. Measure the molecular and stable isotopic composition of organics deposited on rock surfaces and in soils, to link organics on rock surfaces to the various emission sources, and determine which sources contribute the highest quantity of organics to the surface deposition.
3. Identify any organics that are likely to affect weathering of rock art, e.g. by affecting growth of microorganisms (in conjunction with microbiome expert(s)) or interaction with specific minerals (in conjunction with inorganic geochemist(s)).
4. Understand confounding factors introduced by (reported) changed fire management regimes approximately coinciding with the commencement of industrial activity on the Burrup.

4.1.2 Methodology

Organic geochemistry laboratory methodologies are described in Section 3.3.3 of the MSDCA Plan (Curtin University, 2022) and the component study methodology statement:

- COPP21065-PRO-G-113 Organic Geochemistry of Rock Surfaces, Dust and Particulates

4.1.3 Summary of previous work in year one

Sixty-four field rock samples were received (September 2022) following their collection under field campaign 2. Surface samples from six rocks were removed in duplicate as sufficient material was available. In total, 70 surface samples were obtained from the 64 samples received. Six surface samples did not meet the criteria for extraction (see also Curtin University (2023)), hence a total of 64 surface samples were extracted. In addition, 11 fresher rock samples (2 x GPH, 2 x GBR, 2 x GRT, 2 x BAS, 3 x DOL) were taken, extracted, and analysed to estimate a possible contribution

from the interior of the rock to the rock surface (Table *4.1-1*). A detailed list is included in Appendix Table *A-1*.

Table 4.1-1: Overview of surface samples prepared from collected rock specimens.

Samples	Number
Rocks with patinated surface	
Sample rocks received	64
Surface removed (including six duplicates)	70
Samples with insufficient surface material for extraction (material $<$ 3 g)	6
Total number of patinated samples extracted for analysis	64
Rocks with fresher surfaces	
Fresher sample rocks received	11
Samples extracted (including six duplicates)	11

Total organic carbon (**TOC**) was determined in the first year of studies for all extracted samples. The TOC in the patinated surface samples ranged between 0.05 and 1 weight percent (**wt**%), with an average of 0.2 wt% (0.2 wt% **avg.**), and is detailed in the Year One Report (Curtin University, 2023). TOC for the fresher rock samples averaged 0.04 wt% (varied between 0.03 – 0.05 wt%).

Samples (surface and fresher rock) were Soxhlet extracted (72 hours with dichloromethane:methanol solvent; DCM:MeOH, 9:1 vol./vol.). The obtained total lipid extract (**TLE**) was fractionated by small-scale silica gel liquid chromatography into a saturated hydrocarbon fraction, an aromatic hydrocarbon fraction and a polar fraction.

The TLE varied between 0.4 and 8.3 mg (on average 1.7 mg). After fractionation the TLE of the rock surface samples consisted mainly of polar compounds on average representing 75.4% (ranging between 39.8 - 95.2%) of the TLE. Saturated hydrocarbons averaged 20% (ranging between 3.3 and 59.3%) while the aromatic hydrocarbons ranged between 0 and 24% (4.4% avg.) (see Appendix Figure *A-1* saturated, aromatic and polar fraction (%) with TLE (mg)).

The TLE of the fresher rock samples ranged between 0.03 and 0.12 mg (0.03 mg avg.). After fractionation the masses of saturated, aromatic, and polar fractions ranged between 0 and 0.04 mg.

As reported in the Year One Report (Curtin University, 2023), representative vegetation samples were collected for analysis and as a fuel source for biomass combustion experiments. In addition, smoke sampling was conducted during a combined MAC/DBCA cultural burn at Conzinc Bay. These analyses are still in progress and results will be included in future reports.

Analyses

The samples were analysed by a range of instrumentation detailed below (Table *4.1-2*).

Table 4.1-2: Status of analyses in the rock surface and fresher rock samples.

Instrumentation	**Rock Surface Samples**			
		Fraction		
	Bulk	**Saturated**	**Aromatic**	**Polar**
GC-MS	NA	✓	✓	in progress
GCxGC-TOFMS	NA		tested	
GC-TQ	NA	in progress		
GC-irMS (carbon)	NA	in progress	tested	
PY GC-MS	in progress	NA	NA	NA
EA - δ^{13}C(‰)	✓	NA	NA	NA
TOC	✓	NA	NA	NA
	Fresher Rock Samples			
		Fraction		
	Bulk	**Saturated**	**Aromatic**	**Polar**
GC-MS	NA	✓	✓	in progress
GCxGC-TOFMS	NA	NA	NA	NA
GC-TQ	NA	NA	NA	NA
GC-irMS (carbon)	NA	NA	NA	NA
PY GC-MS	in progress	NA	NA	NA
EA - δ^{13}C(‰)	NA	NA	NA	NA
TOC (wt%)	✓	NA	NA	NA

Note: NA denotes not applicable.

4.1.4 Bulk sample analysis

The TOC analyses of the surface samples and fresher rock samples have been completed. The TOC of all rock surface samples ranged between 0.04 and 1 wt%, averaging 0.24% (Curtin University, 2022). TOC of the fresher rock samples averaged 0.04 wt% (ranging from 0.04 – 0.05 wt%).

The stable carbon isotope ratios ($^{13}C/^{12}C$, $\delta^{13}C$) can provide an insight into the source of organic matter and the formation pathways of biomarkers. Measurement of the bulk stable $^{13}C/^{12}C$ of the rock surface samples have been completed. Results were obtained for 59 of the 64 samples. For five samples the carbon signal was outside the linear range of the instrument due to very low % TOC of the samples ($<$ 0.09 wt%). This applied also to the fresher rock samples with TOC values all below 0.05 wt%, hence bulk $\delta^{13}C$ of the fresher rock samples has not been reported. The Pyrolysis Gas Chromatography-Mass Spectrometry (**PY-GC-MS**) analyses are in progress.

4.1.5 Gas chromatography - mass spectrometry analysis (GC-MS)

The GC-MS analysis of the saturated and aromatic hydrocarbon fraction has been completed while the analysis of the polar fraction is in progress.

4.1.5.1 Rock surface samples

Saturated hydrocarbon fraction

The biomarker analysis by GC-MS of the saturated fraction included *n*-alkanes and polycyclic terpenoids (e.g. hopanes and steranes).

The most abundant hydrocarbons in all samples are straight-chain *n*-alkanes. These compounds are ubiquitous and come from a wide range of sources, but the relative abundances of different *n*-alkane carbon numbers can provide an insight into their origin(s). In the samples *n*-alkane distribution varied but overall they were dominated by short-chain (*n*-C_{14}-*n*-C_{20}) and long chain *n*-alkanes (*n*-C_{27} – *n*-C_{33}), on average 47.6% (8.5 – 91.5%) and 35.9% (4.5 – 81.4%), respectively, compared to a lower abundance of mid-chain *n*-alkanes (*n*-C_{21}-*n*-C_{26}) on average 16.4% (1.8 – 38.4%) (Figure *4.1-1*).

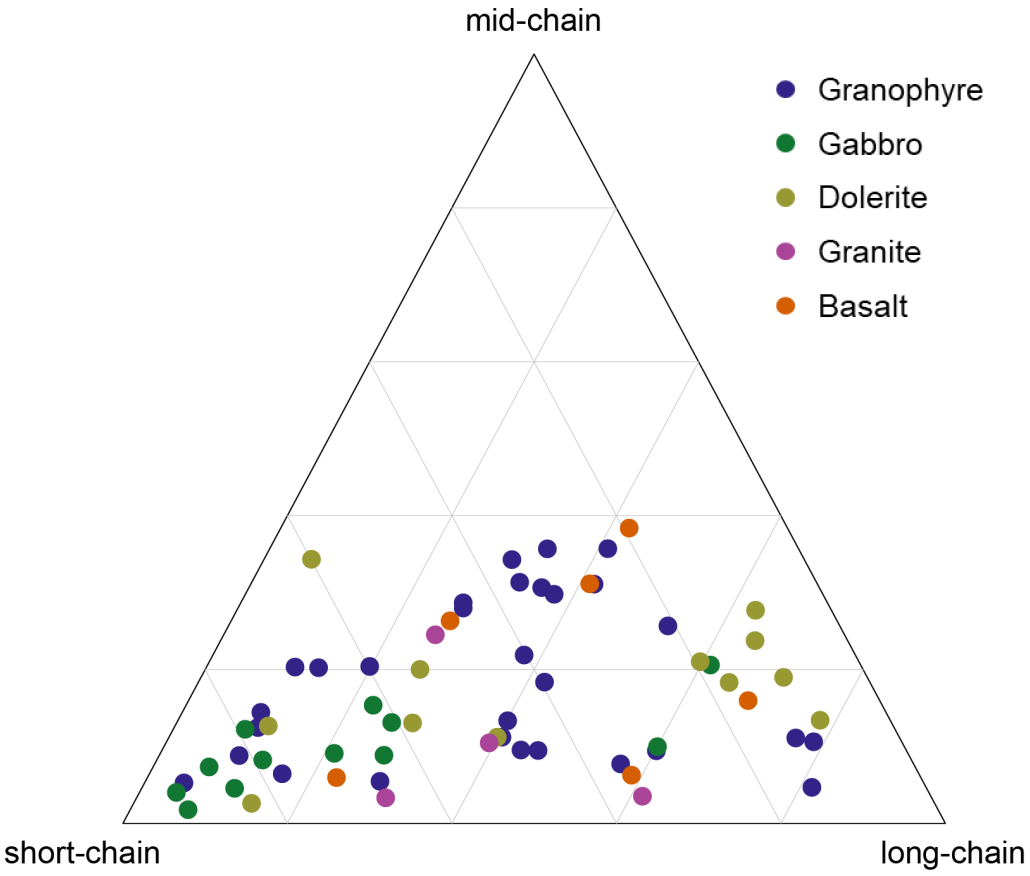

Figure 4.1-1: Ternary diagram of short (n-C_{14}-n-C_{20}), mid (n-C_{21}-n-C_{26}) and long chain n-alkanes (n-C_{27}-n-C_{33}) by rock type.

The chromatograms shown in Figures *4.1-2* to *4.1-4* are representative of the hydrocarbon distributions observed in the rock surface samples.

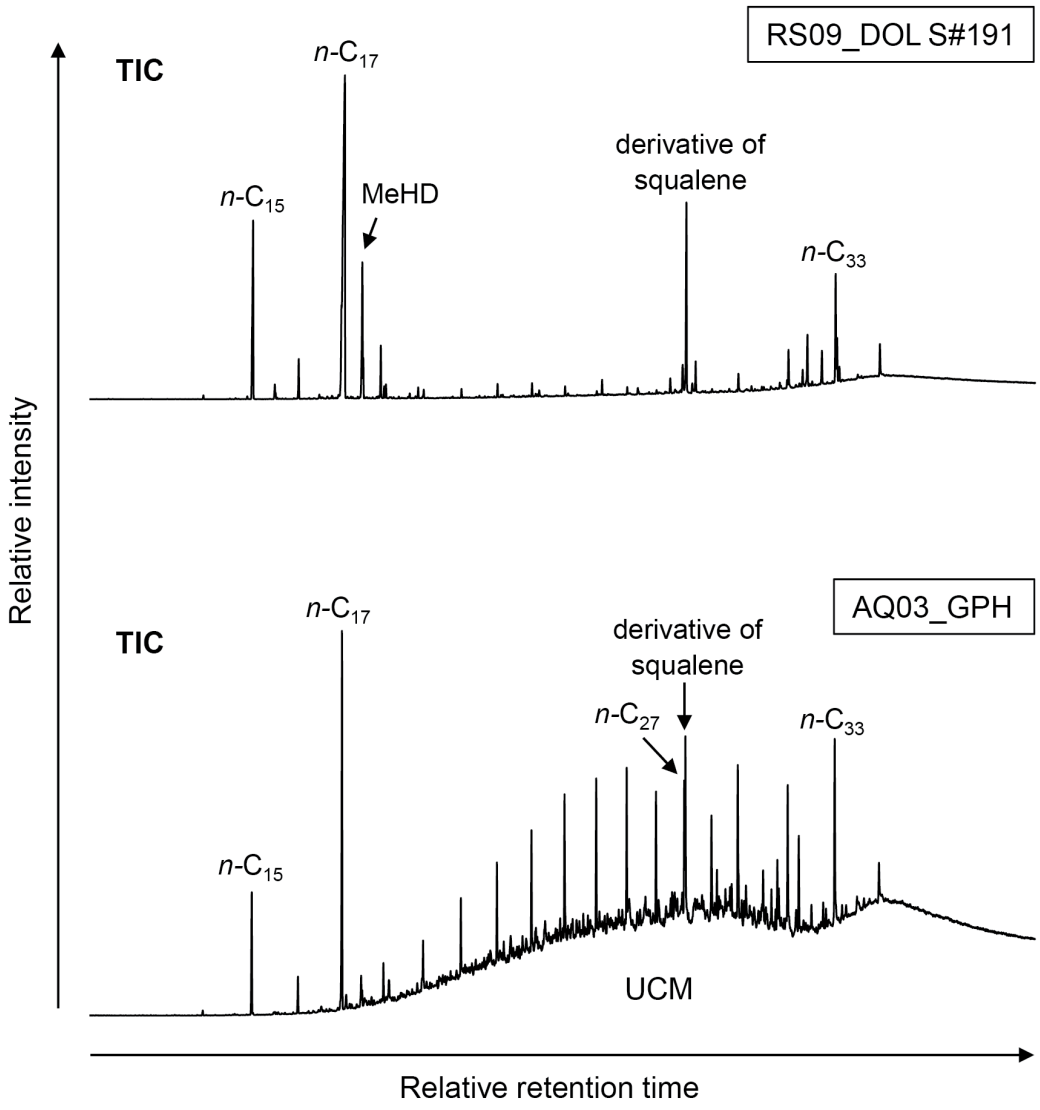

Figure 4.1-2: GC-MS total ion chromatograms (TIC) of the saturated fraction from rock surface sample RS09_DOL S#191 and AQ03_GPH, representative of samples analysed. Observed ions ranged from m/z 50 to m/z 550. The highly raised baseline in AQ03_GPH is due to a large unresolved complex mixture of hydrocarbons (UCM) compared to the only slightly typical raised baseline in RS09_DOL S#191.

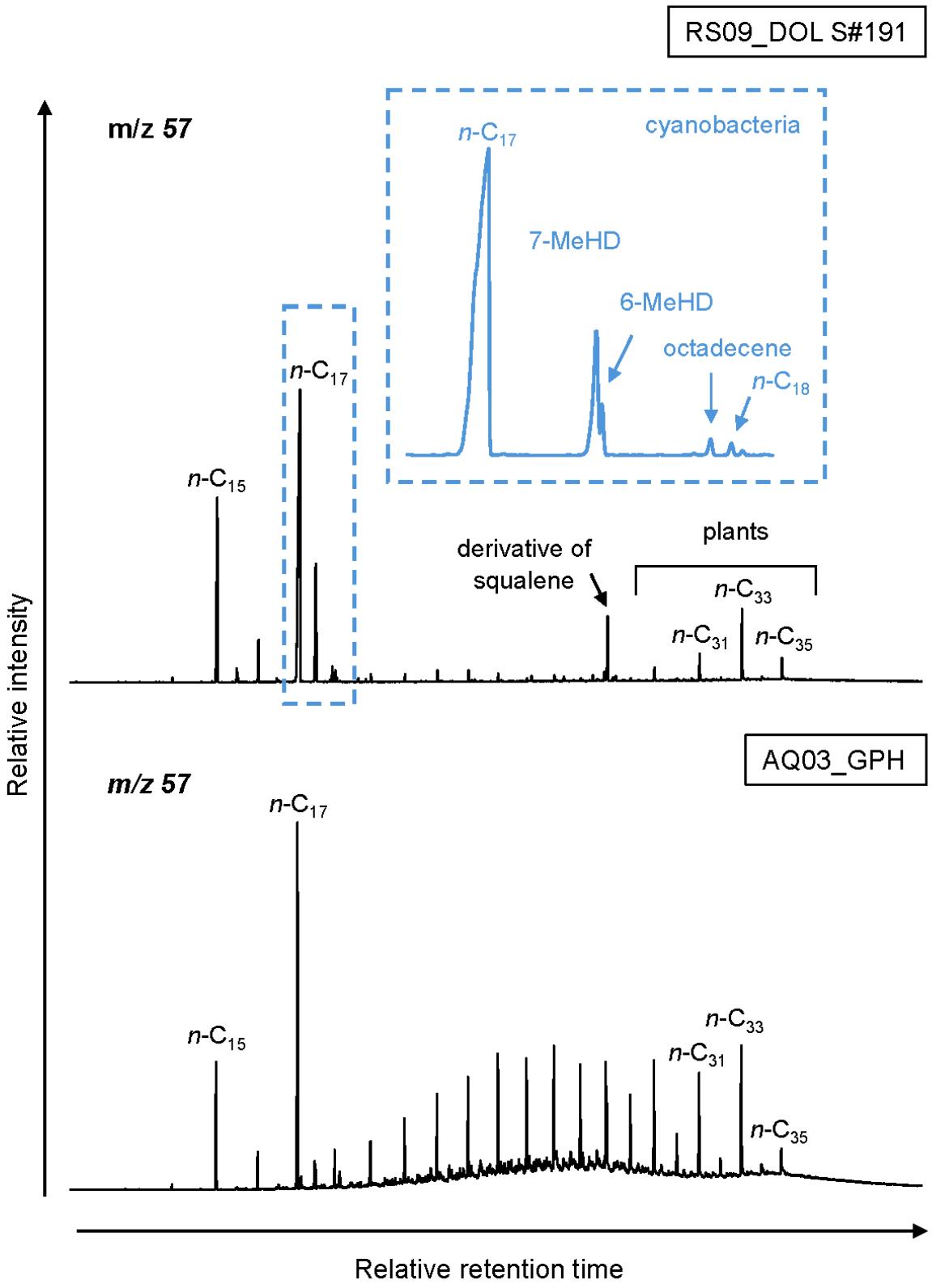

Figure 4.1-3: GC-MS chromatograms of saturated fraction. Extracted ion m/z 57 of sample RS09_DOL S#191 and AQ03_GPH.

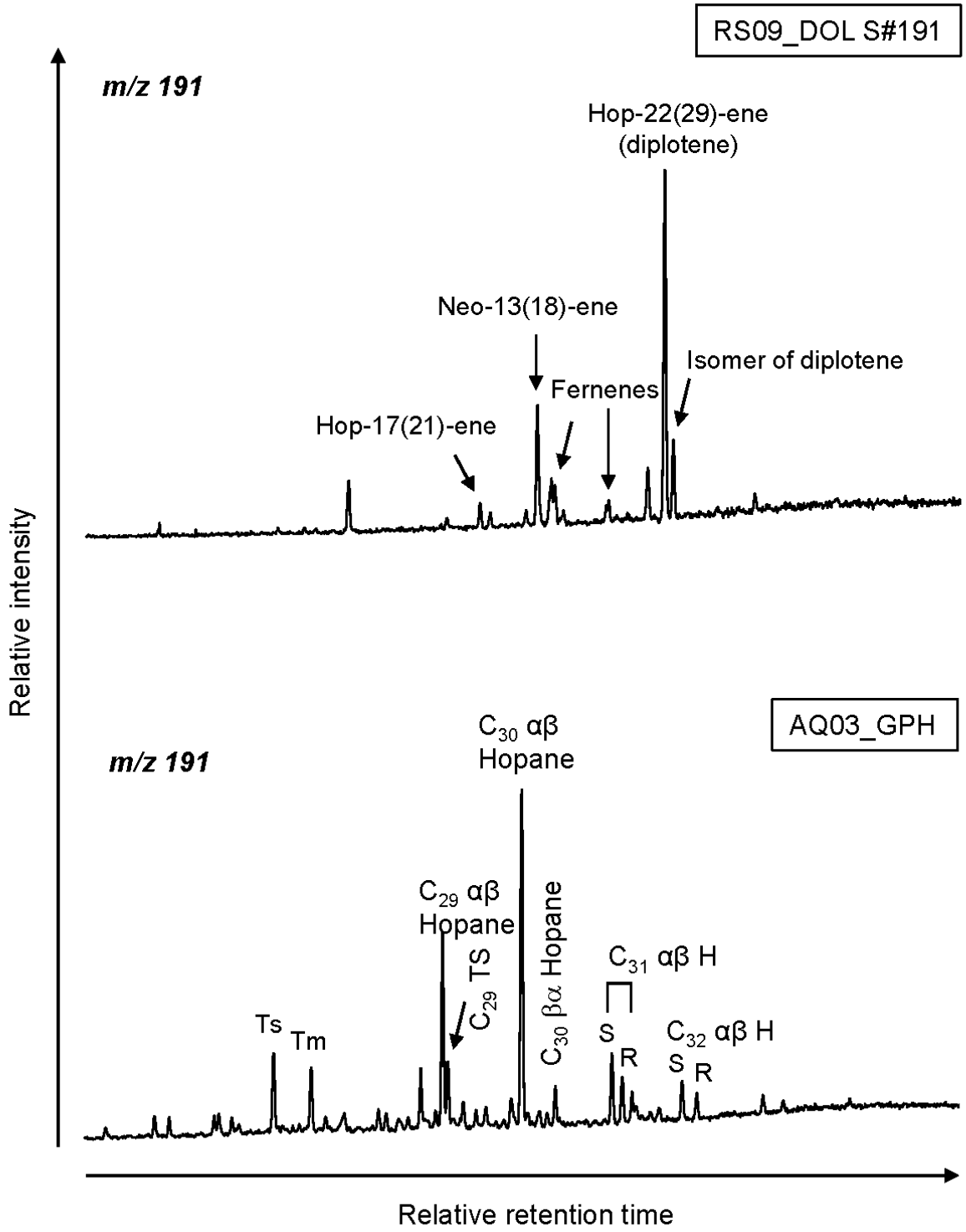

Figure 4.1-4: GC-MS chromatograms of saturated fraction. Extracted ion m/z 191 of sample RS09_DOL S#191 and AQ03_GPH.

The high abundance of heptadecane (*n*-C_{17}) together with 7- and 6-methyl-heptadecane (MeHD) are indicative of photosynthetic cyanobacteria (Hoshino and George, 2015; Kaiser et al., 2020) (Figure *4.1-3*). Such compounds have been previously observed on the surface of samples collected from the Pilbara (Hoshino and George, 2015). The abundant long-chain *n*-alkanes can be attributed to terrestrial plants (Grice and Eiserbeck, 2014; Bush and McInerney, 2013).

Hopanes/hopenes with carbon numbers greater than C_{31} largely derive from the cell membrane lipids of phototrophic cyanobacteria, whereas those less than C_{31} are derived predominantly from bacteria (*e.g.* Atahan et al. (2007)). However, C_{30} hopanes/hopenes/fernenes can also be from land plants and are referred to as phytohopanoids (Ageta et al., 1964; Tripp et al., 2023).

For example, RS09_DOL showed a high relative abundance of hopenes including diplotene, *nor*hopanes, fernenes and C_{30} hopanes which are ascribed to plants and bacteria. In comparison, sample AQ03_GPH contains extended hopanes (C_{31+}) and *n*-C_{15}/*n*-C_{17} alkanes attributed to cyanobacteria. Further, *nor*hopanes, C_{29} and C_{30} hopanes are observed from bacteria and/or plants (Figure *4.1-4*).

All rock surface samples showed very low concentrations of steranes and only a few contained appreciable abundances of steranes using the GC-MS conditions applied to the sample suite. These include C_{27} - C_{29} steranes from algae (C_{27}), fungi (C_{28}) and land plants (C_{29}) (Grice and Eiserbeck, 2014).

However, more sophisticated analyses for all biomarkers (steranes and hopanes) with a higher sensitivity and selectivity (*e.g.* deconvolute signals) will be carried out on all samples later.

Aromatic hydrocarbon fraction

The aromatic fraction can contain a range of low-molecular-weight aromatics *e.g.* phenanthrene and high-molecular-weight polycyclic aromatic hydrocarbons (**PAH**s). PAHs derive from a range of sources not limited to combustion sources from *e.g.* forest fires, hydrothermal sources, and/or natural products (*e.g.* Grice et al. (2009); Holman et al. (2014)).

Most of the samples lack typical aromatics like phenanthrene and PAHs. Most of the samples contain squalene, and a series of dihydrogenated squalene compounds possibly from natural sources e.g. aquatic sources and/or bacteria (Peters et al., 2005)(Figure *4.1-5*). A few samples showed an abundant unresolved complex mixture (**UCM**) – containing thousands of compounds that cannot be separated or identified by one dimensional GC-MS analysis. Reliable identification of compounds within the UCM is challenging and thus requires the use of 2D gas chromatography – time of flight mass spectrometry (**GCxGC-TOFMS**) to deconvolute the UCM and identify specific compounds (Figure *4.1-5*).

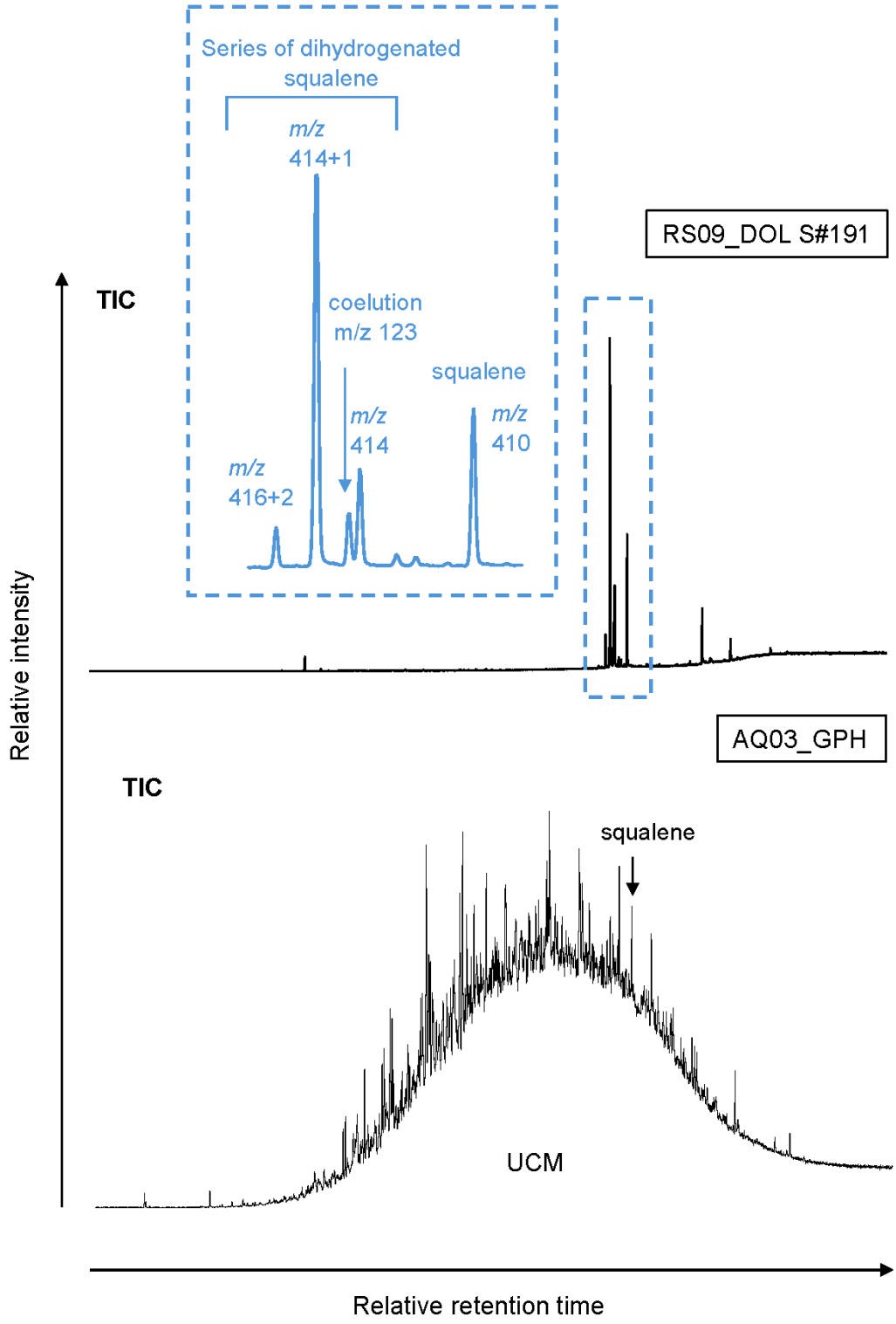

Figure 4.1-5: GC-MS total ion chromatograms (TIC) of the aromatic fraction from rock surface sample RS09_DOL S#191 and AQ03_PH, representative of samples analysed. Observed ions ranged from m/z 50 to m/z 550. Unresolved complex mixture (UCM).

Polar fraction

The GC-MS analyses of the polar fraction is still in progress.

4.1.5.2 Fresher surface samples

The GC-MS analyses of the saturated and aromatic fraction showed no compounds above detection limits - except for some *n*-alkanes in negligible abundance (Appendix Figure *A-2* and *A-3*). Based on these analyses a contribution of organics from the interior to the surface sample can be eliminated. Analysis of the polar fraction is ongoing.

4.1.5.3 Statistical analysis of organic chemistry results

A statistical analysis of TOC and delta 13 C (δ^{13}C) results by site and spatially is given in Section 7.9.

4.2 Geology and inorganic geochemistry laboratory analysis

4.2.1 Objectives

Investigations conducted during the second year of the research were designed to achieve the objectives of the MRAMP monitoring studies plan (point 2, Section 1.3 of the MSDCA Plan (Curtin University, 2022)), to answer the specific questions outlined in Section 4.2.9 of the Year One Report (Curtin University, 2023), based on the preliminary results presented within Section 4.3 of the Year One Report (Curtin University, 2023), and are described in Section 3.2 of this report as part of the fieldwork summary.

4.2.2 Methodology

Inorganic geochemistry laboratory methodologies are described in Section 3.3.2 of the MSDCA Plan (Curtin University, 2022) and the component study methodology statement:

- COPP21065-PRO-G-114 Murujuga Rock Art Monitoring Program: Inorganic Geochemistry Laboratory Analysis.

4.2.3 Geological mapping

Table *4.2-1* displays the geological mapping status for MRAMP study sites.

Table 4.2-1: Geological mapping status for MRAMP study sites.

Site name	Geological map	Site name	Geological map	Site name	Geological map	Site name	Geological map
AQ02_GPH	Completed	RS01_GPH	Completed	EX02_GPH	to be completed	AS-01	to be completed
AQ03_GBR	Completed	RS02_GBR	Completed	EX03_GPH	Completed	AS-02	Completed
AQ03_GPH	Completed	RS03_GPH	to be completed	EX04_GBR	Completed		
AQ03_DOL	Completed	RS04_GBR	Completed	EX05_GPH	Completed		
AQ04_GPH	Completed	RS04_GPH	Completed	EX06_GPH	Completed		
AQ05_GPH	Completed	RS05_GPH	Completed	EX07_GPH	Completed		
AQ06_GBR	Completed	RS06_GPH	Completed	EX08_GPH	to be completed		
AQ06_GPH	Completed	RS07_BAS	to be completed	EX09_GBR	Completed		
AQ07_GPH	to be completed	RS08_DOL	to be completed	EX09_GPH	to be completed		
AQ07_GRT	Completed	RS08_BAS	Completed				
AQ08-GPH	to be completed	RS09_DOL	to be completed				
AQ09_GBR	Completed	RS09_BAS	to be completed				
AQ09_GPH	to be completed	RS10_GBR#4	Completed				
AQ10_GPH	Completed	RS10_GBR#110	Completed				
AQ11_GPH	Completed	RS11_GPH	to be completed				
AQ12_BAS	to be completed	RS13_GBR	to be completed				
AQ13_GPH	Completed	RS14_GPH	Completed				
AQ14_GPH	Completed	RS16_GBR	Completed				
AQ15_GBR	Completed	RS17_GPH	Completed				
AQ16_GBR	Completed	RS18_GPH	Completed				
AQ17_GPH	Completed						
AQ18_GPH	Completed						

4.2.4 X-ray diffraction

The analysis of powdered material comprising the weathered rind and patina by X-ray diffraction (**XRD**) has continued during the second year of research. At the time of this report, the team has completed the analysis and phase identification of 25 granophyre, seven gabbro, three granite, five dolerite and four basalt samples. Of these, XRD quantitative analyses have been performed for 19 granophyre, three gabbro, two granite, two dolerite and two basalt samples. Processing of the data is still ongoing.

The procedure undertaken for the preparation of XRD samples is described in the *Murujuga Rock Art Monitoring Program: Inorganic Geochemistry Laboratory Analysis methodology* (COPP21065-PRO-G-114). Here the results obtained from the identification of mineral phases based on matching of diffraction patterns are summarised in Table *4.2-2* to *4.2-6*. Fluorite is the internal standard used for quantitative analysis of the mineral phases and is not present within the rock.

4.2.5 Macro to microstructural characterisation: fresher rock and weathered rind

Sixty-four thin sections were obtained from rock samples collected across the main five lithologies outcropping at Murujuga that host rock art engravings. Of these, 31 samples are granophyre, 11 gabbro, six granite, nine dolerite and seven basalt. The proportion of rock art occurring on each rock type is not known.

As discussed in the Year One Report (Curtin University, 2023), rocks of all lithologies outcropping at Murujuga are typically characterised by a three layered structure. On a vertical profile, the patina represents the outermost layer of the structure forming a thin external coating of the rocks. The weathered rind comprises the pale orange alteration zone of the rock that is transitional to the underlying fresher rock, which represents the bulk of the lithology.

This section provides a petrological, microstructural and modal description of the fresher rock and weathered rind for each rock type. The petrographic description of granophyre and gabbro provided in Year One Report (Curtin University, 2023) is expanded with additional microstructural and compositional data obtained during year two from a combination of optical microscopy, automated mineralogy (**TIMA**), powder X-ray diffraction, scanning electron microscopy (**SEM**), electron backscattered diffraction (**EBSD**), and electron microprobe (**EMP**). The micro-structures and the chemistry of the patina are described in a separate section of this report (Section 4.2.7.2).

In the TIMA analysis, the phase database comprises mineral end-members rather than solid solution phases and this should be taken into account while reading the report. Moreover, because in the TIMA the classification scheme for mineral identification is largely based on EDS spectra, mineral phases with very similar compositions, if not identical, cannot always be easily distinguished on the base of X-ray only (e.g. clays). Moreover, independently of the precision of the phase library, identification by TIMA-EDS of mineral grains smaller than 5 μm(such as clays, or patina-hosted minerals) is strongly challenged by overlapping of the incident electron beam interaction volume with adjacent grains. Because of these analytical limitations, some phases such as muscovite/illite are grouped together here. In addition, the composition of the Fe-rich patina can be very similar (or at least at the resolution of TIMA) to those of clays and, therefore, they are here grouped together. This compromise mitigates the risk of over- or under-estimation of the modes of Fe-rich patina and clay minerals.

Table 4.2-2: Compilation of identified minerals among the analysed XRD granophyre samples.

	Quartz	Fluorite	Albite	Microcline	Labradorite	Clinochlore	Chamosite	Zoisite	Clinozoisite	Epidote	Stilpnomelane	Pargasite	Kaolinite	Senegalite	Muscovite	Illite	Hematite	Magnetite	Goethite	Jacobsite	Uraninite	Dickite	Nacrite	Indialite
AQ02	X	X	X	X		X							X											
AQ03	X		X	X		X		X									X							
AQ04	X	X	X	X													X							
AQ05	X	X	X	X	X	X								X	X		X		X					
AQ07	X		X	X		X				X	X						X	X	X					
AQ08	X	X	X	X			X		X	X											X			
AQ09	X	X	X	X					X													X		
AQ10_1	X	X	X	X											X		X						X	
AQ10_2	X		X	X		X									X	X	X						X	
AQ11_1	X	X	X	X		X																		
AQ11_2	X		X	X		X						X			X	X								
AQ13	X	X	X	X																				
AQ14	X	X	X	X		X									X									
AQ18	X		X	X		X									X	X		X						
EX03	X	X	X	X		X											X							
EX05	X	?	X	X													X							
EX06	X	X	X	X		X							X				X	X						

	Quartz	Fluorite	Albite	Microcline	Labradorite	Clinochlore	Chamosite	Zoisite	Clinozoisite	Epidote	Stilpnomelane	Pargasite	Kaolinite	Senegalite	Muscovite	Illite	Hematite	Magnetite	Goethite	Jacobsite	Uraninite	Dickite	Nacrite	Indialite
EX08	X	X	X	X		X														X				
EX09	X	X	X	X									X											
RS01	X	X	X	X		X											X							
RS04	X	X	X	X		X			X								X							
RS05	X	X	X	X													X							
RS06	X	X	X	X					X								X							
RS11	X	X	X	X											X		X							
RS17	X		X	X		X					X													X

Table 4.2-3: Compilation of identified minerals among the analysed XRD gabbro samples.

	Quartz	Fluorite	Augite	Enstatite	Albite	Labradorite	Anorthite	Clinochlore	Clinozoisite	Actinolite	Epidote	Muscovite	Illite	Kaolinite	Vermiculite	Chabazite	Magnetite	Birnessite	Rutile	Indialite	Willemseite	Gibbsite	Sphalerite	Galena
AQ15_1	X		X			X		X	X			X		X		X								
AQ15_2	X		X				X	X	X	X		X	X	X	X		X				X	X		
EX04	X	X	X			X		X	X	X		X						X						
EX09	X	X	X		X			X	X	X		X												
RS02	X	X	X		X			X	X	X		X						X						
RS04	X			X			X	X				X				X							X	X
RS13	X		X		X	X		X			X		X			X			X	X				

Table 4.2-4: Compilation of identified minerals among the analysed XRD granite samples.

	Quartz	Fluorite	Albite	Microcline	Clinochlore	Epidote	Phlogopite	Kaolinite	Stilpnomelane	Illite	Rutile	Galena	Ilmenite	Birnessite	Diaspore	Muscovite
AQ07	X	X	X	X	X											
AS02	X		X	X	X				X	X	X	X	X		X	
RS03	X	X	X	X		X	X	X						X		x

Table 4.2-5: Compilation of identified minerals among the analysed XRD dolerite samples.

	Quartz	Fluorite	Albite	Microcline	Augite	Diopside	Clinochlore	Chamosite	Clinozoisite	Hedembergite	Actinolite	Muscovite	Illite	Montmorillonite	Titanite	Hematite	Goethite	Magnetite	Halite	Berlinite
AQ05_1	X	X	X			X	X		X		X	X								
AQ05_2	X		X				X		X	X	X	X			X			X		
AQ05_3	X		X				X		X		X		X		X	X				
AS01_1	X	X	X		X			X			X	X								
AS01_2	X		X		X		X		X		X		X	X	X					
AS02	X		X		X			X	X		X					X	X	X		
RS04	X			X					X									X	X	X

Table 4.2-6: Compilation of identified minerals among the analysed XRD basalt samples.

	Quartz	Fluorite	Albite	Augite	Clinochlore	Chamosite	Clinozoisite	Actinolite	Muscovite	Kaolinite	Titanite	Spinel	Magnetite	Hematite	Halite	TiO_2	Birnessite
AQ12	X	X	X		X			X			X						X
RS08	X		X	X	X	X	X	X	X			X					
RS12	X	X	X			X		X			X		X				
RS15	X									X				X	X	X	

4.2.5.1 Granophyre

Thirty-one granophyre samples have been investigated by optical microscopy and automated mineralogy (TIMA). Of these, 21 have also been observed by SEM to further resolve fine-grained microstructures of the rock. For the mineral composition, 26 powder samples have been analysed by XRD and three using EMP to obtain representative mineral compositions.

Fresher rock

The granophyre fresher rock is fine-grained, felsic, holocrystalline, and aphanitic or porphyritic (Figure *4.2-1*). Mineralogically, the rock is dominated by quartz (~40 vol.% avg.), albite ($An_1Ab_{99}Or_0$, ~32 vol.%) and microcline ($An_0Ab_2Or_{98}$, ~15 vol.% avg.) (Figure *4.2-12*, and Appendix Tables *B-1* to *B-16*). Minor phases are chlorite (clinochlore) and epidote (clinozoisite). Stilpnomelane, Ca- plagioclase (labradorite) and amphibole (pargasite) may be present. Accessory phases are Fe-oxides (hematite and magnetite), ilmenite, titanite, apatite and rare calcite, interpreted as secondary, which occur in variable amounts across the individual samples.

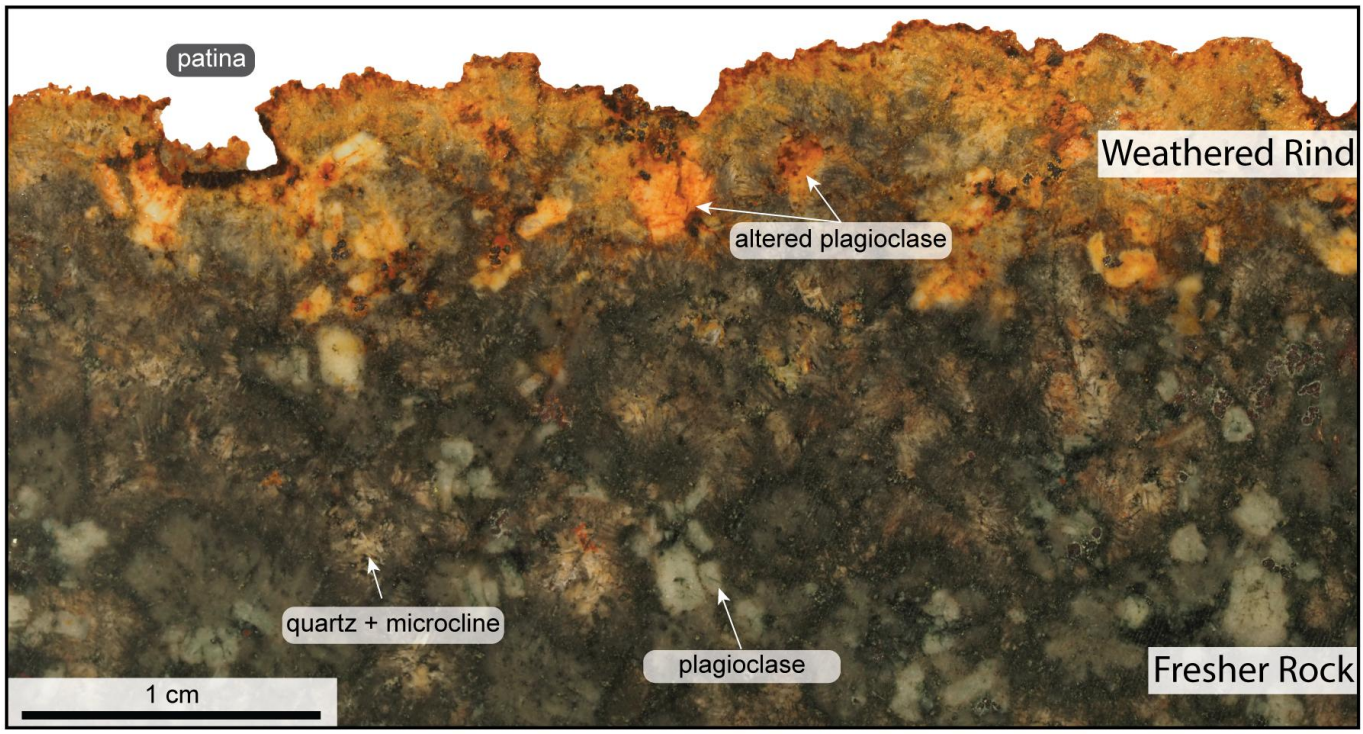

Figure 4.2-1: Core-to-rind cross-section photograph of granophyre rock billet AQ11_GPH. The transition from the fresher rock to the weathered rind domain is indicated by a progressive colour variation to pale orange due to the alteration of minerals present within the fresher rock. A reddish patina is visible as a rim on the outermost part of the profile and a darker patina is localised at the bottom of topographic depressions.

As already observed by previous studies (Ramanaidou and Fonteneau, 2019; Donaldson, 2011), and in the Year One Report (Curtin University, 2023), granophyre is microstructurally characterised by spectacular granophyric intergrowths of acicular quartz and alkali feldspar. Texturally, the rock is porphyritic and displays highly variable microstructural geometries amongst the groundmass

minerals (quartz, albite and microcline) depending on their crystal habits, grain size and relative abundances.

The porphyritic character of the rock is generally due to larger-grained (< 500 μm) subhedral to anhedral phenocrysts of albite (Figure *4.2-2*). Less frequently, plagioclase can be prismatic and elongated (e.g. sample AQ11_GPH). In the fresher rock, a later pervasive hydrothermal alteration of the rock is indicated by the extensive sericitization of plagioclase and abundant chlorite after biotite. Quartz occurs as acicular grains with variable length (usually < 1 mm) and as an anhedral mineral within the groundmass. Microcline is part of the groundmass and occurs with acicular and elongate quartz in the granophyric texture. Labradorite occurs locally within the groundmass, where it is generally associated with microcline. Pale green anhedral chlorite is widespread and large tabular crystals are associated with healed fractures within the rock. Epidote forms grains of variable size, and typically occurs with chlorite. Radiating clusters of bright orange stilpnomelane are present in some rocks (Figure *4.2-3*). Opaque minerals, namely hematite, magnetite and ilmenite, are widespread and commonly form isolated clusters throughout the rock.

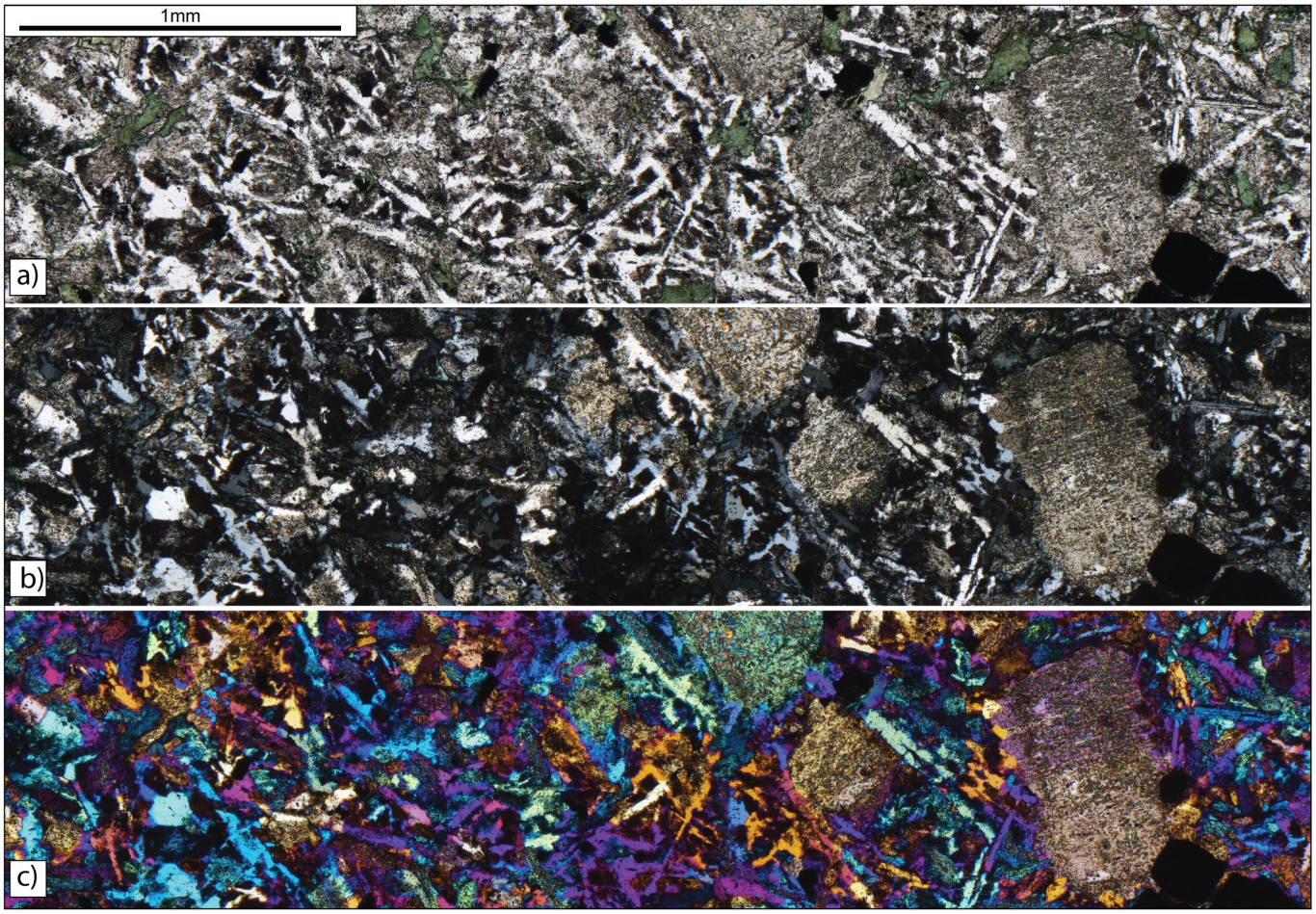

Figure 4.2-2: Plane-polarised (a), crossed-polarised (b) and crossed-polarised with γ-plate (c) photomicrograph of fine-grained spinifex texture in sample AQ06_GPH. Plagioclase phenocrysts characterised by sericite alteration are surrounded by a groundmass of quartz and microcline. Pale green chlorite (a) is widespread in the matrix.

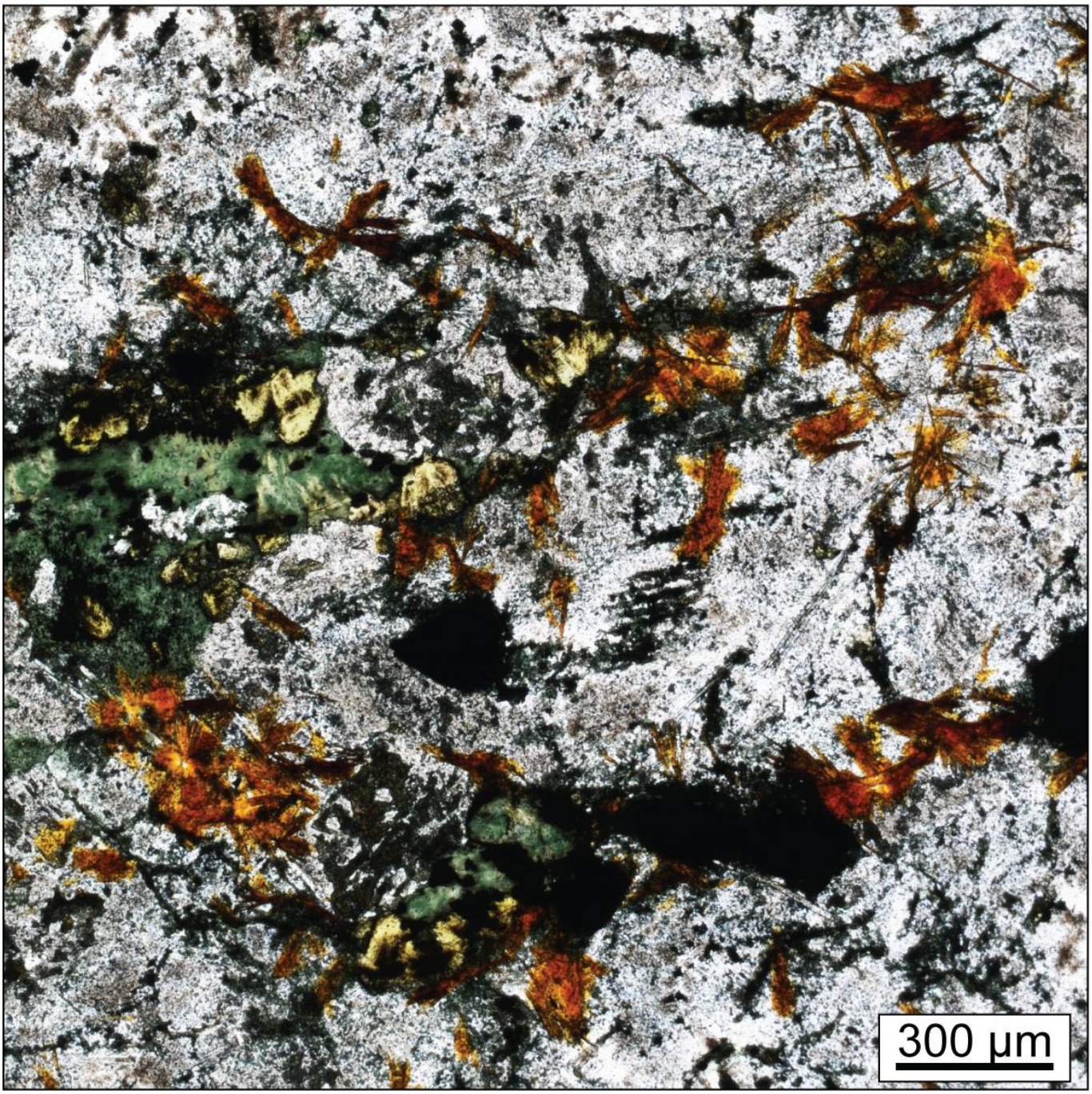

Figure 4.2-3: Photomicrograph of a portion of granophyre sample AQ17_GPH fresher rock displaying chlorite (green), tabular epidote (pale green) and bright orange stilpnomelane characterised by the typical acicular texture.

The texture of the rock can be broadly subdivided into two categories (i) fine-grained acicular or spinifex textures (e.g. samples AQ06, RS01; Figure *4.2-2*) and (ii) fine-grained radiating textures (e.g. samples AQ13, AQ14, RS06; Figure *4.2-4*). The acicular texture is defined by elongated prisms of quartz, and, to a minor extent, chlorite, within a groundmass of alkali feldspar. As suggested in the Year One Report (Curtin University, 2023), the elongated quartz may originally

have formed as tridymite.

The radiating texture is characterised by micro-aggregates of acicular quartz, albite and microcline that project into the surrounding felsic groundmass and are often surrounded by coronae of chlorite and/or epidote. These aggregates, up to 1 mm in diameter, are heterogeneously distributed to give the rock a patchy appearance. This texture resembles the spherulitic structures that are commonly observed in basalts. The spheroidal texture may be interpreted as quench devitrification after magma cooling.

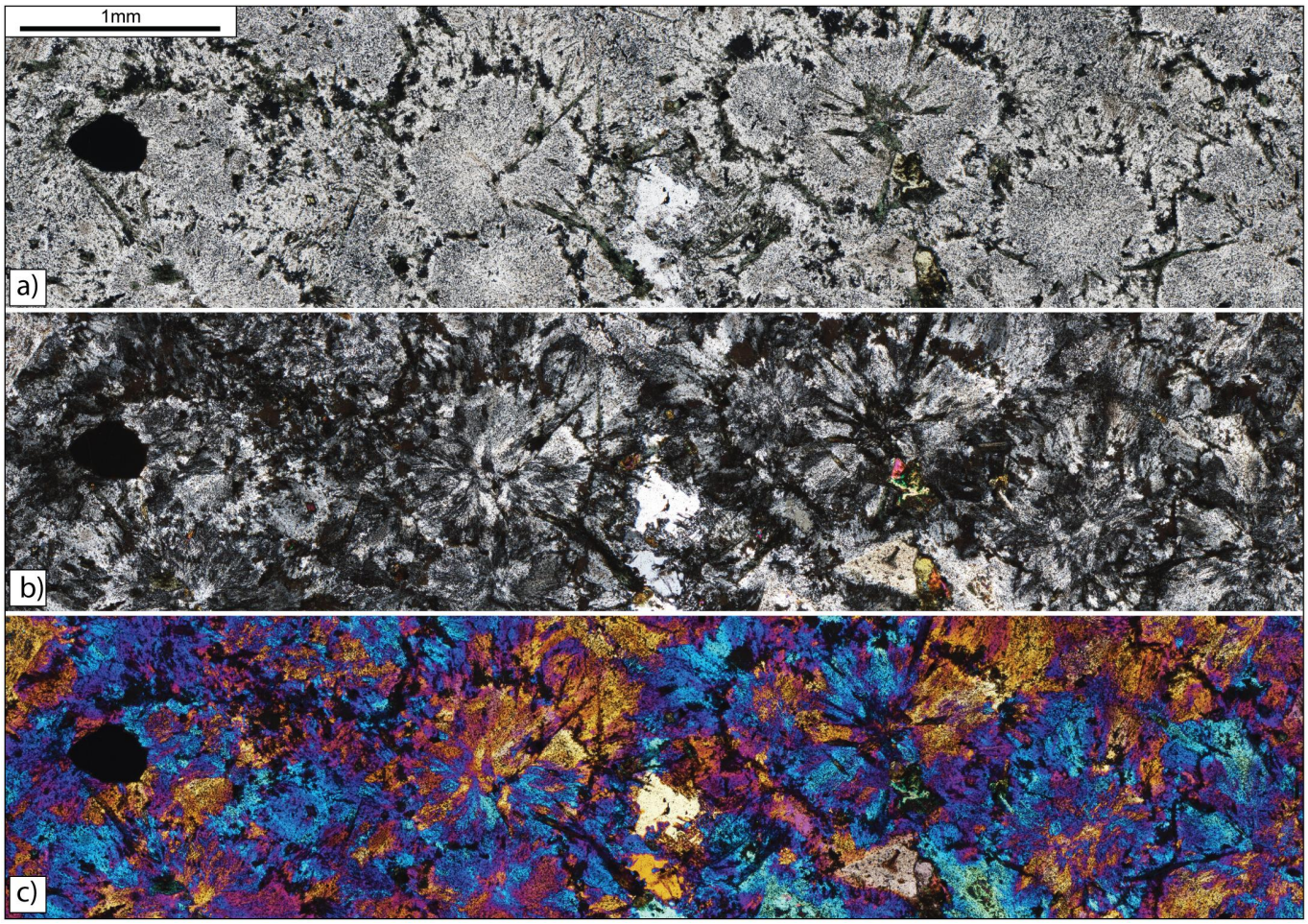

Figure 4.2-4: Plane-polarised (a), crossed-polarised (b) and crossed-polarised with γ-plate (c) photomicrograph of radial texture in sample AQ13_GPH. Pale green chlorite (a) forms coronae around the felsic intergrowth. High birefringent epidote (b) is associated with chlorite in the matrix.

Weathered rind

In cross-section, granophyre weathered rind is optically distinguished by a pale orange to reddish horizon localised within the first few millimetres from the sample surface (Figure *4.2-1*). Amongst the 31 granophyre samples, the extent of this layer is highly variable, from barely present up to $\sim$5mm thick. Optical microscopy observations indicate that the colour variation is related to oxidation and clay alteration of albite and microcline, which confers a paler orange colouration, whereas chlorite and epidote vary from green to brown (Figure *4.2-5*). Grain and phase boundaries

are highlighted by more intense colouration, indicating pathways of localised clay formation.

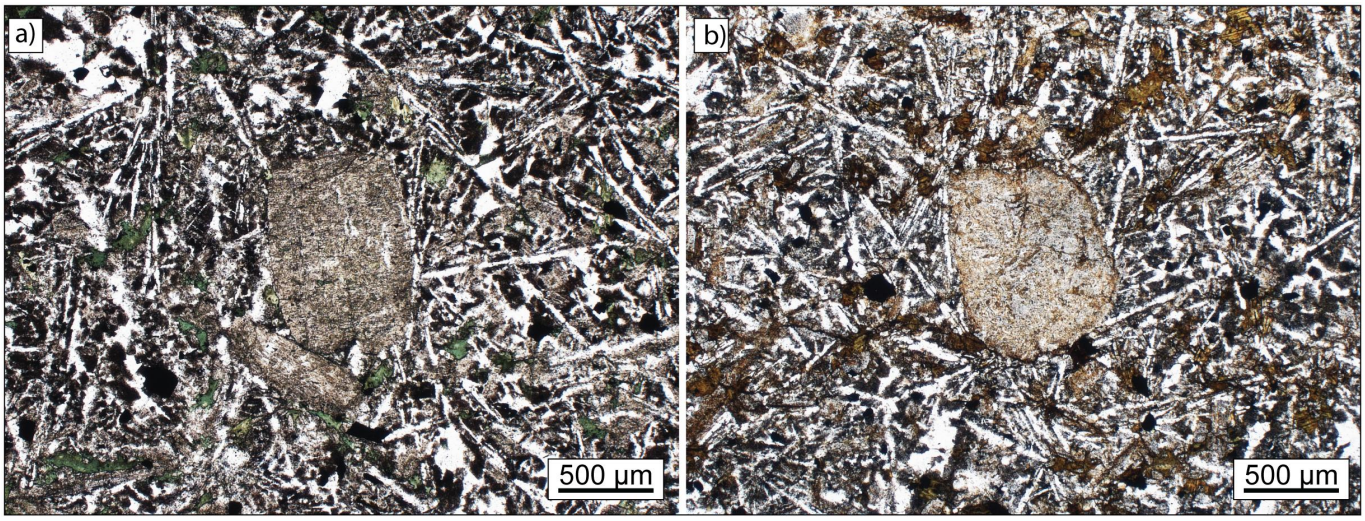

Figure 4.2-5: Plane-polarised photomicrograph of granophyre fresher rock (a) and weathering rind (b) from sample AQ06_GPH. From (a) to (b) the image shows the colour transition to pale orange and brown of large phenocrysts of albite and green chlorite as a consequence of their alteration.

Microstructurally, the weathered rind is characterised by trends of progressively enhanced porosity closer to the surface (Figure *4.2-7* to *4.2-9*). Backscattered and electron backscattered diffraction (EBSD) analyses indicate that sample porosity forms by preferential dissolution of matrix minerals such as albite and microcline while quartz remains substantially unchanged (Figure *4.2-7*). In particular, microcline dissolution leaves behind spectacular skeletal granophyric intergrowths that are now partially empty and surrounded by quartz (Figure *4.2-8*). Larger subhedral voids represent the locations of former albite phenocrysts.

In interpretation of these textures, the possibility of physical removal of portions of crystals by the mechanical stress induced by sample preparation in those regions where the grains are most altered, must be considered (e.g. Figure *4.2-6*). Locally, some samples exhibit planar fractures, often sub-horizontal, interpreted as a record of incipient flaking. These features are visible as isolated or partly isolated flakes in the epoxy resin used to embed the samples before the thin section preparation steps to prevent loss of unconsolidated material (see Section 3.3.2 of the MSDCA Plan (Curtin University, 2023) and COPP21065-PRO-G-114 *Murujuga Rock Art Monitoring Program: Inorganic Geochemistry Laboratory Analysis*).

Given the potential significance of porosity for patina stability, it is useful to consider features that unequivocally or strongly support the formation of porosity by mineral dissolution, and those that may be produced by sample preparation. Features likely to be produced by dissolution include:

- Preferential removal of soluble minerals, such as albite and microcline, where less soluble minerals, such as quartz, remain (e.g. Figure *4.2-8*). Mechanical removal is unlikely to produce this distinction.
- Voids that replicate the shape of a complex mineral. The complex and convoluted shapes of, for example, quartz–feldspar intergrowths, are difficult to produce by mechanical means.

- Gradation in porosity that consists of voids that replicate the shape of individual mineral grains from the fresher rock towards the patina.
- Pore sizes that match the grain size of the rock. Mechanical damage is likely to produce larger voids that cross-cut multiple grains.
- Retention of internal structures, such as exsolution lamellae and cleavage or twin planes that are replaced by other phases. Mechanical damage is unlikely to produce this distinction.
- The formation of gaps between some mineral pairs, such as quartz–feldspar, but not others, such as quartz–quartz (e.g. Figures *4.2-19* and *4.2-27*(b,c)).
- The presence of precursors to mineral dissolution, such as the formation of edge pits and irregular grain boundaries (e.g. Figure *4.2-27*).
- The presence of soft minerals, such as sheet silicates (clays, white micas) adjacent to voids. Mechanical damage would remove these soft minerals as well as the adjacent phase.

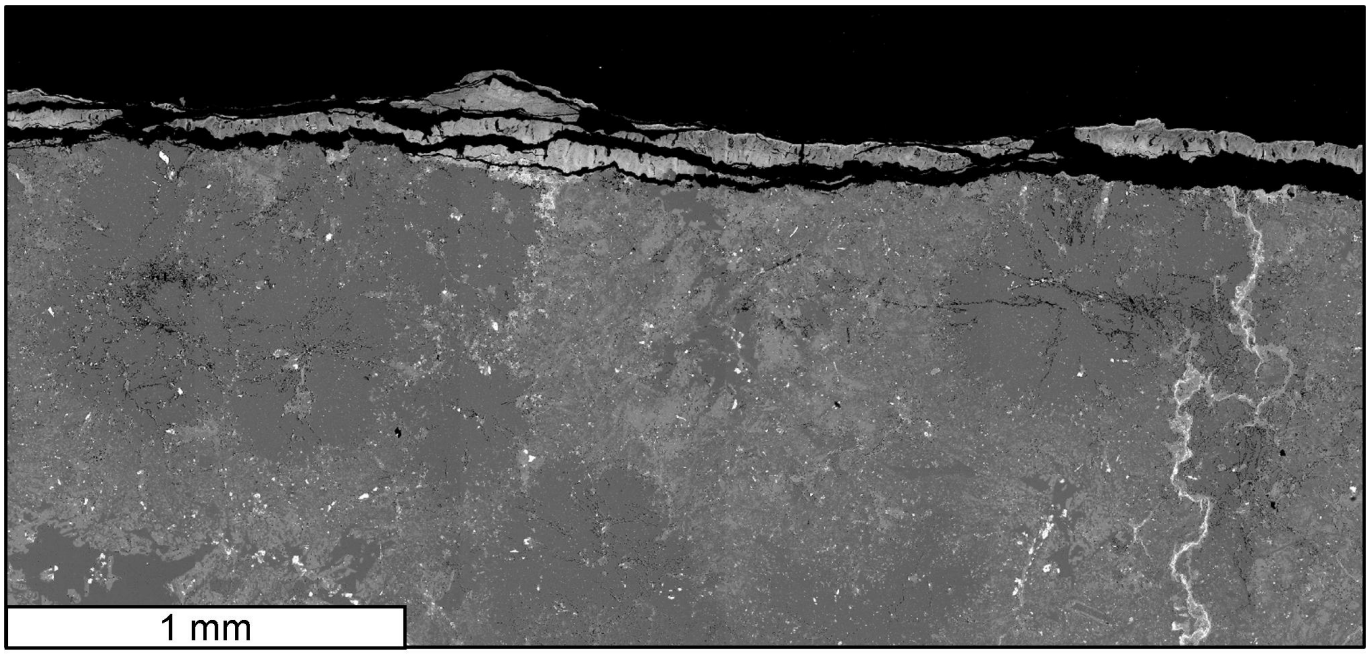

Figure 4.2-6: TIMA-BSE image of patina on granophyre sample AQ14_GPH. The image shows the detachment and internal delamination of the patina from the poorly weathered substrate as a result of sample preparation.

In contrast, features produced by mechanical damage typically form parallel to the patina– weathered rind interface, cross-cut multiple grains, and show planar or close-to-planar interfaces (e.g. Figure *4.2-6*).

At the grain scale, albite is internally characterised by higher densities of etch pits and irregular grain boundaries (Figure *4.2-9*). In places, the mineral is replaced by fine-grained aggregates of kaolinite, illite and muscovite (Figure *4.2-9*). Similarly, microcline is altered and dissolution is indicated by irregular grain boundaries. Importantly, voids along grain boundaries are ubiquitous around the most altered albite grains. These microstructural observations indicate that dissolution of albite and/or microcline is not stoichiometric and mass is not conserved.

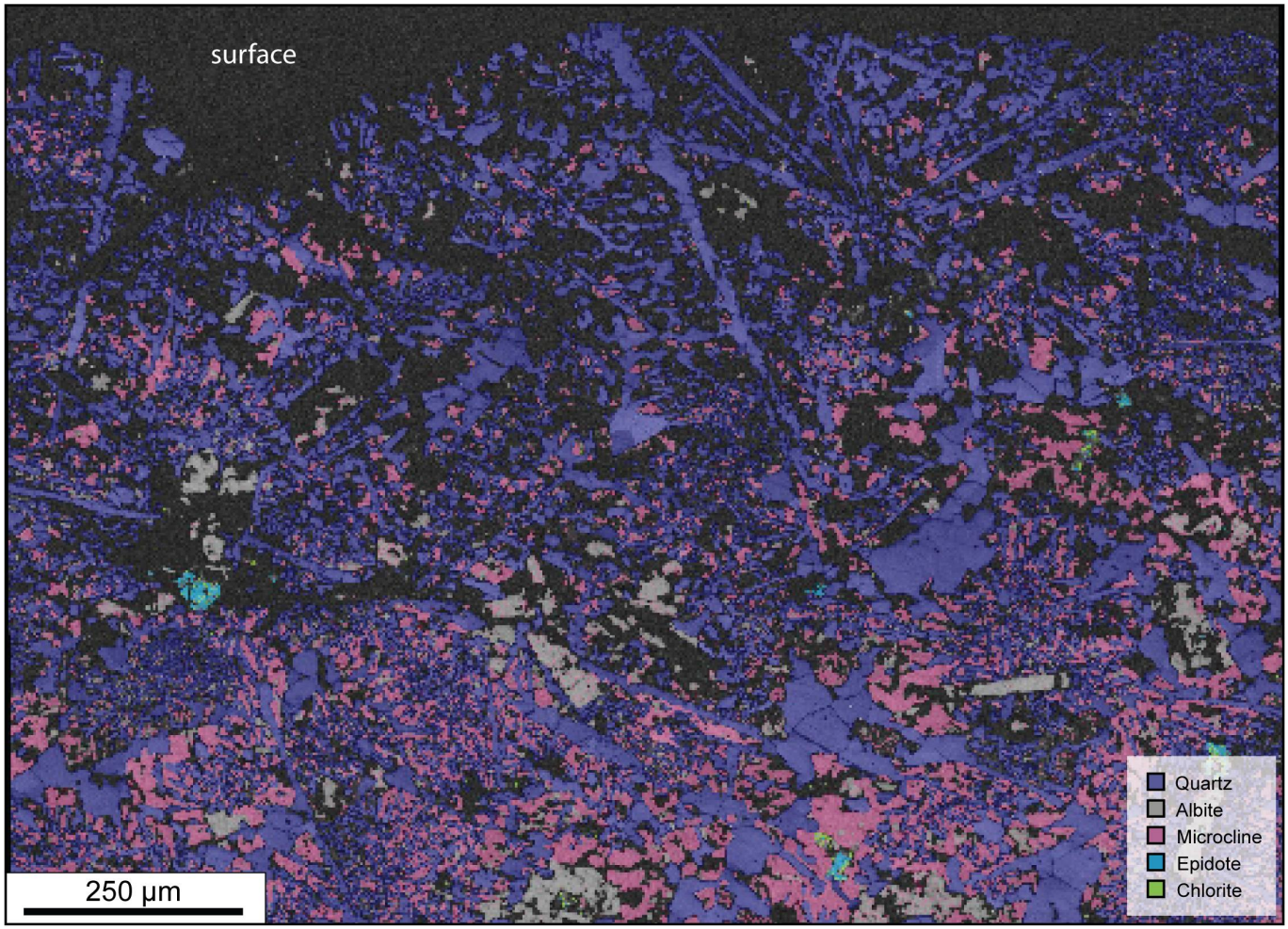

Figure 4.2-7: EBSD phase map of weathered rind-fresher rock transition in granophyre sample AQ08_GPH. Microporosity is generated by the progressive disappearance of plagioclase and microcline, moving from the fresher rock (bottom of the image) towards the surface.

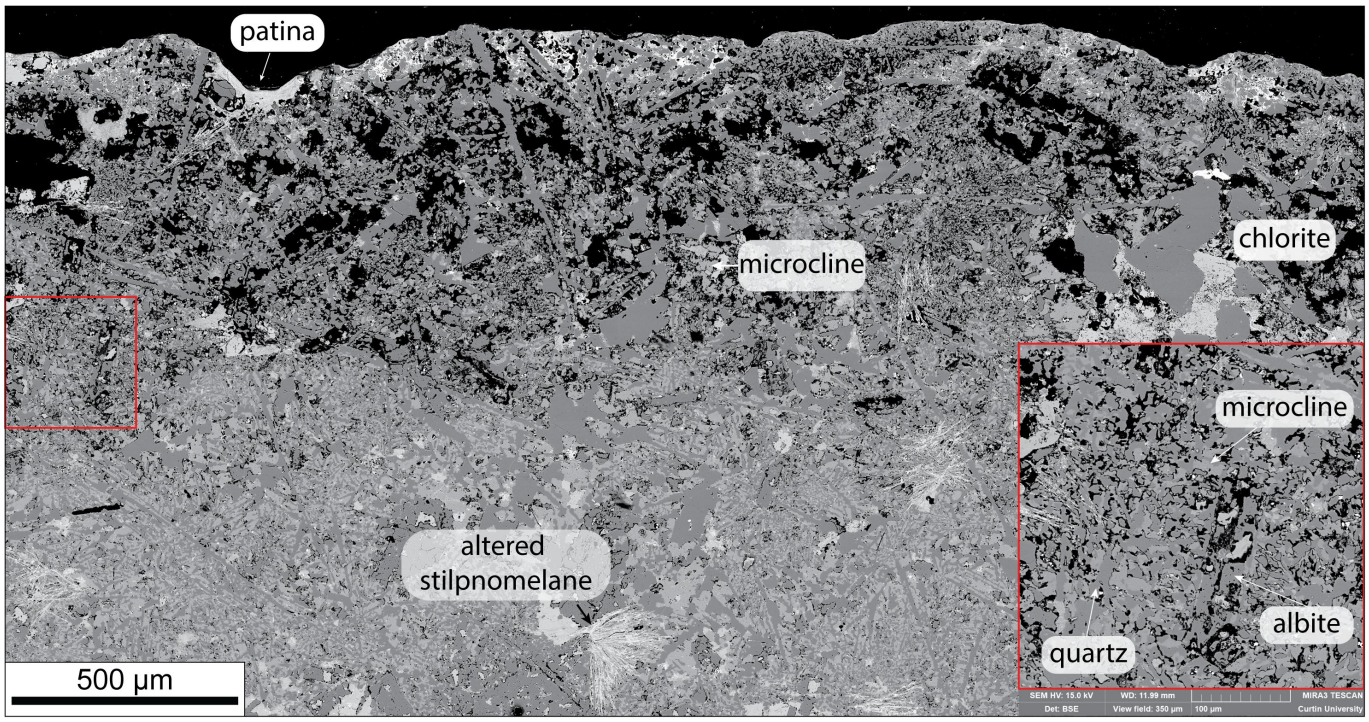

Figure 4.2-8: BSE-SEM large area panorama of the transition region between fresher rock-weathered rind-patina from sample AQ08_GPH. The weathered rind is characterised by enhanced microporosity and the alteration of minerals present within the fresher rock. The red box indicates the location in the image of the close-up inset.

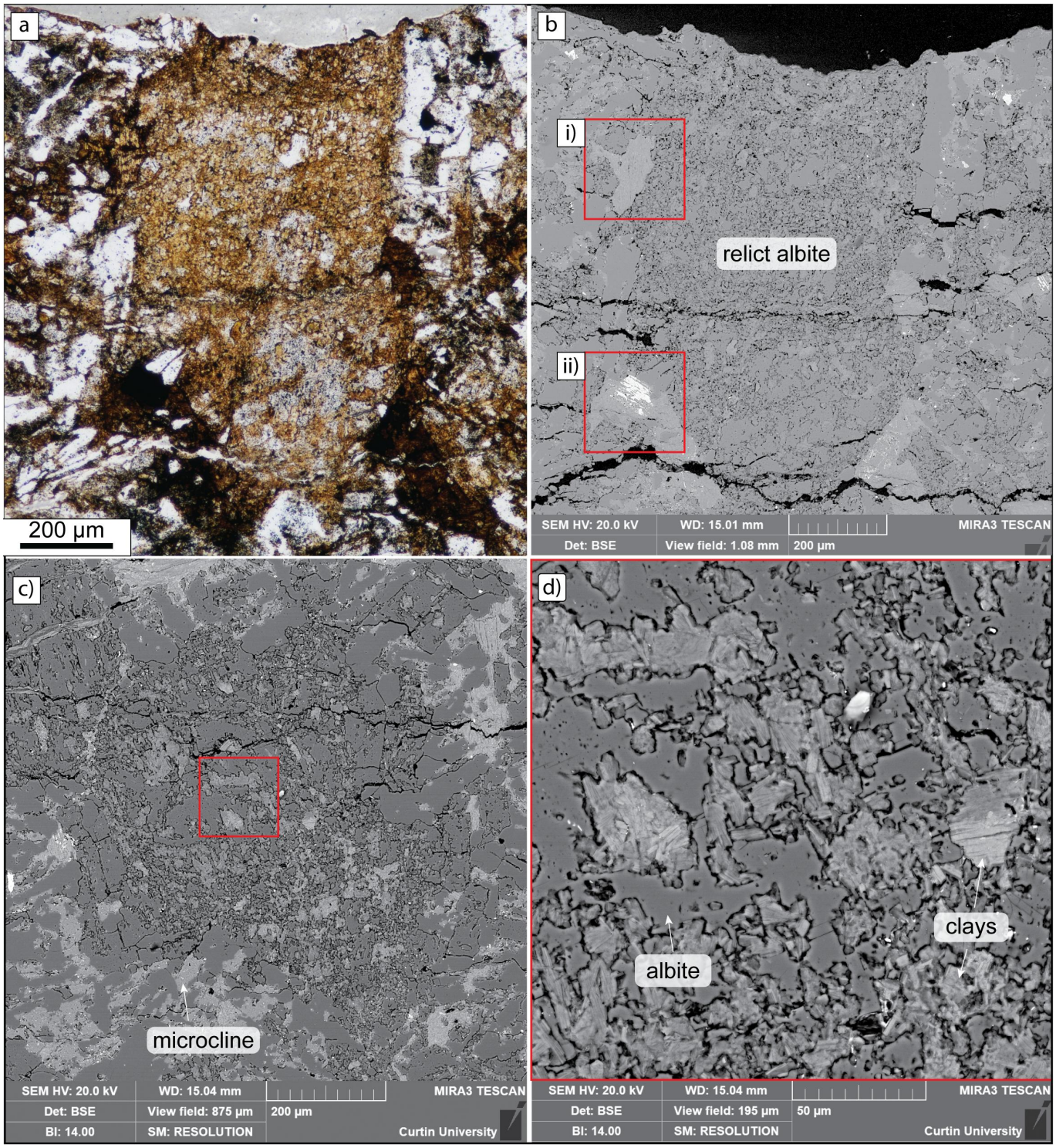

Figure 4.2-9: (a) plane-polarised photomicrograph and (b) BSE-SEM image of albite in the weathering rind of sample AQ06_GPH. In (b), insets (i) and (ii) are shown in Figure 4.2-10. (c) BSE-SEM image of dissolved albite. (d) Close-up image of the area indicated with a red box in (c). Albite is characterised by edge pits and irregular dissolution boundaries. The original portion of the mineral is now replaced by aggregates of clays such as kaolinite, illite and muscovite.

Chlorite alteration is generally pseudomorphic; the original crystal shape is replaced by micro-aggregates of clay minerals, mostly kaolinite and muscovite (Figure *4.2-10*). Oxide minerals such as ilmenite are extensively altered within the weathered zone and mineral dissolution occurs mostly along exsolution lamellae (Figure *4.2-10*).

In addition to the common rock-forming minerals already identified by optical microscopy and automated mineralogy, XRD analyses detected the presence of muscovite, illite, and kaolinite. The oxides are represented by hematite with lesser amounts of magnetite and goethite. Rarely, Al- and Si-bearing phases such as nacrite, dickite, jacobsite (Mn, Fe-oxide), and indialite were identified, but a high proportion of amorphous material may have prevented the identification of some of the minerals present. TIMA analyses confirm that the weathered rind is characterised by an increase in clay modal abundances as the surface is approached, and this increase is linked to the colour variation of the weathered rind (Figure *4.2-11* and *4.2-12*). Moreover, this increase coincides with a decrease in plagioclase mode and, to a minor extent, microcline. Compared to the fresher rock, the percentage of albite decreases by up to 6 vol.% while microcline variations are generally more subtle, of the order of 1 vol.% (Figure *4.2-12*). Abundances of chlorite, epidote and stilpnomelane also decrease from the fresher rock towards the surface, decrease in their modes being compensated by an increase in muscovite, kaolinite, pyrophyllite and K-alteration of chlorite (K-alt-Chlorite). In addition, the increase in the area identified as voids or holes is consistent with the microstructural observations of porosity.

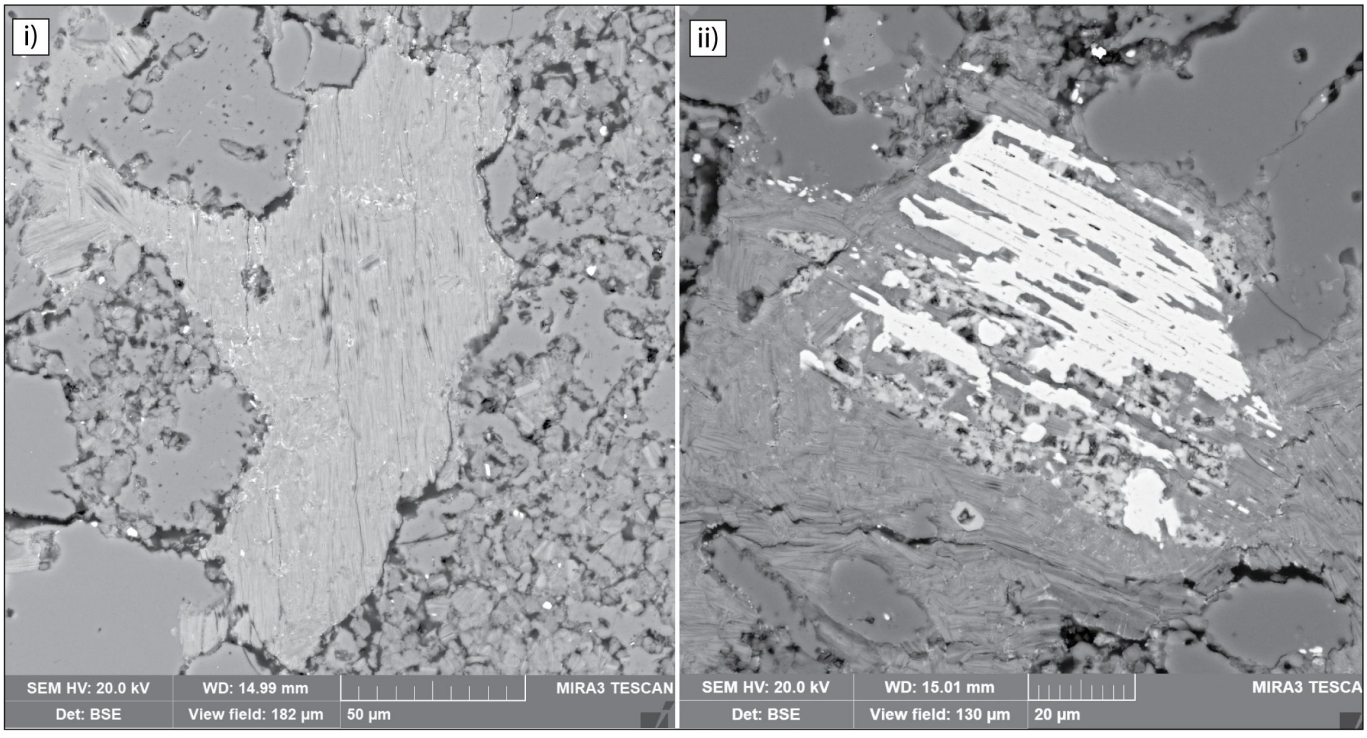

Figure 4.2-10: BSE-SEM image of altered chlorite (i) and altered ilmenite (ii) from Figure 4.2-9.

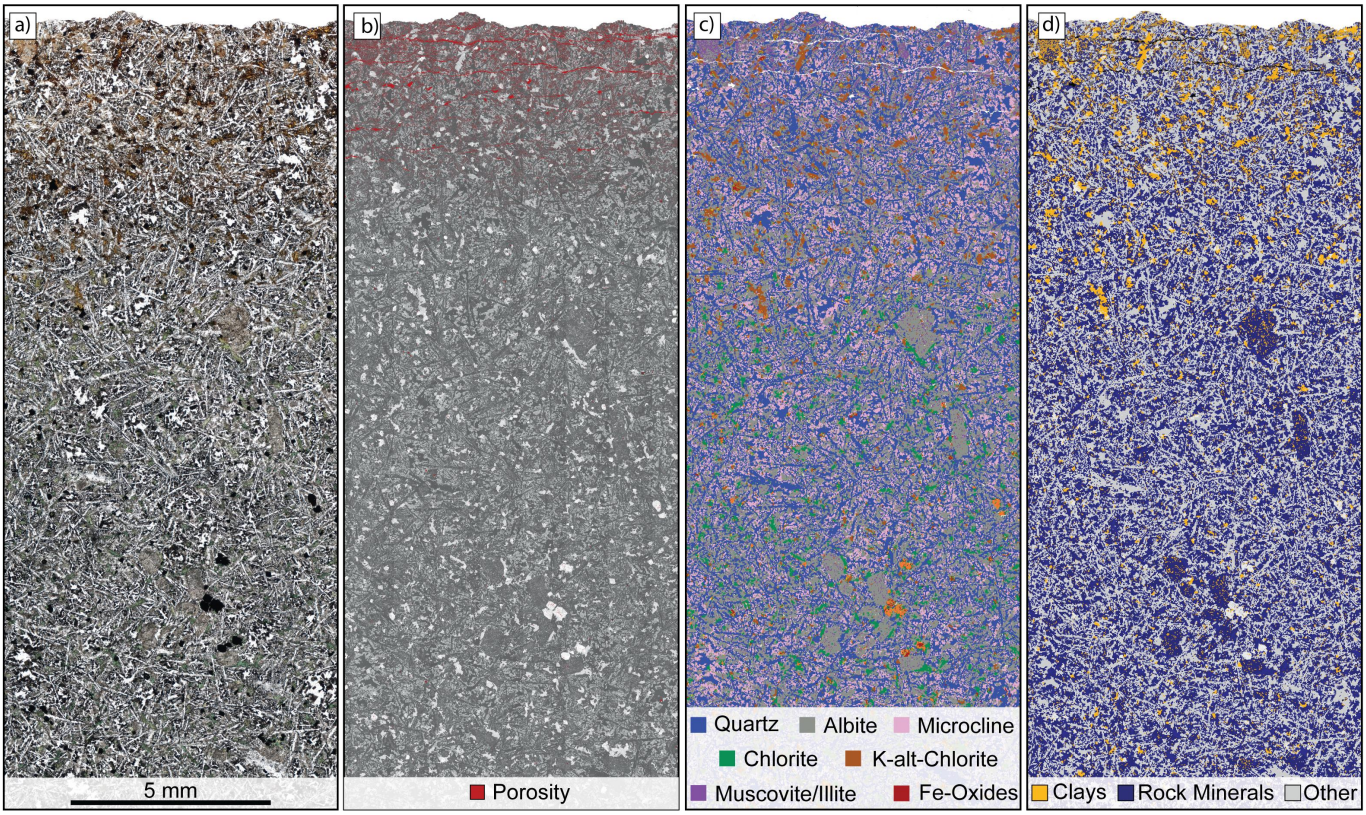

Figure 4.2-11: (a) plane-polarised photomicrograph (b) TIMA-BSE (c) TIMA phase map showing the most abundant phases, and (d) distribution of clays and precursor minerals, shown in the legend as rock forming minerals, for the same portion of sample AQ06_GPH, displaying the transition from fresher rock to weathered rind domain. In (b), the red colour shows the region of the sample with epoxy resin, highlighting the enhanced porosity of the domain. In (d), clay minerals correspond to browner colours shown in (a). Clays include phases identified at the TIMA such as muscovite/illite, K-alt-chlorite, kaolinite and patina.

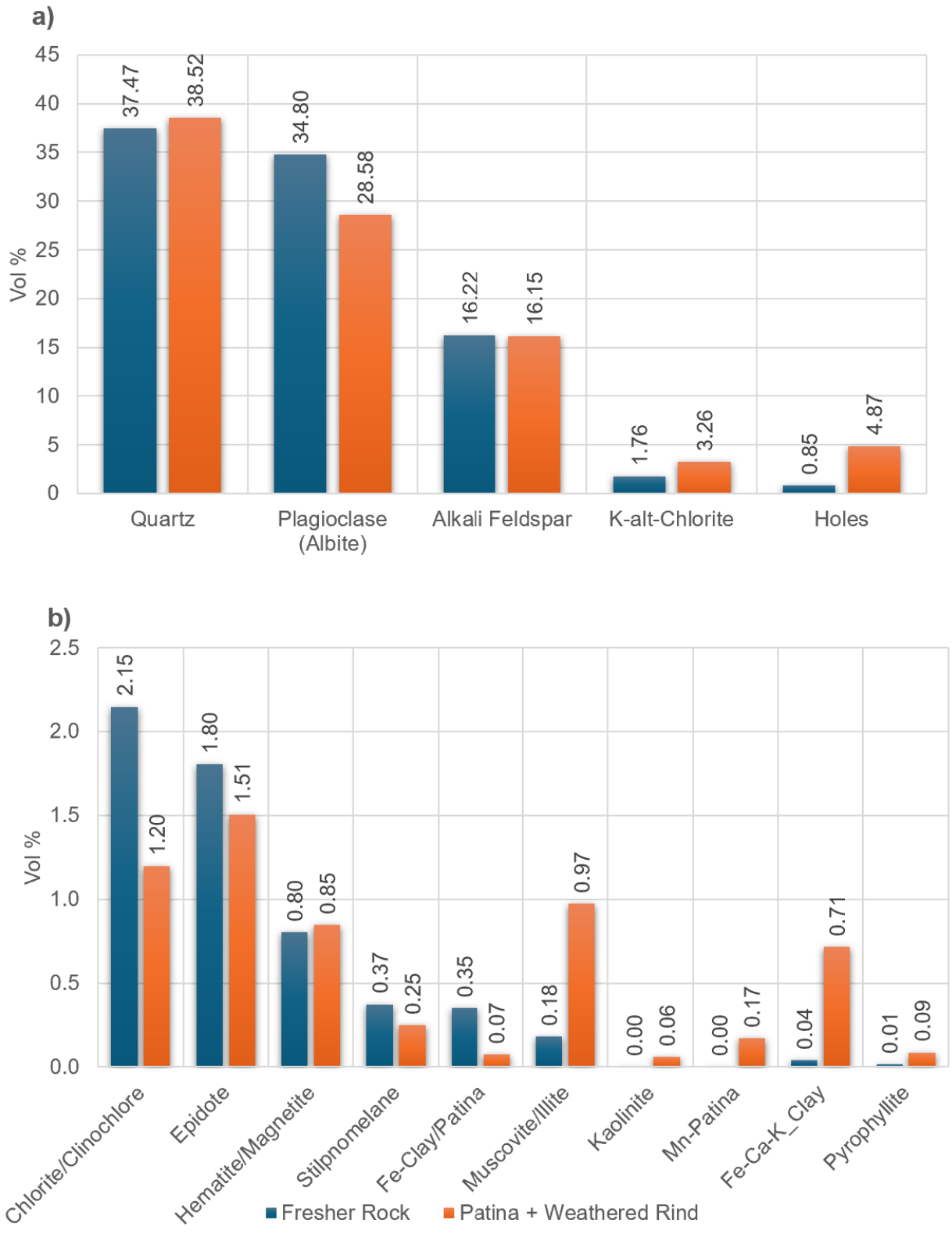

Figure 4.2-12: TIMA modal analysis of the 31 granophyre samples comparing the average abundances of (a) major and (b) minor minerals between the fresher rock and weathered rind domains.

4.2.5.2 Gabbro

Eleven gabbro samples were investigated by optical microscopy and TIMA. Additional SEM observations and XRD analyses were conducted on five selected samples. Mineral compositions were acquired from three representative samples. In this report, no distinction is made between gabbro and “quench” gabbro.

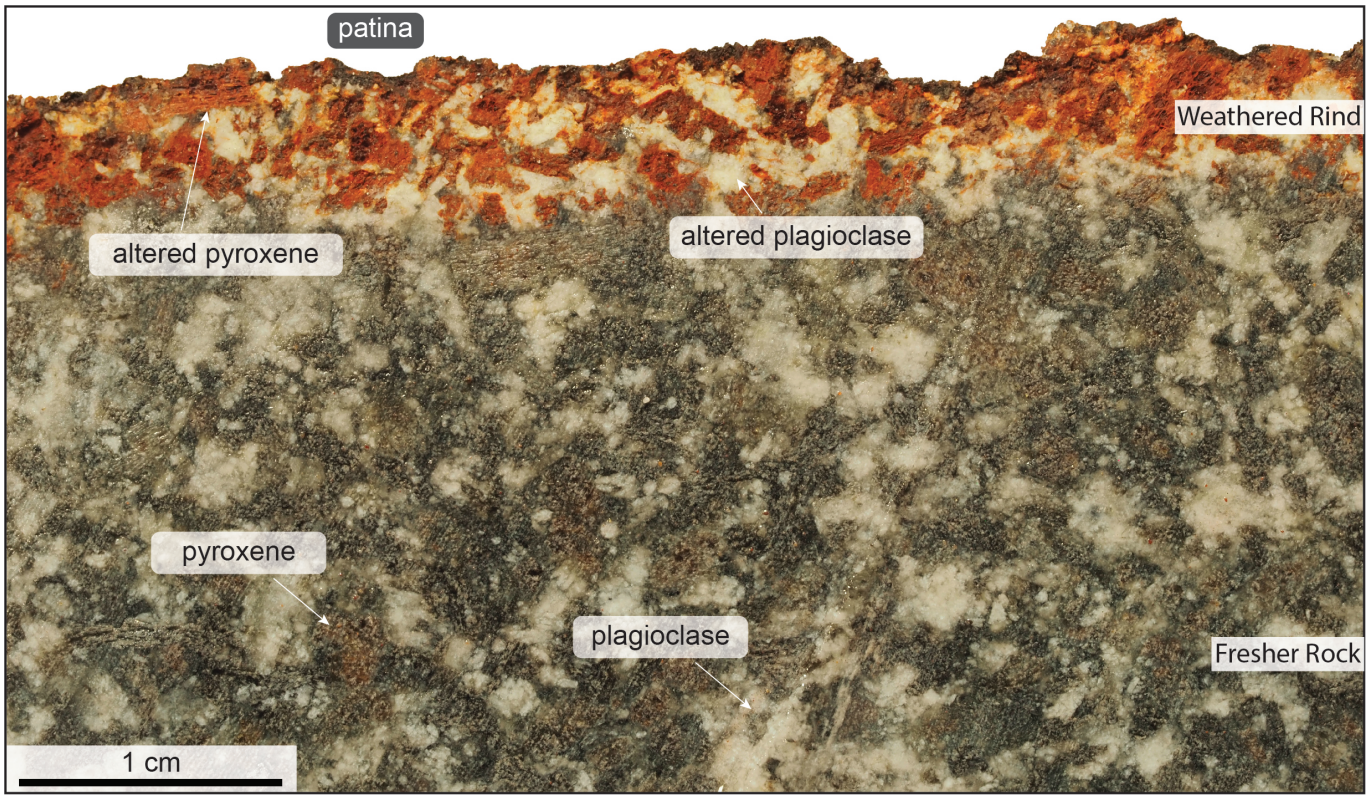

Figure 4.2-13: Core-to-rind cross-section photograph of gabbro rock billet AQ15_GBR. The transition from the fresher rock to the weathered rind domain is indicated by a variation from green to dark orange due to the progressive alteration of precursor minerals within the fresher rock. A dark red patina is visible rimming the outermost part of the profile.

Fresher rock

The lithology is holocrystalline, phaneritic and variably coarse-grained. Generally, the abundances of phenocrysts and groundmass minerals are consistent and homogeneous across the suite of samples (Figure *4.2-22*). The rock is mafic and mostly comprises abundant clinopyroxene (up to ∼50 vol.%) and Ca-plagioclase (∼30 vol.% avg.). Additional minerals include orthopyroxene (enstatite) and quartz (2–20 vol.%, average value of 11.85 vol.%). The high mode of quartz is in excess of that expected for a gabbro *sensu stricto* and may indicate that the field-based terminology requires revision. Secondary phases, in order of abundance, are epidote (up to 15 vol.%), chlorite (∼10 vol.% avg), Na-plagioclase (< 10 vol.%), muscovite, amphibole, and minor orthoclase. Accessory minerals, most commonly Fe- and Ti-bearing oxides (hematite, magnetite and ilmenite), titanite, and apatite occur in various amounts. Sulphides are rare.

Clinopyroxene is of augitic composition (Appendix Figure *B-7*) and forms prismatic elongate crystals

with second-order birefringence that are up to 30 cm long in quench gabbro and show common twinning across the 001 plane (Figure *4.2-14*). Pigeonite exsolution lamellae are ubiquitous. EBSD analysis indicates that they mostly developed along 001 and 100 planes (Figure *4.2-15*, *4.2-16*). Ca-plagioclase is labradorite (An73Ab26Or1), and albite is also present (Appendix Table *B-1* and *B-3*). Plagioclase is coarse-grained, subhedral and generally cloudy because of replacement by secondary dendritic epidote (Figure *4.2-15*). In BSE, labradorite displays asymmetrical darker rims indicating internal chemical zonation (Figure *4.2-15*(b)). Compared to the core, the rim is enriched in Na and K and depleted in Ca (Appendix Tables *B-1* to *B-16*). When present, orthopyroxene (enstatite) varies from subhedral to anhedral with smooth irregular boundaries. Similar to augite, the orthorhombic phase shows lamellae of exsolution. Quartz is generally interstitial but is also observed to form symplectites with feldspar in the quench gabbro samples. Epidote (clinozoisite) occurs as overgrowth on labradorite or as a matrix mineral. Chlorite (clinochlore) occurs as an alteration product of pyroxenes and forms rims and interconnected networks that cross-cut larger grains. Chlorite is often accompanied by fine-grained muscovite and interstitial actinolitic amphibole.

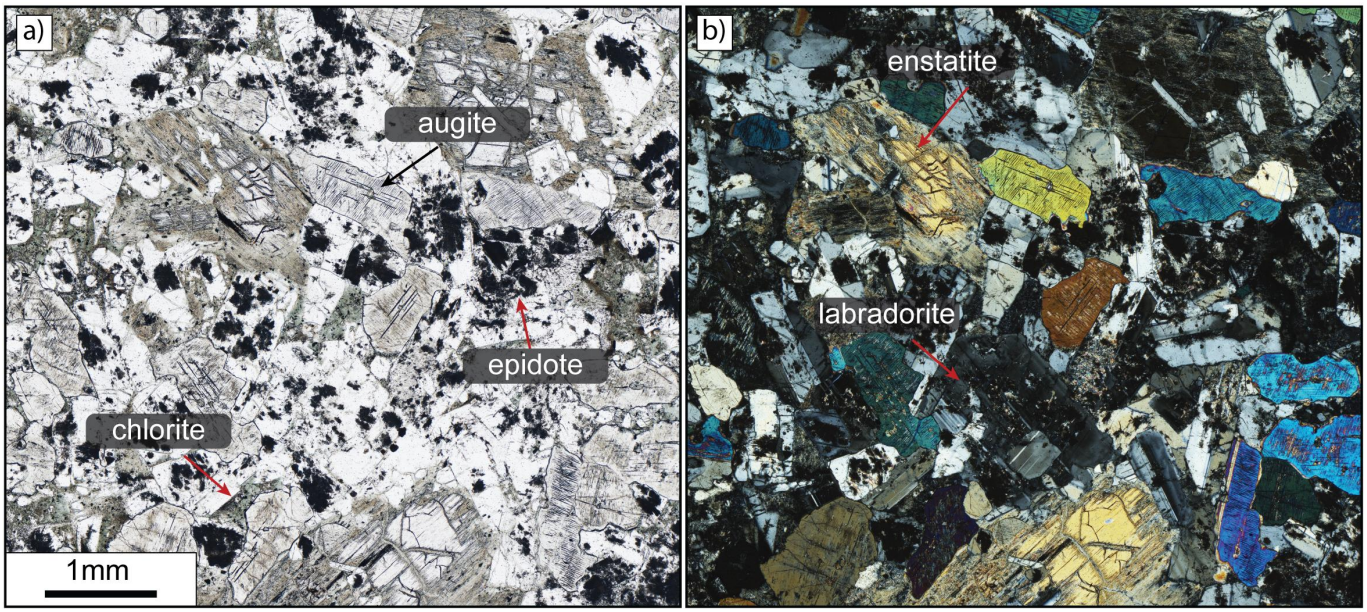

Figure 4.2-14: Plane-polarised (a) and crossed-polarised (b) images of fresher rock part of gabbro from AQ15 study area. Larger tabular grains of augite are distinguishable by their highly birefringent colours. Enstatite is altered and replaced by fine-grained chlorite. In (a) the dark patchy mineral is epidote which replaces prismatic labradorite crystals.

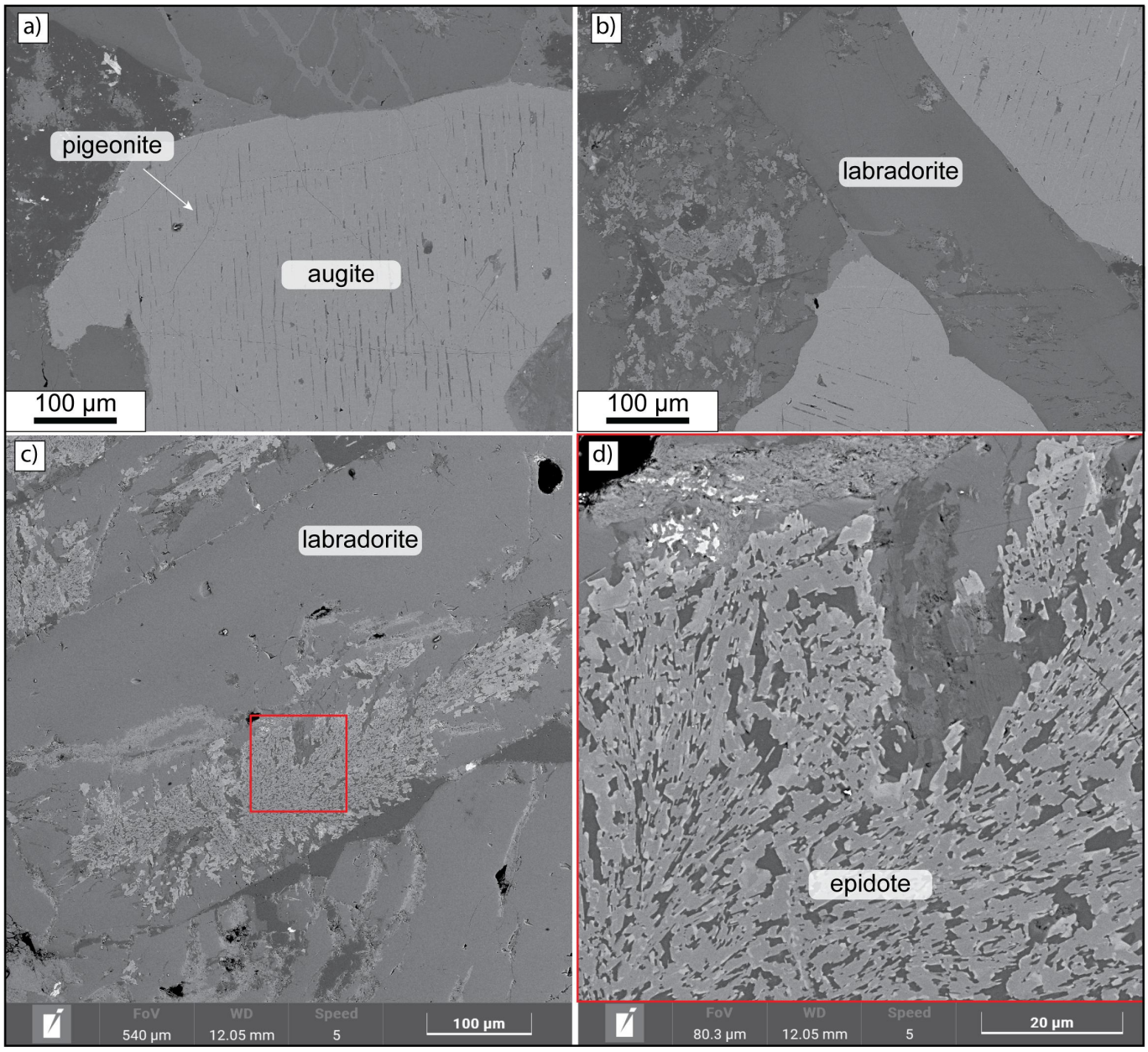

Figure 4.2-15: BSE-SE images of gabbro microstructures. (a) crystal of augite characterised by crystallographically controlled pigeonite exsolution. (b) prismatic labradorite with visible asymmetrical zoning. (c) and (d) secondary dendritic epidote forming at the expenses of labradorite.

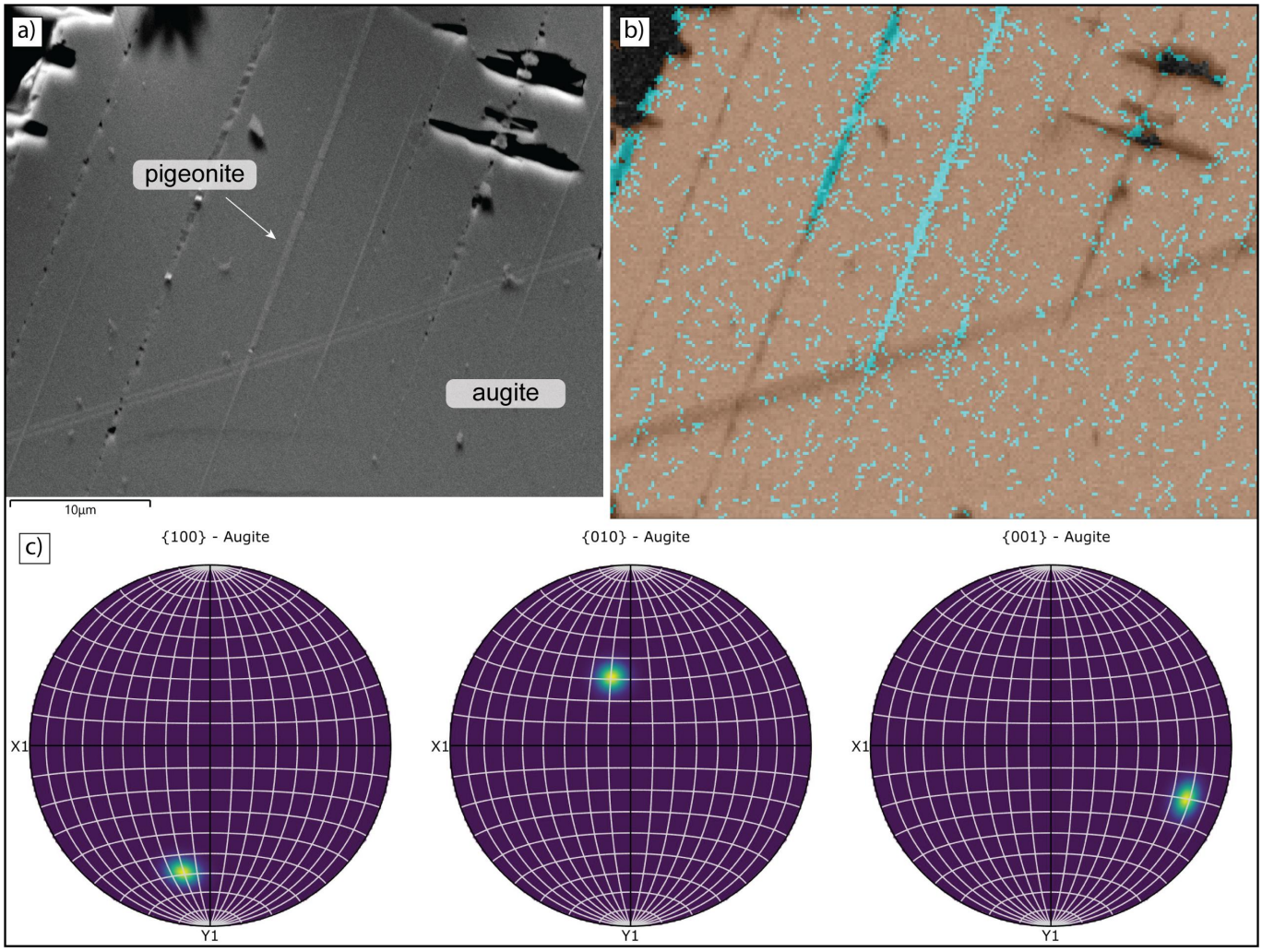

Figure 4.2-16: Crystallographic analysis of pigeonite exsolutions in augite. (a) electron forescattered image, (b) EBSD phase map and (c) pole figures of augite indicating the alignment of pigeonite exsolution along the 001 planes.

Weathered rind

The weathered rind of gabbro is generally well developed, and is highlighted by intense brown to red colouration in sample (Figure *4.2-13*). Optical microscopy observations indicate that the colour variation is largely related pyroxene alteration (Figure *4.2-17*). Exsolution lamellae are highlighted by more intense coloration, indicating localised alteration/oxidation on these planes.

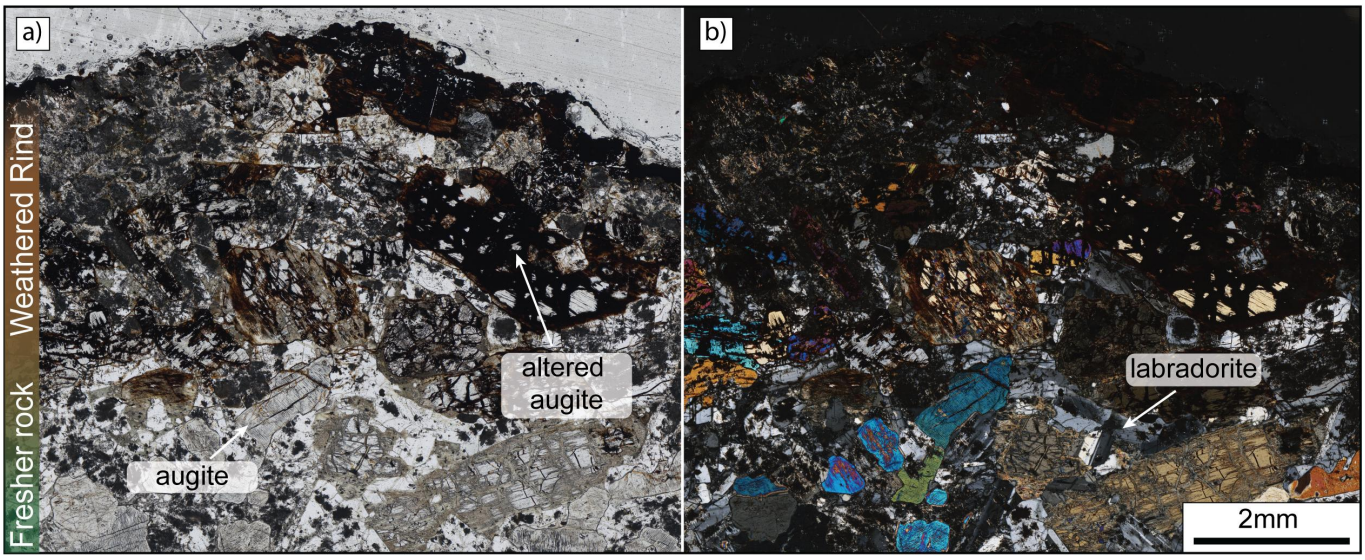

Figure 4.2-17: Plane-polarised (a) and cross-polarised (b) photomicrograph of the region of transition between fresher rock and weathered rind in gabbro from study area AQ15. The colour variation in (a) reflects alteration of augite crystals to dark-red alteration minerals.

Microstructurally, the weathered rind is characterised by a pattern of increased porosity towards the patina. Back-scattered electron images and EBSD analyses indicate that sample porosity is primarily associated with the preferential dissolution of augite and to a lesser extent labradorite (Figure *4.2-18* and *4.2-19*). Compared to augite, orthopyroxene is more affected by chlorite alteration rather than by dissolution. Aggregates of secondary epidote, interpreted as after plagioclase, are preserved.

At the grain scale, dissolution of augite is primarily controlled by crystallography; augite dissolution proceeds via formation of lens-shaped edge pits that initiate along pigeonite exsolution lamellae and expand outwards to form striated surfaces on parallel-edged pits (Figure *4.2-20*). The intersection of multiple pits forms large cavities that are sometimes occupied by muscovite and/or kaolinite. Augite progressively deteriorates until almost the whole grain is dissolved, with only the skeleton of the grain remaining. The skeleton geometry is oriented along distinct crystallographic directions that are decorated by localised enrichment in Fe-oxides (Figure *4.2-20*). Labradorite is also dissolved and replaced by muscovite. In the most weathered portions, generally in regions proximal to the patina, only secondary epidote is left in place and Al-oxides, most likely gibbsite, and quartz, form microscale vermicular aggregates along the original labradorite grain boundaries. Similarly to granophyre, chlorite is replaced by finer aggregates of clays such as kaolinite and illite. Very fine-grained oxides are disseminated within a matrix of muscovite and kaolinite. Quartz remains unaltered across the weathered rind domain.

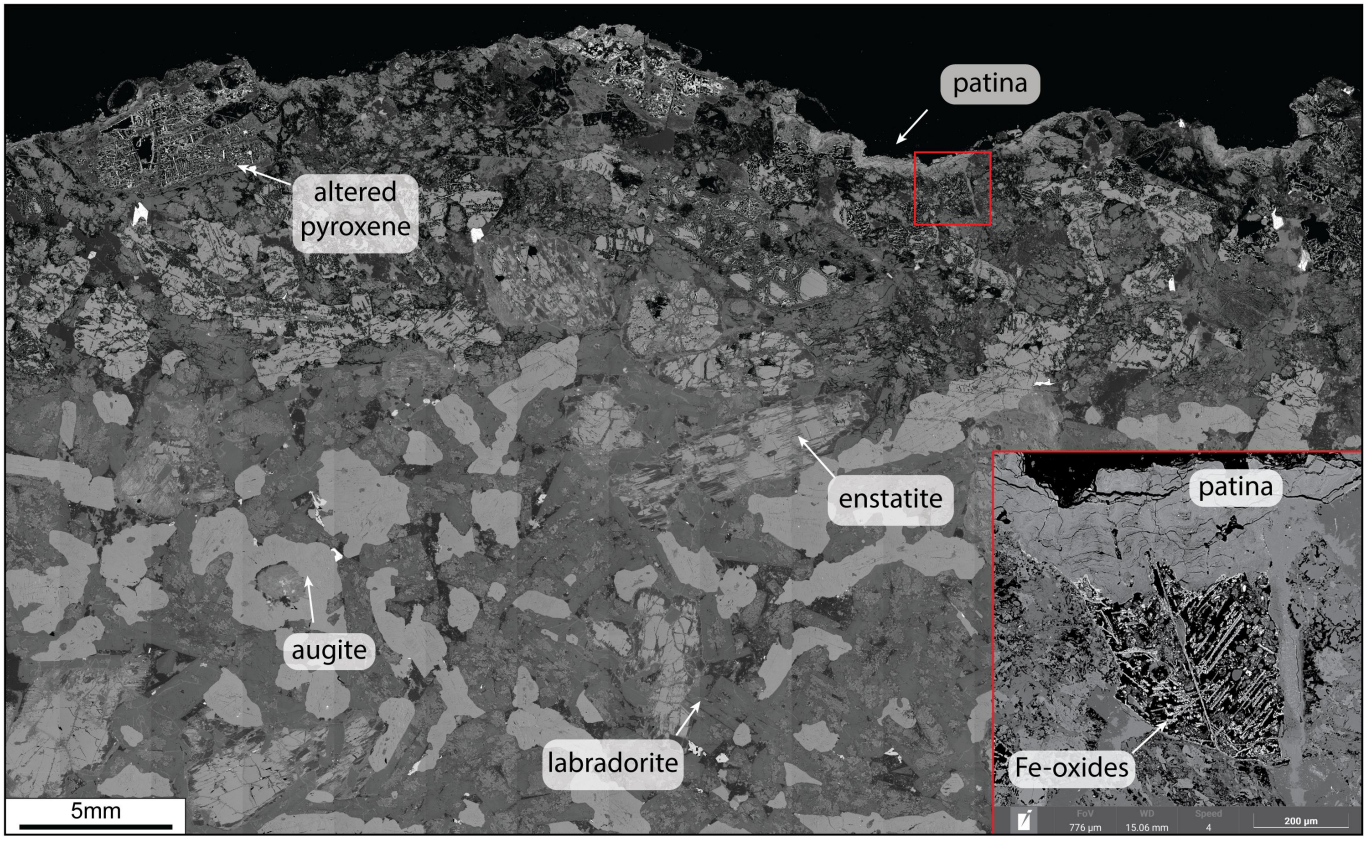

Figure 4.2-18: BSE-SEM large area panorama of the transition region between fresher rock-weathered rind-patina from sample AQ15_GBR. The weathered rind is characterised by enhanced microporosity and the alteration of precursor minerals present within the fresher rock. The red box indicates the location in the image of the close-up inset.

XRD analyses of powdered samples indicate the presence of muscovite and clays such as illite, kaolinite, rare vermiculite and willemseite (talc-pyrophyllite). Oxides comprise magnetite, rutile, birnessite, and rare Al-hydroxides. Other phases observed include chabazite (zeolite), indialite and sulphides (e.g. sphalerite) (Table *4.2-2* to *4.2-6*). Similarly to granophyre observations, TIMA analyses confirm that the colour contrast of the weathered rind relative to the fresher rock is associated with a change in mineralogy (Figure *4.2-21*). Compared to the fresher rock, the weathered rind domain is characterised by variable degrees of augite and labradorite loss. Generally, augite is the most affected mineral phase, decreasing by up to 20 vol.%. To balance this loss, there is an increase in the modes of chlorite, muscovite/illite and iron oxides (Figure *4.2-22*). The enhanced porosity observed optically is measured by TIMA as an increase in the percentage of voids.

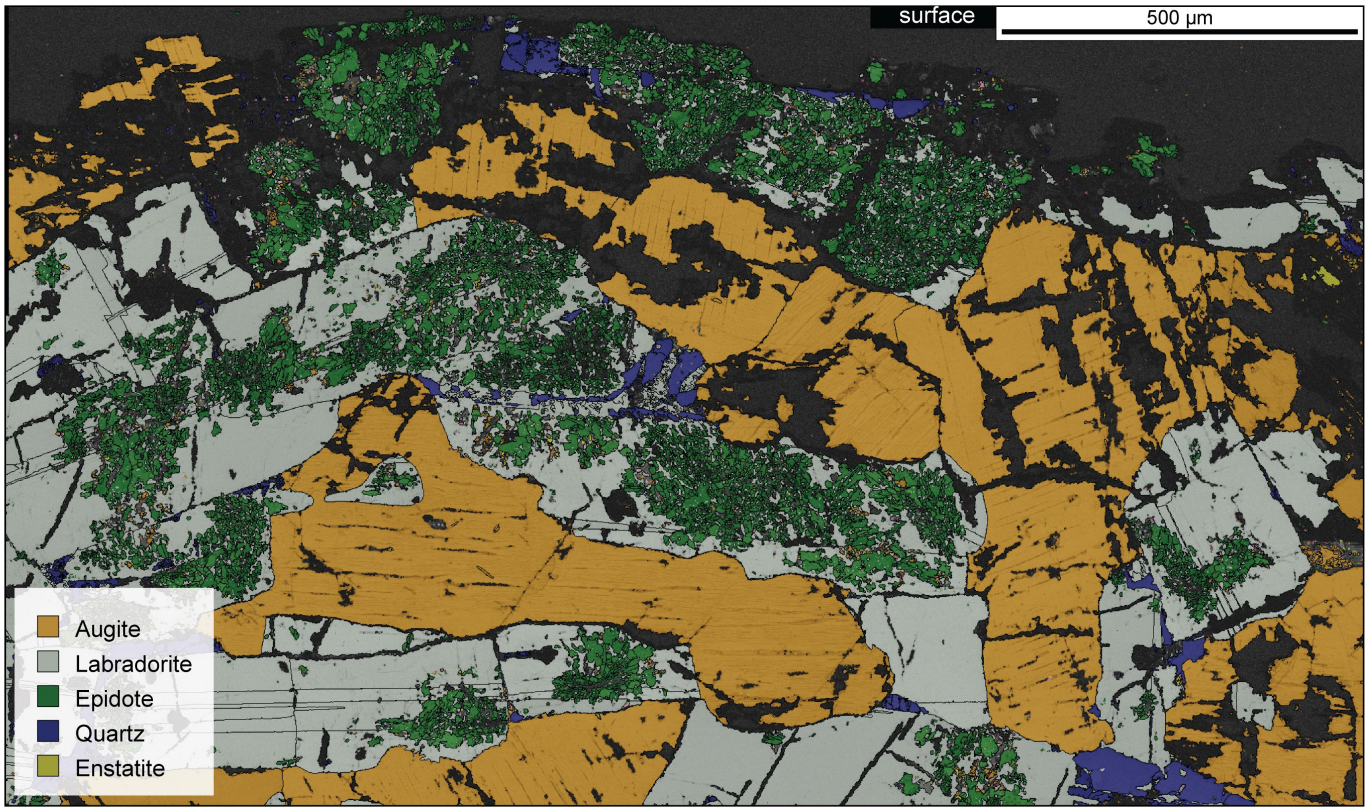

Figure 4.2-19: Large area EBSD phase map showing a region of transition between fresher rock and weathered rind of samples RS16_GBR. The map indicates that porosity is mostly attributed to the alteration and dissolution of augite crystals and to a minor extent labradorite. Phase boundaries are highlighted by a ubiquitous gap between the crystals.

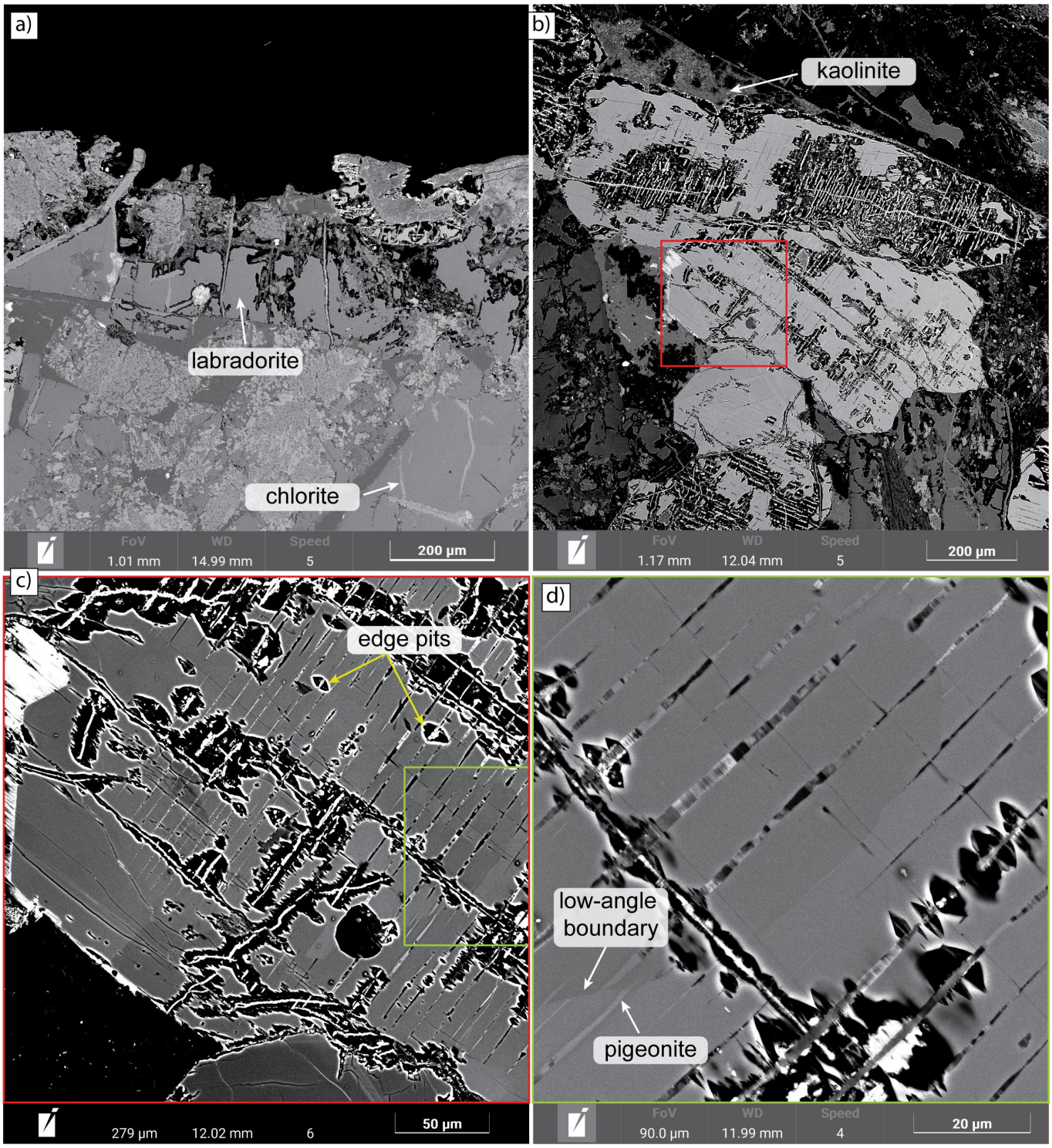

Figure 4.2-20: Grain scale microstructural analysis of gabbro. BSE-SE images of labradorite (a) and augite (b-c) show in detail the patterns of dissolution occurring in the two main rock-forming minerals. (c) is the red box indicated in (b) whereas (d) is a close-up image of the green box in (c). Augite dissolved primarily along pigeonite exsolutions. In (d), variations in BSE grey tones indicate a process of chemical alteration internal to the pigeonite lamellae.

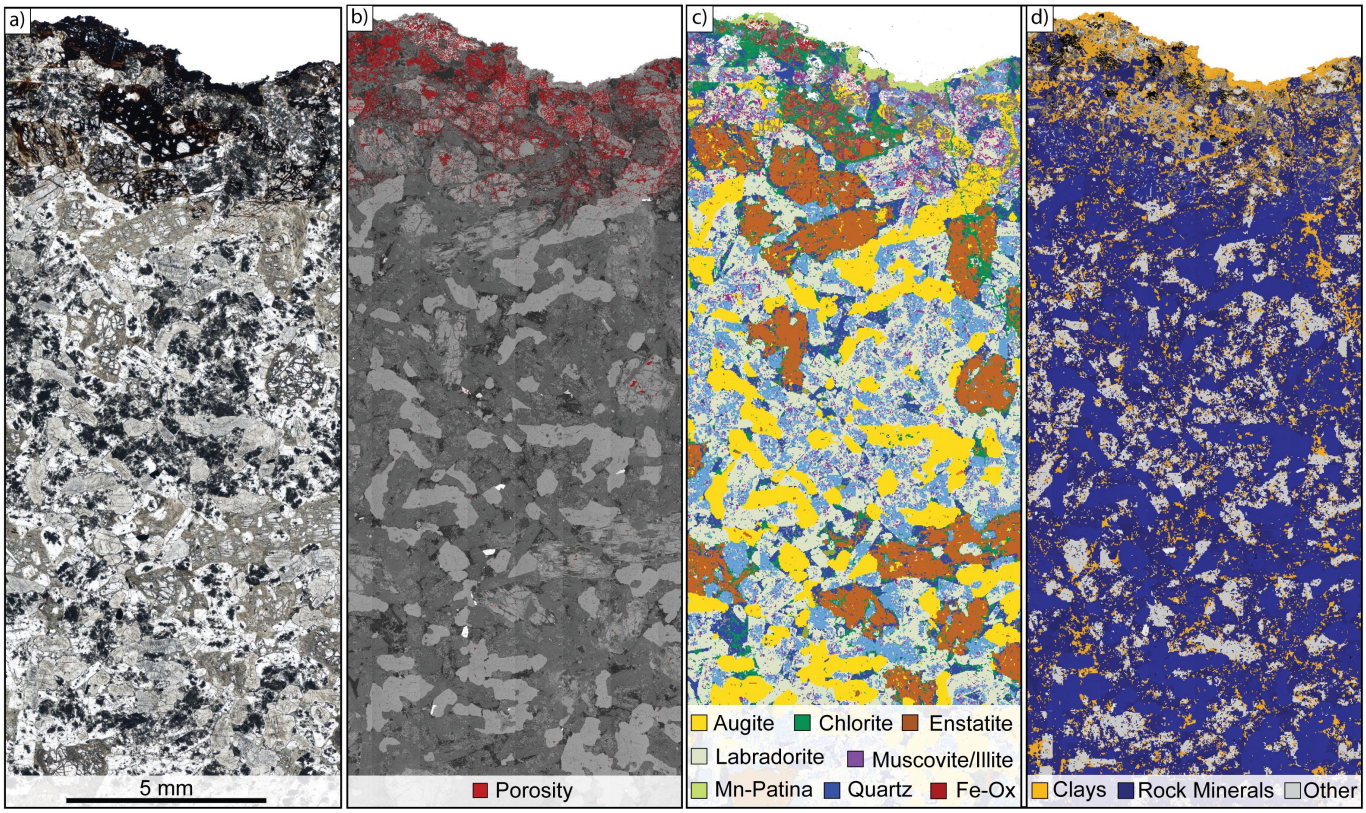

Figure 4.2-21: (a) plane-polarised photomicrograph (b) TIMA-BSE (c) TIMA phase map showing the most abundant phases, and (d) distribution of clays and precursor minerals, shown in the legend as rock forming minerals, for the same portion of sample AQ15_GBR, displaying the transition from fresher rock to weathered rind domain. In (b), the red colour shows the region of the sample with epoxy resin, highlighting the enhanced porosity of the domain. In (d), clay minerals correspond to browner colours shown in (a). Clays include phases identified at the TIMA such as muscovite/illite, K-alt-chlorite, kaolinite and patina.

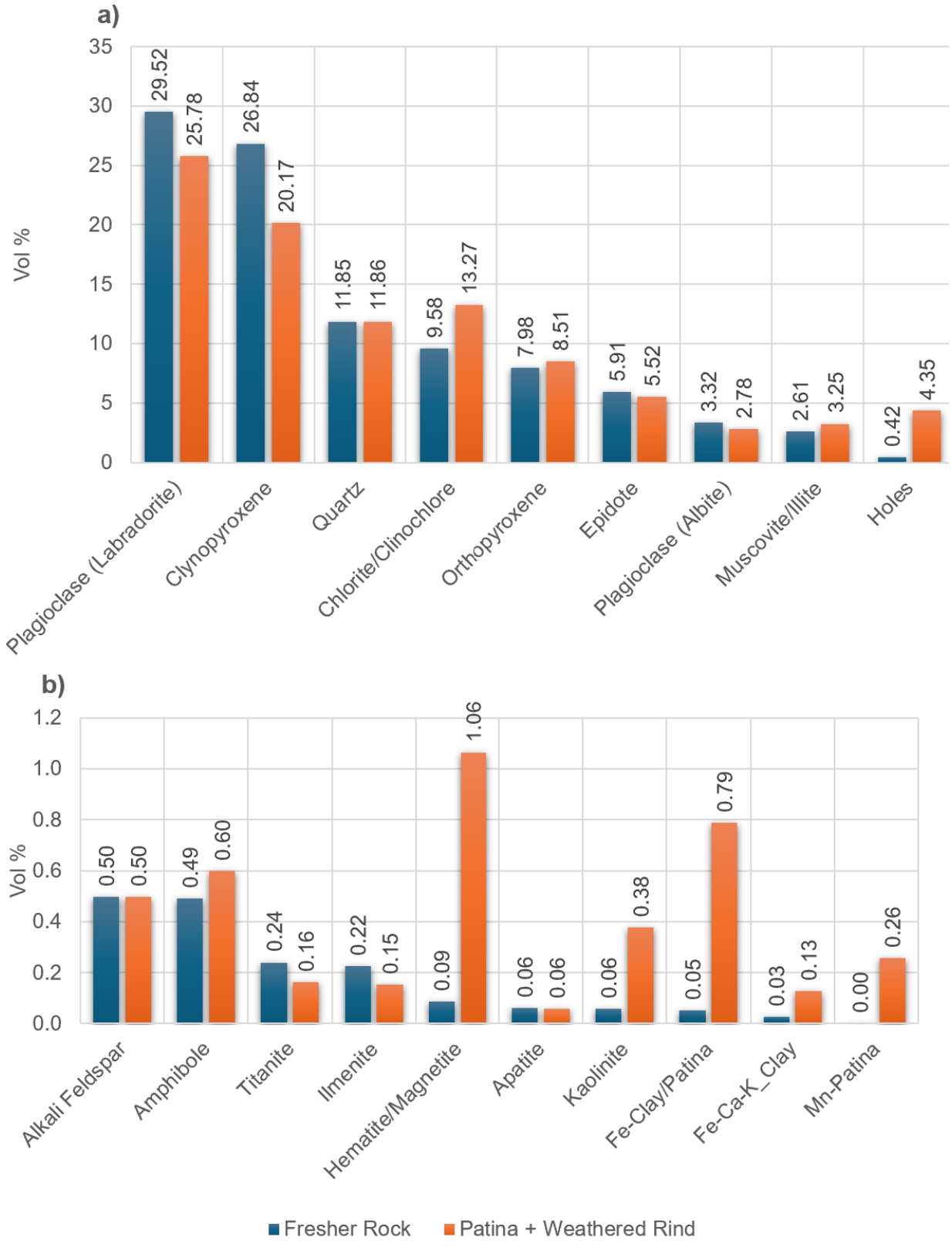

Figure 4.2-22: Summary of TIMA modal analysis of gabbro samples that compares the abundances of (a) major and (b) minor minerals between the fresher rock and weathered rind domains.

4.2.5.3 Granite

Six granite samples were prepared and observed by means of optical microscopy and TIMA. Of these, three samples were investigated by SEM for further characterisation of the microstructures. XRD was conducted on four samples and three additional samples were selected for the mineral chemistry by EMP.

Fresher rock

Murujuga granite is coarse-grained, phaneritic and Na-rich plagioclase (An 2 Ab 97 Or 1, $\sim$40 vol.%), quartz ($\sim$35 vol.%) and microcline ($An_1Ab_2Or_{97}$, $\sim$18 vol.% avg.) are the main minerals. Andesine plagioclase ($An_{29}Ab_{70}Or_1$) is sometimes present in minor amounts ($<$7 vol.%). Epidote, chlorite (clinochlore), muscovite, rare amphibole, stilpnomelane, and phlogopite are minor phases. Apatite, ilmenite, rutile, zircon, galena and Fe-oxides are accessory phases. Compared to granophyre, granite displays widespread alteration in the fresher rock. In particular, sericite alteration of albite is ubiquitous across all parts of all the granite studied. The texture of the rock is dominated by large anhedral crystals of quartz surrounded by a finer-grained groundmass of albite and microcline (Figure *4.2-23*). For this lithology, the use of the γ-plate helps to reveal the presence of pockets of quartz and microcline myrmekite intergrowths (Figure *4.2-24*). Chlorite and epidote form coronae around quartz, replacing biotite, whereas muscovite is associated with altered albite. Quartz grains are characterised by sub-conchoidal fractures, and fractures on a larger scale, that do not show a preferred orientation, cross-cut the thin-section.

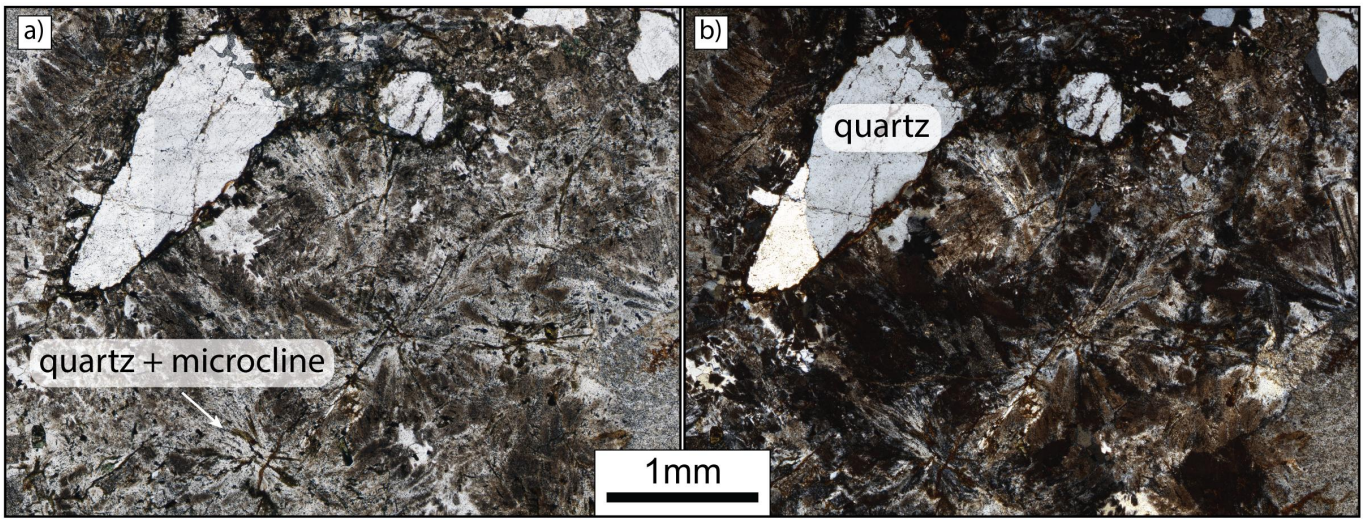

Figure 4.2-23: Plane polarised (a) and crossed-polarised (b) photomicrographs of fresher granite. A large anhedral quartz grain dominates the image and is surrounded by a fine-grained groundmass of felsic minerals.

Weathered rind

Compared to granophyre and gabbro, granite has a much thinner weathered rind and, where present, it is indicated by a faint colour variation from creamy-white to a pale-reddish colour in specimen. Under the optical microscope, the domain is mostly characterised by enhanced alteration surrounding quartz phenocrysts defined by rims of micro-aggregates of dark-brown clays (Figure *4.2-25*).

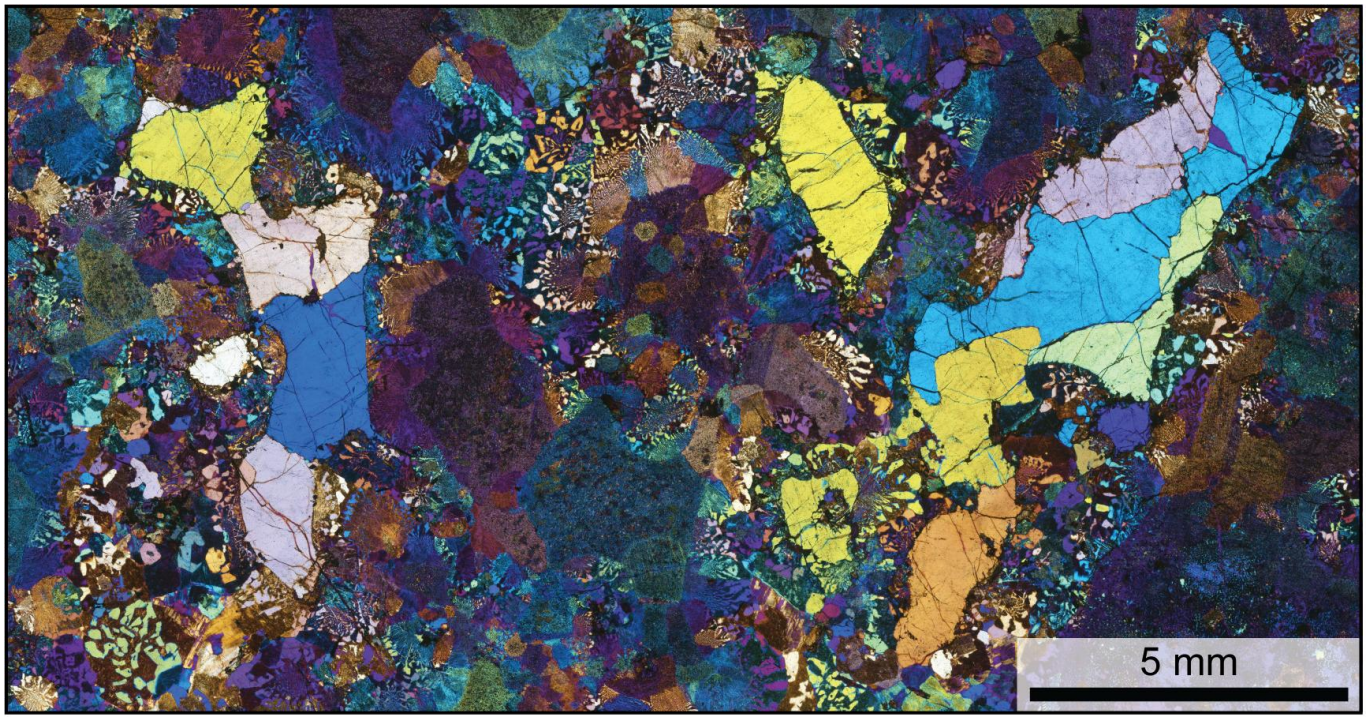

Figure 4.2-24: Cross-polarised panorama image with γ-plate inserted of sample AS02_GRT. Myrmekite of quartz and microcline are visible surrounding larger crystals of quartz.

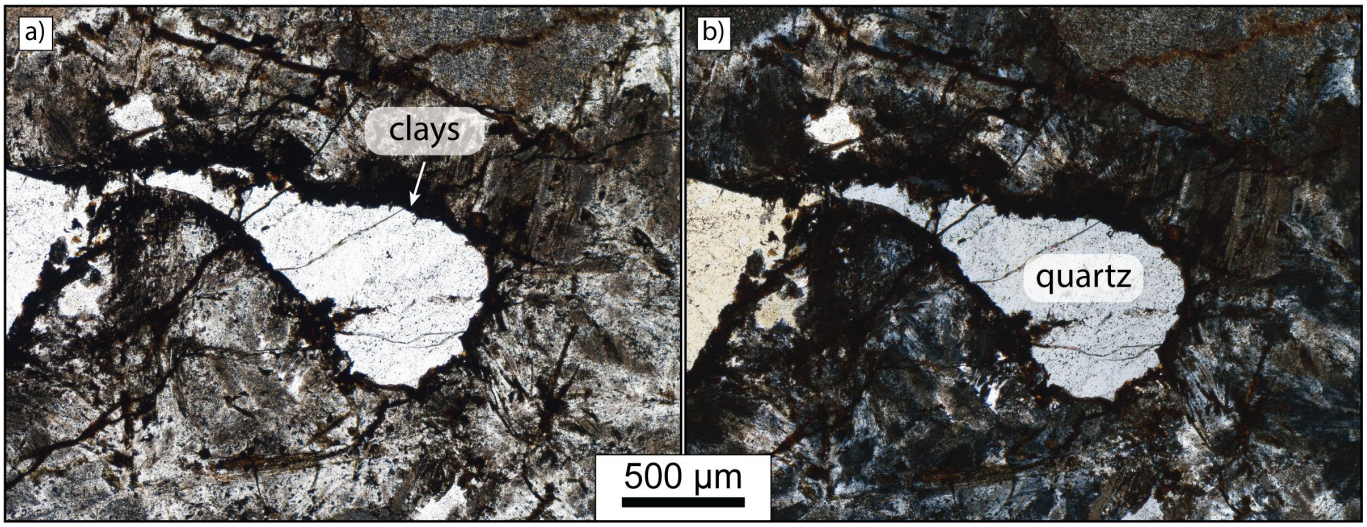

Figure 4.2-25: Plane-polarised (a) and crossed-polarised (b) photomicrographs of the weathered rind in granite. Dark-brown clays form surrounding quartz phenocrysts.

Microstructurally, SEM observations indicate that the region is characterised by a lesser increase in micro-porosity towards the patina compared to the previously described lithologies. Similarly to granophyre, feldspars are the most affected minerals.

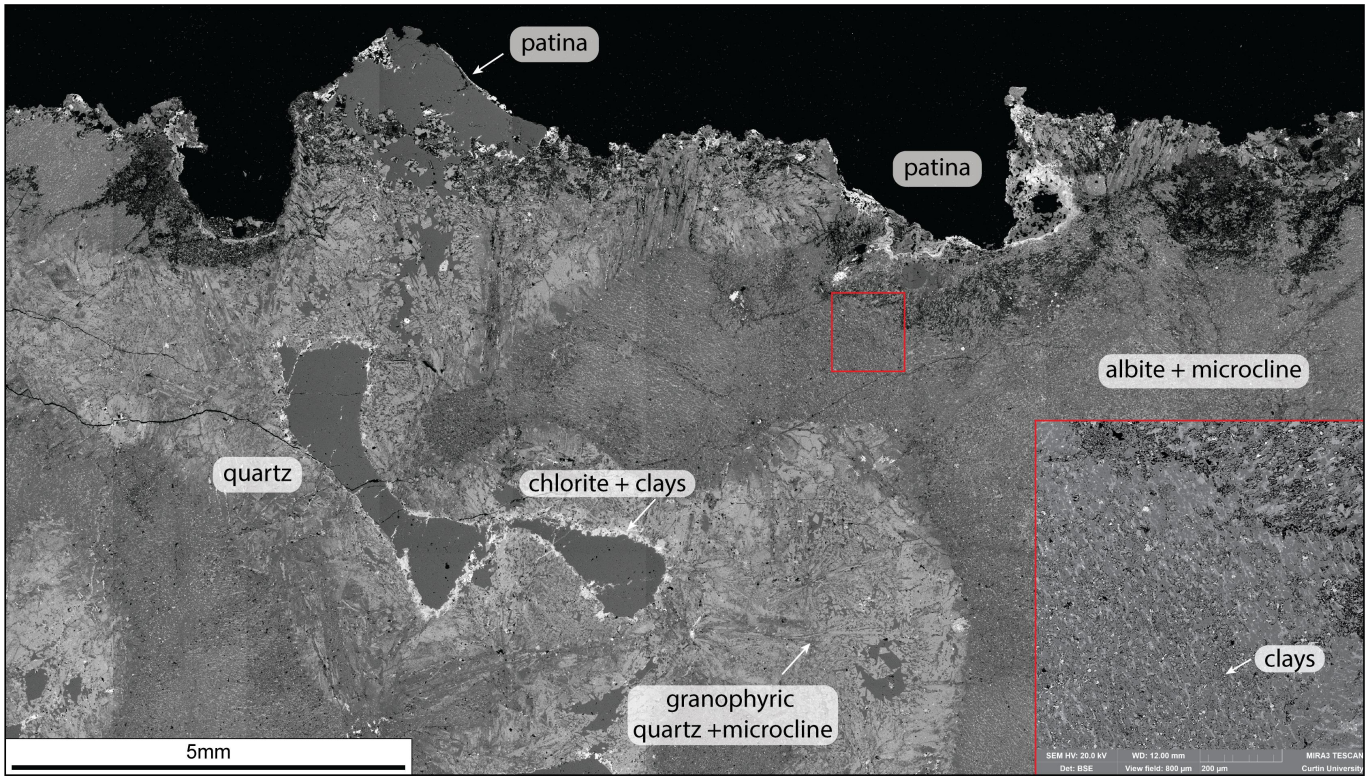

Figure 4.2-26: BSE-SEM large area panorama of the transition between fresher rock-weathered rind-patina from sample AQ07_GRT. The weathered rind is characterised by enhanced microporosity and the alteration of precursor minerals present within the fresher rock. Brighter rims of chlorite and Fe-oxides form rims surrounding quartz. The red box indicates the location in the image of the close-up inset.

At the grain scale, minerals such as albite and microcline are characterised by the development of edge pits and irregular grain boundaries (Figure *4.2-27*). Larger grains of plagioclase are progressively replaced by microscale aggregates of muscovite and kaolinite. Microcline dissolution is highlighted by voids on microcline-quartz contacts within granophyric intergrowths (Figure *4.2-27* (b,c)). In places, clays, mostly illite and muscovite, fill the gaps between minerals. In regions where the weathering rind is more proximal to the surface, the original texture of the rock is almost obliterated and skeletal quartz is surrounded by the remnants of microcline, epidote and Fe-oxides (Figure *4.2-27*(d)), and albite is almost entirely replaced by kaolinite.

Besides minerals present within the fresher rock, XRD analyses detected clays such as kaolinite and illite, and oxides, including diaspore and birnessite (Table *4.2-2* to *4.2-6*). Compared to the fresher rock, TIMA analyses indicate that the weathered rind of granite registers a decrease in rock-forming minerals present within the fresher rock, such as plagioclase and microcline. The fresher rock to weathered rind transition is gradational and involves an increase in clay minerals, in particular illite (∼2 vol.%) and kaolinite from the fresher rock to the weathered rind (Figure *4.2-28* and *4.2-29*). Progressive illitisation is coupled with a decrease in the chlorite mode and changes in chlorite composition associated with potassic alteration (Figure *4.2-28*). The increase in porosity observed optically is shown by TIMA as a higher proportion of holes in the weathered rind compared to the fresher rock.

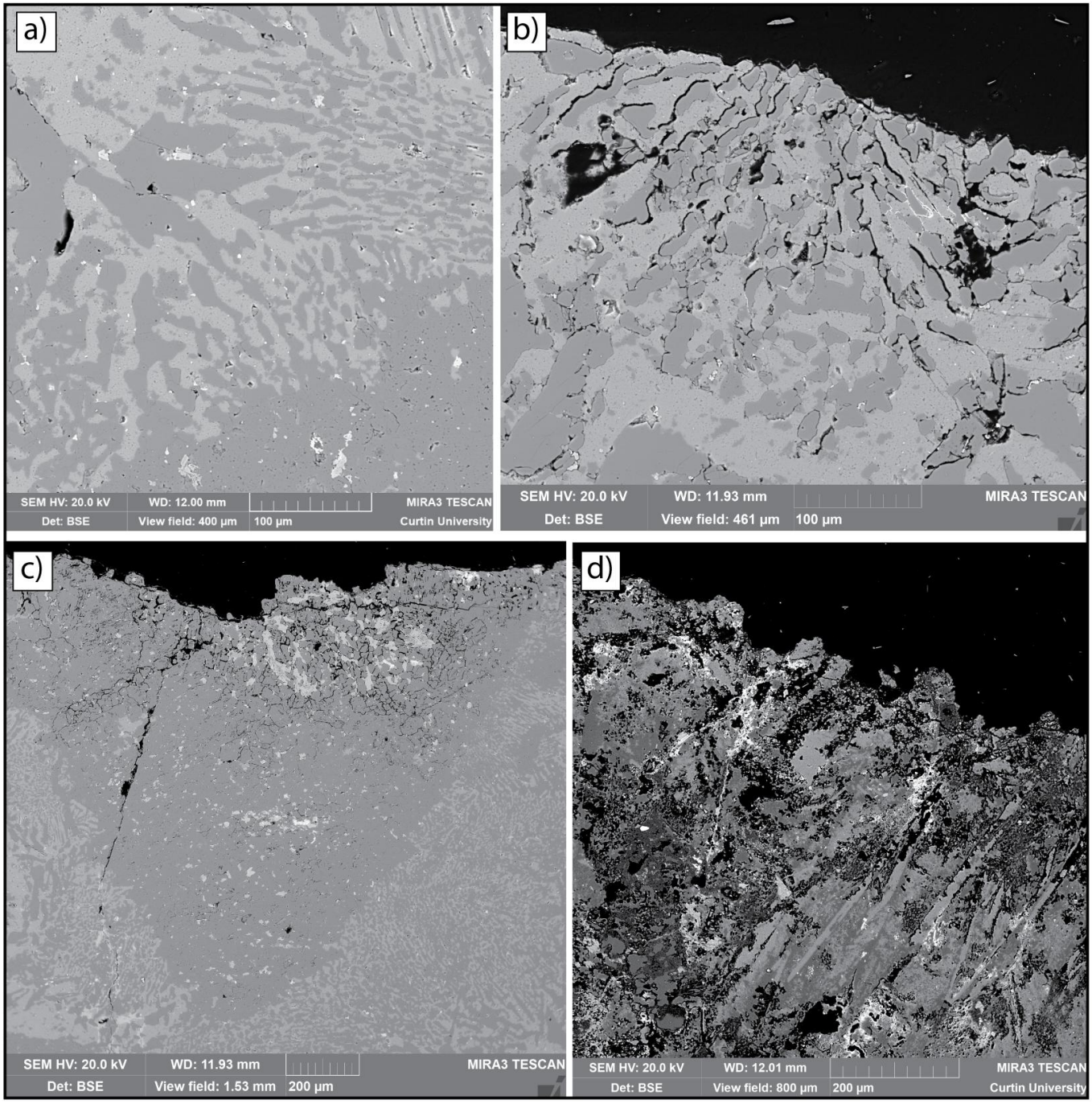

Figure 4.2-27: BSE-SEM images of granite microstructures. (a, b) myrmekitic intergrowth between quartz and microcline. In the micro-texture, the dissolution of microcline forms empty spaces between the minerals. (c) larger albite crystals displaying asymmetric regions of dissolution enhanced at the contact with the surface (top of the image). In (d), the advanced stage of rock-forming mineral dissolution has cancelled the original texture of the rock leaving behind a chaotic microporous texture.

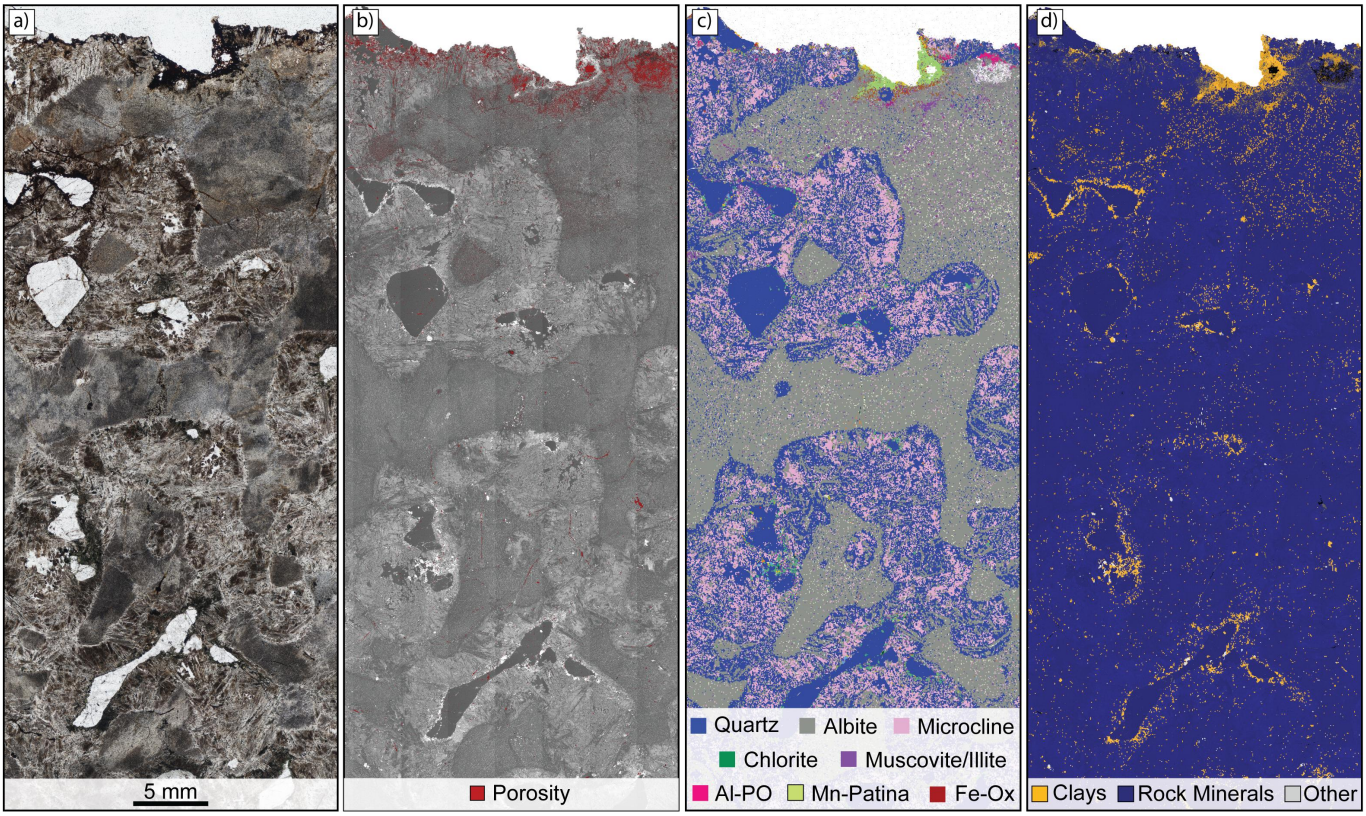

Figure 4.2-28: (a) plane-polarised photomicrograph (b) TIMA-BSE (c) TIMA phase map showing the most abundant phases, and (d) distribution of clays and precursor minerals, shown in the legend as rock forming minerals, for the same portion of sample AQ07_GRT, displaying the transition from fresher rock to weathered rind domain. In (b), the red colour shows the region of the sample with epoxy resin, highlighting the enhanced porosity of the domain. In (d), clay minerals correspond to browner colours shown in (a). Clays include phases identified at the TIMA such as muscovite/illite, K-alt-chlorite, kaolinite and patina.

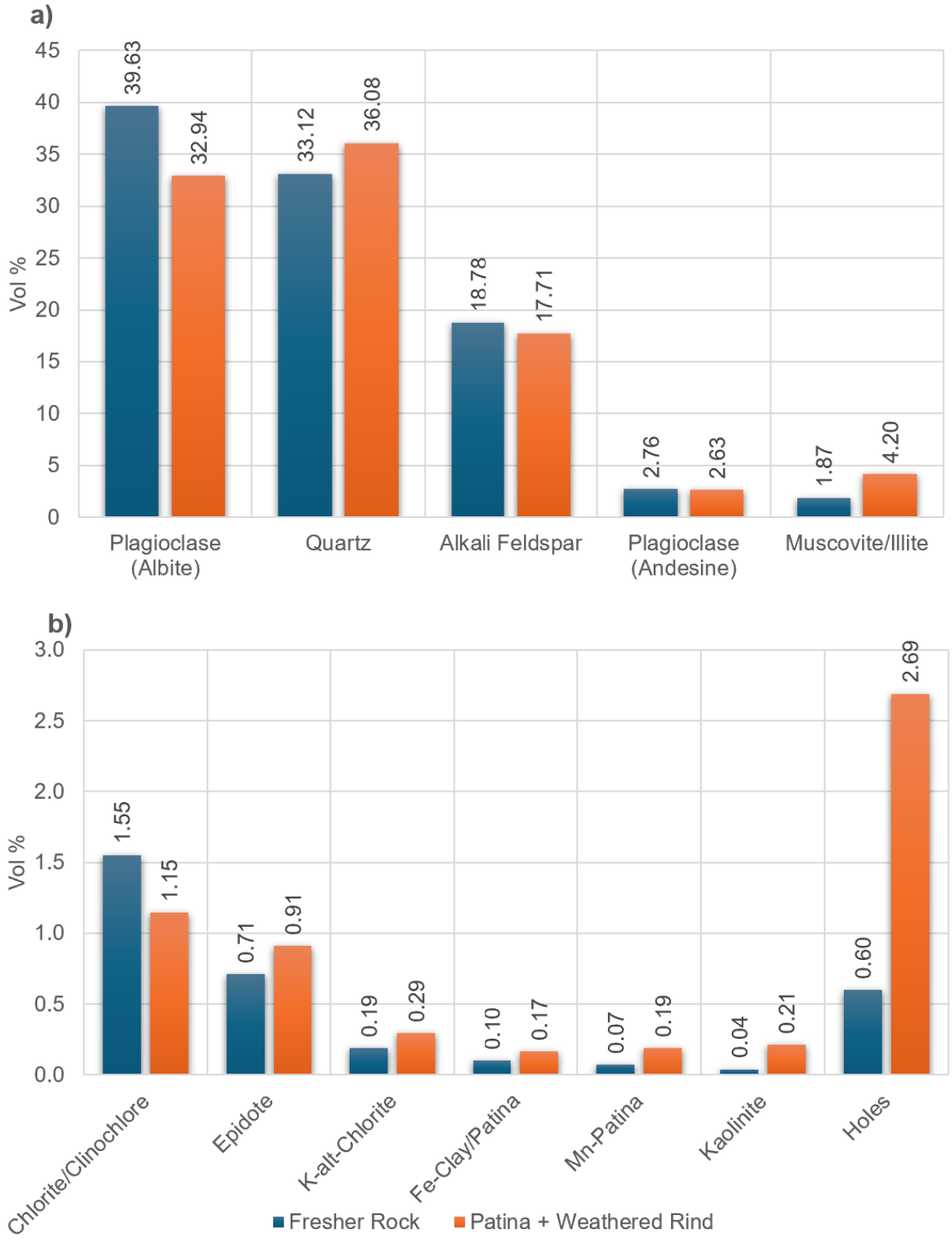

Figure 4.2-29: Summary of TIMA modal analysis of granite samples that compares the abundances of (a) major and (b) minor minerals between the fresher rock and weathered rind domains.

4.2.5.4 Dolerite

Nine dolerite samples were prepared and observed using optical microscopy and TIMA. Of these, four samples were investigated by SEM for further characterisation of the microstructures. To identify the mineralogy of the weathered rind, six samples were analysed by XRD. The mineral compositions were obtained by EMP on three representative samples. In the suite of dolerite samples, RS04_DOL and EX08_DOL are outliers, both in composition and texture (data is not shown but available upon request). RS04_DOL is more similar to a granophyre, whereas EX08_DOL shows characteristics consistent with the basalts. For simplicity, these two samples are not included in the description of this lithology and calculations of modal analysis.

Fresher rock

Dolerite is dark green, medium- to fine-grained ($\sim$300 μm up to 1 mm), holocrystalline and phaneritic. Minerals include augite (up to 28 vol.%), labradorite ($An_{56}Ab_{43}Or_1$, $\sim$26 vol.%), albite ($An_5Ab_{94}Or_1$; up to 25 vol.%) and quartz ($\sim$10 vol.% avg.). Other phases are amphibole (actinolite, $\sim$11 vol.% avg.), epidote (clinozoisite, $\sim$10 vol.% avg.), chlorite (clinochlore), muscovite, and minor microcline. Accessory phases comprise common titanite (up to $\sim$3 vol.%), ilmenite, magnetite, hematite and minor sulphides (pyrite, chalcopyrite and pyrrhotite).

The coarsest grains are dark green augite (up to 1 mm) (Figure *4.2-30*) with habits that range from subhedral stubby prisms to granular anhedral grains. Augite is internally characterised by exsolution lamellae, commonly altered to chlorite, and shows chemical zonation with a brighter rim visible in BSE images (Figure *4.2-30*). The BSE-bright rims are enriched in Fe, Ca, Al, Ti and Mn and depleted in Si and Mg (Appendix Tables *B-1* to *B-16*) relative to the grain cores. Subhedral prismatic labradorite is the most abundant plagioclase and is often overprinted by fine-grained epidote, which is somewhat opaque in transmitted light (Figure *4.2-30*). Albite is anhedral and forms pockets associated with labradorite. Quartz is medium-grained and anhedral, and is typically located between crystals of augite and plagioclase feldspar. Secondary amphibole replaces augite.

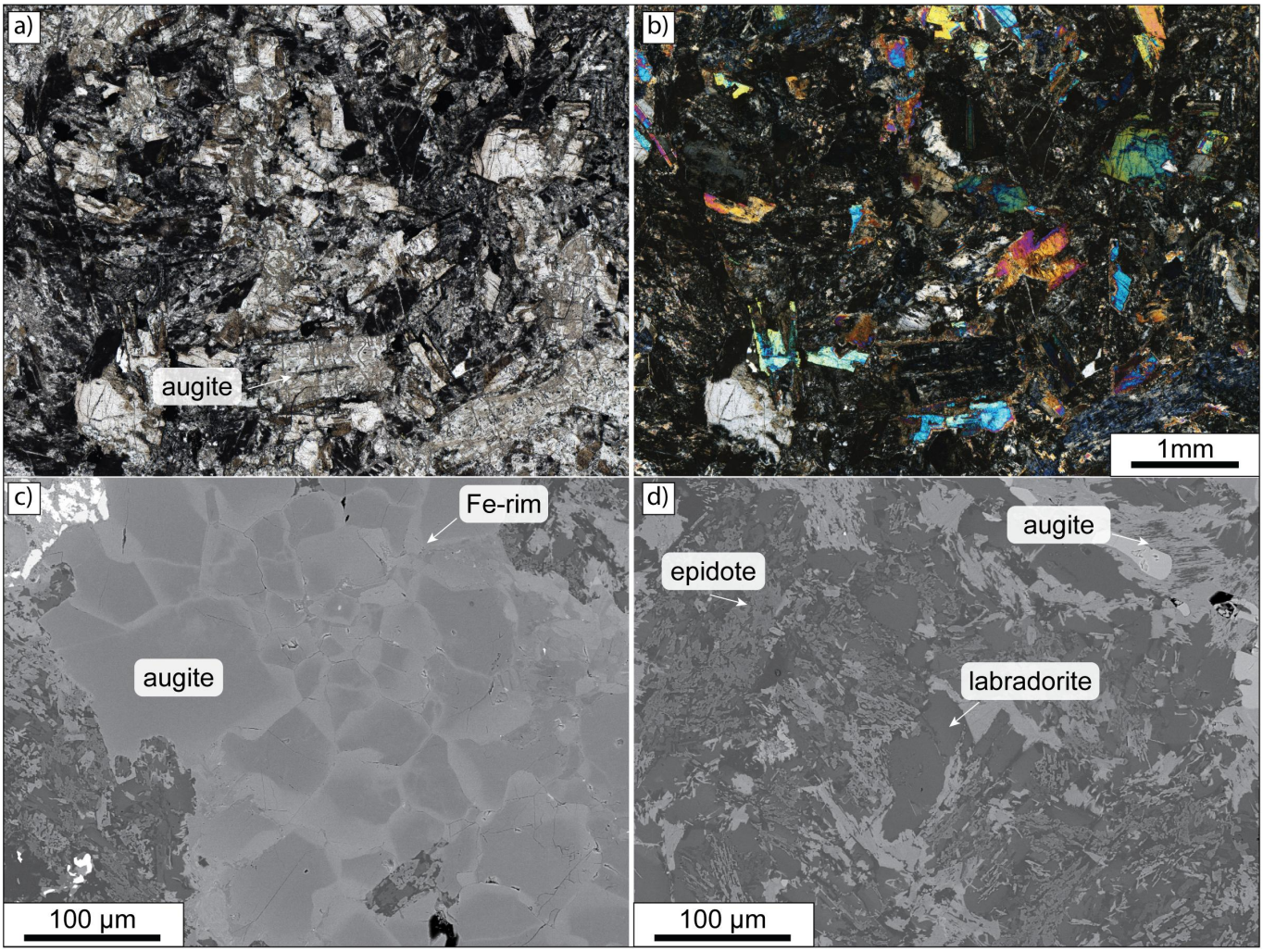

Figure 4.2-30: Plane-polarised (a) and crossed-polarised (b) photomicrographs of dolerite fresher rock. Prismatic crystals of augite are visible and highlighted by high birefringent colours in (b). (c) BSE-SEM image of augite aggregates displaying the internal chemical zonation and (d) secondary epidote replacing labradorite of the rock.

Weathered rind

The weathered rind of dolerite varies from well-developed to very thin and it is generally better developed on the surface of medium-grained samples. Most of the observations made on the gabbro weathered rind (Section 4.2.5.2) apply to dolerite because the two rock types have a similar major element composition. Similarly to gabbro, the weathered rind domain is characterised by an intense brown-to-red colouration, and optical microscopy observations indicate that the colour variation is largely attributable to oxidation and associated alteration of pyroxene (Figure *4.2-31*).

Microstructurally, the weathered rind is characterised by enhanced porosity increasing towards the patina, with similar characteristics to those observed in gabbro (Figure *4.2-32*). In dolerite, porosity is largely attributed to loss of much of the augite, and, to a lesser extent, labradorite.

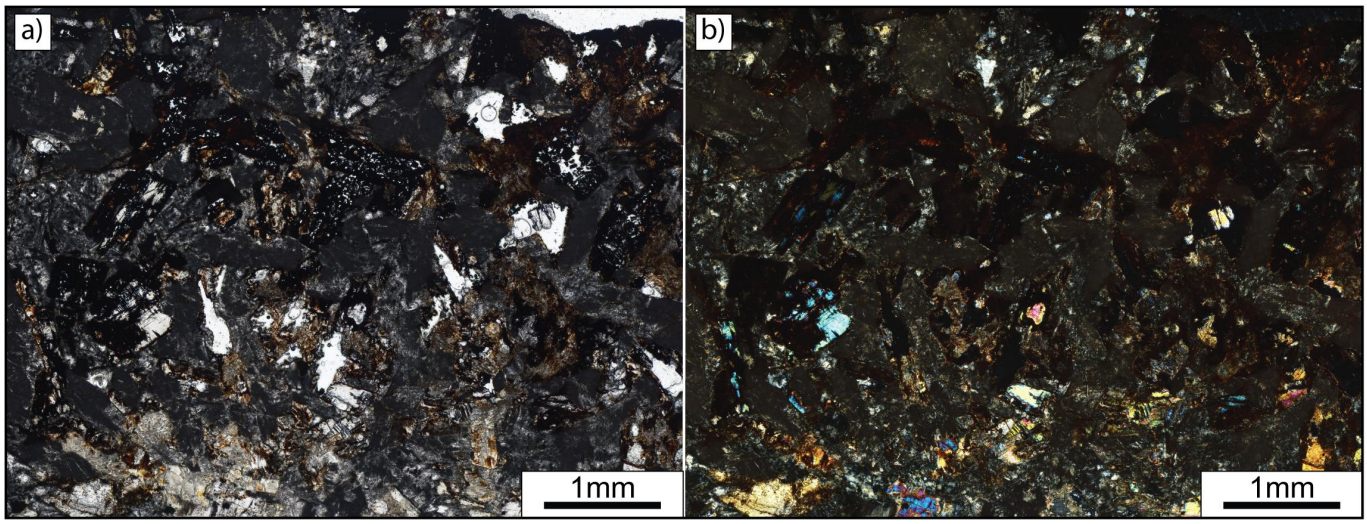

Figure 4.2-31: Plane-polarised (a) and crossed-polarised (b) photomicrograph of the transition from the weathered rind to the fresher rock in dolerite. Despite the bright illumination, the section is quite opaque due the presence of fine-grained Fe-oxides and clays.

At the grain scale, altered augite displays edge pits and irregular boundaries (Figure *4.2-33*). The remaining skeletal crystals are characterised by an internal framework that shows crystallographic control by features such as cleavage, twin planes, exsolution lamellae, and by rims that show local enrichments in iron oxides. Muscovite and clays replace augite and plagioclase. Voids are common on the contacts between altered minerals.

The clay mineral component of the lithology, identified by XRD, includes illite and montmorillonite. In order of decreasing mode, magnetite, hematite and goethite are present. Halite and berlinite ($AlPO_4$) are rare. The TIMA analysis indicates that the weathered rind is characterised by a substantial change in mineralogy compared to the fresher rock. In particular, the phase map shows that the weathered rind is marked by the abrupt disappearance of augite (Figure *4.2-34*), which is compensated by an increase in the modes of muscovite, clays and Fe-oxides. Calculated TIMA mineral abundances are consistent with this finding and indicate a strong decrease in augite ($\sim$7 vol.% avg.), plagioclase, chlorite, titanite, and ilmenite compared to the fresher rock. The average percentage of voids is $\sim$2 vol.% avg greater in the weathered rind than in the fresher rock (Figure *4.2-35*).

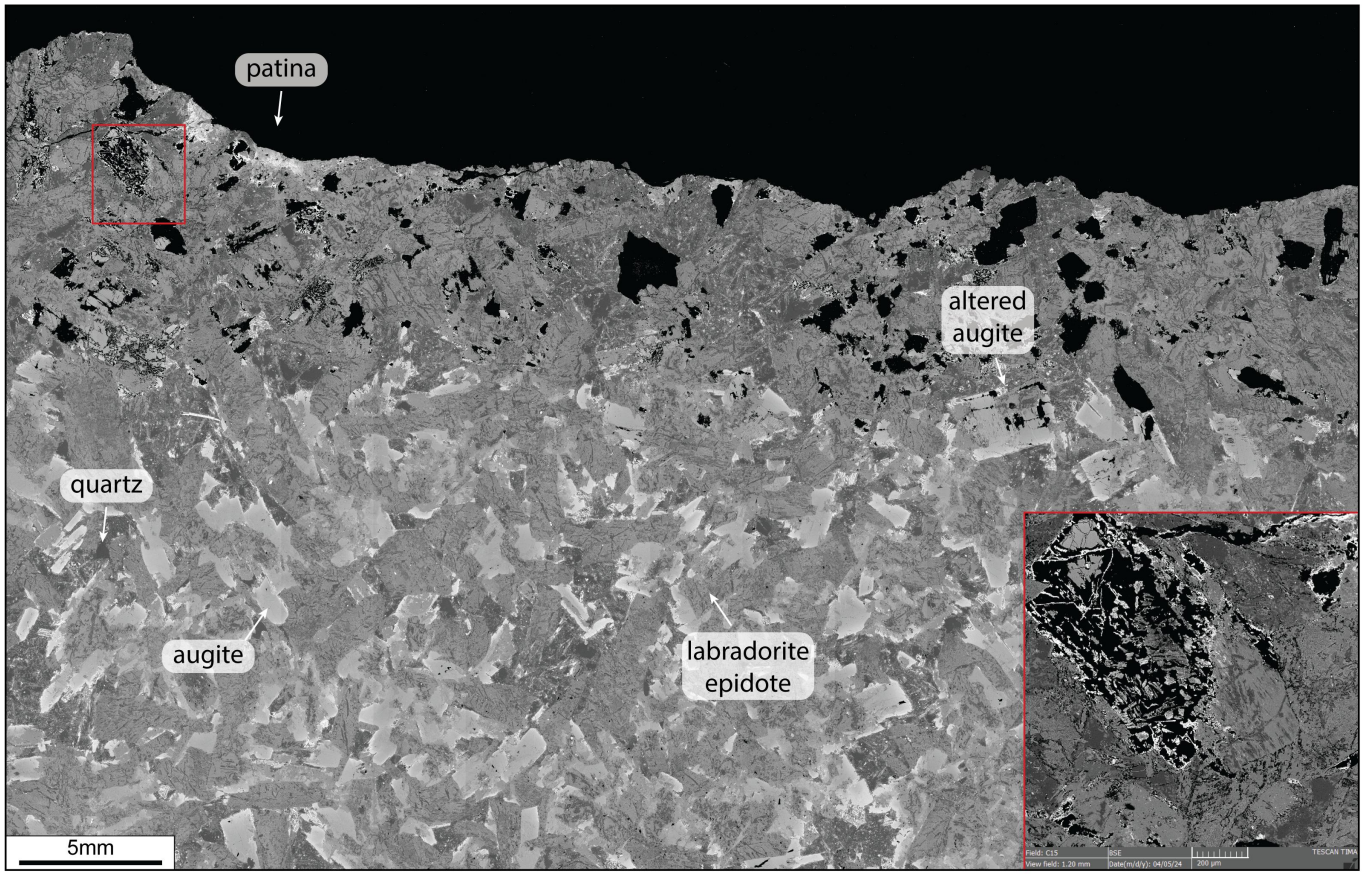

Figure 4.2-32: BSE-SEM large area panorama of the transition from fresher rock to weathered rind to patina from sample AS01_DOL. The weathered rind is characterised by enhanced microporosity and the alteration of minerals present within the fresher rock. The red box indicates the location in the image of the close-up inset. Augite is characterised by bright Fe-rich rims.

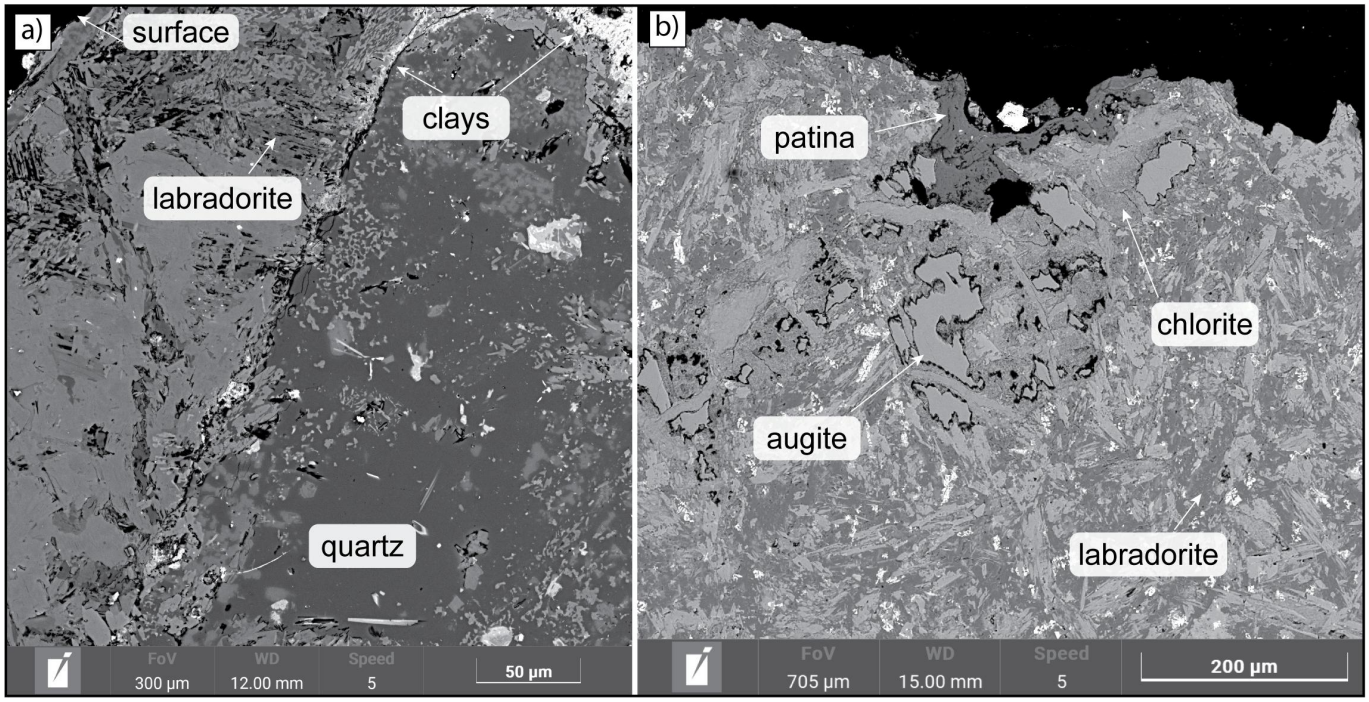

Figure 4.2-33: Grain scale microstructural characterisation of dolerite. (a) BSE-SEM image of altered labradorite crystal at the contact with the surface. Clays occur along the phase boundaries. (b) BSE-SEM image of partially dissolved augite. The crystal is surrounded by chlorite and a groundmass of finer grained labradorite. The brighter material is Fe-rich clays or oxides.

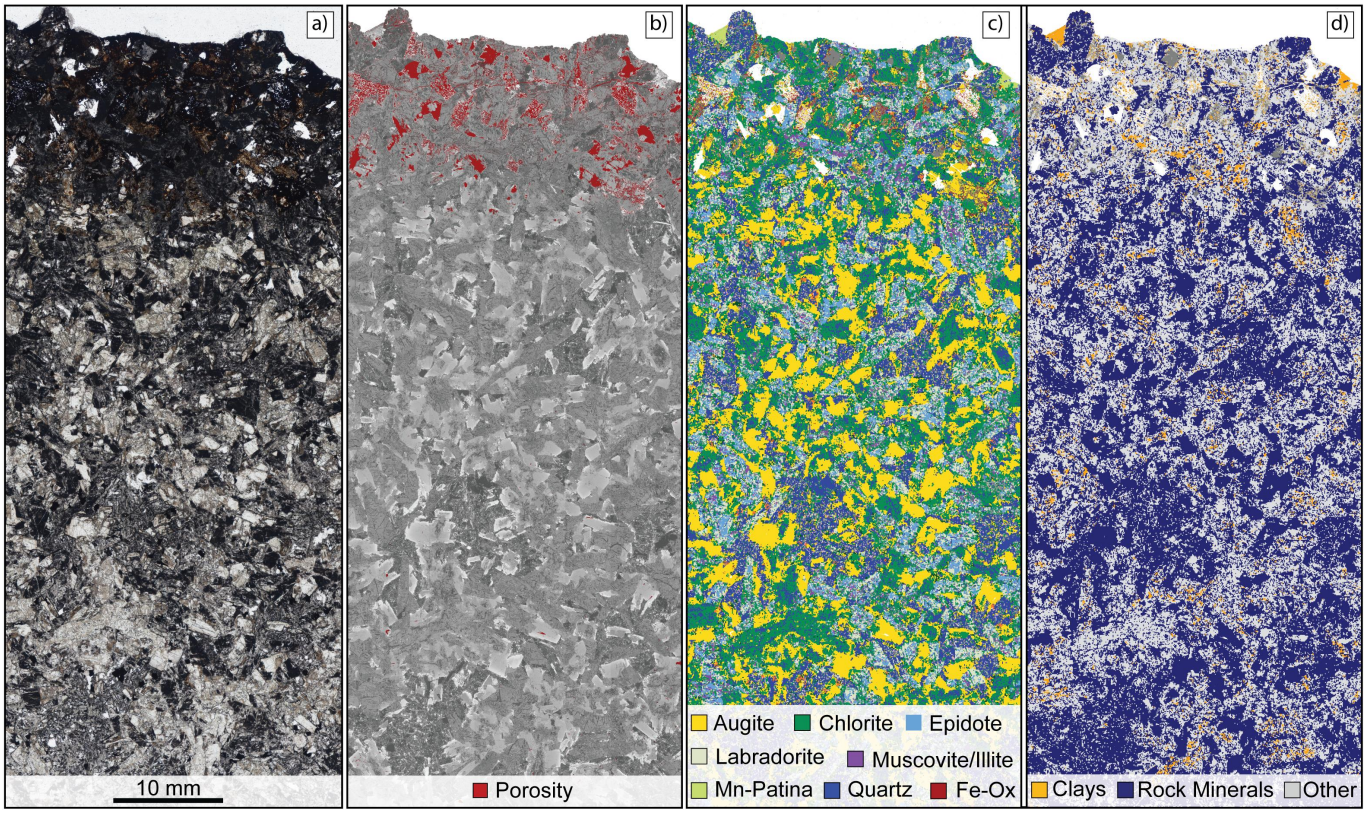

Figure 4.2-34: (a) plane-polarised photomicrograph (b) TIMA-BSE (c) TIMA phase map showing the most abundant phases, and (d) distribution of clays and precursor minerals, shown in the legend as rock forming minerals, for the same portion of sample AS01_DOL, displaying the transition from fresher rock to weathered rind domain. In (b), the red colour shows the region of the sample with epoxy resin, highlighting the enhanced porosity of the domain. In (d), clay minerals correspond to browner colours shown in (a). Clays include phases identified at the TIMA such as muscovite/illite, K-alt-chlorite, kaolinite and patina.

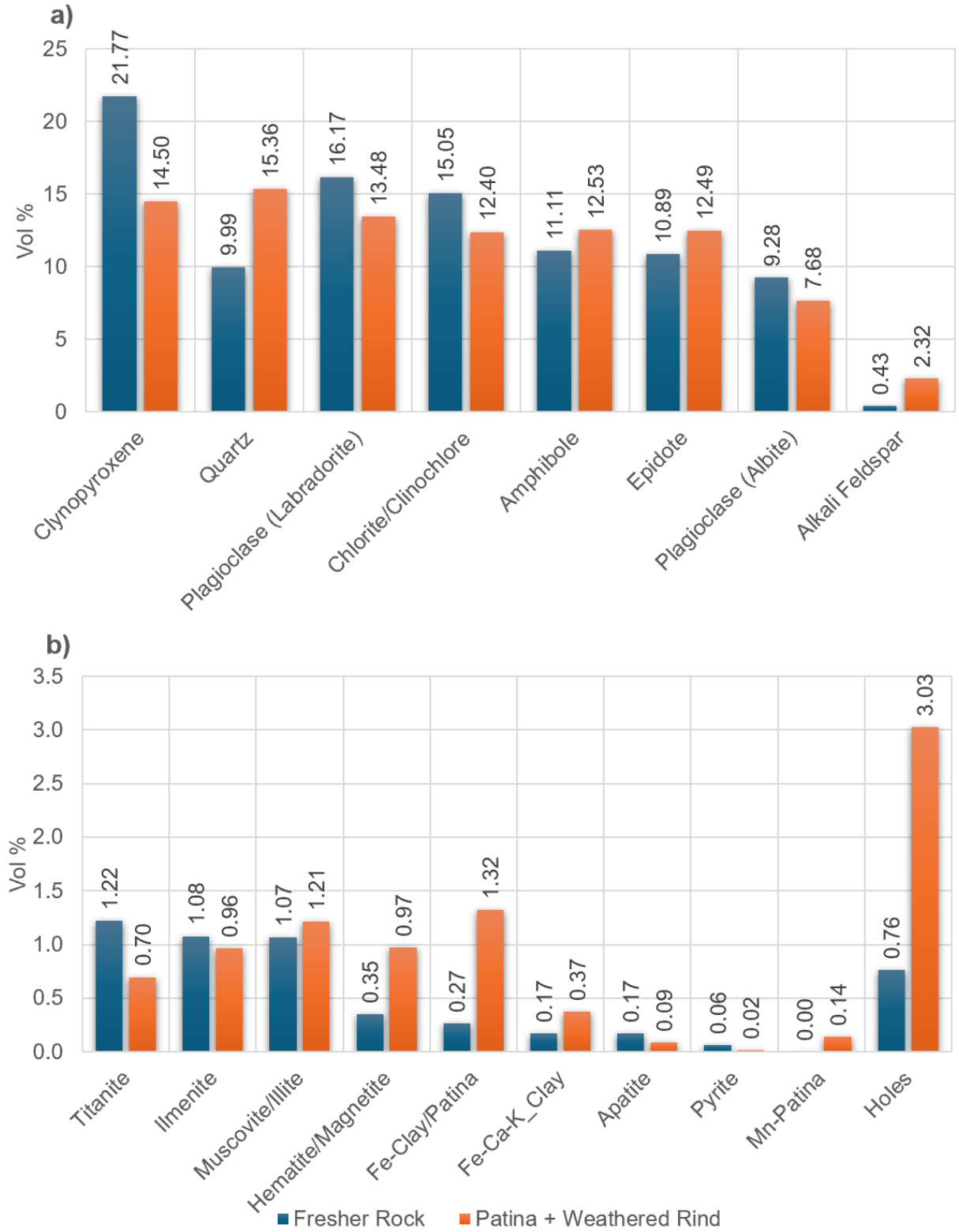

Figure 4.2-35: Summary of TIMA modal analysis of dolerite samples comparing the abundances of (a) major and (b) minor minerals between the fresher rock and weathered rind domains.

4.2.5.5 Basalt

Six basalt rock samples were collected and five polished thin sections of basalt were prepared and investigated by optical microscopy and TIMA. Of these, three samples were investigated by SEM for further characterisation of microstructures, four samples were submitted for XRD analysis, and two were selected for mineral chemistry analysis by EMP. Because of the extreme friability of the material, it was not possible to obtain a thin section from the sample collected from square RS15. Therefore, compositional information on this sample derives only from results obtained by XRD.

Fresher rock

Basalt represents the finest-grained lithology of the study area. Component minerals include albitic plagioclase ($An_2Ab_{97}Or_0$, up to 40 vol.%), sanidine ($An_0Ab_{30}Or_{97}$) and quartz. Mafic minerals include abundant augite (up to ~30 vol.%), chlorite (clinochlore–chamosite), amphibole (actinolite) and epidote (clinozoisite) (Table *4.2-6*). Titanite is present in minor amounts and apatite, ilmenite and sulphides are rare. The texture is generally fine-grained, crystalline, and massive but is locally porphyritic, where micro-phenocrysts of quartz and/or augite are surrounded by an interstitial hypocrystalline groundmass (Figure *4.2-36*). Two samples (RS12_BAS and RS09_BAS) host amygdales filled by radially distributed crystals and surrounded by augite and completely or partially filled by chlorite, epidote, and quartz. In sample RS12_BAS, calcite and euhedral andradite garnet are also present and may represent alteration phases or xenocrysts related to assimilation or partial assimilation of granitic material. Augite is typically anhedral, with brighter rims in BSE-SEM, and commonly surrounded by chlorite and amphibole. Albite is interstitial, forms elongate tabular grains, and is commonly characterised by edge-pits (Figure *4.2-36*).

The presence of albite rather than labradorite, K-feldspar, titanite rather than ilmenite, quartz, and the absence of magnetite are interpreted as a record of hydrothermal alteration on the seafloor or during metamorphism.

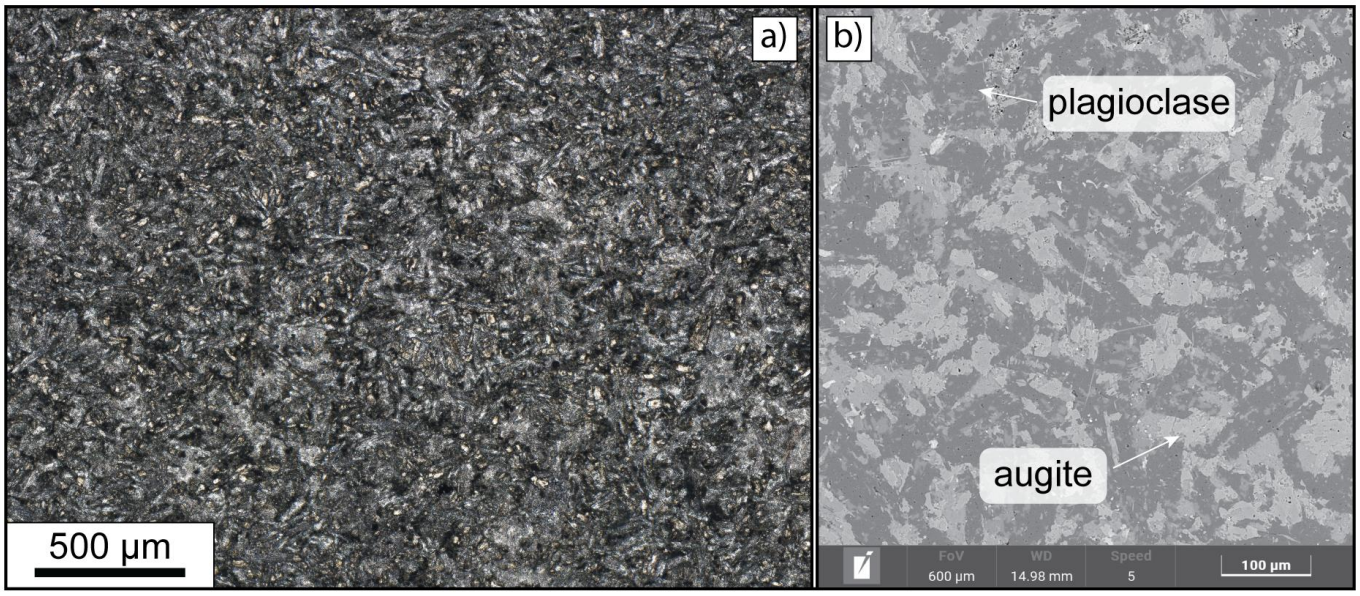

Figure 4.2-36: (a) Plane-polarised photomicrograph of basalt from study area RS09. The matrix of the rock is dominated by fine-grained crystals of plagioclase, which surrounds anhedral augite grains. (b) BSE-SEM image of basalt.

Weathered rind

In most of the available samples, the weathered rind is poorly developed (less than 1 mm in thickness) and ranges from subtle to absent. The colour of the weathered rind ranges from light brown to pale orange. The colour variation is attributed to the preferential alteration and oxidation of pyroxene, which increases in intensity from the fresher rock towards the patina (Figure *4.2-37*).

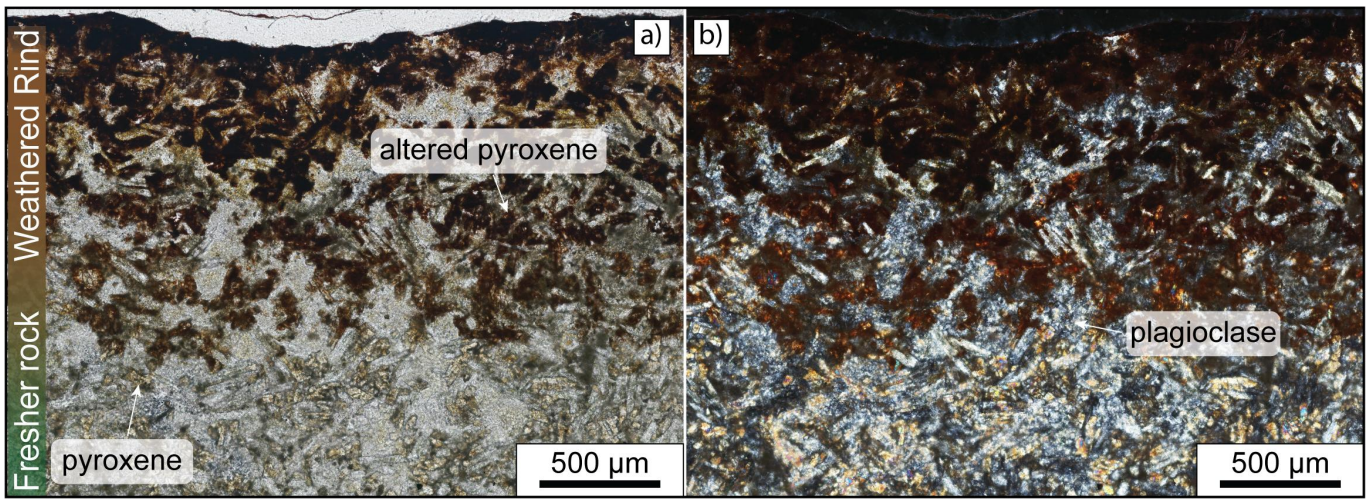

Figure 4.2-37: Plane-polarised (a) and crossed-polarised (b) photomicrograph of the region of transition from the fresher rock to the weathered rind in basalt from study area RS09. The colour variation of the domain is attributed by a distinct alteration of augite.

The SEM observations reveal that the weathered rind of basalt is characterised by the formation

of microporosity. The pore sizes in basalt are much smaller, at $<$100 μm, than pores in the other lithologies. In BSE imaging, the weathered rind forms a darker domain characterised by a decreased mode of augite (Figure *4.2-38*).

On the grain scale, augite and plagioclase both show microstructural evidence of dissolution. The degree of alteration of augite is higher than that of albite, resulting in the formation of near-empty pores within the groundmass with a similar geometry to pre-existing pyroxene grains (Figure *4.2-39*). Dissolution of albite is indicated by increasing edge-pit size from the fresher rock towards the surface.

The XRD analysis of the weathered rind identified muscovite, kaolinite and spinel. Magnetite and hematite are both present. Other minor phases include halite, birnessite and a phase identified as TiO_2 and shows peaks consistent with anatase, which is formed by weathering or hydrothermal alteration of rutile. Modal analyses of basalt are challenged by the very fine grain size of the lithology and, therefore, the obtained values need to be considered indicative. The mineral phase “mixed groundmass” refers to matrix where the grain size is too fine for a diagnostic EDS spectrum to be extracted. Considering the mixed nature of the spectrum and common characteristics of basalt, this it is likely to represent partially or completely devitrified interstitial glass. Despite the limitations of the technique, TIMA results explain the visually observed colour variation of the weathered rind relative to the fresher rock and the increased formation of porosity (Figure *4.2-40*). The calculated mineral abundances indicate a decrease in augite ($\sim$7 vol.% avg.), plagioclase, chlorite, titanite and ilmenite in the weathered rind relative to the fresher rock. The weathered rind is enriched in muscovite, clays and Fe-oxides relative to the fresher rock. On average, the percentage of holes is $\sim$2 vol.% higher in the weathered rind than in the fresher rock (Figure *4.2-41*).

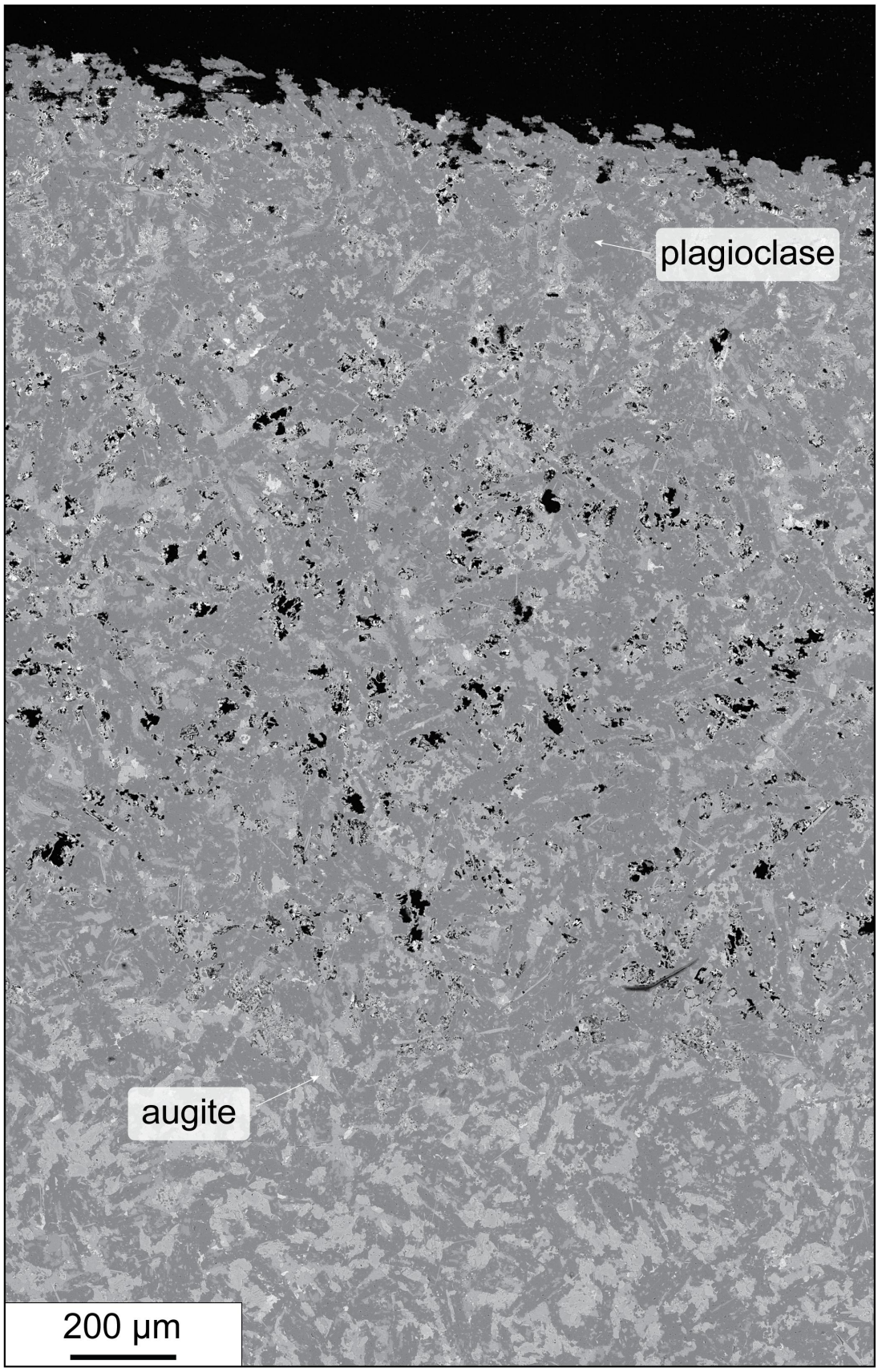

Figure 4.2-38: Large area BSE image of the transition from the fresher rock to the weathered rind in sample AQ12_BAS. The weathered rind is characterised by dissolution of augite and the formation of porosity. Brighter particles indicate the localised formation of Fe-oxides.

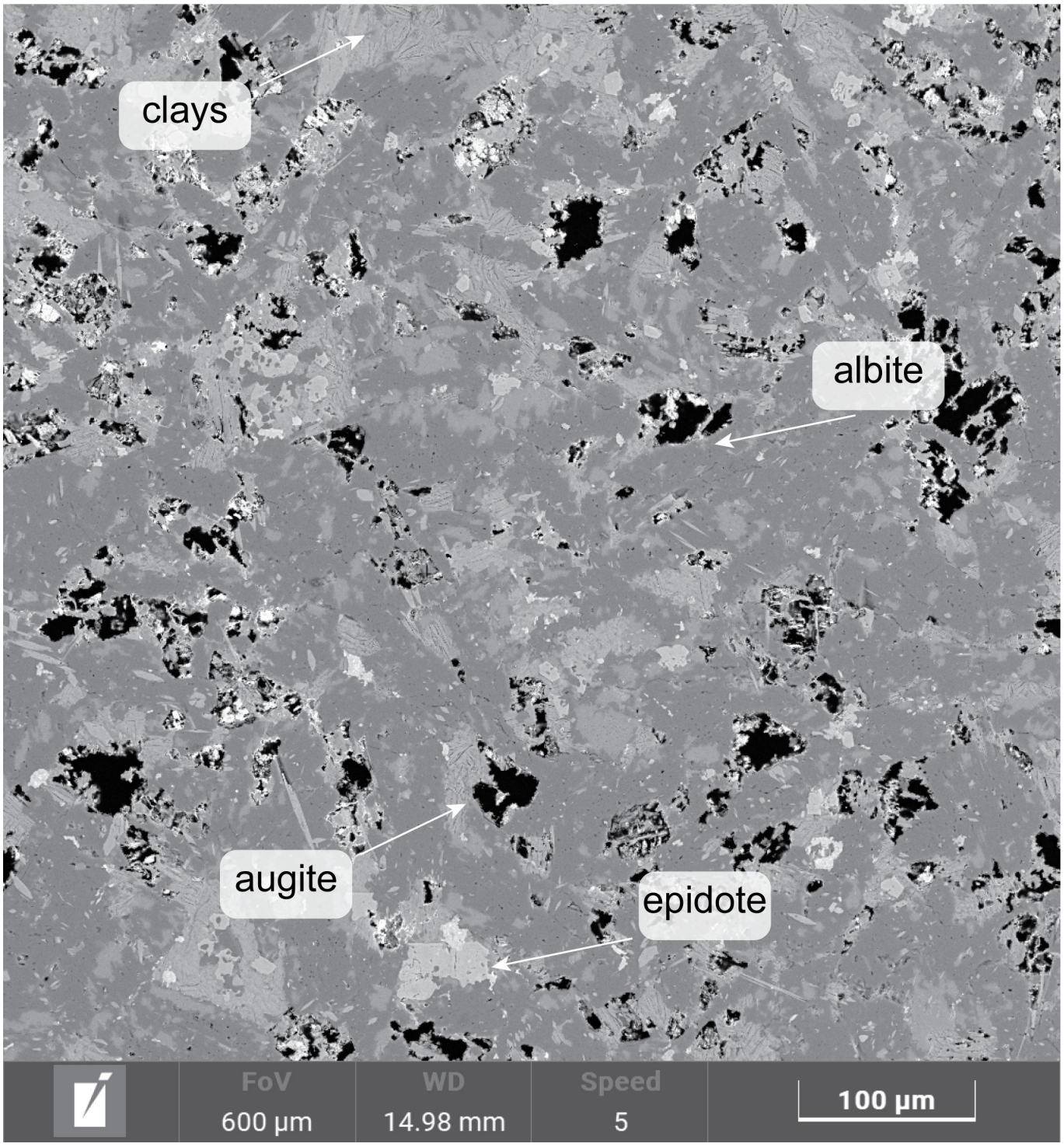

Figure 4.2-39: BSE-SEM image indicating the dissolution of augite and, to a lesser extent, plagioclase.

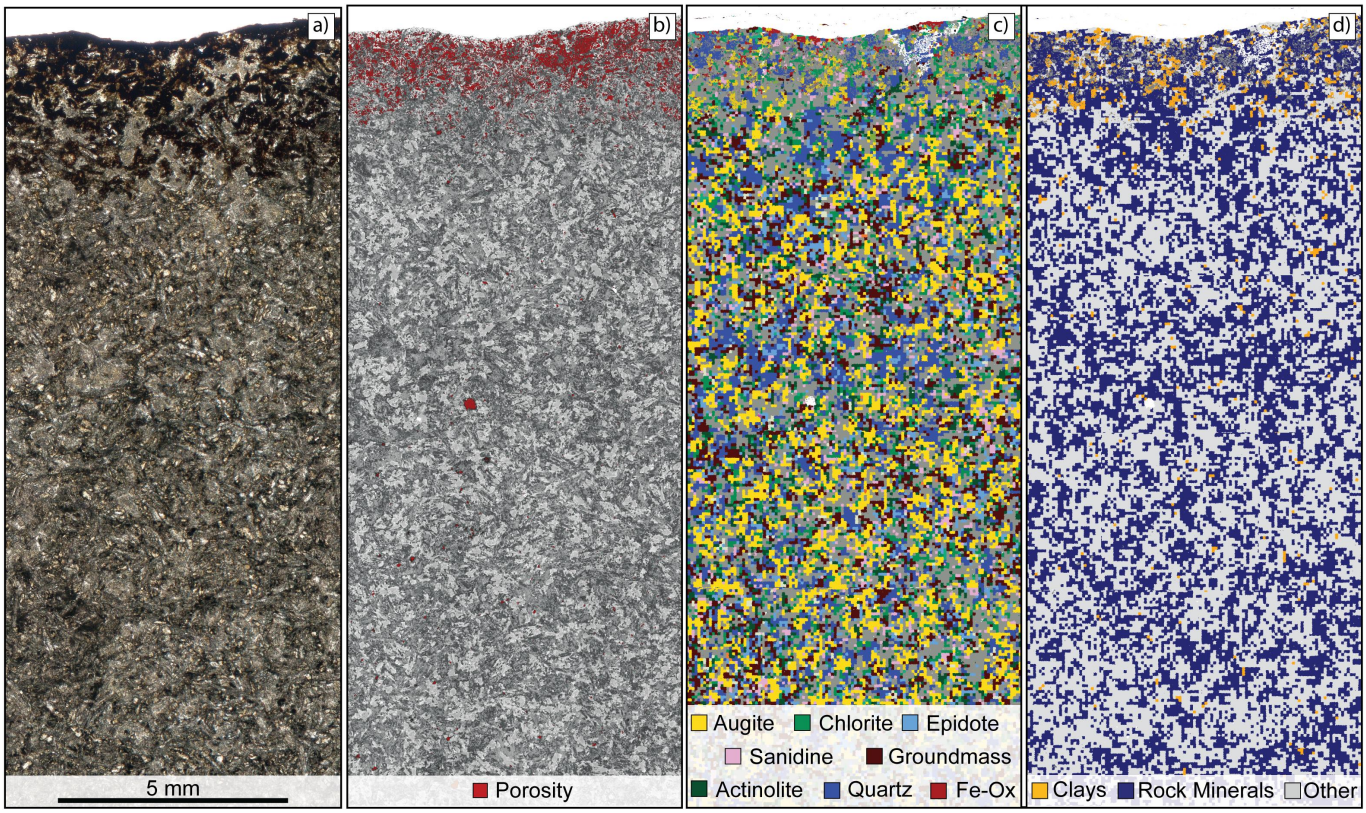

Figure 4.2-40: (a) plane-polarised photomicrograph (b) TIMA-BSE (c) TIMA phase map showing the most abundant phases, and (d) distribution of clays and precursor minerals, shown in the legend as rock forming minerals, for the same portion of sample RS09_BAS, displaying the transition from fresher rock to weathered rind domain. In (b), the red colour shows the region of the sample with epoxy resin, highlighting the enhanced porosity of the domain. In (d), clay minerals correspond to browner colours shown in (a). Clays include phases identified at the TIMA such as muscovite/illite, K-alt-chlorite, kaolinite and patina.

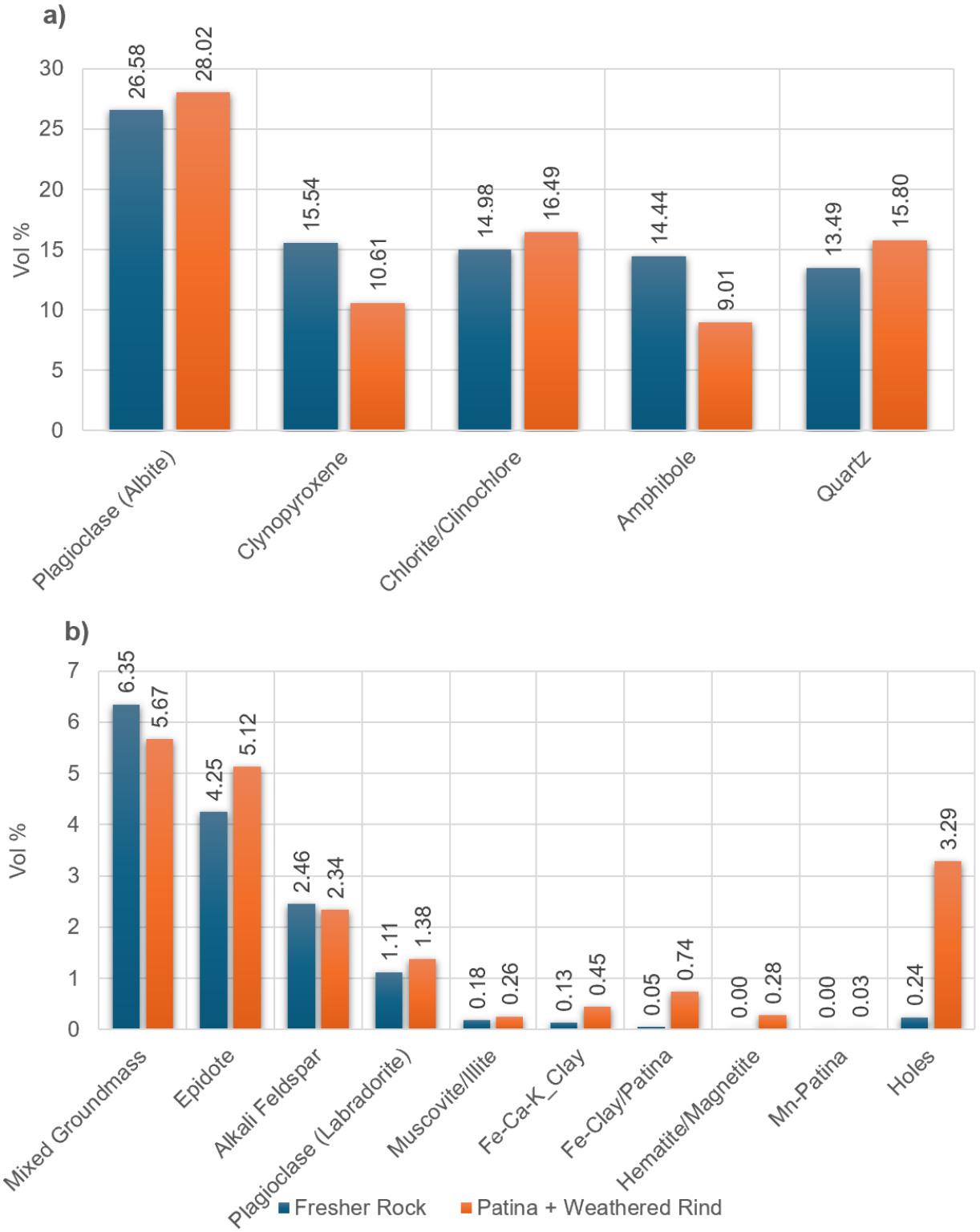

Figure 4.2-41: Summary of TIMA modal analysis of basalt samples that compares the abundances of (a) major and (b) minor minerals between the fresher rock and weathered rind domains.

4.2.6 Geochemical characterisation: weathered rind

This section describes variations in the distribution of major and trace elements within the weathered rind, and on a smaller scale, within the minerals that form the weathered rind in the different rock types, using data obtained by TIMA, EDS and EMP. This work aims to evaluate the geochemical effects of weathering on the rock layers underlying the patina, and the relationship between mineral compositions and the characteristic microstructures described above. The granophyre and granite, and the gabbro, dolerite and basalt, show similar characteristics, so, to avoid repetition, the lithologies are combined to form two groups. Compositions of minerals in the fresher rock and weathered rind are summarised in Appendix Tables *B-1* to *B-16*.

4.2.6.1 Granophyre and granite

TIMA element analyses indicate the presence of compositional variations within the granophyre. In particular, the weathered rind of granophyre is enriched in Fe and K, and depleted, in decreasing order, in Na $>$ Ca $>$ Al $>>$ Mg (Appendix Table *B-28*). At the thin section scale, this variation can be observed in plots of the Fe, Mg, and Ca concentrations of the various samples (Appendix Table *B-28* to *B-32*). The weathered rind is often enriched in P (e.g., Figure *4.2-42*, consistent with previous studies (Ramanaidou and Fonteneau, 2019)). Enrichments in Mn are mostly associated with the patina. A high-resolution, large-area EDS map (LAM-EDS) of the fresher rock–weathered rind transition allows resolution of changes in chemical composition and mineralogy on the transition between, and within, the two domains (Figure *4.2-42*). In particular, Fe enrichment is mostly localised within the patina where it forms a surficial horizon of variable thickness (< 0.5 mm), although Fe is also enriched in the matrix within chlorite and epidote. The distribution of K mimics the granophyric texture characteristic of this rock type. There is a slight decrease in the concentration of K close to the surface and a weak K enrichment at sites of albite dissolution (Figure *4.2-42*). Potassium is also enriched in chlorite and in the patina. The distribution of Al shows similar characteristics; the mapped distribution shows a slight decrease in the weathered rind relative to the fresher rock and an increase within the patina (Figure *4.2-42*). Sodium concentrations decrease towards the surface, consistent with TIMA modal results that show a decrease in the number of large prismatic grains of albite towards the surface, and confirm a trend of progressive Na-depletion with increasing weathering. The LAM also show a pronounced increase in P concentrations within the weathered rind (Figure *4.2-42*).

At the grain scale, SEM–EDS maps reveal relationships amongst the colour of minerals within the weathered rind and their chemistry. Two key examples are considered here (Figure *4.2-43*). In the first, partially altered chlorite located at the visual interface between fresher rock and weathered rind indicates that the colour change is mainly associated with an increase in potassium from the fresher rock to the weathered rind. Microstructurally, this interface coincides with enhanced replacement of the chlorite grain by fine-grained aggregates of clay minerals. Similarly, the chemistry of albite located at the weathered rind–patina interface reveals that the colour change is associated with the presence of K. This is attributed to the ongoing alteration of albite to clay minerals, in agreement with the observations in Figure *4.2-42*.

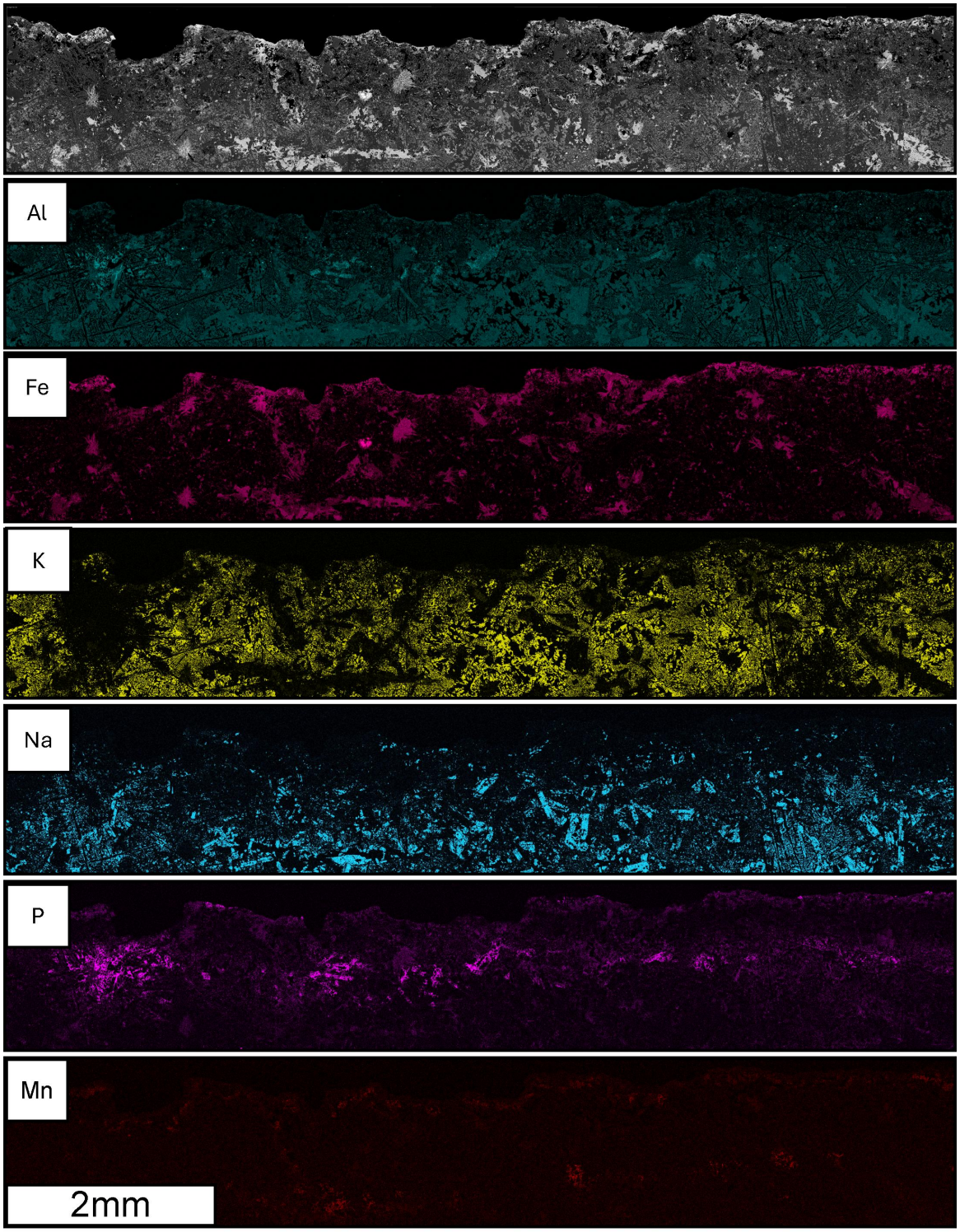

Figure 4.2-42: Large area EDS-SEM map of the transition from fresher rock to the weathered rind and patina from sample AQ08_GPH. In the maps, brighter colours indicate enrichment in the mapped element.

The EMP-derived chemical compositions of the minerals located within the weathered rind shows depletion of albite and microcline in Na, Si and Al relative to the fresher rock (Figure *4.2-44* and Appendix Table *B-28* to *B-32*). Chlorite is depleted in Fe, Mg, and enriched in K within the weathered rind relative to the fresher rock. Potassium is not typically found in chlorite so the K-enrichment is interpreted to reflect alteration of chlorite to a K-bearing sheet silicate, such as illite. Epidote is enriched in Fe and depleted in Mn within the weathered rind relative to the fresher rock. These chemical trends align with the microstructural observations of feldspar dissolution and the associated formation of clay alteration (e.g. illitisation) within the weathered rind.

In granite, the weathered rind is characterised by similar patterns of chemical alteration to those observed in the granophyre. For example, compared to the fresher rock, the weathered rind is depleted in Na $>$ Al $>>$ Ca and enriched in Fe $>$ K $=$ Mg. At the millimetre scale, the weathered rind and patina of granite are enriched in Fe and P relative to the fresher rock, although the average concentrations are within uncertainty for the two lithological types (Appendix Table *B-28* to *B-32*). Iron is heterogeneous within the patina on the rock surface, and is enriched in films that surround large crystals of quartz and are interpreted to host chlorite and clays. Plots of Al distribution indicate localised Al-enrichment within the weathered rind. These Al-enriched regions coincide with altered grains of albite that are replaced by kaolinite and muscovite. Therefore, although the bulk-rock concentration of Al derived from TIMA data is relatively consistent from the fresher rock to the weathered rind, thin-section scale EDS maps on the micrometre scale indicate local redistribution of this element. Phosphorus is also enriched in the weathered rind of granite relative to the fresher rock.

At the grain scale, the chemistry of rock-forming minerals remains substantially unaltered, or at least at the spatial resolution of EMP, without clear patterns of element depletion and/or enrichment (Appendix Tables *B-1* to *B-16*).

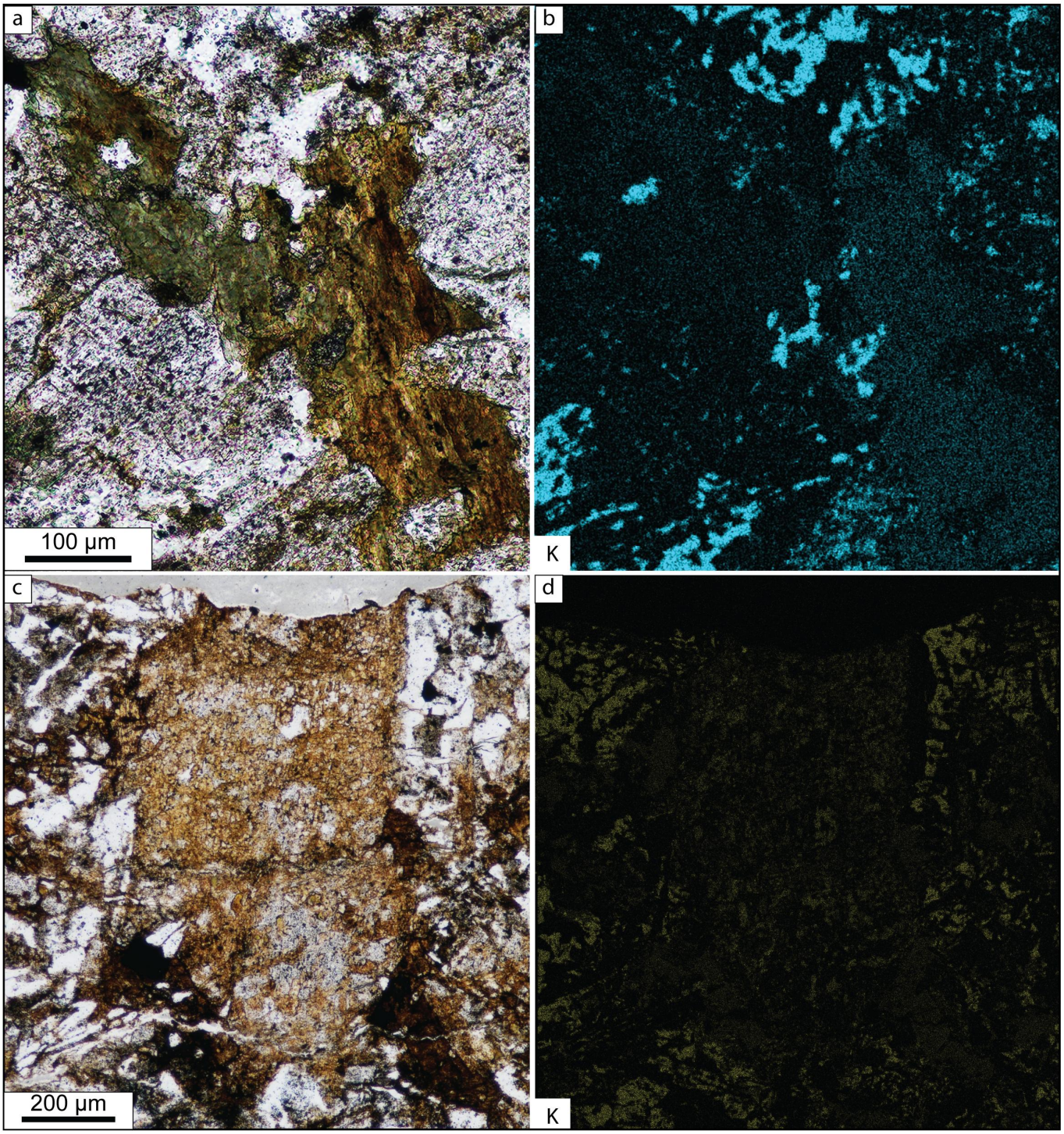

Figure 4.2-43: Plane polarised photomicrograph (a) and potassium element map (b) of a chlorite crystal located at the transition between the weathered rind and fresher rock in sample AQ06_GPH. The brown colouration coincides with a localised enrichment in potassium. (c) and (d) represent the plane polarised light micrograph and K element map of an albite crystal at the weathered rind-patina interface of sample AQ06_GPH. Similarly, the altered regions of the mineral are characterised by higher K concentrations due to the illitisation of albite.

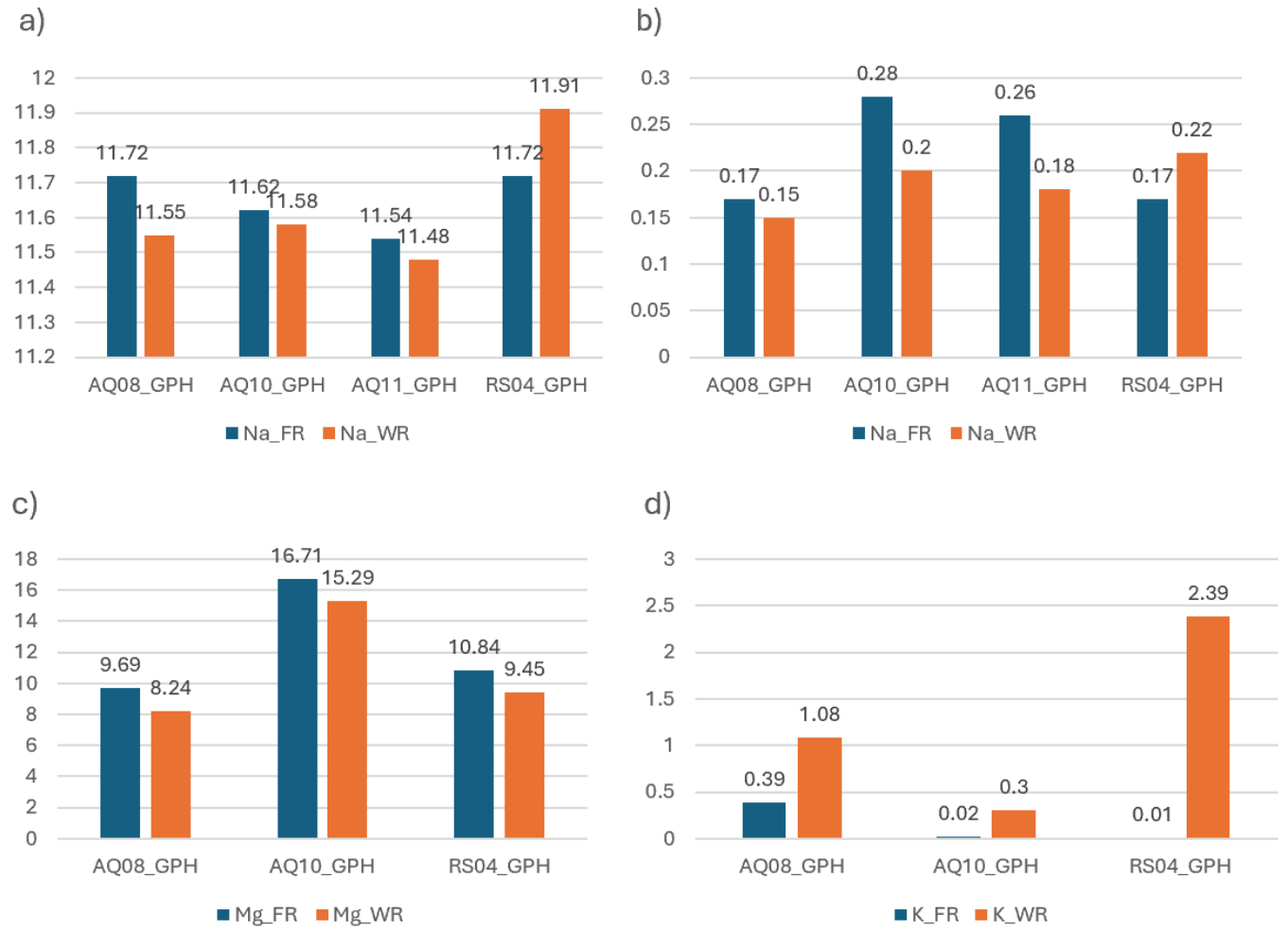

Figure 4.2-44: Comparative chemistry for (a) albite, (b) microcline and (c,d) chlorite in granophyre. The plots indicate the average wt% of the considered element oxide between fresher rock (FR) and weathered rind (WR). Aside from those in RS04_GPH, feldspars of the weathered rind display a common depletion in Na. Across the domains, chlorite is depleted in Mg and enriched in K.

4.2.6.2 Gabbro, Dolerite and Basalt

From the fresher rock to the weathered rind, gabbro shows enrichment in Fe, in agreement with the strong increase in the modal amount of Fe oxides observed by TIMA (Appendix Table *B-29*). In contrast, there is a detectable decrease in the concentrations of Si, Al, Ca and Mg. This elemental difference is visible at the thin section scale in the TIMA element maps (Figure *4.2-45* and Appendix Table *B-28* to *B-32*). In the maps, the weathered rind is generally highlighted by a millimetre-thick Fe-rich zonation where Fe is most enriched within the cores of altered augite crystals, and to a lesser extent, enstatite. Concentrations of Mg and Al are visibly depleted within the weathered rind relative to the fresher rock (Figure *4.2-45*). In the fresher rock, Al is localised in tabular crystals of labradorite (and epidote). This distribution becomes more uniform towards the surface of the rock (top of Figure *4.2-45*). At the surface, the enrichment of Mn indicates the distribution of the patina.

Higher spatial resolution EDS maps show that the compositional variations observed in the TIMA plots reflect mineral compositions (Figure *4.2-46*). For example, large crystals of augite enriched in Fe and Mg compared to the surrounding labradorite (Figure *4.2-46*). The core of the altered augite is characterised by an Fe- and Al-rich framework which represents former pigeonite exsolution lamellae that are now replaced by Fe-oxides and clays. In contrast, the highest Al concentrations are found in labradorite, which also shows zonation in Na. The EDS map shows brighter Na-rich rims at the contact with the altered augite, consistent with the formation of albite during alteration (Figure *4.2-46*).

The composition of clinopyroxene, obtained by EMP, does not show systematic chemical variation. The Fe content of clinopyroxene within the weathered rind ranges from depleted to slightly enriched relative to the fresher rock (Appendix Tables *B-1* to *B-16*) whereas the Mg content of clinopyroxene is either unchanged or increased from the fresher rock to the weathered rind. Labradorite shows two distinct behaviours. Overall, the Ca contents tend to increase moving into the weathered rind, except for sample AQ09_GBR. Contrarily, the Na content is found to either increase or decrease from the fresher rock to the weathered rind (Appendix Tables *B-1* to *B-16*). However, it must be noted that labradorite in gabbro is chemically zoned, so it is difficult to recognise trends of compositional variation across the domains. Comparing the chlorite and epidote analysed within the weathered rind, both the minerals are enriched in Fe, and in the case of chlorite, depleted in Mg compared to the fresher rock. Similarly, muscovite is depleted in K across the two domains, with higher concentrations in the fresher rock (chlorite Appendix Table *B-10* and *B-12*; epidote Appendix Table *B-14* and *B-16*).

In dolerite, the weathered rind is enriched in Fe, Al, K and Ti relative to the fresher rock. In contrast, the fresher rock is enriched in Si $>$ Ca $>$ Mg relative to the weathered rind. The medium-grained samples show a pattern of Fe-enrichment similar to that observed for gabbro. However, in dolerite, the weathered rind is characterised by a sharp decrease in Mg, and to a lesser extent Ca, which coincides with the disappearance of augite (described in Appendix Tables *B-1* to *B-16*). Here, Al and P are also enriched. At the grain scale, the EMP results show that unaltered minerals generally do not show any change in composition from the fresher rock to the weathered rind, although the Fe-rich rims on augite are depleted in Fe within the weathered rind.

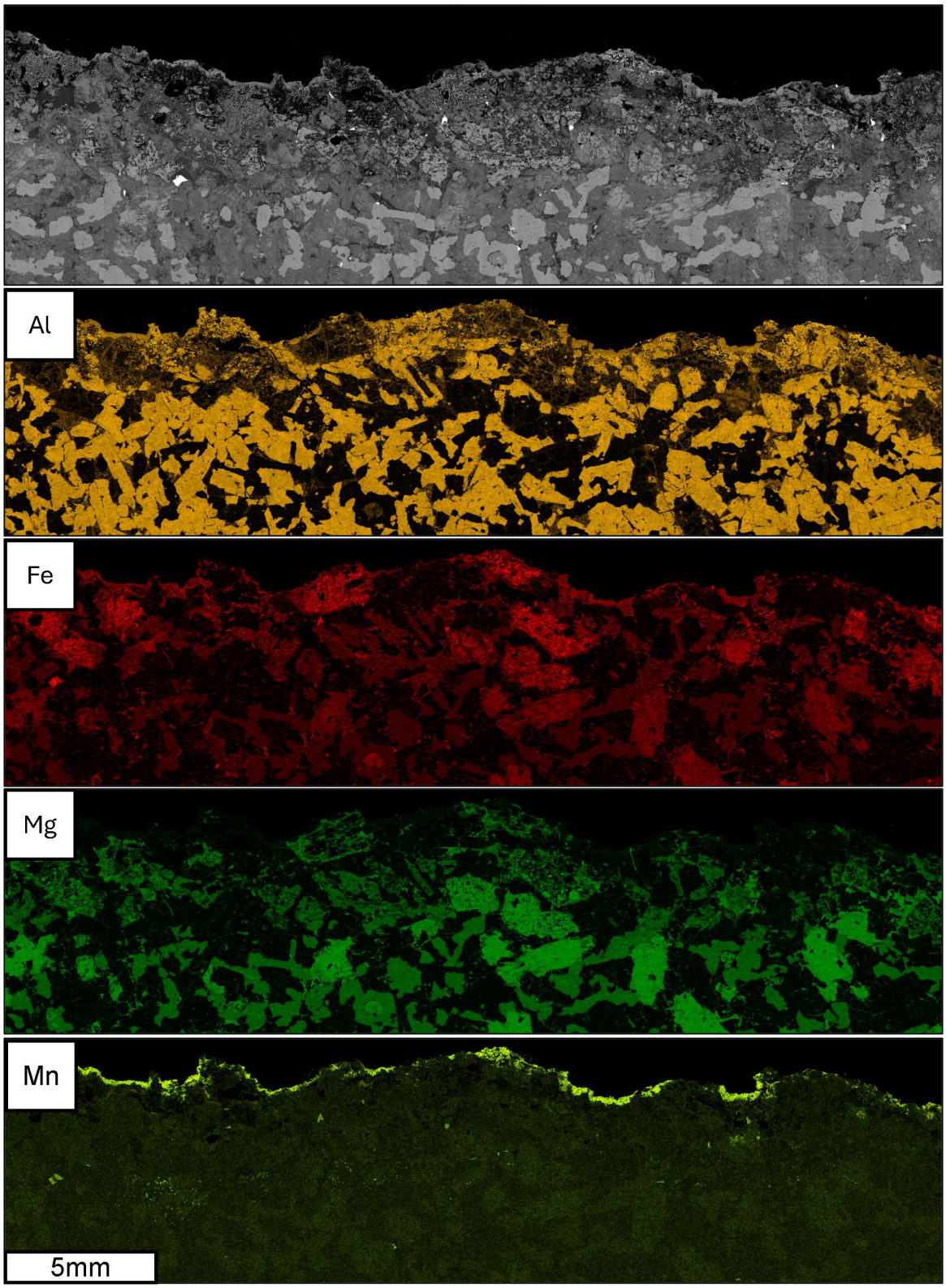

Figure 4.2-45: EDS-TIMA map of sample AQ15_GBR. The maps show that the microstructural transition from the fresher rock to the weathered rind is accompanied by a thin section scale chemical variation. Colour intensity increases with element concentration.

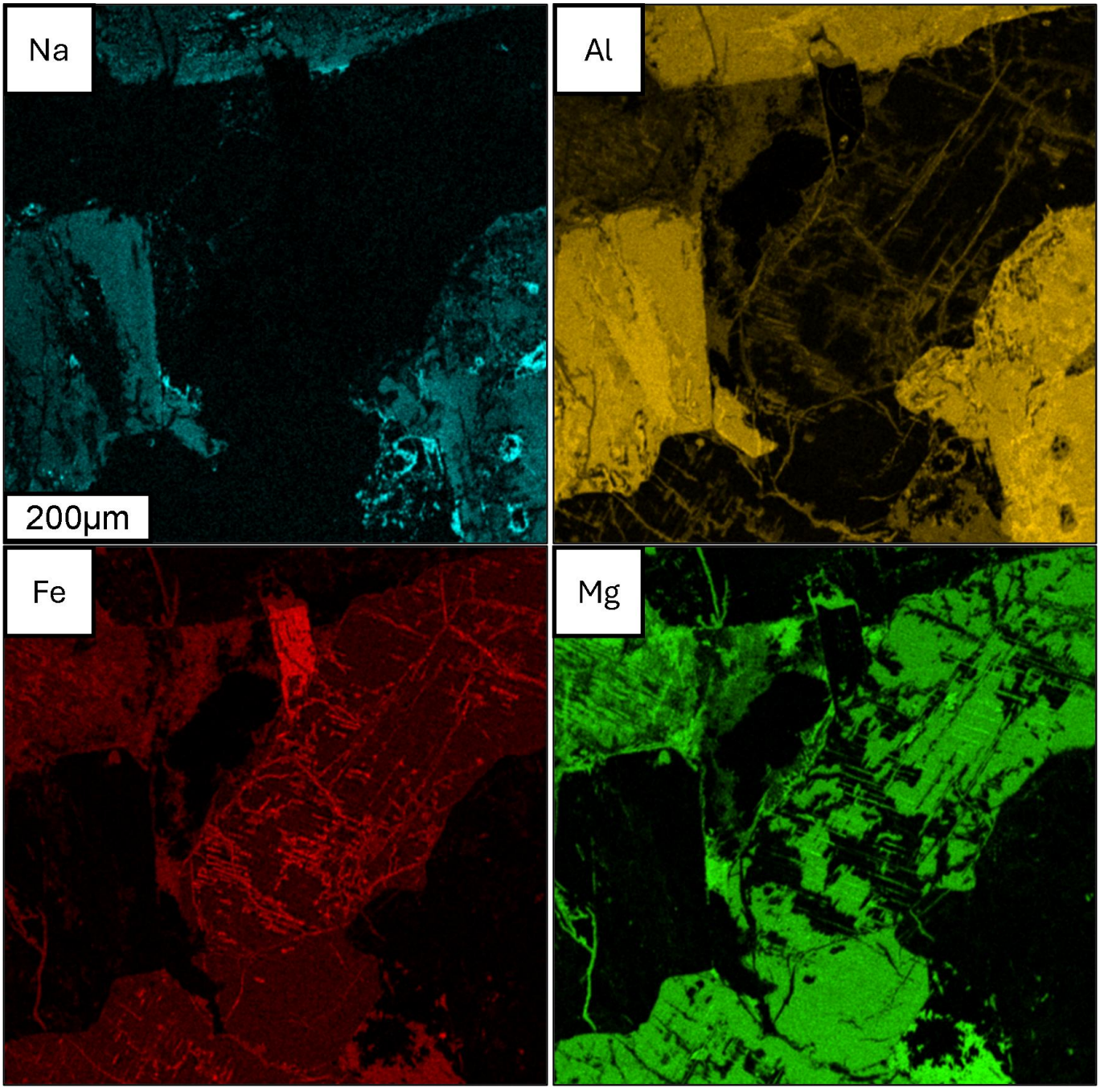

Figure 4.2-46: SEM-EDS map of gabbro acquired over altered augite (central grain) and labradorite (surrounding grains). The distribution of Mg, Fe, Na and Al are heterogeneous. Localised enrichments in Na may represent albite or other Na-rich alteration phases.

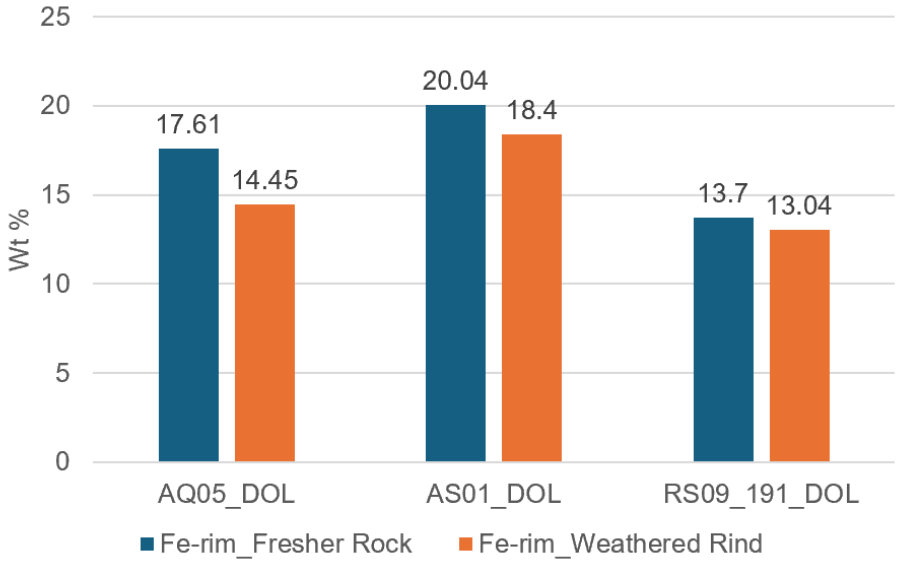

Figure 4.2-47: A comparison of the average wt% FeO in augite rims in the fresher rock and weathered rind. The weathered rind is Fe-depleted relative to the fresher rock.

Basalt shows similar trends to dolerite. The weathered rind is slightly enriched in Al $>$ Fe $>$ Na $>$ Si and depleted in Mg $>$ Ca compared to the fresher rock. At the thin section scale, this compositional change is visible in the TIMA element plot as a thin ($<$0.5 mm) Fe-rich layer, depleted in Mg and Ca compared to the underlying bedrock (Appendix Table *B-32*). The transition from fresher rock to weathered rind appears sharper than in the other lithologies. However, this might be explained by the smaller grain size, such that a transition over a similar number of grains would be much sharper in the basalt than in the gabbro, and micrometre-scale chemical transitions would be difficult to observe because of the limitations of the spatial resolution of analysis. Phosphorus is enriched in the weathered rind relative to the fresher rock and Mn and S are only observed within the patina. The compositions of minerals within the basalt are indistinguishable between the weathered rind and fresher rock (Appendix Table *B-32*).

4.2.7 Macro to microstructural characterisation: patina

The patina (or rock varnish, Dorn (2007)) represents the outermost layer of the rocks at Murujuga and it consists of clay minerals cemented to the host rock by oxyhydroxides of manganese and iron (Dorn, 2013, 2007; Dorn and Krinsley, 2019; Neumann et al., 2022, and references therein). In the field, patina colours include orange, red, dark red and black. Patina occurs on top of the weathered rind. Optical microscopy observations of patina in conventional petrographic thin sections (30 μm in thickness) are challenged by its opacity in transmitted light and the small mineral grain size of the mineral grains. Scanning electron microscopy permits further characterisation of the microstructures, thickness, distribution and morphologies of the patina across granophyre, gabbro, dolerite and granite. At the time of the writing of this report, further investigations are needed to characterise the patina in basalt. Morphological observations were also conducted on selected unpolished billets of patina of granophyre and gabbro.

4.2.7.1 Surface morphologies

Observations conducted on unpolished samples help us to understand the macroscale features of the rock surface and the distribution of the patina (Figure *4.2-48*). The observations included here only report details of granophyre (sample AQ11_GPH) and gabbro (sample AQ15_GBR), and therefore may not be representative across the whole of Murujuga where there is extensive variation in surface topography within samples of each lithology.

In both samples, the topography is highly irregular, characterised by sharply truncated geometries of exposed rock minerals, fractures and cavities almost resembling, in top view, a lunar landscape. In the granophyre, cuspate geometries are defined by fine-grained crystals of quartz interpreted as relicts of the partially dissolved granophyric intergrowths (Figure *4.2-48*(a)). Red-coloured patina is widely distributed. Darker patina is visible at the bottom of deeper cavities. The surface of the gabbro is characterised by potato crisp-like geometries and larger crystals of partially weathered pyroxenes on the macro-scale (Figure *4.2-48*(c)). The skeletal remains of large crystals of augite are recognisable, with shapes controlled by crystal geometry. A fresh fracture on the surface exposes the underlying, orange-weathered rind of altered labradorite, oxidised augite and abundant clays. In this sample, the patina is darker than the patina on the granophyre sample, and it coats the surface topography so that the surface is smoother than the topography of the underlying weathered rind.

Secondary electron SEM images (**SE-SEM**) show the surface topography of granophyre and gabbro in more detail (Figure *4.2-49*(a,b,c)). In this observation mode, the patina appears as a smooth coating sitting on top of the porous and irregular weathering rind of both lithologies. The contact between the weathered rind and the patina is sharp (Figure *4.2-49*(a,b)), in contrast to the gradational fresher rock–weathered rind transition. In the granophyre, in regions where the patina is not present, either because it never formed or because it has been removed by flaking or another process such as dissolution, the underlying weathered rind is exposed, showing aggregates of micropores (Figure *4.2-49*(b,d)). This is in agreement with the microstructural observations conducted in thin section where the pores represent voids left by dissolved feldspars. In places, the patina displays botryoidal textures that resemble, at a much smaller scale, stromatolite morphology (Figure *4.2-49*(e-h)). Fractures and micro cavities are also present (Figure *4.2-49*(f,h)).

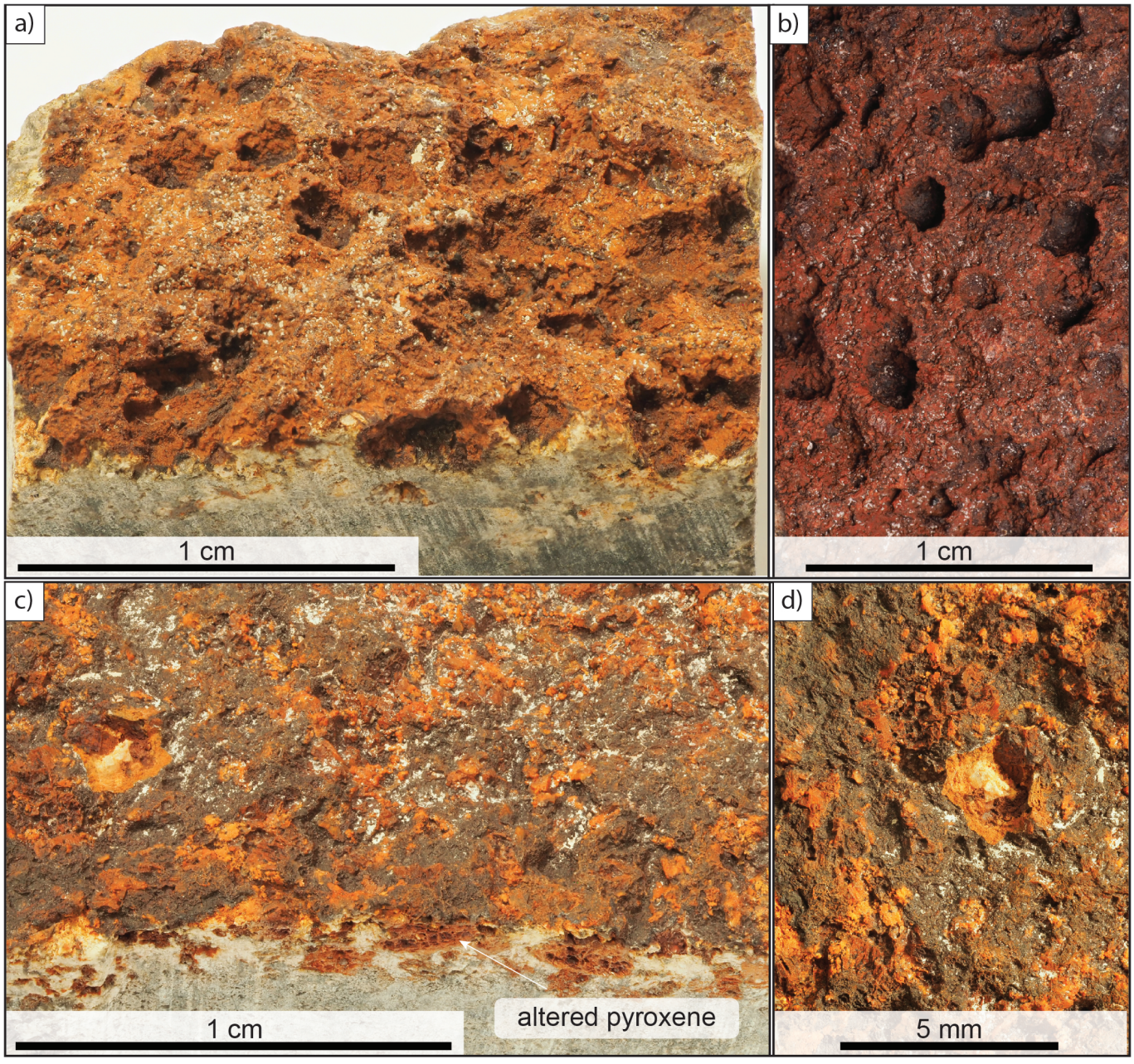

Figure 4.2-48: Macro length-scale characterisation of patina. Images (a) and (c) are of unpolished cut surfaces of rock billets showing cross sections through AQ11_GPH and AQ15_GBR, respectively. Images (b) and (d) are top views of the billets shown in cross-section in images (a) and (c).

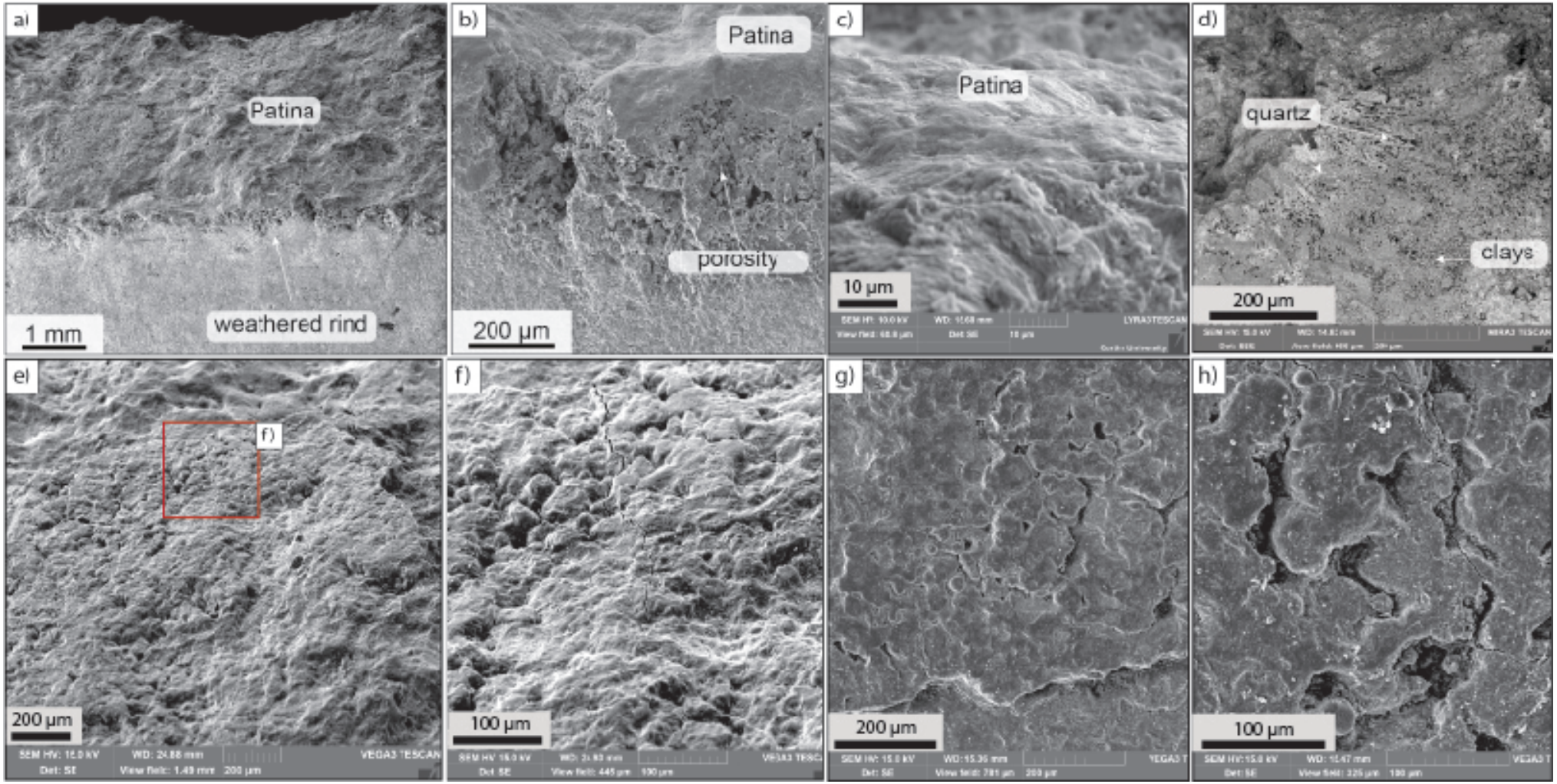

Figure 4.2-49: SE-SEM images of patina from unpolished billets of granophyre (a,b,d,e,f,g,h) and gabbro (c). Features are shown at higher resolution in subsequent images.

4.2.7.2 Cross-sectional microstructures

In this section, microstructural observations from scanning electron microscopy (SEM) analyses of patina found on granophyre, gabbro, granite and dolerite are summarised. At the time of writing of this report, numerous images have been collected across the available samples. Here, the most salient findings are presented Figures *4.2-50* to *4.2-56*. Images at a range of scales, including high resolution BSE panorama images, are shown to provide context (Figures *4.2-57* to *4.2-61*). The BSE brightness increases with average atomic number of the material analysed.

Overall, patina shows highly variable morphology, thickness, distribution and internal structure. In cross-section, the patina appears as laterally discontinuous, complex, micro-deposits, separated from the underlying substrate by a sharp interface, and is most commonly developed on the irregular surfaces of altered minerals that show microstructures defined by the underlying substrate. In granophyre, for example, the underside of the patina fills micropores generated by the dissolution of feldspars, and it is possible to speculate that the geometry of the interface performs an anchoring effect (Figure *4.2-48*(a,b)). Patina can form a very thin film layer that wraps the surface of the outermost minerals of the weathered rind (Figure *4.2-48*(c)). In other places, topographic depressions on the rock surface (i.e. microbasins of Dorn (2007)) host thicker patina (i.e. microdeposit), up to 800 μmthick (Figure *4.2-48*(d), *4.2-55* to *4.2-59*). These observations are in agreement with previous studies conducted on rock coatings elsewhere (Dorn, 2013).

Patina also develops below the rock surface on the walls of fractures within the rock (Figure *4.2-51*(a)) and fills open cavities formed by dissolution of minerals (“hanging patina” Figure *4.2-51*(b)). For example, Figure *4.2-51*(b) shows patina developed within a large subhedral pore, that was most likely previously occupied by albite phenocrysts. An open connecting pathway to the surface is common to all the subsurface patina types. The pathway can be an open fracture or a structurally overlying portion of permeable weathered rind (Figure *4.2-51*(a), *4.2-55*).

Based on the internal texture, the patina can be subdivided into four broad categories: (i) fine-layered, (ii) stromatolitic, (iii) massive and (iv) gravelly. It must be noted that all of these types form on all substrate lithologies. Moreover, variations amongst these types are commonly visible at the micrometre scale within the same patina profile.

(i) Fine-layered patina texture

The fine-layered patina is characterised by significantly consolidated well-organised layers oriented sub-parallel to the underlying substrate and disseminated with small, equigranular bright particles of Fe- or Ti-oxides (Figure *4.2-52*, *4.2-57*, and *4.2-58*). Cavities and fractures commonly crosscut the patina layering. In BSE imaging, the fine-layered structure is highlighted by the alternation of brighter and darker domains indicating a stratification of compositionally different layers. This type of texture is most common within thicker deposits of patina.

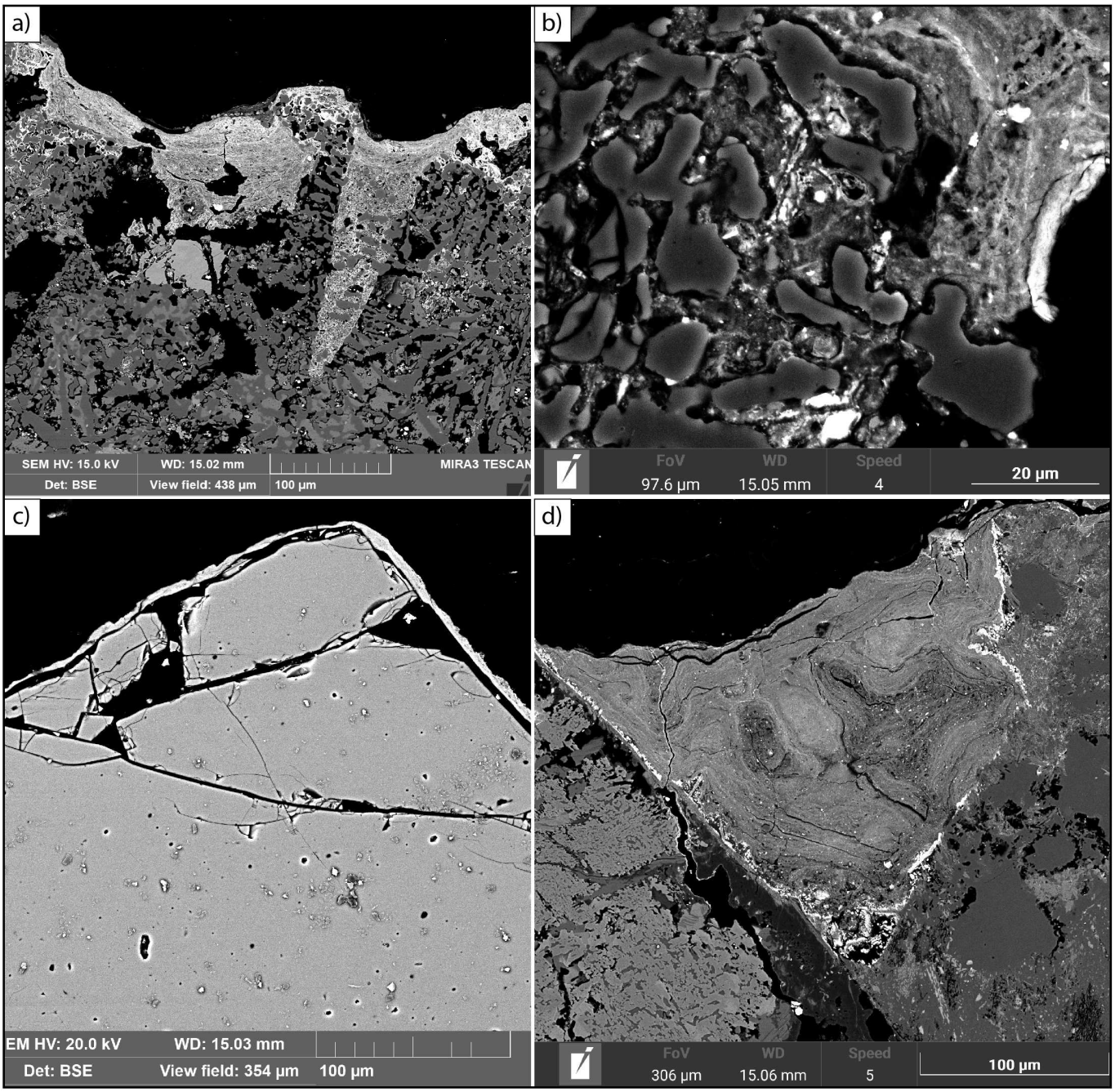

Figure 4.2-50: BSE-SEM images of patina in cross-section. (a) patina fills topographic lows and superficial fractures in sample AQ08_GPH. (b) patina fills micropores between quartz crystals that were part of a granophyric texture. (c) a thin film of patina (bright rim, around 5 μm thick) wraps around the edge of a fractured quartz grain that protrudes from the surface of granite sample AS02_GRT. In (d) a thicker patina ($\sim$300 μm) is found in a topographic depression of sample AQ15_GBR. Note the sub-parallel layering of the patina in the near-surface layers and a bright rim of Fe-oxides at the contact with the substrate.

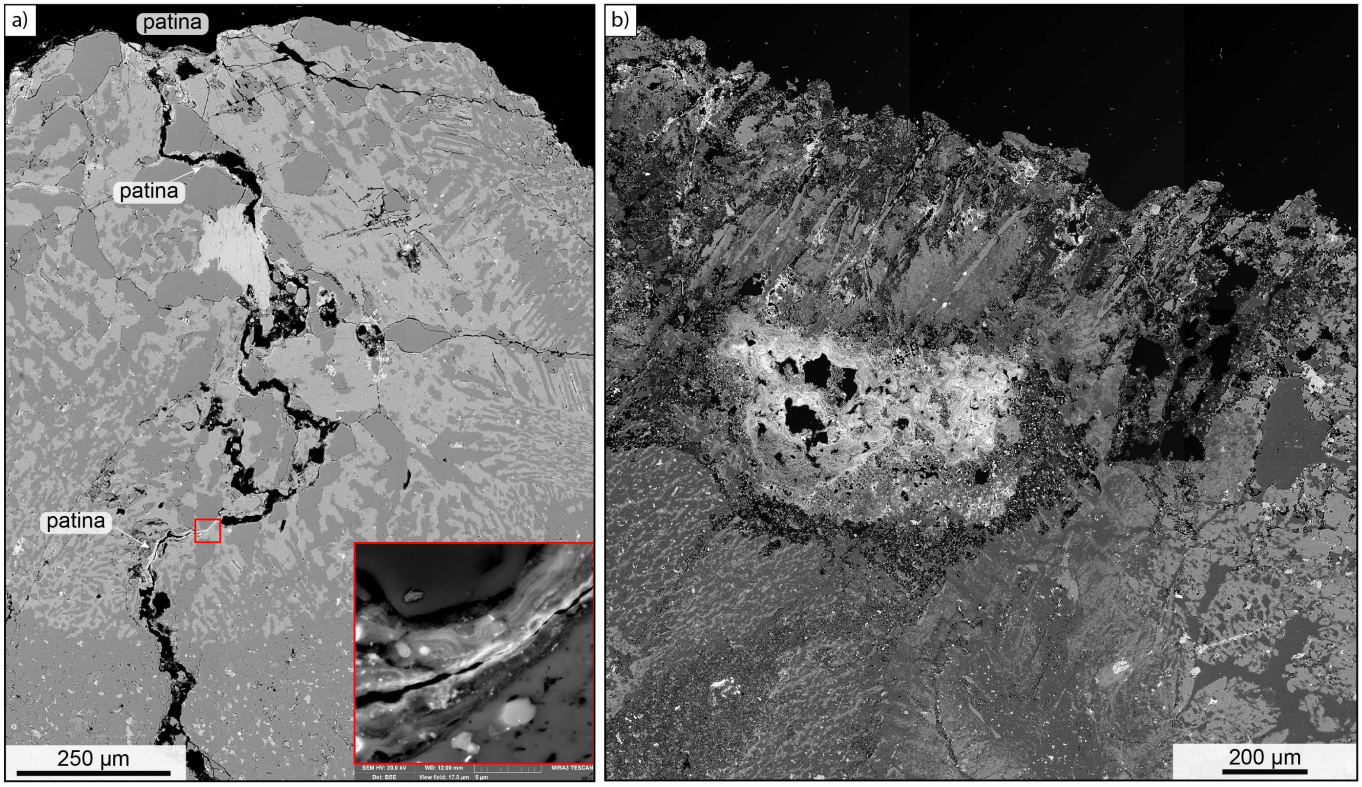

Figure 4.2-51: BSE-SEM images showing the development of patina within a rock fracture (a) and as a hanging patina within the weathered rind of granite (b). Samples AS02_GRT and AQ07_GRT, respectively.

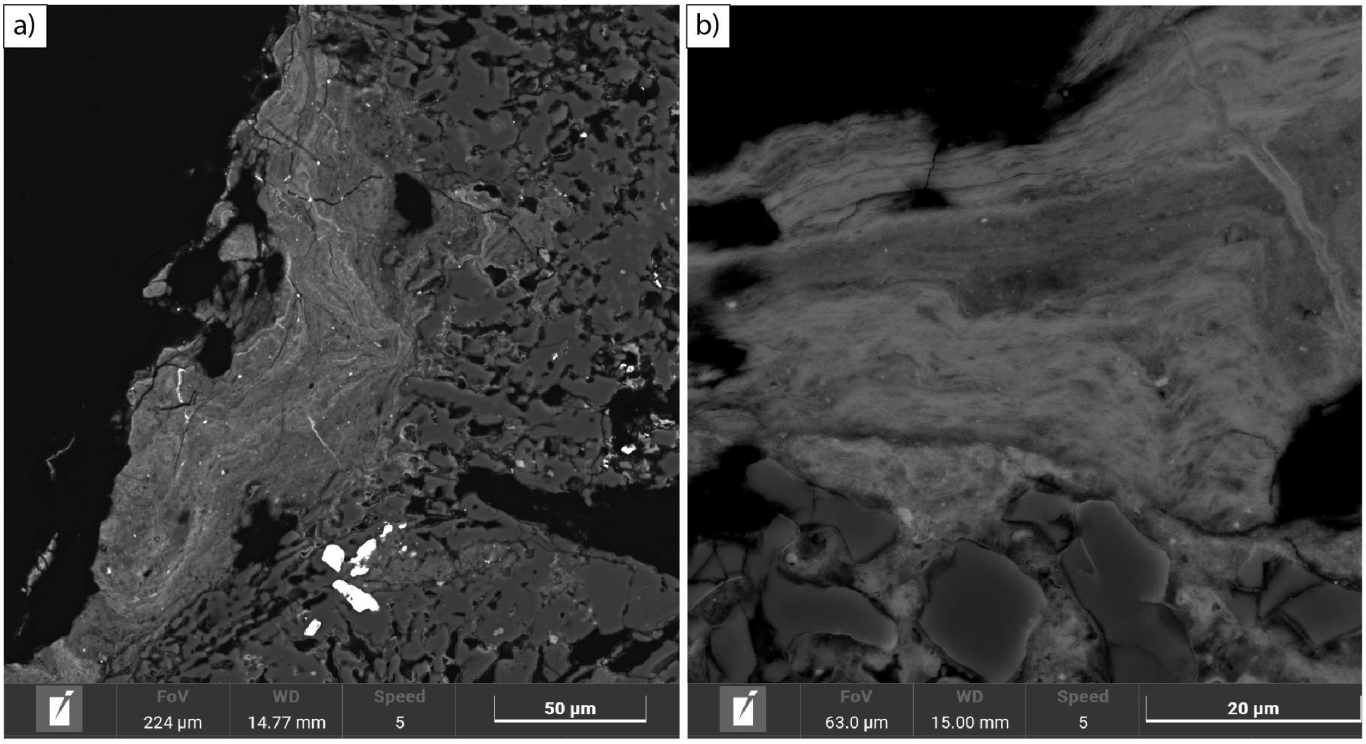

Figure 4.2-52: BSE-SEM images of fine-layered patina on top of altered granophyric intergrowths of quartz and microcline. The internal fine layering is defined by variation in grayscale brightness. At the contact with the substrate, the patina extends into the micropores of the rock. Internally, micro-to-nanoscale bright particles are visible.

(ii) Stromatolitic patina texture

The stromatolitic texture is characterised by layers of patina that form rounded domes (e.g. Figure *4.2-53*, *4.2-58* and *4.2-59*). In BSE images, like the fine-layered patina, the layers that form these structures are characterised by alternating layers with different grayscale brightness, and the presence of microscale bright particles trapped within the layers that compose the domes. These features are very similar to those observed within cross-sections through the botryoidal structures typical of stromatolites although the length-scale is quite different. Domes and columns in patina are not uncommon features and have been previously documented in rock varnish elsewhere (e.g. Corbin et al., 2018, Macholdt et al., 2017, Macholdt et al., 2015, Lingappa et al., 2021 and references therein). These structures indicate that the growth direction of the patina is upward from the previously exposed surface of the rock. Interestingly, the finding of stromatolitic domes in the "hanging patina" indicates that these types of structures can develop in the sub-surface of the patina, for example, the bright ovoid shown in Figure *4.2-51*(b). Moreover, based on their orientation, it is possible to infer that the patina was infilled progressively in concentric layers that accumulated on the inner surface of the void (Figure *4.2-51*(b)).

Sample AQ15_GBR provides an example of the range of morphology and textural variability of stromatolitic type patina from a single sample (Figure *4.2-52*(b), *4.2-58*). At its base, the patina is characterised by stromatolite-type microstructures. These forms are lost towards the top of the sequence, where the patina type is fine-layered. Notably, the change between the two textures is sharp and marked by a truncation surface that resemble features typical of sedimentary sequences that are diagnostic of an unconformity (i.e. a gap in the sedimentary record). Within the top structures, gravelly patina (iv) is also present, and the sequence terminates with a thin BSE-bright layer (< 5 μm). The patina profile is cross-cut by an interconnected network of smooth undulose channels that show bright rims.

(iii) Massive-textured patina

The massive-textured patina is characterised by fine-grained microdeposits that show little or no internal layering, and can reach several hundred micrometres in thickness (Figures *4.2-54*, *4.2-60*). In BSE, internal layering is not clearly distinguishable and the microdeposit is characterised by larger agglomerates of fine-grained material with different orientations. Similar to other patina types, the patina is characterised by disseminated bright particles, fractures, and micrometre-sized cavities. A brighter horizontal thin layer forms a rim on the outermost part of the patina similar to that observed in the stromatolitic type patina (Figure *4.2-53*). Within the patina, a broad undulose BSE-bright structure indicates compositional variability.

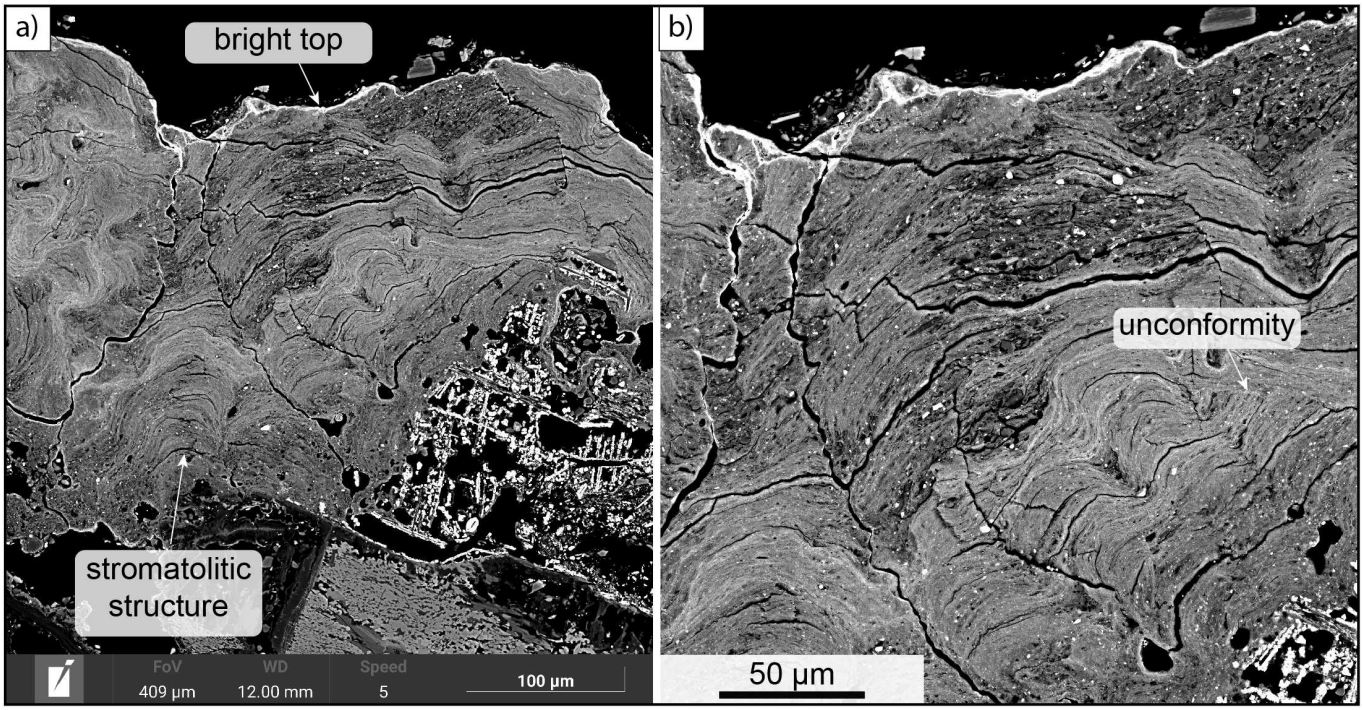

Figure 4.2-53: BSE-SEM images of stromatolitic patina type within gabbro AQ15_GBR. In (a) the patina has developed above a skeletal grain of augite, and is characterised by a sequence of superposed dome-like structures. (b) is a close-up image of (a), and shows an abrupt transition from a stromatolitic morphology to a fine-layered morphology. The top portion of the patina is characterised by an increase of microscale bright particles and a BSE-bright rim.

(iv) Gravelly patina texture

Gravelly patina is characterised by less consolidated, breccia-like disordered structures in which layering is not consistently visible (Figure *4.2-55*). Consolidation refers to the degree of cementation and does not relate to the degree of deformation. The gravelly patina is composed of larger inequigranular and angular mineral fragments of quartz, clays, and Fe- and Ti-oxides that are randomly oriented across the micro deposit. Generally, larger particles are surrounded by brighter films of sheet-like material, interpreted as nanocrystalline clays (Figure *4.2-55*). The shape of quartz clasts is very similar to the shape of quartz within the granophyric substrate, which might indicate that quartz is captured by the patina after it is released from the weathered rind by dissolution of microcline. If quartz grains are indeed locally derived then this observation is a significant finding because it shows that patina components are derived from the rock as well as from external sources, which are considered to dominate the patina (e.g. Dorn et al., 2013). The BSE observations show a sharp compositional difference between the less-well consolidated darker upper patina and better consolidated brighter lower patina, indicating that patina formation is a dynamic process, with modification of patina material post-deposition.

Other types of coating structures observed in the investigated samples comprise grain boundary films and Al–P–S–O-rich concretions. The latter are mostly observed on the granophyre as an infill of micropores formed by the dissolution of microcline in the granophyric structures (Figure *4.2-54*).

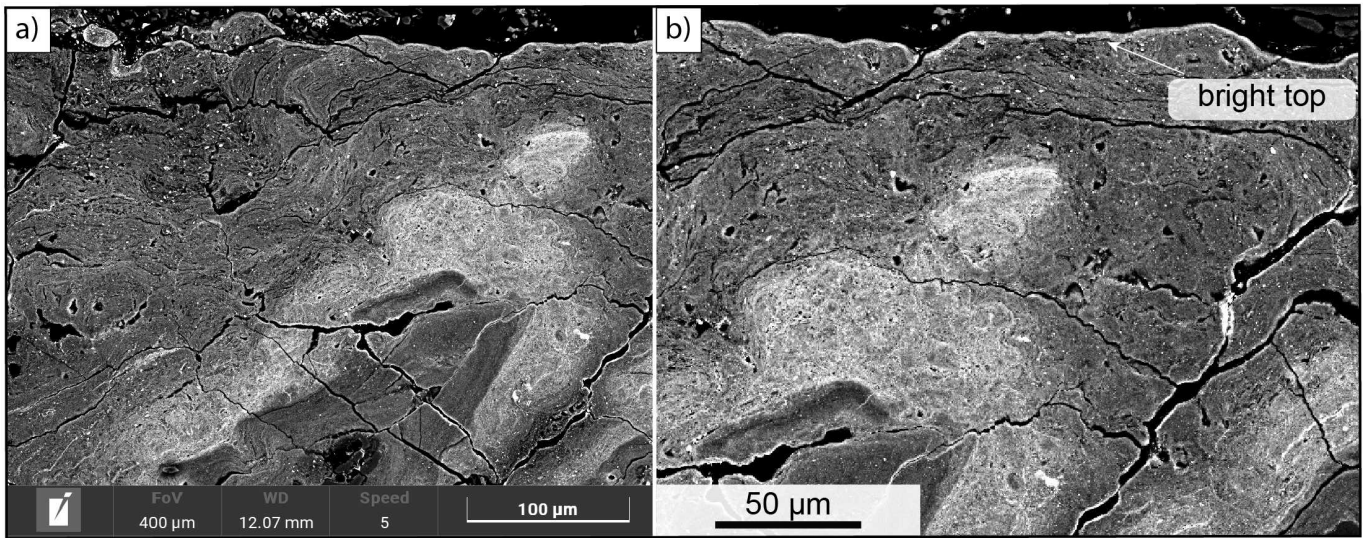

Figure 4.2-54: BSE-SEM images of the massive patina type in sample AQ11_GPH. In (a) the patina is characterised by a broad undulose BSE-bright structure. The close-up image in (b) shows the lack of internal layering within the fine-grained material. Bright particles are disseminated throughout the microdeposit. Voids, fractures and channels are also visible. The channels are highlighted by bright rims.

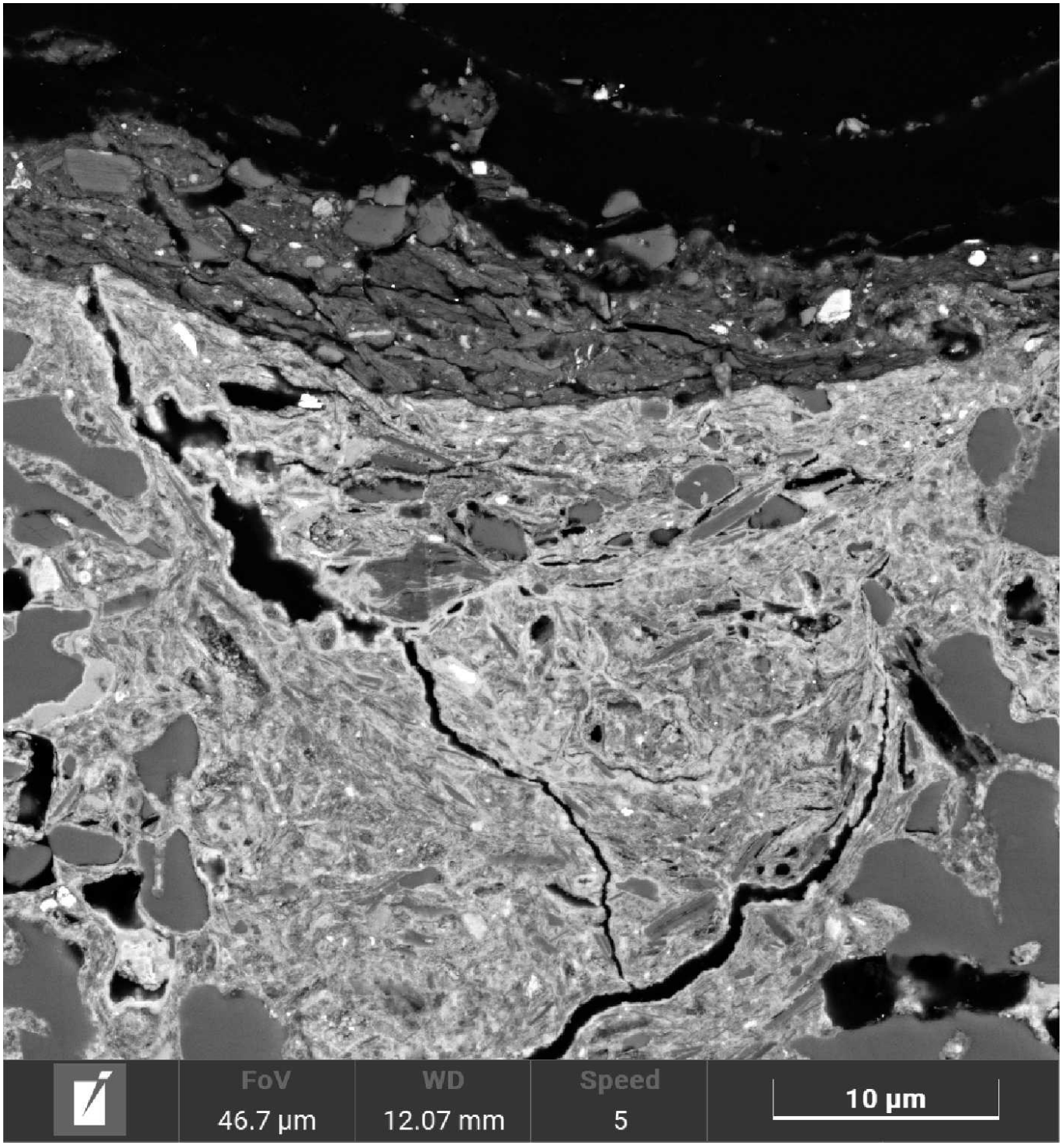

Figure 4.2-55: BSE-SEM image of gravelly patina type on top of a weathered portion of granophyric texture from sample EX05_GPH. In the image, the degree of consolidation decreases towards the top of the sequence. The BSE brightness increases with average atomic number of the material analysed.

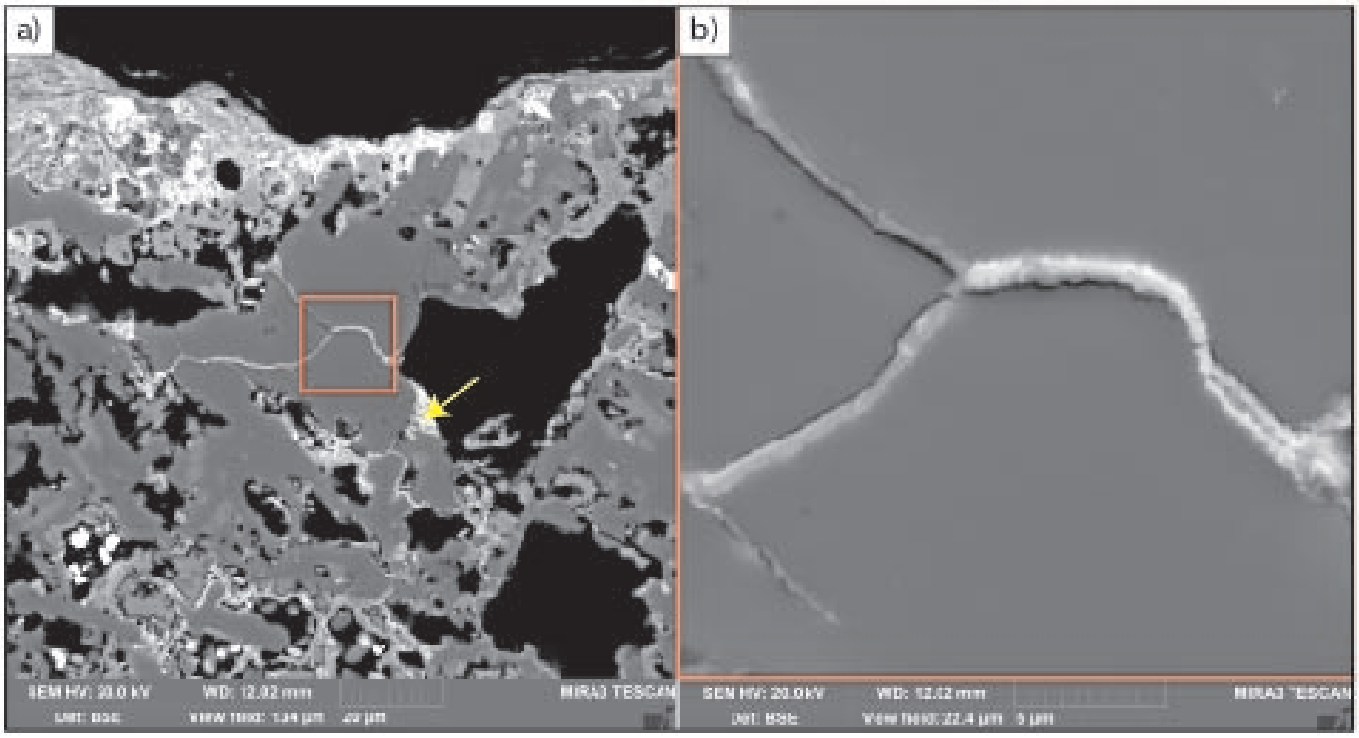

Figure 4.2-56: BSE-SEM images showing variability within rock coatings. Images are from granophyre sample EX05_GPH. In (a) P-rich concretions fill the pores within the granophyre. Example shown by yellow arrow. (b) Close-up image of the quartz grain boundaries highlighted by a thin film of a different BSE-brighter material, shown by the red square in (a). The EDS spectrum of this region (not shown) indicates that the film is enriched in Al, P, S, and Ca. The BSE brightness increases with average atomic number of the material analysed.

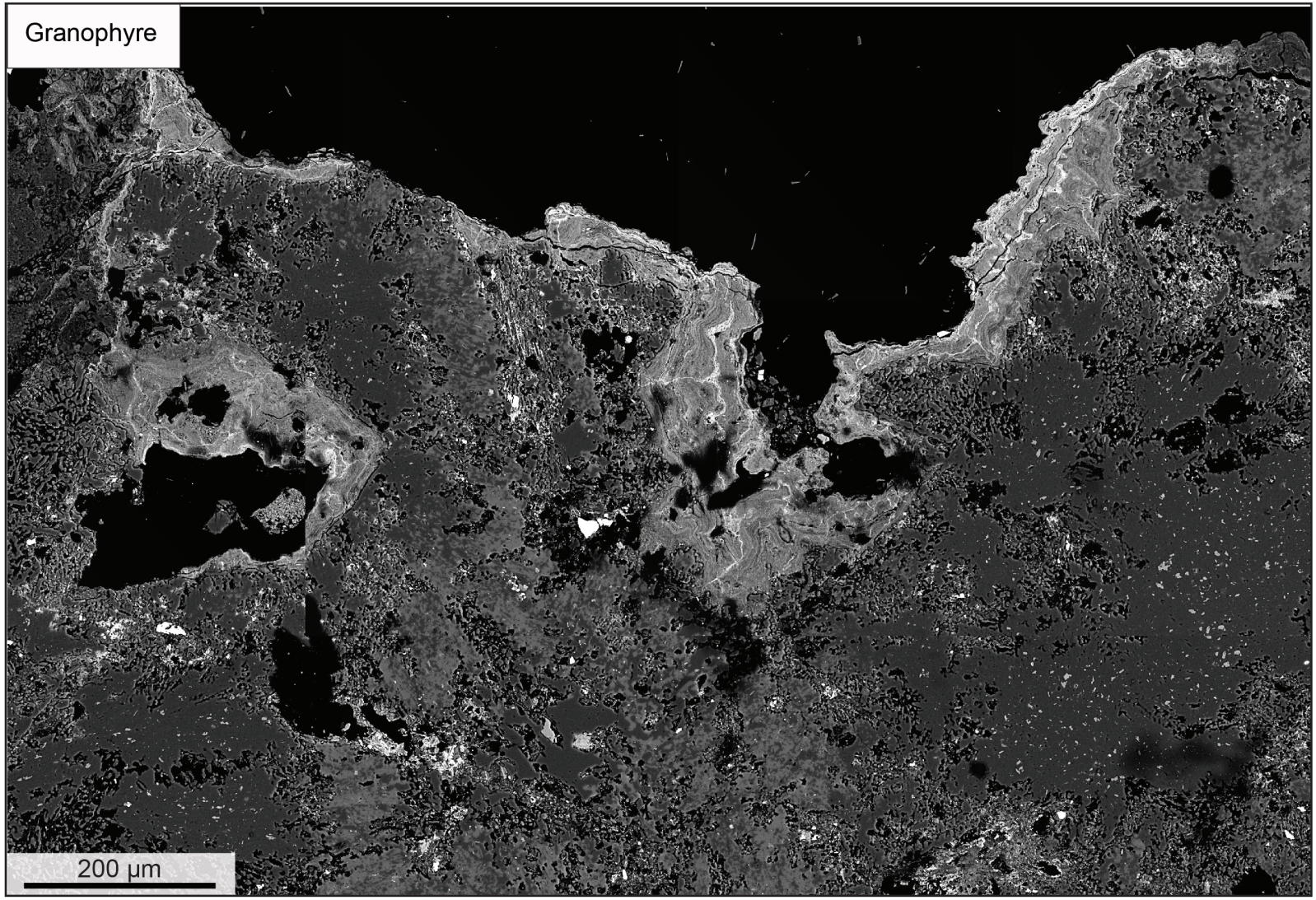

Figure 4.2-57: BSE-SEM large area panorama map of a portion of patina from sample AQ13_GPH. The patina is developed within a topographic depression defined by granophyre microstructures, and "hanging" from the walls of a pore cavity within the weathered rind. Notably, the "hanging" patina is connected to the superficial patina by a thin channel. This patina shows fine-layered and stromatolitic patina types.

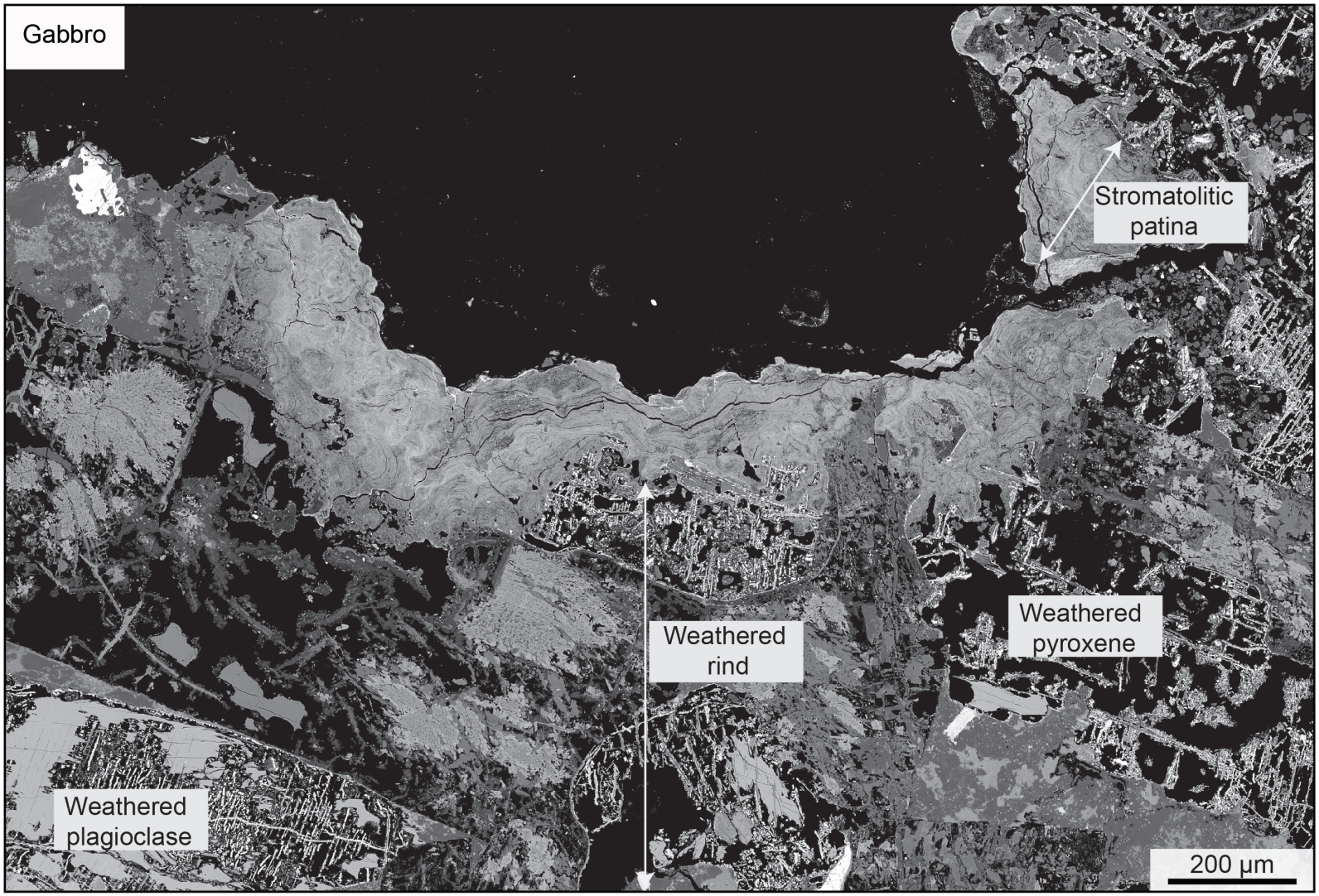

Figure 4.2-58: BSE-SEM large area panorama image of a patina formed on a topographic low of sample AQ15_GBR. The patina is largely characterised by stromatolitic-type textures developing on top of an extensively altered gabbro weathered rind. The substrate is characterised by large relict pyroxene and labradorite crystals.

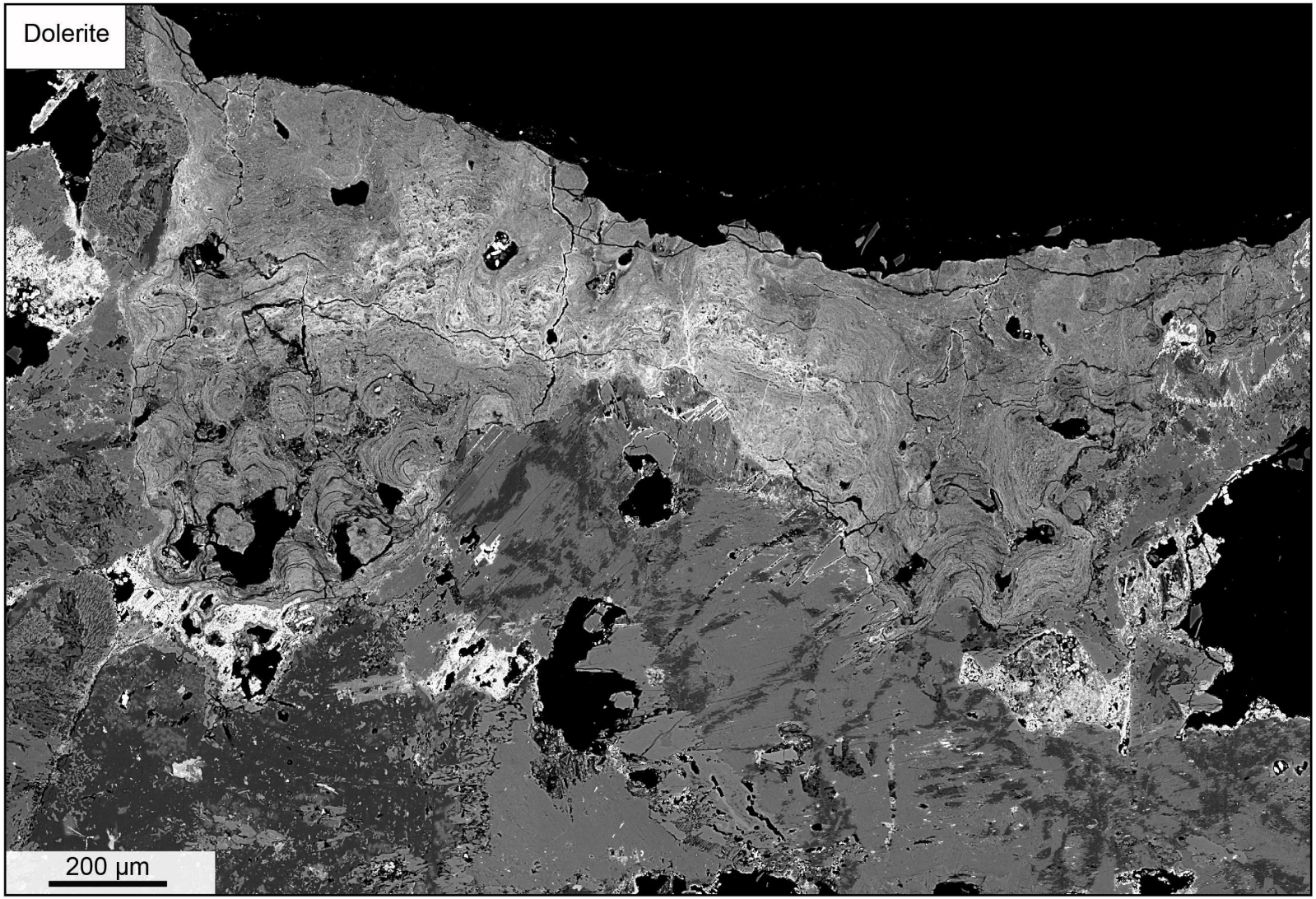

Figure 4.2-59: BSE-SEM large area panorama image of patina from sample AS01_DOL. Within the topographic low, the patina displays stromatolitic structures. In the top region the patina shows a more massive texture.

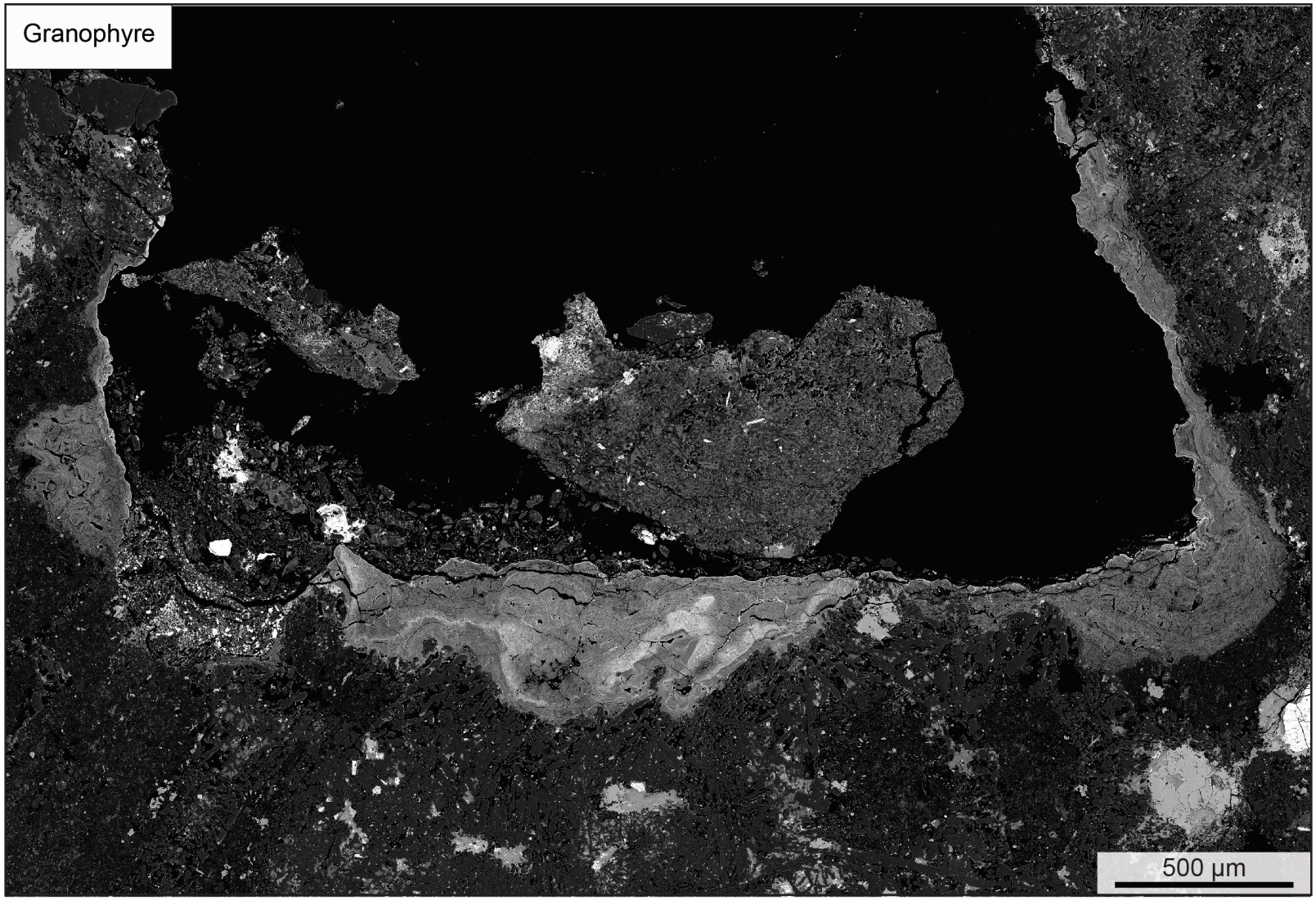

Figure 4.2-60: BSE-SEM large area panorama image of patina from sample AQ11_GPH. The patina develops on a topographic low on top of an altered granophyre with thicker portions in proximity of deeper depressions of the substrate. Internally, the structure is dominantly of the massive type. Patina is also found "hanging" from the walls of the depression.

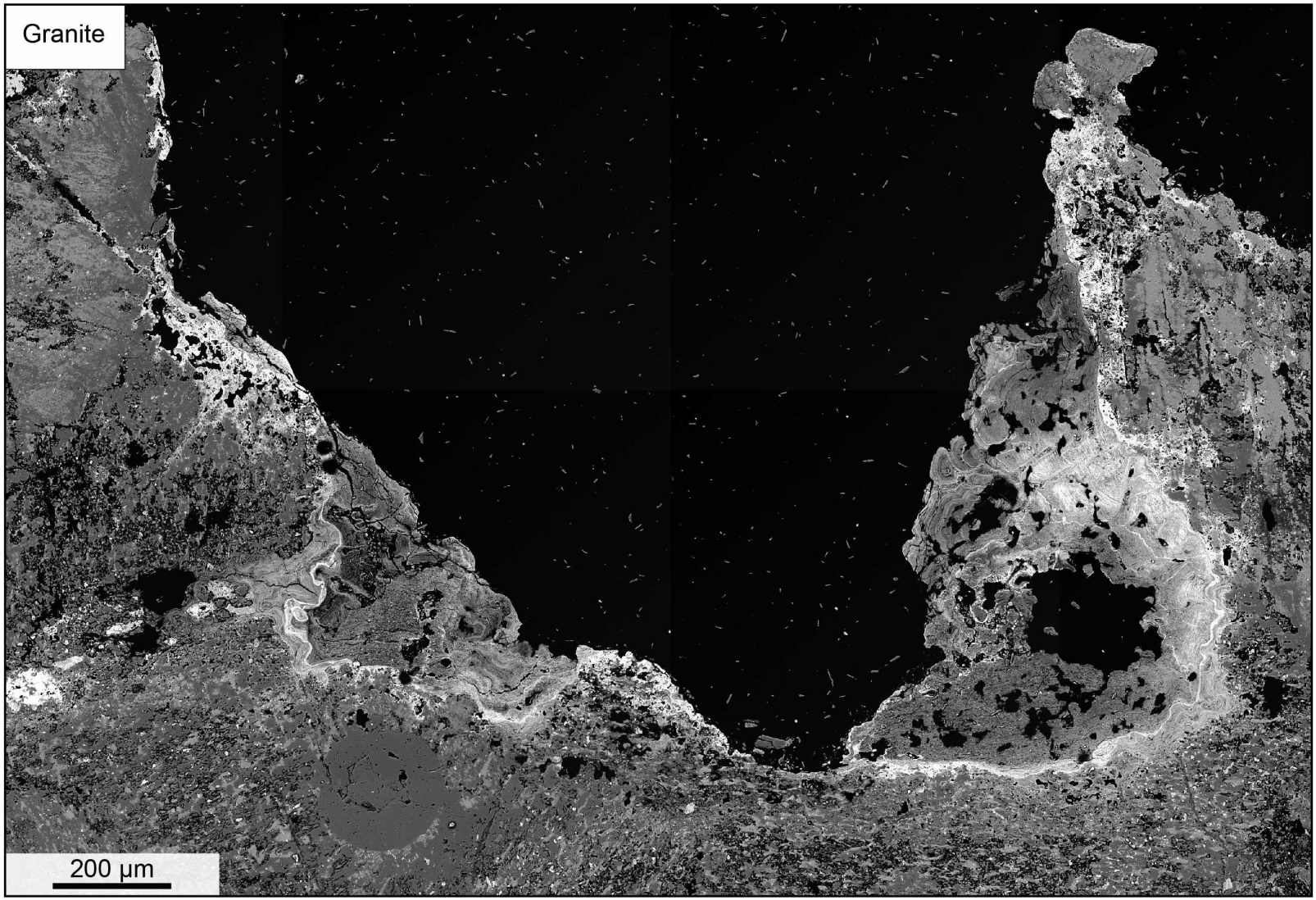

Figure 4.2-61: BSE-SEM large area panorama image of patina from sample AQ07_GRT.

4.2.8 Chemistry of the patina

This section summarises the compositional characterisation obtained by techniques such as EDS, EMP, Time-of-Flight-Secondary Ions Mass Spectrometry (ToF-SIMS), Transmission Electron Microscopy (TEM) and Atom Probe Tomography (APT). These investigations reveal the relationships between the chemistry and the microstructures of the patina described above, and how these relate to the substrate lithology. In particular, nanoscale techniques (ToF-SIMS, TEM and APT) are applied to selected areas of patina to explore for exotic trace elements that could be attributed to an anthropogenic source, but that might not be detectable by the application of conventional techniques with only micrometre-scale resolution (e.g. EDS, EMP). To build a framework of comparative investigation, a small number of samples were selected for analyses based on (i) exposure to industrial emissions, year one findings (Curtin University, 2023), and (ii) the availability of patina. Samples AQ10_GPH, AS01_DOL and AQ15_GBR were considered to represent lower exposure sites. Higher exposure sites are represented by AQ08_GPH, AQ07_GRT, AQ11_GPH and EX03_GPH. The different samples are described in more detail where relevant.

4.2.8.1 Microchemical characterisation of patina

Energy dispersive x-ray spectroscopy

High-resolution SEM-EDS large-area maps provide detailed images of the micrometre-scale distribution of chemical heterogeneities that are also observed in the TIMA element maps (Appendix Table *B-28* to *B-32*). In these coloured maps, brighter colours indicate enriched concentrations of the displayed element.

Sample AQ13_GPH shows a combination of (i) fine-layered, (ii) stromatolitic and (iii) “hanging” patina, as described in Section 4.2.7.2 (Figures *4.2-57*, *4.2-62*). Compared to the underlying substrate, the patina is enriched in Al, Fe, Mg and Mn, and depleted in Si, Na and K. In particular, there is a pronounced difference in the concentrations of Mg, Fe, and Mn which are strongly enriched in the patina. Within the patina, the distribution of the elements is heterogeneous and characterised by compositional gradients. In detail, alternating Fe- and Mn-enriched bands highlight internal layering within the microdeposit. Elements that include Al, Fe and P display higher concentrations on the contact with the substrate and along the rims of the large cavity. In contrast, Mn, Na and K are enriched towards the external surface of the patina. In particular, Mn shows the highest intensities within the outer layers of the patina characterised by stromatolitic structures, and within the cavity. Within the weathered rind of the substrate, Al, Si, Na, and K reveal the distribution of quartz, albite, microcline, and clays. With proximity to the contact between the substrate and the patina, feldspars all show a trend of fading Na and K intensities as they become progressively broken down into smaller isolated grains.

The distribution of major elements within the thick patina localised at the bottom of a topographic low on the surface of granophyre sample AQ11_GPH, which corresponds to the area discussed in Section 4.2.7 and is investigated in detail Figure *4.2-54*, *4.2-60*, *4.2-63*, and Appendix Figure *B-1*. The distributions of Al, Si, K, and Na show that the substrate is characterised by a spinifex-like texture defined by acicular albite and quartz. Of these, K and Al are enriched in portions of the rock where Na is depleted, indicating localised destruction of albite and precipitation of clay minerals. Compared to the fresher rock and weathered rind, the patina is enriched in Al, Fe, Mn, Mg, K and

P. Within the patina, the distribution of elements, particularly Fe and Mn, is heterogeneous. As in sample AQ13_GPH, these two elements form alternating layers of Fe- and Mn-enrichment. Fe is strongly enriched at the patina–substrate contact and forms a thin layer on the very top surface of the patina (see also Appendix Figure *B-1*). Mn is highly enriched within the middle portion of the patina where Mn enrichment defines undulose layers. The presence of an elongate quartz crystal, interpreted as relict, indicates that undulose layering may mirror the irregular topography of the substrate. Contrary to observations of sample AQ13_GPH, the map does not show internal gradients in element concentrations, except for weak zonation in Mg. However, it is possible that element concentrations were lower throughout the patina in this sample, such that variation in those concentrations could not be resolved by EDS. Phosphorus is enriched in the patina and the weathered rind, where P is commonly associated with K and Na.

In gabbro AQ15_GBR, the substrate is dominated by large relict and variably skeletal grains of augite and labradorite (Figure *4.2-53*, *4.2-58*, *4.2-64*, and Appendix Figure *B-1*). The skeletal framework and original rims of augite are enriched in Fe, Mg, and P (see also Appendix Figure *B-1*). Labradorite plagioclase within the weathered rind is very altered; the locations of original tabular crystals are revealed by the distribution of Al- and K-bearing clay minerals, and Na and Ca only present locally. Within the patina, Fe and Mn are the most abundant elements. The distribution of Mn is patchy, and Mn shows the highest concentrations on the margins of stromatolitic structures. Interestingly, the enrichment in Mn extends into parts of the substrate minerals. Fe, and to a minor extent P, are enriched towards the upper surface of the patina. In particular, the top surface of the patina shows a thin BSE-bright layer of Fe (see also Appendix Figure *B-1*). In contrast, Al and Mg are generally enriched at the weathered rind–patina contact and decrease in concentration towards the upper surface of the patina.

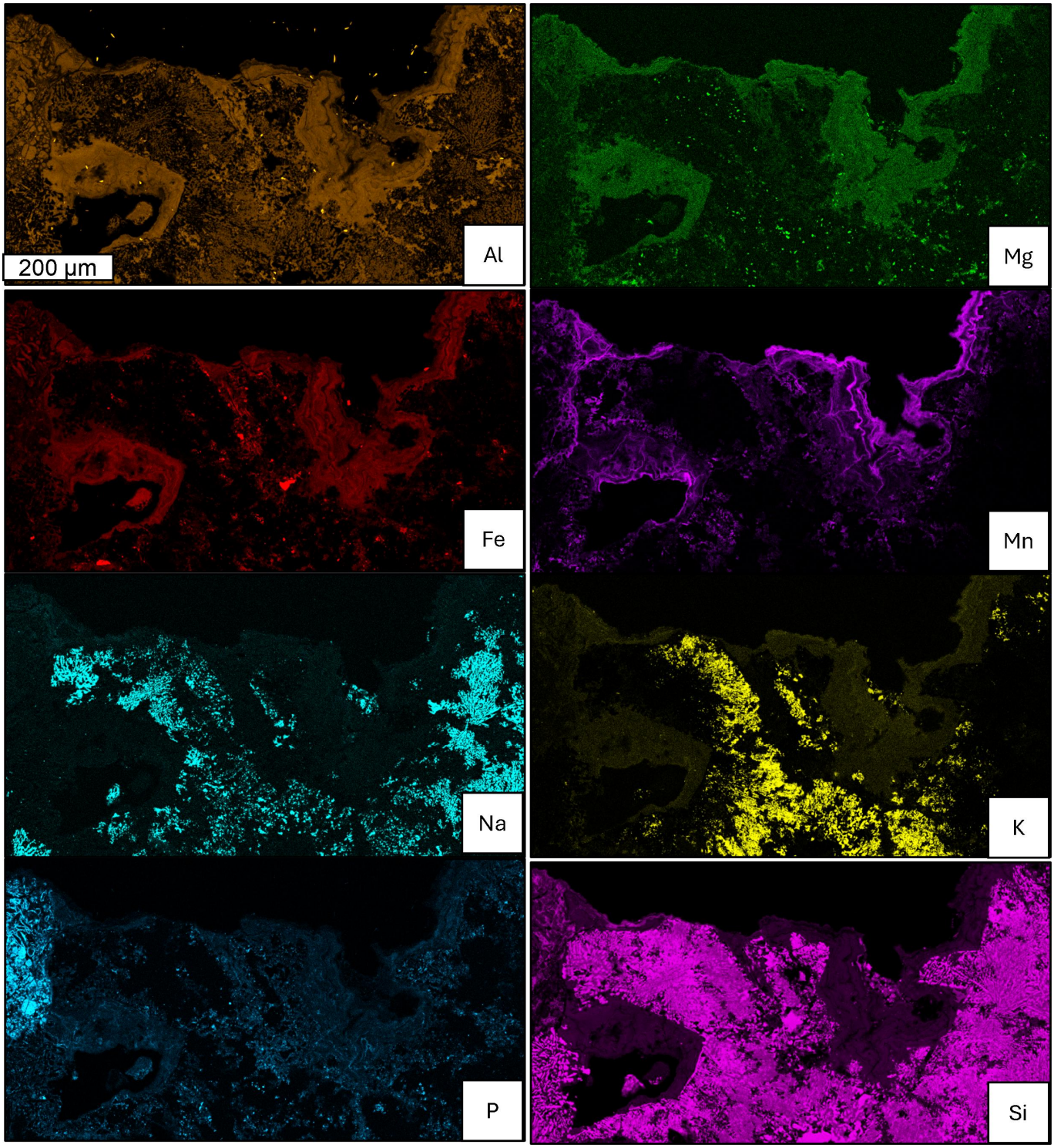

Figure 4.2-62: Compositional characterisation of patina microstructures. Large area EDS-SEM map of part of the patina on sample AQ13_GPH shown in Figure 4.2-57. The distributions of Al, Fe, Mn, K and P are heterogeneous. Mn is mostly enriched in the outermost layers of the patina and Al is enriched in the regions in contact with the substrate.

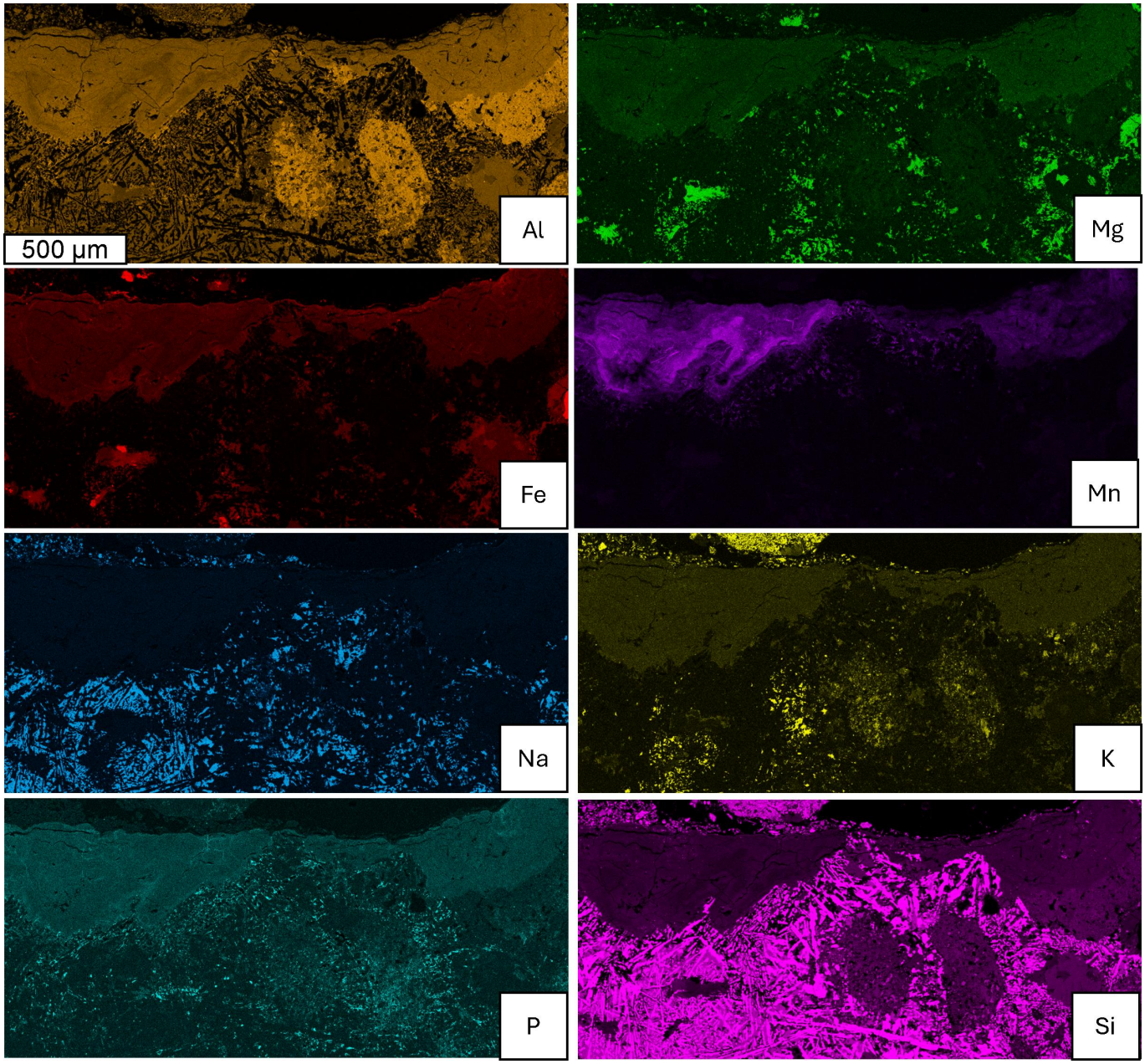

Figure 4.2-63: Compositional characterisation of patina microstructures. Large area EDS-SEM map of part of the patina showed in Figure 4.2-60 of the microstructural section from sample AQ11_GPH. Chemical heterogeneities are mostly observed for Al, Fe and Mn. By far, Mn is the more variable highlighting composite complex structures. Fe is enriched at the structural extremes of the patina forming a thin outermost rim on top of the sequence. P is widespread within the weathered rind.

Electron microprobe

Microprobe analyses of patina were conducted on 15 samples selected across granophyre, gabbro, granite and dolerite lithologies. Where possible, the measurements were conducted across a bottom-to-top vertical profile. This approach permitted investigation of the composition as a function

of vertical position within the patina, and quantification of trends in element concentrations observed by EDS. Element concentrations are highly variable because the patina is physically and chemically heterogeneous. Therefore, to allow a compositional overview, the median oxide concentrations are reported and shown in Table *4.2-7*. This dataset was used to assess the existence of systematic variations in patina composition as a function of rock type, geographical location and position within the patina. Further work is necessary to fully investigate patterns within individual traverses and their relationship to patina microstructures and structural types so the interpretations presented in this report must be considered preliminary.

Median concentrations indicate that the patina is composed of 15–30 wt% SiO_2, 13–26 wt% Al_2O_3, $\sim$1 wt% of MgO and K_2O and generally $<$1 wt% of CaO and Na_2O (Table *4.2-7*). These compositional ranges are consistent with reported compositions of rock varnish elsewhere (e.g. Goldsmith et al., 2014; Macholdt et al., 2015). The concentrations of these elements are relatively consistent and independent of the host lithology (Figure *4.2-65*). The concentrations of Fe, Mn, P and S are more variable and changes in the concentrations of Fe and Mn are the greatest contributors to compositional variability. The highest concentrations of Mn, of up to $\sim$50 wt%, are found in stromatolite-like microstructures (see Appendix Figure *B-1*). In addition, Mn concentration increases with increasing Ba concentration, consistent with the observations of Goldsmith et al. (2014) (Figure *4.2-65* and Appendix Figure *B-2*). Similar positive trends in composition are observed for Si-Al and Na-K (Figure *4.2-65*). Preliminary investigations indicate that median element concentrations do not vary systematically with sample location on Murujuga but further work is necessary to confirm this finding.

The EMP results show a trend of decreasing Mg, Al, and Si concentration from the weathered rind–substrate contact towards the top of the patina, consistent with element distribution shown by the large area EDS maps of gabbro AQ15_GBR (Appendix Figure *B-3*).

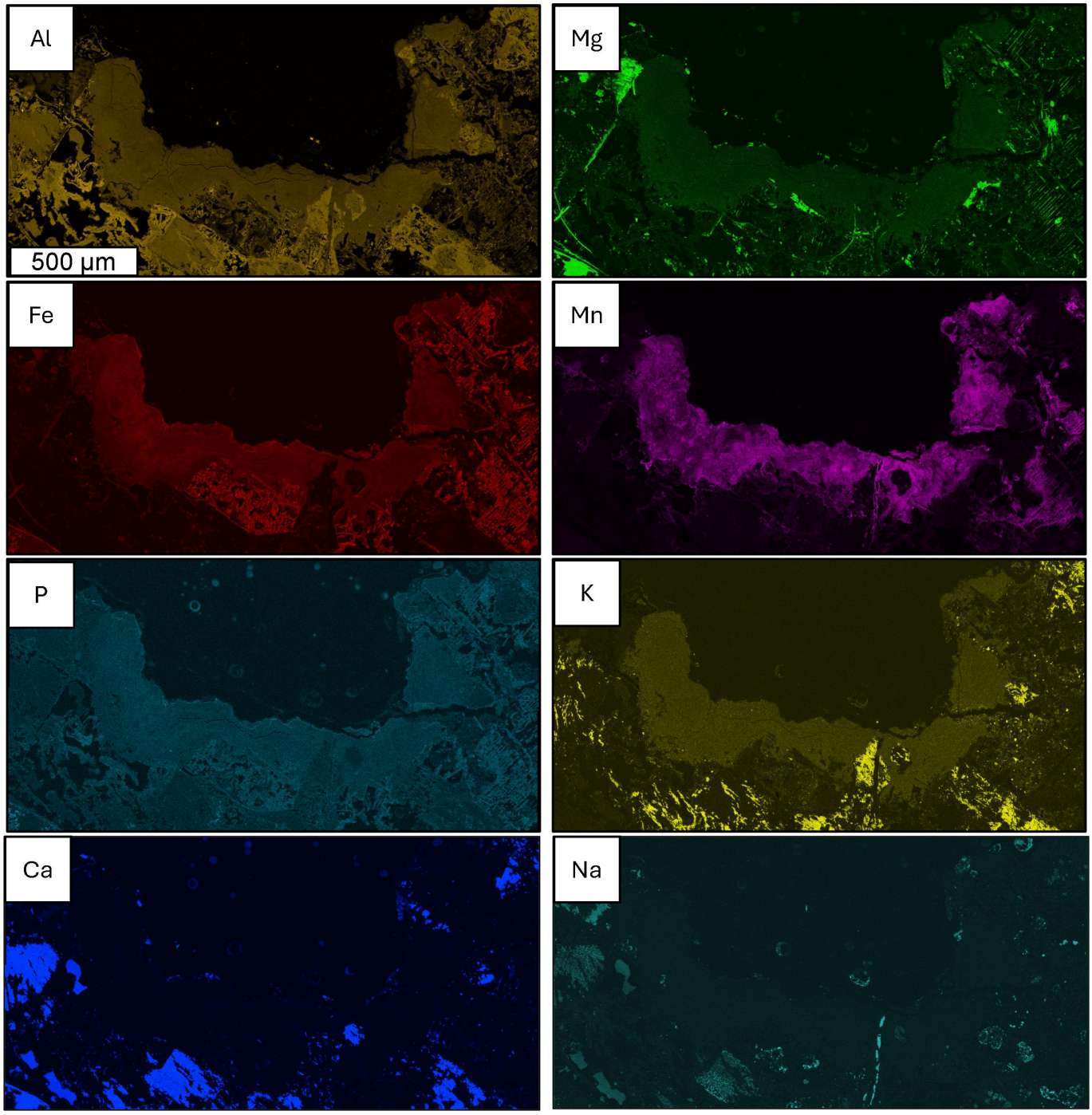

Figure 4.2-64: Compositional characterisation of patina. Large area EDS-SEM map of the patina on sample AQ15_GBR shown in Figure 4.2-58. Fe and Mn are strongly heterogeneous. Al, Mg, Fe and P show systematic changes in abundance, shown by the color intensity, from the top to the bottom of the patina.

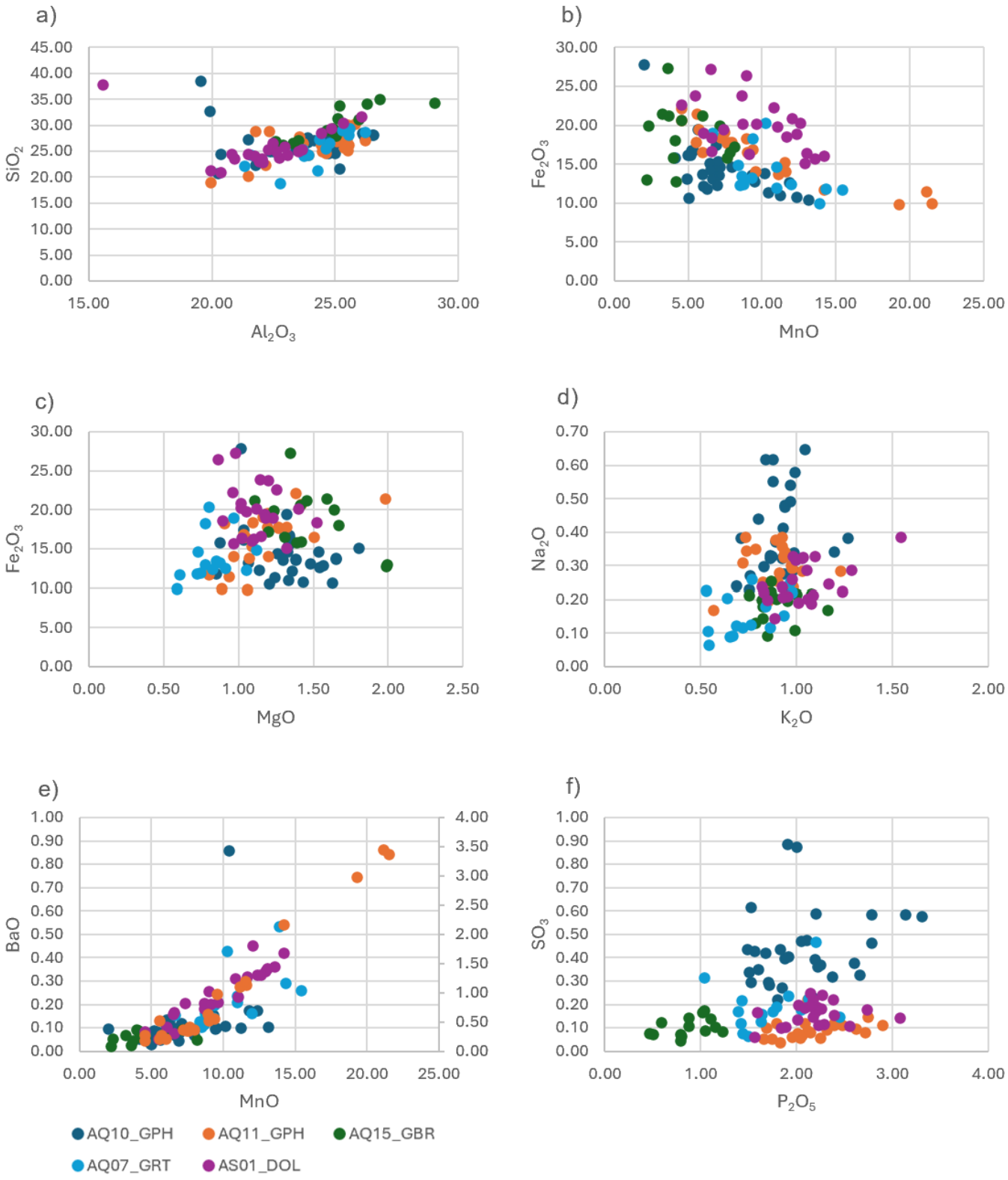

Figure 4.2-65: Compositional scatterplots of EMP data for selected patina traverses. Element concentrations are expressed in wt% of oxides.

Table 4.2-7: Compilation of median concentrations obtained by EMP analysis of patina. Values are expressed in wt%. Unanalysed components such as H_2O are measured by the difference between the total and 100%. BDL: below the detection limit of ~0.05 wt%.

	AQ08_GPH	AQ10_GPH	AQ11_GPH	RS04_GPH	EX03_GPH	EX05_GPH	EX08_GPH	AQ07_GRT	RS03_GRT	AS02_GRT	AQ09_GBR	AQ15_GBR	EX09_GBR	RS09_DOL	AS01_DOL
SiO_2	16.64	26.68	29.38	28.73	18.00	14.51	25.10	23.63	28.93	29.56	22.85	29.77	30.85	32.67	25.74
TiO_2	0.96	0.87	0.72	0.75	1.04	1.14	0.73	0.77	0.62	0.97	0.76	0.67	0.71	1.02	0.79
Al_2O_3	13.70	23.88	26.19	25.07	17.33	14.43	21.55	24.35	21.10	19.16	23.28	24.37	22.42	24.57	22.67
V_2O_3	BDL	BDL	BDL	BDL	0.05	0.05	BDL	BDL	BDL	BDL	BDL	BDL	0.05	BDL	BDL
Cr_2O_3	0.06	BDL	BDL	BDL	0.07	0.18	BDL	BDL	BDL	BDL	BDL	BDL	BDL	BDL	BDL
Fe_2O_3	45.51	16.18	17.20	16.98	39.60	49.20	23.36	14.48	24.91	22.57	25.66	17.84	18.97	22.73	19.91
MnO	0.11	5.95	4.46	8.76	1.87	0.11	5.82	9.34	0.99	0.35	4.09	5.03	6.74	0.14	8.84
MgO	0.28	1.33	1.39	0.97	0.42	0.31	0.95	0.86	1.01	0.93	1.03	1.42	1.53	1.28	1.25
CaO	0.14	0.41	0.24	0.21	0.32	0.26	0.38	0.31	0.26	0.24	0.37	0.24	0.31	0.21	0.43
SrO	BDL	0.07	BDL	BDL	BDL	BDL	BDL	BDL	BDL	BDL	BDL	BDL	BDL	BDL	BDL
BaO	BDL	0.10	0.31	0.21	0.07	0.08	0.12	0.20	BDL	BDL	0.11	0.09	0.11	BDL	0.20
Na_2O	0.14	0.44	0.26	0.26	0.17	0.12	0.27	0.20	0.14	0.17	0.16	0.21	0.28	0.14	0.22
K_2O	0.65	0.92	0.94	0.95	0.73	0.55	0.93	0.68	1.02	0.89	0.74	0.90	1.32	1.04	1.01
P_2O_5	3.98	2.14	1.89	1.36	3.64	4.41	1.92	2.25	3.40	2.18	3.82	0.96	0.72	1.66	2.25
SO_3	0.10	0.34	0.11	0.09	0.15	0.23	0.25	0.15	0.10	0.15	0.15	0.11	0.10	0.05	0.15
Cl	0.11	0.10	BDL	BDL	0.06	0.08	0.09	0.06	0.06	0.11	0.09	BDL	0.06	0.10	BDL
F	BDL	0.06	BDL	0.11	BDL	BDL	BDL	0.10	0.05	BDL	BDL	0.06	0.06	BDL	0.10
Total	83.44	81.30	84.61	85.00	86.68	86.44	83.63	81.11	85.16	82.96	84.96	83.73	85.10	87.32	84.52

4.2.8.2 Nanoscale characterisation

In this section the structural and chemical results obtained from nanoscale observations by the combined use of ToF-SIMS, TEM and APT are summarised.

Time-of-flight-secondary ion mass spectrometry

Seven patinated samples have been analysed by ToF–SIMS, including five granophyre samples, one gabbro sample and one granite sample. Where possible, the same patina area was analysed in negative and positive ion modes. Results obtained in negative ion mode suffered from artifacts generated by the epoxy resin used for preparing the thin sections. Therefore, any interpretation of organic components must be made with care. The samples were selected to permit a comparison between sites exposed to higher and lower amounts of industrial emissions. Samples AQ08_GPH and AQ11_GPH represent higher and AQ10_GPH lower exposure sites respectively. The complete suite of elements identified is provided in the Appendix *B*. The ToF-SIMS results are not quantitative. However, relative concentrations can be determined from the counts per pixel, which are proportional to the concentration of the element of interest in the analysed sample.

The areas of patina investigated for samples AQ08_GPH and AQ11_GPH correspond those shown in Figures *4.2-50*(a) and *4.2-54*, respectively. Microstructurally, samples AQ08_GPH and AQ10_GPH (not shown) show similar patina that is developed on localised topographic irregularities, extends downwards into the weathered rind, and fills features interpreted as pre-existing rock fractures and/or dissolution cavities.

In the positive ion maps, a range of elements and compounds were identified, including silicate mineral-forming elements: (Li, Na, Mg, Al,Si, K, Ca, Ti, Fe); metals, (Cu, Cr, Pb, Rb, Sr, Y, Co, Ni, Ba, Ce, Cs, La, Eu, V, Zr, Mo); ammonium compounds (NH_3, NH_4, alkyls (CH_x)), and ionic compounds (e.g. Ca S). All of the analysed patina samples are enriched in rock-forming elements such as Si, Al, Fe, Mn, and K. Elements Mg, Na, Ca, and Ti are enriched to a lesser extent. These results are consistent with those from EDS (Section 4.2.8.1). In maps of Si, Mg, Fe, K and Ti, the higher lateral resolution of the ToF-SIMS technique permits detailed imaging of compositional variation and reveals that nanoparticles (e.g. quartz and clays) are common and disseminated throughout the patina. While the distribution of the different elements is highly variable there is no obvious systematic pattern to that variability with a few minor exceptions. In the top section of AQ11_GPH patina (Figure *4.2-67*), a thin layer (<5 μm) is enriched in Fe, Cr, Ni, Cu (not shown), Nb, V and Pb. Similarly, AQ08_GPH shows Cr enrichment in a thin layer at the top of the patina. In AQ08_GPH (Figure *4.2-66*), enrichments in Si, Na, and K are spatially associated with enrichments in NH_4. In other samples, the NH_4 compounds are more homogeneously distributed, although they show localised enrichment within the weathered rind (e.g. AQ10_GPH, Figure *4.2-68*). Barium is present in all samples, and its association with Mn, which is confirmed by the EMP results, is particularly evident in AQ11_GPH (Figure *4.2-67*).

In negative ion mode, elements identified include C, F, Cl, P, S, Br; N-bearing compounds (NO_x), and a variety of S-, Si- and C-bearing compounds (see Appendix *B*). The epoxy resin used in sample preparation contains organic compounds, Cl, F, and N, and interferes with the signal from the patina. However, the patina is enriched in O and OH compared to the surrounding host, confirming that oxides and clay minerals are abundant within the microdeposit. Samples AQ08_GPH (Figure *4.2-69*), and AQ11_GPH (Figure *4.2-70*), show higher S counts than

AQ10_GPH (Figure *4.2-71*). Sample AQ08_GPH shows a localised enrichment in P, S, and oxides that include these elements, at the top of the patina (Figure *4.2-69*). In sample AQ11_GPH brighter particles of CaSO are also present (Figure *4.2-70*). Ammonium urate ($C_5H_7N_5O_3$), a compound contained in seabird guano (Ramanaidou and Fonteneau, 2019), is enriched in the weathered rind adjacent to the patina of sample AQ10_GPH (Figure *4.2-71*).

Transmission electron microscopy

TEM was used to investigate nanostructures within an altered albite grain and patina from granophyre sample EX03_GPH. The twofold objectives of these investigations were (a) to observe weathering related albite alteration, and (b) to characterise the structure and chemistry of the patina at the nanoscale.

The TEM foil of plagioclase was prepared from a thin section of sample EX03_GPH and focused on a relict grain within the weathered rind that had undergone extensive alteration and dissolution (Figure *4.2-72*(a)). The foil was extracted from a region of the grain that is characterised by a bright BSE signal, indicating the presence of a compositional gradient between the rim and the interior of the mineral grain (Figure *4.2-72*(b)). The EDS analysis of this region indicated that the brighter layer is depleted in O, Si, Al and Na, and enriched in C (Appendix Figure *B-1*). The TEM analysis of the obtained foil reveals that the internal crystal structure of the plagioclase is characterised by darker curved linear features that are interpreted as local bending or linear defects (e.g. dislocations) of the crystal lattice (Figure *4.2-72*(c)). These features are natural and not an artefact of sample preparation.

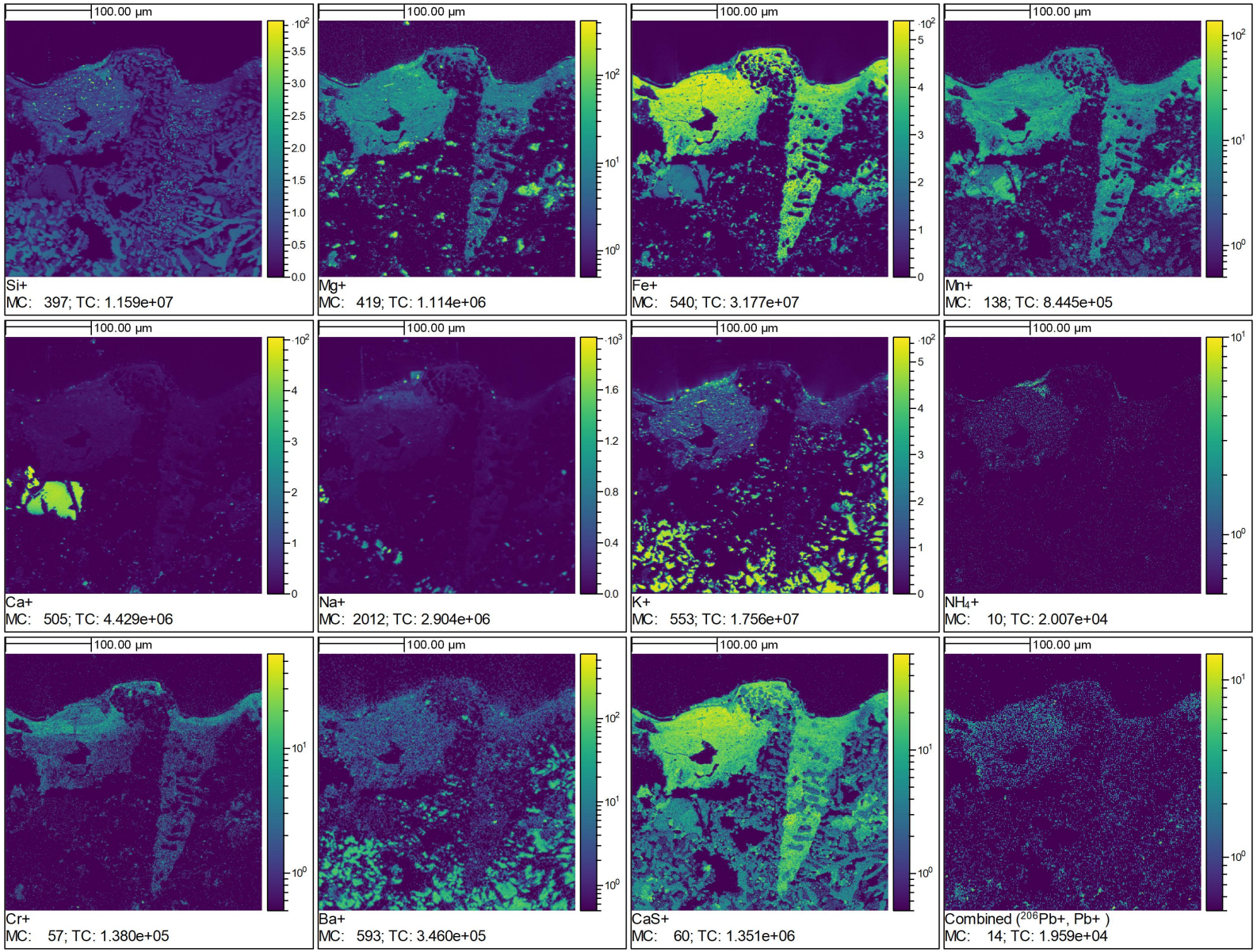

Figure 4.2-66: ToF-SIMS map showing the distribution of selected positive ions for sample AQ08_GPH. Colour scales relate to the number of counts and are not quantitative. The elements are represented by their positive ions.

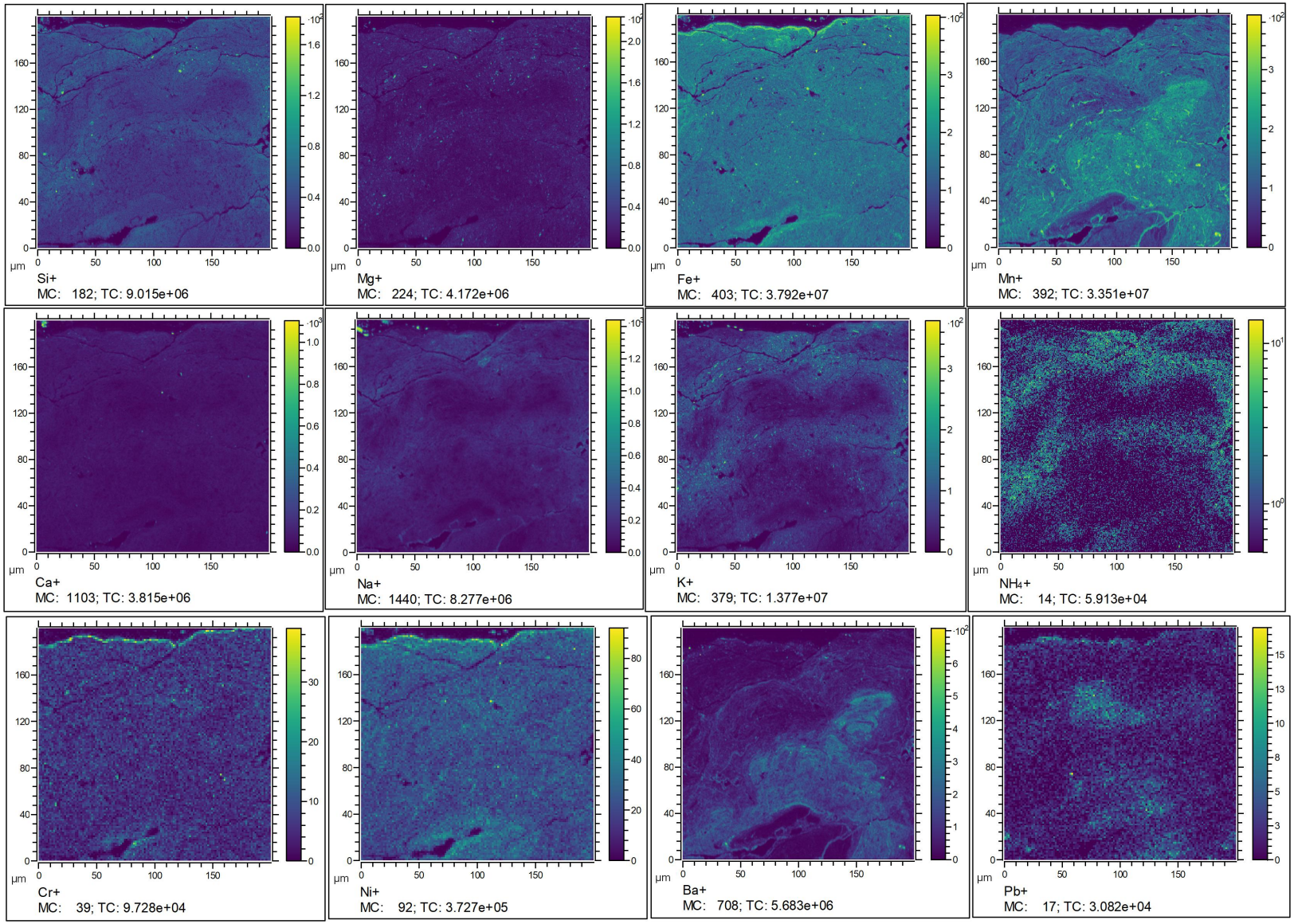

Figure 4.2-67: ToF-SIMS map showing the distribution of selected positive ions for sample AQ11_GPH, highlighting the compositional complexity. Colour scales relate to the number of counts and are not quantitative. The elements are represented by their positive ions.

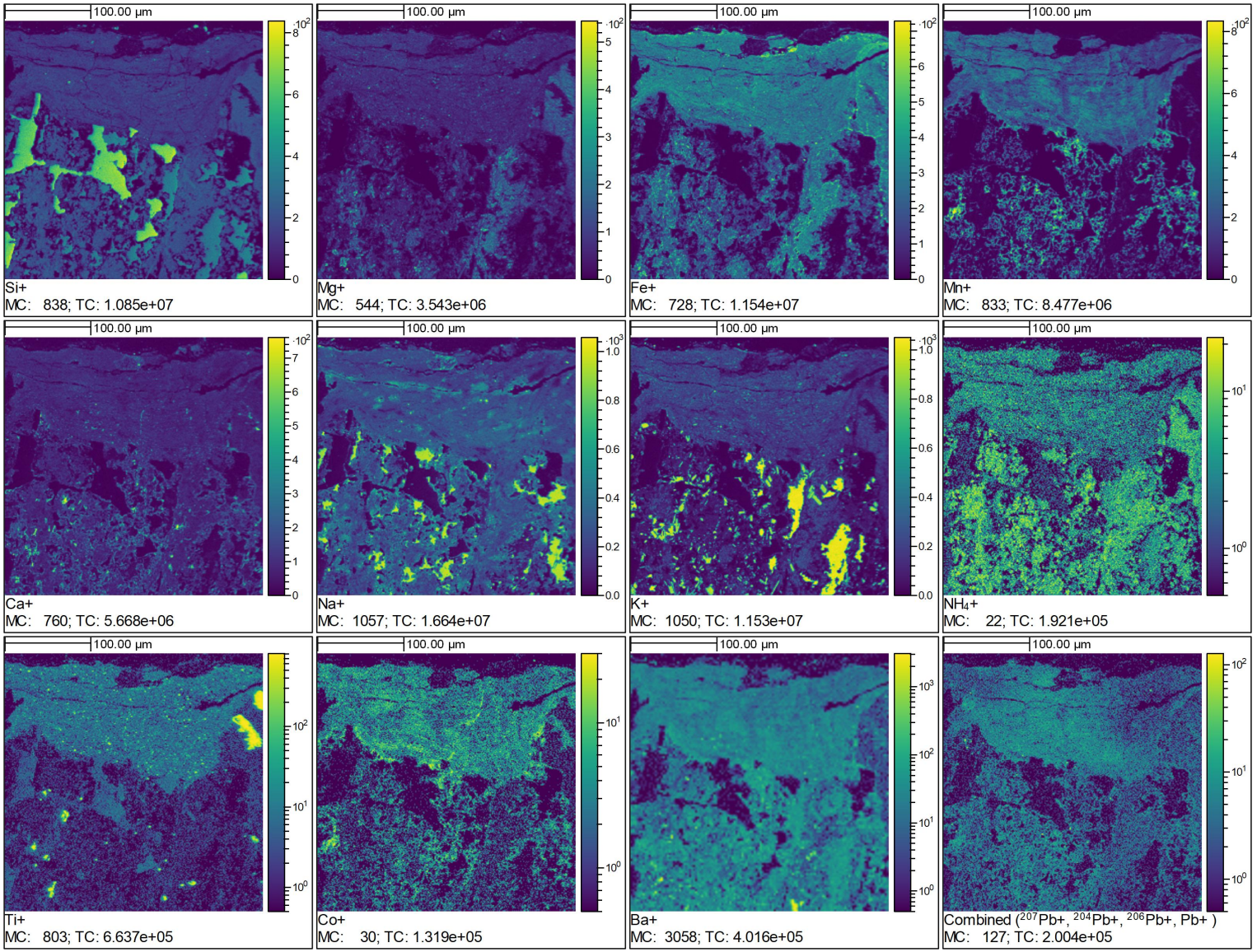

Figure 4.2-68: ToF-SIMS map showing the distribution of selected positive ions for sample AQ10_GPH, highlighting the compositional complexity. Colour scales relate to the number of counts and are not quantitative. The elements are represented by their positive ions.

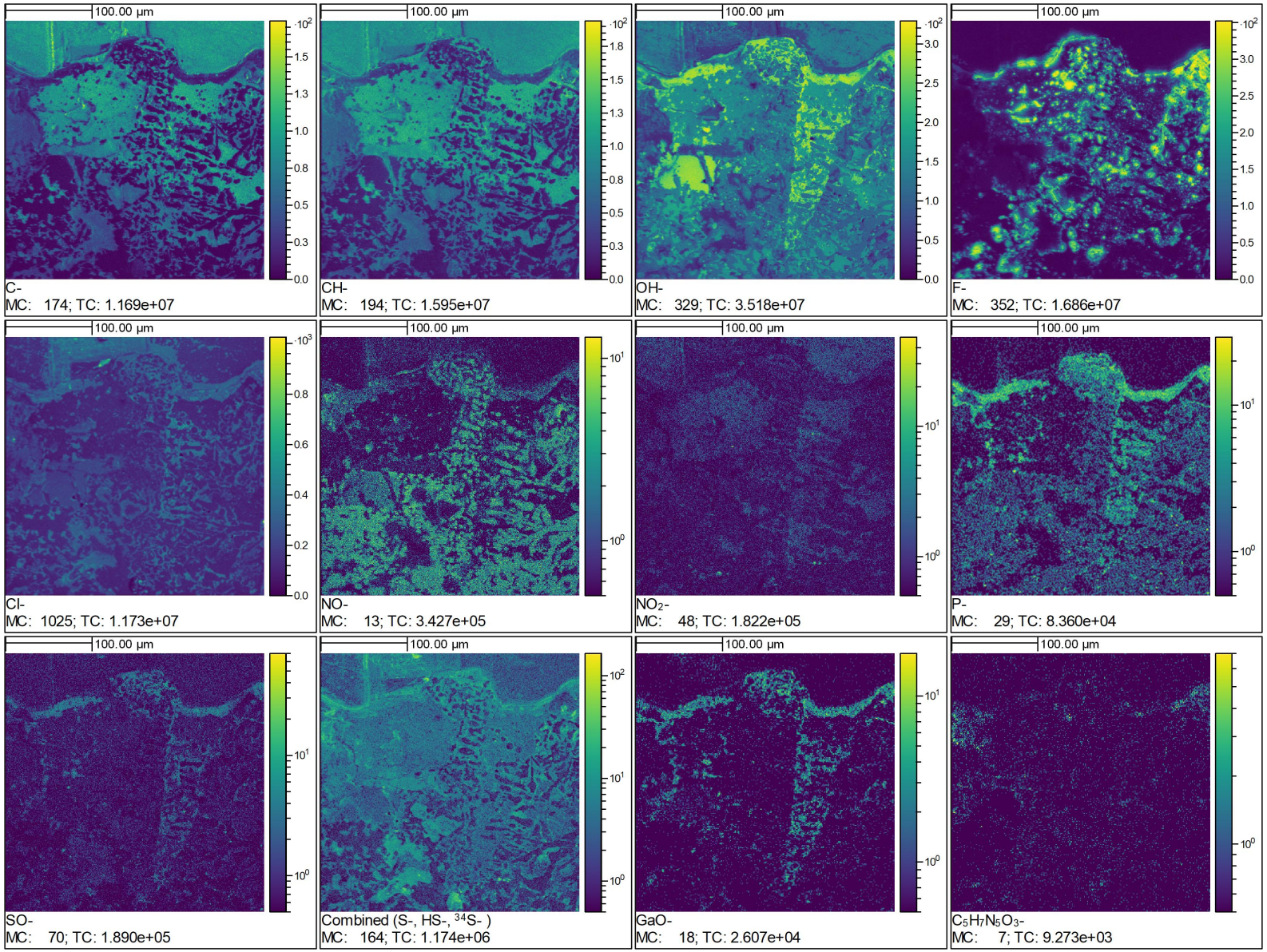

Figure 4.2-69: ToF-SIMS map showing the distribution of selected negative ions for sample AQ08_GPH, highlighting the compositional complexity. Colour scales relate to the number of counts and are not quantitative. The elements are represented by their negative ions.

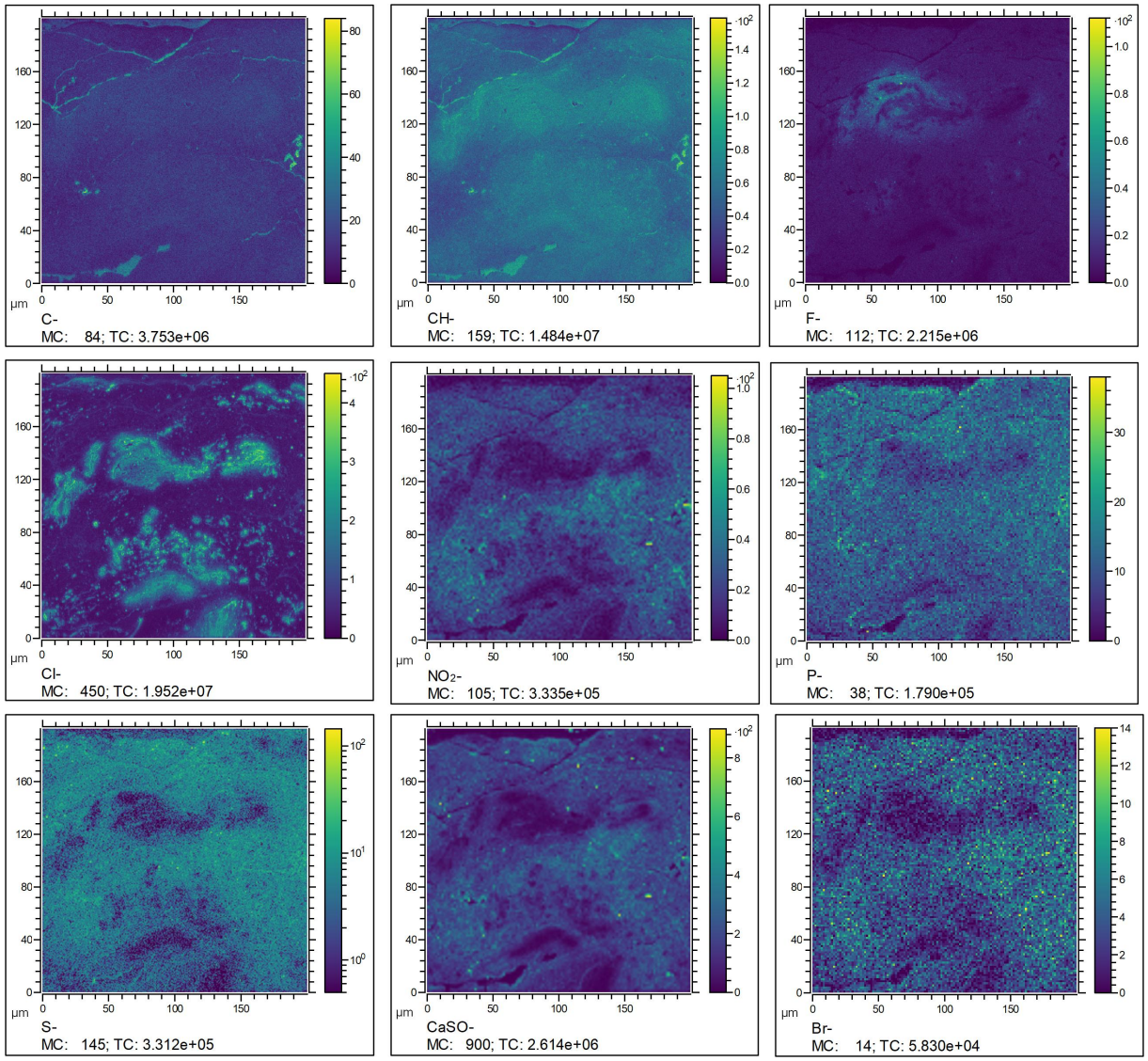

Figure 4.2-70: ToF-SIMS map showing the distribution of selected negative ions for sample AQ11_GPH, highlighting the compositional complexity. Colour scales relate to the number of counts and are not quantitative. The elements are represented by their negative ions. High counts of Cl and F hot spots are attributed to the resin.

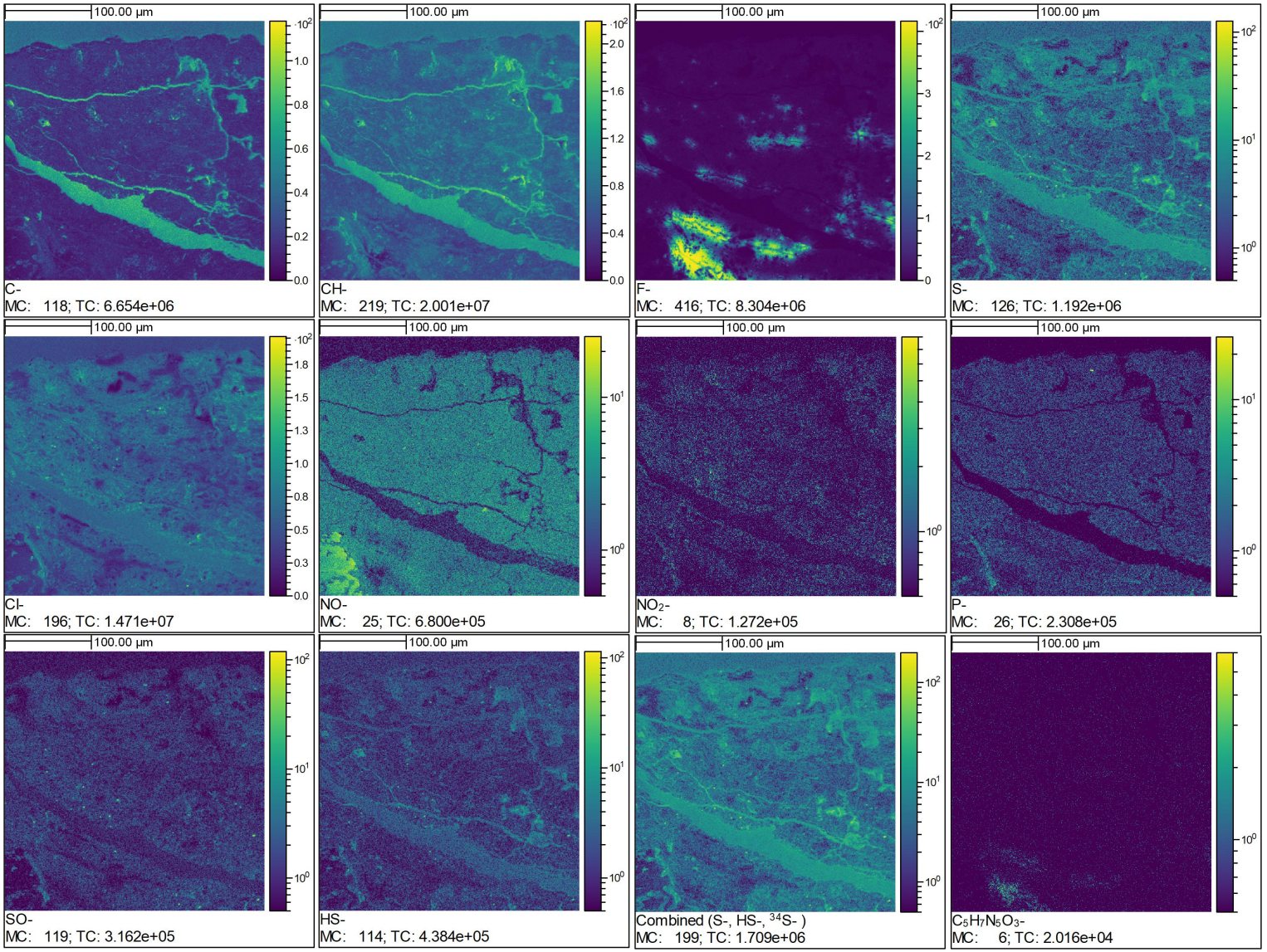

Figure 4.2-71: ToF-SIMS map showing the distribution of selected negative ions for sample AQ10_GPH, highlighting the compositional complexity. Colour scales relate to the number of counts and are not quantitative. The elements are represented by their negative ions. High counts of Cl and F hot spots are attributed to the resin.

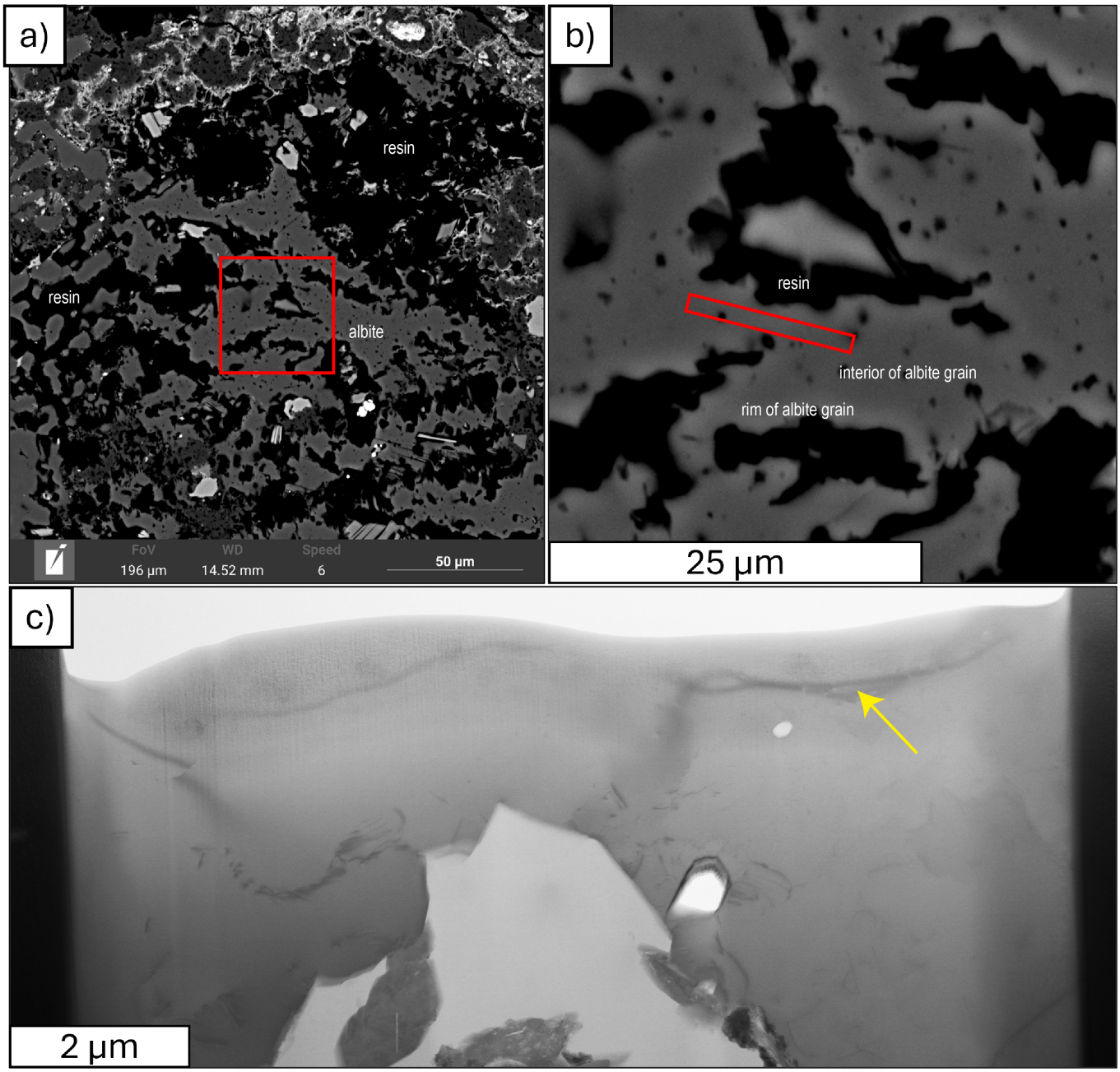

Figure 4.2-72: TEM nanoscale images of albite. (a) Location within the albite crystal selected for analysis. Albite is the mid-grey mineral that occupies most of the field of view. (b) Region of TEM lift out, showing that the rim of the albite grain has a higher BSE brightness than the interior. (c) Bright Field TEM image of the albite foil. Here, the large bright portion of the foil represents resin. The curved lines similar to the one highlighted by a yellow arrow are interpreted as local bending or linear defects (e.g. dislocations) of the crystal lattice.

Observations conducted in high-angle annular dark-field mode (HAADF) indicate that the top portion of the grain is characterised by a thin band that shows a light colour (< 1 μm) (Figure *4.2-73*). In HAADF mode, higher grey-scale intensities (i.e. whiter) are indicative of particles with higher

atomic numbers. Therefore, the top region of the albite grain is compositionally different to the underlying parts of the same grain. Scanning transmission electron microscopy (STEM)-EDS confirms that the brighter domain is depleted in Si, Al, O, and minor Na, and enriched in C, P, S, Cl and Fe relative to the darker domain (Figure *4.2-73*). Nanoclusters of Cl and Na are present within the top region of the foil and may indicate the presence of Na Cl. At the bottom of the foil, fibrous regions visible in HAADF are enriched in Fe and Mn (Figure *4.2-73*).

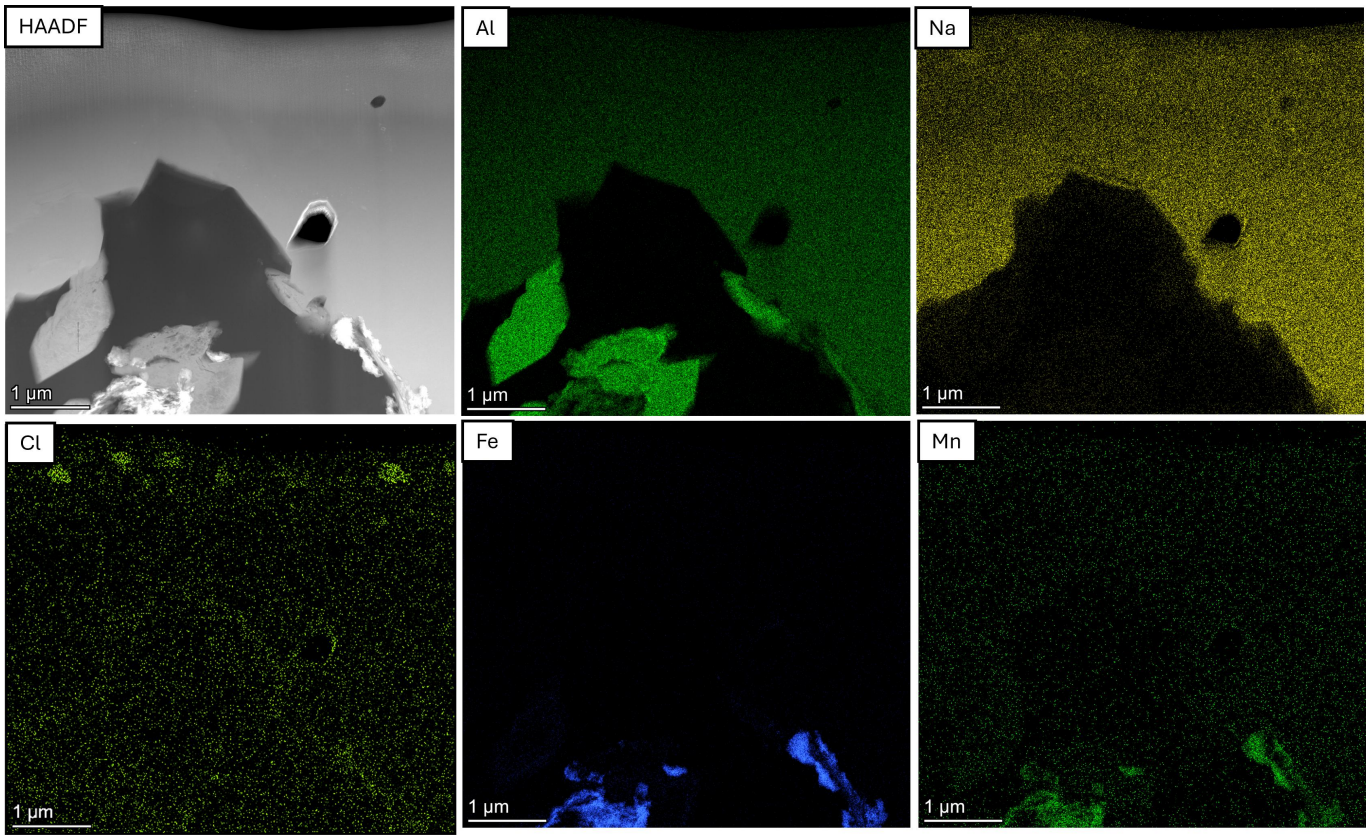

Figure 4.2-73: TEM HAADF image and STEM compositional maps of selected elements. Al, and to a lesser extent Na, decrease in abundance towards the top of the grain. Na and Cl form colocated nanoclusters in the outermost part of the grain.

The TEM foil of the patina was obtained by performing a lift out perpendicular to the patina surface of an unpolished billet of EX03_GPH (not shown). In this way it was possible to obtain a $\sim$5 μm-deep vertical profile of patina. The top of the foil is the top surface of the patina.

Observation of the electron-transparent foil provides a detailed view of the layered nanostructure of the patina (Figure *4.2-74*). The layering is internally defined by larger elongated clasts within a groundmass of nanometre-thick films of brighter material. Within the patina, there is an abundance of disseminated rounded bright particles and nanovugs (nano-scale void, sometimes partially filled by texturally-late material). STEM-EDS maps indicate that the structural layering also corresponds to a nanometre-scale compositional lamination of Mn, Fe and Si (Figure *4.2-74*(b)). The layering is defined by undulose Mn-rich bands that correspond to the intergranular brighter material visible in HAADF imaging (Figure *4.2-74*(a)). The EDS map indicates that the nanometre-size brighter particles disseminated within the matrix are mostly Fe-rich and Ti-rich, and are interpreted as

authigenic oxides. The larger clasts are enriched in Si, Al and K. High spatial resolution images reveal that these grains form flakes and are interpreted as dust-derived clay particles. The clay particles are surrounded by thin films of brighter material (Figure *4.2-74*(e,f)). Elemental abundances obtained by STEM-EDS, integrated over the whole area, show Mn ($\sim$15 wt%) $>$ Al ($\sim$11 wt%) $>$ Fe ($\sim$10 wt%) $>$ Si ($\sim$9 wt%) (Table *4.2-8*). Minor elements such as C (2.5 wt%) and Pb ($\sim$0.2 wt%) are also present. From the bulk analysis, the calculated concentration of nitrogen (N) is only to be considered approximate because quantification of this element by EDS techniques is challenging (Table *4.2-8*). A high-resolution STEM-EDS map of the top region of the patina reveals that the Mn-rich bands are weakly enriched in minor and trace amounts of K, Ca, Cr, Pb and S. Regions of Mn enrichment alternate with nanometre-sized mixtures of Si- and Al-bearing material (Figure *4.2-75*).

Table 4.2-8: Bulk composition of the patina foil obtained by STEM-EDS. The values are background corrected and deconvolution has been applied for gallium (Ga) and plutonium (Pt). Ga is used for TEM specimen preparation and Pt is contained in the top protective layer. σ represents one standard deviation of the element concentration across the mapped area.

Elements	**Wt**%	σ %
C	2.5	7.4
N	1.71	0.46
O	45.96	6.36
Na	0.36	0.13
Mg	0.68	0.16
Al	11.87	2.54
Si	9.38	2.01
P	0.74	0.17
S	0.11	0.03
Cl	0.09	0.02
K	0.48	0.1
Ca	0.23	0.04
Ti	0.44	0.09
Mn	15.22	2.76
Fe	10.03	1.74
Pb	0.19	0.03

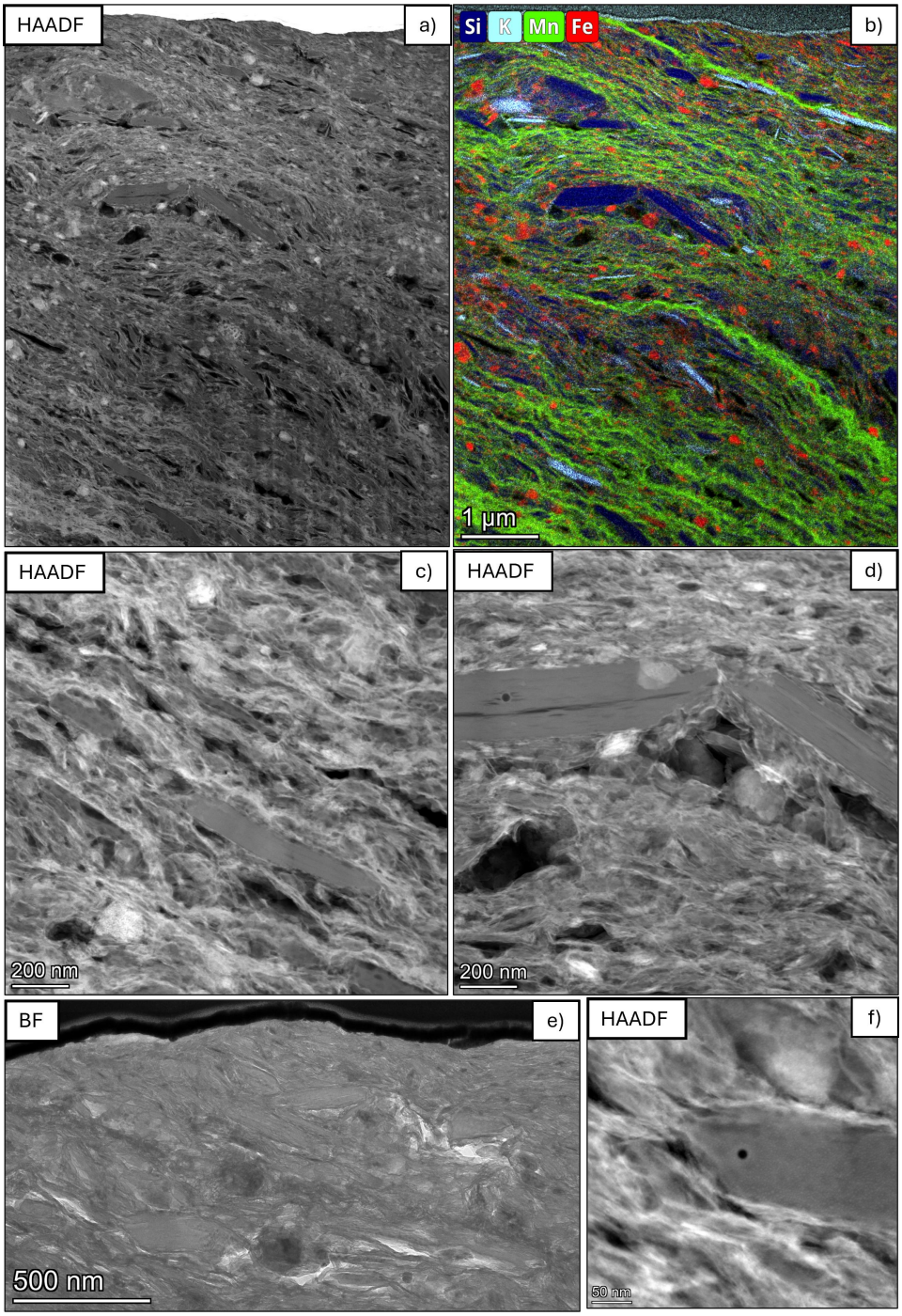

Figure 4.2-74: TEM observations of the patina lamellae. (a) HAADF image of the whole foil and (b) STEM-EDS map showing an overlap of Si, K, Mn and Fe. (c), (d), (e) and (f) show nanoscale structures of the patina. In (c) the fine layering is formed by bands of lighter material containing elongated clasts of clays. (d) close up image of clays within the patina. The flaky character of the clays is also visible. (e) Bright Field TEM image of the top portion of the patina below the protective Pt layer. In bright field, holes appear white revealing porosity within the patina. (f) high resolution STEM-HAADF image of a clay particle surrounded by a film of brighter material. Dark nanometre-sized holes are visible within the brighter matrix.

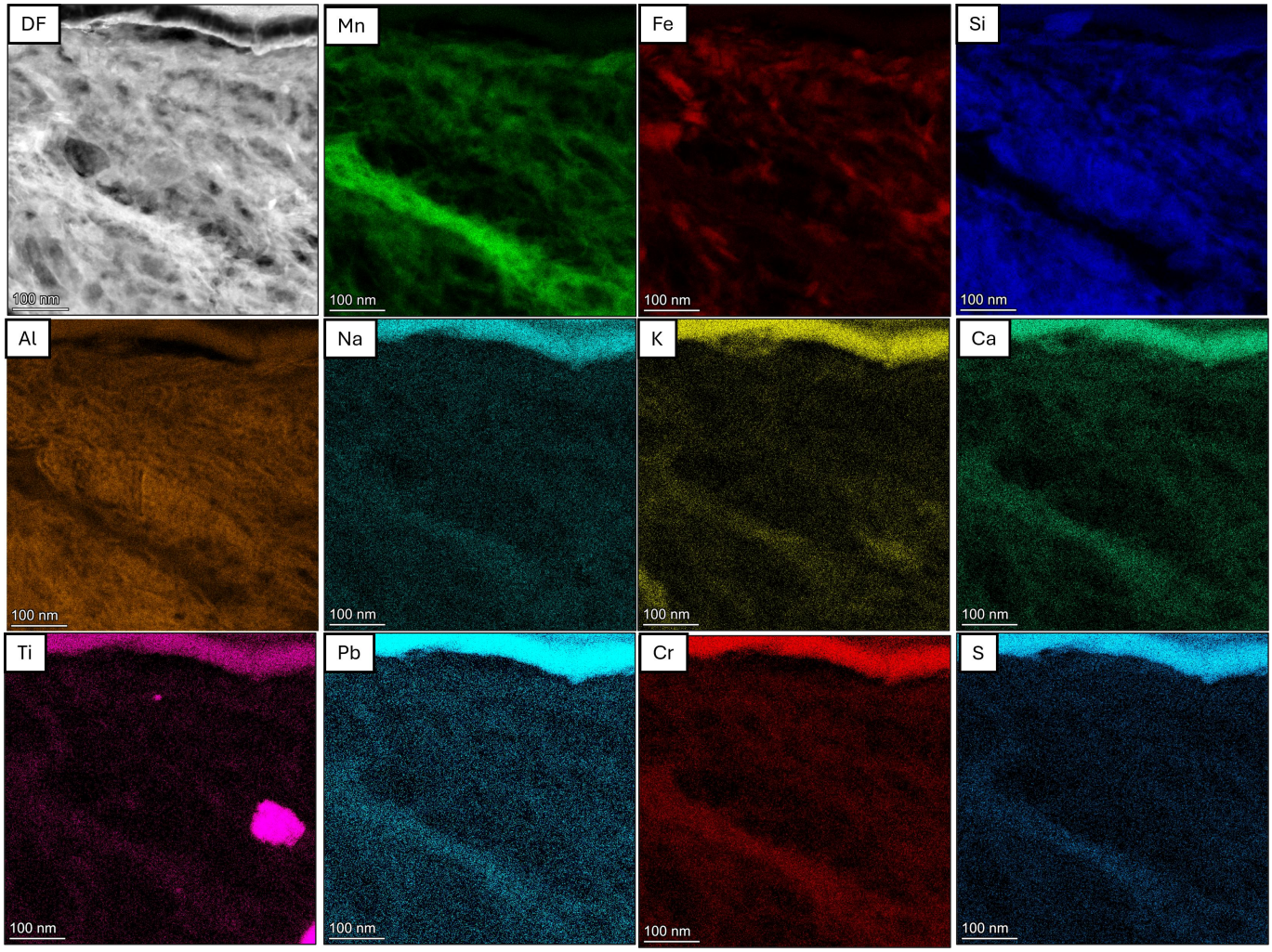

Figure 4.2-75: STEM Dark Field and STEM-EDS maps. Mn-rich bands are enriched in Na, K, Ca, Ti, Pb, Cr and S and depleted in Fe, Si and Al relative to the patina matrix. Ti-bearing nanoparticles are also shown.

Atom probe tomography

Twenty-eight atom probe specimens were prepared from patina across samples AQ11_GPH, AQ15_GBR and AQ09_GBR, which are exposed to different levels of industrial emissions. Measured NO_2 levels are highest at site AQ11, moderate at site AQ09, and lowest at site AQ15 (Figure *7.11-3*). Unfortunately, many of the specimens, which are mechanically weak because of their layered structure and lack of cementation, failed under the applied high electrical field of the measurements. Only seven specimens yielded sufficient APT data for further analysis and interpretation. The rest of the specimens fractured during the very early stages of data acquisition.

The sites for atom probe analyses of AQ11_GPH and AQ15_GBR were chosen based on the 2D compositional results obtained from EDS and ToF-SIMS maps of patina. Relatively low levels of industrial emissions are measured at site AQ15_GBR. Where possible, APT specimens were taken from compositional layers or nanoparticles from either the bottom of the patina, or as close as possible to the surface (Figure *4.2-76*). The rationale behind this strategy was to characterise

the patina–weathered rind and patina–atmosphere interfaces at higher and lower exposure sites, and to compare the sub-nanometre bulk compositions to evaluate the concentrations of exotic elements that may be present at the patina–atmosphere interface and that might be attributable to an anthropogenic source. To date, the successful datasets include data from the top of the patina from samples AQ11_GPH and AQ15_GBR and from the bottom region of sample AQ15_GBR. Unfortunately, specimens prepared from the lower region of AQ11_GPH did not yield usable data. For sample AQ09_GBR, a different approach was used and the specimen was lifted perpendicular to the patina of an unpolished rock billet. This approach was tried to overcome the difficulty of extracting APT specimens from the patina-resin interface. Unfortunately, no successful data was obtained from this sample.

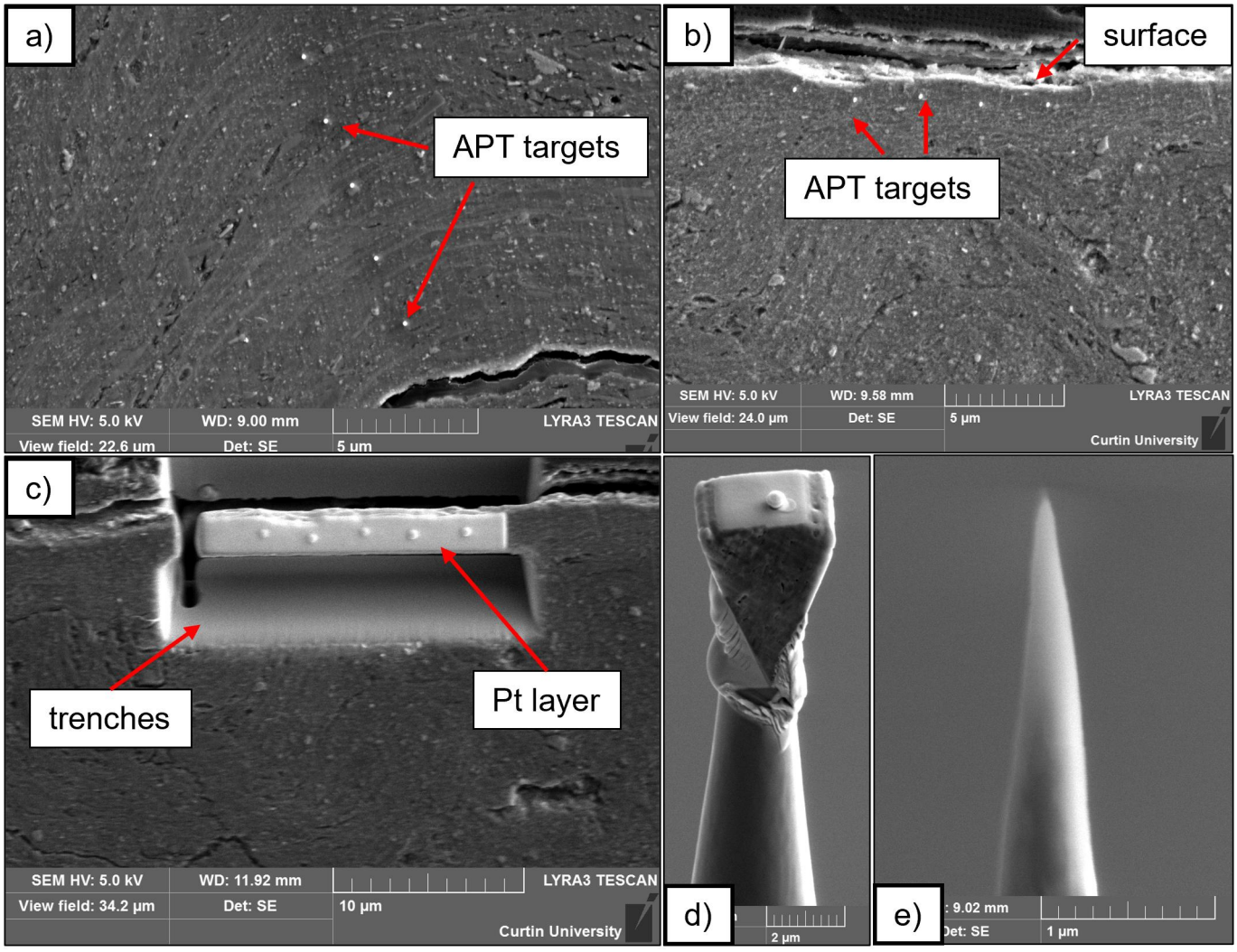

Figure 4.2-76: SE-SEM images showing the APT sample preparation procedure. (a, b) location of APT targets at the bottom of sample AQ15_GPH and top of AQ11_GPH, respectively. Images (c, d and e) displays the steps of wedge lift out, welding and needle shaping. (d) shows wedge precursor of needle M1 from sample AQ11_GPH. (e) shows needle M4 from sample AQ11_GPH.

The mass spectra obtained from the successful measurements are quite complex and record frequent variations of field-evaporated single and molecular ions across the acquired dataset. This

was expected considering the heterogeneous character of the patina. For the acquired dataset, the majority of the peaks in the mass spectra were identified. Each dot in the reconstruction represents one detected charged species, which may be a mono-atomic ion or a molecular species, and which is assigned to a particular element (e.g. Na, H_2O). The obtained bulk compositions of the reconstructed needles are reported in Table *4.2-9*. Most of the totals are above 98%, but specimen M9 returned a total of $\sim$70 wt% and specimen M16 returned a total of 83.8 wt%. These low values indicate that some peaks have not been assigned to elements or species, and further work is necessary to identify missing peaks that may represent a combination of complex molecular ions. H and H-bearing species are detected by ATP, so their presence does not explain the low totals. Because of the low totals, these results are considered preliminary.

In the APT data, the bulk composition of the reconstructed needles is consistent with analysis of silicate material. Across the dataset, the concentration of major elements (Si, Al, Mg, Fe, Mn, Ca, Na, K, Ti, Cl, P and S) is variable. Excluding Fe, Mn, and Si, the APT bulk composition of the patina is similar to that obtained by EMP (Table *4.2-9*). Trace elements detected include As, Ba, Ce, Co, Cr, Cu, In, Li, Ni, Rb, Sr, V, Zn, Sc, Ru, Y, Os, La, Cs and Ce. Additionally, peaks of N and molecular water (H_2O) are present in the mass spectra. In most of the 3D reconstructions, the APT dataset reveals nanoscale chemical heterogeneity. The majority of the structural complexity can be described by local concentrations of Mn, Fe, and Al (Figure *4.2-77* and *4.2-78*). In particular, Mn and Fe define planar interfaces (Figure *4.2-77*) and tubular features (Figure *4.2-78*) in all specimens. Commonly, Na and K form clusters (Figure *4.2-77*(a)) or show enrichment along planar interfaces (Figure *4.2-77*(b)). Some parts of the needle extracted from sample AQ15_GBR, referred to as specimen M9, show enrichment in K and Na on a planar surface located at the interface with portions of the needle characterised by molecular water (Figure *4.2-77*(b)). Molecular water refers to the presence of H_2O rather than OH^- or other O- and H-bearing species, and these observations confirm that molecular water is hosted by the patina. The association of alkali elements and molecular water, combined with a rapid increase in evaporation rates, is produced by evaporation of fluid inclusions during APT analysis (e.g. Reddy et al., 2020). This molecular water is likely to represent nanometer-scale pockets of fluid within the patina. It is not possible to determine the past or future duration of molecular water residence within the patina from the ATP analysis. However, the presence of K and Na with the molecular water argues against an origin related to sample preparation, which uses water with low concentrations of these ions.

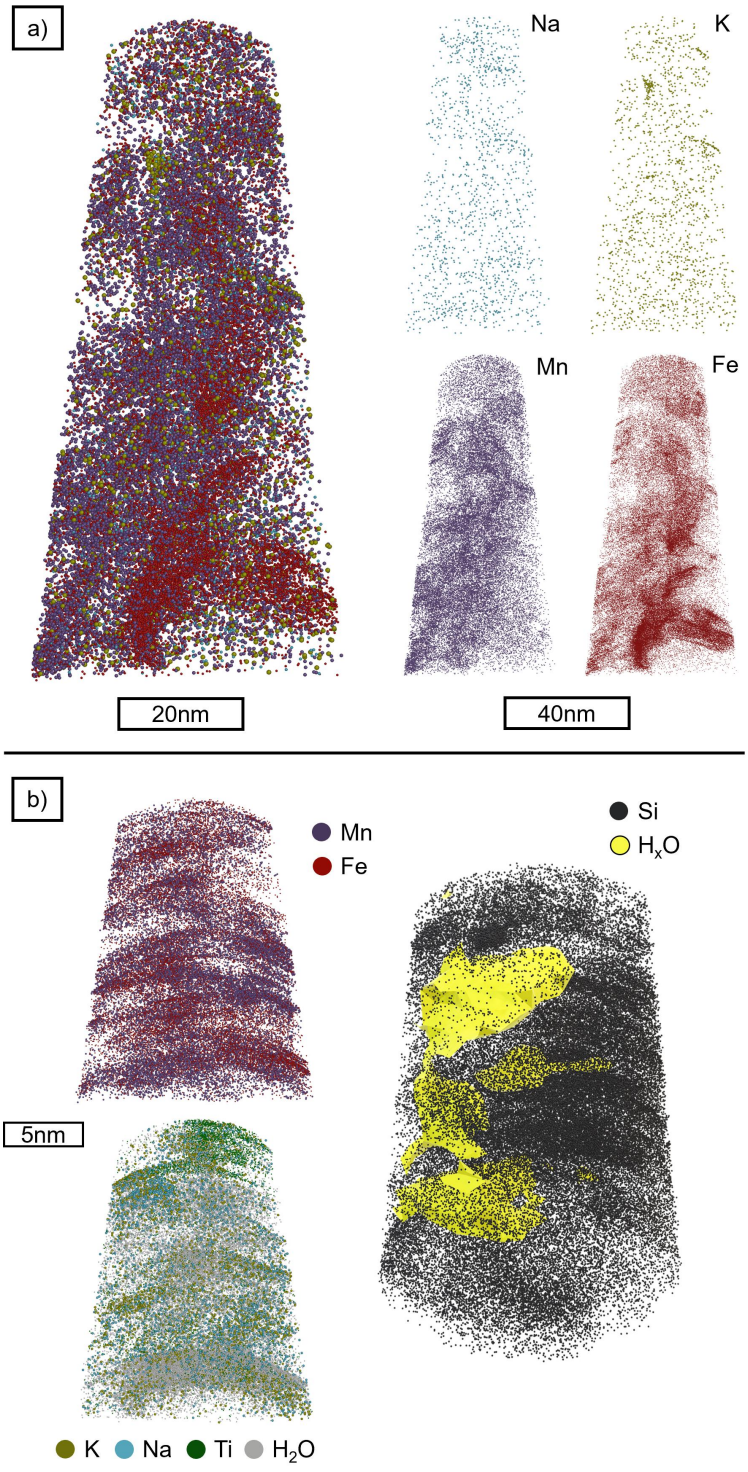

Figure 4.2-77: 3D reconstructions of atom probe specimens for AQ15_GBR. Each dot in the reconstruction represents one detected charged species, which may be a mono-atomic ion or a molecular species, and which is assigned to a particular element (e.g. Na, H_2O). For simplicity, not all inferred atoms are displayed. (a) Specimen M10. Left panel shows superimposed Mn, Fe, K and Na. Right hand panel shows the distributions of these elements individually. The same colour scheme is used for both panels. (b) Specimen M9. Upper left hand panel shows Mn and Fe. Lower left hand panel shows K, Na, Ti, H_2O. Right hand panel shows Si and a surface of constant HxO concentration, in yellow, that highlights the regions of high HxO content. HxO refers to all OH-bearing species.

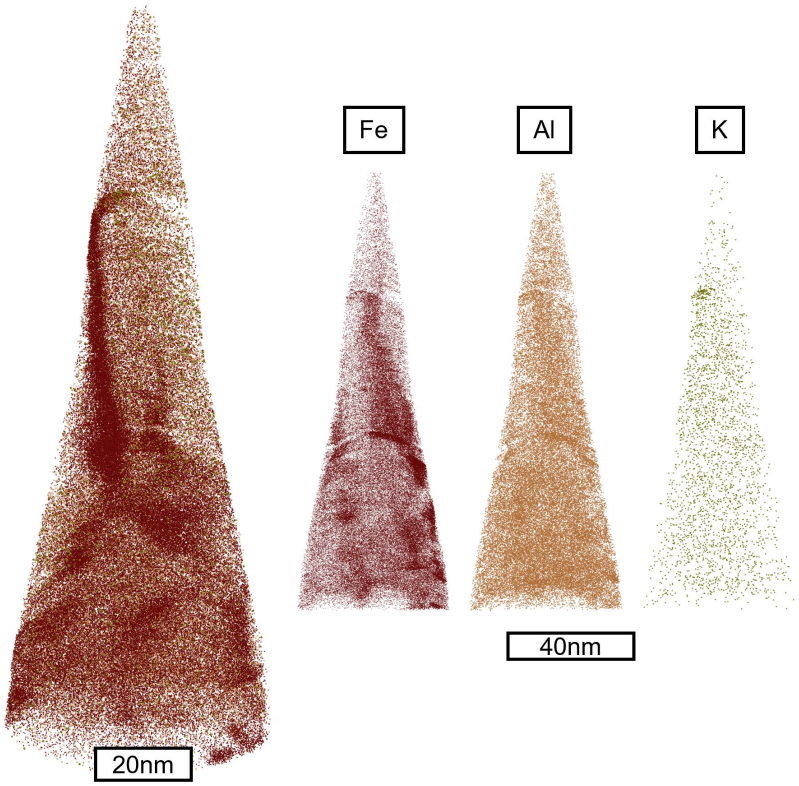

Figure 4.2-78: 3D reconstructions of atom probe specimens for AQ11_GPH. Each dot in the reconstruction represents one detected charged species, which may be a mono-atomic ion or a molecular species, and which is assigned to a particular element (e.g. Na, H_2O). For simplicity, not all inferred atoms are displayed. The maps show tubular heterogeneities of Fe and Al. K forms a cluster on the upper left hand side of the needle, which is collocated with an Fe- and Al-depleted surface.

Table 4.2-9: Bulk composition of the different patina specimens obtained from APT. Values are expressed in atom percent (at.%). σ is one standard deviation on the measured value. Specimen M4 is shown on Figure 4.2-76(d).

	AQ15_GBR										**AQ11_GPH**			
	Bottom						**Top**				**Top**			
	M9	σ	**M10**	σ	**M11**	σ	**M7**	σ	**M8**	σ	**M4**	σ	**M16**	σ
Si	8.24	0.03	13.22	0.03	19.25	0.03	31.82	0.05	27.63	0.11	14.69	0.03	7.21	0.01
Al	7.33	0.03	12.76	0.02	11.62	0.02	5.62	0.03	8.32	0.06	13.01	0.03	7.03	0.01
Ti	0.47	0.01	0.23	0.00	0.21	0.00	0.68	0.01	0.45	0.02	0.11	0.00	0.05	0.00
Fe	1.71	0.02	3.42	0.01	5.28	0.01	13.06	0.04	49.43	0.11	13.13	0.03	9.32	0.01
Mg	1.06	0.01	1.42	0.01	1.22	0.01	0.50	0.01	0.17	0.01	0.81	0.01	14.80	0.02
Mn	5.00	0.02	14.23	0.02	5.40	0.01	2.11	0.02	0.88	0.03	0.04	0.00	0.45	0.00
K	0.29	0.01	0.02	0.00	0.07	0.00	0.08	0.00	0.00	0.00	0.14	0.00	0.71	0.00
Na	0.18	0.01	0.01	0.00	0.00	0.00	0.05	0.00	0.00	0.00	0.01	0.00	0.04	0.00
Ca	0.15	0.01	0.17	0.00	0.13	0.00	0.23	0.01	0.05	0.01	0.20	0.00	0.36	0.00
P	0.35	0.01	0.19	0.01	0.20	0.00	1.04	0.01	0.86	0.02	0.16	0.01	0.61	0.00
S	0.19	0.01	0.10	0.00	0.23	0.01	0.00	0.00	0.00	0.00	0.08	0.00	0.07	0.00
Cl	0.20	0.01	0.12	0.00	0.10	0.00	0.12	0.01	0.00	0.00	0.09	0.00	0.07	0.00
As	0.03	0.00	0.03	0.00	0.03	0.00	0.02	0.00	0.00	0.00	0.00	0.00	0.04	0.00
Ba	0.00	0.00	0.00	0.00	0.02	0.00	0.03	0.00	0.00	0.00	0.00	0.00	0.00	0.00
Ce	0.00	0.00	0.06	0.00	0.04	0.00	0.00	0.00	0.00	0.00	0.00	0.00	0.00	0.00
Co	0.03	0.00	0.04	0.00	0.04	0.00	0.00	0.00	0.00	0.00	0.00	0.00	0.02	0.00
Cr	0.04	0.00	0.01	0.00	0.02	0.00	0.01	0.00	0.00	0.00	0.03	0.00	0.10	0.00
Cu	0.03	0.00	0.01	0.00	0.02	0.00	0.01	0.00	10.07	0.07	0.09	0.00	0.08	0.00

	AQ15_GBR										AQ11_GPH			
	Bottom						Top				Top			
	M9	σ	**M10**	σ	**M11**	σ	**M7**	σ	**M8**	σ	**M4**	σ	**M16**	σ
Ga	0.18	0.01	1.24	0.01	1.21	0.01	0.31	0.01	0.62	0.02	0.72	0.01	0.30	0.00
In	0.03	0.00	0.11	0.00	0.22	0.00	0.52	0.01	0.39	0.02	0.08	0.00	0.03	0.00
Li	0.09	0.00	0.00	0.00	0.00	0.00	0.00	0.00	0.00	0.00	0.00	0.00	0.01	0.00
N	0.23	0.01	0.12	0.00	0.00	0.00	0.02	0.00	0.12	0.02	0.00	0.00	0.28	0.00
Ni	0.03	0.00	0.01	0.00	0.01	0.00	0.03	0.00	0.00	0.00	0.01	0.00	0.12	0.00
O	44.18	0.05	50.89	0.04	53.46	0.03	43.14	0.06	0.00	0.00	54.14	0.04	41.93	0.02
Rb	0.00	0.00	0.02	0.00	0.01	0.00	0.00	0.00	0.00	0.00	0.01	0.00	0.00	0.00
Sr	0.00	0.00	0.00	0.00	0.05	0.00	0.00	0.00	0.00	0.00	0.00	0.00	0.00	0.00
V	0.00	0.00	0.00	0.00	0.04	0.00	0.02	0.00	0.00	0.00	0.01	0.00	0.02	0.00
Zn	0.03	0.00	0.02	0.00	0.02	0.00	0.03	0.00	0.00	0.00	0.01	0.00	0.02	0.00
Sc	0.00	0.00	0.00	0.00	0.00	0.00	0.01	0.00	0.00	0.00	0.00	0.00	0.00	0.00
Ru	0.00	0.00	0.00	0.00	0.00	0.00	0.00	0.00	0.00	0.00	0.02	0.00	0.03	0.00
Y	0.00	0.00	0.00	0.00	0.00	0.00	0.00	0.00	0.00	0.00	0.00	0.00	0.02	0.00
Os	0.00	0.00	0.00	0.00	0.00	0.00	0.00	0.00	0.00	0.00	0.00	0.00	0.01	0.00
Tc	0.00	0.00	0.00	0.00	0.00	0.00	0.00	0.00	0.00	0.00	0.00	0.00	0.00	0.00
La	0.00	0.00	0.00	0.00	0.00	0.00	0.00	0.00	0.00	0.00	0.00	0.00	0.02	0.00
Cs	0.00	0.00	0.00	0.00	0.00	0.00	0.00	0.00	0.00	0.00	0.00	0.00	0.03	0.00
Ce	0.00	0.00	0.00	0.00	0.00	0.00	0.00	0.00	0.00	0.00	0.00	0.00	0.01	0.00
Total	70.07		98.44		98.88		99.45		98.98		97.61		83.80	

4.2.9 Discussion

4.2.9.1 Insights into rock weathering processes: Background

Weathering is a broad term used to describe a range of processes that, when complete, transforms a rock into a mix of disaggregated particles and solutes, and, when incomplete, manifests as disruption and deterioration of rocks on the surface of Earth or other planets. Weathering processes can be grouped into three main categories: mechanical, chemical and biological.

Mechanical weathering includes processes that break down rocks, and their minerals, by physical processes of disaggregation such as fracture propagation (joints) generated by cycles of expansion, plant, and animal activities. Joints can form in rocks below or exposed on the surface by pressure release as the lithospheric load is removed by erosion, or as a result of volumetric expansion. The latter can be induced by temperature fluctuation or by dilation of growing minerals, which provides an example of combined mechanical and chemical weathering. For example, diurnal cycles of thermal expansion and contraction of rocks over geological time lead to fracture propagation, spallation or flaking of the rock surfaces (e.g. Kant et al., 2017 and references therein). Other more localised mechanisms involve stress induced by temperature shock, for example, by fire or lightning strike (Buckman et al., 2021). In addition, salt is a well-known contributor to mechanical weathering (see Oguchi and Yu, 2021 for a review). The crystallisation pressure generated by the growth of salt crystals from liquid water (or moisture) that has infiltrated a rock pore or fracture acts to increase the size of the pore or fracture and can lead to deterioration, over geological timescales, of the internal structure of porous materials. Similarly, clay minerals (e.g. smectites) can incorporate molecules of H_2O within their crystal structure. This generates hydric swelling pressure, exerted by minerals as their volume expands when they come into contact with water. Contrarily, shrinkage occurs when this type of clay dries (shrink-and-swell; Meunier, 2005). At Murujuga, there is large-scale evidence of mechanical weathering in the form of the characteristic and enigmatic “rock piles” landscape (e.g. Donaldson, 2011). Here, fragments of all of the lithologies, especially granophyre, gabbro and dolerite, have physically separated from their parent outcrops by fracturing along rock joints to form the piles of rock boulders and blocks. At a smaller scale, mechanical weathering manifests as rock spalling/flaking and detachment of superficial layers (e.g. Pillans and Fifield, 2013; Smith et al., 2022 and references therein).

Chemical weathering involves the dissolution of minerals and/or their transformation into other minerals. Once at the surface, minerals are commonly metastable because the pressures, temperatures, and fluid availability and composition at the surface are different to those under which the mineral formed. Metastable rock-forming minerals chemically react with the surrounding environment to form crystal phases that are more thermodynamically stable. For example, the Goldich series for igneous rocks (Goldich, 1938) shows that mineral phases formed at the early stages of magma crystallisation (e.g. olivine $>$ pyroxene $>$ Ca-plagioclase $>$ Na-plagioclase $>$ K-feldspar) are the most susceptible to chemical weathering, and react to form clay minerals, quartz, Al- and Fe-oxides (e.g. gibbsite and hematite) under surficial conditions. The rates of weathering and mineral transformation depend on a large number of factors characteristic of the rock, such as the composition of the minerals, their crystallography, and grain size, and environmental factors, such as climate, temperature, precipitation, and *pH*. Water is the most important agent that drives the chemical weathering of minerals and strongly affects weathering rates. Water, in its various forms (dew, precipitation, meteoric) provides a reactive media that allows chemical reactions to

occur and facilitates transport of elements in solution.

4.2.9.2 Insights into rock weathering at Murujuga

Microstructural characterisation of the weathered rind across the various lithologies shows that porosity is ubiquitous and that the porosity decreases towards the fresher rock. The SEM observations show that pores within the weathered rind form by selective mineral dissolution. In granophyre and granite, the dominant weathering reactions typically involve the disappearance of albite and microcline (e.g. Figure *4.2-7*, *4.2-8*). In contrast, within gabbro, dolerite and basalt, chemical weathering mostly affects pyroxene, and to a minor extent Ca-plagioclase (Figure *4.2-18*, *4.2-19*, *4.2-32* and *4.2-38*). At the grain scale, alteration of feldspars and pyroxene by chemical reactions is indicated by the formation of edge-pits and irregular grain boundaries (Yuan et al., 2019; Berner et al., 1980). Crystallographic control of alteration is particularly evident in pyroxene, where dissolution fronts nucleate and propagate within the mineral along exsolution lamellae.

Mineralogically, TIMA analysis of the samples confirms these microstructural observations. The calculated modal percentages record a decrease in the mode of minerals found within the fresher rock from the fresher rock–weathered rind interface towards the weathered rind–patina interface. In most samples, this decrease coincides with an increase in clay mineral abundance. Chemically, the compositional results show a consistent enrichment in Fe within the weathered rinds across all lithologies. In granophyre and granite, Fe-enrichment is associated with an increase in K and loss in Na, Ca, Al and Mg. The spatial distribution of chemical alteration is illustrated by the EDS elemental maps and by microprobe analyses of the minerals. For example, in granophyre, the depletion in Na from the fresher rock–weathered rind interface towards the weathered rind–patina interface revealed by the high-resolution panorama EDS maps is recognisable at the grain scale as Na-depletion within albite and microcline feldspars (Figure *4.2-42* and *4.2-44*).

In the mafic lithologies, Fe-enrichment is associated with depletion in Si, Ca, and Mg. These observations, and particularly the development of porosity and clay mineral formation, are consistent with the formation of the weathered rind by pervasive chemical weathering of the outer few millimetres of the host rocks that involved incongruent dissolution of rock-forming minerals. These results are in agreement with those of previous studies of Murujuga that document progressive alteration of the fresher rock to form weathered rinds (e.g. Donaldson, 2011; Ramanaidou and Fonteneau, 2019; Bednarik, 2012; Pillans and Fifield, 2013), although the results presented here provide an unprecedented level of detail and permit a quantitative description of the chemical weathering process. In particular, these findings align with, and expand on, the comparative mineralogy and chemistry presented by Ramanaidou and Fonteneau (2019). These authors document a decrease in primary minerals (feldspars and augite) in both weathered rind of granophyre and gabbro, respectively, and a concomitant increase in clays and Fe-oxides, which is consistent with the results presented here.

Chemical dissolution of feldspars and pyroxenes within meteoric environments has been studied extensively (e.g. Berner et al., 1980; Yuan et al., 2019). Alteration of feldspars, which involves dissolution, solute transport and secondary mineral re-precipitation plays a fundamental role in the alteration of felsic rocks and the development of soils (see Yuan et al., 2019 for a review). Feldspar dissolution aids the formation of secondary porosity, enhances rock permeability, and promotes the precipitation of clay minerals (e.g. illite, kaolinite and gibbsite) by providing dissolved Na, Ca,

K and Al (Yuan et al., 2019). In this report, the microstructural observations of granophyre and granite reveal, in every sample, voids along feldspar grain boundaries, edge-pits, and irregular compositionally modified grain margins. Moreover, microprobe analyses document preferential loss of Na relative to K, Al, and Si from feldspars of the weathered rind (Figure *4.2-44*). Mechanisms of feldspar dissolution include surface reaction-controlled dissolution, preferential leaching-diffusion, interfacial dissolution-precipitation and diffusion-precipitation dissolution (Yuan et al., 2019 and references therein). In particular, the mechanism of preferential leaching–diffusion leads to non-stoichiometric dissolution and development and evolution of a leached layer (i.e. reaction front) at the surface of the mineral in contact with the reacting solution (Chardon et al., 2006). The EDS analyses of rims of altered albite show depletion in Si, O, Al, Na and increased C, relative to unaltered albite (Appendix Figure *B-5*). TEM-HAADF observations confirm the presence of a compositionally-distinct layer on the margin of albite, $\sim$500 nm thick (Figure *4.2-73*). Based on these observations it is possible to interpret the rims as a leached zone formed by preferential leaching–diffusion mechanisms involving an aqueous solution (Chardon et al., 2006; Yuan et al., 2019). This interpretation is consistent with the development of porosity within the weathered rind. The interpreted nanoclusters of NaCl within the leached zone of the albite foil, and the close proximity of the investigated sample (EX03_GPH) to the coast, indicate that saline solutions may have been involved in hydrolysis and leaching. Such processes may affect other samples from Murujuga, albeit to lesser extents, because no part of Murujuga is more than four kilometres from the coast. Further, EDS and STEM–EDS data reveal C within the leached zone of the albite grain. It is possible to speculate that the presence of C records a biological contribution to the dissolution process and a role for organic acids. Alternatively, it may represent C present in fluid inclusions that formed during conversion of the protolith granophyre to the weathered rock during hydrothermal alteration. It is not possible to distinguish between these hypotheses using inorganic chemical techniques. While it is highly unlikely that any process at Murujuga occurs without a biological/microbial contribution, the role and magnitude of the effect of these contributions remains to be determined. Integration of organic, inorganic, and microbiological investigations are required to better constrain the role of microorganisms. Nevertheless, these results provide important new insights into the mechanism of plagioclase dissolution within granophyre and the role of aqueous solutions.

4.2.9.3 Patina formation: Background

Rock surfaces (*sensu lato*) are often characterised by thin (1–100s μm) orange, brown, dark red, or black coatings (Dorn, 2013). These coatings are sometimes described as rock varnish, and are referred to here as patina. The colour depends on composition and mineral assemblage (see Dorn, 2013, 2020 for a review). For example, dark glossy patinas are associated with high concentrations of Mn-oxides, whereas Fe-oxide-dominated patinas are commonly red or orange. Rock varnish consists of clay minerals and amorphous silica ($\sim$70%), Mn- and Fe-oxides ($\sim$20 %), and minor amounts of other components (Thiagarajan and Aeolus Lee, 2004; Garvie et al., 2008; Goldsmith et al., 2014; Dorn, 2020; Lingappa et al., 2021; Potter and Rossman, 1979). Internally, rock varnish is characterised by micrometre scale laminations and/or stromatolitic structures defined by thin alternating compositionally distinct layers that may be Mn-, Fe- or Si-rich (Dorn, 2007; Macholdt et al., 2017; Dorn and Krinsley, 2019; Lingappa et al., 2021; Krinsley, 1998). Patina forms in a range of environments around the globe, including Murujuga (Bednarik, 2012; Black et al., 2017b;

Dorn, 2020; Curtin University, 2023 and references therein), and have received considerable attention as a possible proxy for paleoclimatic variation (Dorn, 1994). For example, compositional micro-laminations have been interpreted as a record of changes in paleoenvironment, such that Mn-rich bands form in wetter conditions (Dorn, 2007). Rock patina has also been studied in the context of archaeology (Dorn, 2020; Bednarik, 2012) and as a possible indicator of life on Mars (e.g. Randall and Vera, 2004; Lanza et al., 2012).

While there is some consensus that patina is mainly sourced from airborne dust rather than the rock underlying (Krinsley, 1998; Garvie et al., 2008; Goldsmith et al., 2014; Otter et al., 2020), the mechanism(s) responsible for the formation of rock varnish are yet to be proven and proposed conceptual models are divided between abiotic and biotic processes or a combination of both. The biggest challenge for conceptual models is a plausible explanation for the extremely high concentrations of Mn within this patina, which are well above the geological background of the host rocks or surrounding environment. Abiotic models interpret the elevated concentrations of Mn and Fe as a consequence of *pH* variations, where Mn^{2+}, which is relatively soluble, is selectively leached from dust particles by aqueous water solution and then oxidised to form insoluble $Mn^{3,4+}$-oxides (e.g. birnessite), which cement the clay minerals (Otter et al., 2020; Goldsmith et al., 2014). In contrast, biotic models attribute the high concentrations of Mn and Fe to bacterial activity moderated by wetting cycles (e.g. Hoover et al., 2005). Other models, referred to as polygenetic, combine biotic and abiotic processes. For example, abiotic processes may be invoked to explain clay and oxide cementation, while biotic activity, initiated by wetting events, releases Mn and Fe that are then available for cementation (Krinsley et al., 2017; Dorn and Krinsley, 2019; Krinsley, 1998; Lingappa et al., 2021; Chaddha et al., 2024 and references therein).

4.2.9.4 Patina formation at Murujuga

The micro-to-nanoscale observations of the patina reported here amply supplement the preliminary observations provided in the Monitoring Studies Report 2023. The abundance of clay minerals and oxides disseminated within the patina, the alternation of Fe- and Mn-rich bands, and the stromatolitic structures are consistent with features of patina elsewhere (e.g. Dorn, 2007; Garvie et al., 2008; Macholdt et al., 2017; Lingappa et al., 2021). However, some key features may be Murujuga-specific, and/or may be relevant to patina stability and longevity, and these features are summarised below:

1. Microstructural observations indicate that the distribution and occurrence of the patina are largely controlled by the topography of the substrate and its degree of weathering. On all lithologies, thicker patina (up to $\sim$800 μm) is formed within depressions on the substrate.
2. Four main types of patina can be distinguished: fine-layered, stromatolitic, massive and gravelly.
3. Thicker deposits preserve evidence of flaking and re-growth in the form of truncation surfaces (i.e. unconformities) and changes in patina texture, indicating that multiple generations of patina overgrow each other *in situ*.
4. Patina is not limited to the surface of the rocks, but can form along the sides of topographic depressions, along the walls of fractures, “hanging” from the roofs of sub-surface cavities or filling subsurface cavities within the weathered rinds. These patina morphologies are referred

to collectively as sub-surface patina. The formation of sub-surface patina on non-horizontal and inverted surfaces indicates that pools of water are not required for patina formation.

5. High-resolution EDS maps and EMP analyses indicate that patina is compositionally heterogeneous and features, in some cases, alternating Mn- and Fe-rich layers.
6. Fe-films and percolation of Mn within rock fractures to form sub-surface patina may stabilise the weathered rind and patina by providing additional cementation. This cementation is referred to here, and elsewhere in the rock varnish literature, as case-hardening.
7. Median values of most major element concentrations within the patina obtained by EMP indicate that the patina composition does not differ substantially across lithologies. In contrast, Mn and Fe are highly variable within and across samples, but the variability is so large that it is not possible to recognise any systematic variability between lithologies. These findings support a common genetic process that is independent of the lithology of the substrate.
8. Some minor features reflect the substrate lithology and position within the patina. For example, patina is often, but not always, characterised by gradients in Al, with higher Al at the weathered rind–patina interface. Gradients in Mg concentration are observed within patina on gabbro, especially where patina is developed above altered pyroxenes.
9. The stromatolitic patina is characterised by very high concentrations of Mn (up to 50 wt%, Appendix Figure *B-3*). The Mn concentration increases with Ba concentration.
10. ToF–SIMS analyses reveal enrichment of Li, P, S, Ba, Cr, Ni, Rb, Sr, Y, Eu, La, Ce, Cs, Pb, V, Co, U, ammonium compounds (NH_3 and NH_4), nitrogen-, sulphur-, silica- and carbon-bearing compounds (e.g. SO_x, NO_x) within the patina relative to the weathered rind.
11. TEM and APT analyses confirm the presence of nanometre scale clay, Mn- and Fe-oxide aggregates within the patina, and show compositional layering on sub-nanometre length scales.
12. APT reveals the presence of molecular water within the patina.

These findings, combined with findings from the other programs, have important implications for models of patina formation at Murujuga.

4.2.9.5 Co-location of manganese and cyanobacteria

In Section 8.2, Figure *8.2-3* shows the Redundancy Analysis (**RDA**) biplot displaying the relationship between bacteria taxa, inorganic compound concentrations, porosity indices and site information. *Chroococcidiopsidaceae* and *Cyanobacteria* were positively correlated with MnO, BaO, F concentration in patina in dolerite samples, e.g. AS01_DOL (Figures *4.2-79*, *8.2-3*). These results are consistent with the results of another study that Cyanobacteria are associated with elevated manganese concentrations (Lingappa et al., 2021). The Cyanobacteria are thought to accumulate Mn as a way to combat oxidative stress (see Section 8.2 for more details).

The high-resolution EDS map shows localised enrichment of C, Mn, P and Fe-depletion within a stromatolitic part of the patina. It is possible to speculate that the sponge-like, C-rich texture is part of a biotically-mediated structure (Figure *4.2-79*b). It is also possible that the C-bearing

resin contributes to the C-signal. However, the sponge-like structure is brighter on the C image than the resin-filled hole towards the bottom part of the image. Under these circumstances, the C-signal within the sponge-like structure cannot be attributed entirely to the resin. This observation is consistent with those from TOF-SIMS, which also record the presence of C-bearing species within the patina.

The EMP analysis along a stromatolitic patina structure of sample AQ15_GBR indicates a strong localised enrichment of Mn (up to ∼50 wt%) (Appendix Figure *B-3*). These observations support a polygenetic model for patina formation at Murujuga, with a role for abiotic and biotic factors.

4.2.9.6 Dynamic aspects of patina formation at Murujuga

Patina forms from airborne dust that accumulates on the surface of exposed rocks. Thinner patina develops on less weathered surfaces, indicating that a deep weathered rind favours accumulation of thicker patina for structural, chemical, or mechanical reasons (Dorn, 2013; Dorn et al., 2017), or that a deep weathered rind implies an ancient weathering profile locally, with correspondingly ancient, and consequently thick, patina.

The lack of microlamination present in massive and gravelly patina types might reflect that the rate of dust accumulation during the formation of these patina types is more rapid than the rate of biotic processing of the dust to form Mn- and Fe-rich bands (Dorn, 2013; Aulinas et al., 2014).

Patina along walls of topographic depressions, or the roofs of sub-surface cavities, that propagate outwards or downwards against gravity provide additional constraints on patina formation mechanisms (Figure *4.2-52*a, *4.2-57*, *4.2-60*, *4.2-61*). One explanation is that electrostatic forces held the particles together on the cavity walls for long enough that they became abiotically cemented, and chemically modified by bacterial activity (e.g. Dorn, 2013 and references therein). However, this explanation is hard to reconcile with the extreme angles of the cavities (Figure *4.2-60*, *4.2-61*), and new, to the best of our knowledge, observation that patina in contact with walls of cavities and fractures can be laminated (e.g. Figure *4.2-52*, Figure *4.2-57*). An alternative explanation is that moisture percolated downwards along existing pathways, and mobilised and deposited components of surface-deposited dust onto cavity and fracture walls. The presence of an aqueous solution is necessary to explain the extensive chemical dissolution of the weathered rind and gradients of major elements and trace element enrichments within the patina (e.g. Al, Mg). At the nanoscale, APT provides the first evidence for the presence of molecular water trapped within nanometre layers of the patina clays (Figure *4.2-77*d). This aqueous solution may have transported elements within, and external to, the patina–weathered rind system.

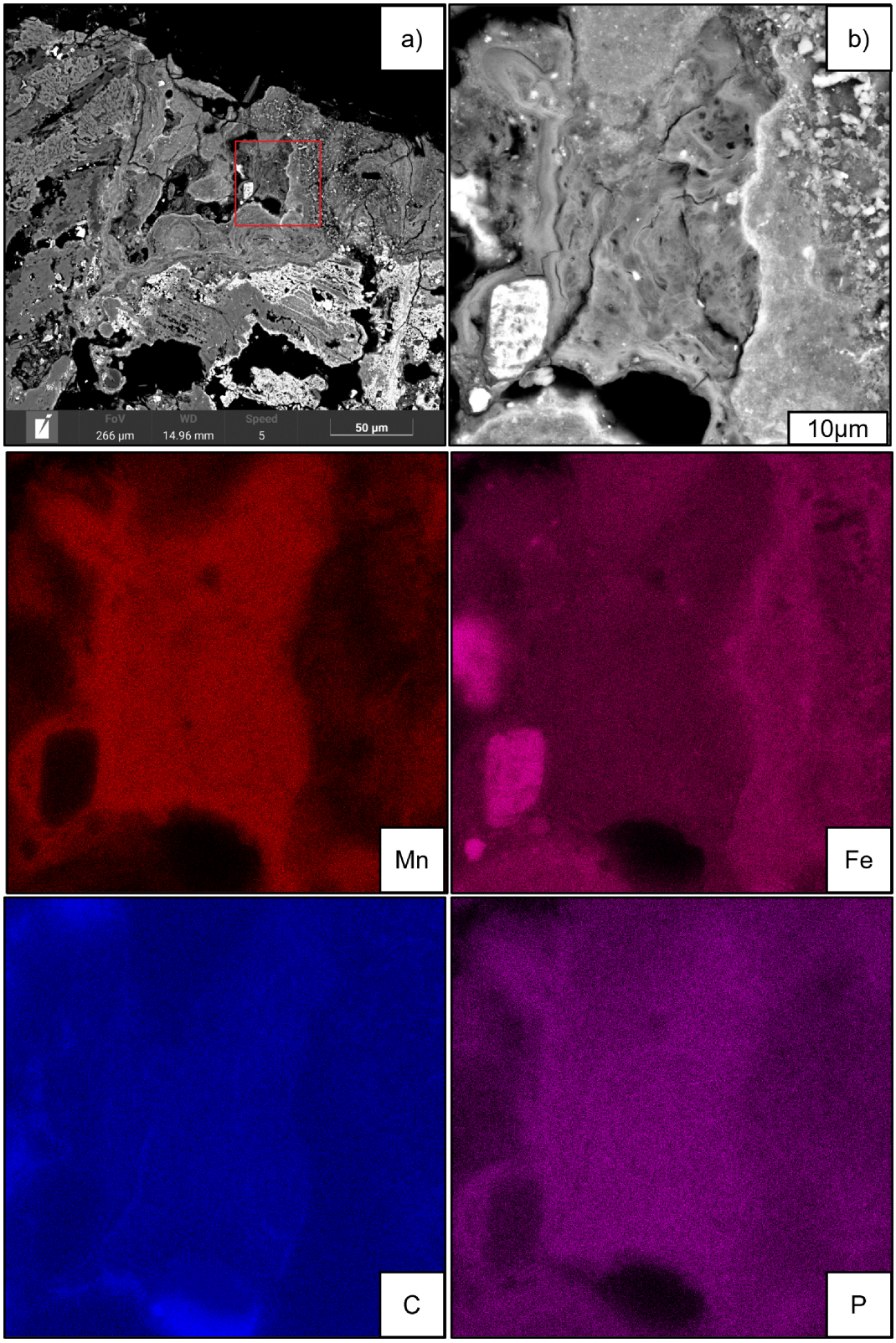

Figure 4.2-79: BSE-SEM images of stromatolitic patina within sample AS01_DOL where (b) is a close-up image of the area indicated by red box in (a). Element maps for Mn, Fe, C, and P are of the region shown in (b). Mn, C, and P show increased enrichment in a sponge-like part of the stromatolitic structure that is depleted in Fe. It is possible to speculate that the sponge-like, C-rich parts of the image form part of a biotically-mediated structure. The brightest C signal is from a pore filled with epoxy resin.

In this model, elements are incorporated into clays within the patina by ionic diffusion (leaching) from an aqueous fluid that interacted with the dissolving substrate or surficial patina (Aulinas et al., 2014; Chaddha et al., 2024). In this scenario, channels within the weathered rind beneath the patina (e.g. left side of Figure *4.2-57*), could have progressively, or episodically, provided constituents for the formation of sub-surface patina, derived from dissolution of surficial patina-hosted minerals. Concomitantly, elements could have been scavenged from the weathered rind by incongruent feldspar dissolution, but the similar compositions of surficial and sub-surface patina indicate that surface patina is the dominant source of elements for the sub-surface patina. Zonation in minerals within the weathered rind and patina might reflect changes in the rates and magnitudes of element transport and supply at different stages of mineral dissolution (Figure *4.2-62*).

Sub-surface voids may be filled or partially filled by sub-surface patina (e.g. Figure *4.2-51* and *4.2-57*). Variation in the degree of filling may reflect local differences in the relative rates of void and patina formation that may be related to differences in the episodicity of fluid ingress. The effects of mineral plucking during sample preparation must be considered. However, based on the criteria listed in Section 4.2.5.1, it is likely that part-filled sub-surface voids are likely to reflect weathering processes rather than preparation artefacts. It is possible to speculate that subsurface and surface patina in sample AQ13_GPH record similar events, based on the similar distribution of bright and dark bands (Figure *4.2-57* and Figure *4.2-62*). A better understanding of sub-surface patina formation and preservation may provide insights into patina stability, because sub-surface patina is protected from the effects of physical weathering and flaking, and only undergoes chemical modification. Further work is necessary to investigate this possibility.

Regardless of the details, the observations are consistent with a growing consensus on the fundamental role of wet surfaces in the formation of patina (Thiagarajan and Aeolus Lee, 2004; Goldsmith et al., 2014; Otter et al., 2020; Chaddha et al., 2024). However, if the previously observed micrometre-scale alternating Mn- and Fe-rich bands indicate variation in paleoeviromental conditions, then it is interesting to consider the meaning of the sub-nanometer scale banding observed by APT.

4.2.9.7 Impact of weathering on patina preservation

To date, the mineralogical and geochemical character of the rocks at Murujuga has been described only by a small number of geological studies, and observations are mainly limited to the gabbro and granophyre lithologies (Donaldson, 2011; Ramanaidou and Fonteneau, 2019; Neumann et al., 2022). In addition, several studies have explored, based on a combination of theoretical approaches and surface electrochemical measurements, the impact of industrial emissions on the rocks at Murujuga, with consequences for the preservation of rock art heritage (see Smith et al., 2022 for a review). These studies focused on the relationship between increased atmospheric acidity and the stability of the Mn-bearing components of the patina (Neumann et al., 2022; Smith et al., 2022). However, these studies have not included detailed characterisation of the patina microstructures and the host rock substrate. In addition, non-anthropogenic processes and their effects on rock weathering and patina preservation have not been fully integrated into these studies.

Data collected during the second year of research provides a comprehensive new database of geological information that allows a better overview of the microstructures, mineralogy and composition of the fresher rock, weathered rind and patina across the main lithologies of Murujuga.

In particular, compared to previous studies, the systematic application of automated mineralogy (TIMA) on a larger number of samples allows for an extended mineralogical analysis providing new insights into previously unreported structural-chemical relationships. Another advantage of the extensive application of TIMA, SEM, and EMP is that it has provided quantification of the mineral assemblage and abundance variations that are responsible for colour variations, and enables the patina to be considered as part of a system that includes both the patina and the weathered rind. Consideration of the patina as part of a larger system is essential if change within the Murujuga rocks is to be placed within a holistic context of microstructural, microchemical, and mineralogical change (Gordon and Dorn, 2005).

From these results, and their comparison with available studies, it becomes clear that chemical weathering might play a key role in controlling the distribution of patina by modifying the morphology of the substrate through microscale transformation of the host rocks (microerosion; Pillans and Fifield, 2013). Highly weathered surfaces show considerable local topography in the form of cavities, holes and fractures. These features commonly host the thickest patina (e.g. Figure *4.2-57*). Therefore, patina formed on these highly weathered surfaces has a greater preservation potential than patina formed on relatively smooth surfaces that may be less strongly weathered, although grain morphologies and textural relationships also control the development of topography on a rock surface. However, if all other factors are equal, patina formed on smooth surfaces is more exposed to mechanical weathering and, consequently, more likely to flake. The converse relationship may also apply; if patina protects the weathered rind from further mineral dissolution, then weathered rind below thick patina may have a greater preservation potential than weathered rind below thin or absent patina. However, further work is necessary to explore this possibility.

The fragile character of the patina is also indicated by its detachment during sample preparation, even when epoxy resin is used to preserve and stabilise the patina (Figure *4.2-6*). Nonetheless, even within a thicker patina that is protected by topography, a microstructural record of flaking indicates the dynamic nature of the patina (e.g. Figure *4.2-53*b).

Besides shaping the morphology of the surface, chemical weathering plays a key role in patina stability by affecting the structural integrity of the underlying substrate. Physical detachment of crystals is a strong influence on weathering rate (e.g. Krklec et al., 2016; Israeli and Emmanuel, 2018). As the rinds develop inward, rock-forming elements are weathered and transported away in solution by incongruent dissolution mechanisms to generate porosity (Oguchi, 2013). Increased porosity allows percolation of meteoric water to deeper levels and ongoing mineral dissolution compromises the stability of the weathered rind until a threshold is reached and portions of the rind will detach or flake (Etienne, 2002; Gordon and Dorn, 2005; Pillans and Fifield, 2013). A range of microstructural findings presented in this report indicate the importance of porosity in generating structural weakness within the weathered rind that can ultimately lead to patina loss (Figure *4.2-80*).

These microstructural observations extend the conceptual model of surface flaking proposed by Pillans and Fifield (2013) by the following considerations:

1. Surficial weathering and patina deposition commence as soon as the rock is exposed at the surface by exhumation or erosion although alteration also occurs below the ground surface.
2. Patina is thinner on smoother surfaces, which may be less intensively weathered, because patina on smooth surfaces is less protected from flaking than patina on rough surfaces, and

may undergo multiple cycles of flaking.

3. Erosion forms topographic irregularities that favour the formation of thicker patina; surface irregularities can form by mechanical fracture, detachment of single grains, or dissolution of minerals exposed at the surface.
4. Flaking might occur multiple times within a single patina profile, so flaking does not necessarily remove the entire patina layer (Figure *4.2-53*b).
5. Within the fresher rock and weathered rind, mineral dissolution contributes to porosity formation. Detachment of patina-bearing rind occurs when a mechanical threshold is reached.

4.2.9.8 Impacts of anthropogenic pollution on weathering processes and patina stability

Rates of chemical dissolution of minerals vary based on their composition, texture, grain size and the chemical composition of coexisting aqueous solutions (Welch and Ullman, 1996). For example, chemical weathering of feldspars is much faster than chemical weathering of quartz in felsic lithologies. In contrast, pyroxene dissolves faster than plagioclase in mafic rocks (e.g. gabbro, basalt, dolerite). Within a single lithology, porosity depends on the grain size of the minerals and the texture of the rock. The rate of mineral dissolution is proportional to the available surface area of that mineral in contact with the dissolving solution. Smaller grain size corresponds to higher total surface areas in any given rock volume and consequently higher surface area available for the dissolution reactions. For example, despite their similar composition, granophyre and granite display different styles of porosity. This could be attributed to faster dissolution of finer-grained granophyre, and to the intricate intergrowth between quartz and feldspars within the granophyre, such that the end product of feldspar dissolution is a void-surrounding framework of quartz crystals (e.g. Figure *4.2-6*).

Meteoric water, and particularly its chemistry, is the main agent responsible for the alteration and dissolution of the minerals. It is well established that changes in *pH* affect the rates of feldspar dissolution (Welch and Ullman, 1996; Yuan et al., 2019; Gudbrandsson et al., 2014). In particular, changes from neutral conditions result in an overall increase in feldspar dissolution rates (see Yuan et al., 2019 for a review). Similar increases in the rate of dissolution are generated by higher concentrations of carbonic acids formed by mixing of meteoric water with CO_2 in the atmosphere (Welch and Ullman, 1996) or formation of organic acids by microbial activity (see Yuan et al., 2019 for references).

The characteristics of the weathered rind and patina determined by EMP, SEM, TIMA, XRD, TOF–SIMS, and APT are highly variable, so that it is difficult to distinguish within-sample variation based on the observations alone. Fortunately, statistical approaches of the relatively large datasets provide a powerful tool that may be used to recognise significant differences amongst samples as a function of their exposure to industrial emissions. These approaches are described further in Section 7.

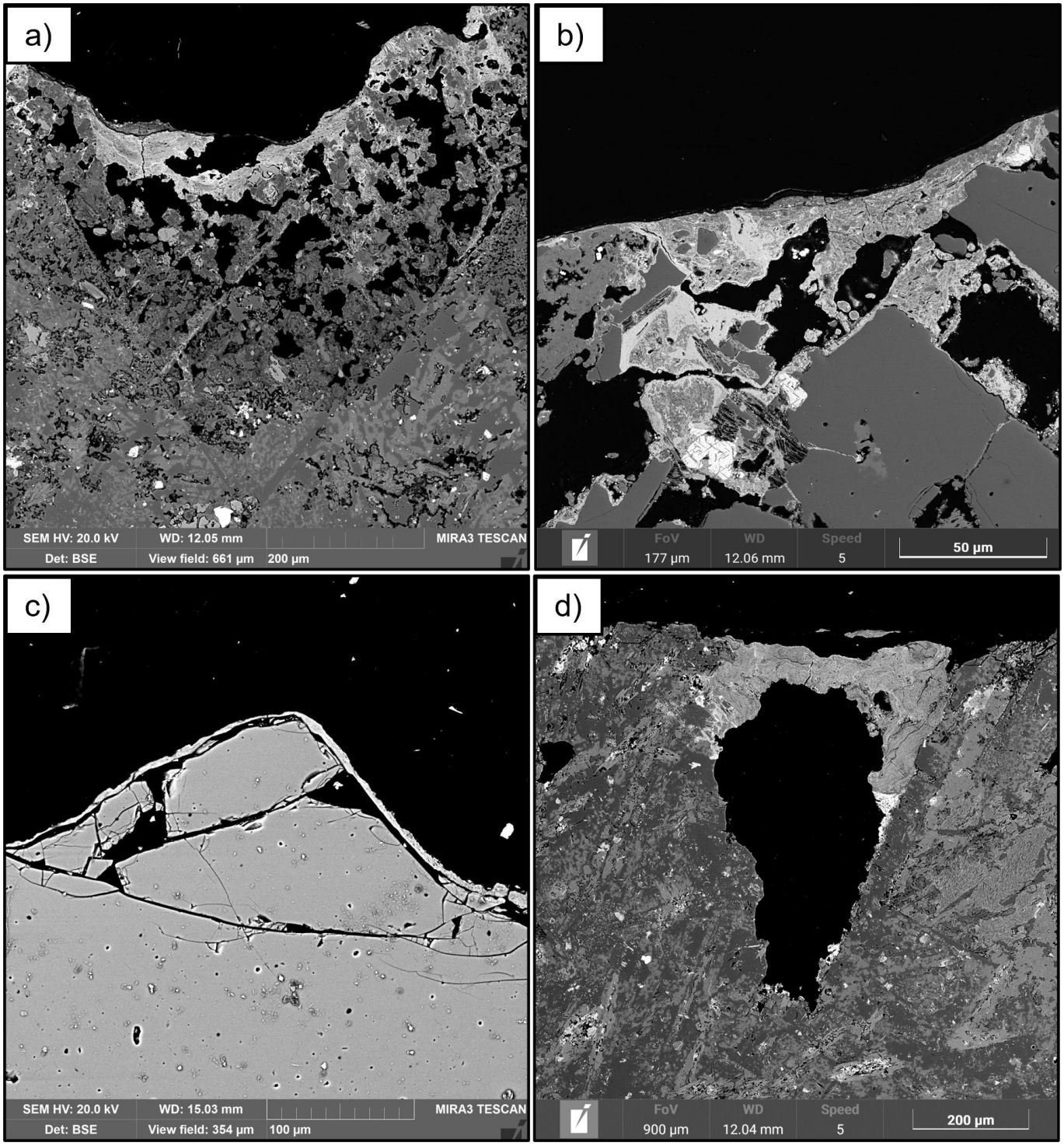

Figure 4.2-80: SEM-BSE images showing areas where patina overlies highly porous weathered rind substrate. As porosity increases, the area of patina:weathered rind contact decreases and the probability of flaking increases. Note the grain-scale features and complex void–mineral interfaces that support mineral dissolution rather than void formation by mechanical preparation.

4.2.10 Thermodynamic modelling

4.2.10.1 Objectives

The objectives of the thermodynamic modelling, taken from the Monitoring Studies Data Collection and Analysis plan are to:

1. Determine the mineralogy for these systems at thermodynamic equilibrium using thermodynamic calculations, and use best practice approaches to estimate the timescales of change, based on measured reaction rates, reaction mechanisms, and the results of other component studies (organic, microbiome, field observations, weathering experiments).
2. Compare the expected and observed mineralogy for sites with different exposure to anthropogenic emissions to (a) obtain proof-of-concept for the thermodynamic calculations; (b) investigate the presence of statistically significant differences among the sites and relate these to industry emissions.

4.2.10.2 Introduction

Equilibrium thermodynamic models use thermodynamic data for minerals, solutes, liquid, and gas phases to predict the characteristics of user-defined systems. Forward models, such as those applied here, predict solute concentrations and speciation, the amounts of minerals and their tendency to precipitate or dissolve in an aqueous solution, at equilibrium, for specified pressures, temperatures, and system compositions. A range of software packages have been developed to perform thermodynamic models, and different packages target different types of systems. At Murujuga, gas, aqueous, and mineral phases interact at relatively low temperatures and atmospheric pressures. Such systems are commonly modelled using the software (Parkhurst and Appelo, 2013), a computer program for simulating chemical reactions and transport processes in natural or polluted water, in laboratory experiments, or in industrial processes. has evolved from precursor programs dating back to the 1980s (Parkhurst et al., 1980), and has been used to simulate processes that include, but are not limited to, ore deposition, hydrogen storage, acid mine drainage and municipal waste-water treatment (Koehn et al., 2022; Masindi et al., 2022; Saeed and Jadhawar, 2024; Mothetha et al., 2023).

The software can be used to model complex ion exchange and kinetically rate limited reactions, amongst other advanced features, but here it is applied in a relatively simple way to derive an understanding of the first-order controls on the stability of minerals within the patina, weathered rind, and fresher rocks at Murujuga. The models applied are based on the assumption of thermodynamic equilibrium, which is seldom achieved in surface settings. In addition, not all of the minerals have been identified in all of the materials, particularly in the patina, and thus any modelling is necessarily a simplification because we cannot predict the stability of minerals we haven't identified. Therefore, the results provide a framework that aids understanding of the patina–weathered rind–fresher rock systems, but they cannot be applied directly to Murujuga because thermodynamic equilibrium is not achieved in these natural systems, and where, instead, biotic and abiotic processes, including catalysis control the rate and reaction pathways that would, on some timescale, lead to equilibrium. In addition, the models simulate systems that are closed to most components, so gains and losses of elements are not simulated quantitatively.

However, it is possible to discuss the consequences of interaction between atmosphere-equilibrated aqueous solutions with patina, weathered rind, and fresher rock, for the end-member case of thermodynamic equilibrium. The results of this work can then be compared to observations of the natural systems at Murujuga to recognise non-equilibrium features and their implications.

4.2.10.3 Methods

Thermodynamic modelling was performed using the software (phreeqc-3.5.0-14000) (Parkhurst and Appelo, 2013), with the Lawrence Livermore National Laboratory llnl.dat database that is distributed with the package. This software was used to simulate interaction between water equilibrated with CO_2 and other atmospheric contaminants with minerals identified within the patina, weathered rind, and fresher rock. In the calculations, equilibration can be envisaged as a one-step process, where a volume of water is added to a volume of rock. In reality, the instantaneous water:rock ratio based on precipitation and interacting rock volumes is likely to be lower than in the simulations, but, so long as no minerals are exhausted, the consequences of equilibrium in the modelled and real systems are likely to be comparable, although the extent to which equilibrium is achieved in the real system is not well known. Issues related to non-equilibrium are discussed below, and these calculations provide guidelines only. The poorly known hydrodynamics of these systems, including instantaneous and time-integrated fluid:rock ratios, limit the value of more complex models.

The modelled mineral assemblage of the patina, weathered rind, and fresher rock were based on the TIMA and XRD results (Table *4.2-2* to *4.2-6*). Mineral modes were taken from the averages provided by the TIMA results. However, variations in mineral modes amongst samples do not affect the results because no mineral is exhausted by the single step of equilibration used in the calculation.

Minor and trace elements, including Ti, P, U, Pb, Zn, and Ni, are hosted by phases such as uraninite, sphalerite, willemite, indialite, a high temperature cordierite polymorph, and senegalite, an aluminium phosphate. These elements and their hosting phases are excluded from the calculations presented here. The concentrations of the trace elements that they host is low in Murujuga rocks and, consequently, the minerals that host these phases are present in such small amounts that they are unable to impose significant controls on the local geochemical environment. Minerals and modes used for calculations are summarised in Table *4.2-10*.

4.2.10.4 Approach

Two sets of calculations were performed. Each set of calculations involved multiple simulations, where the term “simulation” describes a calculation of the consequences of chemical reaction between a fluid and a solid. The thermodynamic data used for the simulations are derived, to a large extent, from laboratory experiments, but the simulations are theoretical and do not represent physical experiments on the material at Murujuga.

In the first set of simulations, atmospheric gases CO_2, NO_2, and SO_2 were first equilibrated with pure water to simulate precipitation at Murujuga. Precipitation includes rain, dew, and mist. Preliminary calculations produced low *pH* values of 1 to 2 for NO_2 partial pressures comparable to those measured at Murujuga ($\log_{10}$ NO_2 c.-8.27), which is attributed to the well-documented incomplete and dynamic equilibration between atmospheric gases (Krissansen-Totton et al., 2018).

To compensate, NO_2, and SO_2 values were adjusted to provide *pH* values of 3.5 to 5 to simulate the formation of acid rain. However, we note that the atmosphere at Murujuga is dust-rich and this, and ocean aerosols may increase *pH* (Section 7.10). For these reasons, the decreases in *pH* calculated here are likely to be larger than those observed in the field.

Then, the solutions formed by equilibration between atmospheric gases and pure water were equilibrated with patina minerals, and the effect of increasing NO_2, SO_2, and NO_2 at fixed SO_2 concentration on solute concentrations, mineral dissolution amounts, and the relative stabilities of Fe- and Mn-oxides and clay minerals were compared (Figure *4.2-81*(a)).

In a second set of simulations, pure water was equilibrated with CO_2 at atmospheric levels, a fixed concentration of SO_2, and four different NO_2 concentrations to simulate precipitation at Murujuga. Gas concentrations were selected using the results of the first set of simulations, after adjustments to compensate for limited equilibration amongst atmosphere gases, and amongst the atmospheric gases and precipitation. The results were used to investigate the effect of increasing NO_2 concentration on solute concentrations, mineral dissolution, and the stability of key minerals (Figure *4.2-81*(b)).

Simulation set 1: Atmosphere-equilibrated rainwater–patina interactions

One litre of water was equilibrated with approximately 2 kilograms of patina, which was assumed to consist of hematite, birnessite, kaolinite, illite, and Mg-montmorillonite. Patina on all rock types was assumed to be identical for the purposes of the model, based on EMP data (Appendix Tables *B-1* to *B-16*). Other minerals were identified by XRD. Some of these minerals do not form under surface conditions and are observed within the fresher rock or weathered rind (e.g. chlorite, clinozoisite, and stilpnomelane). They do not form part of the patina so they were not included in model patina. The selected minerals were identified in a wide range of samples and provide plausible hosts for the major elements of interest (Fe, Mn, Al, K, Si, Mg). Other kaolinite polymorphs were identified, including dickite and nacrite. However, the kaolinite polymorphs have very similar XRD patterns and thermodynamic properties, so they are all considered to be represented by kaolinite in the calculations. Similarly, Fe- and Mn-oxides other than hematite and birnessite were identified, but hematite (Fe_2O_3) and birnessite ($Mn_8O_{14} \cdot 5\,(H_2O)$ are the most common, so they were assumed to be present and the relative stability of a range of other Fe- and Mn-oxides (e.g. magnetite, goethite, $Fe(OH)_2$, hausmannite (Mn_2O_3), bixbyite (Mn_2O_3), and $MNO_2(\gamma)$ was investigated via the calculations.

Simulation 1A: CO_2 equilibrated water plus Fe-bearing patina minerals without NO_2

For comparative purposes, and to provide a baseline, pure water at 30°C was equilibrated with CO_2 at atmospheric concentrations ($\log_{10}$ pCO_2 = -3.5), and this solution was equilibrated with illite, kaolinite, Mg-montmorillonite, hematite, and birnessite. These results are shown on Figures *4.2-82* to *4.2-84* where the y-value is equal to zero.

Simulation 1B: CO_2 and NO_2 equilibrated water plus Fe- and Mn-bearing patina minerals

Pure water at 30°C was equilibrated with CO_2 at atmospheric concentrations ($\log_{10}$ pCO_2 = -3.5), and $\log_{10}$ NO_2 gas partial pressures (equal to fugacity at 1 bar and for an ideal gas) of -12.8, -13.8, and -14.8. These values are considerably lower than measured concentrations of atmospheric NO_2 at Murujuga ($\log_{10}$ NO_2 = -8.27). However, unrealistically low *pH* values of 1 to 2 were calculated for

higher NO_2 partial pressures. These low values were attributed to the well-documented incomplete equilibration between atmospheric gases. The gas-equilibrated solution was then equilibrated with illite, kaolinite, hematite, birnessite, and Mg-montmorillonite, as in simulation 1A. These results are shown on Figures *4.2-82* to *4.2-84* in blue but are mostly overlain by the purple lines relating to simulation 1C.

Simulation 1C: CO_2 and SO_2-equilibrated water plus Fe- and Mn-bearing patina minerals

Pure water at 30°C was equilibrated with CO_2 at atmospheric concentrations ($\log_{10}$ pCO_2 = -3.5), and $\log_{10}$ SO_2 gas partial pressures (equal to fugacity at 1 bar and for an ideal gas) of -12.8, -13.8, and -14.8. These values are considerably lower than the measured partial pressure of atmospheric SO_2 at Murujuga. However, low *pH* values of 1 to 2 were calculated for higher SO_2 partial pressures. As for NO_2, the low values were attributed to the well-documented incomplete equilibration between atmospheric gases (Krissansen-Totton et al., 2018). The gas-equilibrated solution was then equilibrated with illite, kaolinite, hematite, birnessite, and Mg-montmorillonite, as in simulation 1A. These results are shown on Figures *4.2-82* to *4.2-84* in green.

Simulation 1D: CO_2, NO_2- and SO_2-equilibrated water plus Fe- and Mn-bearing patina minerals

Pure water at 30°C was equilibrated with CO_2 at atmospheric concentrations ($\log_{10}$ pCO_2 = -3.5), and $\log_{10}$ NO_2 gas partial pressures (equal to fugacity at 1 bar and for an ideal gas) of -12.8, -13.8, and -14.8, and the SO_2 content of the solution was set to 1×10^{-5} moles kg^{-1}. The gas-equilibrated solution was then equilibrated with patina that comprises illite, kaolinite, hematite, birnessite, and Mg-montmorillonite, as in simulation 1A. These results are shown on Figures *4.2-82* to *4.2-84* in purple.

Simulation set 2: Atmosphere- and/or patina-equilibrated rainwater interactions with weathered rind and fresher rock

Pure water at 30°C was equilibrated with CO_2 at atmospheric concentrations ($\log_{10}$ pCO_2 = -3.5), and $\log_{10}$ NO_2 gas partial pressures (equal to fugacity at 1 bar and for an ideal gas) of -12.8, -13.8, and -14.8, and the SO_2 content of the solution was set to 1×10^{-6} moles kg^{-1}. The gas-equilibrated solution was equilibrated either patina comprising illite, kaolinite, hematite, birnessite, and Mg-montmorillonite, as in simulation 1A, followed by equilibration with weathered rind or fresher rock, or with weathered rind or fresher rock directly (Figure *4.2-81*(b), Table *4.2-10*).

Table 4.2-10: Selected mineral phases and modes for the thermodynamic calculations. Assemblages are based on the XRD and TIMA results. Granophyre mineral modes are based on the minerals featured in Figure 4.2-12. Gabbro mineral modes are based the minerals featured in Figure 4.2-22.

Patina estimated mineral mode	**moles**		
Hematite	3.33		
Birnessite	3.33		
Illite	1.43		
Kaolinite	1.43		
Mg-montmorillonite	0.48		
Granophyre weathered rind	**moles**	**Granophyre fresher rock**	**moles**
Quartz	43.96	Quartz	43.96
Albite	32.97	Albite	32.97
K-Feldspar	16.48	K-Feldspar	16.48
Illite	1.10	Clinochlore	2.20
Clinochlore	2.20	Clinozoisite	1.10
Clinozoisite	1.10		
Hematite	1.10		
Kaolinite	1.10		
Gabbro weathered rind	**moles**	**Gabbro fresher rock**	**moles**
Anorthite	16.85	Anorthite	16.85
Albite	28.09	Albite	28.09
Diopside	19.10	Diopside	19.10
Quartz	12.36	Quartz	12.36
Clinochlore	11.24	Clinochlore	11.24
Epidote	5.62	Epidote	5.62
Illite	3.37		
Hematite	1.12		
Kaolinite	1.12		
Mg-montmorillonite	1.12		

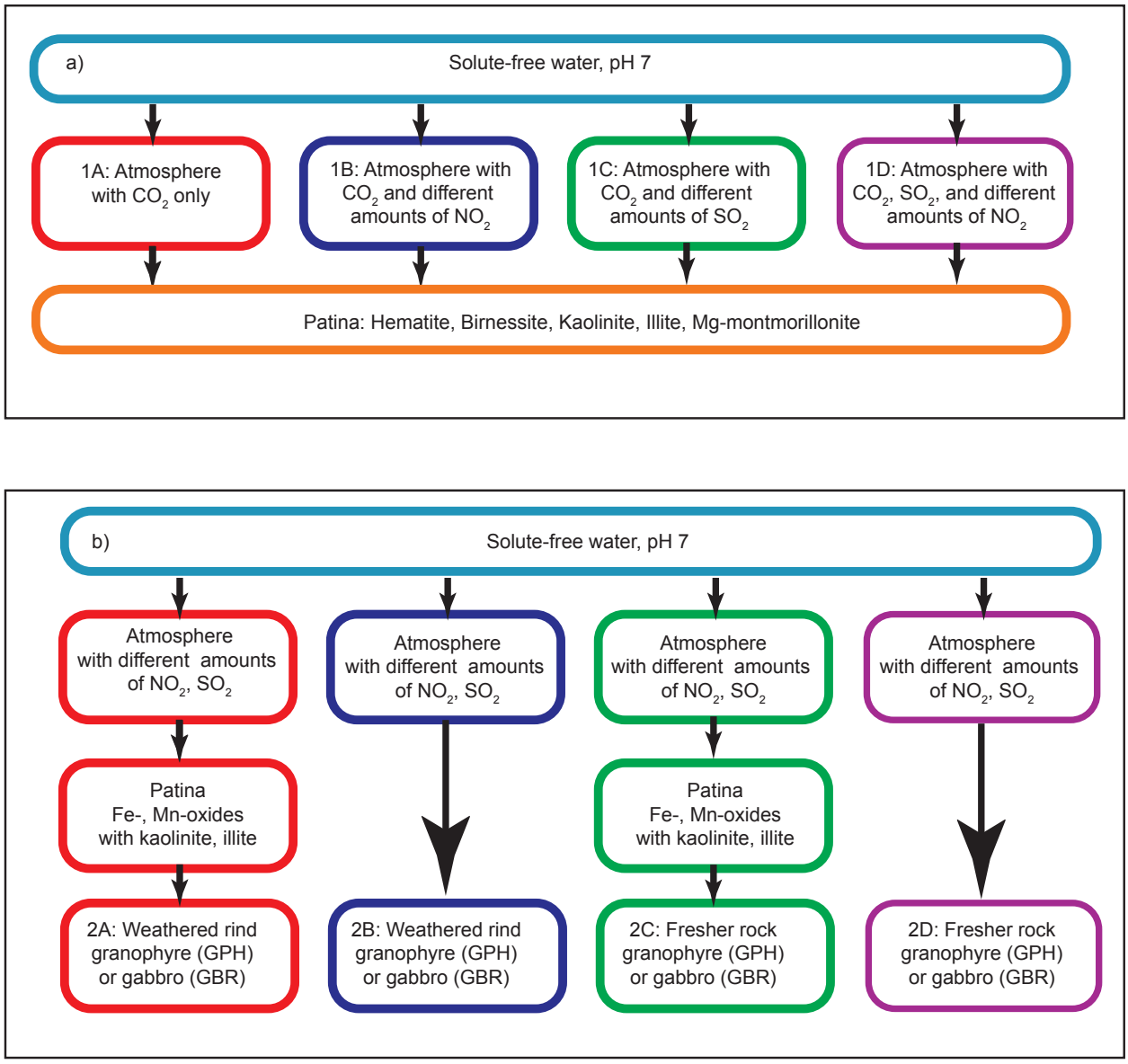

Figure 4.2-81: Schematic illustration of the thermodynamic models presented here. (a) Equilibration of patina with atmosphere-equilibrated solutions (simulation set one). (b) Equilibration of weathered rind and fresher rock with atmosphere- and patina-equilibrated solutions (simulation set 2). Colours match the colours of the lines for the relevant simulations on Figs. 4.2-82–4.2-87.

Preliminary scoping simulations were performed to compare systems where the aqueous phase within the patina, weathered rind, and fresher rock was equilibrated with atmospheric CO_2 (referred to as CO_2-buffered), and those where the the aqueous phase within the patina, weathered rind, and fresher rock was not equilibrated with atmospheric CO_2 (referred to as CO_2-unbuffered). Quartz and K-feldspar within the weathered rind and fresher rock did not dissolve in the CO_2-buffered calculations but did dissolve, in some cases, in the CO_2-unbuffered calculations. Observations of rocks from Murujuga reveal dissolution of quartz and K-feldspar, so the aqueous phase within the patina, weathered rind, and fresher rock was CO_2-unbuffered in the following calculations.

The differences between granophyre and granite, and amongst gabbro, dolerite, and basalt, relate mostly to texture, which was not a variable parameter in the simulations, so granophyre was used to represent granophyre and granite, and gabbro was used to represent gabbro, dolerite, and basalt. Four scenarios were explored (Figure *4.2-81*(b)):

- Simulation 2A (S2A): Solutions equilibrated with atmospheric CO_2, an SO_2 content of 1×10^{-6} moles kg^{-1}, and low, medium, and high concentrations of NO_2, were equilibrated first with patina and then with weathered rind of either gabbro or granophyre. The results of these simulations are shown in red (Figures *4.2-85*, *4.2-86*, *4.2-87*).
- Simulation 2B (S2B): Solutions equilibrated with atmospheric CO_2, an SO_2 content of 1×10^{-6} moles kg^{-1}, and low, medium, and high concentrations of NO_2 were equilibrated with the weathered rind of either gabbro or granophyre. The results of these simulations are shown in blue (Figures *4.2-85*, *4.2-86*, *4.2-87*).
- Simulation 2C (S2C): Solutions equilibrated with atmospheric CO_2, an NO_2 content of 1×10^{-6} moles kg^{-1}, and low, medium, and high concentrations of SO_2 were equilibrated first with patina and then with fresher rock of either gabbro or granophyre. The results of these simulations are shown in green (Figures *4.2-85*, *4.2-86*, *4.2-87*).
- Simulation 2D (S2D): Solutions equilibrated with atmospheric CO_2, an SO_2 content of 1×10^{-6} moles kg^{-1}, and low, medium, and high concentrations of NO_2, were equilibrated with fresher rock of either gabbro or granophyre. The results of these simulations are shown in purple (Figures *4.2-85*, *4.2-86*, *4.2-87*).

Most rocks in the field show a patina above weathered rind and correspond most closely to results of the first simulation within the second set of simulations (red lines on the graphs in Figures *4.2-85*, *4.2-86*, *4.2-87*). However, it may be relevant that no Fe- or Mn-oxides were identified by XRD on samples from high exposure sites AQ09 and AQ11, and in these cases the patina-free simulations 2B and 2D may provide a more realistic guide.

4.2.10.5 Results

Full results and input files are available on request from the Department of Water and Environmental Regulation. Here, we present and discuss *pH*, *pe*, which measures the oxidising or reducing potential of the system, the total solute concentrations for selected elements, the amount of dissolution and precipitation and saturation indices for selected minerals. *pe* is the negative log of the electron activity, and is a linear function of *Eh* at constant temperature (Table *1.4-1*). The total solute concentrations are the sum of the concentrations, in moles per kg of water, of all dissolved species that include the selected element. So, for example, the total concentration of N^{+5}

includes NO_3^-, HNO_3, $MnNO_3^+$, and $FeNO_3^{+2}$. The amount of dissolution (negative) or precipitation (positive) reflects the number of moles of the mineral that dissolve or precipitate when the specified amount of minerals comes into contact with the specified mass of solution, and because these are equilibrium calculations, the amount dissolved depends on the amount of water, but not on the total amount of the mineral phase. The saturation index (SI) represents the thermodynamic driving force for a mineral to precipitate or dissolve. A value of zero indicates that the mineral is in equilibrium with the solution, and typically shows that the mineral has been specified as part of the equilibrium assemblage. A value of greater than zero indicates that the mineral would precipitate from the model system if thermodynamic equilibrium was attained, and a value less than zero indicates that the mineral would dissolve within the model system at thermodynamic equilibrium.

Simulation 1 – Different gas-equilibrated solutions plus patina

In most cases, the NO_2 and NO_2 + SO_2 simulations performed almost identically and are grouped together as 'NO_2 addition' here unless otherwise specified.

pH

The CO_2-equilibrated solution has a calculated *pH* of around 5.6, consistent with that for CO_2-equilibrated water calculated and observed by other methods. The gas-equilibrated solution has a calculated *pH* of around 3.2, 3.9, and 4.5 for $\log_{10}$ NO_2 gas partial pressures of -12.8, -13.8, and -14.8, respectively, and similar values are calculated for the SO_2 and SO_2 plus NO_2-equilibrated solutions. The addition of NO_2 and SO_2 caused a decrease in the *pH* of the atmosphere-equilibrated solution to values of 3.5 to 4.5 for the highest to lowest partial pressures of NO_2 and SO_2, respectively.

Addition of the atmosphere-equilibrated solutions to the patina led to an increase in *pH* to values of above 9 for solutions where NO_2 and SO_2 are absent (Figure *4.2-82*(a)). Increasing NO_2 and SO_2 concentrations are associated with a decrease in *pH* to values of 8–9. Addition of NO_2 affects *pH* more strongly than SO_2.

pe

Addition of NO_2 is associated with an increase in *pe*, while the addition of SO_2 leads to a decrease in calculated *pe* (Figure *4.2-82*(b)). However, in all cases, the dominant Fe, Mn, and S valence states in solution are Fe^{+3}, Mn^{+2}, C^{+4}, and S^{+6}, so all solutions can be considered relatively oxidising.

Solute concentrations

The addition of SO_2 and NO_2 leads to a small decrease ($\sim$30% relative) in the total concentration of Fe^{+3} in solution and a large increase in the concentration of Mn^{+2} of seven orders of magnitude for SO_2 addition, and a smaller increase of two orders of magnitude for NO_2 and SO_2 and NO_2 addition (Figure *4.2-82*(c,d)). The addition of SO_2 and NO_2 also led to increases in K and Si concentrations by a factor of two to three (Figure *4.2-82*(e,f)); larger increases are linked to addition of NO_2, and are attributed to the dissolution of K- and Si-bearing minerals (see below).

Changes in mineral abundance

Mineral abundances are commonly referred to mineral modes, which may be measured by volume, mass, or moles of a mineral per unit volume or mass of rock. Here, the mode is measured in moles per kg of rock. Equilibration of the atmosphere-equilibrated solution causes an increase in

the mode of kaolinite and a decrease in the mode of illite (Figure *4.2-83*(a,b)). Increases in the concentration of SO_2 and NO_2 increase the magnitude of this coupled dissolution and precipitation process by factors of two and 13, respectively. The addition of atmosphere-equilibrated solution to the patina also drives dissolution of hematite in small amounts of around 1×10^{-13} moles of the 3.33 moles present, and dissolution of a higher, but still small, proportion of birnessite (1×10^{-11} to 8×10^{-5} moles of 3.33 moles) (Figure *4.2-83*(c,d). Addition of SO_2 and NO_2 increases the amount of hematite dissolution by a factor of around 20% for the SO_2-bearing solutions, and by a smaller amount for the NO_2-bearing solutions. In contrast, while addition of SO_2 increases birnessite dissolution, addition of NO_2 has a negligible effect (Figure *4.2-83*(c,d)).

Stability of Fe- and Mn-bearing phases

Hematite is the most stable of the Fe-oxides for all simulations (Figure *4.2-84*(a–c)), followed by goethite, magnetite, and $Fe(OH)_2$, which all have negative saturation indices (SI) when hematite is specified as part of the equilibrium assemblage (SI set to zero). The relative stability of all the magnetite and $Fe(OH)_2$ declines with increasing NO_2 concentration, but increases with increasing SO_2 concentration; the reason for this is discussed below. The stability of goethite relative to that of hematite remains unchanged with changes in SO_2 and NO_2 concentration, consistent with similar controls on the stability of this phase and hematite.

Birnessite is the most stable Mn-bearing mineral in solutions where NO_2 and SO_2 are absent. With increasing SO_2, lower oxidation state Mn minerals hausmannite and bixbyite are stabilised relative to birnessite, whereas increasing NO_2, in theory, stabilises $MNO_2(\gamma)$. Birnessite has a Mn-oxidation state of +3.5, hausmannite +2.67, and bixbyite +3. However, $MNO_2(\gamma)$ is exceedingly rare in nature and restricted to hydrothermal systems with temperatures far exceeding those encountered during weathering at Murujuga, so kinetic effects are expected to prevent its formation in natural systems under surface conditions.

Stability of silicate phases

A number of silicate minerals are predicted to be over-saturated in the patina-equilibrated solution, including chlorite, chrysotile, potassium feldspar, a potassium mica, and talc. Many minerals are under-saturated ($SI < 0$), such as gibbsite, which implies that if these minerals were present then they would dissolve, if not kinetically prevented from doing so.

Simulation 2: Atmosphere- and/or patina-equilibrated rainwater interactions with weathered rind and fresher rock

pH

The *pH* of patina- or atmosphere-equilibrated solutions after addition to fresher rock or weathered rind ranges from 8.2 (granophyre, no patina, fresher rock) to 11 (patinated gabbro) (Figure *4.2-85*(a,e)). The addition of NO_2 leads to a decrease in *pH* that ranges from negligible (gabbro, patinated) to approximately one *pH* unit (granophyre, patinated or unpatinated fresher rock), but the *pH* is never lower than 7.1 (granophyre, no patina, fresher rock). The *pH* of granophyre substrates is generally lower than that within the gabbro.

Solutes: sodium, potassium, silicon

The addition of NO_2 increases the Na concentration in the aqueous solution that coexists with the patinated weathered rind of granophyre by a factor of about 3, and of the unpatinated weathered rind by less than 10% relative. In contrast, the addition of NO_2 decreases the Na concentration in the aqueous solution that coexists with patinated and unpatinated fresher rock in the gabbro and granophyre by up to an order of magnitude (Figure *4.2-85*(b,f)).

The addition of NO_2 increases the K concentration of the aqueous solution in most of the granophyre simulations, with the strongest effect, of two orders of magnitude, calculated for the aqueous solution that coexists with the patinated fresher granophyre. The K concentration of the aqueous solution that coexists with the gabbro was unaffected for all but the patinated fresher gabbro simulation, where the K concentration of the aqueous solution that coexists with patinated fresher gabbro increased by two orders of magnitude (Figure *4.2-85*(c,g)).

The addition of NO_2 increases the Si concentration of the aqueous solution that coexists with the granophyre for all but the patina + weathered rind simulation (S2A) by 40–50% relative; the strongest increase was observed for the unpatinated fresher rock simulation. The addition of NO_2 had little or no effect on the Si concentration of the aqueous solution that coexists with the gabbro weathered rind, but the Si concentration of the aqueous solution within the patinated or unpatinated fresher rock (S2C,D) increased by 50% to 80% relative (Figure *4.2-85*(d,h)).

Changes in mineral abundance

Albite dissolution was predicted for all simulations and lithologies (Figure *4.2-86*(a,e)), although dissolution within the gabbro is a factor of around eight less than in the granophyre. Albite dissolution within the weathered rind of the granophyre increases with increasing NO_2, but decreases slightly within the fresher rock. Similar trends are observed for the gabbro, although the magnitude of the change is much smaller, of the order of a few percent relative. For albite, as for other minerals, changes in solubility do not derive directly from reaction between NO_2 or SO_2 and the mineral. Instead, NO_2 or SO_2 affect the *pH* and solubility is a function of *pH*.

In contrast, K-feldpar dissolution is predicted to be minor or negligible for the granophyre, and decreases with increasing NO_2 (Figure *4.2-86*(c)). Diopside dissolution within the gabbro is also predicted to be 0 for the weathered rind, and relatively minor for the fresher rock, at less than 1.5 $\times$ 10^{-5} moles out of the 19 moles present within the modelled assemblage. The largest amount of diopside dissolution is predicted for the unpatinated fresher rock, and increases strongly with increasing NO_2 concentration (Figure *4.2-86*(d)). Anorthite dissolution is predicted for all gabbro simulations, with values or around 1 $\times$ 10^{-4} moles out of the 17 moles present for the weathered rind simulations (S2A,B), and two orders of magnitude less for the fresher rock simulations (S2C,D) (Figure *4.2-86*(g)). Anorthite dissolution increases with increasing NO_2 by around 10% relative for the weathered rind simulations and decreases by a similar amount for the fresher rock simulations (Figure *4.2-86*(g)).

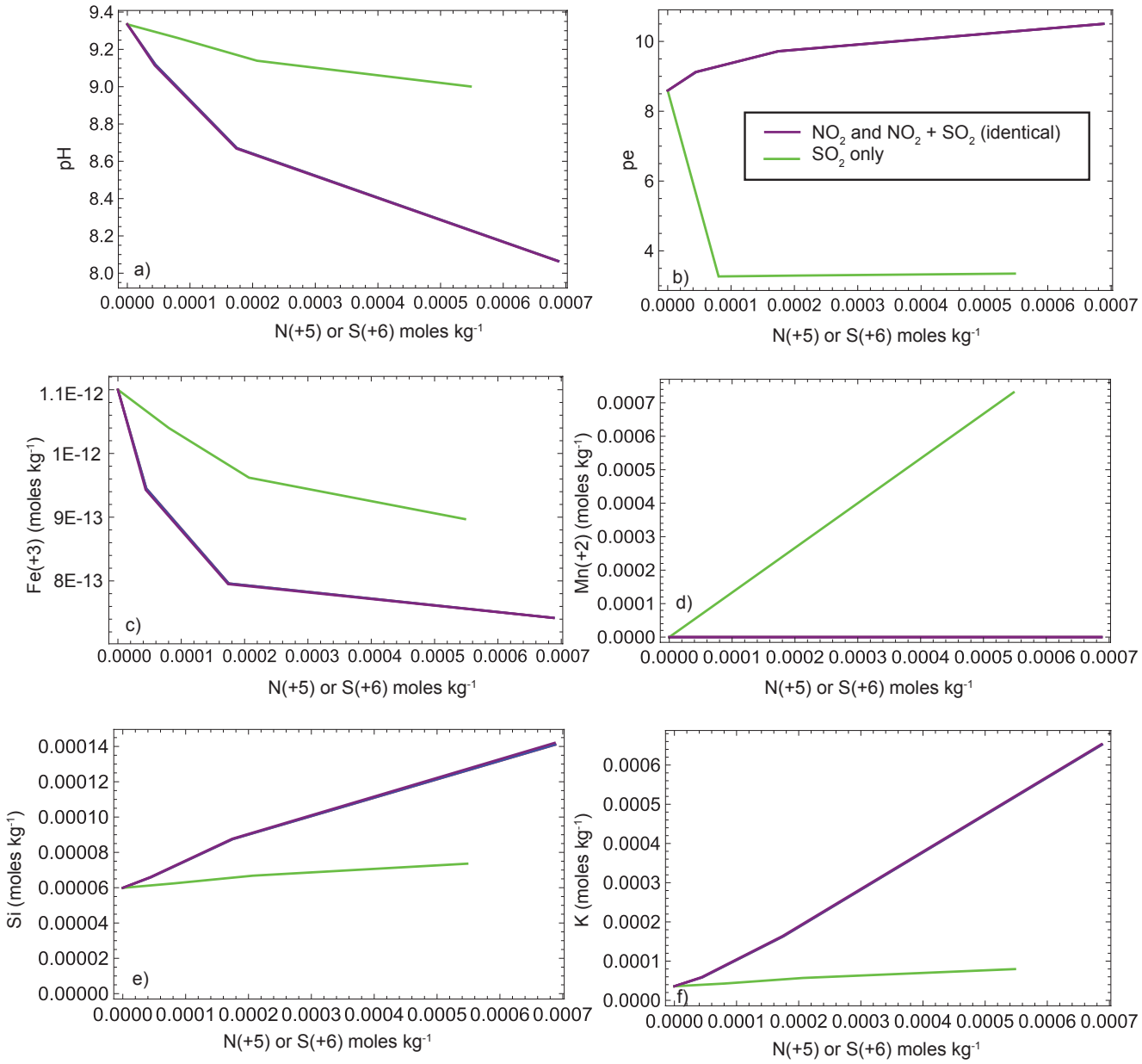

Figure 4.2-82: Selected total solute concentrations for simulation set one as a function of NO_2 or SO_2 concentration. (a) pH; (b) pe; (c) Fe^{3+}; (d) Mn^{+2}; (e) Si; (f) K. Concentrations are in moles per kg of water.

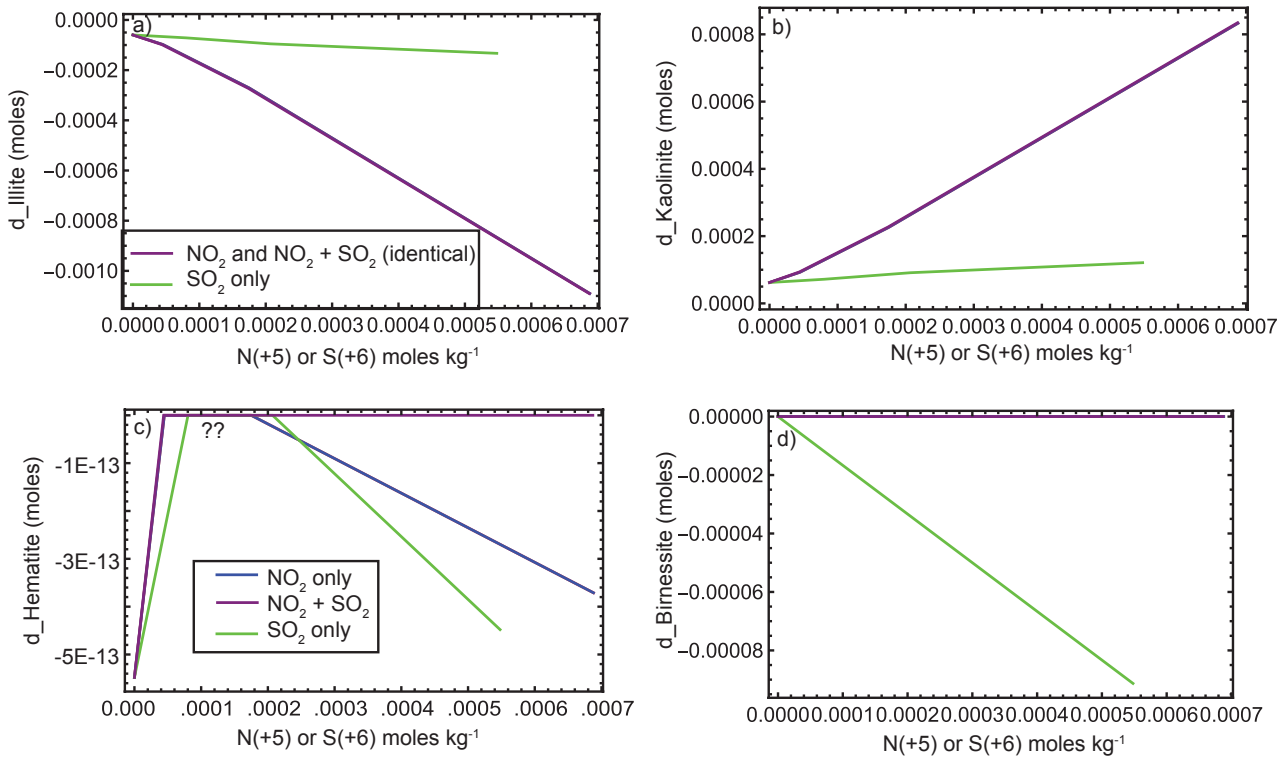

Figure 4.2-83: Selected changes in mineral modes for simulation set one as a function of NO_2 or SO_2 concentration. (a) illite; (b) kaolinite; (c) hematite; (d) birnessite.

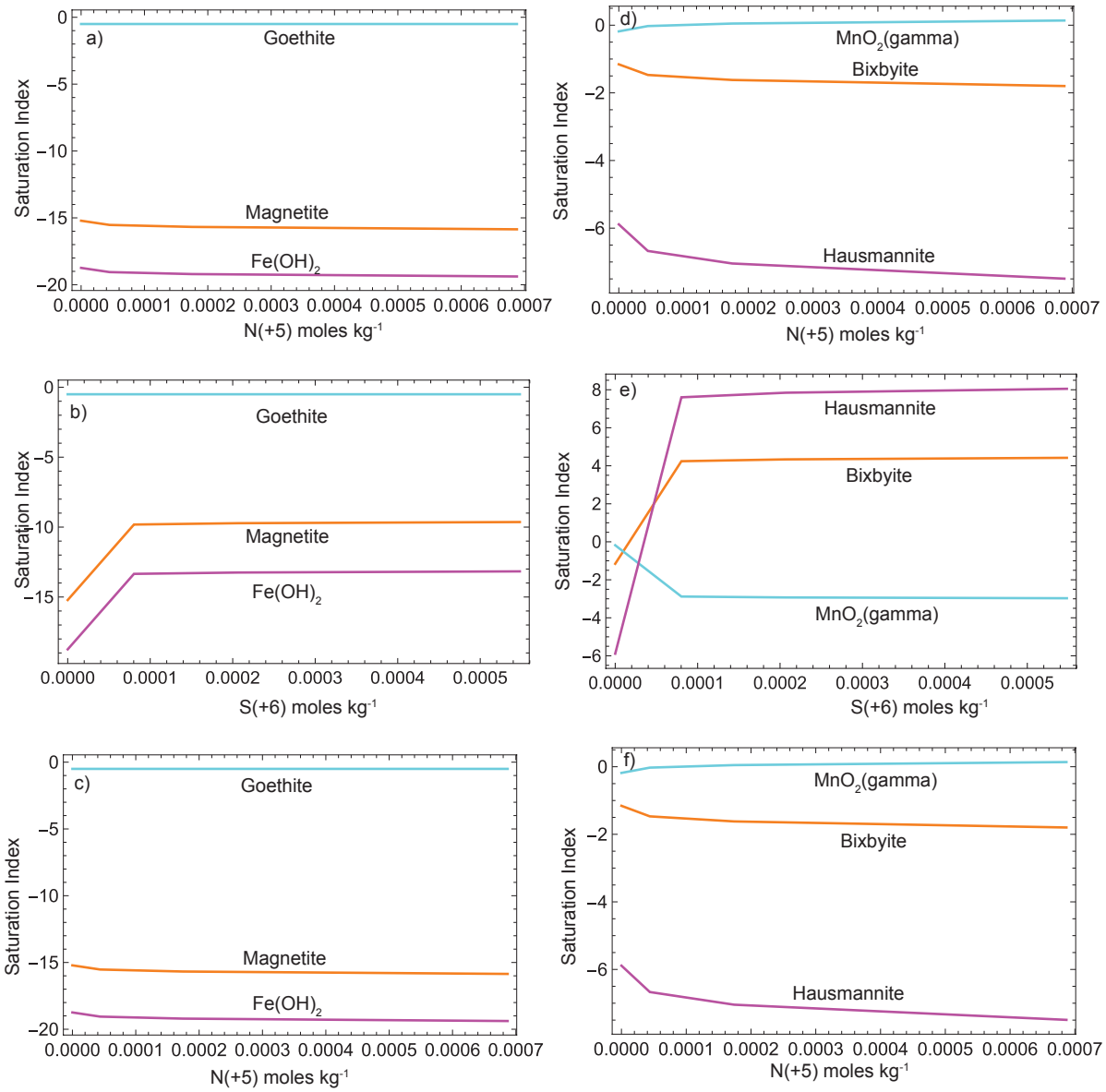

Figure 4.2-84: Selected saturation indices for simulation set one as a function of NO_2 or SO_2 concentration. (a) Fe-oxides in NO_2-bearing solutions; (b) Fe-oxides in SO_2-bearing solutions; (c) Fe-oxides in NO_2- and SO_2-bearing solutions; (d) Mn-oxides in NO_2-bearing solutions; (e) Mn-oxides in SO_2-bearing solutions; (f) Mn-oxides in NO_2- and SO_2-bearing solutions.

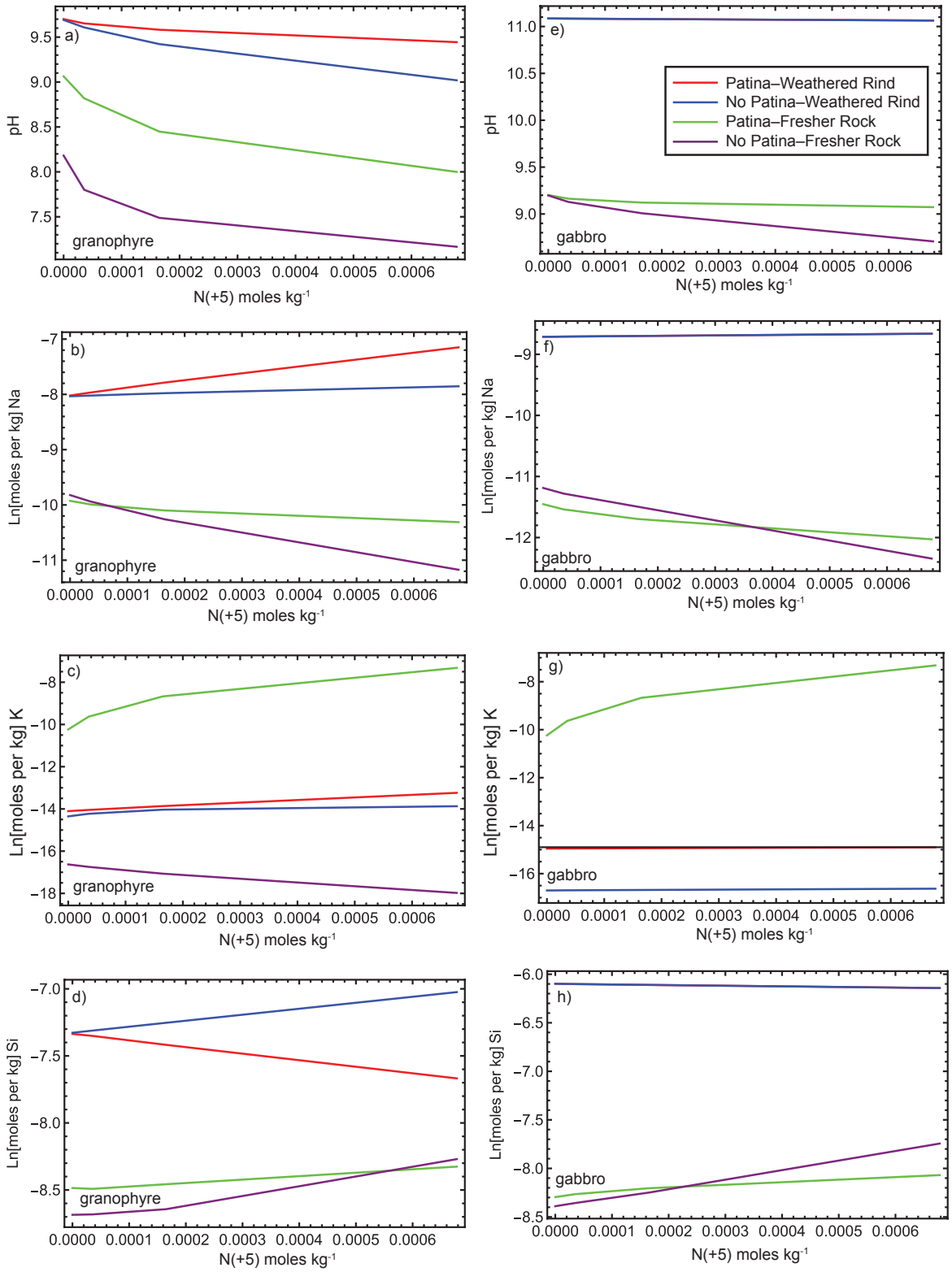

Figure 4.2-85: Selected total solution concentrations for simulation set 2 as a function of NO_2 concentration for patinated and unpatinated weathered rind and fresher rock. (a) pH, granophyre; (b) Na, granophyre; (c) K, granophyre; (d) Si, granophyre; (e) pH, gabbro; (f) Na, gabbro; (g) K, gabbro; (h) Si, gabbro. Concentrations on the y-axis are presented as natural logs for panels b–h. N^{+5} refers to the total concentration of species that include N with a valence of +5.

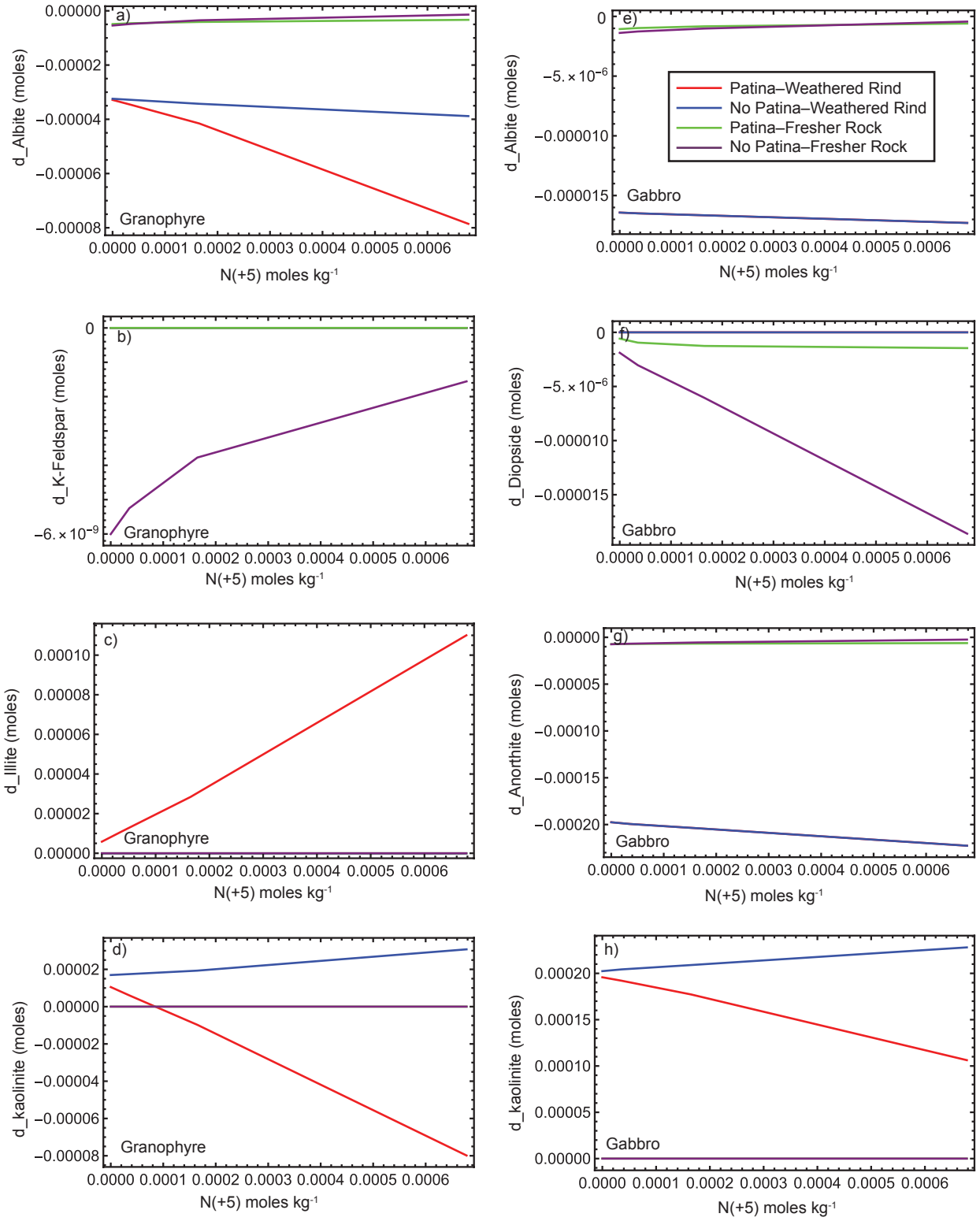

Figure 4.2-86: Selected changes in mineral modes for simulation set 2 as a function of NO_2 concentration for patinated and unpatinated weathered rind and fresher rock. (a) albite, granophyre; (b) K-feldspar, granophyre; (c) illite, granopyhre; (d) kaolinite, granophyre; (e) albite, gabbro; (f) diopsite, gabbro; (g) anorthite, gabbro; (h) kaolinite, gabbro.

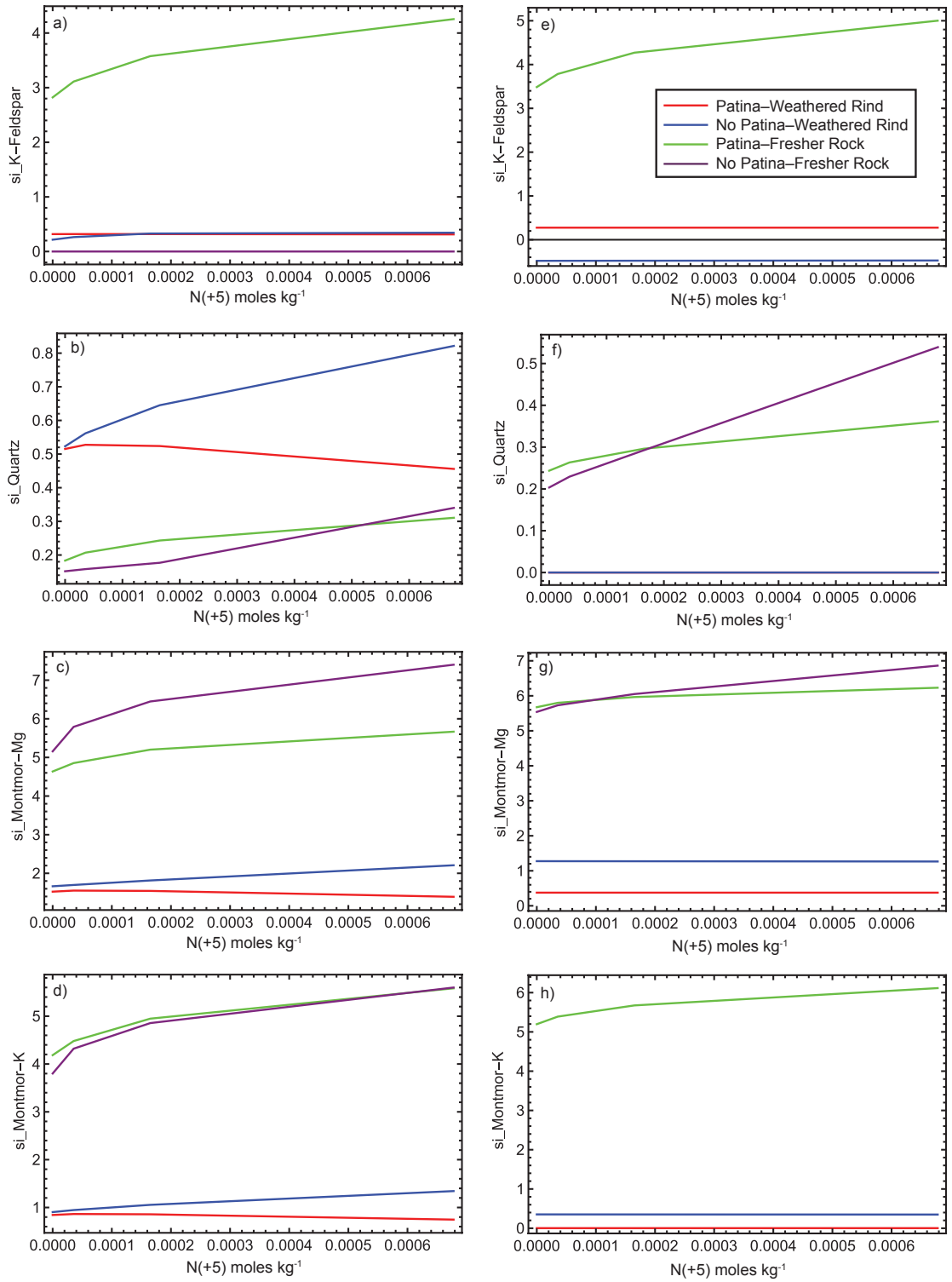

Figure 4.2-87: Selected mineral saturation indices for simulation set 2 as a function of NO_2 concentration for patinated and unpatinated weathered rind and fresher rock. (a) K-feldspar, granophyre; (b) quartz, granophyre; (c) Mg-montmorillonite, granophyre; (d) K-montmorillonite, granophyre; (a) K-feldspar, gabbro; (b) quartz, gabbro; (c) Mg-montmorillonite, gabbro; (d) K-montmorillonite, gabbro.

In the granophyre, kaolinite modes increase with increasing NO_2 for the unpatinated simulation (Scenario 2B) and decrease with increasing NO_2 for the patinated weathered rind (Figure *4.2-86*(d)). The change in kaolinite mode is positive for patinated and unpatinated gabbro weathered rind simulations (Figure *4.2-86*(h)), but the magnitude of the change increases with increasing NO_2 for the unpatinated weathered rind and decreases with increasing NO_2 for the patinated gabbro weathered rind. The decrease in kaolinite mode for the patinated granophyre weathered rind is coupled with an increase in illite mode (Figure *4.2-86*(c)); this trend is opposite to that noted for the patina (see simulation 1 above, and discussion below). Kaolinite is not a component of the fresher rock so there are no changes to its mode for the patinated or unpatinated fresher rock (Figure *4.2-86*(d,h)).

Mineral stability

Potassium-feldspar is predicted to be stable in all simulations except the unpatinated weathered gabbro (Figure *4.2-87* (a,e)), and the saturation index is higher for the patinated simulations than for the unpatinated simulations. Quartz is also predicted to be stable in all but the unpatinated fresher gabbro. The saturation index of quartz is higher in the unpatinated simulations than in the patinated simulations (Figure *4.2-87*(b,f)). Magnesian- and K-bearing montmorillonites are calculated to be supersaturated in all simulations ($SI > 0$) (Figure *4.2-87*(c,d,g,h)); the highest saturation indices are calculated for the patinated and unpatinated fresher rocks. The saturation indices for most of these minerals increases with increasing NO_2 with the exception of quartz in the patinated granophyre weathered rind (Figure *4.2-87*(b)).

4.2.10.6 Discussion

The results of the thermodynamic modelling provide some insights into patina–water–weathered rind–fresher rock systems at Murujuga.

First order processes

Clay minerals control *pH* in the patina

Calculated *pH* values for the patina, weathered rind, and fresher rock at thermodynamic equilibrium with infiltrating fluid are all relatively high and range from 8 to 11. These high values are attributed to reactions amongst the clay minerals. Conversion of illite to kaolinite involves exchange of protons from solution for K derived from illite, so that the number of protons in the solution decreases and the number of K^+ ions increases. Consumption of protons reduces their activity and increases *pH*. Other reactions amongst minerals, or between minerals and aqueous solution, may lead to release of cations. For example, alteration of diopside to form Mg-montmorillonite and dissolved Ca and Mg, increases *pH*. This scenario differs strongly from those proposed by a range of authors who propose that conditions on the rock surface and substrate are controlled by equilibration of Fe- and Mn-oxides with water (e.g. Black et al., 2017a). In reality, the extent to which the clay minerals buffer *pH* depends on the extent of thermodynamic equilibrium (see below).

Addition of NO_2 and SO_2 affect redox-sensitive elements differently

Addition of NO_2 and SO_2 has different effects on *pe* and the stability of Fe- and Mn-oxides (Figure *4.2-87*). The difference is attributed to the different dominant valence states of N, which is dominated by N^{+5}-bearing species in solution, and S, which is dominated by S^{+6}-bearing species in

solution. Oxidation of S^{+4} in SO_2 to S^{+6} in solution requires an electron acceptor for two electrons. In contrast, oxidation of N^{+4} in NO_2 to N^{+5} in NO_3^- and other N^{+5}-bearing species requires an electron acceptor for only one electron. This difference is consistent with the lower *pe* and the stability of Mn-bearing phases with lower average valences in the SO_2-bearing simulations (S1). This observation raises the possibility that Fe- and Mn-oxide phases provide a proxy for changes in the chemistry of the infiltrating solution. However, in reality, the value of such a proxy depends on the extent of thermodynamic equilibrium (see below).

Addition of NO_2 and SO_2 affects different minerals differently

The wide range of trends predicted for different elements in the different simulations of interaction of atmosphere-equilibrated solutions with patina, weathered rind, and fresher rock highlight the complex interactions amongst solution species, primary, and secondary minerals. The results also highlight the sensitivity of the models to the restricted set of relatively simple input parameters provided here. However, a few consistent trends are worthy of mention.

The NO_2- and SO_2-equilibrated solutions that interact with patina generally have higher K and Si concentrations and lower *pH* than NO_2- and SO_2-free solutions, indicating that clay minerals may break down more quickly in the presence of elevated industrial emissions. These minerals buffer the *pH* to high values that minimise dissolution of Fe- and Mn-oxides. However, if clay minerals dissolve more quickly than they are deposited then the patina thickness is likely to decrease. In addition, the ratio of clay minerals to Fe- and Mn-oxides in the patina may provide a proxy for the formation or attrition of patina.

With addition of NO_2 and SO_2 to the infiltrating solutions albite, anorthite, and diopside are predicted to dissolve from the weathered rind and fresher rock of the gabbro. These predictions are consistent with the observed dissolution of augite and labradorite from the Murujuga gabbros. Albite and diopside are considered to be proxies for labradorite and augite for the purposes of the modelling (e.g. Figure *4.2-18*). Quartz is predicted to be stable by the simulations. This prediction is consistent with widespread retention of quartz within the weathered rind of the granophyre. However, K-feldspar is predicted to be stable, but the rocks show widespread K-feldspar dissolution. This contradiction is discussed further below.

Adding a time dimension

The relative rates of patina formation and patina loss, the hydrodynamics and geometry of patina–precipitation interaction, and kinetic limitations and microbiome effects on mineral dissolution rates have not been constrained or are not well known for the Murujuga systems. Here, hydrodynamics refers to the rate of fluid infiltration processes. The geometry of patina–precipitation interaction refers to the area and shape of pores within the patina that are wetted by infiltrated fluids. However, better constraints on these parameters are necessary if we are to add a time dimension to predictions of these dynamic systems. For example, the calculations predict that interaction of 100 cm^3 of liquid water with around 2 kg of patina-covered weathered rind leads to the loss of around 1×10^{-5} moles of albite, if thermodynamic equilibrium is achieved. These values can be scaled to consider interaction of 100 cm^3 of fluid with 5 g of patina, which represents infiltration of one third of the yearly precipitation into 2 cm of weathered rind. The scaled calculations indicate that, each year, 2.5×10^{-8} moles of the 0.0825 moles of albite present in that weathered rind might dissolve if thermodynamic equilibrium is achieved. This dissolution rate is a maximum because it assumes

equilibrium; kinetic rate limitations would decrease the amount dissolved. Under these conditions, it would take 3.3 million years to dissolve all of the albite within the 2 cm thick weathered rind. However, long before complete albite dissolution, removal of a smaller amount of albite might physically destabilise the weathered rind by increasing the porosity to the extent that the patina flakes off. At thermodynamic equilibrium, the rates of dissolution of patina and weathered-rind stabilising minerals are predicted to increase by factors of two or more in response to increasing atmospheric NO_2 and SO_2. It is not known these changes also apply in the real systems, where thermodynamic equilibrium is not achieved. However, if there is a significant increase then this may constitute a significant impact.

Assessment of the impact of mineral dissolution is further complicated by limitations of our observations. To constrain the rate of patina loss or gain, we must consider the gross rate of patina formation, which refers to the rate of patina formation in the absence of any physical or chemical patina-removing processes as well as the rate of patina loss. Consideration of a hypothetical example can be used to illustrate the importance of knowing rates of patina formation as well as rates of patina loss. If the gross rate of patina formation in an emission-unaffected scenario is 20 μm per year, and the net rate is 2 μm per year, then emission-unaffected patina loss is equivalent to 18 μm per year. Under these circumstances, doubling of the rate of patina-stabilising clay mineral dissolution would lead to the loss of 16 μm of patina per year. If, in contrast, the gross rate of formation is 25 μm per year and the net rate is 20 μm per year, then nominal rate of patina loss is 5 μm per year and a tripling of the patina dissolution rate would lead to a reduced, but still positive, patina growth rate of 10 μm per year. To properly assess the longevity of the rock art at Murujuga, it is essential that research focuses on the rates of patina addition, as well as removal.

Caveats

Approach to equilibrium

The calculations presented here are based on chemical equilibrium between the modelled mineral, gas, and aqueous phases. However, conditions at the Earth's surface are not conducive to stable equilibrium. Low pressures and temperatures at the Earth's surface ensure that chemical reactions generally proceed slowly. Therefore, surface environments are characterised by disequilibrium. Indeed, there is abundant evidence of non-equilibrium at Murujuga. This evidence includes the stability of multiple Fe- and Mn-oxide phases, the absence of silicate phases predicted as stable, and the well-documented disequilibrium within Earth's atmosphere. In addition, the microbiome commonly modifies local environments so that variables such as *pe* and *pH* may vary on length-scales as small as a few micrometres. Through these parameters, and the formation of organic acids, the microbiome may impact the composition of the fluid interacting with the patina and rock surfaces, and the availability of various elements. The results of research into the microbiome at Murujuga are presented in Section 4.3. Under these circumstances, the calculations presented here provide only a guide to the direction that reactions may proceed in, and the state that systems may evolve towards. Detailed observations of those systems are required to establish the extent to which thermodynamic equilibrium is approached or achieved for equilibria deemed significant. Such observations will strengthen the conclusions presented here. Significant equilibria include *pH*-buffering clay mineral equilibria with aqueous solutions, Fe- and Mn-oxide dissolution in the patina, and feldspar dissolution within the weathered rind and fresher rock.

Approach to equilibrium: measured versus predicted *pH*

The calculated *pH* values of 8–11 are much higher than the *pH* observed on the rock surface of all rock types by the electrochemical field monitoring. This is partly attributed to incomplete equilibration amongst the patina minerals and the water added to the rock surface over the relatively short time of 2 minutes during the *pH* measurement. Indeed, other workers note that equilibration amongst rocks and solutions occurs over multiple hours to days, rather than minutes (Aho and Weaver, 2006). However, *pH* values above eight are seldom observed in natural or experimental systems for these rock types. Therefore, it is likely that one or more processes that modify *pH*, such as precipitation of secondary minerals or atmospheric interactions, have not been included in the model.

Many of the field measurements of *pH* are close to 5.6. This value is expected for pure water that has equilibrated with atmospheric CO_2, so the primary signal recorded by the field measurements may be that of equilibration between atmospheric CO_2 and the deionised water used for the field measurements. Some field measurements of *pH* are higher than 5.6. There are a number of possible explanations for these higher values. These include partial equilibration with clay minerals within the patina and dissolution of readily soluble surface deposits that produce high *pH* solutions, such as marine salt, soot, or ammonia.

As stated above, water placed on the rock surface for the field measurements is not expected to equilibrate with clay minerals on the time scale of the measurement. However, precipitation may interact with clay minerals that form dust within the atmosphere, where longer timescales are available for water–dust reactions. Indeed, the *pH* of rainwater at Murujuga is relatively high (7–8.5) (Figure *7.10-25*). These high values may indicate partial equilibration with clay minerals, although other explanations, such as interaction with ocean aerosols, cannot be excluded.

If pure deionised water is used for the *pH* measurements then the solutions are effectively unbuffered to pH change. Under these circumstances, the dissolution of tiny quantities of sea salt or other precipitates on the rock surface can cause a relatively large change in the pH. For this reason, and to stabilise *pH* measurements, an ionic strength adjuster was used in field measurements from campaign 5 onwards.

Mineral assemblages

XRD may not have identified all of the minerals present in the rocks because fine-grained and/or amorphous minerals do not produce good XRD peaks. Nevertheless, regardless of the precise identity of the minerals, alteration of silicate minerals, including clay minerals, is likely to be capable of buffering *pH* if fluids interact with rocks for long enough. Similarly, the Fe- and Mn-oxides may not have been identified precisely, but all of the Fe-oxides and Mn-oxides show comparable trends in dissolution and stability in response to changing NO_2 and SO_2 concentrations, so trends, if not absolute values, are likely to be robust if thermodynamic equilibrium is approached. A number of silicate minerals are predicted to be stable, but are not observed (e.g. chrysotile). It is highly likely that kinetic limitations on nucleation prevent precipitation of these, and other, minerals, at Murujuga.

Potassium-feldspar stability

Potassium feldspar (K-feldspar) is predicted to be stable in all of the granophyre simulations except for interaction of unpatinated rock, without a weathered rind, with the atmosphere-equilibrated solution (Figure *4.2-86*(c)). This prediction contrasts with the abundant evidence of dissolution of feldspar within the fresher rock and weathered rind in the Murujuga rocks (e.g. Figure *4.2-7*). Four possible explanations for this apparent contradiction are discussed here:

1. Water may not equilibrate fully with the weathered rind or patina as it infiltrates these layers before contacting the fresher rock. In this case, simulation 2D may represent the reactions that occur even though patina and weathered rind are present in the field.
2. The feldspar that dissolves to form porosity may be albite rather than K-feldspar. Albite replaces K-feldspar as part of the transition from the original fresh rock to hydrothermally altered fresher rocker via greenschist facies metamorphism. Albite dissolves in simulations 2A, B, C, and D (Figure *4.2-86*(a)).
3. The illite to kaolinite reaction, which releases the K that stabilises K-feldspar, does not proceed to equilibrium. In this case, K concentrations in solution in the natural fluid–rock system are lower than predicted. These lower K concentrations might destabilise K-feldspar in the natural systems at Murujuga.

   Ideally, it would be possible to test this hypothesis by a comparison between predicted K concentrations and K concentrations observed in the chamber studies. If the chamber studies rocks reach equilibrium with the atmosphere and aqueous solutions, then the concentrations should be comparable. However, predicted K concentrations in the unpatinated fresh gabbro and granophyre simulations (Simulation 2D) are of the order of 1×10^{-8} moles per litre. These values are below the detection limit of the Inductively Coupled Plasma–Atomic Emission Spectroscopy (ICP–AES) technique used for analysis of the chamber studies product solutions (around 1×10^{-6} moles per litre). Many of the K concentrations measured for the chamber studies experiments are also below the detection limit of the analytical technique, so while the results are broadly consistent with the predictions, they cannot be compared in detail.
4. The calculations have omitted a first-order process or solute that would lead to K-feldspar dissolution. For example, in simulation set 2, quartz and K-feldspar did not dissolve in CO_2-buffered simulations, but did dissolve, in some cases, in the unbuffered simulation. The concentration and speciation of C in the patina and weathered rind may be affected by the microbiome but those processes are not well known or understood and were not included in the calculations. These unconsidered processes may have occurred in the past, under different climatic or temperature conditions, or may occur now, in the present. Further work is necessary to distinguish between these possibilities, and will occur as part of the planned project extension.

Suggestions for further work

Minor and trace element-bearing minerals as proxies

Minor and trace elements such as P, Ti, Pb, Zn, and S may not exert a major control on geochemical environment (e.g. *pH*, redox), but minerals that host these elements may be stable under different conditions. Therefore, the stability of these minerals may provide a useful and practical monitor of

the geochemical environment. Further work is necessary to investigate potential minerals that may be useful for monitoring.

Consequences of evaporation

The calculations simulate the consequences of the addition of water to a patina–weathered rind–fresher rock system. Many minerals are predicted to dissolve, and equilibrium amongst these minerals, and between minerals and the solution, controls *pH* and the release of elements such as Na. As water evaporates within the patina and substrate, solutes become more concentrated and minerals may precipitate. The formation of sub-surface patina provides excellent evidence of element mobilisation by this process (e.g. Figure *4.2-51*), and some of the minerals that we observe may have formed by this process). Further work is necessary to understand the consequences of evaporation and transport within the patina.

Role of the microbiome

Ideally, it would be possible to investigate the changes that the microbiome makes to it's environment. For example, the microbiome may catalyse reactions, or locally alter element concentrations by expelling molecular ions that may enter solution. Changes in fluid composition may enhance or reduce dissolution and precipitation of minerals in the patina and in the underlying weathered/fresher rock. However, such experiments are challenging and beyond the scope of the project at the current time.

Key findings

1. At thermodynamic equilibrium, *pH* in the patina is buffered to relatively high values by clay minerals. However, thermodynamic equilibrium is unlikely to be attained within natural systems at Murujuga.
2. Dissolution of Fe- and Mn-oxides in the patina at thermodynamic equilibrium is predicted to increase by factors of up to three in response to infiltration by NO_2- and SO_2-bearing solutions.
3. Dissolution of albite in the weathered rind at thermodynamic equilibrium is predicted to increase by factors of up to two in response to infiltration by NO_2- and SO_2-bearing solutions.
4. Fe- and Mn-oxide phases, and the ratio of Fe- and Mn-oxides to clay minerals in the patina may record interactions with NO_2- and SO_2-bearing solutions.
5. These calculations provide a framework that aids understanding of the patina-weathered rind-fresher rock systems. However, the results cannot be applied directly to Murujuga because thermodynamic equilibrium is not achieved in the natural systems. In addition, relative rates of patina formation and patina loss, the hydrodynamics and geometry of patina-precipitation interaction, and kinetic limitations and microbiome effects on mineral dissolution rates have not been constrained or are not well known for the Murujuga system. These constraints are necessary if we are to add a time dimension to predictions of these dynamic systems. Given these uncertainties, it is necessary to combine the findings of the inorganic geochemistry program with those of the chamber studies to meet the MRAMP targets.

4.3 Microbiome laboratory analysis

4.3.1 Objectives

From Section 1.6 of the MSDCA Plan (Curtin University, 2022), the objectives of the microbiome investigations are to:

1. Use advanced molecular biological approaches to characterise:
    a) Microbial community composition associated with rock patina and the underlying weathered rind. This answers the question “who is there?”
    b) Diversity and relative abundance of functional genes involved in microbial processes and pathways that may contribute to stabilising or bio-deteriorating (bio-weathering) the rock patina: This answers the question “what are they potentially doing”
    c) Which of these functional genes are expressed transcripts that can potentially be translated into functional proteins/enzymes that carry out these processes.
2. Use advanced bioinformatics tools to:
    a) Build metagenome assembled genomes (MAGs) from the shotgun metagenome dataset of objective 1b and map the functional gene transcripts from objective 1c to the MAGs. This will reveal all sequenced genes belonging to the same species that were expressed at the time of sampling.
    b) Determine the number of mutations that occurred post-mortem in the assembled metagenomic bins (from objective 2a) to distinguish between microbial taxa that have been preserved in the patina as ancient DNA vs. those that represent modern taxa represent. Since this DNA damage increases with time it may be possible to determine the order in which these taxa died.
    c) Estimate the growth rate of the patina associated microbial communities by measuring genome replication rates from shotgun metagenomic bins without the need for cultivation.

4.3.2 Methodology

Microbiome laboratory methodologies are described in Section 3.3.3 of the MSDCA Plan (Curtin University, 2022) and the component study methodology statement:

- COPP21065-PRO-G-112 Murujuga Rock Art Monitoring Program: Microbiome Laboratory Analysis.

Variations from planned methodology

18S rRNA amplicon sequencing has been excluded from the methodology. The rationale for excluding this is the redundancy/overlap of data generated from both ITS and 18S sequencing. These regions are both designed to identify eukaryotic organisms and the ITS amplicon sequencing gives superior taxonomic clarity to fungi and thus is the better candidate.

16S rRNA and ITS amplicon sequencing

DNA was extracted from all sample types (patina, soil and lichen) using the Zymogen DNA/RNA Miniprep kit and was quantified using the NanoDrop™ 3300 Fluorospectrometer. All sample details can be found in the supplementary documents. DNA samples were amplified using reverse transcription polymerase chain reaction (RT-PCR) with both the ITS (ITS1F: TCGTCGGCAGCGTCAGATGTGTATAAGAGACAGCTTGGTCATTTAGAGG AAGTAA, ITS1R: GTCTCGTGGGCTCGGAGATGTGTATAAGAGACAGGCTGCGTTCTTCATCGATGC) and 16S primers (16SV3V 4f-AGRF: TCGTCGGCAGCGTCAGATGTGTATAAGAGACAGCCTAYGGGRBGCASCAG, 16SV3V4r-A GRF: GTCTCGTGGGCTCGGAGATGTGTATAAGAGACAGGCTGCGTTCTTCATCGATGC). Amplification stopped when the amplification curves were ending in the exponential phase. The amplified products were sent to AGRF for indexing and sequencing using the MiSeq platform, generating paired-end 300 base pair reads.

Bioinformatic processing

Sequence quality was assessed using FastQC and MultiQC software on the sequences pre and post trimming (Appendix Figures *C.1-1*, *C.1-2*, *C.1-3* and *C.1-4*) (Ewels et al., 2016). DADA2 software was used to process the amplicon sequences; trimming, denoising, merging, chimera removal and taxonomic assignment (Callahan et al., 2016). Sequences were trimmed with the following constraints; maximum expected error of 2, 10 bases trimmed from the start of all reads, 20 bases trimmed from the end of the forward reads, 50 bases trimmed from the end of the reverse reads. Contaminant reads were removed both manually, by removing any amplicon sequence variants (**ASV**s) that were only present in blank samples, and by using the microDecon package (McKnight et al., 2019). Processed bacterial 16S rRNA reads were taxonomically classified using the SILVA non-redundant database version 138.1. The fungal ITS amplicons were taxonomically assigned using the UNITE database (released on the 29/11/2022). The bacterial and fungal datasets were rarefied to 11,000 and 10,000 sequences per sample, respectively (see Figures *C.1-5* and *C.2-5* in Appendix *C*). Alpha diversity measures were calculated using custom `R` scripts (see Appendix *C*). Non-metric dimensional scaling (NMDS) was performed on bray-curtis dissimilarity matrix generated using the `vegan` package (Dixon, 2003). Microbial abundance heatmaps were created using `ggplot2` (Wickham, 2016). Spearman correlation of the ASV tables to the chemical metadata was done using the `Hmisc` package and plotted using `pheatmap` (Harrell Jr, 2023; Kolde, 2019). Significance testing of the redundancy analysis (RDA) and non-metric multidimensional scaling (**NMDS**) analysis was performed using `anova` function in `R` (R Core Team, 2023).

4.3.3 Work to date

The status of work completed to date is summarised in Table *4.3-1*.

Section 7.8 details the analysis and interpretation of the microbiome in the patina, soil and lichen samples.

Table 4.3-1: Microbiome laboratory analysis work to date.

Analysis	Description	Status
DNA extractions	DNA extractions of all patina, soil and lichen samples from the sample rocks	Completed
RNA extractions	RNA extractions of all patina, soil and lichen samples from the sample rocks	Completed
16S PCR and sequencing of DNA	All DNA samples for PCR amplication of the 16S rRNA amplicon and sent to AGRF for microbial diversity sequencing	Completed
ITS PCR and sequencing of DNA	All DNA samples for PCR amplication of the ITS fungal amplicon and sent to AGRF for microbial diversity sequencing	Completed
Sampling from bacterial and fungal isolates	Sub-sampling 200 SAB and TSA plates for colonies that grew on respective plates innoculated from the sample rocks on site	Completed
PCR and amplicon submission to AGRF of the colony isolates	All samples from the colony plates to be amplified with 16S and ITS primers and sent to AGRF for sequencing to identify what microbes were grown from the sample rocks	In progress
DNA depletion and cDNA synthesis of RNA samples	All patina, soil and lichen RNA samples to be DNase treated and subsequently subject to cDNA synthesis	In progress
16S and ITS PCR and sequencing of cDNA samples	All cDNA samples to be amplified with 16S rRNA primers and ITS primers and sent to AGRF for sequencing to determine the microbial diversity of active microbes at time of sampling	Yet to start
DNA cleanup for metagenome sequencing	DNA samples that failed quality control for metagenome sequencing at AGRF to be concentrated and cleaned	In progress
Meta-transcriptome sequencing	RNA samples need to be submitted to AGRF for meta-transcriptomic sequencing	Yet to start

4.4 Chamber exposure (accelerated degradation) testing

4.4.1 Objectives

From Section 2.2.6 and 3.4 of the MSDCA Plan (Curtin University, 2022), the objective of the chamber exposure testing is to ensure that a dose-response relationship for (elevated) air pollutant concentrations can be established. It remains possible that the current level of anthropogenic emissions at Murujuga may not have a measurable impact on the rock art, or may have an effect below the level of measurement accuracy and precision inherent in field work. If that is the case, no field study of any size will result in a statistically significant outcome. For this reason, chamber studies are vital to give the project certainty in its ability to establish EQC levels. The chamber studies will consider as broad a range of parameters as possible, however will be focused on (a) physicochemical weathering of the rock and measurement of any by-products or results of such weathering and (b) exposure concentrations which may reduce the “health” or growth rates of the most abundant components of the microbiome. Noting that the studies in (b) will include analysis of abiotic products as in (a), in order to account for biotic/abiotic interactions.

4.4.2 Methodology

Information on the chamber exposure methodologies can be found in Section 3.4 of the MSDCA Plan (Curtin University, 2022). Whilst the aims of the experimental program remain the same, the methodology has been significantly revised in response to (1) the geochemistry findings (specifically porosity), and (2) the need for more controlled microbial experiments. The revised methods are detailed in the associated document:

- COPP21065-PRO-G-117 Murujuga Rock Art Monitoring Program: Chamber Exposure Studies.

The design of the experiments is based on observations of typical exposure scenarios at Murujuga. Namely that exposures are predominantly dry with intermittent/infrequent events of rainfall that are slightly alkaline, based on current measurements (refer to Section 7.10.5). Previous studies have focused on an acid (rain) deposition hypothesis, which no longer appears valid based on current observations. Rainfall of sufficient magnitude may be considered conceptually to flush or neutralise reactive air pollution deposition during the dry periods.

In brief, air pollutants in the chamber experiments are generated from hydrocarbon combustion or bottled gases. Rock cubes of fresher or patinated rock are placed in a randomised pattern in a heated incubator (exposure chamber) to replicate solar heating in the field. Likewise, a UV lamp is located inside the chamber to provide photocatalytic generation of secondary air pollutants.

For purely geochemical tests, exposures are conducted for a 6-day incubation period, with air pollution actively introduced at the commencement of the exposure on day one for one hour and then (if repeated) at 24 hour intervals for up to 6-days.

Rock cubes are rinsed in a defined quantity of ultra-pure water then given a “bath” in the same for 30 minutes both pre- and post-exposure. This conceptually replicates rainfall and allows any reaction/decomposition products that may leach into the ultra-pure water to be quantified and related to a dose.

Microbiome experiments have not yet commenced. These will replicate the above however in a smaller chamber in a biocontainment facility. In order to reduce the scope of the geomicrobial chamber studies, a decision has been made to utilise “labelled” cultures of the key species/genera found at Murujuga. This labelling process creates a genetically modified organism, requiring additional protocols. The time points (duration of exposure and overall experiment) for the geomicrobial tests will likely need to be adjusted.

4.4.3 Work to date

A comprehensive suite of abiotic geochemical weathering dose-response tests has been conducted using a blend of diesel and natural gas condensate. Selected tests using heavy fuel oil (**HFO**), a typical shipping fuel, have also been conducted, as have tests using gaseous NH_3.

Confocal microscopy analysis has been conducted on geomicrobiome samples which identified considerable autofluorescence and heterogeneity, hence the need for the more controlled labelled studies, such that precise pre- and post-exposure measurements can be conducted on the same microbes.

Analysis of the chamber studies results is discussed in Section 7.1.

5 Air quality monitoring network establishment and operation

5.1 Objectives

As described in Section 1.8 of the MSDCA Plan (Curtin University, 2022), the objectives of the air quality monitoring network are to deploy and maintain a range of air quality monitoring equipment at appropriate spatial locations such that the air quality across all of the Murujuga region can be determined.

5.2 Methodology

The AQM network includes both passive monitors (with low voltage solar power), and mains powered AQMs to provide accurate real-time monitoring data where existing power infrastructure was available. The passive AQMs are contained within a specifically designed cage, whereas the powered AQMs are built in (and on), modified 20’ (6.1 m) insulated shipping containers.

In order to meet all relevant National Code of Construction standards, the enclosures housing the equipment and relevant components were designed and/or certified according to AS4100; AS1170; AS3600; AS1554; AS1252; AS2923 and the relevant sections of AS3580.

The following documents provide further information on the methodologies relevant to AQM installation, deployment, and operation:

- COPP21065-PRO-G-102 Murujuga Rock Art Monitoring Program: Passive Air Quality Monitoring (AQM) Installation and Commissioning
- COPP21065-PRO-G-103 Murujuga Rock Art Monitoring Program: Passive Air Quality Monitoring (AQM) Sample Collection, Maintenance and Context Observations
- COPP21065-PRO-G-104 Murujuga Rock Art Monitoring Program: Powered Air Quality Monitor Installation and Commissioning
- COPP21065-SPE-G-100 Murujuga Rock Art Monitoring Program: Air Quality Monitoring Station Control Functional Specification.

5.3 Solar/passive sites

The AQMs have been designed to visually blend into the environment as far as possible, and thus were manufactured from weathering steel for installation sites near rock outcrops or finished with a sand-coloured paint (over galvanising) at sites in or near coastal dunes. AQMs installed in and around the Dampier Salt lease, were galvanised (without paint) to provide maximum protection against salt. These latter sites are on a mining lease with no public access so visual amenity considerations are reduced. Figure *5.3-1* shows a weathering steel AQM at the AQ14 site. AQM deployment has been undertaken using the lowest impact means possible for each of the sites.

The solar/passive sites have now been in operation for almost two years since first operational installation. Each of these stations consist of:

- a complete weather station,

- a suite of passive gas samplers,
- a three-bucket deposition sampler,
- a total (flask) deposition sampler,
- rock cube samplers,
- a set of ‘low power’ gas analysers,
- supporting power (solar) and communications infrastructure.

Weather station data and data from the ‘low power’ analysers are live-streamed to Perth for storage and analysis, and are available on a dashboard for viewing in real-time. AQM sites are visited approximately every four weeks for changeover of passive samplers, recovery of deposition samples, and inspection and maintenance.

Rock cube samplers have been deployed at all AQM locations (including existing Industry monitoring sites). These consist of five rock cubes (one of each rock type) that have freshly exposed and sterilised surfaces, to allow us to monitor the establishment of the microbiome on the rocks as well as pH and permeability. They were installed in November 2023 and will be sampled for the first time in October 2024.

5.4 Powered air quality monitoring sites

There are four mains-powered AQMs operating to provide real-time monitoring of NO, NO_2, NH_3, SO_2, O_3 and dust. Powered sites were installed at locations where there was existing power infrastructure. An example of such a site is shown in Figure *5.4-1*, which shows an installed and commissioned AQM. Three of these sites were installed and are operated by the MRAMP researchers, with the fourth being an existing Woodside monitoring station operated by ACOEM/Ecotech. This site (designated EX07) has additional MRAMP owned equipment installed to ensure the above suite of pollutants are all measured. EX07 has a real-time optical particle counter (Palas FIDAS 200), like the three stations operated by the MRAMP researchers, however it features different makes/models of gas analysers, chosen for ease of integration into the existing equipment onsite.

In addition to the species listed above the three MRAMP operated powered AQMs (AQ01, EX02, EX09) feature additional monitoring equipment. These stations include the same monitoring equipment installed at the passive AQMs:

- a complete weather station,
- a suite of passive gas samplers,
- a three-bucket deposition sampler,
- a total (flask) deposition sampler,
- rock cube samplers,
- a set of ‘low power’ gas analysers,
- communications infrastructure.

Figure 5.3-1: Passive AQM AQ14, showing contrast between weathering steel and patinated rock outcrops in the background.

A methane and non-methane hydrocarbon detector have also been installed with the suite of reference grade gas analysers. In addition, AQM EX09 has additional instrumentation, including an aethalometer (black carbon monitor), radon detector, Max-DOAS and an isotopic methane analyser (Picarro). The sites are routinely visited for maintenance, inspection and calibration purposes.

Figure 5.4-1: Powered AQM EX09, as installed on Mount Wongama.

All real-time instruments are internally networked to an onboard PC. This contains a suite of software to handle data logging and transfer as well as remote access to each of the instruments.

5.5 Environmental challenges for AQM equipment operations

Given the nature of the environment there has been the need for some repair and maintenance work to be conducted on the AQMs. Much of this was expected and planned for, with the AQMs located on islands particularly susceptible to corrosion and salt deposition/build-up.

- A small amount of wildlife damage has occurred, likely due to native rodents or birds. In all bar one case this impacted outer protective cable covers only with no loss of data.
- Salt/sea spray exposure required replacement of gate hinges and padlocks at AQ17, AQ18 and AQ10, however this was also partly due to the hinges being painted during manufacture.
- Some faults with system components have occurred with replacement of batteries required at a number of sites, repairs to bucket deposition samplers being required and replacement of faulty data-loggers and Raspberry Pi computers.

Overall, the performance of the AQMs has been reliable, with a schedule of planned maintenance being developed based on our experiences in the field. Most faults can be detected remotely

through diagnostic telemetry, which allows repairs/replacements to be planned and conducted as part of the regular sample changeovers. Occasional, temporary communications outages occur in the region, related to the 4G mobile network, however, the stations are able to automatically reconnect to the network and resume data transfer, once the network is back online. No data is lost as data is stored locally until successfully transmitted.

In summary, the design of the stations is reliable and fit for purpose. Minor revisions to the design have been incorporated to increase reliability and streamline maintenance and repair processes.

5.6 Monitoring equipment calibration and data visualisation

Since the Year One Report (Curtin University, 2023) we have deployed AS3580.10 total deposition samplers (4L flask + 150 mm diameter glass funnel) at all AQM locations operated by the research team. This is to aid in calibration and verification of our novel three bucket deposition sampler, as well as to provide results which are traceable to an Australian Standard.

This page is intentionally blank.

6 Spatial mapping and surface modelling

6.1 Objectives

It is important to understand how environmental and air quality parameters measured at the AQMs relate to the exposures at the rock (art) surfaces being studied. For all sites containing both air quality monitors and rock art or sample rocks included in the study design (i.e. all AQ and EX sites except for AQ01 and EX01), it was important to:

1. Map the topography of the sites, incorporating a region around each sample rock and rock art panel and the AQM location.

2. Triangulate and fill in the mapping between each of (1) and include any nearby features likely to be major air flow paths.

Following the field mapping, processed topographies are provided to the computational fluid dynamics (CFD) team to develop meso-scale models of airflow in the regions above the study targets. This will provide improved determination of pollutant exposures at the rock surface.

6.2 Spatial mapping

6.2.1 Scope of mapping

The sites captured for 3D modelling were AQ02-AQ18, the MAC office (AQA1), and EX02-09. Most of the data capture for these sites was based on an area approximately 250 m^2 around the air quality monitor, and the rock art and sample rocks included in the study square. In some cases, multiple study squares were joined together, and others had to have extended capture areas due to the terrain and spread of features. While most sites could be captured over a single flight campaign, some had to be split up over different campaigns due to the size, schedule of other field activities, or restrictions from local industries or controlled airspace.

To date, all determined sites have been flown and captured. Data captured from all these sites have been fully processed and uploaded to Nextcloud (the cloud-based storage and file sharing service used for the MRAMP data archive) including the GNSS control points, the raster images comprising of the ortho-mosaic and digital elevation model (DEM), and the 3D point cloud.

Conventions for all data capture and processing are:

- The horizontal coordinates are in Map Grid Australia 2020 (MGA2020) Zone 50.
- The vertical coordinates are in Australian Height Datum (AHD), using the AusGeoid2020 model to convert from ellipsoidal to AHD heights.

There are some additional sites and processing steps which remain to be completed. This includes the expansion of the capture around AQ13 and AQ18, capture of the MAC/DBCA cultural burn at Conzinc Bay in Murujuga National Park, capture of some additional sites on behalf of MAC or UWA, and the cleaning of some artefacts due to data captured over water (along the shoreline).

6.2.2 Methodology

For each site, the following process was observed:

- **Establishing a datum point**: A survey mark was established at or near the final location of the AQM installation. The GNSS observations for this point were logged for an extended epoch (ideally two hours or more) to allow for accurate coordinates to be determined through post-processing.
- **Establishing local control**: Temporary control points were placed through the area of capture and picked up with Real Time Kinematic – Global Navigation Satellite Systems (**RTK-GNSS**), in relation to a base station setup over the datum point. These temporary control points were in the form of UAV targets that could then be used to geo-reference and process the imagery captured by the drone flown at the site.
- **Drone flights**: Drone flights of the area were then conducted with sufficient overlap (nominally 75% or better) to ensure a good reconstruction, and at a height to provide an approximate ground sampling distance (GSD) of 20 mm. All flights were conducted after planning approval had been provided to ensure compliance with Civil Aviation Safety Authority (CASA) regulations, and the relevant stakeholders (MAC, local industries, airports, etc) had been engaged and approval gained.
- **Post-processing of control**: The final coordinates of the point were established using post-processing of the logged GNSS data with the AUSPOS service provided through Geoscience Australia. The local control was then adjusted to coincide with the final datum point coordinates, and any check measurements performed during the survey were used to validate the solution.
- **Post-processing of drone imagery**: The drone images and control points were then imported into a photogrammetric software (ContextCapture from Bentley Developer Network). The images were aligned to each other through the automatic generation and matching of tie points, and the UAV targets in the images were extracted and given known coordinates from the control. These UAV targets allowed the alignment and final adjustment to be georeferenced with respect to the ‘real-world’ location of the site.
- **Generation of the final products**: Once the adjustment and geo-reference was complete, a dense 3D point cloud was generated (using dense image matching), and the information was projected onto a 2D surface to produce a 2D ortho-mosaic and a DEM raster for the area.

The raw data, processing files, and the final data (coordinates and photogrammetric products) were then uploaded to Nextcloud. The specifics and variations for each of these steps are explained further in the following sections, and contained in the following document:

- COPP21065-PRO-G-105 Murujuga Rock Art Monitoring Program: Unmanned Aerial Vehicle and Spatial Mapping.

6.2.3 Global navigation satellite system (GNSS) datum point

For each site, a datum point was established with a well-known set of coordinates. This was so that all other control or surveyed points could be determined relative to this mark, and if revisits we required, this point could be used without the need to re-establish primary coordinates to the site. A physical mark (such as a short star iron picket) was placed adjacent to the site of the

AQM installation, or nearby in a suitable location. A GNSS receiver (Trimble R10 or R12LT) was then setup over the mark and data was observed for at least two hours (where possible) to be post-processed later by the online Geoscience Australia service AUSPOS.

AUSPOS uses reference stations around Australia to process baselines to the datum point and perform an adjustment to determine coordinates and their associated uncertainties to 95% confidence interval. The two hour observations allow for the determination of the coordinates to within 20 mm horizontal (MGA2020) and 200 mm vertical (AHD) or 80 mm (to ellipsoid height) at the 95% confidence interval. The final post-processed coordinates are presented in Table *6.2-1* for each site, along with the associated uncertainties. This table is an update of Table 6-1 in the Year One Report (Curtin University, 2023).

Where existing Standard Survey Marks (**SSM**s) were located nearby these were either used as the datum point for the site (EX02, EX06 and EX08), or a check shot from the datum point to the SSM was surveyed to compare results (EX03 and EX09). If an SSM was used as a datum point, a 2-hour observation was still performed and the AUSPOS coordinates compared to the results of the SSM coordinates posted by Landgate. Table *6.2-2* summarises the differences between the checks compared in this manner. This table is an update of Table 6-2 in the Year One Report (Curtin University, 2023).

6.2.4 Local RTK control survey

Spatial mapping for all AQM sites was undertaken in year one, however additional sites related to cultural/prescribed burns or additional sample collection were mapped in year two using the same method (Curtin University, 2023). The method is summarised again here.

To geo-reference the drone imagery and processing outputs, UAV targets were placed around the area to be captured and used as local control. Ideally these were placed around the limits of the area to be captured and several placed through the middle to help locate the extremities of the site, and to help get good elevation data through the middle and stop the final 3D model from flexing or distorting. This was not always possible due to time, terrain, or the size of the area to be captured, but this was performed where possible, and around the main features of interest.

These control points were then surveyed in use Real Time Kinematic (**RTK**) GNSS surveying using two Trimble R10/R12LT receivers and a TCS3/TCS5 handheld controller. A base station was set up over the datum point with “known” coordinates. A rover was then placed over the control point and used to measure the relative vector between the base station and the rover (applying corrections from the base to the rover). This vector was then applied to determine the coordinates of the control point. The uncertainties for these vectors could also be calculated (through the error corrections and propagation) and were checked to ensure errors were kept within a limit of 20 mm (95% confidence interval) horizontally and 30 mm (95% confidence interval) vertically where possible. In addition, the RTK system was set to record five RTK measurements to check for excess movement of the rover over the point, or large differences between the measurements. Measurements to nearby SSMs (if available) were also taken to check the final coordinates with their published known coordinates.

Table 6.2-1: Coordinates and uncertainties of the datum point for the AQ and EX sites. Note CI represents the confidence interval (in meters) and is applied to the uncertainty (standard error).

Site	Date	Occupation	Easting (m)	Northing (m)	Ellipsoid Ht (m) (h)	AHD Ht (m) (H)	E 95% CI	N 95% CI	h 95% CI	H 95% CI
AQ02	4/07/2022	1hr 59m 30s	459525.073	7711460.888	-0.318	7.007	0.013	0.016	0.051	0.213
AQ03	23/06/2022	2hr 51m 00s	464345.785	7710524.565	-3.316	3.972	0.023	0.014	0.055	0.201
AQ04	4/07/2022	2hr 01m 30s	461486.151	7712803.855	-3.996	3.267	0.017	0.015	0.063	0.212
AQ05	21/06/2022	2hr 03m 30s	464451.168	7711835.669	-1.699	5.555	0.019	0.02	0.062	0.204
AQ06	21/06/2022	1hr 49m 30s	465983.135	7712327.107	15.12	22.354	0.016	0.017	0.069	0.201
AQ07-08	28/06/2022	2hr 48m 30s	473091.259	7714348.639	69.754	76.938	0.014	0.013	0.045	0.17
AQ09	30/06/2022	3hr 50m 00s	475962.375	7714646.331	-1.204	5.978	0.015	0.015	0.052	0.174
AQ10	5/07/2022	2hr 03m 30s	446726.447	7720297.835	-1.104	6.082	0.017	0.017	0.061	0.224
AQ11	20/06/2022	2hr 59m 30s	474521.431	7719575.352	32.62	39.668	0.014	0.014	0.044	0.173
AQ12	7/07/2022	1hr 55m 30s	461821.556	7722410.904	10.734	17.612	0.103	0.029	0.132	0.248
AQ13	22/06/2022	2hr 37m 00s	481250.757	7729528.996	8.135	14.933	0.014	0.014	0.049	0.195
AQ14	22/06/2022	1hr 49m 00s	481506.856	7728404.126	16.957	23.778	0.016	0.019	0.071	0.199
AQ15	7/07/2022	2hr 47m 00s	485356.878	7731491.5	-1.852	4.927	0.013	0.012	0.039	0.197
AQ15	7/07/2022	0hr 59m 00s	485356.855	7731491.506	-1.956	4.823	0.135	0.05	0.19	0.271
AQ15	26/10/2022	2hr 13m 00s	485356.887	7731491.523	-1.819	4.96	0.021	0.015	0.056	0.201
AQ16	6/07/2022	1hr 59m 30s	485221.213	7732785.423	2.863	9.614	0.016	0.015	0.061	0.204
AQ17	29/06/2022	1hr 41m 00s	479290.308	7737300.864	8.263	14.916	0.024	0.02	0.093	0.221
AQ18	6/07/2022	1hr 59m 30s	483849.304	7743109.507	-1.464	5.126	0.014	0.016	0.052	0.215
MAC office	20/06/2022	2hr 02m 30s	475589.167	7719412.026	6.185	13.239	0.018	0.016	0.064	0.178
EX02	27/06/2022	2hr 35m 30s	469814.422	7716005.543	8.069	15.197	0.02	0.015	0.064	0.184
EX03	28/10/2022	2hr 03m 30s	474302.366	7719126.336	11.507	18.569	0.023	0.017	0.063	0.178
EX04	24/06/2022	2hr 57m 30s	478597.325	7718196.335	1.989	9.075	0.023	0.019	0.073	0.184
EX05	24/06/2022	2hr 18m 30s	475962.892	7719787.388	16.255	23.297	0.015	0.018	0.058	0.177
EX06	27/06/2022	2hr 35m 00s	477041.351	7719930.687	32.133	39.169	0.018	0.016	0.06	0.179
EX07	Utilised EX08	NA	NA	NA	NA	NA	NA	NA	NA	NA
EX08	28/06/2022	1hr 58m 30s	477378.559	7722168.416	33.717	40.689	0.013	0.016	0.049	0.179
EX09	1/07/2022	2hr 09m 30s	481033.282	7724674.952	19.433	26.343	0.018	0.015	0.053	0.189
EX09-valley	8/07/2022	2hr 50m 00s	480039.185	7723193.169	20.297	27.244	0.012	0.014	0.05	0.185
EX09-Mt Wongama	28/10/2022	2hr 45m 00s	480036.009	7724289.752	112.054	118.973	0.02	0.017	0.066	0.192

Table 6.2-2: Checks performed in field by repeat observations, or by checking against nearby SSM coordinates. Note that "Ell" is ellipsoidal height and "Ortho" is orthometric height.

Location	Notes on Check	△ East	△ North	△ Ell Ht	△ Ortho Ht
AQ07-08	Repeat session 1 (25/10/2022)	-0.010	0.015	0.043	0.043
AQ07-08	Repeat session 2 (25/10/2022)	0.000	-0.011	0.061	0.061
AQ09	Repeat 24/10/2022	0.009	0.005	0.044	0.044
AQ15	Repeat (Same day)	-0.010	0.015	-0.104	-0.104
AQ15	Repeat session (26/10/2022)	-0.009	-0.023	-0.033	-0.033
EX02	Setup on SSM Harbour Mound	-0.003	-0.005	-0.063	-0.080
EX03	Check shot to Dampier 141	-0.013	0.003	0.031	0.031
EX03	Check shot to Damper 141 (Repeat 17/10/23)	0.005	-0.008	0.013	0.013
EX06	Setup on SSM Dampier 140	0.007	0.010	-0.007	-0.007
EX08	Setup on SSM Dampier 148	-0.014	0.002	0.044	0.044
EX09	Check shot to SSM MN931	0.032	-0.017	-0.054	-0.054

In some cases, because the datum point was installed at the same time as the control pickup was performed, there were no known points available. Instead, a set of raw GNSS coordinates was used, and the control pickup was performed in relation to this. Once the known coordinates for the datum point had been post-processed, the differences between the raw coordinates and the processed coordinates were determined. This was then used to correct the control points into the correct location through a block shift (differences in eastings, northings, and elevations applied to each control).

To use this method, a radio link must be established between the base and the rover to transmit observations between them and calculate the relative vector (and uncertainties). Where distances or terrain made this impractical, one of the following was done:

- A new datum point was established.
- The base station was re-positioned over one of the control points, and then measurement resumed from the new location.
- The raw data was observed on the rover, and the vector was post-process in Trimble Business Centre software using PPK (post-processing kinematic) or 'Infill' (Trimble method of infield PPK).

All the RTK uncertainties for the control, are detailed into the summary sections for each site (Appendix *D*.1).

6.2.5 Drone image processing

Before flights were conducted, planning approval was sought through Curtin's remotely piloted aircraft (**RPA**) system. For specific flights, this included getting permission to fly in national parks, over industry operations, and within controlled airspace, as well as arranging for safety alerts to be issued to other pilots through the NOTAM system. The flights were conducted using either a Phantom 4 Pro, or a Phantom 4 RTK drone. In both cases, the DJI flight software DJI Pilot or DroneDeploy was used to plan and fly the mission. The flights were conducted in 'Photogrammetry Mapping' mode, which flew the area in lines over the site with a nominal overlap of 75%, nadir camera (facing down), and a nominal flight height of 70-80 m (with a targeted sampling resolution of 20 mm for the GSD). All flights were planned to try and keep the drone with a visual line of sight (**VLOS**) of 500 m.

To maintain VLOS, some flights had to be split up into sections due to the size of the area being captured. This required the drone to be moved and re-launched in different locations (and for the base station to be moved and set up at an adjacent control point for the Phantom 4 RTK drone). Due to terrain changes and battery limitations, the overlap and flight heights for some areas had to be modified (although the overlap and GSD was maintained where possible). Where the sites had complex topology (such as valleys or large vertical changes) and battery life permitted it, the flights were flown in a 3D grid pattern with the camera at a 75-degree angle. This was to enable a better 3D reconstruction of the terrain, especially in respect to the vertical component.

Before processing the images for each flight, a calibration run for the drones was performed at Curtin during the field campaign. This was done in a carpark with large number of accurately known control targets, flying a grid pattern at different heights (30 m, 50 m, 75 m and 100 m), with different camera angles (nadir and 75 degrees). The calibration allowed for the solution of the internal

camera parameters such as focal length and lens distortion (results are presented in Table *6.2-3* for the Phantom 4 Pro and Table *6.2-4* Phantom 4 RTK cameras respectively). Independent calibration back at Curtin allowed for the results of the processing of the images for the different sites to be checked in terms of the camera parameters, and to limit errors and distortions where UAV targets did not cover the full extent of the area (such as with AQ18).

The processing of the images (and the calibration flights) was performed in the software ContextCapture from Bentley Developer Network. For each site, a project was created, and the images and the UAV control points were imported into the project. The first pass of the software extracted key points (also known as feature or tie points) between the images to align them with one another (hence the importance of adequate overlap between images). Then the control points were identified in all the images, and the known coordinates applied. After this, the photogrammetric adjustment was run to align all the images to each other based on the overlapping key points and control points, to solve the camera parameters in terms of the image locations and orientations (as well as the internal parameters such as focal length and distortions), and to ensure project was georeferenced in relation to the control point coordinates.

In the case of the Phantom 4 RTK drone, the locations of the images were already known. As a result, the camera locations were constrained to these values in the adjustment instead of solving them as unknown as with the Phantom 4 Pro. This reduced the reliance on the UAV targets and helped reduce errors and distortion in the final product. The final adjustment was then checked to see how they compared to the pre-calibrated camera parameters, that enough key points were generated, the final uncertainties of the image positions was small, there were no large reprojection errors, and that final solution agreed to the control points.

Once the images had been aligned and geo-referenced, a dense image matching process was then run to generate a 3D point cloud for each site. This can have some errors due to mismatches between pixels, and some smoothing effects due to the resolution of the matching, but in most cases is considered the raw 3D data generated for the model. A digital surface or elevation model (**DSM**) was then created as a 2D geo-references raster with each pixel containing the projected height value for the location of the terrain (exported as a GeoTIFF format). The 2D raster grid was exported at a nominal resolution of 20 mm per pixel. Finally, an ortho-mosaic was created by projecting and blending the RGB values from the individual images on to the surface.

6.2.6 Summary and issues

In most cases, the process was straightforward, although some issues were experienced during the capture or processing.

The size of the areas, and number of sites to be captured per day, caused issues with balancing battery usage and maintaining the drone. In most cases a 15–20 minute flight using a single battery was possible, resulting in covering an area of 100,000 m^2 to 250,000 m^2 based on the overlap and resolution settings. Often this would mean that two to three batteries were required to cover an average site, with areas such as AQ07–08 and EX09 requiring substantially more. This limited the number of sites that could be flown per day or required breaking the flight into multiple missions (such as AQ15 and EX09).

Table 6.2-3: Phantom 4 Pro specifications and calibrated camera parameters.

Drone	**Phantom 4 Pro**
Camera	DJI FC6310
Image Dimension	4864x3648 (4:3 ratio)
Sensor Size	13.2 mm
Focal length	9.9486 mm (27.1323 mm at 35 mm Equivalent)
Principal Point	X: 2432.55 pixels, Y: 1835.32 pixels
Radial Distortions Co-efficients	K1: 0.00775022, K2: -0.0248404, K3: 0.0251392
Tangential Distortions Co-efficients	P1: 0.00145459 P2: 0.000187166

Table 6.2-4: Phantom 4 RTK specifications and calibrated camera parameters.

Drone	**Phantom 4 RTK**
Camera	DJI FC6310R
Image Dimension	5472x3648 (3:2 ratio)
Sensor Size	12.83 mm
Focal length	8.67998 mm (24.3491 mm at 35mm Equivalent)
Principal Point	X: 2432.55 pixels, Y: 1835.32 pixels
Radial Distortions Co-efficients	K1: -0.279805, K2: 0.117555, K3: -0.0302304
Tangential Distortions Co-efficients	P1: -0.000265225, P2: 0.0000955311

Data was captured in multiple missions for some sites and therefore had to be merged later. This included:

- Pairs of adjacent study squares (AQ07–08 and AQ15–16).
- Sites that experienced delays in capturing, such as AQ09 (because of airspace restriction), EX08 (because of industrial plant boundary restrictions) and EX09 due to scale of the area to be captured.

This introduced some challenges in terms of combining their solution. During the day, lighting conditions and shadowing changed, making it harder to match points between images. This was resolved by planning to ensure sites were covered in a short period of time, or where this was not possible, that the overlapping portions from each session were taken with the shortest time possible. Where this was done over multiple days, either the capture was scheduled during similar time periods, or if not, then the overlapping regions were checked to ensure they aligned, and control targets were placed in these regions where possible to help with this. Looking at the ortho-mosaic for some of these sites (EX08 and EX09 for example), this does present as different colourations in the final image product.

Wind also severely impacted flight time, with sites such as AQ17 (experiencing windspeeds of 30-40 km/h) had flight times less than 10 minutes. Also, in this case, the drone flight planning had to ensure the drone flew parallel to the wind to reduce the buffering effect which causes images to be taken at high angles of nadir (in some cases tracking the horizon). Some images were still affected and had to be removed from the processing, reducing the overlap between some images.

Water in the area (especially where the bottom could not be seen, or along shorelines where the water was not still) also caused distortions and erroneous values in the results. In some cases, no matching points could be found, so they represented a hole in the data. In other cases, they caused mismatching between images that resulting in noisy and erroneous data. These areas still require identification and cropping from the final products generated from the photogrammetry.

Areas with high elevation changes sometimes caused issues with the data. When the drone was launch at a higher elevation, the resolution of lower lying areas was reduced, and it was harder to maintain the regulated flying height of under 120 m from the ground (below the drone). Alternatively, if the drone was launched at a lower elevation, then the required overlap was not met for areas at a higher elevation, resulting in a loss of data. Multiple launches and resets of the drone and flight parameters were required, but in some cases, areas were still impacted. An example of this is the overlapping region between flight campaigns for AQ09 and EX06 where long distances and large elevation changes caused some gaps in the data. Flight planning software can now overcome this with the use of an existing DSM and terrain following functions, but this feature was not available at the time of capture.

The last issue of note was for sites such as AQ18, where large areas were flown beyond the extents of the targets, or for sites such as AQ06 and AQ03, which were flown over large, elongated corridors with no control placed in the middle. In cases without control in the area, it is harder to validate the data and ensure that there is no warping or distortion (normally in the final elevation values). In most cases, the focal length and radial lens distortions parameters have the greatest impact on causing these warping effects. To mitigate this effect the pre-calibrated camera parameters, and (where it was flown) the RTK drone's initial image positions were used to constrain the final

adjustment. However, care should still be taken when using data outside the extent of the control, as it is unchecked by control values.

6.2.7 Completed site summaries

Spatial mapping summaries for the surveyed sites are presented in Appendix *D*. Information provided in the Appendix for each site includes:

- A summary of the site capture metadata
- Position uncertainty values
- Control point summaries
- Tie-point positional uncertainties
- An ortho-mosaic image
- An image of the digital elevation model.

6.3 Computational fluid dynamics modelling

6.3.1 Objectives

Section 4.5 of the MSDCA Plan (Curtin University, 2022) states the objective of the computational fluid dynamics (**CFD**) modelling as assisting interpretation of the field-based air quality monitoring studies. Towards the end of 2023, sufficient data was collected from the air-quality monitors (AQMs) to identify two cases for investigation via CFD modelling. The locations and circumstances identified for investigation were:

- AQ11
  This location showed higher than expected readings for some airborne pollutants, with the potential source not readily identified. Also, this AQM provided real-time air quality data earlier than other sites, so was selected as a means to test the process for working with the available data.
- AQ07 and AQ08
  These two AQMs are co-located. Statistically, these two AQMs assist in quantifying the small-scale variation in the AQ measurements recorded in the monitoring program. The data collected from these AQMs, however, has shown some noticeable variation in the recorded exposures. For this reason, a CFD study was undertaken for the region surrounding these AQMs.

At this point, the CFD studies of these two regions are not complete, but do provide qualitative data to identify flow features potentially affecting the AQM readings. Each of the CFD studies is described in the following sections.

6.3.2 Methodology

The CFD process creates a virtual model of a region of Murujuga, with complete control over the inputs, and with fine spatial resolution. The four main stages in the modelling are:

- defining the inputs (including geometry, emissions, meteorology, etc.),

- creating the model (meshing the domain, setting the boundary conditions),
- running the model (flow, and species transport),
- post-processing (extracting results).

For the MRAMP project, defining the inputs was particularly complex as it was necessary to combine a number of different sources for terrain, meteorology and emissions. A suite of scripts were developed to partially automate the creation of the required input files based on a selected area of interest. This has (and will) allow relatively quick turnaround on results once the need for a particular study has been identified. In the CFD models the largest uncertainties relate to the emission sources particularly those from non or small industry, and in areas away from the main industrial hub. For the wider airshed model (ie. using CAMx), the emission rates and schedules are estimations, generally to match the reported annual emissions. For CFD, these are required to be known (or assumed) at a finer detail. As such, many of the identified sources in the wider airshed model are not characterised to the required detail to be used directly in the CFD modelling.

To account for this variability and uncertainty in the input data, CFD runs will be set up to be comparative and allow trends to be observed, rather than to establish absolute exposures (i.e. relative exposures between sites, or relative exposure versus meteorological conditions). For the MRAMP project OpenFOAM v10 (Greenshields, 2022) has been used for the modelling thus far, and this version will be used for future CFD simulations.

6.3.3 Study of AQ11

The real-time air-quality data for AQ11 showed high readings from the south (when correlated with wind direction), as shown in Figure *6.3-1*. Point emission sources in the airshed modelling did not include any emission sources that were likely to be the cause (the area sources were not of sufficient resolution to include in the CFD model). To overcome this, it was attempted to create a discrete source directly upstream of the AQM, and compare the AQM measured values (from low-power sensors in the AQM, namely particulate matter (PM) in this instance) with exposure at the sample sites (petroglpyhs and rock samples). The resulting plumes were found to affect the AQM readings and not the sample site readings. However, the channelling effect of the local terrain was observed in the results.

6.3.3.1 Simulation parameters

Simulations were made for 16 wind directions at a wind speed of 1 m/s, with some additional simulations to check sensitivity to run time and wind speed. For each simulation the domain was 3 km long (in the direction of flow), and 2 km wide. The terrain was extracted from the Digital Surface Models (DSMs) collected as part of the MRAMP project where available, and a Landgate DSM of the Burrup Peninsula where not. An atmospheric boundary layer profile was applied at the inlet, and the domain height taken as 400 m. Figure *6.3-2* shows the regions covered by MRAMP DSMs and also two sample domains, for southerly and southwesterly wind directions.

Figure 6.3-1: Real-time readings from AQ11 for PM5. Thick solid line is the median/50th percentile, thin solid lines are 25th/75th percentile, and dashed lines 10th/90th for the period of available data. Purple dots represent the known point emission sources, as included in the Murujuga Airshed report (Ramboll Australia, 2022).

a) Aerial Scans around AQ11

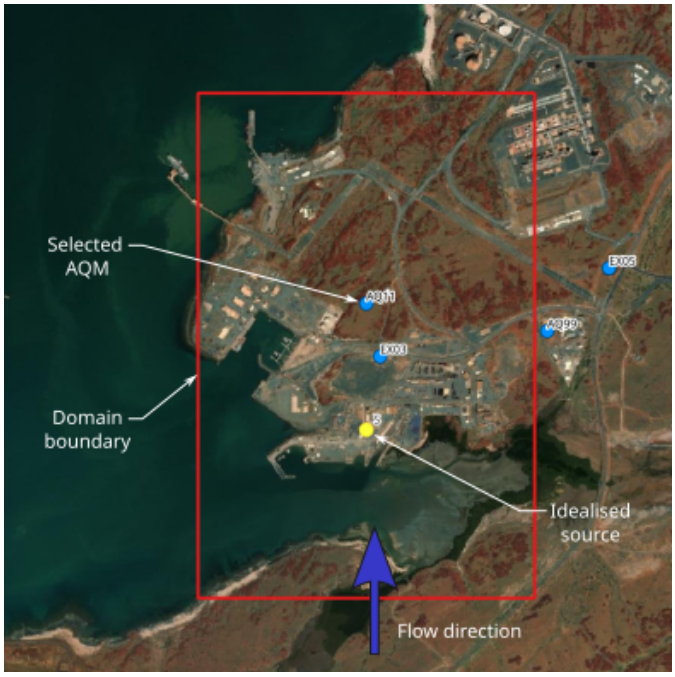

b) Domain for southerly wind direction

c) Domain for south-westerly wind direction

Figure 6.3-2: Sample domains and scans used for AQ11 study.

6.3.3.2 Results & Observations

The simulations were set to run on the Setonix supercomputer at the Pawsey Supercomputing Centre, with each run conducted in two parts, first a flow simulation to establish the flow (including buoyancy where relevant), and a second scalar transport simulation to track the chemical species transport. In post-processing the ground level species concentrations were extracted. These are shown in Figure *6.3-4* for the 16 flow directions (Additional annotations have been added for the AQM and sample sites).

In addition to the surface level sampling, vertical transects were made at the AQM site and sample sites. For comparisons the AQM value was extracted at a height of 2 m, and the sample site values extracted at ground level. Plotting the AQM measurement against sample site exposure allows a correlation to be made between measurement and exposure. However, Figure *6.3-3* shows that for the narrow plumes released from the idealised source, there is almost no resulting exposure at the sample sites, apart for a southwesterly wind direction. It is also observed that the AQM measurements are impacted by the terrain, as the exposure measured on a uniformly flat terrain would be constant irrespective of wind direction.

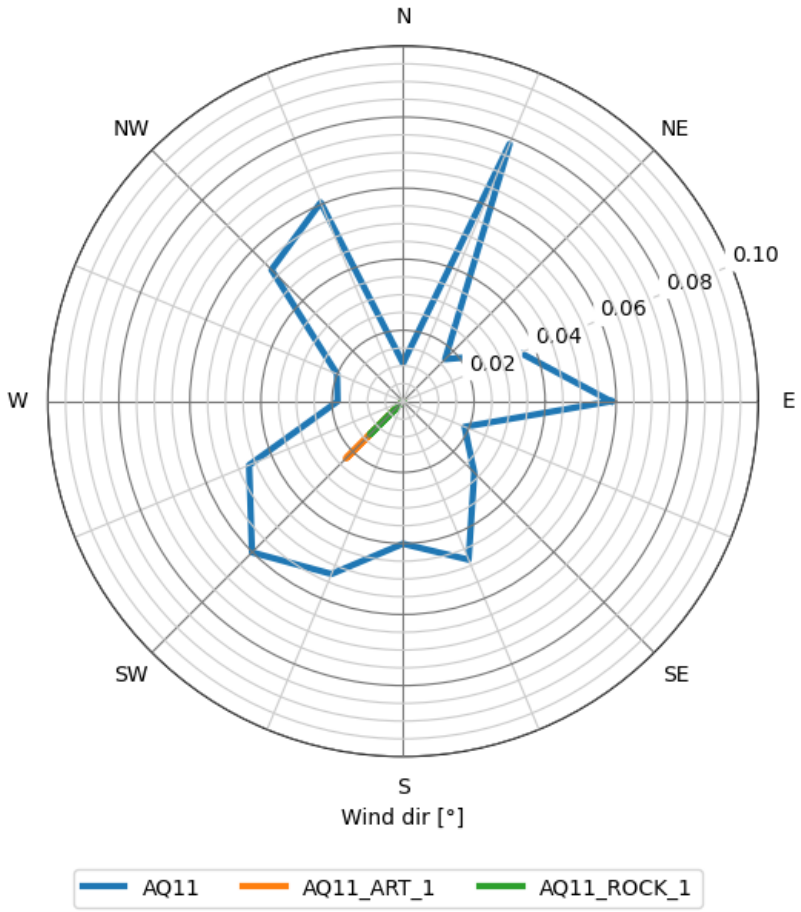

Figure 6.3-3: Comparison between AQM PM measurement and site exposure for an idealised source directly upstream from the AQM.

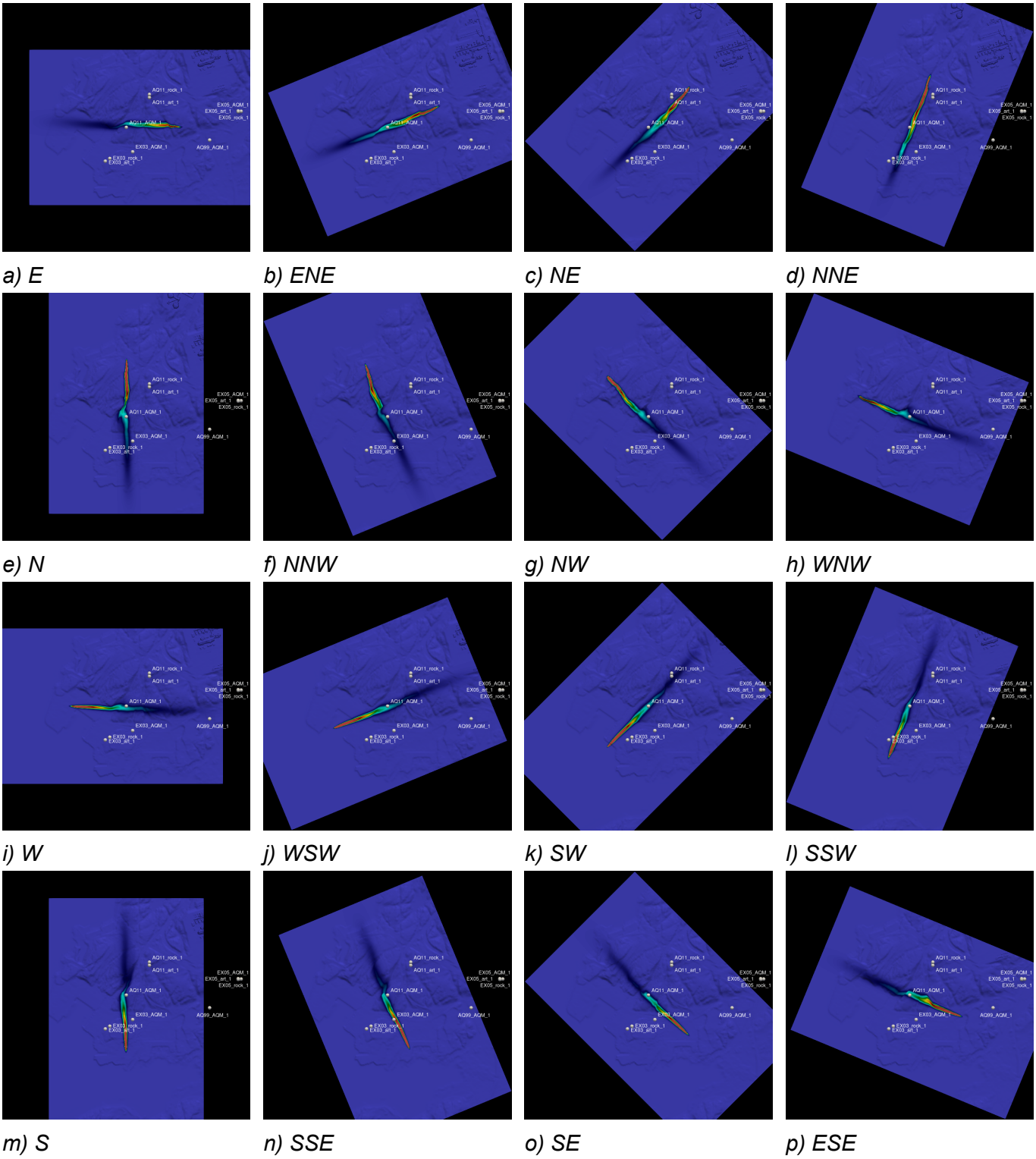

a) E *b) ENE* *c) NE* *d) NNE*

e) N *f) NNW* *g) NW* *h) WNW*

i) W *j) WSW* *k) SW* *l) SSW*

m) S *n) SSE* *o) SE* *p) ESE*

Figure 6.3-4: Ground level concentration of idealised PM10 scalar, for different wind directions.

A key observation from the results is the channelling effect of the terrain. Figure *6.3-5* shows the ground level exposure for a southerly wind direction. This figure shows that part of the plume flows directly over the gorge, while a substantial part of the plume changes direction and flows along the

gorge. At smaller time and spatial scales, this channelling could potentially affect the determined exposure for a particular site, based on the AQM measurements.

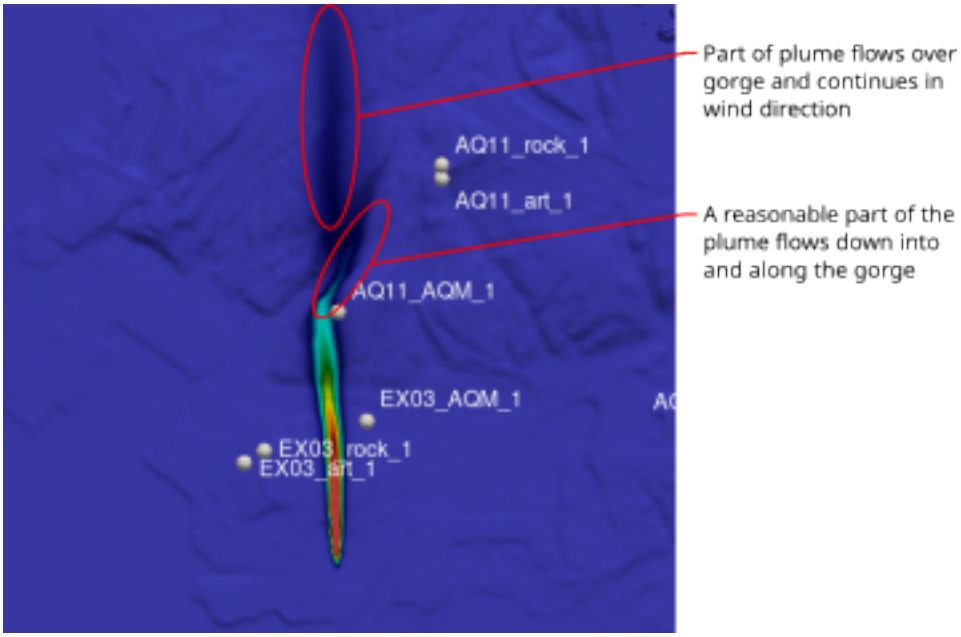

Figure 6.3-5: Southerly wind flowing affected by gorge with idealised source

Currently there is insufficient fine-detailed knowledge of the activities to the south of AQ11 to be able to quantitatively determine the correlation between exposure and measurement.

6.3.4 Study of AQ07 and AQ08

AQ07 and AQ08 are ‘co-located’ to establish the fine scale variation in measurements for the statistical analysis. Air-quality and wind measurements at AQ07 and AQ08 have shown quite large differences although the stations are physically less than 20 m apart. Additionally, AQ07 and AQ08 are positioned at the top of a large quarry (which is not currently operating). CFD modelling was undertaken for the region surrounding the quarry to identify the effect of the quarry on the airflow, and subsequently on the reading taken at the AQMs. At this stage only a preliminary investigation has been undertaken, with additional modelling and analysis on-going.

6.3.4.1 Simulation parameters

The simulations were set up similarly to those for AQ11, however due to the absence of nearby emissions sources only the airflow was modelled. As with AQ11, 16 wind directions were modelled with a nominal windspeed of 1 m/s (at 15 m height). An atmospheric boundary layer profile was modelled at the inlet, and the domain size was 3 km $\times$ 2 km, with a height of 400 m. In addition to the 2D slices extracted for AQ11, the full 3D data was analysed to investigate any complex flow patterns. Figure *6.3-6* shows the region around AQ07/AQ08 that was modelled.

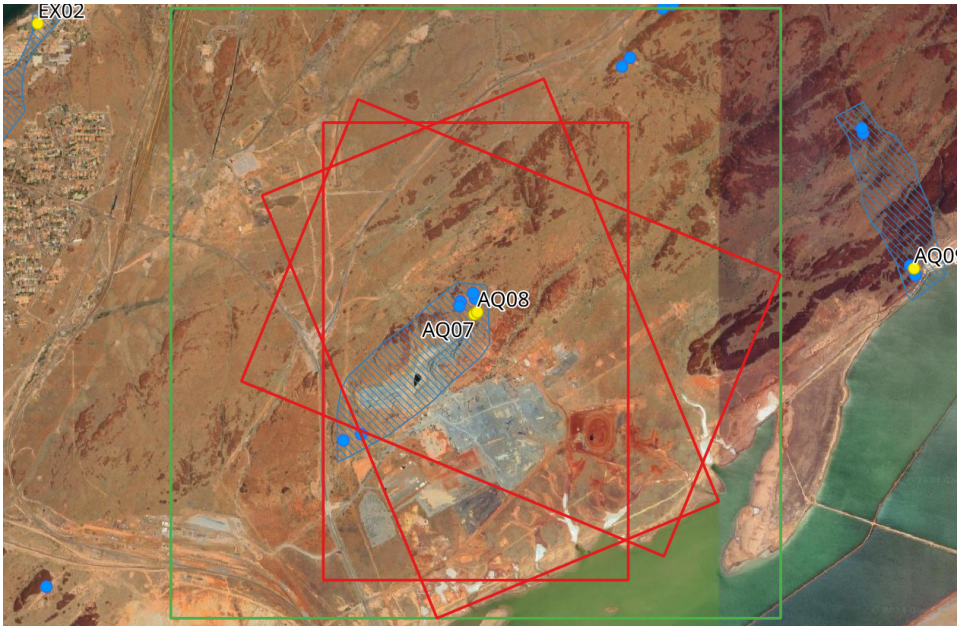

Figure 6.3-6: The region around AQ07/AQ08 that was investigated, domain outlines for S, SSE and ESE are shown, although 16 compass directions were modelled. AQ07 and AQ08 are shown in yellow, while sample sites are shown in blue. The blue cross-hatched region shows the extent of the aerial scan taken for the MRAMP project.

6.3.4.2 Results and observations

As with AQ11, the analysis of AQ07/AQ08 is ongoing. At this point of time only preliminary qualitative analysis has been completed, with further simulations and analysis to follow. The key observation thus far is that the quarry topography has a large influence on the airflow in the region. Figure *6.3-7* shows 3D streamlines of flow in the region around AQ07 and AQ08.

These figures show that the quarry has a large influence on the flow. In particular Figures *6.3-7*c and *6.3-7*d show cases where measurements could impact readings. In Figure *6.3-7*c the streamlines start completely to the west of the AQMs and sample sites, however the quarry causes a large section of the flow to be diverted along it, and the resultant flow passes across both the AQMs and sample sites. In Figure *6.3-7*d the streamlines passing through the AQMs (on the east/right) are unaffected by the quarry, whereas for the western(/left) sample sites the flow has passed through the quarry. This difference in flow path could potentially cause a discrepancy between the modelled exposure at the sample site versus the measured exposure at the AQM. For a southerly wind direction, the potential for different flow paths was investigated further. In Figure *6.3-8* streamlines were released from a line passing through AQ07 and AQ08 (tracked upstream and downstream from the release point). For this flow direction, the ‘source’ of air for AQ07 is from the quarry, while the source of air for AQ08 is from further east.

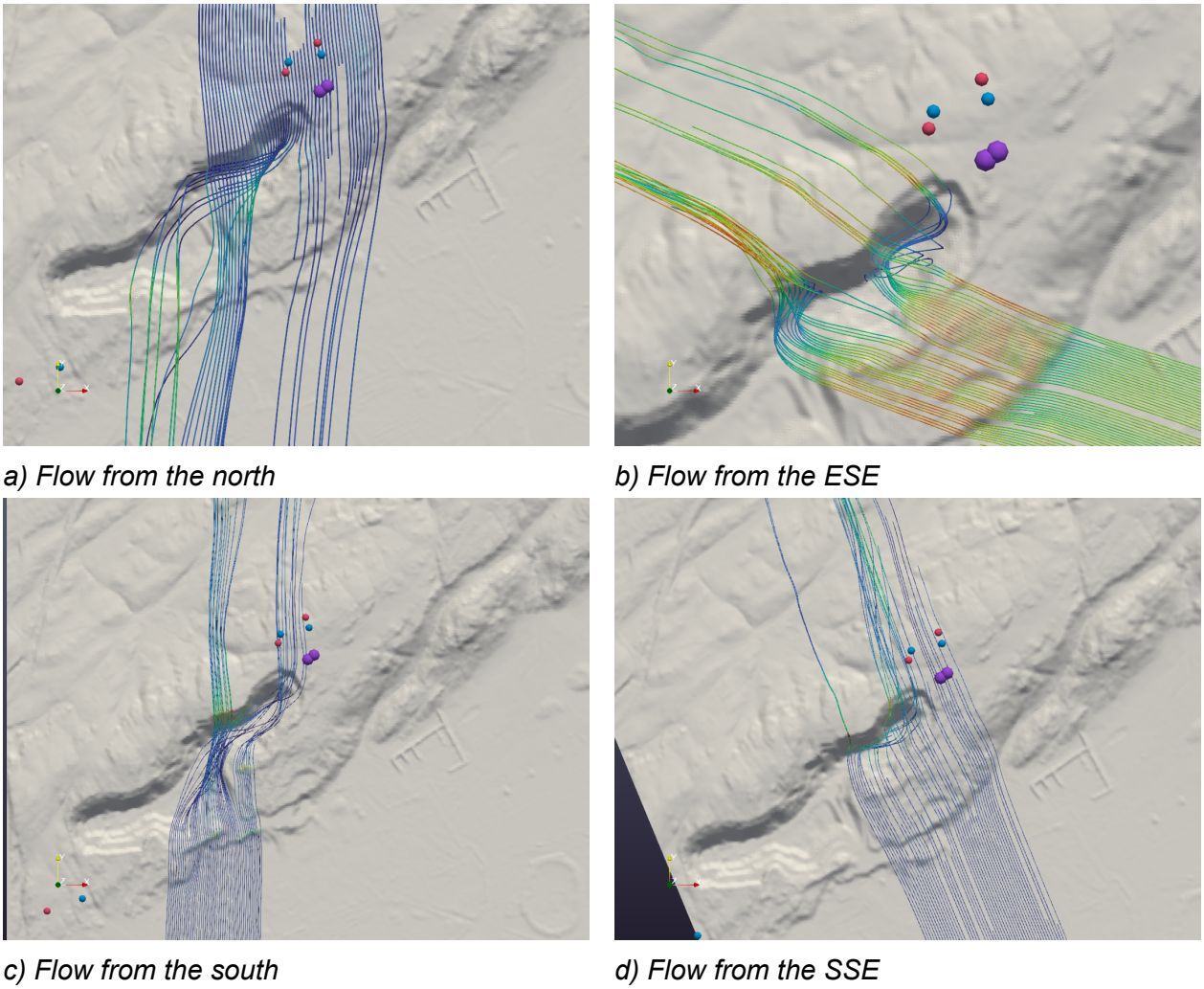

a) Flow from the north

b) Flow from the ESE

c) Flow from the south

d) Flow from the SSE

Figure 6.3-7: A selection of 3D flow streamlines in the vicinity of the quarry. the AQMs are shown in purple and the sample sites (rocks/artworks) are shown in blue and red.

Figure *6.3-9* shows the difference between the measured wind speed and directions at AQ07 and AQ08 for an input wind speed of 1 m/s. The difference between the measured flow at AQ07 and AQ08 is generally quite small (within $\pm$ 6% for magnitude and $\pm$ 2° in direction). These simulations were also run at 0.5 and 5 m/s, and showed that the measured differences (angle and magnitude) are the same for these cases. Together Figures *6.3-8* and *6.3-9* show that it is possible for these AQMs to measure similar wind conditions, but differing exposures.

These results capture the steady flow (nominally for the one hour resolution of the CAMx results) over a relatively large region. There are likely to be transient flow features effects that are not captured by the steady solution. For smaller spatial scales, the flow at AQ07/AQ08 will also be run at a smaller spatial resolution, using the wide area solution to provide the boundary conditions.

6.3.5 Further work

Also of interest for investigation is the industrial hub region (EX-05, EX-06, EX-07, EX-08 and EX-09). These AQMs are sited in or near the industrial hub, and are expected to show higher concentrations of pollutants. Scans for these areas were received in late 2023, with processing of the data underway.

It is important to note that the objective of the CFD modelling is to support the MRAMP air quality monitoring. The CFD results will not feed directly into the EQC but will allow the statistical team to reduce measurement uncertainties by testing and assessing particular localised impacts.

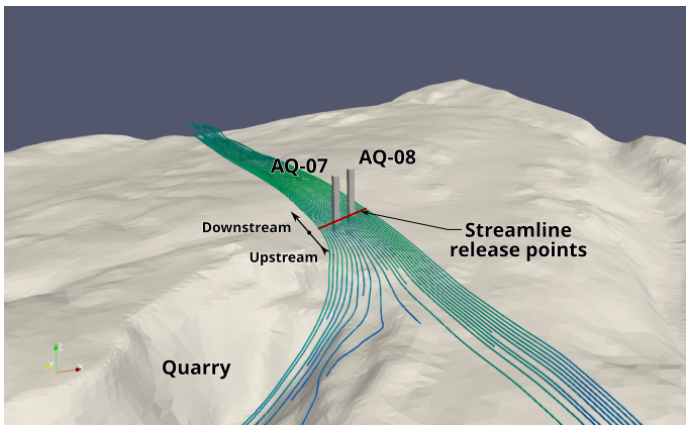

Figure 6.3-8: Streamlines mapped bi-directionally through AQ07 and AQ08, for a southerly wind direction.

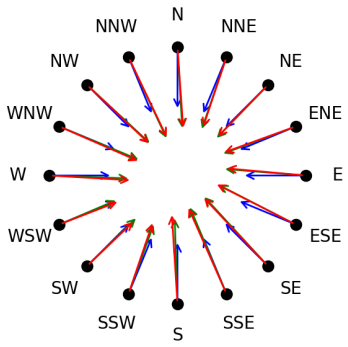

a) modelled wind speed and direction (green=AQ07, red=AQ08) vs nominal wind speed and direction (blue)

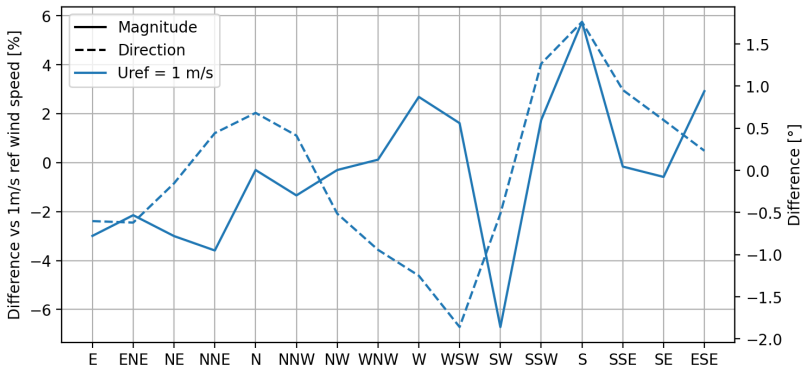

b) Comparison between modelled wind at AQ08 relative to AQ07.

Figure 6.3-9: Comparison between modelled wind at AQ07 and AQ08.

This page is intentionally blank.

7 Statistical analysis of data from each component study

This section reports our analysis of data collected in each of the component studies, focusing on one component study at a time. Relationships between the variables measured in different component studies are investigated in Section 8.

The key findings from the statistical analysis in this section are summarised in Section 7.13.

The plan of the section is as follows. Section 7.1 concerns the chamber experiments in which sample rocks were subjected to high concentrations of pollutants. Section 7.2 concerns the measurements of rock surface colour in the field. Section 7.3 concerns the air quality data supplied by industry. Section 7.4 concerns the measurement of *pH*, *Eh* and Cl^- ion concentration on rock surfaces. Section 7.5 concerns the measurements of rock composition using the pXRF instrument. Section 7.6 concerns rock porosity, as determined from microscope images of thin sections of rock samples. Section 7.7 reports initial analysis of data from the new permeameter instrument, which was deployed in the field in response to our findings about rock porosity. Section 7.8 concerns analysis of the microbiome in the patina, soil and lichen samples. Section 7.9 concerns organic geochemistry. Section 7.10 concerns the data from the three bucket deposition samplers on the *pH* of deposited material and the deposition rate of various chemical species. Section 7.11 concerns the data from the IVL passive sampler tubes on the atmospheric concentrations of various gases. Section 7.12 concerns the data from the real-time air quality monitoring stations. Key findings from this section are summarised in Section 7.13.

7.1 Chamber studies

7.1.1 Background

The chamber exposure experiments (Curtin University, 2023) were designed to provide information about dose-response relationships between the environmental exposure of rock surfaces to industrial emissions, and chemical or microbial changes in the rock surface. These controlled experiments provide cause-and-effect information. In order to ensure data is obtained in as timely a manner as possible, experiments were carried out under “accelerated weathering” conditions which involve relatively short term exposure to higher concentrations of industrial emissions, rather than the chronic exposure to much lower concentrations which is (generally) occurring in the field.

The design of the chamber studies for geochemical processes has been adapted in the light of provisional findings about the porosity and chemical composition of rock surfaces. The modified design enables quantification of the weathering of particular minerals. The selection of analytes in the chamber studies was informed by observations that certain minerals were depleted in the near-surface layer of the rock samples collected from the field.

For expediency, and to reduce the requirement for additional rock samples from Murujuga, all initial experiments to develop EQC were conducted on “Fresher” rock samples — i.e. interior samples that do not contain patina (varnish) or weathered rind. Results from these fresher rock samples will then be confirmed and/or adjusted based on patina experiments which will focus on those elements that are likely to leach from the patina rather than the subsurface rock.

It has also proven necessary to separate geochemical and biological/biogeochemical processes into separate chamber studies. These separate studies will be integrated later, either through combined experiments or data fusion.

7.1.2 Experimental method

The experimental method is detailed in full in the associated document:

- COPP21065-PRO-G-117 Chamber Exposure Studies.

The exposure apparatus is adapted from a previous validated apparatus developed by the authors (Landwehr et al., 2021). The design and development of the method has been informed by other accelerated weathering studies on Murujuga rocks (Neumann et al., 2022) and primarily by the geochemical and porosity findings detailed in this document as they became available in preliminary form.

In brief, prepared cubes of rock were placed in a heated exposure chamber and exposed to measured concentrations of the gases under investigation. Approximately equal numbers of samples from each of the following rock types were used: basalt (BAS), dolerite (DOL), gabbro (GBR), granite (GRT) and granophyre, segregated into coarse (GPHC) and fine (GPHF) crystal size. Single samples of polished granophyre (GPHP), and polished gabbro (GBP) were also included. These were polished and imaged using Scanning Electron Microscopy/ Transmission Electron Microscopy (SEM/TEM) pre- and post-exposure, to confirm the hypothesis of mineral depletion visually as well as chemically.

Rock cubes were rinsed in a defined quantity of ultra-pure water, then given a “bath” in ultra-pure water for 30 minutes both pre- and post-exposure. This conceptually replicates rainfall and allows reaction/decomposition products leaching into the ultra-pure water to be quantified and related to a dose. Pre- and post-exposure samples and blanks were analysed by the ChemCentre using Inductively Coupled Plasma-Atomic Emission Spectroscopy (ICP-AES) to determine the concentrations of leached elements.

Rock cubes were placed in a randomised pattern in a heated incubator (exposure chamber) to replicate solar heating in the field; a different randomisation was used for each exposure scenario. Likewise, a UV lamp was located inside the chamber to provide photocatalytic generation of secondary air pollutants.

Exposures were conducted for a six day incubation period, with air pollution (either from hydrocarbon combustion or bottled gases) actively introduced at the commencement of the exposure on day one for one hour and then (if repeated) at 24 hour intervals for up to six days. This is shown conceptually in Figure *7.1-1*. After the active exposure period, the concentration inside the chamber progressively reduced over the subsequent 23 hours due to reaction or diffusion. For all exposure scenarios, incubation and UV were continued for six days to permit reactions to occur.

Concentrations of gases of interest in the chamber were monitored throughout the experiment, using either a combustion gas analyser (Testo 350, Lenzkirch, Germany) or a dedicated analyser for a particular species (e.g. NH_3, GasBadge Pro, Industrial Scientific, Pittsburgh, PA, USA). For the combustion experiments, due to inherent variability in combustion, the actual exposure amount

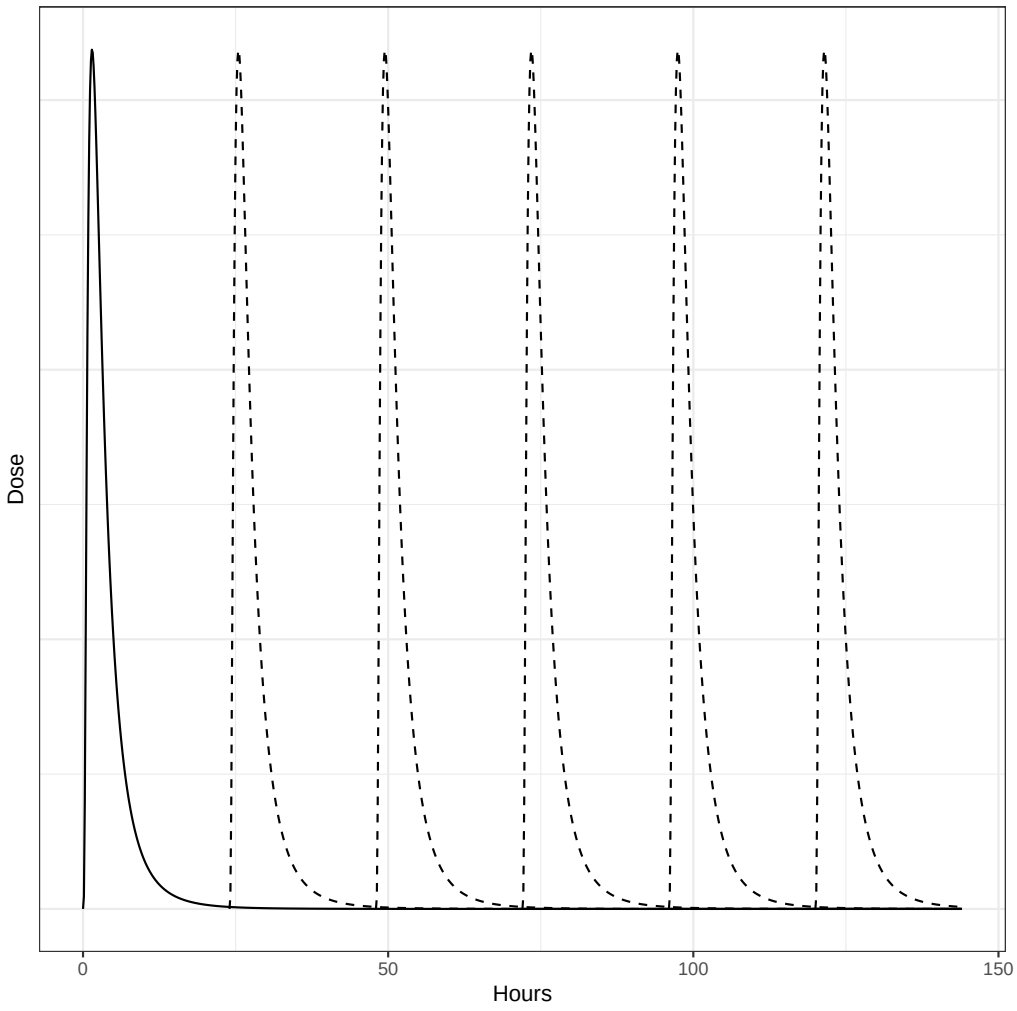

Figure 7.1-1: Design of chamber experiments: Idealised concentration profile of gas/pollutant in chamber against elapsed time of experiment. Solid line shows a single dose experiment which may be re-dosed daily for up to six days (dashed lines).

was not exactly equal to the exposure specified by the design, but was measured accurately by the monitoring equipment.

Analysis of pre- and post-exposure samples and blanks was performed by the ChemCentre. Several metals related to mineral reaction by-products were monitored. Aluminium (Al), Calcium (Ca), Iron (Fe), Potassium (K), Magnesium (Mg), Manganese (Mn), and Sodium (Na) were measured via ICP-AES, which is a relatively sensitive technique with detection limits that range from 0.001 mg per litre for Mn to 0.005 mg per litre for Fe and Al, and 0.1 mg per litre for Ca, Mg, Na, and K. The concentration of Mn was either very low or below detection limit (BDL) for rocks without patina, and the concentration of Fe was consistently BDL in all samples. The concentration of Al showed variability that may be attributable to contamination by Al-bearing components in the experimental apparatus, so this element is not discussed further here. Four elements (Ca, Na, Mg, and K) exhibited a clear dose-response relationship and were selected as the most appropriate analytes for further analysis.

Elements released into solution during the experiments were initially hosted by minerals in the rock samples prior to the experiments. The experiments used cubes of fresher rock (i.e. samples without a surface patina), so the minerals within the fresher rock are the likely sources of the elements measured by ICP-AES. The five different lithologies contain different minerals in different proportions, but Ca is likely to be released from clinopyroxene and plagioclase in the mafic (silica-poor) lithologies (basalt, gabbro, dolerite), and from plagioclase in the felsic (silica-rich) lithologies (granite, granophyre). The main Na-bearing mineral and likely source of most of the Na for all lithologies is albite, which is a Na-rich feldspar, or plagioclase, which is a Na- and Ca-bearing feldspar, although minor Na may be released from amphiboles in the mafic lithologies. The most likely source of Mg is chlorite in all lithologies, and orthopyroxene, clinopyroxene, and amphiboles in the mafic lithologies. Alkali feldspar, which can form orthoclase, microcline, or sanidine, depending on the structure of the mineral, is the most likely source of K, although K may be held within the rock as part of clay minerals, such as illite, that form by alteration of alkali feldspar. Some proportion of all the elements that are released by breakdown of the minerals present in the fresher rock at the start of the experiment may transfer to secondary clay minerals that form as part of the mineral breakdown, and this process reduces the amount of the element that is released and measured in the experimental solutions.

During the experimental program, a 25 mm quartz fibre filter (denoted QTZ, Whatman, Buckinghamshire, UK) was introduced into the design as a (largely) inert substrate to (a) confirm that no particulate contamination was occurring during experiments and (b) act as a substrate for sampling organic and other pollutants for later offline analysis.

7.1.3 Experiments conducted

7.1.3.1 Hydrocarbon exposure experiments

Hydrocarbon exposures to date have consisted of the introduction of cooled, diluted combustion exhaust to the exposure chamber. Exhaust was derived from either:

1. a 50/50 (by volume) combination of natural gas condensate and diesel, or
2. Heavy fuel oil (HFO) - as used by large ships.

Both sources resulted in predominantly NO, NO_2, SO_2 as well as lower levels of CO, uncombusted hydrocarbons, with the balance being air and CO_2. Measured exposure profiles for NOx and SO_2 are shown in Figure *7.1-2*. HFO produced higher SO_2 due to higher fuel sulphur levels, as well as higher hydrocarbons and soot. It is expected that the UV lamp in the exposure chamber in both cases would create secondary air pollutants such as O_3, however this could not be measured at this stage.

7.1.3.2 Ammonia exposure experiment

For the case of ammonia (NH_3), a single six day experiment was conducted using a single exposure of 16 ppm by volume (314 $\mu g/m^3$) NH_3 on day one. A smoothed fit to the measured ammonia exposure profile of the experiment is shown in Figure *7.1-3*.

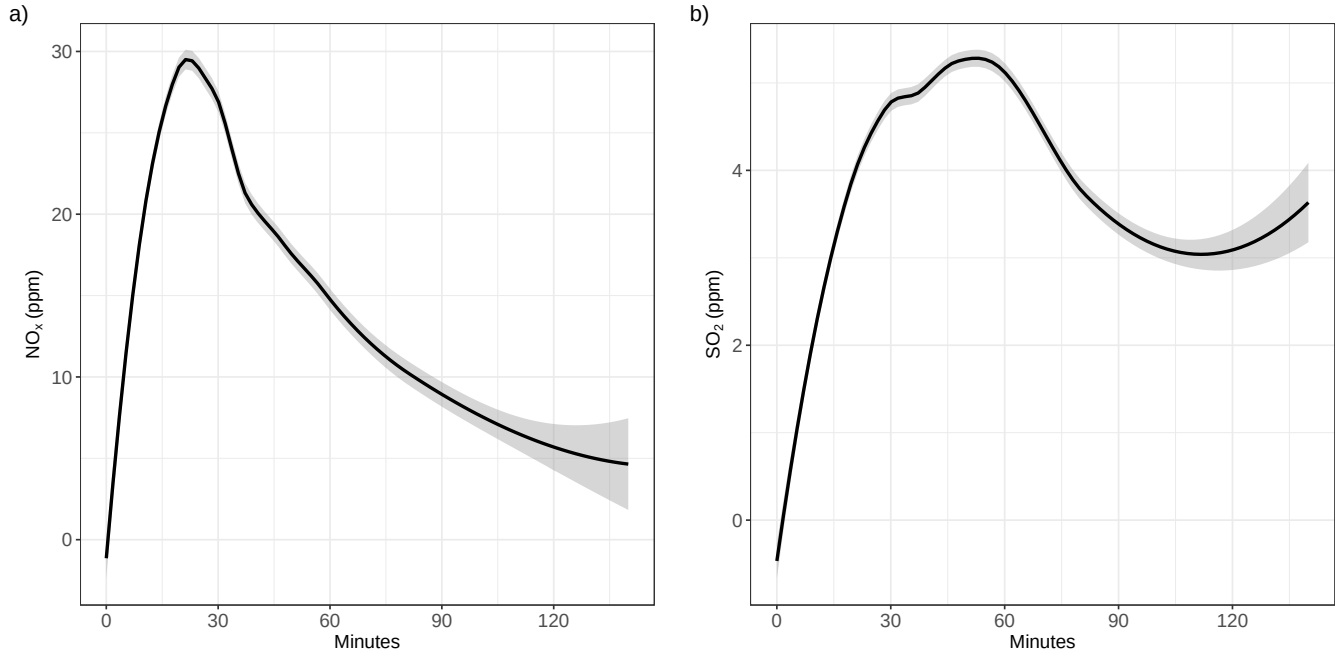

Figure 7.1-2: Measured exposure profiles for (a) NOx and (b) SO_2. The solid black line is the smoothed estimate of exposure; grey shading is the pointwise 95% confidence interval for the true exposure.

7.1.4 Statistical approach

In order to investigate dose–response relationships, both the dose and the response needed to be clearly defined.

7.1.4.1 Dose

The “dose” of a particular gas of interest was defined as the measured concentration of the gas during the chamber exposure, averaged over the six day incubation period.

A complication is that the combustion experiments involved burning fuel and producing a combination of several different pollutant gases in each experiment.

For a given fuel type and combustion apparatus, we provisionally assume that the concentrations of the different pollutant gases are approximately proportional to one another at any moment, and therefore the “doses” of the different pollutant gases are approximately proportional. This allows us to investigate dose-response relationships using the concentration of one particular gas as the “dose”. A more extensive experiment, and more searching multivariate analysis, will be required in order to separate the effects of different gases.

7.1.4.2 Response: change in elemental concentration

To develop a suitable measure of the “response” of rock samples to pollution exposure, we studied changes in the concentration of particular chemical elements in water samples obtained before and

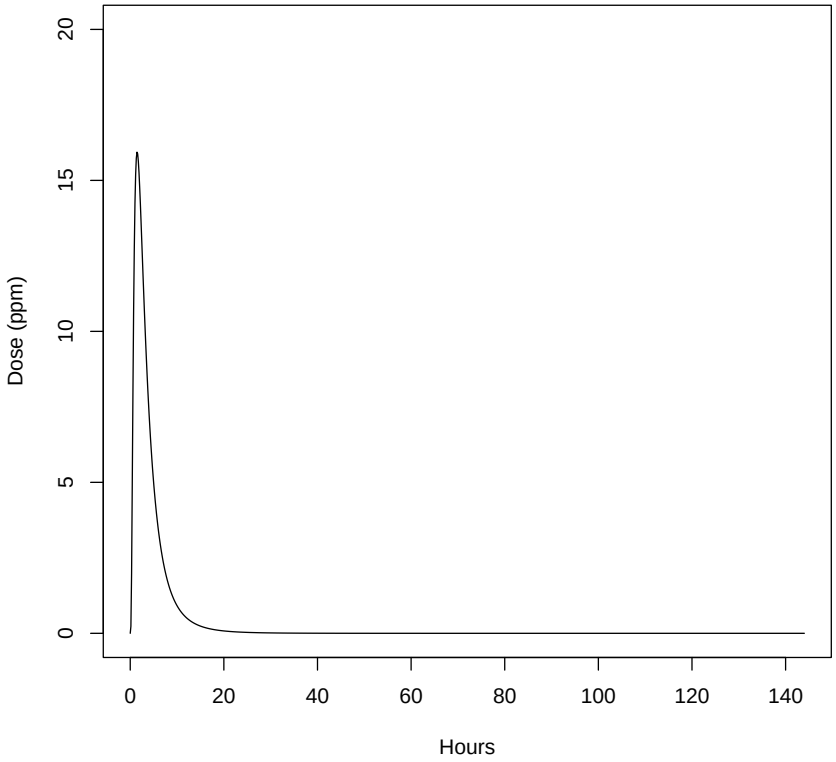

Figure 7.1-3: Measured exposure profile for NH_3.

after exposure to pollutant gases. For initial investigation we calculated the change in concentration as the arithmetic difference between the measurements before and after exposure. That is, the change is the concentration measured after exposure, minus the concentration measured before exposure, expressed in mg/L.

Multivariate analysis indicated a strong positive correlation between the values for Ca, K, Mg and Na. For simplicity, we propose taking the sum total of these values. Our preferred measure of the response is therefore defined as the difference in the sum total of the assayed concentrations of Ca, K, Mg and Na, expressed in mg/L. For the purposes of plotting dose-response curves, the values are peak-normalised (i.e. rescaled so that the maximum value is equal to one).

7.1.4.3 Response: *pH*

Previous literature has conjectured that unusually high or low values of *pH* of the rock surface may be indicators of potential environmental stress and may even have a direct role in the degradation/dissolution of the rock surface. It is well known that NO_2 and SO_2 can be precursors to the formation of nitric and sulphuric acid respectively. Consequently we shall also consider change in *pH* as a response variable in the chamber experiments.

7.1.4.4 Estimation of dose-response relationship

The “dose-response relationship” is a curve which predicts the amount of “response” within the rock surface to a given “dose” of pollutant gas exposure. Knowledge of this relationship would allow policymakers to determine the safe level of exposure and the levels of exposure that should trigger intervention.

Estimation of the dose-response relationship is a form of regression analysis. Many statistical methods are available for this purpose: the best choice of method depends on the expected form of the relationship. It might be reasonable to assume that “response” increases with increasing “dose”, but to ensure transparency, we shall not make that assumption. Neither shall we assume that the relationship follows any particular algebraic form. Instead, we shall use non-parametric regression methods, which assume only that the relationship curve exists and is moderately smooth. The principal method used in our analysis is locally weighted polynomial regression performed in R using `loess` function (Cleveland, 1979).

Concentration data often have a skewed distribution, especially when the concentration values are small. A logarithmic transformation is often appropriate, because it tends to reduce skewness and to improve the performance of regression methods. In this experiment, it would be natural to apply a logarithmic transformation to both the dose and the response. This has not been done in the preliminary analysis reported here. Further analysis and modelling will be undertaken.

7.1.5 Statistical analysis and discussion

Here we report on a preliminary analysis of the data from the experiments described in Section 7.1.3.

7.1.5.1 Changes in elemental concentration

For the “pre-exposure” water samples, concentrations of Ca, K, Mg and Na were generally recorded as below detection limit. Blanks always yielded below detection limit values.

The lowest doses of hydrocarbon combustion gases used in the experiments generally gave rise to little or no response from approximately half of the rock types studied. This dose has been provisionally designated as the Lowest Observed Effect Concentration (LOEC). Coarser-grained rock types tended to exhibit a non-zero response at these lowest doses, whereas fine grained rocks (basalt, dolerite and fine granophyre) generally exhibited no response at this level. However the pointwise 95% confidence bands around the fitted dose-response curves for the combined grouping of rock types extend to zero or lower at this exposure level, providing some support for declaring the LOEC to be the lowest dose used.

It should be noted that the LOEC may be sensitive to the accuracy of the analytical technique used. This is expected to be investigated in the following year through comparison with comparable approaches, such as Inductively Coupled Plasma–Mass Spectrometry (ICP–MS) which offers lower detection limits.

The response from the hydrocarbon combustion experiments appears to be most strongly correlated with NO_x and SO_2; therefore dose-response curves have been estimated for these agents. However

in forthcoming work, more detailed dose response curves for multicomponent doses will be evaluated, as well as single gas exposures (e.g. bottled NO_2, SO_2).

Figure *7.1-4* concerns the dose–response relationship for NO_x. Panel (a) shows boxplots of the response against dose, broken down by rock type. Response generally increases with increasing dose. There does not seem to be evidence that the different rock types have different patterns of response for the higher doses. Panel (b) shows boxplots of response for all rock types combined, together with a smoothed estimate of the dose–response relationship (blue curve) and a pointwise 95% confidence interval. The smoothed estimate and confidence band were obtained by loess regression (Cleveland, 1979).

Figure *7.1-5* shows the corresponding analysis for sulphur dioxide SO_2. Response generally increases with increasing dose.

The dose–response relationship seems to be similar for NO_x and SO_2. Since these two gases were generated together in the same exposure experiment, it may be appropriate to define a new measure of dosage as the sum of the two dose measures. Figure *7.1-6* shows the chemical response (change in total concentration of Ca, K, Na, Mg) against this redefined dose measure (sum of average concentrations of NO_x and SO_2, that is, NO_2 + NO + SO_2). This yields stronger evidence for a dose–response relationship.

For the purposes of developing an interim EQC, this is sufficient evidence to nominate NO_x and SO_2 as potentially harmful agents, with a potentially observable effect on the concentrations of Ca, K, Na, Mg on the rock surface. Refer to the separate interim EQC document (Curtin University, 2025) for further detail.

Heavy fuel oil (HFO) results have been excluded from the dose response curves shown above. Sufficient HFO was only available to conduct a single test with one hour exposures on days one and two of the six day experiment. This resulted in moderate NO_x and the highest SO_2 of all tests. However the data did not follow the same pattern as the dose response curves shown above: see Figure *7.1-7*. It may be that additional effects due to the hydrocarbons or soot particulates associated with the HFO need to be accounted for. It can however be seen that there was no response from the QTZ sample which confirms no external contamination in the results from the apparatus or the fuel. The priority is to undertake experiments with a single gas species; however, further HFO tests may be needed to understand interaction effects. Substantial difficulties in obtaining HFO were experienced in the previous year, but a reliable supplier has now been secured.

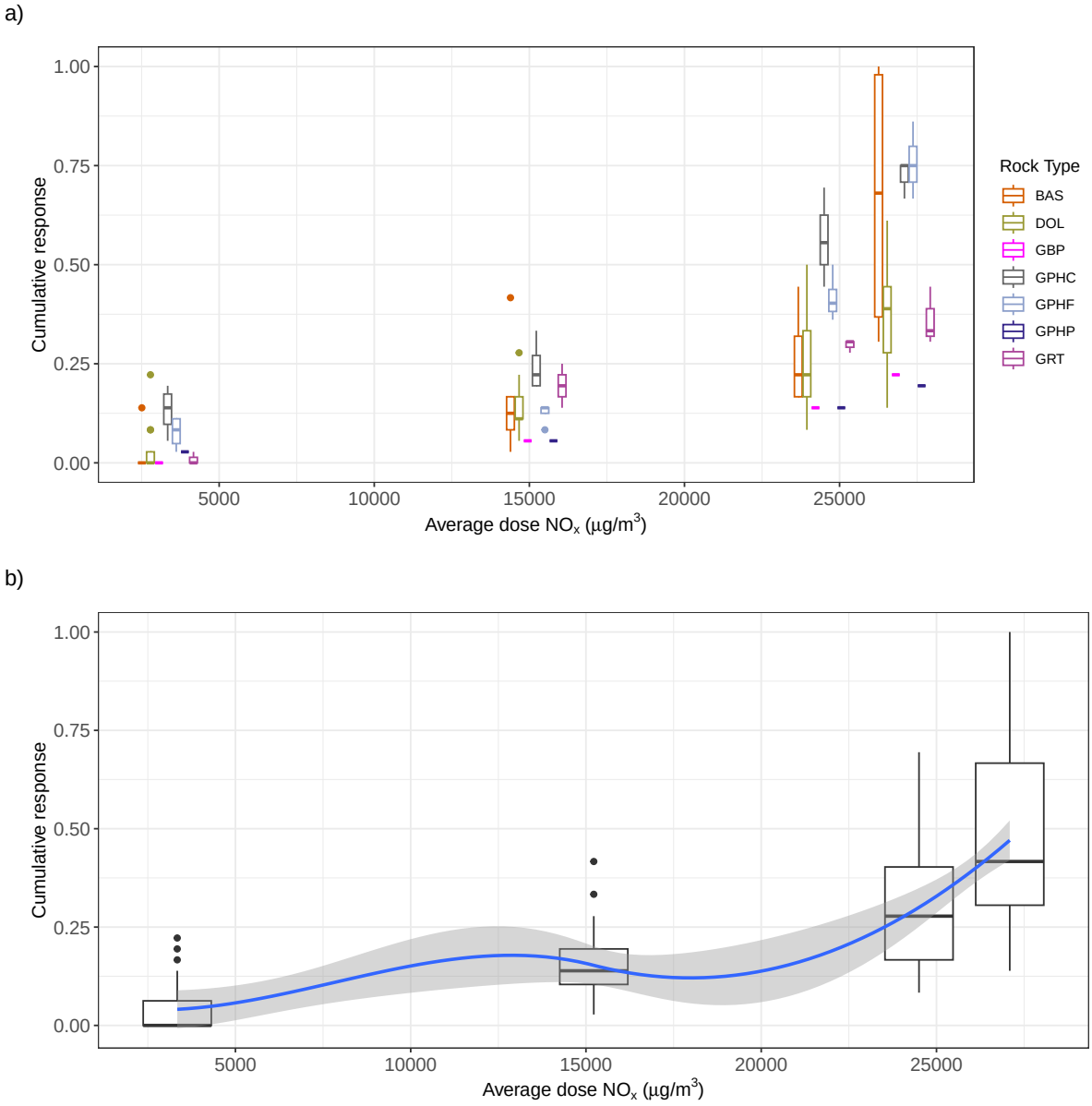

Figure 7.1-4: Boxplots of normalised cumulative response (after minus before exposure) against average dose NO_x, (a) broken down by rock type, and (b) for all rock types combined. Blue curve: smoothed mean response. Grey shading: pointwise 95% confidence intervals. GPHF is fine granophyre and GPHC is coarse granophyre.

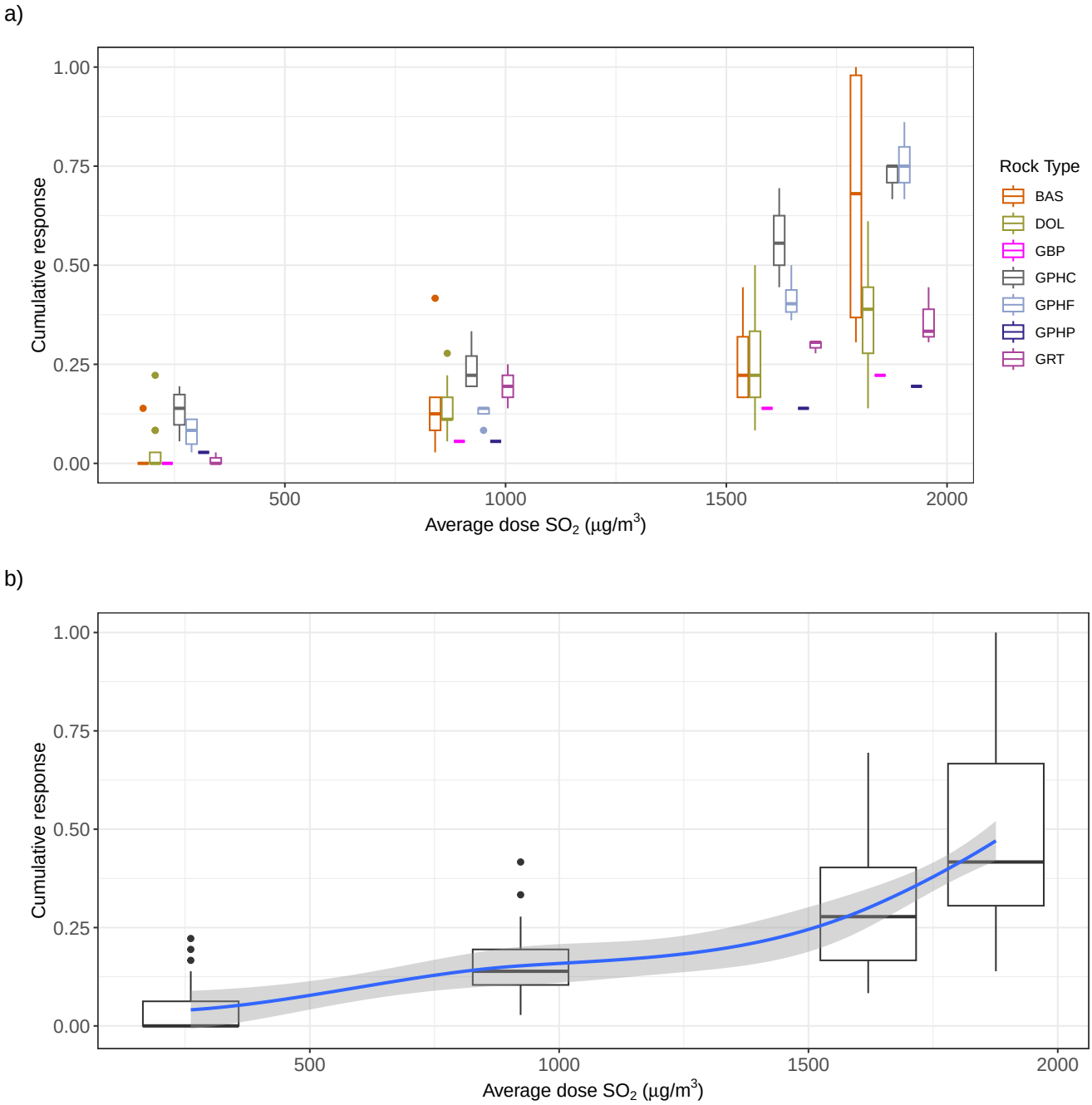

Figure 7.1-5: Boxplots of cumulative response (after minus before exposure) against average dose SO_2, (a) broken down by rock type, and (b) for all rock types combined. The blue curve is the smoothed conditional mean; grey shading is pointwise 95% confidence interval.

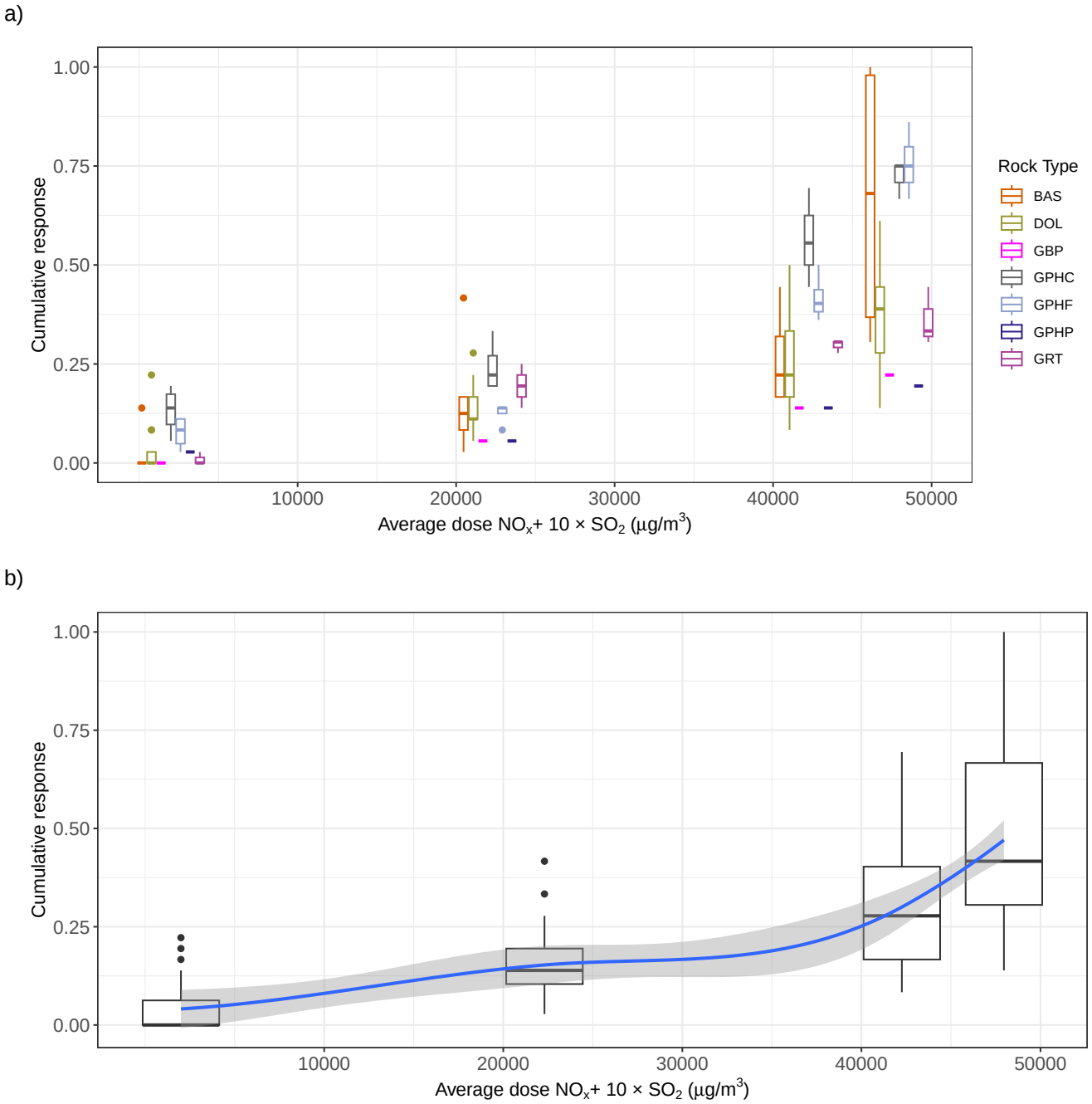

Figure 7.1-6: Boxplots of cumulative response (after minus before exposure) against average dose NO_x plus SO_2, (a) broken down by rock type, and (b) for all rock types combined. The blue curve is the smoothed conditional mean; grey shading is pointwise 95% confidence interval.

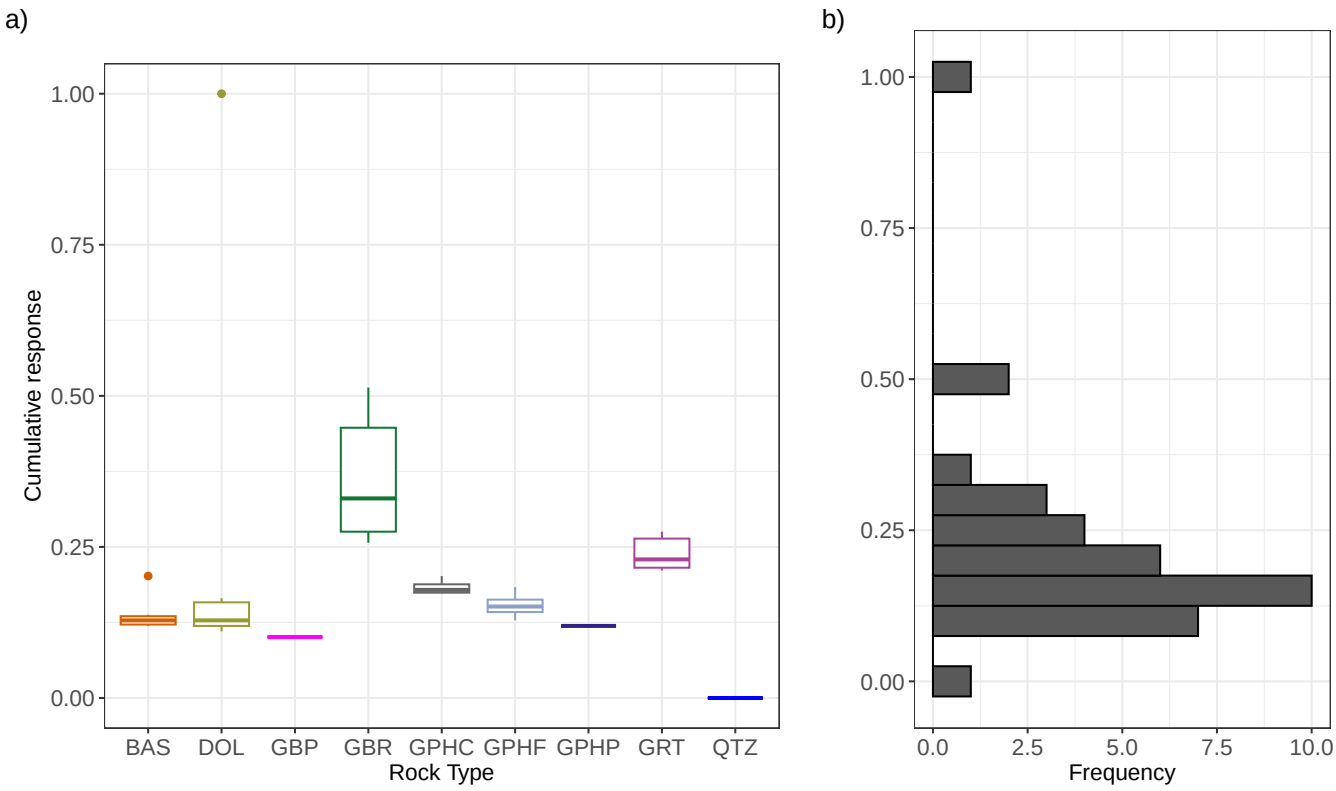

Figure 7.1-7: (a) Boxplots of change in Ca+Mg+Na+K concentration after exposure to HFO, broken down by rock type, and (b) histogram of change in Ca+Mg+Na+K concentration after exposure to HFO. The average HFO is 7174.744 $\mu g/m^3$ NOx and 1898.46 $\mu g/m^3$ SO_2.

7.1.5.2 Changes in *pH*

Figures *7.1-8*, *7.1-9* and *7.1-10* show the after-minus-before change in *pH* against average concentration of NO_x, SO_2, and NO_x + SO_2, respectively. The graphs suggest that *pH* does not respond markedly to increased concentration of these gases. Our provisional conclusion is that there is currently insufficient evidence to base an interim EQC on the conjectured effect of increased NO_x or SO_2 concentration on the *pH* of rock surfaces.

It may be that the time to equilibrium is longer than the time available for measurement in the field. While the dominant process may be an acidic type reaction, the system may react to neutralise this acid, making *pH* a challenging metric.

HFO tests which produced the highest SO_2 did show substantially reduced *pH* after exposure, as shown in Figure *7.1-11*.

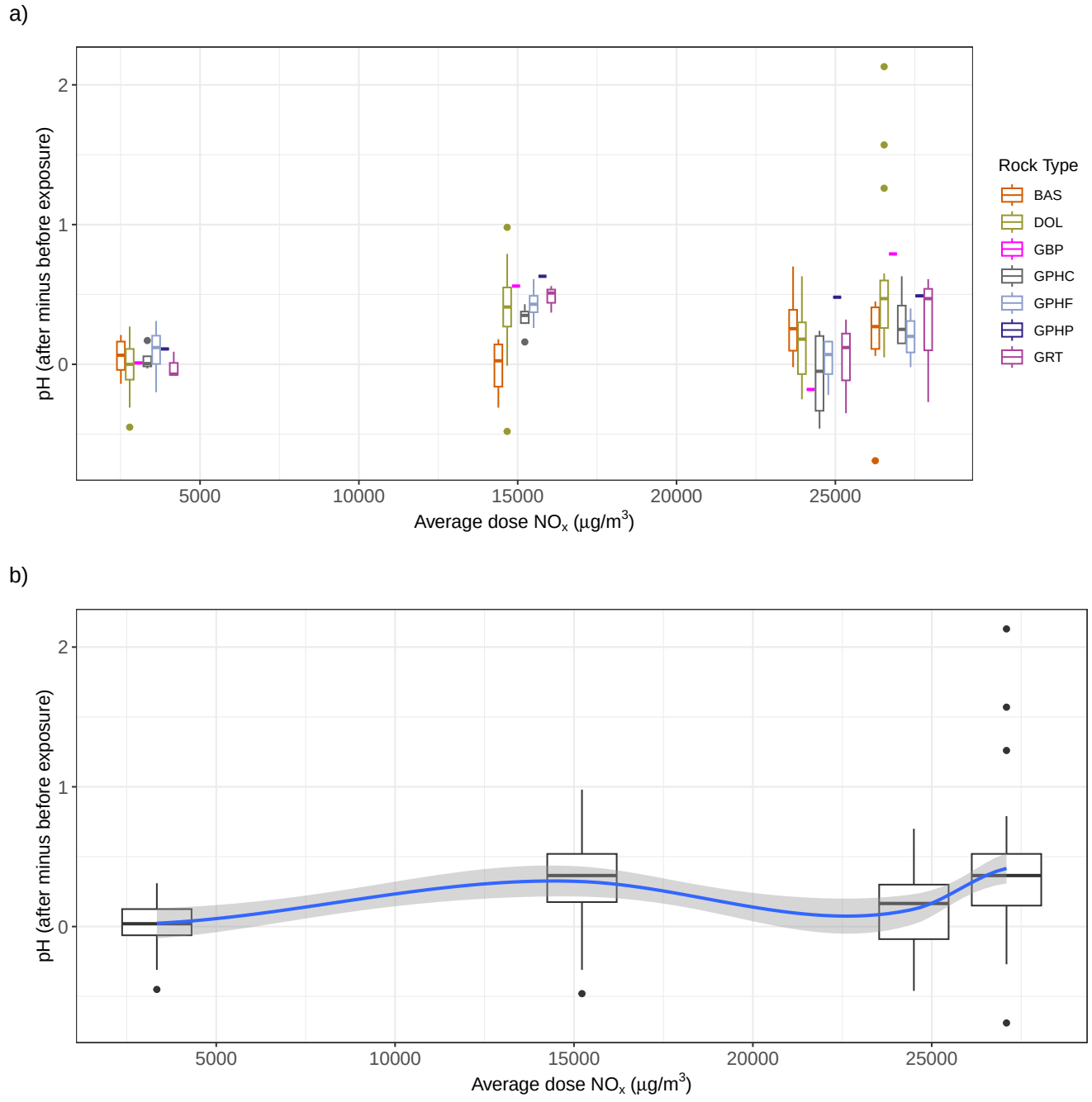

Figure 7.1-8: Boxplots of change in pH (after minus before exposure) against average dose NO_x, (a) broken down by rock type, (b) for all rock types combined. The blue curve is the smoothed conditional mean; grey shading is pointwise 95% confidence interval.

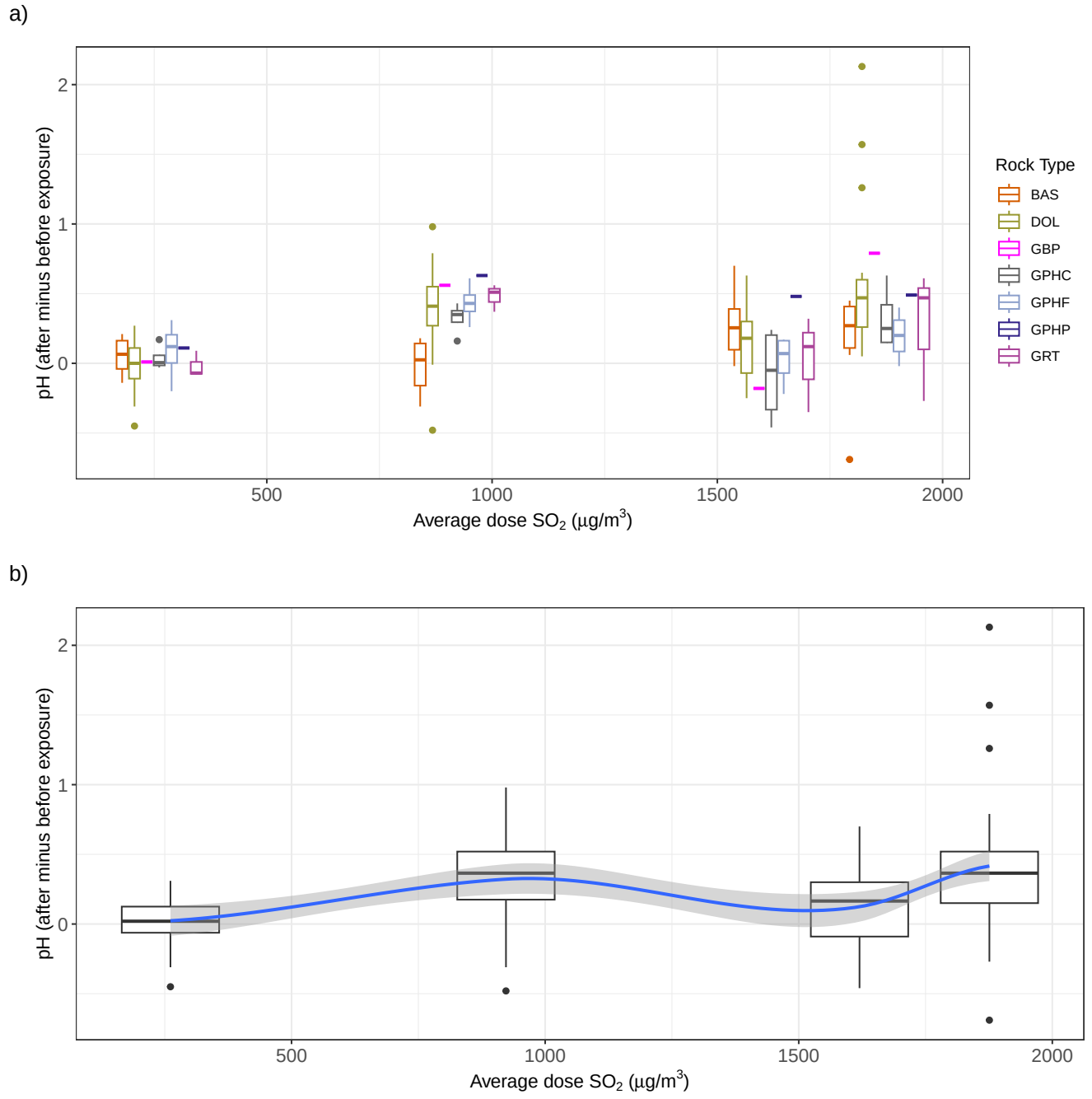

Figure 7.1-9: Boxplots of pH change (after minus before exposure) against average dose SO_2, (a) broken down by rock type, (b) for all rock types combined. The blue curve is the smoothed conditional mean; grey shading is pointwise 95% confidence interval.

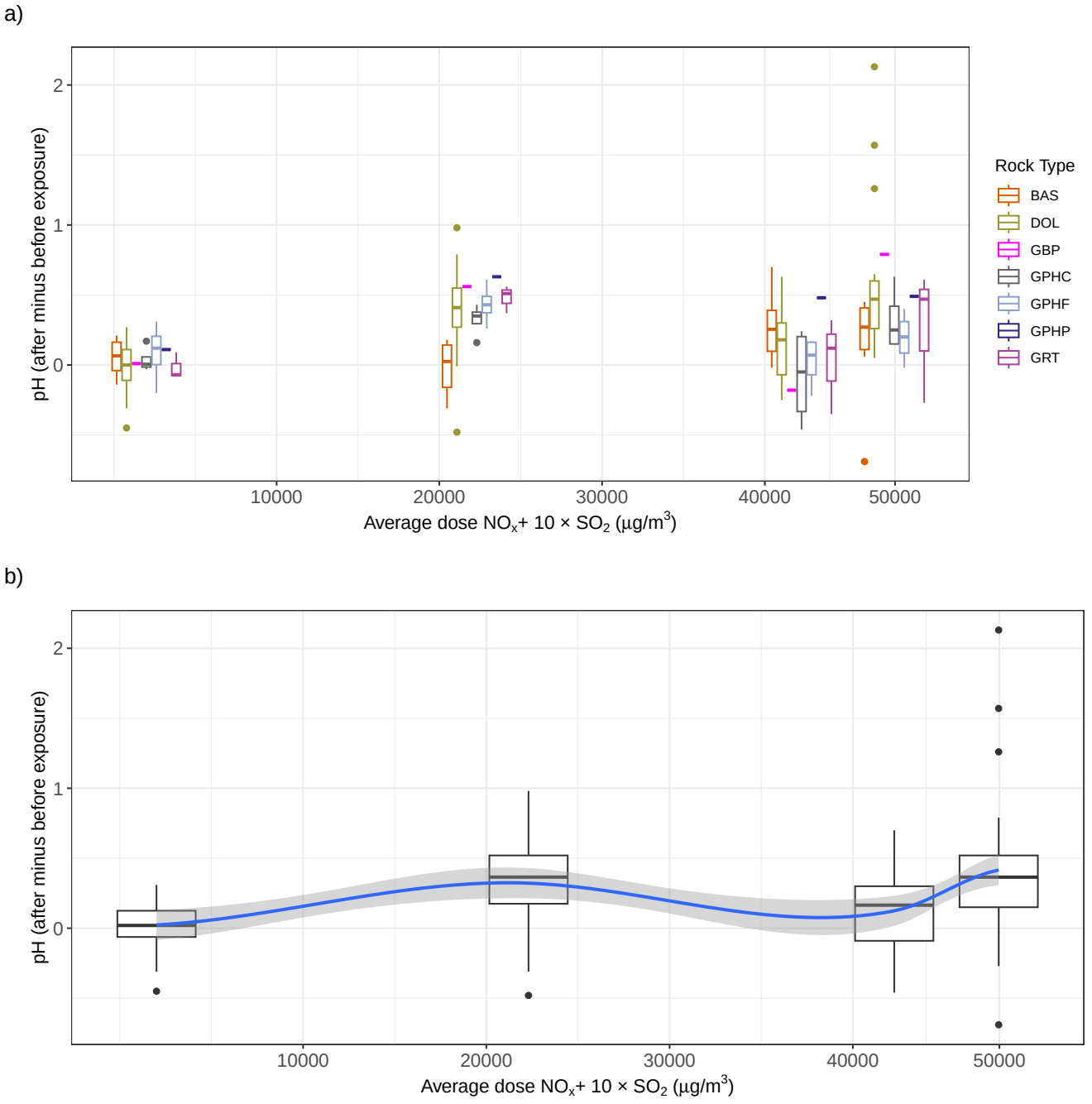

Figure 7.1-10: Boxplots of pH (after minus before exposure) against average dose NO_x plus SO_2. (a) broken down by rock type, and (b) for all rock types combined. The blue curve is the smoothed conditional mean; grey shading is pointwise 95% confidence interval.

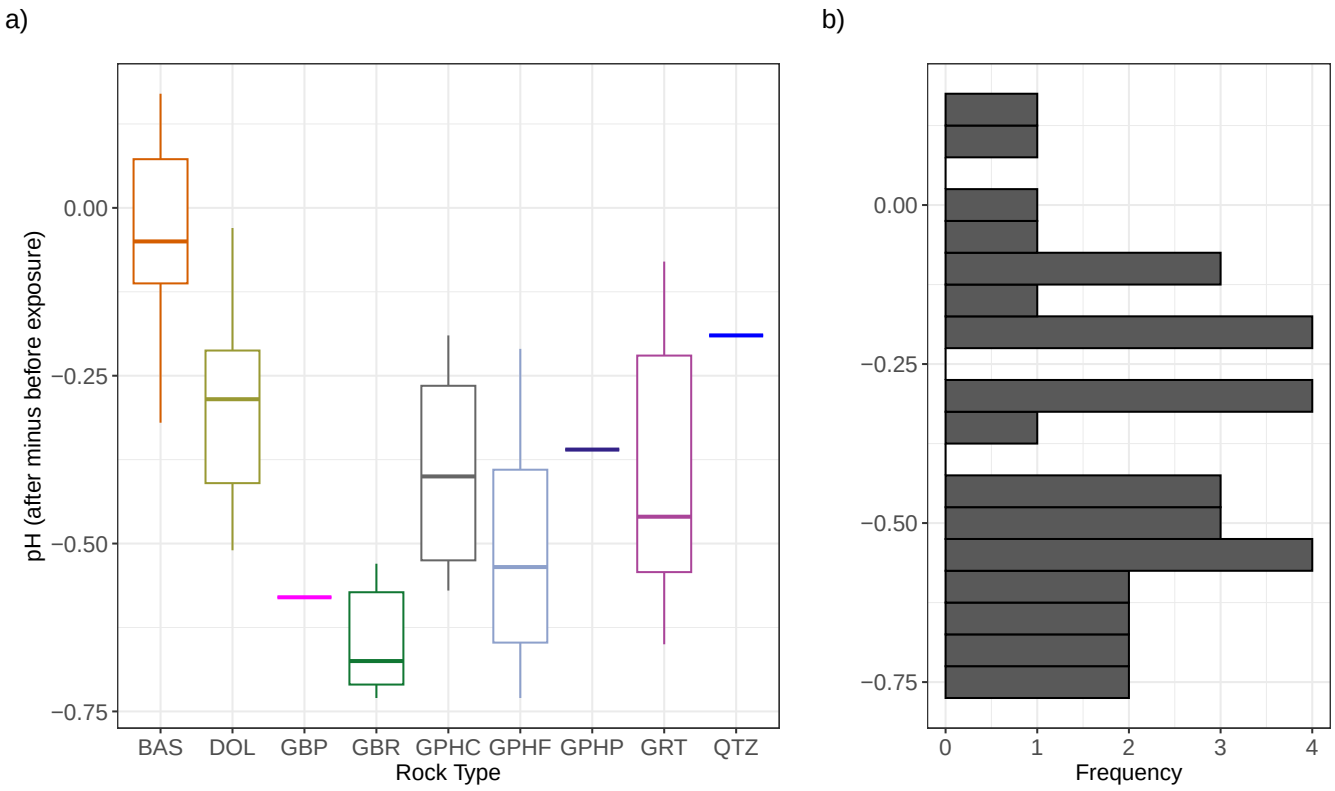

Figure 7.1-11: (a) Boxplots of pH (after minus before exposure) against average dose HFO, broken down by rock type, and (b) histogram of pH (after minus before exposure) for average dose HFO. The average HFO is 7174.744 $\mu g/m^3$ NOx and 1898.46 $\mu g/m^3$ SO_2.

7.1.5.3 Ammonia exposure

Figure *7.1-12* shows boxplots of the response (change in Ca+Mg+Na+K concentration) recorded for the single-dose ammonia experiment (noted in Section 7.1.3).

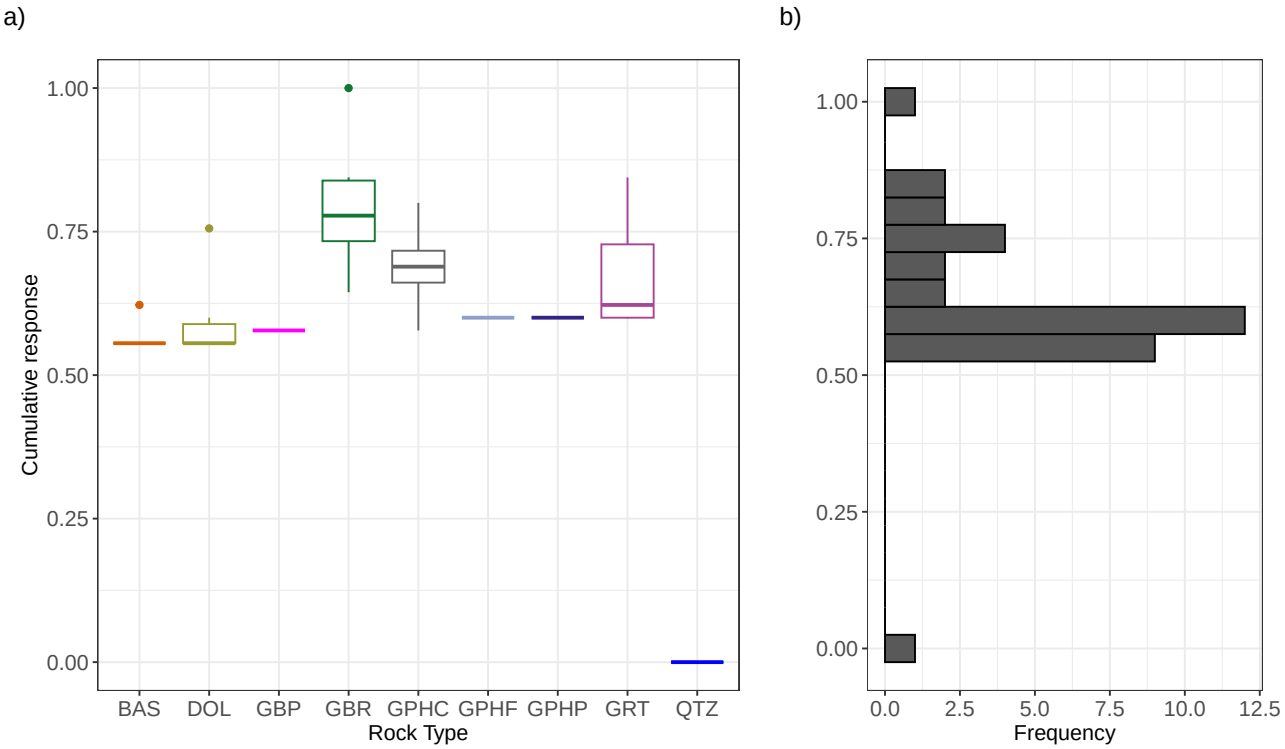

Figure 7.1-12: (a) Boxplots of change in Ca+Mg+Na+K concentration after exposure to ammonia NH_3 broken down by rock type, and (b) histogram of change in Ca+Mg+Na+K concentration after exposure to NH_3. The average dose of NH_3 is 314.752 $\mu g/m^3$.

The median cumulative response (after minus before exposure) for this dose of NH_3 is below 0.25 mg/L, whereas the responses to high doses of NO_x and SO_2 were up to 1.5 mg/L. The response in this experiment is similar or slightly higher than the responses deemed the LOEC in the combustion experiments. It can be observed that the quartz filter demonstrated no response, indicating no contamination.

The two most common rock types, gabbro (GBR) and coarse granophyre (GPHC), have the greatest response to NH_3 in this limited experiment. Fine granophyre (GPHF), polished granophyre (GPHP) and polished gabbro (GBP) showed a weaker effect. Basalt (BAS) showed no effect.

Figure *7.1-13* shows boxplots of the change in *pH* for the ammonia exposure experiment.

Overall, *pH* is increased by exposure to ammonia. The effect is relatively high for basalt (BAS) and granophyre (GPHC, GPHP, GPHF) at about 0.2 to 0.3 units increase, and is smaller for the other rock types. The quartz “blank” shows the equal highest *pH* increase.

Given that the response of this experiment was at or above the response level in the combustion experiments, we can use this exposure level to set a very tentative interim EQC for NH_3 noting that

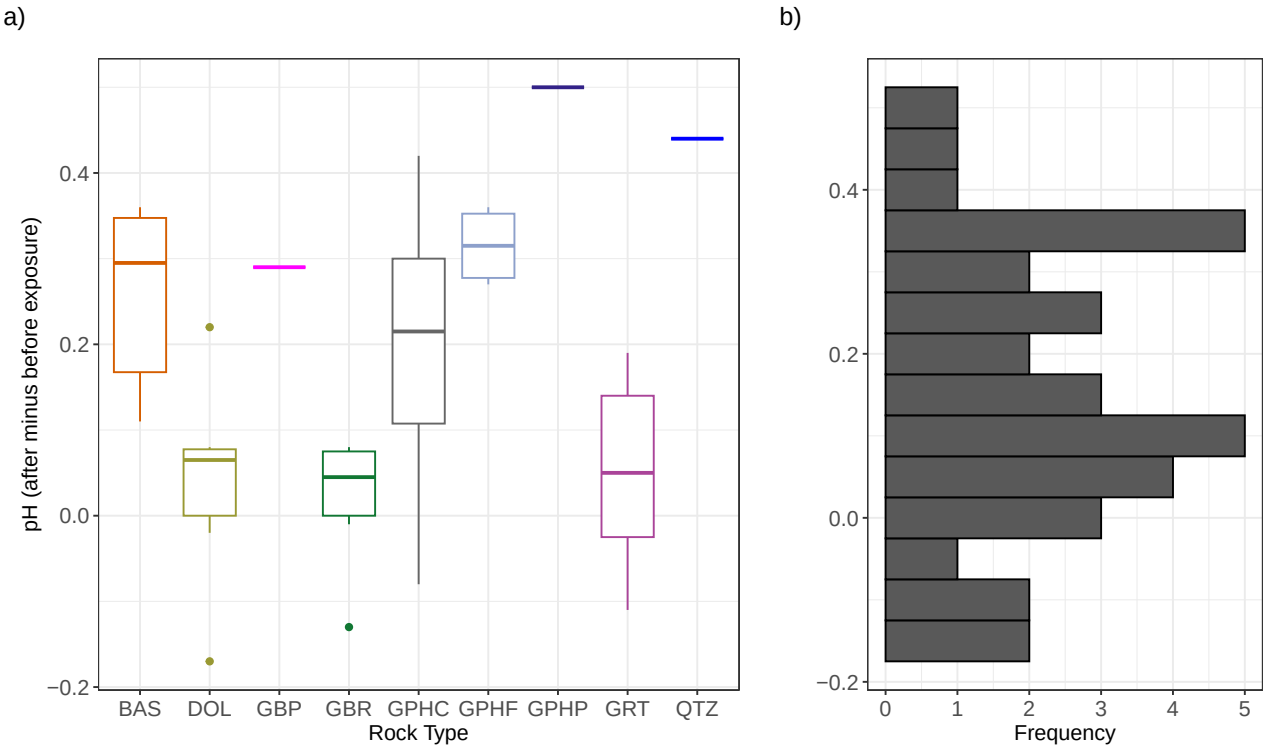

Figure 7.1-13: (a) Boxplots of pH (after minus before exposure) for average dose NH_3 broken down by rock type, and (b) histogram of pH (after minus before exposure) for average dose NH_3. The average dose of NH_3 is 314.752 $\mu g/m^3$.

it will likely be revised once further dose-response experiments can be performed.

7.1.5.4 Confirmation of physical weathering

It is important to verify that the metals detected are the product of dissolution of sensitive minerals. One way to achieve this is confirming no contamination in the chamber experiments through the use of quartz filters and ultrapure water blanks, as above. However the most conclusive means is through microscopy of prepared samples pre- and post-exposure.

Microstructures of plagioclase and pyroxene crystals from a granophyre and gabbro sample, respectively, were investigated by SEM before and after undergoing a full cycle of hydrocarbon weathering experiments. The smooth top surface is an artefact created by coating removal performed on the billet using a VibroMet before exposure. For this reason, observations focused on cavities within minerals, which would not have been modified by the VibroMet polish. Corrugated surfaces and irregular rims within inter-crystal cavities in both minerals provide evidence of the physical consequences of chemical weathering (Figure *7.1-14*).

Notwithstanding the potential effects of changing environmental conditions on the stability of Mn-bearing minerals in the patina (Smith et al., 2022), the holistic investigation of the patina–weathered rind system provided here highlights some previously overlooked important considerations.

At Murujuga, rock lithologies like granophyre, granite and basalt are volumetrically dominated

by feldspars, whereas gabbro and dolerite are volumetrically dominated by pyroxene. Based on microstructural observations, the stability of the weathered rind, and therefore the patina, is strongly controlled by the rates of dissolution of minerals within a fresher rock and weathered rind. Therefore, changes in the chemistry of the fluid phase that affect chemical weathering of the rocks (e.g. changes in *pH*, increased CO_2, organic acids) not only have an impact on the chemical stability of the patina, but also have the potential to modify the natural dissolution rates of minerals within a fresher rock and weathered rind, with consequent changes to the porosity of the weathered rind and the structural stability of the patina.

This work confirms that the processes predicted by the dissolution hypothesis can occur, at least at the exposure levels undertaken in the chamber, albeit at a relatively short duration of six days.

7.1.6 Further work

In terms of chamber exposure experiments, further work will focus on single gas exposures to refine individual dose-response curves and investigation of interactions between air pollutants that may potentiate or mitigate individual responses.

Work will be undertaken to determine whether detection limit has a substantial influence on the determination of the no or lowest effect concentration. More sophisticated statistical approaches to determine these levels, and to determine dose-response curves, will be investigated.

Geomicrobial chamber experiments will also be commenced in the coming months, which will further permit refinement of dose-response curves to account for microbial toxicology.

7.1.7 Discussion

It is well known that “clay minerals” deposited on the rock surface from geogenic dust are an important nutrient source for the microbiome and building block for the patina (under appropriate environmental and climatic conditions). There is also growing evidence in the literature (e.g. McNaughton et al., 2009, 2011) that acid-forming species such as NO_2 may react with clay minerals in environmental dust, moderating pH and reducing potential acidification and associated impacts. Therefore the investigation of these issues, given the high dust levels at Murujuga, are important. Introduction of geogenic dust in the current chamber studies design would however confound the current measurement protocol. Revisions to the experimental design to account for the impact of dust will be required in third year.

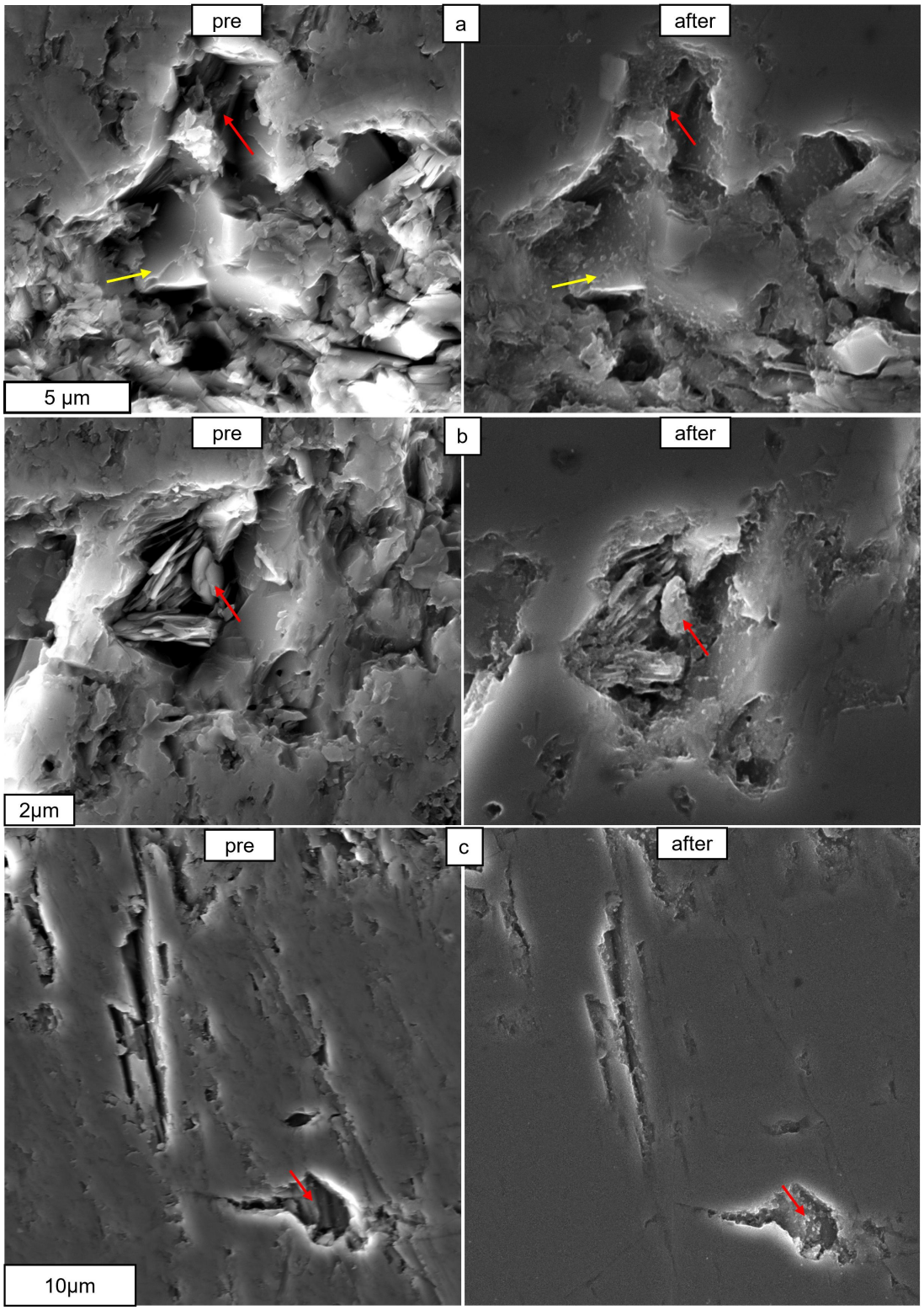

Figure 7.1-14: SE-SEM images of the same regions of a plagioclase crystal. The images are taken before and after a full cycle of chamber studies. The red and yellow arrows point to physical changes induced by chemical alteration. In (a) corrugated surfaces and irregular boundaries are indicative of chemical weathering. In (b) a cluster of clay minerals likely formed by previous hydrolysis of plagioclase is also found dissolving after the experiments. In (c) red arrows indicate physical changes within pyroxene after chamber exposures.

This page is intentionally blank.

7.2 Field colour measurements

This section reports on the measurement of rock surface colour in the field campaigns, and on the statistical analysis of the data obtained.

The Year One Report (Curtin University, 2023) identified concerns about the validity of some of the spectrophotometer data, including the possible sensitivity of the device to ambient temperature. This year, major efforts have been made to ensure the validity of the field colour data, including acquisition of an improved spectrophotometer, improvements to the field technique, development of interactive software to validate the colour data as it is collected, and laboratory experiments to assess the sensitivity of the spectrophotometer to high ambient temperatures. These efforts are also reported in this section.

7.2.1 Field campaigns and colour measurement

The study design calls for repeated measurement of the reflected spectral colour of rock surfaces at exactly the same locations during successive field visits. During the site selection process, the researchers and Rangers identified 54 rock panels across Murujuga that would be measured in this way. On each rock panel there are 10 designated ‘targets’ (precise positions on the panel). The study design requires that each target be measured repeatedly at each visit, yielding at least 10 replicate measurements of each target on each visit.

7.2.2 JAZ instrument

Rock surface colour was measured predominantly using a JAZ spectrophotometer (Ocean Insight, Orlando, FL, USA). The instrument provides its results as data files (with a `.jaz` filename extension) which can be analysed using the commercial software package OceanInsight. The package can display reflectivity spectra as graphical plots and can convert a spectrum to perceptual colour coordinates (L^*, a^*, b^* values) described in Section 7.1.7 of the Year One Report (Curtin University, 2023).

For more penetrating analysis, the ability to analyse the spectral data directly was required. Accordingly, the statistical team and colleagues from the Curtin Institute for Computation have investigated the structure of the JAZ data files.

The JAZ instrument has been superseded and is no longer available new. The technical manual is still available online, but expert support is no longer available. Consequently, some of the following statements represent the statistical team’s best knowledge or interpretation of the available information, rather than being authoritative statements from the manufacturer. The data files contain columns labelled W, D, R, S and P. The statistical team’s interpretation of the manual is that:

- W represents the wavelength of light in nanometres (nm);
- D is the dark field photon count for this wavelength;
- R is the reference (illumination) photon count for this wavelength;
- S is the sample sensed photon count for this wavelength, i.e. colour measurement on the rock target;
- P is the processed (calculated) reflectivity for this wavelength.

The wavelength values W are fractional (rather than integer) values and are not the same sequence of wavelength values in different data files. The team's best explanation is the following:

- The sensor is a linear array of pixels, indexed by the numbers 1 to 2048.
- Each pixel receives photons of light of a particular wavelength, or narrow band of wavelengths.
- Wavelength increases as the pixel index increases.
- However, the precise correspondence between pixel index and wavelength is not constant, because it is affected by the internal state of the device (especially by its temperature).
- The device must be calibrated before use. Whenever the device is recalibrated, the correspondence between pixel index and wavelength is estimated using a cubic polynomial regression, and the coefficients of the regression are stored internally.
- Data files provide the current estimated wavelength value for each pixel according to the last calibration.

That is, the data files are not 'raw' but internally adjusted data. Recalibration changes this internal adjustment.

Future, definitive analysis of these data will need to take into account the presence of errors in the wavelength values themselves, and the changepoints in time when the device is recalibrated. These effects are ignored in the current exploratory analysis which treats the wavelengths as fixed and accurate values.

The manual states that the reflectivity (at each wavelength) is calculated as:

$$P = \frac{S - D}{R - D} \times 100$$

and this formula agrees with direct calculation in the data files.

The JAZ data files provide the photon counts D, R, S and the calculated reflectivity P for a wide range of wavelengths from about 180 to 1030 nm. The visible spectrum is usually taken to be the range between 380 and 780 nm, so the JAZ data reach quite far into the ultraviolet (wavelengths shorter than 380 nm) and infrared (wavelengths longer than 780 nm) bands.

The Year One Report (Curtin University, 2023) identified various anomalies in the field colour data. These anomalies are present (to a diminishing extent) over all seven campaigns; see Appendices *G*.3 and *I*. The statistical team developed interactive software to permit the JAZ operator to check the validity of JAZ data at the time when it is captured. The software was written in R using the `shiny` package (Chang et al., 2024) version 1.7.5. Starting from campaign 6, this interactive software was used in the field. During campaigns 6 and 7, errors in the measurements were still being identified. Consequently, the interactive software was being refined during these campaigns to ensure all faulty targets were identified whilst at the rock art panel; then the expert spectroscopist (Mr Andrew Thorn) could remeasure these targets.

A screenshot of the interactive software for the JAZ instrument is shown in Figure *7.2-1*. To use this interactive software, first the user measures all 10 targets at a rock art panel. Then to check these data using this software, the user selects the site type: AQ, AS, EX or RS. Then the user clicks on the drop down menu to select the site/rock art panel they are currently at. If there are 10 replicate observations for each target, then the user selects "yes" from the drop down menu. If one

or more targets have different numbers of replicates, then the user selects “no”. Then a slide bar for each of the 10 targets appears below the “yes/no” drop down menu. The user slides the bar to the correct number of replicates for each target. Lastly, the user clicks on “Select a folder”; a new window appears where the user can select the folder where the JAZ data is located. Then the software reads in all the data and checks each target for faulty data. On the right-hand side, the software displays which targets are valid and which targets require to be remeasured. At the beginning of campaign 7, the expert spectroscopist requested that the software also display the dark current, reference and percent reflectance over the visible wavelengths (380 to 780 nm).

The JAZ instrument will continue to be used for the remainder of the study program, in order to establish adequate calibration between the JAZ and HDX instruments, and to serve as a backup instrument in the field. However the use of the JAZ instrument will be discontinued at the conclusion of the study when the ongoing Monitoring Program is established.

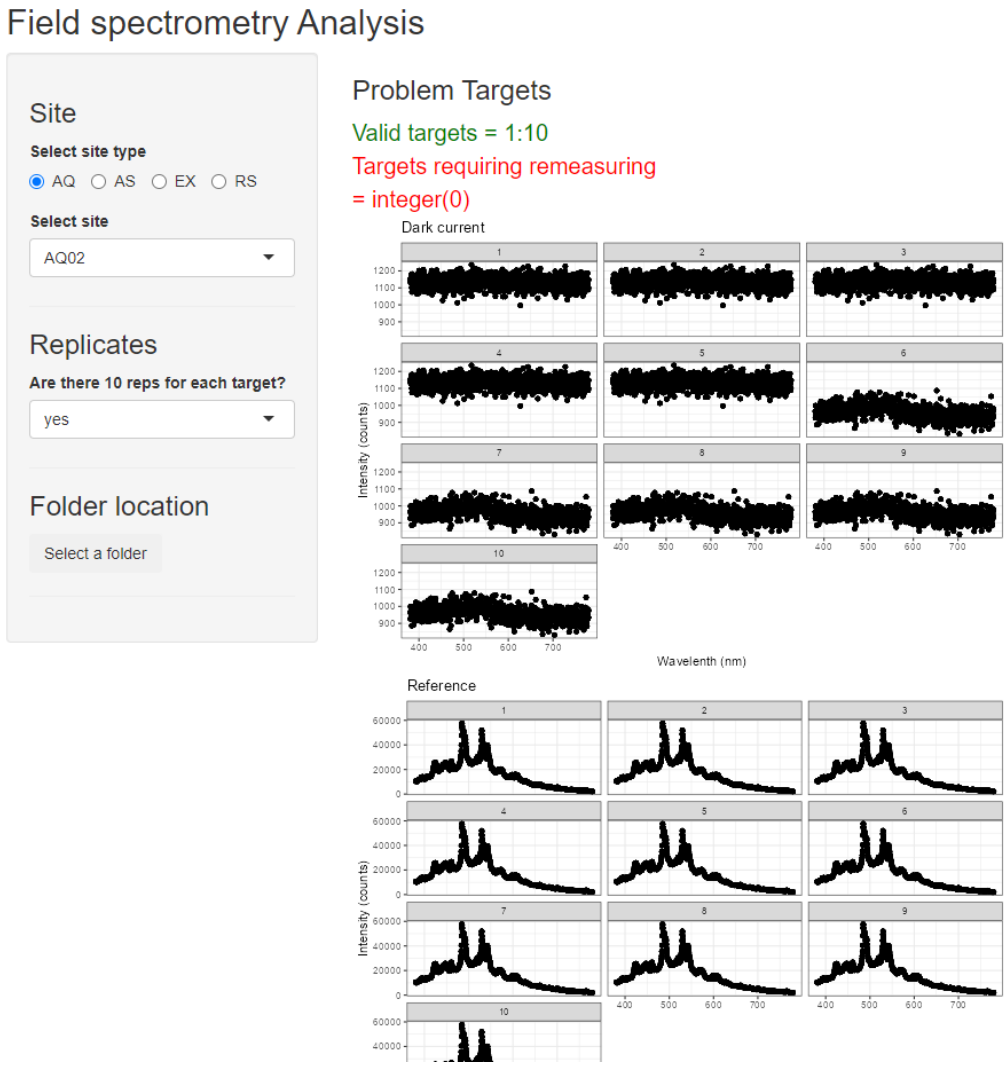

Figure 7.2-1: Screenshot of the interactive software to test the JAZ instrument data in the field

7.2.3 HDX instrument

As the JAZ instrument has been superseded, the project purchased a new spectrophotometer system (HDX, Ocean Insight, Orlando, FL, USA). The product sheet (Ocean Insight, 2024) states that this instrument is engineered to maximise optical resolution, reduce stray light and maintain thermal stability. This instrument also provides data files containing W, D, R, and S columns. From these columns, the percent reflectivity (at each wavelength) is calculated. Unlike the JAZ instrument, the HDX consistently produces the same wavelength values, ranging from 195 to 807 nm.

The HDX instrument was used to take field colour measurements during campaign 7. An interactive software package was developed to assist in taking measurements with the HDX instrument, and to test for any faults on-the-fly whilst taking measurements of the rock art panel. This software is very easy to use and could be used by the MAC Rangers. This interactive software was written in `R` using the `shiny` (version 1.7.5) and `rOmniDriver` packages (Chang et al., 2024; Aphalo, 2024). Unlike the JAZ interactive software, this software is directly connected to the HDX instrument and this software instructs the instrument when to make measurements and when to turn the light in the probe on and off.

Figure *7.2-2* displays screenshots of this HDX software, where (a) is the initial setup page and (b) is the page controlling the field colour measurements. In the initial setup page, the first two steps are the same as the JAZ software. Firstly, the user needs to select which site type, either AQ, AS, EX or RS. Secondly, the user clicks on the "Select site" drop down menu and select which rock art panel ("site") they are about to measure. When a measurement is made, the software automatically creates a ".csv" file containing the site/rock art panel name. Thirdly, they need to click on the "yes/no" button to test if the HDX instrument is connected to the computer. This initialises the connection between HDX and `R`, if the connection fails, e.g. HDX instrument is not connected to the computer, then a red light appears. If the connection is successful, then a green light appears. If the user wishes to change the integration time (time over which the HDX captures incident light), then they click on the drop down menu and select "yes". Below this menu, a slide bar appears and the user can slide to the integration time number they want. The default integration time value is 3,000, this value is recommended in the HDX manual. Lastly, if the user would like any extra information added to the ".csv" file name, other than the site/rock art panel name, then they can type in the box and then click "Save file name".

Once the user has finished the initial setup and there is a connection between the HDX instrument and the computer, then the user should click on the "Field colour measurement" tab (Figure *7.2-2*b). First the user needs to calibrate the instrument. The user firsts clicks on "Store reference". The software will turn on the light in the probe, measure the reference photon counts for each wavelength, and then turn off the light. The reference data undergoes a check by the software to test if the data is faulty, i.e. if the trend is flat then it is deemed faulty (Appendix *G*.3) and a red box appears, otherwise if the data is not faulty then a green box appears. A ".csv" file will automatically be stored, containing all the wavelengths and reference photon counts.

Next the user needs to make a dark current calibration/measurement. When the user clicks on "Store dark current", the software leaves the light off, and measures the dark current photon counts for each wavelength. This data is checked by the software to test if the data is faulty, if the trend is not flat then the data is deemed faulty (Appendix *G*.3) and a red box appears, otherwise if the data

is not faulty then a green box appears. A ".csv" file will automatically be stored, containing all the wavelengths and dark current data.

When the user is ready to measure a target on the rock art panel, in the software they select which target number they are going to measure. To help with positioning the probe onto the target, there is a button to turn the probe light on. When they have finished positioning, then the user clicks to turn the light off. When the user is ready to make a measurement, they click on the "Record spectra" button, the instrument will turn the light on, and take 100 measurements. The percent reflectance data is examined by the software for faults (see Appendix *G*.3), if any faults are detected, a red box is displayed below "Target measurement", otherwise a green box is displayed. Possible faults include extreme weather conditions, the instrument is starting to overheat, the fibre optic cable is broken, or there are connection issues or power supply problems (see Section 7.2.7 for further details). It is recommended to remeasure the target. If the red light still appears again, then the user should restart the instrument and check the fibre optic cable, connections to instrument and computer, and check the batteries. If extreme weather conditions are present, then it is recommended to take the HDX instrument to the air-conditioned car or MAC office, then on another day, to revisit this site and remeasure the targets that had faults. A ".csv" file will automatically be stored, which includes the site name and target number in the file name. The file contains: wavelength (W), dark current (D), reference photon count (R), sample sensed photon count (S), percent reflectance (P), target number, replicate numbers (one to 100), site/rock art panel name and campaign number.

7.2.4 Statistical methodology for analysing percent reflectance

Functional data analysis (FDA) is a statistical methodology used to analyse data sets that consist of functions or curves rather than traditional scalar or vector observations (Ramsay and Silverman, 2005). In traditional statistical analysis, data are often represented as a set of discrete points or measurements. However, in many real-world scenarios, data are collected as functions or curves that vary continuously over some domain (such as time or space). Functional data analysis treats each observed curve or function as a single entity and aims to extract useful information about the overall behaviour of the data set. It focuses on understanding the underlying structure, variability, and relationships within and between the functions themselves, rather than just analysing individual data points.

Here, functional Analysis of Variance (fANOVA) was applied to model the long-term trend in the field colour data (Zhang, 2013). fANOVA is an extension of Analysis of Variance for highly multivariate data, and was used to examine how the mean percent reflectance varies across the campaigns. fANOVA was also used to analyse the laboratory colour measurements of JAZ and HDX instrument. For each replicate or target, a smoothing curve was applied using a cubic spline basis with 20 basis function. This analysis was conducted in `R` using the `fdANOVA` package (Górecki and Smaga, 2019).

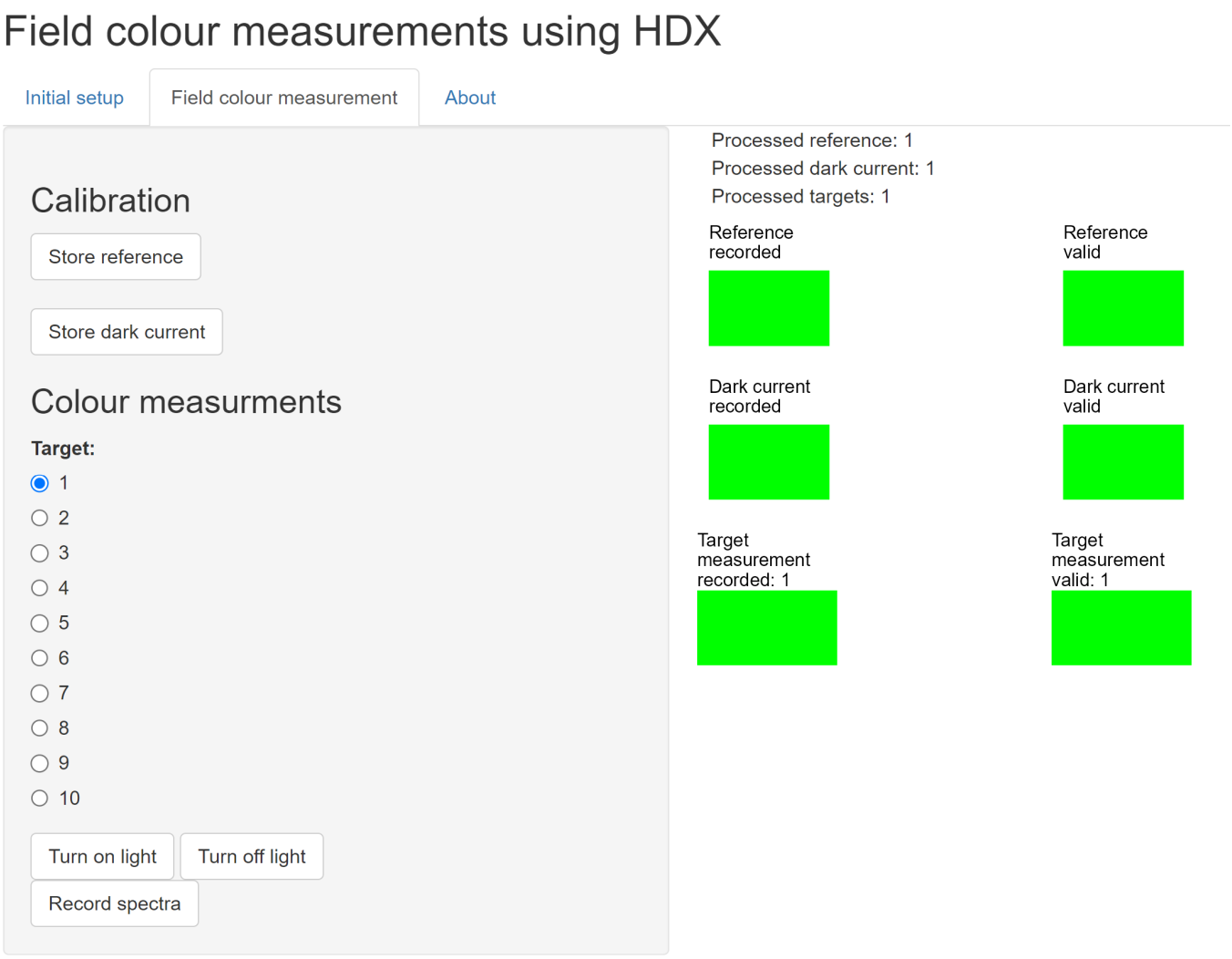

Figure 7.2-2: Screenshot of the interactive software to aid use of the HDX instrument in the field; where (a) initial setup of the HDX and (b) field colour measurements.

7.2.5 Laboratory colour measurements using JAZ instrument

Several experiments using the JAZ instrument were conducted in a laboratory incubator at Curtin University. These experiments are detailed below.

JAZ Test 1: The probe was placed in the incubator and the JAZ instrument was placed outside in ambient conditions. The temperature was raised in 5°C steps from 30-65°C, taking approximately 10 minutes to gain 5°C. The intention was to calibrate just once at the beginning of the experiment. However, the JAZ instrument automatically timed out and switched off twice (at temperature settings 55°C and 65°C), due to long delays between sets of readings. The instrument was recalibrated when it was switched on again. For temperatures 30°C to 50°C, the dark current was not flat, thus deemed faulty (see Appendix *G*.3). Since over 60% of the data were faulty, no plot of the data from this experiment is displayed in this report. However, there is a similar trend in % reflectance for temperatures 55°C to 65°C.

JAZ Test 2: the probe was again placed in the incubator and the JAZ instrument in ambient conditions. The JAZ instrument was recalibrated after each set of 10 readings per temperature increment. The temperature was raised in 5°C steps from 30-65°C. Figure *7.2-3* shows the observed percent reflectance over 250 to 850 nm wavelengths for different temperatures; there is a similar trend in observed percent reflectance for all temperatures.

JAZ Test 3: the probe and instrument were both placed inside incubator for the whole experiment. The Manufacturer advises that the JAZ instrument is functional up to 50°C and displays a saturation message at 50°C, indicating a very precise thermostatic switch to protect the circuitry. In this experiment, there were 5°C increments from 30-45°C. The JAZ instrument was recalibrated after each set of 10 readings per temperature increment.

For this experiment, the observed percent reflectance over 250 to 850 nm wavelengths for the four different temperatures is displayed in Figure *7.2-3*. At 30°C, the dark current was not flat thus was deemed faulty (see Appendix *G*.3). For temperatures 35-45°C, there is a similar trend in observed percent reflectance.

These three experiments demonstrate that the JAZ instrument can operate at high temperatures, even in the extreme air temperatures encountered at Murujuga. However, in such conditions, the rock surface temperatures are often close to or greater than 45°C. Consequently, it is important to store the JAZ instrument in the cool box. It is also important to recalibrate the JAZ instrument before measuring each target on a rock art panel.

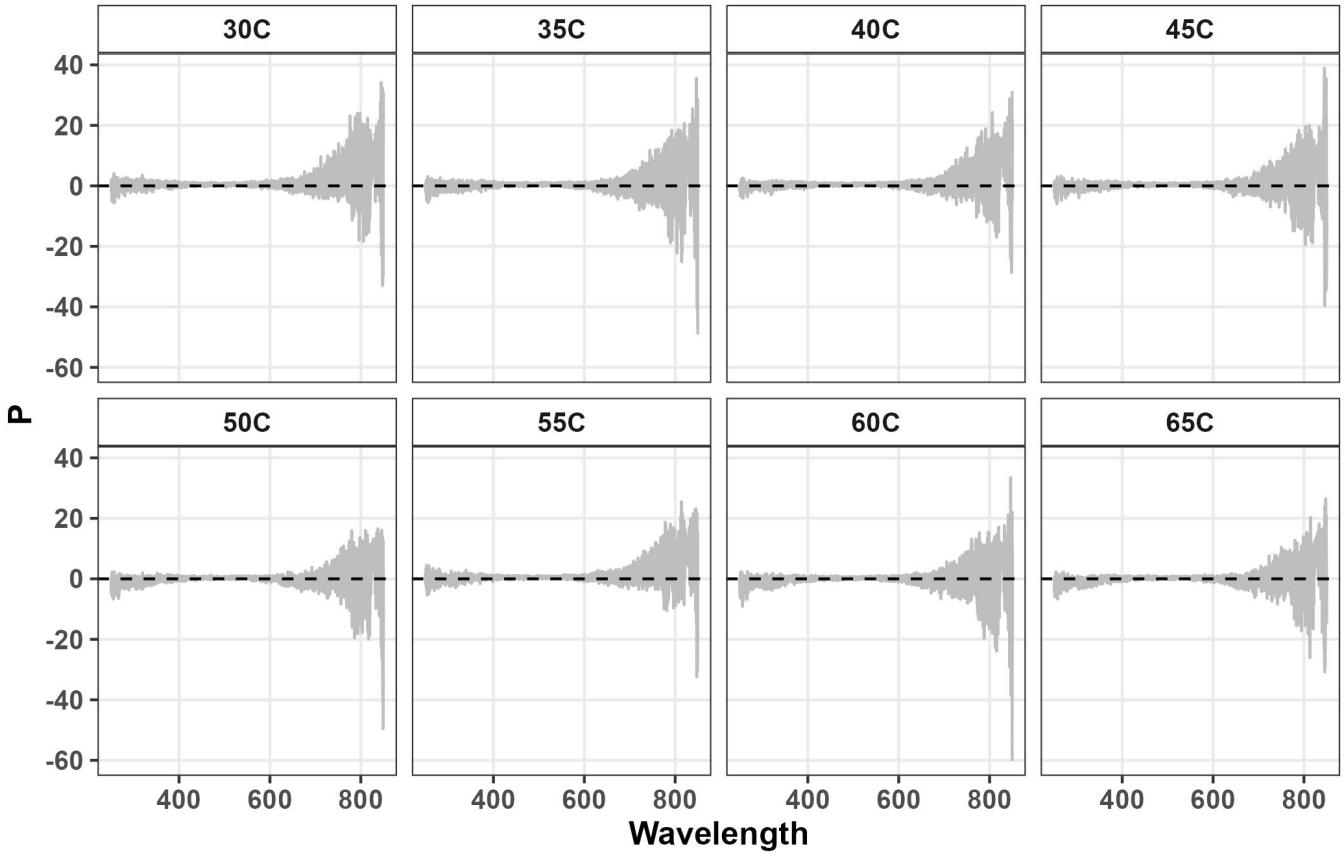

Figure 7.2-3: JAZ Test 2: observed percent reflectance versus wavelength (nm), the probe was in incubator and the JAZ in ambient conditions. The JAZ was recalibrated after each set of 10 readings per temperature increment.

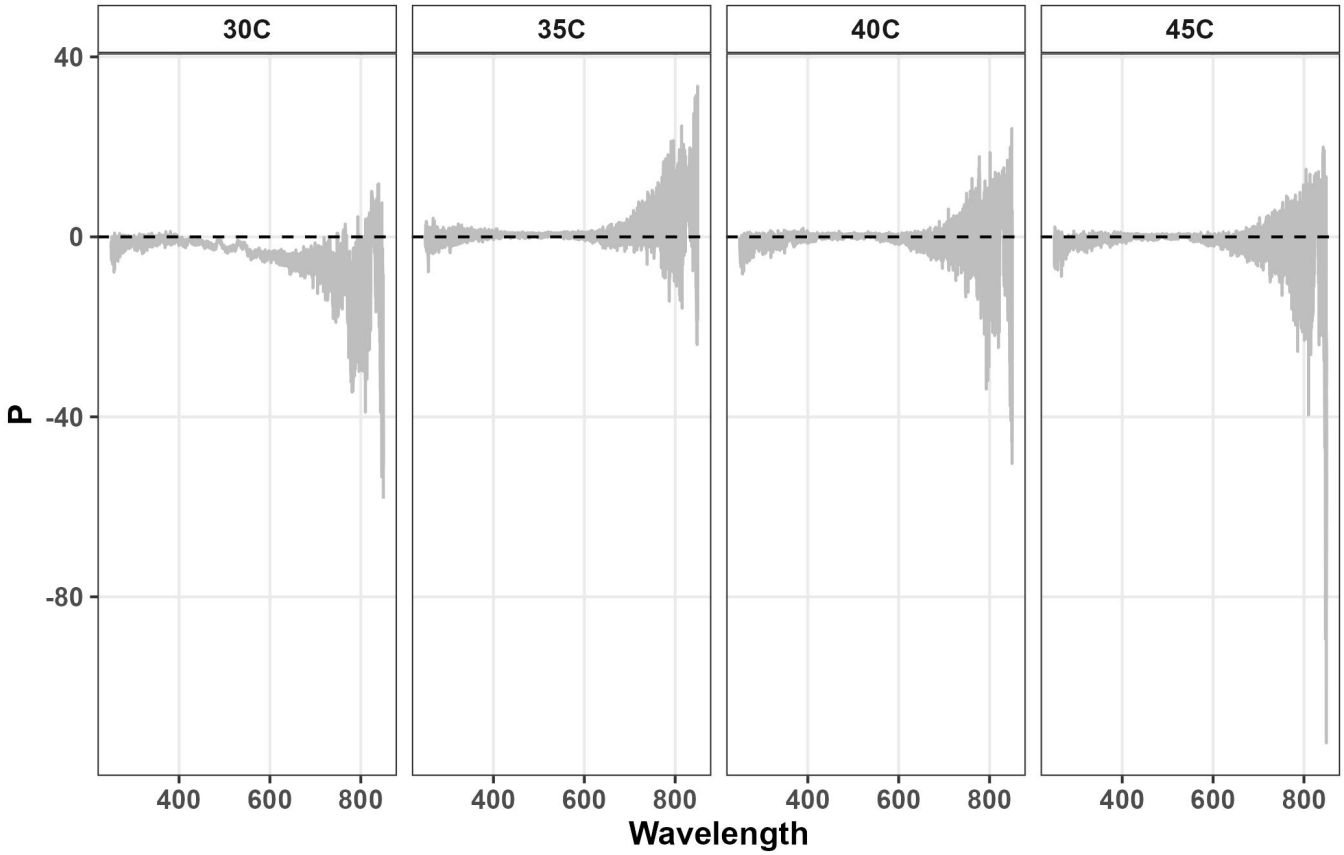

Figure 7.2-4: JAZ Test 3: observed percent reflectance versus wavelength (nm), the probe and JAZ inside incubator for the whole experiment. The JAZ instrument was recalibrated after each set of 10 readings per temperature increment.

7.2.6 Laboratory colour measurements using HDX instrument

A number of experiments with the HDX instrument were conducted in the same laboratory incubator at Curtin University. Details of these four experiments are as follows:

HDX Test 1: The probe was positioned above a black glossy tile in the incubator. The HDX was at ambient temperature for the whole experiment and only calibrated once at the start of the experiment. Measurements started at 31.7°C, 35.8°C, 40°C, and then in 5°C increments until 65°C.

HDX Test 2: Probe, HDX instrument and the light source were all placed inside the incubator. A light target was chosen to assess the saturation threshold more quickly. Measurements were made at 39.4°C, 42°C and 44.5°C. The manual states maximum normal operating temperature is 40°C. Spectrometer was calibrated once at the beginning of the experiment. The ambient temperature started at 36°C. HDX kept operating up to 52°C without giving a saturation message. When the instrument was turned back on after heating to 52°C there was no response, but the instrument started operating normally once cooled in the room to 22°C.

HDX Test 3: The probe was positioned above a black glossy tile in the incubator, plus the calibration thin film (Spectralon reflectance standard, Labsphere, North Sutton, NH, USA) was also in the incubator for the whole time of the experiment. The HDX instrument was at ambient temperature. The spectrometer was calibrated at each temperature increment. The first measurement was taken at 32°C, the second taken at 35°C, then 5°C increments to 65°C. The ambient temperature started at 29°C and finished at 32°C.

HDX Test 4: To test a hypothesis about whether the calibration thin film should be stored in the cool box or kept at ambient conditions matching the probe, this test had the calibration thin film outside the incubator at ambient temperature. The probe was positioned above a black glossy tile in the incubator for the whole experiment. The spectrometer was calibrated at each temperature increment. The first measurement was taken at 26°C, the second taken at 35°C, then like HDX Test 3, 5°C increments to 65°C. Ambient temperature started at 27°C.

Comparing the results of HDX Test 1 (Figure *7.2-5*) with those of HDX Test 3 (Figure *7.2-7*) shows that the calibration of the spectrometer after each temperature step has produced stable estimates. The spectra values from HDX Test 3, excluding outliers, consistently range between zero and 15 for all temperatures. In contrast, the results from HDX Test 1 show an increasing trend in percent reflectance with temperature. This trend is particularly pronounced for wavelengths between 550 and 750 nm. Therefore, it is important that the HDX is calibrated after measuring each target on a rock art panel.

The aim of HDX Test 2 was to test if the HDX instrument could operate in Murujuga without being stored in a cooling system. Figure *7.2-6* clearly demonstrates an increasing trend in percent reflectance as the temperature increases. Therefore, the HDX instrument should be stored in a cooling system when conducting measurements at Murujuga.

The objective of HDX Test 3 and HDX Test 4 was to test a hypothesis about whether the calibration thin film should be stored in the cool box or kept at ambient conditions matching the probe. Figure *7.2-7* and Figure *7.2-8* demonstrates a striking similarity in percent reflectance between

HDX Test 3 and HDX Test 4. Consequently, the location of the calibration thin film becomes inconsequential.

These experiments demonstrate that the HDX instrument could be re-activated at every temperature up to 51°C. This is an adequate operating range for Murujuga. The JAZ has a thermal shut-off at 50°C. The cooling system can keep the HDX instrument at 30°C.

fANOVA was applied to HDX Test 3, to assess whether there were any differences among the mean percent reflectance curves recorded at different temperatures. Figure *7.2-9* shows that 32°C was markedly higher than the other temperatures. All other temperatures had a similar trend between wavelengths of 300 to 700 nm.

In conclusion, these experiments demonstrate that the HDX instrument can also operate at high ambient temperature, even at the extreme temperatures encountered at Murujuga. Similar to the JAZ instrument, it is important to store the HDX instrument in the cool box. Additionally, it is important to recalibrate the HDX instrument before measuring each target on a rock art panel.

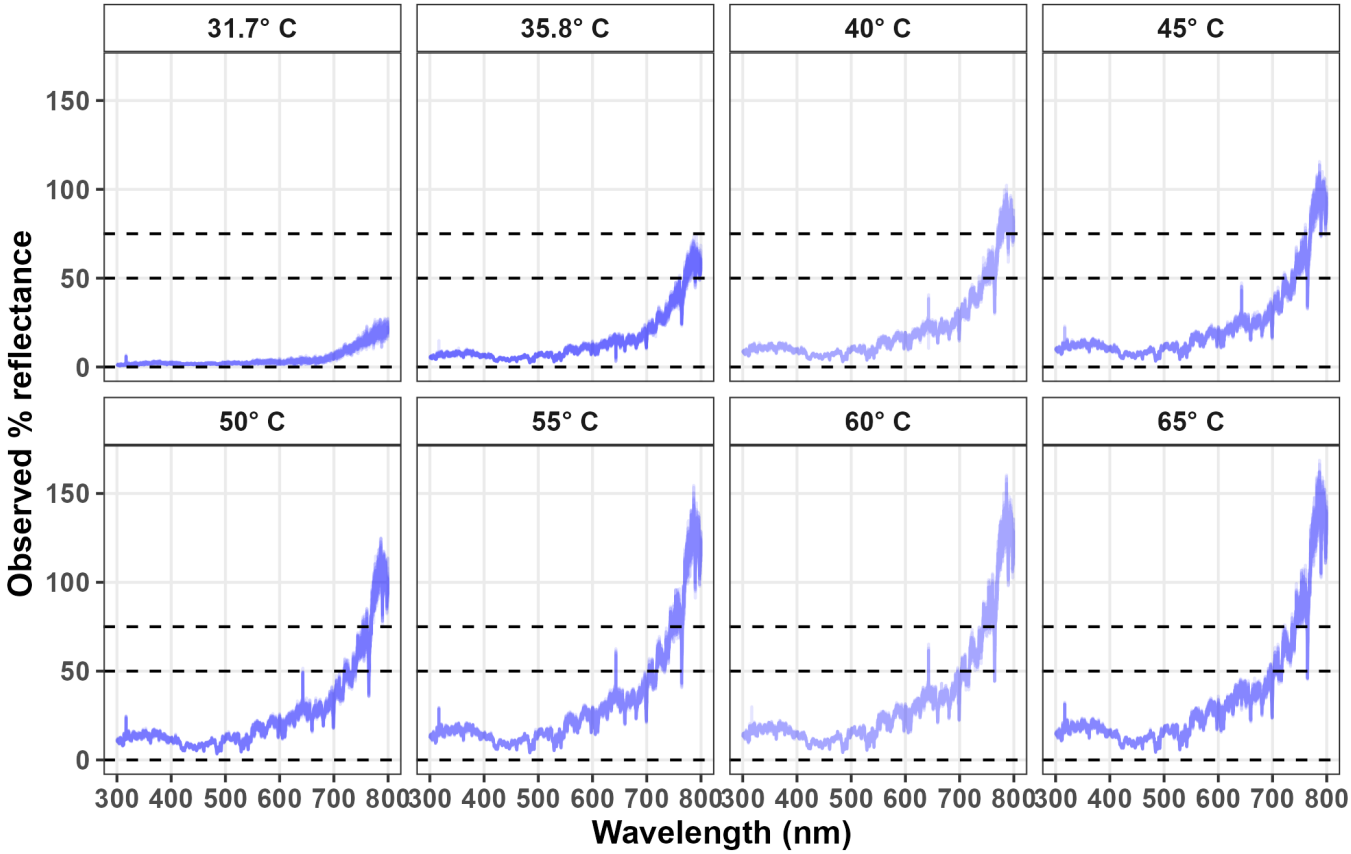

Figure 7.2-5: HDX Test 1: observed percent reflectance versus wavelength (nm). The HDX placed outside the incubator, probe applied to black glossy tile inside the incubator; and HDX calibrated once at the start. The blue colour variation in the plots is due to the differing number of replicates at different temperatures.

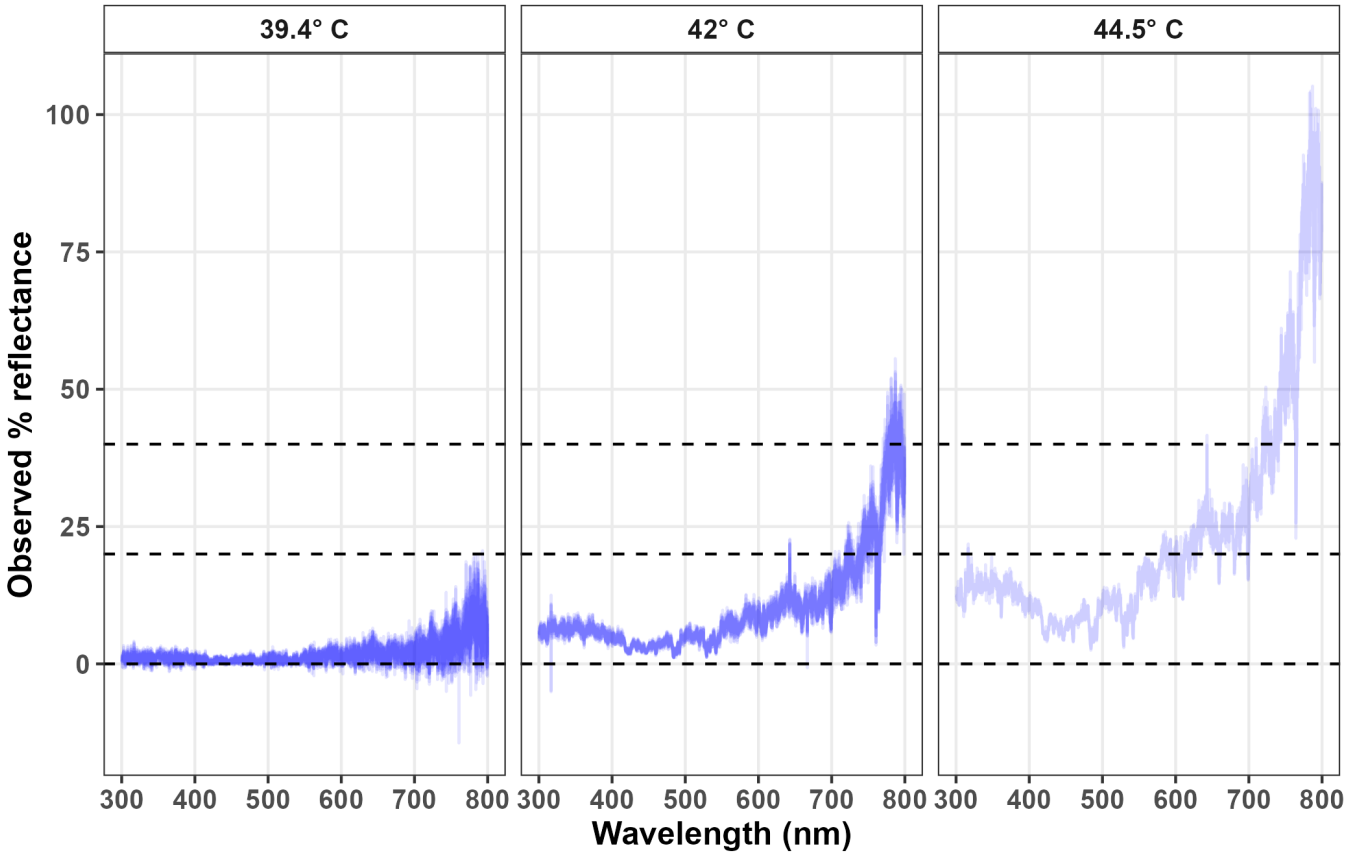

Figure 7.2-6: HDX Test 2: observed percent reflectance versus wavelength (nm). The probe, HDX and light source placed inside the incubator. HDX calibrated once at the start of the experiment. The blue colour variation in the plots is due to the differing number of replicates at different temperatures.

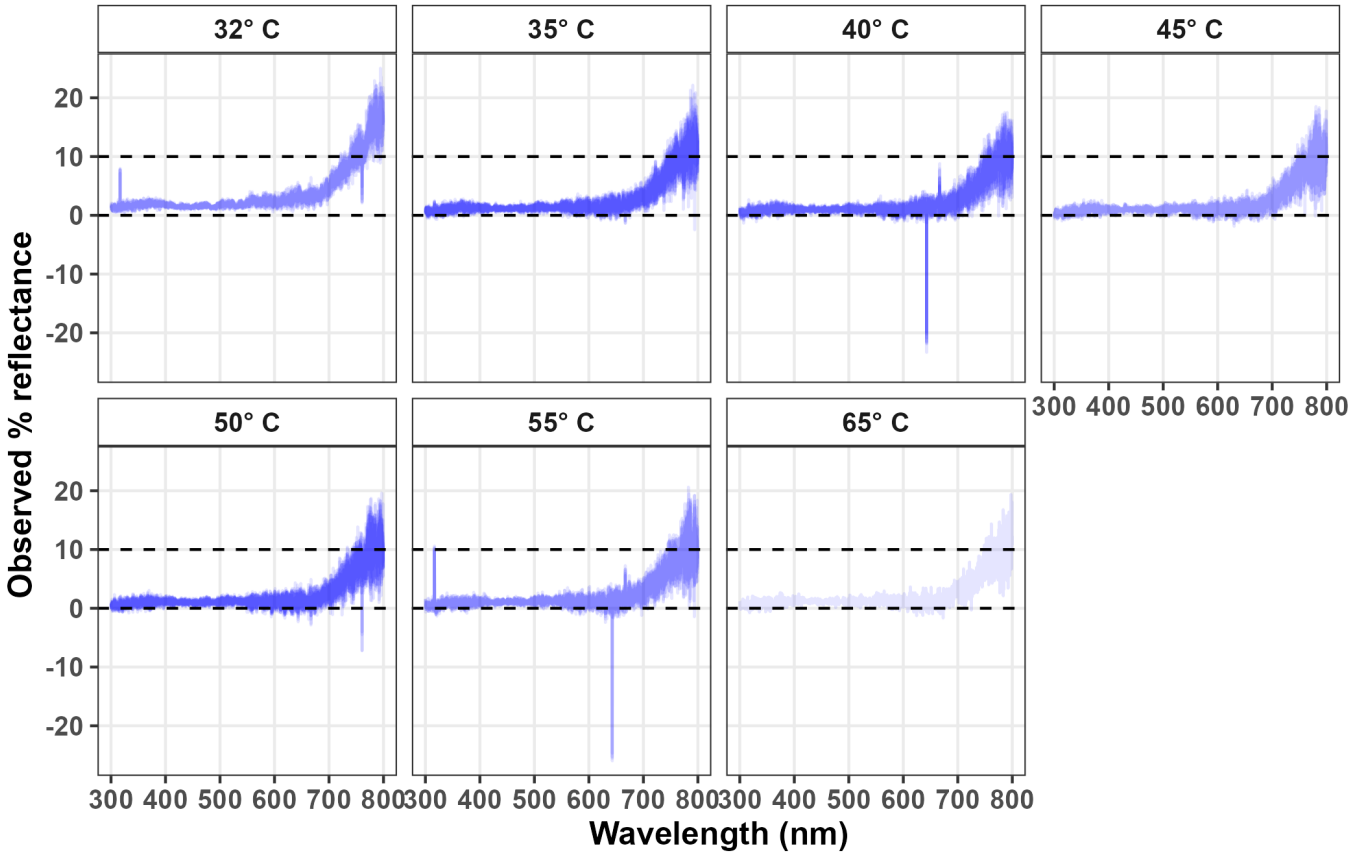

Figure 7.2-7: HDX Test 3: observed percent reflectance versus wavelength (nm). The calibration thin film and the probe applied to black glossy tile in incubator for entire experiment; and the HDX calibrated after each temperature increment. The blue colour variation in the plots is due to the differing number of replicates at different temperatures.

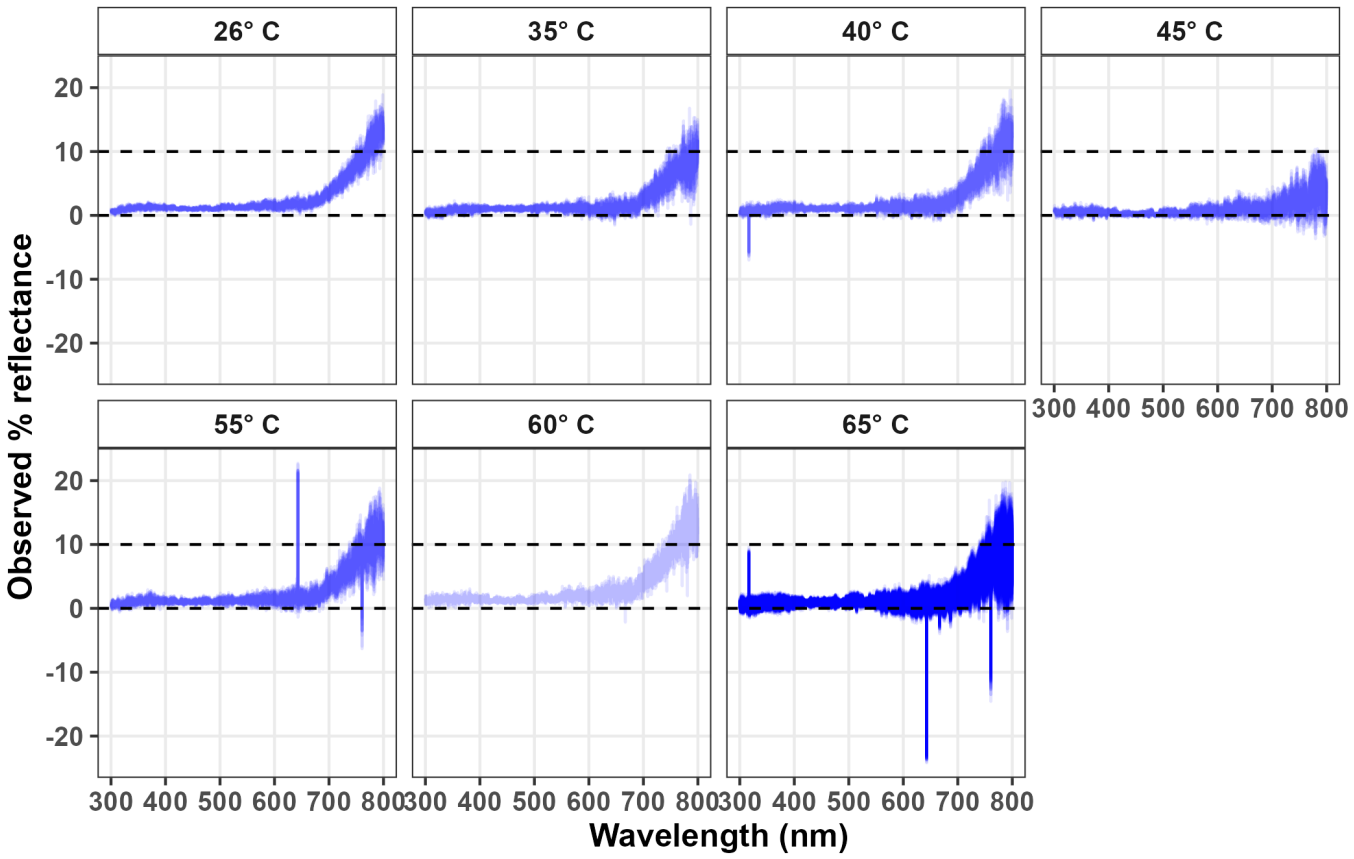

Figure 7.2-8: HDX Test 4: observed percent reflectance versus wavelength (nm). The probe applied to black glossy tile in incubator for entire experiment; calibration thin film in ambient temperature for entire experiment; and the HDX calibrated at each temperature increment. The blue colour variation in the plots is due to the differing number of replicates at different temperatures.

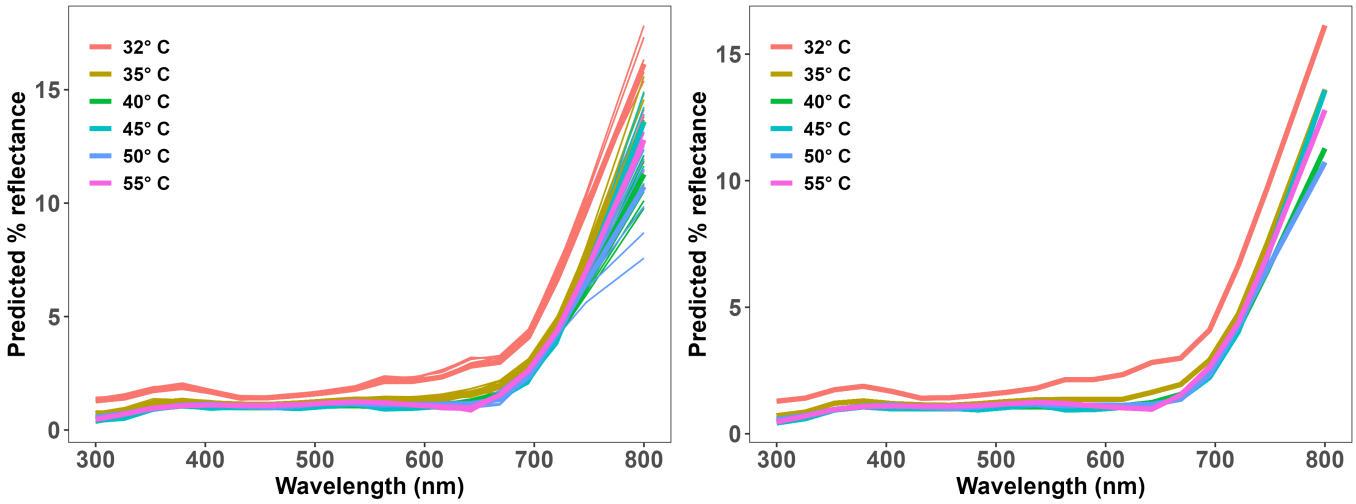

Figure 7.2-9: Predicted percent reflectance vs wavelength (nm) for HDX Test 3. The left panel has a smooth curve for each replicate for each temperature; and right panel has a smooth curve for each temperature over all replicates.

7.2.7 Campaign 7 and HDX instrument problems

At the beginning of campaign 7, the expert spectroscopist (Mr Andrew Thorn) started using the HDX instrument. Below is a list of problems which he noted with the instrument.

- The HDX was struggling to operate in the extreme weather conditions in the field, including very hot air temperatures and rock surfaces.
- Optic fibres were damaged, one of seven peripheral light transmitters stopped working. The identical optic fibre from the JAZ was used for remaining measurements and a new cable has been ordered.
- The connection between the HDX spectrometer, light source and computer were very unreliable.
- Challenges arose with the power supply of the HDX instrument.

The chief issue appears to be connectivity with a proprietary multi-pin connector embedded in the HDX circuit board, which experienced failures under the conditions at Murujuga. To address this, the instrument was returned to the vendor (Quark Photonics) to be inspected. the faults could not be replicated by the vendor. The instrument is now being shipped to Curtin University. Before the next campaign, the MRAMP electronics technicians will investigate and develop a reliable solution.

Because of the above problems, early in campaign 7 the expert spectroscopist switched to using the JAZ instrument and 91% of rock art panels were measured using this instrument.

Nine sites were measured by the HDX instrument. Three sites were measured by both instruments. These sites were:

- AQ12_BAS
- RS10_GBR1
- RS10_GBR2.

7.2.8 Analysis of the field colour measurements using the JAZ instrument

Over the seven campaigns, a total of 334 rock art panels have been measured by the JAZ instrument (Table *7.2-1*). After campaign 4, each RS site was measured only once in either campaign 5, 6 or 7 (Section 3.3). Over the seven campaigns, almost 65% of the rock art panels were deemed valid. For campaign 1, only 28% of rock art panel measurements were deemed valid. By campaign 7, 97% of the JAZ measurements were deemed valid.

During campaigns 5, 6 and 7, the field colour measurements were sent to the statistical team either nightly or within a few days after the expert spectroscopist (Mr Andrew Thorn) visited the rock art panels. The data were analysed and additional faults were identified. If time permitted, Mr Thorn would revisit the rock art panels to remeasure the targets identified as faulty. This iterative process allowed for the continual refinement of the JAZ interactive software, incorporating additional fault detection criteria.

In campaign 7, the interactive software identified 19 rock art panels with faults, and Mr Thorn was able to remeasure these panels in a single visit. Unfortunately, one rock art panel measured by the JAZ instrument was deemed faulty by the statistical team but could not be revisited. This rock art panel was measured fairly early in campaign 7, and the dark current was not flat, resulting

in fluctuating percent reflectance values, which were deemed faulty (refer to Appendix *G*.3). Fortunately, this rock art panel was measured early in the campaign, and the JAZ interactive software was updated the next day to detect this specific fault.

Table 7.2-1: Total number of valid, total number measured and percentage of valid rock art panels measured at each of the 7 campaigns.

	Campaign 1	Campaign 2	Campaign 3	Campaign 4	Campaign 5	Campaign 6	Campaign 7 JAZ	Campaign 7 HDX	Total JAZ
Total valid	15	37	37	35	28	23	36	8	211
Total measured	54	54	54	54	41	40	37	9	334
Percent valid	27.78%	68.52%	68.52%	64.81%	68.29%	57.50%	97.30%	88.89%	63.17%

Figure *7.2-10* shows an example of four rock art panels measured by the JAZ instrument for campaigns 1 to 7. Some of the lines have an irregular “wiggly” appearance, due to large variation between the 10 targets, resulting in a fluctuating predicted percent reflectance.

For the rock surface AQ03_GPH, campaigns 4 and 5 have a similar trend over 300 to 700 nm wavelengths, with campaign 6 having the highest predicted percent reflectance overall wavelengths (Figure *7.2-10*a). Campaign 3 has a “wiggly” line because there was a big variation between targets. Note for AQ03_GPH, campaigns 1, 2 and 7 were not included in Figure *7.2-10*a) because of faulty data.

For AQ11_GPH, campaign 2 has the lowest predicted percent reflectance overall wavelengths, campaign 1 is roughly in the middle, and campaign 6 has the highest predicted percent reflectance (Figure *7.2-10*b). During campaign 7, AQ11_GPH was measured by the HDX instrument in the morning and afternoon, see Figure *7.2-12*.

Results for AQ12_BAS are similar to those for AQ11_GPH, with campaign 2 having the lowest predicted percent reflectance overall wavelengths, campaign 1 is roughly in the middle, and campaign 7 having the highest predicted percent reflectance (Figure *7.2-10*c). Campaign 3 was not included because of faulty data.

For EX06_GPH, ignoring campaign 5, this rock art panel is similar to AQ11_GPH and AQ12_BAS, with campaign 2 having the lowest predicted percent reflectance overall wavelengths and campaign 7 having the highest predicted percent reflectance (Figure *7.2-10*d). Campaign 1 had faulty data, thus was not included in this plot.

7.2.9 Analysis of the field colour measurements using the HDX instrument

Figure *7.2-11* shows an example of a rock art panel (AQ08_GPH) measured by the HDX instrument during campaign 7. The other eight rock art panels that were measured by the HDX had similar

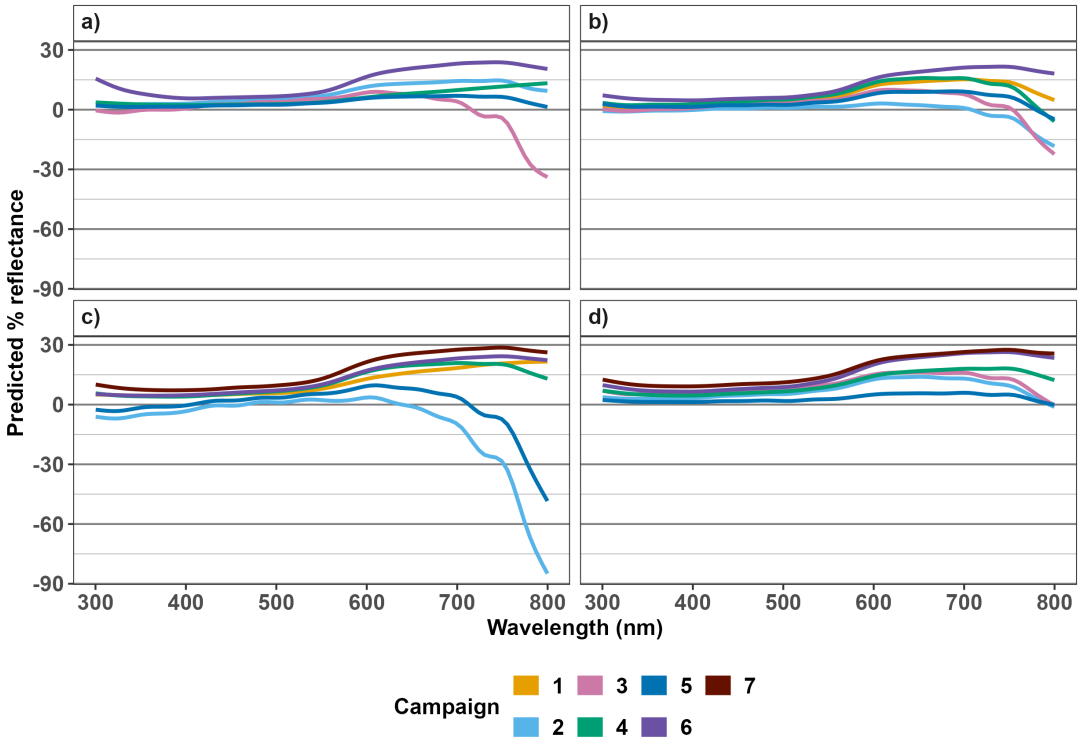

Figure 7.2-10: Predicted percent reflectance vs wavelength (nm) for (a) AQ03_GPH, (b) AQ11_GPH, (c) AQ12_BAS and (d) EX06_GPH, with a different colour for each campaign.

trends. Unfortunately, for AQ03_GPH, three targets were faulty due to sample photon count (S column) recorded zero for all wavelengths (see Appendix *G*.3). Based on these measurements, the HDX interactive software was updated to include testing for this fault.

In campaign 7, two measurements were taken with the HDX instrument at AQ11_GPH, one in the morning and the other in the afternoon. The relative humidity in the morning was 100-84% and dropped to around 67% in the afternoon; the surface moisture in the morning was 18% and in the afternoon was 12-14%. Figure *7.2-12* shows percent reflectance versus wavelength (nm) for the morning and afternoon measurements. All targets except for target nine, the morning measurements were lower than the afternoon measurements. Future experiments in the incubator at Curtin University should focus on investigating the effects of humidity on HDX measurements.

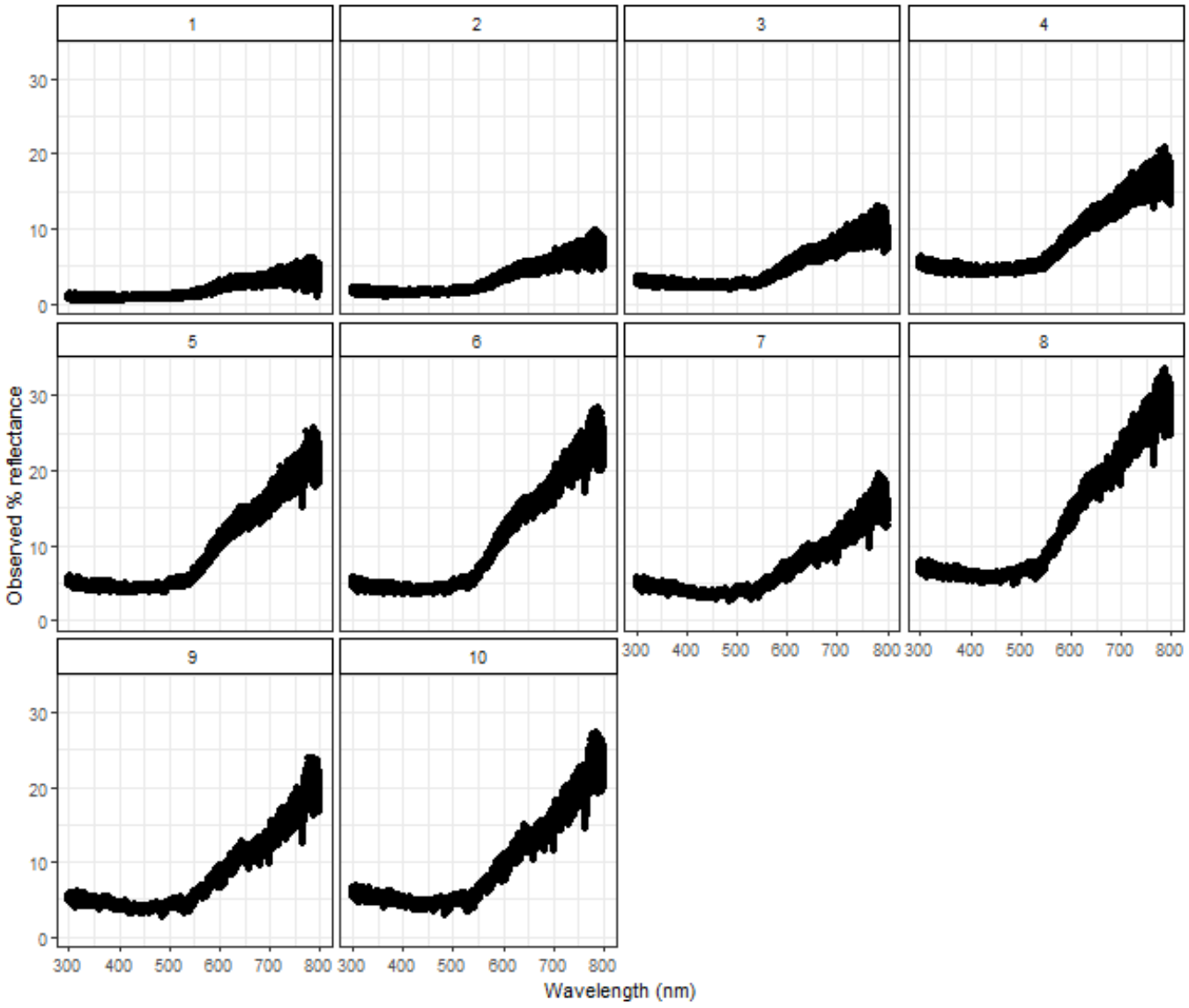

Figure 7.2-11: Art panel AQ08_GPH observed percent reflectance versus wavelength (nm), where each panel is a target number.

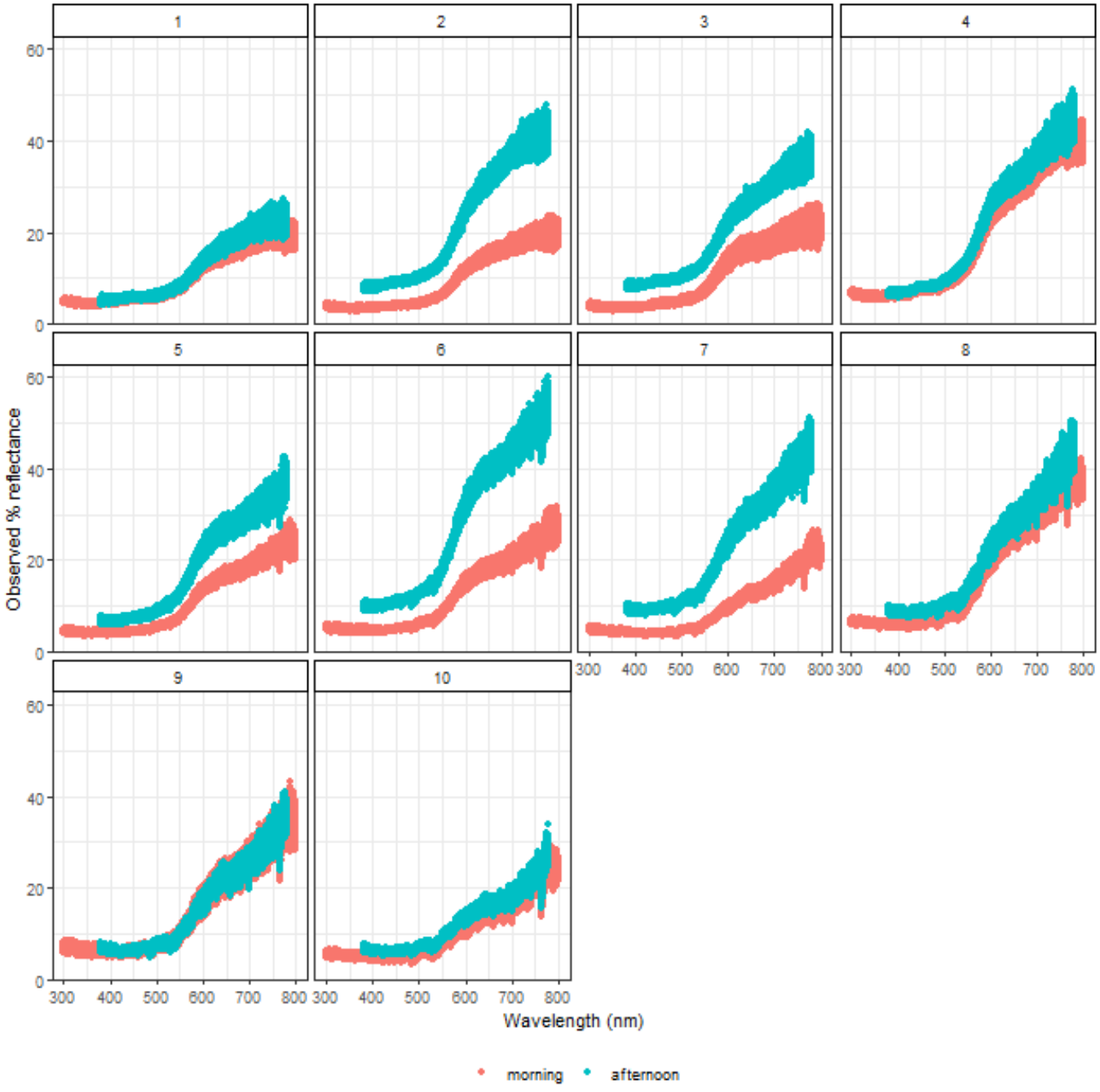

Figure 7.2-12: Art panel AQ11_GPH observed percent reflectance versus wavelength (nm), where red were the morning measurements and teal the afternoon measurements, each panel is a target number.

7.2.10 Comparison between JAZ and HDX instrument for campaign 7

As discussed above in Section 7.2.7, three rock art panels were measured by both the JAZ and HDX instrument during campaign 7. Regrettably, the data recorded from rock art panel RS10_GBR1 was deemed faulty because the dark current was not flat (refer to Appendix *G*.3), resulting in fluctuating percent reflectance values. Unfortunately, the test of the dark current was not in the JAZ interactive software when the expert spectroscopist (Mr Andrew Thorn) visited this site. This test was added to the software the following day. Consequently, it is not possible to compare the results obtained from the two instruments for RS10_GBR1.

Figure *7.2-13* shows the predicted percent reflected versus wavelength (300 to 700 nm) for rock art panel AQ12_BAS. Note campaign 3 was excluded due to faulty data. For campaigns 2 and 5 the lines are “wiggly”; this is again due to large variation between the 10 targets, resulting in a fluctuating predicted percent reflectance. For campaign 7, a comparison between the two instruments shows that between the 300 to 600 nm wavelengths the predicted percent reflectance for the HDX is about 10% higher than the JAZ; at 700 nm the HDX is 30% higher than the JAZ.

Figure *7.2-14* shows the predicted percent reflected versus wavelength (300 to 700 nm) for rock art panel RS10_GBR2. Note that campaign 2 was excluded due to faulty data. This rock art panel was not recorded in campaigns 5 and 6 (see Section 3.3). For RS10_GBR2, campaigns 1 and 3 are fairly flat over 300 to 700 nm. Just comparing the JAZ lines, campaigns 4 and 7 have a similar trend, but campaign 4 the predicted reflectance is about 5% lower at 300 nm wavelength and 15% lower at 700 nm. Now, comparing the JAZ versus HDX for campaign 7, at 300 nm wavelengths the predicted percent reflectance is the same. But starting around 400 nm wavelengths, the JAZ starts having a higher predicted percent reflectance, and at 700 nm the JAZ has a predicted percent reflectance of 15% higher than the HDX.

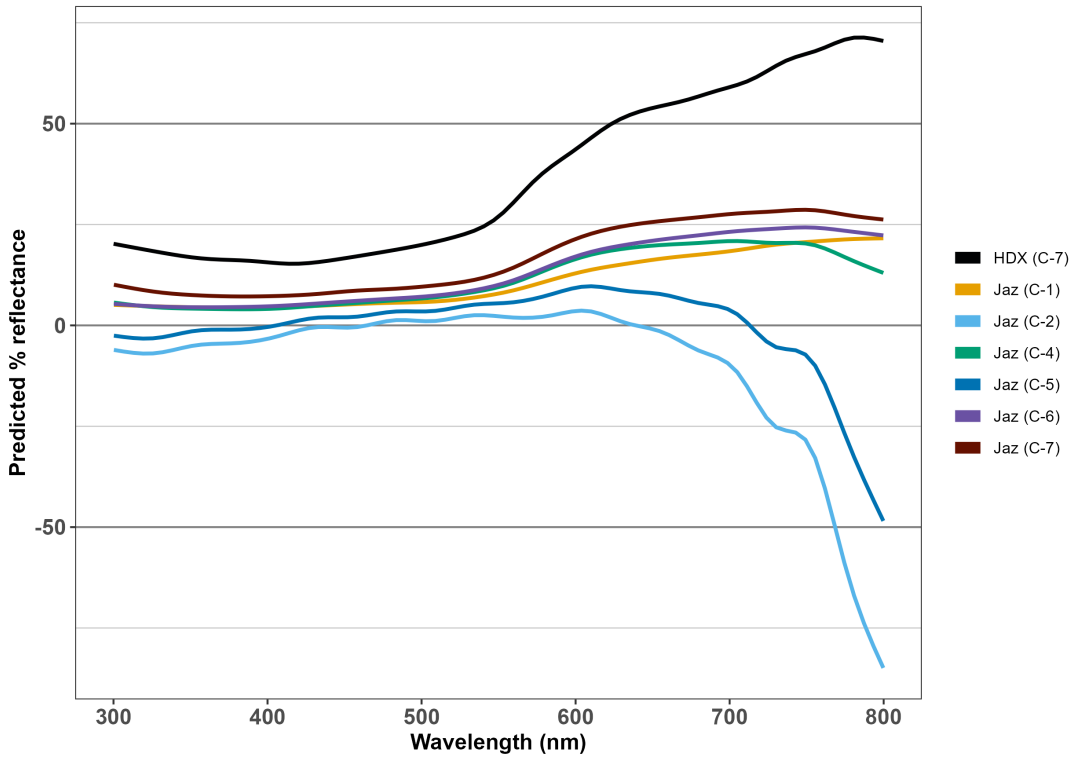

Figure 7.2-13: Art panel AQ12_BAS predicted percent reflectance versus wavelength (nm), with a smooth curve for each campaign measured by the JAZ and HDX instruments.

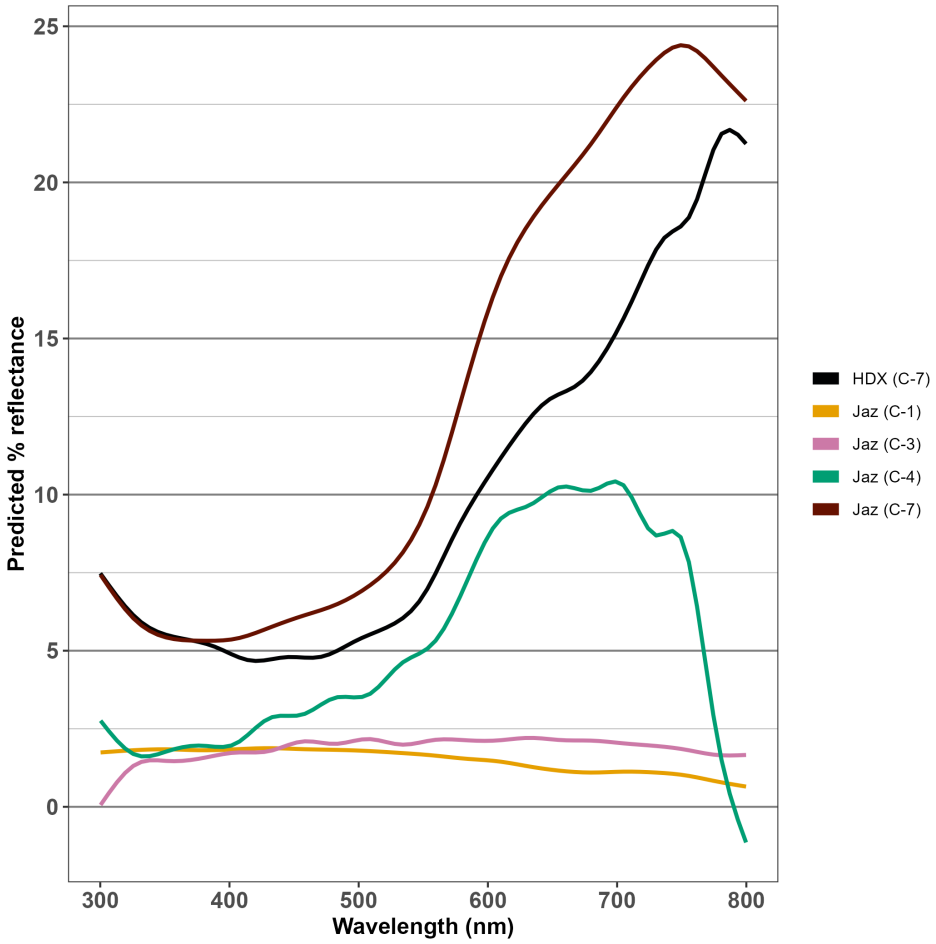

Figure 7.2-14: Art panel RS10_GBR2 predicted percent reflectance versus wavelength (nm), with a smooth curve for each campaign measured by the JAZ and HDX instruments.

This page is intentionally blank.

7.3 Industry data

The research contract states that our analysis should also take account of previously existing data where possible.

The industrial installations on Murujuga collect data on air quality using passive sampler tubes (of the brands IVL and Radiello). Our study design and analysis plan envisages that these data will be compared with the results of our own IVL passive sampler measurements, as a cross-check on reliability, and in order to gain more information about long-term trends.

Woodside and Yara have provided the MRAMP research team with their previously collected results from these samplers. Substantial work is still required to extract numerical data from the supplied records, which are mostly PDF documents or scanned images of printed reports from the IVL and Radiello laboratories. There is apparently no standard format for the assay results from the laboratories. Consequently, the MRAMP team is not yet able to incorporate industry data in the analysis.

Figure *7.3-1* shows the IVL gas sample data provided by Woodside. These data are gas concentrations for each site, collected from five sites from October 2021 to October 2022 inclusive.

Our own passive sampler data are presented in Section 7.11. Comparison between the industry data and our own data is reported in Section 8.5.

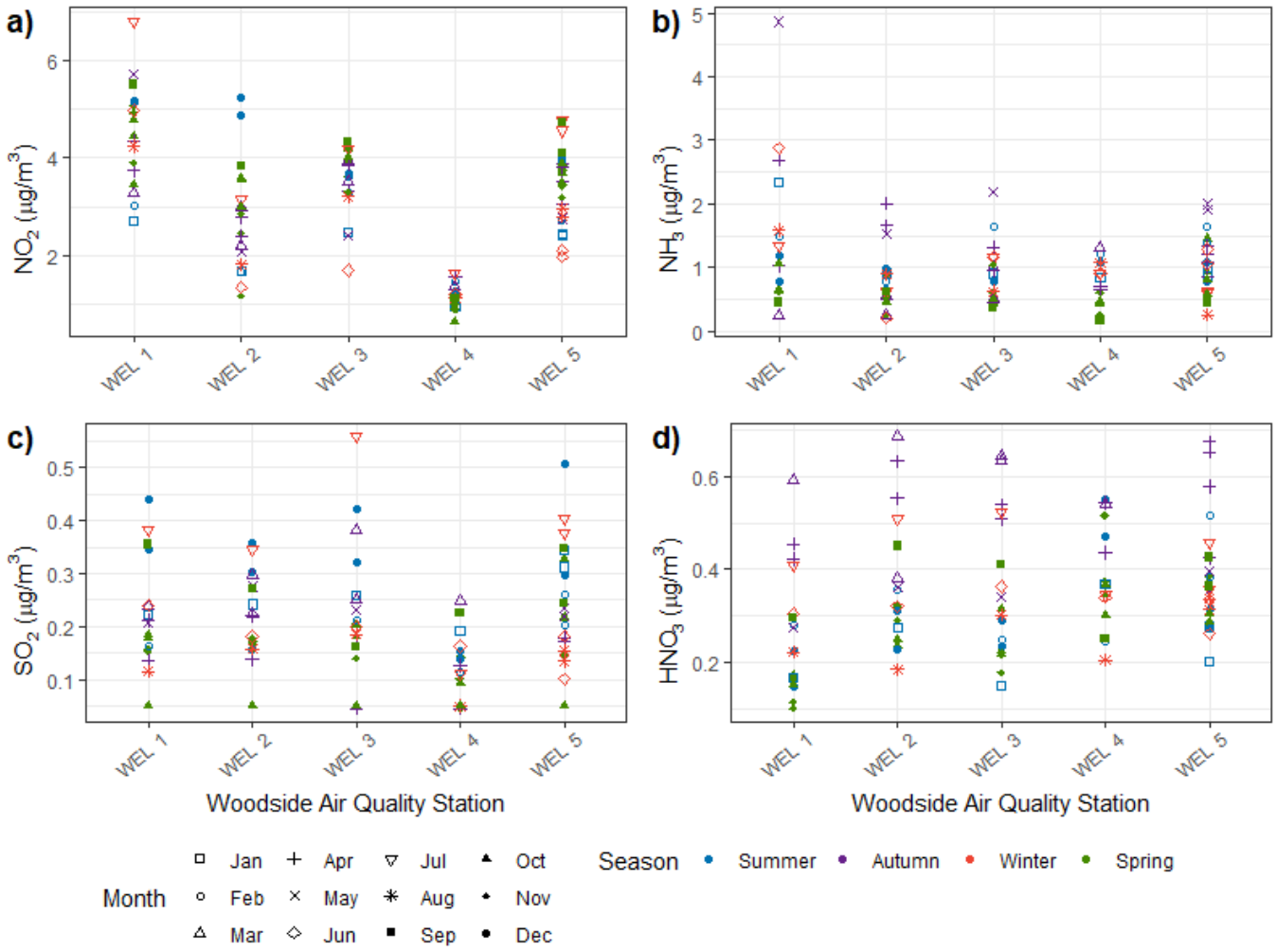

Figure 7.3-1: Woodside IVL passive sample data for five sites. The colours show the season while shapes show individual months.

7.4 Inorganic geochemistry – *pH*, *Eh*, Cl^-

7.4.1 Background

The acidity of rock surfaces has been an important topic of previous research on rock art. Our study design involves measuring acidity (*pH*), oxidation-reduction potential (*Eh*, *ORP*) and chloride ion concentration (Cl^-) on selected rock surfaces during each field campaign.

The Year One Report (Curtin University, 2023) dealt with the observations of *pH*, *Eh* and concentration of Cl^- from the first four field campaigns. Campaign 1 yielded results that were quite different in some respects from those obtained in the subsequent campaigns 2, 3 and 4. This discrepancy could have been explained either by seasonal effects (because campaign 1 was conducted at the end of a very long spell of hot dry weather, while the other campaigns were conducted in wetter conditions) or by startup effects (such as operator learning curves, revisions of technique, and deterioration of reagents). In order to resolve these competing explanations it was important to continue the field work into the second year of the project.

A further three field campaigns have now been completed. A few rainy days were also reported during campaigns 1, 4, and 7, with campaign 7 having more than 10 mm of rain.

Table *7.4-1* shows the campaign dates, the number of days since the most recent rain that occurred before the start of the campaign, any occurrence of rain during the campaign, and the median *pH* recorded.

Table 7.4-1: Overall campaign data: start and end dates, days since last rain (before start of campaign), rain recorded during campaign, and median pH.

Campaign	Start Date	End Date	Days since last rain				Rain during		Median
			Any rain	>10 mm	>20 mm	>40 mm	Any rain	>10 mm	*pH*
1	15/03/2022	08/04/2022	24	33	289	314	**Y**	N	6.63
2	20/06/2022	22/07/2022	9	19	19	21	N	N	4.78
3	10/10/2022	03/11/2022	37	37	131	133	N	N	4.50
4	27/02/2023	24/03/2023	4	7	274	276	**Y**	N	4.44
5	01/07/2023	26/07/2023	10	11	11	11	N	N	4.46
6	14/10/2023	08/11/2023	115	116	116	116	N	N	5.81
7	26/02/2024	12/03/2024	3	251	251	251	**Y**	**Y**	6.03

This section reports a combined analysis of the results from all campaigns 1 to 7.

7.4.2 *pH* observations

Figure *7.4-1* shows boxplots and individual values of *pH* recorded in each campaign. The striking difference between campaign 1 and campaigns 2–4 was noted in the previous annual report (Curtin University, 2023): the median *pH* in campaign 1 is close to 7, while the median in each of campaigns 2–4 is close to 4.3. With the additional data from campaigns 5–7, we note that the median *pH* recorded in campaign 5 is again close to 4.3, while in campaigns 6 and 7 the median is close to 6.

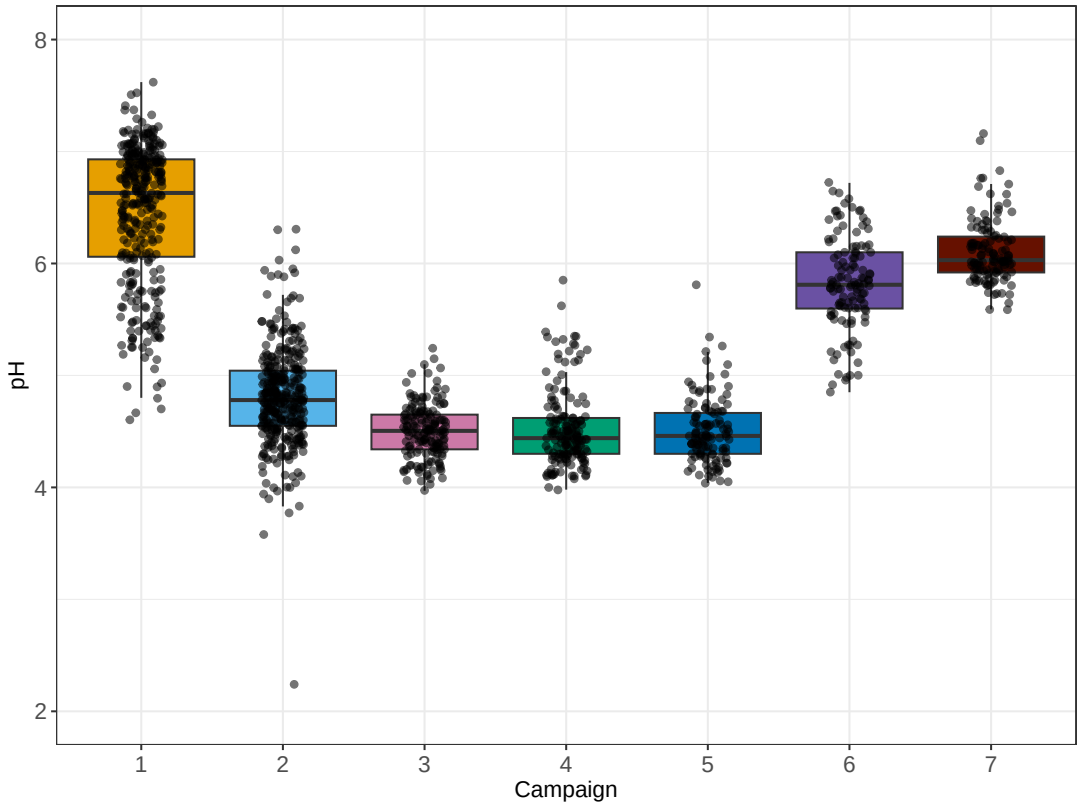

Figure 7.4-1: Boxplots of pH by campaign.

Figure *7.4-2* shows boxplots of *pH* broken down by rock type, within each campaign. Differences between campaigns are much greater than differences between rock types within a campaign. There is weak evidence for differences between rock types.

Possible explanations for the large differences between campaigns include the following:

- Data may reflect real fluctuations in rock surface *pH* (e.g. seasonal effects related to temperature, rainfall and other environmental factors).
- Lower *pH* for campaigns 2 to 5 may reflect biotic or other activity associated with rainfall.
- Campaigns 1 and 6 may have higher *pH* because of methodological factors (trial effects and equipment failure in campaign 1, introduction of ionic strength adjuster (ISA) in campaign 6).

Evidence for a seasonal effect (i.e. periodic variation with a period of one year) is inconclusive. Even though the *pH* data from campaigns 2 and 5 (both conducted in July) are quite similar, there are substantial differences between the results from campaigns 4 and 7 (both conducted in February–March) and between the results from campaigns 3 and 6 (both conducted in October–November).

Recent rainfall appears to be highly influential. Campaigns 1 and 6 were preceded by long dry periods, whereas campaigns 2–4 were preceded by, or took place during, rain. Water in equilibrium with atmospheric CO_2 is expected to have a *pH* around 5.6; this is consistent with the observed *pH* values in campaign 6. If this explanation is valid, it would indicate that rock surface chemistry is dynamic, and that *pH* fluctuates on timescales longer than a year, which would make *pH* a poor choice for the Environmental Quality Criterion.

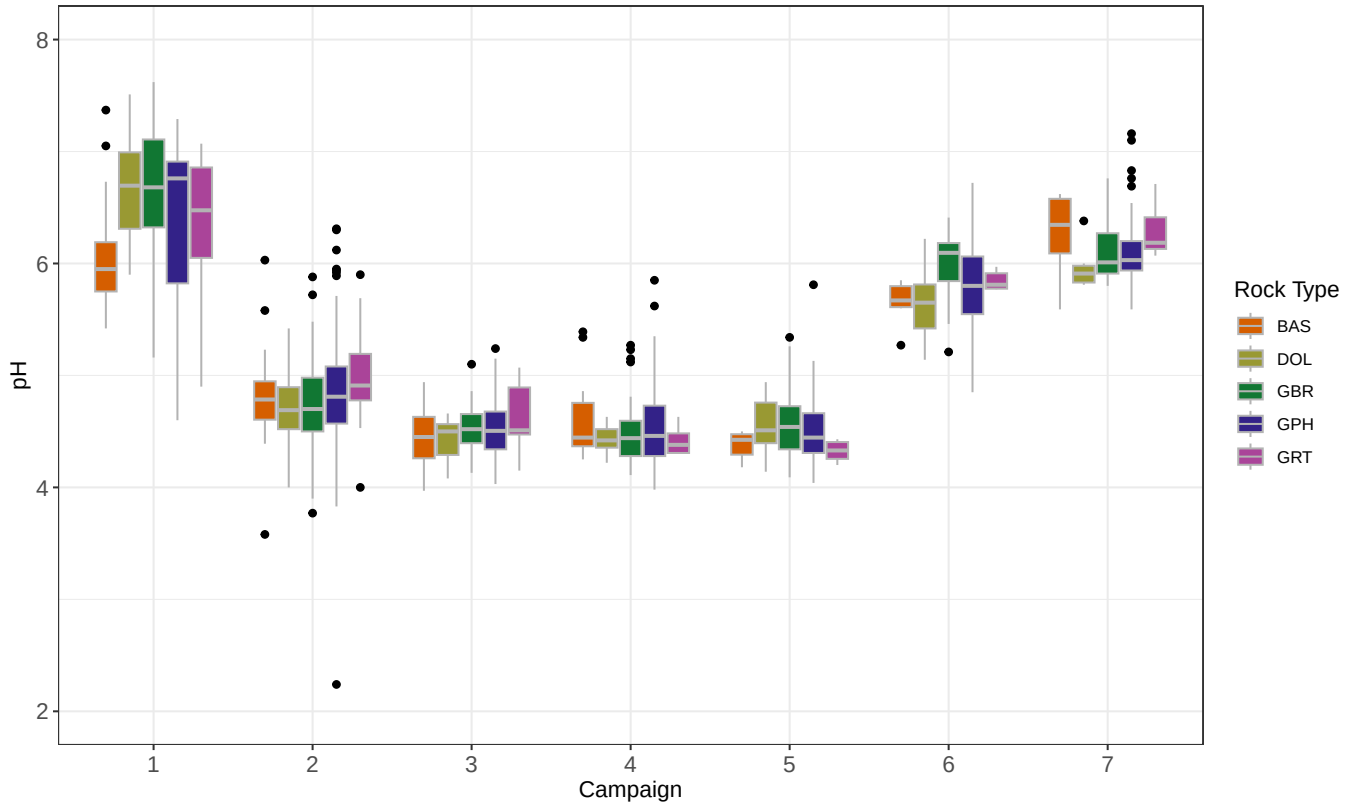

Figure 7.4-2: Boxplots of pH by rock type for each campaign.

Evidence for consistent differences in *pH* between different rock types (a rock type "effect") is mixed. Figure *7.4-3* shows boxplots of *pH* after subtracting the median *pH* for the relevant campaign. Data from campaigns 1, 6 and 7 suggest that there may be a rock effect. However, data from the other campaigns 2–5 did not support this so strongly, or gave conflicting estimates. For example, in campaign 2, the median *pH* for granite (GRT) is higher than for other rock types, but in campaign 5, the median *pH* for granite is lower than for other rock types. The possibility of an interaction between rock type and seasonal/weather effects (i.e. different seasonal effects on different rock types) should still be considered.

It is important to assess evidence for any spatial trend in electrochemistry, because such trends could be associated with the gradient in exposure to industrial output. Figure *7.4-4* shows spatially smoothed *pH* surfaces for each campaign obtained by the Nadaraya-Watson smoothing technique (Appendix *F*.1). The standard colour map for *pH* values is used in all panels, despite the very different values of *pH* obtained in the different campaigns. Spatial variations in *pH* are much smaller than the differences between campaigns.

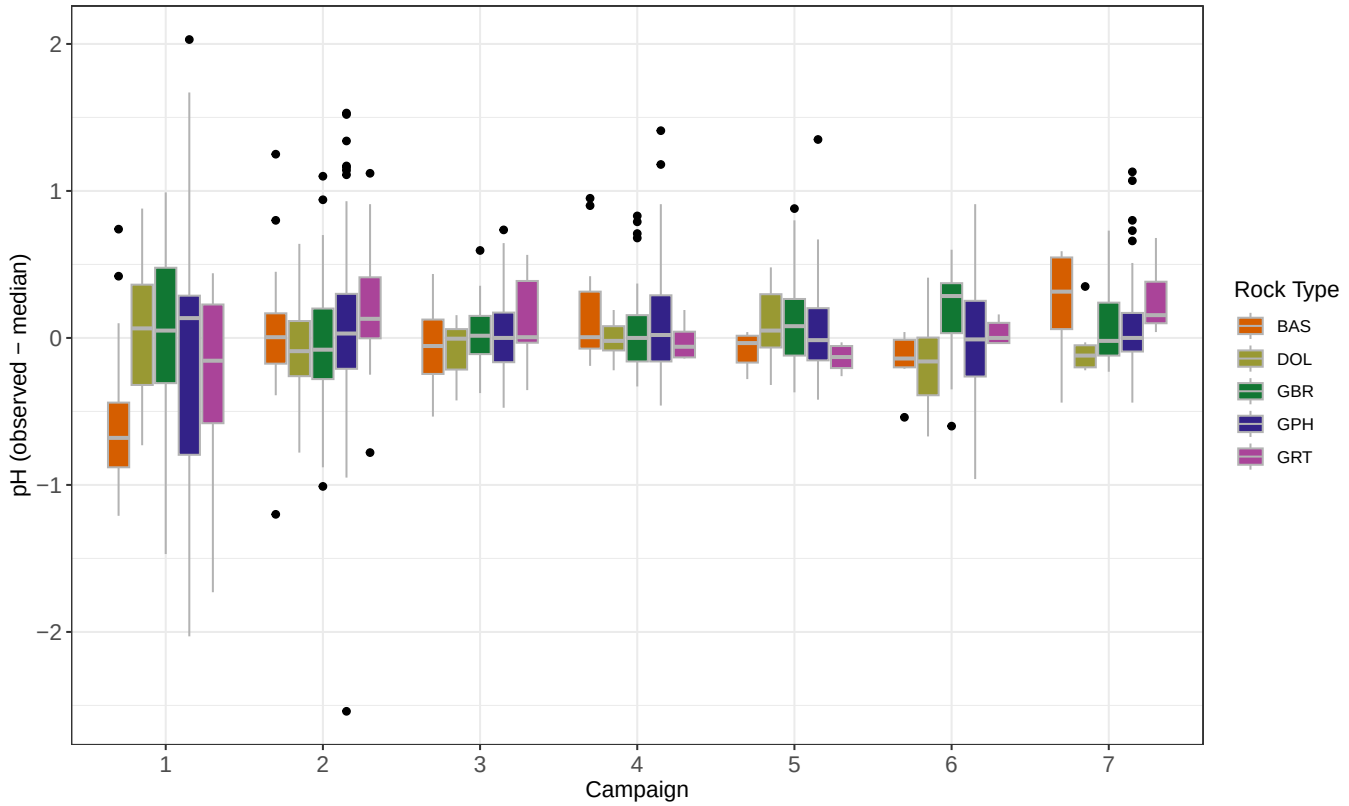

Figure 7.4-3: Boxplots of observed pH minus campaign median pH, by rock type for each campaign.

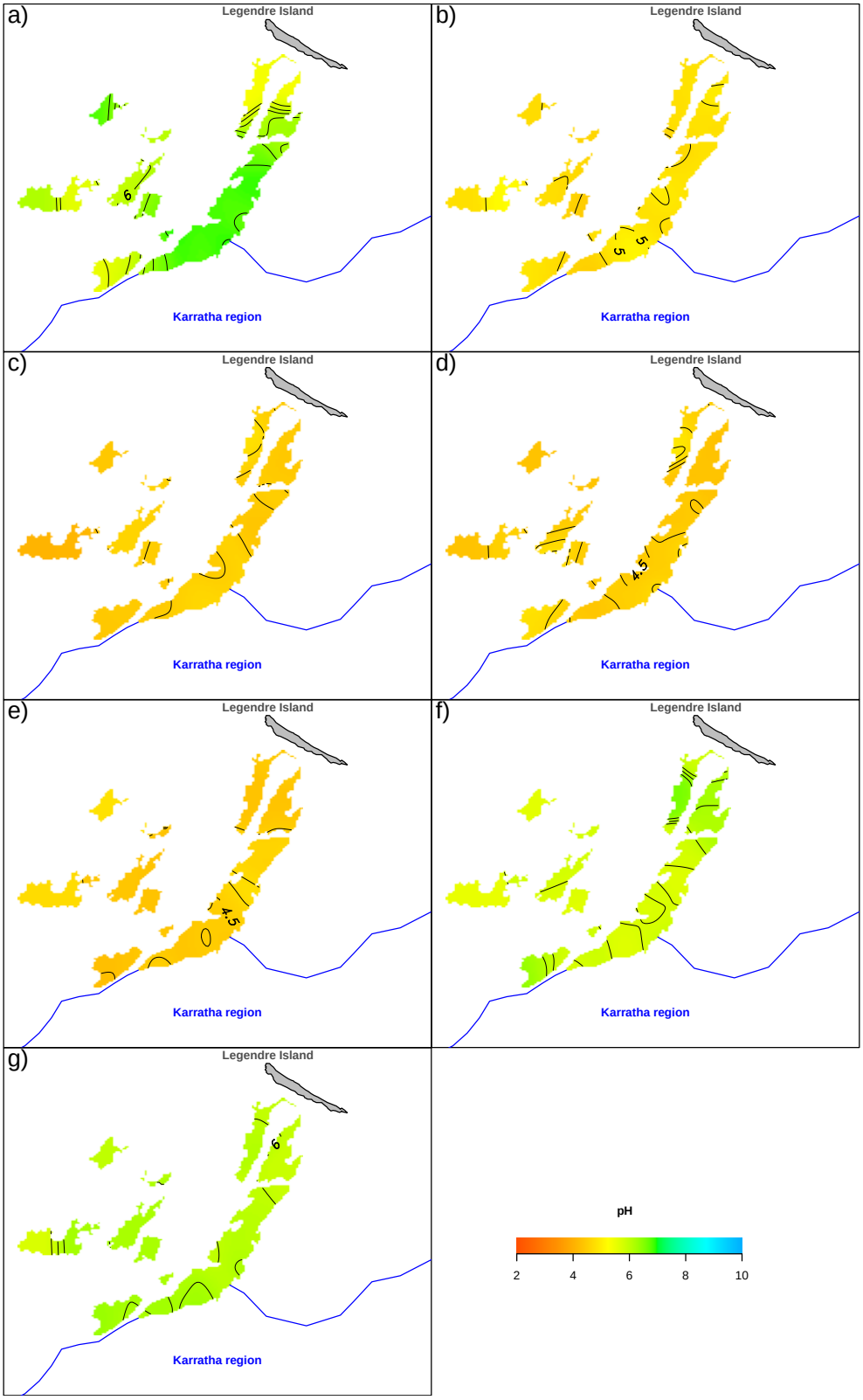

Figure 7.4-4: Spatially smoothed pH values of campaigns 1 to 7 in panels a) to g), respectively. Colour map overlaid with contour lines. Blue line represents Karratha coastline; grey polygon is Legendre Island.

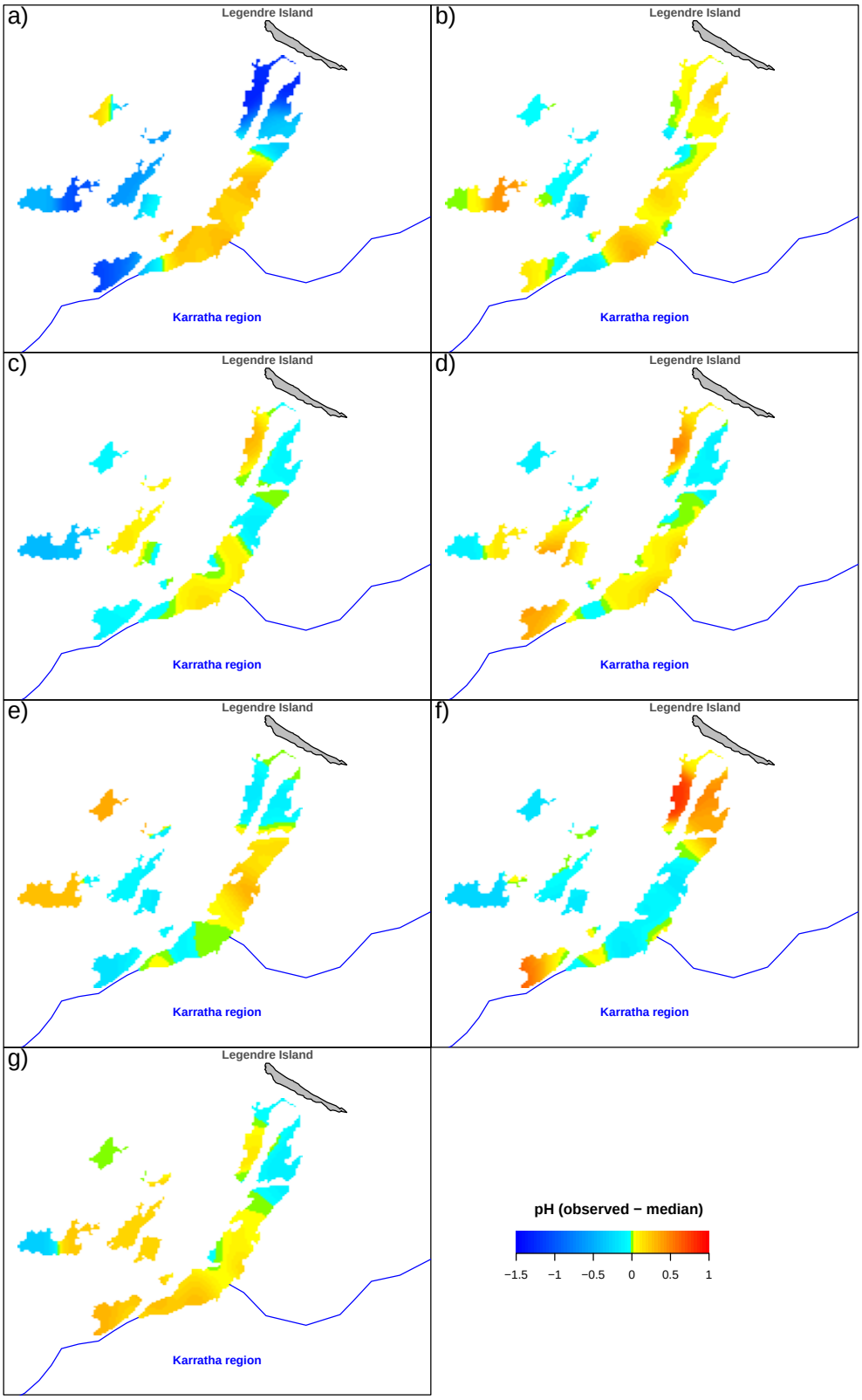

Figure 7.4-5: Spatially smoothed observed pH minus campaign median pH of campaigns 1 to 7 in panels a) to g), respectively.

7.4.3 Chloride ion (Cl^-) observations

Chloride ion Cl^- concentration (in parts per million) was measured three times at each sample rock in each campaign, starting from campaign 2, because of a device breakdown in campaign 1. In campaign 5, the effect of using an Ionic Strength Adjuster (ISA) in the measurement technique was investigated, by measuring chloride concentration with and without using an ISA.

The recorded values of Cl^- concentration vary over several orders of magnitude, and are strongly skewed to the right. Accordingly, a logarithmic transformation was used to analyse these data.

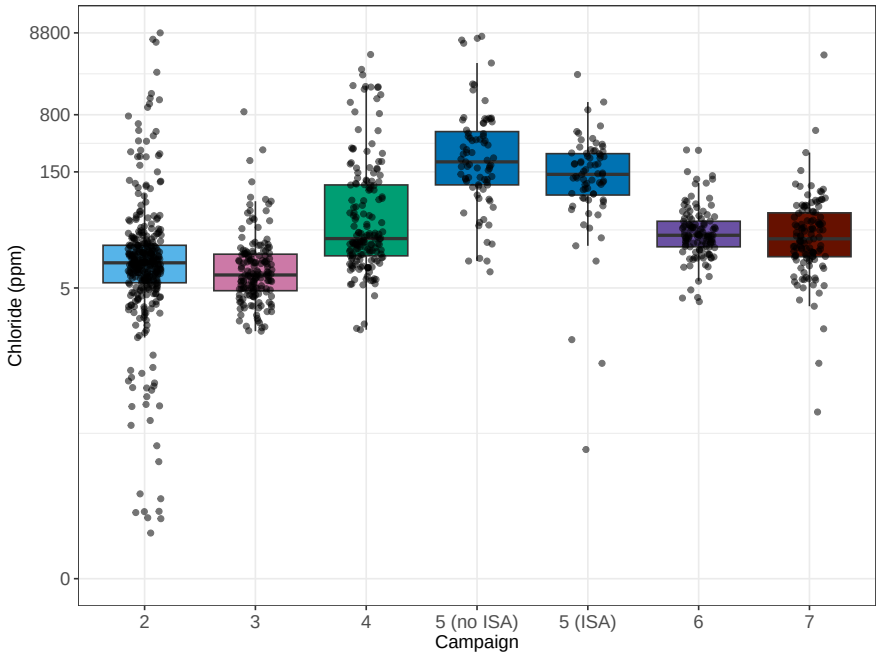

Figure 7.4-6: Boxplots of Cl^- concentration by campaign. Note logarithmic scale. ISA (Ionic Strength Adjuster).

Figure *7.4-6* show boxplots, on a logarithmic scale, of Cl^- concentration for each campaign. For campaign 5, there are separate boxplots for the results with and without ISA.

There are substantial differences in Cl^- concentration between campaigns. The median chloride concentration in each campaign is very high for campaign 5, with and without ISA; it is very low in campaigns 2 and 3 which give similar results; and it is moderate in campaigns 4, 6 and 7 which give similar results.

There is also substantial variability within each campaign. Figure *7.4-7* shows boxplots, again on a logarithmic scale, of Cl^- concentration for each rock type in each campaign. There does not appear to be a systematic effect associated with rock type. There are numerous extreme values.

Figure *7.4-8* shows spatially smoothed Cl^- concentration for each campaign. A common colour map has been used, shown at bottom right. The upper ribbon shows the colour map over the entire range of values from zero to 450 ppm, while the lower ribbon is a magnified display of the colour map for the range from zero to 50 ppm. The use of a common colour map allows immediate

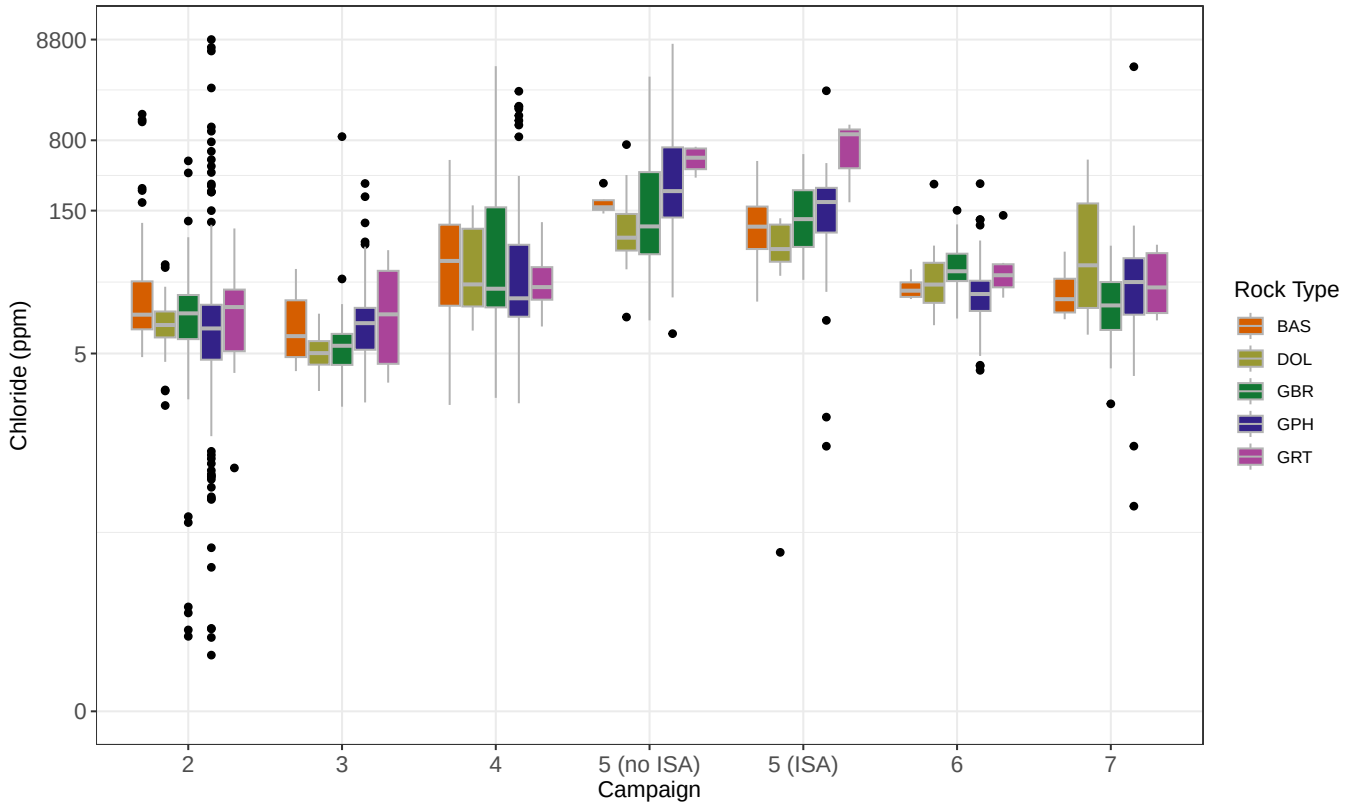

Figure 7.4-7: Boxplots of Cl^- concentration by rock type for different campaigns. Note logarithmic scale. ISA (Ionic Strength Adjuster).

recognition of the systematic differences between campaigns. There does not appear to be a consistent spatial trend in Cl^- values.

One question for further investigation is whether Cl^- concentration measurements are elevated at sites near the sea, which might be expected due to the greater availability of salt (NaCl).

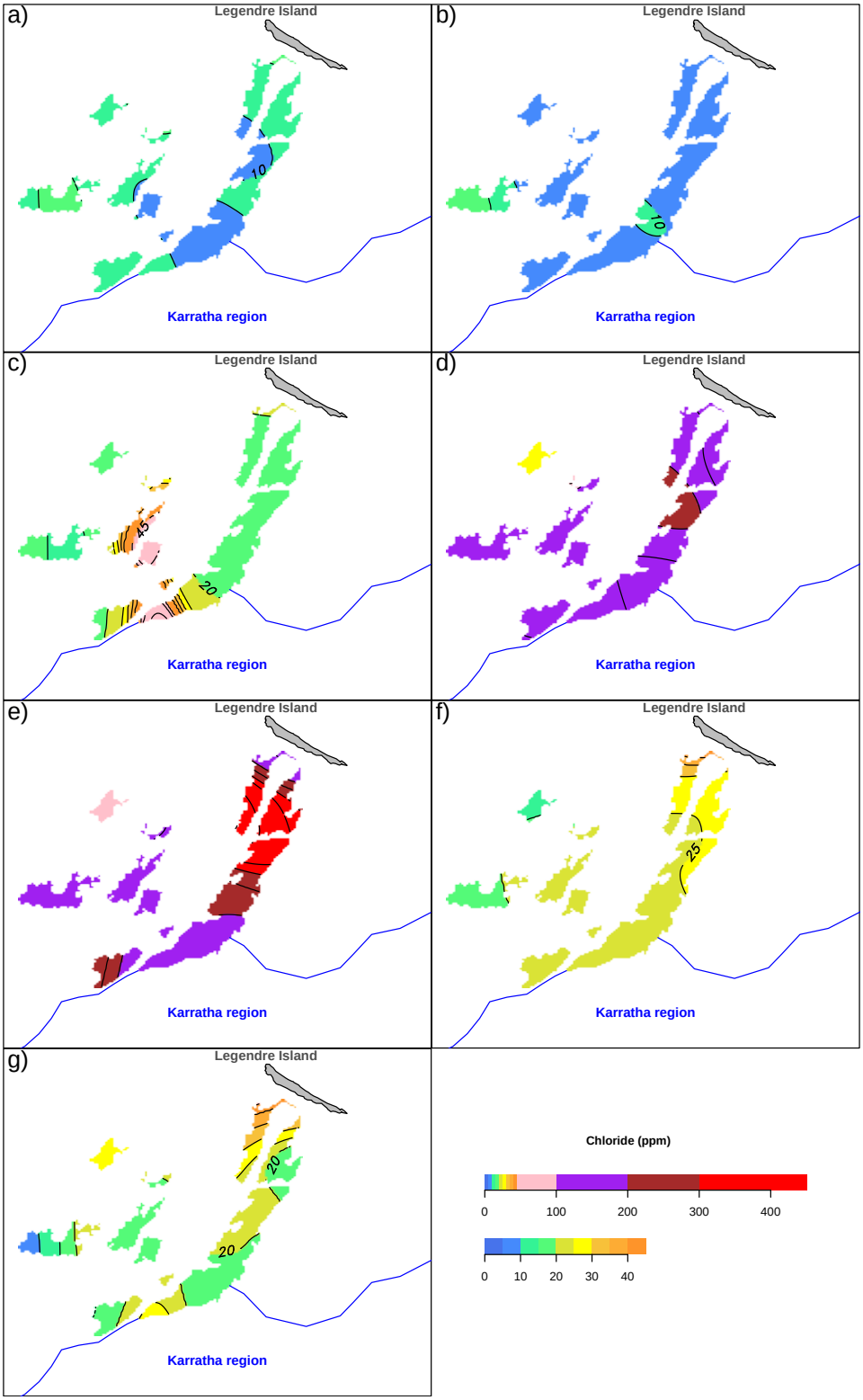

Figure 7.4-8: Spatially smoothed chloride ion (Cl^-) concentration of campaigns 2 to 4 (a,b,c), campaign 5 with and without ISA (d,e), and campaigns 6 and 7 (f,g). Colour map overlaid with contour lines.

7.4.4 Oxidation-reduction potential (*ORP*) observations

Figure *7.4-9* shows boxplots of *ORP* measurements in millivolts (mV) for each campaign, starting from campaign 2. Values range between 80-400 mV with quartiles at about 200, 250 and 300 mV. Boxplots and histograms suggest good approximation by a normal distribution for exploratory purposes. There are slight differences between campaigns, and substantial variability between campaigns.

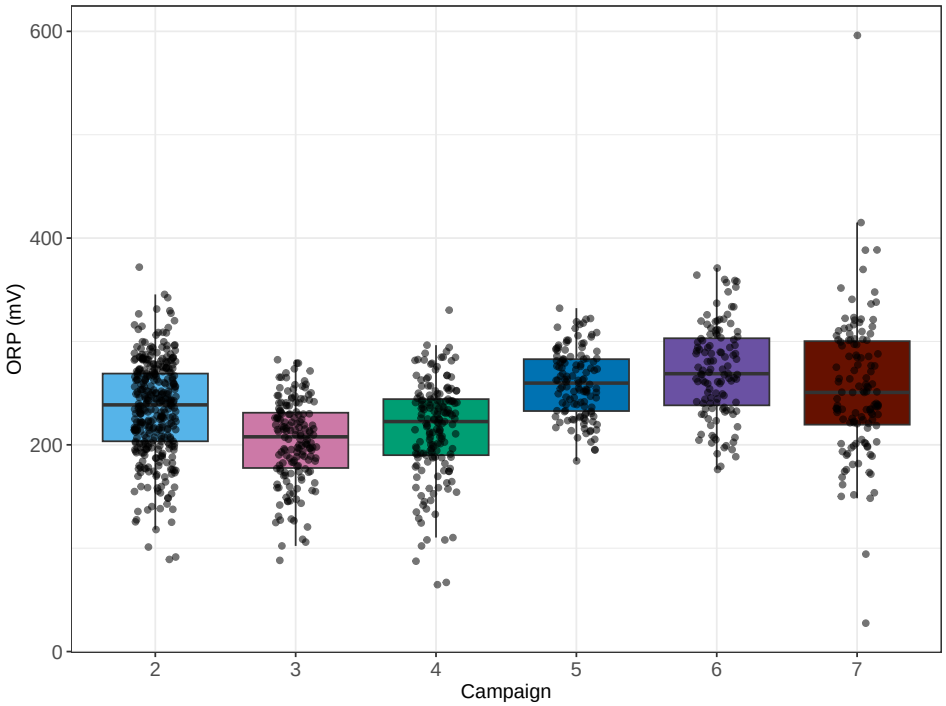

Figure 7.4-9: Boxplots of ORP by campaign.

Figure *7.4-10* shows boxplots of *ORP* for each rock type in each campaign. This does not suggest a consistent effect of rock type. Residual variability is large.

Figure *7.4-11* shows spatially smoothed *ORP* surfaces for each campaign. Estimates of the spatial trend are similar in panels (a)–(c), obtained from campaigns 2–4 respectively, and are similar in panels (d)–(f), obtained from campaigns 5–7, but the two groups of panels indicate different spatial trends. Further evaluation of these results will be undertaken.

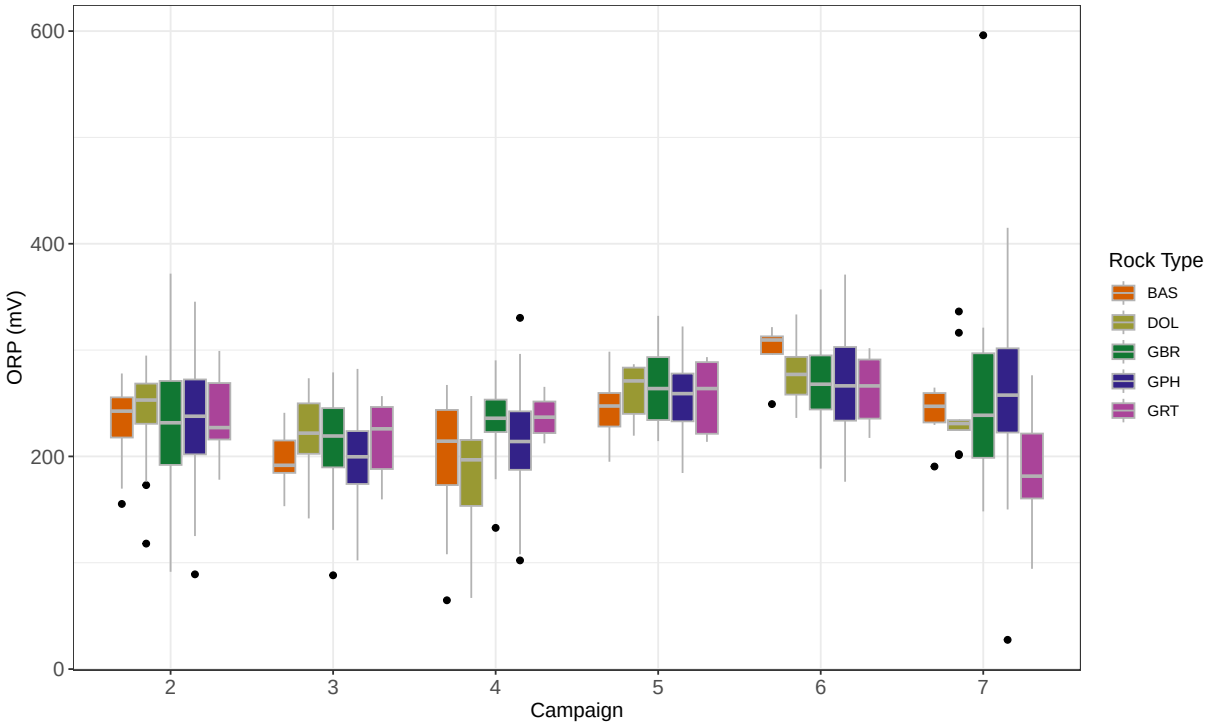

Figure 7.4-10: Boxplots of ORP by rock type for different campaigns.

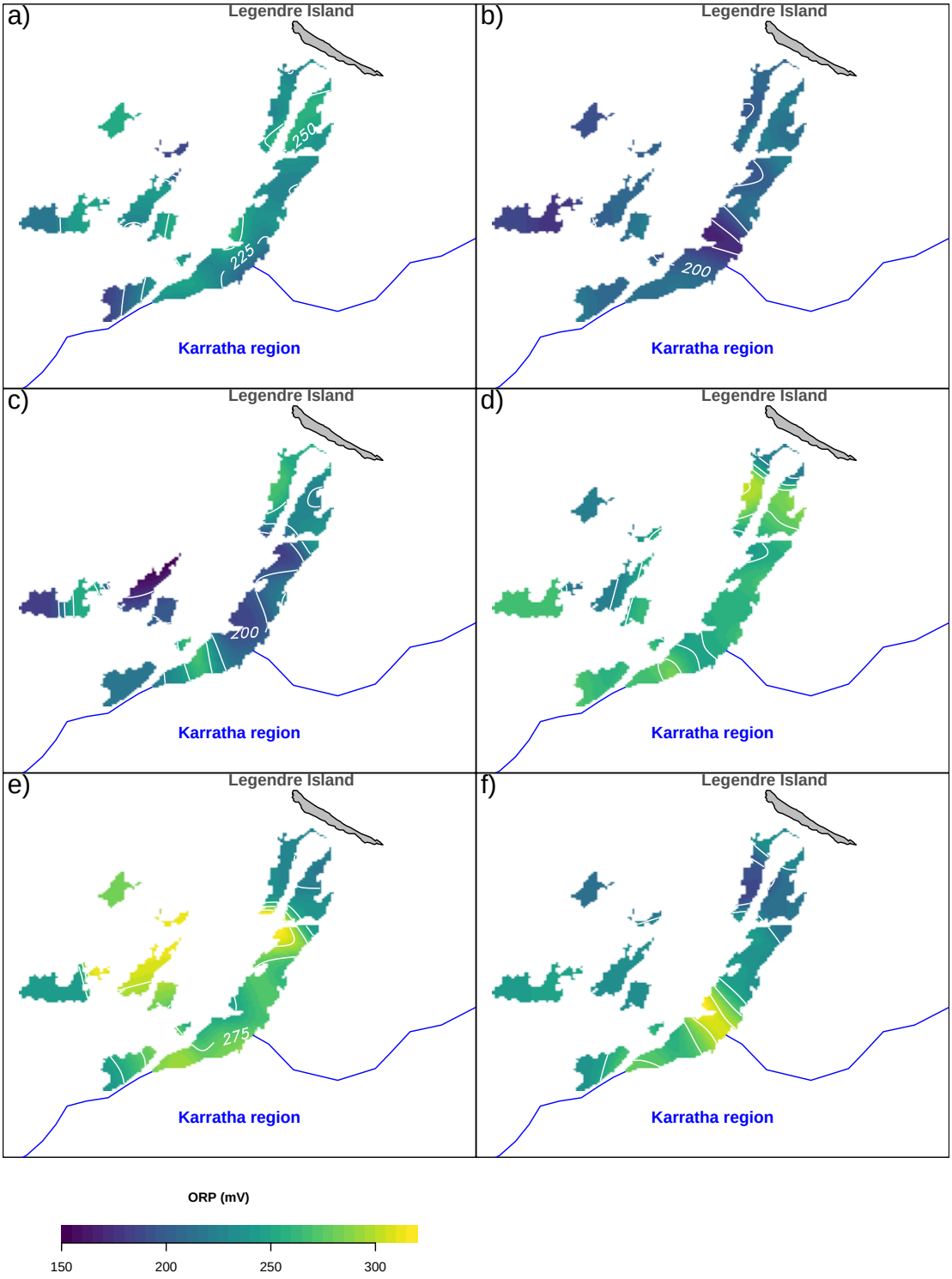

Figure 7.4-11: Spatially smoothed ORP from data from campaigns 2 (a) to 7 (f), respectively. Colour map overlaid with contour lines.

7.4.5 Multivariate association between *pH*, *ORP* and Cl^-

Figures *7.4-12–7.4-18* show a scatterplot matrix for investigating relationships between *pH*, *ORP* and the decimal logarithm of Cl^- concentration for campaigns 2 to 7. The upper right panels in these figures show the corresponding Pearson sample correlation.

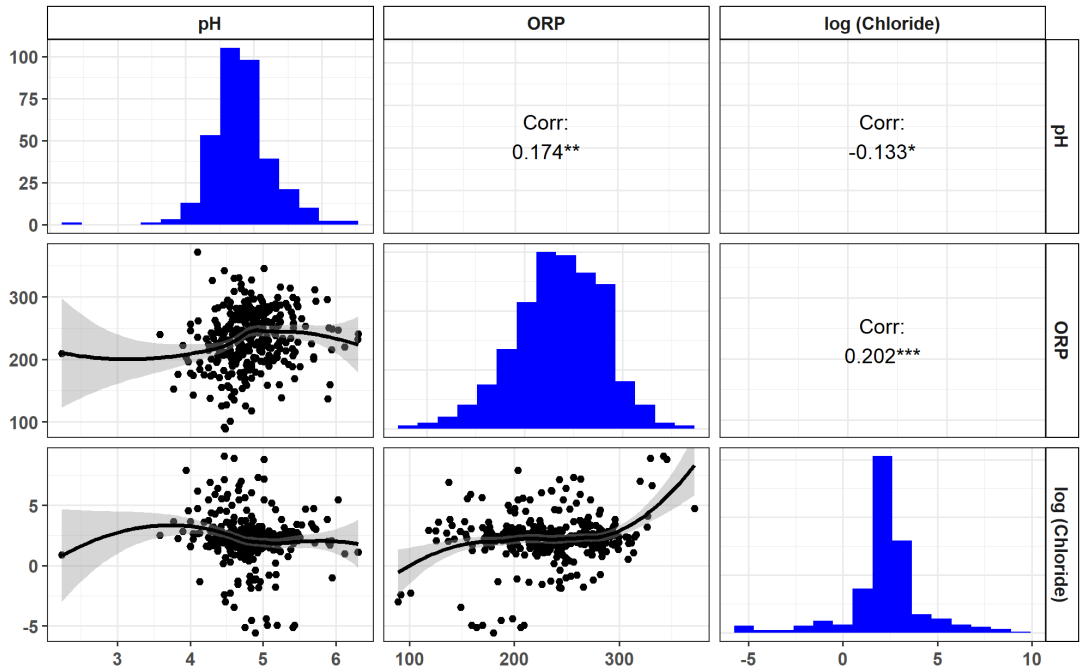

Figure 7.4-12: Campaign 2 pairwise scatterplots between pH, ORP and logarithm of chloride concentration. Where the panels above the diagonal show the correlation between two variables; panels on the diagonal show the histogram of each variable; panels below the diagonal show a scatterplot between two variables.

Pearson correlation coefficients are denoted by stars based on their significance levels. The lower panels show scatterplots with loess curves that visually display the relationship between variables (positive, negative or no relationship).

- No stars (zero stars): The correlation coefficient is not statistically significant.
- One star (*): The correlation coefficient is significant at the 0.05 level (two-tailed test).
- Two stars (**): The correlation coefficient is significant at the 0.01 level (two-tailed test).
- Three stars (***): The correlation coefficient is significant at the 0.001 level (two-tailed test).

In summary, pairwise associations between *pH*, *ORP* and logarithm of Cl^- concentration were either statistically non-significant at the 0.05 level or were weak as measured by the linear (Pearson) sample correlation. Further multivariate analysis of these data will be undertaken in the context of the overall study design, but this preliminary analysis suggests no strong association between these variables.

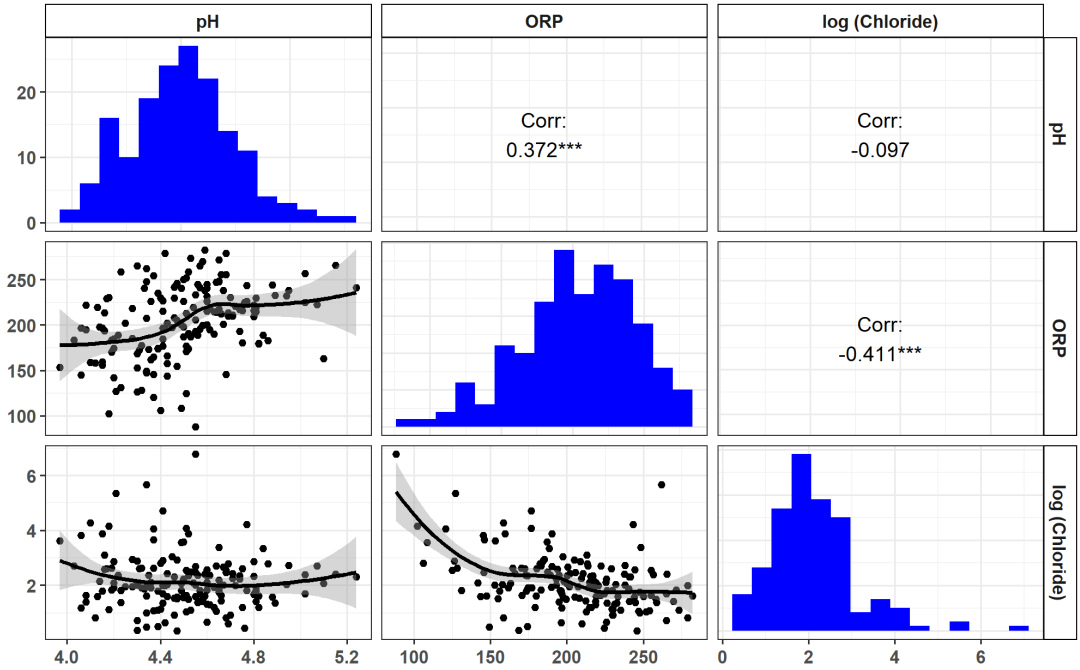

Figure 7.4-13: Campaign 3 pairwise scatterplots between pH, ORP and log of chloride concentration. Where the panels above the diagonal show the correlation between two variables; panels on the diagonal show the histogram of each variable; panels below the diagonal show a scatterplot between two variables.

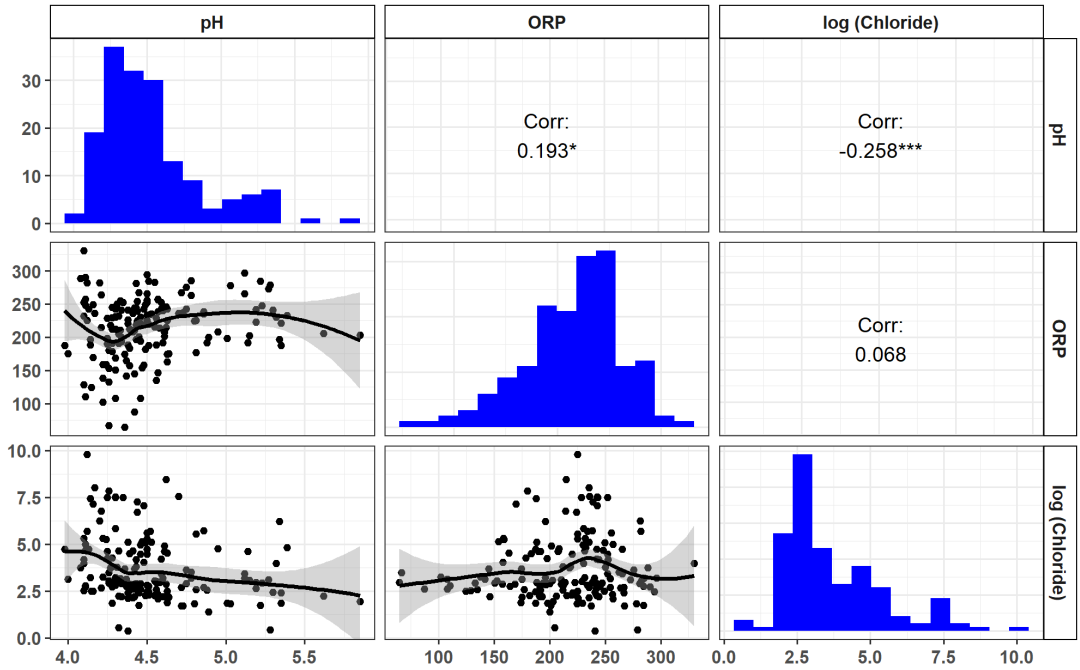

Figure 7.4-14: Campaign 4 pairwise scatterplots between pH, ORP and log of chloride concentration. Where the panels above the diagonal show the correlation between two variables; panels on the diagonal show the histogram of each variable; panels below the diagonal show a scatterplot between two variables.

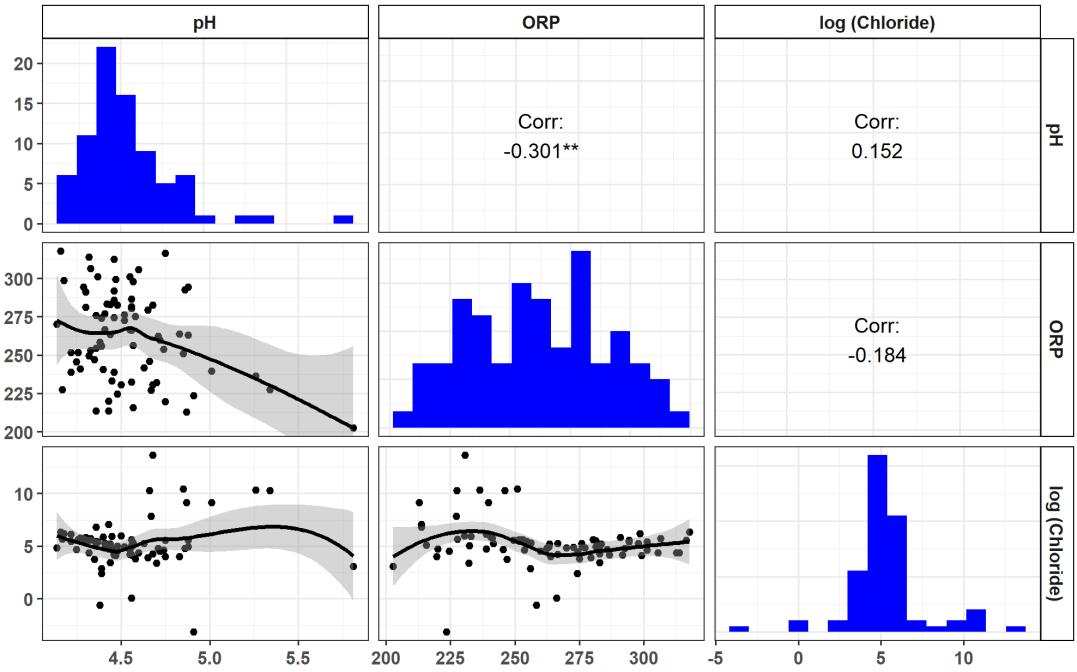

Figure 7.4-15: Campaign 5 pairwise scatterplots between pH, ORP and log of chloride concentration (with ISA). Where the panels above the diagonal show the correlation between two variables; panels on the diagonal show the histogram of each variable; panels below the diagonal show a scatterplot between two variables.

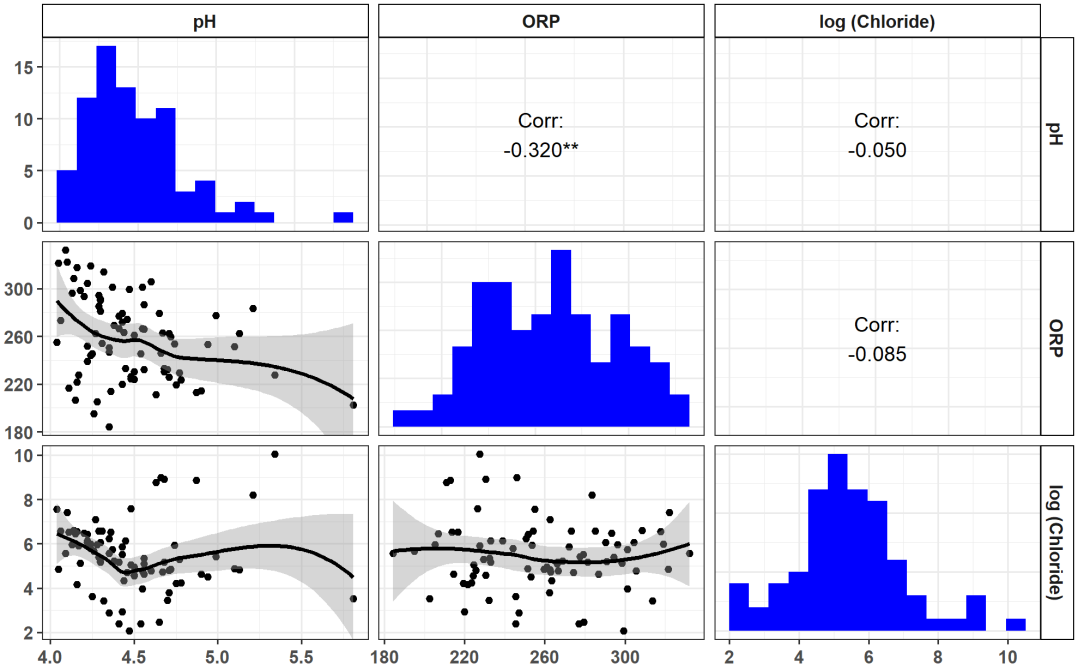

Figure 7.4-16: Campaign 5 pairwise scatterplots between pH, ORP and log of chloride concentration (without ISA). Where the panels above the diagonal show the correlation between two variables; panels on the diagonal show the histogram of each variable; panels below the diagonal show a scatterplot between two variables.

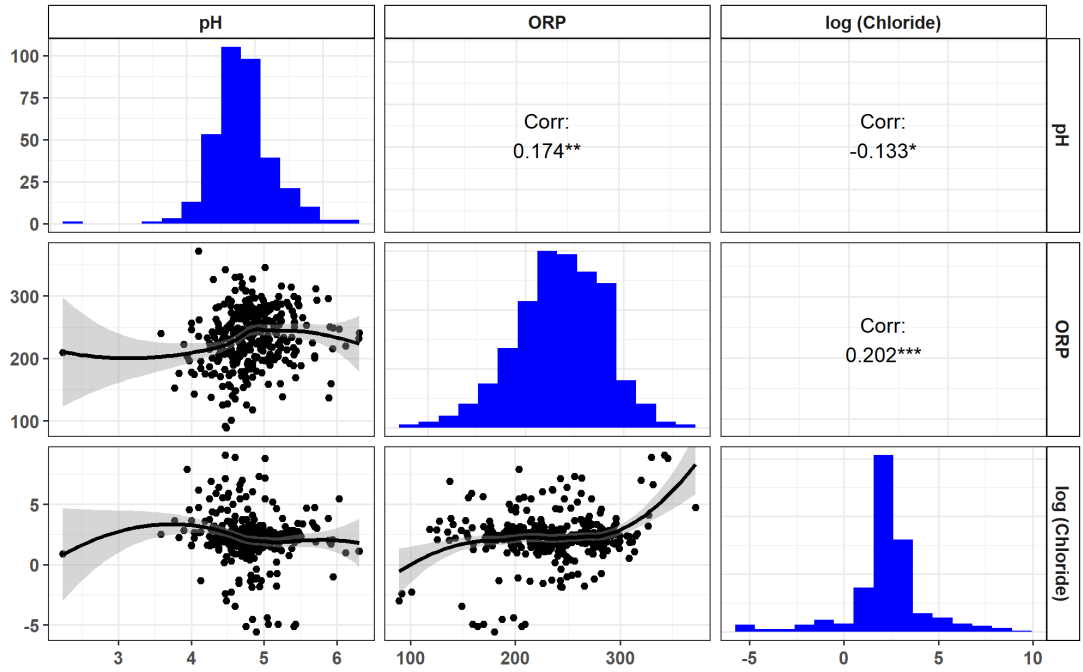

Figure 7.4-17: Campaign 6 pairwise scatterplots between pH, ORP and log of chloride concentration. Where the panels above the diagonal show the correlation between two variables; panels on the diagonal show the histogram of each variable; panels below the diagonal show a scatterplot between two variables.

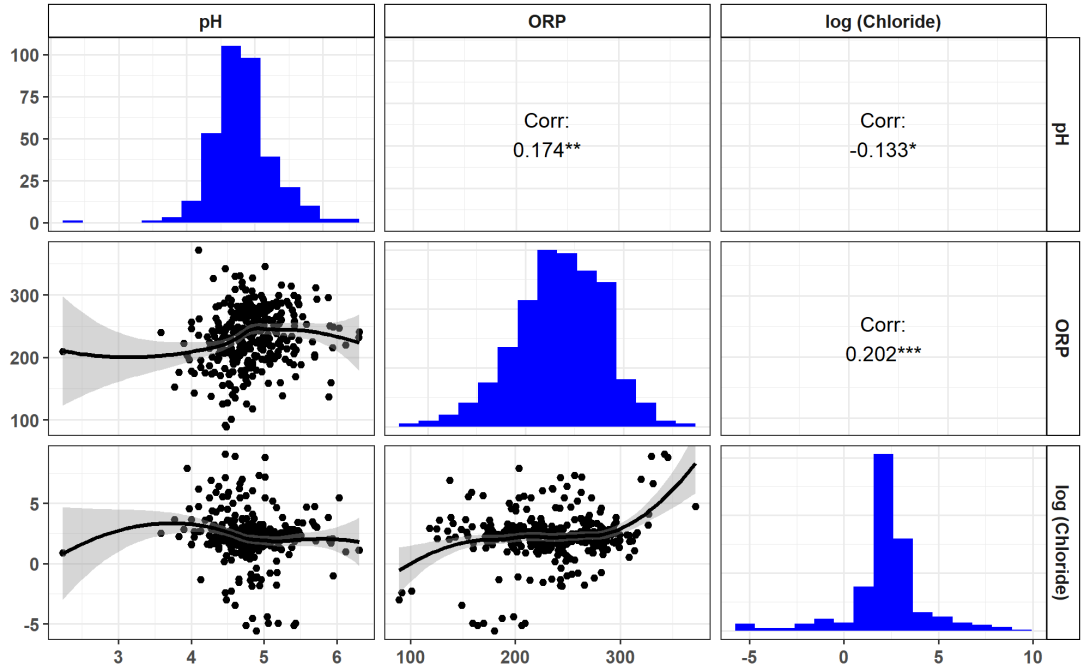

Figure 7.4-18: Campaign 7 pairwise scatterplots between pH, ORP and log of chloride concentration. Where the panels above the diagonal show the correlation between two variables; panels on the diagonal show the histogram of each variable; panels below the diagonal show a scatterplot between two variables.

7.4.6 Influence of bushfire emissions on rock surface *pH*

As mentioned in Section 4.1, a cultural burn was undertaken in the Conzinc Bay area at the end of campaign 5. Smoke and burnt vegetation were sampled for organics analysis, however the impact of bushfire smoke on the rocks is also of importance, insofar as it allows researchers to study both natural and anthropogenic exposures and impacts. An important parameter for study is rock surface *pH*.

Unfortunately for the research, the burn was conducted with strong easterly winds, and consequently bushfire emissions were only measured to any substantial extent at AQ10, more than 30 km from the fire. None of the rock art panels selected for the study were immediately downwind of the fire. In order to study the impact of bushfires in more detail, three additional sample rocks (not containing rock art) were selected downwind of the burn area. Two of these contained visible soot deposition, and one did not. Triplicate *pH* measurements were conducted on each of the three new sample rocks, as well as the closest (upwind) rock art panels (RS11, AQ13, AQ14). The new sample rocks were subsequently resampled in campaigns 6 and 7.

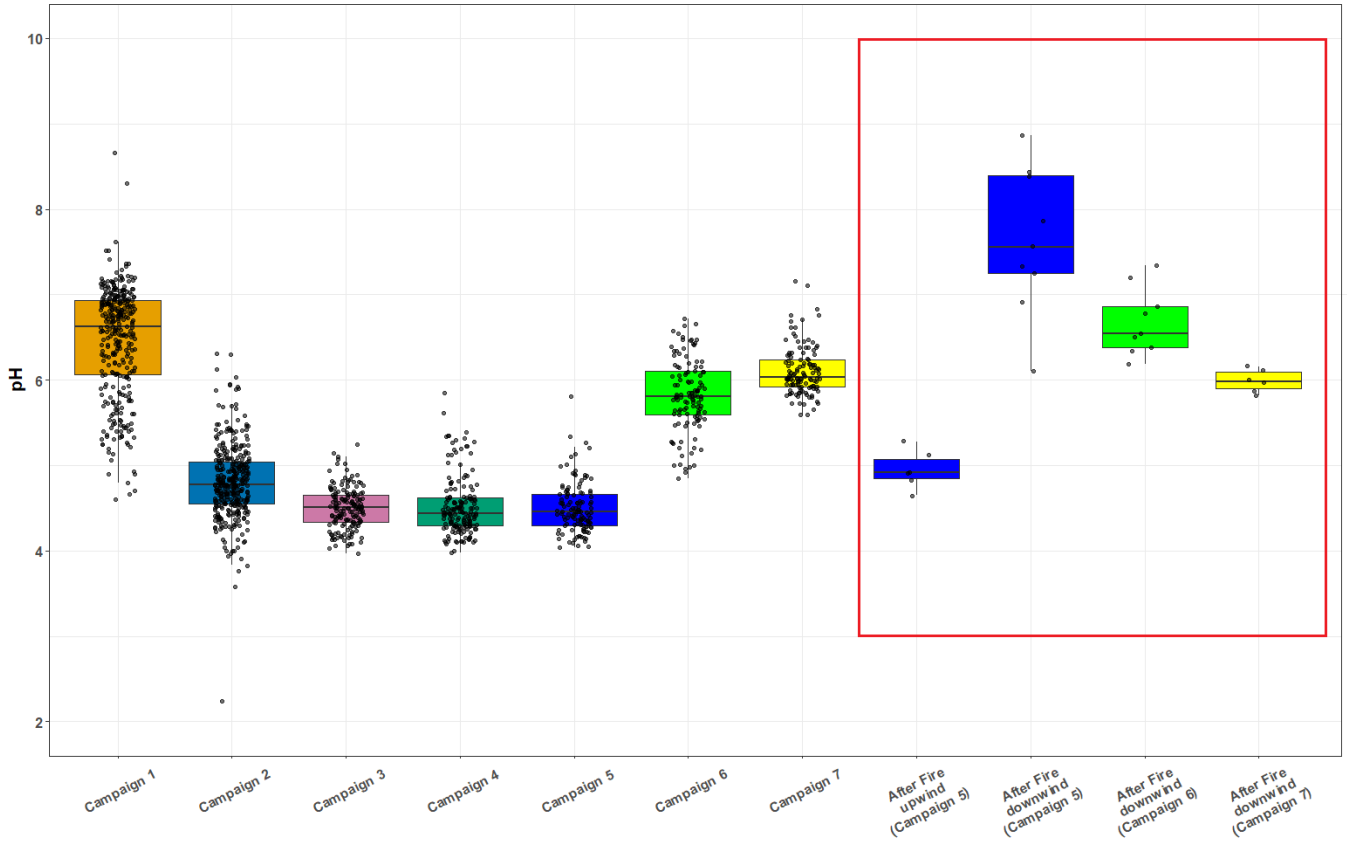

Figure 7.4-19: Boxplot of rock surface pH in bushfire exposed samples (red inset), shown with campaign 1-7 pH for comparison.

Figure *7.4-19* shows the fire-related samples in the red inset, together with the campaign 1-7 measurements for reference. It can be seen that the downwind samples had substantially elevated *pH* compared to both prior measurements and the upwind sample measurements. The upwind

sample measurements were comparable to the upper end of campaign 5 measurements and were consistent with tests immediately pre-fire on the same panels. *pH* did not appear to be correlated with the level of soot deposition: the triplicate samples on the rock with no visible soot deposition were not markedly different from the samples on the other two rocks with triplicate samples.

It can be seen that over campaign 6 and 7 the *pH* values on these sample rocks decreased, ultimately returning to a level commensurate with other measurements from campaign 7.

7.5 Inorganic geochemistry – pXRF

7.5.1 Background

The portable X-Ray Fluorescence (pXRF) instrument is a hand-held device for measuring the elemental composition of rocks. The instrument is placed on or against the rock surface and activated by pressing a trigger. The instrument readout is a list of elements (or their oxides such as SiO_2) present in the rock, with their corresponding percentages by mass. The pXRF is less reliable than a laboratory instrument, but has the great advantage of being portable and usable in the field.

pXRF measurement was included in the original study design (Curtin University, 2022) in order to obtain supplemental information about the geology across the peninsula. Patinated rocks of different types can look very similar to researchers who are not familiar with the different rock types at Murujuga, so the pXRF was used to provide supporting information to confirm rock identification. The pXRF provides information from the top few millimetres of the sampled rock, so it samples the patina, weathered rind, and fresher rock. Further investigations were undertaken to assess the utility of the pXRF as a tool to assess patina composition and patina thickness.

pXRF readings were taken in all seven field campaigns on the same rock surfaces in each campaign.

7.5.2 Multivariate analysis

Redundancy Analysis (RDA) is a multivariate counterpart of linear regression combined with some features of principal component analysis (Legendre and Legendre, 2012). This method is used to explore the relationships between two sets of variables: explanatory variables and response variables. In this section, RDA was applied to investigate the relationship between the chemical elements from the pXRF and the rock types. RDA helps determine the extent to which the chemical elements explain the differences between the rock types. This exploratory analysis is reasonable because rock types are defined partially by their geochemistry, so that it would be expected to see strong associations between particular rock types and particular elements.

RDA was conducted in `R` using the function `rda` in the `vegan` package. All pXRF elements were normalised by the `Hellinger` normalisation (Legendre and Gallagher, 2001); other normalisation methods were also tested and gave similar results. The rock types were encoded as dummy variables, with one variable for each rock type. Each dummy variable is a binary variable that indicates the absence (value of zero) or presence (one) of the corresponding rock type.

Figures *7.5-1* to *7.5-7* show the RDA biplots for the pXRF and rock type data from campaigns 1 through 7, respectively. The horizontal and vertical axes represent the first and second principal components of the RDA analysis, which capture the maximum variance explained by the pXRF element abundances.

In these plots, blue arrows represent the pXRF elements, and red labels denote the rock types. The length of the arrows reflects the strength of the correlation between the elements and the rock types; longer arrows indicate stronger correlations. The angle between arrows shows the correlation between elements: smaller angles (close to 0 degrees) signify a strong positive correlation, larger angles (close to 180 degrees) indicate a strong negative correlation, and angles close to 90 degrees suggest no correlation.

The position of the red rock type labels relative to the arrows illustrates the strength and direction of the correlation with the pXRF elements. A label pointing in the direction of an arrow indicates a positive correlation with that element, while a label pointing in the opposite direction indicates a negative correlation. Labels closer to an arrow suggest a stronger association with that element. Rock types clustered together suggest similarity with respect to the elements analysed by pXRF.

Each principal component is a weighted average of the pXRF values. The first principal component is the weighted average which has the maximum possible variance; the horizontal axis label shows the fraction of total variance explained by the first principal component. The second principal component is the weighted average which has maximum possible variance subject to the condition that it is uncorrelated with the first principal component. The vertical axis label shows the fraction of total variance explained by the second principal component. Adding these two numbers, the first two principal components in campaigns 1 to 7 capture about 45%, 43%, 64%, 66%, 61%, 59%, 65% of the variation, respectively.

In campaign 1, granophyre (GPH) was positively correlated with high levels of Thorium (Th) and Rubidium (Rb) and negatively correlated with Copper (Cu) (Figure *7.5-1*). Dolerite (DOL) was positively correlated with Titanium (Ti). Gabbro (GBR) and basalt (BAS) was positively correlated with Copper (Cu), Magnesium Oxide (MgO), Aluminum Oxide (Al_2O_3) and Chlorine (Cl). Granite (GRT) is positively correlated with Lead (Pb) and Strontium (Sr).

There are some differences between the RDA plots for campaigns 1 to 7 (Figures *7.5-1* to *7.5-7*). However, GPH was positively correlated with Thorium (Th) for all seven campaigns and positively correlated with Rubidium (Rb) for majority of the campaigns. DOL was positively correlated with Titanium (Ti) for all campaigns except for campaign 7.

In the Year One Report (Curtin University, 2023) based on data from campaigns 1 to 4, it was argued that the rocks are unlikely to have changed their composition from one campaign to another, except that some minerals in the surface layers might dissolve in water and be gradually removed over time. It was argued that these plots are mainly of use for cross-checking the internal consistency of the technique. Year two results also confirmed that Figures *7.5-1* to *7.5-7* are broadly consistent. The vertical axes (second principal component scores) in Figures *7.5-2* and *7.5-6* are reversed relative to other biplots, which is quite normal because the sign of a principal component is not well defined in the mathematical sense.

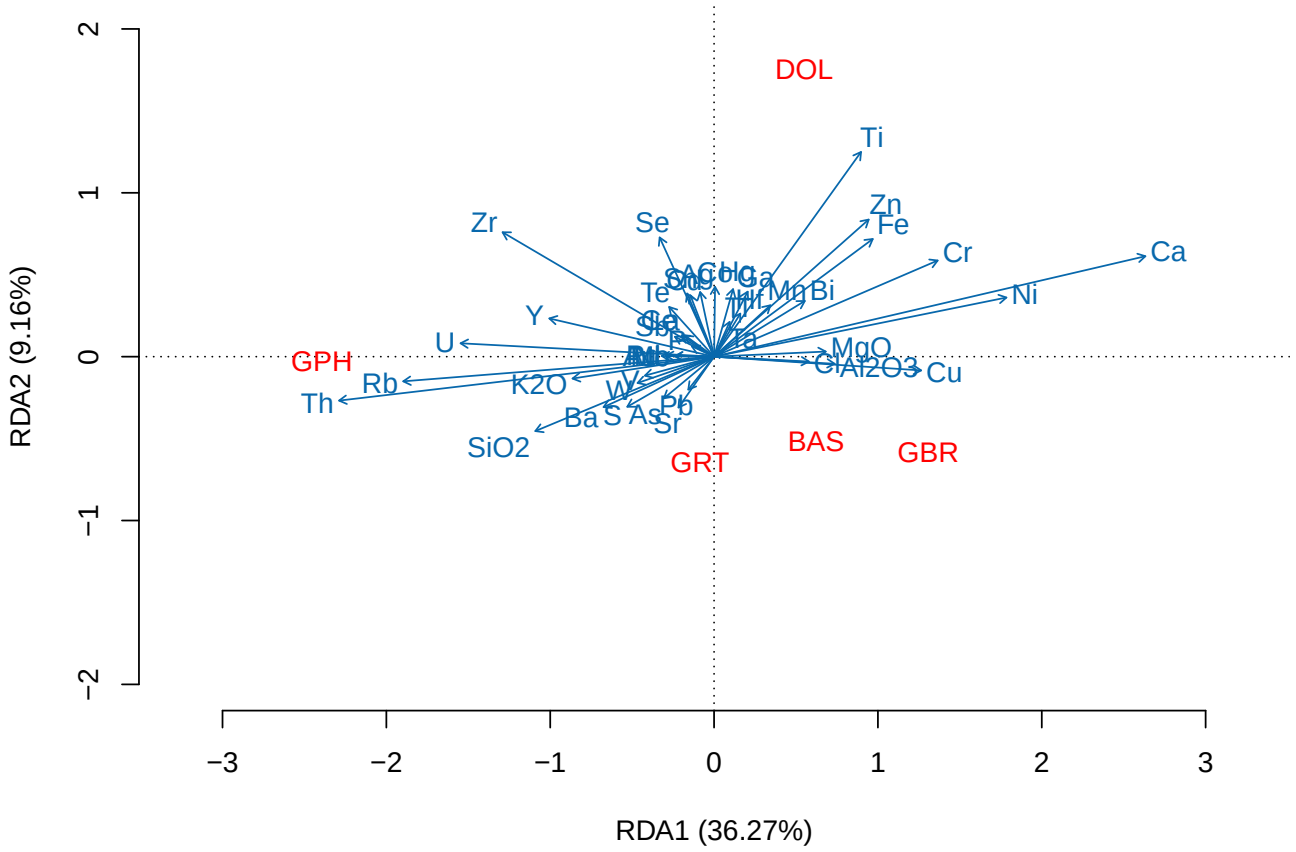

Figure 7.5-1: RDA biplot showing the relationship between chemical elements from the pXRF and rock types in campaign 1. Percentage in parentheses is the percentage of total variation explained by the RDA.

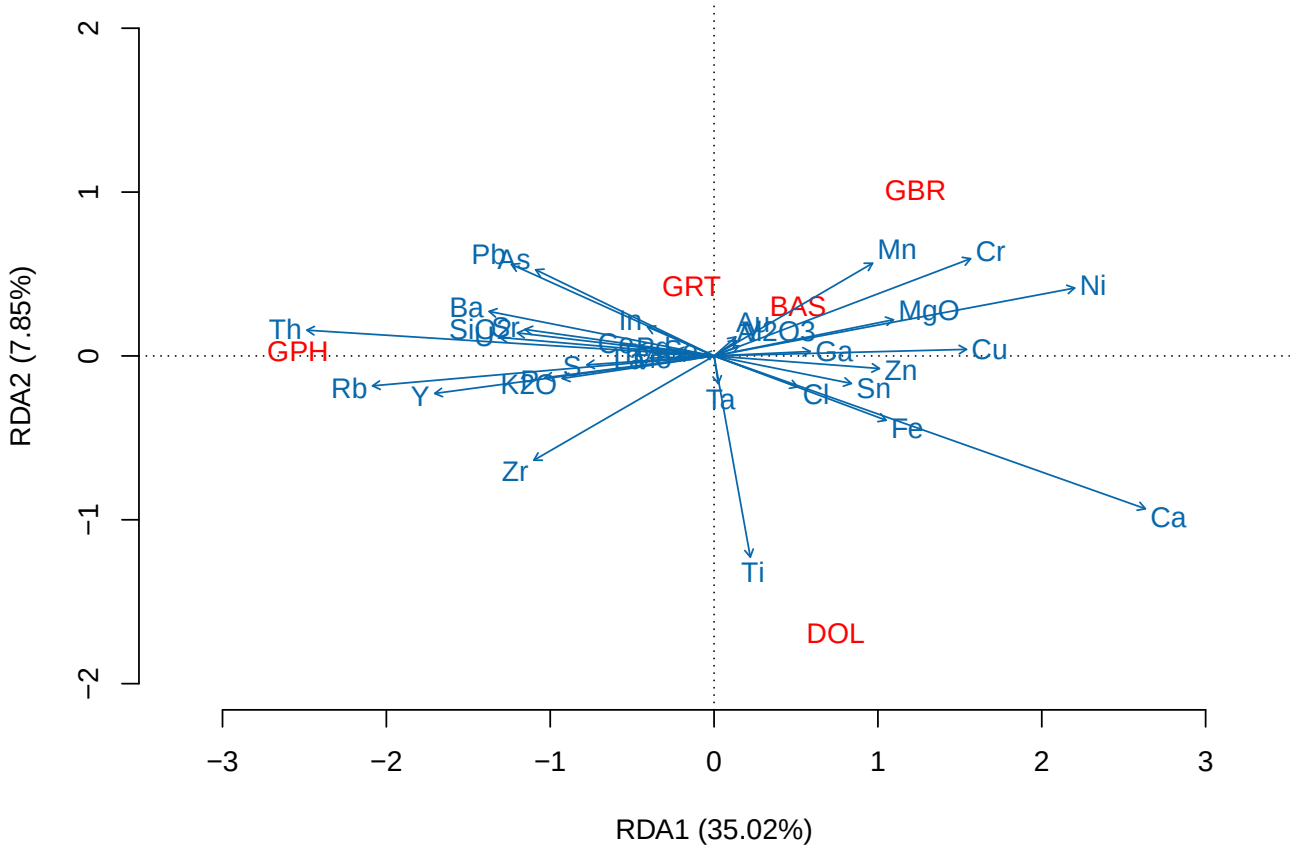

Figure 7.5-2: RDA biplot showing the relationship between pXRF chemical elements and rock types in campaign 2.

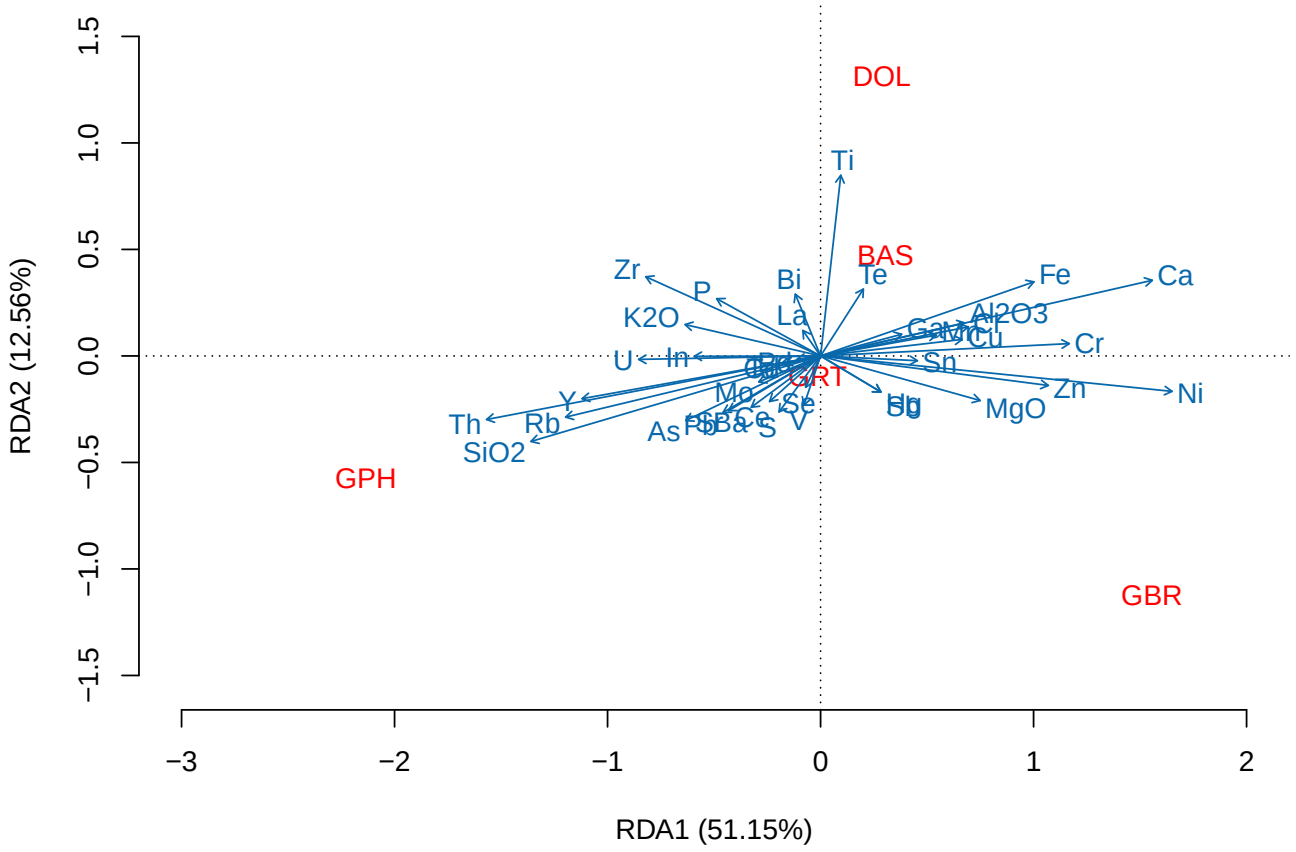

Figure 7.5-3: RDA biplot showing the relationship between pXRF chemical elements and rock types in campaign 3.

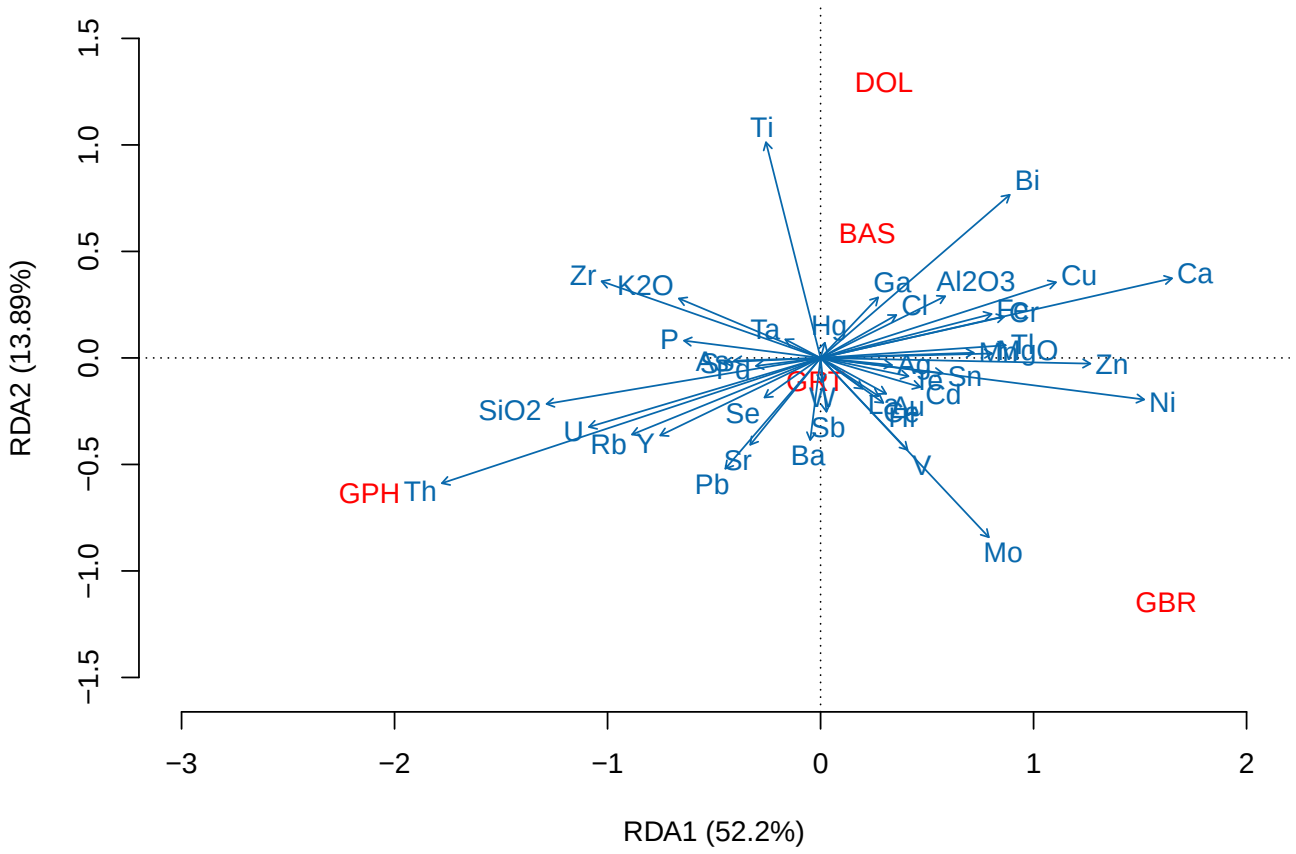

Figure 7.5-4: RDA biplot showing the relationship between pXRF chemical elements and rock types in campaign 4.

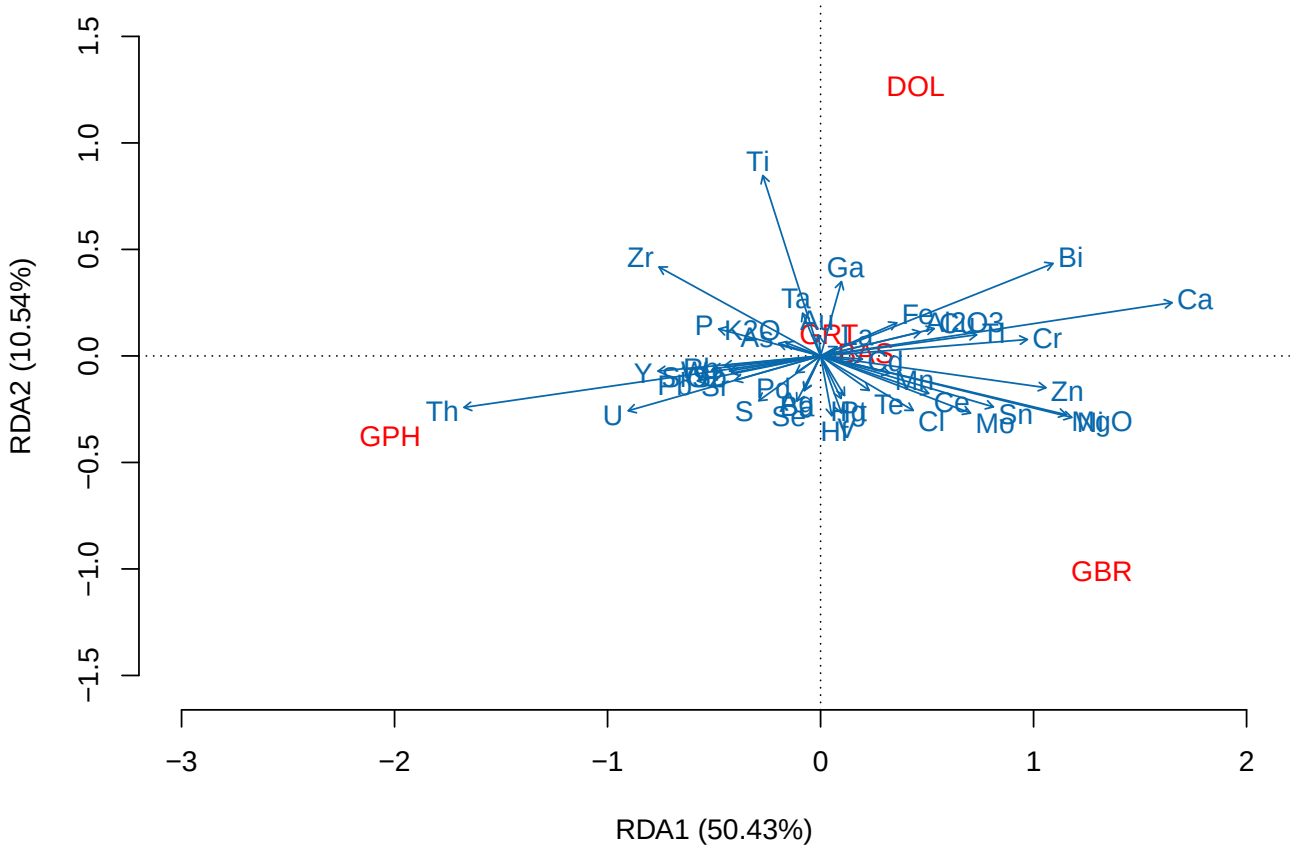

Figure 7.5-5: RDA biplot showing the relationship between pXRF chemical elements and rock types in campaign 5.

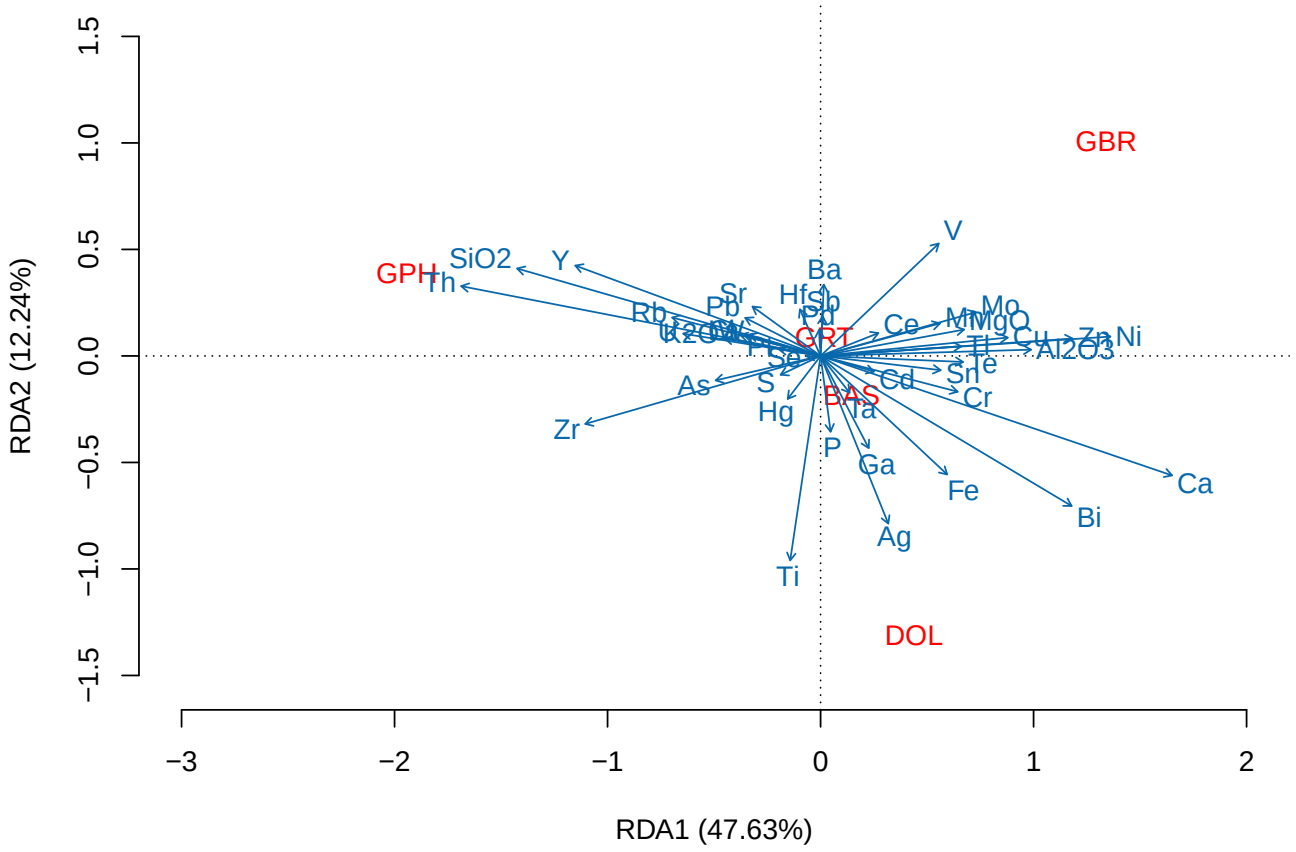

Figure 7.5-6: RDA biplot showing the relationship between pXRF chemical elements and rock types in campaign 6.

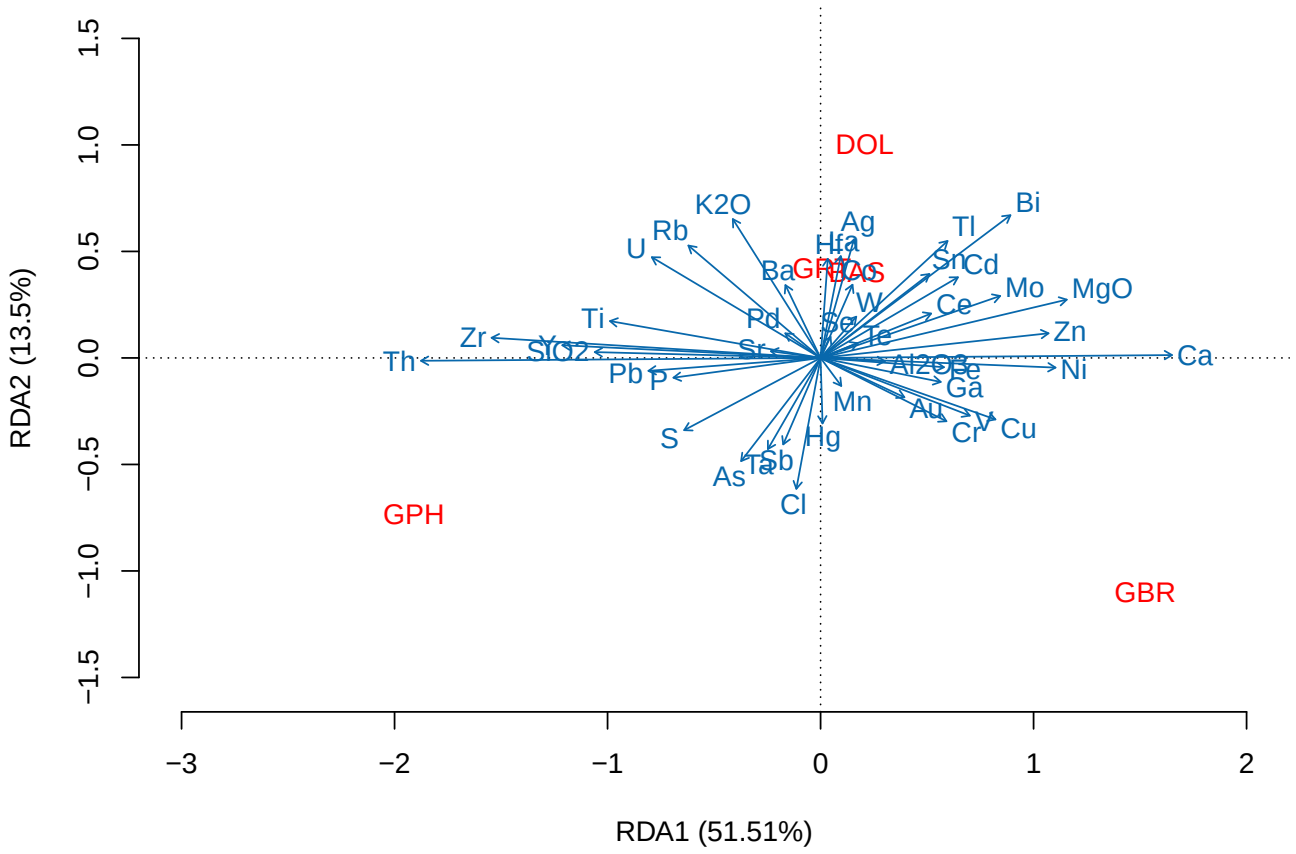

Figure 7.5-7: RDA biplot showing the relationship between pXRF chemical elements and rock types in campaign 7.

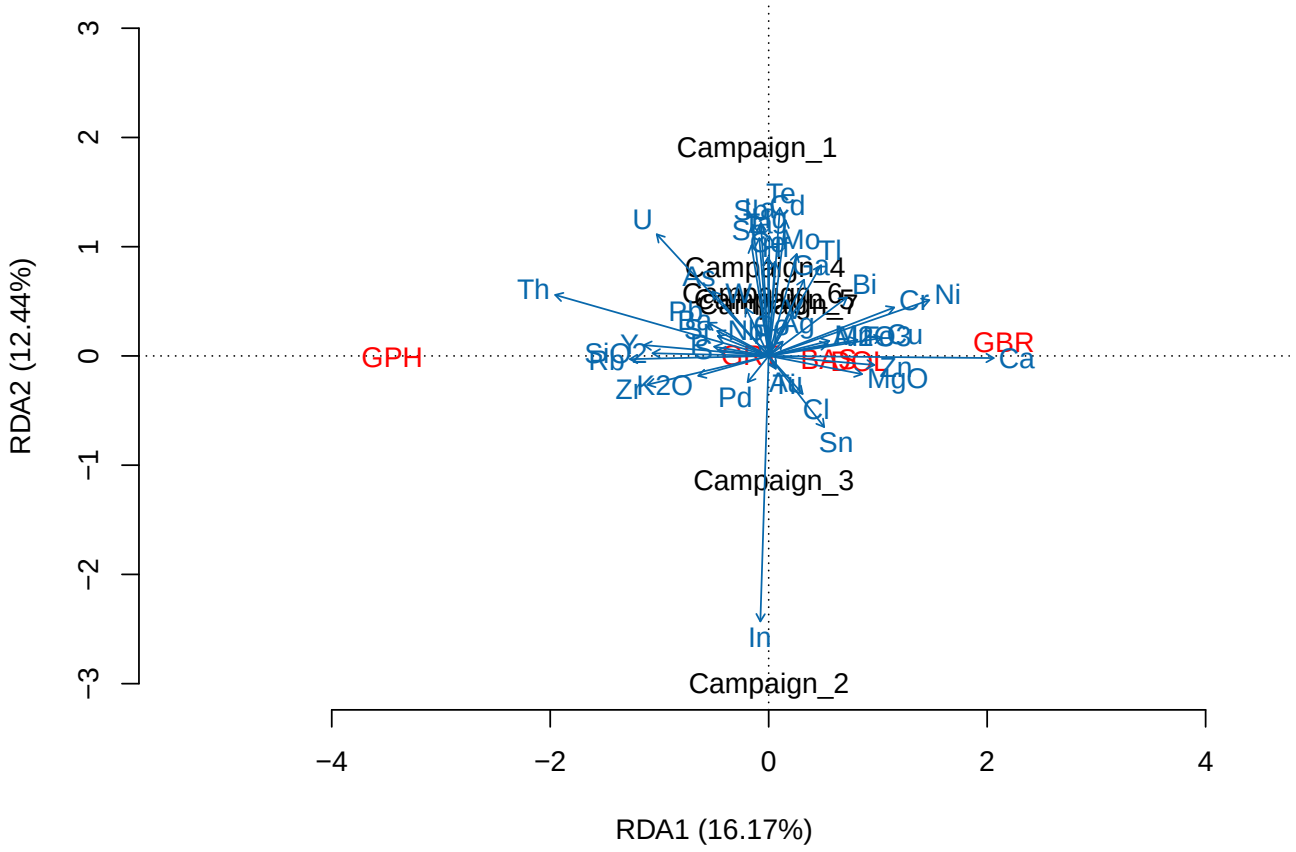

Figure 7.5-8: RDA biplot showing the relationship between pXRF chemical elements, rock types and the seven campaigns.

Figure *7.5-8* shows a biplot for the pooled pXRF data from all seven campaigns, adding the campaign number as an explanatory variable. It does not suggest a difference between campaigns. However, this does suggest that the pXRF data was positively correlated between campaign 1 and 4, and also between campaign 2 and 3.

7.5.3 Ratios of pairs of elements

The ratios of pairs of elements were used to assess the utility of pXRF as a way to monitor patina composition and thickness. The concentration of elements thought to be enriched in the patina (e.g. Ti, Cl, Mn, S, V) were compared with the concentrations of elements thought to be enriched in the substrate (e.g. Si). In this analysis, it was hypothesised that highly patinated samples would have a stronger signal from patina-hosted elements such as Ti, and a weaker signal from weathered rind and fresher rock-hosted elements such as Si. If this signal is a first-order control on element ratios then the pXRF could be used to map patina thickness across Murujuga. The distribution of single elements was also considered. However, element ratios measured by the pXRF are much more consistent than absolute values, so ratios were preferred for this assessment.

The composition of the substrate varies with rock type; granite and granophyre have higher silica contents than basalt, dolerite, and gabbro. This variation provides a possible confounding factor to the proposed analysis. To explore the extent of this variation and the effect that it might have on Si/Ti measurements, boxplots of the ratio of silica to titanium were constructed (Figure *7.5-9*), classified by rock type and by campaign. Note the logarithmic scale on the vertical axis.

There were a few extremely high values amongst these ratios. The technique of winsorization described in Appendix *F*.1 increases robustness and resistance to outliers by reducing extreme values without removing them. Figure *7.5-10* shows the boxplots of the SiO_2 to Ti ratio after winsorization.

The Ti/Si values vary systematically with rock type (Figure *7.5-10*), so the different rock types were separated in the following analysis. Figure *7.5-11* shows spatially smoothed Si/Ti values for rocks classified as granophyre only (the spatial region with granophyre samples only considered for prediction), calculated from the pXRF data from campaigns 1 to 7. Assayed values of SiO_2 and Ti lower than 50 ppm, and missing values, were reset to 50 ppm. The individual ratios exhibited considerable variation and a strongly skewed distribution, so the smoothing was performed on a logarithmic scale.

The panel for campaign 5 shows substantially higher values of Si/Ti in the north (Gidley and Dolphin Islands). Also, campaign 7 has the highest ratio in the northern part of the peninsula. Campaign 3 has the lowest ratio over the entire region. There is no apparent spatial trend in element composition ratios within a particular rock type. The same analysis was done for some other major element ratios, including the ratios of manganese to silica, sulphur to silica, chlorine to silica, and vanadium to silica. No systematic trends in these ratios were observed.

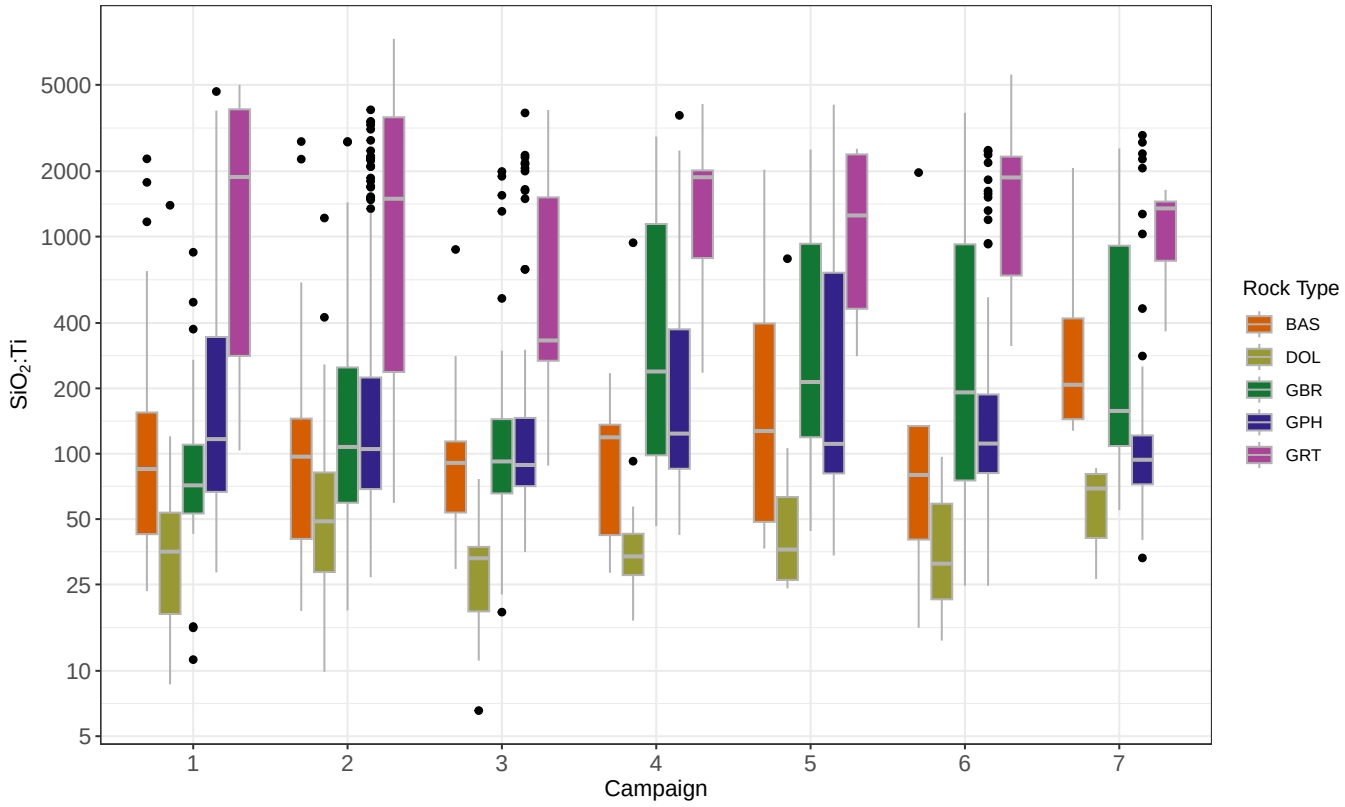

Figure 7.5-9: Boxplots of SiO_2:Ti by campaign. Note logarithmic scale.

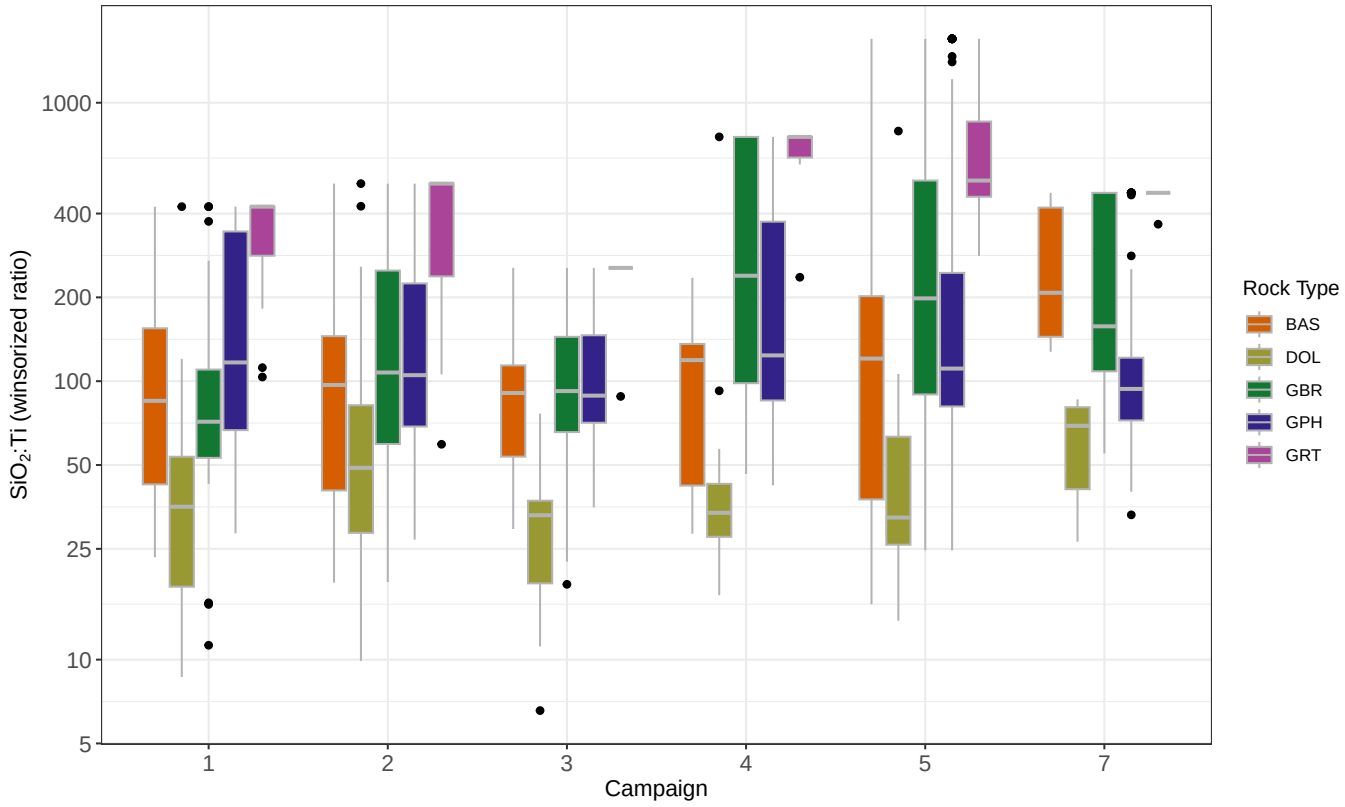

Figure 7.5-10: Boxplots of SiO_2:Ti ratio by campaign after winsorization. Note logarithmic scale.

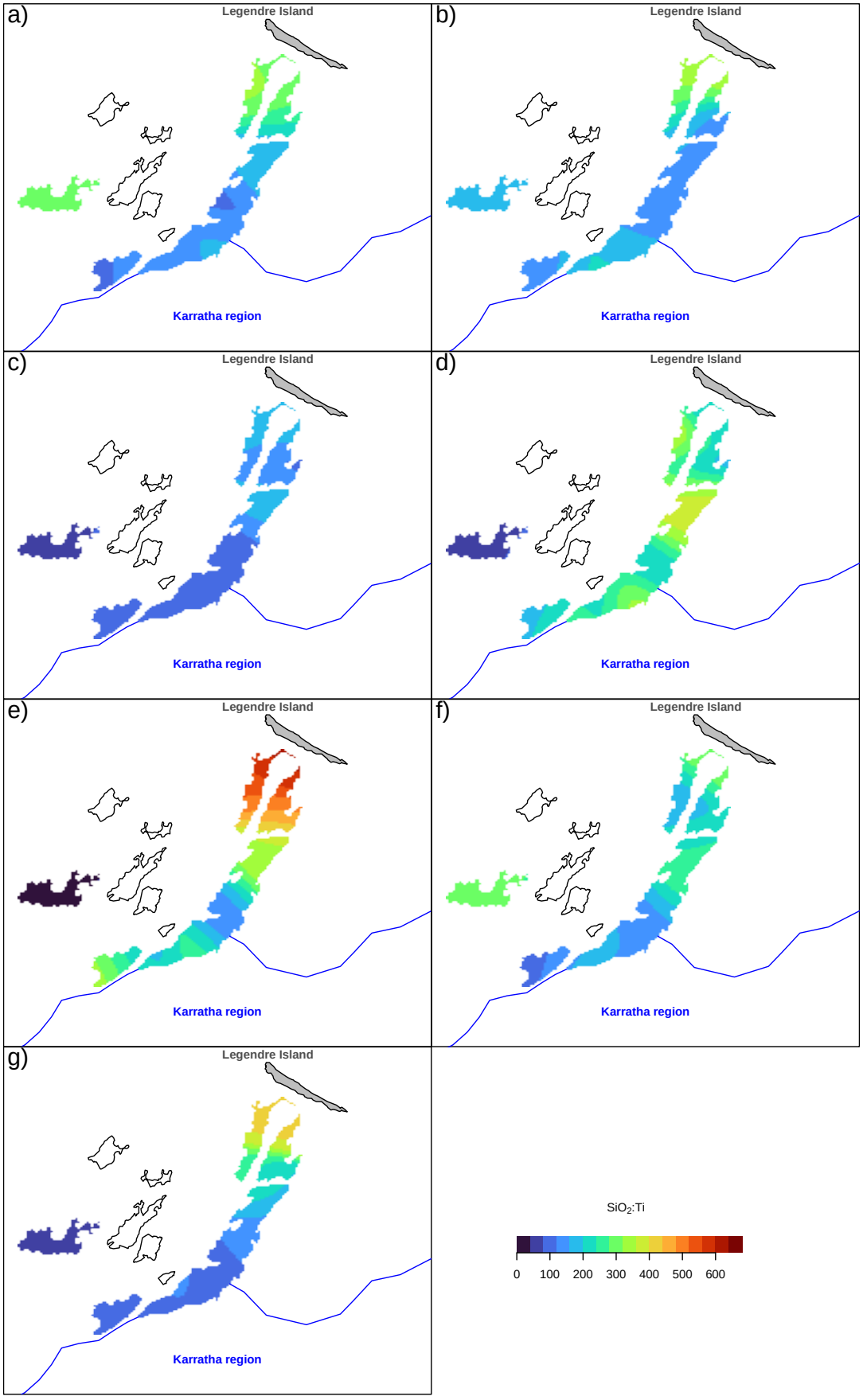

Figure 7.5-11: Spatial smoothing of SiO_2:Ti ratio in granophyre (GPH) of campaigns 1 (a) to 7 (g), respectively. The white colour polygons are the islands with zero granophyre samples.

7.6 Inorganic geochemistry – porosity

7.6.1 Background

Microstructure of rock samples was investigated by preparing thin sections and visualising them under various modes of microscopy.

Figure *7.6-1* shows a back-scattered electron microscope image of a thin section of sample rock (granophyre from site AQ03). Lighter areas in this greyscale image represent rock components of different kinds, while the very darkest areas are void space that is not occupied by rock. This void space is occupied by the epoxy resin in which the rock samples were embedded for section preparation. The large black area at the top of the image is empty space outside the rock sample; the macroscopic surface of the rock is the lighter area that is in contact with this black area.

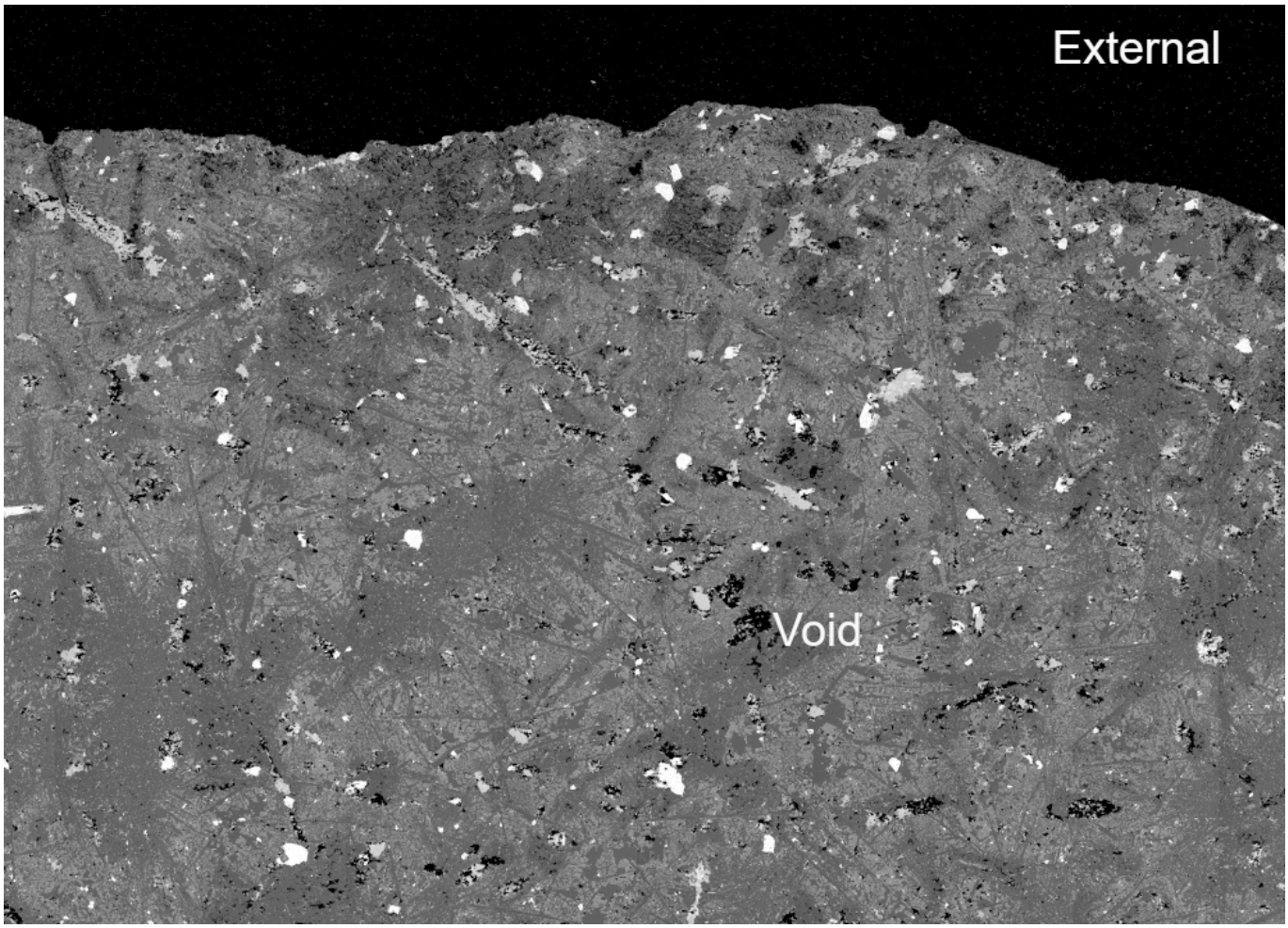

Figure 7.6-1: Scanning electron microscope, back-scattered electron image of a thin section of granophyre sample from site AQ03. Surface at the top of image. The physical size of the image is about 10 mm wide by 7.5 mm high. Black area at top is exterior. Smaller, dark areas within sample are voids: one void is labelled in the figure.

In this section of the report, such images are analysed to estimate rock porosity, and to determine how the porosity changes as a function of depth below the rock surface. Porosity estimates obtained

from rocks at different spatial locations are compared. Spatial variation in porosity across Murujuga is investigated. The methods for quantifying porosity are detailed in Appendix *F*.2 and summarised below.

7.6.2 Image processing

The rock sample images represent a physical size of 39 to 44 mm wide and 4.5 to 13.2 mm high. Each image was based on a square pixel raster, with pixel side lengths between 2.0 and 2.5 μm in different images, so that the raster was typically 20,000 pixels wide and 2,000 to 6,000 pixels high (40 megapixels to 180 megapixels).

Figure *7.6-1* is approximately 10 mm by 7.5 mm in real size. This is part of an original sample image that is 42.4 mm wide by approximately 8 mm wide with a pixel size of 2 μm by 2 μm.

Images needed to be cropped to remove any physical edges visible on the sides or bottom of the image. To help make processing times manageable and to allow multiple samples per site, the images were then cropped into four fields of approximately equal physical size.

The grey-scale images were then converted to binary images in which the value one (white) represents rock and the value zero (black) represents void space. A simple threshold operation was used. Figure *7.6-2* shows the result of thresholding Figure *7.6-1*. The result depends on the choice of greyscale threshold; a range of thresholds was considered, and the results are quite insensitive to the threshold choice.

The large void space at the top of the image is exterior to the rock. The amount of void space in the interior of the rock appears to reduce progressively from top to bottom in Figure *7.6-2*, that is, moving deeper into the fresh rock and further away from the macroscopic surface. The objective of this analysis is to quantify the change in void space by inferring the porosity of the rock at different depths below the surface.

The macroscopic surface of the rock sample was identified from the image data by finding the largest connected component of void space, and nominating this as the “exterior” of the rock. In order to avoid artefacts in which large cracks were labelled as “exterior” to the rock, some images were first smoothed using mathematical morphology operations (Serra, 1982; Soille, 2003), in particular, morphological opening. The results are somewhat sensitive to the choice of opening radius, and require human judgement in some extreme cases. Further details of this procedure are given in Appendix *F*.2.3.

Depth (distance from the macroscopic surface of the rock) was then computed for each pixel in the image, using the distance transform (Rosenfeld and Pfalz, 1968). Figure *7.6-3* illustrates an example. Panel (a) shows the input binary image, and panel (b) shows the distance values, represented as colours according to the colour ribbon at right. For example, blue colours represent distances (depths) shorter than about 750 μm.

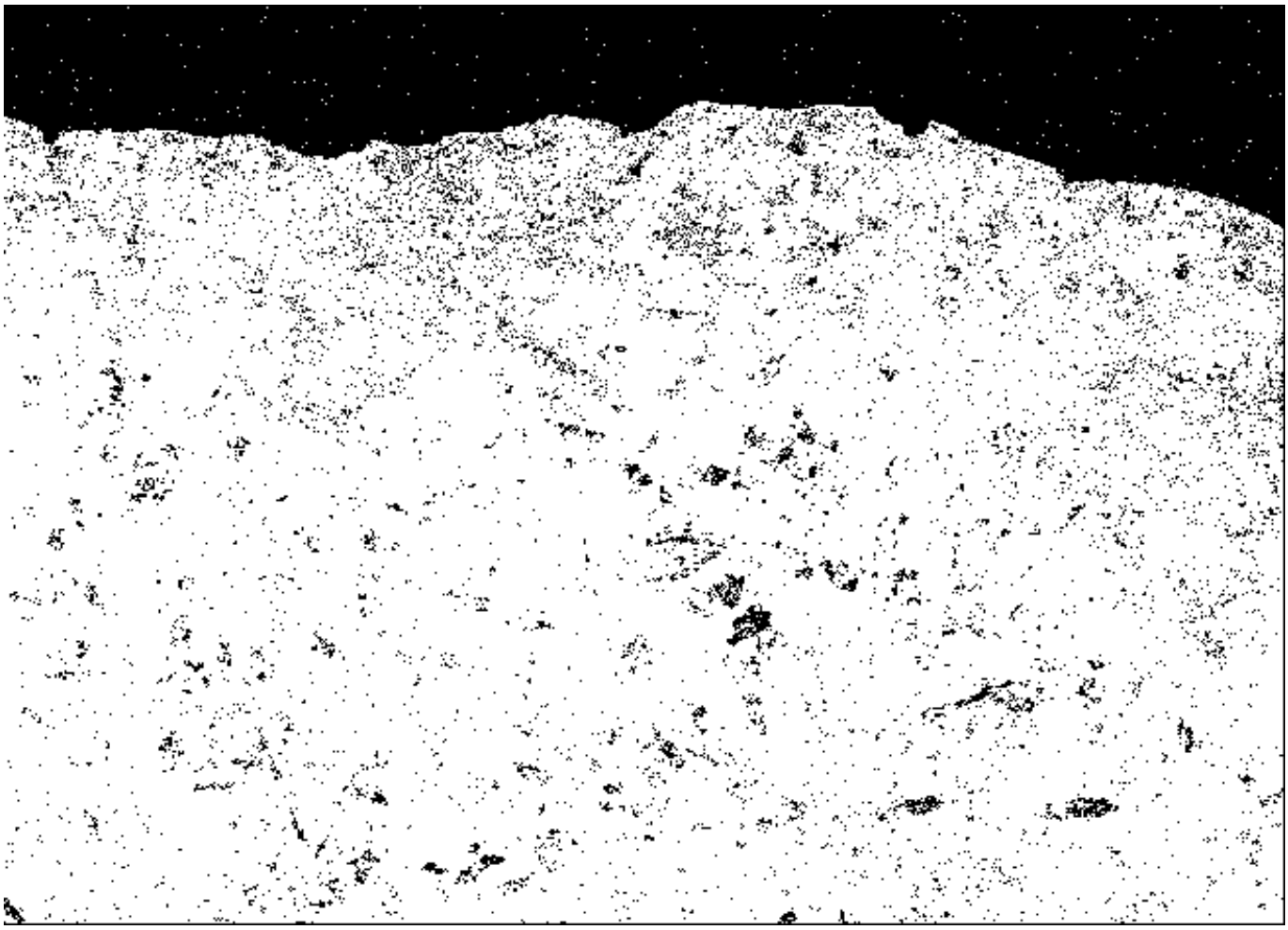

Figure 7.6-2: Binary image obtained by thresholding the granophyre AQ03 image in Figure 7.6-1. Binary value one (white) interpreted as rock; binary value zero (black) interpreted as void space.

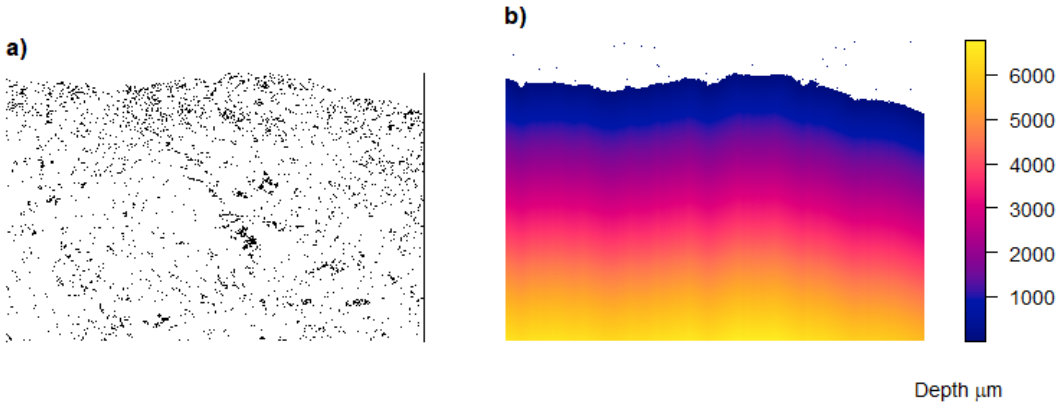

Figure 7.6-3: Distance transform. (a) binary image; (b) distance transform of "top". Granophyre from site AQ03, field four of four.

7.6.3 Porosity curves

For each greyscale input image, the processing steps described above yield three digital output images: a binary image T identifying the "exterior" (with value one in the exterior and zero in the interior of the rock), a binary image V indicating the presence of void (with value one in void space and zero in rock), and a numerical image D giving the distance from the pixel in question to the rock surface.

The data pairs (D, V) for each pixel where $T = 0$ were then extracted. Nonparametric regression was then applied to the (D, V) data to obtain a smooth estimate of porosity as a function of depth $p(d)$ as described in Appendix *F*.2.5. Figure *7.6-4* shows an example.

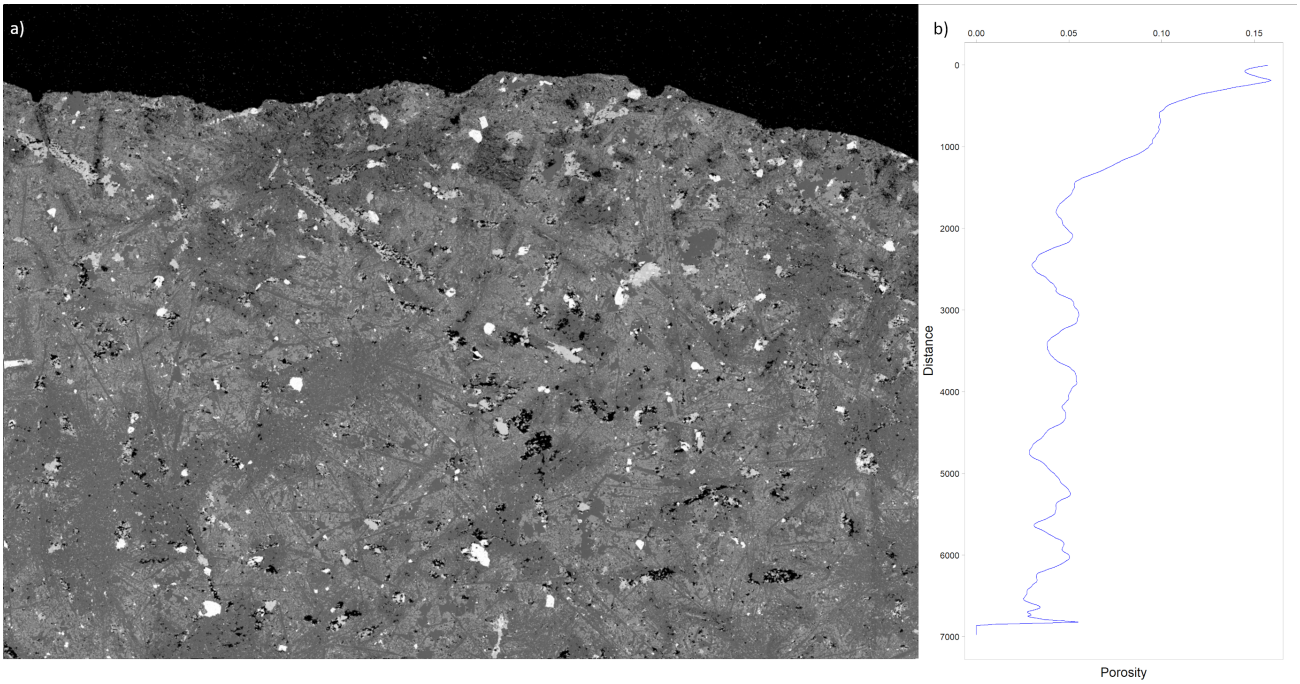

Figure 7.6-4: Estimation of porosity as a function of depth. (a) grey scale backscattered electron image microscope from Scanning electron microscope. (b) smoothed estimate of porosity as a function of depth. Granophyre, site AQ03, field 3 of 4. Porosity values are fractions between zero and one.

This approach produces estimates of *volumetric* porosity as a function of depth. Volumetric porosity of rock is the fraction of volume of 3D space inside the rock which is occupied by voids. Thus a porosity value of 0.2 would indicate that 20% of the macroscopic volume of material is occupied by void space. A version of Delesse's Principle (Delesse, 1847) is used to obtain valid estimates of 3D volumetric porosity from the 2D section, as explained in Appendix *F*.2.2. A porosity value of 0.2 on the horizontal axis in Figure *7.6-4* indicates that the estimated volumetric porosity at that depth is 20%.

7.6.4 Porosity index

The next step in the investigation is to compare the porosity of different rock samples, and to determine whether differences in porosity are associated with other variables, such as exposure to

pollutants. For such purposes, it is useful to define a single numerical summary index of porosity for each sample. Various options for such an index are proposed in Appendix *F*.2.6. Here two of those options are considered, which are calculated from the porosity curve:

- **Average porosity (to 3.1 mm)**: the average of the estimated porosity $p(d)$ over the range of depths d from 0 mm (the surface) to 3.1 mm (the depth of the narrowest sample).
- **Maximum porosity**: the maximum of the estimated porosity $p(d)$ over all observed depths d.

These indices are porosity values (fractions between zero and one), with zero indicating solid rock without pores, and one indicating void space.

Average porosity is equivalent to the standard estimate of volumetric porosity for the region extending from the surface to a depth of 3.1 mm. It reflects the condition of the rock surface to a depth of 3.1 mm. Maximum porosity reflects the condition of the material lying immediately below the surface, because all the porosity curves estimated from the samples reached their maximum porosity value at a very shallow depth.

Very high values of average porosity suggest a rock texture that is deeply penetrated by void space. Very high values of maximum porosity suggest a rock texture in which the patina is a thin cap over a very porous 'honeycomb' layer.

Porosity index values for all samples for four morphological opening radii (0 μm, 10 μm, 20 μm, and 40 μm) are depicted graphically in Appendix *G*.1 in Figure *G.1-9*.

The index used in the following figures is the average porosity over depths 0 to 3.1 mm, with the surface defined by an opening radius of 20 μm, and using the automatically selected bandwidth for smoothing the porosity curve. Porosity values are fractions between zero and one.

Figure *7.6-5* shows a histogram of the porosity index values obtained for the 99 granophyre rock samples. This right-skewed histogram could be approximated by a gamma distribution (with fitted shape parameter 1.58) as shown by the blue curve, or by a mixture of two normal distributions.

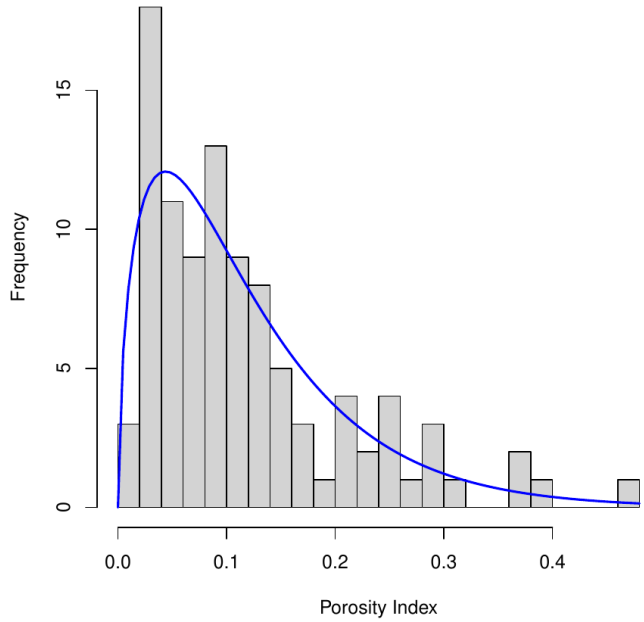

Figure 7.6-5: Histogram of values of average porosity index for 99 granophyre rock samples at sites across Murujuga. Blue curve shows fitted gamma distribution.

7.6.5 Spatial variation in porosity

Spatial variation in porosity is a key question for investigation. Here an exploratory analysis is presented, using the numerical indices of porosity described above.

Figure *7.6-6* shows the values of the porosity index computed from granophyre rock sample images obtained from sites across Murujuga. The Murujuga region is shown in perspective view looking from the south-west. The porosity values are depicted as vertical spikes, with height proportional to the porosity index value, as shown in the accompanying legend, with the base of the spike placed at the geographic location of the site from which the rock sample was taken. The head of each spike is drawn as a circular bubble. Bubbles lying along the same vertical spike represent porosity values taken from different rock samples at the same geographic location. Most of the sites are on the main peninsula, with a few sites on the northern and western islands. This reflects the distribution of granophyre.

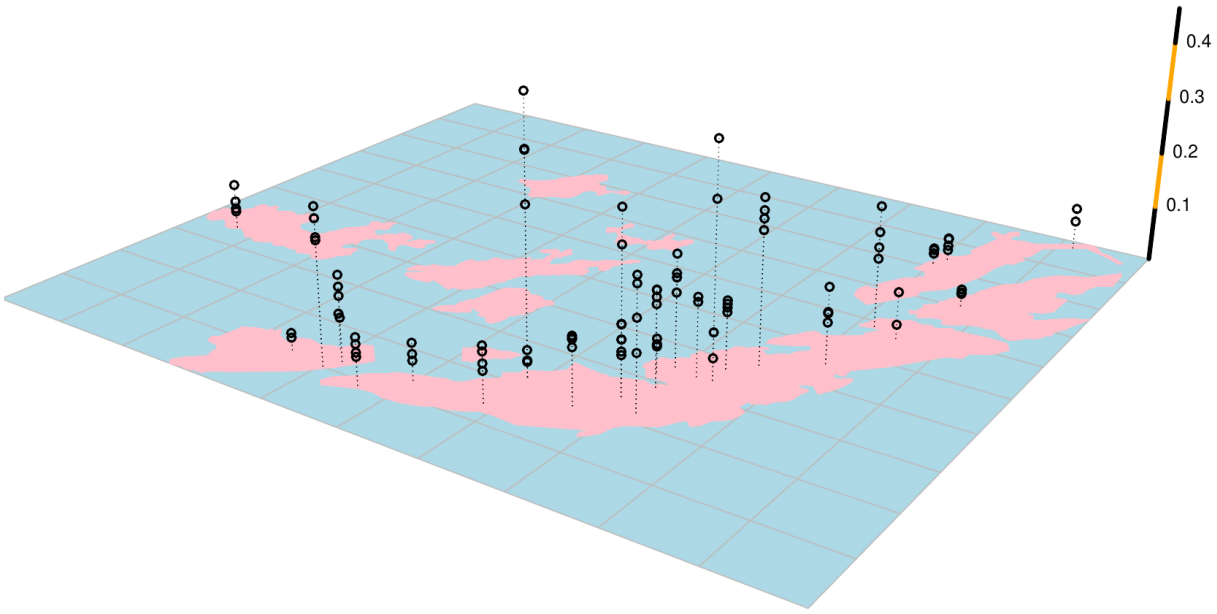

Figure 7.6-6: Average porosity index of granophyre rock samples at sites across Murujuga. Perspective view showing porosity index values as vertical spikes.

The average porosity values tend to be lower in the north and west (the left and right extremes of the figure). Larger values are observed close to the industrial area and towns. This impression is further supported by Figure *7.6-7* which shows the mean of the porosity estimates at each sample location.

Spatial smoothing of these porosity index values may provide useful information about overall trends in porosity across Murujuga. The Nadaraya-Watson smoothing technique (described in Appendix *F*.1) effectively calculates, at each geographic location, a weighted average of the porosity index values observed at nearby sites. Figure *7.6-8* shows the spatially smoothed value of the average porosity index obtained from the point data shown in Figure *7.6-6* using the Nadaraya-Watson smoother. The smoothed average porosity values tend to be higher on the Burrup Peninsula and lower on the northern and western islands, as expected from the point data.

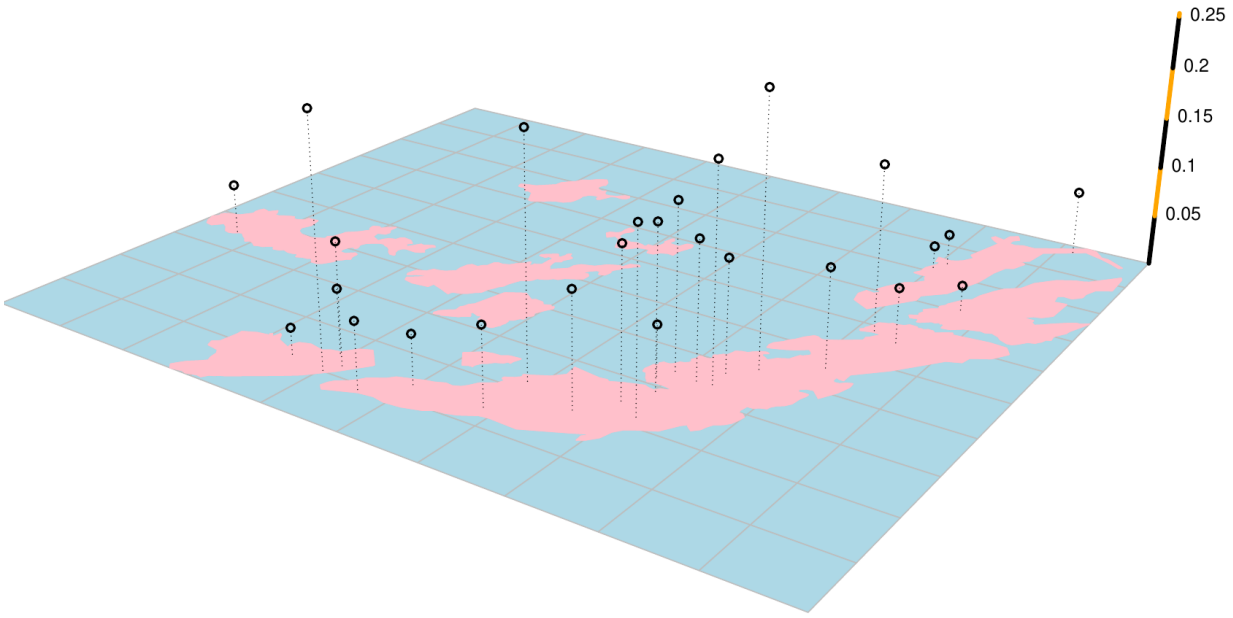

Figure 7.6-7: Mean estimated porosity at each sample location. Perspective view showing mean porosity value at each location as a vertical spike.

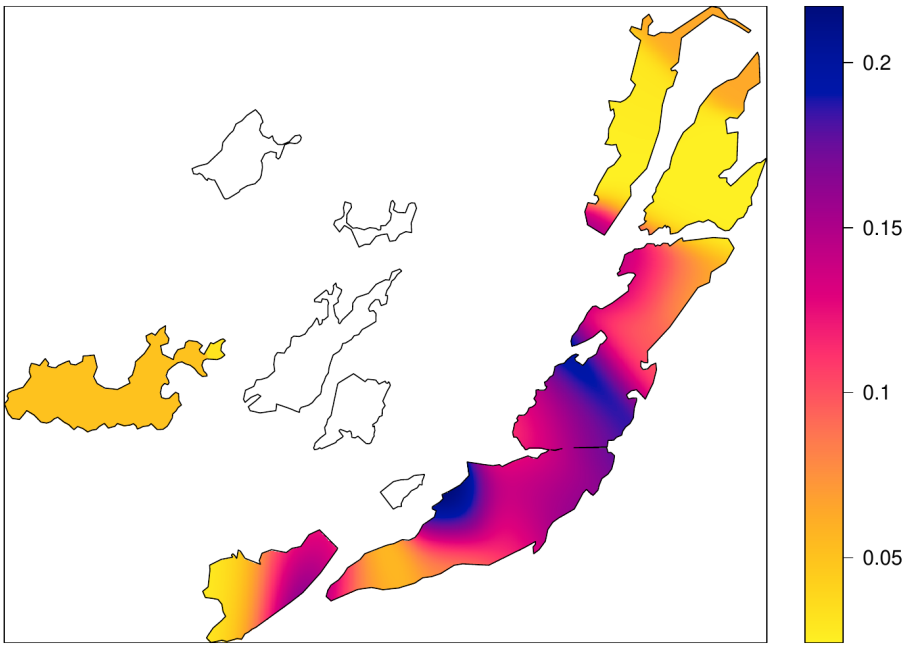

Figure 7.6-8: Spatially smoothed (Nadaraya-Watson) average porosity (for depths from 0 to 3.1 mm) for morphological opening radius = 20 μm.

There is a similar outcome for smoothed surfaces of the maximum porosity index, shown in Figure *G.1-13* in Appendix *G*.1.3.

7.6.6 Significance test of elevated porosity

Figure *7.6-8* above, and similar figures in Appendix *G*.1.3, suggest that there is an area of Murujuga where rock porosity is elevated in comparison to the overall tendency. It is important to assess whether this deviation is statistically significant.

Appendix *F*.3 describes the "pointwise" Monte Carlo test of the null hypothesis of spatially constant mean porosity against the one-sided alternative hypothesis of elevated porosity at a given location.

For the purposes of this test, a single numerical index of porosity is selected. The 'porosity' of an individual rock surface is now taken to be a single numerical value, calculated using one of the indices described above. The 'mean porosity' over a spatial region is defined as the average of the values of the porosity index for all rocks in the region. Likewise the mean porosity in the vicinity of some location is defined as the average of the porosity index values in that vicinity.

At every location across Murujuga, a separate statistical test is conducted, in which the null hypothesis that

> "the average porosity index of rocks in the vicinity of this location is *equal to* the average porosity index of rocks at all other locations"

is tested against the one-sided alternative hypothesis that

> "the average porosity of rocks in the vicinity of this location is *greater than* the average porosity of rocks at some other locations."

Each hypothesis test results in a p-value (probability value) which provides a measure of the strength of evidence to reject the null hypothesis. The smaller the p-value, the stronger the evidence against the null hypothesis.

Figure *7.6-9* shows the results of the pointwise Monte Carlo test applied to the porosity index data in Figure *7.6-6*. Panel (a) of Figure *7.6-9* shows the p-value of the pointwise Monte Carlo test at each spatial location. The p-values are quite small for some locations, suggesting strong evidence against the null hypothesis.

In panel (b) of Figure *7.6-9*, locations are coloured orange and labelled `SIGNIF` when the p-value of the pointwise Monte Carlo test is less than or equal to 0.05, so that the test result is statistically significant, according to standard criteria. Other locations are labelled `NONSIG` for non-significant. Loosely speaking, the locations coloured orange are those where there is statistically significant evidence of elevated porosity.

Some important caveats about the interpretation of the pointwise test are explained in Appendix *F*.3. Figure *7.6-9* indicates that, if a geographic location had been nominated in advance and the test had been performed at this location, the result would have been statistically significant, and the hypothesis of constant mean porosity would have been rejected, if the specified location had been one of the locations shown in orange in panel (b) of Figure *7.6-9*.

Even if the null hypothesis of constant mean porosity were true, random variability would cause fluctuations in the observed porosity, so that the pointwise test would be likely to produce spuriously significant results in some locations (indeed, this should occur at about 5% of locations by area

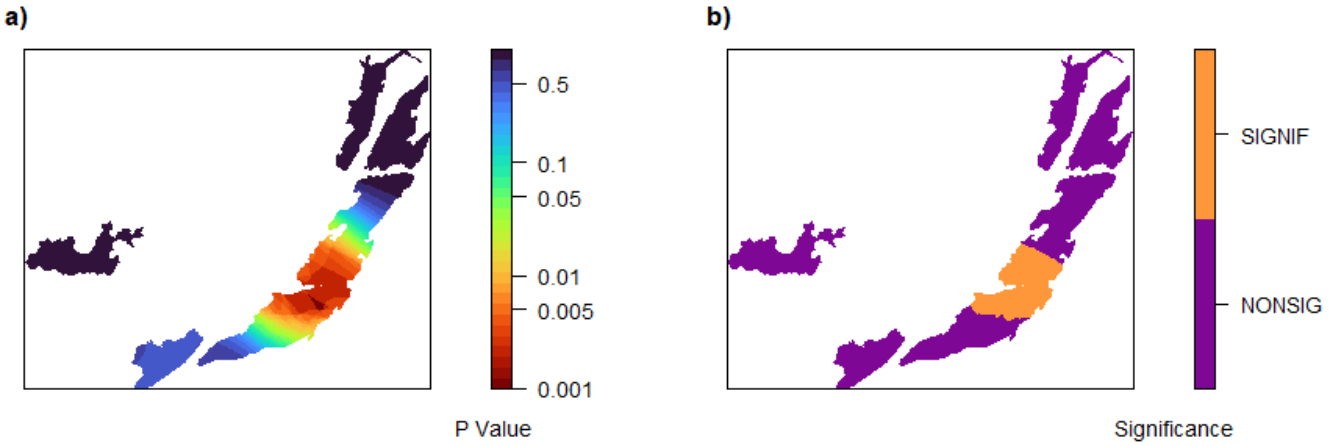

Figure 7.6-9: Results of pointwise Monte Carlo test of the null hypothesis of uniform porosity against the alternative of locally elevated porosity: (a) p-value of the test at each spatial location; (b) orange colour identifies locations where the test is statistically significant.

across the peninsula). The counterpart of Figure *7.6-9* would then show disorganised patches where the result of the pointwise test is (spuriously) significant.

To deal with this issue, Appendix *F*.3 also describes the "global" test of the null hypothesis of constant mean against the alternative hypothesis of elevated porosity in some region (where the region of elevated porosity is not specified in advance).

The p-value for this global test is 0.039 for the data shown here. Similar results are obtained using different porosity indices and algorithm parameter settings, as reported in Appendix *G*.1.3.1. It is provisionally concluded that

1. there is statistically significant ($p < 0.05$) evidence that there is an area of elevated porosity at Murujuga;
2. the best current estimate of the area of elevated porosity is indicated by the orange area in panel (b) of Figure *7.6-9*.

This page is intentionally blank.

7.7 Inorganic geochemistry – permeameter

7.7.1 Background

The finding that rock porosity is elevated in some locations at Murujuga, documented in Section 7.6, requires further investigation. The method used to quantify porosity involved destructive sampling of rock and intensive labour, and has yielded only a small dataset.

It would be desirable to find a non-destructive method of measuring porosity that could be deployed in the field. This would allow collection of larger datasets and repeated measurements at the same location, making it possible to detect change in porosity over time.

The team conducted additional field observations using a portable handheld device (TinyPerm 3) which measures the *permeability* ("air permeability") of the rock surface (Figure *7.7-1*). Air permeability of a material is a measure of the propensity of the material to allow air, at a slightly elevated air pressure, to move through the material. It may be interpreted as an alternative measure of porosity for some materials, but is also related to the sizes of cracks and channels at the surface of a dense material. Permeability is expressed in Darcy (D) or milliDarcy (mD). Typically cited values of permeability are 1 Darcy for sand, 10^{-8} Darcy for solid granite and 10^{5} Darcy for gravel.

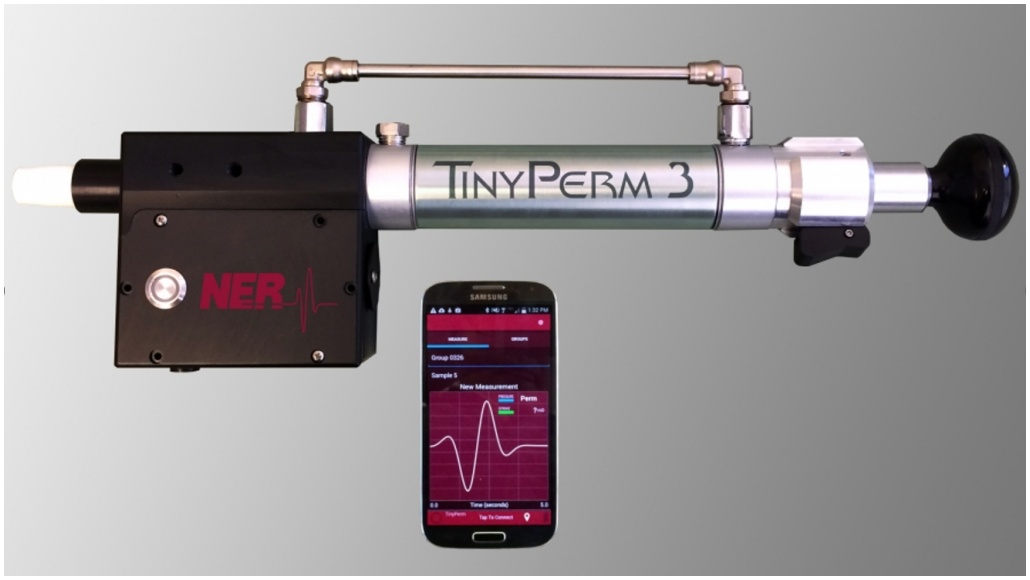

Figure 7.7-1: TinyPerm 3 and the Android device (NER website)

The instrument consists of a metal cylinder with a rubber nozzle at one of its extremities. It measures the vacuum created over the specimen surface by the stroke of a syringe at the nozzle's opposite side. The TinyPerm 3 records the transient vacuum and the syringe volume over time and transmits real-time data to an Android device via Bluetooth. The TinyPerm 3 measures the air permeability of the rock matrix and open fractures (10 μm–-2 mm in size) on outcrops, down to a depth of about 18 mm (Skurtveit et al., 2021). The apparatus gives reliable permeability measures from 1 mD to 10 D for an intact rock.

7.7.2 Measurement method

During campaign 7, TinyPerm 3 was used at 29 of the 41 visited rock art panels, in a trial to assess whether the instrument was able to produce reliable, repeatable measurements of permeability. As this instrument had not previously been used by the team, the methods were developed and updated throughout the campaign.

Geochemical data were recorded on three representative spots on each rock art panel. The TinyPerm 3 was used to obtain five permeability measures from each spot. If the permeability is of the order of a few mD then each measurement can take several minutes to complete. Lengthy measurements are less reproducible than shorter measurements because it is difficult to maintain consistent pressure on the instrument plunger, particularly where the rock surface is difficult to access. To mitigate these issues, the TinyPerm 3 algorithm has an option, referred to as the Extrapolation Data function, which reduces the time required for measurement. If this function is enabled, the permeability is calculated by extrapolating data collected over a measurement of user-determined length, referred to as the Extrapolation Time, if pressure has not dropped by a user-determined amount, referred to as the Decay Amount within that time. For the Murujuga measurements, the Extrapolation Time and Decay Amount were set to 30 s and 50%, respectively, as recommended by the manufacturer.

7.7.3 Validation of technique

Permeability measurements were performed on rock art panels visited in campaign 7 at the same time as the wet geochemistry measurements of *pH*, *ORP* and Cl^- were performed. Since these different measurements all interact with the rock surface, it was conceivable that they could interfere with each other. Accordingly, at eight of the field sites, permeability was measured both before and after conducting the wet geochemistry sampling. Figure *7.7-2* shows a boxplot of these 'before' and 'after' permeability measurements. A two-sample t-test was conducted on 'after' minus 'before' permeability measurements and concluded that there is no statistically significant difference between the permeameter readings before and after the wet geochemistry procedure (p-value = 0.335).

In the current method, the Extrapolation Time is set to 30 s and the permeameter is applied to a dry surface.

The permeameter procedure involves holding the device against the rock surface for either 30 or 60 seconds. Possible sensitivity to the duration of measurement was investigated by a small experiment at one field site, EX06_GPH. The TinyPerm3 measured the rock art panel for 30 seconds (repeated $n = 9$ times) and 60 seconds (repeated $n = 9$ times). The results are depicted in Figure *7.7-3*. A two-sample t-test indicated no statistically significant difference between the two groups of measurements (p-value = 0.412); this test was repeated with the outlier (63.173 mD) removed and the conclusion remained (p-value = 0.087).

No anomalous behaviour was observed.

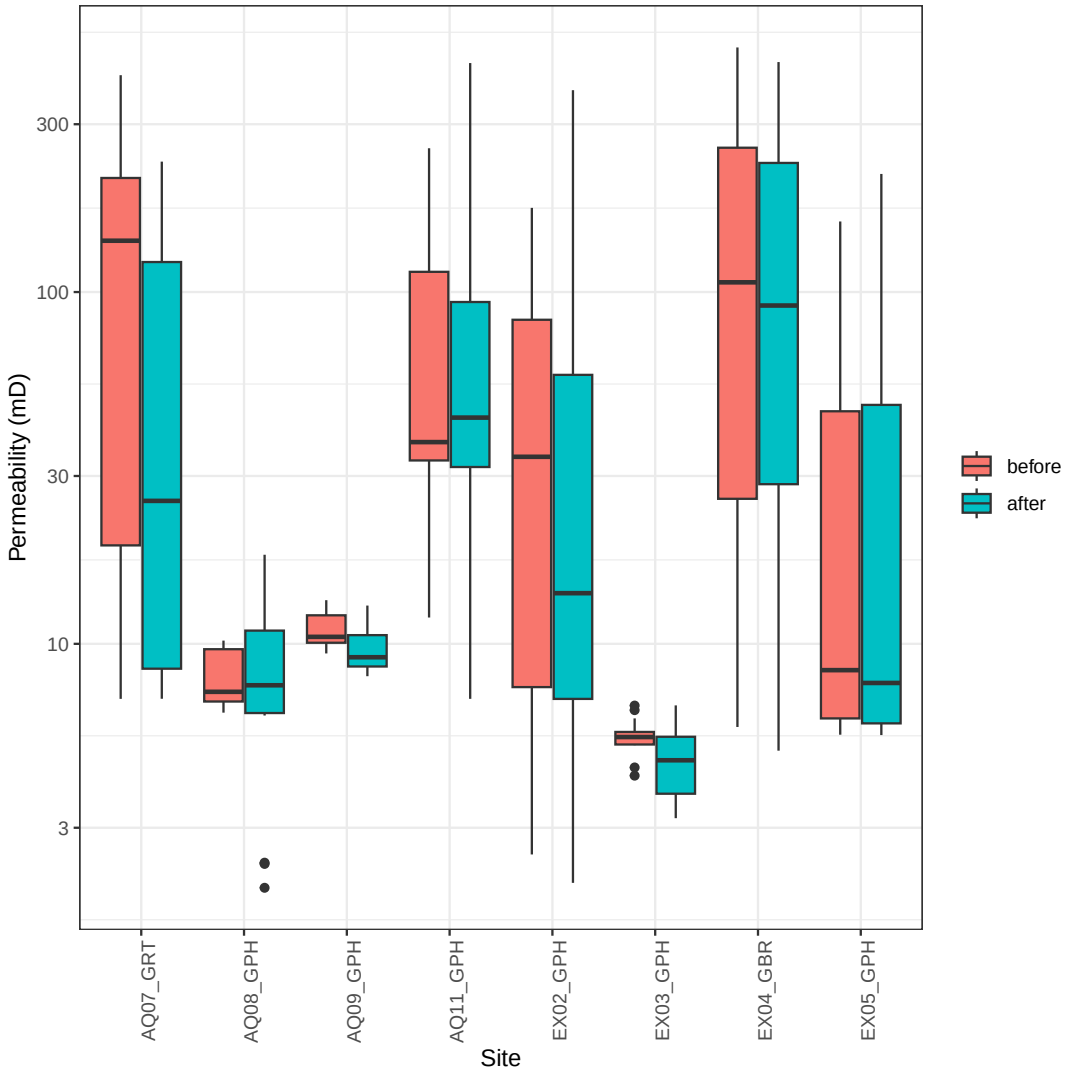

Figure 7.7-2: Boxplots of permeability measurements taken from eight sites before and after wet geochemistry sampling was conducted. Note logarithmic scale.

7.7.4 Permeability observations

Figure *7.7-4* displays (on a logarithmic scale) the full set of permeameter measurements obtained in campaign 7 by rock type. Granite has the highest median value and basalt has the lowest. The other three rock types (dolerite, gabbro and granophyre) have similar permeability.

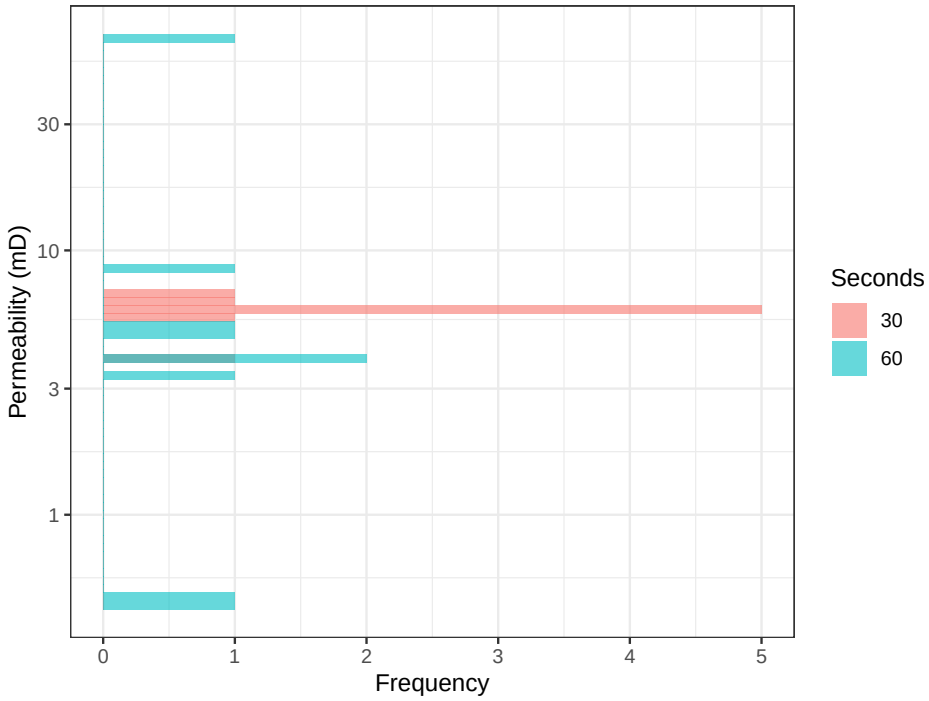

Figure 7.7-3: Histogram of 30 and 60 second permeability measurements at site EX06_GPH. Note logarithmic scale.

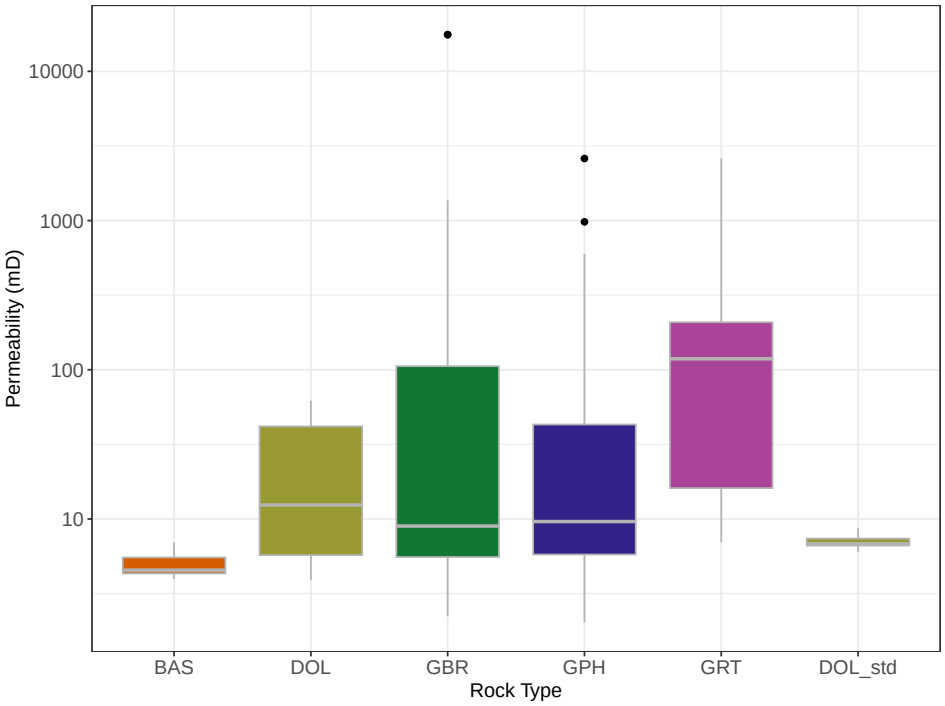

Figure 7.7-4: Permeability measurements for each rock type. Note logarithmic scale.

The data mostly ranged between 1 and 100 mD, and there were some extreme outliers. Also, there was a very high value of 408775.8 mD. Since there were extreme outliers in the permeability

readings, winsorization (Appendix *F*.1) was applied to reduce the impact of possible spurious outliers on subsequent analysis by limiting extreme values in the observed data without deleting extremes altogether. Figure *7.7-5* shows the boxplots of permeability after winsorization. Some of the rock art panels exhibited quite large variability in the permeability readings, typically with a relatively large median value, whereas other panels have lower variability and lower median values.

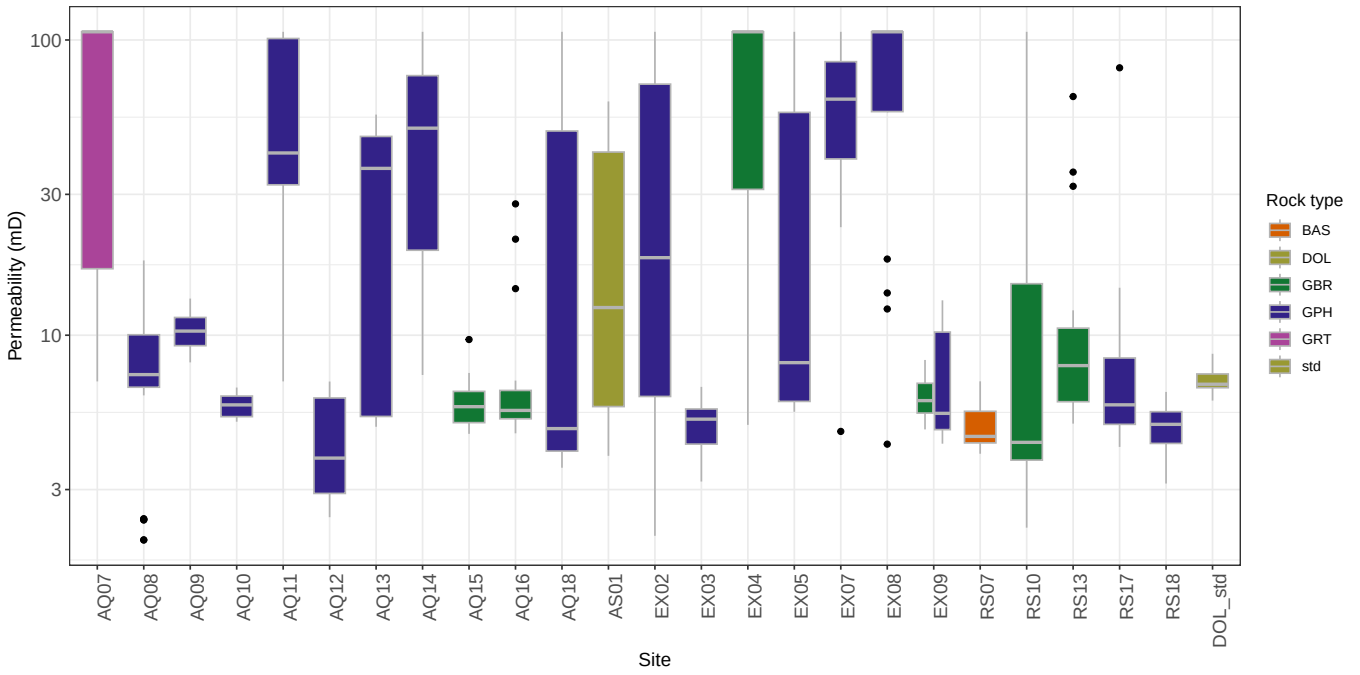

Figure 7.7-5: Permeability measurements for all sites and the dolerite standard. Note logarithmic scale.

Figure *7.7-6* shows (a) spatial point data and (b) spatial smoothing plots of the winsorized permeability measurements for granophyre only. The pattern of spatial variation in permeability appears broadly similar to that observed for the porosity data. The presence of extreme values in the permeability data was an additional challenge that was not present in the porosity data. Further investigation and observation is required; however this appears to be a promising approach for field monitoring.

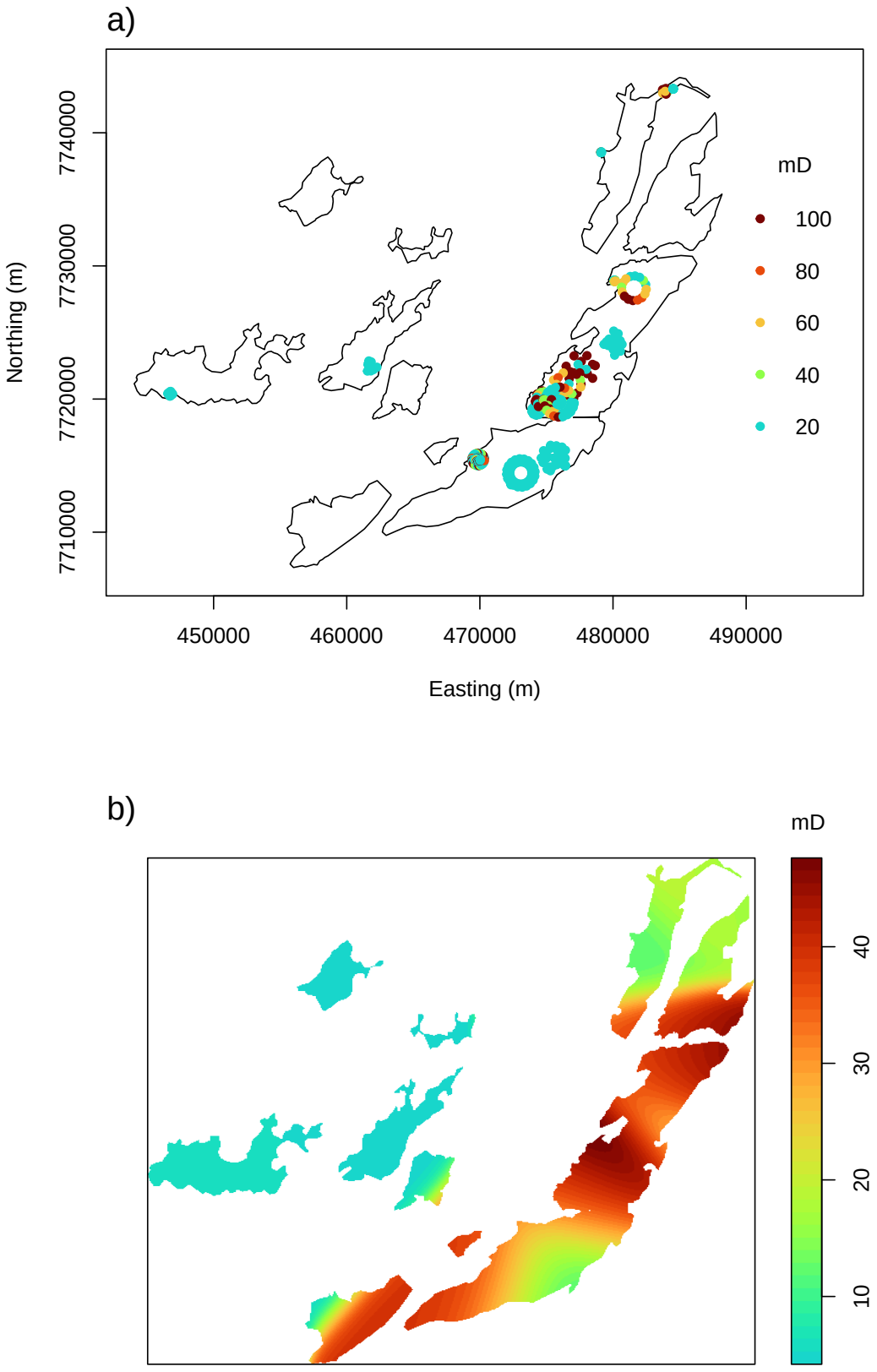

Figure 7.7-6: a) Spatial point data and b) spatial smoothing plots of winsorized permeability measurements, for granophyre.

7.8 Microbiome

7.8.1 Background

The microbiome (the collection of all microbes) present on the rock surface is an important element in understanding the patina, and in predicting the possible effects of environmental pollution.

Samples of material from the patina, the underlying weathered rind, lichen patches, and soil, were collected at the MRAMP study sites during each field campaign. The samples were analysed by cultivation-independent sequencing analysis of environmental barcoding genes, encoding for

- *16S ribosomal RNA* relevant to bacteria and archaea, and
- *ITS*, best suited for fungi.

As noted in the Murujuga Rock Art Monitoring Program: Monitoring Studies Data Collection and Analysis Plan (MSDCA Plan) (Curtin University, 2022), the identification of organisms based on sequencing analysis of these barcoding genes does not mean that the microbes were alive and active at the time of sampling. The MSDCA Plan involves a separate analysis of the *metatranscriptome* to identify the functional genes involved in various microbial processes were expressed at the time of sampling. This metatranscriptome analysis has not been completed at the time of this report.

7.8.2 Statistical methodology

The exploratory analysis of the microbiome data presented here has largely been conducted by members of the microbiome team, using methods that are widely accepted in the bioinformatics literature. The statistical team provided advice and additional analysis. Formal statistical analysis will be reported in subsequent reports.

Briefly, an *amplicon* is a fragment of DNA or RNA. The sequencing technology produces, for each sample of material, a list of *amplicon sequence variants* (ASV's or 'reads') that were present in the sample, along with their observed frequencies in an amplified version of the sample. Frequencies are un-normalised. An ASV may uniquely identify a species, but more commonly it identifies only a genus, family, order, class or phylum of organisms.

Statistical analysis of the amplicon sequence data is challenging because there are different sample sizes in the sequence data and they contain a high proportion of zeros. These differences in sample sizes can be due to: uncertainties in sequence quantification; variation in the loading concentrations or volumes for each sample; and efficiency of the sequencing process for each sample. To address these problems in the data, the data was normalised using rarefaction (`rarefy` function in `R` package `vegan`) which randomly sub-samples the data to a selected sample size (11000 and 10000 for the bacterial and fungal datasets respectively (Section 4.3)). Future work will investigate various normalisation methods and how these techniques affect the diversity indices (McMurdie and Holmes, 2014; Weiss et al., 2017; Cameron et al., 2021; Hong et al., 2022). Since these data contain a high proportion of zeros, future work will also explore negative binomial and zero-inflated mixed models (e.g. Brooks et al., 2017; Ho et al., 2019; Zhang and Yi, 2020).

7.8.3 Analysis of bacteria

Actinobacteria was the most abundant bacterial phylum in the patina samples, followed by *Cyanobacteria* and *Proteobacteria* (Figure *7.8-1*). *Actinobacteria* and *Cyanobacteria* are commonly identified as the major phyla in rock patina microbiomes, due to their ability to attach to the rock surface and penetrate into the rock, and *Cyanobacteria*'s ability to fix atmospheric carbon dioxide via photosynthesis (reviewed in Gorbushina (2007); Dorn (2024)). Although these three phyla are the most abundant in the patina samples on average, not all individual patina samples from Murujuga conform to this abundance profile. The RS15_BAS patina had a 66% abundance of *Halobacterota* and had a very low percentage of *Actinobacteria* and *Proteobacteria*.

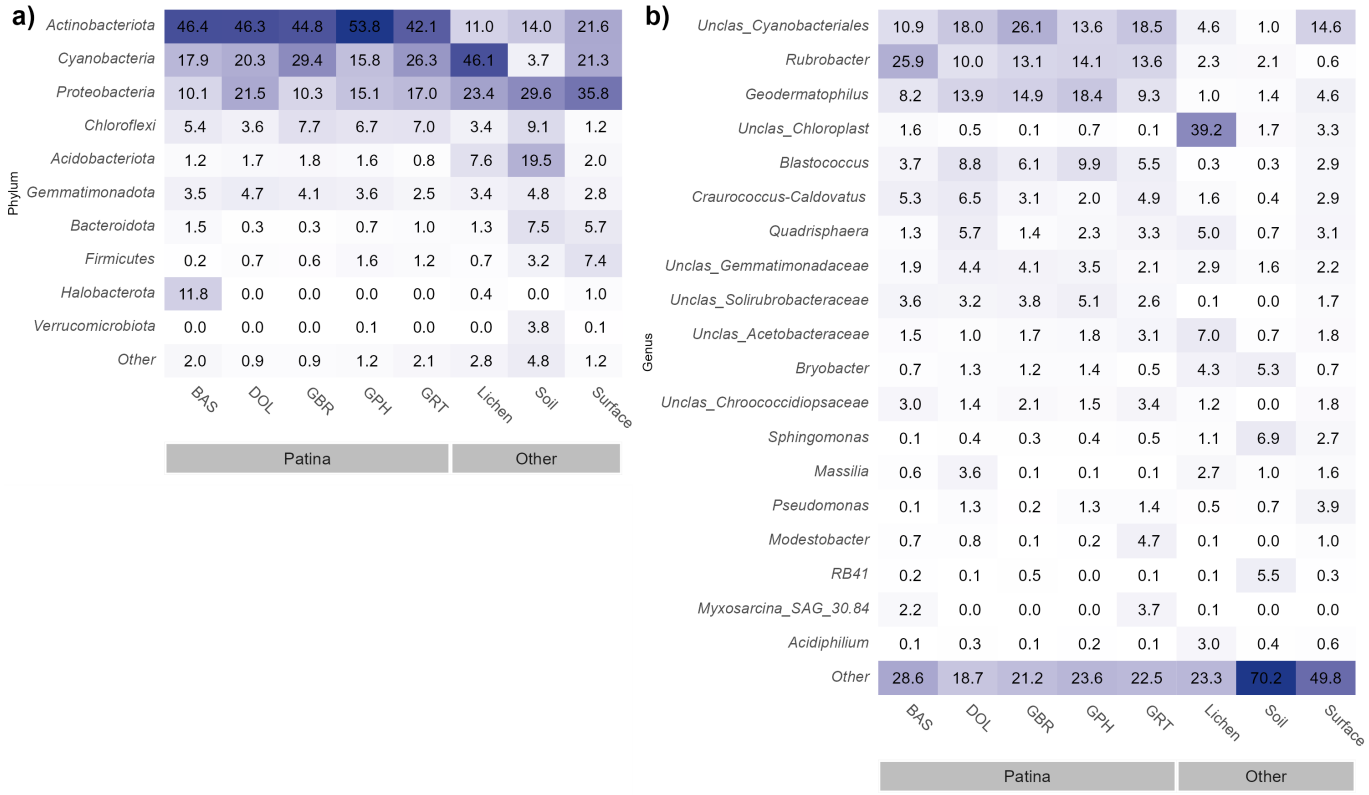

Figure 7.8-1: Relative abundance of the 16S rRNA amplicon data grouped by sample type. Patina samples are grouped by which rock type they were sampled from. (a) relative abundance at Phylum level. (b) relative abundance at Genus level. Note that "Unclas" is "unclassified".

Some 72% of all *Actinobacteriota* reads in the dataset were classified as *Geodermatophilus* spp. (29%), *Rubrobacter* spp. (28%), and *Blastococcus* spp. (15%). *Rubrobacter* is a genus that is aerobic, heterotrophic, can use oxygen and nitrate as a terminal electron acceptor, are resistant to irradiation and desiccation, and are commonly found on rock surface microbiomes (Albuquerque et al., 2014; Chen et al., 2020; Rosado et al., 2020). The *Geodermatophilus* genus is also known for its extreme resistance to UV irradiation, its ability to oxidize manganese and its production of extracellular functional amyloid (Montero-Calasanz et al., 2013; Hezbri et al., 2015, 2016; Antonelli et al., 2020). *Blastococcus*, much like the other *Actinobacteria* genera in this dataset, has been identified and isolated from other stone surface environments and is known for its resistance to desiccation, UV irradiation and heavy metals (Hezbri et al., 2018; Louati et al., 2022; Kammoun

et al., 2023). Some 72% of all reads classified in the *Cyanobacteria* phylum could not be classified past the *Cyanobacteriales* order. Current efforts are being made to understand if further taxonomic classification of the reads can be achieved.

The abundance data were spatially mapped across the peninsula to get a better understanding of how the Phyla and Genera described are distributed (Figure *7.8-2*). *Geodermatophilus* spp. and *Blastococcus* spp. have a higher abundance in the patina samples on the main island surrounding the industrial area, and the abundance reduces on the surrounding islands. *Rubrobacter* spp. and *Cyanobacteriales* have the opposite pattern, decreasing in abundance on the main island and becoming more abundant on the surrounding islands.

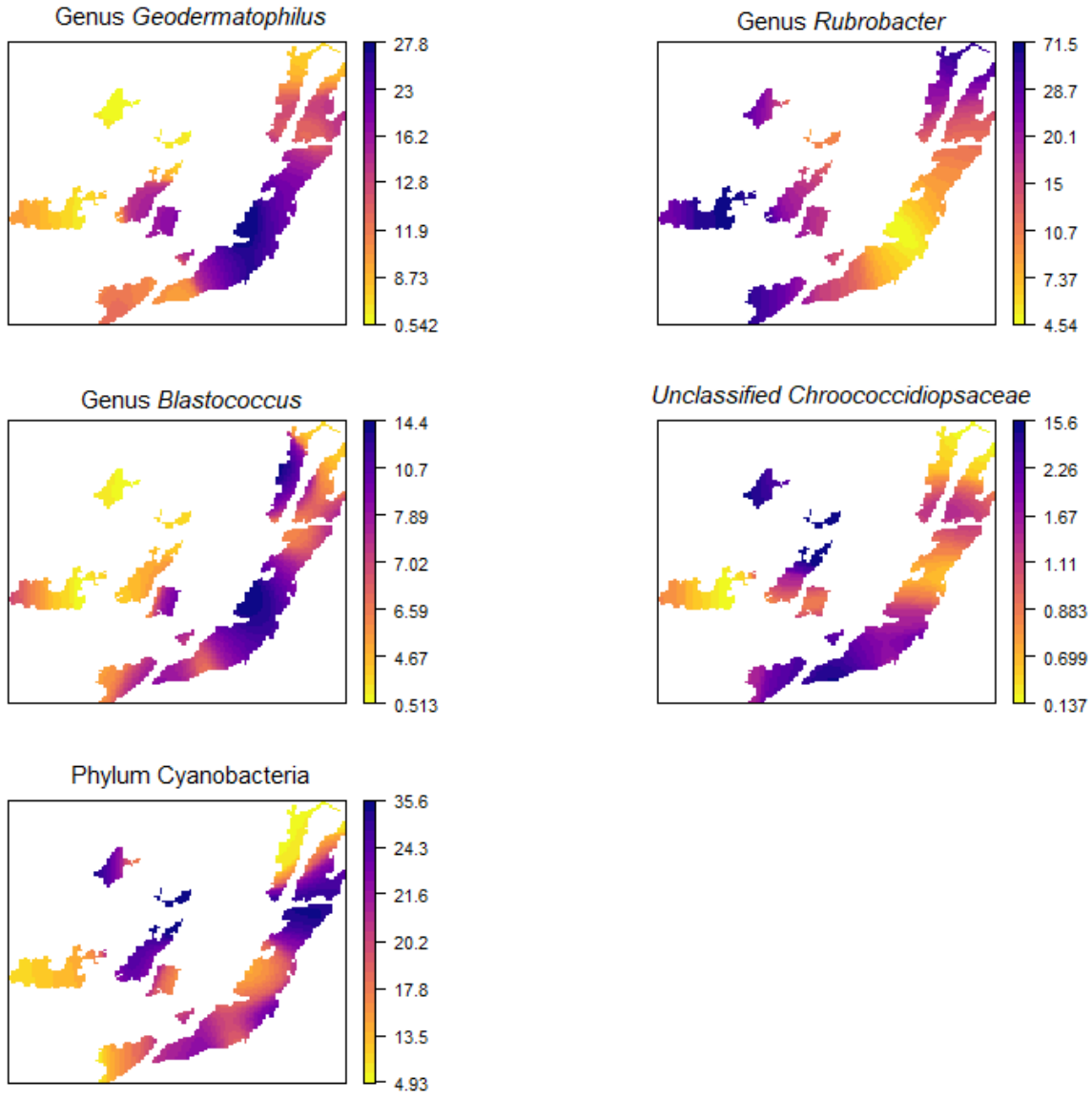

Figure 7.8-2: Spatially smoothed relative abundance (%) of selected taxa.

Alpha diversity is a metric used commonly in microbial ecology to understand the diversity of species, in this case ASVs, in a sample (Feranchuk et al., 2018). By comparing the alpha diversity

indices between samples in this dataset we can understand if there is any relationship between species diversity and any environmental parameter we are interested in. Alpha diversity analysis of the data based on rock type revealed the microbial communities collectively in the gabbro patinas had the highest average diversity, however only marginally (Figure *C.1-6*). When assessing the alpha diversity on a sample basis, both wet and dry season gabbro patina samples at the RS02 site had the highest Shannon diversity index compared the other patina samples. The majority of patina samples had Shannon diversity measures between 2.5 and 3.5, indicating low diversity of ASVs in the patina samples. Samples with the lowest diversity included AQ07_GPH, AQ18_GPH, EX03_GPH, EX05_GPH and RS07_BAS with Shannon diversity measures below 2.5 (Figure *7.8-3*). Investigations so far have not indicated any evidence of relationships between the microbial diversity of these samples and the environmental data; see Section 8.2.

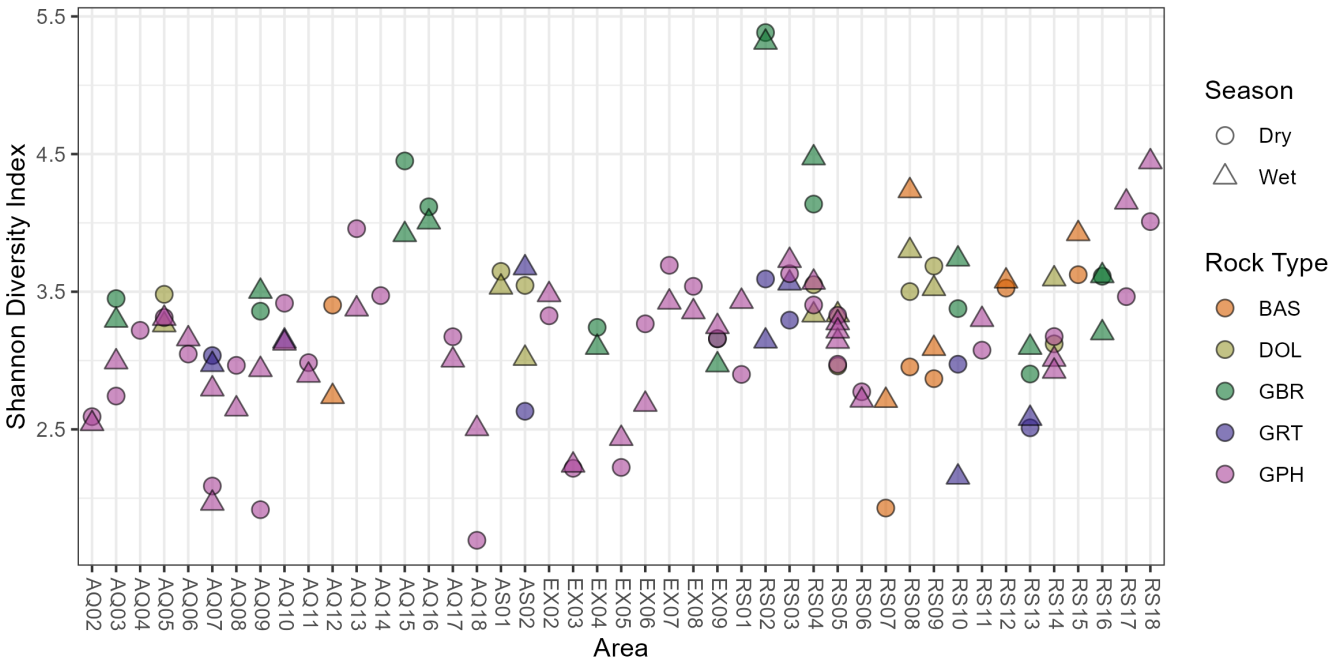

Figure 7.8-3: Shannon diversity index of patina samples grouped by rock type, season and area.

Beta diversity is a metric that expresses the similarity or dissimilarity of multiple samples to each other (Armstrong et al., 2022). Non-metric multidimensional scaling of the microbial communities with all the samples shows a clear grouping of the lichen and soil samples away from the patina samples (Figure *7.8-4*). Surface samples are grouped with the patina samples. It is clear through this ordination that the soil and lichen samples form a distinct microbial community and are dissimilar to the patina samples. Analysis of similarity (ANOSIM; R package `vegan`, Monte Carlo test using 999 random permutations) of the ordination grouped by sample types reports an R value of 0.6 and a p-value of 0.001, indicating statistically significant evidence of a moderate difference between the microbial communities from different sample types. When looking at the patina samples only, NMDS analysis and ANOSIM suggest that the patina microbial communities are not different based on the rock type they were sampled from, however are slightly different based on the area they were sampled from (Figure *C.1-7*).

Evidence for association between the abundance of particular bacteria, or the diversity of bacterial

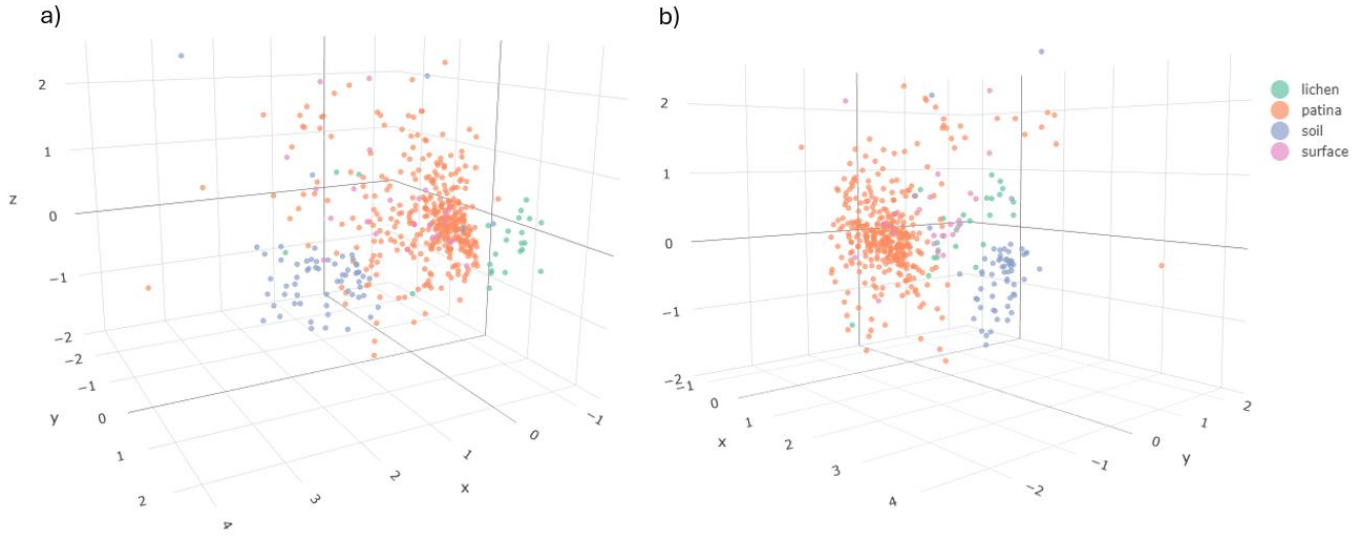

Figure 7.8-4: (a) NMDS ordination based on Bray-Curtis dissimilarity matrix of all samples grouped by sample type. (b) NMDS ordination based on Bray-Curtis dissimilarity matrix of patina samples grouped by rock type.

communities, and other variables of interest such as the rock composition, is investigated in Section 8.2.

7.8.4 Analysis of fungi

The *Ascomycota* phylum almost exclusively constitutes the fungal community of the patina, lichen and surface samples (Figure *7.8-5*). Approximately 38% of all *Ascomycota* reads could not be classified past phylum level, much like the *cyanobacterial* reads. Further efforts to achieve phylogenetic clarity of these reads are underway. The genus *Spissiomyces* makes up 24% of the *Ascomycota* reads; it is found in high abundance in the patina samples and in low abundance in the soil, lichen and surface samples. *Spissiomyces* was first described in 2015, isolated from rock samples in China (Su et al., 2015). These species produce slow growing, highly melanised hyphal colonies. Although the stress capabilities of *Spissiomyces* spp. have not been directly observed, it is evident in the literature that rock-inhabiting fungi and their highly melinated cell walls confer many stress adaptations, including resistance to UV irradiation, desiccation and extreme temperatures (Ruibal et al., 2009; Liu et al., 2022).

The Shannon index of diversity for the fungal communities ranged from 0.1 to 4.4 (Figure *7.8-6*). On average, the fungal diversity in the patina samples was higher during the dry season sampling (1.9 and 2.3 average Shannon diversity index in dry and wet seasons respectively) (Figure *C.2-6*).

NMDS of all sample types revealed the separation of patina, lichen and surface samples away from the soil samples (Figure *7.8-7*). ANOSIM analysis (using 999 random permutations) of the ordination based on sample type had an R value of 0.39, with a p-value of 0.001, suggesting some difference between samples of different sample types, however with overlap. The ordination of only the patina samples failed to show any differentiation of the samples based on rock type (Figure *C.2-7*) (R = 0.124, p = 0.001). Similarly to the bacterial microbial communities, ANOSIM

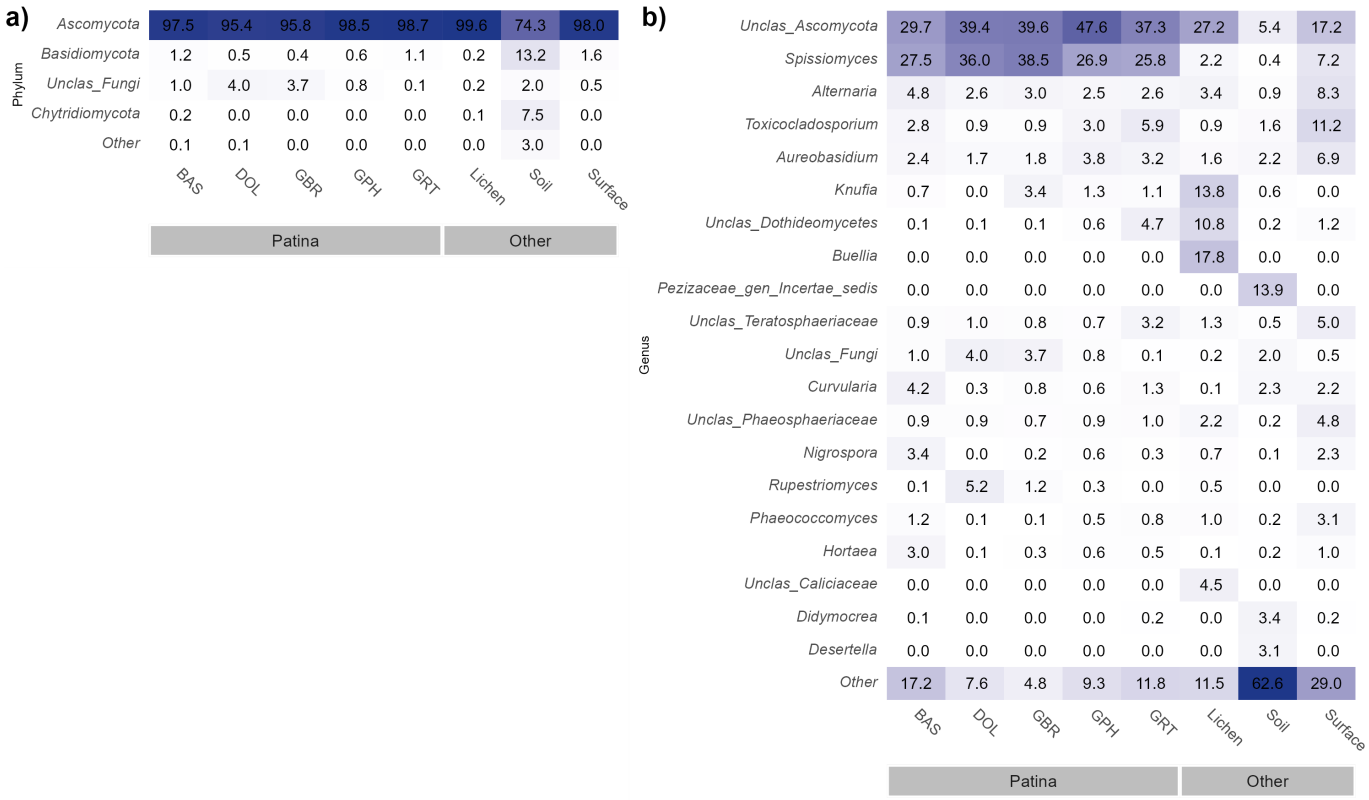

Figure 7.8-5: Relative abundance of the ITS amplicon data grouped by sample type. Patina samples are grouped by rock type. (a) relative abundance at Phylum level. (b) relative abundance at Genus level. Note that "Unclas" is "unclassified".

suggests that the samples are different based on area as opposed to rock type (R = 0.45, p = 0.001).

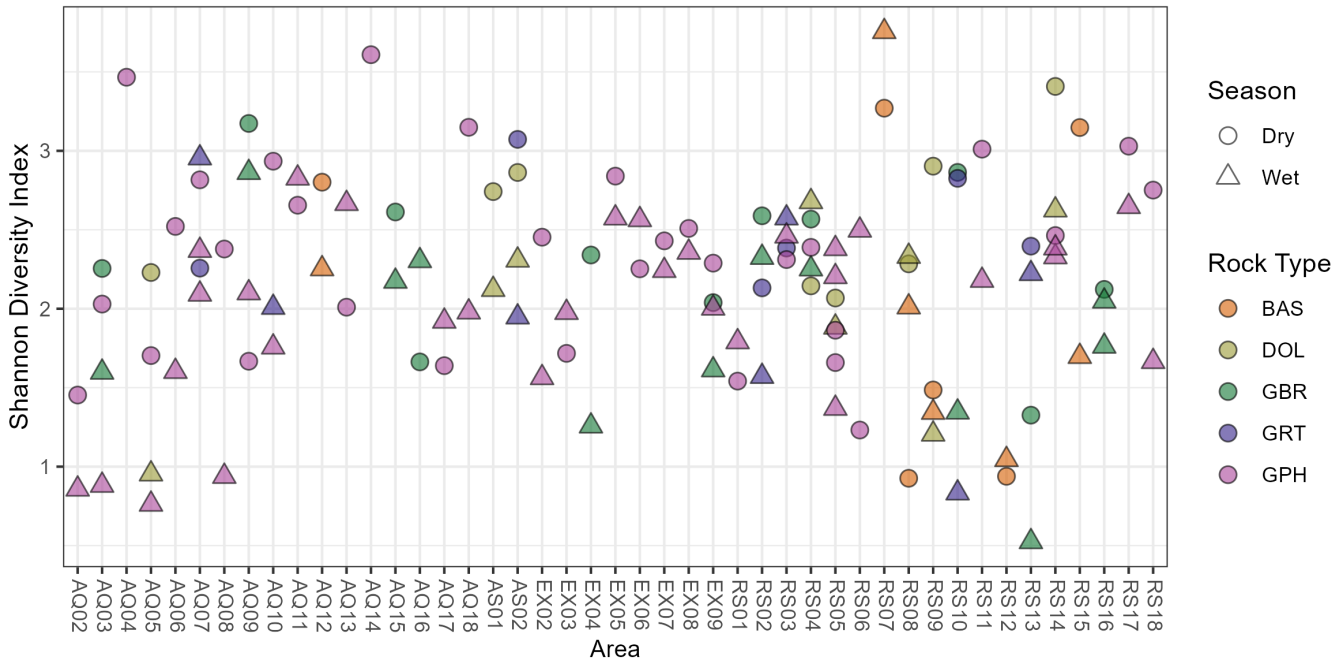

Figure 7.8-6: Fungal ITS Shannon diversity index of patina samples grouped by rock type, season and area.

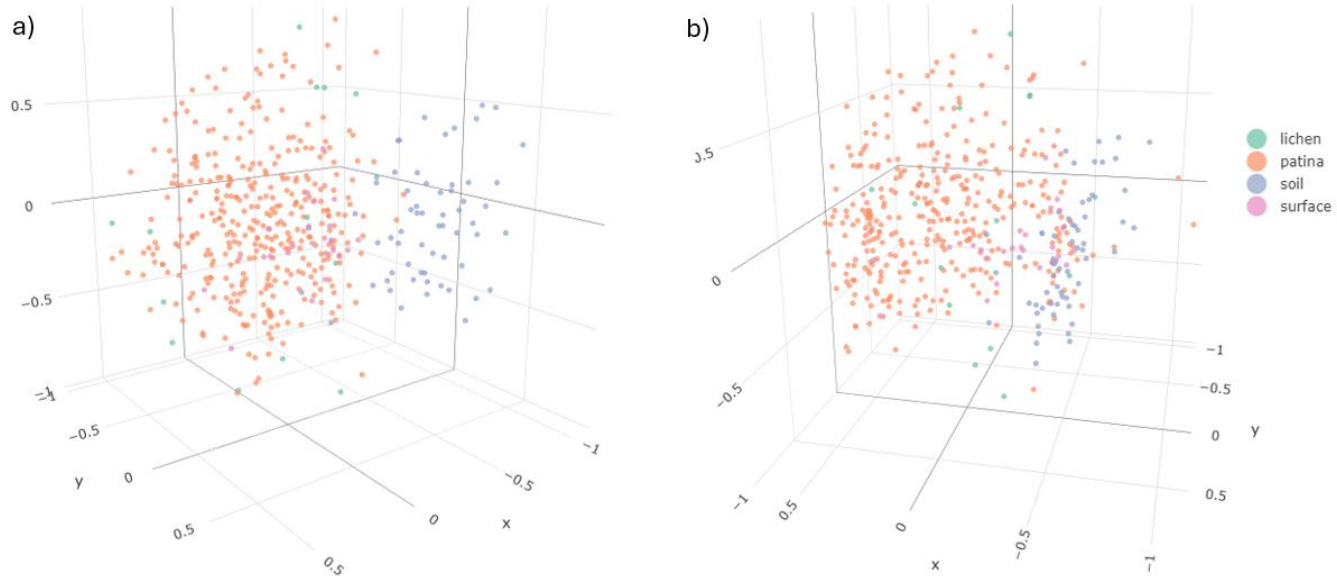

Figure 7.8-7: NMDS ordination based on Bray-Curtis dissimilarity matrix of all samples grouped by sample type, stress = 0.20.

This page is intentionally blank.

7.9 Organic geochemistry

7.9.1 Background

The organic geochemistry component of the project aims to better understand the origin and fate of organic compounds (commonly referred to as biomarkers or molecular fossils) and their stable isotopic compositions ($^{13}C/^{12}C$, D/H, $^{15}N/^{14}N$, $^{34}S/^{35}S$), for the purposes of this work, in samples from Murujuga (Peters et al., 2005; Dawson et al., 2007; Vitzthum von Eckstaedt et al., 2012). Biomarkers derive from lipids and pigments from the three domains of life — archaea, bacteria and eukaryotes (Grice and Eiserbeck, 2014) — which are extracted from powdered rock samples with organic solvents. Biomarker characterisation employs analytical instrumentation to separate and determine the structure of organic molecules in complex mixtures. These structures may then be traced back to known biological precursors (Grice and Eiserbeck, 2014). The most common analytical technique is gas chromatography-mass spectrometry (GC-MS), which separates organic mixtures and determines the molecular structure of individual organic molecules. Other techniques including thermal desorption GC-MS (for analysis of volatile organics in atmosphere and emissions), metastable reaction monitoring (for highly selective analysis of specific biomarkers), and 2D GC-MS (for analysis of highly complex mixtures).

Stable isotope analysis measures the ratio of heavy and light stable isotopes of a particular element (e.g. $^{13}C/^{12}C$ ratio for carbon, $^{15}N/^{14}N$ ratio for nitrogen). These measurements are reported relative to an international reference scale and are expressed as delta (δ) values in parts per thousand (‰, “per mil”). For example

$$\delta^{13}C = \left(\frac{\left(^{13}C/^{12}C\right)_{\text{sample}}}{\left(^{13}C/^{12}C\right)_{\text{standard}}} \right) \times 1000.$$

The international reference standard for stable carbon isotope measurements is Vienna Peedee Belemnite (VPDB) (Coplen et al., 2006). The stable carbon isotope ratio ($\delta^{13}C$) helps to indicate the source of an organic compound, as different carbon sources and biosynthetic processes produce different $^{13}C/^{12}C$ ratios (Grice and Brocks, 2011). Stable isotope ratios can be measured on whole samples (bulk isotope analysis), or on individual compounds within an organic mixture (compound-specific isotope analysis, CSIA).

The following results were obtained from bulk organic geochemical analyses, which are done using whole samples without prior separation of organic material. These can therefore be performed on small samples which do not have sufficient mass for compound-specific analysis (e.g. less than 5 g). Total organic carbon (TOC) indicates the total concentration of organic matter in a sample from all sources, measured in wt%. Bulk stable carbon isotope measurements give a single $\delta^{13}C$ value for all organic carbon in a sample, providing an initial indication of carbon source.

It is not necessarily expected that TOC and $\delta^{13}C$ on their own will necessarily provide conclusive information, however when combined with other measures such as microbiome, biomass combustion (bushfire) data and anthropogenic air pollution data they may add further evidence to other areas of investigation or may suggest areas where further source apportionment of the organic compounds is needed.

7.9.2 Exploratory data analysis of TOC and δ^{13}C

By analysing TOC and δ^{13}C, combined with more detailed compositional data, it may be possible to apportion organic chemicals to microbiome, biomass and anthropogenic sources in the Murujuga environment. Biomass (and biomass combustion) from different sources often possess different δ^{13}C ratios. δ^{13}C analysis may help distinguish between different sources of hydrocarbons and assesses the contribution of anthropogenic activity to carbon bound in the rock patina.

However, it is not expected that this will be possible from the current data; more extensive laboratory analysis and comprehensive statistical data fusion are likely to be needed for this to occur. The current section details our exploratory analysis of TOC and δ^{13}C data recorded so far. More comprehensive studies and analysis are planned for subsequent reports.

Figure *7.9-1* shows histograms of TOC and δ^{13}C from all available samples. The data set contained 64 observations. TOC ranges from 0.0 wt% to 1.0 wt%; it exhibits a right-skewed distribution with a median of approximately 0.18 wt% and has three observations exceeding 0.5 wt%. δ^{13}C is approximately uniformly distributed between -27 and -17.

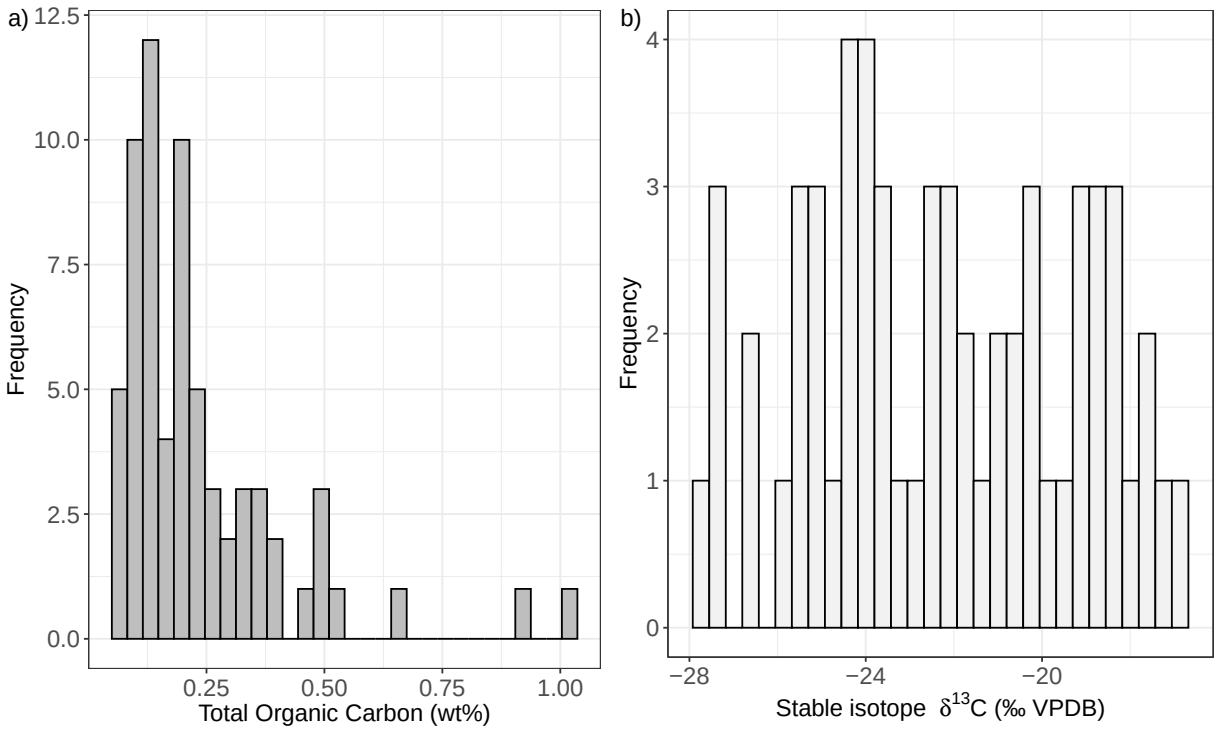

Figure 7.9-1: Histograms of total organic carbon (TOC) and stable carbon isotopes (δ^{13}C) based on 64 observations.

Figure *7.9-2* shows boxplots of the same data broken down by rock type, and Figure *7.9-3* by site location, using a logarithmic axis scale for TOC. In these data, basalt (BAS) has the highest average δ^{13}C and lowest average TOC, while granite (GRT) has the lowest δ^{13}C and highest TOC. However the sample size is too small to support formal conclusions.

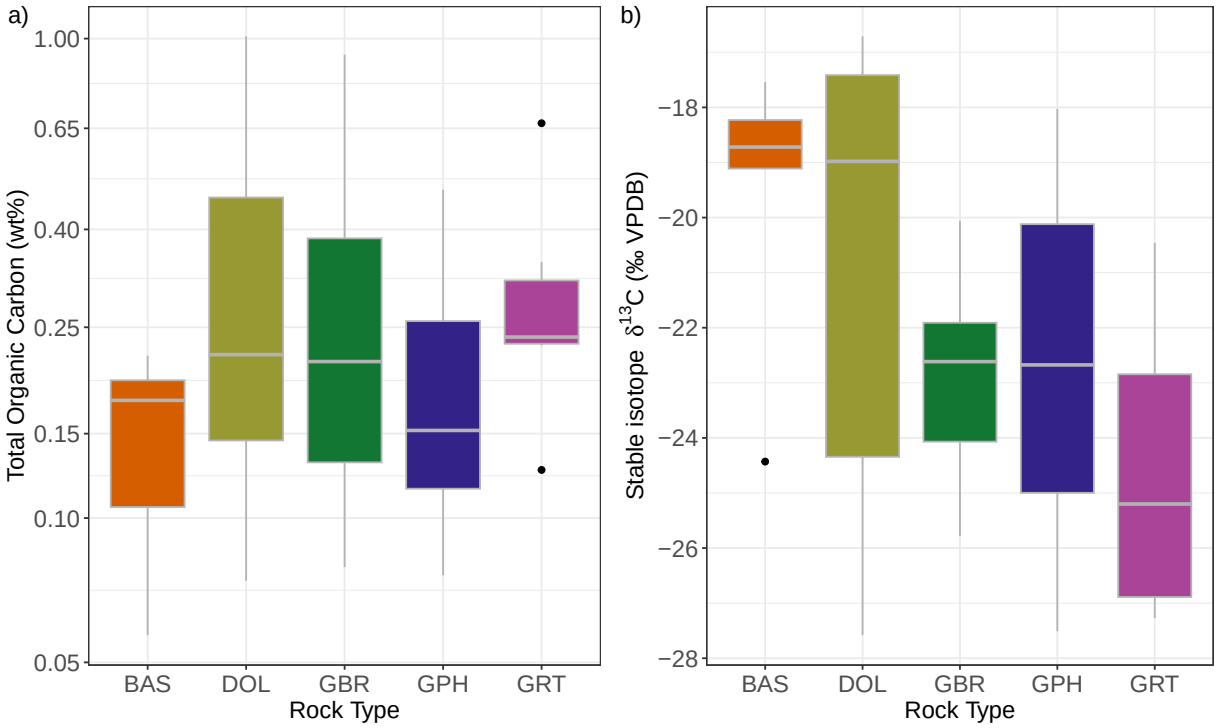

Figure 7.9-2: Boxplots of a) total organic carbon (TOC) and b) stable carbon isotope ($\delta^{13}C$) for different rock types. Note logarithmic scale of TOC.

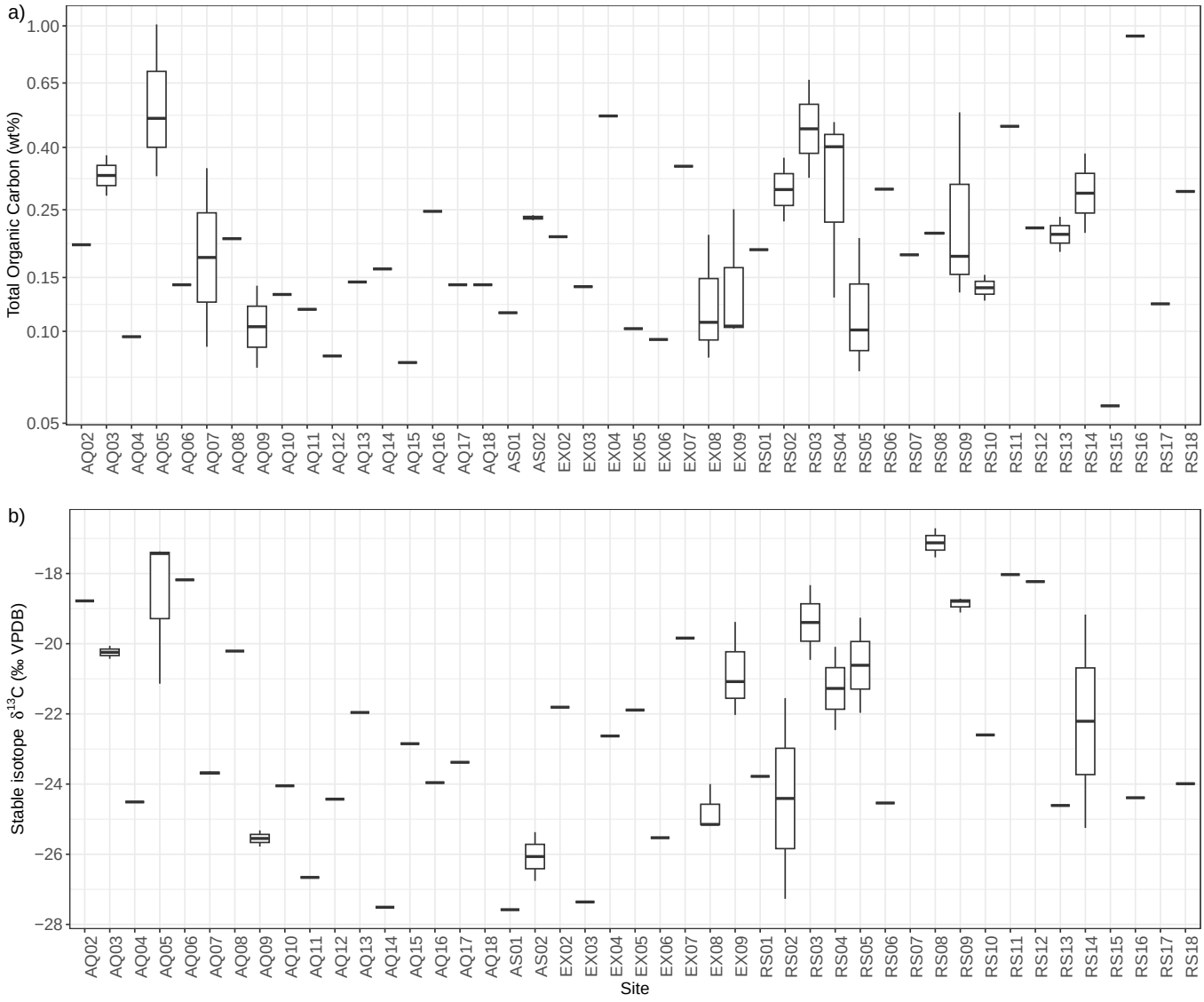

Figure 7.9-3: Boxplots of (a) total organic carbon (TOC) and (b) stable carbon isotope ($\delta^{13}C$) for different sites. Note logarithmic scale of TOC.

Figure *7.9-4* shows a scatter plot of TOC vs δ^{13}C, coloured by rock type, with a logarithmic scale for TOC. The Pearson sample correlation coefficient of 0.36 implies a moderate strength of association between δ^{13}C and TOC, while the scatterplot suggests that increasing δ^{13}C is associated with increasing variability in TOC; these observations warrant further investigation.

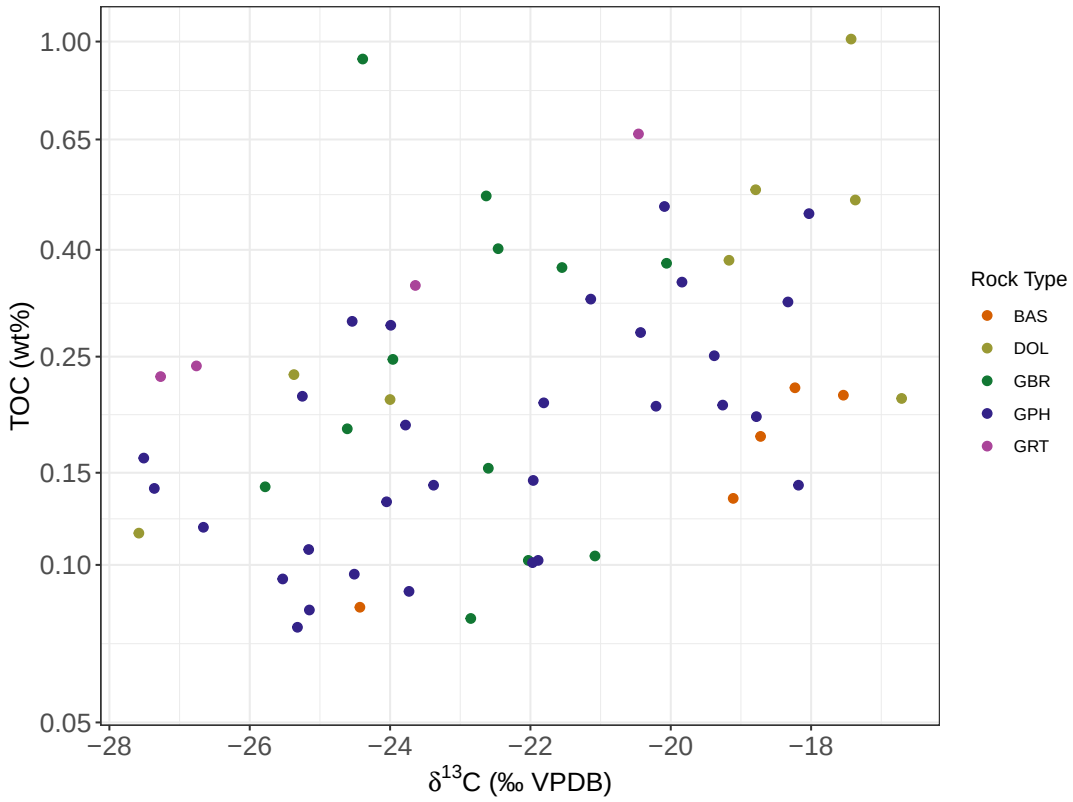

Figure 7.9-4: Scatterplot of total organic carbon (TOC) against stable isotope ratio (δ^{13}C). Logarithmic scale for TOC. Pearson sample correlation coefficient 0.36.

7.9.3 Spatial smoothing of TOC and δ^{13}C observations

It is of interest to identify any spatial trends in organic geochemistry which might exist across the Murujuga region.

Figure *7.9-5*(a) shows the measured TOC values encoded as colours and plotted at the geographic locations where the samples were taken. There are a few relatively high TOC values – close to 1 wt% in the north (Dolphin Island – RS16_GBR) and south (AQ05_DOL), which are depicted as black dots.

Figure *7.9-5*(b) shows the spatially smoothed (locally weighted average) TOC surface computed using Nadaraya-Watson smoothing (Appendix *F*.1). Figure *7.9-6* shows similar spatial plots for δ^{13}C.

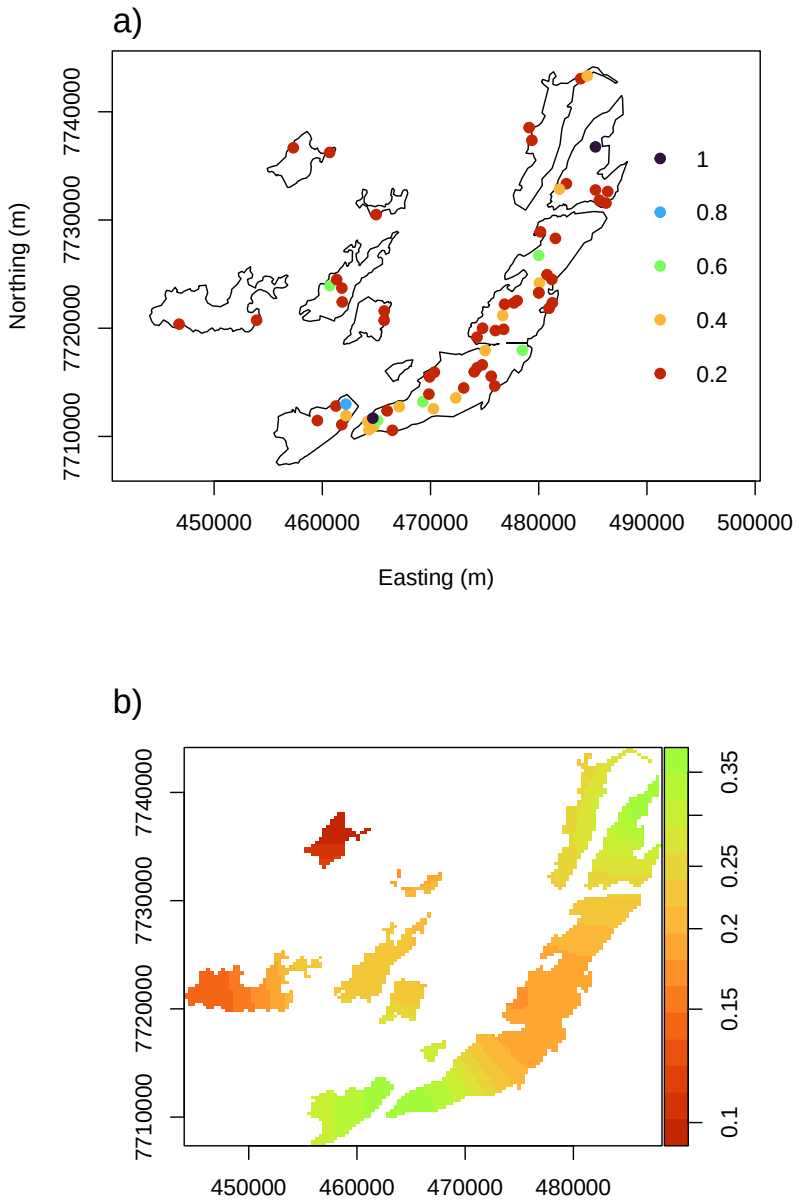

Figure 7.9-5: a) spatial plot of sampled TOC values at each site and b) spatially smoothed average TOC (logarithmic colour scale).

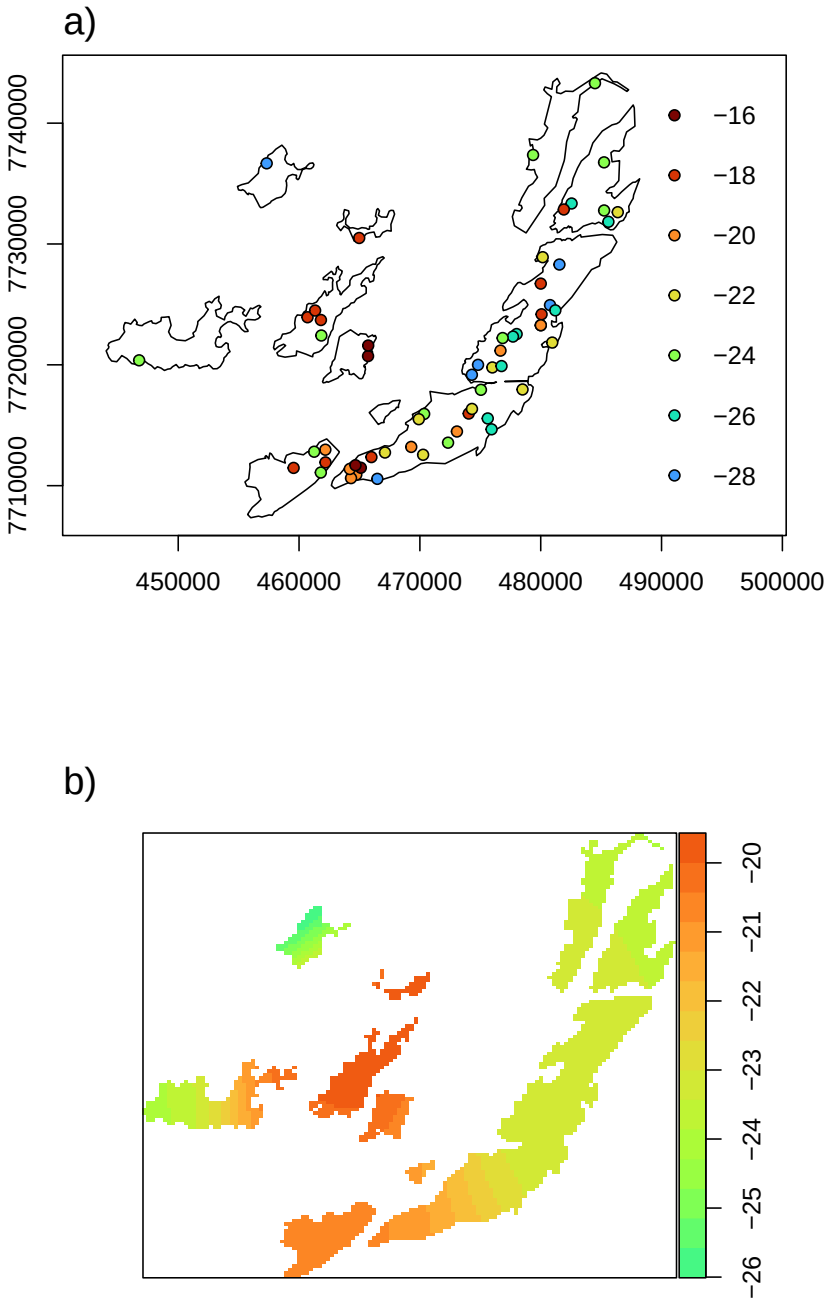

Figure 7.9-6: a) spatial plot of sampled stable isotope ($\delta^{13}C$) at each site and b) spatially smoothed average $\delta^{13}C$.

The application of spatial smoothing to analytical sample data has not previously occurred in the field of organic geochemistry, to our knowledge. Some of the authors of this document have expressed concerns about the appropriateness and validity of spatial smoothing in this context. Spatial smoothing is simply a form of averaging, which is unobjectionable in many contexts. The main objection in the context of organic geochemistry is that each analytical result is a separate experiment, and calculating an average of several discrete analytical results is inappropriate or invalid. From a statistical viewpoint, it must be acknowledged that the Nadaraya-Watson estimator is optimal when there is an underlying “true” average value at each location, and when this true value is either constant or varies gently across spatial locations. If these assumptions do not hold, then the estimator may be inappropriate or misleading. Consequently, caution needs to be applied in any interpretation of the results.

Despite the notes of caution above, there do appear to be promising avenues of investigation for potential source apportionment of the organic species and investigation of anthropogenic contributions to TOC in the patina.

7.10 Deposition sampler data

7.10.1 Background

The three bucket deposition sampler developed for this project is described in the original MSDCA Plan (Curtin University, 2022), as well as in the following documents:

- COPP21065-PRO-G-102 Passive Air Quality Monitoring (AQM) Installation and Commissioning;
- COPP21065-PRO-G-103 Passive Air Quality Monitoring (AQM) Sample Collection, Maintenance and Context Observations;
- COPP21065-SPE-G-100 Air Quality Monitoring Station Control Functional Specification

In contrast to the AS3580.10 “total flask” method, or wet deposition devices, the “three bucket” deposition sampler is designed to collect separate dry, wet and mist deposition samples. However, it is currently undergoing cross-validation against the AS3580.10 total flask method. The sampler’s default position is the dry deposition, with the sampler rotating to mist and wet deposition sampler positions based on weather conditions (the specific control parameters are given in the above documentation, as well as the original MSDCA Plan (Curtin University, 2022)). Due to the typically arid conditions at Murujuga, the samplers spend the majority of time with the dry deposition bucket open. However localised or widespread mist deposition events have been found to occur at times, which emphasises the benefit of the novel sampler design.

At each sample changeover (approximately four weeks), the three buckets at each site are swapped for an alternate set. The collected sample is recovered at the MRAMP laboratory at the MAC office. Processing is as per the methods above. The buckets are then cleaned and dried for the next changeover. Samples are transported to Perth for analysis at the ChemCentre. Based on the known time each bucket was open and the fixed quantity of ultrapure water used to extract the residual sample, the results obtained from the laboratory analysis can be expressed in terms of an average deposition rate.

7.10.2 Exploratory analysis of dry deposition sampler data

Since the bucket samplers tend to remain in the ‘dry’ position for the vast majority of the time, the analysis below concentrates on data from the dry deposition samples, as this dataset has the largest sample size and likely represents the main exposure mode for the Murujuga rocks.

Figure *7.10-1* shows boxplots of *pH* values of dry deposition samples collected between May 2023 and February 2024, broken down by the date of sample collection. The *pH* varies between 5.5 and 8 with the majority of the samples above 6.5. The relatively high *pH* is most likely attributable to salt (mainly NaCl) deposition and geogenic dust/clay mineral deposition. Particularly notable is that the dry buckets from June 23, 2023 show comparatively low *pH* (with a median of 6), which coincides with a period of low dust/deposition as the likely cause.

Figure *7.10-2* shows boxplots of the same *pH* data (May 2023 to February 2024), instead broken down by site. AQ01 shows by far the highest median *pH* of $\sim$8. This may be due to its location in a dusty flood plain and/or the site’s very different geology compared to the Dampier archipelago. AQ11, AQ12, EX02, and EX09 have the next highest median *pH* values of about 7.5. Other sites have median *pH* between 6.5 and 7.5. The lowest median *pH* values were at AQ18 and AQ17

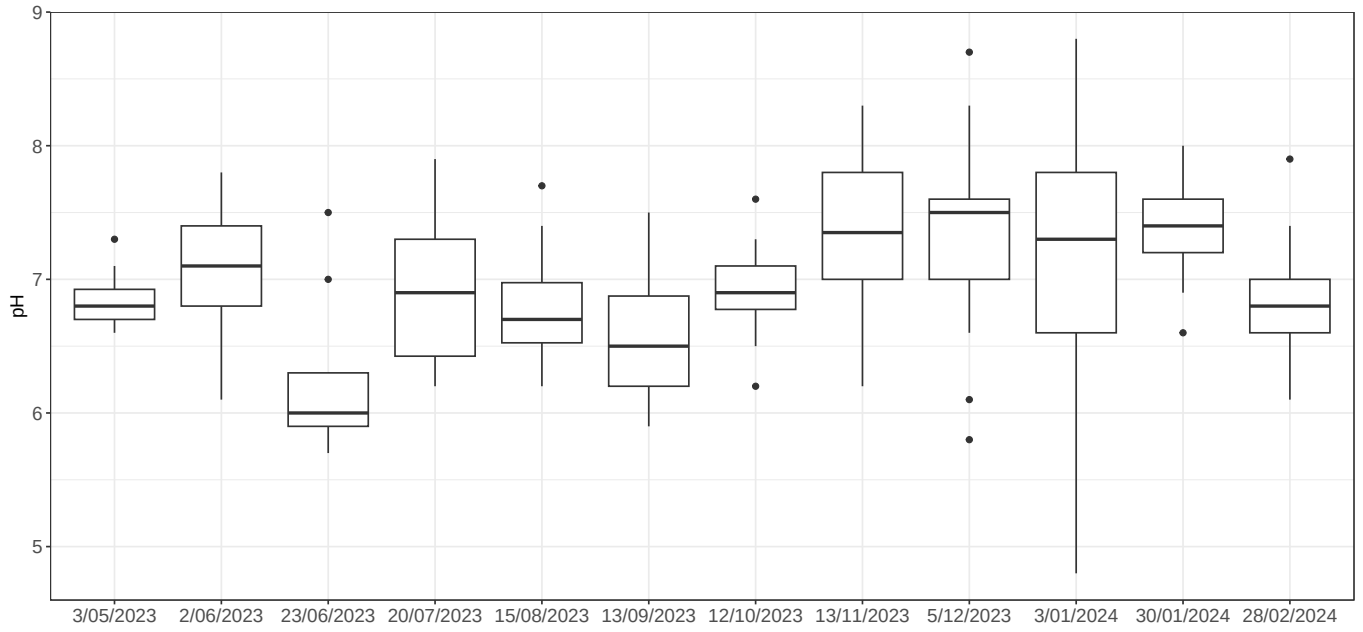

Figure 7.10-1: Boxplots of pH for the dry deposition samples by different sampling periods.

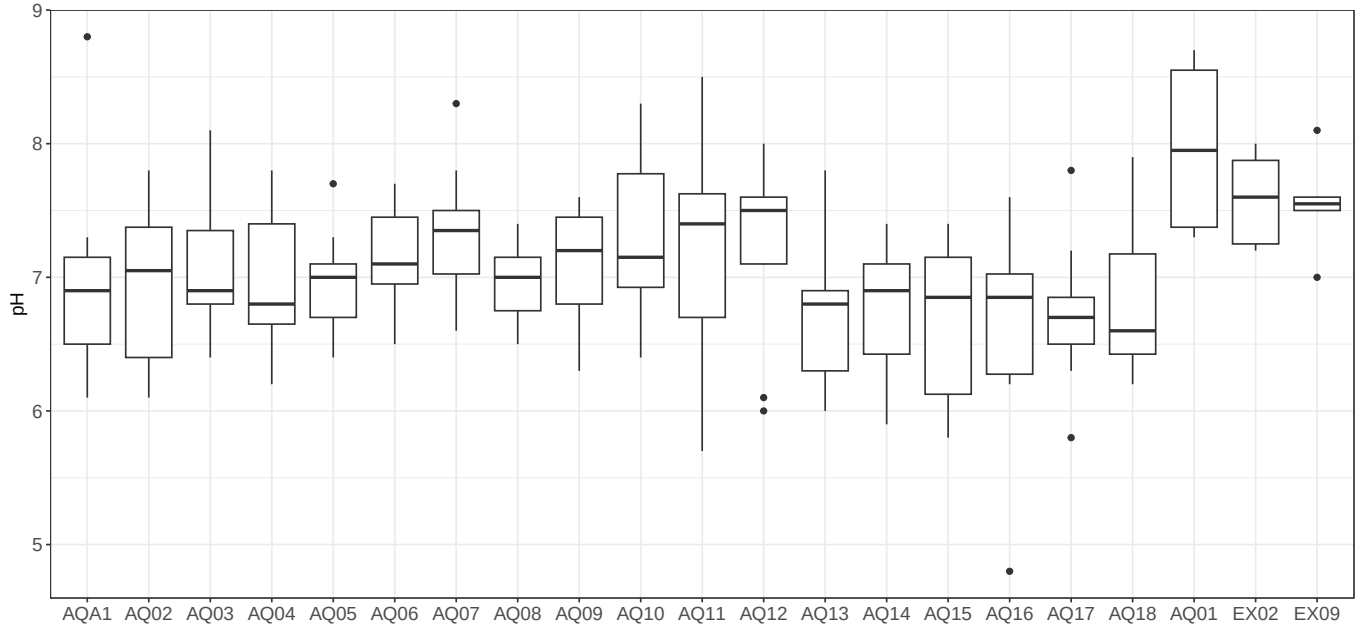

Figure 7.10-2: Boxplots of pH for the dry deposition samples by different sampling sites.

with values 6.6 and 6.7 respectively. It can be seen from the passive sampler results that these latter two sites generally have the highest SO_2, however they are also have low deposition rates of dust/clay minerals.

Dry deposition samples generally showed an approximately neutral *pH*, which is very similar

to the *pH* measured on the rock surfaces in campaigns 6 and 7 (October–November 2023, February–March 2024).

Chemical analysis of the bucket samples also provided assayed concentrations of Ca^{2+}, K^{+}, Mg^{2+}, Cl^{-}, Na^{+}, SO_4^{2-}, NH_4^{+}, NO_3^{-}, P and NO_2^{-}. The concentration of NO_2^{-} was below the detection limit and is not considered further in our analysis.

The concentration values provided by the ChemCentre give the concentration (mg/L) of chemical species in the original 60 ml of water added during sample processing. However the 60 ml value is somewhat arbitrary and does not account for differing water quantity (e.g. rainfall in wet buckets) or different open area of the collector (e.g. the AS3580.10 samplers use a 150 mm funnel as a collector). For these reasons, and to account for slight differences in time between sample collection, samples were standardised to a deposition rate measured in $\mathrm{ng/m^2/day}$, nanograms per square metre per day.

In the following analysis we have converted the assayed concentrations in the dry bucket samplers to deposition rates in $\mathrm{ng/m^2/day}$.

Figures *7.10-3* and *7.10-4* show boxplots of the calculated deposition rates of Ca^{2+}, K^{+}, and Mg^{2+} broken down by sampling date and by location, respectively.

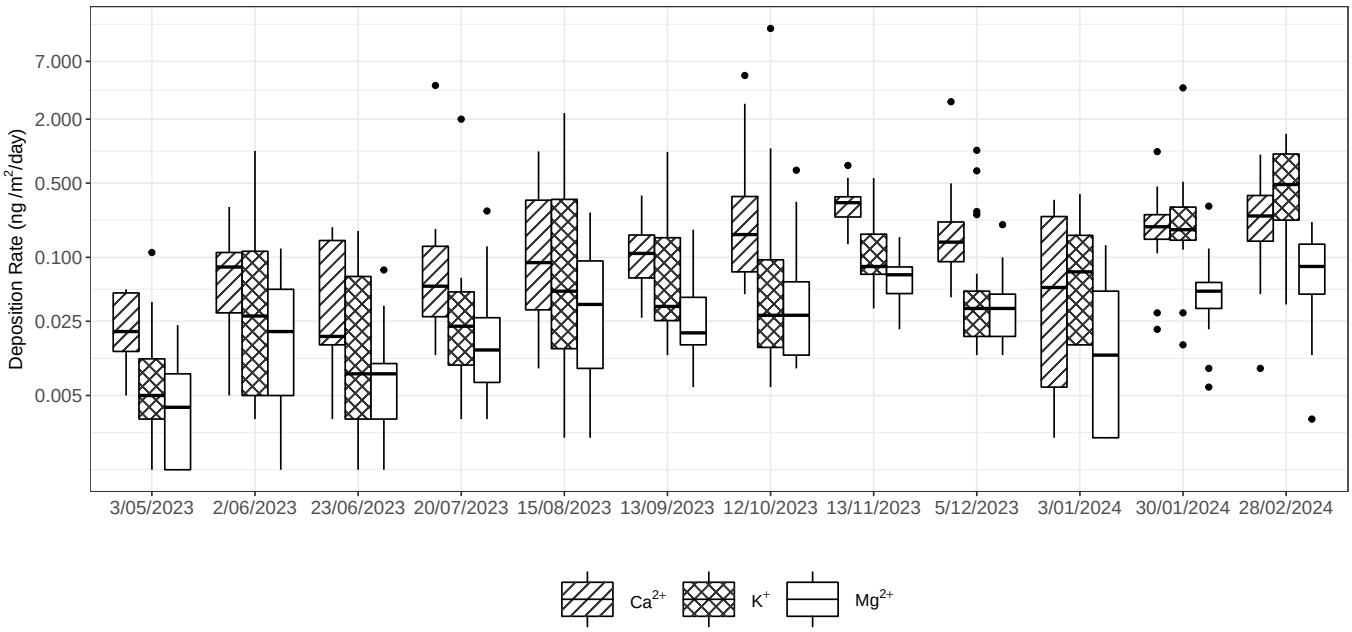

Figure 7.10-3: Boxplots of Ca^{2+}, K^{+}, and Mg^{2+} deposition rates for the dry deposition samples by different sampling periods. Note logarithmic scale.

Ca^{2+}, K^{+} and Mg^{2+} are all likely to arise mainly from geogenic sources and to be indicators of dust and clay mineral deposition — although other sources such as combustion/bushfires remain possible. The ratio of these three species appears to be roughly constant, with some variation between sites. Further data analysis will be undertaken. A possible explanation for systematic differences between sites is a composition/size relationship due to differences in dust transport

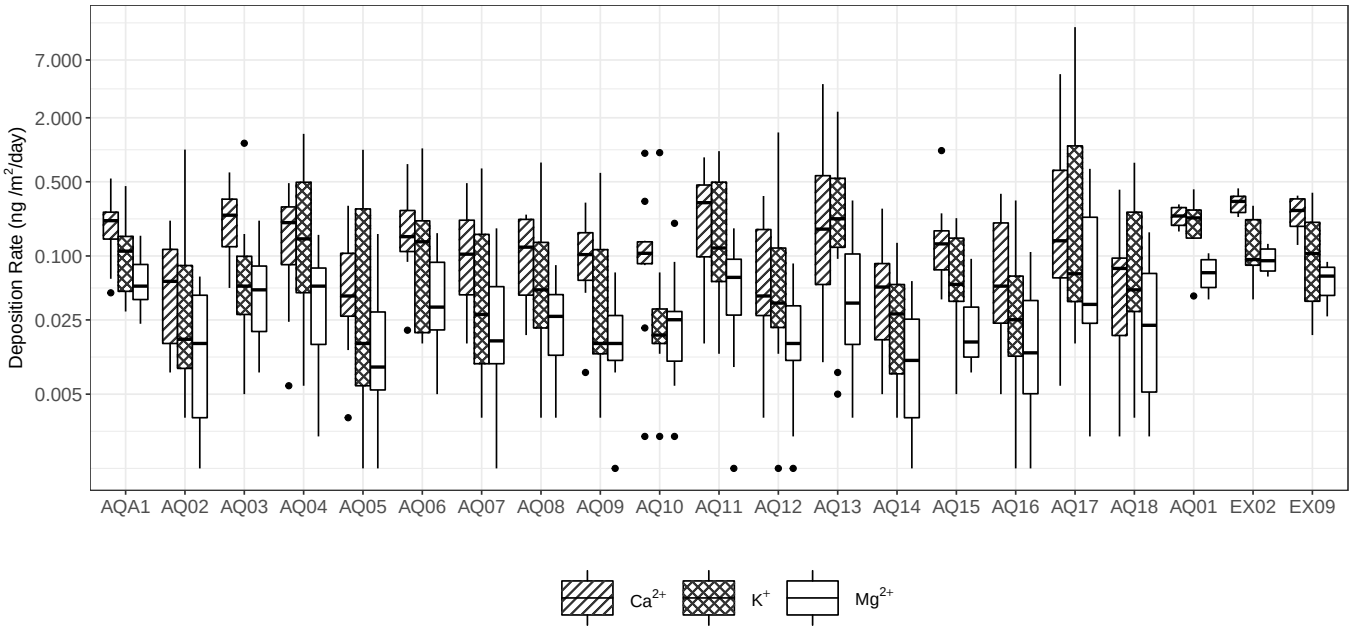

Figure 7.10-4: Boxplots of Ca^{2+}, K^{+}, and Mg^{2+} deposition rates for the dry deposition samples by different sampling sites. Note logarithmic scale.

distances. This may need investigation.

Figures *7.10-5* and *7.10-6* show boxplots of Cl^{-}, Na^{+}, and SO_4^{2-} deposition rates by sampling date and site, respectively. In contrast to the previous species, these three species may originate from geogenic dust, sea salt/sea spray (including anthropogenically generated NaCl from cooling towers) and (in the case of sulphates and SO_4^{2-}) may arise from combustion or biomass sources. Again the ratios at each location appear consistent. These data and subsequent deposition data will undergo more detailed investigation in the next reporting period.

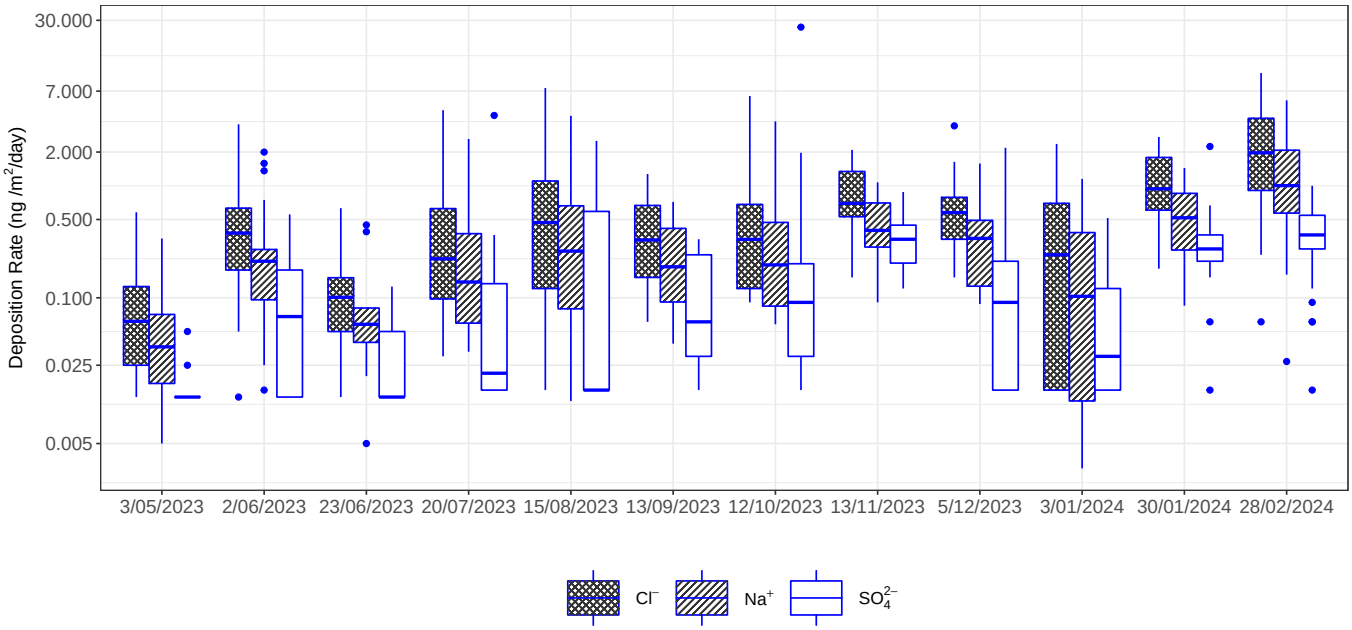

Figure 7.10-5: Boxplots of Cl^-, Na^+, and SO_4^{2-} deposition rates for the dry deposition samples by different sampling periods. Note logarithmic scale.

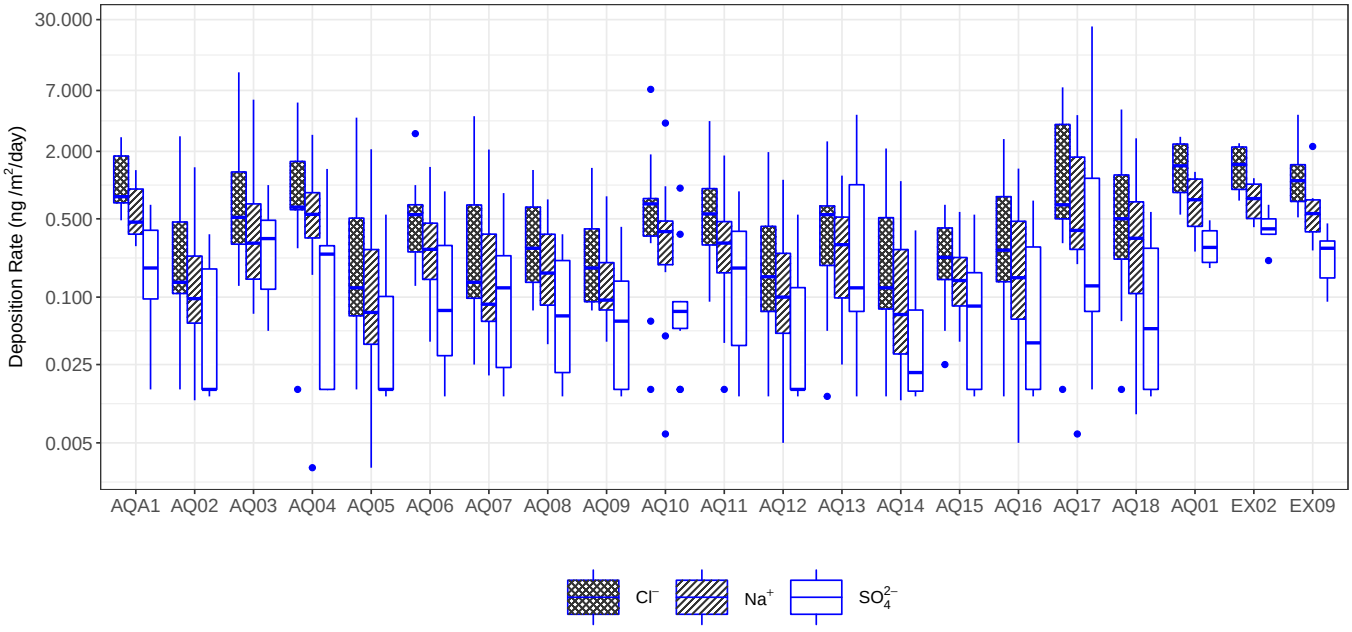

Figure 7.10-6: Boxplots of Cl^-, Na^+, and SO_4^{2-} deposition rates by different sampling sites. Note logarithmic scale.

Boxplots of NH_4^+, NO_3^-, and P deposition rates for each sampling date and location are shown in Figures *7.10-7* and *7.10-8*. These species may also arise from a range of natural, anthropogenic,

marine and terrestrial sources. The relationships are more variable - possibly due to lower levels - and require further investigation in future.

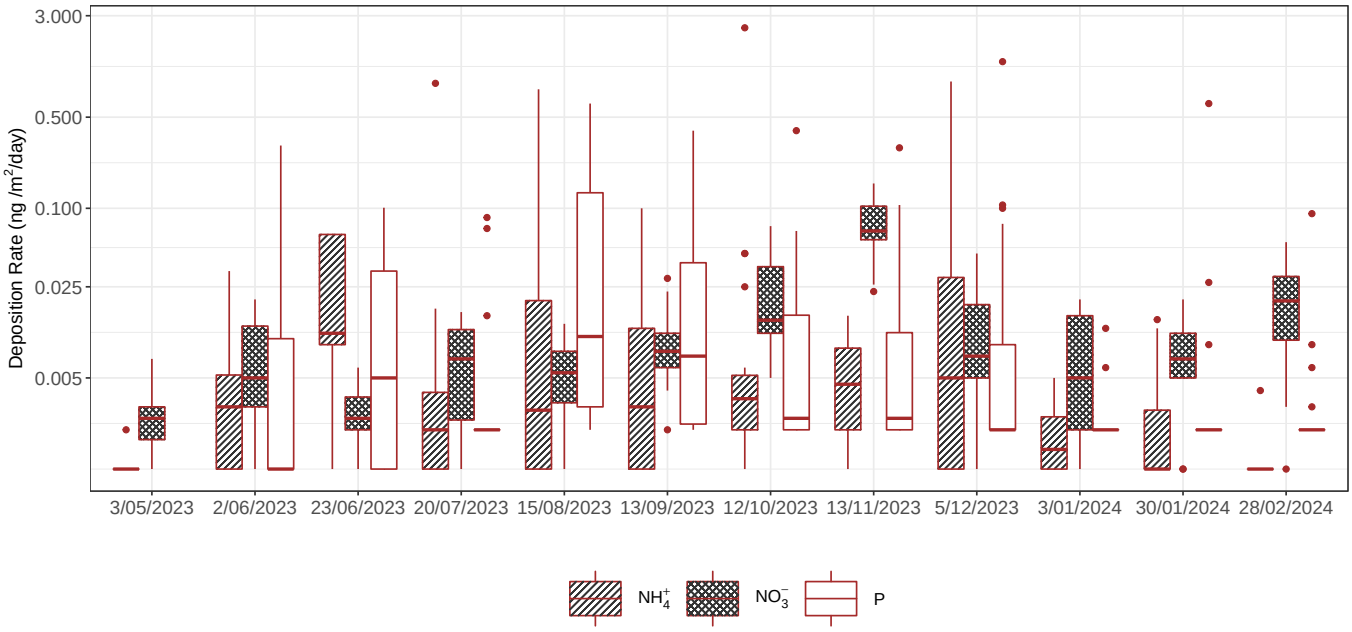

Figure 7.10-7: Boxplots of NH_4^+, NO_3^-, and P deposition rates for the dry deposition samples by different sampling periods. Note logarithmic scale.

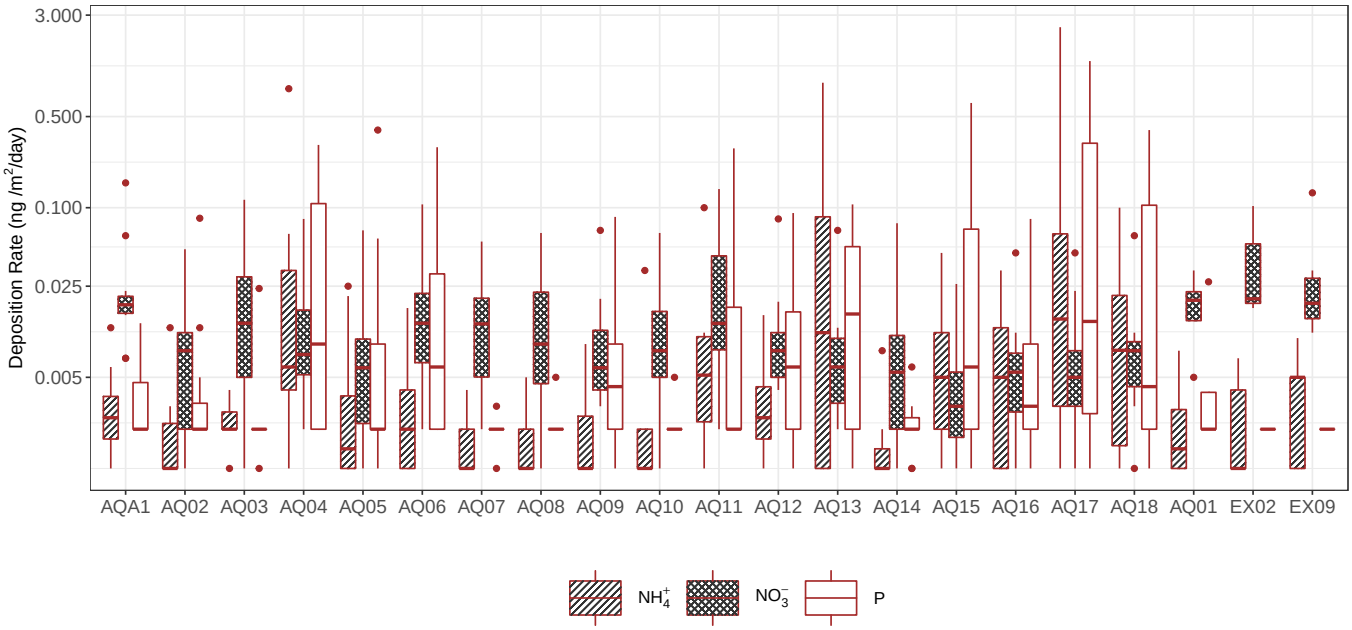

Figure 7.10-8: Boxplots of NH_4^+, NO_3^-, and P deposition rates for the dry deposition samples by different sampling sites. Note logarithmic scale.

Figure *7.10-9* shows the average *pH* and deposition rates of chemical species at each AQM site and *7.10-10* shows the median *pH* and deposition rates of chemical species at each AQM site. In each plot panel, sites are ordered by increasing value of the deposition rate, separately for each chemical species. It can be seen that AQ01 has the highest *pH* in both cases, whereas AQ17 has the highest mean values for many chemical species, largely due to a small number of high measurements (extreme outliers). Overall, however, some clear trends are appearing across the sites, which require more comprehensive investigation in conjunction with other datasets.

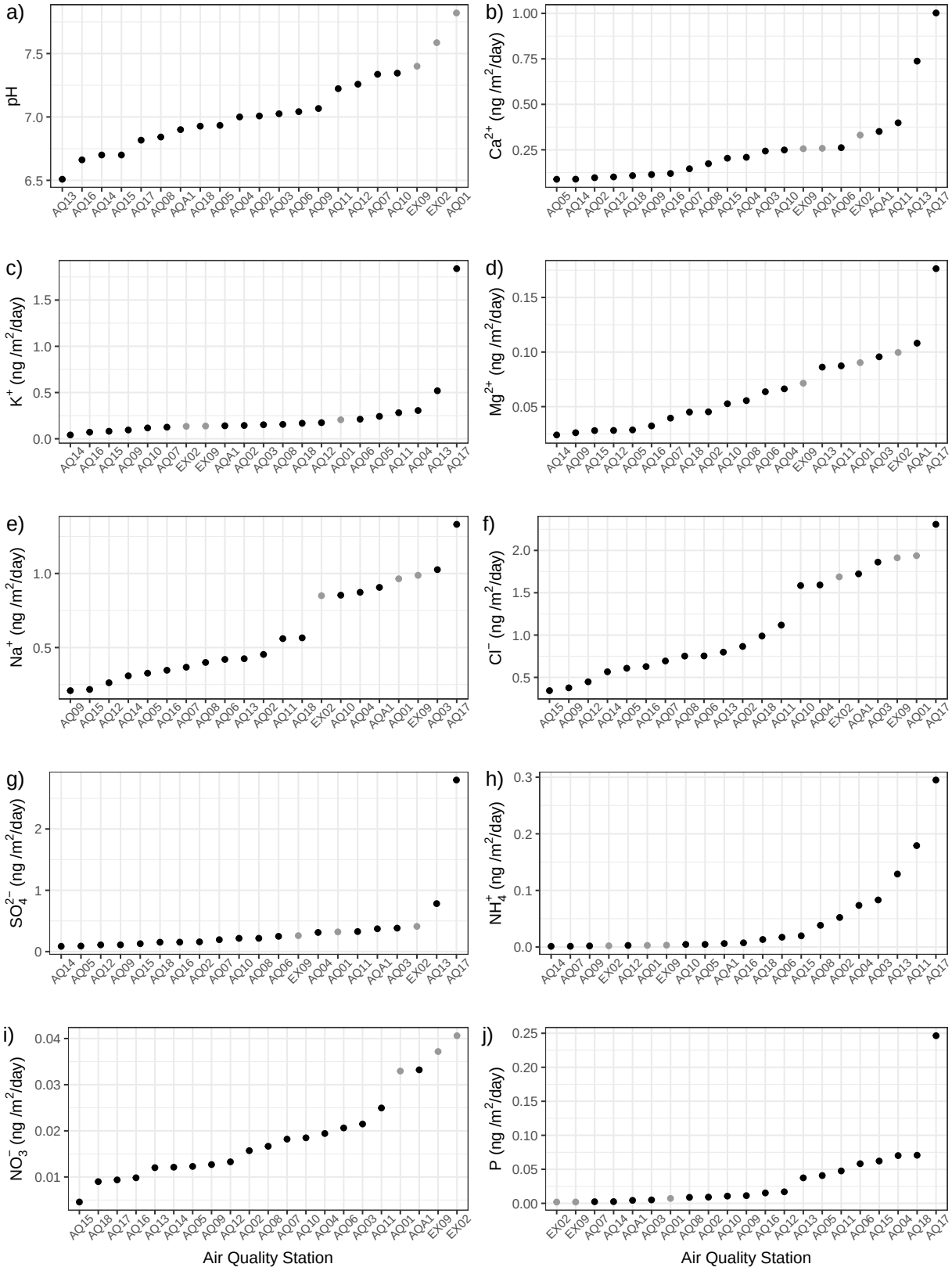

Figure 7.10-9: Average pH and deposition rates by AQM. Data represent approximately 18 months of observation (8/02/2023 to 25/03/2024) except for EX02, EX09 and AQ01 (indicated by grey dots) where less than 12 months of data are available.

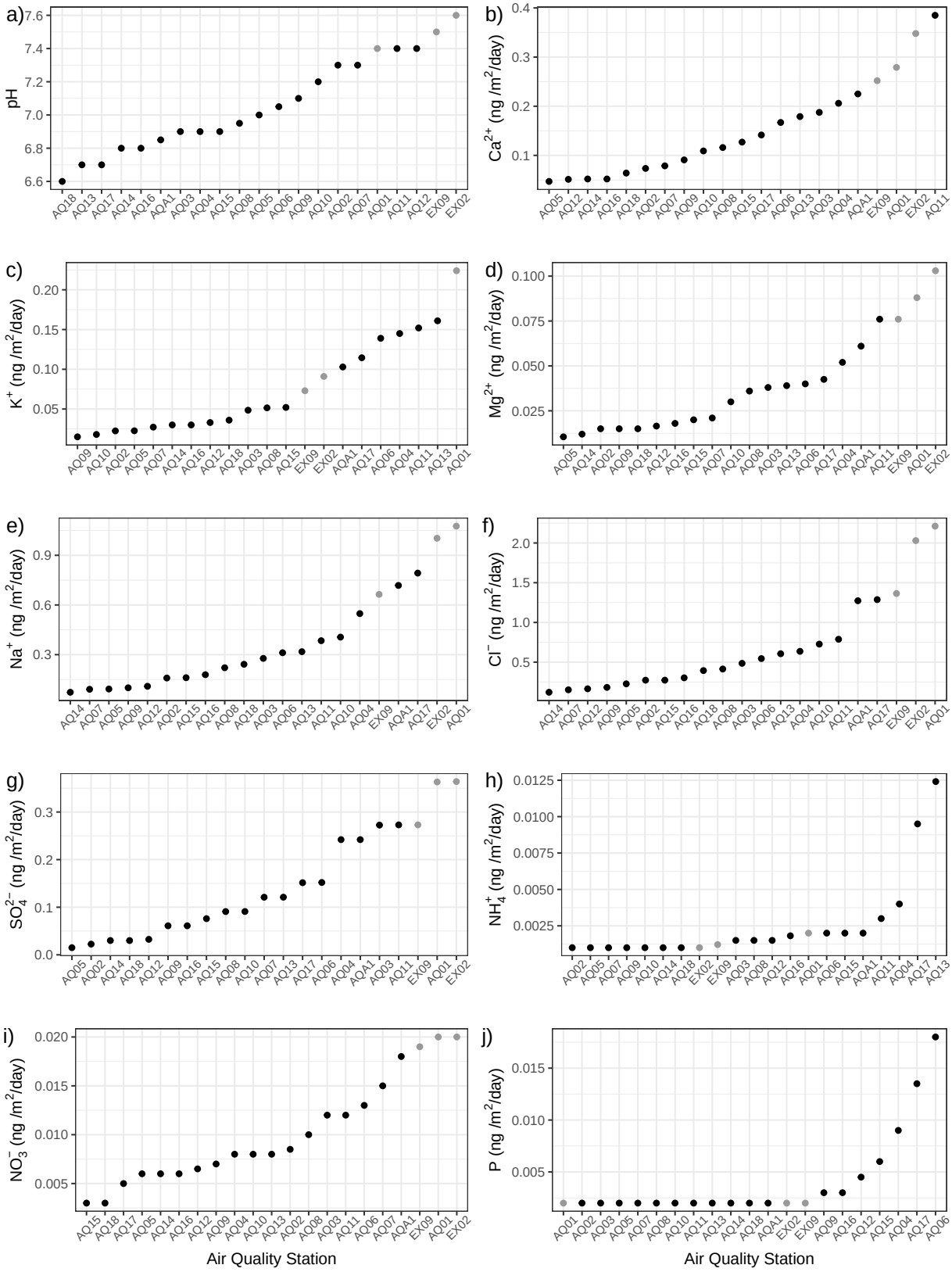

Figure 7.10-10: Median pH and deposition rates by AQM. Data from 8/02/2023 to 25/03/2024 that is approximately 18 months, apart from EX02 and EX09 and AQ01 where less than 12 months of data are available (grey points).

7.10.3 Analysis of co-located sites

The study design specified that one pair of sites should be placed in close proximity to one another, in order to assess variability over small spatial scales, which is an important unknown in many studies. This purpose is served by sites AQ07 and AQ08, which are located approximately 20 metres apart on a small plateau above a quarry pit and roughly equidistant between the (Karratha) airport to the south east, solar salt mine to the south and the main industrial and port facilities spanning an arc from the west to the north.

The first deposition samples from AQ07 and AQ08 were collected in July 2023.

Figure *7.10-11* shows boxplots of deposition rates for different chemical species at AQ07 and AQ08.

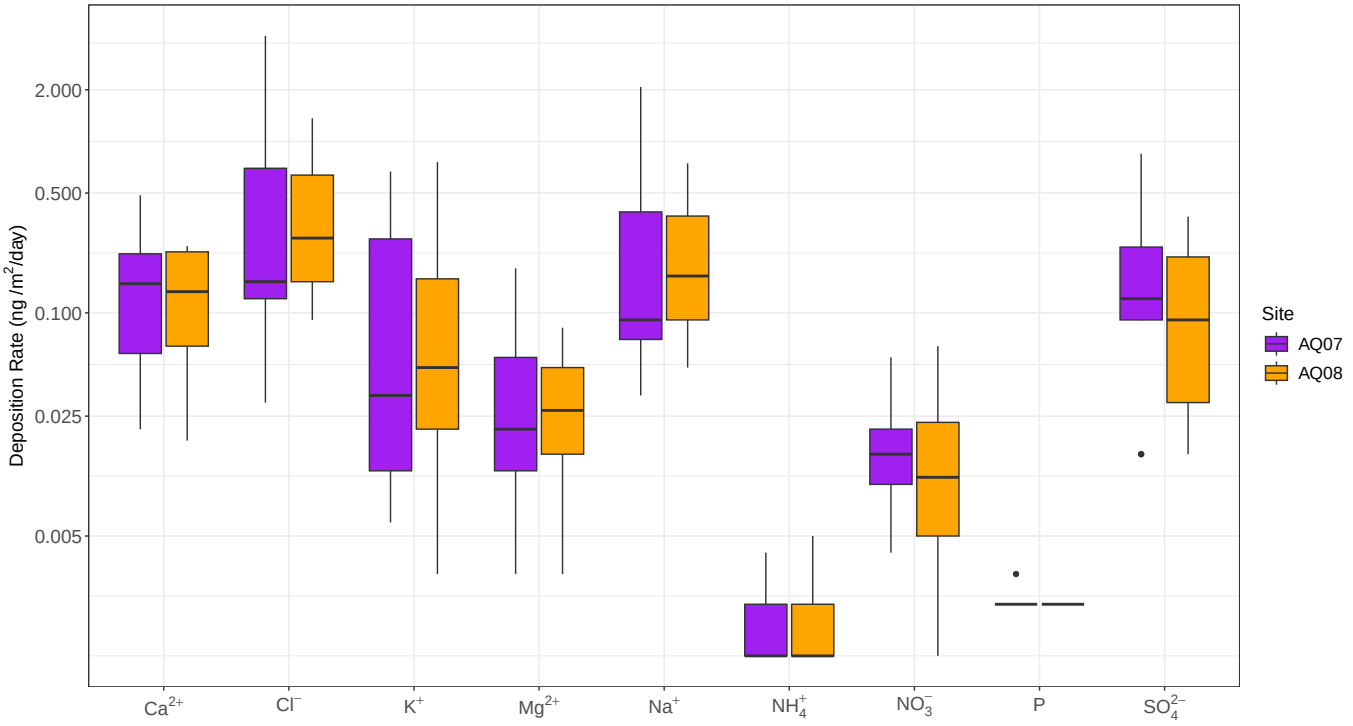

Figure 7.10-11: Boxplots of deposition rates of chemical species from dry deposition samples of co-located AQ07 and AQ08 sites. Note logarithmic scale.

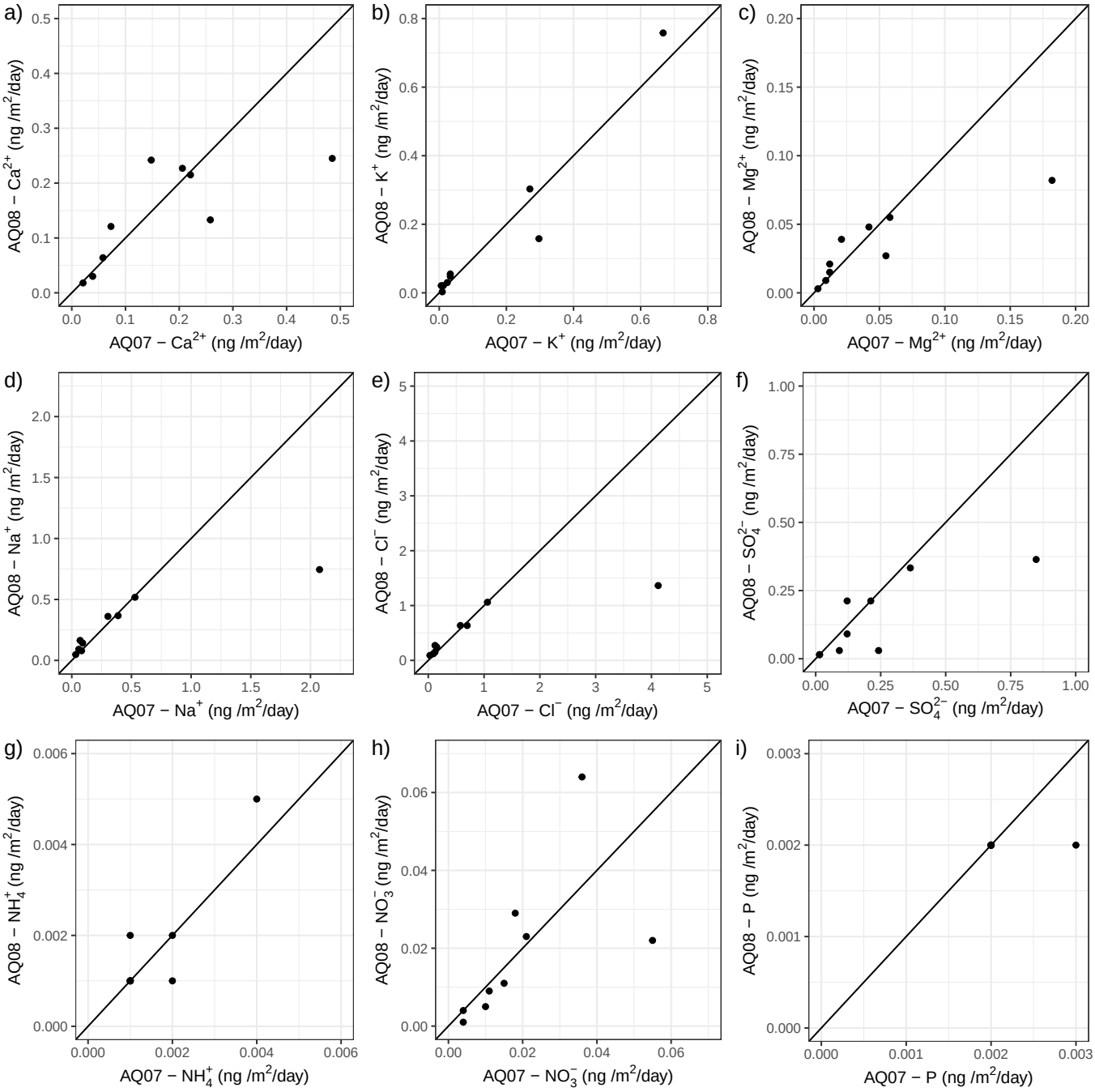

Figure 7.10-12: Scatterplots of the AQ07 vs AQ08 values, for each chemical species. The black line is $y = x$.

Figure *7.10-12* shows scatterplots of the deposition rates observed at AQ07 and AQ08, separately for each chemical species. Observations at the two sites generally agree well, except for NH_4^+ and P, which had many values below detection limits.

Differences between the observations at the two sites may be attributed to short-scale variability (including intrinsic variability of the sampler and assay technique), provided that there is no evidence

of systematic difference. For each chemical species we performed a Wilcoxon rank sum test (Mann-Whitney test) comparing the distributions of the deposition rates at the two sites. The p-values from these tests are reported in the right-hand column of Table *7.10-1* and suggest that there is no evidence for systematic discrepancy between the two sites. Likewise the p-values from the Levene test of equal variances are non significant.

The estimated deposition rates are normally or non-normally distributed, which is evident from histograms and from the the p-values of the Shapiro-Wilk test of normality reported in Table *7.10-1*.

Table 7.10-1: p-values of Shapiro-Wilk test for normality of each sample in AQ07 and AQ08. p-values of Levene's test for homogeneity of variance across AQ07 and AQ08. p-values of the Wilcoxon rank-sum test which compares the distribution of two independent groups (AQ07 and AQ08). Bold figures indicate p-values which are statistically significant at the 5 % level.

Sample	Number of observations (AQ07 and AQ08)	Shapiro-Wilk Normality Test (AQ07)	Shapiro-Wilk Normality Test (AQ08)	Levene's Test	Wilcoxon Rank-Sum Test
Ca^{2+}	18	0.146	0.147	0.372	0.929
Cl^-	18	$<$ **0.001**	0.086	0.461	0.626
K^+	18	**0.001**	$<$ **0.001**	0.986	0.724
Mg^{2+}	18	$<$ **0.001**	0.658	0.433	1
Na^+	18	**0.001**	0.149	0.484	0.691
NH_4^+	18	**0.026**	**0.015**	0.685	0.849
NO_3^-	18	0.075	**0.032**	0.769	0.894
P	18	**0.001**	NA	0.332	0.374
SO_4^{2-}	18	**0.009**	0.062	0.597	0.593

Figure *7.10-13* shows a multiple time series plot of dry bucket sample deposition rates against collection date. Circles represent AQ07 and triangles represent AQ08. The overall impression is that colours cluster together, indicating that the differences between AQ07 and AQ08 are generally much smaller than the variability over time. Na^+ and Cl^- deposition rates increase from July 2023 to September 2023, then drop in October 2023, again increasing from November 2023 to February 2024. Mg^{2+} and Ca^{2+} deposition rates increase from July 2023 to February 2024, while there is a slight drop in 03/01/2024. K^+ and SO_4^{2-} deposition rates are quite high between January–February 2024 compared to July–December 2023. NO_3^- is low in July and August 2023, and high in October-November 2023, and February 2024. NH_4^+ and P did not show notable variation with the time, compared to the scale of variability for the other species.

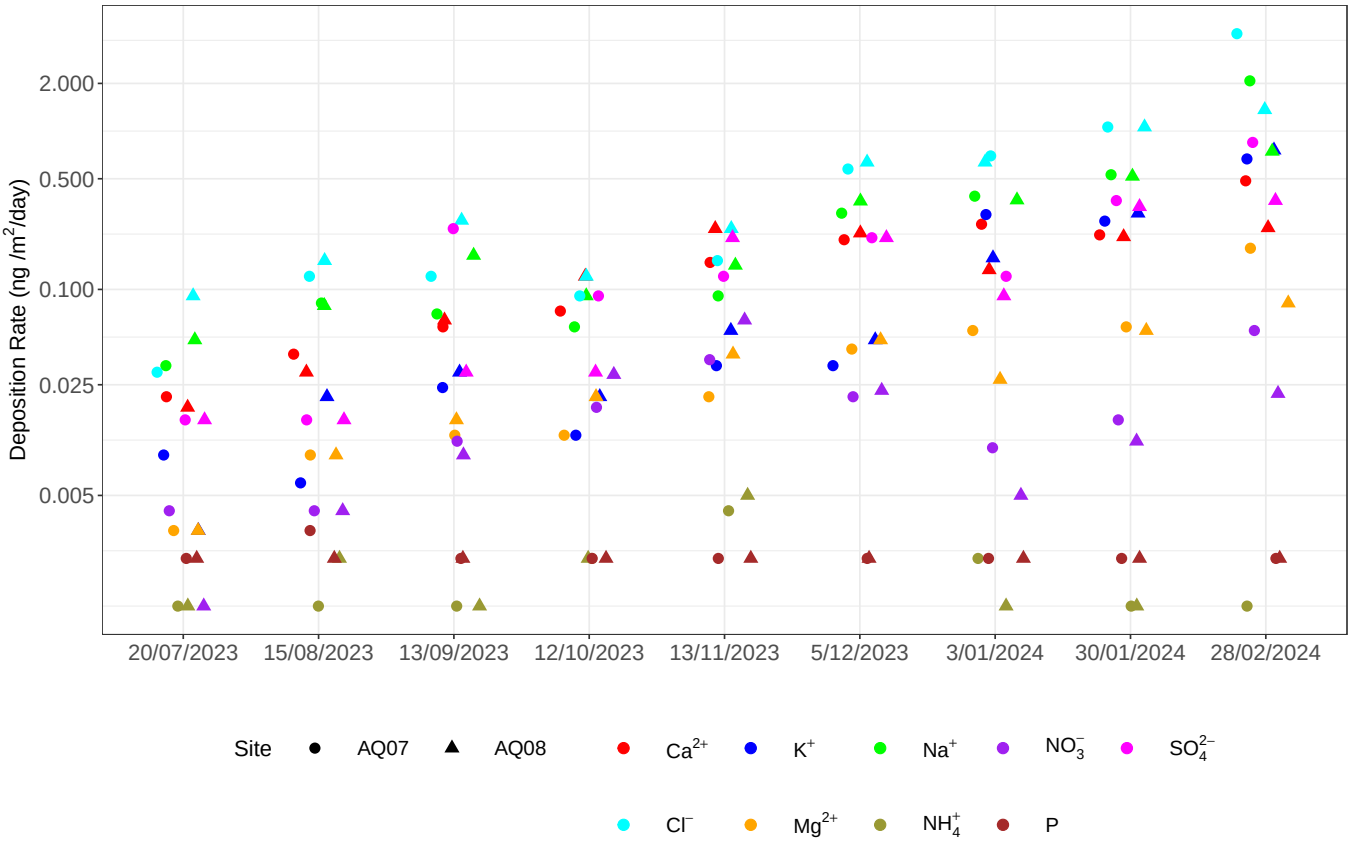

Figure 7.10-13: Time series plots of deposition rates of chemical species, from dry deposition samples at co-located AQ07 and AQ08 sites, against collection date. Note logarithmic scale. Points were jittered to avoid overlap.

7.10.4 Spatial smoothing of deposition sampler data

Figure *7.10-14* shows the result of Nadaraya-Watson spatial smoothing of the dry bucket sample *pH* for each collection date. Other than 23 June 2023 and 13 September 2023, all other *pH* smoothed values are between 6.5 and 7.5, and there is relatively little spatial variation.

Figures *7.10-15* to *7.10-23* show the Nadaraya-Watson spatial smoothed surfaces for dry bucket deposition rates for each of the species Ca^{2+}, K^{+}, Mg^{2+}, Cl^{-}, Na^{+}, SO_4^{2-}, NH_4^{+}, NO_3^{-}, and P.

Ca^{2+} and Mg^{2+} deposition rates show very similar spatial patterns of variation. There is a high deposition rate of Ca^{2+} and Mg^{2+} in August 2023 to the north (near Dolphin Island), as well as in November 2023 and February 2024 near Dampier and the southern Burrup Peninsula. Ca^{2+} and Mg^{2+} deposition rates were generally higher near the Dampier and southern Burrup regions from September 2023 to February 2024. Also, February 2024 showed the highest Ca^{2+} and Mg^{2+} deposition rates in the north west of the Dampier archipelago. In May–June 2023, there is not much spatial variation in Ca^{2+} and Mg^{2+} across sites.

The spatial variation in K^{+} deposition rate is almost similar to Ca^{2+} and Mg^{2+} in most months, but

there are some differences. August, October, and December 2023 have high deposition rates of K^+ in the north (Dolphin and Gidley Islands). K^+ deposition rates were also high in the south (Dampier and southern Burrup regions) in January-February 2024. Also, the highest K^+ deposition rate was observed near the west and east Lewis islands in February 2024. In other months, there is little spatial variation in the K^+ deposition rate across sites.

Spatial variation in Na^+ and Cl^- deposition rates is very similar. Generally, Na^+ and Cl^- deposition rates over the Murujuga region are higher in all months except May and June 2023. However, there are some regions with notably higher deposition rates. In February 2024, very high Na^+ and Cl^- deposition rates were observed in Dampier, southern Burrup, east and west Lewis Islands and West Intercourse Island. Dolphin and Gidley Islands also had higher Na^+ and Cl^- deposition rates in August 2023. In addition, slightly higher Na^+ and Cl^- deposition rates were observed near Burrup and Dampier in January 2024.

The deposition rates of SO_4^{2-} in February 2024 are very high around Dampier, southern Burrup, the East and West Lewis islands, and West Intercourse islands. Higher SO_4^{2-} deposition rate was also observed near Dampier and southern Burrup in November 2023 and January 2024. Furthermore, Dolphin and Gidley Islands showed very high SO_4^{2-} deposition rates in August 2023. All the other months had quite low SO_4^{2-} deposition rates.

Spatial smoothing showed high levels of K^+, Na^+, Cl^- and SO_4^{2-} on Rosemary Island; however, as no monitoring stations exist on this island such interpolations must be treated with caution.

The spatial patterns of variation in NH_4^+ and P deposition rate are very similar. In particular, high deposition rates of NH_4^+ and P were observed in the north (Dolphin and Gidley Islands) during August and October 2023 and early December 2024. From July to December 2023, NH_4^+ and P deposition rates were higher near the southern Burrup regions. Moreover, an interesting fact is that, in February 2024, only NH_4^+ deposition rate was extremely low (and P also low), over Murujuga whereas other deposition rates were very high.

All over Murujuga, samples collected on 13th November 2023 showed relatively high NO_3^- deposition rates.

For cross-checking purposes, analysis was repeated after applying winsorization to all deposition rate data to moderate the effects of extreme values. After winsorization, NO_3^- ranged between 0 and 0.02 ng/m^2/day except that NO_3^- on 13/11/2023 ranged between 0.023 and 0.036 ng/m^2/day. We concluded that the spatial smoothing results appear to be resistant to extremes, and the extreme NO_3^- observed on 13th November 2023 may require further analysis or comparison with other component studies. Apart from this date, NO_3^- is very high in Dampier (near industrial installations) in October 2023, December 2023, and February 2024. In general, NO_3^- is somewhat higher in the Dampier and southern Burrup regions from September 2023 to February 2024, whereas NO_3^- is very low from May to August 2023 over the Murujuga region.

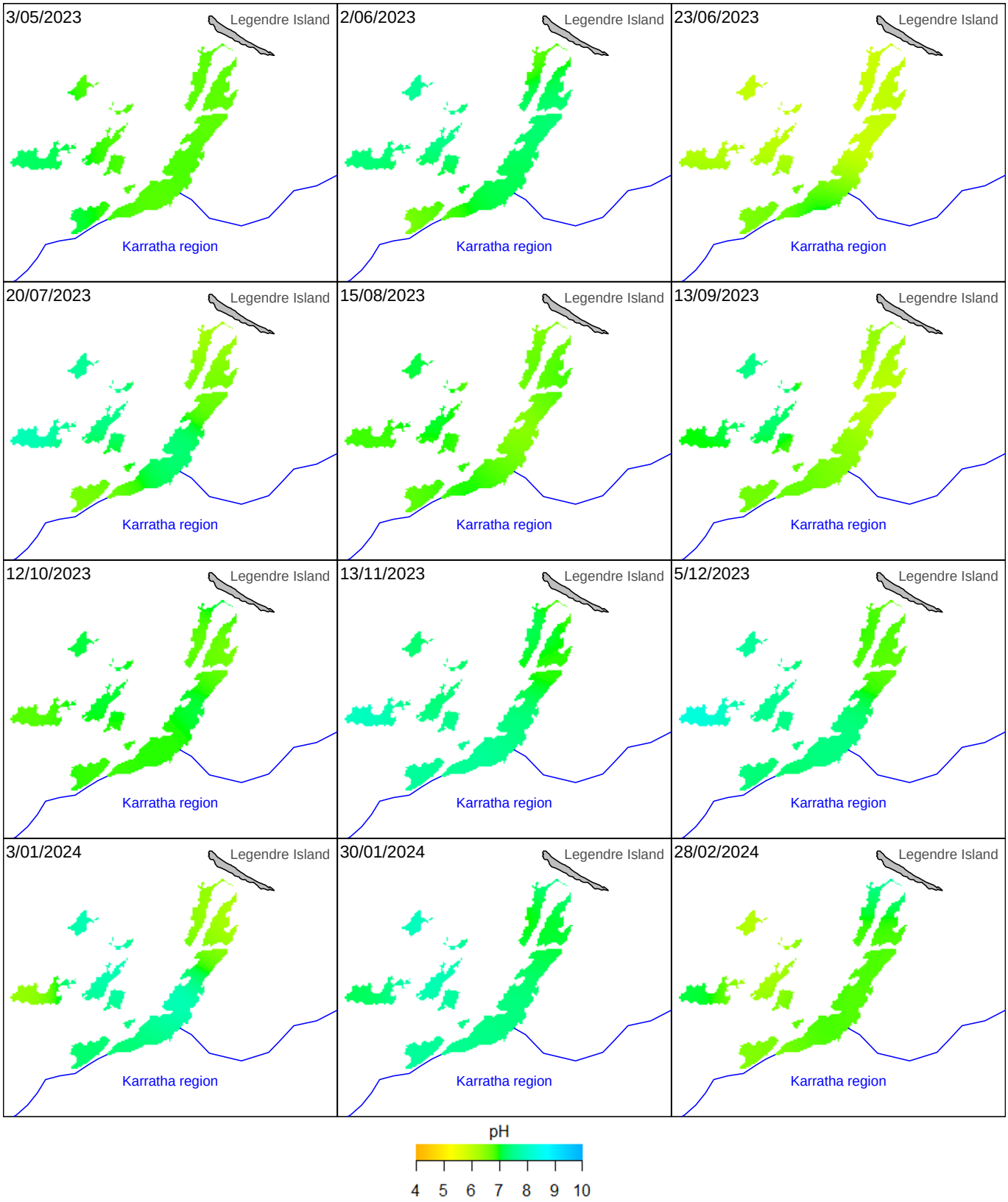

Figure 7.10-14: Spatially smoothed average pH for the dry deposition samples by different sampling periods. The blue line represents the Karratha coastline. The grey polygon is Legendre Island.

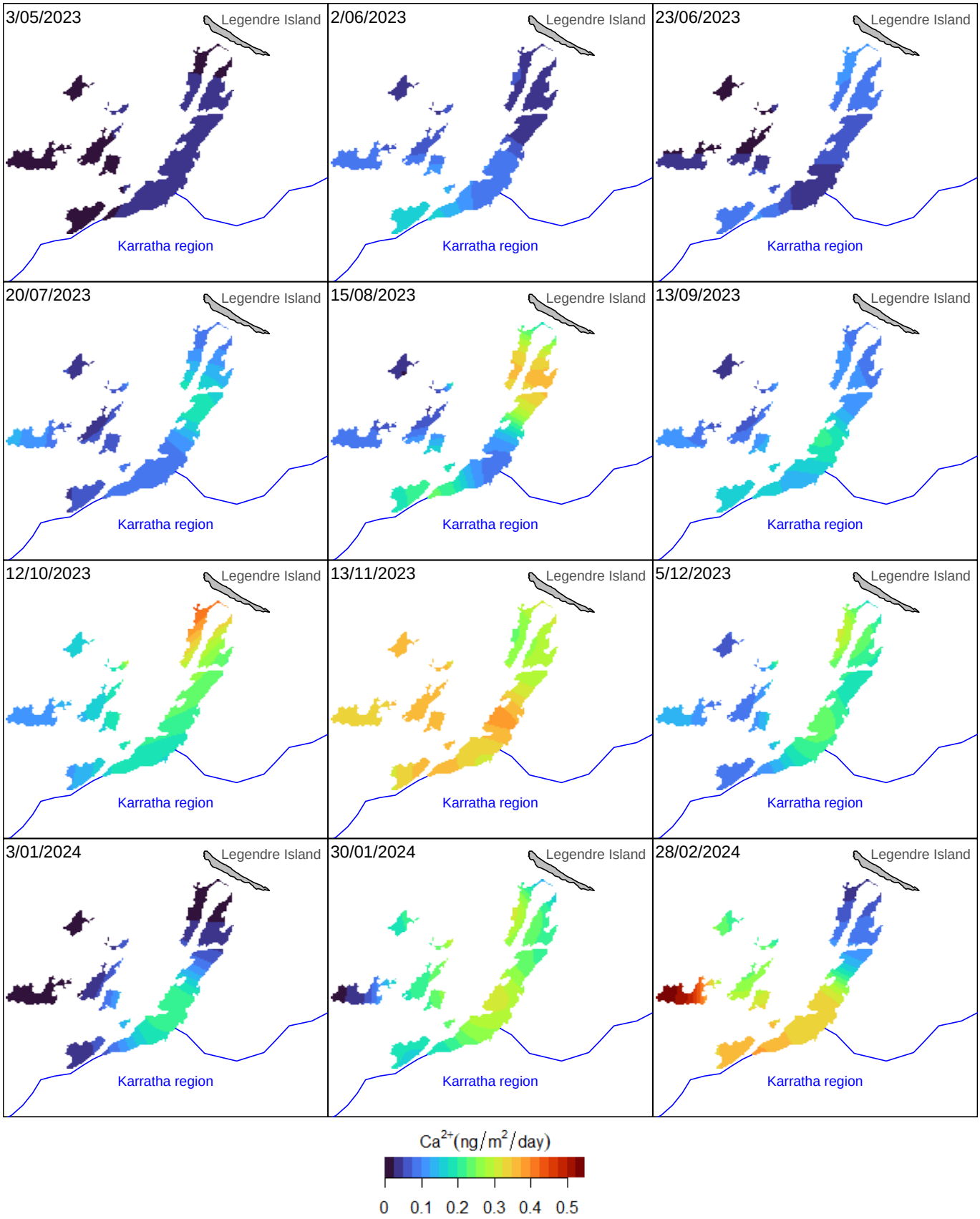

Figure 7.10-15: Spatially smoothed average Ca^{2+} deposition rate for the dry deposition samples by different sampling periods.

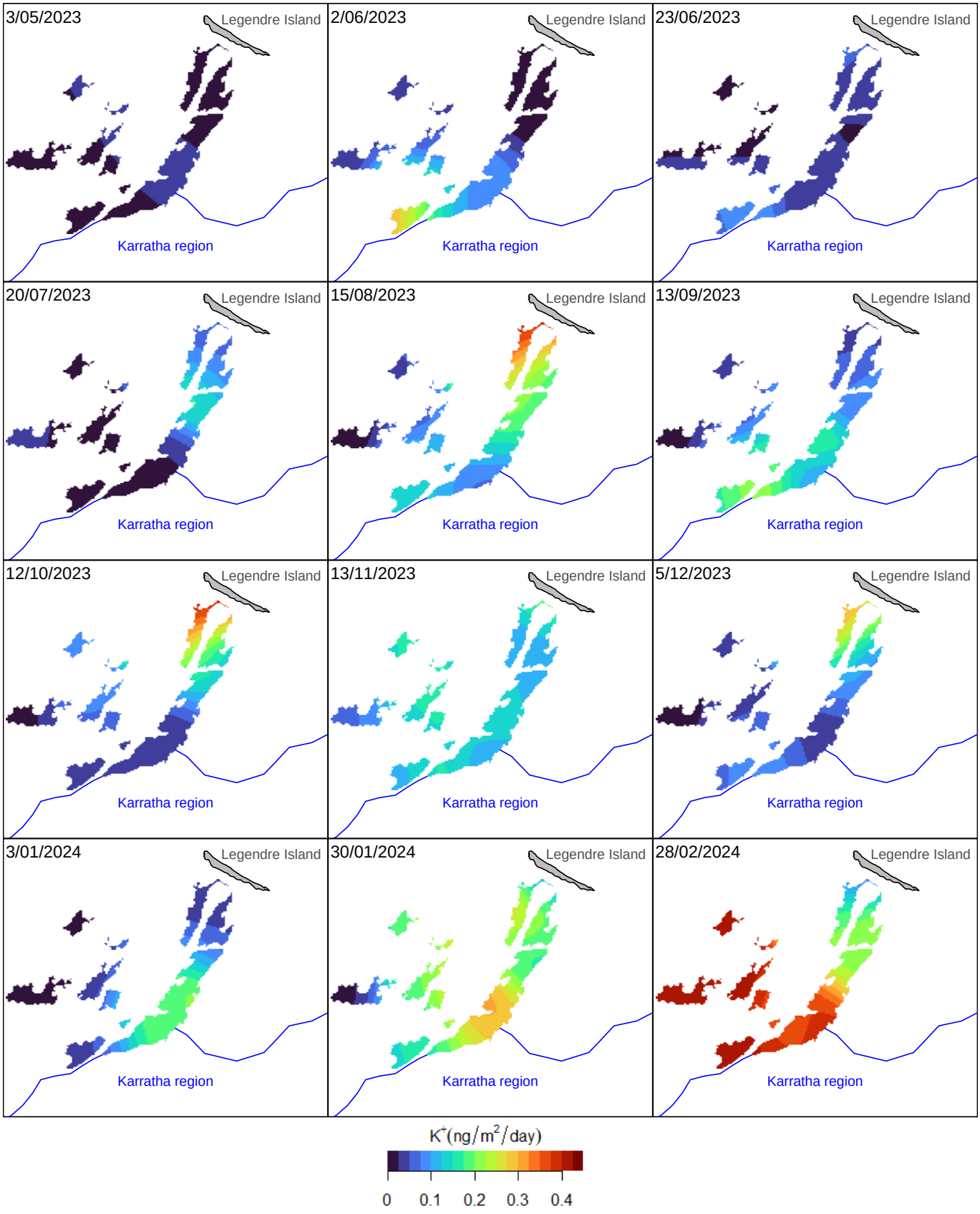

Figure 7.10-16: Spatially smoothed average K^+ deposition rate for the dry deposition samples by different sampling periods.

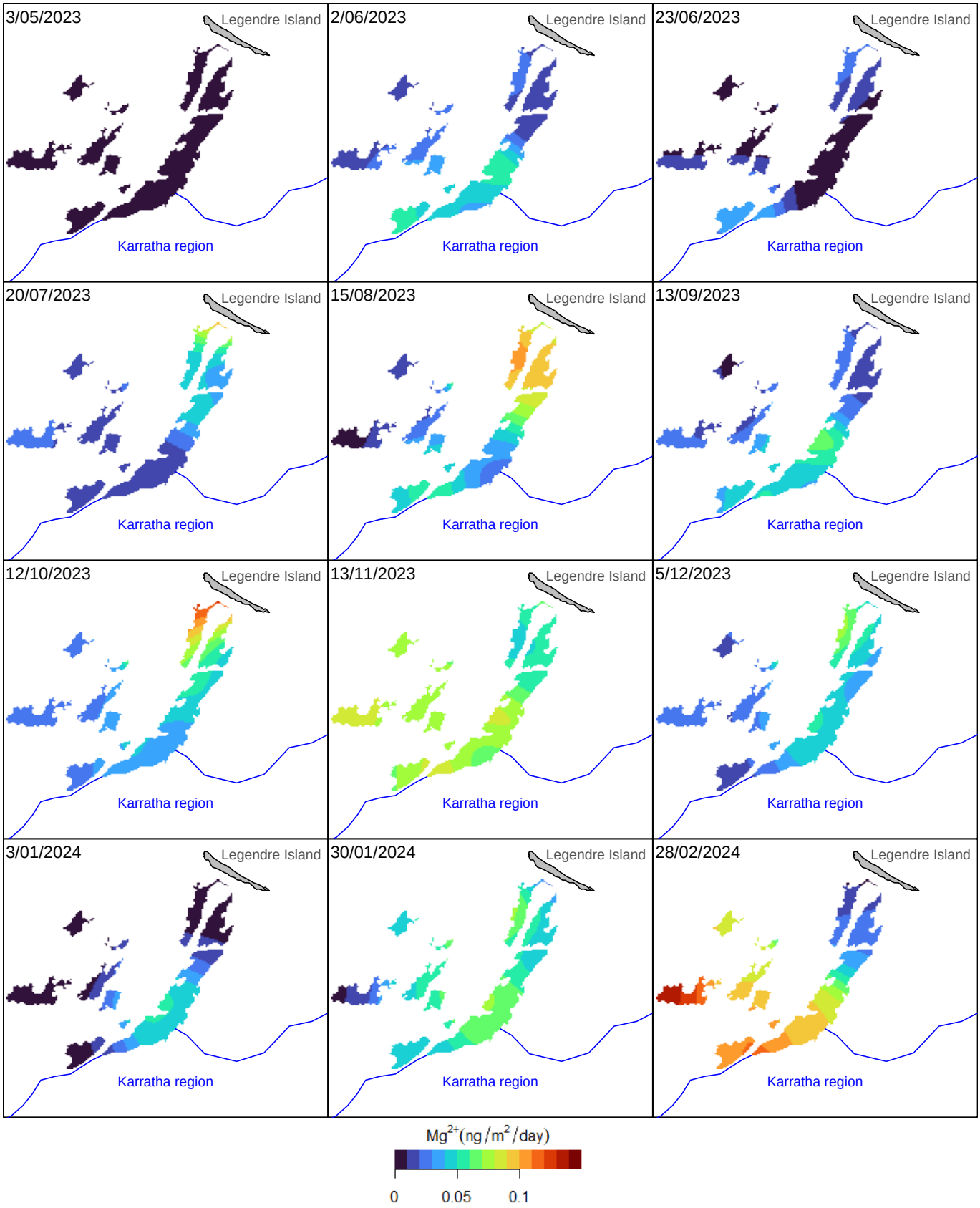

Figure 7.10-17: Spatially smoothed average Mg^{2+} deposition rate for the dry deposition samples by different sampling periods.

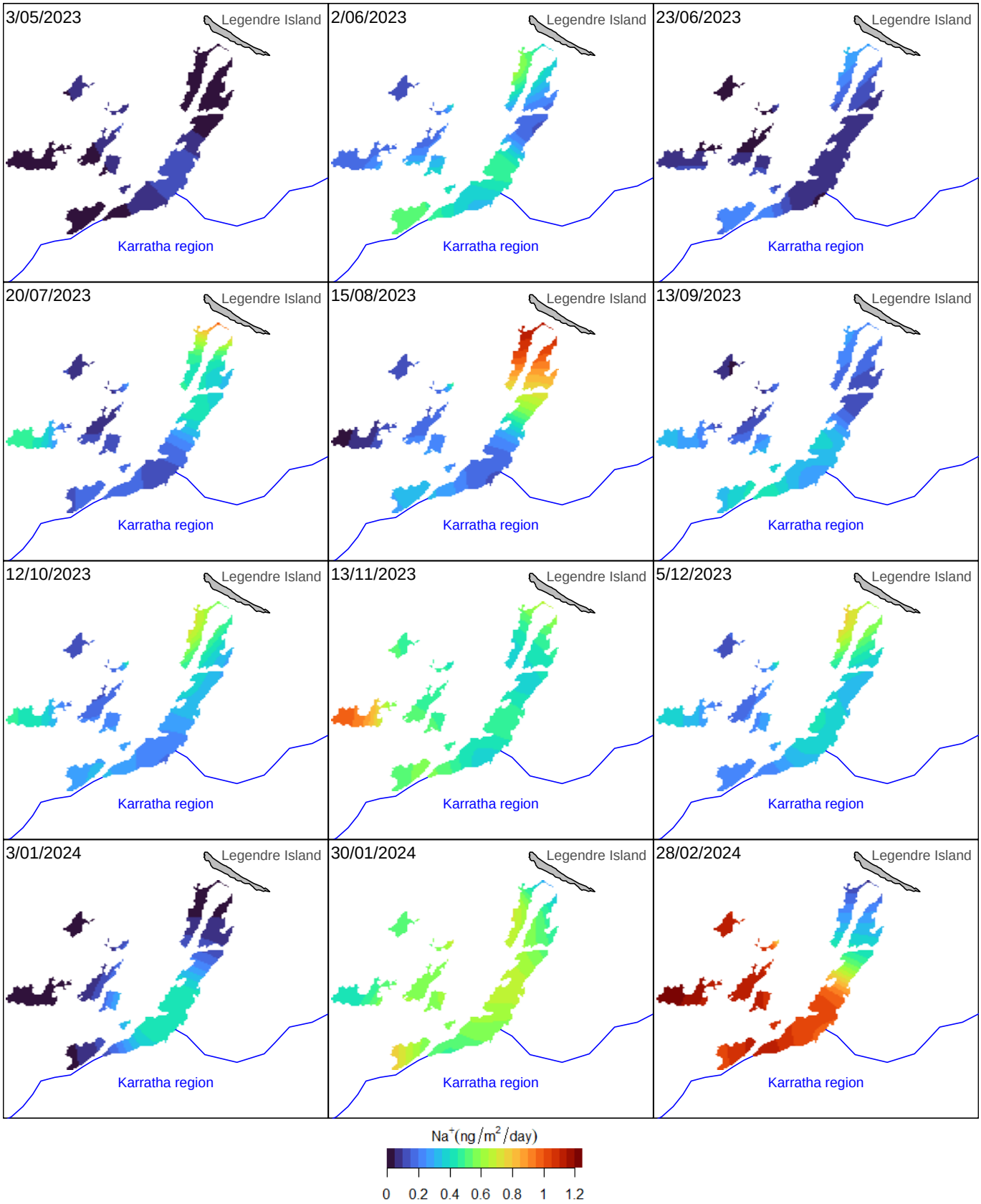

Figure 7.10-18: Spatially smoothed average Na^+ deposition rate for the dry deposition samples by different sampling periods.

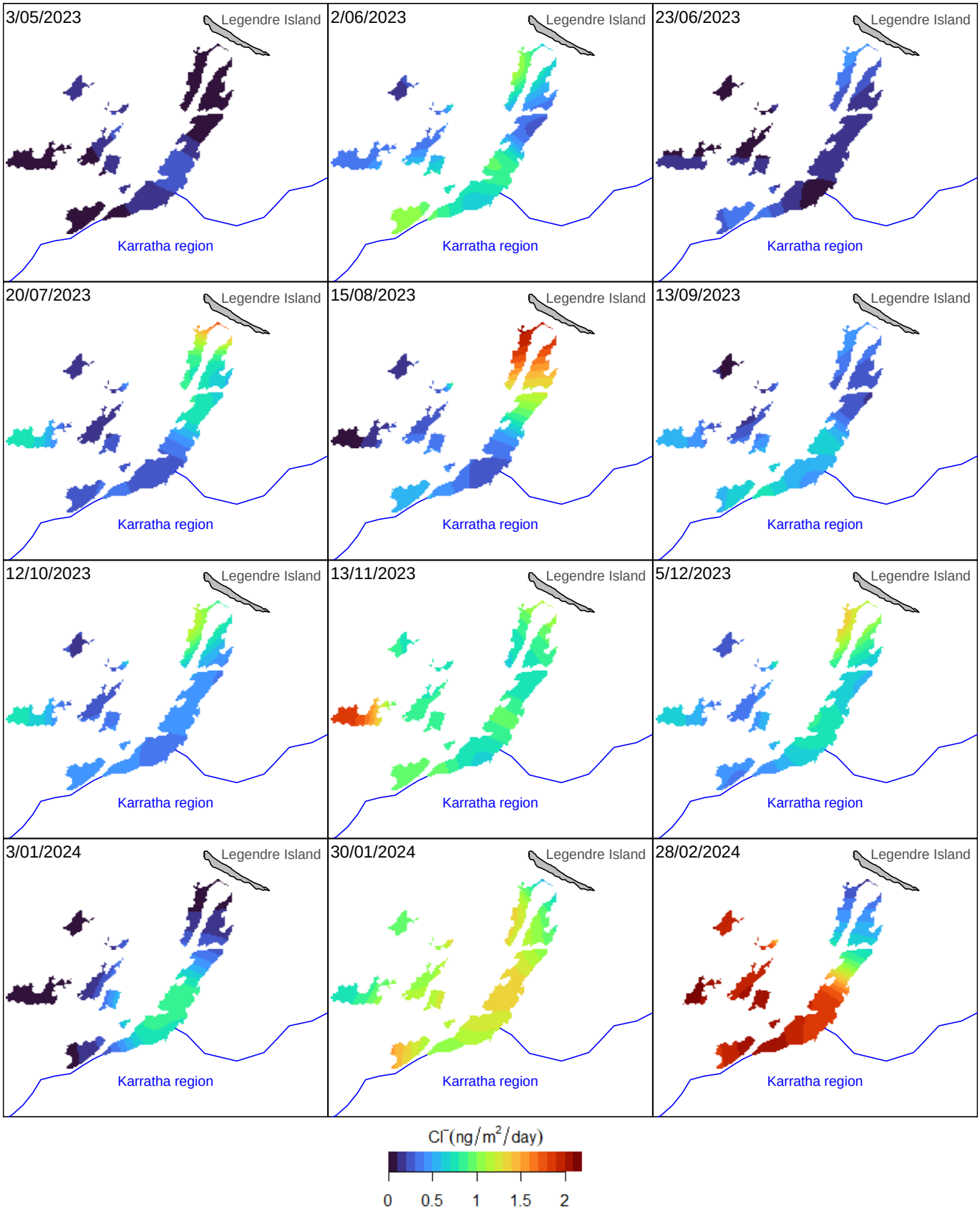

Figure 7.10-19: Spatially smoothed average Cl^- deposition rate for the dry deposition samples by different sampling periods.

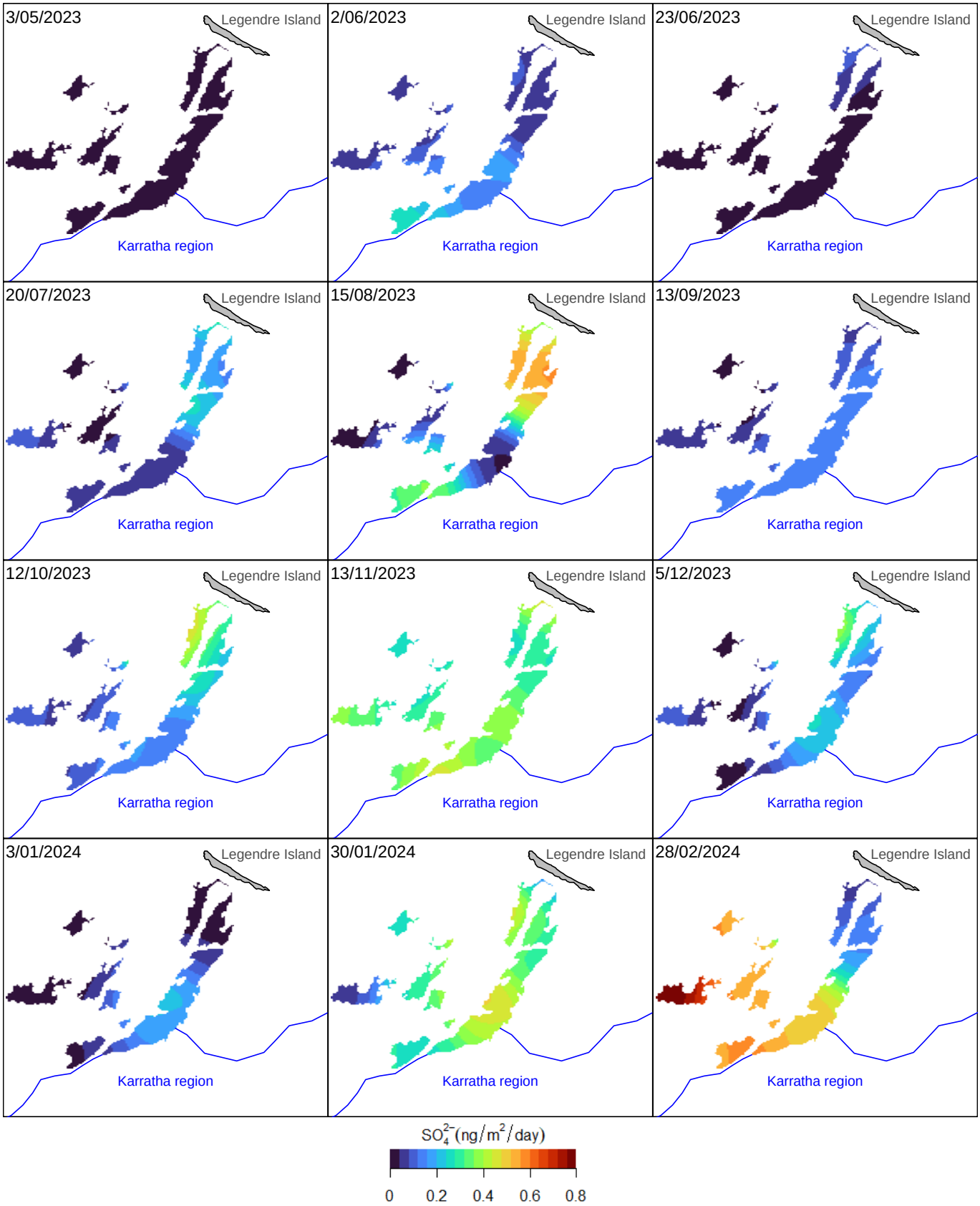

Figure 7.10-20: Spatially smoothed average SO_4^{2-} deposition rate for the dry deposition samples by different sampling periods.

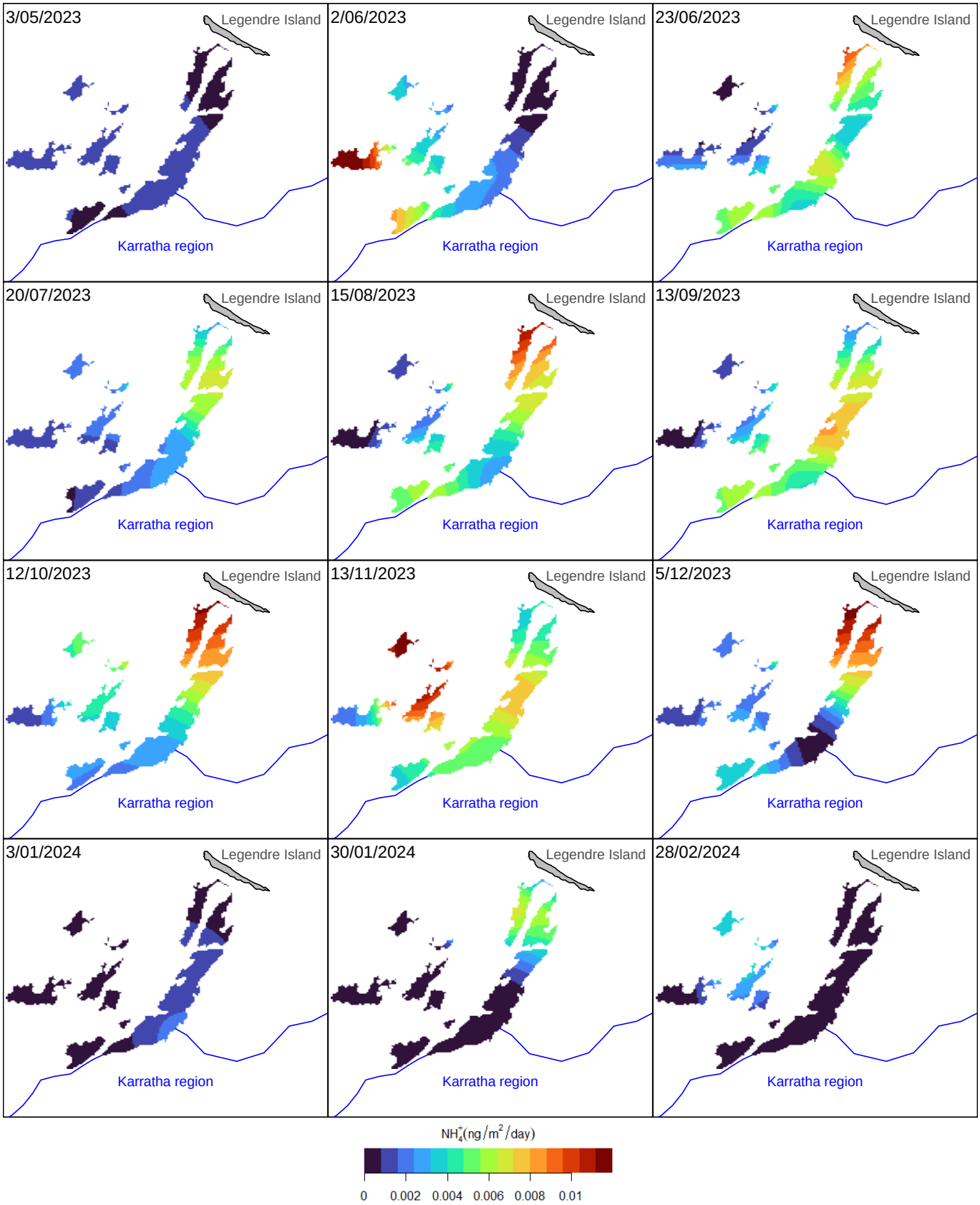

Figure 7.10-21: Spatially smoothed average NH_4^+ deposition rate for the dry deposition samples by different sampling periods.

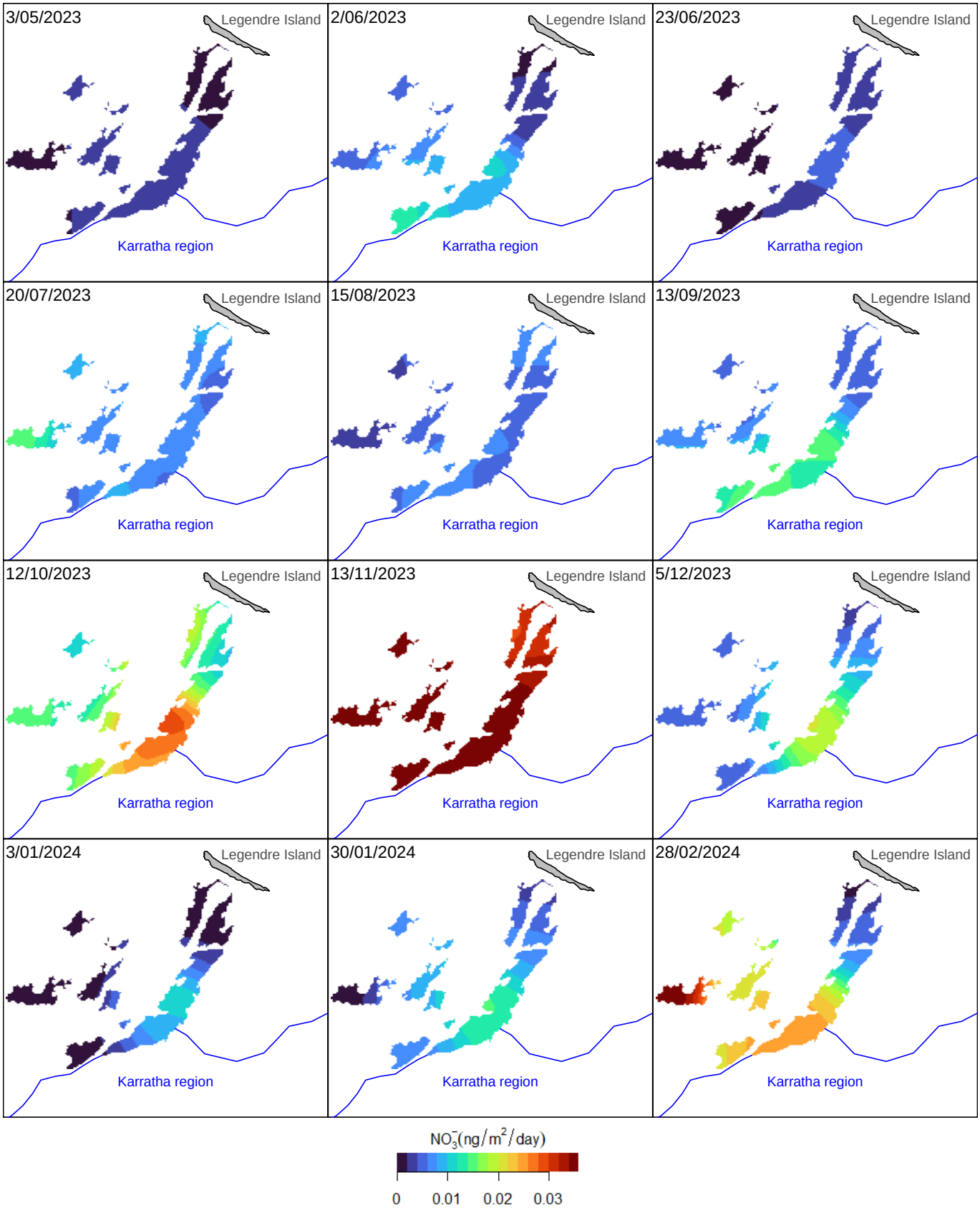

Figure 7.10-22: Spatially smoothed average NO_3^- deposition rate for the dry deposition samples by different sampling periods.

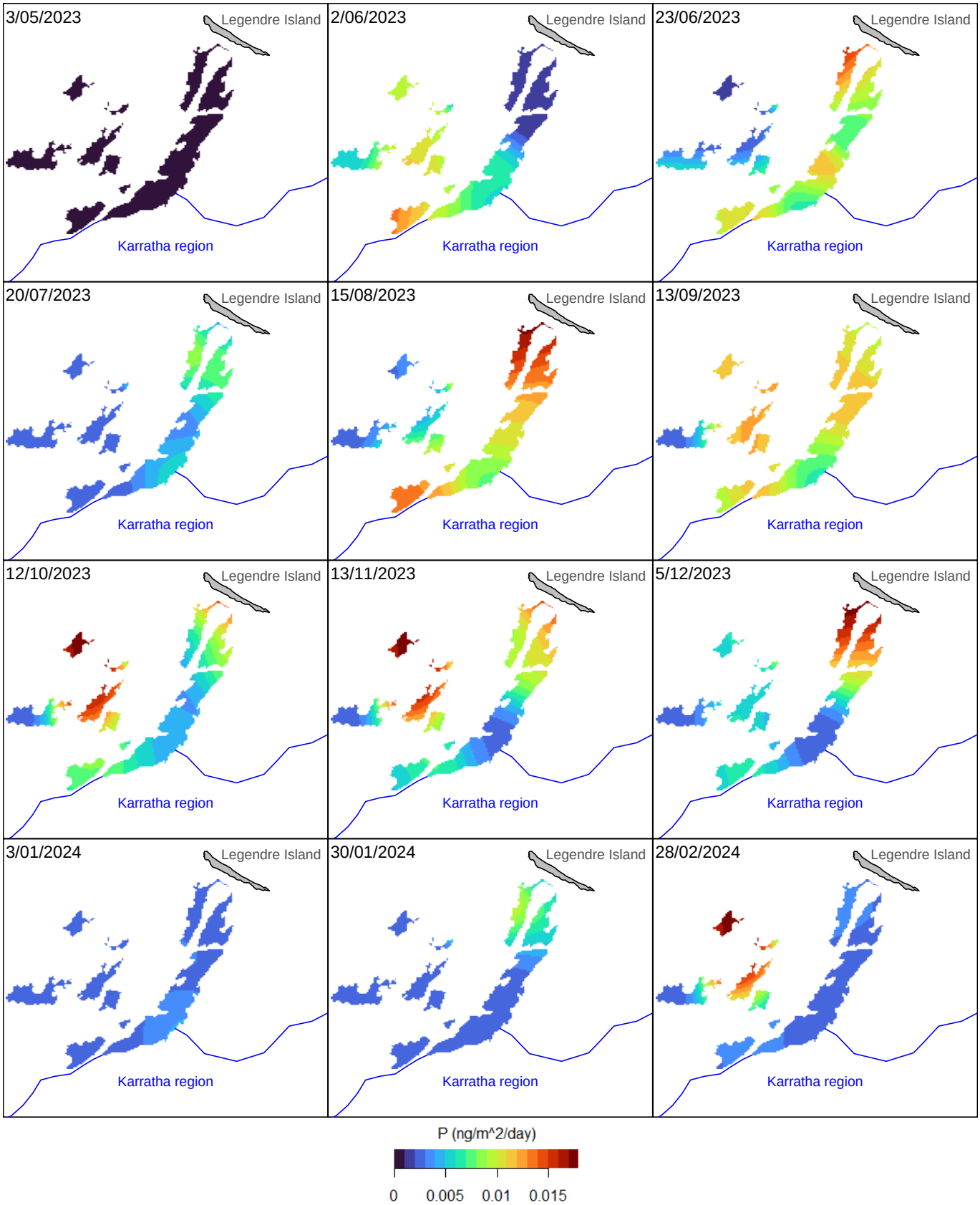

Figure 7.10-23: Spatially smoothed average P deposition rate for the dry deposition samples by different sampling periods.

In Figure *7.10-24*, there is no notable difference in *pH* among dry, wet, and mist deposition samples. 50 ml water (H_2O) was added from March 2023 to June 2023, and 60 ml water (H_2O) was added from July 2023 to date.

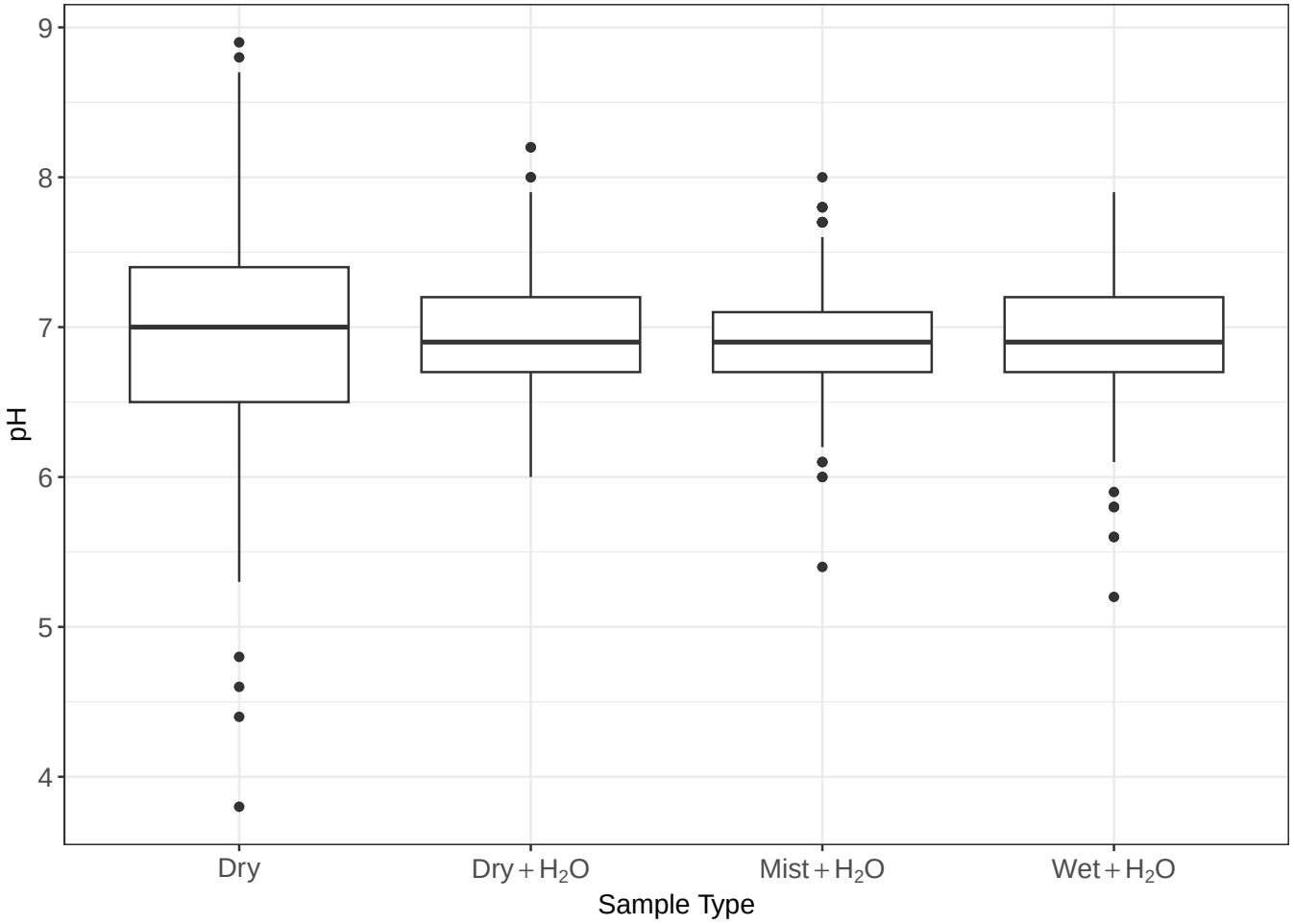

Figure 7.10-24: Boxplots of pH by Dry, Wet, and Mist deposition samples (H_2O is distilled water).

7.10.5 Rainfall *pH*

A dominant narrative in previous studies and commentary has been increasing acidification at Murujuga (i.e. increasingly acidic rainfall). Therefore it was considered important to collate data on current and historic rainfall *pH*.

Figure *7.10-25* shows historic and recent rainfall data from Murujuga. The red dots were *pH* measurements reported by Bednarik (2007), which have been digitally extracted from the published material. Personal communication has established that the horizontal bars published in the original paper represent single points at the centroid of the bar and have been extracted as such. The recent data represents *pH* measurements by the West Australian Biogeochemistry Centre (Greg Skrypek, UWA) using specialised rain collectors (Palmex Ltd. (Croatia)) which have been co-located at four MRAMP AQMs (AQ01, AQ10, AQ14, AQ18). It can be seen that the recent measurements are

neutral or slightly alkaline. This is thought to be due to the contribution of salt(s) and or dust(/clay minerals). The rainfall *pH* values agree relatively well with the deposition sampler data.

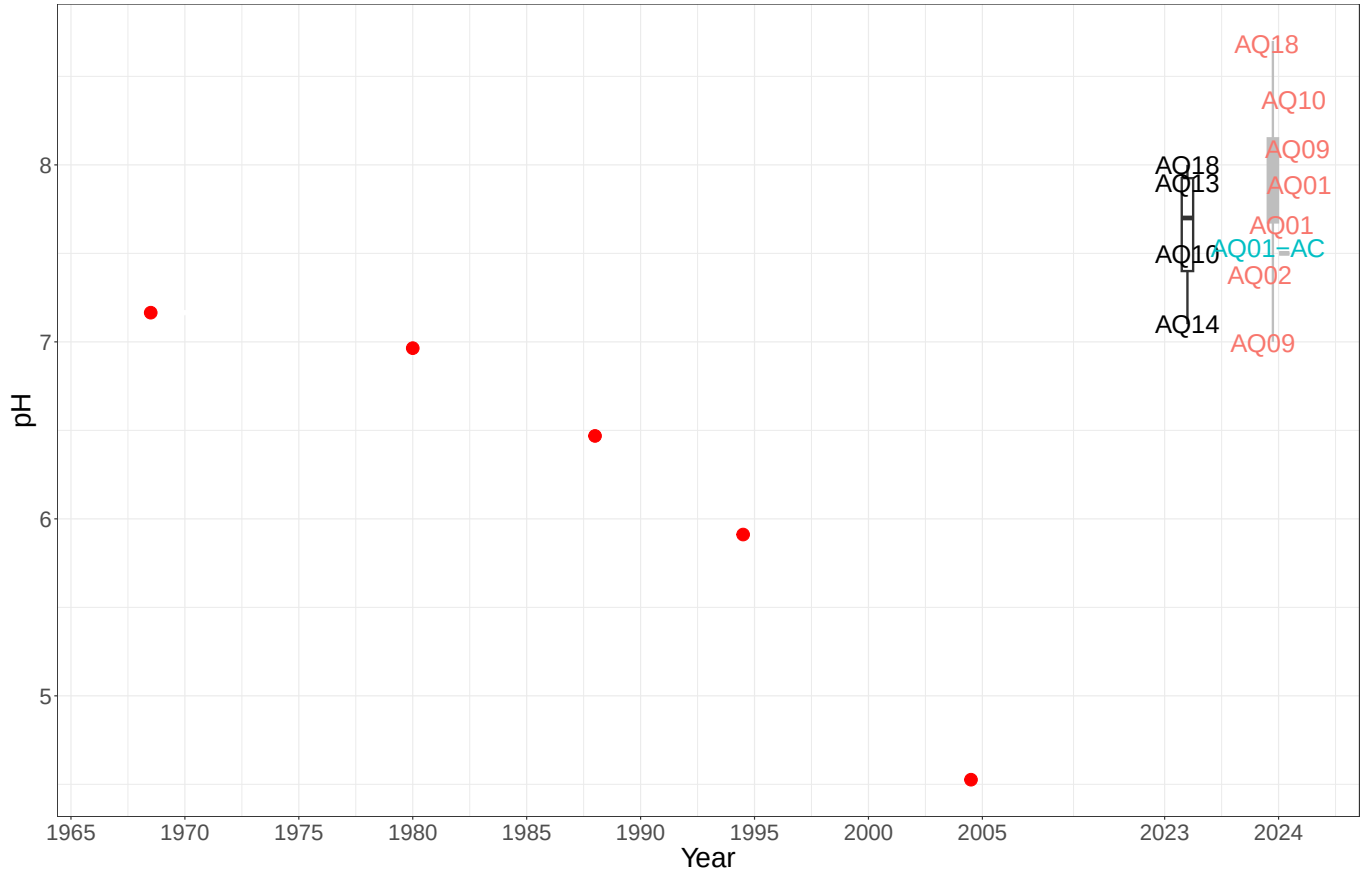

Figure 7.10-25: Historical measurements of rainfall pH plotted against year of observation. The red dots are digitised from Bednarik (2007). Boxplots show recent data from Greg Skrypek, UWA.

Given both the deposition sampler and rainfall *pH* data, the historic rainfall acidification reported by Bednarik (2007) does not appear to be currently occurring. It is unfortunate that a more extensive rainfall pH record for the region does not appear to be available. Globally, rainfall *pH* is generally 5.0-6.0 in what are considered relatively unpolluted regions. Values below this are considered acid rain. Rainfall *pH* above 7 is usually considered to be due to salt/sea spray or alkaline dust/clay minerals as discussed above. It is possible that rainfall was more acidic in the past when NO_2 and SO_2 levels in the airshed were higher, e.g. when additional sources such as higher sulphur fuels were combusted.

7.11 Passive samplers

7.11.1 Background

This study uses passive diffusion samplers, deployed at different sites across Murujuga, to measure the monthly (typically every 4 weeks) average concentration of several gas species and volatile organic compounds in the environment. These measurements provide valuable information about the spatial distribution and seasonal pattern of these analytes, at relatively low cost.

We utilise IVL passive diffusion samplers (IVL Swedish Environmental Research Institute, 2024) each of which is specialised for measuring either NO_2, NH_3, O_3, SO_2, HNO_3 or volatile organic compounds (VOCs). Samplers are deployed at 21 air quality monitoring stations (AQMs) across Murujuga. At each AQM, the samplers are mounted together in a dedicated housing, exposed to the ambient air, while protected from direct sunlight and rain. Samplers are deployed in duplicate, that is, two identical sampler tubes are deployed for each analyte at each AQM for each sample period. The placement of the 12 sampler tubes within the housing is randomised. Samplers are deployed for approximately four weeks, after which they are retrieved and sent for laboratory analysis by IVL. The weather station at each site is used to determine the mean temperature over the sampling period to allow the laboratory to determine diffusive rates for each species, at each site. The VOC samplers are assayed for benzene, toluene, ethylbenzene, m-,p-xylene, o-xylene, n-octane, and n-nonane. All other samplers are assayed for the gas species to which they are dedicated.

7.11.2 Exploratory data analysis of passive sampler data

7.11.2.1 Observations ascribed to calendar months

Each passive sampler observation was ascribed to the calendar month having the longest overlap with the sampling period. The number of months of data available varied between gases, with at most 12 months available (November 2022 to October 2023) at the time of analysis, partly due to the time required for laboratory assay. However some months are missing: NO_2 data is only available to August 2023 due to an issue with IVL samplers; May 2023 and October 2023 samples are missing for SO_2; and October samplers are missing for HNO_3.

7.11.2.2 Values below detection limit

In some of the data, particularly from our VOC samplers, the assayed concentration may be reported as below detection limit (BDL).

Chemical analyses to determine the concentrations of sampled quantities typically adopt an abundance of caution, not to declare presence of a quantity when the sample is in fact a ‘blank’. An instrument comes with a prespecified limit of detection (**LOD**), which is the lowest concentration level that can be determined to be statistically different from that of a blank, although what “statistically different” means is a matter of some interpretation (Currie, 1988; Lambert et al., 1991). Then any concentration below the instrument’s LOD is denoted in the database as BDL, or similar. Assay results from the passive samplers, particularly those for VOC, return BDLs on occasions.

A BDL is not a missing value, since it carries information that the instrument found a value that was small. In the exploratory statistical analysis below, where variabilities in the different quantities are

explored in search of potential signals, we replaced the non-numeric 'BDL' with a value equal to half the LOD (Hornung and Reed, 1990; Finkelstein and Verma, 2001; Ganser and Hewett, 2010).

For a statistically rigorous treatment of these data at the final confirmatory stage of analysis, one can consider each measurements to be an imperfect observation of the true latent process, where the imperfection is due to measurement error and left censoring below the LOD (Cressie et al., 2007). This approach is deferred until the final Monitoring Studies Report.

7.11.2.3 Summary statistics

Figures *7.11-1* and *7.11-2* show histograms of the passive sampler data, overlaid with kernel density estimates. These were produced using all the available data for each analyte, pooled over all AQM stations and over all months.

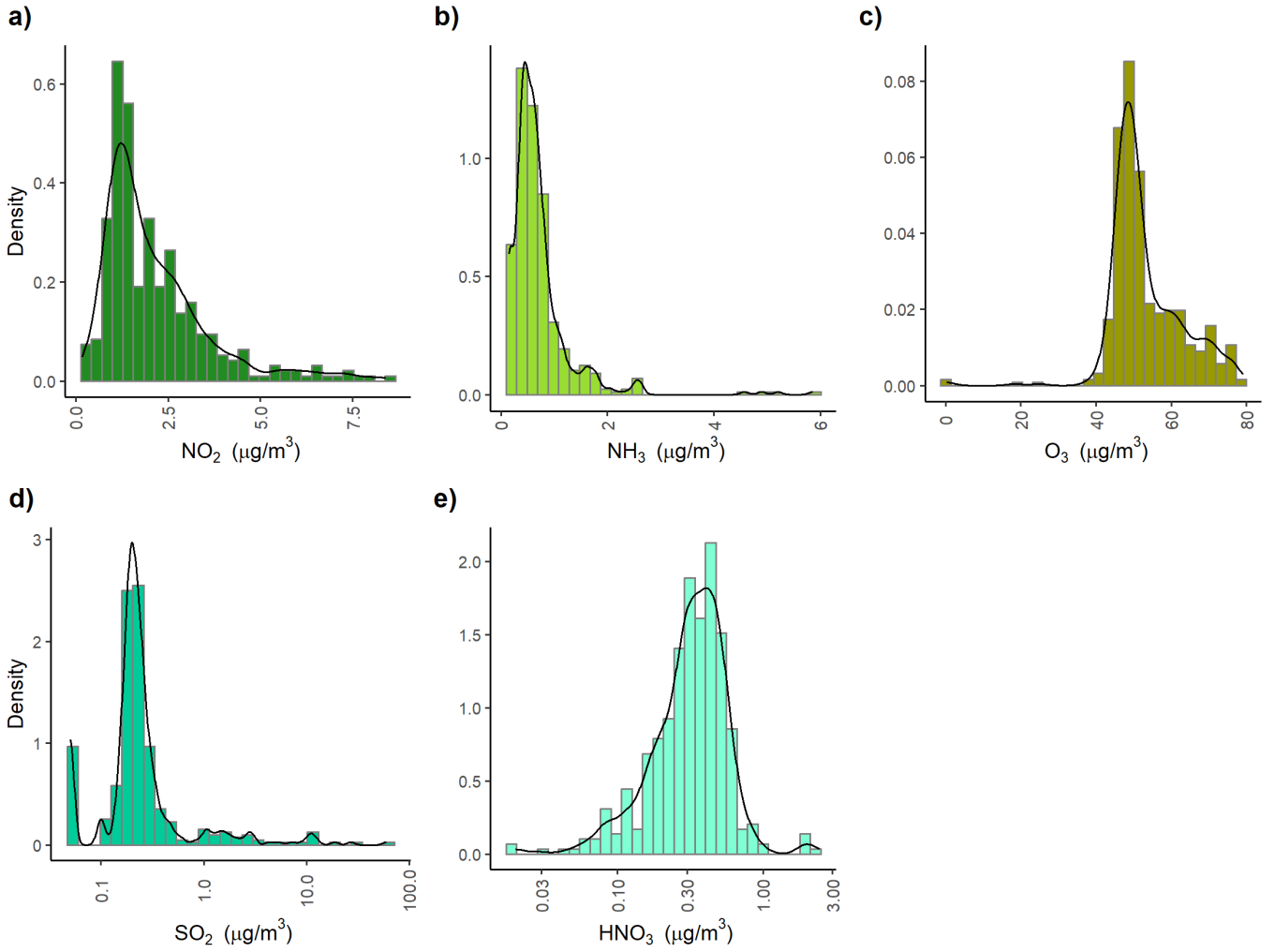

Figure 7.11-1: Histograms of IVL sampler gas concentration observations across all stations and months. Separate gases are shown for each panel: (a) NO_2, (b) NH_3, (c) O_3, (d) SO_2 and (e) HNO_3. Panels (d) and (e) use logarithmic scale on horizontal axis.

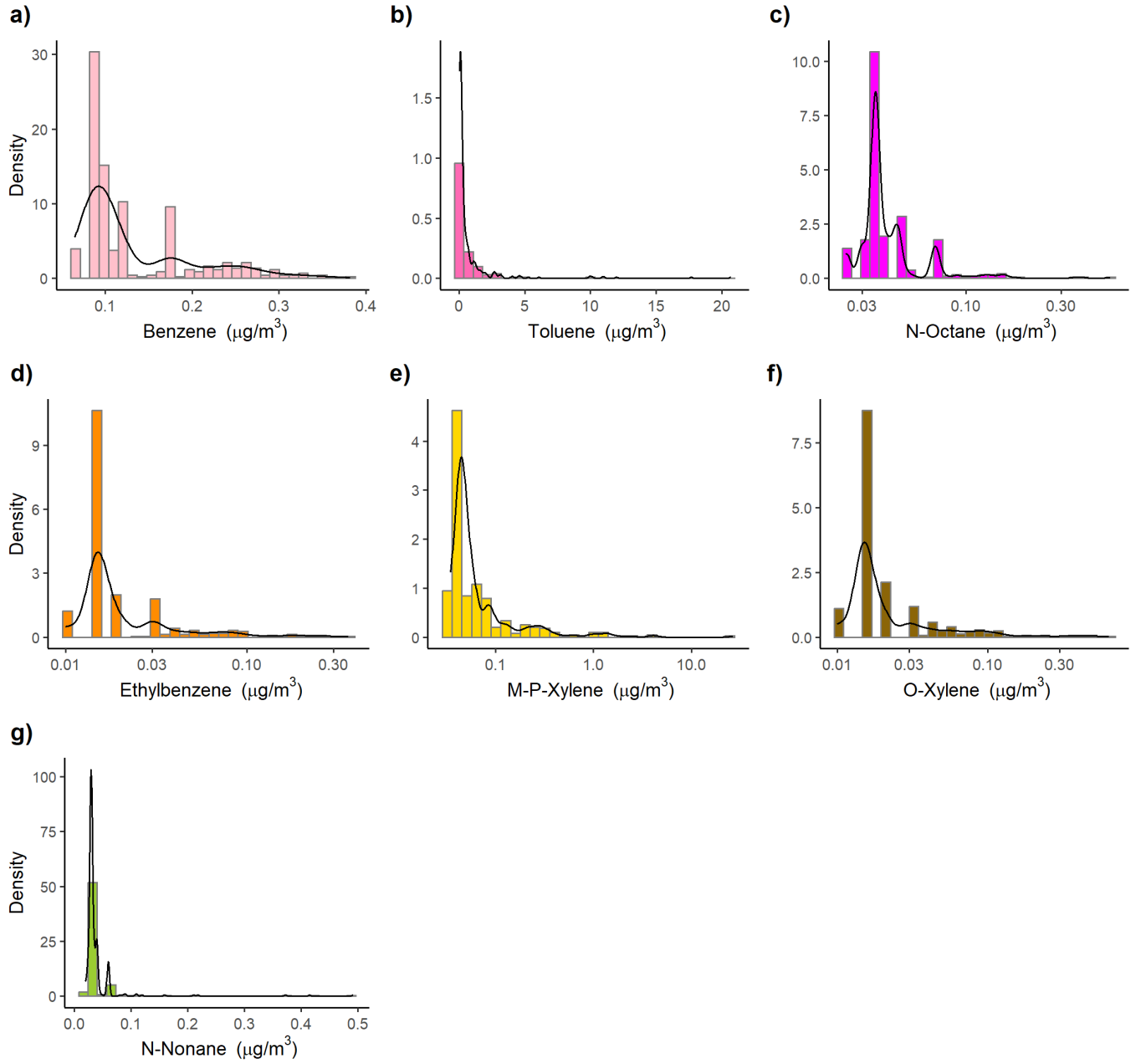

Figure 7.11-2: Histograms of IVL sampler VOC measurements each VOC species. Panels: (a) benzene, (b) toluene, (c) n-octane, (d) ethylbenzene, (e) m-p-xylene, (f) o-xylene, and (g) n-nonane. Panels (c), (d), (e), and (f) use logarithmic scale on horizontal axis.

The histograms give a general indication of the spread of values of monthly average concentration that are observed at Murujuga. They reflect all sources of variability that affect the passive samplers, including differences between locations, seasonal effects, weather variability and other factors. Due to the highly skewed distributions observed for some variables, a logarithmic scale is used on the horizontal axis for the histograms of SO_2 and HNO_3 in panels (d)–(e) of Figure *7.11-1*, and n-octane, ethylbenzene, m-p-xylene and o-xylene in panels (c)–(f) of Figure *7.11-2*.

Table *7.11-1* reports overall summary statistics for the same data. Again these were computed from all the available data for each analyte, pooled over all AQM stations and over all months. Columns in the table show the sample mean, sample variance, sample standard deviation, and the ratio of the standard deviation to the mean.

Table 7.11-1: Overall summary statistics for passive sampler data. Mean, variance, standard deviation (SD) and ratio of standard deviation to mean, for assayed concentration of each analyte in $\mu g/m^3$, using data from all AQM stations and sampling months.

Gas	Mean	Variance	SD	SD/Mean
NO_2	2.234	2.301	1.517	0.679
NH_3	0.707	0.373	0.611	0.863
O_3	52.890	90.253	9.500	0.180
SO_2	0.808	14.394	3.794	4.693
HNO_3	0.359	0.064	0.253	0.703
benzene	0.134	0.005	0.074	0.551
toluene	0.758	4.126	2.031	2.679
n-octane	0.047	0.002	0.041	0.870
ethylbenzene	0.030	0.002	0.041	1.373
m-p xylene	0.198	1.907	1.381	6.963
o-xylene	0.036	0.004	0.067	1.844
n-nonane	0.041	0.002	0.041	1.006

The overall mean concentrations indicate approximately the levels of chronic exposure to these gases and compounds in the Murujuga region overall. The overall estimates of variance and standard deviation are more difficult to interpret, since they include the effects of any systematic differences between locations, seasonal variation, weather variability and other sources of variation.

For SO_2 the standard deviation is 4.7 times the mean. For the other gases (NO_2, NH_3, O_3, HNO_3), the standard–deviation–to–mean ratio was less than 1. Similarly, most VOCs show a standard-deviation-to-mean ratio of less than 1, although this may be due to the large number of values which are below detection limit.

7.11.2.4 Gas species NO_2, NH_3, O_3, SO_2, HNO_3 and spatial location

Figure *7.11-3* shows, in separate panels for each gas species, the individual estimates of atmospheric gas concentration from the IVL passive gas samplers, plotted against the air quality station identifier. Data points are coloured according to the meteorological season, and plotted as different symbols according to the month of exposure, defined as the calendar month which covered the majority of the exposure period.

The ordering of the air quality stations on the horizontal axis is the same in each panel of Figure *7.11-3*: stations are ordered by increasing value of the station's overall average concentration of NO_2. This facilitates comparison between different panels in the figure.

Panel (a) of Figure *7.11-3* shows estimated gas concentrations for NO_2 on the vertical axis against station identifier on the horizontal axis. It indicates substantial systematic differences between

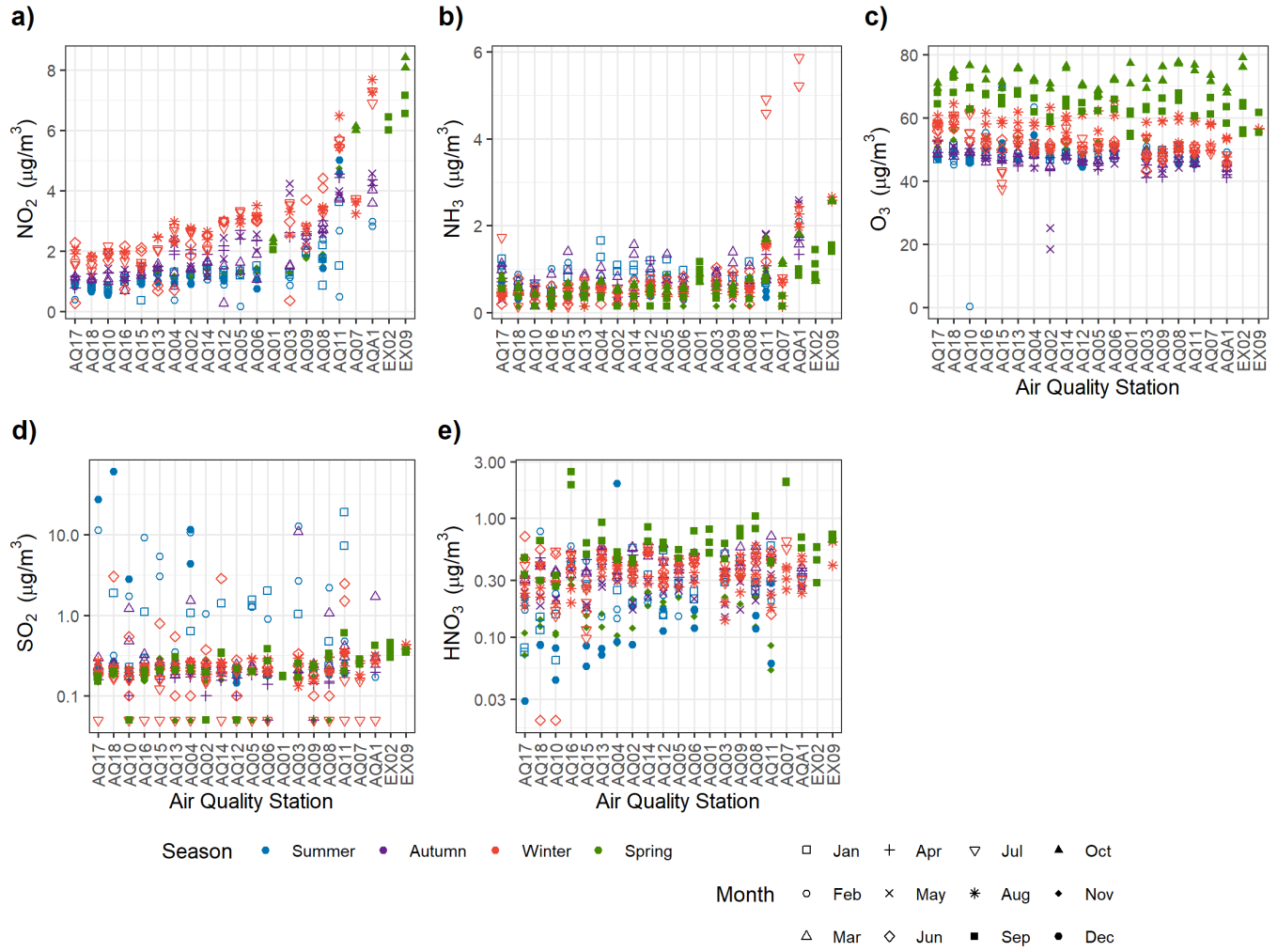

Figure 7.11-3: Plots of IVL sampler gas concentration estimates against air quality station identifier, labelled by season (colour) and month (shape). Separate gases are shown for each panel: (a) NO_2, (b) NH_3, (c) O_3, (d) SO_2 and (e) HNO_3. In each panel, stations are ordered by their overall average concentration of NO_2. Note that panels (d) and (e) use logarithmic scales, due to the highly skewed distributions of the data for these plots.

the NO_2 levels at different sites. One possible explanation is a spatial gradient in exposure to NO_2 related to distance from the industrial areas. Reading off the horizontal axis, we learn that measurements are lowest at stations AQ18 and AQ17 (which are sited on the northernmost islands), and are highest at AQ11 and AQA1 (which are sited close to Dampier port) along with AQ07 and EX09 (which are relatively close to Dampier). The spatial pattern of NO_2 readings is considered further in Section 7.11.6. The substantial systematic differences in NO_2 values also justify our decision to rank the monitoring sites by increasing NO_2 rather than some other criterion.

The pattern of colours in panel (a) also suggests a seasonal pattern in NO_2 concentration, with higher readings for winter months overall, lower readings for summer months, and intermediate values in autumn. Only a few measurements are available for spring, due to difficulties with a batch of NO_2 samplers. Further monitoring is required in order to confirm the apparent seasonal pattern.

Ammonia (NH_3) concentrations are shown in Figure *7.11-3*(b). There is a slight suggestion of a relationship where NH_3 increases with increasing NO_2. There is little evidence of a seasonal pattern. For most stations, observations of NH_3 stay relatively low across all months, with some slightly higher measurements in March and January. Three of the four highest measurements (at AQ07, AQ11 and AQA1) were recorded in winter (July and August). The other station (EX02) only has measurements available for October. The highest value is for AQ11 in winter, which coincides with the highest winter NO_2 readings.

Note that the interpretation of panels (b)–(e) in Figure *7.11-3* is different from the interpretation of panel (a). Any apparent "trend" in panels (b)–(e) would suggest a relationship in which the concentration of one gas increases with increasing NO_2. However the shape of panel (a) is simply a representation of the distribution of values of NO_2 concentration.

Ozone (O_3) concentrations shown in Figure *7.11-3*(c) exhibit relatively small differences between stations, but there is a distinct seasonal pattern, with consistently high measurements for spring samples, lower measurements for summer and autumn samples, with winter samples in between. We note that O_3 gas concentration tends to be higher in sites AQ17 and AQ18, which are the sites located furthest north from Dampier port. A possible explanation is the dispersion of the gases and VOCs involved in O_3 production.

Sulphur dioxide (SO_2) concentrations shown in Figure *7.11-3*(d) exhibit the widest range of values and the most skew distribution, hence a logarithmic scale is used to display these data. Most values range between 0.1 and 1 $\mu g/m^3$. However, particularly over the summer months and March, there are several very high readings. Some of the highest readings were obtained from AQ18 and AQ17, well to the north of the port, but there are also high readings from AQ11 (in the port) and AQ03 and AQ04, well to the west of Dampier port. The SO_2 data also include numerous observations that are below detection limit (BDL); these are visible at the bottom of the plot. Most of these occur in the month of July, but some occur in spring and autumn.

Nitric acid (HNO_3) concentrations shown in Figure *7.11-3*(e) exhibit variation over two orders of magnitude, so again we have used a logarithmic scale to show these data. Measurements are highest for AQ07 and AQ16, though we do not have summer readings for these sites. The sites with the lowest HNO_3 values are AQ10, AQ15, AQ17 and AQ18. All these stations are all either to the west or north of the port. There is also a seasonal pattern, with measurements highest for spring samples, followed by winter samples and then lowest for summer samples.

It should be noted that the air quality values above are analysed with respect to spatial and seasonal trends. Changing levels of industrial activity (e.g. altered production/shipping rates, shutdown/maintenance and other activities may also produce what appear to be seasonal trends in emissions. While source apportionment is not an aim of the current project, it would be prudent to investigate in the third year of studies if the variations found can be more attributed to weather and climate variation or variation in industrial activity.

7.11.2.5 Volatile organic compounds (VOC) and spatial location

Figure *7.11-4* shows plots of the IVL passive sampler estimates of the concentration of each volatile organic compound, plotted against the air quality monitoring station identifier. In each plot, AQM stations are ordered by the overall average concentration of NO_2. Overall, the VOC measurements

include a high proportion of BDL observations. The detection limit varies according to the gas and the observation period. For some statistical analysis and graphics, BDL observations are assigned the value $(\text{Detection Limit})/2$. This can lead to bias in some calculations but can provide valuable insight during exploratory analysis.

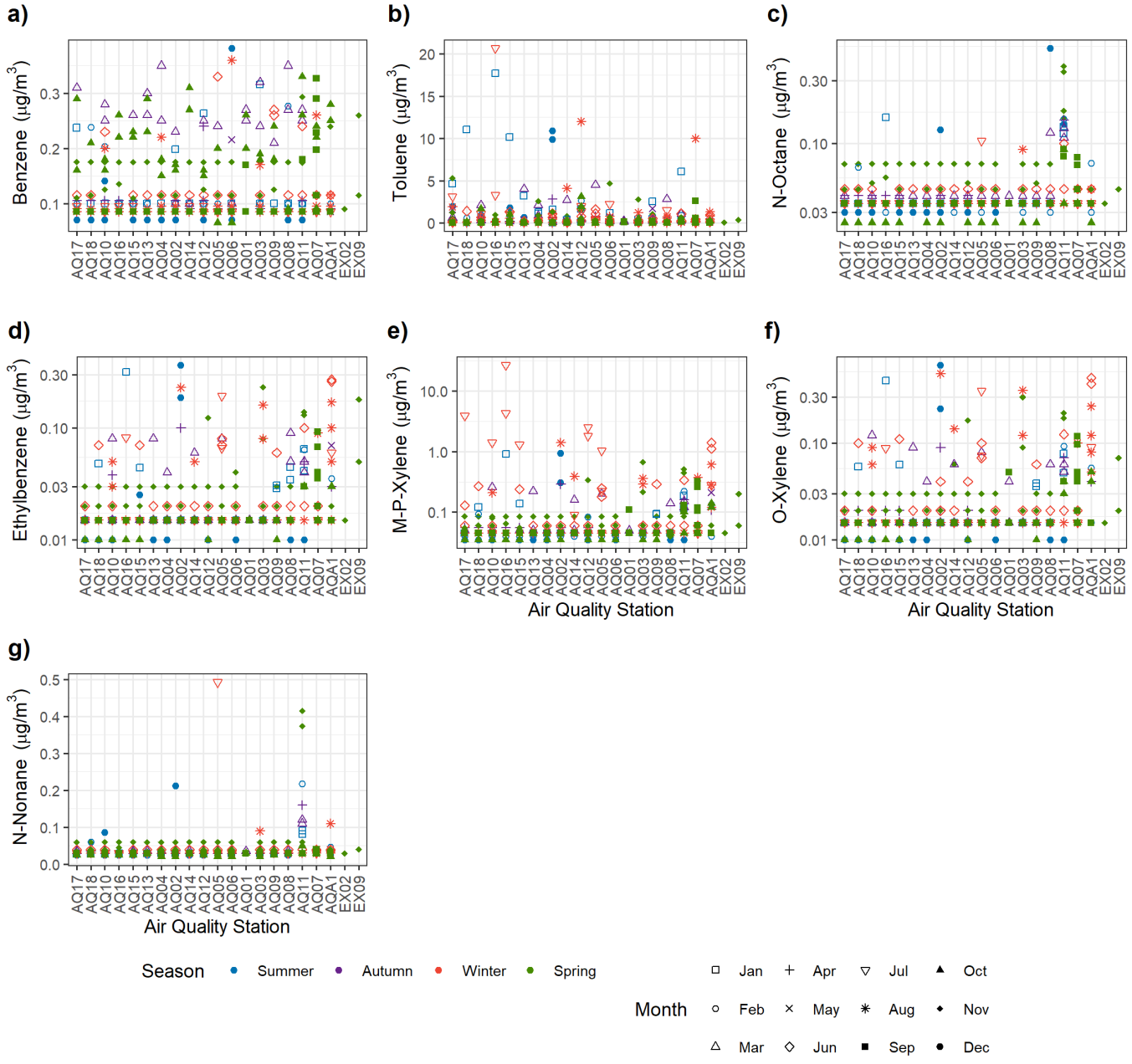

Figure 7.11-4: Plots of IVL sampler VOC measurements against air quality station for each VOC species, labelled by season (colour) and month (shape). AQM stations are ordered by increasing average NO_2 concentration. Panels: (a) benzene, (b) toluene, (c) n-octane, (d) ethylbenzene, (e) m-p-xylene, (f) o-xylene, and (g) n-nonane. Panels (c), (d), (e), and (f) are plotted on logarithmic scales.

Benzene concentration, shown in Figure *7.11-4*(a), exceeds the detection limit most frequently in autumn (March) and spring (September and October), though there are a few higher winter readings (June and August). There is no evidence of systematic differences in benzene concentration across the stations. The highest concentration measured was at station AQ06 for December, but the next highest reading was at the same station in August.

Toluene concentration, Figure *7.11-4*(b), shows a very high number of BDL observations. The above-detection- limit readings vary widely, without a consistent pattern being evident.

N-octane concentration data, Figure *7.11-4*(c), consists mostly of BDL observations. Only nine stations have measurements above the detection limit. Most of these measurements are at AQ11, which has detectable levels for most months. Note there is also a wide range in detection limits for different months.

Ethylbenzene concentration data, Figure *7.11-4*(d), includes readings above the detection limit for many winter observations (June, July and August) and early spring (September), but also some in summer and early autumn (December to March). There is some suggestion of a 'reversal' pattern in which stations furthest from the port show higher readings in summer, while stations closer to the port generally show higher readings in winter.

M-p-xylene, Figure *7.11-4*(e), shows consistently higher measurements for the winter samples, with a few observations above detection limits for spring, summer and autumn months. There is variation between stations across the winter measurements, with the highest readings at AQ16 and usually further away from the port area. The lowest readings (all BDL values) are at various stations including AQ04, AQ06, AQ01 and EX02. (EX02 only has a single observation.)

O-xylene, Figure *7.11-4*(f), shows some similarities to ethylbenzene, with more measurements above the detection limit during the winter months, and some systematic differences between stations. The highest readings are at AQ06 for December and August, with high readings also at AQ16 (January), AQA1 (June), AQ05 (July) and AQ03 (August and December). These coincide with high readings for ethylbenzene.

N-nonane, Figure *7.11-4*(g), has most observations above the detection limits recorded at AQ11, similar to n-octane. There are very few other stations with readings above the detection limit, and no consistency between such readings. There is a very high reading at AQ05 in July, while in the same month the reading at AQ11 is below detection limit.

7.11.3 Correlations between different gases

An important objective for statistical analysis is to determine whether the different gas species exhibit similar patterns in concentration, both across space (gradients across the Murujuga region) and over time (seasonal patterns). Such findings may inform our scientific understanding and the Environmental Quality Criteria.

A definitive answer to this question requires formal statistical modelling and analysis of the monitoring data involving all the observation variables jointly. This approach was outlined in the original MSDCA Plan (Curtin University, 2022). Results of this analysis will be provided in the final report.

As an exploratory step, in this subsection we explore *apparent* correlations between the assayed concentrations of different gas species measured by the passive samplers.

An important caveat is that “correlation is not causation”, especially in this context where there are several lurking variables including spatial location, calendar time, and seasonal weather. Empirical correlations observed between the concentrations of two gas species, without allowing or adjusting for these lurking variables, could be entirely spurious correlations. ‘Joint’ analysis (in which all variables are analysed together) and ‘marginal’ analysis (in which only one or two variables are analysed) can produce contradictory results due to Simpson’s Paradox (Yule, 1903; Simpson, 1951).

Figure *7.11-3* (b) shows, on the vertical axis, the assayed concentration of NH_3 from each passive sampler tube, and on the horizontal axis, the identifier of the AQM at which the tube was deployed. Stations are ranked along the horizontal axis according to their annual average NO_2 value. There is a slight suggestion of an increasing trend, which is to say that NH_3 appears to increase with increasing NO_2. To assess the evidence for this apparent trend, we calculate the average NH_3 and NO_2 concentrations for each station (averaging with weights proportional to the number of days in each sample period), and compute the Spearman rank correlation ρ (rho) between these two sets of values.

The Spearman rank correlation is a standard tool of non-parametric statistics, defined as a measure of agreement between the orderings of the two variables (Corder and Foreman, 2014; Zar, 1972). It is the tool of choice in situations where the data may include extreme values, and where it is not appropriate to assume a linear relationship between the variables. The rank correlation ρ takes a value between -1 and +1. A value of +1 would indicate that, when stations are ranked by increasing value of average NO_2, they are also correctly ranked by increasing value of NH_3: the station with the largest NO_2 also has the largest NH_3, and so on. A value of 1 would indicate that these two rankings are exactly the reverse of one another: the station with the largest NO_2 has the smallest NH_3 and so on. A value of 0 indicates no correspondence between the two rankings.

Tests of statistical significance are also available for the Spearman rank correlation. In keeping with the exploratory approach, we use the simplest of these tests, the classical Spearman two-sample test, which assumes that the observations from different stations are statistically independent of one another. The validity of this assumption is questionable for these data, because all stations are subjected to similar weather and possibly similar gas exposure patterns at any given time. The IVL laboratory analysis adjusts for the recorded temperature at each site. Our judgement is that the classical test can be used for exploratory purposes. A small p-value for this test suggests evidence that the observed correlation was not merely the result of chance, but reflects an association between the two gases. The p-value expresses the strength of evidence rather than the strength of the observed correlation. We used the software implementation in the R function `cor.test` which computes tail probabilities by the Best-Roberts approximation (Zar, 1972; Best and Roberts, 1975; R Development Core Team, 2018).

For the NH_3 and NO_2 annual average concentrations, Figure *7.11-3* (b), the calculated Spearman rank correlation is 0.67 and the p-value of the classical two-sample Spearman test is 0.001. The latter indicates that the evidence for an association is significant.

Table *7.11-2* shows the corresponding results for each pair of gas species. Overall the rank

correlations suggest moderate positive associations between NO_2 versus NH_3 and HNO_3, a moderate positive association between HNO_3 versus NH_3 and O_3, and weak negative associations between SO_2 versus NO_2 and HNO_3. However there are only three statistically significant results, namely for NO_2 versus NH_3, NO_2 versus HNO_3, and HNO_3 versus O_3, where there is strong evidence for moderately strong positive associations.

Table 7.11-2: Correlations between different gas species; annual average data. For each pair of gas species, the table entry shows the Spearman rank correlation ρ between the station average concentrations (averaged over all available IVL passive sampler assay results for each station) of the two gases. Statistically significant correlations are shown in bold type and annotated with one, two or three asterisks representing statistical significance at the 0.05, 0.01 and 0.001 level respectively.

	NO_2	NH_3	HNO_3	O_3	SO_2
NO_2		**0.67****	**0.54****	0.04	-0.42
NH_3	**0.67****		0.28	0.12	0.03
HNO_3	**0.54****	0.28		**0.62****	-0.40
O_3	0.03	0.12	**0.62****		0.03
SO_2	-0.42	0.04	-0.40	0.03	

For comparison, we also computed the Spearman rank correlation between gas concentrations broken down by month and station. For each calendar month and each station for which IVL assay results are available, we compute the average of the assayed concentrations for each gas. With a few exceptions, each such average value is the average of exactly two observations (the results from the duplicate sampler tubes at a given station during a given month). Data may be missing for some combinations of station, month and gas species. The interpretation of correlations and p-values is more tendentious in this case, because the test assumes that observations taken at the same site but during different months are independent.

Table *7.11-3* shows the Spearman rank correlations for the monthly data. According to this analysis, SO_2 has a significant negative correlation with NO_2 and a statistically significant positive correlation with NH_3. Both correlations are relatively weak (absolute value of Spearman's rho is less than 0.4). NO_2 has a statistically significant positive correlation with NH_3 and HNO_3. This latter correlation is expected since HNO_3 can be formed as a byproduct of NO_2. Again both correlations are relatively weak. NH_3 has a statistically significant positive correlation with HNO_3 and a negative correlation with O_3.

Sample correlations in monthly data (Table *7.11-3*) include the effect of seasonal patterns and other variability over time, whereas correlations in annual average data (Table *7.11-2*) are more directly reflective of spatial gradients of gas concentration. The stronger correlations found in the annual average data suggest that spatial location is one of the most influential factors in predicting gas concentration. The weaker correlations found in the monthly data have several possible causes, including the higher variability of the monthly observations.

The above correlations show associations between gases but did not account for variables such as time of year or site location. To address this, RDA analysis, introduced in Section 7.5, was applied. RDA explores the relationship between two sets of variables, here it was used to examine

Table 7.11-3: Correlations between different gas species; monthly data. For each pair of gas species, the table entry shows the Spearman rank correlation ρ between the monthly mean concentrations of the two gases at each station for each month. Values marked with one, two or three asterisks indicate results that are statistically significant at the levels 0.05, 0.01 and 0.001 respectively.

	NO_2	NH_3	HNO_3	O_3	SO_2
NO_2		**0.20***	**0.33***	0.04	-**0.32***
NH_3	**0.20***		**0.29***	-**0.29***	**0.28***
HNO_3	**0.33***	**0.29***		0.02	-0.06
O_3	0.04	-**0.29***	0.0.02		-0.08
SO_2	-**0.32***	**0.28***	-0.06	-0.08	

the relationship between IVL gas measurements and site-specific information, including time of year, site location and elevation. RDA was conducted in `R` using the function `rda` in the `vegan` package. IVL gas measurements were normalised using the `Hellinger` normalisation (Legendre and Gallagher, 2001). Time of year was based on the month of each IVL sample, encoded as an integer from 1 to 12. In order to identify seasonal effects, the analysis employed sine and cosine terms:

$$\text{Month sin} = \sin(\frac{2\pi(\text{month})}{12})$$

$$\text{Month cos} = \cos(\frac{2\pi(\text{month})}{12})$$

The site location was defined by northing, easting, and elevation (measured in metres) for each AQM. These variables were standardised using the `range` method to a value between zero and one, using the function `decostand` in the `vegan` package in `R`.

Figure *7.11-5* shows the RDA biplot displaying the relationship between the IVL gas measurements and time of year (month sin and cos). This RDA explains 38.6% of the total variation explained by the first two principal components.

NO_2 is negatively correlated with SO_2. Since NH_3 is approximately 90 degrees from NO_2 and SO_2, this indicates no correlation. There is some level of correlation between NH_3 and HNO_3, because there is approximately 30 degree angle between these two gases, although the correlation is not particularly strong. NH_3 is positively associated with month sin, while SO_2 is positively correlated with month cos, but neither are strongly correlated.

There were correlations between gas measurements, location (northing and easting) and elevation. However, when combined with time of year, these correlations were much weaker.

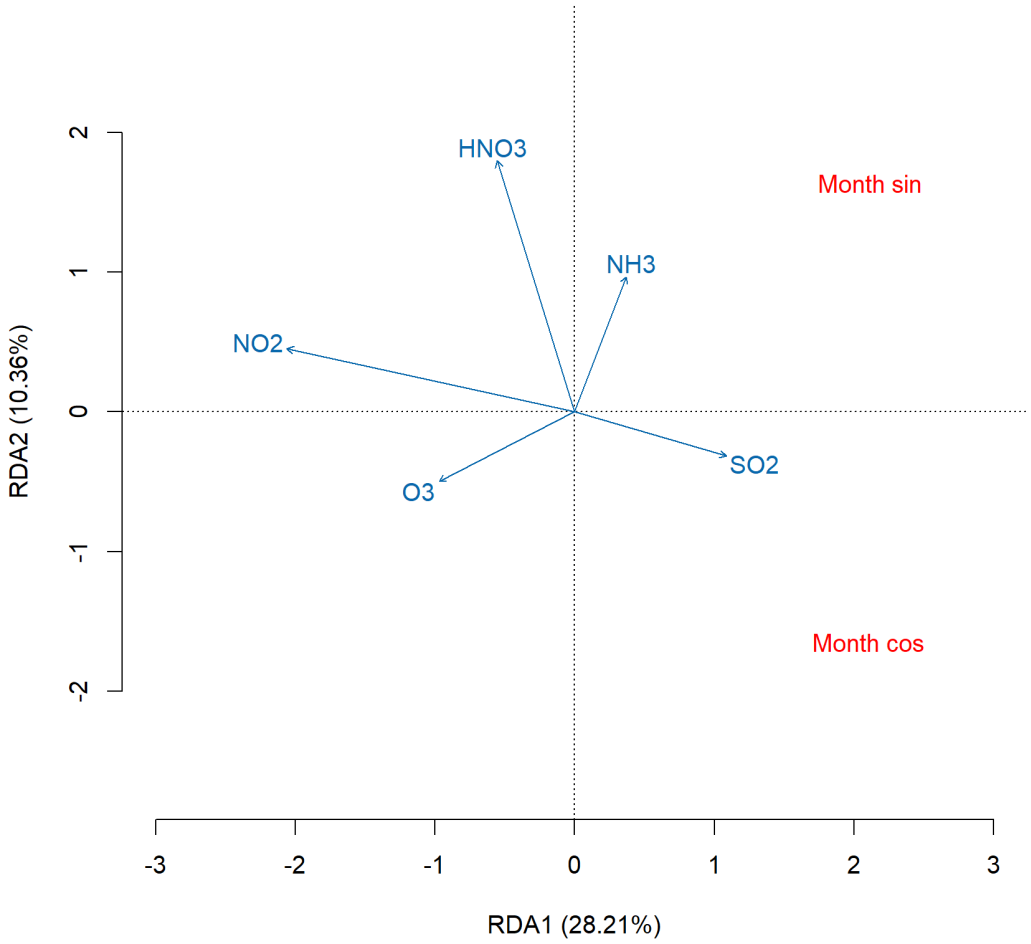

Figure 7.11-5: RDA biplot showing the relationship between gas measurements (NO_2, SO_2, NH_3, HNO_3, O_3) and month sin and cos.

7.11.4 Residual variability

Passive sampler tubes are deployed in duplicate pairs: two identical sampler tubes for each analyte are deployed within the same housing at each AQM for each month. These duplicate observations are valuable because any discrepancies between the results obtained for these identical pairs of sampler tubes are attributable to 'residual' variability in the measurement technique itself.

Residual variability is a very important consideration in the statistical analysis. An estimate of residual variance is often needed to determine whether a result is statistically significant. In order to distinguish "signal" from "noise", one must know how large the "noise" is.

The actual causes of residual variability are not important for the purposes of this investigation. Causes may include intrinsic variability of laboratory technique, variability in the production of the sampler tubes, and variability associated with deployment in the field, such as very short scale differences in exposure within the sampler housing. We treat all these sources as 'residual' variation in our analysis.

In this section we estimate the amount of residual variability, and also investigate whether the residual variance depends on the mean concentration of the analyte. Information about this "variance-mean relationship" is important background for choosing an appropriate statistical model for the data distribution, which supports the formal statistical modelling and analysis that is planned for the final stage of the research.

We apply the following principle. If X_1 and X_2 are duplicate measurements of the same quantity, assumed to be independent samples from the same probability distribution, then their average

$$\overline{X} = \frac{1}{2}(X_1 + X_2)$$

is an unbiased estimate of the mean μ of the distribution,

$$S^2 = \frac{1}{2}(X_1 - X_2)^2$$

is an unbiased estimate of the variance σ^2 of the distribution. The standard deviation σ of the distribution can be estimated by

$$S = \sqrt{S^2} = \frac{1}{\sqrt{2}}\,|X_1 - X_2|$$

although this is a biased estimator of σ.

For each analyte, our overall estimate of residual variance is computed by first calculating the individual estimates S^2 of the residual variance from each pair of duplicate measurements, then computing the average of these variance estimates, obtaining the "pooled" estimate of residual variance. This is the primary goal of analysis.

Unlike the residual variance estimates, the sample means $\overline{X}$ obtained from duplicate samples are likely to vary widely between different sites if there is a spatial pattern or gradient of concentration of the analyte, and are likely to vary between different months because of seasonal effects.

Table 7.11-4: Summary statistics for duplicate measurements from passive samplers. Overall mean, pooled estimate of residual variance, and ratio of residual standard deviation to overall mean, for each analyte. Mean measures are in $\mu g/m^3$.

Gas	Mean of Means	Residual Variance	Residual SD/Mean	Residual/Total Variance
NO_2	2.155	0.129	0.166	6%
NH_3	0.703	0.023	0.215	6%
O_3	53.461	3.544	0.035	4%
SO_2	0.825	13.989	4.535	97%
HNO_3	0.365	0.017	0.360	27%
benzene	0.134	0.002	0.330	36%
toluene	0.583	1.541	2.131	37%
n-octane	0.045	0.000	0.232	6%
ethylbenzene	0.029	0.001	0.814	33%
m-p xylene	0.202	1.595	6.249	84%
o-xylene	0.035	0.002	1.267	45%
n-nonane	0.040	0.001	0.721	50%

Table *7.11-4* reports summary statistics for the duplicate pairs of observations. It shows the mean of the means of duplicate pairs, the mean of the residual variance estimates S^2, the ratio of the residual standard deviation to the overall mean, and the ratio of residual variance to total variance.

The column of 'means of means' in Table *7.11-4* is almost identical to the column of means in Table *7.11-1* and has the same interpretation.

The column labelled 'residual variance' in Table *7.11-4* provides estimates of the intrinsic variability of the measurement technique. This is the primary goal of analysis.

The next column reports the ratio of estimated residual standard deviation to the overall mean.

The last column in Table *7.11-4* is the fraction of variance explained by residual variability; this is computed as the ratio of the residual variance in Table *7.11-4* to the overall variance in Table *7.11-1*. Residual variability accounts for only 6% of the variation in NO_2 measurements (0.129/2.301 = 0.056) but 97% of variation in SO_2 measurements (13.989/14.394=0.972). The fraction of variance explained is effectively the "noise-to-signal ratio" for a single measurement.

Various additional factors must be considered in the interpretation of these results. Previous analysis in Curtin University (2022) showed that SO_2 measurements did not conform to a normal distribution and were better described as following a heavy tailed, right-skewed distribution. Some of the VOC measurements contain high numbers of BDL values, and the treatment of BDL values may have introduced artefacts.

The key to correct statistical analysis and modelling of these data is an understanding of the variance-mean relationship. In order to investigate this, we plot the individual estimates S^2 of variance against the corresponding individual estimates $\overline{X}$ of the mean. Figure *7.11-6* shows this scatterplot for each of the gas species NO_2, NH_3, O_3 and HNO_3. There is no evidence that the

variance depends on the mean, suggesting that the foregoing analysis was appropriate.

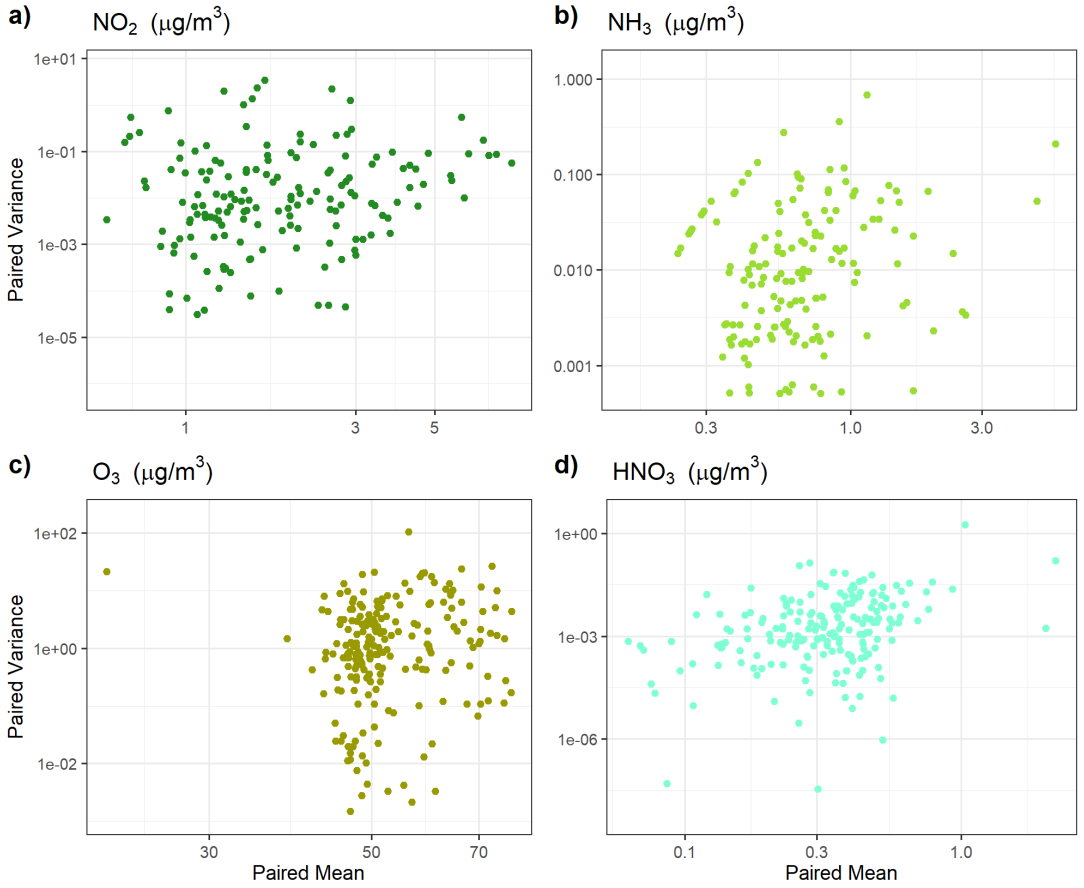

Figure 7.11-6: Paired variance versus paired mean for gas species (a) NO_2, (b) NH_3, (c) O_3, and (d) HNO_3. Where for example 1e-06 means $10^{-}6$, or 0.000001.

For SO_2, the top two panels of Figure *7.11-7* are scatterplots of residual variance estimates against paired means, with both variables shown on a logarithmic scale. Colours represent months in the top left plot, and AQM stations in the top right plot. Residual variance estimates are plotted against calendar month in the bottom left panel, and against AQM station identifier in the bottom right panel. The top row strongly suggests an increasing relationship between variance and mean.

Further plots of residual variance versus station and month are given in Appendix *G*.4 .

For the volatile organic compounds, Figures *7.11-8* and *7.11-9* show paired residual variance estimates versus paired means. Logarithmic axis scales have been used throughout. Some plots lack adequate numbers of observations above the detection limit.

Toluene (Figure *7.11-8*(b)) ethyl benzene (Figure *7.11-8*(d)) m-p-xylene (Figure *7.11-9*(a)) o-xylene (Figure *7.11-9*(b)) and n-nonane (Figure *7.11-9*(c)) suggest an increasing relation between variance and mean. There are numerous caveats including the small sample size, the wide range of reported values, the high frequency of BDL observations, and the fact that all VOC species are assayed from the same sampler tube.

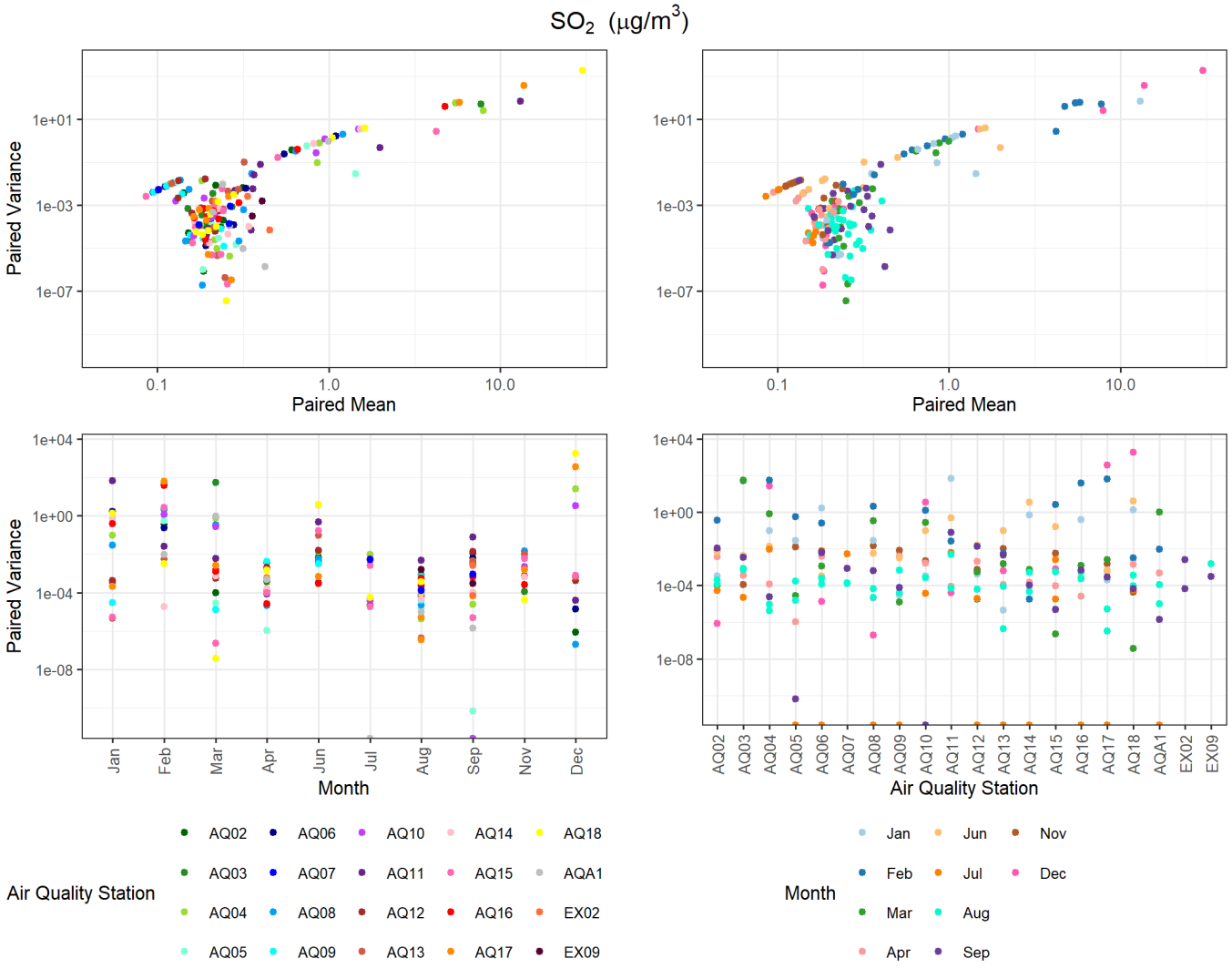

Figure 7.11-7: SO_2 paired residual variance estimates against paired means (top) and paired residual variance by station and month (bottom). Right panels show stations by colour, while left panels show months by colour. Logarithmic scale is used for both mean and variance.

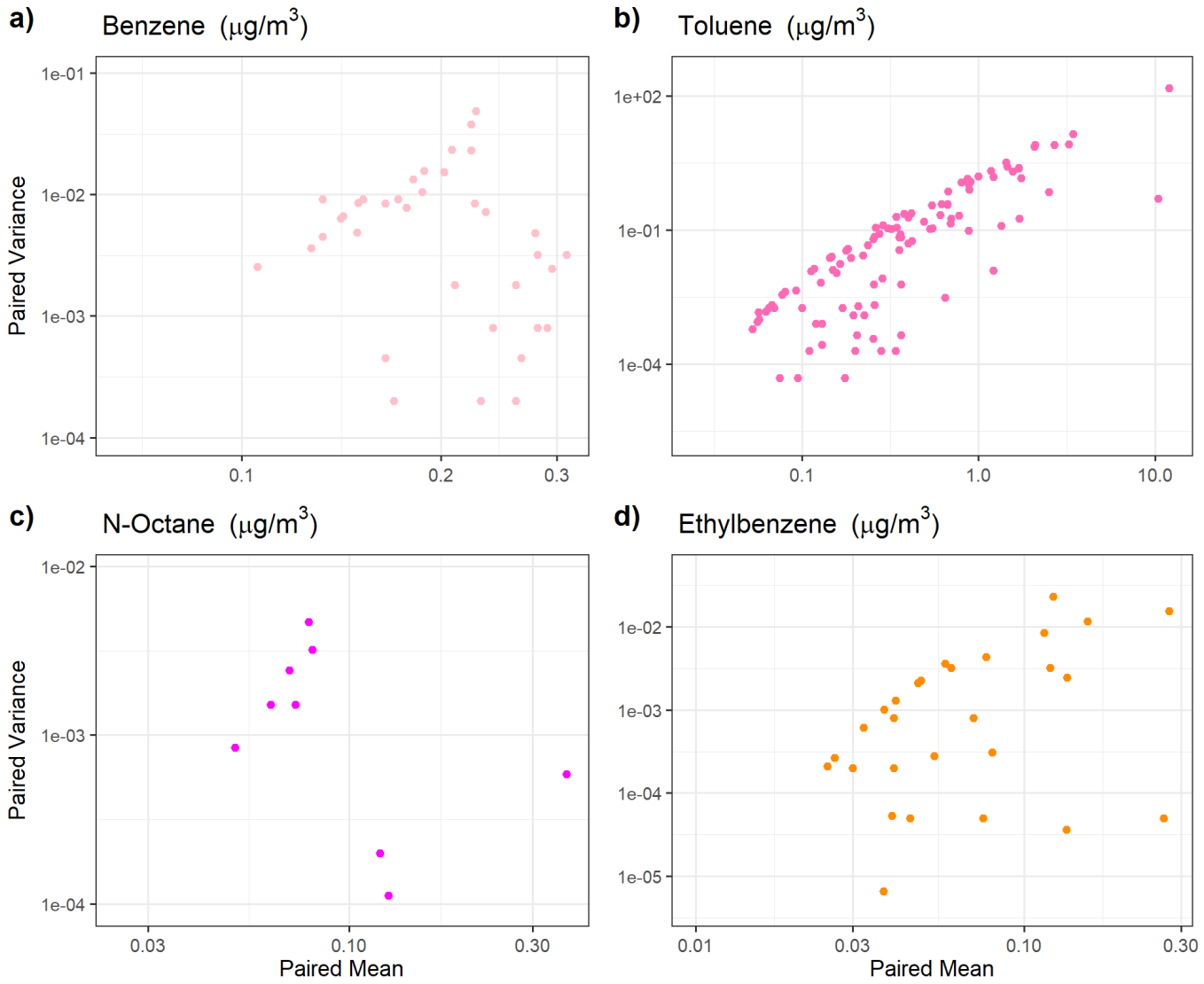

Figure 7.11-8: Pairwise variance by pairwise mean for VOC species (a) benzene, (b) toluene, (c) n-octane, and (d) ethylbenzene.

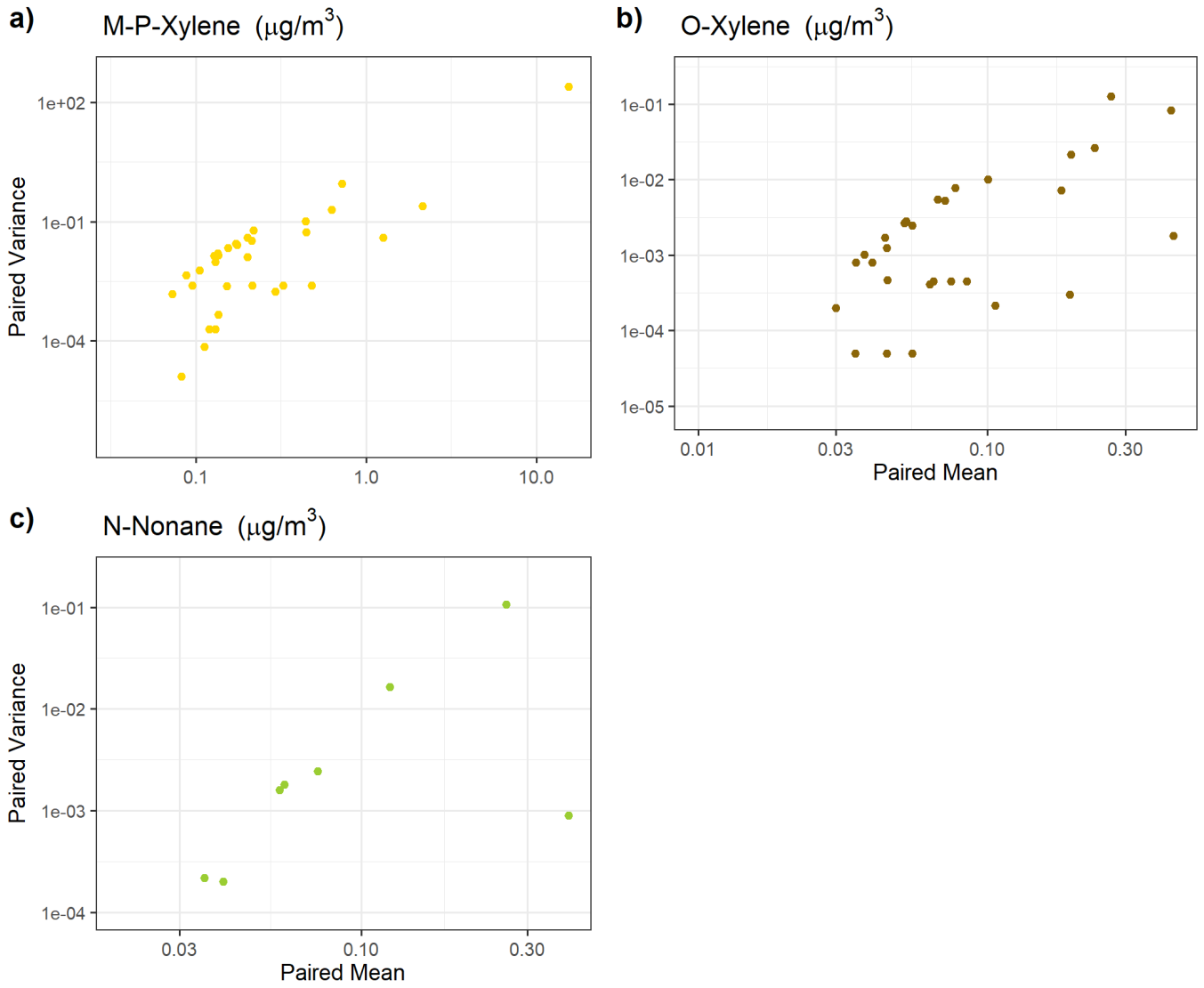

Figure 7.11-9: Pairwise variance by pairwise mean for VOC species (a) m-p-xylene, (b) o-xylene, and (c) n-nonane.

7.11.5 Short-scale variability

Another important consideration in statistical analysis of spatial data is the magnitude of short-scale variability. In the context of environmental monitoring, discrepancies between observations at sites which are very close together could arise from micro-environmental conditions such as localised airflow patterns and physical obstacles. Again the specific causes of short-scale variability are not important for the statistical analysis, but the magnitude of variability has a large influence on assessments of statistical significance. The MSDCA Plan (Curtin University, 2022) specified that two air quality monitoring stations should be placed close together, in order to assess the magnitude of short-scale variability.

Two monitoring stations, AQ07 and AQ08, were established approximately 25 metres apart, on a small plateau, roughly equidistant from the airport and the main industrial and port facilities.

Passive samplers were deployed at AQ08 from November 2022 onward, and at AQ07 from June 2023 onward. At the time of preparation of this report, IVL assay reports for the gas species were available for the sampling months up to and including October 2023; however, not all results were available for every sampling period for each gas. The assay results for VOC samplers were available for months up until December 2023, but these data included a large number of below detection limit (BDL) values. The data analysis reported below is based on all data for which corresponding observations are available for both AQ07 and AQ08. The maximum sample size is only 5 months, and the results in this subsection are very preliminary.

7.11.5.1 Gas species NO_2, NH_3, O_3, SO_2 and HNO_3

Figures *7.11-10* and *7.11-11* compare the passive sampler measurements for the two sites. Boxplots in Figure *7.11-10* summarise the marginal distributions of individual sampler results for each station. The distributions are generally similar between the two stations. In panel (a), there is a relatively small overlap between the two filled rectangles, which represent the inter-quartile ranges of NO_2 concentration values for the two sites. This may be partly attributable to the small sample sizes. In panel (e) the interquartile ranges for HNO_3 also have a relatively small overlap, and several outliers are present. Figure *7.11-11* shows scatterplots of the sample mean gas concentrations for each sampling period for station AQ07 versus station AQ08. The diagonal line corresponds to perfect agreement between the two stations. All gases show a reasonable agreement between observations at the two stations, given the small sample sizes. Figure *7.11-11*(e) for HNO_3 contains outliers.

The main objective of our exploratory analysis is to determine the magnitude of short-range variability. If X_1, X_2 denote the duplicate passive sampler results for a particular gas for a particular month at AQ07, and Y_1, Y_2 are the results for the same gas and month at AQ08, write $\overline{X} = (X_1 + X_2)/2$ and $\overline{Y} = (Y_1 + Y_2)/2$ for the sample means for that month. Then $(\overline{X} - \overline{Y})^2$ is an unbiased estimator of $\tau^2 + \sigma^2$ where σ^2 is the residual variance for each observation and τ^2 is the expected squared difference between the true concentrations at sites AQ07 and AQ08. Using the previously-described estimates of residual variance σ^2, we may then calculate estimates of the short-scale mean square τ^2 by subtraction.

Table *7.11-5* shows the results of this calculation. The estimate of $\sigma^2 + \tau^2$ is calculated as the average of the values $(\overline{X} - \overline{Y})^2$ over all months where data are available for both stations. The

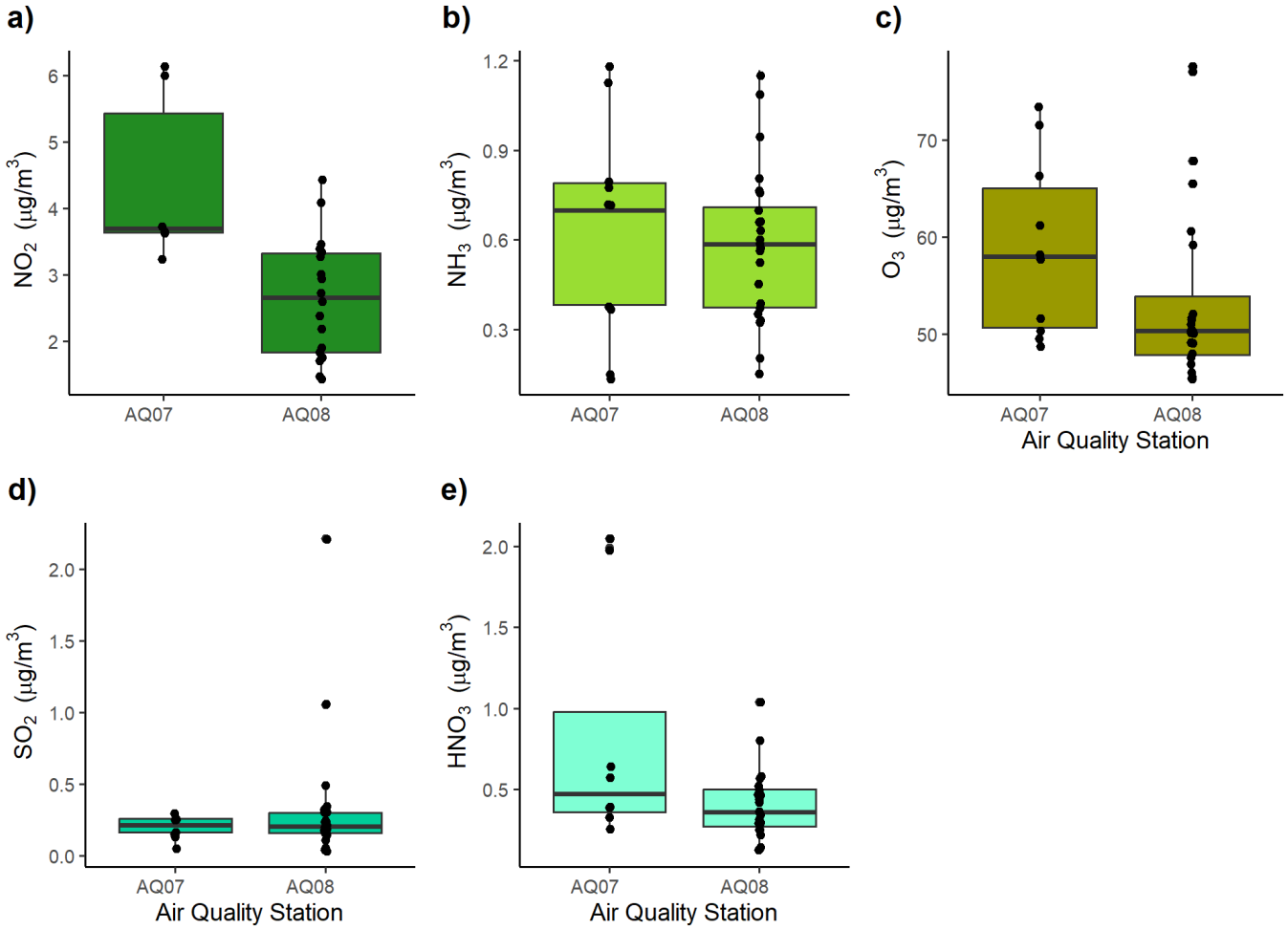

Figure 7.11-10: Boxplots of passive sampler gas concentration measurements for stations AQ07 and AQ08 for gas species (a) NO_2, (b) NH_3, (c) O_3, (d) SO_2, and (e) HNO_3.

number n of months for which data were available is indicated. The estimate of τ^2 is then obtained by subtracting the estimate of σ^2 given in Table *7.11-4*. Some of the estimates are negative and have been recorded as NA. Given the small sample size, negative estimates are not unexpected, and the results in Table *7.11-5* are only provisional or 'pilot' estimates of short-scale variability.

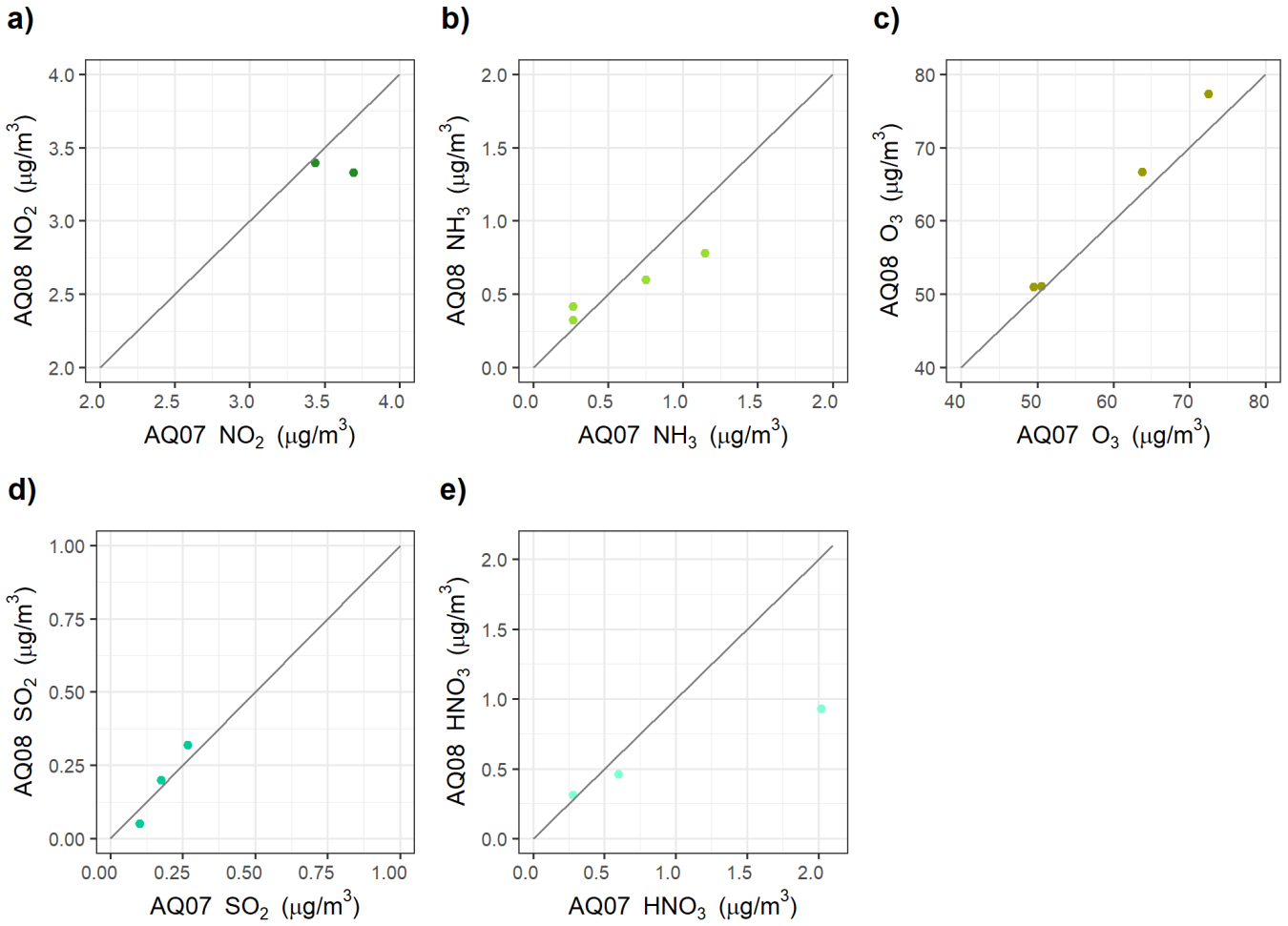

Figure 7.11-11: Scatterplots of monthly sample mean gas concentration for station AQ07 versus station AQ08 for gas species (a) NO_2, (b) NH_3, (c) O_3, (d) SO_2, and HNO_3. Plots show the sample mean gas concentration for each sample period for each station.

Table 7.11-5: Calculation of raw estimates of the short-range mean square difference τ^2 between true values of gas concentrations at the sites AQ07 and AQ08. Columns give the number n of months for which paired data were available, the estimate of $\sigma^2 + \tau^2$ described in the text, and the resulting estimate of τ^2. Negative estimates are recorded as NA.

Gas	n	$\sigma^2 + \tau^2$	τ^2
NO_2	2	0.066	NA
NH_3	4	0.041	0.018
O_3	4	8.890	5.346
SO_2	3	0.002	NA
HNO_3	3	0.406	0.389

7.11.5.2 Volatile organic compounds

Figures *7.11-12* and *7.11-13* compare VOC concentrations at the two sites. Figure *7.11-12* presents boxplots of the VOC assay results for the two sites. Many results for AQ08 are BDL values, resulting in very narrow interquartile ranges (filled rectangles) in the boxplots. Figure *7.11-13* presents scatterplots of the monthly sample mean values at the two sites. The abundance of BDL values for AQ08 is reflected in the almost horizontal line of data points in many of the scatterplots. Toluene, Figure *7.11-12*(b) is the only VOC showing a reasonable number of data values above the detection limit for both stations; it shows reasonable agreement between the stations, although there are still many BDL observations for AQ08. It is unclear why there should be a higher frequency of BDL results for AQ08 than for AQ07, given that the sample tubes for the two stations were deployed together and retrieved together. The number of BDL observations hampers the analysis of short-scale variability for the VOC data.

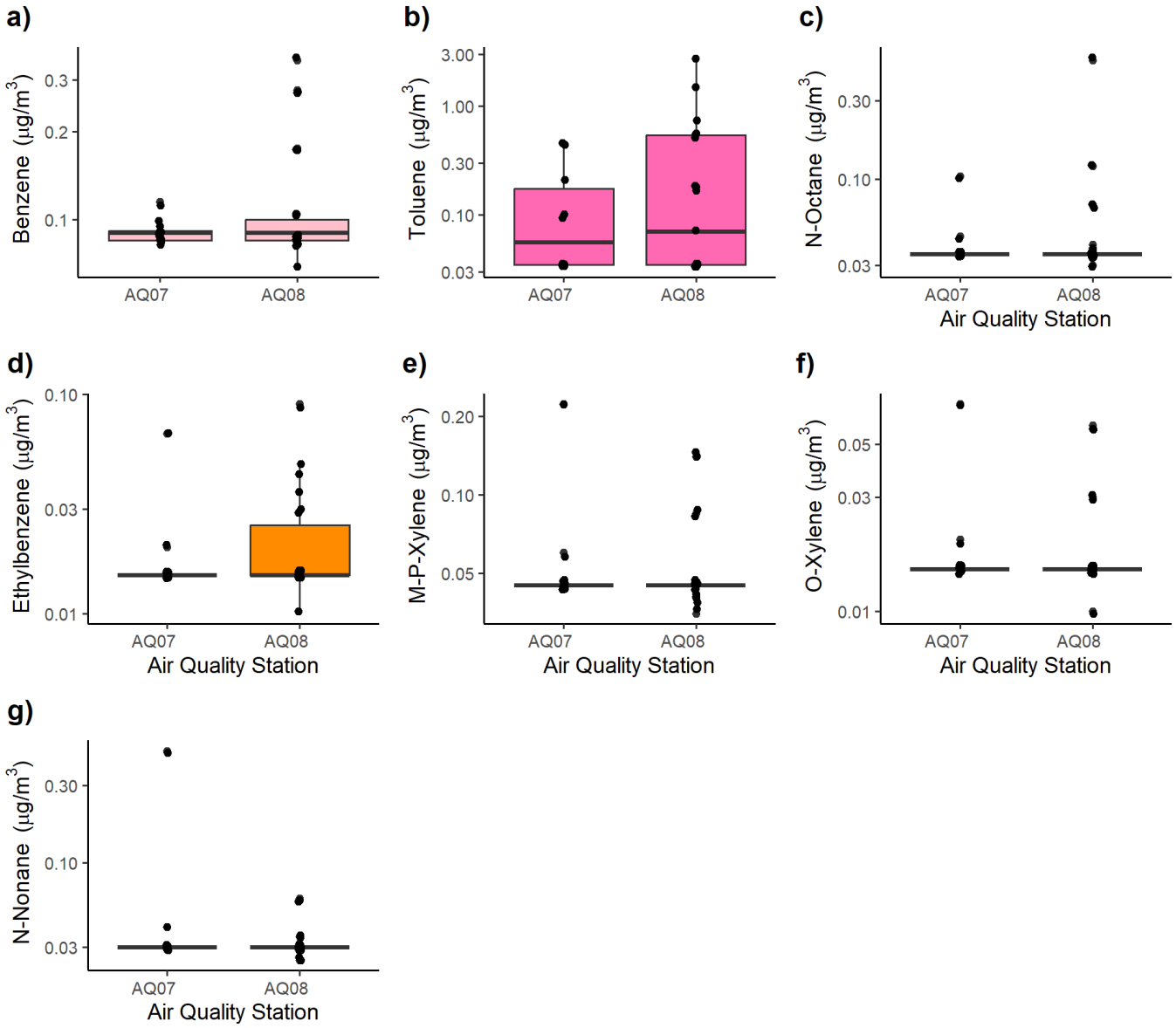

Figure 7.11-12: Boxplots comparing VOC measurements between stations AQ07 and AQ08 using a logarithmic scale for VOC species (a) benzene, (b) toluene, (c) n-octane, (d) ethylbenzene, (a) m-p-xylene, (b) o-xylene, and (c) n-nonane.

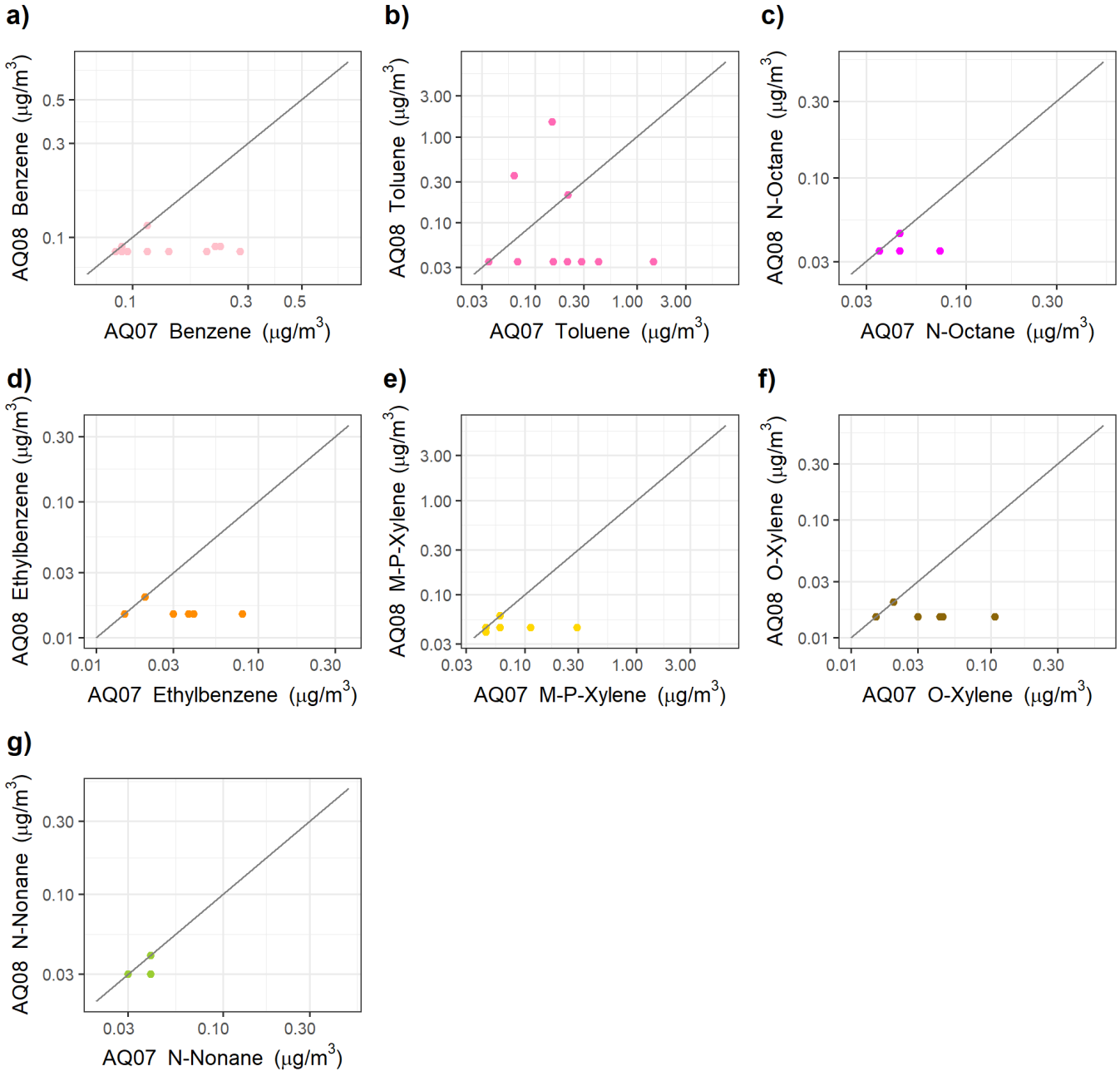

Figure 7.11-13: Scatterplot of sample mean VOC concentration for station AQ07 versus station AQ08 using a logarithmic scale for VOC species (a) benzene, (b) toluene, (c) n-octane, (d) ethylbenzene, (a) m-p-xylene, (b) o-xylene, and (c) n-nonane. Plots show the sample mean gas concentration for each sample period.

7.11.6 Spatial pattern of gas concentration

A key question is whether there is a persistent gradient in the environmental concentration of pollutant gases across the Murujuga region. The passive sampler data provide monthly estimates of gas concentration at 21 locations across Murujuga. For exploratory purposes, the passive sampler data for each month were spatially smoothed to produce colour images of the spatially-varying average gas concentration for each month.

Smoothing was performed using the Nadaraya-Watson technique described in Appendix *F*.1 and demonstrated in Section 7.4. The smoothed value at each pixel is a weighted average of the passive sampler observations at different AQMs, where the weights depend on the distance from the query pixel to the AQM location.

Figures *7.11-14* to *7.11-19* show the spatially smoothed passive sampler estimates of concentration for each gas species. For each figure, the different panels (associated with different months) are depicted using a common colour map, shown at the right of each panel. This assists the reader in visualising seasonal variation.

Since the concentration values can vary by several orders of magnitude, a nonlinear colour map has been used in these figures, in order to preserve important detail. The colour map is based on the Probability Integral Transformation (Appendix *F*.1.4.3), that is, colours effectively represent percentiles of the smoothed values. Similar map techniques are commonly used for climate forecasting. The colour map is annotated with seven tick marks which divide the distribution of pixel values into six bands containing equal numbers of values.

Figure *7.11-14* shows spatially smoothed monthly average NO_2 concentration for each month from November 2022 to August 2023. Overall differences in colour between panels indicate that the NO_2 level varies substantially over time, being lowest in January and February and highest in June, July and August. This is consistent with the evidence for seasonal variation seen in Figure *7.11-3*(a).

Closer examination of Figure *7.11-14* suggests that NO_2 concentrations are consistently higher close to the Dampier port area. This question can be assessed using the concordance technique described in Appendix *F*.1.6. Panel (a) of Figure *7.11-15* shows the consensus rank image. Values close to 1 are seen in the area near the Dampier port. These values indicate that, at any given time, this area consistently experienced the highest levels of NO_2 concentration across the Murujuga region. Values close to 0 are seen in the far west and north of the Murujuga region, and indicate that these localities consistently experienced the lowest levels of NO_2. Panel (b) of Figure *7.11-15* shows the disagreement (standard deviation of ranks) image. Low values of disagreement indicate that the spatial pattern of relative concentrations is quite consistent over different months.

Figure *7.11-16* shows the spatially smoothed average concentration of NH_3 for each month from November 2022 to October 2023. The first two months have lower overall levels of NH_3 than the subsequent months.

The panels for April 2023 to October 2023 exhibit a consistent spatial pattern in which the NH_3 levels are highest near the Dampier port area. The panel for November 2022 follows a similar spatial pattern at a lower concentration level. This common spatial pattern is similar to the pattern observed for NO_2.

However, a contrasting spatial pattern is observed in the panels for December 2022 to February

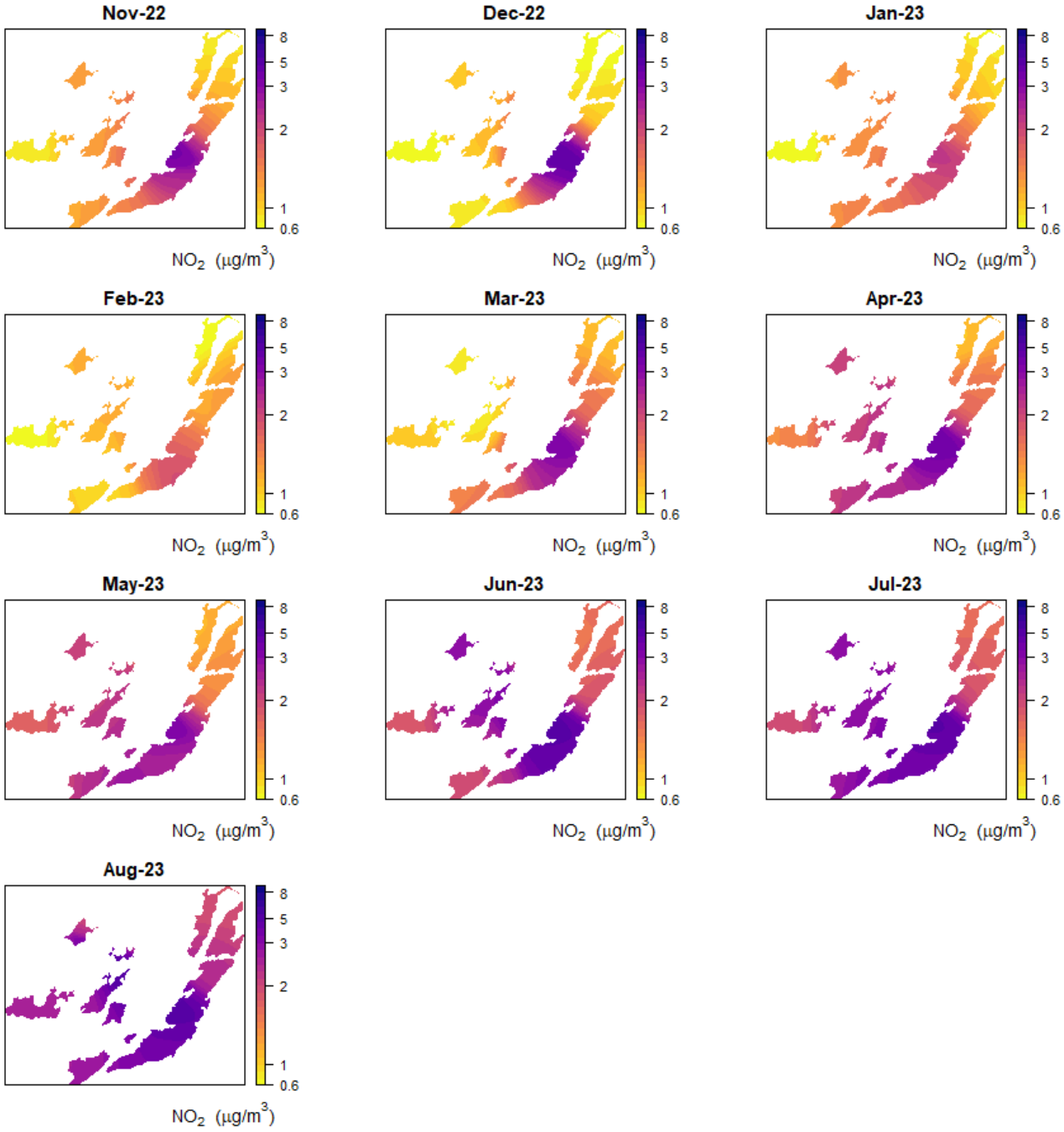

Figure 7.11-14: Spatially smoothed monthly average concentration of NO_2 by sampling period. Common colour map based on percentiles.

2023, in which NH_3 concentrations are highest in the north or west corners of the region.

Appendix *G*.4.1 presents consensus rank images for NH_3 which support the assertions above.

The similarity between the spatial patterns of NH_3 and NO_2 concentration, observed in the data for 8 out of 12 months, may account for the positive correlation between NO_2 and NH_3 concentrations found in Tables *7.11-2* and *7.11-3* of Section 7.11.3.

a) b)

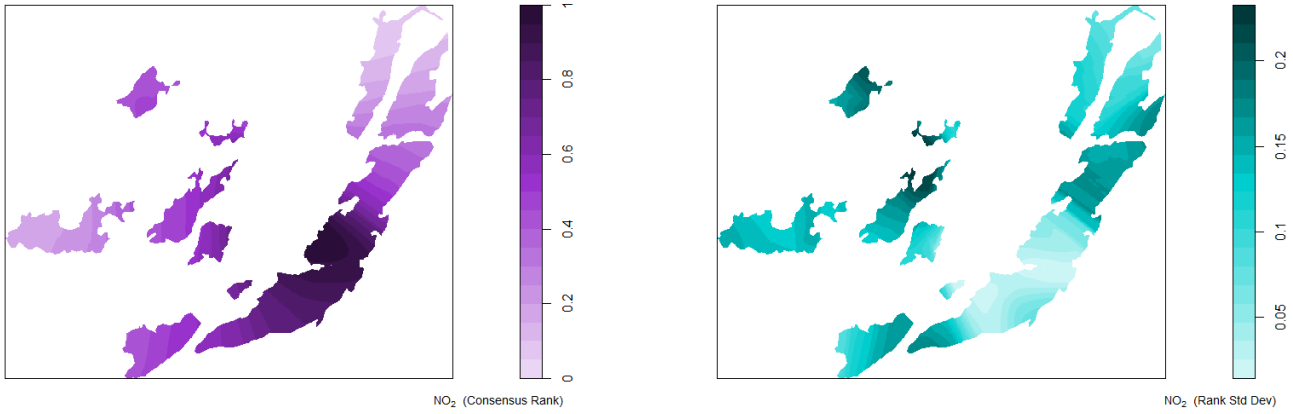

Figure 7.11-15: Assessment of concordance between spatial patterns of NO_2 concentration in different months, estimated from spatially smoothed passive sampler data. (a) consensus ranks; (b) disagreement (standard deviation).

Figure *7.11-17* shows spatially smoothed monthly average O_3 concentration for November 2022 to October 2023. The overall level of O_3 concentration appears to rise progressively from December 2022 to October 2023. These images suggest a moderately consistent spatial pattern in which O_3 concentration is highest at the northern part of Murujuga — in contrast to the spatial pattern observed for NO_2 and NH_3. Appendix *G*.4.1 presents consensus rank images which support this assertion.

Figure *7.11-18* shows spatially smoothed monthly average SO_2 concentration for November 2022 to September 2023. Data for May 2023 are unavailable. There is little consistency in the spatial pattern of SO_2 concentration between different periods. Overall levels of SO_2 also fluctuate quite substantially. The passive sampler data for SO_2 have a wide range of values, and include some extreme values. Some of the highest levels were recorded at AQ18 and AQ17 in December 2023, although there were also large discrepancies between the values obtained for the duplicate samplers. Other high values have been recorded at these same sites in other months, suggesting that the observations may reflect actual conditions that occasionally lead to high SO_2 levels in the northern islands.

Finally, Figure *7.11-19* shows spatially smoothed monthly average HNO_3 concentration for November 2022 to September 2023. Overall levels of HNO_3 vary widely between different months, with relatively low levels in November and December 2022, and high levels in March and September 2023. No consistent spatial pattern is observed. For several months, HNO_3 concentration was approximately constant over most of the region (November 2022, December 222, May 2023 and September 2023).

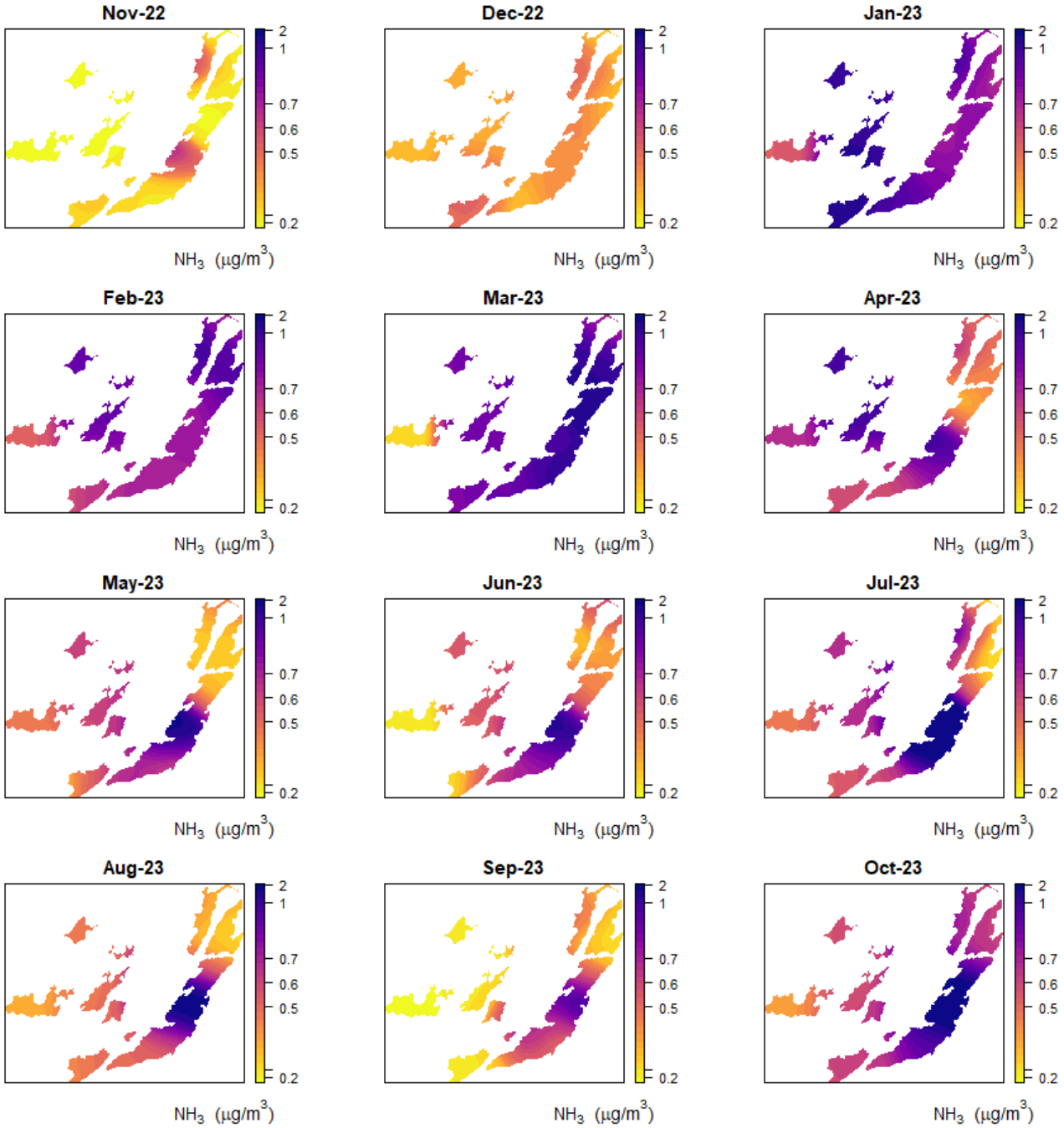

Figure 7.11-16: Spatially smoothed monthly average concentration of NH_3 by sampling period. Common colour map based on percentiles.

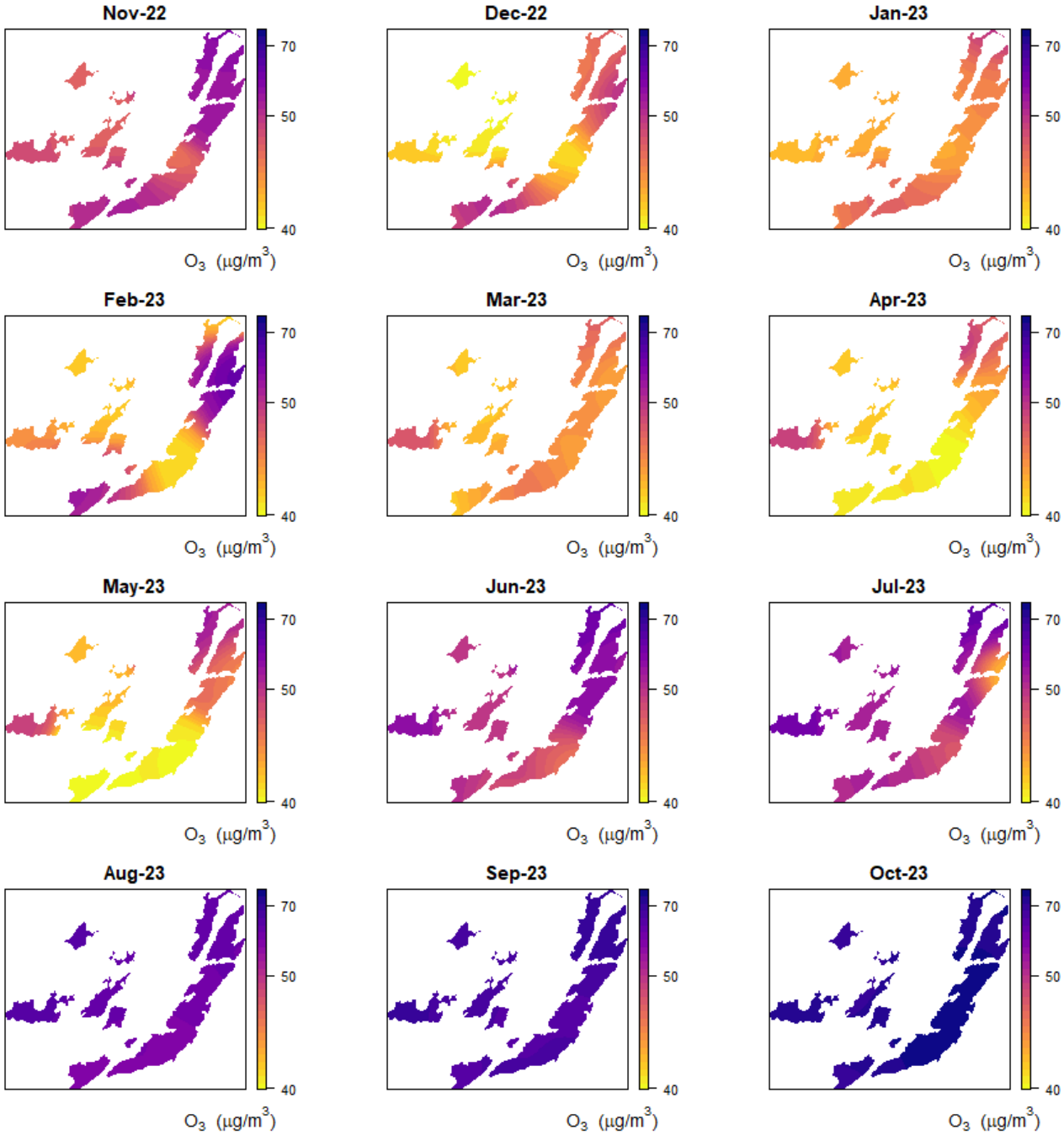

Figure 7.11-17: Spatially smoothed monthly average concentration of O_3 by sampling period. Common colour map based on percentiles.

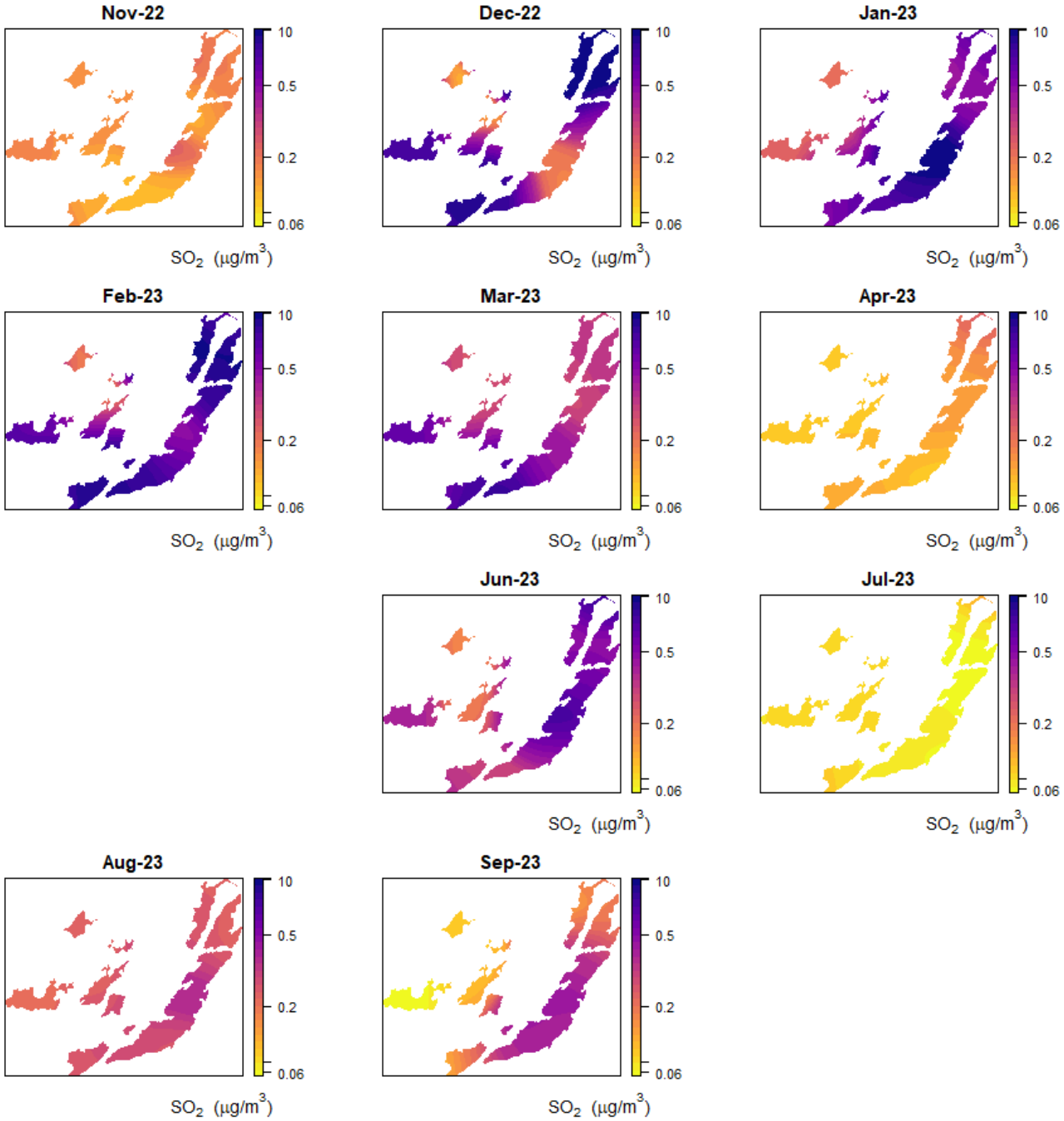

Figure 7.11-18: Spatially smoothed monthly average concentration of SO_2 by sampling period. Common colour map based on percentiles.

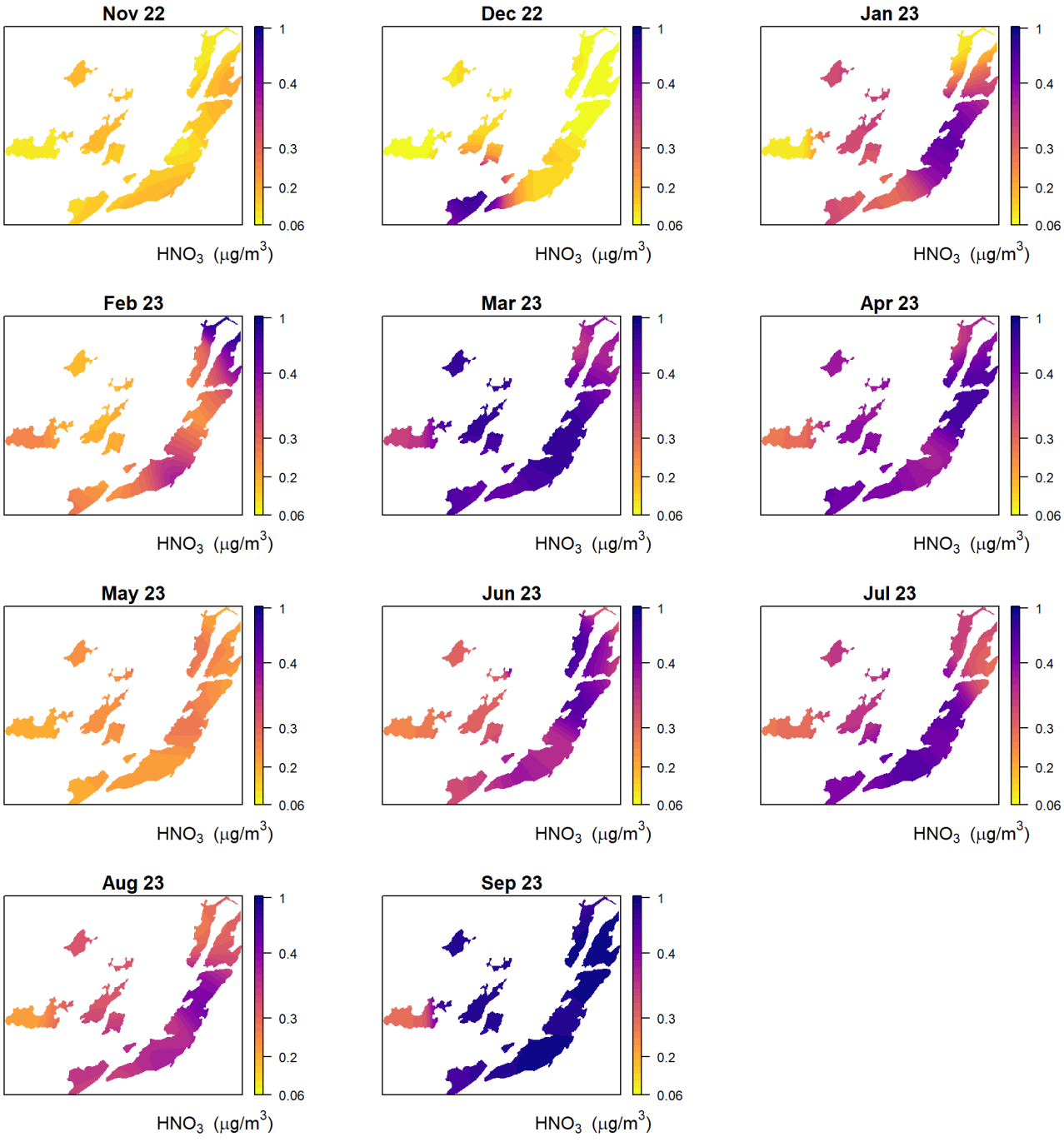

Figure 7.11-19: Spatially smoothed monthly average concentration of HNO_3 by sampling period. Common colour map based on percentiles.

This page is intentionally blank.

7.12 Real time powered sites

Three of the air quality monitoring stations operated by MRAMP include instruments for real-time monitoring of gas concentration and particulates. These instruments require mains electrical power. Data from a similar monitoring station operated by other users is also available.

Data from each of the three powered sites operated by MRAMP researchers is live-streamed from the AQM's computer to our data store. As the suite of instruments is logging continuously, the volume of data produced is quite high. Many of the instruments allow multiple data channels to be logged. To limit the volume of data, we limit the transfer to the measurement results of the species/substance(s) in question, as well as information viewed as critical for remote monitoring and diagnostics of system health (e.g. instrument sample flow rates, converter temperatures, system alerts). This allows early detection of any factors which may impact the reliability of results, as well as early identification of any need for maintenance or repairs.

Data from the fourth powered site (operated by ACOEM/Ecotech) is received monthly and added to our data store. This is received in the form of a validated report, with five minute averaged, hourly averaged, and daily averaged data for all species/substances. At the time of writing this report, the latest data received was from April 2024.

7.12.1 Gaseous species

The gas analysers were deployed incrementally at each powered AQM, and brought online when installed, following initial zeroing and calibration. More data is available for some instruments than others, owing to availability of calibration gases and a few cases of equipment failure, specifically:

- A leak in the zero air generator at EX02, resulting in the inability to reach the required pressure of zero air. This was repaired on site by the research team, with a vendor-supplied replacement part, but it resulted in an inability to provide sufficient dilution air for calibration purposes.
- Failure of a thermal converter at EX09 requiring return to the vendor for repairs. This is expected to be returned and redeployed by June 2024. Resulting in nitrogen measurements for EX09 being unavailable.
- A fault in SO_2 and O_3 monitors at EX07 resulting in data for February 2024 being invalidated.
- A recent leak in the zero air generator at AQ01, which is identical to that earlier experienced in the instrument at EX02. We are currently waiting on a replacement part.
- A recent fault in the Teledyne T201 sensor at EX02 resulting in the instrument not responding as expected to ammonia calibration gas. We are in contact with the vendor to identify required repairs.
- The inbuilt software component of the gas instruments, that facilitates data transfer for external processing, has intermittently stopped working from time to time, requiring manual restarting on site. The vendor has been contacted for advice.
- There were some power surges or power failures on site which caused the logging software on the AQM computer to stop executing. This resulted in data not being uploaded to data storage, and the software needing to be restarted on the PC once power was restored. After such events, data must be recovered manually from individual instruments.

Negative values of concentration were occasionally recorded. For this exploratory analysis, negative values were re-set to zero when the data was extracted and collated for analysis. In the event where there are concerns about data validity (e.g. substantial drift between calibrations, data collected immediately after a power outage, data collected when instruments were reporting important alerts) the relevant data have been excluded.

Data for gas species has been plotted in the figures below, with values from all four powered sites displayed, where available. Concentrations are reported in parts per billion (ppb).

As illustrated in Figure *7.12-1*, SO_2 is consistently present at all sites at low concentrations, typically around the $\sim$1.5 ppb range. There are occasional higher readings which may be related to activities near each site.

At a shorter time scale, there is some evidence of daily patterns in readings. The SO_2 data for a selected week (in early February 2024) is shown in Figure *7.12-2*. For each of the three sites shown, there is a daily pattern with peaks occurring at regular intervals. This effect is most pronounced at EX02.

A regular daily cycle in SO_2 concentration could be explained by diurnal variation in weather including temperature and wind direction. However, differences between the three sites in the magnitude and timing of the peaks are more easily explained by localised events involving emission of SO_2.

The Teledyne T201 instrument reports NO, NO_2, NOx, NH_3 and total nitrates (TNX). The instrument at EX09 was taken offline, once the fault with the thermal converter was identified. This remained offline until the May 2024 sample changeover, when the thermal converter from EX02 was moved to EX09 to allow the T201 to be brought back online. Given the issues experienced with the T201 at EX02, this was viewed as a prudent step to get data collection back online, while the thermal converter from EX09 was with the vendor for repair. The thermal converter has now been repaired and is ready to be shipped back to site for re-installation. This has resulted in no data for nitrogen species being recorded for the first part of the year. The T201 at EX09 was however one of the first instruments brought online, so some data is available for NO and NO_2 for late December 2023 to early January 2024. This corresponds to the last time a calibration was performed prior to the thermal converter fault being detected.

Data for NO is shown in Figure *7.12-3*. The plots show a number of peaks, rising well above typical levels observed at each site. The peaks do not exhibit a regular periodic pattern. Indeed these time series do not even appear to be statistically stationary over time. There is insufficient data available to assess consistency between the time series from the different sites. Very limited data are available for EX09, but the few available readings are broadly comparable with the readings from EX07 for the corresponding time period.

Since NO is converted to NO_2 during daylight hours, the irregularity of the time series for NO is most likely attributable to combustion processes taking place around the AQM sites. However the data also needs to be considered in relation to weather conditions, especially wind direction. The Ramboll modelling has shown that there can be long range transport of gaseous species within the region, particularly in the direction of prevailing winds.

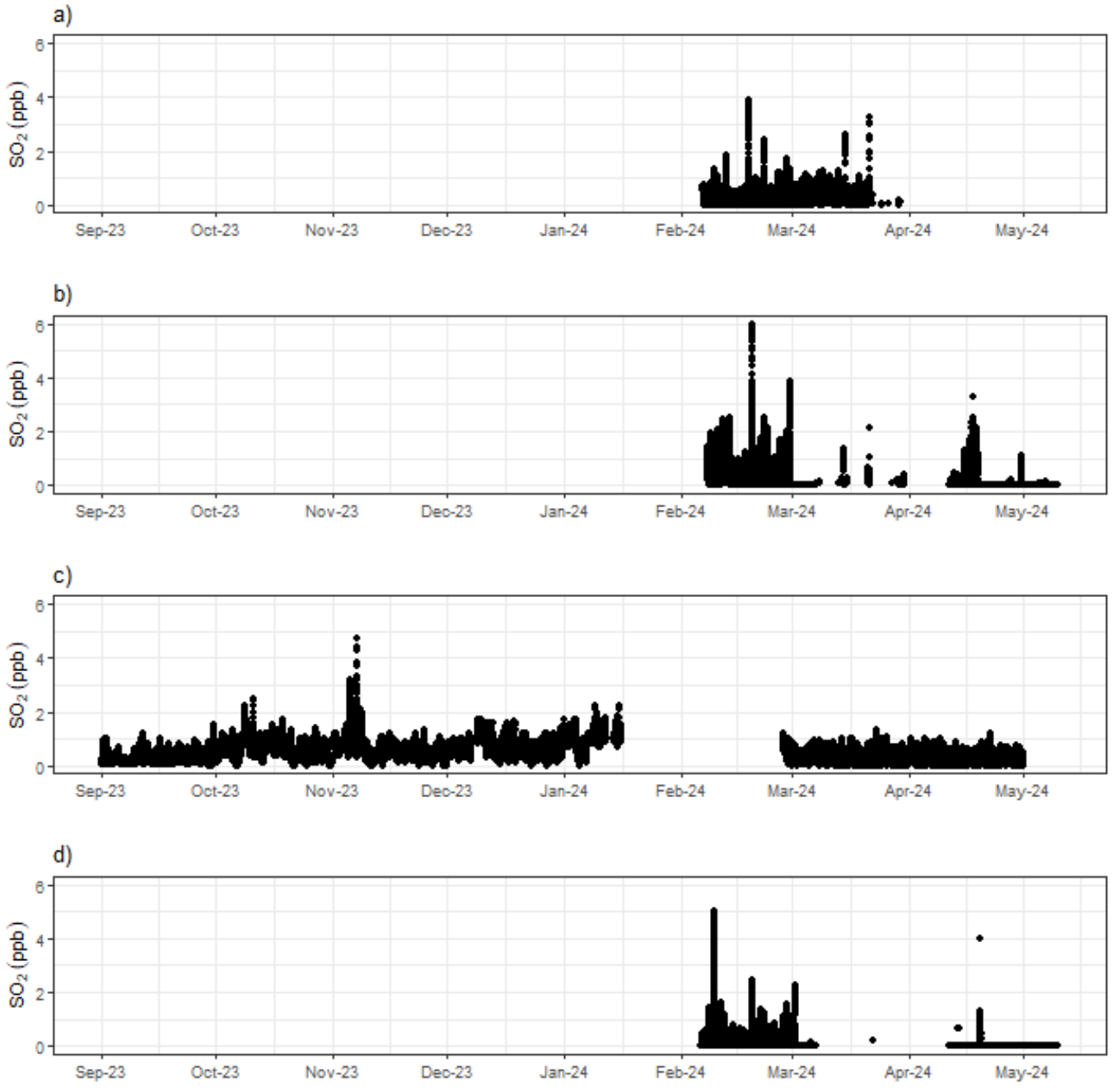

Figure 7.12-1: Time series plots for SO_2 concentration to date, for sites (a) AQ01, (b) EX02, (c) EX07 and (d) EX09. Data have been excluded where the validity is in question.

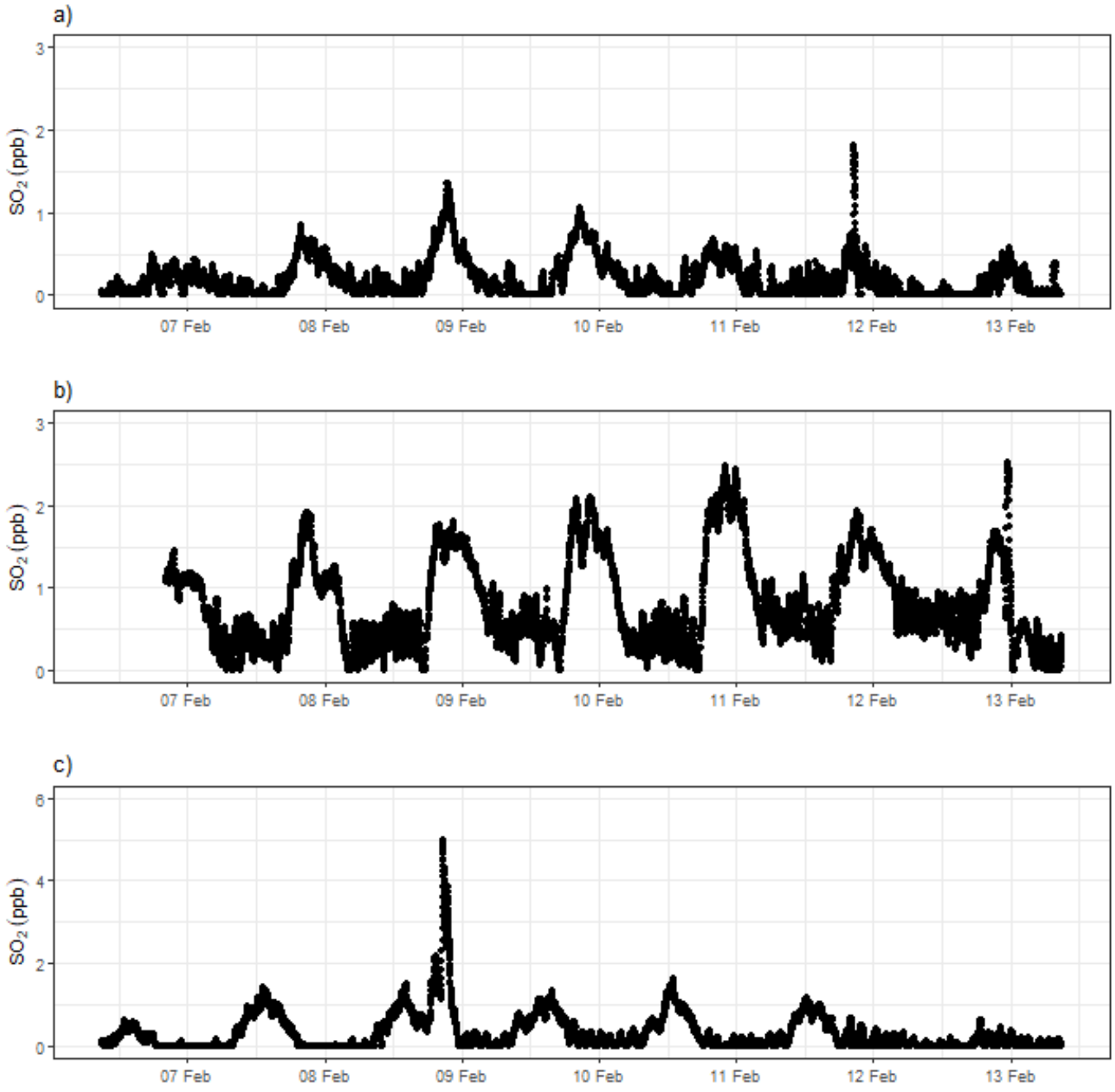

Figure 7.12-2: Time series plots for SO_2 concentration over one week in February 2024, at sites (a) AQ01, (b) EX02 and (c) EX09.

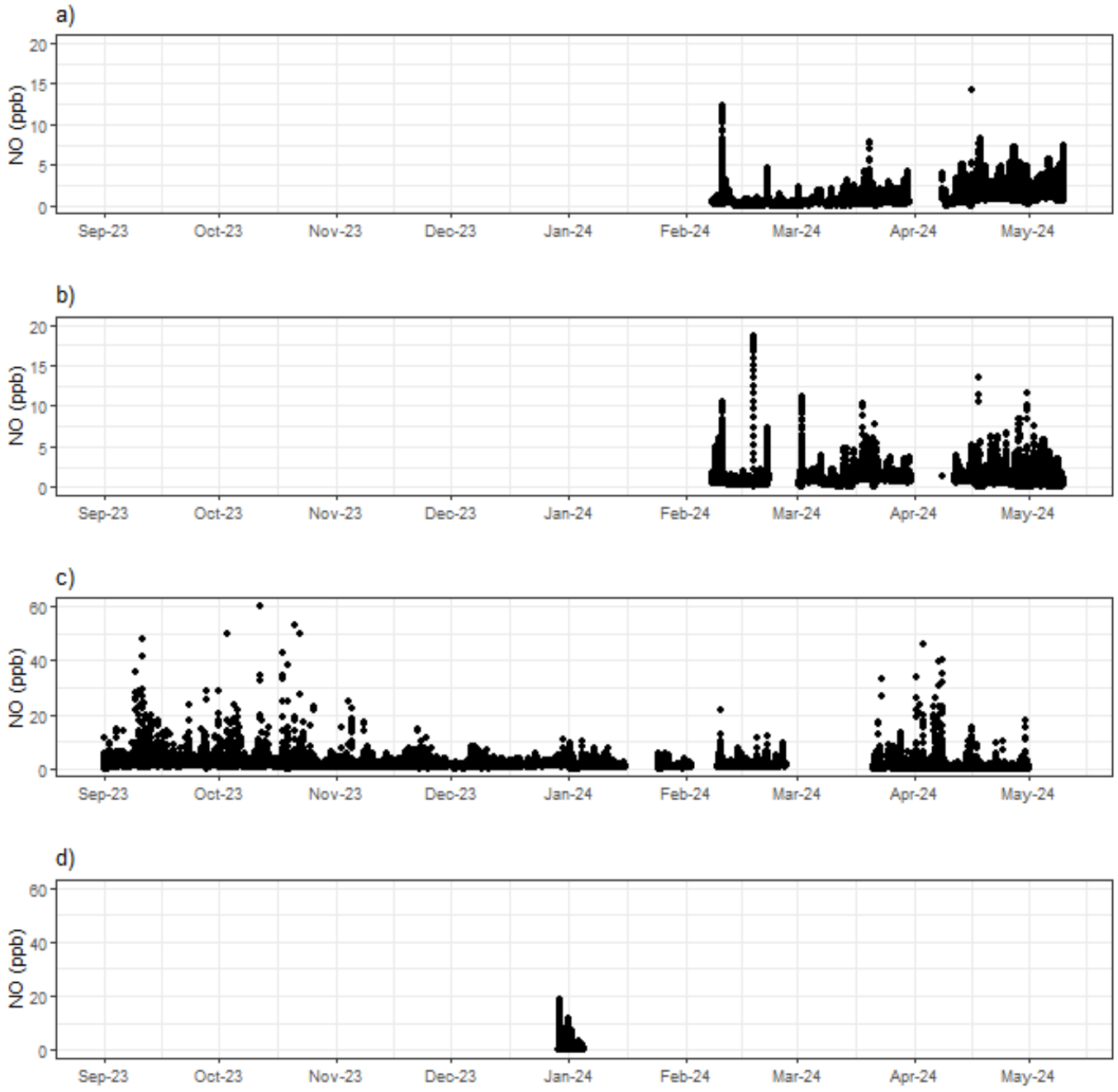

Figure 7.12-3: Time series plots for NO to date, where (a) AQ01, (b) EX02, (c) EX07 and (d) EX09. Data have been excluded where the validity is in question.

NO_2 data are shown in Figure *7.12-4*. The observed values for NO_2 are typically lower at AQ01 and EX02 than at EX07, however there is insufficient overlap between these time series to draw conclusions. The limited data available for EX09 show higher NO_2 values than at EX07 for the corresponding time period.

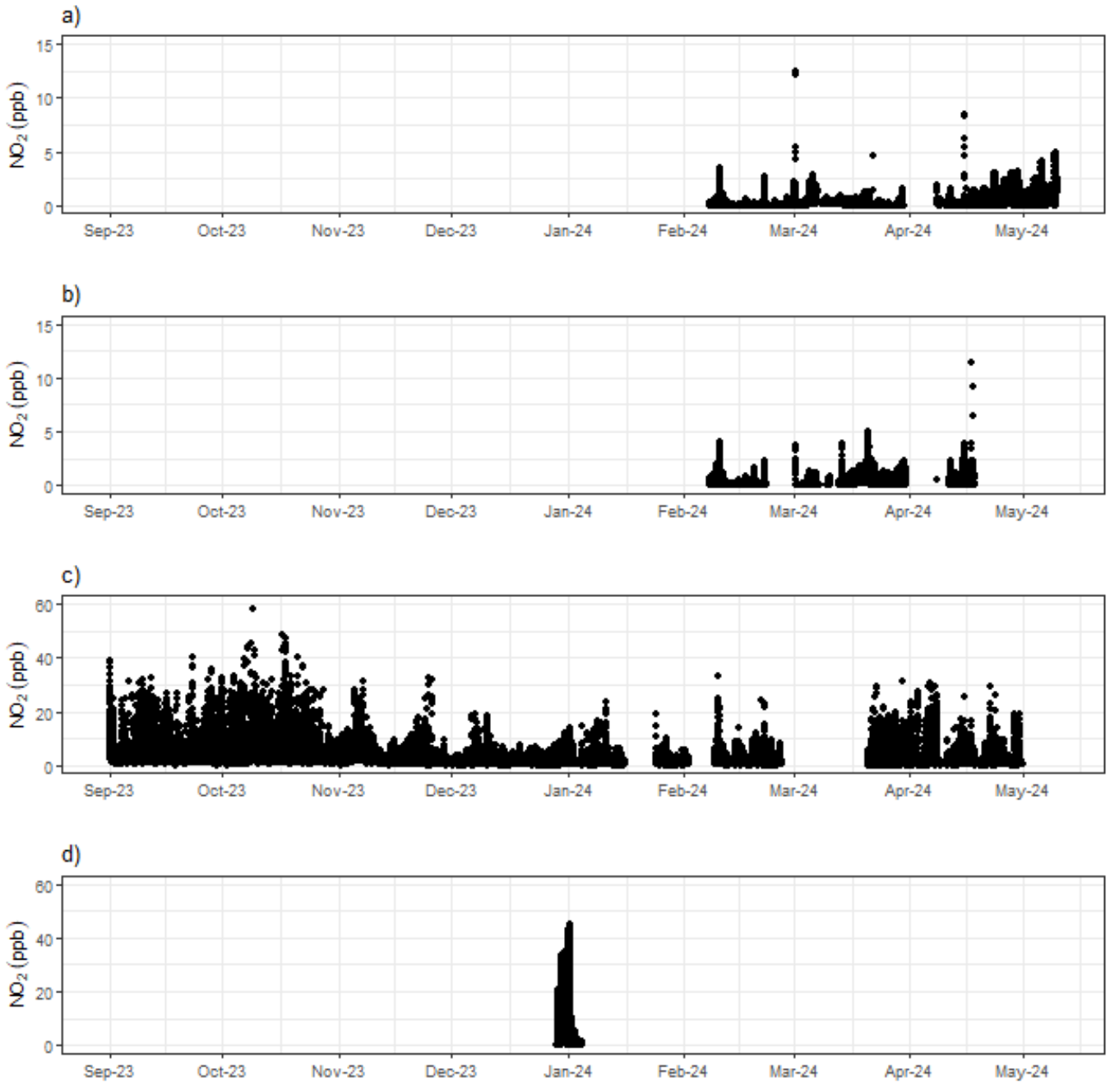

Figure 7.12-4: Time series data for NO_2, where (a) AQ01, (b) EX02, (c) EX07 and (d) EX09. Data have been excluded where the validity is in question.

Available results for ammonia are shown in Figure *7.12-5*. These time series show all data from EX07 since the commissioning of the new ammonia instrument at the site. There is limited ammonia

data from the other sites owing to the issues noted above with the T201 instrument at EX02, and owing to the T201 at EX09 being offline while the thermal converter was undergoing repair. There is some uncertainty about the ammonia data measured at other sites, because the T201 at EX02 did not respond to calibration gas in the way expected. We are in contact with the vendor to address this. The ammonia data that are available appear to be relatively consistent at each site, where the dates/times overlap.

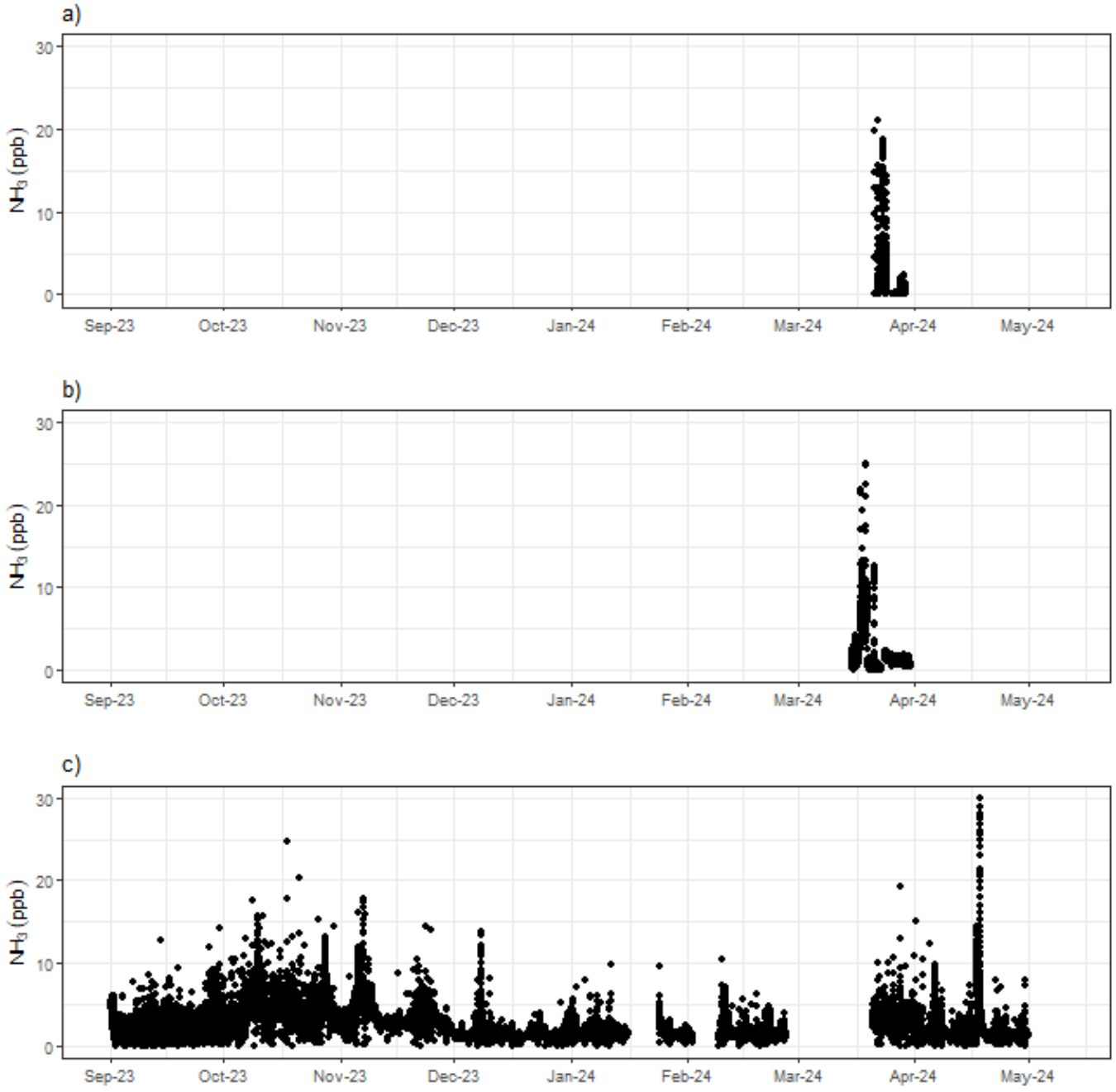

Figure 7.12-5: Time series data for NH_3 for (a) AQ01, (b) EX02 and (c) EX07. Data have been excluded where the validity is in question.

Ozone data are shown in Figure *7.12-6*. While O_3 appears to be consistently present, there are some notable peak values (e.g. November 2023). From the data available it appears that O_3 levels are typically higher at EX07, but in the absence of overlapping data this is difficult to determine definitively. The effect of other factors, such as wind direction, still need to be considered.

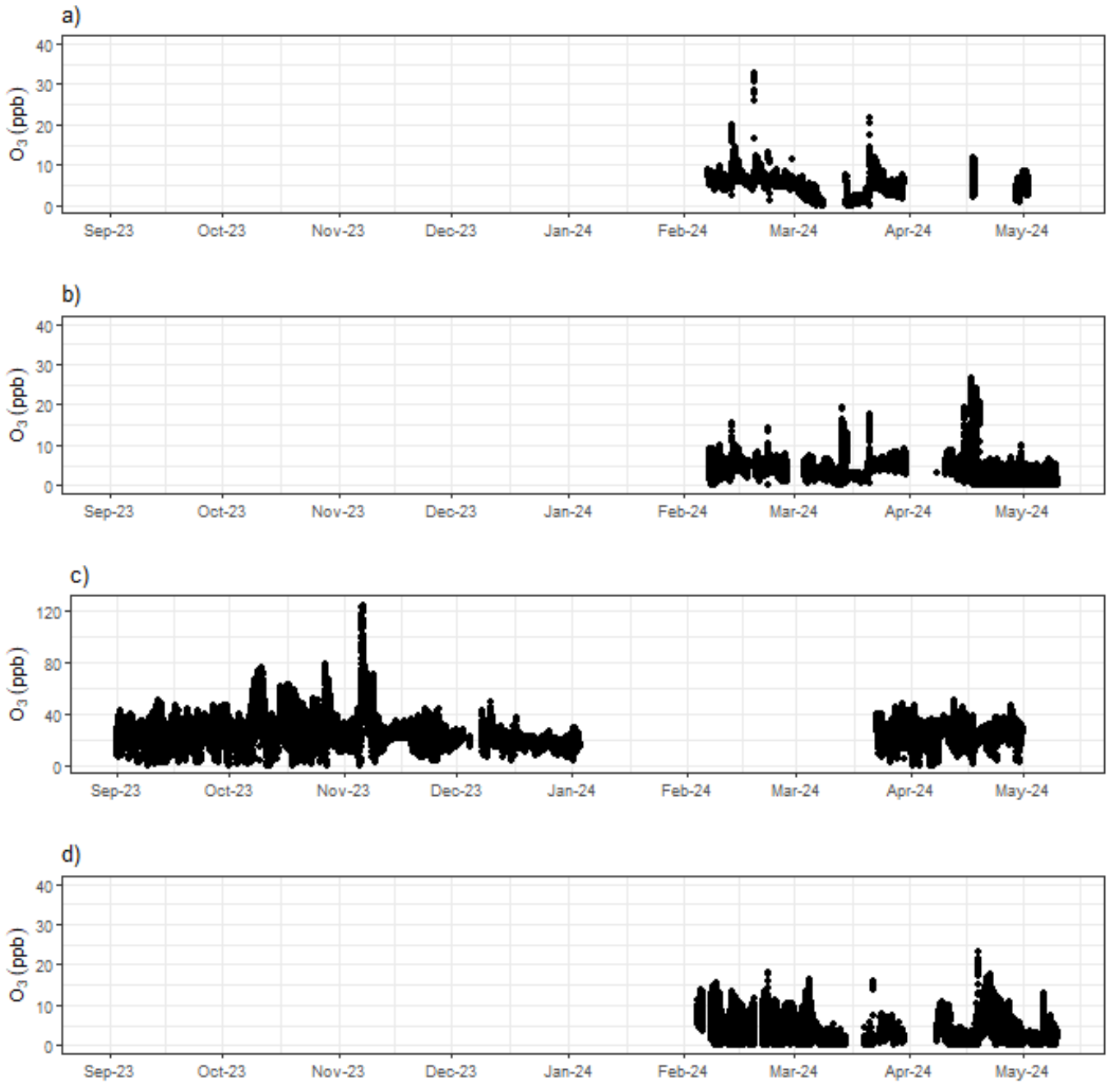

Figure 7.12-6: Time series plots for O_3 at (a) AQ01, (b) EX02, (c) EX07 and (d) EX09.

Statistical modelling of these gas concentration time series data will need to take account of the highly skewed distributions of concentration values. In particular, prediction of exceedances will depend on a good understanding of the tails of the distributions. Suitable distribution models

include the compound-Poisson and extreme-value distribution families.

7.12.2 Particulates

Palas Fidas 200 instruments are deployed at the four powered AQMs. These count particles across a range of size fractions, with time series plots for $PM_{2.5}$ and PM_{10} shown below (Figure *7.12-7* and *7.12-8*). These were brought online as they were installed and following an initial calibration check. Some challenges were encountered after initial installation, owing to the humidity in the environment, but these have now been addressed. Particle data for AQ01, EX02 and EX09 is unavailable owing to equipment failure, the systems at AQ01, EX02 and EX09 have suffered the same malfunction at different times, due to a corrupted internal data storage drive. The manufacturer is currently sending out new components that should run more reliably. These systems have also had (or are in the process of having) their power supplies replaced. All replacement components have been obtained directly from the manufacturer under warranty. Current status of instruments;

- Unit at EX02 has had the power supply replaced, now waiting on hard drive delivery, expected redeployment June 2024.
- Unit at EX02 has had the power supply replaced, now waiting on hard drive delivery, expected redeployment June 2024.
- Unit at EX09 experienced the same power supply and software issues as the other instruments, awaiting repair and hard drive delivery, expected redeployment July 2024.

$PM_{2.5}$ data are shown in Figure *7.12-7*. This shows that levels were low for September and October 2023, before increasing in November where steadily increasing values were observed daily up until maximum (five minute average) concentration of 0.726 mg/m^3 (726 μg/m^3). This is by far the highest measurement observed so far, with a number of subsequent peaks over 0.2 mg/m^3 observed through December 2023 and January 2024. While it is noted that the Murujuga region and the Pilbara in general has higher levels of natural dust than other parts of Australia, the November 2023 peak is particularly high and would fall into the 'extremely poor' air quality index (AQI) based on the DWER criteria (DWER, 2024). It should also be noted that while the AQI offers a useful reference, or basis of comparison, for dust levels the criteria are based on health measures which may not have any relevance to what is happening in terms physico-chemical processes on the rocks and/or rock art panels. It is anticipated that over the next year, more complete real-time dust data will be available and that this will bear a correlation to the monthly deposition samples. Further understanding of the role of dust in the environment, as it pertains to the condition of rock art, may yield an alternative reference point for comparison.

PM_{10} data are shown in Figure *7.12-8*. This shows a similar trend to the data for $PM_{2.5}$ only with higher mass concentrations (as would be expected). A similar pattern is shown in Figure *7.12-9* for total suspended particulates (TSP), again with higher mass concentrations.

The distribution of $PM_{2.5}$, PM_{10} and TSP is highly skewed. Extreme-value distributions are likely to be appropriate models for these data.

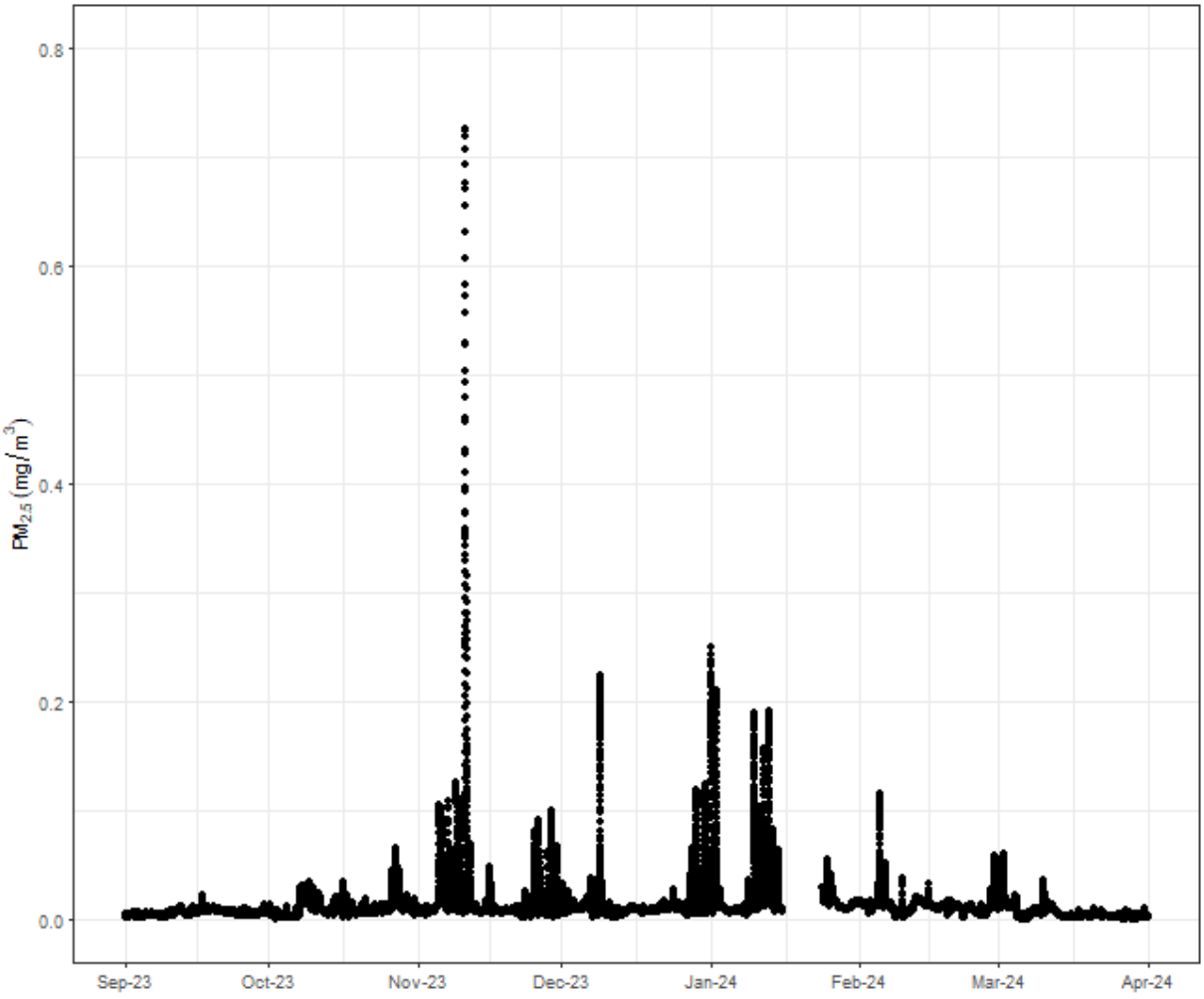

Figure 7.12-7: Time series plot of $PM_{2.5}$ at EX07 since instrument commissioning. Data have been excluded where the validity is in question.

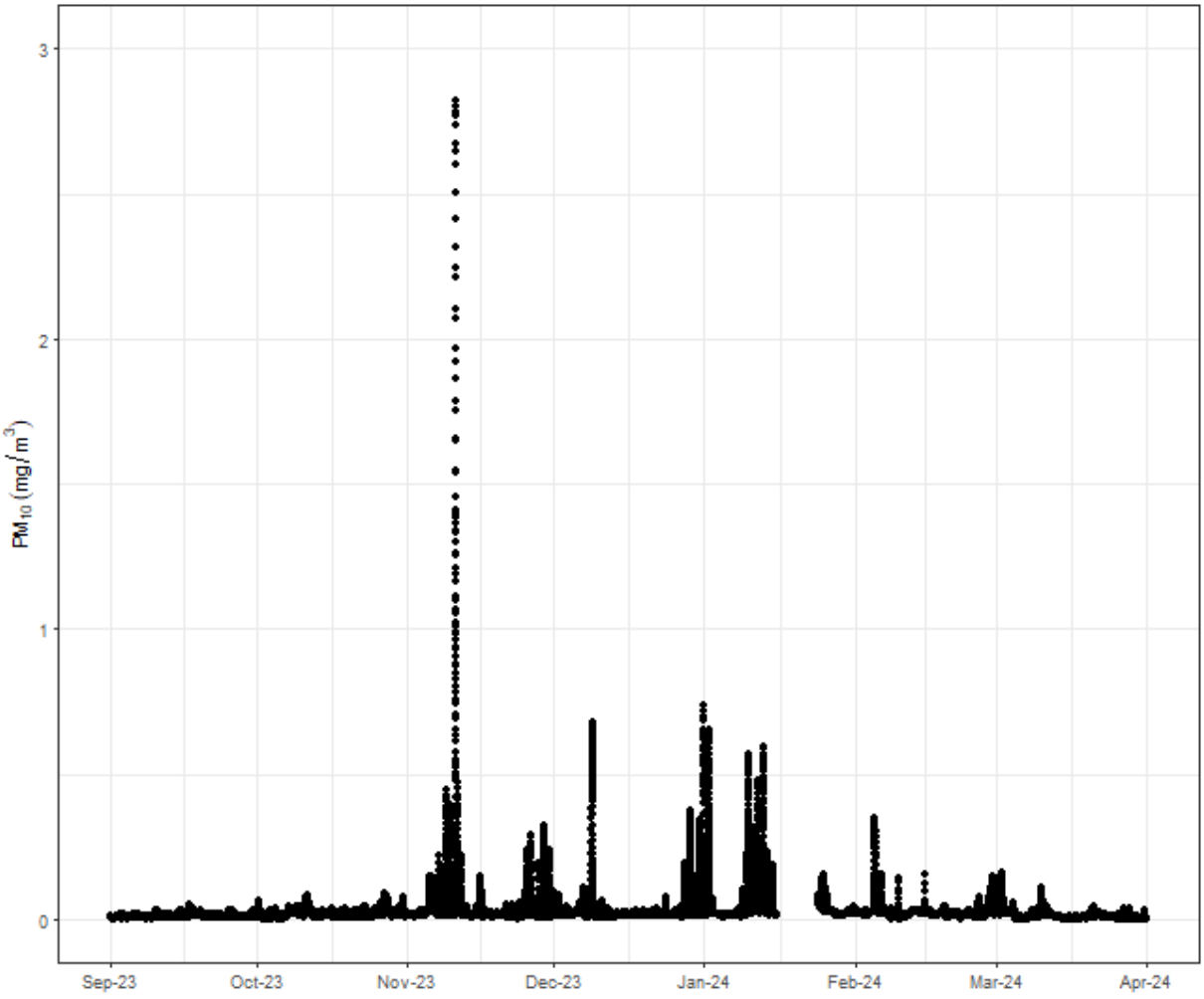

Figure 7.12-8: Time series plot of PM_{10} at EX07 since instrument commissioning. Data have been excluded where the validity is in question.

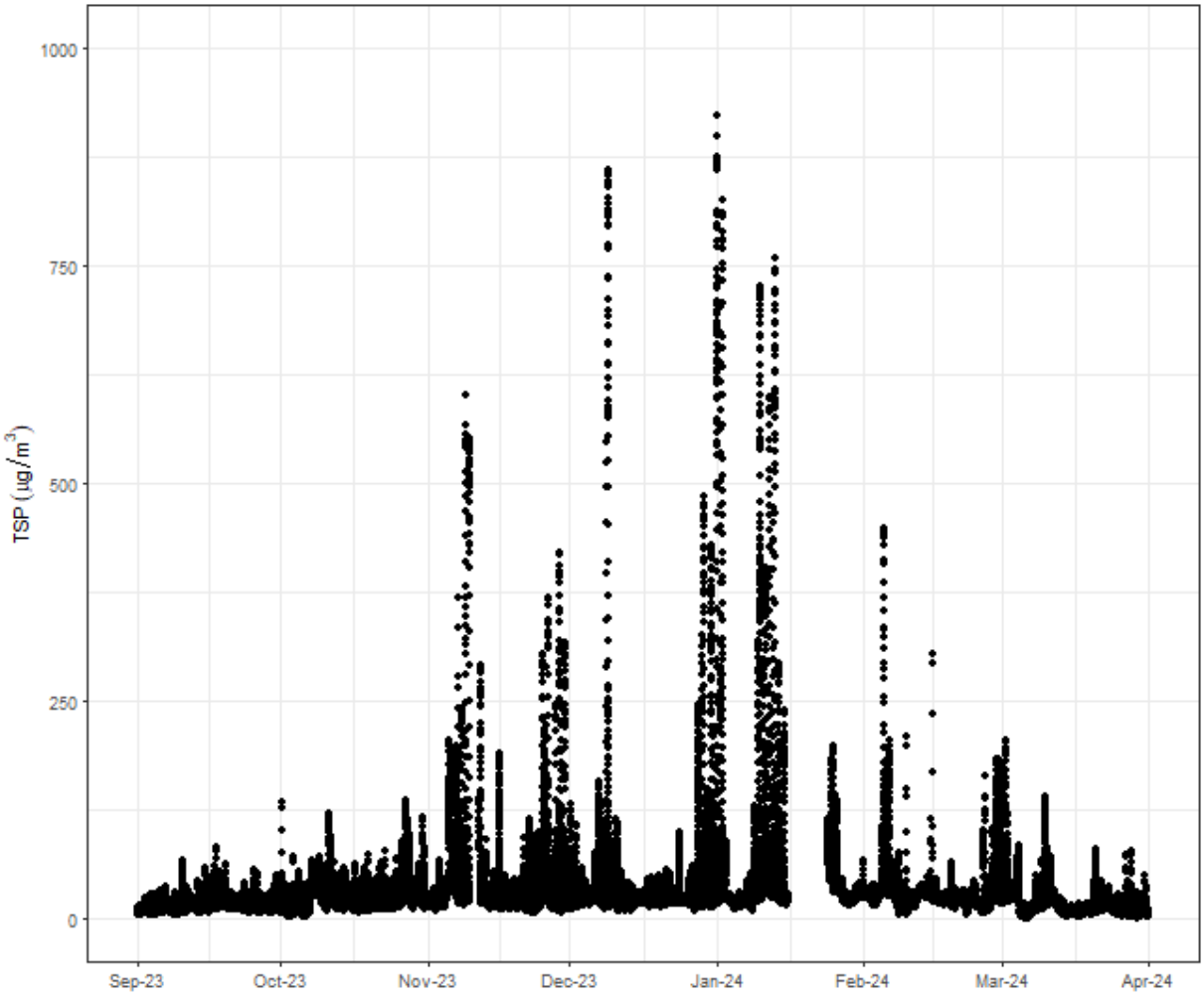

Figure 7.12-9: Time series plot of total suspended particulates (TSP) at EX07 since instrument commissioning. Data have been excluded where the validity is in question.

7.12.3 Scanning instruments

7.12.3.1 Aethalometer

Given the proximity of the study area to major shipping routes, flares from the natural gas plants, and the likelihood of bushfire events (controlled or otherwise) it is important to consider the presence of carbon in the atmosphere, and any impacts this may have either directly, or indirectly, e.g. through secondary aerosol formation. It has also been suggested that carbon/soot may cause "micro-delamination" on rock art panels (Dorn, 2020). To allow the direct measurement of carbon in the air we have deployed an aethalometer (Maggee AE43) at the EX09 site. This site has higher elevation than other sites and effectively overlooks both industry and the northern part of the Burrup Peninsula. It is also the closest powered site to major shipping routes, and offers to be best chance to capture shipping, as well as other, emissions.

The instrument was initially commissioned while the EX09 AQM was at its temporary location (at the MAC office) and then re-commissioned after relocation to the Mt Wongama site (the permanent EX09 location, as indicated in Figure *3.1-1*. Observations from the commissioning period (late September to early October 2023) and from the subsequent permanent installation (November 2023 onward) are included in Figure *7.12-10*. There is also a short period of data shown for early September 2023, which corresponds to the initial set up of the instrument.

Figure *7.12-10* shows black carbon (BC) concentration (black dots), the weekly average black carbon concentration (yellow diamonds), as well as the weekly average biomass-derived black carbon (BB) concentration (blue diamonds). It is clear that black carbon concentration can reach high levels at certain times. The highest weekly average black carbon concentration (4.6 μ g/m^3) was observed when the AQM was deployed at the MAC office, which may be the result of flaring at the natural gas plant, though further investigation is required. A notable observation over the data collection period is the percentage of biomass derived carbon, which is regularly in excess of 20%. Some of these periods correspond to controlled burns in the Murujuga National Park, but this also suggest long distance transport of inland bushfire smoke. Future further analysis of black carbon results and wind direction may reveal additional evidence to support this.

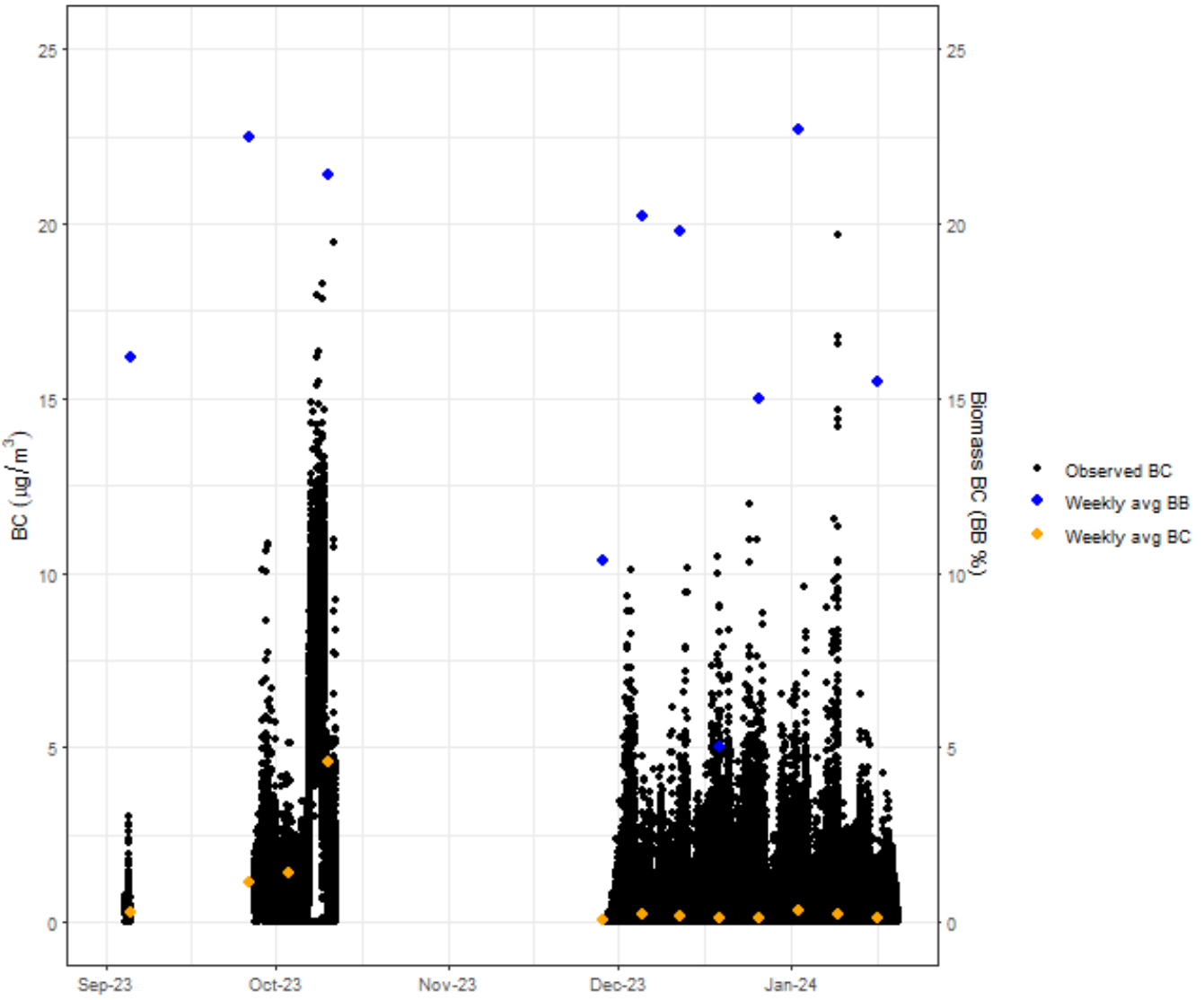

Figure 7.12-10: Time series plot of black carbon (BC) and biomass-derived black carbon (BB) from Aethalometer instrument. Observations from September to October 2023 were obtained during initial startup and commissioning at the MAC office. Data from late November 2023 onward were obtained at the EX09 Mt Wongama site.

7.12.3.2 Picarro

As indicated in the previous section, the EX09 site is well located to capture a range of air quality measurements. For this reason, this site was chosen for the installation of additional instrumentation, to allow a more thorough investigation of the chemical species present in the air. In particular, this was the site chosen to deploy the isotopic methane analyser (Picarro G2210-i). This instrument was commissioned in December 2023 at the Mt Wongama site. Data are unavailable for the first half of February due to the Picarro being offline.

Figure *7.12-11* shows the CO_2 levels for the site, starting from December 2023. The data typically

sit around the 400 ppm level, in line with global averages, with a number of periodic peaks (several per month) approaching or exceeding 500 ppm. In some cases these reach concentrations above 2000 ppm. These may correspond to flaring events at the gas plant(s), other combustion processes (e.g. bush fires) or emissions from ammonia production facilities. Given that the levels of CO_2 reach these higher levels from time to time, the impacts on the environment need to be considered. This could include atmospheric processes involving CO_2 (such as acidification), as well as the impact of CO_2 on the microbiome. Given the results so far, further investigation of CO_2 is warranted.

Figure *7.12-12* shows the methane levels for the site. The methane levels are typically around or above the global background methane concentration of 1.9 ppm (Skeie et al., 2023). There are a number of peaks observed with the methane concentration at times exceeding 3 ppm. This may be explained by the proximity of the monitoring station to the gas plant, so further analysis and consideration of the carbon isotopes in the methane is required. Higher levels of methane may mean more potential for secondary organic aerosol formation, but this requires further investigation.

Ethane results have also been obtained over the same monitoring period and are shown in Figure *7.12-13*. These are typically low, with only a few days reaching concentrations over 20 ppb. Notably, the higher ethane concentrations do not always correspond to days with higher methane concentrations.

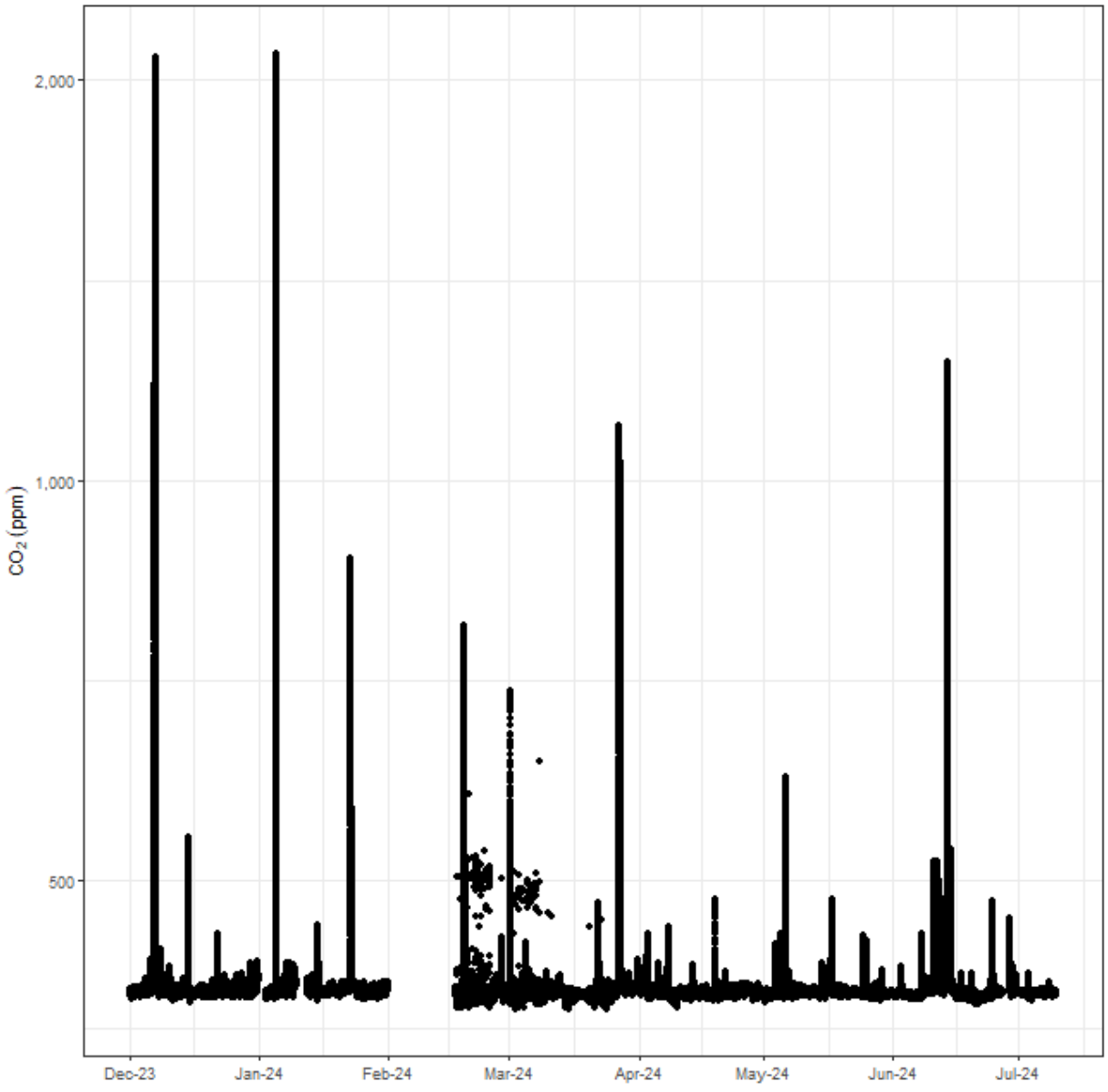

Figure 7.12-11: Time series plot of CO_2 from Picarro instrument at EX09 since instrument commissioning.

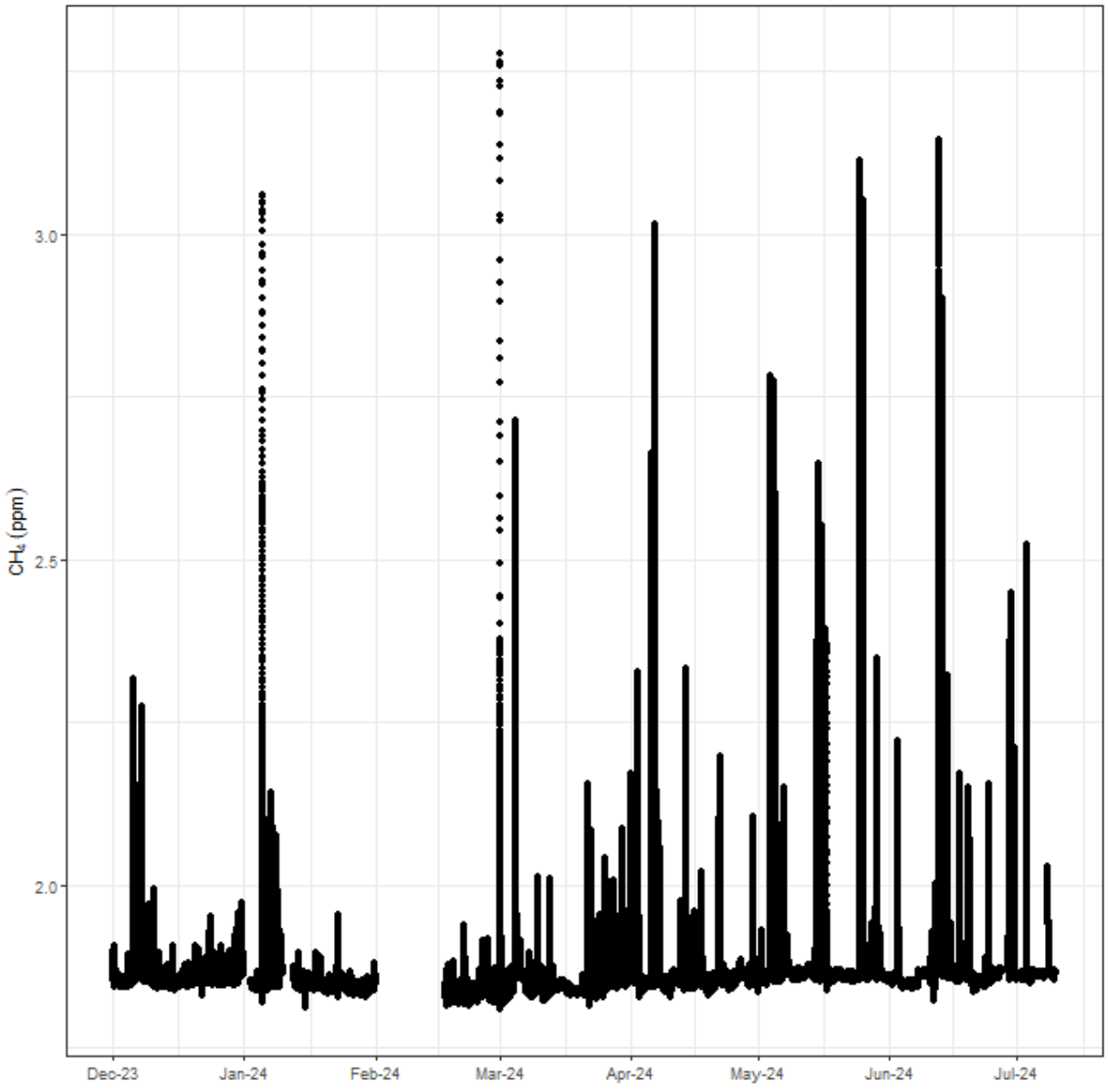

Figure 7.12-12: Time series plot of CH_4 from Picarro instrument at EX09 since instrument commissioning.

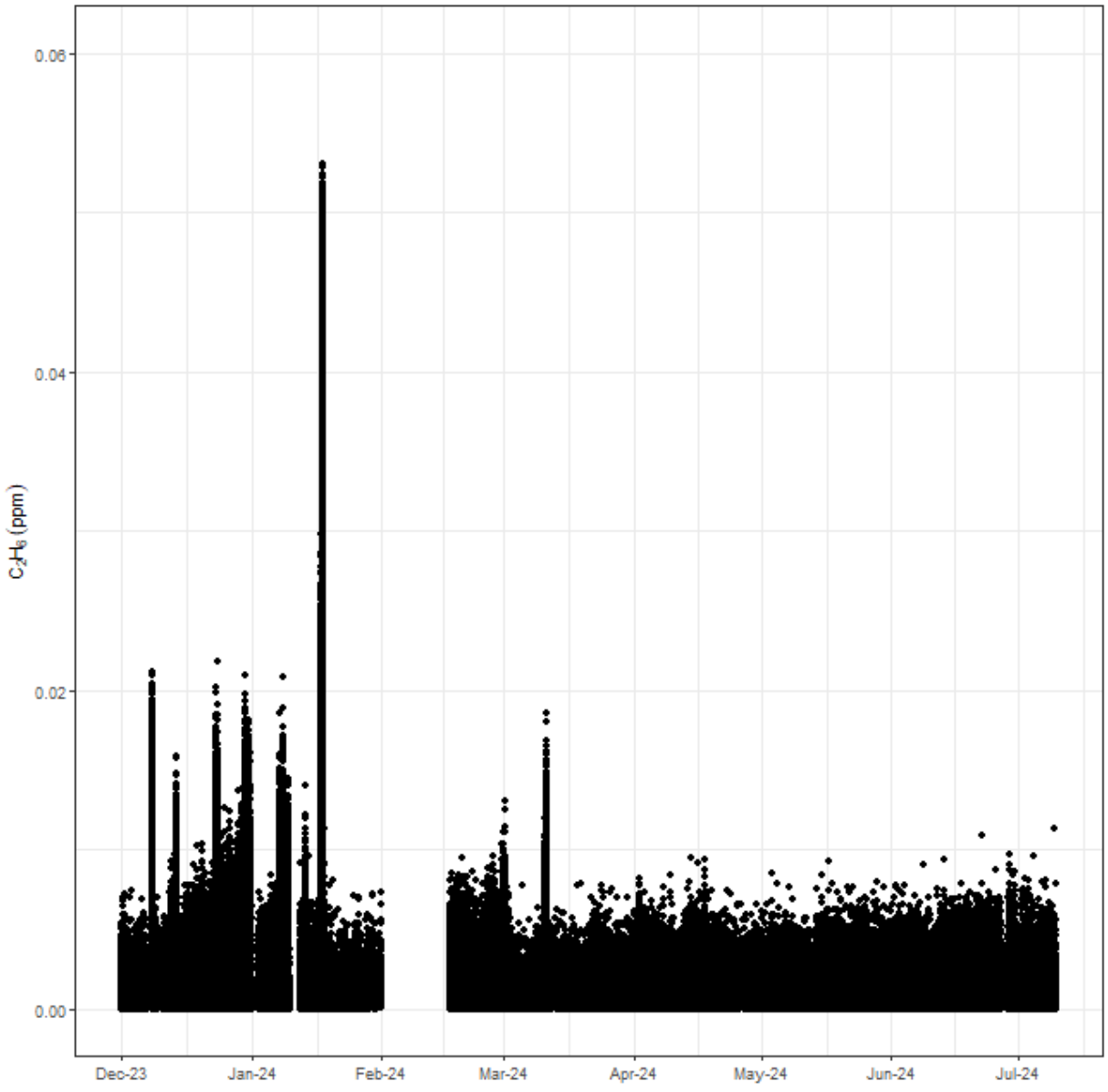

Figure 7.12-13: Time series plot of C_2H_6 from Picarro instrument at EX09 since instrument commissioning.

7.12.3.3 MAxDOAS

The Multi AXis Differential Optical Absorption Spectrometer (MAxDOAS) operates in a similar manner to satellite remote sensing, except that it is able to measure horizontally, vertically and angles in between. It has an effective measurement path length of 15 to 25 km depending on atmospheric conditions. It is only able to measure during daylight conditions. Data can be extracted and processed to obtain approximate concentrations of NO_2, SO_2 and selected other species such as formaldehyde (CH_2O). The MAxDOAS is currently sited at EX09 (Mt Wongama) and is oriented such that an angle of 0° represents due west (W), 90° represents a vertical orientation and 180° represents due east (E).

Figure *7.12-14* provides a comparison between gas concentrations near ground level (1°/ W) elevation versus 10° elevation in the same direction, for NO_2 and CH_2O. It can be seen that NO_2 exhibits strong vertical distribution characteristics (higher near ground level) as well as temporal variation. CH_2O however is much more uniform both vertically and temporally.

Figure *7.12-15* provides a comparison between the concentrations of NO_2 and CH_2O at ground level, in westerly (0°) and easterly (180°) directions. It can be seen that NO_2 exhibits substantial variation, likely due to prevailing wind direction. CH_2O however is much more uniform in both directions. This appears to be a trend for secondary air pollutants (e.g. including O_3), due to the need for a reaction between (most likely) NO_2, CH_4 or another volatile organic and OH radicals formed through photocatalytic processes.

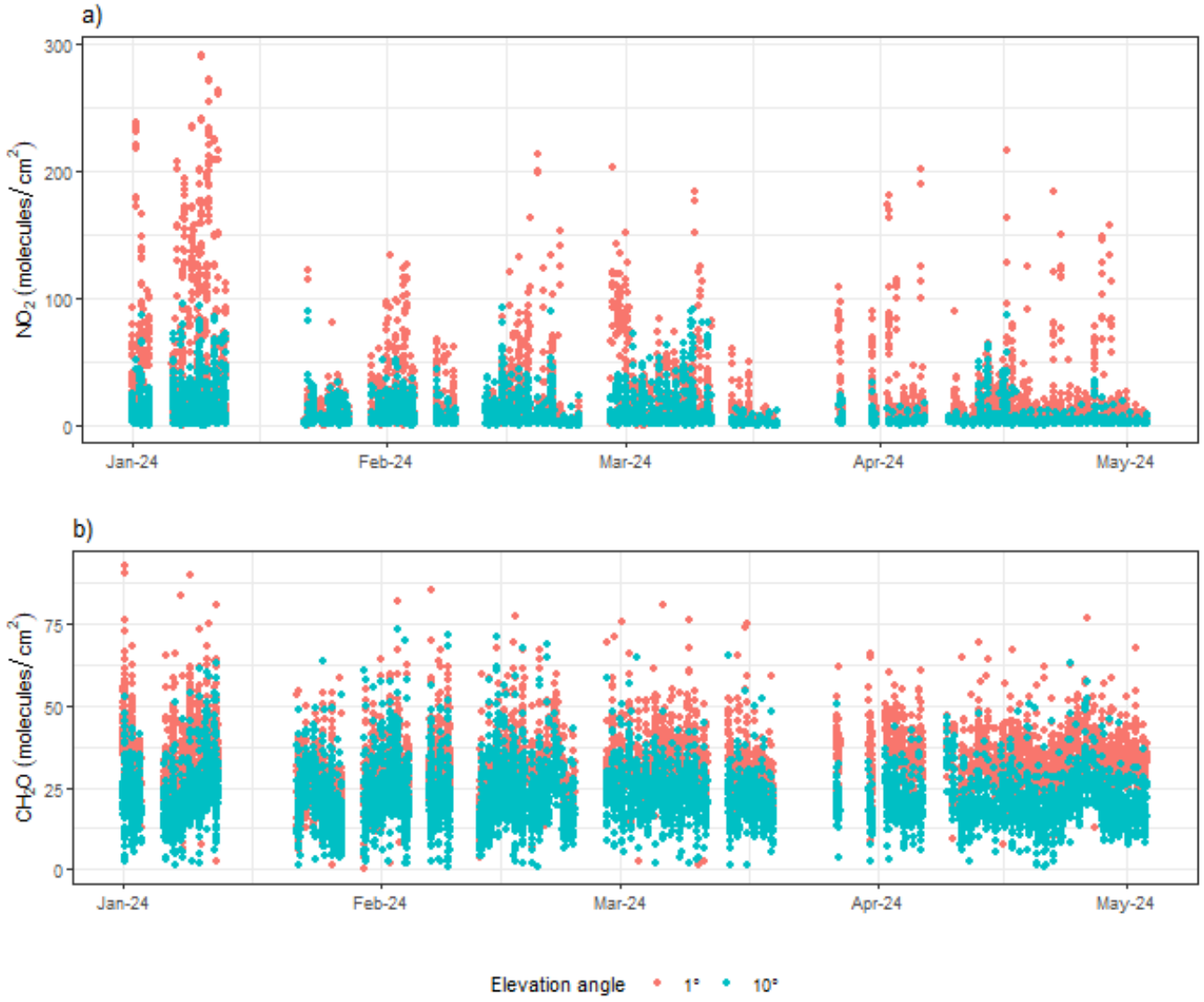

Figure 7.12-14: Differential slant column densities (dSCDs) from MAX-DOAS at 1° and 10° elevation angle. Note that the NO_2 and CH_2O have been divided by 10^{15} (one thousand trillion) to simplify the tick marks on the y-axis.

Figure 7.12-15: Differential slant column densities (dSCDs) from MAX-DOAS at 0° (W) and 180° (E). Note that the NO_2 and CH_2O have been divided by 10^{15} (one thousand trillion) to simplify the tick marks on the y-axis.

This page is intentionally blank.

7.13 Key findings from statistical analysis

This section summarises the key findings from the statistical analysis of data from each individual component study, as reported above.

Relationships between the variables measured in different component studies are investigated in Section 8 and summarised in Section 8.6.

7.13.1 Chamber studies

The analysis of chamber experiments in Section 7.1 confirmed that the gases SO_2, NO_2, and NH_3 may cause alteration of the rock surface. We proposed that the total concentration of SO_2, NO_x (treated as NO_2) and the concentration of NH_3 may serve as the measures of exposure that are required in order to formulate an EQC.

We estimated a dose-response relationship between changes in chemical composition (K+Ca+Mg+Na) and level of exposure to SO_2 and/or NO_x. Using this dose-response relationship it is possible to calculate an estimate of the threshold levels of exposure.

We established that *pH* is elevated after exposure to NH_3. Further chamber experiments would be required in order to establish a dose-response relationship and an EQC threshold for NH_3.

7.13.2 Field measurement of colour

The measurement of rock surface colour in the field has been an important component of previous studies of the Murujuga rock surfaces, and is also an important component of MRAMP. Previous studies were criticised for technical and methodological failings of their colour analysis. Accordingly the MRAMP study design and fieldwork have involved very extensive work to eliminate technical problems.

MRAMP is the first research project, to our knowledge, in which the colour of Murujuga rock surfaces has been analysed using the full spectral reflectance curve, rather than the simpler CIELAB coordinates which are derived from the spectral reflectance curve. This has been done partly in the hope of extracting more detailed and sensitive information about colour changes in the rock surfaces, and partly in order to validate the colorimetry technique more fully.

The validity of data produced by the JAZ spectrometer was a major focus of statistical investigation in the Year One Report (Curtin University, 2023). The spectral reflectance curves recorded in the field by the JAZ instrument were found (by our analysis) to be invalid in an unacceptably large fraction of cases. While this was concerning, it also supported our choice to investigate the full spectral reflectance curve, since the JAZ instrument still produces apparently reasonable values of the CIELAB coordinates without a warning, even when the underlying spectral reflectance curve is invalid.

Our analysis in the Year One Report raised questions about the sensitivity of the JAZ instrument to thermal noise, especially in the very hot conditions prevailing at Murujuga.

In the second year of research studies, we have deployed the JAZ instrument alongside the HDX instrument, which is a successor to the JAZ instrument, for comparison and validation.

We also conducted an experiment in which both JAZ and HDX instruments were placed in an incubator and operated at increasing temperatures. The experiment confirmed that the devices are sensitive to increasing internal heat, but also demonstrated that both instruments could be operated successfully — even at the extreme temperatures experienced at Murujuga — provided they are stored in a cool box between exposures, and are recalibrated before measuring each target.

For the field colour data measured by the JAZ instrument, the typical trend over the seven campaigns is that campaign 2 has the lowest percent reflectance, campaign 1 data are roughly in the middle, and campaigns 6 and 7 had the highest percent reflectance.

In campaign 7, we measured colour using the new HDX at nine rock art panels; the rest of the rock art panels were measured by the JAZ instrument, and three rock art panels were measured by both instruments.

Interactive software was developed for the JAZ and HDX instrument to identify errors in the colour measurements whilst visiting a rock art panel. This software was used during campaigns 6 and 7. During these campaigns, we were still refining the software to ensure all faults were identified while the operator was at the rock art panel, allowing the operator to remeasure these targets. By the use of this software, we have reduced the occurrence of faulty observations to a very low level. In the first field campaign, only 28% of rock art panel measurements were deemed valid; by campaign 7, over 97% of the JAZ measurements were deemed valid.

7.13.3 Industry data

Industry stakeholders have provided their observations of gas concentration using IVL and Radiello passive samplers. Preliminary analysis indicates no major discrepancies between the industry data and MRAMP data. Some higher concentrations were observed in the MRAMP data, particularly for SO_2. This is probably attributable to the much broader spatial extent of the MRAMP monitoring site network.

7.13.4 Inorganic geochemistry — *pH*, *Eh*, Cl^-

Analysis in Section 7.4 found striking differences in *pH* between different campaigns. Rainfall appears to have a substantial effect on *pH* over short periods, while differences due to spatial location and rock type appear to be far smaller.

Similar comments apply to the measures of chloride ion Cl^- concentration.

For the oxidation–reduction potential (*ORP*) measurements, differences between campaigns were relatively small, compared to the residual variability. No systematic differences were detected between rock types, or between spatial locations.

The three measurements *pH*, *ORP* and Cl^- did not appear to be correlated with each other.

It is provisionally concluded that measurements of rock surface *pH*, *ORP* and Cl^- concentration are not strong candidates for EQC development.

7.13.5 Inorganic chemistry – pXRF

The pXRF instrument provides readings of elemental composition of rock surfaces in situ, and is a useful aid in studying the geology of an area.

pXRF readings of the same rocks recorded during different field campaigns were compared. The readings are not expected to change from month to month, but there is variability between repeated measurements, due to the fact that the instrument is manually positioned over the rock surface, and possibly due to other factors. This analysis serves as a check on internal consistency of the technique. Redundancy analysis indicated that the results are consistent between campaigns.

Ratios of the percentages of two elements are often used to characterise rock types. We investigated the ratio of silica (SiO_2) to titanium (Ti) calculated from the pXRF readings for all rocks classified as belonging to a specific type, such as granophyre. The ratios had a highly skew distribution. There was no evidence of a spatial trend in the ratio of silica to titanium in granophyre. Similar conclusions were reached for other elemental ratios.

7.13.6 Inorganic geochemistry – porosity

In Section 7.6 it was concluded that there is statistically significant evidence of elevated porosity of granophyre surfaces in an area within the Murujuga study region.

The strongest evidence of elevated porosity was obtained at locations in the general vicinity of Dampier and King Bay. This finding emerged automatically from the analysis; the Dampier–King Bay area was not nominated for special attention in advance.

The conclusion that there is significant evidence of elevated porosity was based solely on the observed spatial variation in porosity index across the Murujuga study region. The analysis did not take account of any other explanatory variables which might have an effect on porosity. Such questions are tackled in Section 8.4.

7.13.7 Inorganic geochemistry – permeameter

A permeameter instrument was only recently added to the project, in an effort to obtain more information about variation in the microstructure of rock surfaces. Permeability measurements obtained in campaign 7 were, even for the same rock panel, highly variable in some cases. Rock panels where the permeameter readings were highly variable typically also had a high median permeameter reading. This may be related to the overall condition of the rock surface. Further investigation is required.

7.13.8 Microbiome

Analysis of microbial communities found in samples from the patina, from soil and from lichen was reported in Section 7.8. The microbiome of patina was distinctly different from that found in soil or lichen. The microbiome of patina had relatively low diversity, consisting mainly of genera that are known to tolerate high levels of UV radiation. There was some evidence of spatial variation in the patina microbiome, with certain species found to be more common in areas close to industry, while

other species predominated on the more remote islands. Fungal diversity in the patina appeared to be greater during dry periods than in wet periods.

7.13.9 Organic geochemistry

Section 7.9 described the organic chemistry data, which provide estimates of total organic carbon (TOC) percentage and the stable isotope ratio index $\delta^{13}C$ from samples extracted from rocks at the field sites.

Our exploratory analysis of these data has concentrated on the distribution of the data, overall summaries, and evidence for differences between sites, differences between rock types, and overall spatial trends, if present.

Samples from basalt recorded the highest $\delta^{13}C$ and lowest TOC. There was a moderate correlation between TOC and $\delta^{13}C$, which warrants further investigation. There was moderate evidence for a spatial trend across the peninsula in both TOC and $\delta^{13}C$, which also warrants validation and further investigation. A few very high values TOC and very large negative values of $\delta^{13}C$ were observed.

It is not expected that TOC and $\delta^{13}C$ on their own will necessarily provide conclusive information; however, when combined with other measures such as microbiome, biomass combustion (bushfire) data and anthropogenic air pollution data, they may add further evidence to other areas of investigation or may suggest areas where further source apportionment of the organic carbon compounds is needed.

7.13.10 Deposition sampler data

Analysis of data from the three bucket deposition sampler apparatus (Section 7.10) was confined to the “dry” bucket which is exposed to the atmosphere for the vast majority of the time).

The *pH* values exhibited appreciable differences between different dates, with particularly low *pH* values appearing to coincide with periods where low quantities of dust were deposited. There were some systematic differences between *pH* values at different sites.

Calculated deposition rates of Ca^{2+}, K^{+}, Mg^{2+}, Cl^{-}, Na^{+}, $SO_4{}^{2-}$, $NH_4{}^{+}$, $NO_3{}^{-}$ and P did not exhibit large seasonal variation nor systematic difference between sites.

7.13.11 Passive samplers

Passive sampler tubes are exposed in the field for one month, and retrieved for chemical analysis, which provides estimates of the average atmospheric concentration of various gases over the relevant month. Our analysis of the passive sampler data was reported in Section 7.11.

Gases associated with industrial output show strong seasonal changes in concentration. Some gases, particularly NO_2, also show consistent spatial patterns. NO_2 concentration is clearly higher close to the Dampier port area, but other gases show different patterns.

The study design specified that passive samplers should be placed at the AQ sites in duplicate (two identical tubes in the same housing) for each gas of interest. This allows us to validate the passive sampler data, and to estimate the intrinsic variability of the technique, and thereby to estimate

the underlying natural variation in gas concentration. Analysis of these duplicate observations indicated that the intrinsic variability of the technique is generally acceptable. SO_2 is the exception, and continues to show much higher relative differences across the IVL samplers.

The study design also specified that two monitoring sites should be placed close together. This allows us to estimate the short-scale spatial variability in gas concentration, also serves to validate the overall design of the monitoring installations. Analysis of passive sampler data from the two co-located sites AQ07 and AQ08 indicated good agreement between the two sites for NO_2, SO_2, NH_3, O_3 and HNO_3.

VOC monitoring data are available up to December 2023. These measurements continue to show quite low levels with many observations classified as Below Detection Limit. For n–octane and n–nonane, detectable levels are nearly all recorded from the site near the Dampier port.

7.13.12 Real time powered sites

The real-time air quality monitoring systems provide data on the atmospheric concentrations of important gases at the three site locations every five minutes. Data from a fourth real-time monitoring station are also provided to us retrospectively every month.

A striking feature of these data is the presence of sharp peaks in gas concentration at certain times of day. Particularly high peaks are observed for NO, and peaks are also observed for SO_2 and NO_2. Peaks are also observed in the atmospheric density of particulate matter $PM_{2.5}$. These peaks may be associated with combustion events and may depend on the prevailing wind direction. The presence of short-term peaks in gas concentration may influence the appropriate choice of EQC.

Various technical difficulties were encountered while installing and validating the real-time monitoring systems. The ammonia instrument is not yet validated. The data that has been collected so far is voluminous but represents a relatively short duration of observation, which limits our ability to draw conclusions.

This page is intentionally blank.

8 Associations between variables

This section presents our statistical investigation of relationships or associations between variables recorded in the different component studies. Some of the analysis provides a cross-check on the validity of the techniques. Other analysis provides new findings on relationships between processes occurring at Murujuga. Key findings of this section are summarised in Section 8.6.

The plan of the section is as follows. Section 8.1 compares the bucket deposition samplers with the passive samplers. Section 8.2 compares the microbiome data obtained from rock surfaces with the underlying rock composition and porosity. Section 8.3 compares the passive sampler data with the Ramboll model predictions. Section 8.4 investigates whether the elevated porosity of rock surfaces in the vicinity of the industrial/port/town area can be explained by other variables. Section 8.5 compares IVL passive sampler data provided by Woodside with IVL passive sampler data collected in the MRAMP. Finally Section 8.6 summarises key findings.

8.1 Deposition versus passive samplers

8.1.1 Background

The three-bucket deposition samplers (Section 7.10) collect material deposited from environmental air into the “dry” bucket unless precipitation is occurring. The passive samplers (Section 7.11) are continuously exposed to environmental air. Both the passive samplers and bucket samplers are collected periodically, but the sampled material is assayed for different sets of chemical species and particle populations. For validation and calibration, it is important to compare the two kinds of observations, although they are not strictly equivalent measurements.

8.1.2 Comparison of “dry” deposition with passive samplers

There are some difficulties in reconciling the time series of deposition sampler data and passive sampler data because of asynchronous dates, missing data and artefacts. This requires further methodological development.

One important question is whether there are systematic differences between the sites (for example, differences due to a consistent gradient across Murujuga in the level of exposure to industrial output) and, if so, whether the same pattern of systematic differences is observed in the dry deposition samples and in the passive samples. Accordingly, passive SO_2 and dry deposition SO_4^{2-} sampler data were compared, passive NH_3 and dry deposition NH_4^+ sampler data were compared, and passive NO_2 and dry deposition NO_3^- sampler data were compared, in Figures *8.1-1* to *8.1-3*. Each plot shows “skeleton 2D boxplots” in which the central dot is the median of each variable (that is, the median of passive sample concentration estimates is plotted against the median of deposition concentrations) and the line segments represent the 95% confidence intervals for the true mean values of each variable, computed using the standard formula for independent Normally distributed observations.

When interpreting Figures *8.1-1* to *8.1-3*, it needs to be understood that the medians and confidence intervals for each site were computed from all the available data for the site in question, collected at different calendar dates. Seasonal variation was not explicitly taken into account. The sample

median for each site can be interpreted as an estimate of the overall annual median value at that site. The confidence interval for each site is an interval estimate of the overall annual average at that site; however, it is conservative (its coverage probability is likely to be much greater than the nominal 95%). The width of the confidence interval was calculated under the assumption that the monthly observations are independent; seasonal variation is conflated with random variation, leading to an inflated estimate of variability and an excessively wide confidence interval.

Figure *8.1-1* suggests that passive sample SO_2 and dry deposition sample SO_4^{2-} are positively associated.

Figure *8.1-2* suggests that passive sample NO_2 and dry deposition sample NO_3^- are strongly positively associated. We note the extreme values observed at sites AQA1, EX02 and EX09.

Figure *8.1-3* suggests only weak evidence of association between passive sample NH_3 and dry deposition sample NH_4^+.

Table *8.1-1* shows the Pearson and Spearman rank correlation correlation coefficients between the median of “dry” deposition vs passive samplers. The passive sample NO_2 and dry deposition sample NO_3^- have a statistically significant, strong positive relationship.

Table 8.1-1: Pearson and Spearman rank correlation coefficients between corresponding measurements from the “dry” deposition samplers and passive samplers. Statistically significant correlations are shown in bold type, and annotated with one asterisk for $p < 0.05$, two asterisks for $p < 0.01$ and three asterisks for $p < 0.001$.

“dry” deposition	passive sampler	Pearson	Spearman
SO_4^{2-}	SO_2	0.373	0.309
NO_3^-	NO_2	**0.782*****	**0.627****
NH_4^+	NH_3	-0.035	0.090

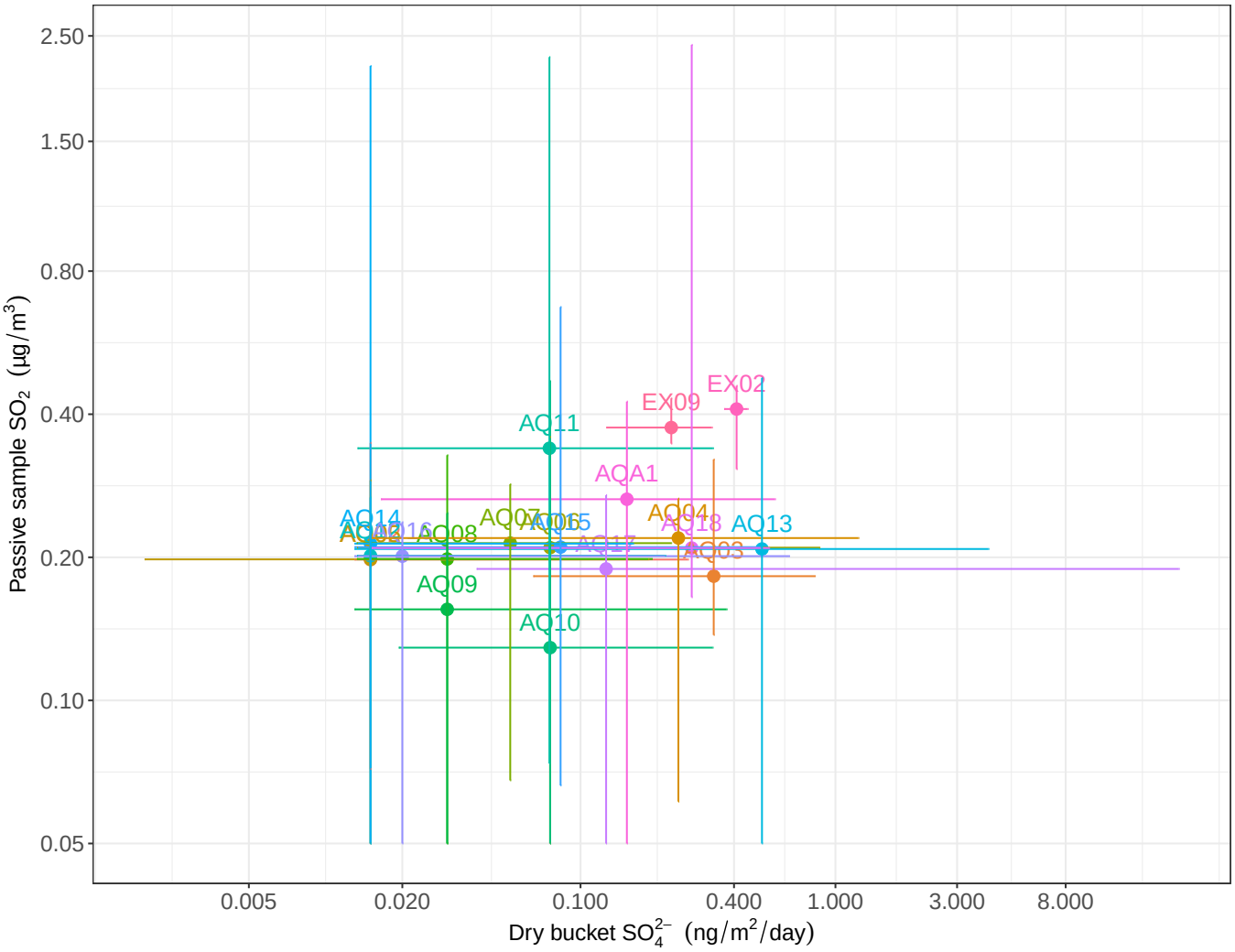

Figure 8.1-1: Simplified 2D boxplots of dry bucket SO_4^{2-} and passive sampler SO_2 from each AQ and EX site. The points are the median SO_4^{2-} and the median SO_2, and the horizontal and vertical lines are are approximately 95% confidence intervals for the means. Note logarithmic scale in both axes. Data between May 2023 and December 2023.

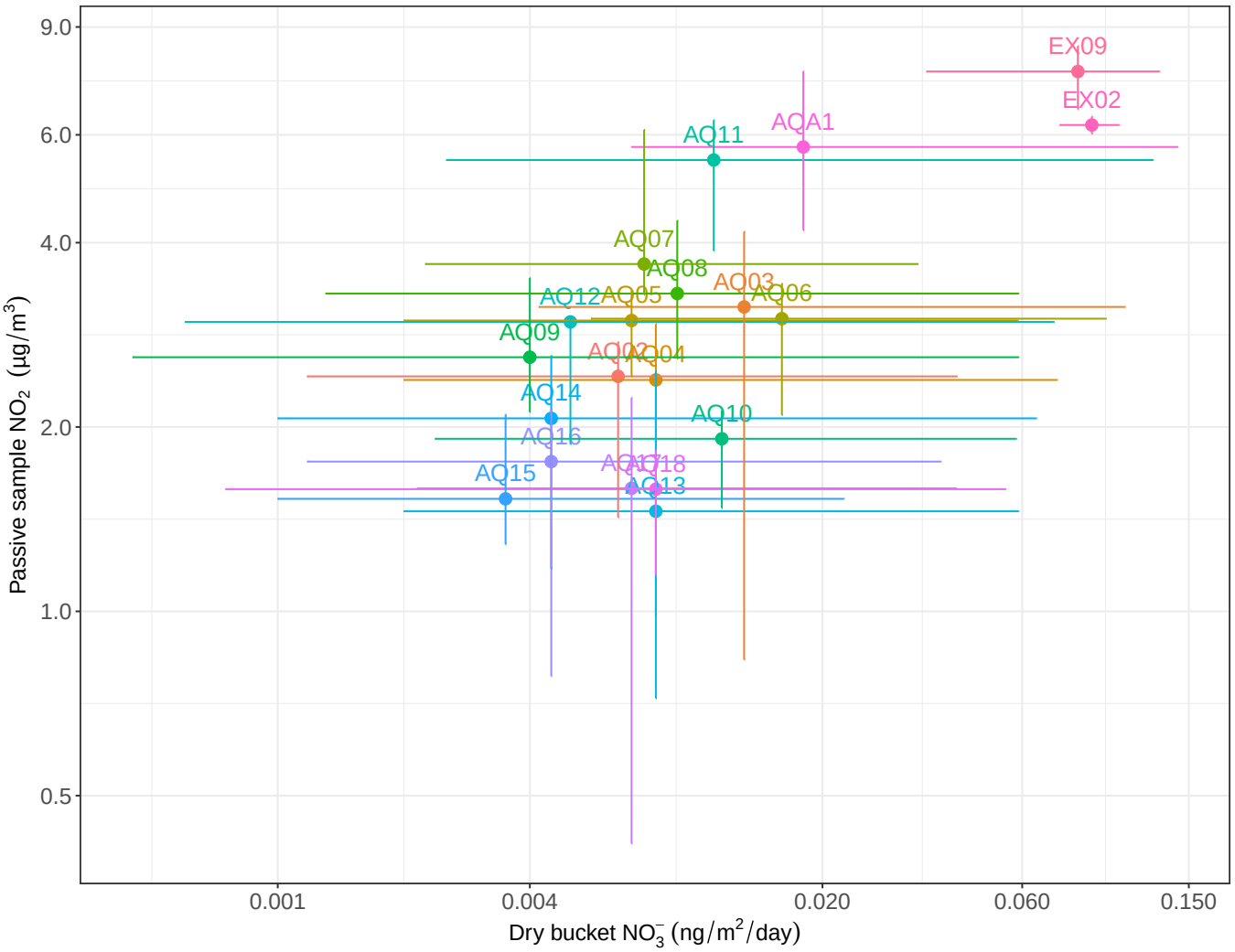

Figure 8.1-2: Simplified 2D boxplots of dry bucket NO_3^- and passive samples NO_2 from each AQ and EX site. The points are the median NO_3^- and the median NO_2, and the horizontal and vertical lines are approximately 95% confidence intervals for the means. Note logarithmic scale in both axes. Data between May 2023 and December 2023.

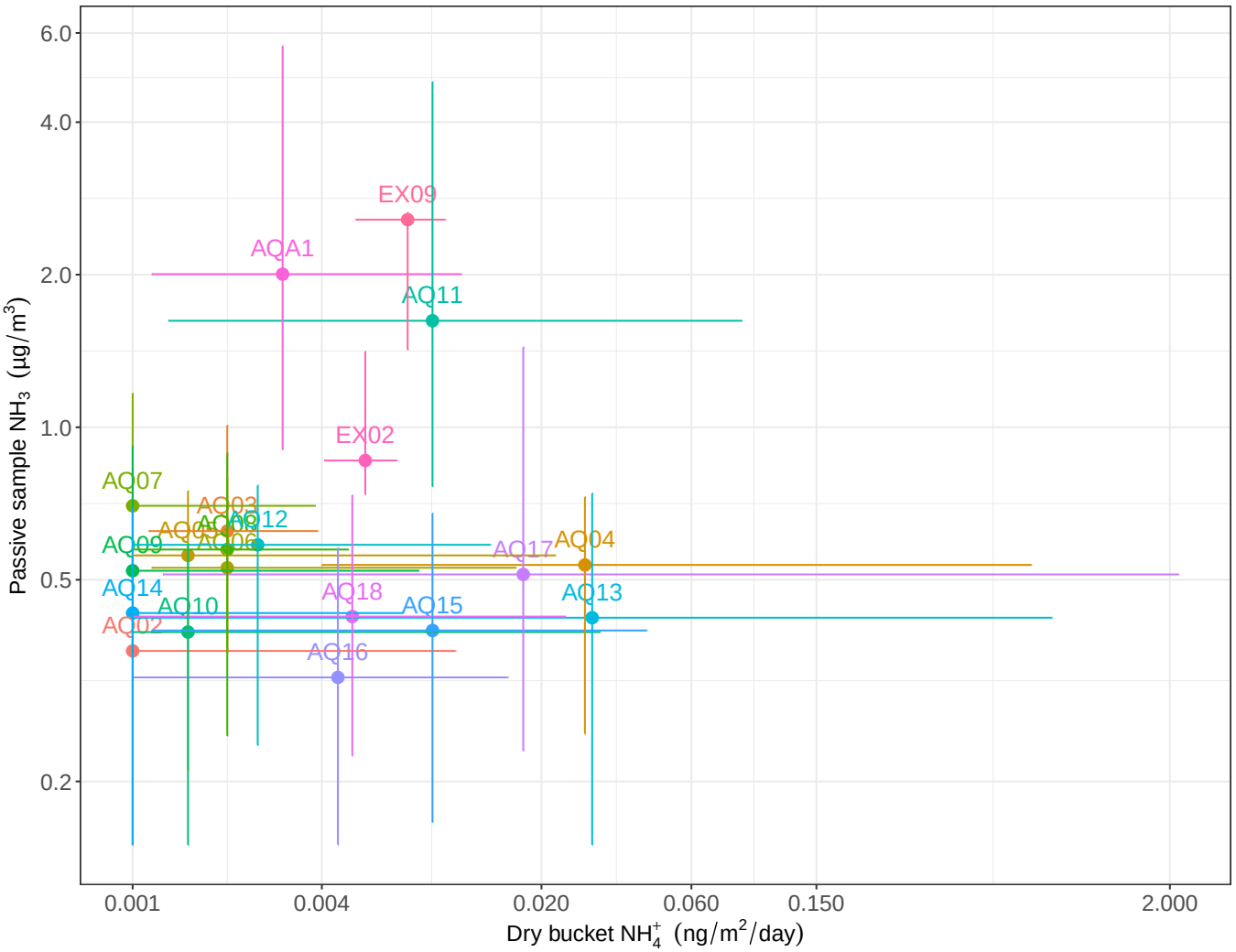

Figure 8.1-3: Simplified 2D boxplot of dry bucket NH_4^+ and passive sampler NH_3 from each AQ and EX site. The points are the median NH_4^+ and the median NH_3, and the horizontal and vertical lines are approximately 95% confidence intervals for the means. Note logarithmic scale in both axes. Data between May 2023 and December 2023.

We expect that further statistical analysis and modelling, to be conducted in the next report, will explicitly include seasonal effects, and will provide more accurate confidence intervals for annual average values and seasonal trends, enabling a more searching analysis of relations between the variables.

8.2 Microbiome versus other variables

8.2.1 Background

It is important to investigate the underlying connection between the chemistry, structures and processes of patina formation occurring at Murujuga.

Current literature aimed at understanding the formation of rock varnish and the enrichment of manganese and iron in the varnish, points to the dual action of biotic and abiotic processes (reviewed in Dorn, 2024). Recent research has highlighted the role of photosynthetic bacteria in manganese enrichment in desert varnish (Lingappa et al., 2021; Yeager, 2019). Lingappa et al. (2021) show evidence that *Cyanobacteria*, and specifically *Chroococcidiopsis*, is able to accumulate high quantities of Mn^{2+} which allows it to combat oxidative stress. Lingappa et al. (2021) hypothesise that during periods of water availability, *Cyanobacteria* sequester manganese in their cells as part of their anti-oxidant strategy, and following cell death, the biomass provides an enriched manganese source that is oxidised and cemented into the varnish layers. Manganese accumulation has been observed not only in *Cyanobacteria*, but also in the extreme radiation resistant *Deinococcus radiotolerans* (Daly et al., 2004).

We have observed a range of concentrations of manganese in the patinas sampled in this research (Section 4.2.8.1), as well as an abundance of microbes (Section 7.8) that have been hypothesised to be involved in patina formation. It is of interest to investigate whether increased abundance of these microbes is associated with an increase in MnO concentrations. This will give us an indication as to whether microbes believed to be associated with patina formation are still present and may be contributing to the increased MnO concentrations. It is currently hypothesised, but not proven, that patina is not currently being formed at Murujuga any more. If this is true, then this might affect weathering rates because the substrate, without the patina coverage, might become more exposed to physical or chemical weathering. Conversely, patination may increase dissolution within the weathered rind, if aqueous solutions that pass through the patina become more susceptible to mineral dissolution by the addition of organic acids or other components. These details are not yet known.

8.2.2 Association between microbiome and rock composition

The elemental composition of rocks was measured in the field using the pXRF instrument (Section 7.5). Here we investigate evidence for an association between the composition or diversity of microbial communities and the elemental composition of the host rock.

Spearman rank correlations, between the pXRF data taken from the sample rocks and the microbial community abundance, were calculated to assess evidence for any association between the abundance of microbial taxa and the elemental composition of the host rock.

For bacteria, the top 50 most abundant genera in the dataset were used. Multiple genera were positively correlated with Fe, Mn, As and Pb, as shown in Figure *8.2-1*. This figure is a heat map diagram which depicts the Spearman correlation values as colours, organised in a table in which the rows represent microbial taxa and the columns represent elements. Rows have been arranged in an order which maximises the separation of clusters of taxa that were identified using a hierarchical clustering algorithm, with the clustering dendrogram depicted at the left of the table.

Similarly, columns have been arranged in an ordering which separates clusters of elements, with the clustering dendrogram shown at the top of the diagram. Blocks of consistently red or consistently blue colour in the diagram suggest a relationship between clusters of taxa and clusters of elements.

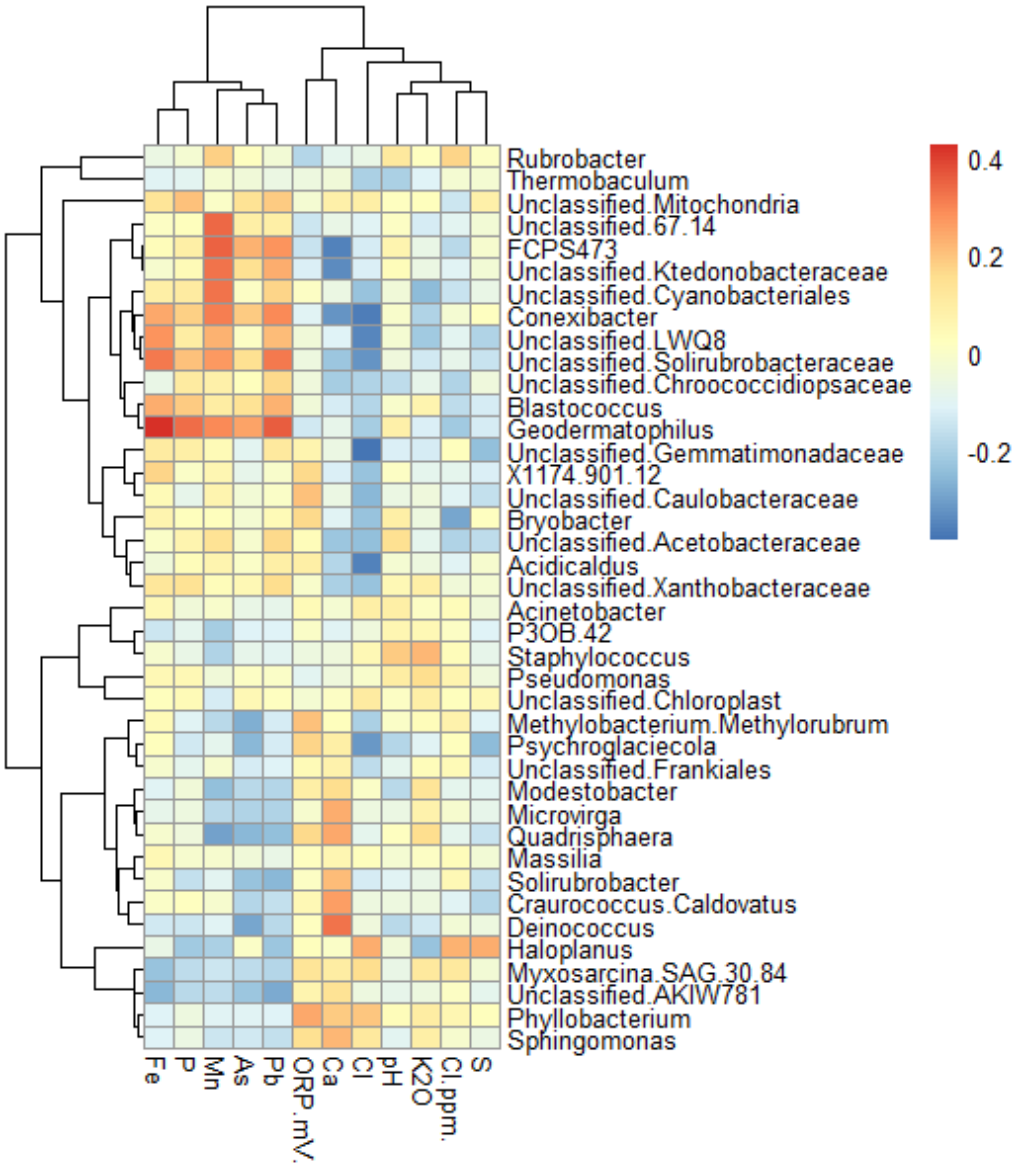

Figure 8.2-1: Heatmap display of Spearman rank correlation between the pXRF elemental composition data and the abundance of the top 50 genera across patina samples.

Spearman rank correlation of the fungi genera with the pXRF elemental data and other rock surface measurements indicates the unclassified *Ascomycota* have a moderate positive correlation with Pb, P, Fe and Mn as shown in Figure *8.2-2*. Fe and Mn are important elements to consider in this dataset due to their association with the formation of the patina on the rocks. *Spissiomyces* has a moderate negative correlation with S. These elements will be important in further analysis to understand how these fungal communities in Murujuga are responding to their environment and what that might mean for the patina's integrity.

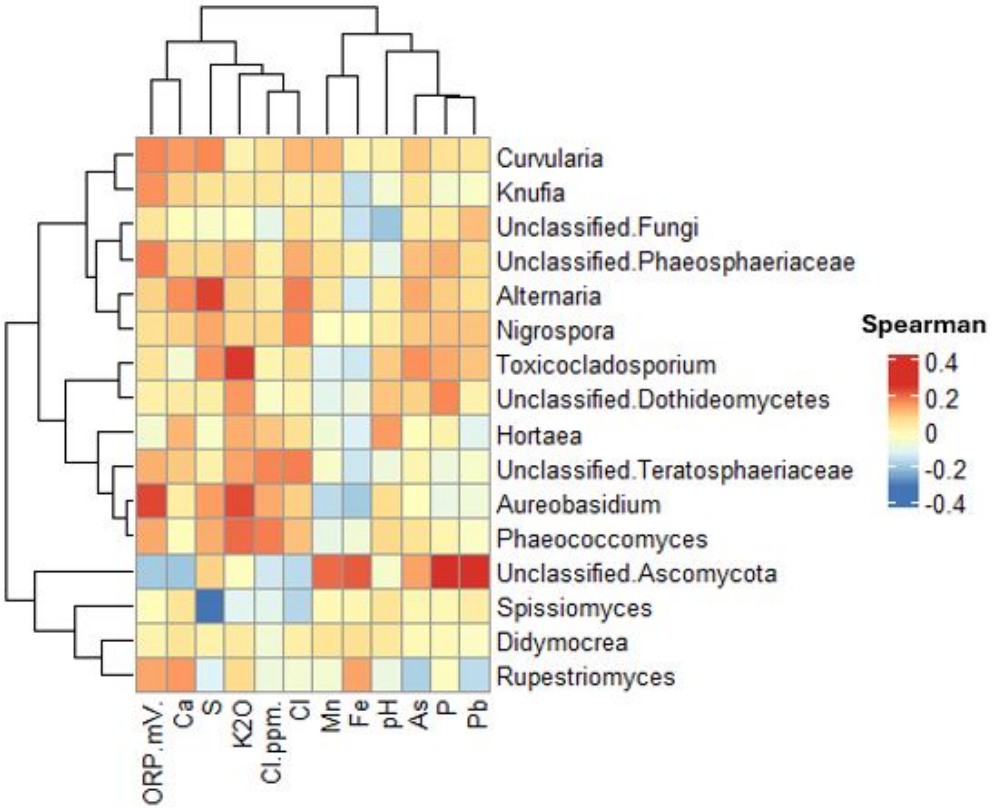

Figure 8.2-2: Heatmap display of Spearman rank correlation of the environmental data with the abundance of Fungi Genera across patina samples.

8.2.3 Association between bacteria and inorganic compound concentrations

Micro- and macro-structural characterisation of the patina, including the concentrations of inorganic compounds in the rock, was reported in Section 4.2.7. There is particular interest in manganese oxide MnO, as explained above.

This section investigates whether any of the abundant bacteria identified in the 16S amplicon data are positively or negatively associated with the MnO concentrations (from the EMP analysis of the patina). Both abundance values and MnO concentration values do not follow a normal distribution. Specifically, the MnO data contain a large number of values close to zero, while the abundance data contain a large number of zeros. Therefore, associations between these variables were investigated using the Spearman rank correlation. The classical Spearman correlation test (with two-sided alternative) was applied to assess whether there was an association between MnO concentrations and abundance of different bacteria. Detailed description of the Spearman rank correlation is provided in Section 7.11.3. This analysis will help determine if any particular bacteria are associated with sample rocks that has a higher MnO concentration, which is associated with a thicker patina.

Table *8.2-1* shows the Spearman rank correlations with MnO. *Cyanobacteria* abundance in both wet and dry sampling seasons had highly significant evidence of positive correlation with MnO concentrations, however the estimated correlation was only moderately large (ρ = 0.42) in the dry

season and rather weak (ρ = 0.23) in the wet season. A similar trend was also observed for taxa within the *Cyanobacteria*. For the family *Chroococcidiopsidaceae* both sampling seasons yielded a significant positive correlation with MnO, the dry season having a moderate correlation and the wet season having a weak correlation. *Blastococcus* spp. had a negligible negative correlation with the MnO concentrations, of which dry season was not significant. *Geodermatophilus* spp. was the only genus with a statistically significant but weak negative correlation with MnO in both seasons, suggesting *Geodermatophilus* spp. are less abundant on patinas that have thicker patina. *Rubrobacter* spp. had a significant weak positive correlation with MnO, across both sampling seasons.

This analysis strongly suggests that the *Cyanobacteria* phylum and *Chroococcidiopsidaceae* family have an increased abundance on sample rocks with a higher MnO concentration. This is important information since *Cyanobacteria* have been identified as important microbial players in concentrating manganese in desert varnish. Although, this analysis alone is not sufficient to conclude that patina formation is still occurring at Murujuga.

Table 8.2-1: Spearman rank correlation ρ between bacterial taxa and MnO. Statistically significant correlations are shown in bold type and annotated with one, two or three asterisks representing statistical significance at the 0.05, 0.01 and 0.001 level respectively.

Bacterial taxon	Season	Spearman's rho
Cyanobacteria	"wet"	$\mathbf{0.23}^{***}$
Cyanobacteria	"dry"	$\mathbf{0.42}^{***}$
Chroococcidiopsidaceae	"wet"	$\mathbf{0.28}^{***}$
Chroococcidiopsidaceae	"dry"	$\mathbf{0.39}^{***}$
Blastococcus	"wet"	$-\mathbf{0.12}^{***}$
Blastococcus	"dry"	-0.04
Geodermatophilus	"wet"	$-\mathbf{0.27}^{***}$
Geodermatophilus	"dry"	$-\mathbf{0.30}^{***}$
Rubrobacter	"wet"	$\mathbf{0.27}^{***}$
Rubrobacter	"dry"	$\mathbf{0.37}^{***}$

8.2.4 Association between bacteria and rock porosity

Next, evidence for an association between the composition or diversity of bacterial communities and the porosity of the rock surface is investigated. Numerical indices of porosity of the surface layers of sample rocks were determined in Section 7.6. The selected index was the average porosity (depths 0 to 3.1 mm), which were computed from granophyre rock sample images obtained from sites across Murujuga, with morphological opening radius 20 μm.

Both porosity and abundance data are non-negative. The distribution of the average porosity is approximately lognormal or gamma (Figure *7.6-5* on page 291), while the bacterial abundance data contain a large number of zeros (as described above). Therefore, Spearman rank correlation was again used to assess association between the porosity index and the abundance of different bacteria. Section 7.8 found some species to be more common in areas close to industry, while

other species predominated on the more remote islands. This analysis will help determine whether any particular bacteria are associated with sample rocks that have higher porosity.

Bacterial abundance at different taxonomy levels were compared to the average porosity (Table *8.2-2*). Unlike MnO, only the *Cyanobacteria* phylum and *Chroococcidiopsidaceae* spp. had a significant positive correlation with porosity for both seasons. All other taxonomy tested had no significant correlation with porosity. *Cyanobacteria* and Cyanobacterial biofilms have been previously identified as major sources of rock pitting and bioweathering (Ljaljević-Grbić et al., 2010; Rabbachin et al., 2022). This analysis is insufficient to infer that the *Cyanobacteria* at Murujuga are responsible for high porosity. It will be essential to see the meta-transcriptomic sequencing to assess the abundant of genes involved in biofilm formation, Mn accumulation, mineral transformation, etc., in order to gain a clearer understanding of how *Cyanobacteria* at Murujuga are interacting with the rock surface and the environment surrounding.

Table 8.2-2: Spearman rank correlation ρ between each bacterial taxon and average porosity (0 to 3.1 mm depth). Statistically significant correlations are shown in bold type and annotated with one, two or three asterisks representing statistical significance at the 0.05, 0.01 and 0.001 level respectively.

Bacterial taxon	Season	Spearman rho
Cyanobacteria	"wet"	**0.23*****
Cyanobacteria	"dry"	**0.22*****
Chroococcidiopsidaceae	"wet"	**0.15*****
Chroococcidiopsidaceae	"dry"	**0.21*****
Blastococcus	"wet"	0.30
Blastococcus	"dry"	-0.03
Geodermatophilus	"wet"	0.08
Geodermatophilus	"dry"	0.05
Rubrobacter	"wet"	-0.02
Rubrobacter	"dry"	-0.08

8.2.5 Association between bacteria, inorganic compound concentrations and rock porosity

In this section, Redundancy Analysis (RDA) was applied to explore the relationship between bacterial taxa, inorganic compound concentrations, porosity indices and site information (for an outline of RDA see Section 7.5). The analysis above, using Spearman rank correlation, only investigated the association between microbial taxa and the MnO concentrations from the EMP analysis of the patina. Here all concentrations from the EMP analysis were included in the RDA. All abundance data for bacterial taxa analysed above were included as input to this RDA. This analysis also included both of the porosity indices described in Section 7.6, namely the average porosity (depths 0 to 3.1 mm depth) and maximum porosity. Various site information was included as input to the RDA, including the season (wet and dry), rock type, site names, elevation, northing and easting.

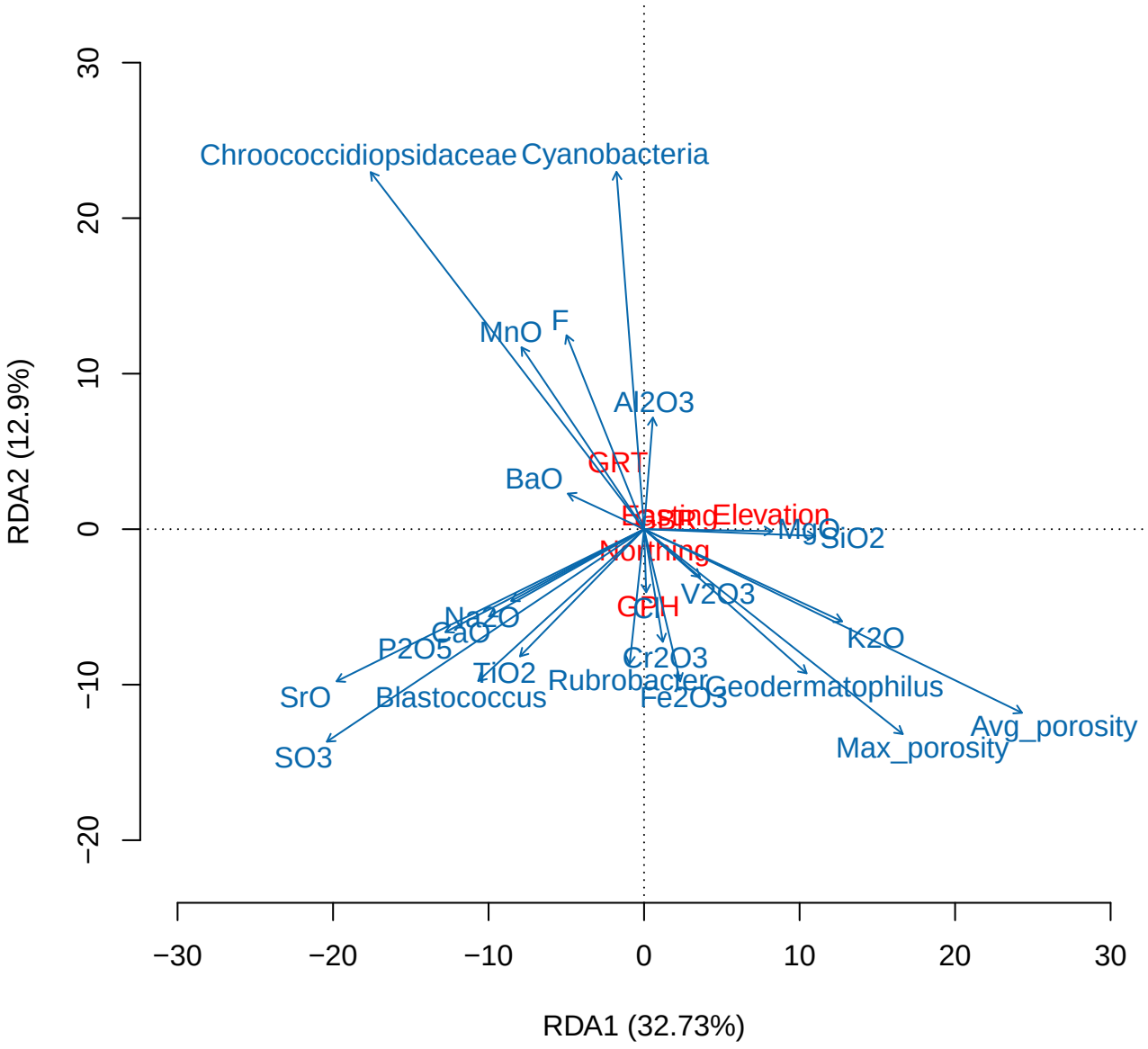

Figure 8.2-3: RDA biplot showing the relationship between bacteria taxa, inorganic compound concentrations, porosity indices and site information. Percentage in parentheses is the percentage of total variation explained by the RDA.

Figure *8.2-3* shows the RDA biplot displaying the relationship between bacteria taxa, inorganic compound concentrations, porosity indices and site information. The results indicate that almost 46% of the total variation is explained by the first two principal components.

Chroococcidiopsidaceae was negatively correlated with both porosity indices (average and maximum)

and *Geodermatophilus*. *Chroococcidiopsidaceae* was positively correlated with MnO, BaO, F and granite (GRT).

Cyanobacteria was positively correlated with F, Al_2O_3 and GRT. *Cyanobacteria* was negatively correlated with *Rubrobacter*, *Geodermatophilus*, granophyre (GPH), Cr_2O_3, Fe_2O_3 and maxium porosity.

Elevation was not correlated with all bacteria taxa, except for *Geodermatophilus*, but elevation was positively correlated with MgO and SiO_2. Since the arrow corresponding to elevation is inclined at a 30 to 45 degree angle to the arrow representing *Geodermatophilus*, and similarly to both the maximum and average porosity, this indicates some level of correlation, though it is not particularly strong.

Blastococcus is positively correlated with TiO_2, SO_3, SrO, P_2O_5, CaO and Na_2O.

Note that season and site names were excluded from this biplot because these variables had an almost negligible effect on the total variation explained by the RDA.

This page is intentionally blank.

8.3 Ramboll model versus passive sampler data

8.3.1 Background

A pivotal issue is whether there are measurably different levels of exposure to industrial output at different locations across Murujuga. Previous studies were criticised for assuming, without evidence, that some locations at Murujuga are not exposed to any industrial output and can therefore serve as "control" locations. Instead, the MRAMP study relies on the expectation that there will be a spatial gradient across Murujuga in the level of exposure to industrial output, so that when the level of exposure at each location is known, a regression analysis can identify any relationship that might exist between the exposure to industrial output and the deterioration of rock condition.

Supporting evidence for the existence of such a gradient was presented in the original study design using an early version of the Ramboll data (Ramboll Australia, 2022). These data are outputs of a model which incorporates meteorological inputs (actual weather observations and interpolated weather states according to a weather-forecasting model) and known or assumed sources of pollution, to predict atmospheric concentrations of various gases at a grid of spatial locations at different times.

8.3.2 Data extraction and processing

The Ramboll models used meteorological inputs taken from the calendar year 2014, which was considered a typical year for the weather around Murujuga. The weather forecasts were cross-checked against actual meteorological observations from 2014. There are two datasets available from the Ramboll model outputs:

- for the calendar year 2014, incorporating current known sources of emissions; and
- for a hypothetical year 2030, assuming the same meteorological inputs as 2014 but with additional proposed/approved industrial facilities included.

Both the 2014 and 2030 scenarios were evaluated as part of the analysis and no substantial differences in the relationships were found using either dataset.

The Ramboll data are available at grid resolutions of 1.3 km and 4 km, but for statistical analyses only the 1.3 km grid data were extracted, which match the grid cells used in the MSDCA Plan study design. Gas concentrations in the model were provided in μ mol/m^3 (micromoles per cubic metre) and were converted to ng/m^3 (nanograms per cubic metre) for analysis.

In the Year One Report (Curtin University, 2022), Ramboll model predictions of gas concentration were used as a proxy for field observations of gas concentration, which were unavailable at that time. In this section, the Ramboll model predictions are compared to the IVL passive sampler data. Passive samplers were deployed in the field over varying time periods of approximately three to four weeks, and subsequently analysed in the IVL laboratory to provide a calculated average concentration of the nominated gas species over the exposure period. For mapping purposes, these observations were mapped to the month in which the majority of the sampling period occurred (the majority month).

In order to compare the observed concentrations of gases at the AQM sites with their predicted concentrations under the Ramboll model, the Ramboll predictions for each grid cell containing an

AQM site were extracted, yielding a time series of one year's duration for each gas and each site. Average and maximum values for each calendar month were then computed for each site. The sites AQA1 (a test site next to the MAC office) and AQ01 were unintentionally omitted.

The mean and maximum Ramboll gas predictions needed to be converted to μ g/m^3. In the previous report, Ramboll predictions were believed to be in milli-mols per cubic metre. However, after further review, this has been revised to parts per million by volume (ppmV). This may result in some mismatch between values in this report compared to the Year One Report, but as this is a simple matter of scaling, it should not affect conclusions about the patterns of gas concentration and field observations from the earlier campaigns.

Gases were compared first by month, where Ramboll months corresponded to the majority month of IVL sampling period. An averaged IVL value across all the sampling periods was also determined for each gas by calculating the weighted average of the IVL estimates of gas concentration with weights proportional to the duration of the sample period. Ramboll data was averaged over the majority months corresponding to the sample periods.

8.3.3 Comparison to Ramboll gas predictions

8.3.3.1 Passive sampler data against average gas concentration in the relevant month

Figure *8.3-1* compares the IVL gas measures with both the mean monthly Ramboll and maximum monthly Ramboll estimates for each AQM station. In these plots the colours indicate months, with data available for all 12 months from November 2022 to October 2023 for some gases. Appendix *G*.5 shows the monthly comparisons for each gas in separate panels.

In Figure *8.3-1*, overall the Ramboll maximum estimates per month (triangles) are a good deal higher than both the Ramboll average monthly estimates and IVL measurements, as would be expected. The IVL observations are generally lower than the mean monthly Ramboll estimates for SO_2, NO_2 and HNO_3.

Figure *8.3-1*(a) shows values for SO_2. In this plot the Ramboll mean estimates (plus signs) are generally higher than the IVL measurements (squares), but there are some overlaps, especially for the very high IVL observations. SO_2 IVL measurements are similar to the Ramboll estimates for January through March, and then seem to be distinctly lower for most other months. The IVL data does show some very high values, similar to maximum values for a few stations, particularly in February and December (plus one high observation each in January and March). Both the IVL observations and Ramboll estimates show quite a lot of variation across stations, but there is no clear trend and the variations are not always the same. (Figure *G.5-4* on page 716 in Appendix *G*.5 shows the SO_2 IVL measurements and Ramboll estimates for each month individually.)

Figure *8.3-1*(b) shows values for NO_2. In this plot the Ramboll mean estimates (plus +) are generally higher than the IVL measurements (squares). Although the NO_2 IVL measurements are up to an order of magnitude lower than the Ramboll estimates in some places, they show similar trends across most months. (Figure *G.5-1* in Appendix *G*.5 shows the NO_2 IVL measurements and Ramboll estimates for each month individually.)

Figure *8.3-1*(c) displays the values for NH_3. The IVL measurements and the Ramboll estimates overlap to a large extent but a number of IVL measures are higher than the Ramboll estimates.

There are also a number of IVL measurements that were below the detection limits. Figure *G.5-2* in Appendix *G*.5 shows the NH_3 IVL measurements and Ramboll estimates for each month individually. From January to April and in December, the NH_3 Ramboll predictions are lower than the IVL measurements, but for the other months, they are similar. Again there are similar trends between IVL observations and Ramboll predictions across stations.

Figure *8.3-1*(d) shows values for HNO_3. Figure *G.5-5* in Appendix *G*.5 shows the HNO_3 IVL measurements and Ramboll estimates for each month individually. Ramboll predictions seem fairly flat across different months and stations, while the IVL observations show distinct monthly variations, differences between stations also seem to vary monthly.

Values for O_3 are displayed in Figure *8.3-1*(e) and in Figure *G.5-3* in Appendix *G*.5 for each month individually. There is substantial agreement between the IVL measurements and the Ramboll estimates, but some IVL measurements are higher than the Ramboll estimates, particularly June, September and October. Conversely, most IVL measurements are slightly lower in February and March. Although there are distinct monthly differences, the variations between stations appear relatively small.

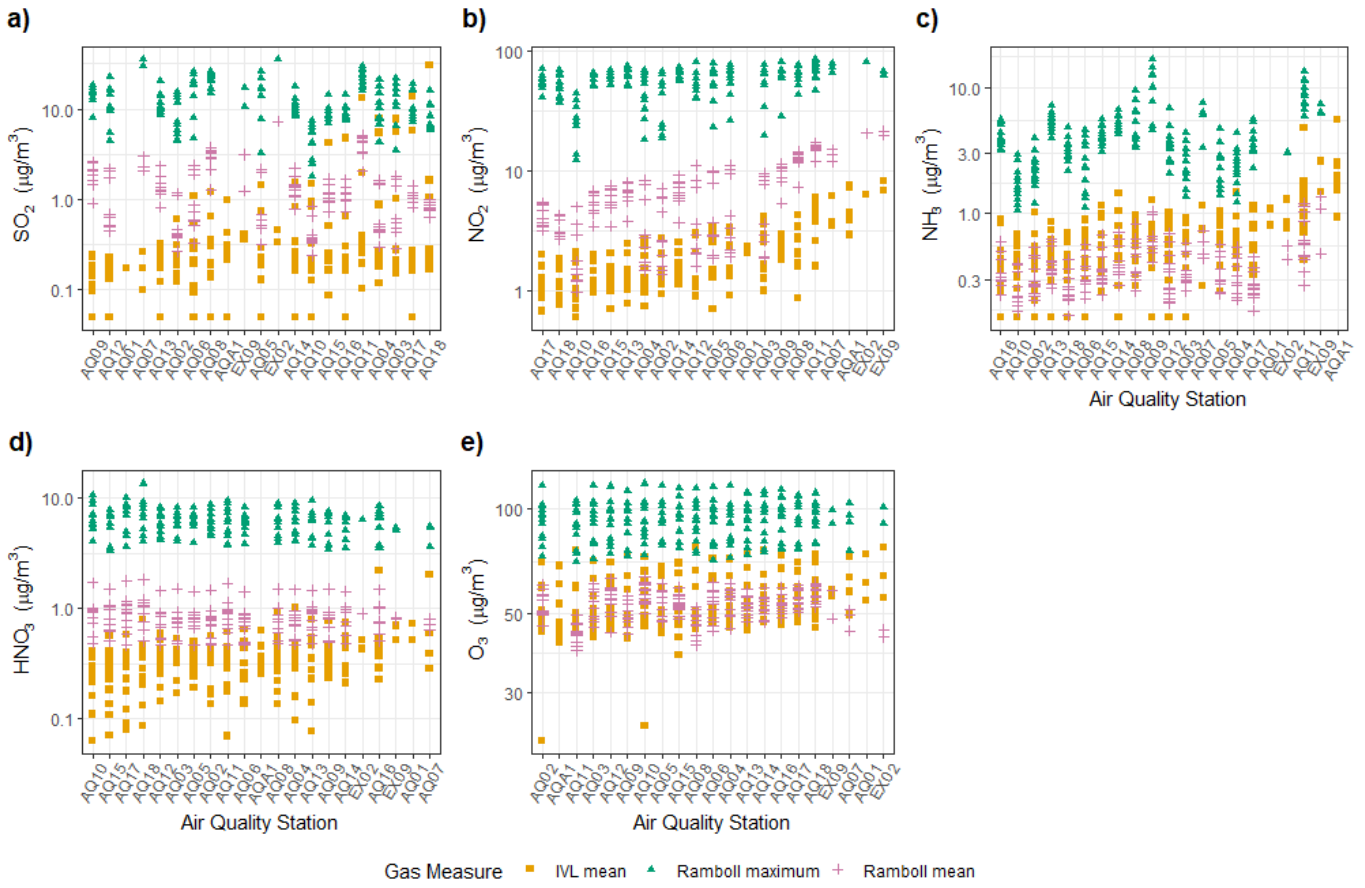

Figure 8.3-1: Gas concentrations measured by passive IVL samplers, and mean and maximum monthly Ramboll predictions, by station for each gas. Gases shown are (a) SO_2, (b) NO_2, (c) NH_3, (d) HNO_3 and (e) O_3.

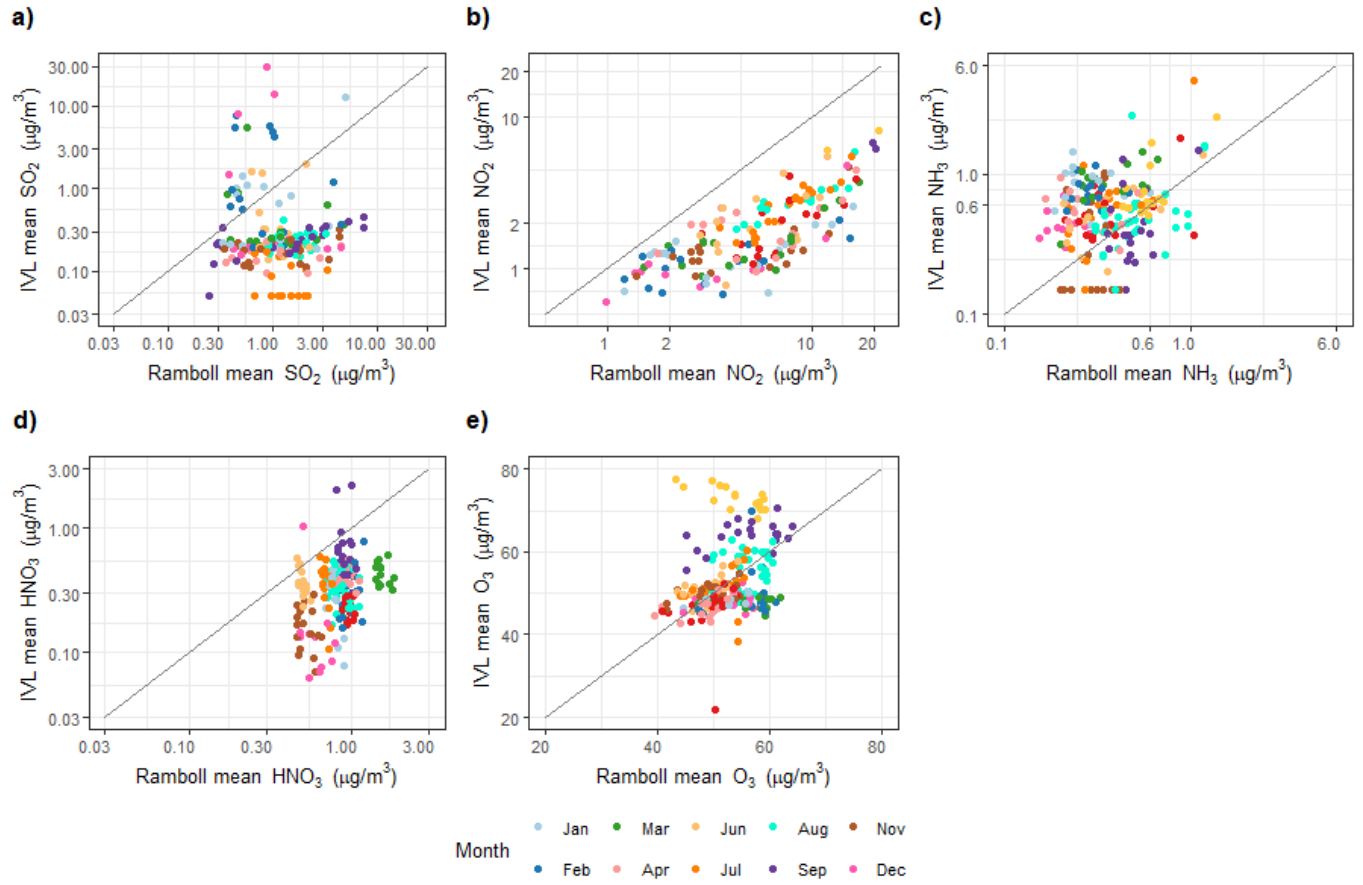

Figure 8.3-2: Passive IVL samplers by mean Ramboll predictions, coloured by month for each gas. Gases shown are (a) SO_2, (b) NO_2, (c) NH_3, (d) HNO_3 and (e) O_3.

Figure *8.3-2* and *8.3-3* show scatterplots of the IVL passive sampler measurements versus the Ramboll monthly estimates for each gas; the points in Figure *8.3-2* are coloured by month and Figure *8.3-3* the points are coloured by AQM station. Table *8.3-1* shows the results for the Spearman rank correlation test between the IVL measurements and monthly mean Ramboll predictions, displaying the sample rank correlation (Spearman's rho) and p-values for each gas.

Figures *8.3-2*(a) and *8.3-3*(a) show no clear pattern relating SO_2 IVL passive sampler measurements with Ramboll monthly estimates. There was a wide range of SO_2 IVL values, so a log scale has been used. Table *8.3-1* shows there was no significant correlation between SO_2 IVL and Ramboll values. Figure *8.3-2*(a) shows there was a number of very high SO_2 readings in February, March and December. Figure *8.3-3*(a) shows strong vertical grouping which relates to specific AQM stations.

For NO_2, there appears to be an approximately linear relationship between IVL measurements versus Ramboll monthly estimates (Figure *8.3-2*(b) and *8.3-3*(b)). Table *8.3-1* shows a significant strong correlation between NO_2 IVL measurements and Ramboll predictions. Figure *8.3-3*(b) shows NO_2 Ramboll predictions for a few stations cluster in distinct ranges.

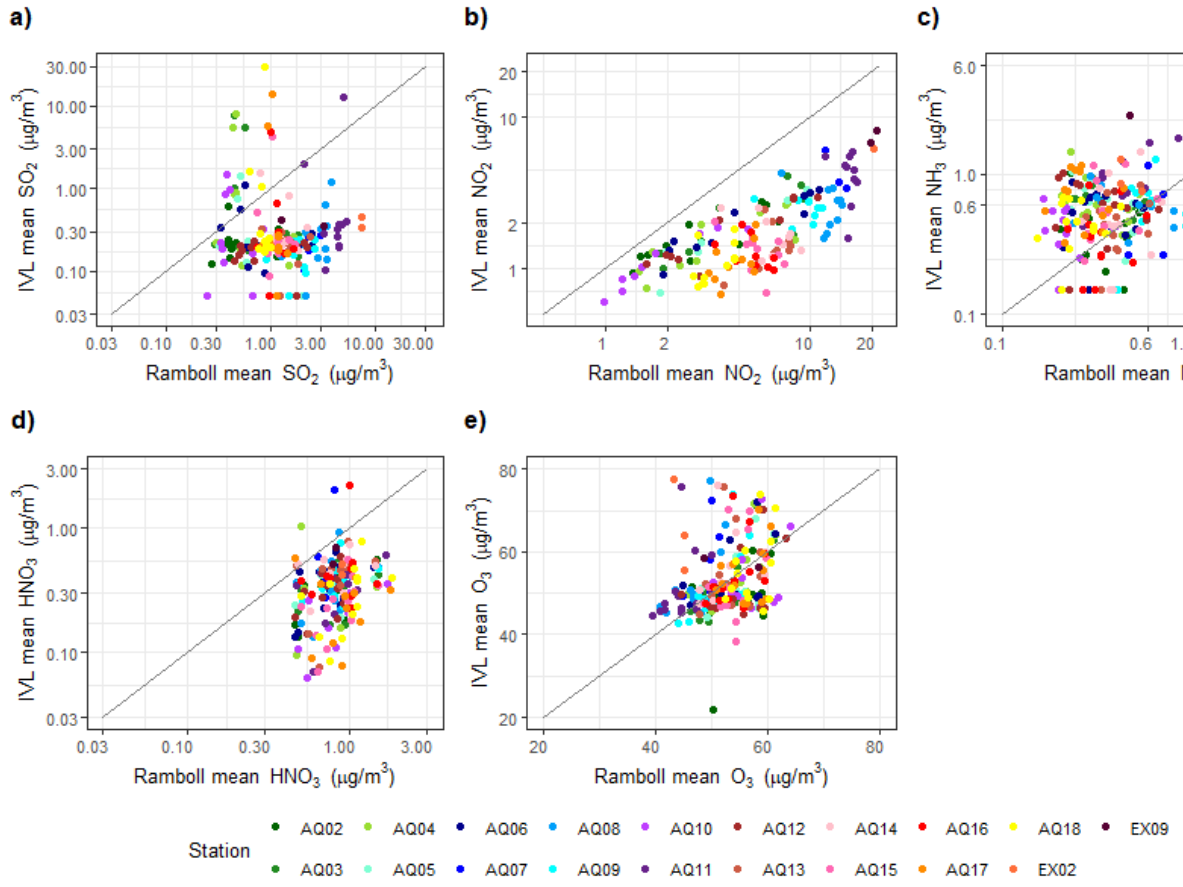

Figure 8.3-3: Passive IVL samplers by mean Ramboll predictions, coloured by AQM station for each gas. Gases shown are (a) SO_2, (b) NO_2, (c) NH_3, (d) HNO_3 and (e) O_3.

For NH_3, there is no clear relationship between IVL measurements and Ramboll monthly predictions (Figure *8.3-2*(c) and *8.3-3*(c)). Table *8.3-1* shows a marginally non-significant correlation between NH_3 IVL measurements and Ramboll predictions. Figure *8.3-2*(c) shows no particularly distinct monthly relationships. Figure *8.3-3*(c) shows NH_3 Ramboll predictions for a few stations cluster in distinct ranges.

For HNO_3, there is no clear relationship between IVL measurements and Ramboll monthly predictions (Figure *8.3-2*(d) and *8.3-3*(d)). Figure *8.3-2*(d) shows some monthly observations are grouped in distinct clusters, for example March, in which the March Ramboll predictions are the highest compared to other months. Figure *8.3-3*(d) shows HNO_3 predictions have no clear relationship with the AQM stations. Table *8.3-1* shows a statistically significant correlation between HNO_3 IVL measurements and Ramboll predictions. This finding is particularly influenced by the results for March.

For O_3, there appears to be a weak linear relationship between IVL measurements and Ramboll monthly predictions (Figure *8.3-2*(e) and *8.3-3*(e)). Table *8.3-1* shows a significant correlation between O_3 IVL measurements and Ramboll predictions. Figure *8.3-2*(e) shows monthly linear relationships, for example June, July and September, however these relationships do not have the same slopes. Figure *8.3-3*(e) shows O_3 predictions have no clear relationship to the AQM stations.

Table 8.3-1: Spearman rank correlation between the IVL measurements and monthly mean Ramboll predictions, for each gas species.

Gas	Spearman rho
SO_2	-0.017
NO_2	**0.705*****
NH_3	**0.138***
HNO_3	**0.246****
O_3	**0.305*****

In summary, there is strong positive correlation between Ramboll estimates and passive IVL measures for NO_2, indicating that the Ramboll NO_2 estimates have provided good working predictions of NO_2 concentration for the purposes of the study design. The other gases (except SO_2) show weak correlations between IVL measures and Ramboll estimates. This may be due to differences between the actual weather conditions of a single year and the idealised weather conditions used in the Ramboll model. However, it is reassuring to see that the mean Ramboll estimates and IVL measures are not too far apart in magnitude. SO_2 measures show no correlation between Ramboll estimates and passive IVL measures. The IVL SO_2 observations have generally exhibited wider variance and a non-normal distribution compared to other gases (Curtin University, 2022), which may be contributing to the lack of correlation. Additionally, sources of SO_2, especially those related to shipping, may be more dispersed and transitional, making modelling difficult.

8.3.3.2 Results for annual mean and maximum gas predictions over all sampling periods

Figure *8.3-4* compares IVL observations averaged across all sampling periods to date (noting that some AQM stations were installed for less than 12 months) with the annual average and maximum Ramboll predictions for the appropriate grid square where the relevant AQM is located. Averaged IVL data generally show clear trends across the stations, as expected, as the stations are ordered by overall measured gas concentration. Averaged Ramboll predictions follow trends for IVL gases for NO_2 (strongly) and to some extent for NH_3 and O_3. However, for SO_2, HNO_3 and O_3 the Ramboll predictions are flatter than the IVL measurements.

Figure *8.3-4*(a) shows that the SO_2 IVL observations exhibit a strong increase in values across the stations. For the first half of the AQM stations displayed in Figure *8.3-4*(a) (AQ09 to AQ05), the average Ramboll predictions are up to an order of magnitude higher than the IVL measurements, but for AQ03 to AQ18 the IVL measurements exceed the Ramboll predictions.

Figure *8.3-4*(b) shows that NO_2 IVL values also exhibit a reasonably strong increase across AQM stations. The trend is flattened here due to the much higher Ramboll predicted maximum values, which are at least four times greater than the mean Ramboll predictions and IVL observations. For NO_2, the mean Ramboll predictions are similar to the IVL measurements overall, closely matching the IVL values in the lower range but tending to exceed them in the higher range.

NH_3 IVL measurements increase from 0.3 to over 2 $\mu g/m^3$ across the AQM stations (Figure *8.3-4*(c)). The mean Ramboll predictions are mostly lower than the IVL measurements, with only three stations overlapping.

HNO_3 IVL measurements increase from 0.1 to 1 μ g/m^3 (Figure *8.3-4*(d)). Whereas the Ramboll predicted mean values are quite flat across the AQM stations and only overlap with the IVL measurements for EX09 and AQ07.

O_3 IVL measurements increase from 50 to 70 μ g/m^3 (Figure *8.3-4*(d)). While there is an overlap between the measured IVL values and the predicted Ramboll values for the lower three quarters of the stations, the Ramboll predictions are lower for the stations with higher measured IVL values. Note that AQ01 and EX02 were installed later, thus only have a smaller number of IVL measurements, which might account for the difference between the IVL measurements and the Ramboll predictions for these two stations. Maximum Ramboll predicted values are almost double the average Ramboll values, but also decrease for the last few stations.

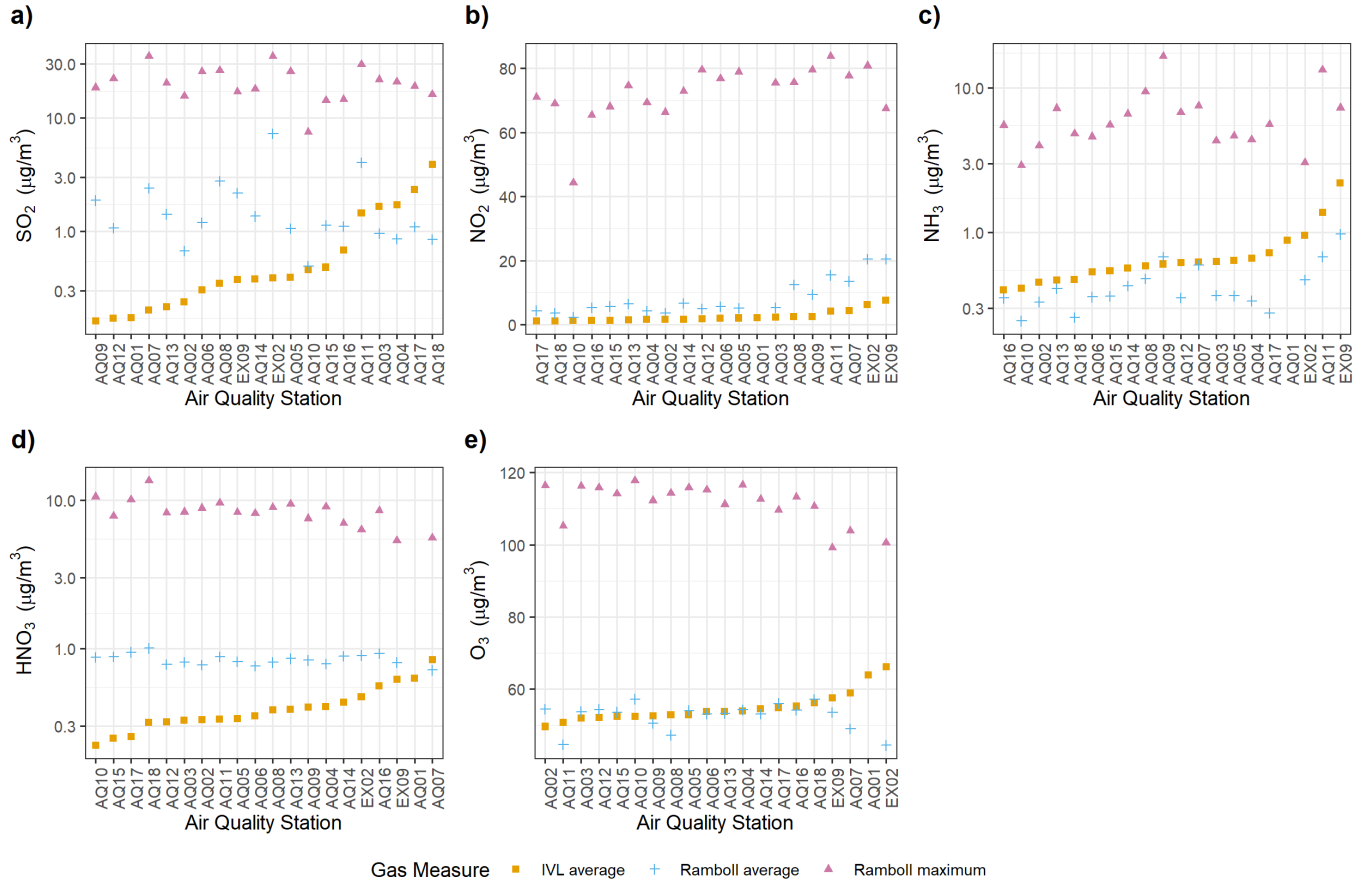

Figure 8.3-4: Passive IVL samplers and mean Ramboll predictions averaged across all sample periods by station for each gas and overall maximum Ramboll prediction. Gases shown are (a) SO_2, (b) NO_2, (c) NH_3, (d) HNO_3 and (e) O_3.

Figure *8.3-5* shows the relationship between the IVL observations averaged across all sampling periods and the Ramboll predictions averaged across corresponding months. Table *8.3-2* shows the Spearman's rank correlation test results between the averaged IVL measurements and averaged Ramboll predictions for each gas.

For SO_2, there is no correlation between the averaged IVL measurements and the averaged Ramboll predictions (Figure *8.3-5*(a) and Table *8.3-2*).

For NO_2, there is significant evidence of a positive linear relationship between the averaged IVL measurements and the averaged Ramboll predictions (Figure *8.3-5*(b) and Table *8.3-2*).

For NH_3, there is also a significant positive relationship between the averaged IVL measurements and the averaged Ramboll predictions (Figure *8.3-5*(c) and Table *8.3-2*)

For HNO_3 and O_3, there is no correlation between the averaged IVL measurements and the averaged Ramboll predictions (Figure *8.3-5*(d) and (e) and Table *8.3-2*).

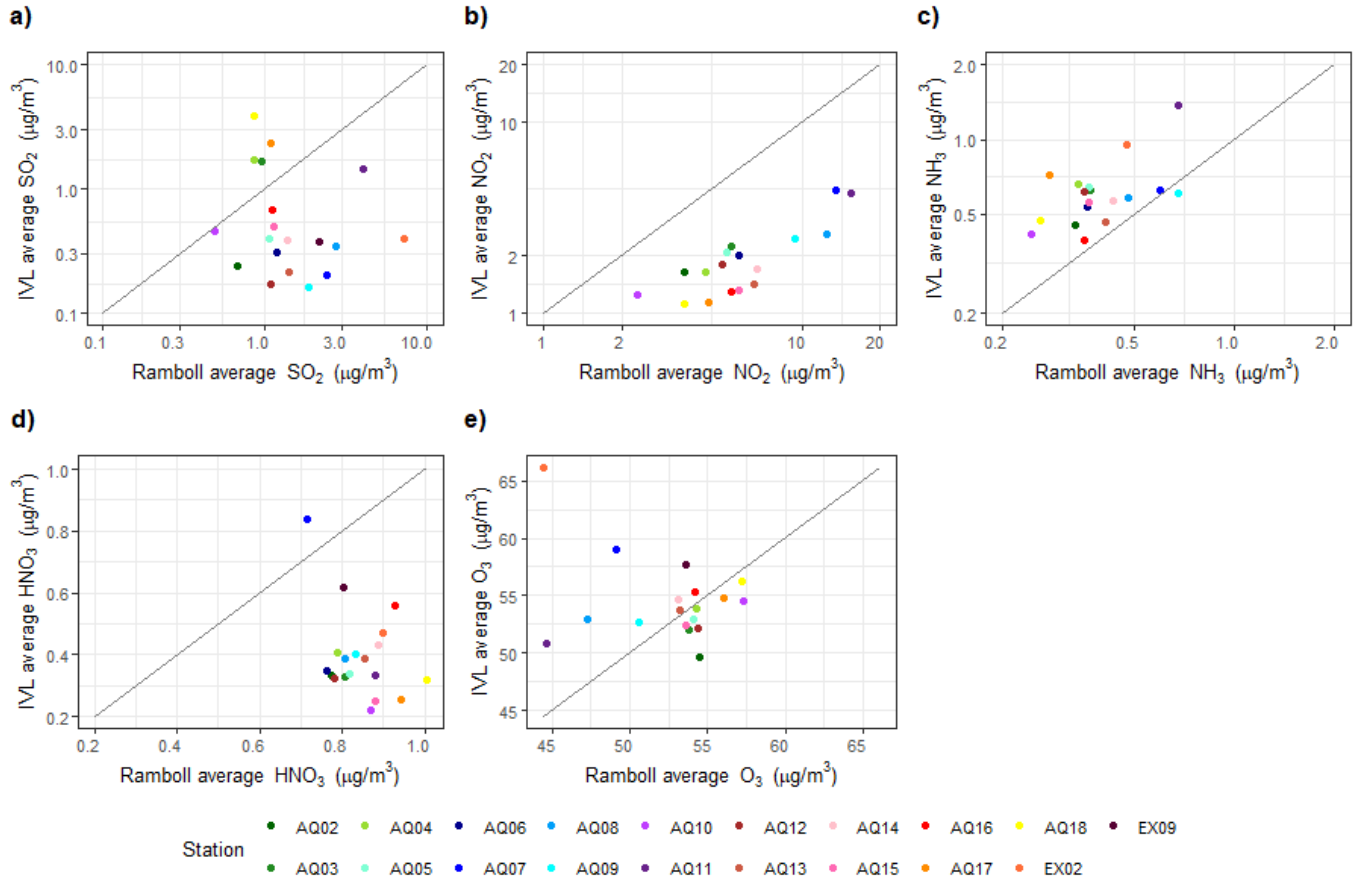

Figure 8.3-5: Passive IVL samplers by mean Ramboll predictions averaged across all sample periods by station for each gas. Gases shown are (a) SO_2, (b) NO_2, (c) NH_3, (d) HNO_3 and (e) O_3.

Table 8.3-2: Spearman rank correlation between averaged IVL measurements and averaged monthly Ramboll predictions for each gas species.

Gas	Spearman rho
SO_2	-0.361
NO_2	**0.779*****
NH_3	**0.519***
HNO_3	-0.218
O_3	-0.153

8.4 Porosity versus explanatory variables

8.4.1 Background

In Section 7.6 it was concluded that there is statistically significant evidence of elevated porosity of rock surfaces in an area within the Murujuga study region. The strongest evidence of elevated porosity was obtained at locations in the general vicinity of Dampier and King Bay.

This conclusion was based solely on the observed spatial variation in porosity index across the Murujuga study region. It did not take account of any other factors which might have caused porosity to be *naturally* elevated in the Dampier–King Bay region in the absence of industrial output. That issue will now be addressed.

The major challenge is to identify a suitable explanatory variable. Many observable quantities appear to be *correlated* with porosity, such as the chemical composition of the rock surface, physical parameter readings, and potentially, microbiome abundance. However, these quantities cannot serve as indices of the *natural* propensity of the rock material to have higher or lower porosity in the absence of industrial output. These quantities are correlated with the "response" (change in porosity) as well as the "explanatory variables". Treating such quantities as explanatory variables involves a kind of circular logic which leads to inconclusive results. This is a common problem in observational studies (Cox and Snell, 1981).

In order to examine alternative explanations for the observed elevated porosity, we require a measurable quantity that can serve as a surrogate for the propensity of the rock surface, in the pre-industrial environment, to have higher or lower porosity.

Candidates for the explanatory variable include:

- height of the rock above the surrounding terrain;
- spatial orientation (dip and/or strike) of the rock surface;
- total hours of direct sunlight per year on the rock surface;
- annual total solar flux on the rock surface.

Further work is needed to examine and validate these candidates and to identify alternative candidates.

One possible strategy for selection of an explanatory variable is to restrict attention to areas that are very distant from the industrial output sources, provisionally treat these areas as if they were completely unexposed to industrial output, and identify the explanatory variables which have the greatest predictive power for porosity in these areas. This would require more rock sampling in the remote areas.

8.4.2 Porosity after accounting for height above terrain

This sub-section demonstrates a technique that could be used to assess evidence for a region of elevated porosity after accounting for the effect of an explanatory variable. For demonstration purposes, the explanatory variable is chosen to be the height of the rock above the surrounding terrain. This choice has the advantage that a rock's height above terrain was determined long before industry arrived on the peninsula (ignoring rock falls and deliberate displacement). However,

height could be confounded with distance from industry, because the selection of locations for industrial installations is probably biased toward flatter terrain. We ignore such concerns for the sake of the demonstration.

A straightforward technique to test for the presence of an area of elevated porosity in the Murujuga region, after accounting for the effect of rock height above terrain, is as follows.

1. Obtain porosity index values y_i and heights z_i at each site x_i, for $i = 1, \ldots, n$.
2. Examine the relationship (if any) between z and y regardless of spatial location, using techniques such as the Pearson correlation, Spearman rank correlation, visual inspection of scatterplots, linear or polynomial regression, nonparametric smooth regression.
3. Select a regression model which predicts the expected porosity y as a function of the rock height z.
4. Compute the residuals $r_i = y_i - \widehat{y}_i$ for each site $i = 1, \ldots, n$ where $\widehat{y}_i$ is the predicted porosity for rock height z_i.
5. Apply spatial smoothing to the residuals r_i using the techniques described in Appendix *F*.1.
6. Perform a Monte Carlo test of the null hypothesis of constant mean residual against the alternative hypothesis of elevated mean residual, using the techniques described in Appendix *F*.3.

Analysis reported in Appendix *G*.2 found little evidence of a relationship between porosity index and height above terrain. Nevertheless, the demonstration continues. Figure *8.4-1*(a) shows a scatterplot of porosity index against rock height, and the predicted porosity according to the fitted beta regression model

$$\log \frac{\text{Porosity}}{1 - \text{Porosity}} = -2.54 + 0.028\,\text{Height} - 0.0002\,\text{Height}^2.$$

(Some figures refer to height as “elevation” but we use the term height to avoid confusion.) The negative coefficient for squared height implies that the predicted relationship has an inverted U shape. Grey shading indicates a pointwise 95% confidence band for the mean, computed using a naive bootstrap (the data were randomly resampled 1000 times; the model was fitted to each resampled dataset; the fitted curve was computed for each model; and the upper and lower 2.5% pointwise quantiles were computed.) Figure *8.4-1*(b) shows the raw residuals for this model, again plotted against rock height. Appendix *G*.2 provides further details of this model, including diagnostics.

Figure *8.4-2* shows the raw residuals, for the beta regression of porosity on rock height, plotted at the geographic locations of the sample rocks. Residuals tend to be negative on the northern and western islands, and tend to be positive near the centre of the peninsula.

Figure *8.4-3* shows the spatially smoothed residuals. The northern and western islands have large negative values of the smoothed average residual, while two areas, just north and south of the port, have moderately large positive values. The Monte Carlo test described in Appendix *F*.3 was applied to the residuals. In this context, the null hypothesis is that the mean residual is constant across the peninsula, which would imply that the observed spatial variation in porosity is explained by the dependence of porosity on rock height.

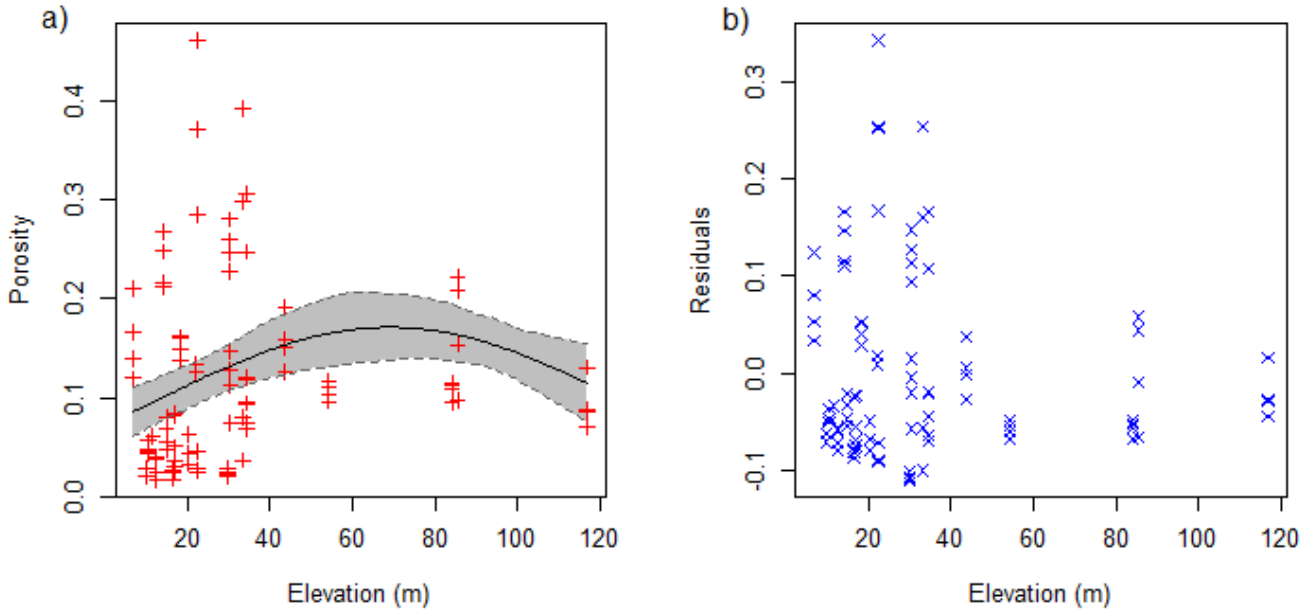

Figure 8.4-1: Regression model for porosity index as a function of rock height above terrain. (a) observed average porosity (+) and predicted porosity (black line) versus rock height. Grey shading is pointwise 95% confidence interval for true relationship. (b) raw residuals (×) versus rock height. Porosity index is average porosity at depths 0 to 1.3 mm, opening radius 20 μm.

Figure *8.4-4* shows the result of the pointwise Monte Carlo test of the null hypothesis against the two-sided alternative. Panel (a) shows p-values for the pointwise Monte Carlo test, and panel (b) identifies all locations where the test result is statistically significant.

Our interpretation of Figure *8.4-4* is that there are areas of Murujuga where the porosity is both statistically significantly less than, and statistically significantly greater than, the porosity predicted by the regression model, according to the pointwise test. The global Monte Carlo test described in Appendix *F*.3 yielded a p-value of 0.02 indicating statistically significant evidence.

The main weakness of this analysis is that rock height has not proved to be a good choice for the explanatory variable that might explain the spatial variation in porosity observed in Section 7.6.5. There is only weak evidence at best for a relationship between porosity and rock height; the fitted model used in the analysis may be a result of over-fitting; the conclusions are equivocal.

This section has described and demonstrated a technique that could be used to assess whether any given variable might explain the observed spatial variation in porosity. In the case detailed above, the result of this assessment procedure was negative: variations in rock height above the surrounding terrain are not sufficient to explain the observed spatial variation in porosity. Further work will be performed to investigate other possible candidates for the explanatory variable.

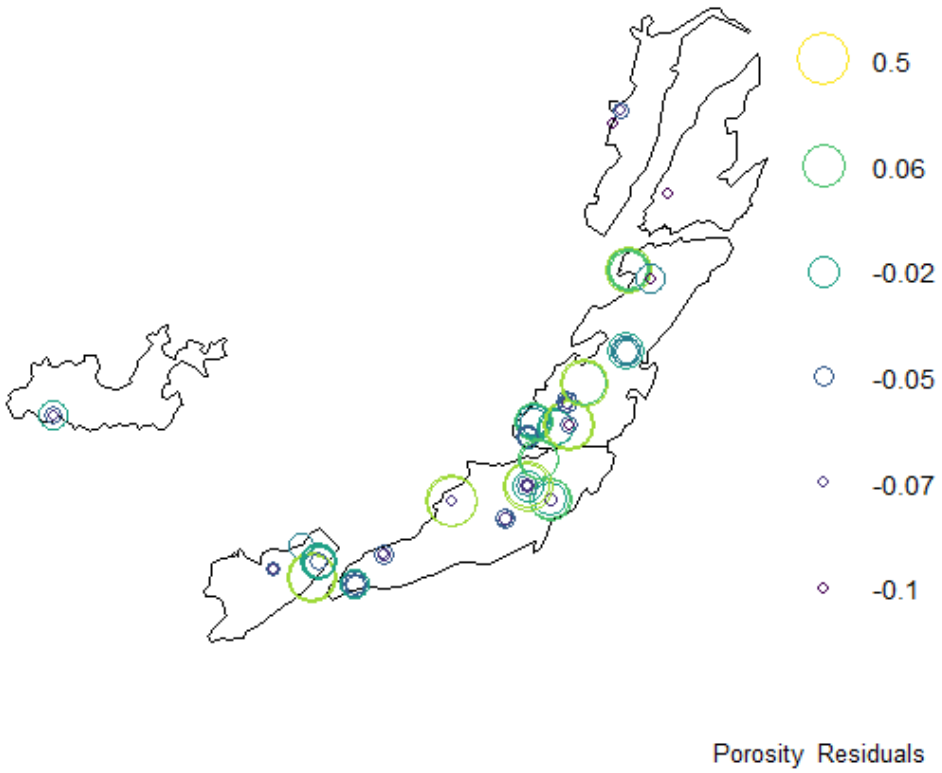

Figure 8.4-2: Spatial plot of raw residuals from the beta regression of porosity against rock height.

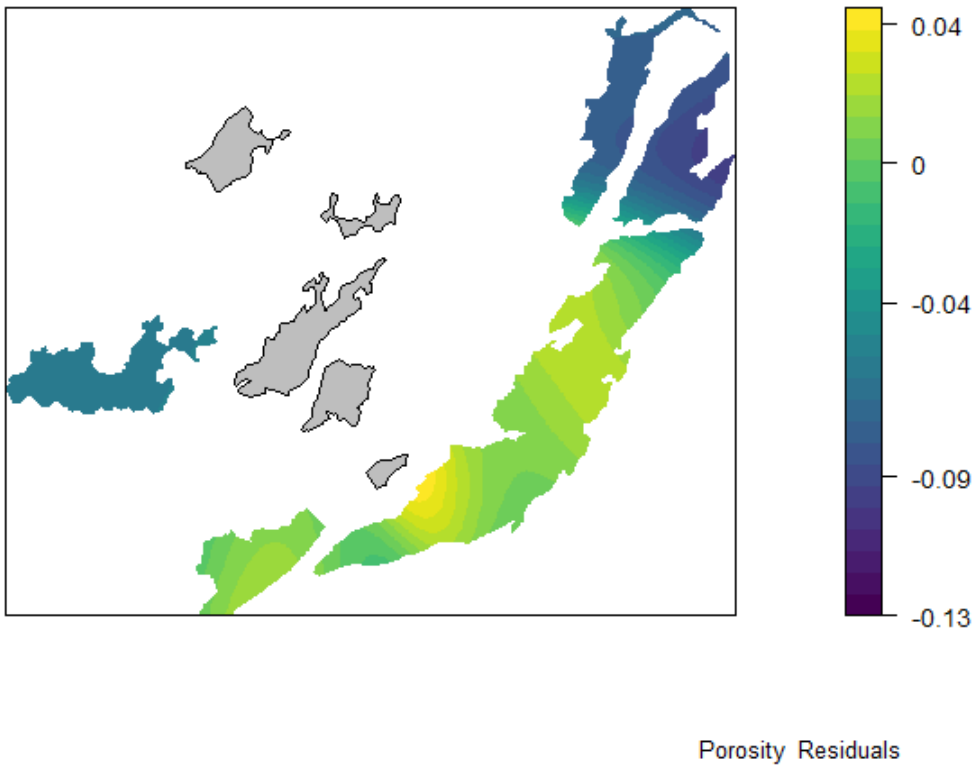

Figure 8.4-3: Spatially smoothed average raw residual from the beta regression model of porosity against rock height.

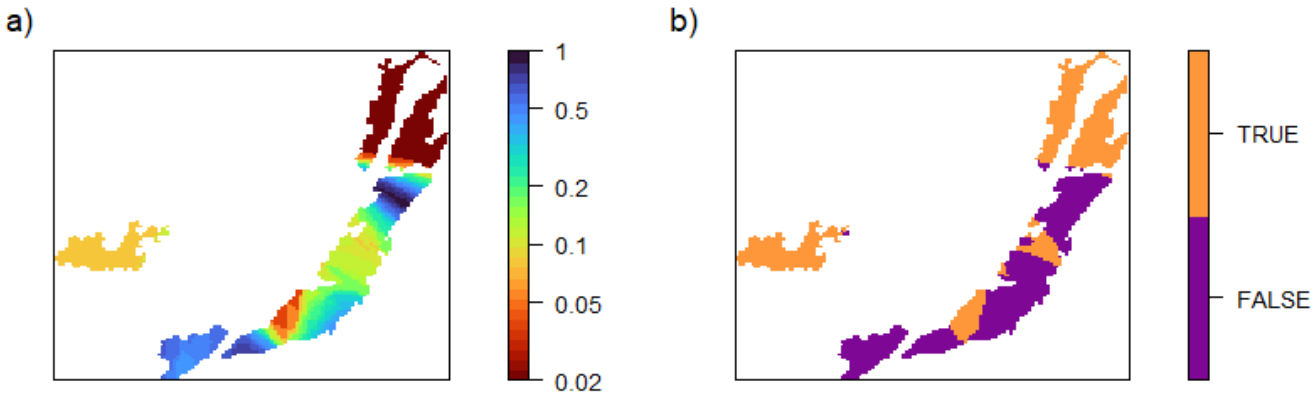

Figure 8.4-4: Pointwise Monte Carlo test of constant mean residual against a two-sided alternative. Beta regression of Porosity versus rock height. (a) p values for the pointwise test. (b) locations where the pointwise test result is statistically significant.

8.5 Passive sampler data from MRAMP study and from industry

The MRAMP study scope stipulates that our analysis should also take account of previously existing data where possible. Section 7.3 summarised data provided by Woodside from IVL passive samplers deployed at five sites from October 2021 to October 2022 inclusive. Section 7.11 presented data collected from the IVL passive samplers deployed by MRAMP. We now compare the two sets of data.

Direct correlation between the datasets is not appropriate because the Woodside and MRAMP data sets were collected over different areas and different periods. The Woodside sites are positioned over a smaller area than the MRAMP network. Woodside's observations are from a period preceding the start of MRAMP field work.

Comparing the Woodside data in Figure *7.3-1* on page 252 to the MRAMP data in Figure *7.11-3* on page 349, the range of observed concentrations for most gases is narrower in the Woodside data than the MRAMP data, probably reflecting the more restricted monitoring area.

Woodside NO_2 observations in Figure *7.3-1* panel (a) are in a similar range to the MRAMP observations in Figure *7.11-3* panel (a). Most of the highest readings are from either winter or spring for the Woodside data. The MRAMP NO_2 observations are generally highest for the winter months, but very few spring observations are available.

Woodside NH_3 observations in Figure *7.3-1* panel (b) are in a similar range to the MRAMP observations in Figure *7.11-3* panel (b). The Woodside data is similar for four of the stations (WEL 2 to WEL 5) while WEL 1 has somewhat higher values. This data also tends to be highest for Autumn, which is similar to middle MRAMP readings (AQ14 to AQ05 in Figure *7.11-3* panel (b)).

Woodside SO_2 observations in Figure *7.3-1* panel (c) have a much smaller range than the MRAMP observations in Figure *7.11-3* panel (d), with all measurements less than 0.6 μg/m^3. The largest values of SO_2 concentration in the MRAMP data are associated with the northernmost monitoring station, which is not close to any of the Woodside sites. The Woodside SO_2 measurements are mainly grouped together across different months, but there are some high December measurements, which largely corresponds to the MRAMP findings.

Woodside HNO_3 observations in Figure *7.3-1* panel (d) are in a similar range to the MRAMP observations in Figure *7.11-3* panel (e). The Woodside data is highest in the Autumn months, while the MRAMP data is highest in Spring. This may reflect the local area differences and weather differences between the two observation periods.

This page is intentionally blank.

8.6 Key findings from statistical comparative analysis

8.6.1 Deposition samplers vs passive samplers

As a further check on the validity of techniques, we compared the results from the passive sampler tubes (Section 7.11 and the bucket deposition samplers (Section 7.10) for similar pairs of chemical species.

Passive sample SO_2 and dry deposition sample SO_4^{2-} showed a strong relationship. Passive sample NO_2 and dry deposition sample NO_3^- also showed a strong relationship. However, passive sample NH_3 and dry deposition sample NH_4^+ were only moderately strongly related.

8.6.2 Microbiome vs other component studies

It is important to investigate whether variations in the abundance of different taxa of micro-organisms, or variations in the diversity of microbial communities, are associated with variations in the chemical composition or microstructure of rock surfaces and host rock.

Amongst the micro-organisms that were commonly present in patina samples, many bacterial taxa were positively correlated with the proportion of Fe, Mn, As and Pb measured by the pXRF instrument; some taxa of fungi were moderately positively correlated with Pb, P, Fe and Mn; and *Spissomyces* was moderately negatively correlated with S.

MnO concentration in thin sections of rock surface layers can be regarded as a surrogate for patina thickness. *Cyanobacteria* abundance had statistically significant positive correlation with MnO concentration, stronger in the dry season than in the wet season.

Cyanobacteria abundance also had statistically significant positive correlation with porosity as measured by the average porosity index. This might be expected, since *Cyanobacteria* biofilms have been identified as sources of rock pitting and weathering. However, this analysis is not sufficient to infer that *Cyanobacteria* are causing increased porosity; it will be essential to investigate this further when we have data from meta-transcriptomic sequencing.

8.6.3 Ramboll predictions vs passive sampler observations

A key assumption of our study design (Curtin University, 2022) is that the atmospheric concentrations of pollutant gases at Murujuga are not uniform but exhibit a spatial gradient of some kind. This gradient allows us to determine the relationship between the degree of exposure to pollutants and the degree of degradation experienced by the rock surfaces.

The study design was based on predictions of the atmospheric concentrations of pollutant gases across the study region in a ‘typical’ year, computed by a model developed by Ramboll (Ramboll Australia, 2022). These model predictions can now be assessed against actual observations of gas concentration provided by the IVL passive samplers.

Analysis in Section 8.3 found that the predicted and observed concentrations of each gas have approximately the same range of values.

In order to assess evidence for the predicted spatial gradient in concentration, we compared for each study site the yearly average of the Ramboll model predictions for that site with the yearly

average of the IVL passive sampler observations at the same site. For NO_2 there was a strong positive correlation between model predictions and passive sampler observations. For the other gases, except SO_2, there were weak correlations between the model predictions and observations. These findings are encouraging given that only two years' worth of observations have been collected so far.

For SO_2 there was little relationship between model predictions and observations at the same sites. The observed pattern of SO_2 includes high concentrations at locations in the north of the Burrup Peninsula where the Ramboll model predictions are much lower. It is conceivable that the Ramboll model omitted some undocumented sources of SO_2, perhaps associated with shipping.

Discrepancies which might arise, between the spatial gradient of gas concentration predicted by the Ramboll model and the spatial gradient actually observed, do not invalidate the study design. Ramboll predictions were used to design the optimal placement of air quality monitoring stations. Errors in the Ramboll predictions would imply only that the placement of the monitoring stations was not optimal.

These findings suggest that the sampling design is appropriate.

8.6.4 Porosity versus explanatory variables

In Section 7.6 it was concluded that there is statistically significant evidence of elevated porosity of rock surfaces in an area within the Murujuga study region. The strongest evidence of elevated porosity was obtained at locations in the general vicinity of Dampier and King Bay. This conclusion was based solely on the observed spatial variation in porosity index across the Murujuga study region. It did not take account of any other factors which might have caused porosity to be *naturally* elevated in the Dampier—King Bay region in the absence of industrial output.

Analysis of porosity after allowing for other factors was explored in Section 8.4. The major challenge is to identify an explanatory variable which measures the *natural* propensity of the rock material to have higher or lower porosity in the absence of industrial output. We described a simple technique which could be used to assess whether porosity is statistically significantly elevated in an area of Murujuga after allowing for the explanatory variable.

One possible choice of explanatory variable is the height of the sample rock above the surrounding terrain. For demonstration purposes, we used this as the explanatory variable. The results were not useful because there was no apparent relationship between porosity and height. However, this method could be used in future if a suitable explanatory variable can be identified.

8.6.5 Industry data and MRAMP data from passive samplers

Section 7.11 presented data collected from the IVL passive samplers deployed by MRAMP. Section 7.3 summarised data provided by Woodside from IVL passive samplers deployed at five sites from October 2021 to October 2022 inclusive. These data were compared in Section 8.5.

Observations in the two datasets were broadly comparable. Discrepancies can be explained by the fact that the Woodside sites extend over a smaller area than the MRAMP network, and Woodside's observations are from a period preceding the start of MRAMP field work.

The Woodside data will be included in future analysis and modelling of gas concentrations across Murujuga.

This page is intentionally blank.

9 General summary

9.1 Summary

This document represents the collective progress of the Murujuga Rock Art Monitoring Program research studies over the past two years. The extensive program of monitoring and the high spatial resolution of data collection, combined with rigorous laboratory investigation and innovative statistical techniques, have enabled us to establish important spatial patterns in porosity, microbiome and chemistry. The evidence for these patterns would have been unlikely to be statistically significant if a smaller number of study sites had been selected.

The porosity of the weathered rind (subsurface layer) of granophyre rock surfaces was found to be higher in a region close to Dampier and the main industrial precinct, and lower elsewhere. This pattern may represent anthropogenic impact; further investigation and confirmation is required. Given that previous industrial emissions in the region of highest porosity were two-to-three times higher in the past, these past emissions may be the major contributor. However, it is not yet known if industrial emissions have contributed to patina formation or any changes in patina formation rates as industrial emissions have increased and decreased over time. This area is the subject of active investigation.

Preliminary analysis of the microbiome dataset and data synthesis with geochemical data shows that *Geodermatophilus* appears to be more abundant where porosity is elevated and *Chroococcidiopsidaceae* is apparently more abundant when porosity is lower. This requires further investigation to determine if these correlations are causal or opportunistic colonisation with respect to porosity. Furthermore, this analysis also suggests that surface manganese (a key component in desert varnish) is lower where porosity is elevated.

The chamber studies have confirmed a mechanism by which rock surfaces exposed to air pollution could undergo an increase in porosity, as observed in field samples. This has been confirmed chemically (through analysis of leachate) and physically (through high resolution pre- and post-exposure analysis of minerals via imaging). A clear path forward to develop EQC from field and chamber observations has been established. This will be integrated with separate experiments to investigate microbiome sensitivity to air pollutants. The contribution of the microbiome and organic acids to this process is yet to be studied.

Microstructural and geochemical analysis indicated that the development of pores and the formation of patina are complex processes. While the action of NO_2 and SO_2 contribute to these processes, the historic “acidification” or “acid rain” hypothesis from the literature (Bednarik, 2007; Smith et al., 2022) does not appear to be supported by the current studies. Data from rainfall and dust deposition samplers show that the environment of Murujuga tends towards slightly alkaline/basic and this is consistent with the results of thermodynamic modelling, although care must be taken with this interpretation because the modelling assumes thermodynamic equilibrium, which is unlikely to be reached in the natural environment.

Air quality data show good agreement with spatial trends in previous modelling, albeit with average levels slightly lower than modelled values, with the notable exception of NH_3, which appears to be emitted into the airshed at a higher rate than previously predicted. Higher levels of the secondary air pollutant O_3 (relative to the Ramboll model), have also been observed. Interesting spatial

and diurnal trends in NO_2 are emerging from real-time and scanning instrument data. Moderate levels of formaldehyde (CH_2O) have also been observed, which is an intermediate product in the decomposition of methane. There is not yet any suggestion this is significant with respect to accelerated weathering of the rock art, however sufficiently high concentrations of CH_2O or O_3 at ground level could be expected to impact the micriobiome. Relatively high levels of black carbon (soot) have also been observed (compared to published global air quality data). Again this requires further investigation due to suggestions it may contribute to delamination. Some black carbon is due to natural sources such as bushfires, however the majority as measured (at EX09) appears to be anthropogenic in origin. Observations during bushfire events suggest that fire exposures are more acute however much more localised and short term in nature.

High-resolution spatial mapping coupled with computational fluid dynamics (**CFD**) simulations suggest that pollutants may be channeled or concentrated in geographic features such as gorges, which frequently contain a particularly high concentration of engravings. It has also been observed experimentally, and predicted using CFD models, that due to frequent high wind speeds and point source emissions, air pollutants will often remain concentrated in narrow plumes, thereby exposing a relatively small geographic swath of land to higher emissions. CFD simulations have been adapted to incorporate micro-scale processes incorporating the porous surface layer under moderate-high humidity conditions. This is intended to aid in understanding how gases such as NO_2 may react directly with moist pores in rock under nominally dry conditions, as appears to be the case from the chamber studies.

Spectral imaging of rock art is now producing high quality results after much work on optimising the method and error detection. However, there remain questions over the utility of high resolution spectrophotometry versus more simplified photogrammetric approaches for ongoing studies.

pH measurements from inert surfaces such as the deposition samplers and rainfall samplers clearly show that wet and dry deposition over the past two years has generally been neutral or alkaline. *pH* measurements on rock surfaces are more challenging and to interpret due to the relatively small contribution from the rock surface and complex interactions which may occur on the rock prior to and during measurement, as well as isolating relative contributions from deposited matter or organic acids formed by the microbiome. However, measurements on the surface of bushfire-exposed rocks showed a clear (alkaline) signal which reverted to baseline over 9-12 months post exposure. Another important consideration in rock *pH* measurement is the contribution of clay minerals (e.g. dust) which are expected to be alkaline, as well as (neutral) sea spray. It is likely that a more extensive dataset of rock pH measurements, combined with a more detailed analysis of deposition sampler data, will allow useful conclusions to be drawn from the rock *pH* measurements.

9.2 Further work

The remaining components of the MSDCA Plan (Curtin University, 2022) will be progressed as planned.

Given the findings on porosity and confirmation of the mechanisms in the chamber studies, some additions to the methodology have been approved:

- Collection of additional rock samples from islands or regions not in the current study design to confirm the porosity gradient over the entire range of relevant rock types.

- Evaluation of a field permeameter as a non-invasive field appropriate surrogate for porosity measurement. Results are promising, however more field data are needed. If successful, this method could be added to the monitoring plan to monitor porosity change over time.
- More comprehensive characterisation of bulk dust samples, and exploration of the role of dust in the *pH* and thermodynamics of the system, and in moderating *pH* from acid-gas species.
- Comprehensive consideration of the utility of rock surface *pH* and the potential for it to be included or excluded from ongoing monitoring under the EQMF.
- Investigation of the correlation between porosity and the two key microbiome genera and determination if the chicken or the egg came first.

Work will also progress to further synthesise and understand the rich data collected to date and additional monitoring and laboratory data that will be available as data collection continues. The chamber studies will be continued and more sophisticated models developed to refine NOEC/LOEC and thus EQC. Investigation of the impacts of peak air pollutant levels (both from chamber and field data) will be a focus of further work.

9.3 Conclusion

The MRAMP research studies have made substantial progress in all areas and developed guideline Interim EQC for three key air pollutants as well as a standard EQC for one pollutant.

There exist many opportunities for increased integration and analysis of combined datasets, which will be explored in further work.

Overall, it appears that some anthropogenic impacts have occurred, however at this stage these are most likely attributable to historic (higher) emission levels, rather than current levels. The likely dominant mechanism for any effect appears to be direct impact of emissions rather than rainfall, which is not currently acidic as previous research has suggested.

This page is intentionally blank.

APPENDICES

A Organic geochemistry – additional tables and figures

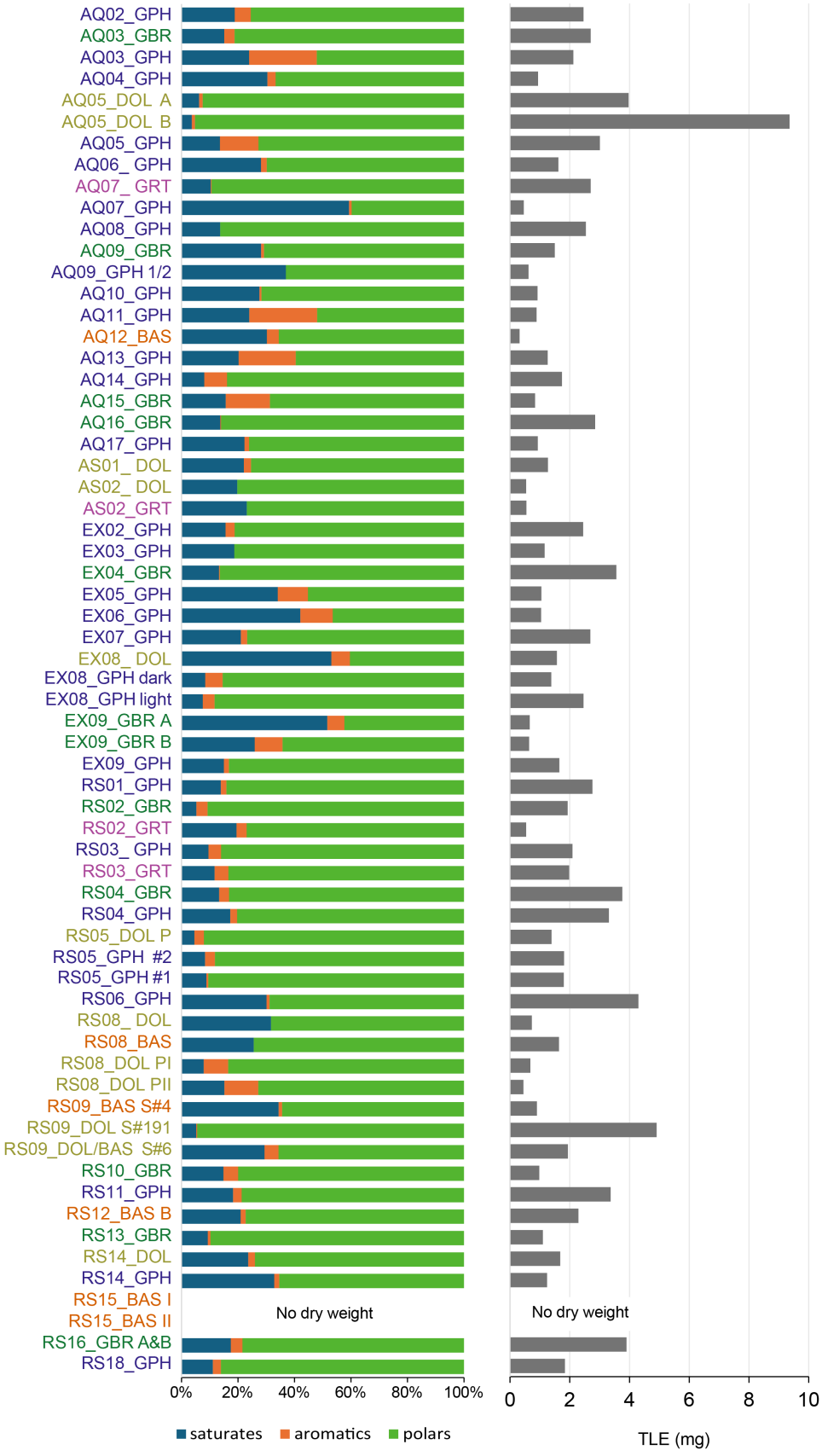

Figure A-1: Total lipid extract (TLE, mg) and saturated, aromatic and polar fraction (%) of rock surface samples.

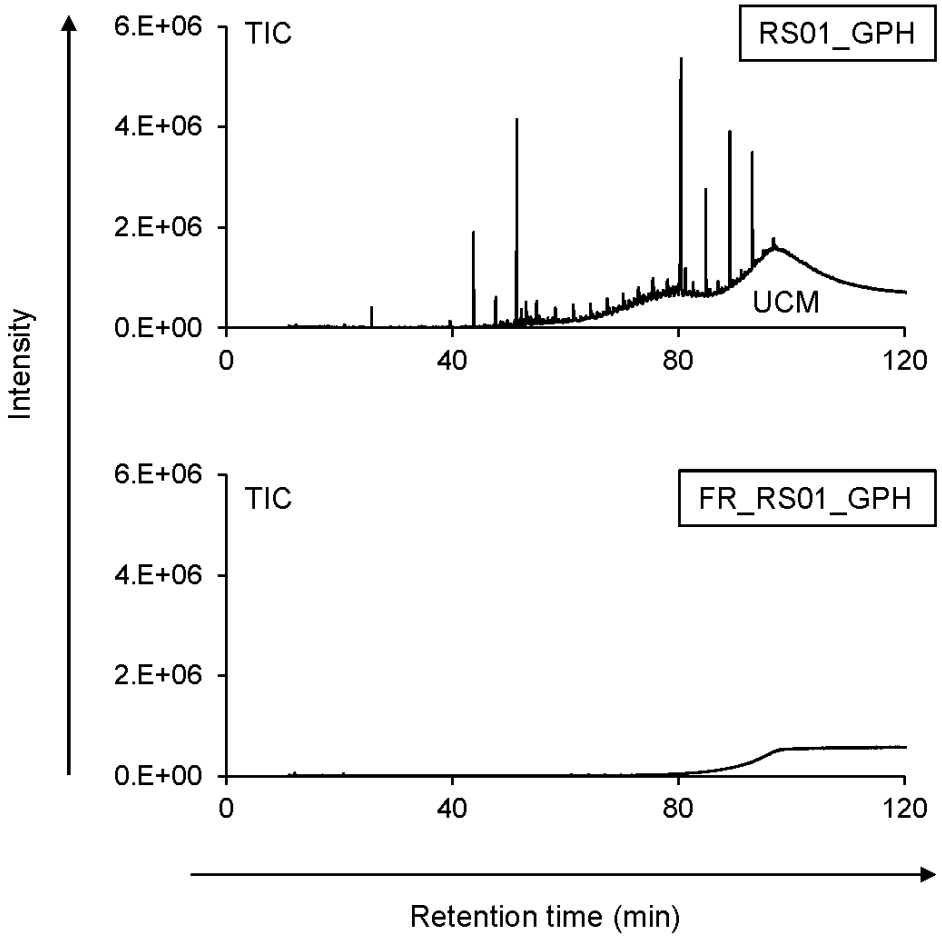

Figure A-2: GC-MS total ion chromatograms (TIC) of the saturated fraction. Comparing rock surface sample RS01_GPH with fresher rock sample FR_RS01_GPH. Observed ions ranged from m/z 50 to m/z 550. Unresolved complex mixture (UCM).

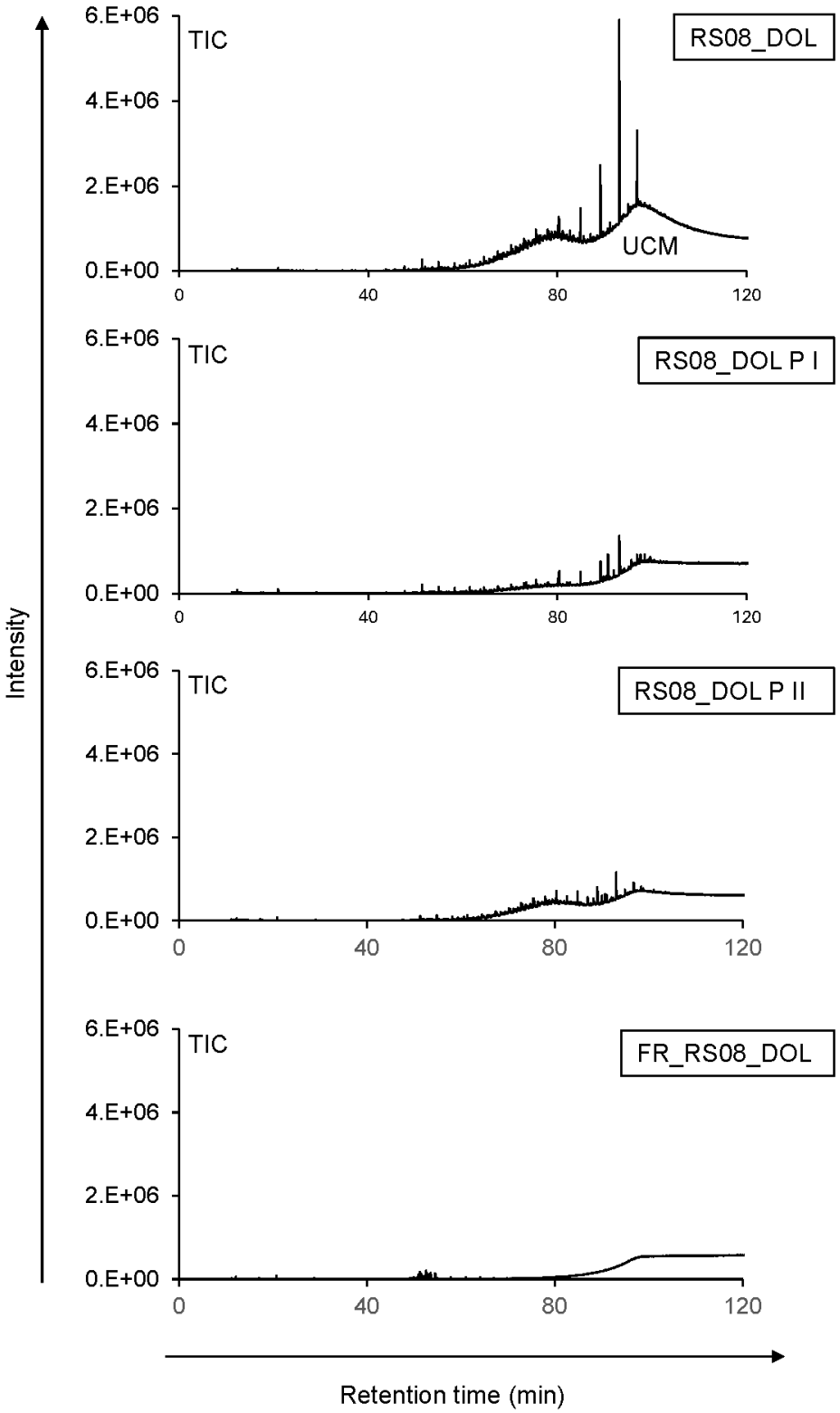

Figure A-3: GC-MS total ion chromatograms (TIC) of saturated fraction. Comparing rock surface sample RS08_DOL, mixed samples RS08_DOL PI and PII with fresher rock sample FR_RS08_DOL. Observed ions ranged from m/z 50 to m/z 550. Unresolved complex mixture (UCM).

Table A-1: List of Samples.

Sample	Fresher Rock Sample	Comment
AQ02_GPH		
AQ03_GBR		
AQ03_GPH		
AQ04_GPH		
AQ05_DOL A		
AQ05_DOL B		
AQ05_GPH		
AQ06_ GPH		
AQ07_ GRT		
AQ07_GPH		
AQ08_GPH		
AQ09_GBR		
AQ09_GPH 1/2		
AQ10_GPH		
AQ11_GPH		
AQ12_BAS		
AQ13_GPH		
AQ14_GPH		
AQ15_GBR		
AQ16_GBR		
AQ17_GPH	X	
AQ18_GPH		not extracted $<$3 g
AS01_ DOL		
AS02_ DOL	X	
AS02_GRT	X	
EX02_GPH		
EX03_GPH		
EX04_GBR		
EX05_GPH		
EX06_GPH		
EX07_GPH		

Sample	Fresher Rock Sample	Comment
EX08_ DOL		
EX08_GPH dark		darker sections removed
EX08_GPH light		lighter sections removed
EX09_GBR A		
EX09_GBR B		
EX09_GPH		
RS01_GPH	X	
RS02_GBR		
RS02_GRT		
RS03_ GPH		
RS03_GRT	X	
RS04_GBR	X	
RS04_GPH		
RS04_DOL		not extracted <3 g
RS05_GPH #1		
RS05_GPH #2		
RS05_DOL P	X	
RS06_GPH		
RS07_BAS		not extracted <3 g
RS08_ DOL	X	
RS08_DOL PI		
RS08_DOL PII		
RS08_BAS		
RS09_BAS S#4	X	
RS09_DOL/BAS S#6		
RS09_DOL S#191		
RS10_GBR		
RS10_ GRT		not extracted <3 g
RS11_GPH		
RS12_BAS B	X	
RS13_GBR		
RS13_GRT		not extracted <3 g
RS14_DOL		

Sample	Fresher Rock Sample	Comment
RS14_GPH		
RS15_BAS I		
RS15_BAS II		deeper layer
RS16_GBR A&B	X	
RS17_GPH		not extracted $<$3 g
RS18_GPH		

This page is intentionally blank.

B Geology and inorganic geochemistry – additional tables and figures

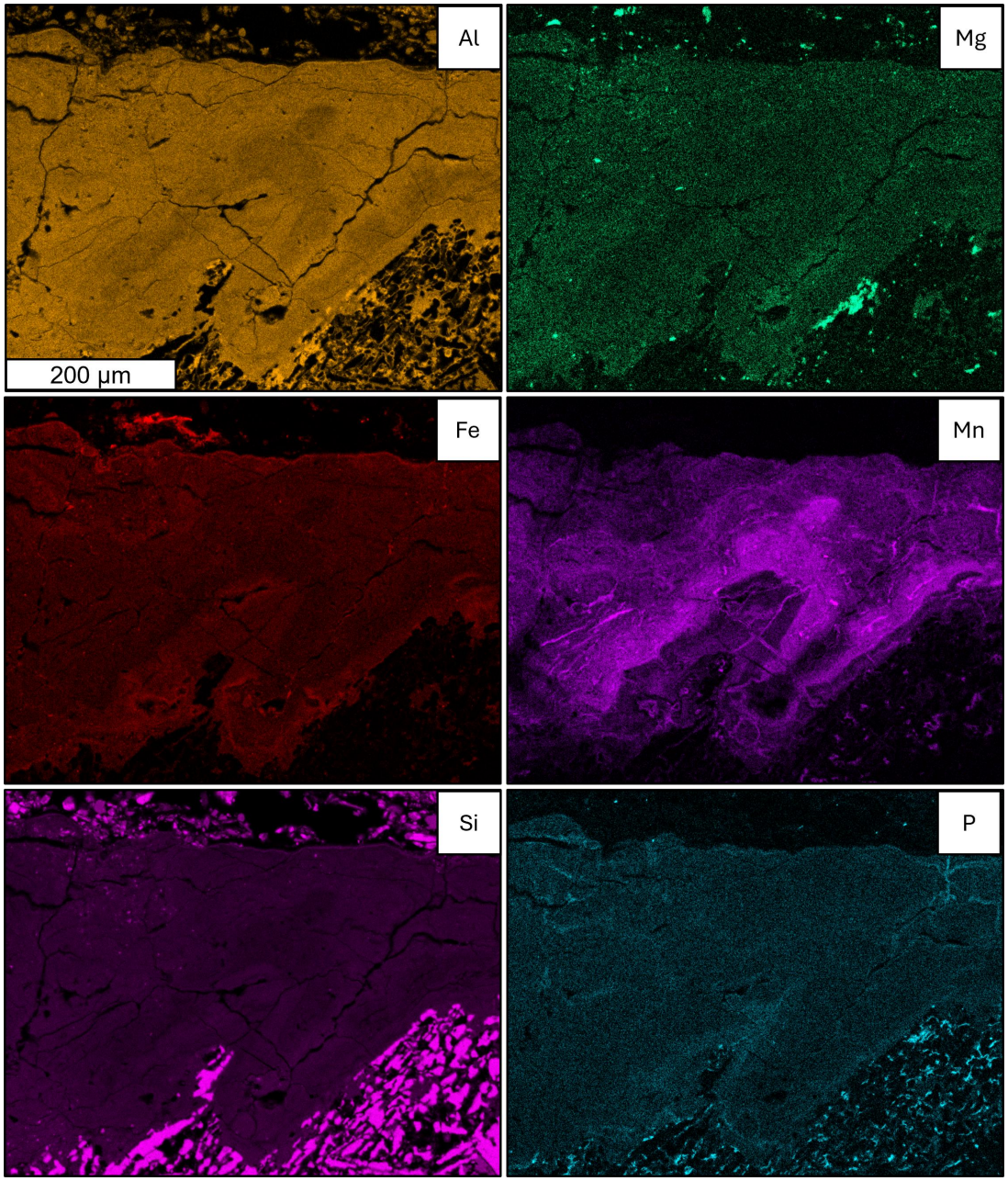

Figure B-1: SEM–EDS element distribution map of the region of the sample between the patina (top layer) and weathered rind (bottom layer) of sample AQ11_GPH, chemical heterogeneities are mostly observed for Al, Fe, Mn and P. Of these, Mn is by far the most variable, highlighting composite complex structures. Fe is enriched at the structural extremes of the patina forming a thin outermost rim on top of the sequence. P is widespread within the weathered rind.

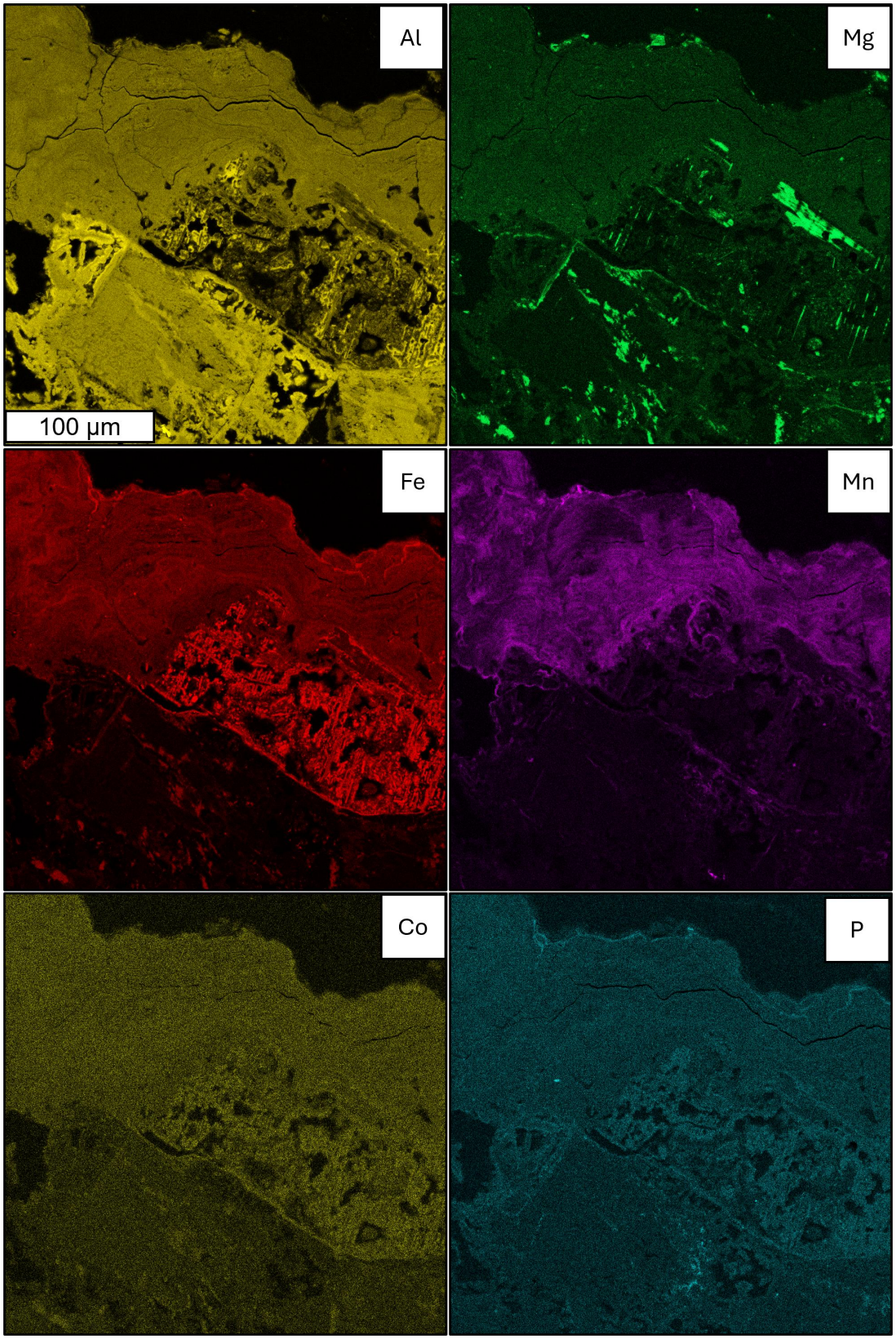

Figure B-2: SEM-EDS element distribution map of the region of the sample between the patina (top) and weathered rind (bottom) of sample AQ15_GBR. In the image, Fe and Mn are strongly heterogeneous. Al, Mg, Fe and P show systematic changes in abundance from the top to the bottom of the patina. In the Fe map, higher concentrations highlight the framework of a ghost pyroxene crystal. In the patina, Co and P are also present.

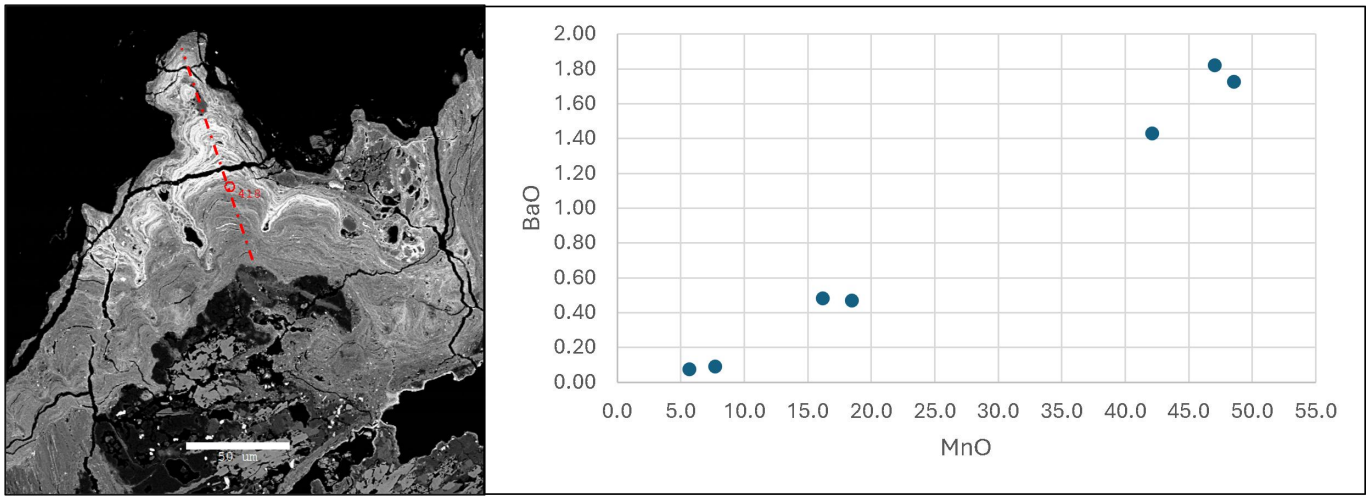

Figure B-3: Microstructural-compositional link between stromatolitic patina and the Mn-Ba concentration relationship. Left panel shows BSE-SEM image of stromatolitic patina occurring in a portion of sample AQ15_GBR. Right panel shows the EMP concentration of MnO versus BaO along a bottom to top profile across the botryoidal structure. The graph indicates that higher concentrations of MnO coincide with high values of BaO. Concentration values are expressed in wt%.

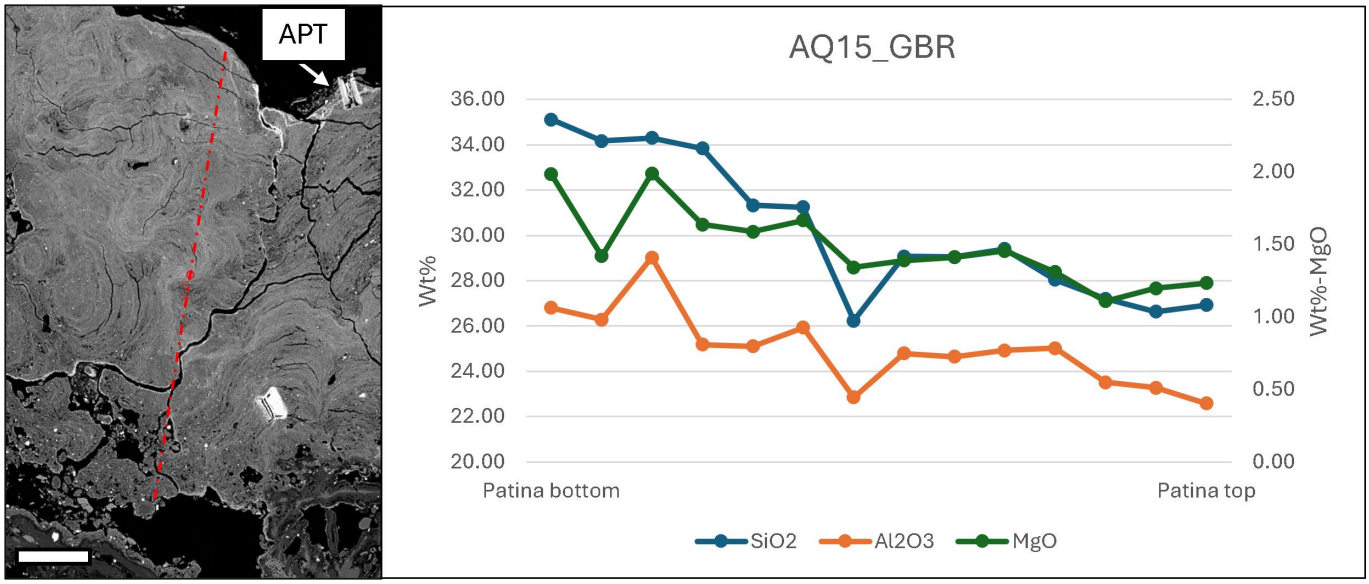

Figure B-4: Microstructural-compositional link between patina and immediate substrate in sample AQ15_GBR. The profile across the BSE-SEM image of the patina obtained by EMP (left panel) indicates the variation in concentration of SiO_2, Al_2O_3 and MgO as a function of the position in the patina (right panel). Notably, there is a trend of depletion moving away from the weathered rind for the considered elements. Concentration values are expressed in wt% oxides.

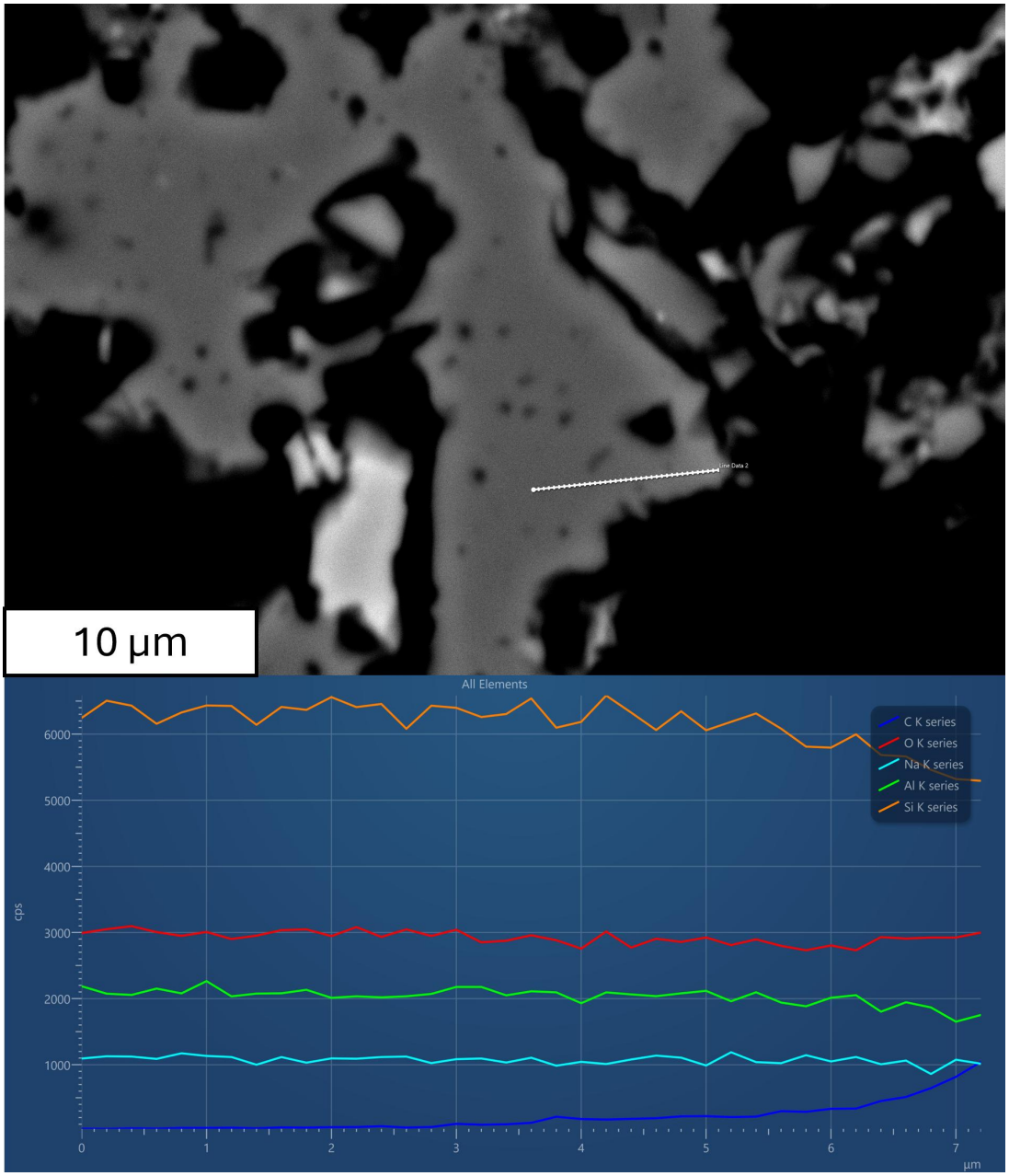

Figure B-5: (top) BSE-SEM image of albite rims within sample EX03_GPH investigated by TEM. (bottom) SEM-EDS line analysis across the albite rim indicated in the image. The brighter rim of the grain in BSE coincides with an increase in C and a depletion in Si and Al. A faint depletion in Na is also visible.

Table B-1: Summary of the plagioclase EMP analyses where WR refers to 'weathered rock' and FR refers to 'fresher rock' (part 1).

Plagioclase	AQ08_GPH		AQ10_GPH		AQ11_GPH		RS04_GPH		AQ07_GRT		RS03_GRT		AS02_GRT		AS02_GRT	AQ09_GBR		AQ09_GBR	
	WR	**FR**	**WR**	**FR**	**WR**	**FR**	**WR**	**FR**	**WR**	**FR**	**WR**	**FR**	**WR**	**FR**	**FR**	**WR**	**FR**	**WR_rim**	**FR_rim**
SiO_2	67.91	68.24	67.79	68.02	67.37	67.69	68.46	68.08	67.63	70.23	67.70	67.61	67.30	66.75	60.20	49.88	50.06	52.42	46.99
TiO_2	BDL	BDL	BDL	BDL	BDL	BDL	BDL	BDL	BDL	BDL	BDL	BDL	BDL	BDL	BDL	BDL	BDL	BDL	BDL
Al_2O_3	19.74	19.81	19.77	19.82	19.88	19.91	19.85	19.89	20.05	18.35	20.11	20.08	19.87	20.81	25.19	31.65	31.34	29.75	33.63
FeO	0.12	0.13	0.12	0.08	0.13	0.06	0.11	0.17	0.12	0.10	0.06	0.06	BDL	BDL	0.09	0.60	0.71	0.55	0.61
MnO	BDL	BDL	BDL	BDL	BDL	BDL	BDL	BDL	BDL	BDL	BDL	BDL	BDL	BDL	BDL	BDL	BDL	BDL	BDL
MgO	BDL	BDL	BDL	BDL	BDL	BDL	BDL	BDL	BDL	BDL	BDL	BDL	BDL	BDL	BDL	0.10	0.08	0.08	0.07
CaO	0.17	0.13	0.20	0.19	0.26	0.24	0.12	0.11	0.46	0.42	0.48	0.48	0.32	1.16	6.17	14.41	14.25	12.22	16.65
SrO	BDL	BDL	BDL	BDL	BDL	BDL	BDL	BDL	BDL	BDL	BDL	BDL	BDL	BDL	BDL	BDL	BDL	BDL	BDL
BaO	BDL	BDL	BDL	BDL	BDL	BDL	BDL	BDL	BDL	BDL	BDL	BDL	BDL	BDL	0.07	BDL	BDL	0.05	BDL
Na_2O	11.55	11.72	11.58	11.62	11.48	11.54	11.91	11.72	11.23	10.16	11.34	11.41	11.37	11.02	8.09	3.23	3.27	4.36	2.00
K_2O	0.05	BDL	0.10	0.10	0.11	0.10	BDL	0.07	0.17	0.31	0.11	0.09	0.07	0.11	0.13	0.15	0.16	0.22	0.07
Rb_2O	BDL	BDL	BDL	BDL	BDL	BDL	BDL	BDL	BDL	BDL	BDL	BDL	BDL	BDL	BDL	BDL	BDL	BDL	BDL
TOT	99.56	100.08	99.61	99.87	99.27	99.59	100.55	100.10	99.74	99.65	99.85	99.78	99.03	99.94	100.00	100.12	99.93	99.71	100.08
An	0.80	0.60	0.92	0.91	1.21	1.13	0.54	0.53	2.18	2.16	2.27	2.27	1.55	1.52	29.44	70.52	70.05	59.98	81.82
Ab	98.93	99.17	98.54	98.51	98.18	98.31	99.21	99.08	96.83	96.02	97.09	97.20	98.04	97.87	69.80	28.58	29.01	38.72	17.78
Or	0.27	0.23	0.54	0.58	0.61	0.57	0.24	0.39	0.99	1.82	0.64	0.53	0.42	0.61	0.76	0.90	0.94	1.30	0.40

Table B-2: Summary of the standard deviation (SD) of the plagioclase EMP analysis of the minerals (part 1).

SD	AQ08_GPH		AQ10_GPH		AQ11_GPH		RS04_GPH		AQ07_GRT		RS03_GRT		AS02_GRT		AS02_GRT	AQ09_GBR		AQ09_GBR	
	WR	**FR**	**WR**	**FR**	**WR**	**FR**	**WR**	**FR**	**WR**	**FR**	**WR**	**FR**	**WR**	**FR**	**FR**	**WR**	**FR**	**WR_rim**	**FR_rim**
SiO_2	0.36	0.46	0.74	0.36	0.36	0.47	0.57	0.60	1.74	7.53	0.90	0.32	0.55	0.44	0.24	1.54	2.16	1.06	1.25
TiO_2	0.02	0.02	0.01	0.01	0.02	0.01	0.01	0.01	0.05	0.03	0.02	0.02	0.03	0.02	0.00	0.03	0.02	0.01	0.02
Al_2O_3	0.16	0.18	0.21	0.18	0.24	0.10	0.25	0.23	0.97	4.75	0.37	0.16	0.21	0.26	0.12	1.17	1.52	0.74	0.92
FeO	0.11	0.15	0.16	0.07	0.06	0.05	0.03	0.14	0.12	0.12	0.05	0.04	0.05	0.04	0.01	0.11	0.06	0.03	0.03
MnO	0.01	0.02	0.04	0.01	0.01	0.01	0.06	0.02	0.01	0.01	0.02	0.01	0.01	0.01	0.00	0.01	0.01	0.02	0.02
MgO	0.01	0.04	0.02	0.02	0.01	0.01	0.01	0.06	0.02	0.04	0.02	0.02	0.01	0.01	0.02	0.01	0.03	0.01	0.02
CaO	0.09	0.05	0.08	0.05	0.13	0.16	0.04	0.05	0.21	0.14	0.18	0.17	0.09	0.15	0.12	1.36	1.73	0.71	0.84
SrO	0.02	0.02	0.02	0.03	0.03	0.02	0.02	0.04	0.03	0.03	0.02	0.02	0.02	0.02	0.03	0.02	0.03	0.02	0.01
BaO	0.02	0.02	0.02	0.02	0.01	0.02	0.02	0.01	0.02	0.02	0.02	0.02	0.02	0.03	0.04	0.02	0.02	0.01	0.01
Na_2O	0.12	0.15	0.24	0.15	0.21	0.30	0.21	0.28	0.60	2.39	0.23	0.13	0.20	0.30	0.06	0.73	0.96	0.42	0.51
K_2O	0.01	0.01	0.09	0.11	0.09	0.08	0.01	0.05	0.19	0.28	0.09	0.08	0.14	0.17	0.05	0.05	0.08	0.03	0.03
Rb_2O	0.02	0.01	0.02	0.02	0.02	0.01	0.01	0.01	0.02	0.01	0.02	0.02	0.01	0.02	0.04	0.02	0.01	0.02	0.01

Table B-3: Summary of the plagioclase EMP analysis as annotated in Table B-1 (part 2).

Plagioclase	AQ15_GBR		AQ15_GBR		EX09_GBR	AQ05_DOL		AQ05_DOL (alb)		RS09_191_DOL		RS09_191_DOL (alb)		AQ12_BAS		RS07_BAS
	WR	**FR**	**WR_rim**	**FR_rim**	**FR**	**WR**	**FR**	**WR**	**FR**	**WR**	**FR**	**WR**	**FR**	**WR**	**FR**	**FR**
SiO_2	48.16	49.11	49.08	51.64	46.07	62.30	63.12	67.69	67.99	55.16	56.22	68.21	67.01	66.81	66.66	66.18
TiO_2	BDL	BDL	BDL	0.05	0.05	BDL	BDL	BDL	BDL	0.07	0.06	BDL	BDL	BDL	BDL	BDL
Al_2O_3	32.81	32.31	32.21	30.46	28.56	23.59	22.75	20.23	20.24	28.17	27.66	20.63	21.11	19.97	19.92	20.51
FeO	0.61	0.60	0.65	0.62	2.20	0.37	0.32	0.32	0.32	0.77	0.77	0.20	0.32	0.14	0.17	0.24
MnO	BDL	BDL	BDL	BDL	BDL	BDL	BDL	BDL	BDL	BDL	BDL	BDL	BDL	BDL	BDL	BDL
MgO	0.06	0.07	0.06	0.05	0.06	BDL	BDL	BDL	BDL	0.06	0.06	BDL	BDL	BDL	BDL	BDL
CaO	15.66	14.94	15.02	12.95	18.19	4.95	3.96	0.53	0.55	10.17	9.43	0.34	0.95	0.24	0.16	0.78
SrO	BDL	BDL	BDL	BDL	0.09	BDL	BDL	BDL	BDL	0.05	BDL	BDL	BDL	BDL	BDL	0.05
BaO	BDL	0.05	BDL	0.06	BDL	0.06	0.15	BDL	BDL	BDL	BDL	BDL	BDL	BDL	BDL	BDL
Na_2O	2.46	2.91	2.82	3.86	2.75	8.46	8.91	11.40	11.39	5.24	5.96	11.09	11.28	11.26	11.87	11.39
K_2O	0.13	0.16	0.17	0.32	BDL	0.36	0.65	0.06	0.06	0.17	0.13	0.05	0.08	0.10	0.06	0.09
Rb_2O	BDL	BDL	BDL	BDL	BDL	BDL	BDL	BDL	BDL	BDL	BDL	BDL	BDL	BDL	BDL	BDL
TOT	99.96	100.24	100.07	100.04	98.02	100.16	99.90	100.28	100.61	99.89	100.35	100.49	100.83	98.57	98.86	99.30
An	77.28	73.31	73.94	63.74	78.42	23.96	18.98	2.50	2.58	51.20	56.18	1.66	4.38	1.19	0.75	3.59
Ab	21.98	25.78	25.09	34.37	21.48	73.95	77.29	97.19	97.07	47.77	42.98	98.07	95.19	98.23	98.93	95.93
Or	0.74	0.91	0.97	1.89	0.10	2.09	3.73	0.31	0.35	1.03	0.84	0.28	0.43	0.58	0.32	0.48

Table B-4: Summary of the SD of the plagioclase EMP analysis of the minerals (part 2).

SD	AQ15_GBR		AQ15_GBR		EX09_GBR	AQ05_DOL		AQ05_DOL (alb)		RS09_191_ DOL		RS09_191_ DOL (alb)		AQ12_BAS		RS07_BAS
	WR	**FR**	**WR_rim**	**FR_rim**	**FR**	**WR**	**FR**	**WR**	**FR**	**WR**	**FR**	**WR**	**FR**	**WR**	**FR**	**FR**
SiO_2	1.46	1.87	1.27	2.04	-	1.79	-	0.21	0.28	2.01	1.54	0.25	0.73	1.47	1.16	1.20
TiO_2	0.01	0.02	0.01	0.02	-	0.02	-	0.01	0.02	0.03	0.03	0.01	0.01	0.01	0.02	0.02
Al_2O_3	0.92	1.48	0.84	1.55	-	1.16	-	0.03	0.13	1.03	0.87	0.10	0.59	0.43	0.35	0.17
FeO	0.05	0.08	0.04	0.06	-	0.11	-	0.13	0.11	0.15	0.11	0.16	0.05	0.25	0.05	0.06
MnO	0.01	0.01	0.01	0.01	-	0.01	-	0.01	0.01	0.01	0.01	0.01	0.02	0.05	0.01	0.01
MgO	0.01	0.01	0.01	0.02	-	0.05	-	0.02	0.03	0.02	0.02	0.00	0.03	0.05	0.02	0.01
CaO	0.95	1.49	0.85	1.59	-	1.37	-	0.11	0.04	1.38	1.20	0.03	0.70	0.25	0.08	0.48
SrO	0.03	0.03	0.02	0.02	-	0.02	-	0.04	0.02	0.03	0.02	0.00	0.05	0.03	0.02	0.06
BaO	0.02	0.01	0.02	0.01	-	0.03	-	0.02	0.01	0.02	0.02	0.02	0.02	0.02	0.01	0.02
Na_2O	0.55	0.76	0.49	0.81	-	0.77	-	0.16	0.10	0.67	0.56	0.10	0.02	1.17	0.38	0.24
K_2O	0.05	0.12	0.04	0.13	-	0.14	-	0.03	0.01	0.07	0.03	0.01	0.00	0.13	0.02	0.02
Rb_2O	0.02	0.02	0.02	0.02	-	0.02	-	0.02	0.02	0.01	0.02	0.01	0.02	0.02	0.02	0.01

Table B-5: Summary of the alkali K-feldspar EMP analysis as annotated in Table B-1.

Alkali Feldspar	AQ08_GPH		AQ10_GPH		AQ11_GPH		RS04_GPH		AQ07_GRT		RS03_GRT		AS02_GRT		AQ12_BAS		RS07_BAS	
	WR	**FR**	**WR**	**FR**	**WR**	**FR**	**WR**	**FR**	**WR**	**FR**	**WR**	**FR**	**WR**	**FR**	**WR**	**FR**	**WR**	**FR**
SiO_2	64.10	64.51	64.14	64.29	63.72	63.93	64.29	64.43	64.38	63.97	64.70	64.59	63.86	64.25	64.55	65.26	65.11	64.56
TiO_2	BDL	BDL	BDL	BDL	BDL	BDL	BDL	BDL	0.06	0.06	0.05	0.10	BDL	BDL	BDL	BDL	BDL	BDL
Al_2O_3	18.45	18.56	18.51	18.49	18.42	18.60	18.57	18.66	18.73	18.56	18.53	18.53	18.60	18.79	18.83	19.04	18.76	18.56
FeO	0.19	0.14	0.31	0.17	0.18	0.16	0.09	0.14	0.25	0.13	0.31	0.12	0.05	BDL	0.07	0.17	0.58	0.32
MnO	BDL	BDL	BDL	BDL	BDL	BDL	BDL	BDL	BDL	BDL	BDL	BDL	BDL	BDL	BDL	BDL	BDL	BDL
MgO	BDL	BDL	BDL	BDL	BDL	BDL	BDL	BDL	BDL	BDL	BDL	BDL	BDL	BDL	BDL	BDL	0.18	BDL
CaO	BDL	BDL	BDL	BDL	BDL	BDL	BDL	BDL	0.12	0.22	0.07	0.10	BDL	0.12	0.14	BDL	0.08	0.15
SrO	BDL	BDL	BDL	BDL	BDL	BDL	BDL	BDL	BDL	BDL	BDL	BDL	BDL	BDL	BDL	BDL	BDL	BDL
BaO	0.31	0.32	0.28	0.21	0.28	0.35	0.35	0.33	0.42	0.41	0.24	0.27	0.30	0.33	0.70	0.43	0.49	0.46
Na_2O	0.15	0.17	0.20	0.28	0.18	0.26	0.22	0.17	0.23	0.30	0.17	0.16	0.23	0.32	0.10	0.33	0.26	0.28
K_2O	16.36	16.33	16.27	16.24	16.31	16.24	16.34	16.43	16.28	16.09	16.38	16.45	16.25	16.15	15.65	15.54	15.52	15.56
Rb_2O	0.08	0.08	0.07	0.07	0.08	0.07	0.07	0.07	0.07	0.07	0.06	0.05	0.05	0.07	BDL	BDL	0.05	0.05
TOT	99.62	100.12	99.82	99.75	99.20	99.64	99.94	100.24	100.54	99.80	100.50	100.36	99.35	100.03	100.08	100.85	101.04	99.99
An	0.09	0.13	0.12	0.10	0.14	0.15	0.09	0.13	0.61	1.11	0.38	0.51	0.15	0.59	0.76	0.23	0.45	0.76
Ab	1.41	1.53	1.83	2.57	1.68	2.36	2.01	1.55	2.10	2.69	1.51	1.47	2.11	2.93	0.99	3.15	2.46	2.63
Or	98.51	98.34	98.04	97.33	98.18	97.49	97.91	98.32	97.29	96.20	98.11	98.03	97.74	96.48	98.25	96.61	97.09	96.61

Table B-6: Summary of the SD of the alkali K-feldspar EMP analysis.

SD	AQ08_GPH		AQ10_GPH		AQ11_GPH		RS04_GPH		AQ07_GRT		RS03_GRT		AS02_GRT		AQ12_BAS		RS07_BAS	
	WR	**FR**	**WR**	**FR**	**WR**	**FR**	**WR**	**FR**	**WR**	**FR**	**WR**	**FR**	**WR**	**FR**	**WR**	**FR**	**WR**	**FR**
SiO_2	64.10	64.51	64.14	64.29	63.72	63.93	64.29	64.43	64.38	63.97	64.70	64.59	63.86	64.25	64.55	65.26	65.11	64.56
TiO_2	0.00	0.01	0.01	0.00	0.01	0.01	0.01	0.00	0.06	0.06	0.05	0.10	0.00	0.01	0.02	0.01	0.01	0.02
Al_2O_3	18.45	18.56	18.51	18.49	18.42	18.60	18.57	18.66	18.73	18.56	18.53	18.53	18.60	18.79	18.83	19.04	18.76	18.56
FeO	0.19	0.14	0.31	0.17	0.18	0.16	0.09	0.14	0.25	0.13	0.31	0.12	0.05	0.02	0.07	0.17	0.58	0.32
MnO	0.00	0.01	0.00	-0.01	0.00	0.00	0.01	0.01	0.01	0.01	0.00	0.01	0.00	0.00	0.00	0.00	0.00	0.01
MgO	0.00	0.00	0.03	0.00	0.00	0.00	-0.01	0.00	0.00	0.01	0.01	0.00	0.00	-0.01	0.00	0.01	0.18	0.02
CaO	0.02	0.03	0.02	0.02	0.03	0.03	0.02	0.03	0.12	0.22	0.07	0.10	0.03	0.12	0.14	0.04	0.08	0.15
SrO	-0.03	-0.03	-0.01	-0.02	-0.02	-0.01	-0.02	-0.03	-0.01	-0.01	-0.02	-0.01	-0.01	-0.02	-0.01	-0.02	-0.01	0.01
BaO	0.31	0.32	0.28	0.21	0.28	0.35	0.35	0.33	0.42	0.41	0.24	0.27	0.30	0.33	0.70	0.43	0.49	0.46
Na_2O	0.15	0.17	0.20	0.28	0.18	0.26	0.22	0.17	0.23	0.30	0.17	0.16	0.23	0.32	0.10	0.33	0.26	0.28
K_2O	16.36	16.33	16.27	16.24	16.31	16.24	16.34	16.43	16.28	16.09	16.38	16.45	16.25	16.15	15.65	15.54	15.52	15.56
Rb_2O	0.08	0.08	0.07	0.07	0.08	0.07	0.07	0.07	0.07	0.07	0.06	0.05	0.05	0.07	0.02	0.04	0.05	0.05

Table B-7: Summary of the clinopyroxene EMP analysis as annotated in Table B-1.

Clinopyroxene	AQ09_GBR		AQ15_GBR		EX09_GBR		AQ05_DOL (core)		AS01_DOL (core)		RS09_191_ (core)		AQ05_DOL (rim)		AS01_DOL (rim)		RS09_191_ DOL (rim)		AS12_BAS		RS07_BAS	
	WR	**FR**	**WR**	**FR**	**WR**	**FR**	**WR**	**FR**	**WR**	**FR**	**WR**	**FR**	**WR**	**FR**	**WR**	**FR**	**WR**	**FR**	**WR**	**FR**	**WR**	**FR**
SiO_2	52.45	51.88	52.53	52.46	52.26	52.07	51.70	51.99	53.94	52.65	51.27	52.38	50.51	50.83	50.78	50.88	50.99	51.20	53.05	51.36	52.73	52.46
TiO_2	0.47	0.62	0.60	0.50	0.48	0.53	0.57	0.49	0.26	0.42	0.66	0.51	0.68	0.55	0.69	0.66	0.83	0.81	0.17	0.15	0.15	0.22
Al_2O_3	1.56	1.52	1.34	1.46	1.59	1.53	2.54	2.39	1.31	1.67	2.77	2.44	2.31	1.74	1.32	1.23	2.00	2.07	1.31	3.35	1.09	1.55
Cr_2O_3	0.18	0.13	0.12	0.10	0.33	0.27	0.07	0.13	0.28	0.22	0.22	0.23	BDL	BDL	0.06	BDL	BDL	0.09	0.08	0.05	0.05	BDL
FeO	9.69	11.59	9.50	9.44	10.59	10.31	11.56	10.81	11.24	11.70	9.86	7.62	14.45	17.61	18.40	20.04	13.04	13.70	6.87	8.52	10.32	8.00
MnO	0.24	0.28	0.24	0.23	0.25	0.23	0.31	0.26	0.22	0.26	0.23	0.18	0.31	0.37	0.34	0.37	0.30	0.32	0.39	0.31	0.24	0.32
MgO	15.68	14.47	15.27	15.35	14.98	14.86	15.32	16.32	16.69	16.57	15.40	16.78	13.81	13.43	12.56	12.44	14.27	13.93	14.24	12.59	14.09	13.98
CaO	19.38	19.03	20.06	20.15	18.78	19.71	18.00	17.44	14.92	16.64	18.44	19.58	17.06	15.30	15.56	14.25	17.56	17.58	22.84	22.41	21.15	22.40
Na_2O	0.19	0.21	0.22	0.21	0.26	0.26	0.22	0.19	0.12	0.15	0.29	0.23	0.25	0.19	0.13	0.12	0.28	0.26	0.27	0.23	0.19	0.24
K_2O	BDL	BDL	BDL	BDL	BDL	BDL	BDL	BDL	BDL	BDL	BDL	BDL	BDL	BDL	BDL	BDL	BDL	BDL	BDL	BDL	BDL	BDL
TOT	99.86	99.71	99.87	99.89	99.54	99.77	100.28	100.03	98.99	100.28	99.18	99.95	99.41	100.02	99.83	100.02	99.30	99.94	99.23	98.99	100.04	99.24

Table B-8: Summary of the SD of the clinopyroxene EMP analysis.

SD	AQ09_GBR		AQ15_GBR		EX09_GBR		AQ05_DOL (core)		AS01_DOL (core)		RS09_191_ (core)		AQ05_DOL (rim)		AS01_DOL (rim)		RS09_191_ DOL (rim)		AS12_BAS		RS07_BAS	
	WR	**FR**	**WR**	**FR**	**WR**	**FR**	**WR**	**FR**	**WR**	**FR**	**WR**	**FR**	**WR**	**FR**	**WR**	**FR**	**WR**	**FR**	**WR**	**FR**	**WR**	**FR**
SiO_2	0.36	0.45	0.24	0.09	1.11	0.23	0.72	1.06	1.84	0.50	0.41	0.34	-	1.07	0.49	1.26	0.46	0.56	0.12	4.85	0.72	0.49
TiO_2	0.10	0.17	0.04	0.05	0.13	0.12	0.12	0.05	0.26	0.07	0.14	0.05	-	0.01	0.15	0.16	0.09	0.11	0.01	0.08	0.03	0.06
Al_2O_3	0.09	0.08	0.13	0.05	0.27	0.19	0.46	0.77	0.34	0.19	0.59	0.24	-	0.51	0.17	0.32	0.25	0.38	0.14	7.18	0.28	0.32
Cr_2O_3	0.03	0.05	0.02	0.02	0.12	0.13	0.06	0.10	0.13	0.06	0.28	0.13	-	0.01	0.03	0.11	0.04	0.08	0.04	0.05	0.04	0.05
FeO	1.32	0.80	0.19	0.24	0.46	0.26	2.90	6.15	2.47	2.55	3.28	0.46	-	4.59	3.43	6.40	1.87	2.67	0.35	1.64	0.51	1.63
MnO	0.02	0.03	0.02	0.02	0.02	0.02	0.12	0.13	0.04	0.05	0.07	0.02	-	0.09	0.06	0.11	0.06	0.06	0.04	0.10	0.04	0.09
MgO	0.76	0.87	0.15	0.11	0.43	0.37	1.79	2.79	1.46	0.66	1.00	0.57	-	3.35	2.45	2.97	0.94	1.06	0.15	4.47	0.52	0.93
CaO	0.80	0.88	0.21	0.31	2.16	0.27	0.79	1.83	2.40	1.73	2.36	0.58	-	0.14	0.04	2.28	0.70	1.08	0.16	0.83	0.34	0.97
Na_2O	0.02	0.03	0.02	0.01	0.06	0.04	0.03	0.01	0.04	0.03	0.15	0.02	-	0.01	0.01	0.04	0.01	0.02	0.02	0.09	0.02	0.05
K_2O	0.03	0.00	0.00	0.00	0.01	0.00	0.00	0.00	0.01	0.00	0.08	0.00	-	0.00	0.00	0.00	0.00	0.00	0.00	0.02	0.01	0.01

Table B-9: Summary of the orthopyroxene EMP analysis as annotated in Table B-1, includes the SD.

Orthopyroxene	**AQ09_GBR**		**AQ15_GBR**	
	WR	**FR**	**WR**	**FR**
SiO_2	54.55	54.03	54.05	54.01
TiO_2	0.14	0.11	0.13	0.20
Al_2O_3	0.98	1.00	0.81	0.73
Cr_2O_3	0.22	0.28	0.10	0.07
FeO	14.74	17.04	18.04	18.68
MnO	0.30	0.34	0.36	0.38
MgO	26.74	25.07	24.18	24.12
CaO	1.97	1.94	2.26	2.01
Na_2O	BDL	BDL	BDL	BDL
K_2O	BDL	BDL	BDL	BDL
TOTAL	99.67	99.82	99.96	100.21
SD	**AQ09_GBR**		**AQ15_GBR**	
	WR	**FR**	**WR**	**FR**
SiO_2	0.19	0.50	0.27	0.29
TiO_2	0.03	0.01	0.01	0.03
Al_2O_3	0.11	0.06	0.05	0.03
Cr_2O_3	0.04	0.02	0.02	0.01
FeO	0.65	1.97	0.26	0.14
MnO	0.02	0.03	0.02	0.02
MgO	0.59	1.48	0.24	0.16
CaO	0.12	0.03	0.38	0.09
Na_2O	0.01	0.01	0.01	0.01
K_2O	0.00	0.00	0.00	0.00

Table B-10: Summary of the chlorite EMP analysis as annotated in Table B-1 (part 1).

Chlorite	AQ08_GPH		AQ10_GPH		AQ11_GPH	RS04_GPH		AQ09_GBR	AQ15_GBR		EX09_GBR		AQ07_GRT		RS03_GRT
	WR	**FR**	**WR**	**FR**	**WR**	**WR**	**FR**	**FR**	**WR**	**FR**	**WR**	**FR**	**WR**	**FR**	**FR**
SiO_2	25.95	25.46	28.22	26.39	26.23	29.58	24.53	29.66	30.97	29.37	27.61	27.03	24.60	25.01	30.08
TiO_2	0.39	0.10	BDL	BDL	BDL	0.05	BDL	BDL	BDL	BDL	BDL	BDL	0.06	BDL	0.07
Al_2O_3	18.14	18.61	19.88	18.87	17.93	17.73	18.09	15.66	13.51	16.00	18.70	20.23	19.02	18.63	18.99
V_2O_3	BDL	BDL	BDL	BDL	BDL	BDL	BDL	BDL	BDL	BDL	BDL	0.05	BDL	BDL	BDL
Cr_2O_3	BDL	BDL	BDL	BDL	BDL	0.05	BDL	BDL	BDL	BDL	1.29	0.37	BDL	BDL	BDL
Fe_2O_3	30.07	32.02	23.40	24.26	28.66	26.98	32.22	20.87	18.50	20.90	19.99	20.64	32.03	32.21	20.94
MnO	0.58	0.56	0.31	0.34	0.79	1.30	0.71	0.12	0.17	0.28	0.32	0.30	0.62	0.63	0.48
MgO	8.24	9.69	15.29	16.71	13.25	9.45	10.84	20.10	22.75	20.30	19.06	18.63	9.38	10.24	15.08
CaO	0.14	0.05	0.05	0.05	BDL	0.09	BDL	0.33	0.05	BDL	0.13	0.09	0.06	0.17	0.10
SrO	BDL	BDL	BDL	BDL	BDL	BDL	BDL	BDL	BDL	BDL	BDL	BDL	BDL	BDL	BDL
BaO	0.10	BDL	BDL	BDL	BDL	0.06	BDL	0.02	BDL	BDL	BDL	BDL	0.09	BDL	0.05
Na_2O	BDL	BDL	0.05	BDL	BDL	0.07	BDL	0.01	BDL	BDL	BDL	BDL	0.06	BDL	0.07
K_2O	1.08	0.39	0.30	BDL	0.11	2.39	BDL	BDL	BDL	BDL	BDL	BDL	0.18	BDL	1.27
P_2O_5	0.81	0.21	0.08	BDL	BDL	0.17	BDL	BDL	BDL	BDL	BDL	BDL	0.40	0.08	BDL
SO_3	0.10	BDL	BDL	BDL	BDL	BDL	BDL	BDL	BDL	BDL	BDL	BDL	0.06	BDL	BDL
Cl	BDL	BDL	BDL	BDL	BDL	BDL	BDL	0.08	BDL	BDL	BDL	BDL	BDL	BDL	BDL
F	0.08	0.07	0.05	0.06	BDL	0.07	0.05	BDL	BDL	BDL	BDL	BDL	BDL	BDL	0.13
H_2O	11.17	11.07	11.64	11.53	11.26	11.28	11.03	11.77	11.93	11.76	11.76	11.76	11.07	11.06	11.73
TOTAL	96.91	98.34	99.32	98.28	98.40	99.26	97.57	98.66	97.87	98.73	99.01	99.12	97.69	98.13	99.02

Table B-11: Summary of the SD of the chlorite EMP analysis (part 1).

SD	AQ08_GPH		AQ10_GPH		AQ11_GPH	RS04_GPH		AQ09_GBR	AQ15_GBR		EX09_GBR		AQ07_GRT		RS03_GRT
	WR	**FR**	**WR**	**FR**	**WR**	**WR**	**FR**	**FR**	**WR**	**FR**	**WR**	**FR**	**WR**	**FR**	**FR**
SiO_2	1.34	1.58	2.91	0.60	1.03	3.39	0.03	0.65	10.84	1.14	1.42	0.02	1.37	0.76	3.81
TiO_2	1.08	0.09	0.01	0.03	0.01	0.02	0.01	0.04	0.05	0.01	0.02	0.01	0.05	0.01	0.14
Al_2O_3	0.75	0.41	0.52	0.38	0.31	1.17	0.15	0.70	5.96	1.17	1.76	0.06	0.46	0.41	1.72
V_2O_3	0.02	0.02	0.02	0.02	0.02	0.02	0.01	0.01	0.01	0.01	0.02	0.01	0.02	0.02	0.02
Cr_2O_3	0.01	0.03	0.01	0.02	0.01	0.07	0.02	0.01	0.03	0.01	0.85	0.25	0.02	0.03	0.02
Fe_2O_3	1.63	1.71	2.07	0.45	1.02	3.61	0.02	0.93	5.00	1.43	0.71	0.00	1.03	0.28	3.20
MnO	0.13	0.06	0.06	0.01	0.07	0.49	0.01	0.01	0.42	0.07	0.05	0.00	0.05	0.02	0.12
MgO	0.76	0.68	2.38	0.43	0.29	0.79	0.34	0.71	4.53	1.68	1.26	0.07	0.78	0.36	1.79
CaO	0.07	0.04	0.02	0.01	0.02	0.05	0.04	0.02	0.03	0.00	0.17	0.06	0.02	0.25	0.05
SrO	0.04	0.03	0.02	0.02	0.02	0.02	0.02	0.02	0.02	0.02	0.01	0.02	0.03	0.02	0.02
BaO	0.07	0.05	0.02	0.01	0.01	0.06	0.02	0.01	0.03	0.01	0.01	0.01	0.09	0.01	0.09
Na_2O	0.03	0.04	0.05	0.02	0.02	0.05	0.01	0.03	0.09	0.01	0.01	0.02	0.03	0.02	0.04
K_2O	0.39	0.48	0.52	0.02	0.14	1.99	0.01	0.00	0.02	0.00	0.01	0.01	0.18	0.01	1.50
P_2O_5	0.46	0.31	0.13	0.01	0.05	0.10	0.03	0.01	0.05	0.02	0.02	0.00	0.50	0.20	0.03
SO_3	0.07	0.04	0.03	0.03	0.02	0.02	0.04	0.01	0.01	0.03	0.02	0.00	0.08	0.04	0.05
Cl	0.02	0.01	0.01	0.01	0.01	0.01	0.01	0.02	0.00	0.00	0.00	0.00	0.02	0.01	0.01
F	0.05	0.01	0.02	0.03	0.03	0.06	0.00	0.01	0.02	0.03	0.02	0.04	0.02	0.03	0.04
H_2O	0.12	0.12	0.20	0.03	0.08	0.15	0.00	0.06	0.55	0.09	0.07	0.02	0.07	0.03	0.20

Table B-12: Summary of the chlorite EMP analysis as annotated in Table B-1 (part 2).

Chlorite	AS02_GRT		AQ05_DOL		RS09_191_DOL		AS01_DOL		AQ12_BAS	RS07_BAS	
	WR	**FR**	**WR**	**FR**	**WR**	**FR**	**WR**	**FR**	**WR**	**WR**	**FR**
SiO_2	25.85	26.26	26.77	29.38	28.89	29.41	28.87	29.33	27.33	26.49	27.54
TiO_2	0.05	0.05	BDL	0.07	0.07	0.05	BDL	BDL	BDL	BDL	BDL
Al_2O_3	18.67	18.94	17.87	16.68	13.53	13.67	17.07	16.33	18.47	19.88	19.28
V_2O_3	BDL	BDL	0.05	0.06	BDL	BDL	BDL	BDL	BDL	BDL	BDL
Cr_2O_3	BDL	BDL	BDL	BDL	BDL	BDL	0.26	0.35	BDL	BDL	BDL
Fe_2O_3	31.05	30.69	28.02	29.19	30.49	30.92	20.12	20.04	24.65	22.67	22.37
MnO	0.36	0.33	0.33	0.45	0.20	0.20	0.24	0.22	0.33	0.32	0.31
MgO	10.78	11.24	12.59	11.98	13.27	13.14	19.90	20.42	15.34	16.98	16.47
CaO	0.07	0.10	0.06	0.06	0.12	0.26	0.08	BDL	0.13	0.11	0.16
SrO	BDL	BDL	BDL	BDL	BDL	BDL	BDL	BDL	BDL	BDL	BDL
BaO	0.07	BDL	0.12	BDL	BDL	BDL	BDL	BDL	BDL	BDL	BDL
Na_2O	0.06	BDL	0.05	BDL	BDL	BDL	BDL	BDL	BDL	BDL	BDL
K_2O	0.08	0.19	0.15	0.44	0.07	0.05	BDL	BDL	0.12	BDL	0.13
P_2O_5	0.08	0.07	0.06	BDL	BDL	BDL	BDL	BDL	BDL	BDL	BDL
SO_3	BDL	BDL	0.08	BDL	BDL	BDL	BDL	BDL	BDL	BDL	BDL
Cl	BDL	BDL	BDL	BDL	BDL	BDL	BDL	BDL	BDL	BDL	BDL
F	BDL	BDL	BDL	BDL	BDL	BDL	BDL	BDL	BDL	BDL	BDL
H_2O	11.16	11.19	11.35	11.31	11.23	11.21	11.81	11.81	11.54	11.64	11.69
TOTAL	98.39	99.12	97.55	99.65	97.97	98.96	98.48	98.62	98.05	98.25	98.15

Table B-13: Summary of the SD of the chlorite EMP analysis as annotated in Table B-1 (part 2).

SD	AS02_GRT		AQ05_DOL		RS09_191_DOL		AS01_DOL		AQ12_BAS	RS07_BAS	
	WR	**FR**	**WR**	**FR**	**WR**	**FR**	**WR**	**FR**	**WR**	**WR**	**FR**
SiO_2	0.74	0.89	2.00	5.46	0.52	1.60	1.34	1.40	1.44	-	0.86
TiO_2	0.07	0.07	0.01	0.14	0.06	0.03	0.01	0.00	0.01	-	0.01
Al_2O_3	0.81	0.51	2.25	3.27	0.60	0.79	2.18	1.91	0.56	-	0.85
V_2O_3	0.02	0.02	0.04	0.05	0.03	0.02	0.01	0.04	0.03	-	0.02
Cr_2O_3	0.03	0.03	0.03	0.02	0.02	0.02	0.25	0.26	0.02	-	0.02
Fe_2O_3	1.53	0.40	1.80	0.72	0.78	0.87	0.66	0.52	0.49	-	0.53
MnO	0.11	0.03	0.07	0.16	0.03	0.04	0.03	0.01	0.01	-	0.01
MgO	1.04	0.56	2.32	1.73	0.56	0.22	0.77	1.03	0.61	-	0.44
CaO	0.03	0.09	0.04	0.04	0.05	0.31	0.11	0.02	0.07	-	0.19
SrO	0.03	0.02	0.02	0.03	0.01	0.02	0.02	0.02	0.02	-	0.01
BaO	0.10	0.03	0.22	0.01	0.03	0.02	0.02	0.03	0.02	-	0.03
Na_2O	0.02	0.02	0.06	0.08	0.05	0.02	0.03	0.00	0.02	-	0.03
K_2O	0.09	0.23	0.11	0.54	0.00	0.06	0.03	0.00	0.14	-	0.15
P_2O_5	0.11	0.07	0.07	0.02	0.06	0.01	0.02	0.01	0.02	-	0.01
SO_3	0.08	0.01	0.11	0.02	0.03	0.02	0.01	0.03	0.04	-	0.06
Cl	0.02	0.01	0.01	0.01	0.01	0.01	0.01	0.00	0.01	-	0.01
F	0.04	0.03	0.03	0.01	0.02	0.02	0.07	0.04	0.02	-	0.03
H_2O	0.07	0.03	0.11	0.10	0.05	0.07	0.04	0.02	0.05	-	0.05

Table B-14: Summary of the epidote EMP analysis as annotated in Table B-1 (part 1).

Epidote	AQ08_GPH		AQ11_GPH		RS04_GPH		AQ09_GBR		AQ15_GBR		EX09_GBR	RS03_GRT	
	WR	**FR**	**WR**	**FR**	**WR**	**FR**	**WR**	**FR**	**WR**	**FR**	**FR**	**WR**	**FR**
SiO_3	37.26	37.27	37.05	37.25	36.89	36.98	38.46	39.20	40.70	42.26	40.03	37.39	37.18
TiO_3	0.05	0.13	0.05	BDL	0.06	BDL	BDL	BDL	BDL	BDL	0.07	0.06	0.06
Al_2O_4	22.50	21.68	21.47	21.55	20.15	20.89	28.67	29.04	30.74	30.78	31.41	22.77	22.84
V_2O_4	BDL	BDL	BDL	0.10	BDL	BDL	BDL	BDL	BDL	BDL	BDL	BDL	BDL
Cr_2O_4	BDL	BDL	BDL	BDL	BDL	BDL	BDL	BDL	BDL	BDL	BDL	BDL	BDL
Fe_2O_4	14.96	15.95	16.01	15.06	17.64	16.75	7.54	6.56	3.20	2.21	3.04	13.98	13.90
MnO	0.22	0.26	0.21	0.32	0.15	0.22	0.08	0.07	0.06	0.05	0.10	0.25	0.26
MgO	BDL	BDL	BDL	0.35	0.05	BDL	BDL	BDL	0.06	0.07	0.06	0.05	0.11
CaO	22.98	22.90	22.87	22.70	22.69	22.60	23.98	23.55	22.79	21.32	23.37	22.78	22.69
SrO	BDL	0.08	BDL	0.18	0.28	0.33	BDL	BDL	0.09	0.08	0.17	0.32	0.29
BaO	BDL	BDL	BDL	BDL	BDL	BDL	BDL	BDL	BDL	BDL	BDL	BDL	BDL
Na_2O	BDL	BDL	BDL	BDL	BDL	BDL	BDL	0.25	0.74	1.50	0.49	BDL	BDL
K_2O	BDL	BDL	BDL	BDL	BDL	BDL	BDL	BDL	BDL	BDL	BDL	BDL	BDL
P_2O_6	BDL	BDL	BDL	BDL	BDL	BDL	BDL	BDL	BDL	BDL	BDL	BDL	BDL
SO_4	BDL	BDL	BDL	BDL	BDL	BDL	BDL	BDL	BDL	BDL	BDL	BDL	BDL
Cl	BDL	BDL	BDL	BDL	BDL	BDL	BDL	BDL	BDL	BDL	BDL	BDL	BDL
F	BDL	BDL	BDL	0.05	BDL	BDL	BDL	BDL	-0.01	BDL	BDL	BDL	BDL
H_2O	1.87	1.87	1.87	1.87	1.85	1.86	1.93	1.94	1.97	1.98	1.96	1.88	1.88
TOT	99.94	100.24	99.69	99.50	99.84	99.76	100.76	100.67	100.42	100.33	100.71	99.56	99.28

Table B-15: Summary of the SD of the epidote EMP analysis as annotated in Table B-1 (part 1).

SD	AQ08_GPH		AQ11_GPH		RS04_GPH		AQ09_GBR		AQ15_GBR		EX09_GBR	RS03_GRT	
	WR	**FR**	**WR**	**FR**	**WR**	**FR**	**WR**	**FR**	**WR**	**FR**	**FR**	**WR**	**FR**
SiO_3	0.22	0.32	0.24	0.65	0.24	0.15	0.12	1.70	1.85	2.81	0.54	0.29	0.09
TiO_3	0.02	0.35	0.01	0.02	0.03	0.02	0.01	0.01	0.02	0.02	0.03	0.03	0.02
Al_2O_4	1.44	0.71	0.12	1.05	1.23	1.11	1.09	1.01	1.65	1.90	1.86	0.82	0.67
V_2O_4	0.02	0.02	0.01	0.06	0.03	0.03	0.01	0.01	0.01	0.03	0.00	0.03	0.04
Cr_2O_4	0.02	0.02	0.01	0.03	0.02	0.02	0.01	0.01	0.02	0.02	0.03	0.02	0.01
Fe_2O_4	1.80	0.74	0.27	0.94	1.25	1.16	1.27	2.15	1.24	0.36	1.95	1.03	0.98
MnO	0.12	0.17	0.11	0.10	0.09	0.12	0.04	0.04	0.01	0.02	0.10	0.13	0.22
MgO	0.04	0.03	0.03	0.48	0.11	0.01	0.01	0.02	0.04	0.02	0.05	0.05	0.19
CaO	0.09	0.33	0.15	0.10	0.26	0.51	0.16	1.07	1.77	2.65	0.90	0.30	0.49
SrO	0.04	0.21	0.04	0.26	0.29	0.46	0.02	0.02	0.04	0.02	0.14	0.14	0.07
BaO	0.02	0.02	0.02	0.02	0.01	0.03	0.01	0.01	0.03	0.01	0.02	0.02	0.03
Na_2O	0.01	0.01	0.02	0.04	0.02	0.01	0.01	0.56	0.88	1.22	0.39	0.03	0.02
K_2O	0.01	0.01	0.01	0.00	0.01	0.01	0.01	0.01	0.01	0.00	0.00	0.02	0.03
P_2O_6	0.03	0.03	0.01	0.03	0.01	0.02	0.01	0.02	0.01	0.02	0.02	0.02	0.01
SO_4	0.02	0.02	0.01	0.01	0.01	0.01	0.01	0.01	0.03	0.02	0.01	0.03	0.02
Cl	0.00	0.00	0.01	0.00	0.01	0.01	0.00	0.01	0.01	0.02	0.01	0.01	0.01
F	0.03	0.02	0.02	0.03	0.02	0.01	0.00	0.01	0.00	0.00	0.00	0.03	0.03
H_2O	0.01	0.01	0.00	0.00	0.01	0.01	0.01	0.02	0.01	0.01	0.01	0.01	0.01

Table B-16: Summary of the epidote EMP analysis as annotated in Table B-1 (part 2).

Epidote	AS02_GRT		AQ05_DOL		RS09_191_DOL		AS01_DOL		AQ12_BAS		RS07_BAS	
	WR	**FR**	**WR**	**FR**	**WR**	**FR**	**WR**	**FR**	**WR**	**FR**	**WR**	**FR**
SiO_3	36.44	37.52	37.75	37.51	37.65	37.96	45.69	45.29	31.65	37.70	37.45	38.86
TiO_3	0.06	0.06	0.05	0.05	0.05	0.11	BDL	BDL	0.06	0.10	BDL	BDL
Al_2O_4	20.87	22.83	22.88	22.34	23.93	21.46	28.43	27.77	20.21	23.99	23.87	19.90
V_2O_4	0.05	BDL	0.13	0.11	BDL	BDL	BDL	BDL	BDL	0.09	0.08	0.08
Cr_2O_4	BDL	BDL	BDL	BDL	BDL	BDL	BDL	BDL	BDL	BDL	BDL	BDL
Fe_2O_4	15.45	13.83	14.30	14.98	12.94	16.27	3.05	3.76	18.53	12.92	12.86	10.49
MnO	0.08	0.09	0.13	0.07	0.10	0.12	0.05	0.07	0.18	0.07	0.10	0.11
MgO	BDL	BDL	BDL	BDL	0.28	2.92	0.43	0.12	6.73	BDL	BDL	3.05
CaO	21.98	23.12	23.13	23.15	22.46	17.63	18.04	18.63	11.49	23.08	22.78	22.54
SrO	0.23	0.12	0.09	0.09	0.12	0.17	0.10	0.20	BDL	BDL	0.32	0.15
BaO	BDL	BDL	BDL	BDL	BDL	BDL	BDL	BDL	BDL	BDL	BDL	BDL
Na_2O	BDL	BDL	BDL	BDL	0.05	0.23	2.72	2.56	BDL	BDL	BDL	BDL
K_2O	BDL	BDL	BDL	BDL	BDL	0.05	BDL	BDL	0.19	BDL	BDL	BDL
P_2O_6	BDL	BDL	BDL	BDL	BDL	BDL	BDL	BDL	BDL	BDL	BDL	BDL
SO_4	BDL	BDL	BDL	BDL	BDL	BDL	BDL	BDL	BDL	BDL	BDL	BDL
Cl	BDL	BDL	BDL	BDL	BDL	BDL	BDL	BDL	BDL	BDL	BDL	BDL
F	0.06	BDL	BDL	BDL	BDL	BDL	BDL	BDL	BDL	BDL	BDL	BDL
H_2O	1.87	1.88	1.88	1.87	1.89	1.89	2.00	1.99	1.89	1.89	1.89	1.90
TOT	97.14	99.53	100.37	100.21	99.56	98.88	100.64	100.53	91.14	100.04	99.46	97.30

Table B-17: Summary of the SD of the epidote EMP analysis as annotated in Table B-1 (part 2).

SD	AS02_GRT		AQ05_DOL		RS09_191_DOL		AS01_DOL		AQ12_BAS		RS07_BAS	
	WR	**FR**	**WR**	**FR**	**WR**	**FR**	**WR**	**FR**	**WR**	**FR**	**WR**	**FR**
SiO_3	1.65	0.10	0.44	0.29	0.73	3.53	0.71	2.48	8.27	0.11	0.40	5.80
TiO_3	0.07	0.00	0.02	0.04	0.02	0.20	0.00	0.00	0.04	0.05	0.01	0.06
Al_2O_4	1.52	1.47	0.65	0.74	1.63	6.63	1.06	0.80	4.58	0.66	1.61	8.15
V_2O_4	0.06	0.03	0.06	0.08	0.03	0.03	0.01	0.02	0.05	0.02	0.04	0.04
Cr_2O_4	0.05	0.04	0.02	0.02	0.01	0.02	0.00	0.04	0.01	0.01	0.01	0.06
Fe_2O_4	1.78	1.97	0.77	0.98	1.86	7.89	0.49	0.39	7.52	1.14	1.86	3.20
MnO	0.06	0.04	0.07	0.02	0.01	0.04	0.05	0.04	0.10	0.02	0.03	0.07
MgO	0.04	0.00	0.01	0.01	0.24	3.63	0.47	0.04	9.51	0.01	0.02	5.16
CaO	2.18	0.34	0.11	0.25	0.63	6.20	0.24	2.00	16.09	0.06	0.30	0.26
SrO	0.10	0.06	0.07	0.09	0.05	0.15	0.01	0.00	0.04	0.01	0.12	0.21
BaO	0.02	0.03	0.02	0.03	0.01	0.02	0.05	0.00	0.02	0.02	0.03	0.01
Na_2O	0.02	0.01	0.04	0.02	0.04	0.28	0.25	1.25	0.03	0.00	0.04	0.09
K_2O	0.00	0.01	0.01	0.01	0.01	0.07	0.00	0.01	0.25	0.00	0.02	0.01
P_2O_6	0.02	0.01	0.02	0.02	0.01	0.02	0.02	0.02	0.01	0.02	0.03	0.01
SO_4	0.02	0.01	0.03	0.01	0.03	0.01	0.01	0.03	0.02	0.01	0.03	0.02
Cl	0.01	0.00	0.00	0.00	0.00	0.02	0.01	0.02	0.06	0.00	0.00	0.02
F	0.10	0.02	0.02	0.02	0.02	0.01	0.01	0.01	0.04	0.04	0.01	0.03
H_2O	0.01	0.01	0.01	0.01	0.01	0.03	0.00	0.02	0.00	0.01	0.01	0.02

Table B-18: Summary of the amphibole EMP analysis as annotated in Table B-1, includes the SD.

Amphibole	AQ09_GBR	EX09_GBR	AQ05_DOL		RS09_191_DOL	
	WR	WR	WR	FR	WR	FR
SiO_2	49.05	55.67	45.22	45.37	48.86	45.71
TiO_2	0.07	0.41	0.97	1.18	0.32	1.17
Al_2O_3	4.53	1.50	5.14	5.16	3.86	6.24
V_2O_3	BDL	BDL	BDL	BDL	BDL	0.15
Cr_2O_3	0.17	0.11	BDL	BDL	BDL	BDL
Fe_2O_3	16.53	11.33	29.95	29.00	19.19	22.56
MnO	0.40	0.23	0.43	0.35	0.36	0.23
MgO	16.05	16.19	5.22	5.71	12.21	9.68
CaO	5.99	11.42	8.54	8.85	9.52	9.38
SrO	0.13	BDL	BDL	BDL	BDL	BDL
BaO	0.08	BDL	BDL	BDL	BDL	BDL
Na_2O	0.35	0.09	1.47	1.42	0.65	1.49
K_2O	0.08	BDL	0.46	0.53	0.37	0.37
P_2O_5	1.63	BDL	BDL	BDL	0.05	BDL
SO_3	0.05	BDL	BDL	BDL	BDL	BDL
Cl	0.05	BDL	0.35	0.40	0.12	0.25
F	BDL	BDL	0.33	0.34	0.07	0.35
H_2O	7.13	2.12	1.89	1.89	2.01	1.95
TOTAL	102.32	99.16	100.01	100.24	97.66	99.59
SD	**AQ09_GBR**	**EX09_GBR**	**AQ05_DOL**		**RS09_191_DOL**	
	WR	**WR**	**WR**	**FR**	**WR**	**FR**
SiO_2	4.63	2.17	0.71	1.12	-	1.77
TiO_2	0.03	0.56	0.26	0.35	-	0.43
Al_2O_3	1.77	0.68	0.37	0.58	-	1.47
V_2O_3	0.01	0.02	0.02	0.02	-	0.07
Cr_2O_3	0.21	0.03	0.03	0.02	-	0.02
Fe_2O_3	1.84	0.60	1.72	0.85	-	0.96
MnO	0.01	0.00	0.08	0.08	-	0.05
MgO	0.03	0.74	0.42	0.38	-	0.38
CaO	0.15	0.69	0.87	0.82	-	0.41
SrO	0.17	0.02	0.03	0.02	-	0.01
BaO	0.08	0.00	0.02	0.03	-	0.04
Na_2O	0.13	0.01	0.14	0.12	-	0.42
K_2O	0.01	0.02	0.11	0.19	-	0.11
P_2O_5	2.22	0.00	0.03	0.03	-	0.00
SO_3	0.07	0.03	0.02	0.02	-	0.02
Cl	0.04	0.01	0.05	0.08	-	0.06
F	0.02	0.01	0.33	0.14	-	0.16
H_2O	7.16	0.02	0.02	0.01	-	0.01

Table B-19: Summary of the muscovite EMP analysis as annotated in Table B-1, includes the SD.

Muscovite	AQ09_GBR		AQ15_GBR		EX09_GBR		RS03_GRT	AQ05_DOL		AS01_DOL
	WR	FR	WR	FR	WR	FR	WR	WR	FR	WR
SiO_2	47.77	47.11	45.52	46.17	40.86	48.13	47.67	47.45	47.65	49.01
TiO_2	BDL	BDL	BDL	0.05	0.05	BDL	0.06	BDL	0.05	BDL
Al_2O_3	36.09	35.57	37.28	36.71	30.27	33.09	27.27	32.73	30.37	30.21
V_2O_3	BDL	BDL	BDL	BDL	BDL	BDL	BDL	BDL	BDL	BDL
Cr_2O_3	BDL	BDL	BDL	BDL	BDL	BDL	BDL	BDL	BDL	BDL
Fe_2O_3	1.29	1.09	0.95	0.97	6.65	1.75	5.34	2.91	4.49	2.50
MnO	0.05	BDL	0.10	0.12	0.12	BDL	BDL	BDL	0.05	BDL
MgO	0.19	1.17	0.36	0.50	6.31	1.52	2.46	0.73	1.19	2.23
CaO	0.46	0.06	BDL	BDL	0.09	BDL	0.07	0.10	0.08	BDL
SrO	BDL	BDL	BDL	BDL	BDL	BDL	BDL	BDL	BDL	BDL
BaO	0.11	0.27	BDL	BDL	0.16	0.29	0.13	0.16	0.20	0.05
Na_2O	1.15	0.17	0.14	0.16	0.12	0.09	0.05	0.30	0.23	0.01
K_2O	10.15	11.36	9.60	11.23	5.76	11.17	9.69	10.77	10.87	11.48
P_2O_5	BDL	BDL	BDL	BDL	0.07	BDL	0.08	BDL	BDL	BDL
SO_3	BDL	BDL	BDL	BDL	BDL	BDL	BDL	BDL	BDL	BDL
Cl	BDL	BDL	BDL	BDL	BDL	BDL	BDL	BDL	BDL	BDL
F	BDL	BDL	BDL	BDL	BDL	BDL	0.09	BDL	BDL	BDL
H_2O	4.52	4.50	4.56	4.51	7.09	4.49	4.44	4.48	4.43	4.48
TOTAL	101.80	101.27	98.68	100.45	97.59	100.62	97.37	99.73	99.57	100.05

SD	AQ09_GBR		AQ15_GBR		EX09_GBR		RS03_GRT	AQ05_DOL		AS01_DOL
	WR	FR	WR	FR	WR	FR	WR	WR	FR	WR
SiO_2	-	-	0.50	0.05	8.82	0.83	1.21	1.20	-	-
TiO_2	-	-	0.01	0.05	0.02	0.00	0.03	0.02	-	-
Al_2O_3	-	-	0.44	0.21	7.23	0.83	1.15	2.73	-	-
V_2O_3	-	-	0.02	0.01	0.00	0.00	0.04	0.01	-	-
Cr_2O_3	-	-	0.02	0.01	0.01	0.00	0.02	0.02	-	-
Fe_2O_3	-	-	0.01	0.01	8.15	0.29	0.26	1.41	-	-
MnO	-	-	0.05	0.04	0.10	0.01	0.02	0.02	-	-
MgO	-	-	0.11	0.32	8.92	0.67	0.18	0.54	-	-
CaO	-	-	0.03	0.01	0.00	0.01	0.04	0.11	-	-
SrO	-	-	0.05	0.02	0.01	0.01	0.04	0.02	-	-
BaO	-	-	0.03	0.00	0.14	0.10	0.05	0.08	-	-
Na_2O	-	-	0.01	0.02	0.10	0.04	0.02	0.28	-	-
K_2O	-	-	1.57	0.30	4.50	0.04	0.60	0.33	-	-
P_2O_5	-	-	0.02	0.02	0.03	0.01	0.09	0.02	-	-
SO_3	-	-	0.04	0.03	0.02	0.02	0.03	0.03	-	-
Cl	-	-	0.01	0.02	0.03	0.01	0.00	0.01	-	-
F	-	-	0.01	0.03	0.03	0.01	0.01	0.02	-	-
H_2O	-	-	0.05	0.00	4.36	0.00	0.02	0.03	-	-

Table B-20: Summary of the kaolinite EMP analysis of the mineral, includes the SD.

Kaolinite	**AQ11_GPH**	**AQ09_GBR**
	WR	**WR**
SiO_2	43.94	36.88
TiO_2	BDL	0.05
Al_2O_3	38.64	40.63
V_2O_3	BDL	BDL
Cr_2O_3	BDL	BDL
Fe_2O_3	1.11	3.11
MnO	0.52	1.22
MgO	0.58	0.96
CaO	0.17	0.26
SrO	BDL	BDL
BaO	0.48	BDL
Na_2O	0.10	0.31
K_2O	1.30	0.11
P_2O_5	0.21	1.26
SO_3	BDL	0.09
Cl	BDL	BDL
F	BDL	BDL
H_2O	13.61	13.49
TOTAL	100.92	98.38
SD	**AQ11_GPH**	**AQ09_GBR**
	WR	**WR**
SiO_2	1.44	-
TiO_2	0.01	-
Al_2O_3	1.06	-
V_2O_3	0.03	-
Cr_2O_3	0.03	-
Fe_2O_3	0.28	-
MnO	0.70	-
MgO	0.21	-
CaO	0.08	-
SrO	0.05	-
BaO	0.79	-
Na_2O	0.02	-
K_2O	1.26	-
P_2O_5	0.11	-
SO_3	0.29	-
Cl	0.00	-
F	0.03	-
H_2O	0.18	-

Table B-21: Summary of the clays EMP analysis as annotated in Table B-1, includes the SD.

Clays	AQ11_GPH	RS03_GRT	AS02_GRT	AQ05_DOL	RS09_191_DOL	RS09_191_DOL
	WR	WR	WR	WR	WR	WR
SiO_2	34.88	35.84	35.97	23.69	21.45	30.38
TiO_2	BDL	BDL	0.05	0.29	27.53	BDL
Al_2O_3	25.21	24.73	11.85	14.13	10.50	17.74
V_2O_3	BDL	BDL	BDL	0.05	0.55	BDL
Cr_2O_3	BDL	BDL	BDL	BDL	BDL	BDL
Fe_2O_3	15.02	11.70	33.69	23.53	13.24	19.56
MnO	0.44	0.21	0.22	4.70	0.24	0.21
MgO	8.24	7.61	2.34	4.42	3.13	11.46
CaO	0.17	0.71	0.16	6.26	10.71	0.21
SrO	BDL	0.29	BDL	0.05	BDL	BDL
BaO	0.14	0.14	0.17	0.88	BDL	0.07
Na_2O	0.08	0.08	0.53	0.10	0.11	0.26
K_2O	1.06	2.22	1.61	1.04	0.21	1.02
P_2O_5	0.33	2.16	0.31	5.15	1.63	2.76
SO_3	0.10	0.24	BDL	0.11	BDL	0.21
Cl	BDL	BDL	BDL	BDL	0.05	BDL
F	0.05	0.08	BDL	0.21	0.07	BDL
H_2O	BDL	BDL	BDL	BDL	BDL	BDL
TOTAL	85.80	86.03	86.96	84.67	89.46	83.97
SD	**AQ11_GPH**	**RS03_GRT**	**AS02_GRT**	**AQ05_DOL**	**RS09_191_DOL**	**RS09_191_DOL**
	WR	**WR**	**WR**	**WR**	**WR**	**WR**
SiO_2	3.59	2.87	7.68	4.26	-	-
TiO_2	0.02	0.03	0.05	0.29	-	-
Al_2O_3	3.28	6.51	6.10	5.05	-	-
V_2O_3	0.03	0.02	0.02	0.03	-	-
Cr_2O_3	0.01	0.02	0.01	0.04	-	-
Fe_2O_3	3.54	6.45	7.84	12.61	-	-
MnO	0.25	0.12	0.11	6.82	-	-
MgO	1.33	5.20	2.76	4.90	-	-
CaO	0.08	0.97	0.10	8.19	-	-
SrO	0.02	0.44	0.03	0.05	-	-
BaO	0.13	0.19	0.11	1.32	-	-
Na_2O	0.01	0.03	0.44	0.06	-	-
K_2O	0.25	1.17	1.26	0.77	-	-
P_2O_5	0.35	3.36	0.28	6.35	-	-
SO_3	0.12	0.41	0.04	0.11	-	-
Cl	0.00	0.04	0.01	0.04	-	-
F	0.03	0.04	0.04	0.27	-	-
H_2O	0.00	0.00	0.00	0.00	-	-

Table B-22: Summary of the AlPO EMP analysis as annotated in Table B-1, includes the SD.

AlPO	**AQ07_GRT**
	WR
SiO_2	1.81
TiO_2	0.09
PbO	BDL
Al_2O_3	45.22
V_2O_3	BDL
Cr_2O_3	BDL
Fe_2O_3	1.06
MnO	BDL
MgO	BDL
CaO	0.07
SrO	BDL
BaO	BDL
Na_2O	0.07
K_2O	0.11
P_2O_5	30.13
SO_3	BDL
Cl	BDL
F	-0.08
TOTAL	78.58
SD	**AQ07_GRT**
	WR
SiO_2	1.57
TiO_2	0.11
Al_2O_3	0.04
V_2O_3	0.90
Cr_2O_3	0.02
Fe_2O_3	0.01
MnO	0.62
MgO	0.02
CaO	0.02
SrO	0.06
BaO	0.05
Na_2O	0.02
K_2O	0.16
P_2O_5	0.14
SO_3	1.58
Cl	0.04
F	0.01
H_2O	0.03

Table B-23: Summary of the apatite EMP analysis as annotated in Table B-1, includes the SD.

Apatite	**AS02_GRT**	**RS09_191_DOL**
	FR	**WR**
SiO_2	BDL	0.68
TiO_2	BDL	BDL
Al_2O_3	BDL	BDL
V_2O_3	BDL	BDL
Cr_2O_3	BDL	BDL
Fe_2O_3	0.69	0.77
MnO	0.30	0.06
MgO	0.15	0.20
CaO	53.35	52.78
SrO	BDL	BDL
BaO	BDL	BDL
Na_2O	0.19	BDL
K_2O	BDL	BDL
P_2O_5	40.73	37.39
SO_3	BDL	BDL
Cl	0.14	1.13
F	3.63	2.64
H_2O	BDL	BDL
TOTAL	99.18	95.65
SD	**AS02_GRT**	**RS09_191_DOL**
	FR	**WR**
SiO_2	0.01	-
TiO_2	0.00	-
Al_2O_3	0.01	-
V_2O_3	0.04	-
Cr_2O_3	0.02	-
Fe_2O_3	0.10	-
MnO	0.09	-
MgO	0.03	-
CaO	0.43	-
SrO	0.03	-
BaO	0.02	-
Na_2O	0.04	-
K_2O	0.00	-
P_2O_5	0.38	-
SO_3	0.01	-
Cl	0.03	-
F	0.04	-
H_2O	0.00	-

Table B-24: Summary of the ilmenite EMP analysis as annotated in Table B-1, includes the SD.

Ilmenite	**RS09_191_DOL**
	FR
SiO_2	BDL
TiO_2	51.06
Al_2O_3	BDL
V_2O_3	0.17
Cr_2O_3	BDL
Fe_2O_3	44.69
MnO	2.08
MgO	0.06
CaO	BDL
SrO	BDL
BaO	BDL
Na_2O	BDL
K_2O	BDL
P_2O_5	BDL
SO_3	BDL
Cl	BDL
F	BDL
H_2O	BDL
TOTAL	98.07
SD	**RS09_191_DOL**
	FR
SiO_2	0.03
TiO_2	0.82
Al_2O_3	0.03
V_2O_3	0.08
Cr_2O_3	0.00
Fe_2O_3	1.88
MnO	0.10
MgO	0.02
CaO	0.00
SrO	0.03
BaO	0.01
Na_2O	0.04
K_2O	0.00
P_2O_5	0.01
SO_3	0.02
Cl	0.01
F	0.03
H_2O	0.00

Table B-25: Summary of the oxide EMP analysis as annotated in Table B-1.

Oxides	AQ08_GPH		AQ10_GPH		AQ11_GPH		RS04_GPH		AQ15_GBR	EX09_GBR	RS03_GRT	AS02_GRT	AQ05_DOL		RS09_191_DOL
	WR	**FR**	**WR**	**FR**	**WR**	**FR**	**WR**	**FR**	**WR**	**FR**	**FR**	**FR**	**WR**	**FR**	**WR**
SiO_2	0.37	0.40	0.14	0.09	1.04	1.99	0.62	0.18	2.30	7.44	1.87	0.14	2.49	11.43	10.55
TiO_2	1.07	2.44	0.78	0.02	3.26	2.19	3.27	3.88	0.02	2.86	2.03	5.72	0.05	0.05	0.54
ZnO	BDL	BDL	BDL	BDL	BDL	BDL	BDL	BDL	BDL	0.42	BDL	2.42	0.06	0.06	0.08
PbO	BDL	BDL	BDL	BDL	BDL	BDL	BDL	BDL	BDL	BDL	BDL	BDL	BDL	BDL	BDL
Al_2O_3	0.14	0.06	BDL	BDL	0.73	0.19	0.10	0.05	1.89	3.23	0.19	3.77	0.57	0.64	5.50
V_2O_3	BDL	BDL	0.05	0.06	BDL	0.05	BDL	BDL	0.05	1.23	0.05	0.18	0.07	BDL	0.05
Cr_2O_3	BDL	0.06	BDL	BDL	BDL	BDL	BDL	BDL	BDL	6.18	BDL	BDL	BDL	BDL	BDL
FeO	88.65	88.11	91.14	93.25	84.30	85.78	87.68	85.97	70.42	64.46	84.14	81.04	74.55	64.23	60.07
NiO	BDL	BDL	BDL	BDL	BDL	BDL	BDL	BDL	0.26	BDL	BDL	BDL	BDL	BDL	0.14
Cu_2O	BDL	BDL	BDL	BDL	BDL	BDL	BDL	BDL	0.07	BDL	BDL	BDL	0.06	BDL	0.14
MnO	0.16	0.22	BDL	BDL	0.14	0.09	0.27	0.58	0.08	0.46	BDL	BDL	0.48	BDL	0.10
MgO	BDL	BDL	BDL	BDL	0.05	BDL	BDL	BDL	0.15	3.53	BDL	BDL	0.34	0.50	0.33
CaO	0.05	0.11	BDL	BDL	0.07	1.59	0.17	0.05	0.21	1.97	1.51	0.09	0.34	0.23	0.71
SO_3	BDL	BDL	BDL	BDL	BDL	BDL	BDL	BDL	1.37	BDL	BDL	BDL	0.13	BDL	0.78
As_2O_3	BDL	BDL	BDL	BDL	BDL	BDL	BDL	BDL	0.07	BDL	BDL	BDL	BDL	BDL	BDL
Cl	BDL	BDL	BDL	BDL	0.05	0.06	BDL	0.05	0.08	BDL	BDL	BDL	BDL	0.17	BDL
TOT	90.53	91.44	92.22	93.54	89.70	91.96	92.20	90.84	76.95	91.79	89.82	93.36	79.18	77.43	79.04

Table B-26: Summary of the SD of oxides EMP analysis as annotated in Table B-1.

SD	AQ08_GPH		AQ10_GPH		AQ11_GPH		RS04_GPH		AQ15_GBR	EX09_GBR	RS03_GRT	AS02_GRT	AQ05_DOL		RS09_191_DOL
	WR	**FR**	**WR**	**FR**	**WR**	**FR**	**WR**	**FR**	**WR**	**FR**	**FR**	**FR**	**WR**	**FR**	**WR**
SiO_2	0.07	0.27	0.04	0.03	0.76	0.36	0.76	0.36	0.56	3.29	-	0.09	0.42	-	-
TiO_2	1.47	1.95	1.08	0.00	4.51	0.43	4.51	0.43	0.01	2.86	-	6.65	0.06	-	-
ZnO	0.01	0.01	0.00	0.02	0.01	0.02	0.01	0.02	0.05	0.06	-	2.10	0.02	-	-
PbO	0.01	0.01	0.01	0.00	0.02	0.02	0.02	0.02	0.01	0.02	-	0.01	0.00	-	-
Al_2O_3	0.12	0.05	0.02	0.02	1.05	0.04	1.05	0.04	1.40	2.26	-	3.27	0.38	-	-
V_2O_3	0.00	0.01	0.00	0.00	0.01	0.02	0.01	0.02	0.03	0.13	-	0.04	0.01	-	-
Cr_2O_3	0.03	0.02	0.02	0.05	0.02	0.01	0.02	0.01	0.01	0.30	-	0.01	0.02	-	-
FeO	1.69	0.31	1.90	0.10	7.31	2.44	7.31	2.44	2.89	7.84	-	10.35	0.40	-	-
NiO	0.01	0.02	0.02	0.00	0.01	0.00	0.01	0.00	0.40	0.01	-	0.01	0.03	-	-
Cu_2O	0.01	0.01	0.01	0.01	0.01	0.03	0.01	0.03	0.01	0.01	-	0.01	0.03	-	-
MnO	0.27	0.27	0.01	0.01	0.16	0.02	0.16	0.02	0.05	0.05	-	0.02	0.29	-	-
MgO	0.01	0.00	0.01	0.00	0.03	0.01	0.03	0.01	0.02	3.14	-	0.01	0.09	-	-
CaO	0.02	0.05	0.00	0.00	0.04	0.31	0.04	0.31	0.03	2.05	-	0.04	0.04	-	-
SO_3	0.01	0.00	0.00	0.01	0.01	0.00	0.01	0.00	0.88	0.00	-	0.01	0.07	-	-
As_2O_3	0.02	0.01	0.01	0.01	0.00	0.01	0.00	0.01	0.03	0.01	-	0.01	0.02	-	-
Cl	0.01	0.00	0.00	0.00	0.08	0.02	0.08	0.02	0.00	0.00	-	0.01	0.00	-	-

Table B-27: Summary of the stilpnomelane EMP analysis as annotated in Table B-1, includes the SD.

Stilpnomelane	**AQ08_GPH**
	FR
SiO_2	47.09
TiO_2	BDL
Al_2O_3	6.15
FeO	27.44
MnO	1.22
MgO	5.66
CaO	0.17
SrO	BDL
BaO	0.50
Na_2O	0.54
K_2O	1.93
Rb_2O	BDL
H_2O	8.09
TOTAL	98.83
SD	**AQ08_GPH**
	FR
SiO_2	0.56
TiO_2	0.06
Al_2O_3	0.11
FeO	3.15
MnO	0.59
MgO	0.12
CaO	0.06
SrO	0.02
BaO	0.03
Na_2O	0.20
K_2O	0.42
Rb_2O	0.02

Table B-28: The average (AVG) and standard deviation (SD) of the granophyre elemental analysis obtained by TIMA.

	Fresher rock		Weathered Rind + Patina	
Elements wt%	**AVG**	**SD**	**AVG**	**SD**
Oxygen	49.05	0.47	48.99	0.59
Silicon	35.08	1.02	35.17	1.05
Aluminum	6.26	0.71	6.09	0.72
Sodium	2.88	0.86	2.49	0.95
Iron	2.63	0.62	2.87	0.98
Potassium	2.27	0.72	2.48	0.83
Calcium	1.02	0.41	0.84	0.39
Magnesium	0.51	0.23	0.43	0.24
Titanium	0.20	0.13	0.20	0.12
Hydrogen	0.04	0.02	0.03	0.02
Carbon	0.01	0.01	0.00	0.01
Phosphorus	0.01	0.01	0.01	0.01
Fluorine	0.00	0.00	0.01	0.02
Manganese	0.00	0.01	0.01	0.02
Sulphur	0.00	0.00	0.00	0.00
Barium	0.00	0.00	0.00	0.00
Unspecified	0.03	0.04	0.37	0.50
The rest	0.00	0.00	0.00	0.00
Total	100.00		100.00	

Table B-29: Summary of the gabbro elemental analysis obtained by TIMA.

	Fresher rock		Weathered Rind + Patina	
Elements wt%	**AVG**	**SD**	**AVG**	**SD**
Oxygen	43.8	1.8	44.0	1.7
Silicon	27.1	1.2	26.0	1.6
Aluminum	11.1	1.8	10.3	2.1
Calcium	6.7	3.7	6.4	3.4
Iron	5.7	1.6	7.3	2.9
Magnesium	4.4	1.4	4.4	1.1
Potassium	0.5	0.3	0.5	0.4
Sodium	0.4	0.3	0.4	0.2
Titanium	0.2	0.2	0.1	0.1
Fluorine	0.0	0.0	0.0	0.0
Hydrogen	0.0	0.0	0.0	0.0
Phosphorus	0.0	0.0	0.0	0.0
Sulphur	0.0	0.0	0.0	0.0
Chromium	0.0	0.0	0.0	0.0
Manganese	0.0	0.0	0.0	0.0
Unspecified	0.2	0.2	0.4	0.3
The rest	0.0	0.0	0.0	0.0
Total	100.0		100.0	

Table B-30: Summary of the granite elemental analysis obtained by TIMA.

	Fresher rock		Weathered Rind + Patina	
Elements wt%	**AVG**	**SD**	**AVG**	**SD**
Oxygen	49.03	0.57	49.02	0.59
Silicon	35.42	0.96	35.52	0.99
Aluminum	7.03	0.54	6.69	0.73
Sodium	3.30	0.29	2.79	0.42
Potassium	2.80	0.39	2.96	0.70
Calcium	0.85	0.41	0.81	0.44
Iron	0.63	0.28	0.83	0.28
Magnesium	0.51	0.24	0.67	0.33
Titanium	0.04	0.03	0.04	0.04
Hydrogen	0.03	0.01	0.04	0.01
Fluorine	0.02	0.01	0.05	0.02
Phosphorus	0.01	0.01	0.02	0.04
Zirconium	0.00	0.00	0.01	0.01
Manganese	0.00	0.00	0.01	0.01
Unspecified	0.32	0.28	0.54	0.29
The rest	0.01	0.00	0.01	0.00
Total	100.00		100.00	

Table B-31: Summary of the dolerite elemental analysis obtained by TIMA.

	Fresher rock		Weathered Rind + Patina	
Elements wt%	**AVG**	**SD**	**AVG**	**SD**
Oxygen	44.40	1.36	44.06	1.30
Silicon	24.72	0.82	23.92	0.90
Iron	9.65	1.23	11.17	1.66
Calcium	8.16	1.42	7.59	1.45
Aluminum	6.05	0.98	6.30	0.85
Magnesium	4.78	0.48	4.36	0.51
Sodium	0.87	0.58	0.80	0.44
Titanium	0.94	0.50	1.15	0.69
Potassium	0.24	0.10	0.28	0.13
Sulphur	0.07	0.06	0.03	0.04
Hydrogen	0.05	0.01	0.06	0.01
Phosphorus	0.03	0.03	0.04	0.03
Manganese	0.02	0.01	0.02	0.00
Fluorine	0.02	0.01	0.02	0.01
Barium	0.00	0.01	0.00	0.00
Unspecified	0.01	0.01	0.19	0.12
The rest	0.01	0.01	0.01	0.01
Total	100.00		100.00	

Table B-32: Summary of the basalt elemental analysis obtained by TIMA.

	Fresher rock		Weathered Rind + Patina	
Elements wt%	**AVG**	**SD**	**AVG**	**SD**
Oxygen	44.63	4.58	44.91	4.85
Silicon	26.14	4.11	26.34	5.44
Iron	6.04	1.66	6.43	2.53
Aluminum	5.46	2.65	5.85	2.83
Magnesium	4.59	0.93	3.82	1.31
Calcium	4.37	3.05	3.69	3.09
Sodium	2.28	1.16	2.49	1.38
Potassium	0.34	0.33	0.35	0.31
Titanium	0.06	0.03	0.07	0.04
Hydrogen	0.04	0.02	0.03	0.04
Manganese	0.02	0.01	0.01	0.01
Sulphur	0.01	0.01	0.00	0.00
Carbon	0.00	0.01	0.00	0.00
Barium	0.00	0.00	0.00	0.01
Fluorine	0.00	0.00	0.00	0.01
Unspecified	6.02	6.79	6.00	6.55
The rest	0.00	0.00	0.01	0.00
Total	100.00		100.00	

This page is intentionally blank.

C Microbiome

C.1 Bacterial 16S rRNA amplicon sequencing processing

C.1.1 16S rRNA sequence quality reports

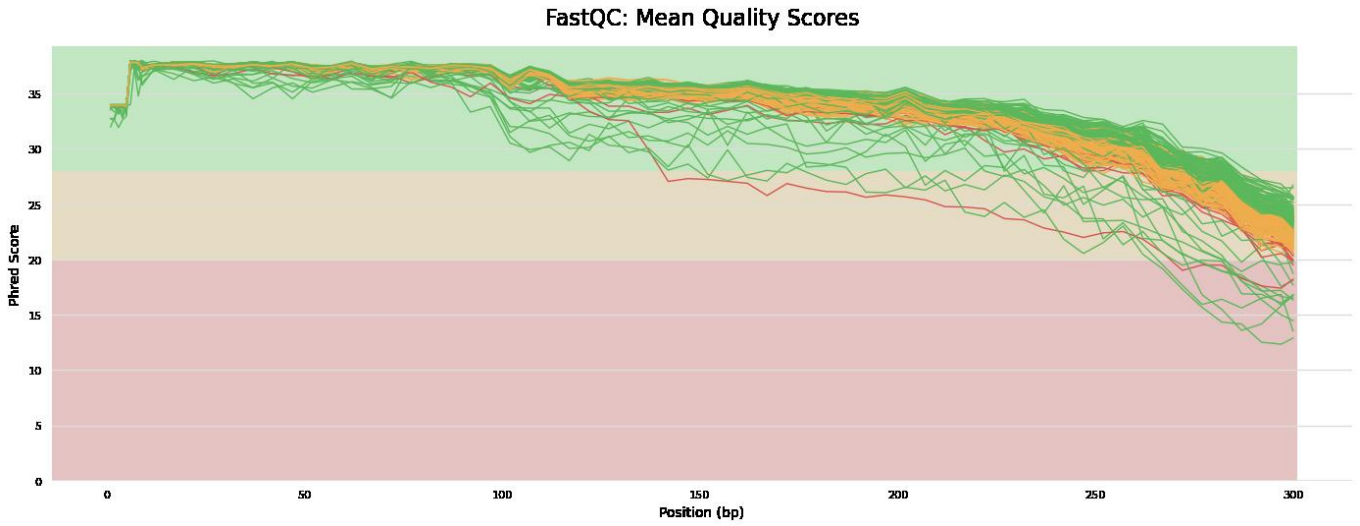

Figure C.1-1: MultiQC report of the raw 16S rRNA V3–V4 forward sequences.

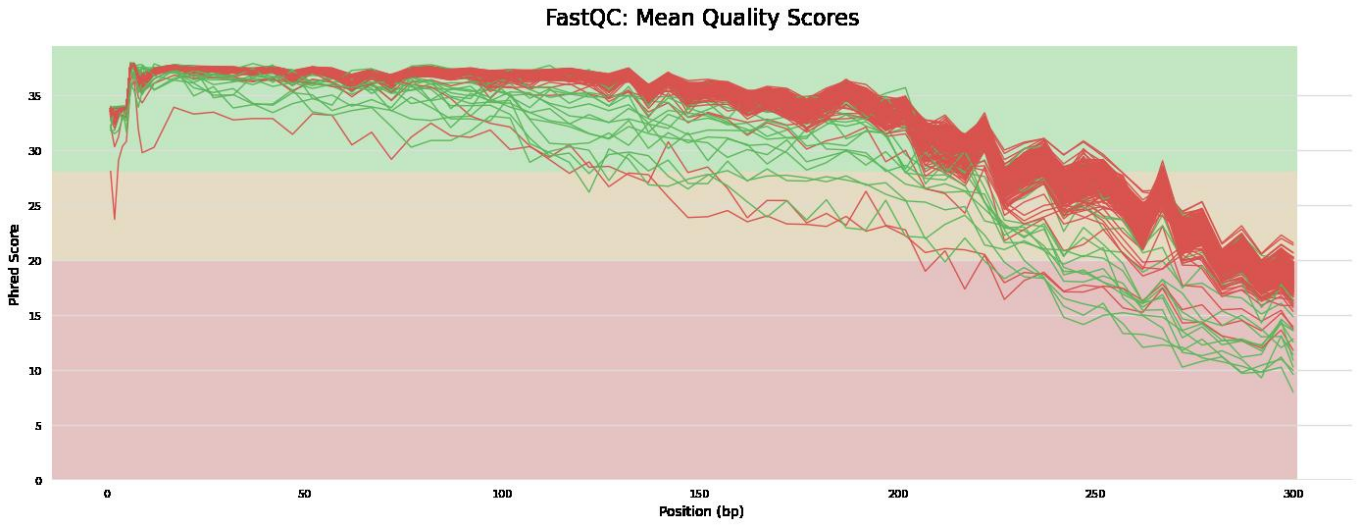

Figure C.1-2: MultiQC report of the raw 16S rRNA V3–V4 reverse sequences.

Figure C.1-3: MultiQC report of the trimmed 16S rRNA V3-V4 forward sequences.

Figure C.1-4: MultiQC report of the trimmed 16S rRNA V3-V4 reverse sequences.

C.1.2 16S rarefication

Bacterial 16S rRNA samples were rarefied to 11,000 reads per sample. This resulted in the removal of 11 samples from the dataset due to low read numbers; P4_F11, P4_G2, P5_E8, P5_F3, P6_D8, P1_A1, P1_E2, P2_D8, P2_E8, P3_A8 and P3_F10. See Figure *C.1-5*.

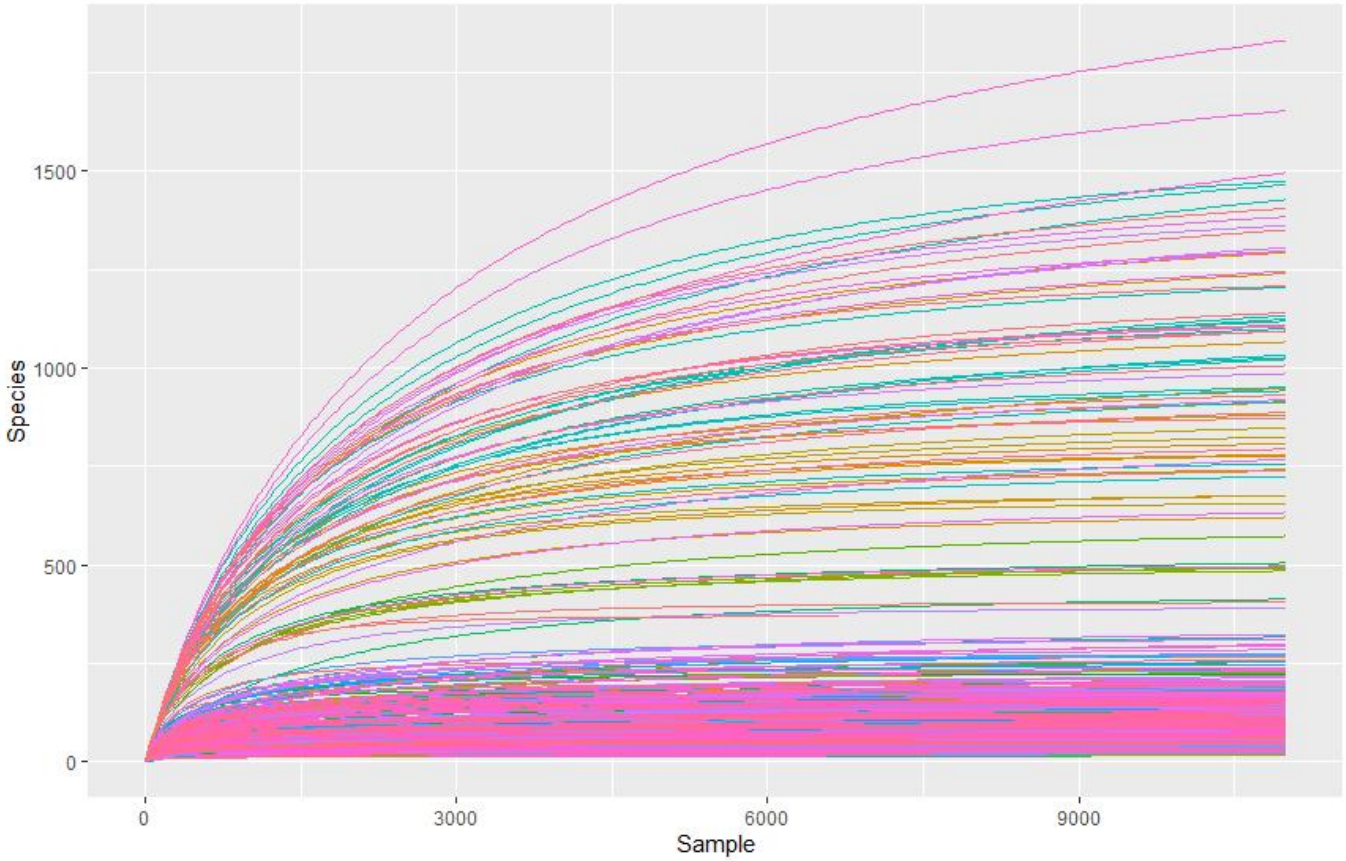

Figure C.1-5: Post rarefication of the 16S rRNA samples to 11,000 reads per sample.

Additional 16S rRNA analysis

The custom R functions used calculate Shannon, Simpson and Observed Species values are as follows, where `x` denotes a numeric vector of abundances for each taxon.

```
richness <- function(x) { sum(x>0) }
shannon <- function(x) {
  rabund <- x[x>0]/sum(x)
  -sum(rabund * log(rabund))
}
simpson <- function(x) {
 n <- sum(x)
 sum(x*(x-1)/(n*(n-1)))
}
```

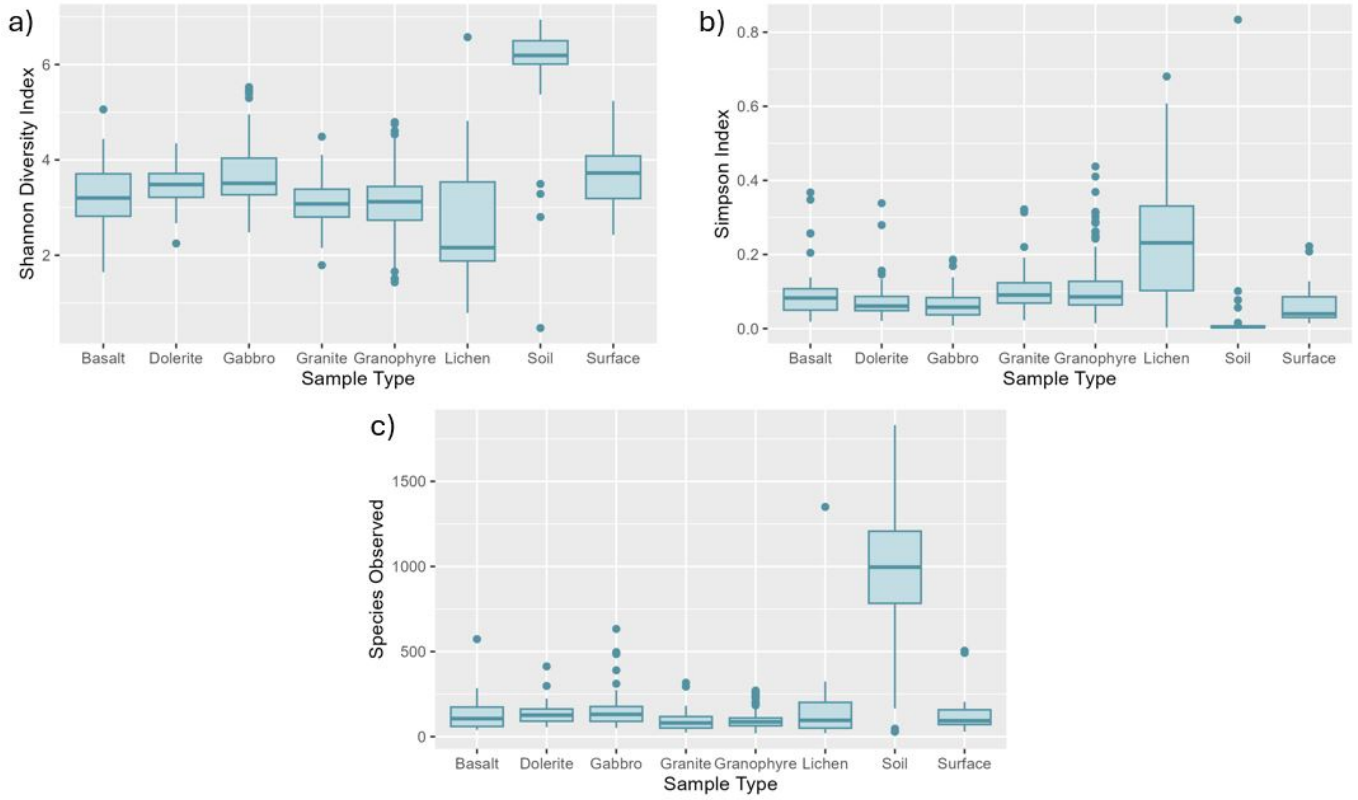

Figure C.1-6: Bacterial 16S alpha diversity grouped by sample type. a) Shannon diversity. b) Simpson diversity. c) ASVs observed

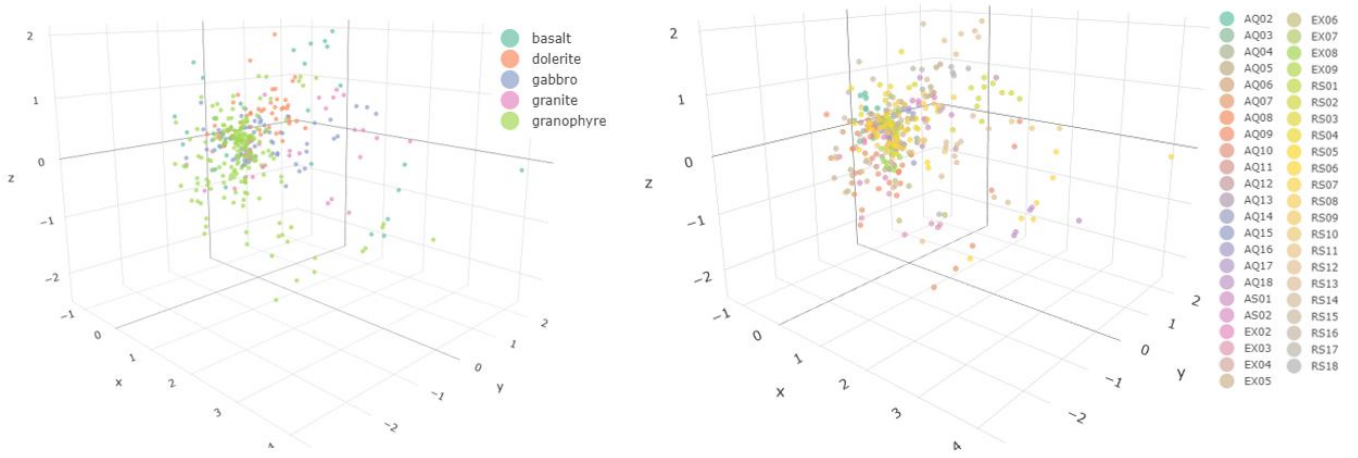

Figure C.1-7: Bacterial 16S NMDS ordination of patina samples, stress value 0.15. a) NMDS coloured based on rock type the patina was sampled from. b) NMDS coloured based on area the patina was sampled from.

C.2 Fungal ITS amplicon sequencing processing

C.2.1 ITS sequence quality reports

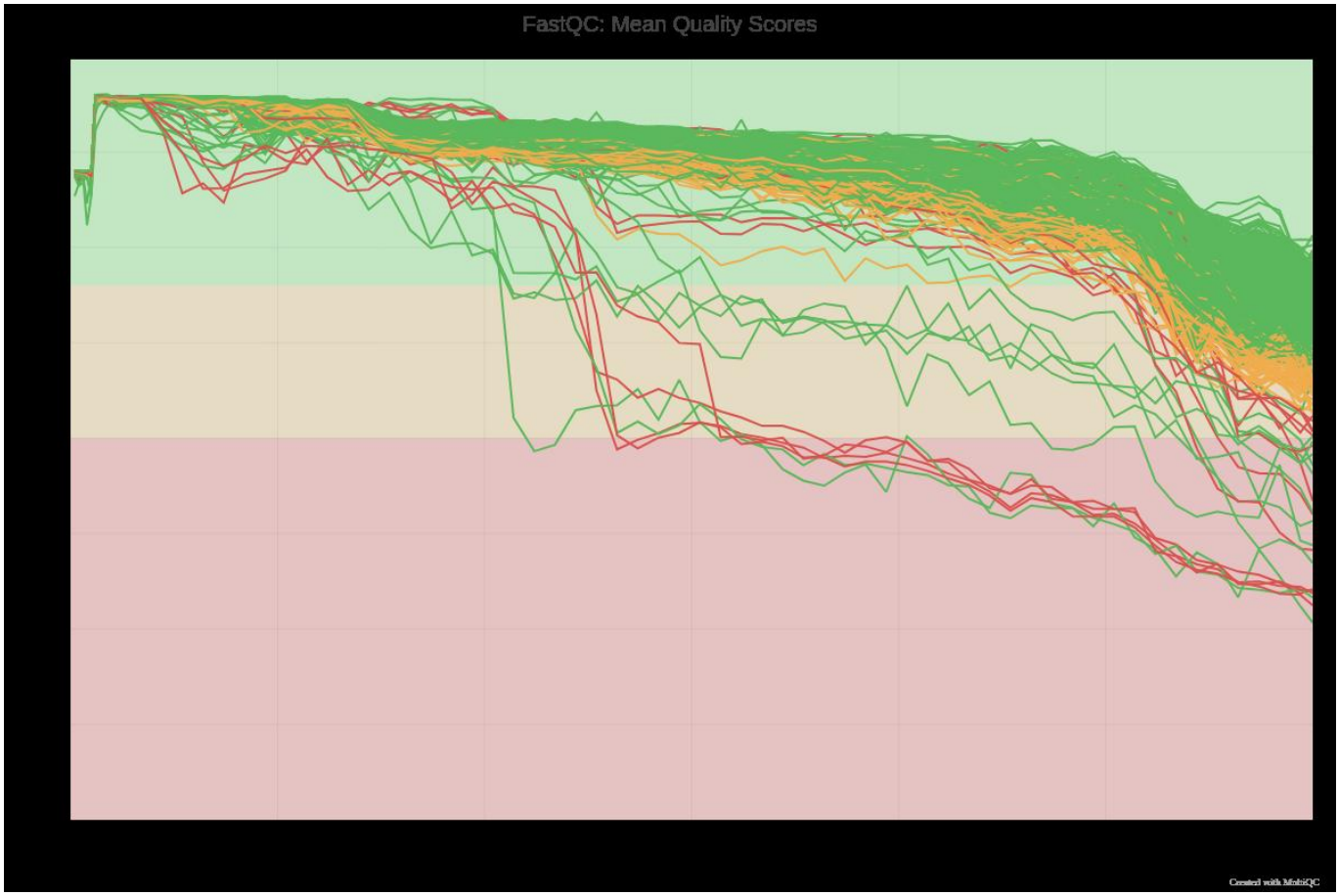

Figure C.2-1: MultiQC report of the raw ITS forward sequences.

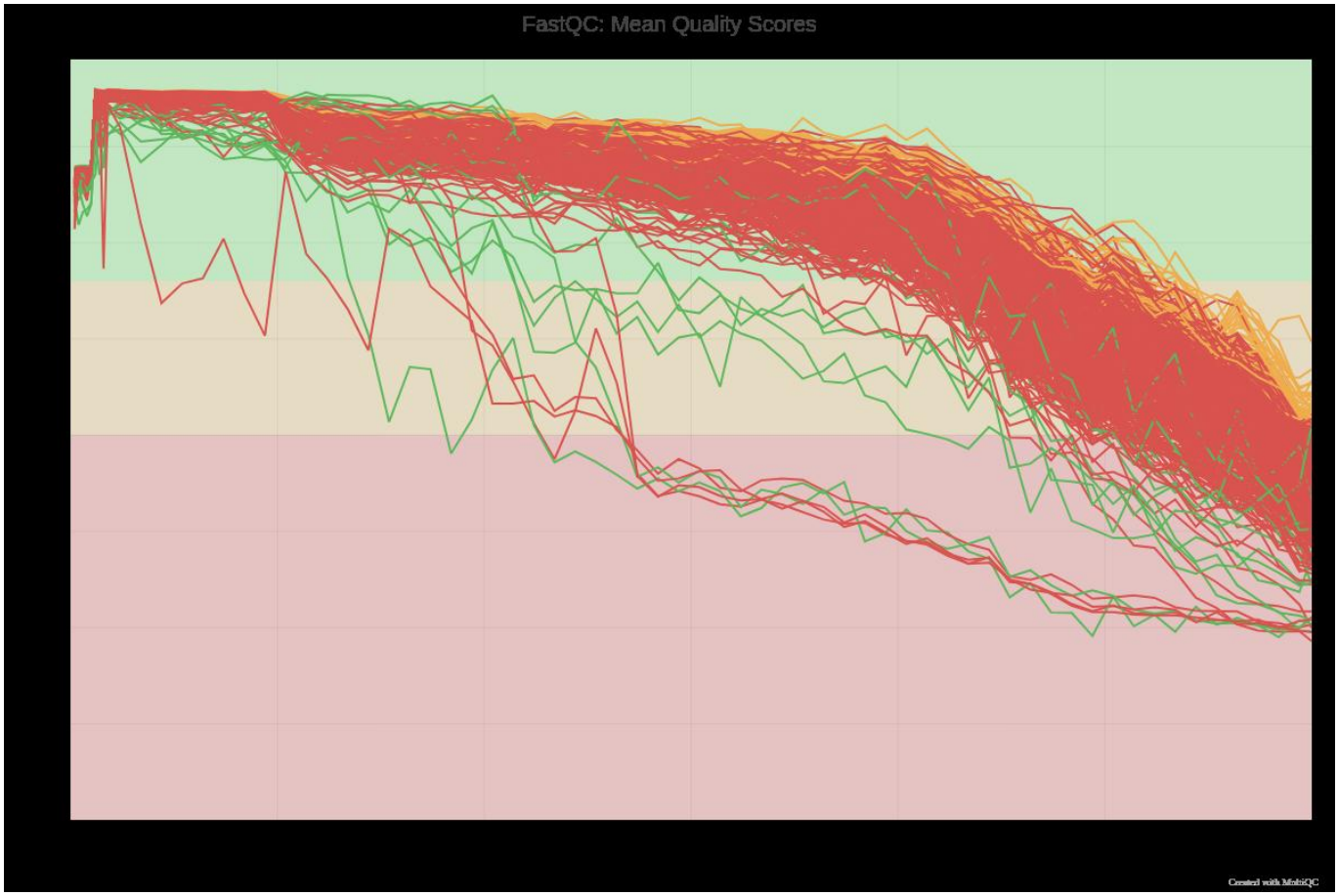

Figure C.2-2: MultiQC report of the raw ITS reverse sequences.

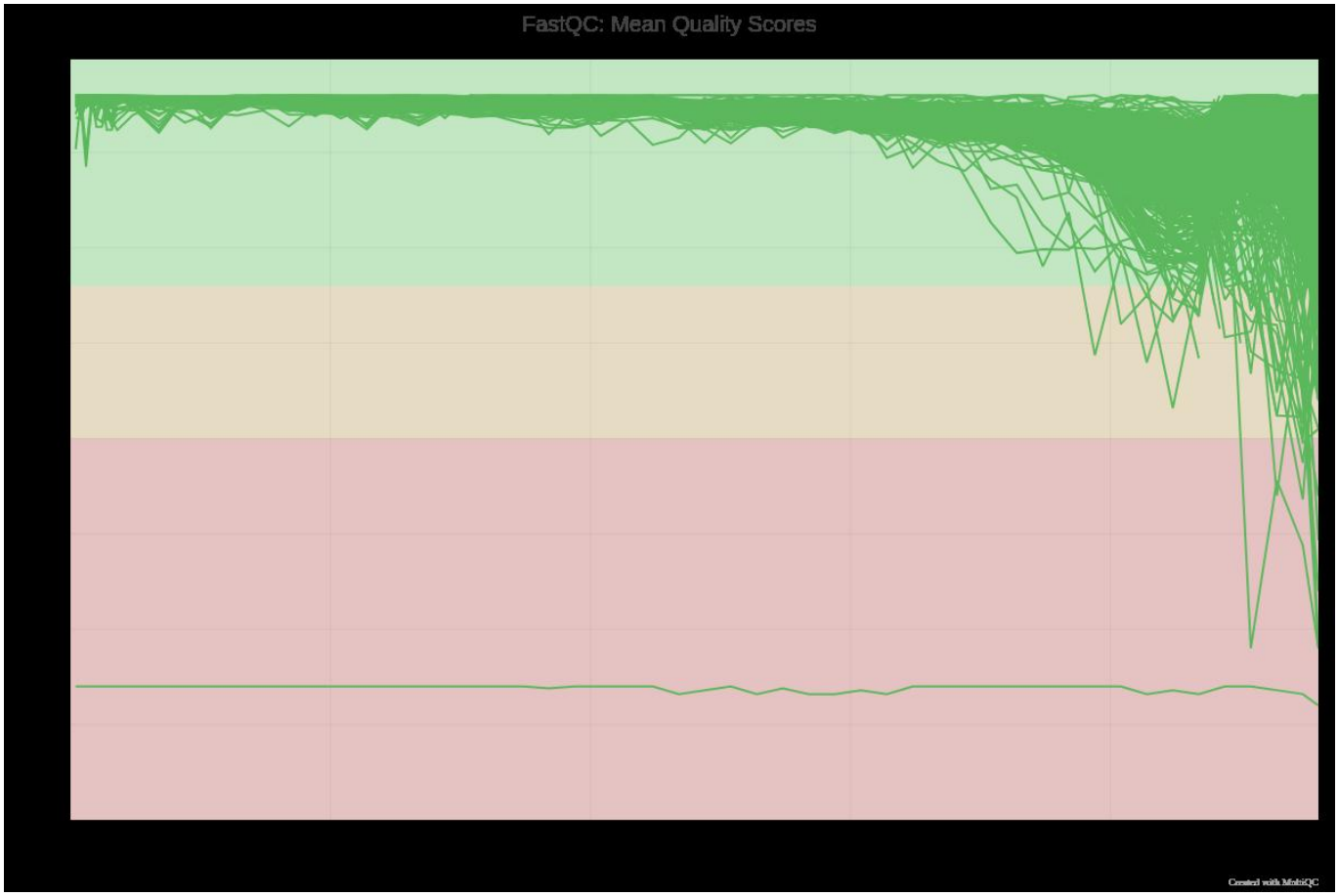

Figure C.2-3: MultiQC report of the trimmed ITS forward sequences.

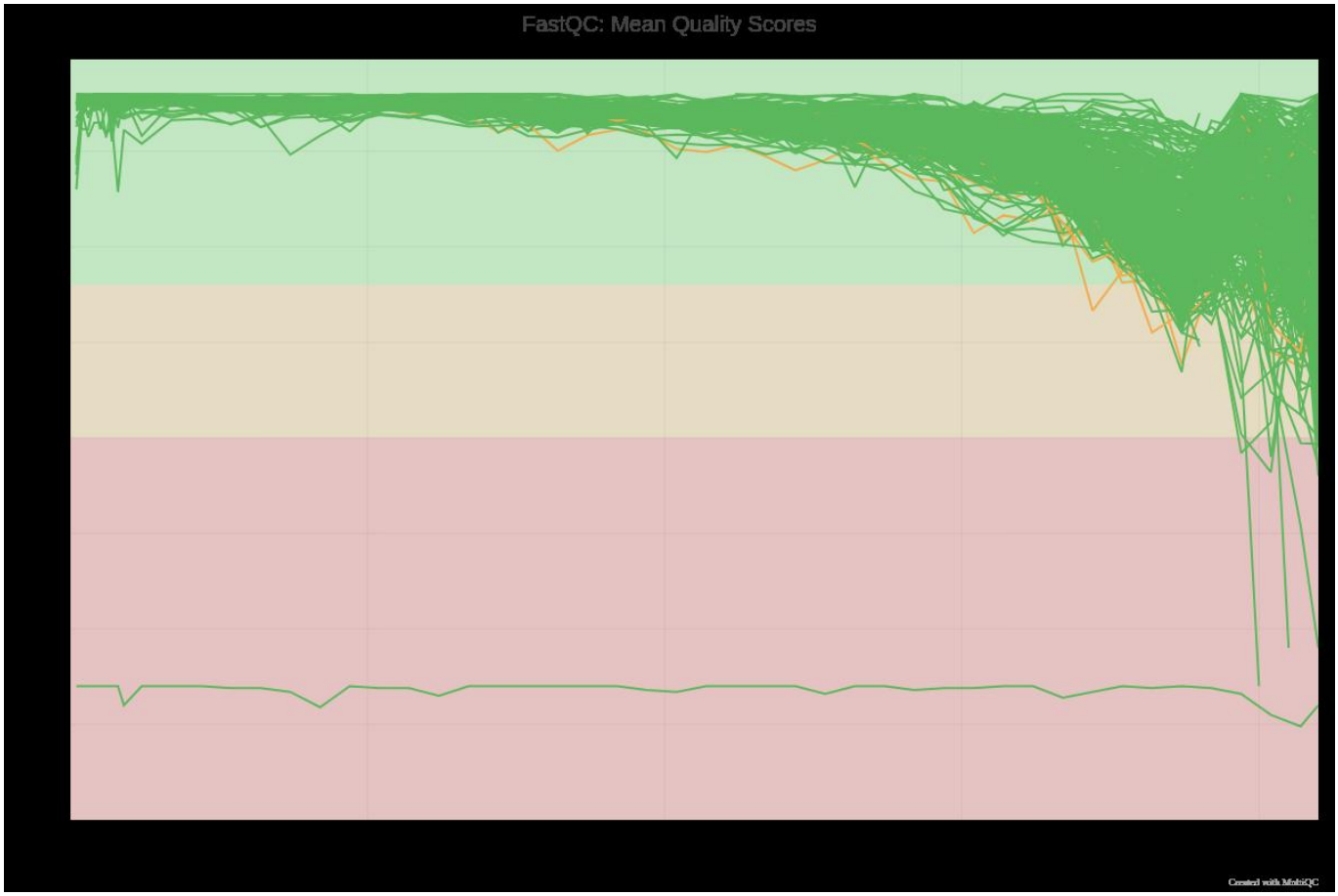

Figure C.2-4: MultiQC report of the trimmed ITS reverse sequences.

C.2.2 ITS rarefication

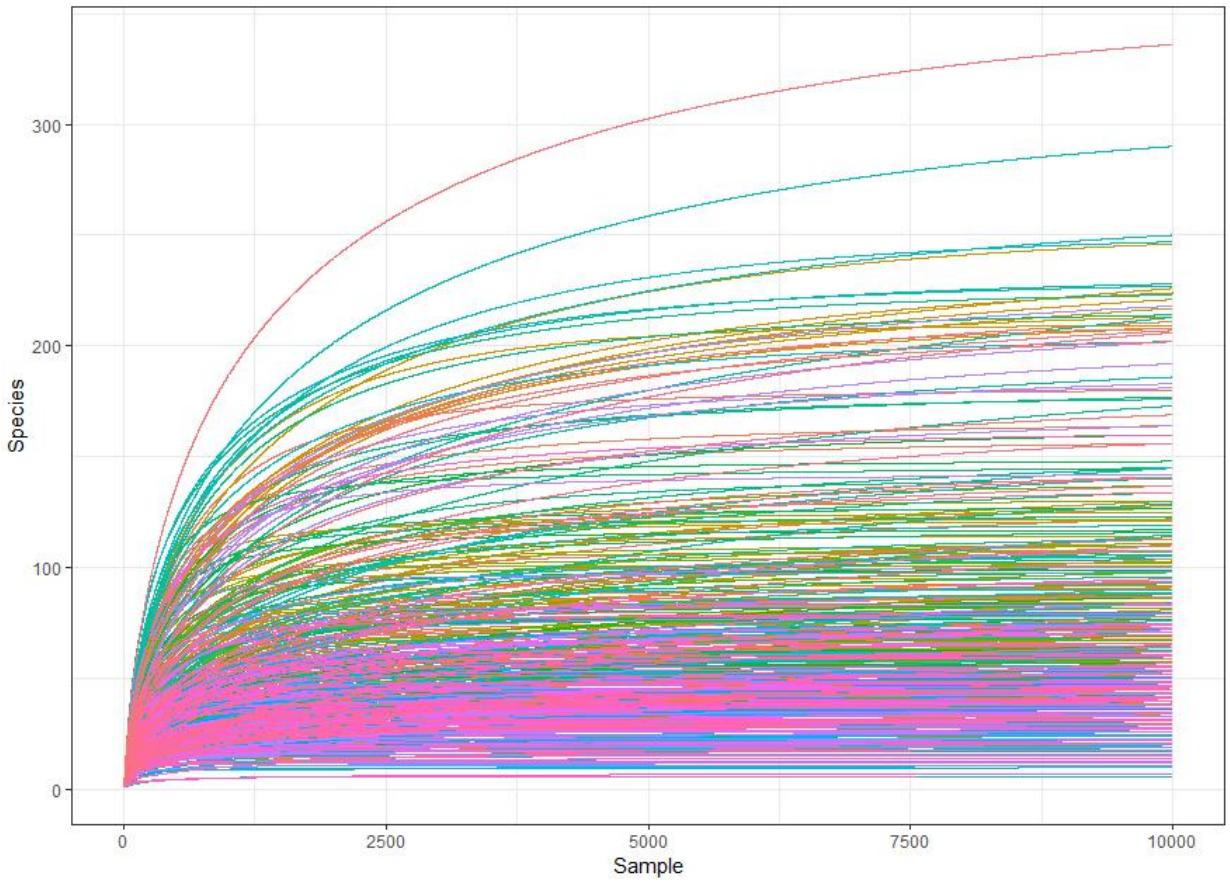

Figure C.2-5: Post rarefication of the ITS samples to 10,000 reads per sample.

C.2.3 ITS additional analysis

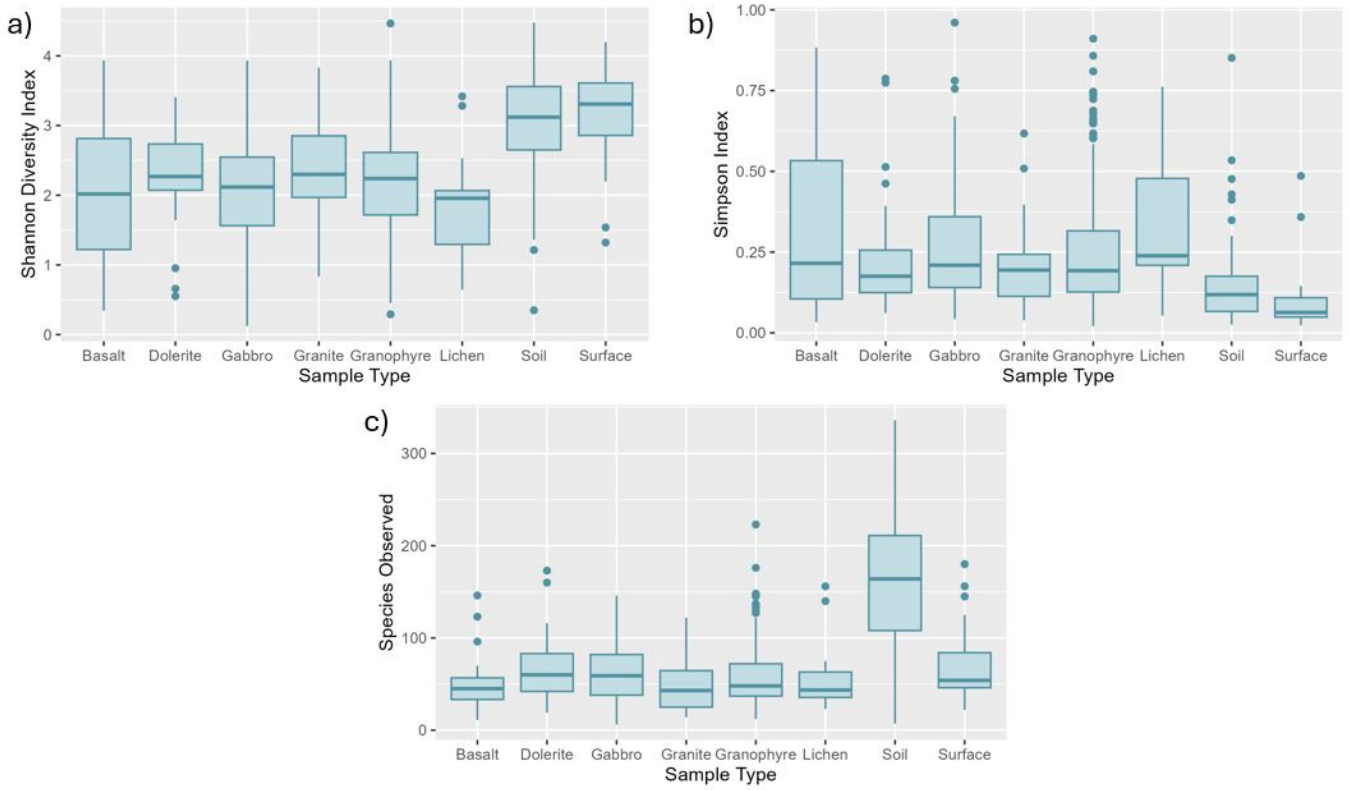

Figure C.2-6: Fungal ITS alpha diversity grouped by sample type. a) Shannon diversity. b) Simpson diversity. c) ASVs observed

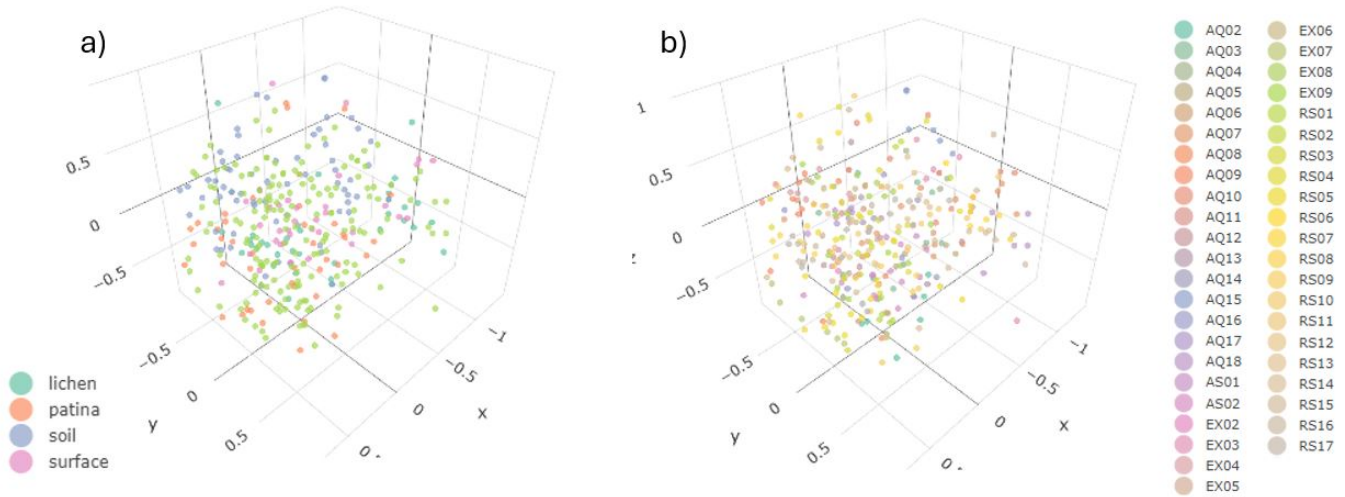

Figure C.2-7: Fungal ITS NMDS ordination of patina samples, stress value 0.21. a) NMDS coloured based on rock type the patina was sampled from. b) NMDS coloured based on area the patina was sampled from.

C.3 Microbiome sample log

Table C.3-1: Sample Log.

Sample name	Date sampled	Sample type	Season	ITS plate	16S plate	16S reads	16S inclusion	ITS reads	ITS inclusion
AQ02_soil	16/03/2022	soil	Wet	P3_A7	P3_E4	37582	Included	32904	Included
AQ02G_1	16/03/2022	patina	Wet	P1_D10	P1_E1	50363	Included	30147	Included
AQ02G_2	16/03/2022	patina	Wet	P1_D11	P1_F8	47962	Included	30614	Included
AQ02G_3	16/03/2022	patina	Wet	P1_D12	P1_F9	56745	Included	33764	Included
AQ02G_A	4/07/2022	patina	Dry	P4_C1	P4_F3	29421	Included	53747	Included
AQ02G_B	4/07/2022	patina	Dry	P4_C2	P4_B12	21540	Included	38333	Included
AQ02G_C	4/07/2022	patina	Dry	P3_G11	P4_F4	25138	Included	21395	Included
AQ02G_soil	4/07/2022	soil	Dry	P4_A10	P4_D10	28335	Included	39688	Included
AQ03G_1/3	29/03/2022	patina	Wet	P6_F3	P6_G10	26165	Included	40532	Included
AQ03G_2/3	29/03/2022	patina	Wet	P2_C12	P2_A12	38892	Included	41998	Included
AQ03G_3/3	29/03/2022	patina	Wet	P2_D1	P2_B1	39598	Included	27983	Included
AQ03G_A	NA	patina	Dry	P6_F2	P6_G9	19714	Included	37770	Included
AQ03G_B	NA	patina	Dry	P5_H11	P5_G8	15790	Included	55597	Included
AQ03G_C	NA	patina	Dry	P5_H12	P5_G9	18221	Included	39005	Included
AQ03G_soil	NA	soil	Wet	P2_B12	P2_D12	36655	Included	29051	Included
AQ03G_soil	NA	soil	Dry	P6_E1	P6_E8	56308	Included	35458	Included
AQ03GB_A	NA	patina	Dry	P5_E5	P6_B1	48663	Included	28255	Included
AQ03GB_B	NA	patina	Dry	P6_A1	P6_B2	49170	Included	37956	Included
AQ03GB_ bottom	29/03/2022	patina	Wet	P2_C8	P2_A8	23486	Included	25888	Included
AQ03GB_C	NA	patina	Dry	P5_E6	P6_B3	54970	Included	29976	Included
AQ03GB_lower	29/03/2022	patina	Wet	P2_C6	P2_A6	40621	Included	4678	Excluded
AQ03GB_right	29/03/2022	patina	Wet	P2_C7	P2_A7	29150	Included	31649	Included
AQ03GB_soil	NA	soil	Dry	P6_B1	P6_F5	32013	Included	36847	Included
AQ04G_A	NA	patina	Dry	P5_B4	P5_E6	41585	Included	38070	Included
AQ04G_B	NA	patina	Dry	P5_B5	P5_E7	34090	Included	37234	Included
AQ04G_C	NA	patina	Dry	P4_H5	P5_C2	46619	Included	36824	Included
AQ05D_1/3	28/03/2022	patina	Wet	P6_E11	P6_H7	29676	Included	20943	Included
AQ05D_2/3	28/03/2022	patina	Wet	P1_E9	P1_G3	73735	Included	6988	Excluded

Sample name	Date sampled	Sample type	Season	ITS plate	16S plate	16S reads	16S inclusion	ITS reads	ITS inclusion
AQ05D_3/3	28/03/2022	patina	Wet	P1_E10	P1_G4	57046	Included	5571	Excluded
AQ05D_A	NA	patina	Dry	P6_E10	P5_F8	25442	Included	728539	Included
AQ05D_B	NA	patina	Dry	P4_G7	P5_G5	13416	Included	12396	Included
AQ05D_C	NA	patina	Dry	P5_D12	P5_F9	21168	Included	42773	Included
AQ05D_soil	28/03/2022	soil	Wet	P2_B8	P2_G2	42856	Included	30566	Included
AQ05G_1/3	28/03/2022	patina	Wet	P1_F7	P1_F3	58617	Included	36784	Included
AQ05G_2/3	28/03/2022	patina	Wet	P1_F8	P1_G6	51874	Included	33937	Included
AQ05G_3/3	28/03/2022	patina	Wet	P1_F6	P1_G5	43238	Included	50460	Included
AQ05G_A	NA	patina	Dry	P5_B7	P5_F5	36824	Included	30164	Included
AQ05G_B	NA	patina	Dry	P5_D11	P5_F6	32628	Included	41836	Included
AQ05G_C	NA	patina	Dry	P4_H10	P5_B1	36931	Included	50903	Included
AQ05G_ lichen	28/03/2022	lichen	Wet	P2_B9	P2_D9	45437	Included	23460	Included
AQ06_soil	28/03/2022	soil	Wet	P2_B10	P2_D10	61794	Included	27443	Included
AQ06G_1/3	28/03/2022	patina	Wet	P1_E11	P1_E9	44024	Included	29334	Included
AQ06G_2/3	28/03/2022	patina	Wet	P1_E12	P1_C10	37689	Included	32952	Included
AQ06G_3/3	28/03/2022	patina	Wet	P1_B5	P1_A4	40819	Included	46088	Included
AQ06G_A	NA	patina	Dry	P4_C3	P4_C1	51346	Included	45682	Included
AQ06G_B	NA	patina	Dry	P4_C4	P4_A9	33308	Included	49434	Included
AQ06G_C	NA	patina	Dry	P4_C5	P4_A10	32731	Included	58155	Included
AQ07_ lichen-WGR	6/04/2022	lichen	Wet	P3_E5	P3_E3	34827	Included	44602	Included
AQ07_soil	6/04/2022	soil	Wet	P3_E4	P3_F2	43209	Included	42128	Included
AQ07G_1	25/03/2022	patina	Wet	P1_F9	P1_D11	35464	Included	20764	Included
AQ07G_1	NA	patina	Dry	P4_C8	P4_A12	31322	Included	40980	Included
AQ07G_1/3	6/04/2022	patina	Wet	P1_H8	P1_H11	42225	Included	42465	Included
AQ07G_2	25/03/2022	patina	Wet	P1_D2	P1_B9	20274	Included	21305	Included
AQ07G_2	NA	patina	Dry	P3_H4	P4_C5	48674	Included	22308	Included
AQ07G_2/3	6/04/2022	patina	Wet	P1_H9	P1_H12	16386	Included	40833	Included
AQ07G_3	25/03/2022	patina	Wet	P1_D1	P1_B8	37751	Included	25721	Included
AQ07G_3	NA	patina	Dry	P4_C9	P4_C6	61674	Included	23120	Included
AQ07G_3/3	6/04/2022	patina	Wet	P1_H10	P2_A1	67743	Included	31601	Included

Sample name	Date sampled	Sample type	Season	ITS plate	16S plate	16S reads	16S inclusion	ITS reads	ITS inclusion
AQ07G_soil	NA	soil	Dry	P4_E2	P4_G8	13743	Included	27360	Included
AQ07GR_1	28/07/2022	patina	Dry	P6_C1	P6_D12	28239	Included	28488	Included
AQ07GR_2	28/07/2022	patina	Dry	P6_C2	P6_E1	68068	Included	24886	Included
AQ07GR_3	28/07/2022	patina	Dry	P6_C3	P6_E2	33328	Included	15338	Included
AQ07GR_low	6/04/2022	patina	Wet	P1_H6	P1_H9	60073	Included	28335	Included
AQ07GR_right	6/04/2022	patina	Wet	P1_H5	P1_H8	46077	Included	43066	Included
AQ07GR_ right2	6/04/2022	patina	Wet	P1_H7	P1_H10	34963	Included	42315	Included
AQ07GR_soil	28/07/2022	soil	Dry	P6_D6	P6_F12	29317	Included	43472	Included
AQ07GR_ surfA	6/04/2022	surface	Wet	P2_C9	P2_A9	47313	Included	23690	Included
AQ07GR_ surfB	6/04/2022	surface	Wet	P2_C10	P2_A10	38086	Included	11323	Included
AQ07GR_ surfR	6/04/2022	surface	Wet	P2_C11	P2_A11	30383	Included	23634	Included
AQ08G_1	25/03/2022	patina	Wet	P1_E8	P1_E8	39584	Included	27263	Included
AQ08G_1	28/07/2022	patina	Dry	P3_H3	P4_F6	31218	Included	26661	Included
AQ08G_2	25/03/2022	patina	Wet	P1_F1	P1_C12	52067	Included	32022	Included
AQ08G_2	28/07/2022	patina	Dry	P4_C6	P4_C4	38788	Included	28577	Included
AQ08G_3	25/03/2022	patina	Wet	P1_B9	P1_C11	26957	Included	17633	Included
AQ08G_3	28/07/2022	patina	Dry	P4_C7	P4_A11	31707	Included	43839	Included
AQ08G_soil	28/07/2022	soil	Dry	P3_G3	P4_D12	19832	Included	10364	Included
AQ09_soil	30/03/2022	soil	Wet	P2_C1	P2_E1	45753	Included	26415	Included
AQ09G_1	30/06/2022	patina	Dry	P5_A9	P5_B9	40943	Included	37042	Included
AQ09G_1/3	29/03/2022	patina	Wet	P2_E3	P1_H2	48671	Included	15449	Included
AQ09G_2	30/06/2022	patina	Dry	P5_C10	P5_B10	29139	Included	13979	Included
AQ09G_2/3	29/03/2022	patina	Wet	P2_E4	P1_H3	57213	Included	14231	Included
AQ09G_3	30/06/2022	patina	Dry	P5_C11	P5_B11	22490	Included	33164	Included
AQ09G_3/3	29/03/2022	patina	Wet	P2_E5	P2_B8	17402	Included	32188	Included
AQ09GB_1	30/07/2022	patina	Dry	P3_H5	P4_C7	41081	Included	41007	Included
AQ09GB_2	30/07/2022	patina	Dry	P3_H6	P4_F7	38584	Included	44994	Included
AQ09GB_3	30/07/2022	patina	Dry	P3_H7	P4_C8	46469	Included	45801	Included

Sample name	Date sampled	Sample type	Season	ITS plate	16S plate	16S reads	16S inclusion	ITS reads	ITS inclusion
AQ09GB_left	30/03/2022	patina	Wet	P2_D6	P2_B3	84223	Included	38402	Included
AQ09GB_right	30/03/2022	patina	Wet	P2_D7	P2_B4	48569	Included	37480	Included
AQ09GB_top	30/03/2022	patina	Wet	P2_D5	P2_B2	57367	Included	30280	Included
AQ10G_1/3	21/03/2022	patina	Wet	P3_C4	P3_D4	43737	Included	6319	Excluded
AQ10G_2/3	21/03/2022	patina	Wet	P3_C3	P3_A11	26385	Included	170519	Included
AQ10G_3/3	21/03/2022	patina	Wet	P3_C2	P3_A10	31501	Included	18867	Included
AQ10G_A	NA	patina	Dry	P5_E8	P5_G11	16918	Included	44489	Included
AQ10G_B	NA	patina	Dry	P5_E9	P6_B6	93117	Included	47606	Included
AQ10G_C	NA	patina	Dry	P5_E10	P6_B7	17113	Included	37721	Included
AQ10G_soil	NA	soil	Dry	P6_B2	P6_F7	57737	Included	51132	Included
AQ10GR_1	NA	patina	Wet	P1_A5	P1_B3	65870	Included	41847	Included
AQ10GR_2	NA	patina	Wet	P1_A6	P1_B4	38439	Included	46587	Included
AQ10GR_3	NA	patina	Wet	P1_A7	P1_B5	49690	Included	39879	Included
AQ11G_1	NA	patina	Wet	P2_H4	P3_A9	31166	Included	42726	Included
AQ11G_2	NA	patina	Wet	P2_H3	P2_G11	28575	Included	25991	Included
AQ11G_3	NA	patina	Wet	P2_H2	P3_A8	9967	Included	19798	Included
AQ11G_A	NA	patina	Dry	P5_B8	P5_C5	60987	Included	31030	Included
AQ11G_B	NA	patina	Dry	P5_B9	P5_C6	71278	Included	33757	Included
AQ11G_C	NA	patina	Dry	P5_B10	P5_C7	46104	Included	15064	Included
AQ12_soil	7/07/2022	soil	Dry	P3_G7	P4_E7	19454	Included	34580	Included
AQ12B_1	7/07/2022	patina	Dry	P4_H6	P5_E11	11705	Included	31341	Included
AQ12B_2	7/07/2022	patina	Dry	P4_H7	P5_E12	29837	Included	42658	Included
AQ12B_3	7/07/2022	patina	Dry	P5_B6	P5_F1	40701	Included	13851	Included
AQ12B_ blackvarnish	18/03/2022	patina	Wet	P2_B1	P2_D2	53918	Included	41122	Included
AQ12B_lichen	18/03/2022	lichen	Wet	P2_A4	P2_D1	50860	Included	2106	Excluded
AQ12B_R1	18/03/2022	patina	Wet	P3_E1	P3_C6	52430	Included	32605	Included
AQ12B_R2	18/03/2022	patina	Wet	P3_A3	P3_C7	39778	Included	30502	Included
AQ12B_R3	18/03/2022	patina	Wet	P3_E2	P3_E1	41161	Included	11261	Included
AQ12B_soil	18/03/2022	soil	Wet	P2_A12	P2_F12	27353	Included	31476	Included
AQ13G_1	24/03/2022	patina	Wet	P2_E6	P2_F1	65251	Included	17373	Included
AQ13G_2	24/03/2022	patina	Wet	P2_E7	P2_B9	21333	Included	8159	Excluded

Sample name	Date sampled	Sample type	Season	ITS plate	16S plate	16S reads	16S inclusion	ITS reads	ITS inclusion
AQ13G_3	24/03/2022	patina	Wet	P2_E8	P2_B10	49145	Included	2093	Excluded
AQ13G_A	NA	patina	Dry	P6_B9	P6_D8	32881	Included	12391	Included
AQ13G_B	NA	patina	Dry	P6_A6	P6_D5	54702	Included	29997	Included
AQ13G_C	NA	patina	Dry	P6_B10	P6_D9	53031	Included	15877	Included
AQ13G_soil	NA	soil	Dry	P6_B3	P6_F10	36574	Included	33272	Included
AQ14G_A	NA	patina	Dry	P5_F4	P5_H1	25365	Included	39489	Included
AQ14G_B	NA	patina	Dry	P6_A4	P6_B12	109891	Included	24427	Included
AQ14G_C	NA	patina	Dry	P6_A5	P6_D4	7779	Excluded	24214	Included
AQ14G_soil	NA	soil	Dry	P5_H7	P6_F9	29820	Included	33374	Included
AQ15_lichen	7/06/2022	lichen	Dry	P4_E6	P4_E8	44577	Included	19632	Included
AQ15_soil	NA	soil	Wet	P3_A2	P2_H3	81881	Included	46768	Included
AQ15GB_1	7/06/2022	patina	Dry	P4_H8	P5_F2	40216	Included	23472	Included
AQ15GB_1	NA	patina	Wet	P3_D6	P3_D10	17335	Included	27033	Included
AQ15GB_2	7/06/2022	patina	Dry	P4_H9	P5_F3	17	Excluded	12773	Included
AQ15GB_2	NA	patina	Wet	P2_H10	P3_C1	39757	Included	22809	Included
AQ15GB_3	7/06/2022	patina	Dry	P5_D10	P5_F4	0	Excluded	23093	Included
AQ15GB_3	NA	patina	Wet	P3_D7	P3_D11	20857	Included	30502	Included
AQ16GB_?	NA	NA	Wet	P1_G9	P1_E2	87	Excluded	36403	Included
AQ16GB_1	NA	patina	Wet	P2_D12	P2_E10	45282	Included	23478	Included
AQ16GB_2	NA	patina	Wet	P2_E1	P2_E11	56105	Included	49102	Included
AQ16GB_3	NA	patina	Wet	P2_E2	P2_E12	29061	Included	32378	Included
AQ16GB_A	NA	patina	Dry	P5_D7	P5_E8	4349	Excluded	43671	Included
AQ16GB_B	NA	patina	Dry	P5_D8	P5_E9	29315	Included	30485	Included
AQ16GB_C	NA	patina	Dry	P5_D9	P5_E10	41202	Included	35646	Included
AQ16GB_soil	NA	soil	Dry	P3_G6	P4_E6	33565	Included	41682	Included
AQ17_soil1	16/03/2022	soil	Wet	P3_F5	P3_F9	15719	Included	43330	Included
AQ17_soil2*	16/03/2022	soil	Wet	P3_A9	P2_H9	26156	Included	7563	Excluded
AQ17_soil3*	16/03/2022	soil	Wet	P3_A10	P2_H10	17727	Included	14323	Included
AQ17G_1	16/03/2022	patina	Wet	P2_G1	P2_C8	42946	Included	18620	Included
AQ17G_1	29/07/2022	patina	Dry	P4_D2	P4_G2	7547	Excluded	40004	Included
AQ17G_2	16/03/2022	patina	Wet	P2_G2	P2_C9	41111	Included	40482	Included
AQ17G_2	29/07/2022	patina	Dry	P4_D3	P4_G3	32621	Included	31388	Included

Sample name	Date sampled	Sample type	Season	ITS plate	16S plate	16S reads	16S inclusion	ITS reads	ITS inclusion
AQ17G_3	16/03/2022	patina	Wet	P2_G3	P2_C10	24380	Included	32152	Included
AQ17G_3	29/07/2022	patina	Dry	P4_D4	P4_G4	21716	Included	42839	Included
AQ17G_maz	16/02/2022	NA	Wet	P3_B7	P3_C12	28273	Included	7753	Excluded
AQ17G_soil	29/07/2022	soil	Dry	P3_G4	P4_G9	16963	Included	46517	Included
AQ18G_A	NA	patina	Dry	P4_F11	P5_F7	28529	Included	46228	Included
AQ18G_B	NA	patina	Dry	NA	P5_C3	32329	Included	NA	Excluded
AQ18G_black	NA	patina	Wet	P1_A3	P1_A11	31161	Included	35823	Included
AQ18G_C	NA	patina	Dry	P4_F12	P5_C4	41086	Included	54438	Included
AQ18G_red1	NA	patina	Wet	P1_A2	P1_A10	55791	Included	48124	Included
AQ18G_red2	NA	patina	Wet	P1_A4	P1_A12	38302	Included	44047	Included
AQ18G_soil	NA	soil	Dry	P4_B4	P4_E9	35258	Included	44312	Included
AS01_lichen	22/03/2022	lichen	Wet	P3_E3	P3_F1	49685	Included	43256	Included
AS01_soil	22/03/2022	soil	Wet	P3_B2	P3_E2	49561	Included	4673	Excluded
AS01D_black	22/03/2022	patina	Wet	P2_F10	P2_F6	32075	Included	5353	Excluded
AS01D_bottom	NA	patina	Dry	P4_C11	P4_F12	30303	Included	28601	Included
AS01D_left	22/03/2022	patina	Wet	P2_F11	P2_F7	48631	Included	18854	Included
AS01D_lichen	NA	lichen	Dry	P4_E3	P4_E1	51805	Included	9769	Excluded
AS01D_right	22/03/2022	patina	Wet	P2_F9	P2_C6	48921	Included	28179	Included
AS01D_soil	NA	soil	Dry	P4_A12	P4_E2	28282	Included	55617	Included
AS01D_surf	NA	surface	Dry	P4_D1	P4_B1	42791	Included	47719	Included
AS01D_ topleft	NA	patina	Dry	P4_C12	P4_G1	40522	Included	22185	Included
AS01D_ topright	NA	patina	Dry	P4_C10	P4_F11	190	Excluded	29052	Included
AS02_soil	31/03/2022	soil	Wet	P3_A11	P3_E9	25863	Included	31702	Included
AS02_soil	31/03/2022	soil	Wet	P3_F6	P3_F10	6688	Excluded	28233	Included
AS02D_1	7/01/2022	patina	Dry	P6_A2	P6_B4	61054	Included	36370	Included
AS02D_2	7/01/2022	patina	Dry	P5_E7	P5_G10	17285	Included	42156	Included
AS02D_3	7/01/2022	patina	Dry	P6_A3	P6_B5	77341	Included	50555	Included
AS02D_low	3/03/2022	patina	Wet	P2_F5	P2_C2	41553	Included	40799	Included
AS02D_mid	3/03/2022	patina	Wet	P2_F4	P1_H7	46172	Included	37888	Included
AS02D_soil	7/01/2022	soil	Dry	P6_D2	P6_F6	26800	Included	35888	Included

Sample name	Date sampled	Sample type	Season	ITS plate	16S plate	16S reads	16S inclusion	ITS reads	ITS inclusion
AS02D_top	3/03/2022	patina	Wet	P2_F3	P2_C1	28045	Included	38570	Included
AS02GR_1	44568	patina	Dry	P4_G11	P4_H9	20329	Included	41768	Included
AS02GR_2	44568	patina	Dry	P4_G12	P4_H10	22170	Included	57310	Included
AS02GR_3	7/01/2022	patina	Dry	P5_A5	P4_H11	17626	Included	48254	Included
AS02GR_lower	31/03/2022	patina	Wet	P2_C5	P1_H1	43818	Included	40317	Included
AS02GR_mid	31/03/2022	patina	Wet	P2_C4	P1_G12	42504	Included	41278	Included
AS02GR_soil	7/01/2022	soil	Dry	P3_G5	P4_G10	13577	Included	24438	Included
AS02GR_upper	31/03/2022	patina	Wet	P2_C3	P2_E4	52148	Included	17271	Included
CaCO3	24/03/2022	NA	Wet	P1_G12	P2_A5	44095	Included	34750	Included
EX02_soil	28/03/2022	soil	Wet	P2_B11	P2_G3	49915	Included	27004	Included
EX02_soil	NA	soil	Dry	P6_D9	P6_G4	24264	Included	29565	Included
EX02G_1	27/07/2022	patina	Dry	P4_E7	P4_F8	26715	Included	46654	Included
EX02G_1/3	28/03/2022	patina	Wet	P2_D4	P2_E7	44033	Included	35628	Included
EX02G_2	27/07/2022	patina	Dry	P3_H8	P4_F9	44774	Included	32049	Included
EX02G_2/3	28/03/2022	patina	Wet	P2_D3	P2_E6	56866	Included	35403	Included
EX02G_3	27/07/2022	patina	Dry	P4_E8	P4_F10	32335	Included	45117	Included
EX02G_3/3	28/03/2022	patina	Wet	P2_D2	P2_E5	25613	Included	39221	Included
EX03_soil	31/03/2022	soil	Wet	P2_B3	P2_D4	51871	Included	86009	Included
EX03G_1	20/07/2022	patina	Dry	P5_B1	P5_A9	56827	Included	9123	Excluded
EX03G_2	20/07/2022	patina	Dry	P5_B2	P5_A10	53565	Included	22339	Included
EX03G_3	20/07/2022	patina	Dry	P5_B3	P5_C1	21484	Included	28399	Included
EX03G_left	31/03/2022	patina	Wet	P3_A4	P2_H4	47160	Included	25661	Included
EX03G_mid	31/03/2022	patina	Wet	P3_A5	P2_H5	38316	Included	30427	Included
EX03G_right	31/03/2022	patina	Wet	P3_A6	P2_H6	41585	Included	16847	Included
EX03G_surf	20/07/2022	surface	Dry	P4_H4	P5_A11	37496	Included	51440	Included
EX04GB_1/3	5/04/2022	patina	Wet	P1_F11	P1_D12	52855	Included	29817	Included
EX04GB_2/3	5/04/2022	patina	Wet	P1_F10	P1_F5	58267	Included	29389	Included
EX04GB_3/3	5/04/2022	patina	Wet	P1_F12	P1_F7	56336	Included	35718	Included
EX04GB_A	NA	patina	Dry	P4_B7	P4_B7	44738	Included	25300	Included
EX04GB_B	NA	patina	Dry	P4_B8	P4_B8	44395	Included	34917	Included
EX04GB_C	NA	patina	Dry	P4_B9	P4_B9	45639	Included	27909	Included
EX05_lichen	5/04/2022	lichen	Wet	P2_B6	P2_D8	6571	Excluded	3984	Excluded

Sample name	Date sampled	Sample type	Season	ITS plate	16S plate	16S reads	16S inclusion	ITS reads	ITS inclusion
EX05_soil	5/04/2022	soil	Wet	P2_B7	P2_G1	36892	Included	31913	Included
EX05G_A	NA	patina	Dry	P5_A2	P5_B5	47302	Included	43891	Included
EX05G_B	NA	patina	Dry	P5_A3	P5_B6	51711	Included	51274	Included
EX05G_bottom	5/04/2022	patina	Wet	P1_B6	P1_A5	55725	Included	31587	Included
EX05G_C	NA	patina	Dry	P5_A4	P5_B7	42559	Included	35167	Included
EX05G_left	5/04/2022	patina	Wet	P1_B8	P1_A7	41977	Included	28803	Included
EX05G_right	5/04/2022	patina	Wet	P1_B7	P1_A6	51890	Included	16602	Included
EX06_lichen	NA	lichen	Wet	P3_E9	P3_E5	36707	Included	19637	Included
EX06G_1	27/07/2022	patina	Dry	P5_F5	P5_H2	20386	Included	34617	Included
EX06G_1	NA	patina	Wet	P2_H1	P2_G10	43248	Included	35442	Included
EX06G_2	27/07/2022	patina	Dry	P5_F6	P5_H3	25856	Included	39198	Included
EX06G_2	NA	patina	Wet	P2_G12	P2_G9	40917	Included	45916	Included
EX06G_3	27/07/2022	patina	Dry	P5_F7	P5_H4	22090	Included	34630	Included
EX06G_3	NA	patina	Wet	P2_G11	P2_G8	21999	Included	23798	Included
EX06G_lichen	27/07/2022	lichen	Dry	P6_D4	P6_E10	48031	Included	15980	Included
EX07G_1	20/07/2022	patina	Dry	P5_C7	P5_D6	50645	Included	39090	Included
EX07G_2	20/07/2022	patina	Dry	P5_C8	P5_D7	34111	Included	42726	Included
EX07G_3	20/07/2022	patina	Dry	P5_C9	P5_D8	42592	Included	46445	Included
EX07G_bottom	NA	patina	Wet	P1_F5	P1_D9	47990	Included	33552	Included
EX07G_left	NA	patina	Wet	P1_F3	P1_D7	51361	Included	33585	Included
EX07G_right	NA	patina	Wet	P1_F4	P1_D8	46657	Included	24573	Included
EX07G_soil	20/07/2022	soil	Dry	P4_E5	P4_G11	14254	Included	24388	Included
EX07G_surf	20/07/2022	surface	Dry	P4_H1	P4_H12	17073	Included	48742	Included
EX08G_1	22/07/2022	patina	Dry	P5_F10	P6_C2	36319	Included	51232	Included
EX08G_2	22/07/2022	patina	Dry	P5_F11	P6_C3	36676	Included	34194	Included
EX08G_3	22/07/2022	patina	Dry	P6_A7	P6_C4	44514	Included	9977	Excluded
EX08G_bottom	NA	patina	Wet	P1_C8	P1_D6	58187	Included	13761	Included
EX08G_right	NA	patina	Wet	P1_C7	P1_B2	70757	Included	38309	Included
EX08G_top	NA	patina	Wet	P1_G5	P1_B1	44085	Included	36371	Included
EX09_lichen	31/03/2022	lichen	Wet	P3_B4	P3_E10	32144	Included	8120	Excluded
EX09_soil	1/04/2022	soil	Wet	P3_F4	P3_E8	39595	Included	36443	Included
EX09G_1	20/07/2022	patina	Dry	P5_E1	P5_G1	38511	Included	42775	Included

Sample name	Date sampled	Sample type	Season	ITS plate	16S plate	16S reads	16S inclusion	ITS reads	ITS inclusion
EX09G_2	20/07/2022	patina	Dry	P5_E2	P5_C8	61025	Included	39087	Included
EX09G_3	20/07/2022	patina	Dry	P5_B11	P5_G2	39819	Included	19744	Included
EX09G_left	1/04/2022	patina	Wet	P3_C1	P3_A7	48650	Included	22860	Included
EX09G_mid	1/04/2022	patina	Wet	P3_B12	P3_A6	40959	Included	14895	Included
EX09G_right	1/04/2022	patina	Wet	P3_B11	P3_A5	36113	Included	30112	Included
EX09G_soil	20/07/2022	soil	Dry	P3_G8	P4_G12	23843	Included	26200	Included
EX09G_surf	NA	surface	Dry	P5_G10	P6_A4	43449	Included	52459	Included
EX09GB_1	1/07/2022	patina	Dry	P6_E4	P6_G11	42412	Included	46228	Included
EX09GB_2	1/07/2022	patina	Dry	P5_F2	P6_B10	57384	Included	47465	Included
EX09GB_3	1/07/2022	patina	Dry	P5_F3	P6_B11	32446	Included	43844	Included
EX09GB_lichen	1/07/2022	lichen	Dry	P6_D3	P6_E9	41917	Included	9824	Excluded
EX09GB_lower	31/03/2022	patina	Wet	P6_E5	P6_G12	20424	Included	10540	Included
EX09GB_mid	31/03/2022	patina	Wet	P2_G9	P3_A3	33786	Included	39633	Included
EX09GB_top	31/03/2022	patina	Wet	P2_G10	P3_A4	30973	Included	37592	Included
FC	17/03/2022	NA	Wet	P1_A1	P1_A1	9134	Excluded	18641	Included
RS0?8?3_ lichen	NA	lichen	Wet	P2_A9	P2_E3	50503	Included	20393	Included
RS01_soil	17/03/2022	soil	Wet	P2_B4	P2_D5	30655	Included	32646	Included
RS01G_bottom	9/11/2022	patina	Dry	P6_C6	P6_E4	51853	Included	35629	Included
RS01G_middle	8/11/2022	patina	Dry	P6_C5	P6_E3	27615	Included	42297	Included
RS01G_R1	17/03/2022	patina	Wet	P3_C12	P3_B8	14078	Included	28126	Included
RS01G_R2	17/03/2022	patina	Wet	P3_C11	P3_B7	32790	Included	29201	Included
RS01G_R3	17/03/2022	patina	Wet	P3_C10	P3_B6	46765	Included	38719	Included
RS01G_soil	8/11/2022	soil	Dry	P6_B5	P6_G1	29494	Included	37587	Included
RS01G_surf	7/11/2022	surface	Dry	P5_G3	P5_H8	25797	Included	48413	Included
RS01G_top	7/11/2022	patina	Dry	P6_C4	P6_C5	64443	Included	36838	Included
RS02_lichen	NA	lichen	Wet	P2_A7	P2_D11	47742	Included	5371	Excluded
RS02_soil	29/03/2022	soil	Wet	P2_C2	P2_G4	35552	Included	37508	Included
RS02GB_1/3	29/03/2022	patina	Wet	P2_E12	P2_B12	31040	Included	24791	Included
RS02GB_2/3	29/03/2022	patina	Wet	P2_F1	P2_F4	37984	Included	17661	Included
RS02GB_3/3	29/03/2022	patina	Wet	P2_F2	P2_F5	42096	Included	9828	Excluded
RS02GB_A	NA	patina	Dry	P5_C2	P5_D1	32150	Included	31489	Included

Sample name	Date sampled	Sample type	Season	ITS plate	16S plate	16S reads	16S inclusion	ITS reads	ITS inclusion
RS02GB_B	NA	patina	Dry	P5_A1	P5_D2	31107	Included	54203	Included
RS02GB_C	NA	patina	Dry	P5_C3	P5_D3	33859	Included	41521	Included
RS02GB_ lichen	NA	lichen	Dry	P4_E4	P4_E3	34276	Included	10099	Included
RS02GB_soil	NA	soil	Dry	P4_B2	P4_E4	17913	Included	22162	Included
RS02GR_A	NA	patina	Dry	P6_E6	P6_H10	30121	Included	45756	Included
RS02GR_B	NA	patina	Dry	P5_F8	P6_D11	34008	Included	35530	Included
RS02GR_C	NA	patina	Dry	P5_F9	P6_C1	67296	Included	32617	Included
RS02GR_left	29/03/2022	patina	Wet	P1_H1	P2_B5	43585	Included	36317	Included
RS02GR_right	29/03/2022	patina	Wet	P2_D8	P2_B6	31485	Included	27673	Included
RS02GR_soil	NA	soil	Dry	P6_B6	P6_G3	26814	Included	25383	Included
RS02GR_top	29/03/2022	patina	Wet	P6_E7	P6_H1	33448	Included	42993	Included
RS03_L1R1	17/03/2022	patina	Wet	P3_D8	P3_C2	42354	Included	36623	Included
RS03_L1R2	17/03/2022	patina	Wet	P3_D9	P3_C3	92383	Included	39475	Included
RS03_L1R3	17/03/2022	patina	Wet	P3_D10	P3_C4	37598	Included	43461	Included
RS03_L2R1	17/03/2022	patina	Wet	P3_C6	P3_B2	41649	Included	28127	Included
RS03_L2R2	17/03/2022	patina	Wet	P2_H5	P3_B1	41343	Included	34927	Included
RS03_L2R3	17/03/2022	patina	Wet	P3_C5	P3_A12	24687	Included	28719	Included
RS03_soil	17/03/2022	soil	Wet	P3_E11	P3_E6	34760	Included	38342	Included
RS03_soilL2	17/03/2022	soil	Wet	P3_E10	P3_F6	35323	Included	33624	Included
RS03G_bottom	7/11/2022	patina	Dry	P4_D10	P4_D2	39570	Included	40205	Included
RS03G_right	NA	patina	Dry	P6_C11	P6_E7	40675	Included	33985	Included
RS03G_soil	NA	soil	Dry	P6_D8	P6_G2	21537	Included	23033	Included
RS03G_surf	7/11/2022	surface	Dry	P4_A9	P4_B6	52334	Included	57165	Included
RS03G_top	7/11/2022	patina	Dry	P4_D9	P4_D1	27523	Included	23290	Included
RS03GR_ bottom	7/11/2022	patina	Dry	P4_D8	P4_C12	29279	Included	42019	Included
RS03GR_right	7/11/2022	patina	Dry	P4_D7	P4_C11	42695	Included	19244	Included
RS03GR_top	7/11/2022	patina	Dry	P3_F9	P4_B5	42581	Included	20425	Included
RS04_lichen	30/03/2022	lichen	Wet	P2_A8	P2_E2	48224	Included	8312	Excluded
RS04_NA	NA	patina	Wet	P3_B8	P3_D1	35899	Included	4123	Excluded
RS04_NA	NA	patina	Wet	P3_B9	P3_D2	42161	Included	7213	Excluded

Sample name	Date sampled	Sample type	Season	ITS plate	16S plate	16S reads	16S inclusion	ITS reads	ITS inclusion
RS04_NA	NA	patina	Wet	P3_B10	P3_D3	62347	Included	7007	Excluded
RS04_R1	17/03/2022	patina	Wet	P2_G8	P3_C11	29753	Included	37076	Included
RS04_R2	17/03/2022	patina	Wet	P2_G6	P3_A1	46568	Included	19295	Included
RS04_R3	17/03/2022	patina	Wet	P2_G7	P3_A2	38782	Included	27752	Included
RS04_soil	17/03/2022	soil	Wet	P3_E12	P2_H7	20483	Included	40425	Included
RS04_soil	1/04/2022	soil	Wet	P3_F3	P3_F8	31817	Included	42773	Included
RS04_ SRBslocoords	NA	NA	Wet	P2_F12	P2_G5	41195	Included	27546	Included
RS04D_1	18/07/2022	patina	Dry	P5_F12	P5_H5	23938	Included	39961	Included
RS04D_2	18/07/2022	patina	Dry	P5_G1	P5_H6	30006	Included	36567	Included
RS04D_3	18/07/2022	patina	Dry	P5_G2	P5_H7	21143	Included	38151	Included
RS04D_soil	18/07/2022	soil	Dry	P3_G2	P4_G7	24498	Included	34882	Included
RS04G_1	18/07/2022	patina	Dry	P3_F11	P4_D6	28730	Included	6794	Excluded
RS04G_2	18/07/2022	patina	Dry	P3_F12	P4_D7	34114	Included	9099	Excluded
RS04G_3	18/07/2022	patina	Dry	P3_G9	P4_E10	30760	Included	16057	Included
RS04GB_1	18/07/2022	patina	Dry	P4_B5	P4_E11	32176	Included	39177	Included
RS04GB_2	18/07/2022	patina	Dry	P4_B6	P4_E12	31638	Included	39216	Included
RS04GB_3	18/07/2022	patina	Dry	P3_G10	P4_F1	30894	Included	36655	Included
RS04GB_left	30/03/2022	patina	Wet	P1_D9	P1_G8	38037	Included	23743	Included
RS04GB_lichen	18/07/2022	lichen	Dry	P4_E1	P4_D9	43882	Included	13696	Included
RS04GB_little	30/03/2022	patina	Wet	P1_G1	P1_G7	62606	Included	22677	Included
RS04GB_right	30/03/2022	patina	Wet	P1_G2	P1_G9	37042	Included	16054	Included
RS05D_1	22/07/2022	patina	Dry	P6_C12	P6_C9	77265	Included	27254	Included
RS05D_2	22/07/2022	patina	Dry	P6_A10	P6_C10	58280	Included	28773	Included
RS05D_3	22/07/2022	patina	Dry	P5_G11	P6_C11	43707	Included	36659	Included
RS05D_left	1/04/2022	patina	Wet	P3_C9	P3_B5	43014	Included	29829	Included
RS05D_mid	1/04/2022	patina	Wet	P3_C8	P3_B4	41007	Included	22706	Included
RS05D_right	1/04/2022	patina	Wet	P3_C7	P3_B3	43939	Included	27918	Included
RS05D_soil	22/07/2022	soil	Dry	P6_D10	P6_G5	26127	Included	40617	Included
RS05D_surf	22/07/2022	surface	Dry	P5_G12	P6_A5	64097	Included	48787	Included
RS05G_bottom	1/04/2022	patina	Wet	P1_D4	P1_F4	38325	Included	9433	Excluded
RS05G_left	1/04/2022	patina	Wet	P1_D5	P1_F6	84561	Included	16786	Included

Sample name	Date sampled	Sample type	Season	ITS plate	16S plate	16S reads	16S inclusion	ITS reads	ITS inclusion
RS05G_right	1/04/2022	patina	Wet	P1_D3	P1_B10	49567	Included	24810	Included
RS05G_ SR2-left	6/04/2022	patina	Wet	P1_H2	P1_H4	62071	Included	40047	Included
RS05G_ SR2-middle	6/04/2022	patina	Wet	P1_H3	P1_H5	42653	Included	46543	Included
RS05G_ SR2-right	6/04/2022	patina	Wet	P1_H4	P1_H6	55629	Included	34860	Included
RS05G1_1	21/07/2022	patina	Dry	P6_A11	P6_D1	52138	Included	41424	Included
RS05G1_2	21/07/2022	patina	Dry	P6_A12	P6_D2	48010	Included	43254	Included
RS05G1_3	21/07/2022	patina	Dry	P6_D1	P6_F4	40378	Included	37650	Included
RS05G1_soil	21/07/2022	soil	Dry	P6_D11	P6_G6	41064	Included	19621	Included
RS05G1_surf	21/07/2022	surface	Dry	P5_H5	P6_A9	78232	Included	46437	Included
RS05G2_1	22/07/2022	patina	Dry	P5_H1	P6_A6	53679	Included	29248	Included
RS05G2_2	22/07/2022	patina	Dry	P5_H2	P6_C12	34330	Included	30738	Included
RS05G2_3	22/07/2022	patina	Dry	P5_H3	P6_A7	49488	Included	38168	Included
RS05G2_soil	22/07/2022	soil	Dry	P6_F6	P7_A1	49991	Included	14404	Included
RS05G2_surf	22/07/2022	surface	Dry	P5_H4	P6_A8	29985	Included	38903	Included
RS06G_1	18/07/2022	patina	Dry	P4_B10	P4_B10	43715	Included	21694	Included
RS06G_2	18/07/2022	patina	Dry	P4_B11	P4_F2	43322	Included	9807	Excluded
RS06G_3	18/07/2022	patina	Dry	P4_B12	P4_B11	33689	Included	9723	Excluded
RS06G_lower	1/04/2022	patina	Wet	P1_B2	P1_C7	34254	Included	41348	Included
RS06G_mid	1/04/2022	patina	Wet	P1_A10	P1_E5	46789	Included	9941	Excluded
RS06G_upper	1/04/2022	patina	Wet	P1_E4	P1_G1	48771	Included	1734	Excluded
RS07B_1/3	21/03/2022	patina	Wet	P2_H7	P3_D5	37068	Included	51270	Included
RS07B_2/3	21/03/2022	patina	Wet	P2_H8	P3_D6	36786	Included	42738	Included
RS07B_3/3	21/03/2022	patina	Wet	P2_H9	P3_B12	26265	Included	34128	Included
RS07B_A	NA	patina	Dry	P4_G1	P5_F10	32295	Included	47766	Included
RS07B_B	NA	patina	Dry	P4_G2	P5_F11	27798	Included	45236	Included
RS07B_C	NA	patina	Dry	P4_G3	P5_F12	23013	Included	45406	Included
RS08B_1	NA	patina	Wet	P2_D9	P2_E8	1408	Excluded	26230	Included
RS08B_2	NA	patina	Wet	P2_D10	P2_B7	46858	Included	14528	Included
RS08B_3	NA	patina	Wet	P2_D11	P2_E9	47914	Included	37971	Included

Sample name	Date sampled	Sample type	Season	ITS plate	16S plate	16S reads	16S inclusion	ITS reads	ITS inclusion
RS08B_ bottomleft	NA	patina	Dry	P4_D12	P4_D5	30434	Included	19400	Included
RS08B_ bottomright	NA	patina	Dry	P3_F10	P4_D4	30970	Included	38180	Included
RS08B_top	NA	patina	Dry	P4_D11	P4_D3	13695	Included	27693	Included
RS08D_1	NA	patina	Wet	P2_F6	P2_C3	45045	Included	17323	Included
RS08D_2	NA	patina	Wet	P2_F7	P2_C4	54368	Included	43576	Included
RS08D_3	NA	patina	Wet	P2_F8	P2_C5	48152	Included	38335	Included
RS08D_ bottomleft	NA	patina	Dry	P6_C10	P6_E6	47641	Included	42960	Included
RS08D_ bottomright	NA	patina	Dry	P6_D12	P6_E5	60727	Included	42058	Included
RS08D_lichen	NA	lichen	Dry	P6_D7	P6_D3	40443	Included	34862	Included
RS08D_surf	NA	surface	Dry	P5_G8	P6_A2	28382	Included	49765	Included
RS08D_surf	NA	surface	Dry	P5_G9	P6_A3	39559	Included	54551	Included
RS08D_top	NA	patina	Dry	P6_C8	P6_C8	36326	Included	39150	Included
RS09B_R1	18/03/2022	patina	Wet	P3_D2	P3_B11	38356	Included	44876	Included
RS09B_R2	18/03/2022	patina	Wet	P2_H6	P3_B10	39889	Included	40585	Included
RS09B_R3	18/03/2022	patina	Wet	P3_D1	P3_B9	18599	Included	31884	Included
RS09B_soil	18/03/2022	soil	Wet	P3_A8	P3_E7	32904	Included	26245	Included
RS09D_A	7/08/2022	patina	Dry	P3_G12	P4_F5	25965	Included	30658	Included
RS09D_B	7/08/2022	patina	Dry	P3_H1	P4_C2	38358	Included	29363	Included
RS09D_C	7/08/2022	patina	Dry	P3_H2	P4_C3	40221	Included	27341	Included
RS09D_R1	18/03/2022	patina	Wet	P3_D3	P3_D7	41481	Included	167525	Included
RS09D_R2	18/03/2022	patina	Wet	P3_D4	P3_D8	21921	Included	37141	Included
RS09D_R3	18/03/2022	patina	Wet	P3_D5	P3_D9	36546	Included	28489	Included
RS09D_soil	18/03/2022	soil	Wet	P3_F1	P3_F7	22217	Included	28984	Included
RS09D_soil	7/08/2022	soil	Dry	P4_A11	P4_D11	27375	Included	14552	Included
RS09DB_A	44780	patina	Dry	P5_C12	P5_D12	21444	Included	19457	Included
RS09DB_B	44780	patina	Dry	P5_D1	P5_E1	41819	Included	42662	Included
RS09DB_C	44780	patina	Dry	P4_H3	P5_A2	43376	Included	35353	Included
RS09DB_soil	44780	soil	Dry	P4_B3	P4_E5	23109	Included	27925	Included

Sample name	Date sampled	Sample type	Season	ITS plate	16S plate	16S reads	16S inclusion	ITS reads	ITS inclusion
RS10-1GR_3	25/03/2022	patina	Wet	P1_C9	P1_D10	51113	Included	32996	Included
RS10-1QGB_1	25/03/2022	patina	Wet	P1_C10	P1_F1	35245	Included	21186	Included
RS10-1QGB_2	25/03/2022	patina	Wet	P1_C12	P1_F2	59498	Included	15100	Included
RS10GB_1	21/07/2022	patina	Dry	P5_A6	P5_D9	44896	Included	51835	Included
RS10GB_2	21/07/2022	patina	Dry	P5_A7	P5_D10	38691	Included	39379	Included
RS10GB_3	21/07/2022	patina	Dry	P5_A8	P5_D11	31775	Included	23983	Included
RS10GB_surf	21/07/2022	surface	Dry	P4_H2	P5_A1	55424	Included	52047	Included
RS10GR_1	21/07/2022	patina	Dry	P4_E11	P4_H3	29377	Included	59667	Included
RS10GR_2	21/07/2022	patina	Dry	P4_E12	P4_H4	23079	Included	50706	Included
RS10GR_3	21/07/2022	patina	Dry	P4_F1	P4_H5	25984	Included	55844	Included
RS10GR_surf	21/07/2022	surface	Dry	P4_F2	P4_H6	26840	Included	46996	Included
RS11G_1	24/03/2022	patina	Wet	P1_E1	P1_F10	38474	Included	48566	Included
RS11G_2	24/03/2022	patina	Wet	P1_G7	P1_C2	90802	Included	28403	Included
RS11G_3	24/03/2022	patina	Wet	P1_G8	P1_C3	56526	Included	16688	Included
RS11G_A	NA	patina	Dry	P5_E11	P5_G12	18679	Included	37876	Included
RS11G_B	NA	patina	Dry	P5_E12	P6_B8	31744	Included	45320	Included
RS11G_C	NA	patina	Dry	P5_F1	P6_B9	50593	Included	40988	Included
RS11G_soil	NA	soil	Dry	P5_H6	P6_F8	37329	Included	44673	Included
RS12_soil	18/03/2022	soil	Wet	P3_F2	P2_H8	43203	Included	47720	Included
RS12B_1	29/07/2022	patina	Dry	P6_F4	P6_H4	31663	Included	19301	Included
RS12B_2	29/07/2022	patina	Dry	P6_B11	P6_F3	29981	Included	17411	Included
RS12B_3	29/07/2022	patina	Dry	P6_B12	P6_D10	51440	Included	40738	Included
RS12B_lichen	29/07/2022	lichen	Dry	P6_D5	P6_E11	37483	Included	4148	Excluded
RS12B_R1	18/03/2022	patina	Wet	P6_F5	P6_H5	27695	Included	25081	Included
RS12B_R2	18/03/2022	patina	Wet	P3_D11	P3_C5	38277	Included	30524	Included
RS12B_R3	18/03/2022	patina	Wet	P3_D12	P3_D12	40021	Included	31675	Included
RS12B_soil	29/07/2022	soil	Dry	P6_B4	P6_F11	41480	Included	52547	Included
RS13G_NA	NA	NA	Wet	P1_C6	P1_D5	38501	Included	23200	Included
RS13GB_1/3	23/03/2022	patina	Wet	P1_A11	P1_A2	47066	Included	26952	Included
RS13GB_2/3	23/03/2022	patina	Wet	P1_A12	P1_A3	56569	Included	35337	Included
RS13GB_3/3	23/03/2022	patina	Wet	P1_B1	P1_C6	32918	Included	45391	Included

Sample name	Date sampled	Sample type	Season	ITS plate	16S plate	16S reads	16S inclusion	ITS reads	ITS inclusion
RS13GB_ bottom	15/07/2022	patina	Dry	P5_A12	P5_A7	50155	Included	37934	Included
RS13GB_left	15/07/2022	patina	Dry	P5_D2	P5_B12	26081	Included	47969	Included
RS13GB_right	15/07/2022	patina	Dry	P5_D3	P5_E2	36043	Included	23771	Included
RS13GB_surf	15/07/2022	surface	Dry	P4_F9	P5_A8	15615	Included	61758	Included
RS13GR_1/2	23/03/2022	patina	Wet	P1_C11	P1_B7	39618	Included	7546	Excluded
RS13GR_2/2	23/03/2022	patina	Wet	P1_G6	P1_B6	39340	Included	27045	Included
RS13GR_ bottom	15/07/2022	patina	Dry	P4_F7	P5_A5	44154	Included	53441	Included
RS13GR_ middle	15/07/2022	patina	Dry	P5_A11	P5_A4	46359	Included	13619	Included
RS13GR_surf	15/07/2022	surface	Dry	P4_F8	P5_A6	46401	Included	52377	Included
RS13GR_top	15/07/2022	patina	Dry	P5_A10	P5_A3	46970	Included	21322	Included
RS14_lichen	24/03/2022	lichen	Wet	P3_B3	P3_C8	39331	Included	5041	Excluded
RS14_lichen	NA	lichen	Wet	P2_A5	P2_D6	73328	Included	1500	Excluded
RS14D_1	23/03/2022	patina	Wet	P1_F2	P1_E10	39715	Included	19270	Included
RS14D_2	23/03/2022	patina	Wet	P1_B3	P1_C8	18248	Included	144751	Included
RS14D_3	23/03/2022	patina	Wet	P1_B4	P1_C9	33487	Included	30531	Included
RS14D_bottom	17/07/2022	patina	Dry	P6_C7	P6_C6	48323	Included	9143	Excluded
RS14D_lichen	17/07/2022	lichen	Dry	P5_H8	P6_A10	71135	Included	58588	Included
RS14D_right	17/07/2022	patina	Dry	P5_G4	P5_H9	19427	Included	42117	Included
RS14D_soil	23/03/2022	soil	Wet	P2_B2	P2_D3	37233	Included	31006	Included
RS14D_surf	17/07/2022	surface	Dry	P5_G5	P5_H10	13864	Included	40629	Included
RS14G_1	24/03/2022	patina	Wet	P1_D6	P1_B11	34593	Included	37177	Included
RS14G_1	NA	patina	Wet	P1_C4	P1_D4	53389	Included	19908	Included
RS14G_2	24/03/2022	patina	Wet	P1_D7	P1_B12	37107	Included	34097	Included
RS14G_2	NA	patina	Wet	P1_C5	P1_E12	28416	Included	31085	Included
RS14G_3	24/03/2022	patina	Wet	P1_D8	P1_C1	58726	Included	36628	Included
RS14G_bottom	17/07/2022	patina	Dry	P5_G6	P5_H11	21682	Included	33618	Included
RS14G_middle	17/07/2022	patina	Dry	P6_A8	P6_C7	49691	Included	39751	Included
RS14G_surf	17/07/2022	surface	Dry	P5_G7	P6_A1	41442	Included	51411	Included
RS14G_top	17/07/2022	patina	Dry	P6_A9	P5_H12	12758	Included	40937	Included

Sample name	Date sampled	Sample type	Season	ITS plate	16S plate	16S reads	16S inclusion	ITS reads	ITS inclusion
RS15B_ leftbottom	13/07/2022	patina	Dry	P4_F6	P5_C12	28876	Included	50571	Included
RS15B_lichen	13/07/2022	lichen	Dry	P4_B1	P4_A8	46647	Included	63157	Included
RS15B_red	21/03/2022	patina	Wet	P2_A1	P2_F9	46372	Included	50188	Included
RS15B_red2	21/03/2022	patina	Wet	P1_H12	P2_F8	60576	Included	36047	Included
RS15B_right	13/07/2022	patina	Dry	P4_F4	P5_B4	45579	Included	51437	Included
RS15B_surf	13/07/2022	surface	Dry	P4_F5	P4_H7	21825	Included	50340	Included
RS15B_top	13/07/2022	patina	Dry	P4_F3	P5_C11	21657	Included	57504	Included
RS15B_white	21/03/2022	patina	Wet	P1_H11	P2_C7	61174	Included	34149	Included
RS16_ lichen-white	15/03/2022	lichen	Wet	P2_A6	P2_D7	38242	Included	5485	Excluded
RS16_ lichen-yellow	15/03/2022	lichen	Wet	P2_B5	P2_A4	47153	Included	15480	Included
RS16GB_1	19/07/2022	patina	Dry	P5_D4	P5_E3	30609	Included	47253	Included
RS16GB_2	19/07/2022	patina	Dry	P5_D5	P5_E4	31180	Included	38747	Included
RS16GB_3	19/07/2022	patina	Dry	P5_D6	P5_E5	36508	Included	35662	Included
RS16GB_R1	15/03/2022	patina	Wet	P1_C3	P1_D3	39856	Included	24157	Included
RS16GB_R2	15/03/2022	patina	Wet	P1_C2	P1_D2	49611	Included	36826	Included
RS16GB_R3	15/03/2022	patina	Wet	P1_C1	P1_E11	40285	Included	46018	Included
RS16GB_ SRR1	15/03/2022	patina	Wet	P1_B12	P1_A9	38304	Included	31852	Included
RS16GB_ SRR2	15/03/2022	patina	Wet	P1_B11	P1_D1	28705	Included	38763	Included
RS16GB_ SRR3	15/03/2022	patina	Wet	P1_B10	P1_A8	43908	Included	10	Excluded
RS16GB_surf	19/07/2022	surface	Dry	P4_F10	P5_A12	21069	Included	50326	Included
RS17_soil1	16/03/2022	soil	Wet	P3_E6	P3_F3	38236	Included	40499	Included
RS17_soil2	16/03/2022	soil	Wet	P3_E7	P3_F4	32002	Included	37523	Included
RS17_soil3	16/03/2022	soil	Wet	P3_E8	P3_F5	29440	Included	34471	Included
RS17G_1	16/03/2022	patina	Wet	P2_H11	P2_G12	46341	Included	28444	Included
RS17G_2	16/03/2022	patina	Wet	P2_H12	P2_H1	30386	Included	28571	Included
RS17G_3	16/03/2022	patina	Wet	P3_A1	P2_H2	52327	Included	46310	Included

Sample name	Date sampled	Sample type	Season	ITS plate	16S plate	16S reads	16S inclusion	ITS reads	ITS inclusion
RS17G_left	13/07/2022	patina	Dry	P4_A2	P4_B4	35529	Included	61330	Included
RS17G_right	13/07/2022	patina	Dry	P4_A4	P4_A3	46467	Included	59254	Included
RS17G_soil	13/07/2022	soil	Dry	P3_G1	P4_D8	29998	Included	50982	Included
RS17G_surf	13/07/2022	surface	Dry	P4_A1	P4_A1	40030	Included	68325	Included
RS17G_top	13/07/2022	patina	Dry	P4_A3	P4_A2	36688	Included	68606	Included
RS18c_R1	15/03/2022	patina	Wet	P1_E7	P1_G2	55664	Included	29163	Included
RS18c_R2	15/03/2022	patina	Wet	P1_E5	P1_E6	79748	Included	37014	Included
RS18c_R3	15/03/2022	patina	Wet	P1_E6	P1_E7	43824	Included	43981	Included
RS18G_bottom	14/07/2022	patina	Dry	P5_C6	P5_D5	39581	Included	54914	Included
RS18G_left	14/07/2022	patina	Dry	P5_C4	P5_D4	33561	Included	40022	Included
RS18G_right	14/07/2022	patina	Dry	P5_C5	P5_B8	34585	Included	57750	Included
RS18G_surf	14/07/2022	surface	Dry	P4_G10	P4_H8	20152	Included	49204	Included
RS5G_ SR2-left	6/04/2022	patina	Wet	P2_E9	P2_B11	29912	Included	35379	Included
RS5G_ SR2-middle	6/04/2022	patina	Wet	P2_E10	P2_F2	48204	Included	32961	Included
RS5G_ SR2-right	6/04/2022	patina	Wet	P2_E11	P2_F3	43661	Included	29671	Included
SR1	19/07/2022	NA	Dry	P4_A5	P4_A4	43338	Included	58621	Included
SR2	19/07/2022	NA	Dry	P4_A6	P4_A5	39462	Included	48443	Included
SR3	19/07/2022	NA	Dry	P4_A7	P4_A6	35744	Included	66076	Included
Srsurf	19/07/2022	surface	Dry	P4_A8	P4_A7	39438	Included	64886	Included

This page is intentionally blank.

D Spatial mapping and surface modelling

D.1 Spatial mapping site summaries

The following is a summary of the sites AQ and EX, which have been processed and uploaded to Nextcloud, containing the following information:

- **Summary of capture:** This includes the drone (and camera) used, the number of images processed versus number captured, the average resolution or ground sampling and the type of control used to geo-reference the final model (and the number of control and how it was captured). Also summarised is the median number of key points per image (feature points used to match points between images), the number of tie points used in aligning the images together to create the 3D model, and the average reprojection error (error of the projected image point to the observed point). The last values are an indication of the strength and the errors in the 3D.
- **Position uncertainties:** These are the uncertainties of the final calculated camera locations of the final adjustment. These locations are used in the projections and matching of the image points to re-create the 3D scene captured.
- **Control points:** These are the summary of the control points used to georeferenced the 3D model to the real-world location. This contains the initial accuracy of the points from the RTK pickup (relative to the base station or site datum point), the number of images they occur in, the errors (median and RMS) of the control in terms of the generated 3D model. This is separated into 3D, horizontal and vertical errors (with vertical normally being higher than horizontal).
- **Positional uncertainties:** These figures contain the positional uncertainties of the generated tie points over the region. It gives an indication of the distribution of the tie points, and their errors and uncertainties in image matching in the adjustment. This can be used to determine some of the errors and missing information in the final 3D model.
- **Ortho-mosaic:** The orthographic mosaic of the area depicts the area captured, as well as the location of the control points used in the adjustment and processing of the images. This is created by projecting the images onto the terrain surface and stitching them together into a continuous mosaic.
- **Digital elevation model:** The Digital Elevation Model (**DEM**) provides information on the heights and topology of the region of capture.

AQ02 site summary

Table D.1-1: AQ02 site summary.

Drone	**Phantom 4 Pro**
Camera Model	DJI FC6310
Images	558/558
Ground Coverage	2405601 m^2
Average ground resolution	17.4834 mm/pixel
Geo referencing	7 Control points (RTK)
Key Points	Median of 49313 key points per image
Tie Points	255109 points (median of 27060 points per photo)
Reprojection Errors (Median)	0.39 pixels
Reprojection Errors (RMS)	0.53 pixels
Distance to Rays (RMS)	0.0639 metres

Table D.1-2: AQ02 Position uncertainties (camera locations).

	X (metres)	**Y (metres)**	**Z (metres)**
Minimum	0.0018	0.0016	0.0008
Mean	0.003	0.003	0.0014
Maximum	0.0346	0.0444	0.023

Table D.1-3: AQ02 control points. Where "H" is horizontal and "V" is vertical.

Name	Accuracy (m)	Num of Photos	RMS of Reproject Error (pixels)	RMS of Dist to Rays (m)	3D Error (m)	Horizontal Errors (m)	Vertical Error (m)
uav01	H: 0.012 V: 0.026	16	0.6	0.051	0.0058	X: 0.0048 Y: -0.0008	0.0031
uav02	H: 0.011 V: 0.024	21	0.73	0.0629	0.0061	X: -0.0055 Y: -0.0006	-0.0027
uav03	H: 0.009 V: 0.018	40	0.64	0.0575	0.0051	X: -0.0001 Y: -0.0009	0.005
uav04	H: 0.010 V: 0.020	41	0.69	0.0808	0.0078	X: 0.0024 Y: 0.007	-0.0026
uav05	H: 0.010 V: 0.019	7	0.55	0.0793	0.0124	X: 0.0005 Y: 0.0015	0.0123
uav06	H: 0.015 V: 0.027	32	0.66	0.0693	0.0057	X: -0.0005 Y: -0.0004	-0.0057
uav07	H: 0.010 V: 0.018	21	0.59	0.0602	0.0038	X: 0.0008 Y: -0.0014	0.0035
Global RMS			0.64	0.0667	0.0072	X: 0.0029 Y: -0.0028	0.0059
Median			0.64	0.0629	0.0058	X: 0.0005 Y: -0.0006	0.0031

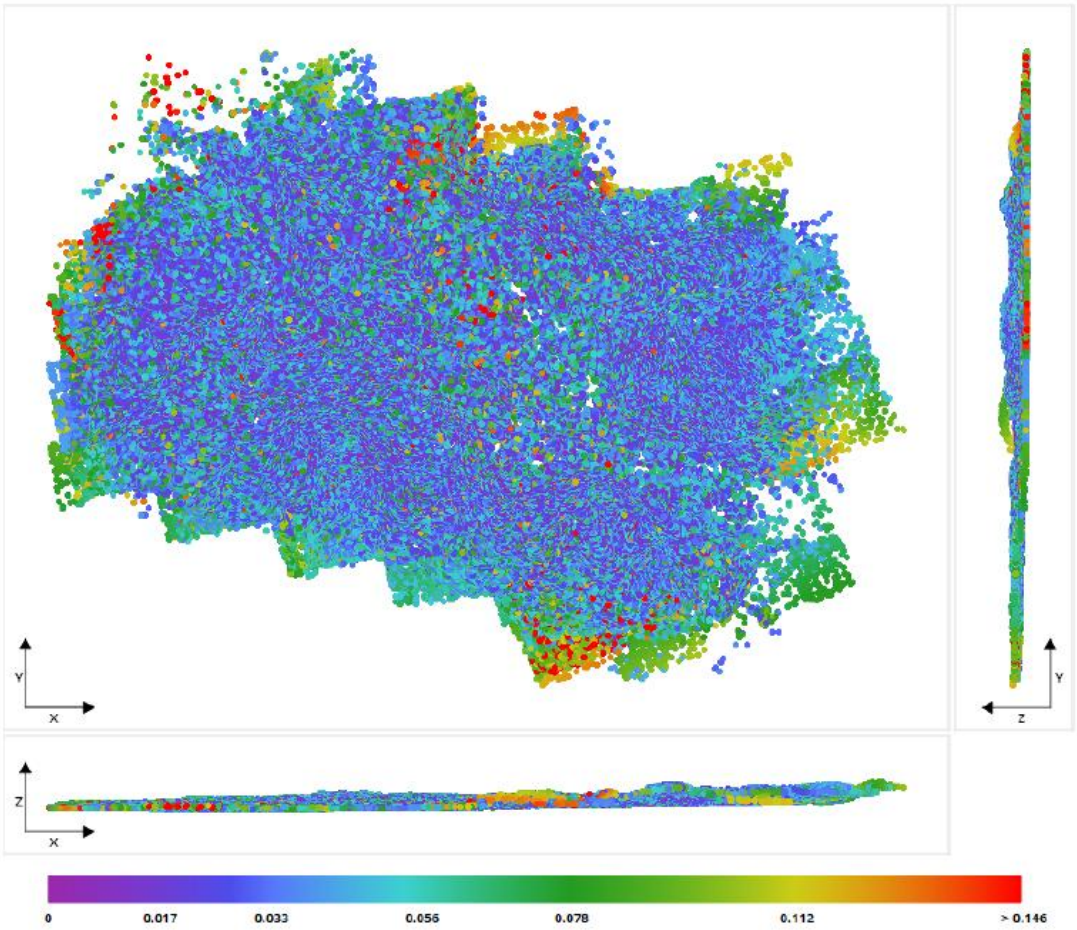

Figure D.1-1: Position uncertainties for AQ02: Top view (XY plane), side view (ZY plane) and front view (XZ plane) displays of all tie points, with colours representing uncertainty in the individual point position. The values are in metres, with a minimum uncertainty of 0.0051 metres and a maximum of 0.6867 metres. The median position uncertainty equals 0.0335 metres.

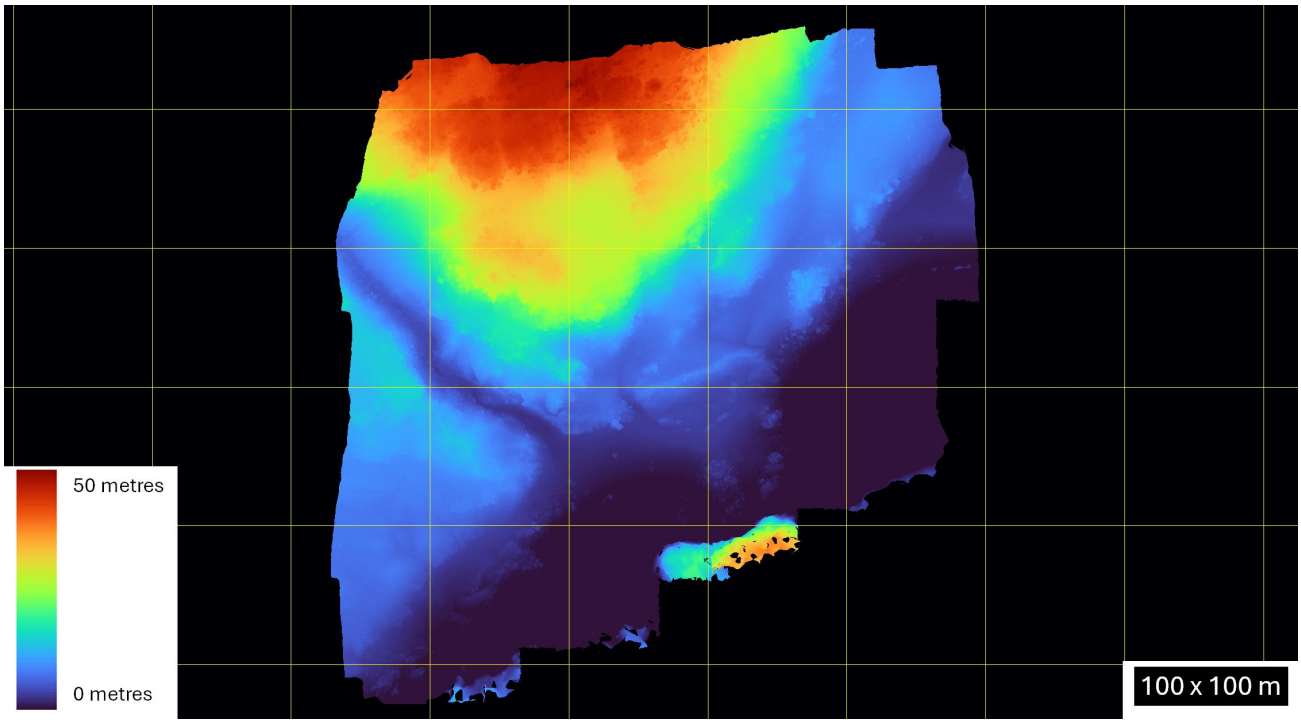

Figure D.1-2: Ortho-mosaic for AQ02. Plotted with control points and 100 x 100 m grid spacing.

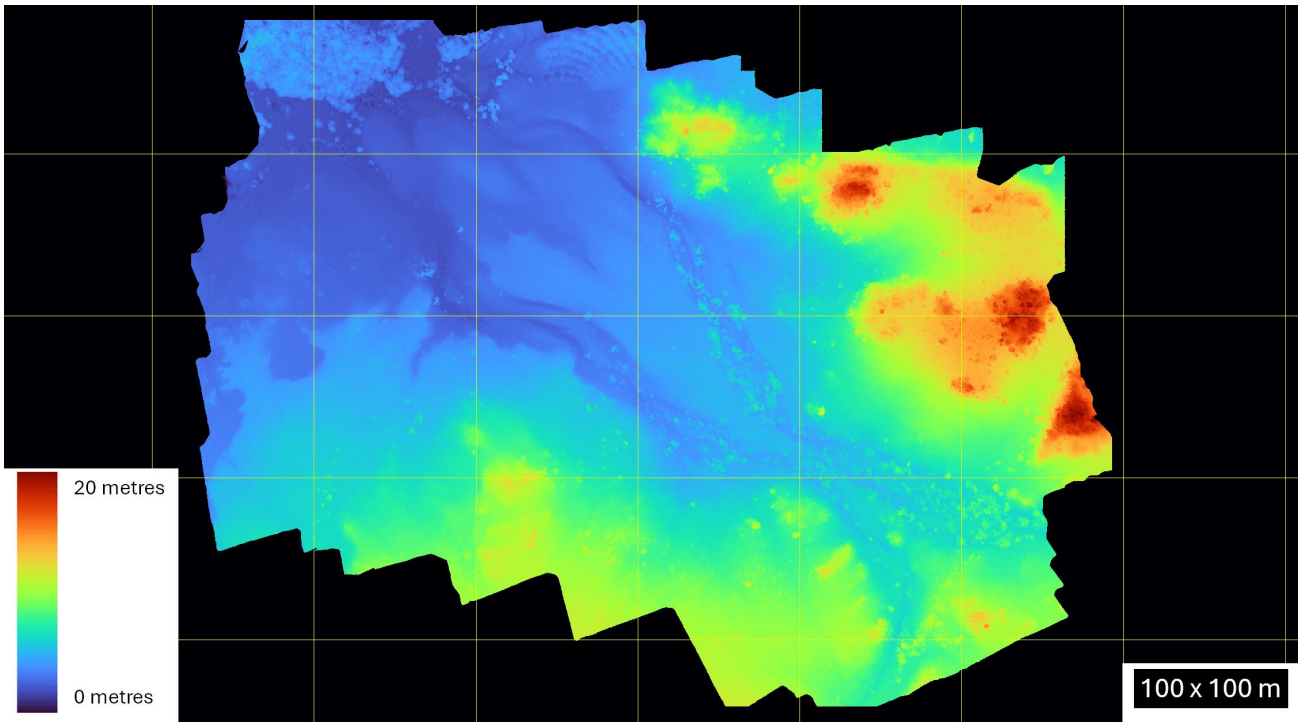

Figure D.1-3: DEM for AQ02. Plotted with 100 x 100 m grid spacing.

AQ03 site summary

Table D.1-4: AQ03 site summary.

Drone	**Phantom 4 Pro**
Camera Model	DJI FC6310
Images	895/865
Ground Coverage	0.821 m^2
Average ground resolution	18.4324 mm/pixel
Geo referencing	8 control points (RTK)
Key Points	Median of 48451 key points per image
Tie Points	383184 points (median of 2014 points per photo)
Reprojection Errors (Median)	0.35 pixels
Reprojection Errors (RMS)	0.49 pixels
Distance to Rays (RMS)	0.0636 metres

Table D.1-5: AQ03 Position uncertainties (camera locations).

	X (metres)	**Y (metres)**	**Z (metres)**
Minimum	0.002	0.0022	0.0008
Mean	0.0039	0.0052	0.0022
Maximum	0.3231	0.6447	0.5063

Table D.1-6: AQ03 control points.

Name	Accuracy (m)	Num of Photos	RMS of Reproject Error (pixels)	RMS of Dist to Rays (m)	3D Error (m)	Horizontal Errors (m)	Vertical Error (m)
uav01	H: 0.008 V: 0.018	17	0.45	0.0797	0.0043	X: -0.0014 Y: 0.0010	0.0039
uav02	H: 0.009 V: 0.022	16	0.49	0.0791	0.004	X: -0.0010 Y: 0.0005	-0.0038
uav03	H: 0.009 V: 0.018	13	0.55	0.0717	0.0033	X: 0.0014 Y: -0.0011	-0.0028
uav04	H: 0.008 V: 0.015	11	0.44	0.0579	0.0045	X: -0.0002 Y: 0.0039	-0.0022
uav05	H: 0.006 V: 0.012	11	0.48	0.0743	0.0059	X: 0.0025 Y: -0.0046	0.0026
uav06	H: 0.017 V: 0.035	15	0.41	0.0732	0.0039	X: -0.0006 Y: -0.0032	-0.0021
uav07	H: 0.015 V: 0.03	17	0.39	0.0807	0.0059	X: 0.0030 Y: -0.0011	0.0049
uav08	H: 0.015 V: 0.03	14	0.44	0.086	0.0032	X: -0.0019 Y: 0.0016	-0.002
Global RMS			0.46	0.0758	0.0045	X: 0.0017 Y: 0.0026	0.0032
Median			0.45	0.0791	0.0042	X: -0.0002 Y: 0.0005	-0.002

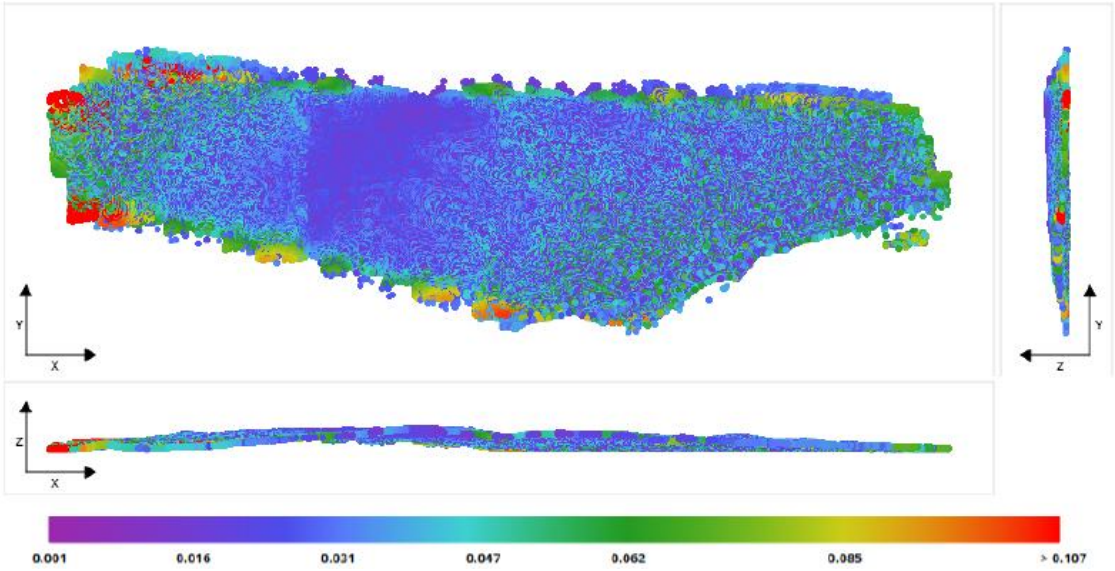

Figure D.1-4: Position uncertainties for AQ03: Top view (XY plane), side view (ZY plane) and front view (XZ plane) displays of all tie points, with colours representing uncertainty in the individual point position. The values are in metres, with a minimum uncertainty of 0.0051 metres and a maximum of 0.6867 metres. The median position uncertainty equals 0.0335 metres.

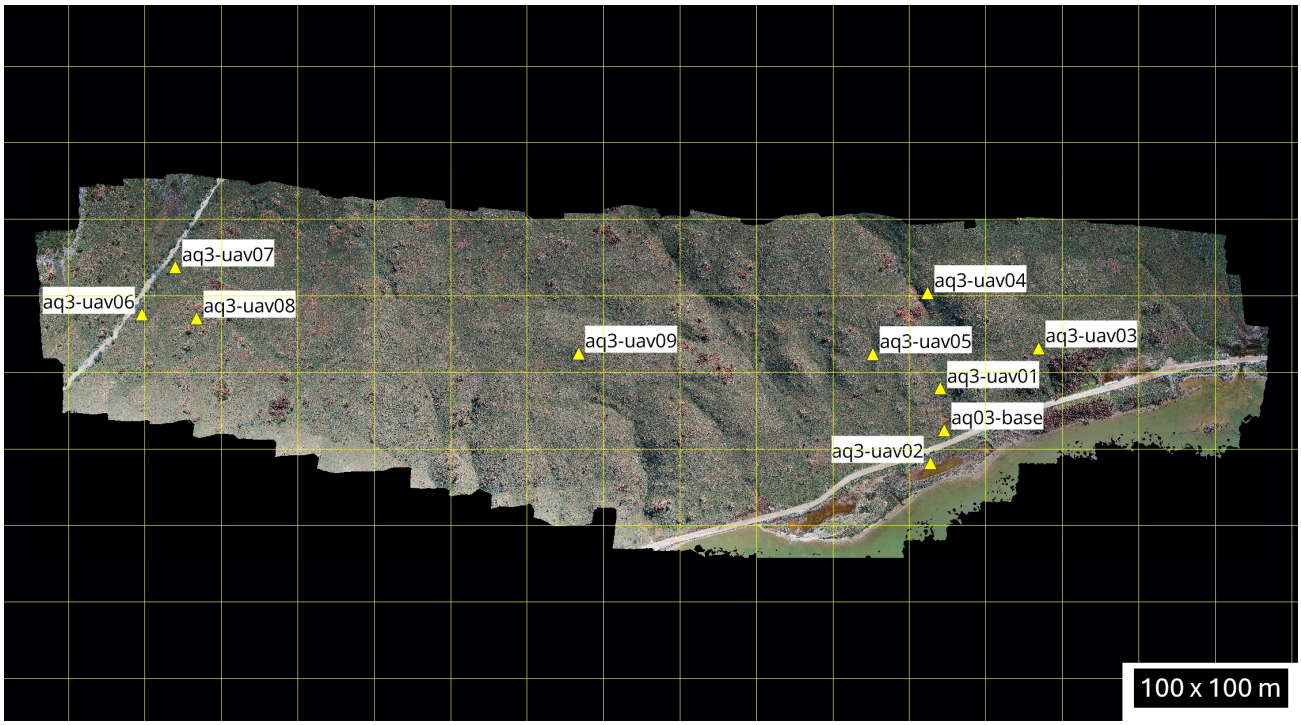

Figure D.1-5: Ortho-mosaic for AQ03. Plotted with control points and 100 x 100 m grid spacing.

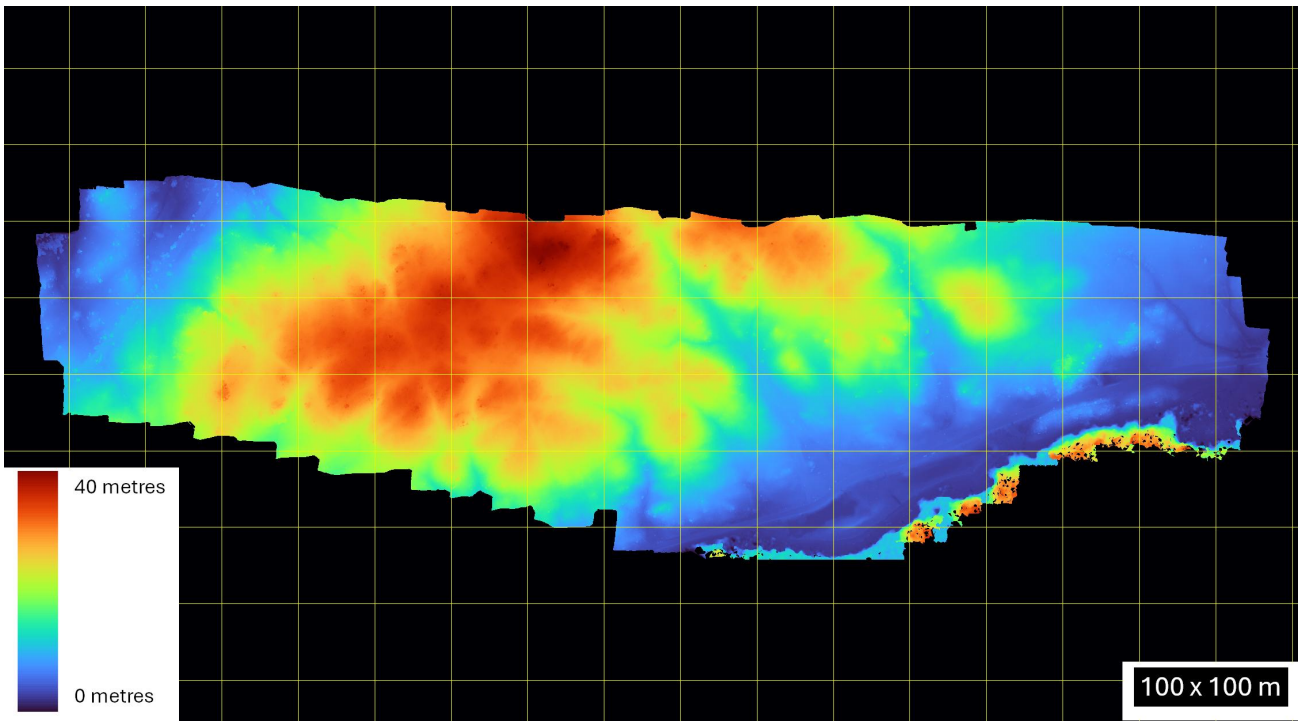

Figure D.1-6: DEM for AQ03. Plotted with 100 x 100 m grid spacing.

AQ04 site summary

Table D.1-7: AQ04 site summary.

Drone	**Phantom 4 Pro**
Camera Model	DJI FC6310
Images	558/558
Ground Coverage	2405601 m^2
Average ground resolution	17.4834 mm/pixel
Geo referencing	7 control points (RTK)
Key Points	Median of 49313 key points per image
Tie Points	255109 points (median of 27060 points per photo)
Reprojection Errors (Median)	0.39 pixels
Reprojection Errors (RMS)	0.53 pixels
Distance to Rays (RMS)	0.0639 metres

Table D.1-8: AQ04 Position uncertainties (camera locations).

	X (metres)	**Y (metres)**	**Z (metres)**
Minimum	0.0018	0.0016	0.0008
Mean	0.003	0.003	0.0014
Maximum	0.0346	0.0444	0.023

Table D.1-9: AQ04 control points.

Name	Accuracy (m)	Num of Photos	RMS of Reproject Error (pixels)	RMS of Dist to Rays (m)	3D Error (m)	Horizontal Errors (m)	Vertical Error (m)
uav01	H: 0.008 V: 0.020	25	0.65	0.0849	0.0027	X: 0.0009 Y: 0.0024	0.0009
uav02	H: 0.007 V: 0.017	18	0.54	0.0656	0.0082	X: -0.008 Y: 0.0017	0
uav03	H: 0.009 V: 0.020	18	0.69	0.0574	0.00124	X: 0.0036 Y: -0.0107	0.005
uav04	H: 0.008 V: 0.017	20	0.69	0.0619	0.0084	X: 0.0077 Y: 0.0024	0.0023
uav05	H: 0.010 V: 0.022	18	0.84	0.06	0.0136	X: -0.0126 Y: 0.0050	-0.0011
uav06	H: 0.008 V: 0.017	19	0.44	0.062	0.0043	X: -0.0033 Y: 0.0027	-0.001
uav07	H: 0.008 V: 0.017	26	0.65	0.0879	0.0031	X: -0.0016 Y: -0.0021	0.0017
uav08	H: 0.008 V: 0.016	25	0.81	0.0952	0.0122	X: 0.0120 Y: -0.0010	-0.0017
Global RMS			0.67	0.0732	0.0091	X: 0.0075 Y: -0.0046	0.0022
Median			0.69	0.0656	0.0084	X: 0.0009 Y: 0.0024	0.0009

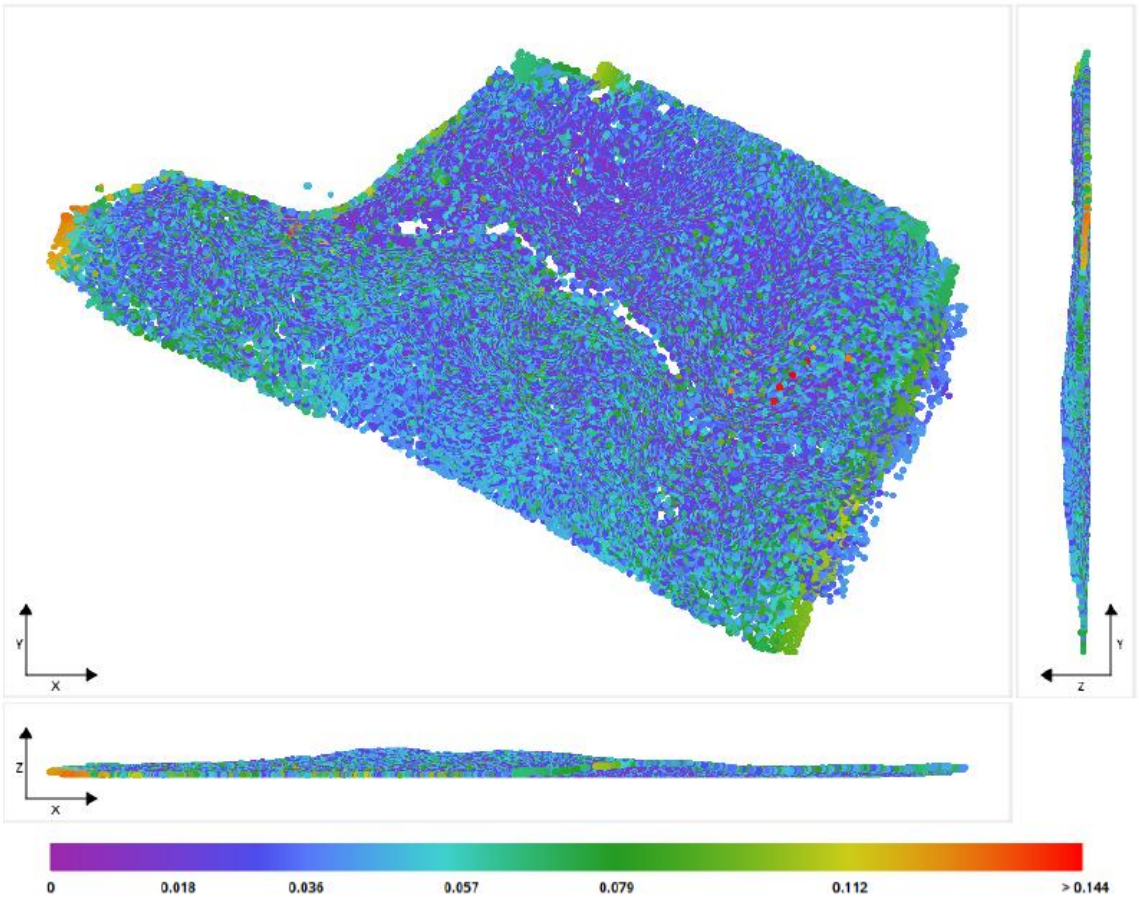

Figure D.1-7: Position uncertainties for AQ04: Top view (XY plane), side view (ZY plane) and front view (XZ plane) displays of all tie points, with colours representing uncertainty in the individual point position. The values are in metres, with a minimum uncertainty of 0.0051 metres and a maximum of 0.6867 metres. The median position uncertainty equals 0.0335 metres.

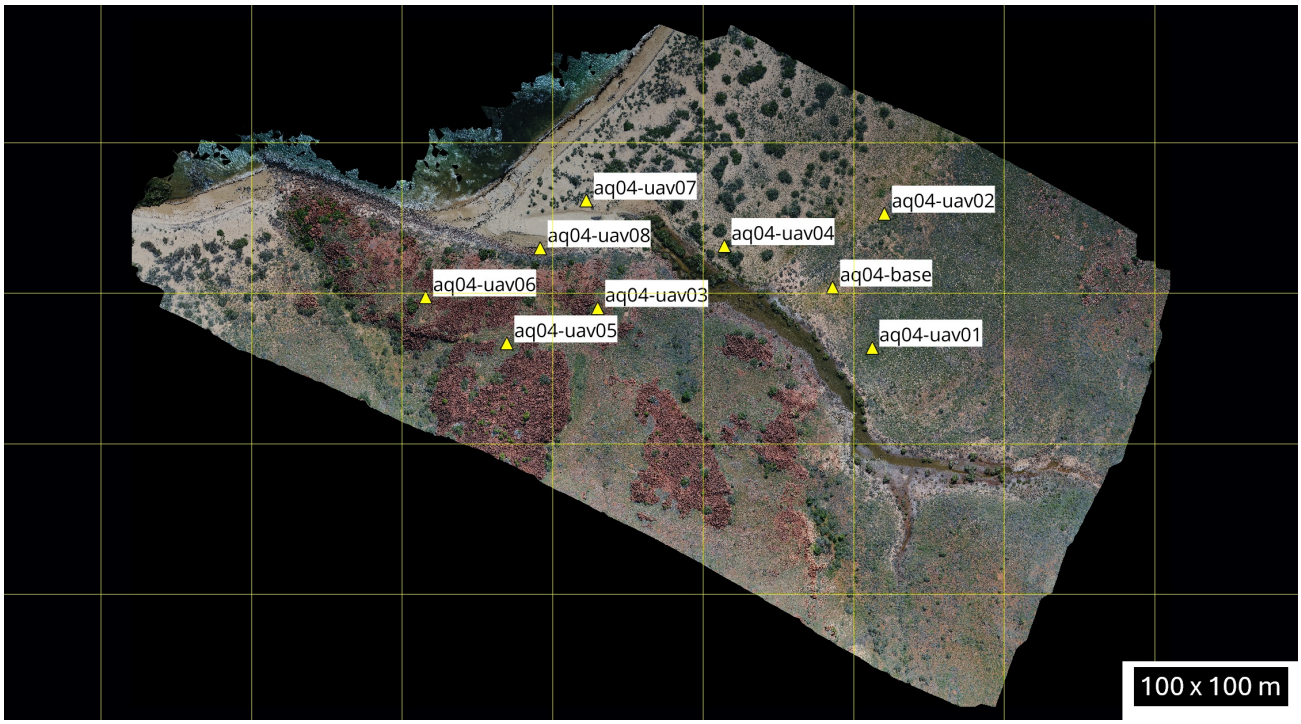

Figure D.1-8: Ortho-mosaic for AQ04. Plotted with control points and 100 x 100 m grid spacing.

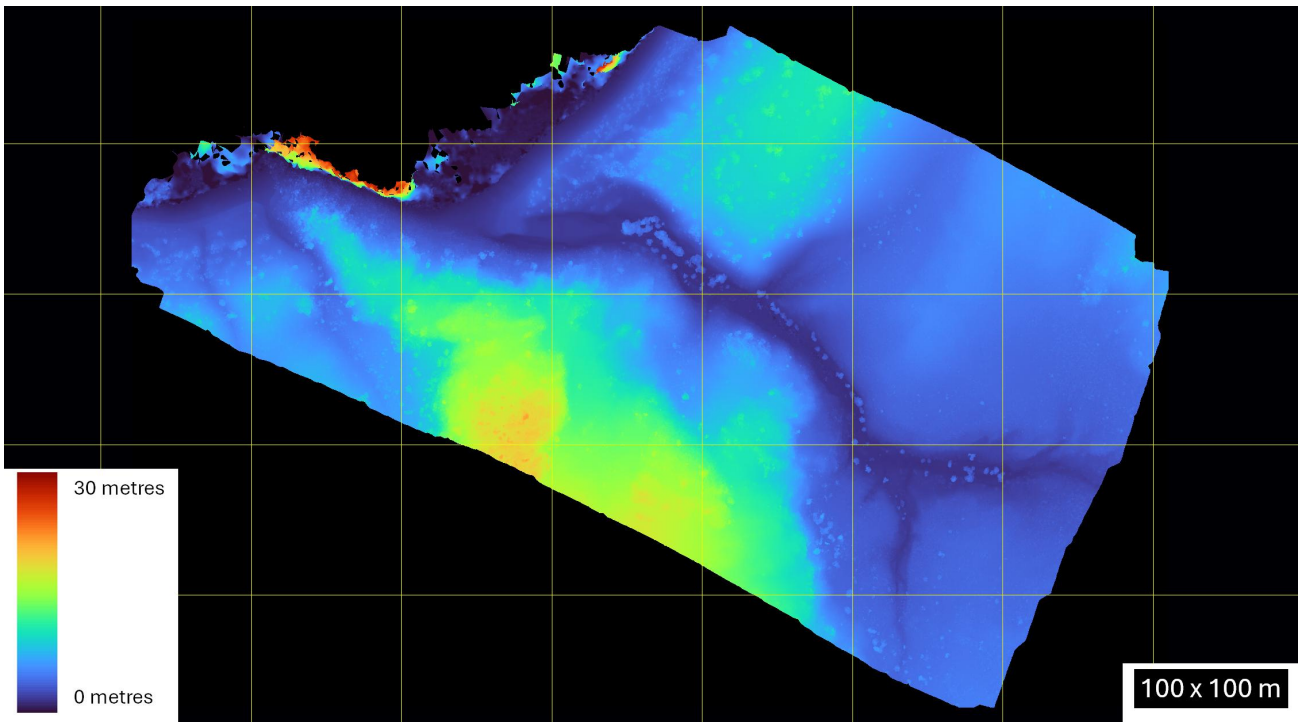

Figure D.1-9: DEM for AQ04. Plotted with 100 x 100 m grid spacing.

AQ05 site summary.

Table D.1-10: AQ05 site summary

Drone	**Phantom 4 Pro**
Camera Model	DJI FC6310
Images	584/588
Ground Coverage	0.542 km^2
Average ground resolution	19.59255 mm/pixel
Geo referencing	6 control points (RTK)
Key Points	Median of 49584 keypoints per image
Tie Points	292382 points (median of 2707 points per photo)
Reprojection Errors (Median)	0.36 pixels
Reprojection Errors (RMS)	0.49 pixels
Distance to Rays (RMS)	0.0712 metres

Table D.1-11: AQ05 Position uncertainties (camera locations).

	X (metres)	**Y (metres)**	**Z (metres)**
Minimum	0.0023	0.002	0.0009
Mean	0.0033	0.003	0.0013
Maximum	0.0281	0.0202	0.0118

Table D.1-12: AQ05 control points.

Name	Accuracy (m)	Num of Photos	RMS of Reproject Error (pixels)	RMS of Dist to Rays (m)	3D Error (m)	Horizontal Errors (m)	Vertical Error (m)
uav01	H: 0.007 V: 0.021	13	0.42	0.0874	0.0053	X: 0.0028 Y: 0.0035	-0.0029
uav02	H: 0.016 V: 0.051	14	0.77	0.0529	0.0124	X: 0.0082 Y:-0.0092	0.0016
uav03	H: 0.015 V: 0.045	16	0.45	0.0694	0.005	X:-0.0049 Y:-0.0008	0.0051
uav04	H: 0.011 V: 0.033	20	0.61	0.0751	0.0097	X: 0.0041 Y: 0.0087	0.0008
uav05	H: 0.011 V: 0.031	22	0.61	0.0946	0.0077	X:-0.0075 Y:-0.0014	0.0012
Global RMS			0.67	0.0732	0.0091	X: 0.0075 Y:-0.0046	0.0022
Median			0.69	0.0656	0.0084	X: 0.0009 Y: 0.0024	0.0009

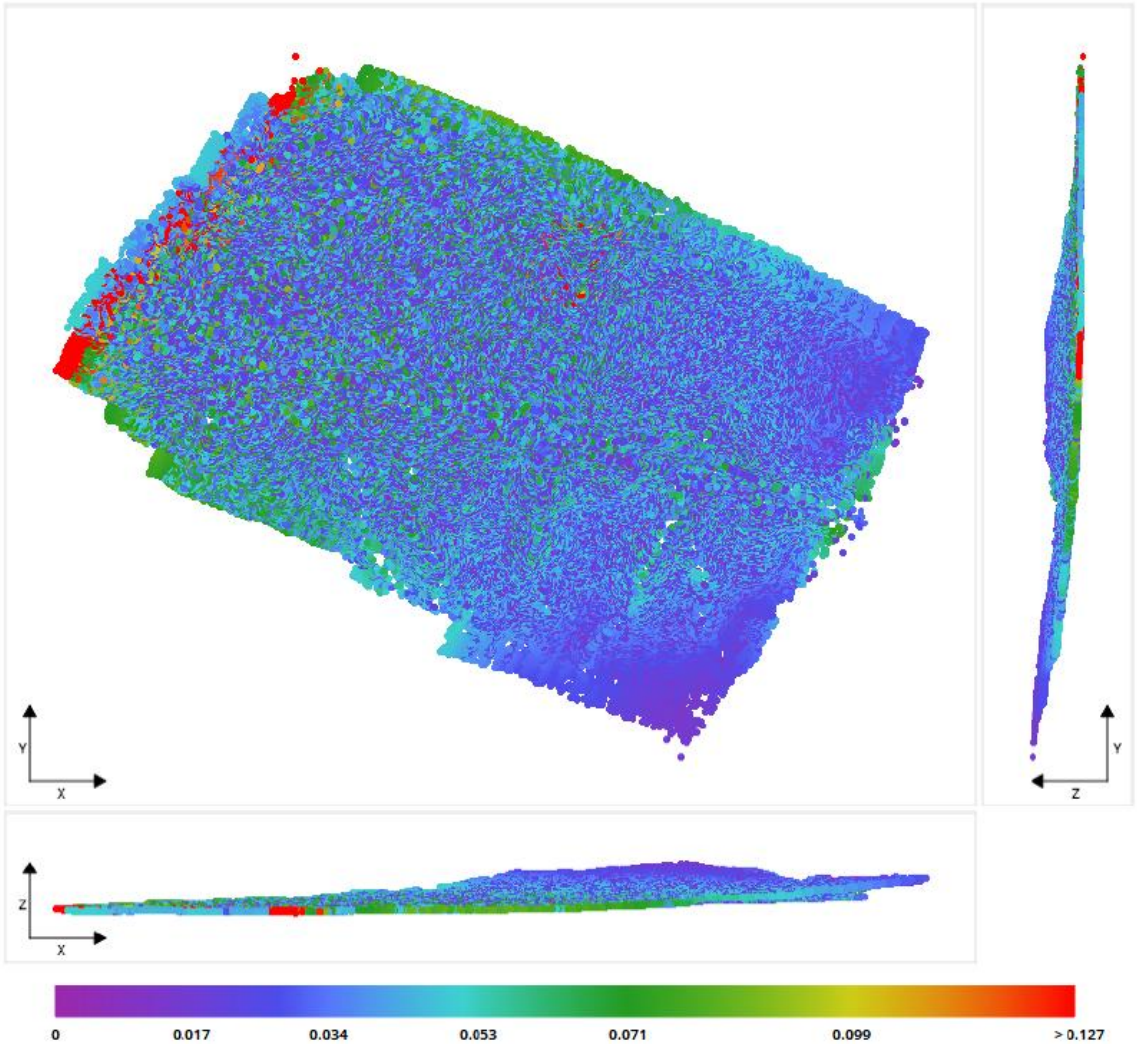

Figure D.1-10: Position uncertainties for AQ05: Top view (XY plane), side view (ZY plane) and front view (XZ plane) displays of all tie points, with colours representing uncertainty in the individual point position. The values are in metres, with a minimum uncertainty of 0.0051 metres and a maximum of 0.6867 metres. The median position uncertainty equals 0.0335 metres.

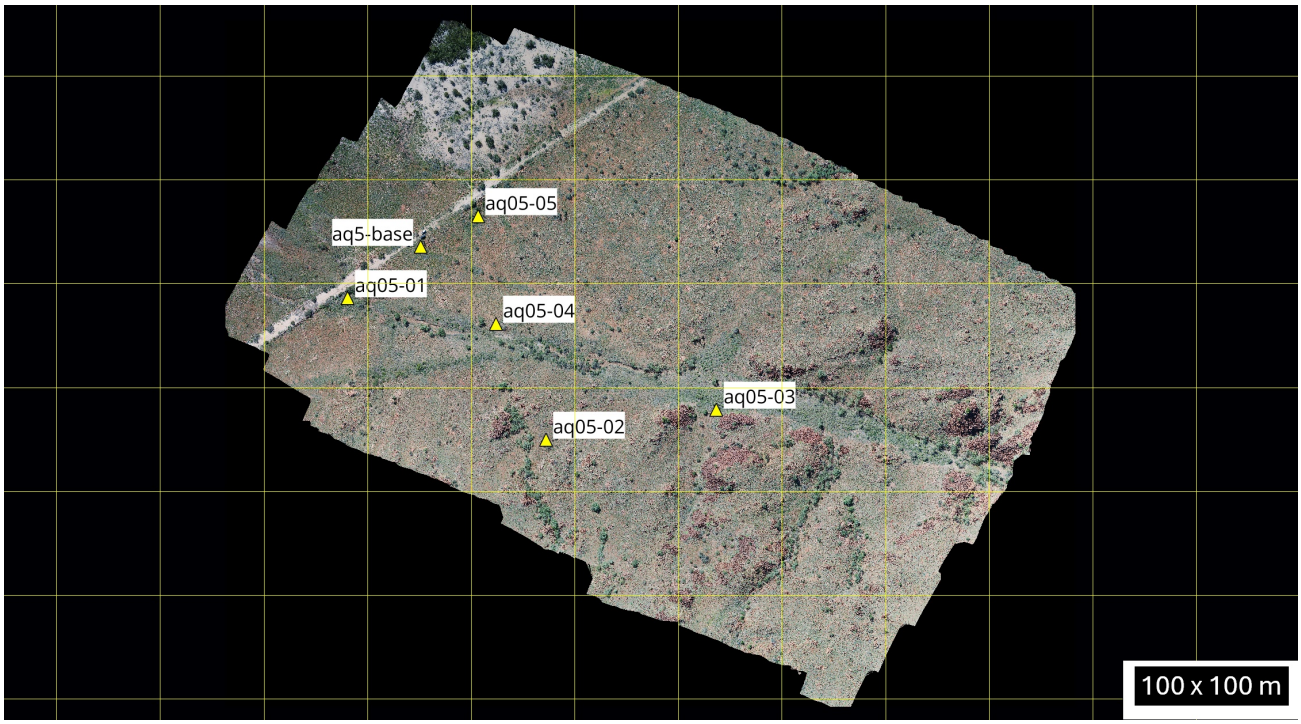

Figure D.1-11: Ortho-mosaic for AQ05. Plotted with control points and 100 x 100 m grid spacing.

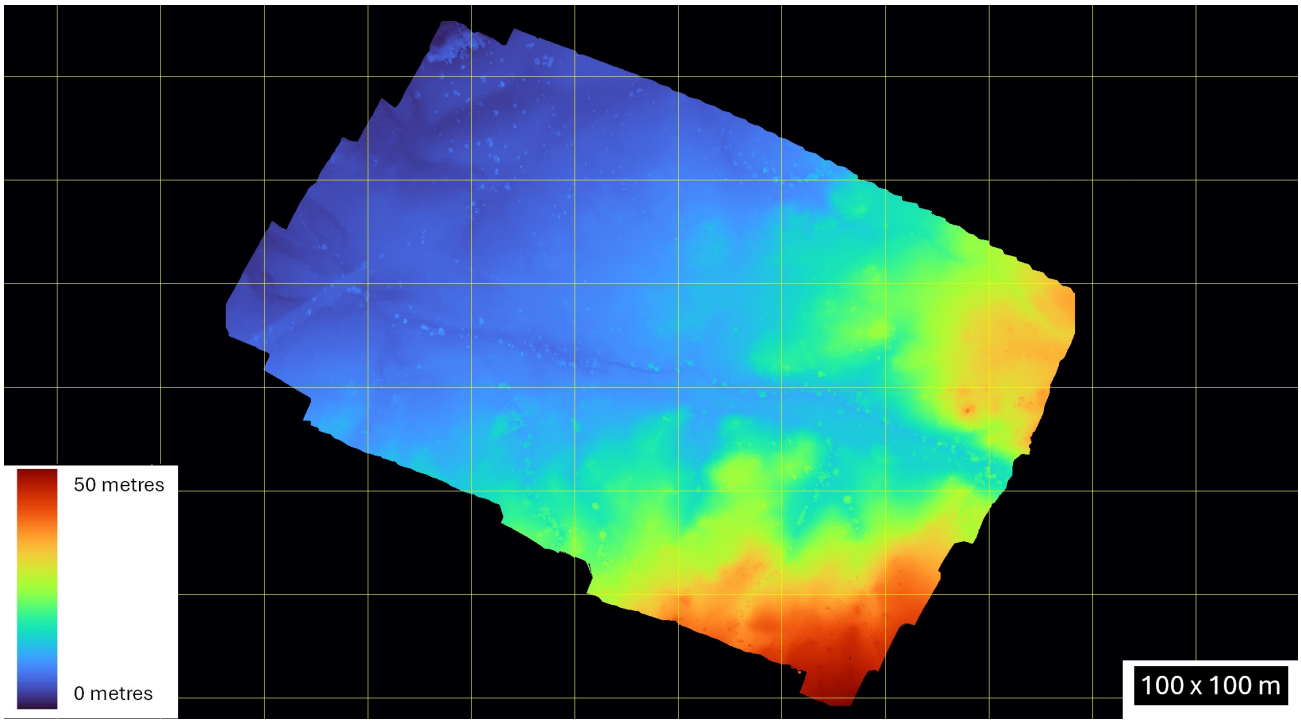

Figure D.1-12: DEM for AQ05. Plotted with 100 x 100 m grid spacing.

AQ06 site summary

Table D.1-13: AQ06 site summary.

Drone	**Phantom 4 Pro**
Camera Model	DJI FC6310
Images	1182/1206
Ground Coverage	0.752 km^2
Average ground resolution	18.107 mm/pixel
Geo referencing	6 control points (RTK)
Key Points	Median of 49214 key points per image
Tie Points	522901 points (median of 2187 points per photo)
Reprojection Errors (Median)	0.34 Pixels
Reprojection Errors (RMS)	0.48 pixels
Distance to Rays (RMS)	0.0641 metres

Table D.1-14: AQ06 Position uncertainties (camera locations).

	X (metres)	**Y (metres)**	**Z (metres)**
Minimum	0.0017	0.00196	0.00088
Mean	0.00301	0.00333	0.00143
Maximum	0.02368	0.0231	0.01523

Table D.1-15: AQ06 control points.

Name	Accuracy (m)	Num of Photos	RMS of Reproject Error (pixels)	RMS of Dist to Rays (m)	3D Error (m)	Horizontal Errors (m)	Vertical Error (m)
uav01	H: 0.010 V: 0.022	22	0.55	0.06852	0.00514	X: 0.0033 Y: 0.0028	-0.0028
uav02	H: 0.010 V: 0.021	32	0.56	0.09782	0.00692	X:-0.0000 Y:-0.0066	0.0022
ro01	H: 0.006 V: 0.015	18	0.42	0.06493	0.00596	X: 0.0043 Y:-0.0004	-0.0041
ro02	H: 0.008 V: 0.019	18	0.57	0.06802	0.00764	X: -0.0002 Y: 0.0067	-0.0037
ro03	H: 0.001 V: 0.02	15	0.54	0.0752	0.00786	X:-0.0031 Y:-0.0061	0.0038
uav03	H: 0.010 V: 0.022	27	0.56	0.08464	0.00302	X:-0.0011 Y: 0.0023	0.0017
Global RMS			0.54	0.07738	0.00631	X: 0.0026 Y: 0.0048	0.0032
Median			0.56	0.0752	0.00692	X:-0.0000 Y: 0.0023	0.0017

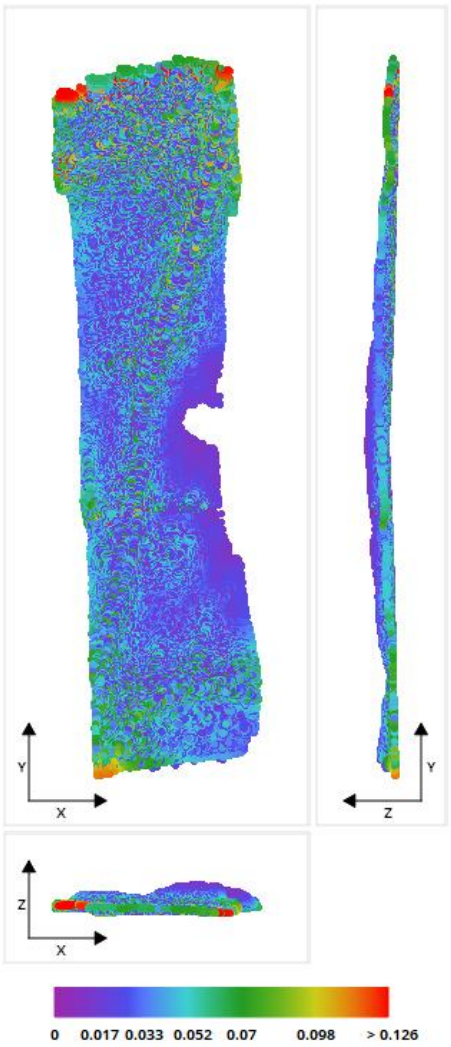

Figure D.1-13: Position uncertainties for AQ06: Top view (XY plane), side view (ZY plane) and front view (XZ plane) displays of all tie points, with colours representing uncertainty in the individual point position. The values are in metres, with a minimum uncertainty of 0.0051 metres and a maximum of 0.6867 metres. The median position uncertainty equals 0.0335 metres.

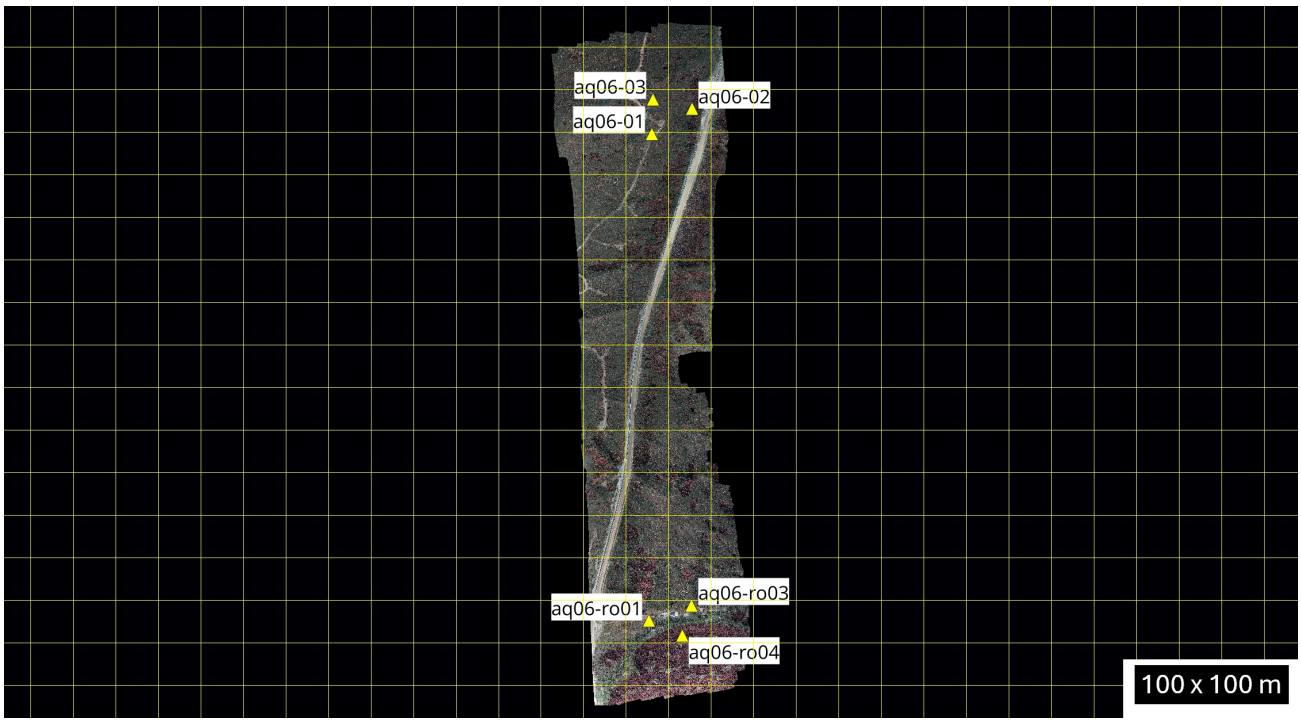

Figure D.1-14: Ortho-mosaic for AQ06. Plotted with control points and 100 x 100 m grid spacing.

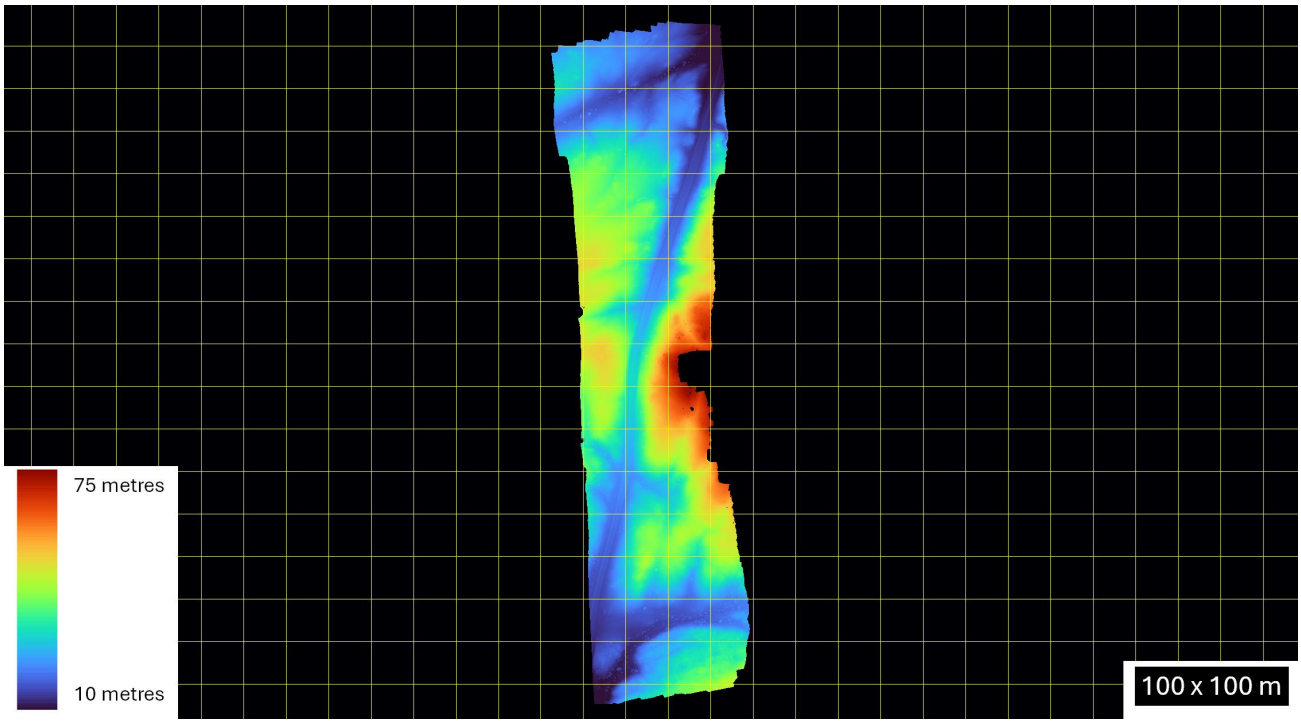

Figure D.1-15: DEM for AQ06. Plotted with 100 x 100 m grid spacing.

AQ07 and AQ08 site summary

Table D.1-16: AQ07 and AQ08 site summary.

Drone	**Phantom 4 Pro**
Camera Model	DJI FC6310R
Images	1182/2139
Ground Coverage	1.566 km^2
Average ground resolution	20.423502 mm/pixel
Geo referencing	10 control points (RTK)
Key Points	Median of 44758 key points per image
Tie Points	1052911 points (median of 2666 points per photo)
Reprojection Errors (Median)	0.30 pixels
Reprojection Errors (RMS)	0.42 pixels
Distance to Rays (RMS)	0.0318 metres

Table D.1-17: AQ07 and AQ08 Position uncertainties (camera locations).

	X (metres)	**Y (metres)**	**Z (metres)**
Minimum	0.00084	0.00076	0.00064
Mean	0.00298	0.0028	0.00133
Maximum	0.54585	0.08446	0.04552

Table D.1-18: AQ07 and AQ08 control points.

Name	Accuracy (m)	Num of Photos	RMS of Reproject Error (pixels)	RMS of Dist to Rays (m)	3D Error (m)	Horizontal Errors (m)	Vertical Error (m)
uav01	H: 0.009 V: 0.013	28	0.47	0.0316	0.0022	X:-0.0002 Y: 0.0011	-0.0018
uav02	H: 0.015 V: 0.024	12	0.42	0.0126	0.0006	X:-0.0005 Y:0.0002	-0.0001
uav03	H: 0.008 V: 0.014	39	0.35	0.0262	0.0011	X: 0.0002 Y:-0.0004	0.0009
uav04	H: 0.018 V: 0.040	14	0.53	0.0423	0.0083	X: 0.0044 Y:-0.0051	-0.0048
uav05	H: 0.018 V: 0.041	34	0.66	0.0474	0.009	X:-0.0078 Y: 0.0043	-0.0014
uav06	H: 0.018 V: 0.043	14	0.54	0.034	0.0059	X: 0.0010 Y: 0.0045	-0.0037
uav07	H: 0.017 V: 0.043	31	0.74	0.0429	0.0066	X:-0.0010 Y: -0.0064	0.0011
uav08	H: 0.016 V: 0.043	29	0.52	0.035	0.0098	X: 0.0035 Y:-0.0006	0.0091
uav09	H: 0.017 V: 0.043	37	0.58	0.0437	0.0084	X: 0.0046 Y: 0.0037	0.006
uav11	H: 0.007 V: 0.019	92	0.5	0.0538	0.0026	X:-0.0021 Y: 0.0014	0.0007
Global RMS			0.54	0.0386	0.00638	X: 0.0035 Y: 0.0035	0.00405
Median			0.53	0.0423	0.00655	X: 0.0002 Y: 0.0011	0.00067

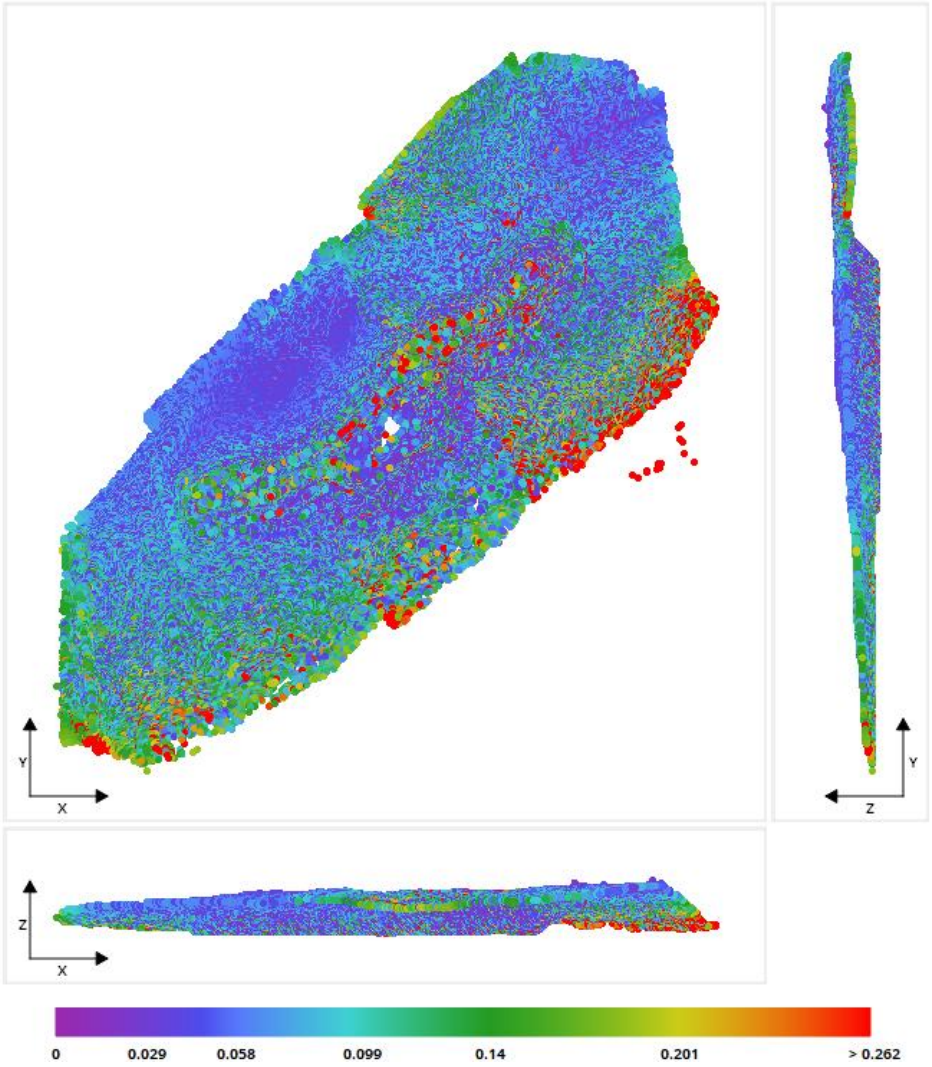

Figure D.1-16: Position uncertainties for AQ07 and AQ08: Top view (XY plane), side view (ZY plane) and front view (XZ plane) displays of all tie points, with colours representing uncertainty in the individual point position. The values are in metres, with a minimum uncertainty of 0.0051 metres and a maximum of 0.6867 metres. The median position uncertainty equals 0.0335 metres.

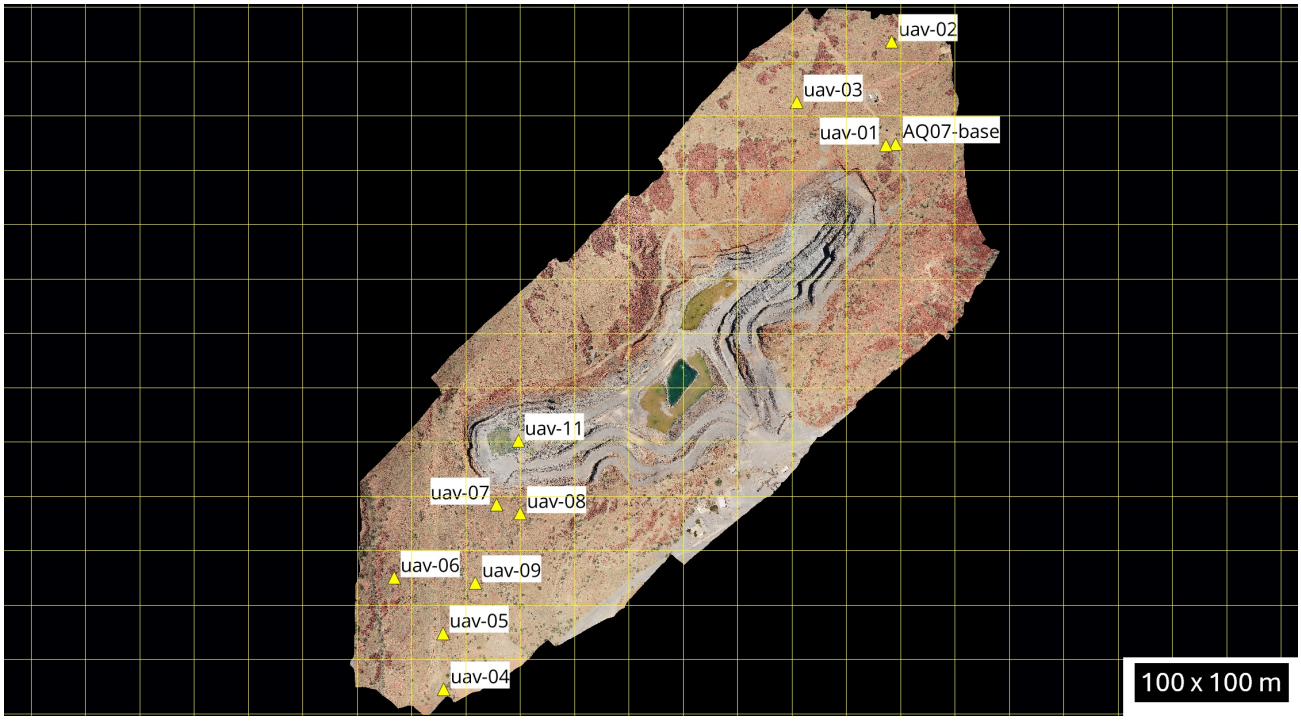

Figure D.1-17: Ortho-mosaic for AQ07 and AQ08. Plotted with control points and 100 x 100 m grid spacing.

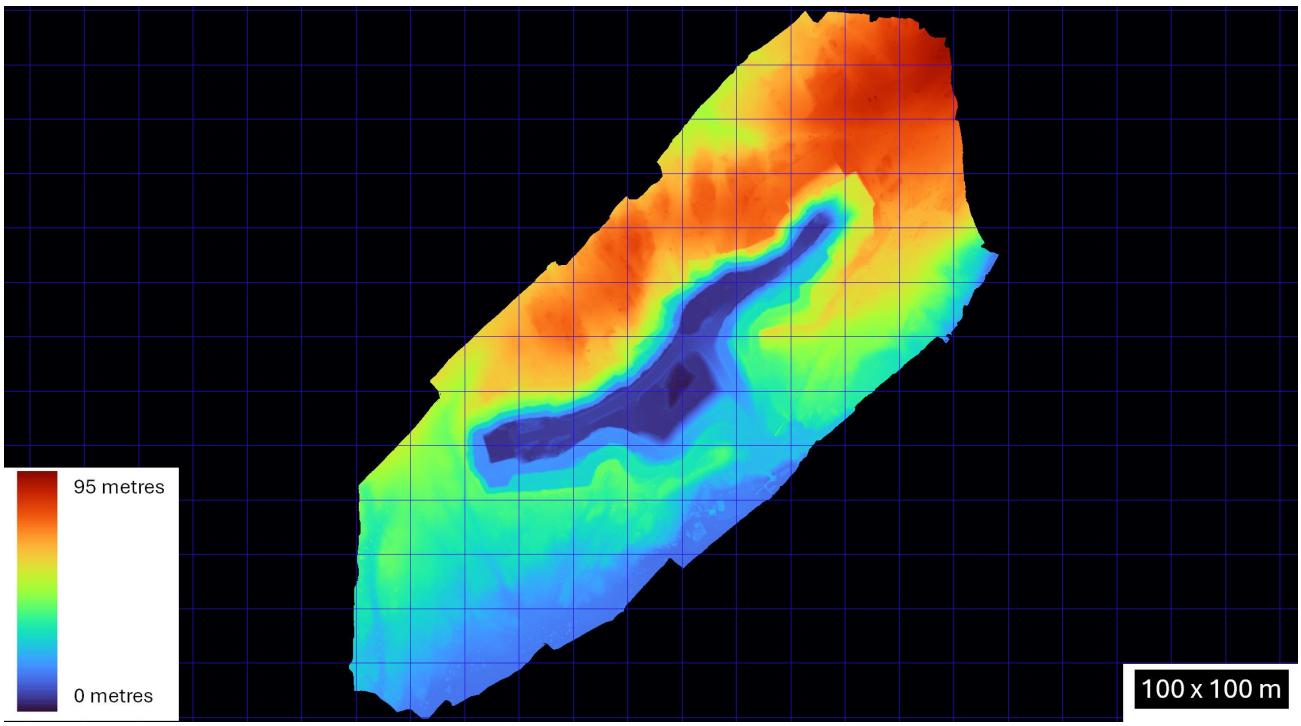

Figure D.1-18: DEM for AQ07 and AQ08. Plotted with 100 x 100 m grid spacing.

AQ09 (North) site summary

Table D.1-19: AQ09 (North) site summary.

Drone	**Phantom 4 Pro**
Camera Model	DJI FC6310
Images	929/929
Ground Coverage	0.398 km^2
Average ground resolution	14.29764 mm/pixel
Geo referencing	13 control points (RTK)
Key Points	Median of 49176 key points per image
Tie Points	331916 points, with a median of 1843 points per photo.
Reprojection Errors (Median)	0.45 pixels
Reprojection Errors (RMS)	0.61 pixels
Distance to Rays (RMS)	0.0609 metres

Table D.1-20: AQ09 (North) Position uncertainties (camera locations).

	X (metres)	**Y (metres)**	**Z (metres)**
Minimum	0	0	0
Mean	0.00293	0.00276	0.0014
Maximum	0.03418	0.01619	0.01691

Table D.1-21: AQ09 (North) control points.

Name	Accuracy (m)	Num of Photos	RMS of Reproject Error (pixels)	RMS of Dist to Rays (m)	3D Error (m)	Horizontal Errors (m)	Vertical Error (m)
s2-uav019	H: 0.012 V: 0.034	5	2.09	0.1062	0.0432	X: -0.0263 Y: -0.0259	0.0224
s2-uav021	H: 0.011 V: 0.028	12	2.78	0.05823	0.0498	X: 0.0156 Y: -0.0329	-0.034
s2-uav023	H: 0.014 V: 0.024	12	2.16	0.08137	0.0437	X: 0.0292 Y: 0.0235	0.0225
s1-uav53	H: 0.017 V: 0.032	5	2.41	0.11425	0.0587	X: 0.0228 Y: 0.0148	-0.0521
s1-uav101	H: 0.015 V: 0.035	37	2.45	0.0671	0.0586	X: 0.0152 Y: 0.0151	-0.0545
s1-uav102	H: 0.019 V: 0.05	46	2.06	0.06995	0.0522	X: 0.0039; Y: -0.0129	-0.0505
s1-uav103	H: 0.015 V: 0.044	42	0.95	0.05426	0.0225	X: 0.0041 Y: 0.0024	0.022
s1-uav104	H: 0.017 V: 0.048	29	2.79	0.06936	0.085	X: -0.0103 Y: -0.0099	0.0838
s1-uav105	H: 0.019 V: 0.031	12	0.9	0.06939	0.0258	X: -0.0114 Y: -0.0008	0.022
s1-uav106	H: 0.0230 V: 0.038	30	0.62	0.08829	0.0131	X: -0.0077 Y: 0.0029	0.0102
s1-uav107	H: 0.020 V: 0.032	30	0.83	0.10652	0.0244	X: -0.0073 Y: 0.0049	-0.0228
s1-uav108	H: 0.018 V: 0.030	45	0.63	0.11233	0.0129	X: -0.0092 Y: 0.0031	0.0085
s1-uav109	H: 0.020 V: 0.033	44	0.71	0.10486	0.0148	X: -0.0131 Y: 0.0004	0.0069
s2-uav019	H: 0.012 V: 0.034	5	2.09	0.1062	0.0432	X: -0.0264 Y: -0.0259	0.0224
Global RMS			1.85	0.0873	0.0442	X: 0.0156 Y: 0.0154	0.0384
Median			2.06	0.0814	0.0432	X: -0.0073 Y: 0.0024	0.0085

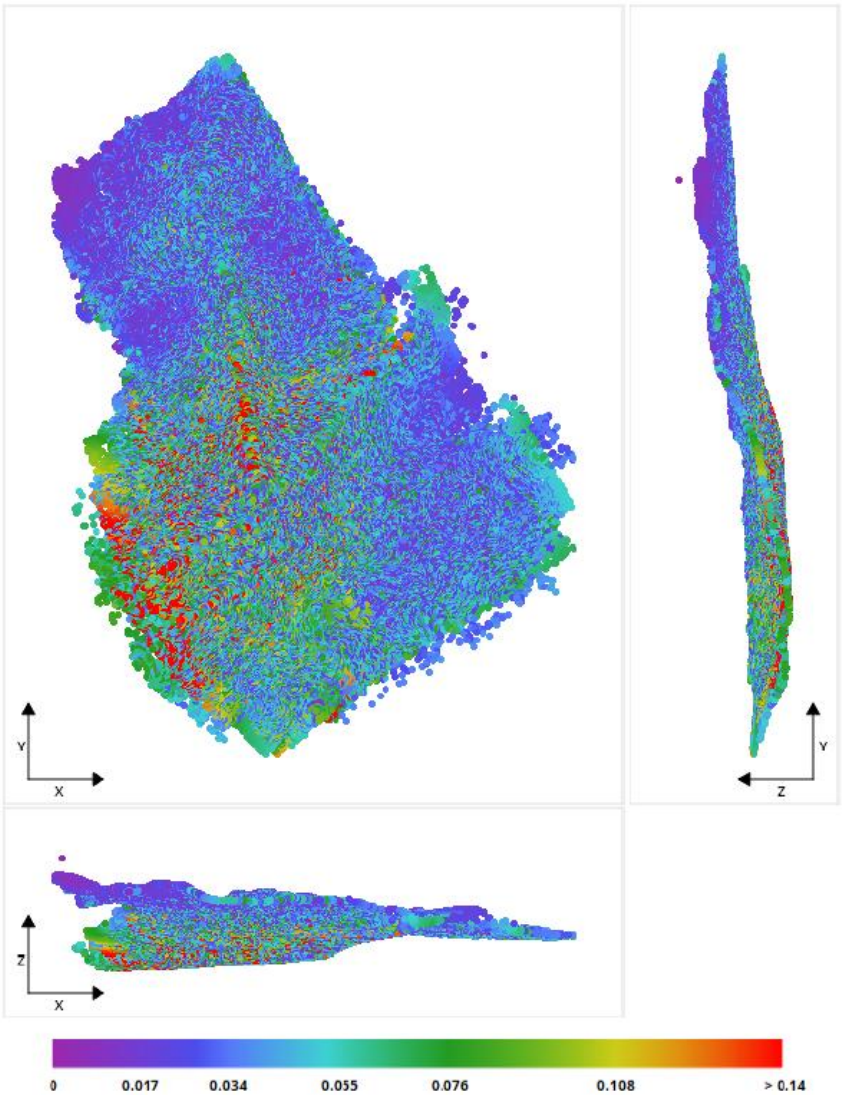

Figure D.1-19: Position uncertainties for AQ09 (North): Top view (XY plane), side view (ZY plane) and front view (XZ plane) displays of all tie points, with colours representing uncertainty in the individual point position. The values are in metres, with a minimum uncertainty of 0.0051 metres and a maximum of 0.6867 metres. The median position uncertainty equals 0.0335 metres.

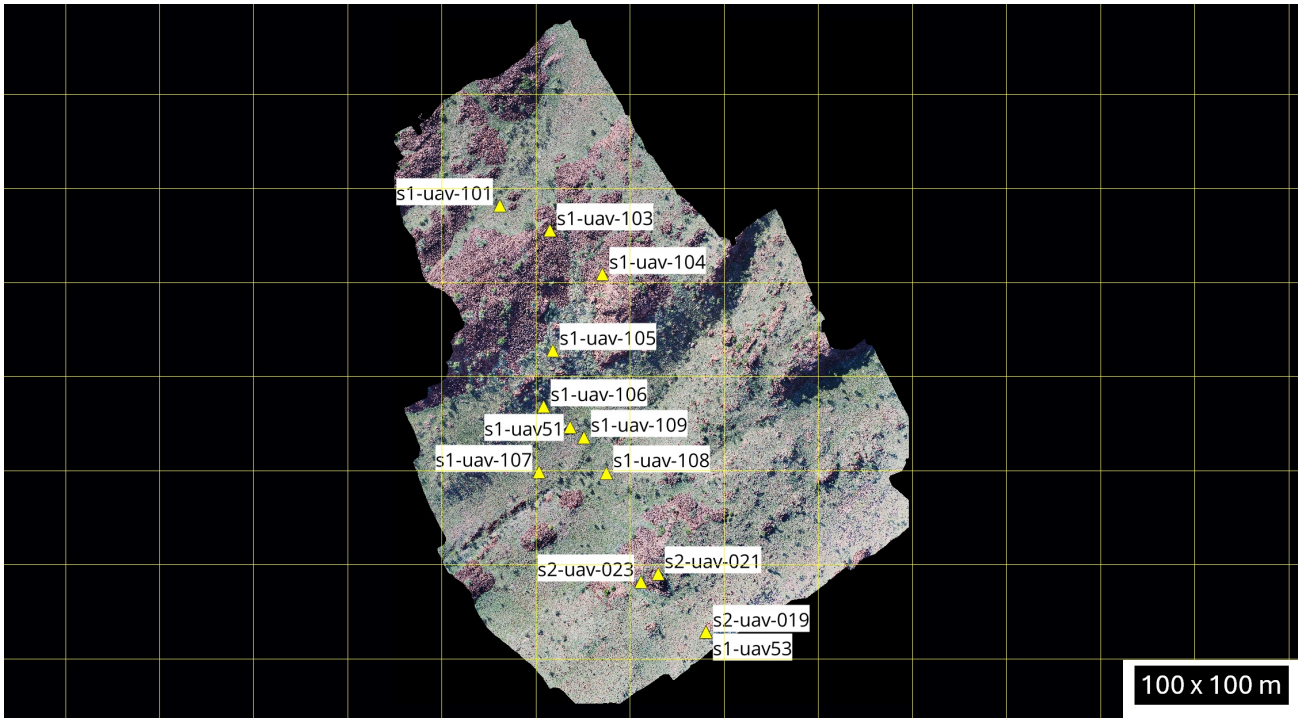

Figure D.1-20: Ortho-mosaic for AQ09 (North). Plotted with control points and 100 x 100 m grid spacing.

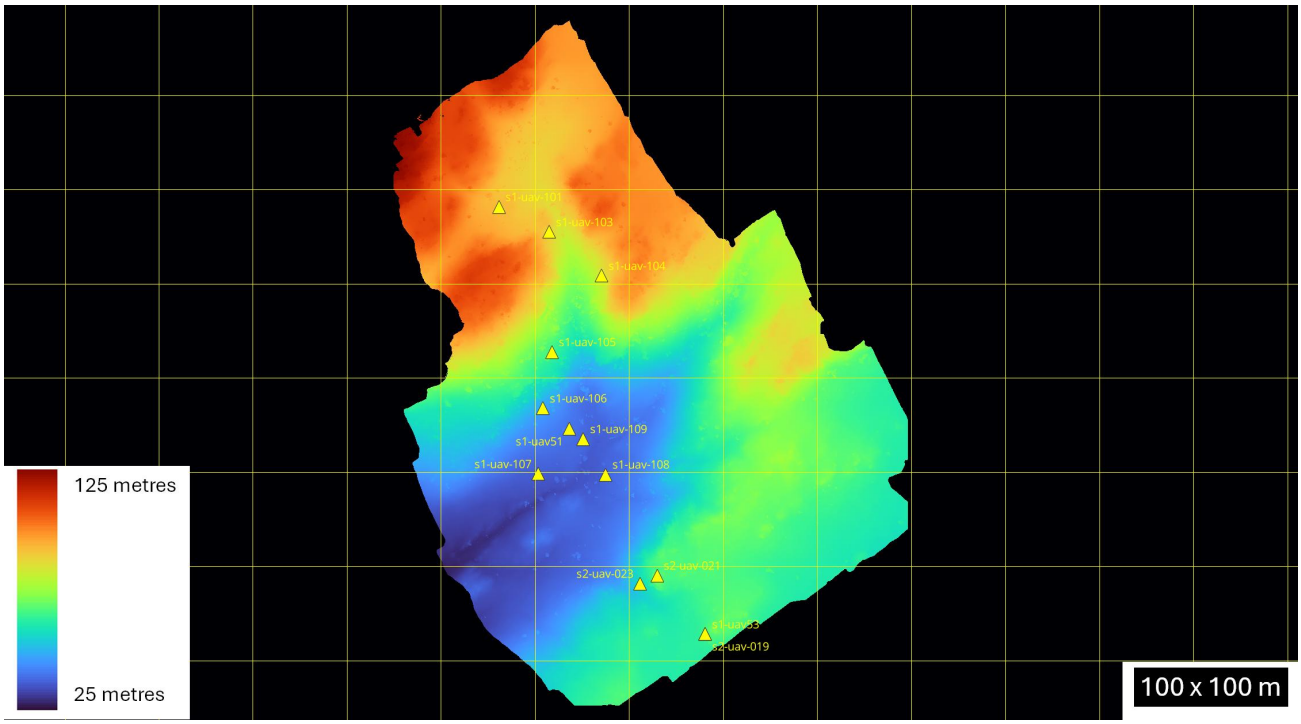

Figure D.1-21: DEM for AQ09 (North). Plotted with 100 x 100 m grid spacing.

AQ09 (South) site summary

Table D.1-22: AQ09 (South) site summary.

Drone	**Phantom 4 Pro**
Camera Model	DJI FC6310R
Images	1410/1555
Ground Coverage	0.598 km^2
Average ground resolution	20.44146 mm/pixel
Geo referencing	12 control points (RTK)
Key Points	Median of 48050 keypoints per image
Tie Points	375406 points, with a median of 1532 points per photo
Reprojection Errors (Median)	0.40 pixels
Reprojection Errors (RMS)	0.56 pixels
Distance to Rays (RMS)	0.02758 metres

Table D.1-23: AQ09 (South) Position uncertainties (camera locations).

	X (metres)	**Y (metres)**	**Z (metres)**
Minimum	0.00066	0.00116	0.00055
Mean	0.00605	0.0062	0.00329
Maximum	1.00474	1.10623	0.38588

Table D.1-24: AQ09 (South) control points.

Name	Accuracy (m)	Num of Photos	RMS of Reproject Error (pixels)	RMS of Dist to Rays (m)	3D Error (m)	Horizontal Errors (m)	Vertical Error (m)
s2-uav001	H: 0.007 V: 0.014	95	0.48	0.02982	0.00495	X: -0.0028 Y: -0.0020	0.0035
s2-uav003	H: 0.008 V: 0.016	79	0.69	0.03377	0.02157	X: 0.0002 Y: 0.0076	0.0202
s2-uav006	H: 0.009 V: 0.018	123	0.58	0.03423	0.00957	X: 0.0088 Y: 0.0017	-0.0032
s2-uav008	H: 0.010 V: 0.018	89	0.75	0.03329	0.01452	X: 0.0088 Y: -0.0108	0.004
s2-uav010	H: 0.012 V: 0.020	67	0.6	0.02984	0.01101	X: -0.0048 Y: -0.0060	-0.0079
s2-uav012	H: 0.014 V: 0.036	86	0.59	0.03136	0.0089	X: -0.0011 Y: 0.0069	-0.0055
s2-uav014	H: 0.014 V: 0.023	96	0.56	0.02987	0.00772	X: 0.0057 Y: 0.0042	-0.0024
s2-uav015	H: 0.011 V: 0.019	81	0.54	0.0264	0.00772	X: 0.0026 Y: -0.0039	-0.0061
s2-uav016	H: 0.010 V: 0.026	11	1	0.02333	0.02676	X: -0.0101 Y: -0.0033	0.0246
s2-uav019	H: 0.012 V: 0.034	6	1.98	0.01635	0. 0227	X: -0.0139 Y: -0.0081	-0.0721
s2-uav023	H: 0.014 V: 0.024	3	2.52	0.02726	0.0798	X: 0.0342 Y: -0.0010	0.0721
s1-uav02	H: 0.009 V: 0.018	113	0.44	0.03203	0.0064	X: -0.0033 Y: -0.0011	0.0054
Global RMS			5.02	0.04755	0.027	X: 0.0119 Y: 0.0056	0.0236
Median			0.6	0.0298	0.011	X: 0.0002 Y: -0.0011	-0.0024

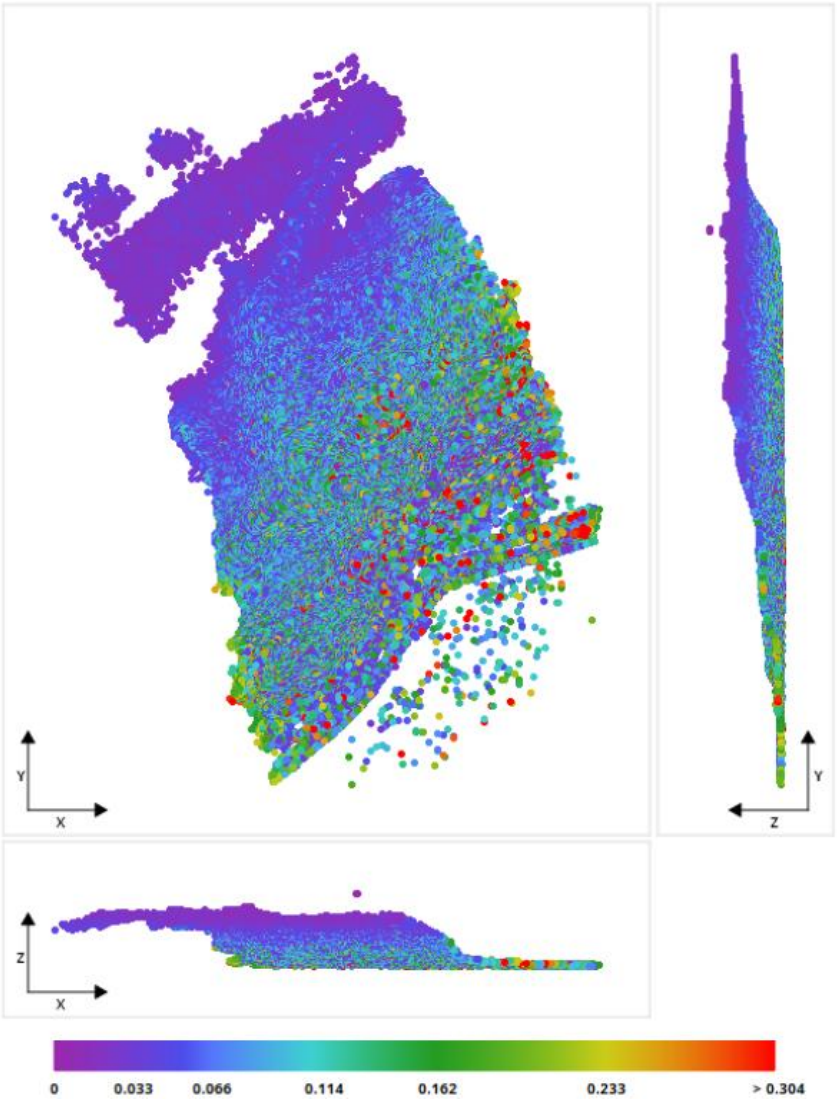

Figure D.1-22: Position uncertainties for AQ09 (South): Top view (XY plane), side view (ZY plane) and front view (XZ plane) displays of all tie points, with colours representing uncertainty in the individual point position. The values are in metres, with a minimum uncertainty of 0.0051 metres and a maximum of 0.6867 metres. The median position uncertainty equals 0.0335 metres.

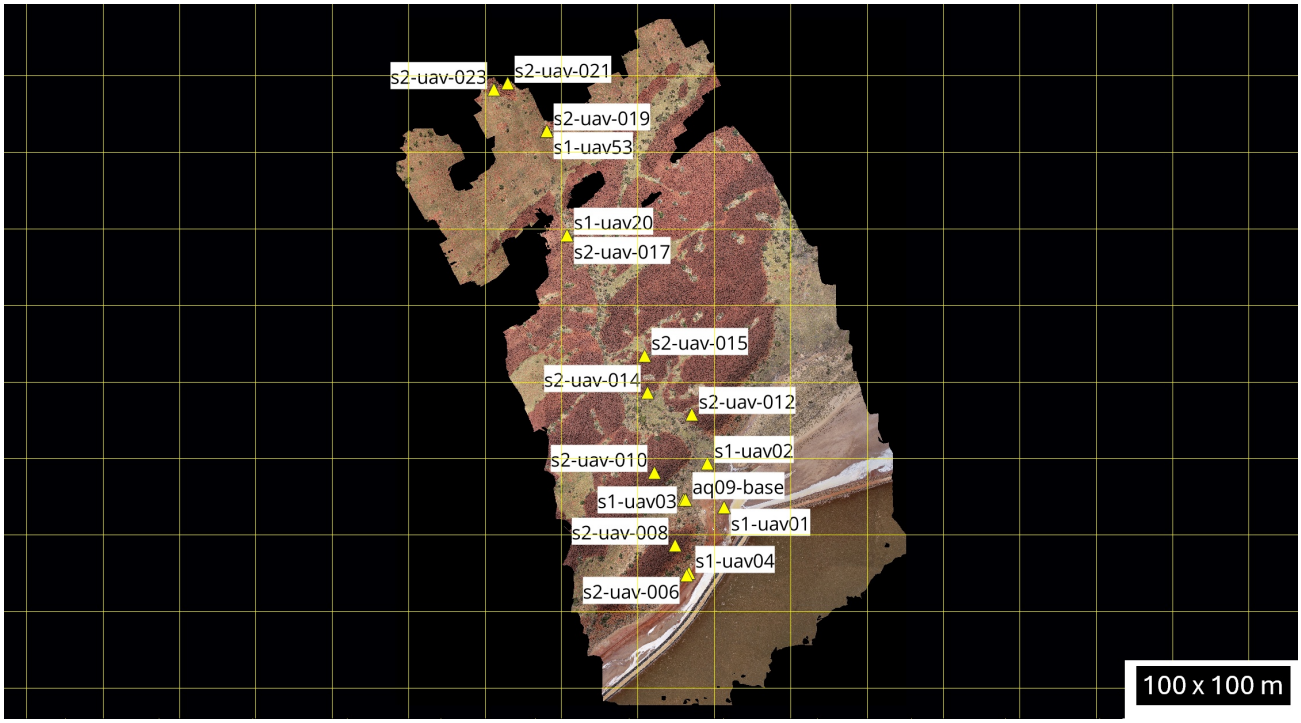

Figure D.1-23: Ortho-mosaic for AQ09 (South). Plotted with control points and 100 x 100 m grid spacing.

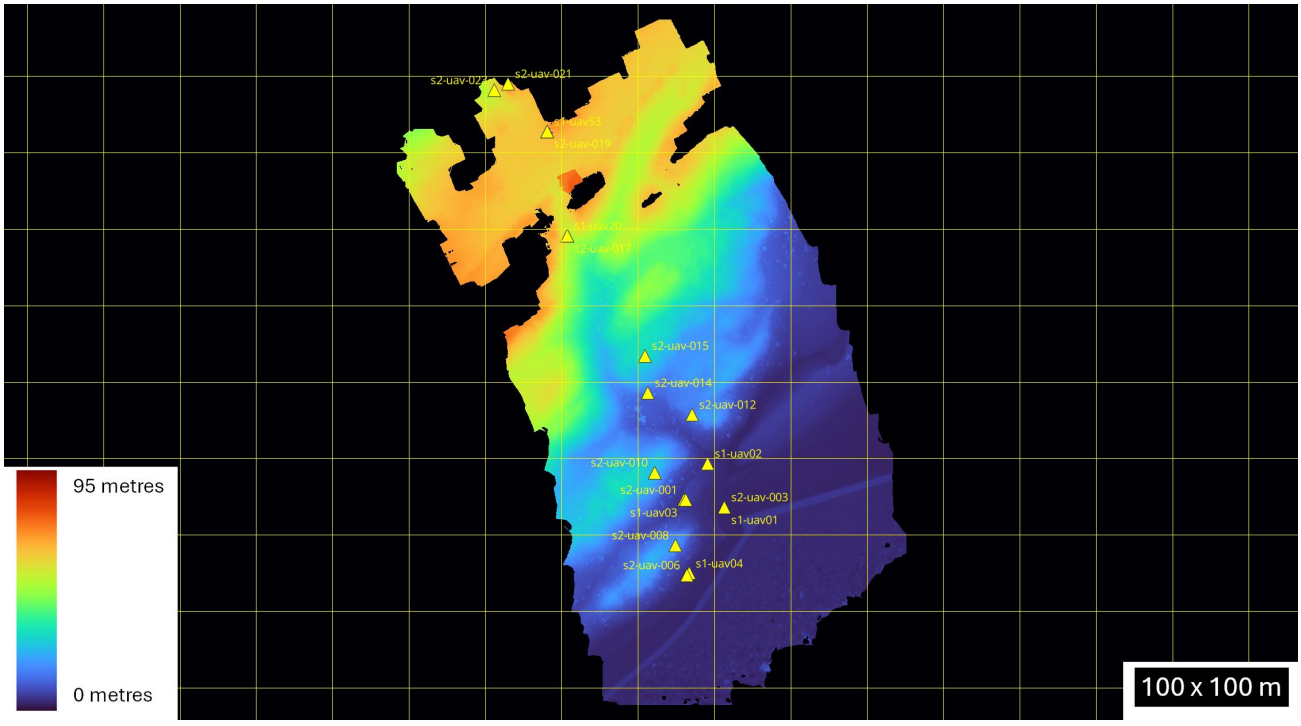

Figure D.1-24: DEM for AQ09 (South). Plotted with 100 x 100 m grid spacing.

AQ10 site summary

Table D.1-25: AQ10 site summary.

Drone	**Phantom 4 Pro**
Camera Model	DJI FC6310
Images	696/702
Ground Coverage	232224 m^2
Average ground resolution	21.31051 mm/pixel
Geo referencing	6 control points (RTK)
Key Points	Median of 45698 key points per image
Tie Points	254559 points (median of 2719 points per photo)
Reprojection Errors (Median)	0.44 pixels
Reprojection Errors (RMS)	0.60 pixels
Distance to Rays (RMS)	0.05843 metres

Table D.1-26: AQ10 Position uncertainties (camera locations).

	X (metres)	**Y (metres)**	**Z (metres)**
Minimum	0.00156	0.00144	0.00081
Mean	0.00486	0.0051	0.00251
Maximum	0.12754	0.20019	0.0579

Table D.1-27: AQ10 control points.

Name	Accuracy (m)	Num of Photos	RMS of Reproject Error (pixels)	RMS of Dist to Rays (m)	3D Error (m)	Horizontal Errors (m)	Vertical Error (m)
uav01	H: 0.009 V: 0.021	30	0.82	0.0516	0.011	X: -0.0012 Y: 0.0011	-0.0027
uav02	H: 0.013 V: 0.027	30	0.88	0.0542	0.0129	X: 0.0026 Y: -0.0117	-0.005
uav03	H: 0.013 V: 0.028	35	0.86	0.0612	0.0139	X: -0.0056 Y: 0.0042	0.012
uav04	H: 0.008 V: 0.018	50	0.98	0.0813	0.011	X: 0.0051 Y: -0.0096	-0.0018
uav05	H: 0.008 V: 0.018	47	0.62	0.0721	0.0045	X: 0.0028 Y: 0.0034	-0.0001
uav06	H: 0.009 V: 0.020	64	0.68	0.0782	0.0038	X: -0.0029 Y: 0.0021	-0.001
Global RMS			0.82	0.0674	0.0103	X: 0.0037 Y: 0.0078	0.0055
Median			0.86	0.0721	0.011	X: 0.0026 Y: 0.0034	-0.0009

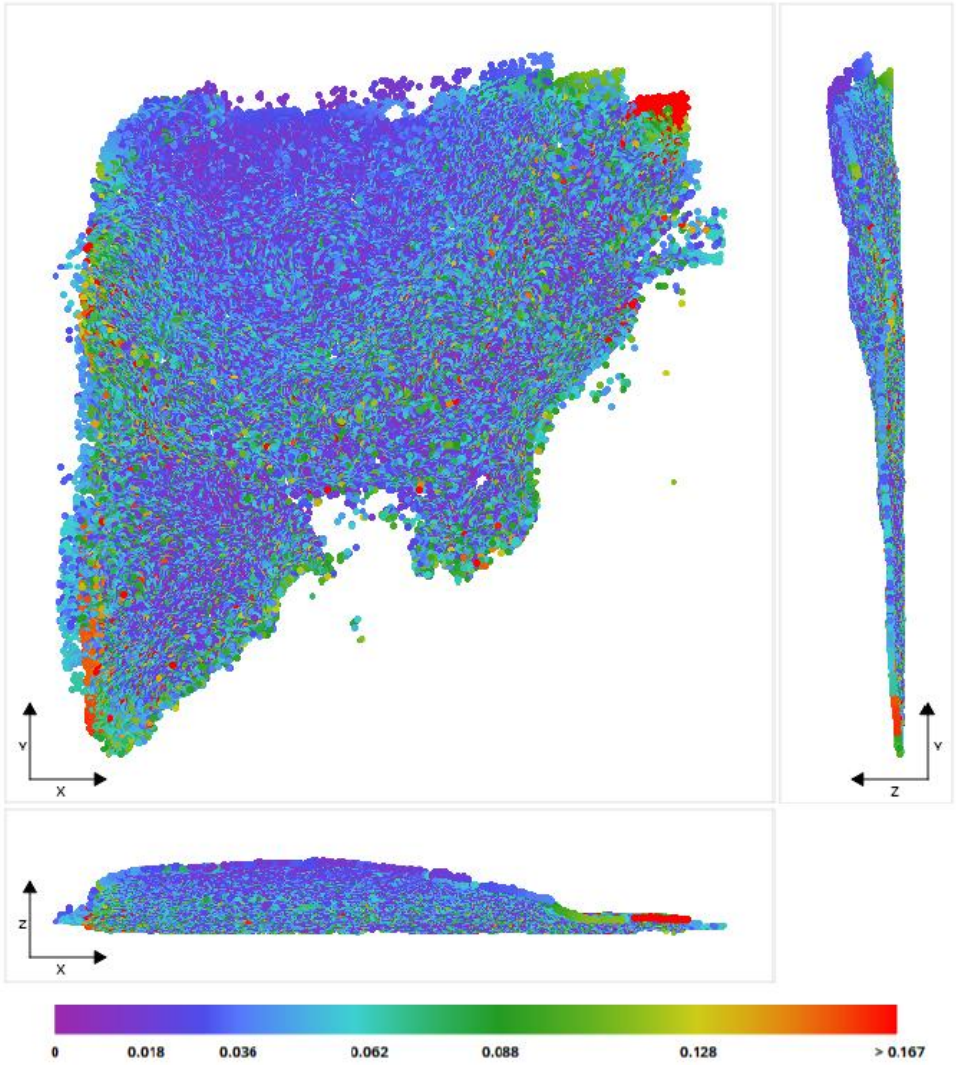

Figure D.1-25: Position uncertainties for AQ10: Top view (XY plane), side view (ZY plane) and front view (XZ plane) displays of all tie points, with colours representing uncertainty in the individual point position. The values are in metres, with a minimum uncertainty of 0.0051 metres and a maximum of 0.6867 metres. The median position uncertainty equals 0.0335 metres.

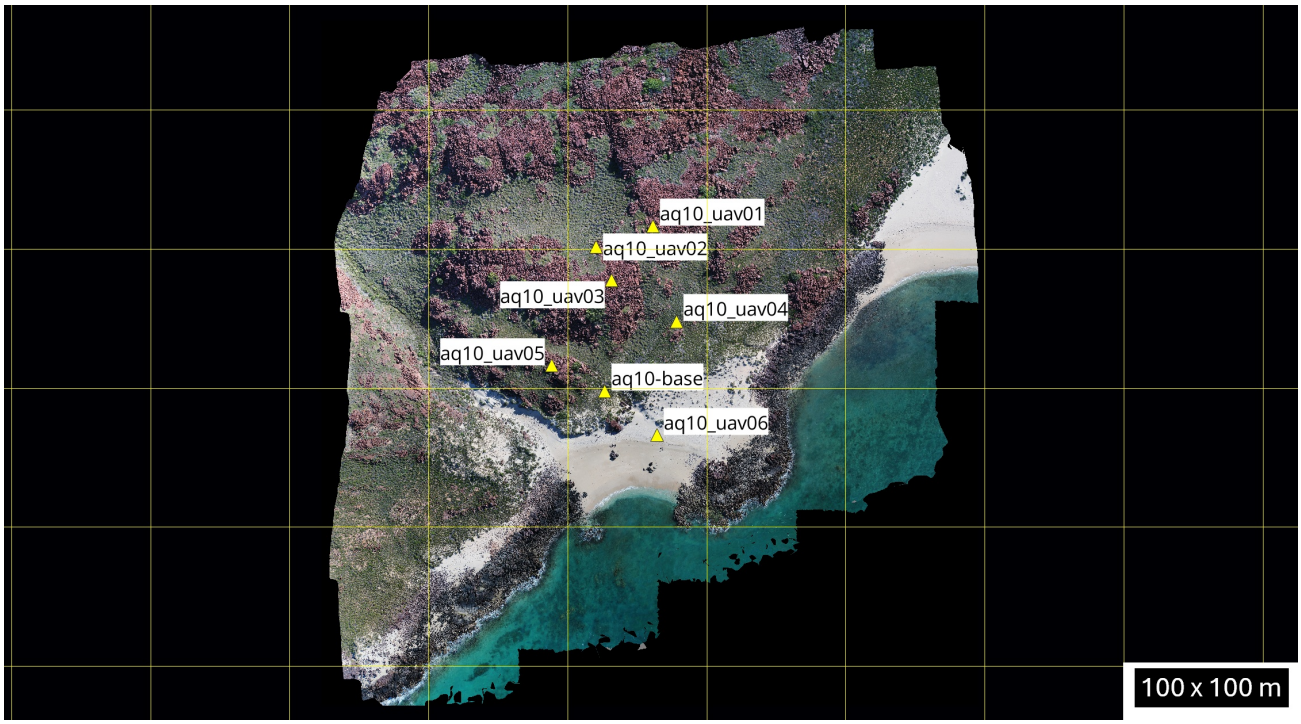

Figure D.1-26: Ortho-mosaic for AQ10. Plotted with control points and 100 x 100 m grid spacing.

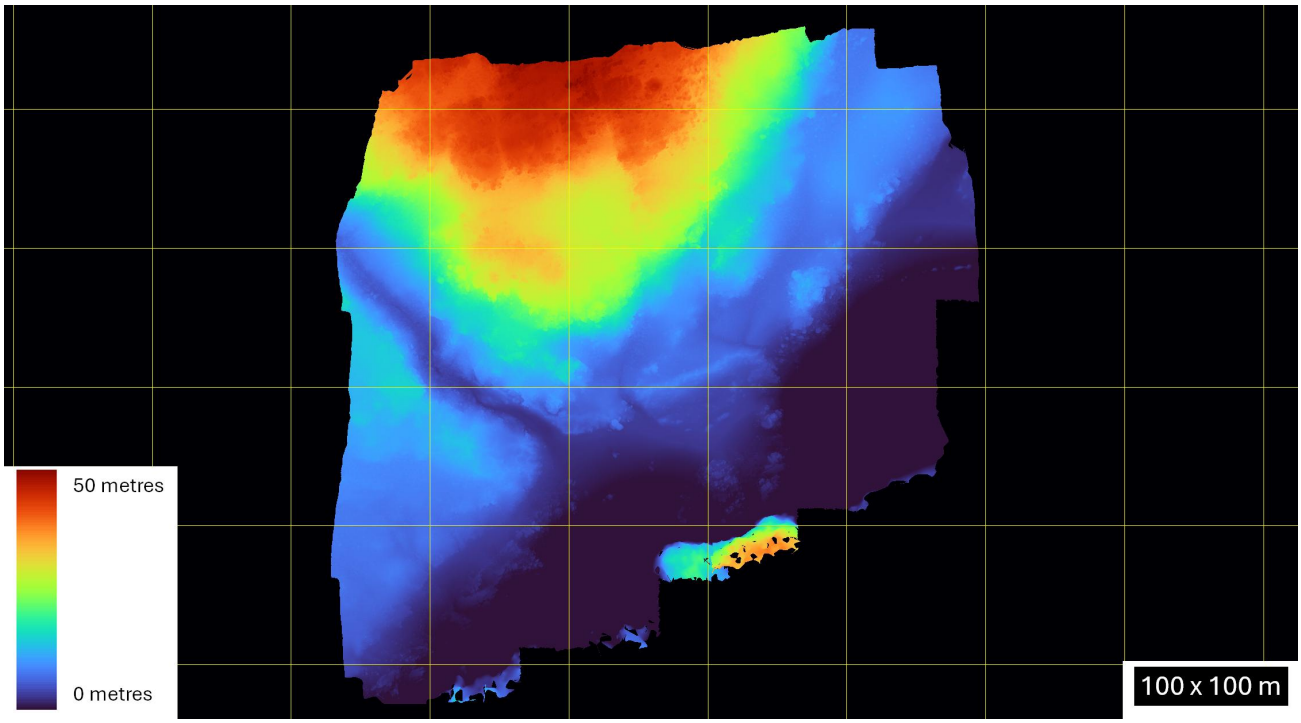

Figure D.1-27: DEM for AQ10. Plotted with 100 x 100 m grid spacing.

AQ11 site summary

Table D.1-28: AQ11 site summary.

Drone	**Phantom 4 Pro**
Camera Model	DJI FC6310
Images	891/891
Ground Coverage	0.583 km^2
Average ground resolution	22.2477 mm/pixel
Geo referencing	11 control points (RTK)
Key Points	Median of 45698 key points per image
Tie Points	430657 points (median of 3254 points per photo)
Reprojection Errors (Median)	0.40 pixels
Reprojection Errors (RMS)	0.52 pixels
Distance to Rays (RMS)	0.0765 metres

Table D.1-29: AQ11 Position uncertainties (camera locations).

	X (metres)	**Y (metres)**	**Z (metres)**
Minimum	0.0017	0.0019	0.0009
Mean	0.0028	0.0028	0.0013
Maximum	0.0081	0.0094	0.003

Table D.1-30: AQ11 control points.

Name	Accuracy (m)	Num of Photos	RMS of Reproject Error (pixels)	RMS of Dist to Rays (m)	3D Error (m)	Horizontal Errors (m)	Vertical Error (m)
uav1	H: 0.007 V: 0.015	45	0.56	0.0951	0.0034	X: 0.0009 Y: 0.0024	0.0022
uav2	H: 0.009 V: 0.021	24	0.55	0.0889	0.0078	X: 0.0021 Y: 0.0012	-0.0075
uav3	H: 0.009 V: 0.020	37	0.63	0.0955	0.0124	X: 0.0019 Y: -0.0062	0.0106
uav4	H: 0.009 V: 0.020	59	0.53	0.0887	0.0043	X: -0.0033 Y: -0.0027	0.0001
uav5	H: 0.009 V: 0.021	45	0.5	0.0815	0.005	X: 0.0021 Y: -0.0002	0.0045
uav6	H: 0.009 V: 0.021	76	0.49	0.0989	0.0054	X: -0.0013 Y: 0.0040	-0.0034
uav7	H: 0.008 V: 0.017	53	0.56	0.0922	0.0049	X: 0.0037 Y: -0.0003	0.0032
uav8	H: 0.009 V: 0.021	32	0.42	0.0712	0.002	X: 0.0003 Y: -0.0015	0.0012
uav9	H: 0.009 V: 0.021	37	0.56	0.079	0.0057	X: 0.0012 Y: 0.0013	-0.0054
uav10	H: 0.010 V: 0.022	22	0.64	0.0815	0.0073	X: -0.0027 Y: -0.0066	-0.0017
uav11	H: 0.010 V: 0.022	11	0.63	0.0451	0.0092	X: 0.0004 Y: 0.0068	0.0062
Global RMS			0.56	0.0847	0.0067	X: 0.0021 Y: 0.0039	0.0051
Median			0.56	0.0887	0.0054	X: 0.0009 Y: -0.0002	0.0012

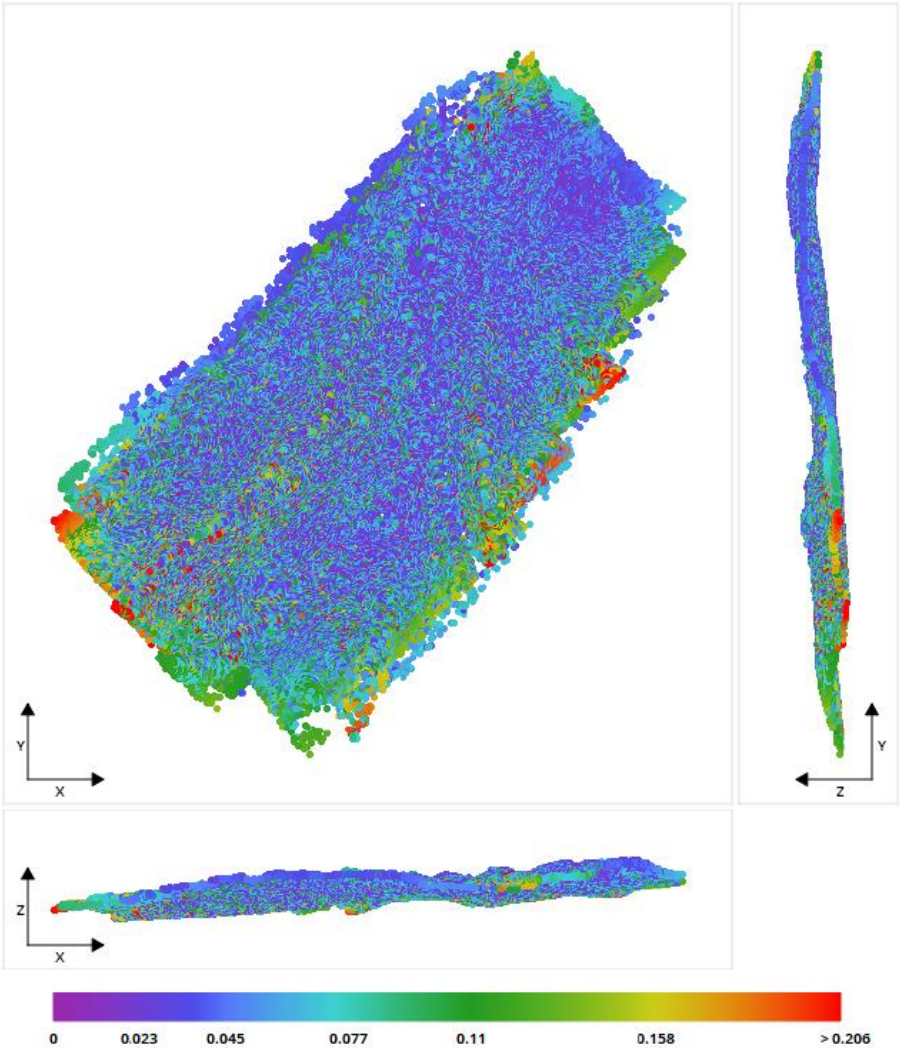

Figure D.1-28: Position uncertainties for AQ11: Top view (XY plane), side view (ZY plane) and front view (XZ plane) displays of all tie points, with colours representing uncertainty in the individual point position. The values are in metres, with a minimum uncertainty of 0.0051 metres and a maximum of 0.6867 metres. The median position uncertainty equals 0.0335 metres.

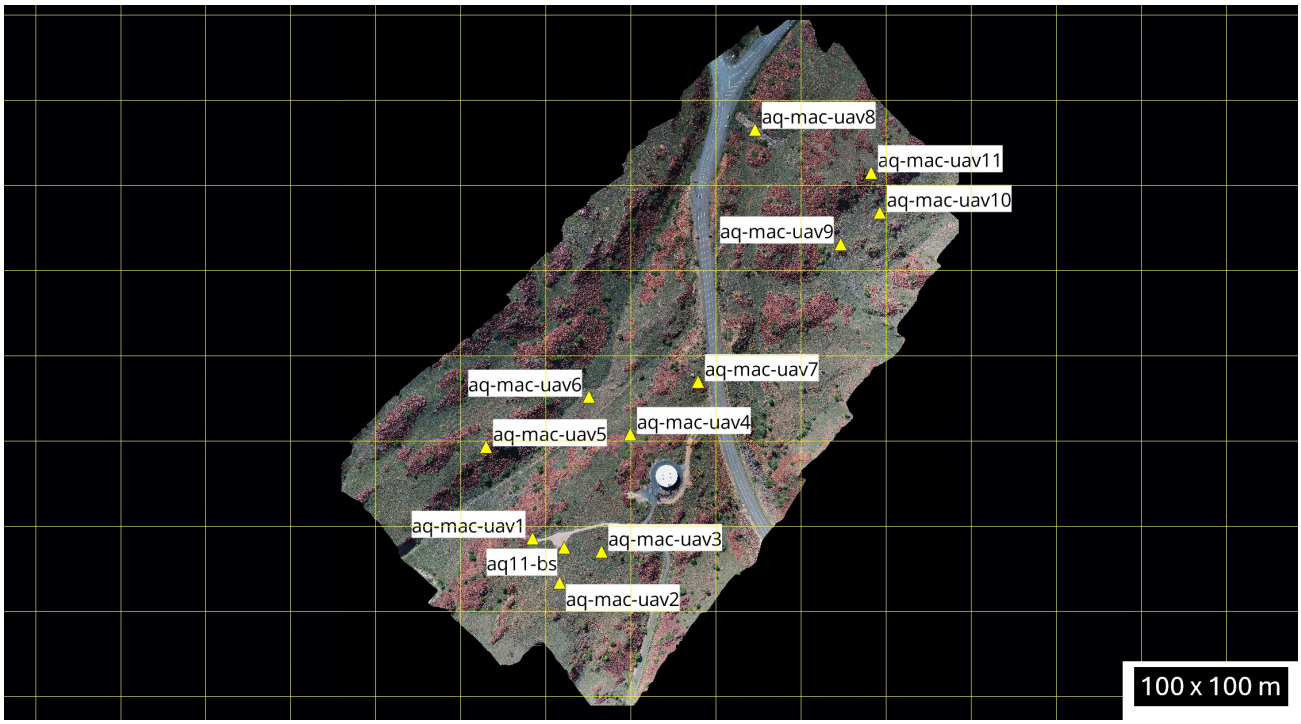

Figure D.1-29: Ortho-mosaic for AQ11. Plotted with control points and 100 x 100 m grid spacing.

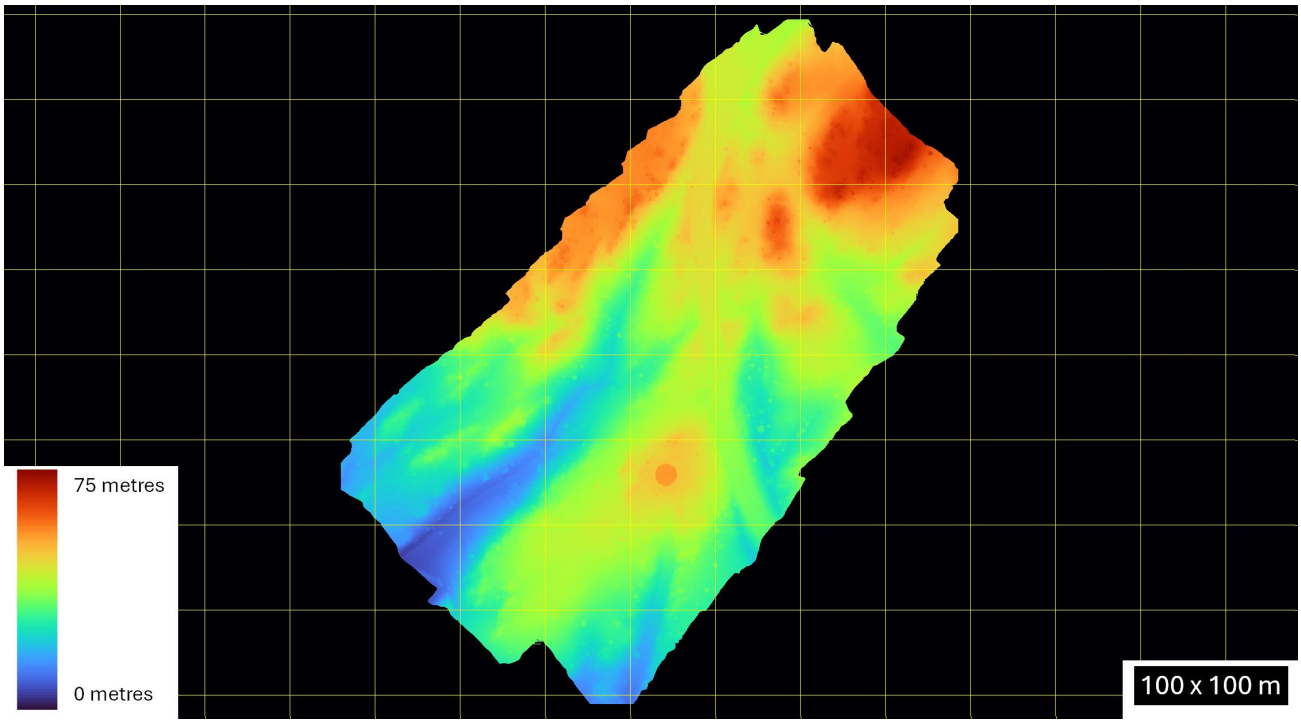

Figure D.1-30: DEM for AQ11. Plotted with 100 x 100 m grid spacing.

AQ12 site summary

Table D.1-31: AQ12 site summary.

Drone	**Phantom 4 Pro**
Camera Model	DJI FC6310
Images	538/558
Ground Coverage	0.154 km^2
Average ground resolution	15.7102 mm/pixel
Geo referencing	6 control points (RTK)
Key Points	Median of 49804 keypoints per image
Tie Points	214954 points (median of 2303 points per photo)
Reprojection Errors (Median)	0.39 pixels
Reprojection Errors (RMS)	0.52 pixels
Distance to Rays (RMS)	0.05288 metres

Table D.1-32: AQ12 Position uncertainties (camera locations).

	X (metres)	**Y (metres)**	**Z (metres)**
Minimum	0.00125	0.00113	0.00071
Mean	0.00254	0.00251	0.00132
Maximum	0.01828	0.02811	0.01335

Table D.1-33: AQ12 control points.

Name	Accuracy (m)	Num of Photos	RMS of Reproject Error (pixels)	RMS of Dist to Rays (m)	3D Error (m)	Horizontal Errors (m)	Vertical Error (m)
uav1	H: 0.007 V: 0.015	67	0.52	0.0533	0.0073	X: -0.0034 Y: -0.0006	0.0064
uav2	H: 0.010 V: 0.022	27	0.6	0.0807	0.0099	X: 0.0072 Y: -0.0066	0.0015
uav3	H: 0.009 V: 0.021	21	0.51	0.0666	0.0049	X: -0.0043 Y: -0.0024	0.0003
uav4	H: 0.011 V: 0.025	47	0.65	0.0732	0.0101	X: -0.0044 Y: 0.0046	-0.0079
uav5	H: 0.011 V: 0.028	61	0.8	0.0587	0.0145	X: 0.0079 Y: 0.0103	0.0065
uav6	H: 0.014 V: 0.034	56	0.64	0.0637	0.0122	X: 0.0019 Y: -0.0083	-0.0086
Global RMS			0.63	0.0666	0.0103	X: 0.0053 Y: 0.0064	0.0061
Median			0.64	0.0666	0.0101	X: 0.0019 Y: -0.0006	0.0015

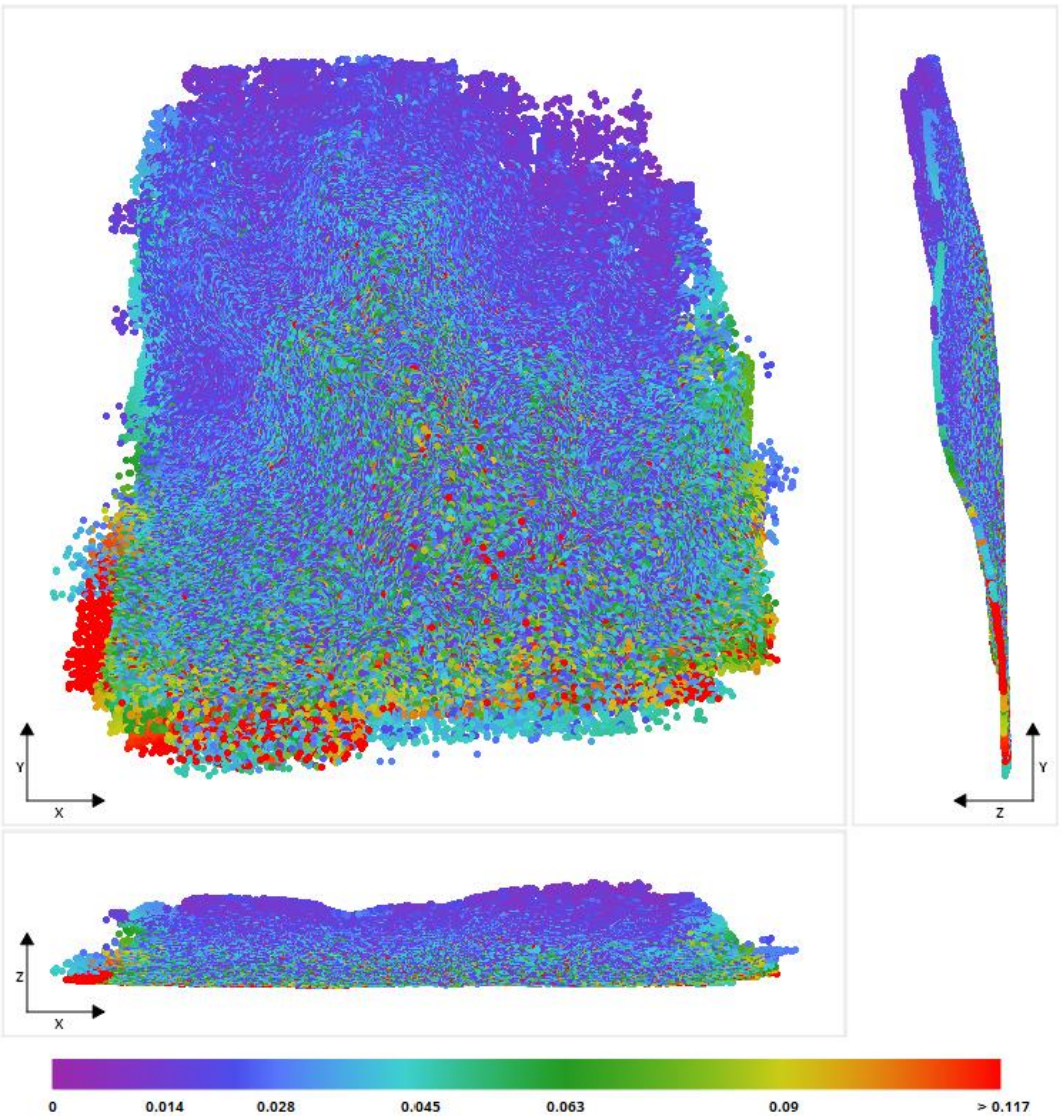

Figure D.1-31: Position uncertainties for AQ12: Top view (XY plane), side view (ZY plane) and front view (XZ plane) displays of all tie points, with colours representing uncertainty in the individual point position. The values are in metres, with a minimum uncertainty of 0.0051 metres and a maximum of 0.6867 metres. The median position uncertainty equals 0.0335 metres.

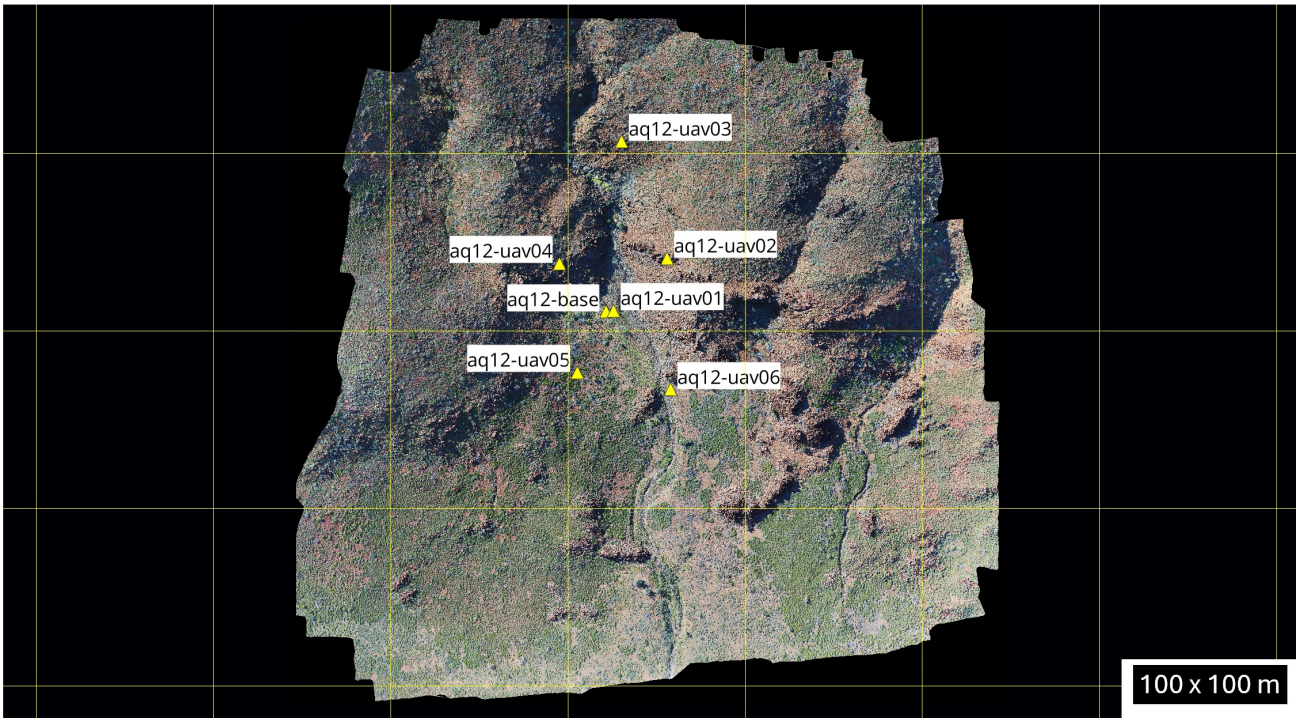

Figure D.1-32: Ortho-mosaic for AQ12. Plotted with control points and 100 x 100 m grid spacing.

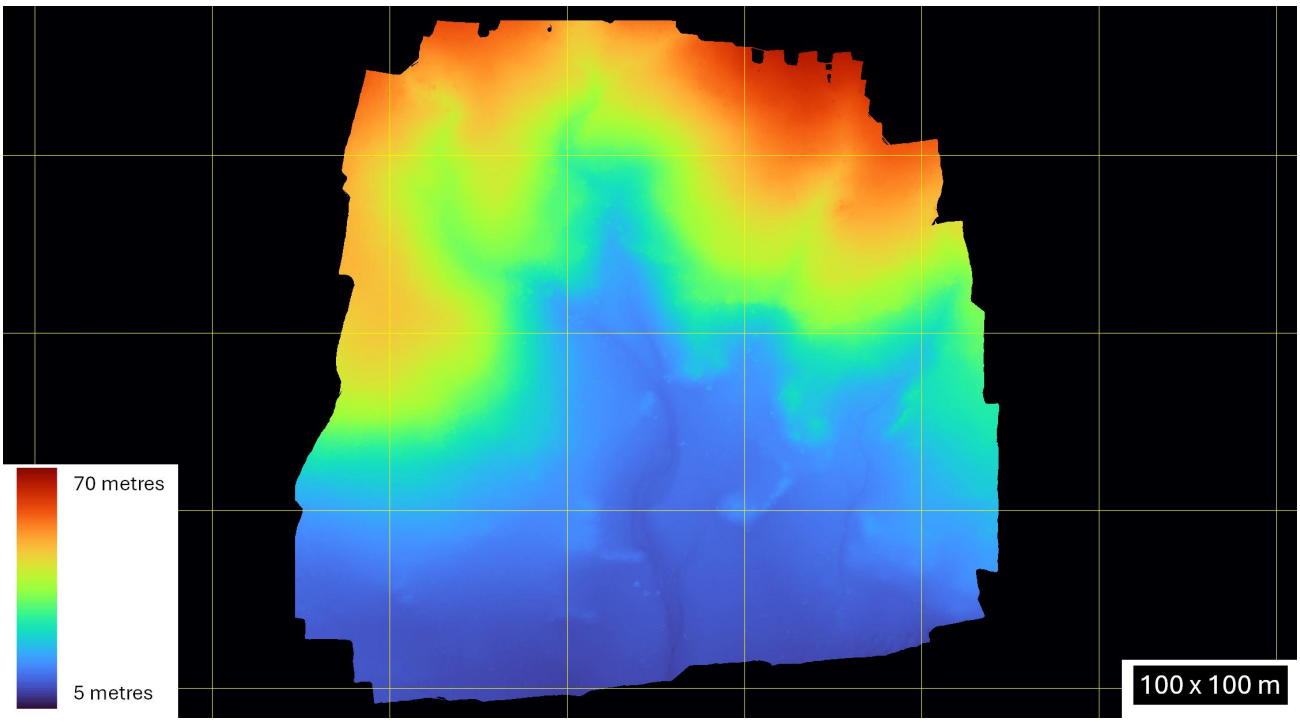

Figure D.1-33: DEM for AQ12. Plotted with 100 x 100 m grid spacing.

AQ13 site summary

Table D.1-34: AQ13 site summary.

Drone	**Phantom 4 Pro**
Camera Model	DJI FC6310
Images	1015/1031
Ground Coverage	1.429 km^2
Average ground resolution	20.89304 mm/pixel
Geo referencing	9 control points (RTK)
Key Points	Median of 48126 key points per image
Tie Points	429123 points (median of 2019 points per photo)
Reprojection Errors (Median)	0.35 pixels
Reprojection Errors (RMS)	0.48 pixels
Distance to Rays (RMS)	0.07165 metres

Table D.1-35: AQ13 Position uncertainties (camera locations).

	X (metres)	**Y (metres)**	**Z (metres)**
Minimum	0.00214	0.00205	0.00076
Mean	0.00622	0.00588	0.00248
Maximum	0.17971	0.13379	0.05232

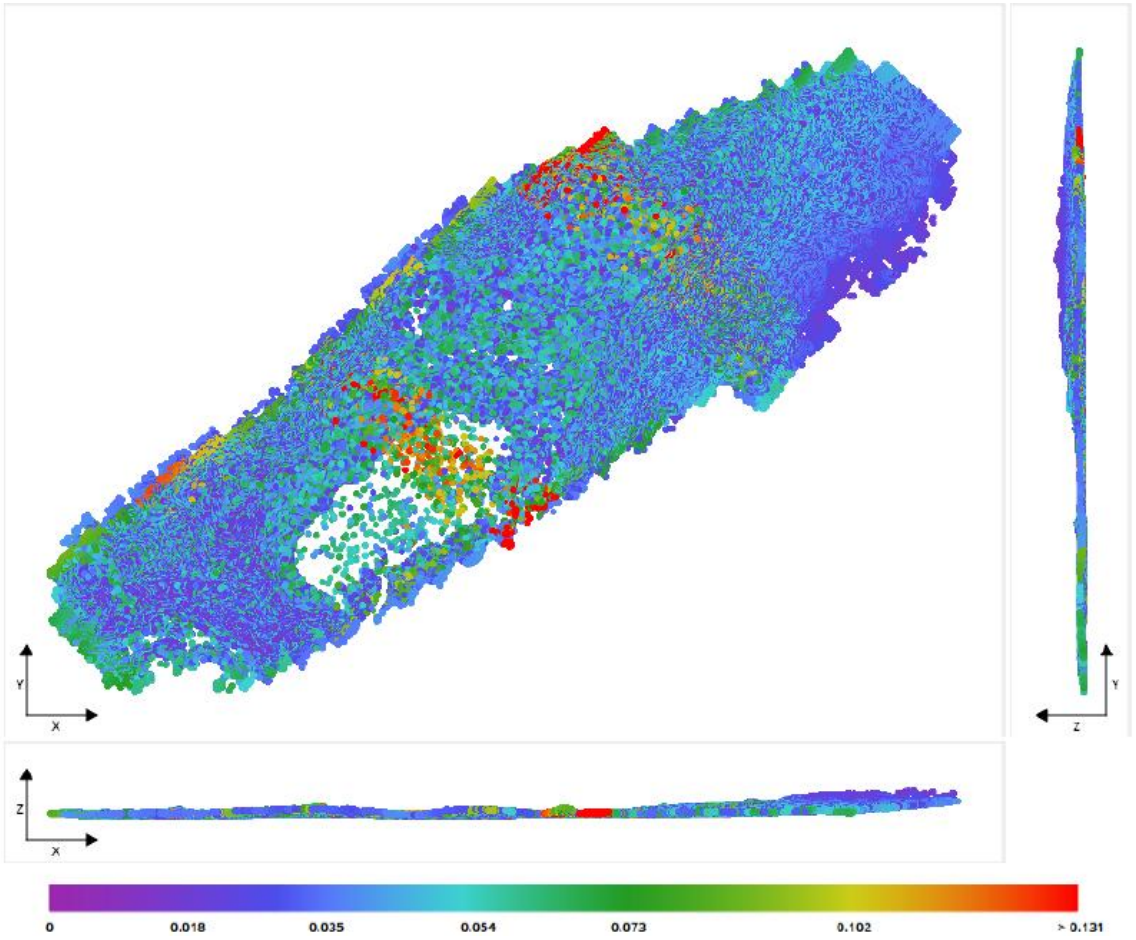

Figure D.1-34: Position uncertainties for AQ13: Top view (XY plane), side view (ZY plane) and front view (XZ plane) displays of all tie points, with colours representing uncertainty in the individual point position. The values are in metres, with a minimum uncertainty of 0.0051 metres and a maximum of 0.6867 metres. The median position uncertainty equals 0.0335 metres.

Table D.1-36: AQ13 control points.

Name	Accuracy (m)	Num of Photos	RMS of Reproject Error (pixels)	RMS of Dist to Rays (m)	3D Error (m)	Horizontal Errors (m)	Vertical Error (m)
uav1	H: 0.014 V: 0.031	12	0.47	0.0556	0.0029	X: 0.0016 Y: 0.0024	0
uav2	H: 0.011 V: 0.022	14	0.54	0.774	0.0059	X: -0.0017 Y: 0.0056	0.0007
uav3	H: 0.010 V: 0.022	12	0.65	0.0572	0.0087	X: 0.0029 Y: -0.0076	-0.0031
uav4	H: 0.013 V: 0.032	13	0.41	0.0713	0.036	X: -0.0029 Y: -0.0020	0.0009
uav5	H: 0.007 V: 0.015	24	0.35	0.0795	0.0044	X: 0.0021 Y: 0.0020	-0.0033
uav6	H: 0.010 V: 0.022	9	0.29	0.0676	0.0023	X: -0.0007 Y: -0.0017	0.0014
uav7	H: 0.010 V: 0.022	9	0.39	0.0539	0.004	X: -0.0023 Y: 0.0005	-0.0032
uav8	H: 0.010 V: 0.021	14	0.54	0.0845	0.0057	X: 0.0027 Y: 0.0030	0.004
uav9	H: 0.010 V: 0.020	9	0.32	0.0684	0.004	X: -0.0018 Y: -0.0034	0.0008
Global RMS			0.45	0.0692	0.005	X: 0.0022 Y:0.0038	0.0024
Median			0.41	0.0684	0.004	X: -0.0007 Y:0.0005	0.0007

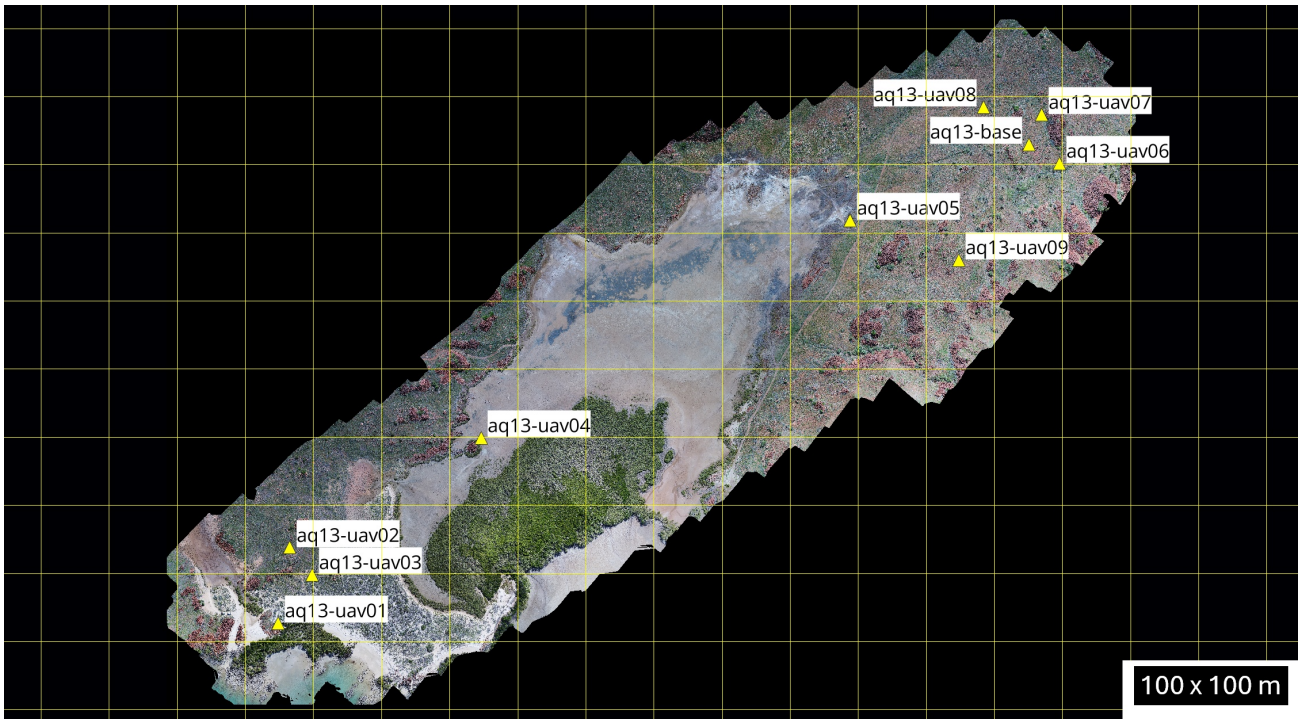

Figure D.1-35: Ortho-mosaic for AQ13. Plotted with control points and 100 x 100 m grid spacing.

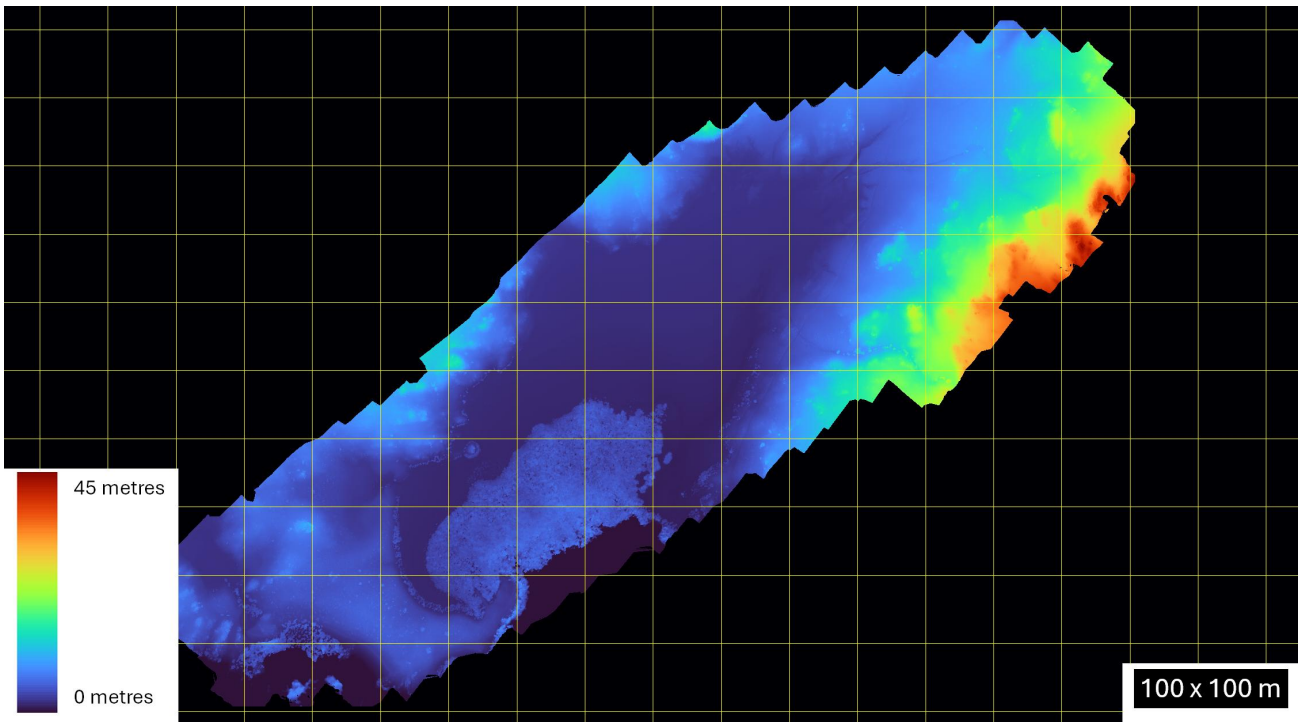

Figure D.1-36: DEM for AQ13. Plotted with 100 x 100 m grid spacing.

AQ14 site summary

Table D.1-37: AQ14 site summary.

Drone	**Phantom 4 Pro**
Camera Model	DJI FC6310
Images	623/623
Ground Coverage	0.2600 km^2
Average ground resolution	20.8253 mm/pixel
Geo referencing	5 control points (RTK)
Key Points	Median of 50196 key points per image
Tie Points	309201 points (median of 2822 points per photo)
Reprojection Errors (Median)	0.37 pixels
Reprojection Errors (RMS)	0.50 pixels
Distance to Rays (RMS)	0.0728 metres

Table D.1-38: AQ14 Position uncertainties (camera locations).

	X (metres)	**Y (metres)**	**Z (metres)**
Minimum	0.0018	0.002	0.0008
Mean	0.003	0.003	0.0015
Maximum	0.0301	0.0649	0.0583

Table D.1-39: AQ14 control points.

Name	Accuracy (m)	Num of Photos	RMS of Reproject Error (pixels)	RMS of Dist to Rays (m)	3D Error (m)	Horizontal Errors (m)	Vertical Error (m)
uav1	H: 0.008 V: 0.020	26	0.38	0.0822	0.0018	X: -0.0005 Y: 0.0016	-0.0006
uav2	H: 0.009 V: 0.021	42	0.44	0.0938	0.0028	X: -0.0020 Y: -0.0020	-0.0002
uav3	H: 0.010 V: 0.023	42	0.42	0.0891	0.0032	X: 0.0003 Y: -0.0027	-0.0017
uav4	H: 0.010 V: 0.024	47	0.43	0.0779	0.0046	X: 0.0034 Y: 0.0021	0.0021
uav5	H: 0.010 V: 0.024	43	0.41	0.0942	0.0016	X: 0.0007 Y: -0.0004	0.0014
Global RMS			0.42	0.0877	0.003	X: 0.0018 Y: -0.0019	0.0014
Median			0.42	0.0891	0.0028	X: 0.0003 Y: -0.0004	-0.0002

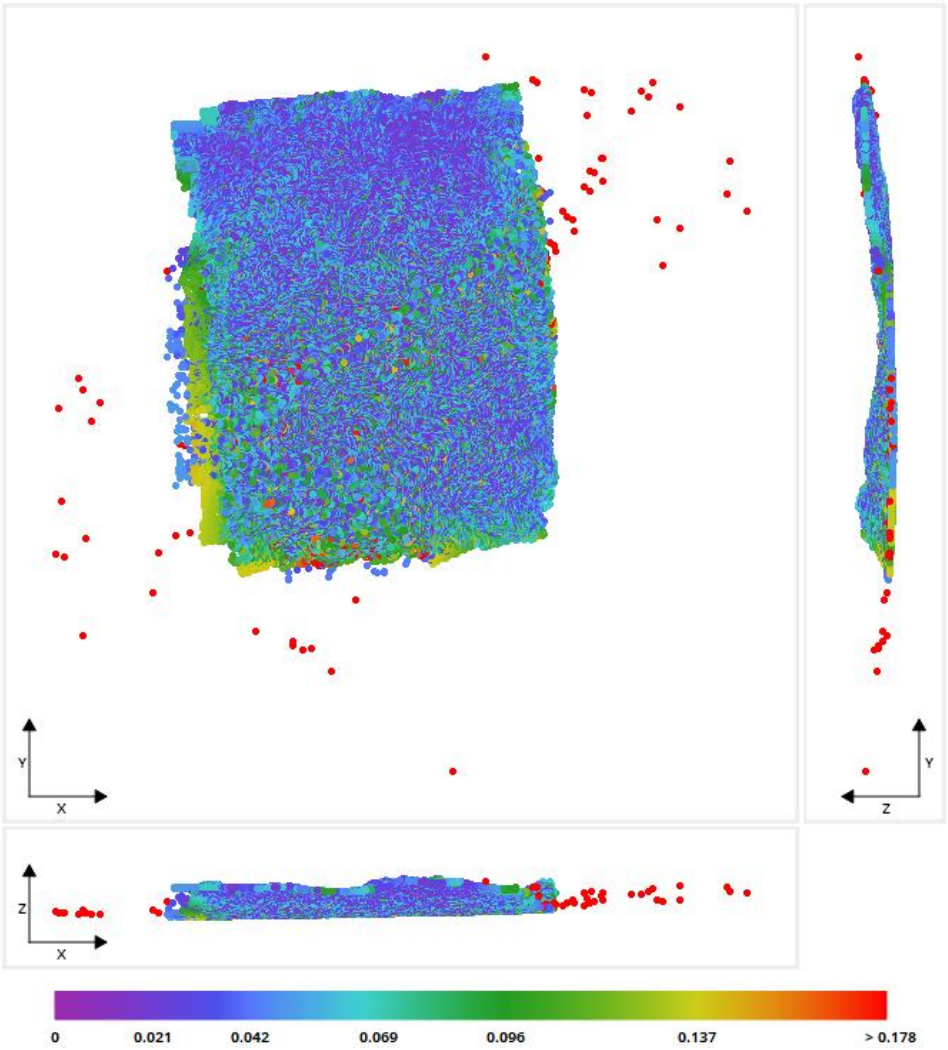

Figure D.1-37: Position uncertainties for AQ14: Top view (XY plane), side view (ZY plane) and front view (XZ plane) displays of all tie points, with colours representing uncertainty in the individual point position. The values are in metres, with a minimum uncertainty of 0.0051 metres and a maximum of 0.6867 metres. The median position uncertainty equals 0.0335 metres.

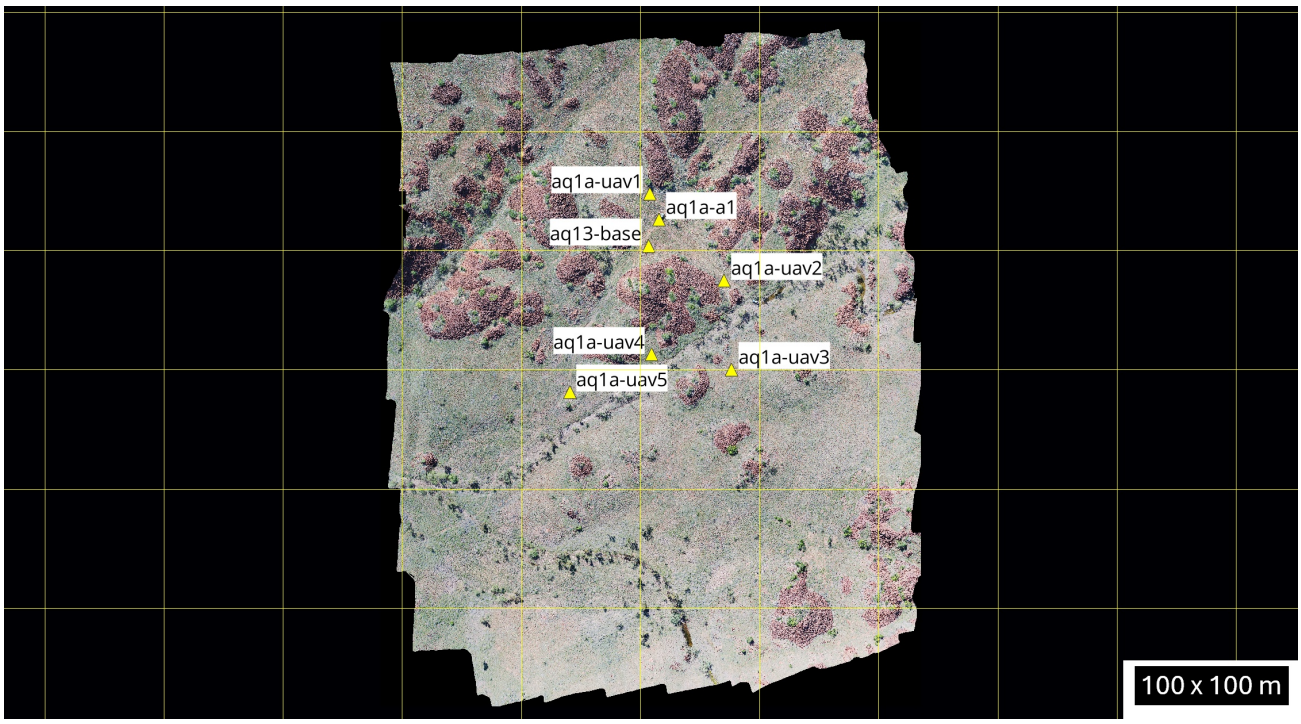

Figure D.1-38: Ortho-mosaic for AQ14. Plotted with control points and 100 x 100 m grid spacing.

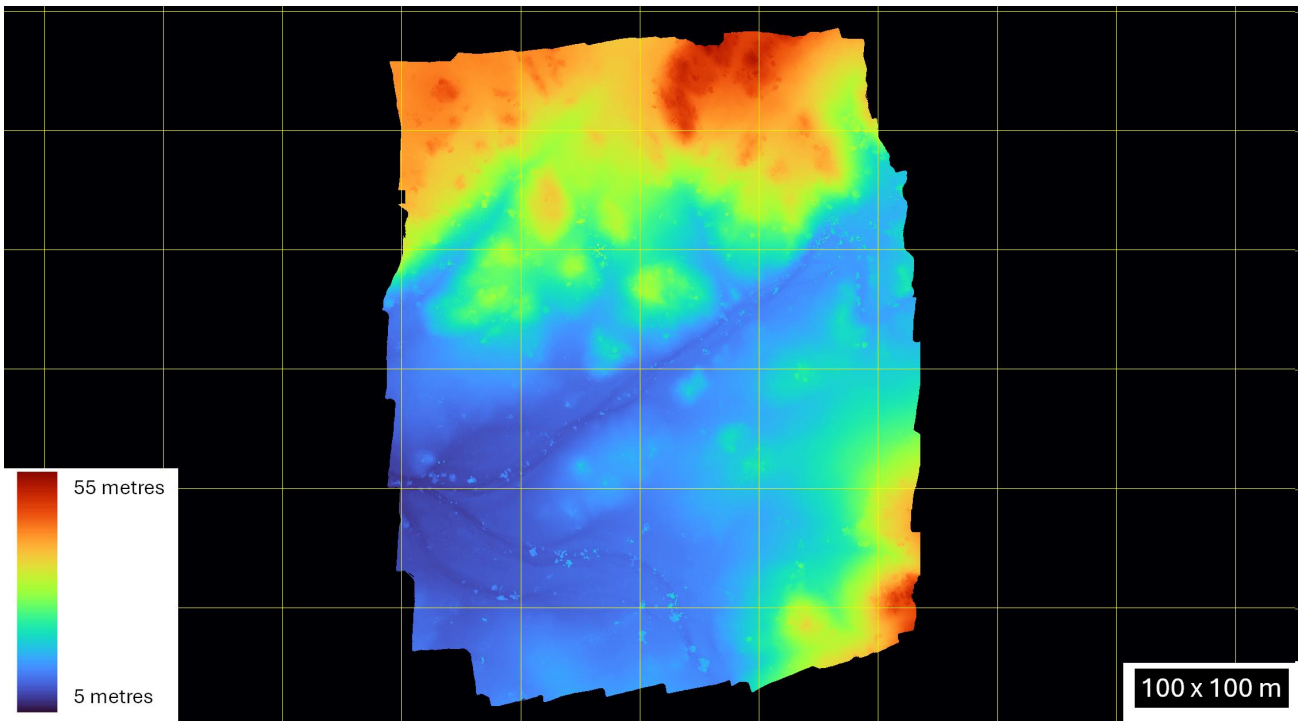

Figure D.1-39: DEM for AQ14. Plotted with 100 x 100 m grid spacing.

AQ15 (Southwest) site summary

Table D.1-40: AQ15 (Southwest)site summary.

Drone	**Phantom 4 Pro**
Camera Model	DJI FC6310
Images	253/264
Ground Coverage	0.080 km^2
Average ground resolution	15.5958 mm/pixel
Geo referencing	4 control points (RTK)
Key Points	Median of 44541 key points per image
Tie Points	86829 points (median of 1819 points per photo)
Reprojection Errors (Median)	0.39 pixels
Reprojection Errors (RMS)	0.55 pixels
Distance to Rays (RMS)	0.042 metres

Table D.1-41: AQ15 Position uncertainties (camera locations).

	X (metres)	**Y (metres)**	**Z (metres)**
Minimum	0.0015	0.0013	0.0011
Mean	0.0053	0.0076	0.0037
Maximum	0.1153	0.3218	0.122

Table D.1-42: AQ15 control points.

Name	Accuracy (m)	Num of Photos	RMS of Reproject Error (pixels)	RMS of Dist to Rays (m)	3D Error (m)	Horizontal Errors (m)	Vertical Error (m)
uav1	H: 0.008 V: 0.010	42	0.56	0.0576	0.0059	X: 0.0010 Y: -0.0034	-0.0047
uav2	H: 0.008 V: 0.017	38	0.44	0.0464	0.0066	X: -0.0034 Y: 0.0012	0.0055
uav3	H: 0.010 V: 0.019	29	0.45	0.0431	0.0045	X: 0.0030 Y: 0.0022	0.0024
uav4	H: 0.015 V: 0.024	33	0.46	0.0524	0.0052	X: 0.0010 Y: 0.0024	-0.0046
Global RMS			0.48	0.0502	0.0056	X: 0.0024 Y: 0.0024	0.0044
Median			0.46	0.0524	0.0059	X: 0.0010 Y: 0.0023	0.0024

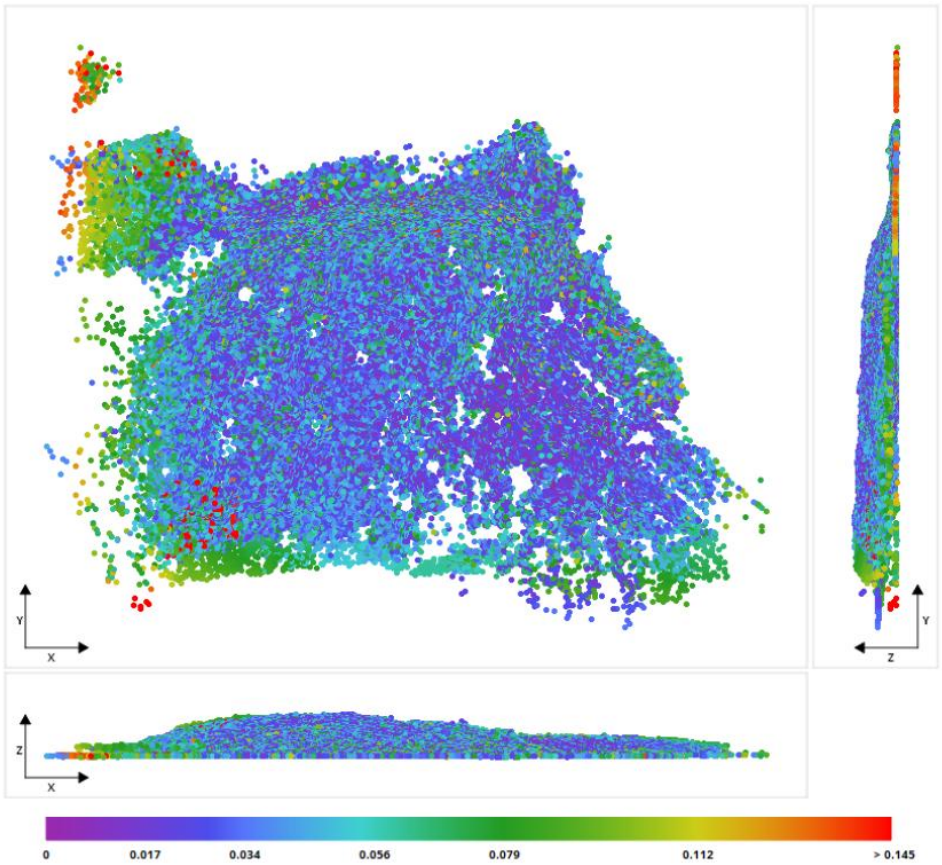

Figure D.1-40: Position uncertainties for AQ15 (Southwest): Top view (XY plane), side view (ZY plane) and front view (XZ plane) displays of all tie points, with colours representing uncertainty in the individual point position. The values are in metres, with a minimum uncertainty of 0.0051 metres and a maximum of 0.6867 metres. The median position uncertainty equals 0.0335 metres.

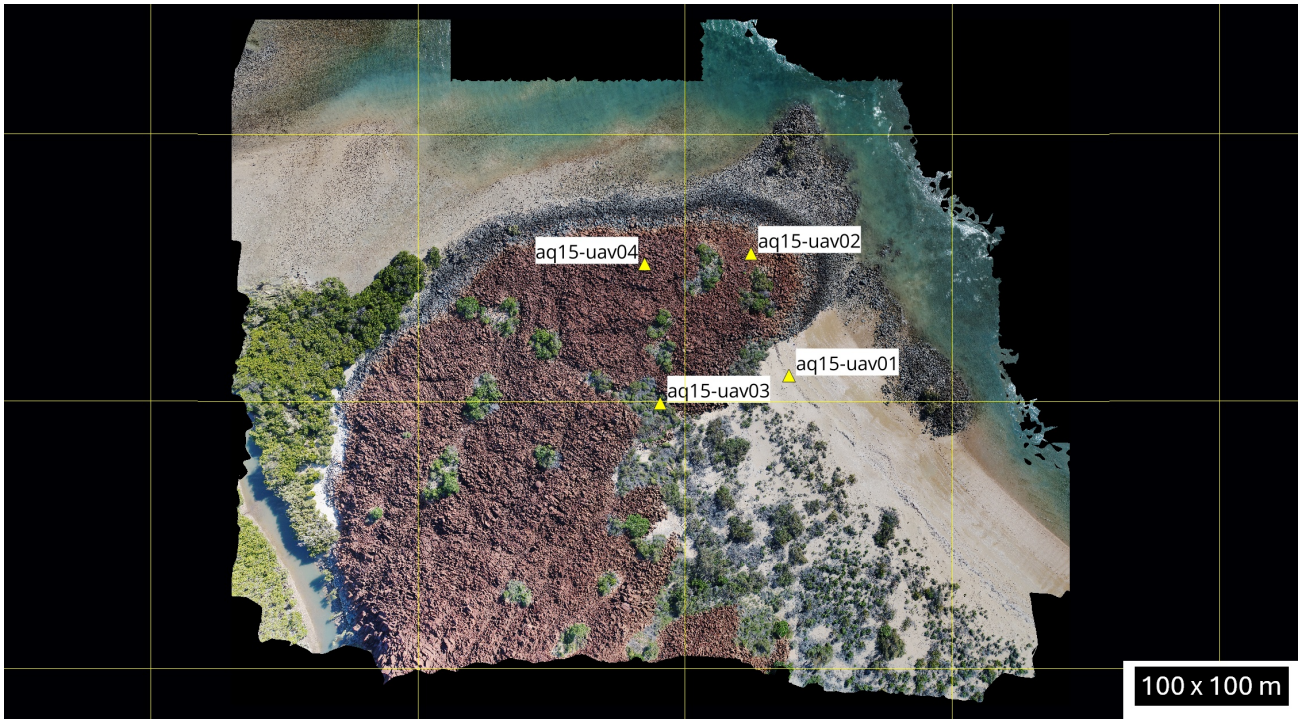

Figure D.1-41: Ortho-mosaic for AQ15 (Southwest). Plotted with control points and 100 x 100 m grid spacing.

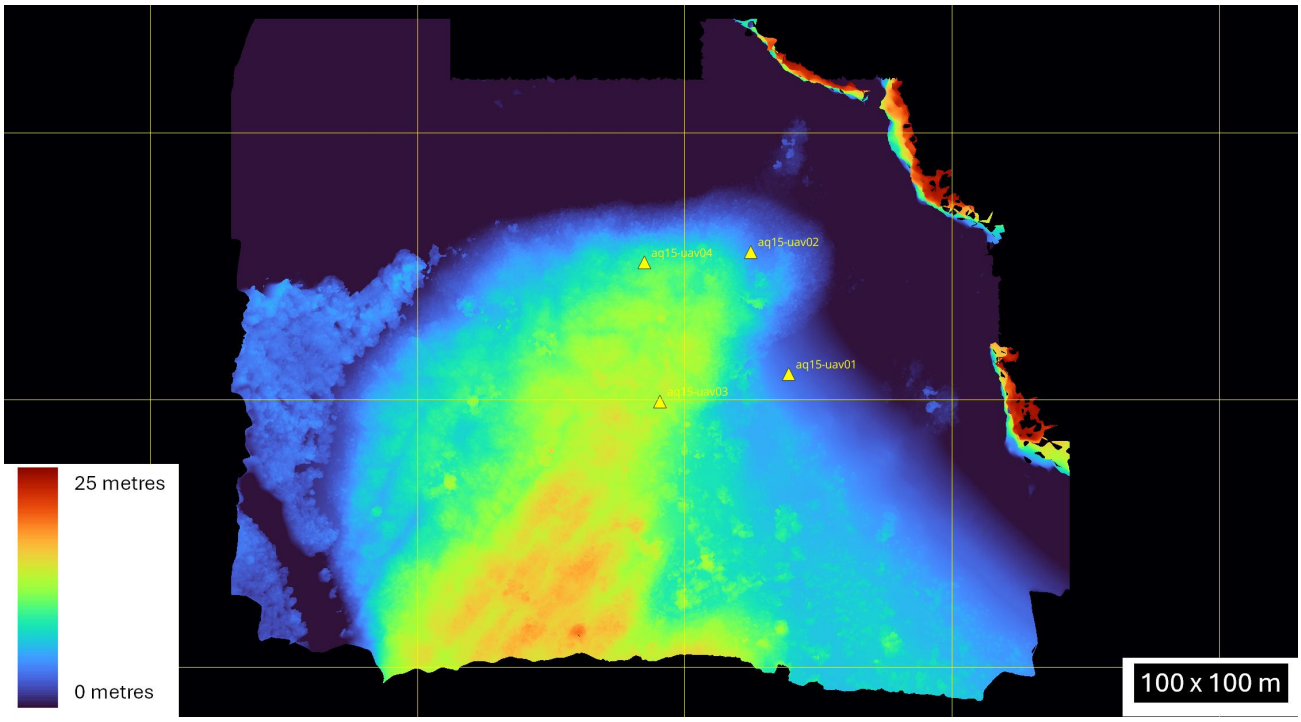

Figure D.1-42: DEM for AQ15 (Southwest). Plotted with 100 x 100 m grid spacing.

AQ15 and AQ16 site summary

Table D.1-43: AQ15 and AQ16 site summary.

Drone	**Phantom 4 Pro**
Camera Model	DJI FC6310, DJI FC6310R
Images	3266/3457
Ground Coverage	2.026 km^2
Average ground resolution	24.0049 mm/pixel
Geo referencing	20 control points (RTK)
Key Points	Median of 49160 key points per image
Tie Points	1157124 points (median of 2017 points per photo)
Reprojection Errors (Median)	0.36 pixels
Reprojection Errors (RMS)	0.51 pixels
Distance to Rays (RMS)	0.05072 metres

Table D.1-44: AQ15 and AQ16 Position uncertainties (camera locations).

	X (metres)	**Y (metres)**	**Z (metres)**
Minimum	0.00094	0.00096	0.00083
Mean	0.03028	0.02607	0.00528
Maximum	11.3306	6.61264	1.52591

Table D.1-45: AQ15 and AQ16 control points.

Name	Accuracy (m)	Num of Photos	RMS of Reproject Error (pixels)	RMS of Dist to Rays (m)	3D Error (m)	Horizontal Errors (m)	Vertical Error (m)
uav1	H: 0.009 V: 0.021	32	0.69	0.0733	0.00744	X: 0.0068 Y: -0.0003	0.003
uav2	H: 0.008 V: 0.020	35	0.73	0.0661	0.01005	X: -0.0096 Y: 0.0002	-0.003
uav3	H: 0.010 V: 0.023	34	0.73	0.0638	0.00928	X: 0.0027 Y: -0.0085	0.0027

Name	Accuracy (m)	Num of Photos	RMS of Reproject Error (pixels)	RMS of Dist to Rays (m)	3D Error (m)	Horizontal Errors (m)	Vertical Error (m)
uav4	H: 0.009 V: 0.021	36	0.66	0.0682	0.00633	X: -0.0010 Y: 0.0053	-0.0034
uav5	H: 0.009 V: 0.021	37	0.53	0.0558	0.00421	X: -0.0035 Y: 0.0005	0.0022
uav6	H: 0.009 V: 0.021	38	0.77	0.0703	0.01055	X: 0.0102 Y: 0.0027	0.0006
uav7	H: 0.008 V: 0.021	32	0.79	0.0606	0.00868	X: -0.0057 Y: -0.0062	-0.0021
uav5	H: 0.012 V: 0.024	26	0.55	0.1178	0.00828	X: -0.0035 Y: -0.0010	0.0074
uav6	H: 0.014 V: 0.028	39	0.63	0.0817	0.01436	X: 0.0023 Y: -0.0048	-0.0133
uav7	H: 0.012 V: 0.022	34	1.27	0.0862	0.02683	X: -0.0235 Y: 0.0115	-0.0058
uav8	H:0.390 V: 0.023	19	0.77	0.0872	0.01583	X: 0.0098 Y: -0.0097	0.0077
uav9	H: 0.013 V: 0.026	23	1.12	0.0739	0.01883	X: -0.0062 Y: 0.0171	0.0049
uav11	H: 0.014 V: 0.029	34	0.96	0.0833	0.02227	X: 0.0185 Y: -0.0007	-0.0123
uav15	H: 0.011 V: 0.023	37	0.58	0.0881	0.00702	X: -0.0065 Y: 0.0008	0.0026
uav16	H: 0.011 V: 0.023	38	0.74	0.0839	0.00614	X: 0.0060 Y: -0.0010	-0.0006
uav17	H: 0.007 V: 0.015	37	0.86	0.0856	0.01395	X: 0.0059 Y: 0.0125	-0.0018
uav18	H: 0.007 V: 0.015	38	0.82	0.0968	0.01138	X: -0.0047 Y: -0.0103	-0.0011
uav10	H: 0.014 V: 0.028	26	1.3	0.094	0.02496	X: 0.0101 Y: -0.0197	0.0115
Global RMS						X: 0.0094 Y: 0.0086	0.0062

Name	Accuracy (m)	Num of Photos	RMS of Reproject Error (pixels)	RMS of Dist to Rays (m)	3D Error (m)	Horizontal Errors (m)	Vertical Error (m)
Median						X: 0.0023 Y: -0.0003	0.0006

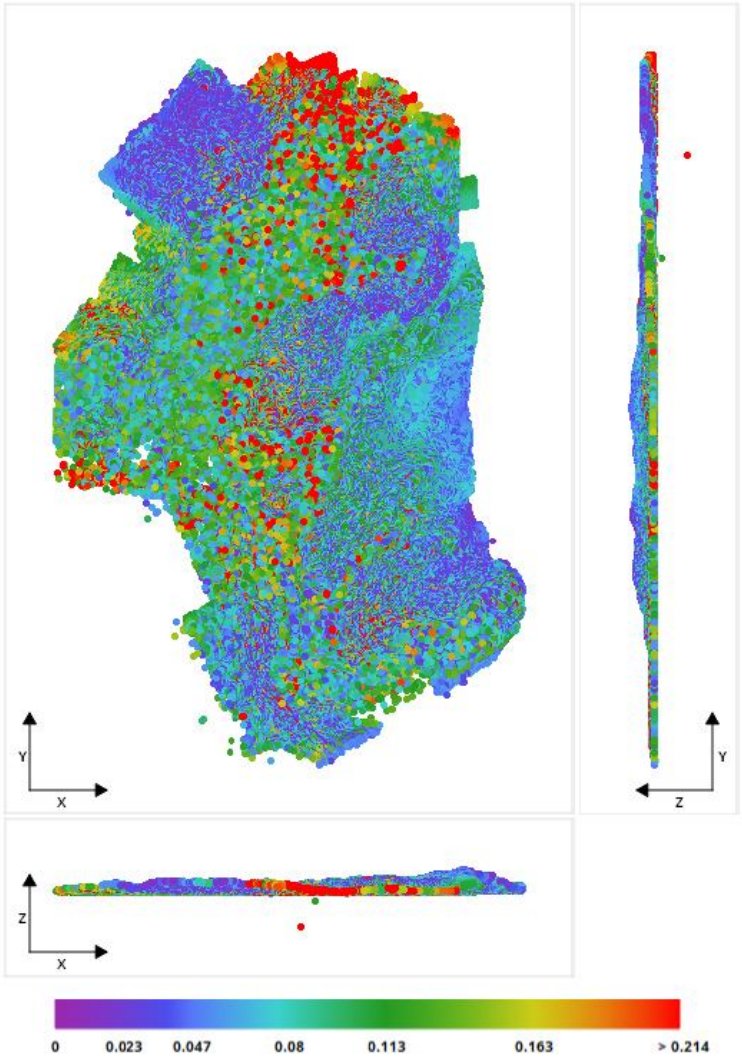

Figure D.1-43: Position uncertainties for AQ15 and AQ16: Top view (XY plane), side view (ZY plane) and front view (XZ plane) displays of all tie points, with colours representing uncertainty in the individual point position. The values are in metres, with a minimum uncertainty of 0.0051 metres and a maximum of 0.6867 metres. The median position uncertainty equals 0.0335 metres.

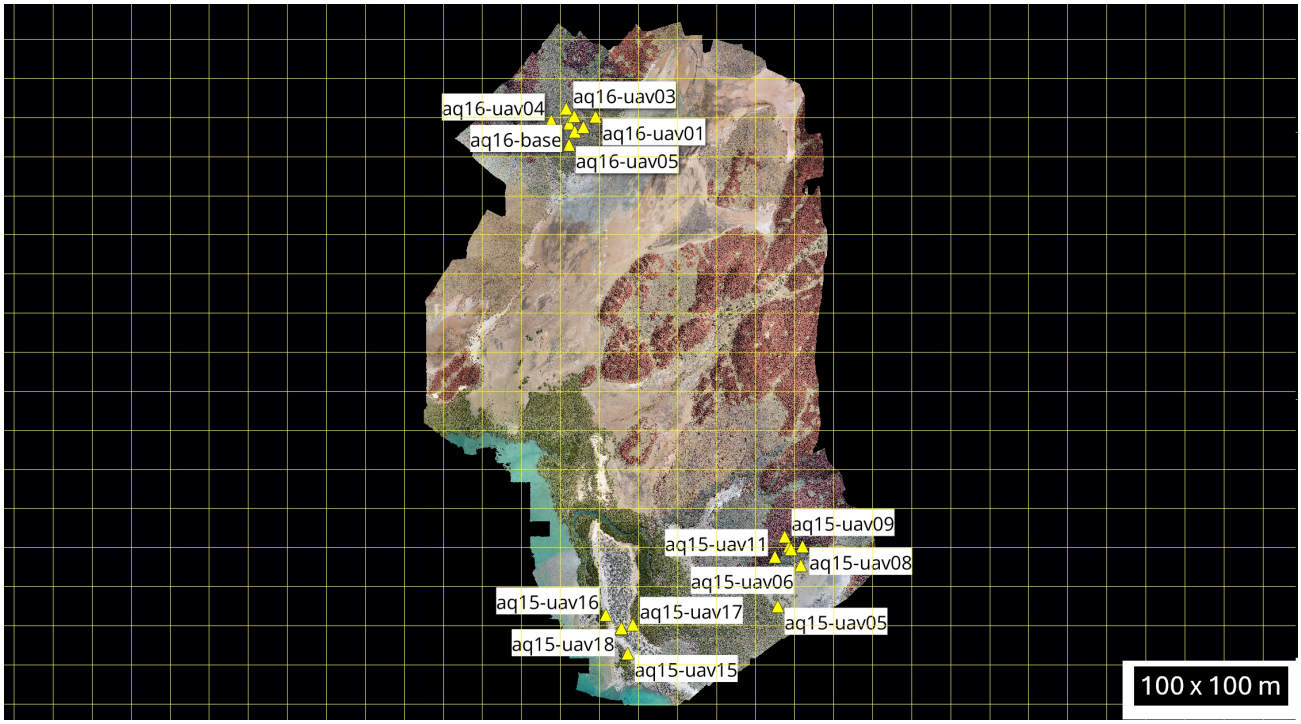

Figure D.1-44: Ortho-mosaic for AQ15 and AQ16. Plotted with control points and 100 x 100 m grid spacing.

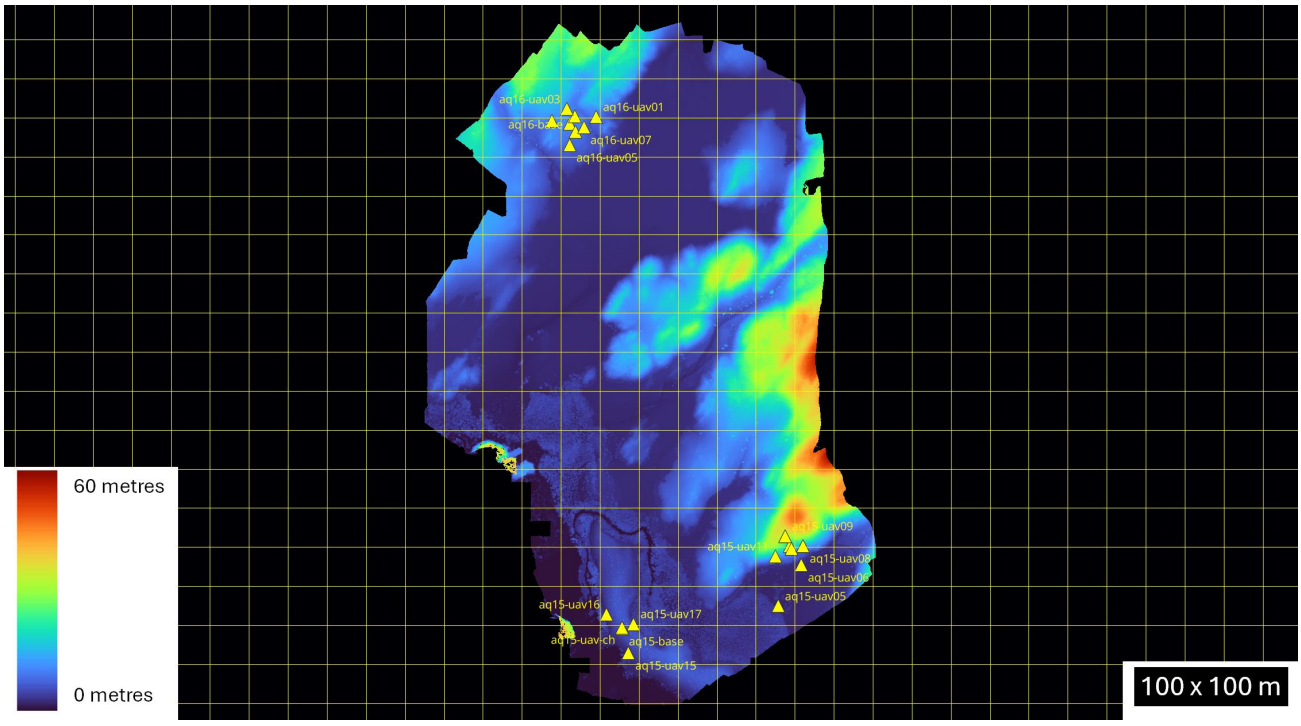

Figure D.1-45: DEM for AQ15 and AQ16. Plotted with 100 x 100 m grid spacing.

AQ17 site summary

Table D.1-46: AQ17 site summary.

Drone	**Phantom 4 Pro**
Camera Model	DJI FC6310
Images	465/465
Ground Coverage	0.234 km^2
Average ground resolution	18.0112 mm/pixel
Geo referencing	6 control points (RTK)
Key Points	Median of 48954 key points per image
Tie Points	139706 points (median of 1515 points per photo)
Reprojection Errors (Median)	0.47 pixels
Reprojection Errors (RMS)	0.62 pixels
Distance to Rays (RMS)	0.064 metres

Table D.1-47: AQ17 Position uncertainties (camera locations).

	X (metres)	**Y (metres)**	**Z (metres)**
Minimum	0.0017	0.002	0.001
Mean	0.0035	0.0036	0.0017
Maximum	0.0151	0.0181	0.0129

Table D.1-48: AQ17 control points.

Name	Accuracy (m)	Num of Photos	RMS of Reproject Error (pixels)	RMS of Dist to Rays (m)	3D Error (m)	Horizontal Errors (m)	Vertical Error (m)
uav30	H: 0.008 V: 0.018	28	0.49	0.0652	0.0029	X: -0.0009 Y: -0.0018	0.0021
uav32	H: 0.009 V: 0.019	34	0.58	0.0679	0.0066	X: -0.0049 Y: -0.0042	0.0014
uav38	H: 0.011 V: 0.022	25	0.64	0.0551	0.0084	X: 0.0076 Y: -0.0004	0.0036
uav39	H: 0.010 V: 0.020	26	0.56	0.0681	0.0036	X: 0.0032 Y: -0.0008	0.0015
base	H: 0.015 V: 0.015	16	0.84	0.0522	0.0119	X: -0.0062 Y: -0.0007	-0.0102
uav37	H: 0.008 V: 0.016	24	0.72	0.0693	0.011	X: 0.0045 Y: 0.0067	-0.0075
Global RMS			0.65	0.0633	0.0082	X: 0.0050 Y: 0.0034	0.0055
Median			0.64	0.0679	0.0084	X: 0.0032 Y: -0.0007	0.0015

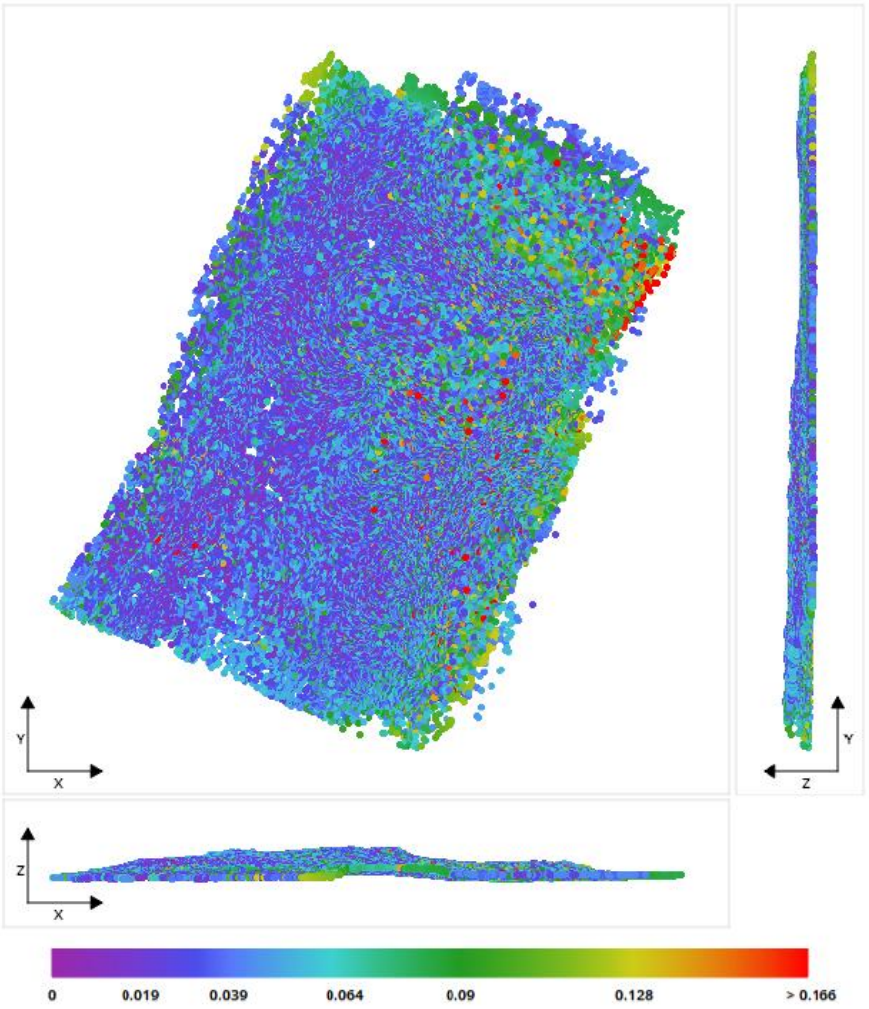

Figure D.1-46: Position uncertainties for AQ17: Top view (XY plane), side view (ZY plane) and front view (XZ plane) displays of all tie points, with colours representing uncertainty in the individual point position. The values are in metres, with a minimum uncertainty of 0.0051 metres and a maximum of 0.6867 metres. The median position uncertainty equals 0.0335 metres.

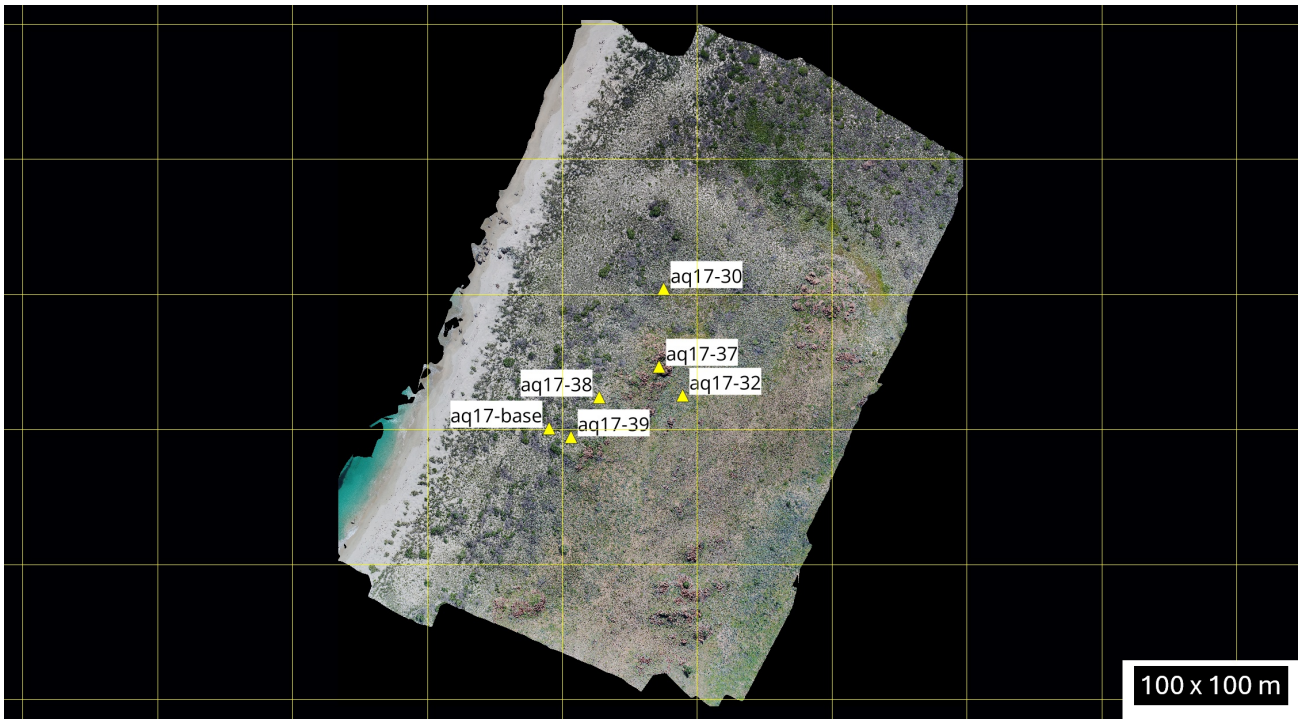

Figure D.1-47: Ortho-mosaic for AQ17. Plotted with control points and 100 x 100 m grid spacing.

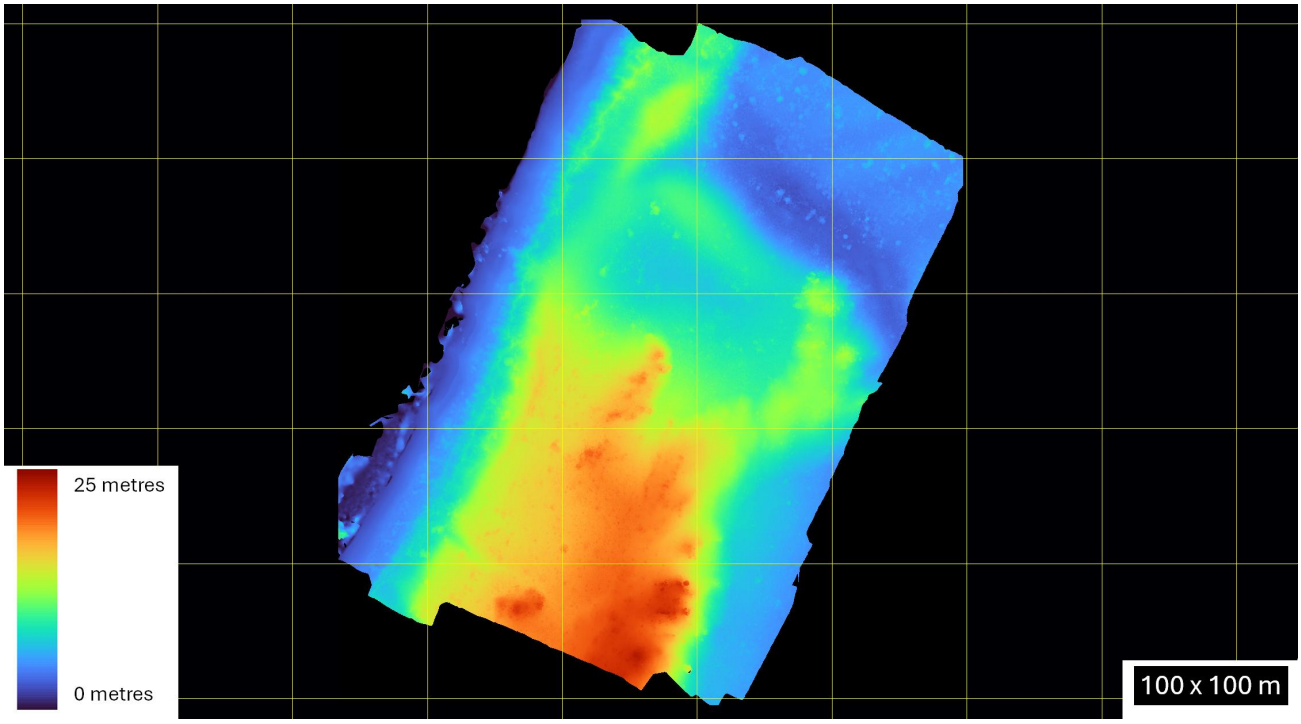

Figure D.1-48: DEM for AQ17. Plotted with 100 x 100 m grid spacing.

AQ18 site summary

Table D.1-49: AQ18 site summary.

Drone	**Phantom 4 Pro**
Camera Model	DJI FC6310
Images	990/1013
Ground Coverage	0.613 km^2
Average ground resolution	19.543 mm/pixel
Geo referencing	7 control points (RTK)
Key Points	Median of 48423 key points per image
Tie Points	329748 points (median of 1941 points per photo)
Reprojection Errors (Median)	0.39 pixels
Reprojection Errors (RMS)	0.52 pixels
Distance to Rays (RMS)	0.067 metres

Table D.1-50: AQ18 Position uncertainties (camera locations).

	X (metres)	**Y (metres)**	**Z (metres)**
Minimum	0.0021	0.0018	0.0008
Mean	0.0085	0.0084	0.0042
Maximum	1.258	1.2265	0.6421

Table D.1-51: AQ18 control points.

Name	Accuracy (m)	Num of Photos	RMS of Reproject Error (pixels)	RMS of Dist to Rays (m)	3D Error (m)	Horizontal Errors (m)	Vertical Error (m)
uav01	H: 0.005 V: 0.013	46	1.63	0.0745	0.0253	X: 0.0166 Y: 0.0166	-0.0095
uav02	H: 0.007 V: 0.017	50	1.26	0.0822	0.016	X: -0.0137 Y: 0.0061	-0.0055
uav03	H: 0.007 V: 0.018	49	1.44	0.0797	0.0253	X: 0.0023 Y: -0.0216	0.009
uav04	H: 0.008 V: 0.018	47	0.98	0.0763	0.0084	X: 0.0004 Y: -0.0137	0.0059
uav05	H: 0.008 V: 0.018	47	1.23	0.0778	0.0188	X: -0.0046 Y: 0.0137	-0.0119
uav06	H: 0.008 V: 0.018	47	0.85	0.0717	0.0045	X: -0.0031 Y: -0.0023	-0.0023
uav07	H: 0.008 V: 0.018	43	1.37	0.0836	0.0209	X: 0.002 Y: -0.0184	0.0097
Global RMS			1.26	0.0781	0.0182	X: 0.0050 Y: 0.0034	0.0083
Median			1.26	0.0778	0.0188	X: 0.0032 Y: -0.0007	0.0023

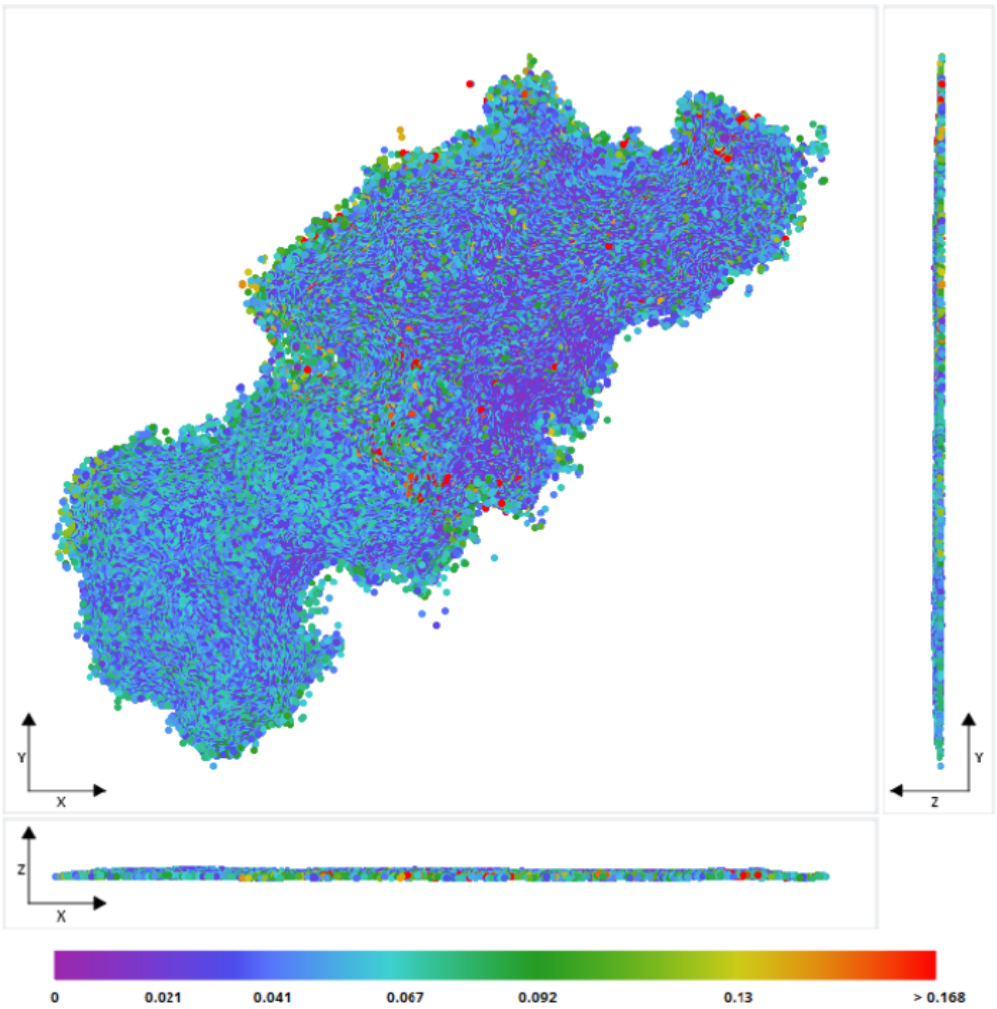

Figure D.1-49: Position uncertainties for AQ18: Top view (XY plane), side view (ZY plane) and front view (XZ plane) displays of all tie points, with colours representing uncertainty in the individual point position. The values are in metres, with a minimum uncertainty of 0.0047 metres and a maximum of 0.6218 metres. The median position uncertainty equals 0.0414 metres.

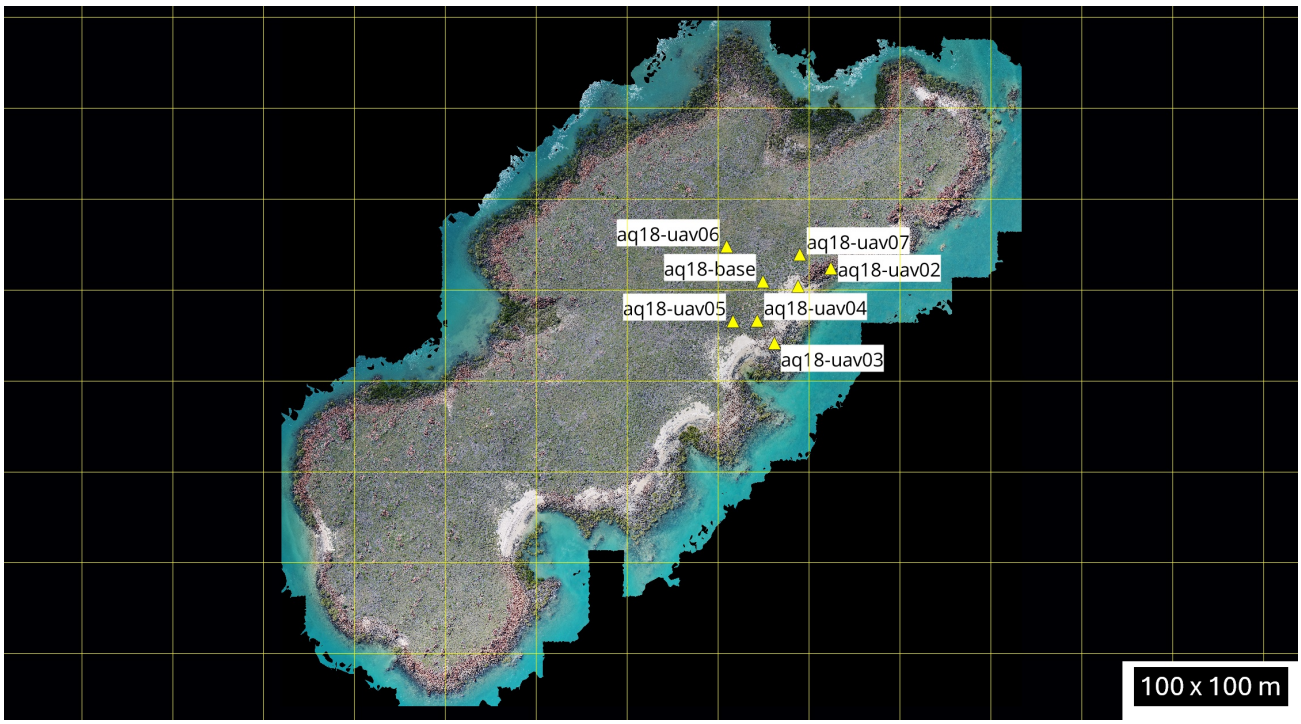

Figure D.1-50: Ortho-mosaic for AQ18. Plotted with control points and 100 x 100 m grid spacing.

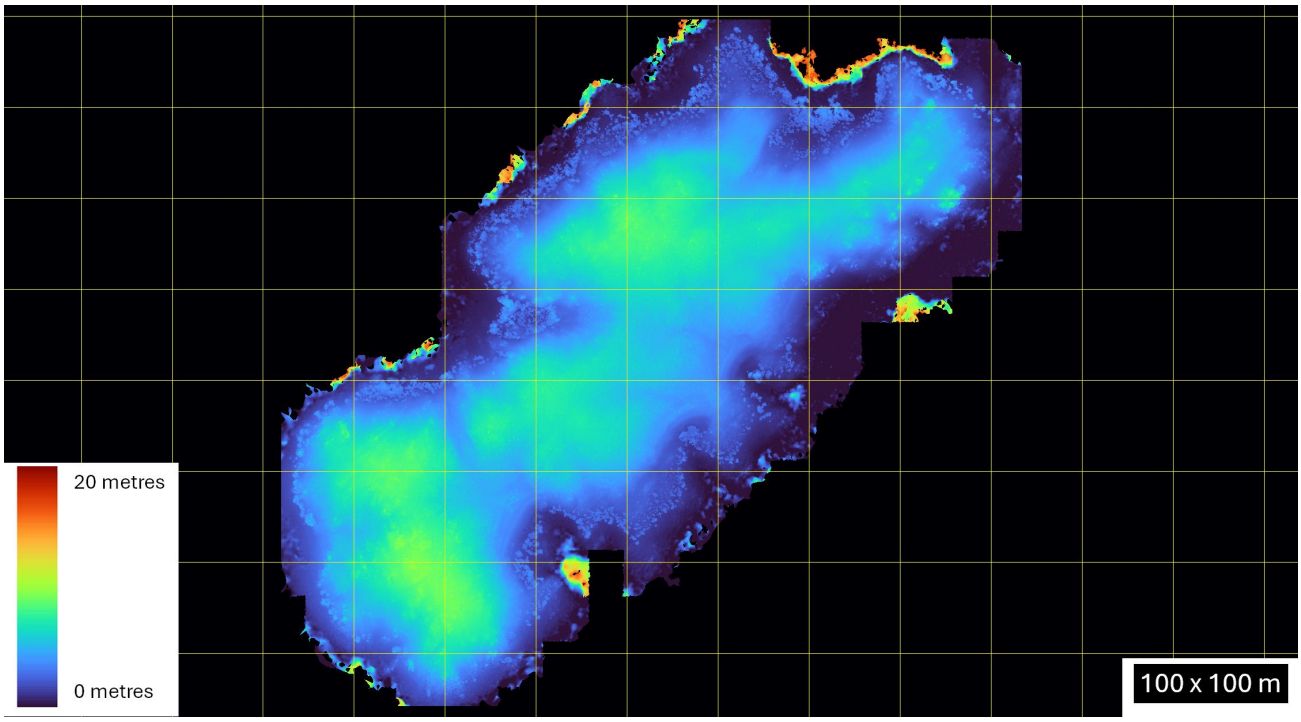

Figure D.1-51: DEM for AQ18. Plotted with 100 x 100 m grid spacing.

EX02 (Northeast) site summary

Table D.1-52: EX02 (Northeast) site summary.

Drone	**Phantom 4 Pro**
Camera Model	DJI FC6310
Images	302/303
Ground Coverage	0.126 km^2
Average ground resolution	16.888 mm/pixel
Geo referencing	4 control points (RTK)
Key Points	Median of 39117 key points per image
Tie Points	85862 points (median of 1679 points per photo)
Reprojection Errors (Median)	0.44 pixels
Reprojection Errors (RMS)	0.59 pixels
Distance to Rays (RMS)	0.0473 metres

Table D.1-53: EX02 (Northeast) Position uncertainties (camera locations).

	X (metres)	**Y (metres)**	**Z (metres)**
Minimum	0.0019	0.0017	0.0013
Mean	0.0042	0.0049	0.003
Maximum	0.0975	0.1306	0.0776

Table D.1-54: EX02 (Northeast) control points.

Name	Accuracy (m)	Num of Photos	RMS of Reproject Error (pixels)	RMS of Dist to Rays (m)	3D Error (m)	Horizontal Errors (m)	Vertical Error (m)
uav101	H: 0.014 V: 0.031	47	1.63	0.52	0.0515	X: -0.0047 Y: 0.0003	-0.0028
uav102	H: 0.007 V: 0.016	41	1.26	0.9	0.0554	X: 0.0098 Y: 0.0066	-0.0056
uav103	H: 0.019 V: 0.042	42	0.64	0.73	0.0533	X: -0.0015 Y: -0.0063	0.0071
uav104	H: 0.016 V: 0.035	39	1.44	0.57	0.0557	X: 0.0002 Y: -0.0017	0.0047
Global RMS			0.65	0.7	0.054	X: 0.0055 Y: 0.0047	0.0053
Median			0.64	0.73	0.0554	X: 0.0002 Y: 0.0003	0.0047

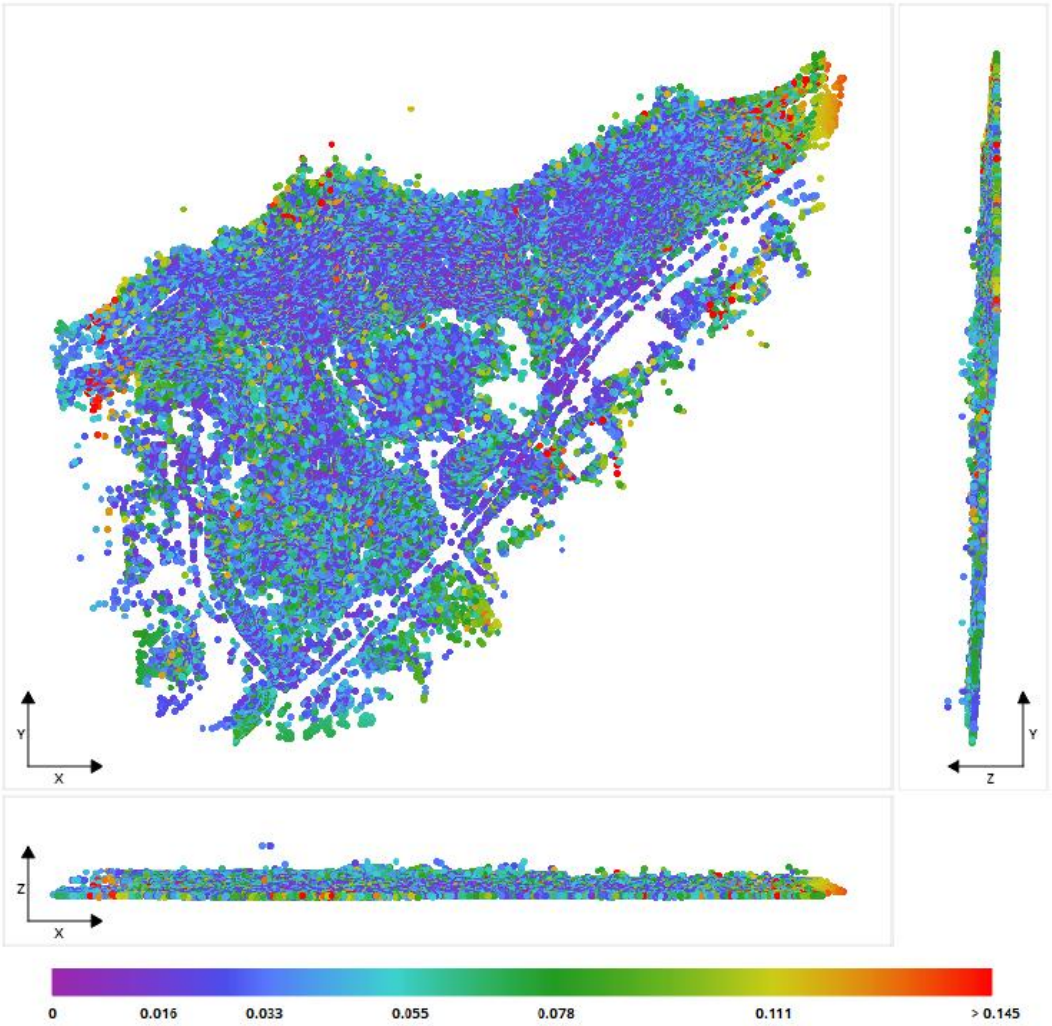

Figure D.1-52: Position uncertainties for EX02 (Northeast): Top view (XY plane), side view (ZY plane) and front view (XZ plane) displays of all tie points, with colours representing uncertainty in the individual point position. The values are in metres, with a minimum uncertainty of 0.0051 metres and a maximum of 0.6867 metres. The median position uncertainty equals 0.0335 metres.

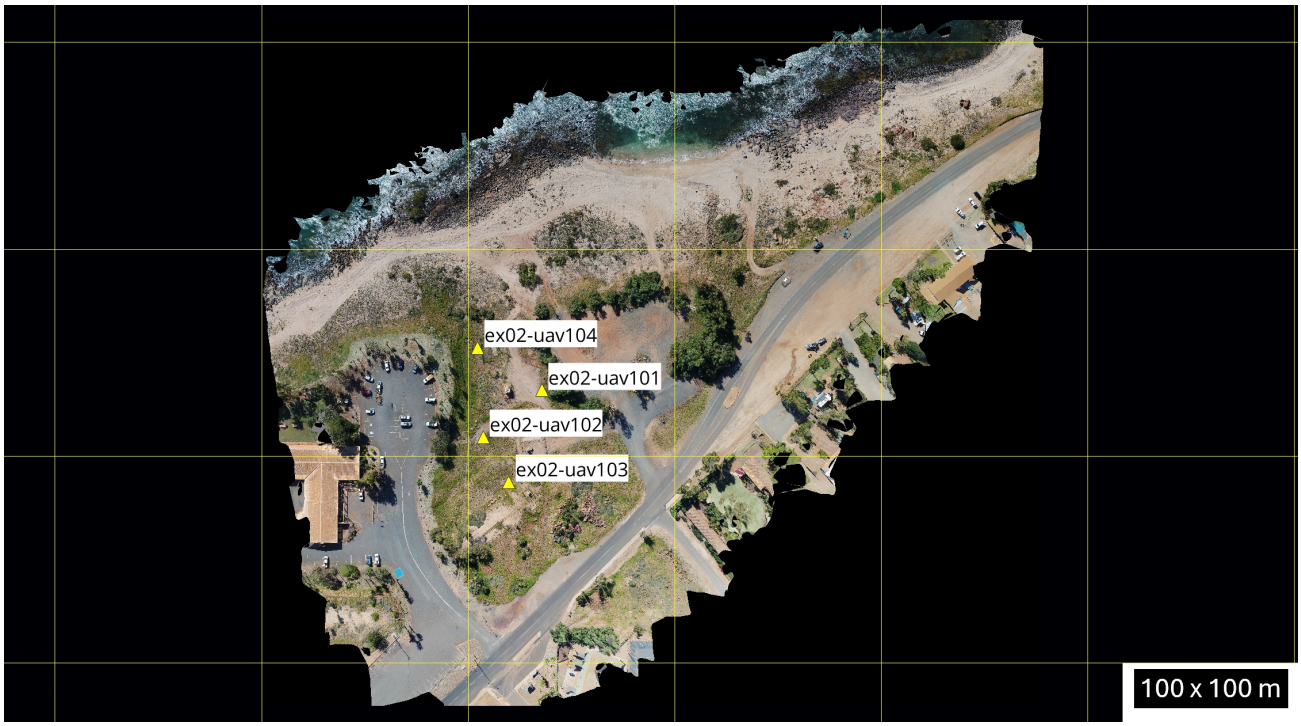

Figure D.1-53: Ortho-mosaic for EX02 (Northeast). Plotted with control points and 100 x 100 m grid spacing.

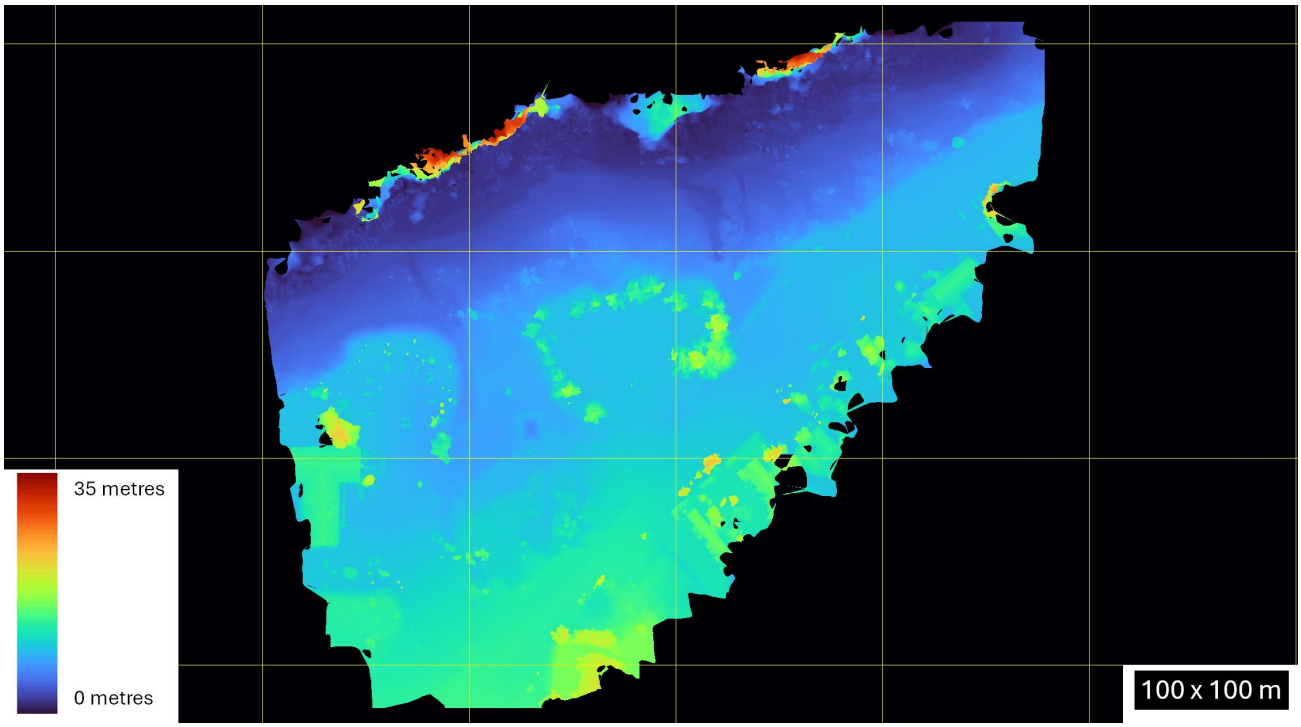

Figure D.1-54: DEM for EX02 (Northeast). Plotted with 100 x 100 m grid spacing.

EX02 (Southwest) site summary

Table D.1-55: EX02 (Southwest) site summary.

Drone	**Phantom 4 Pro**
Camera Model	DJI FC6310
Images	640/640
Ground Coverage	0.310 km^2
Average ground resolution	18.2752 mm/pixel
Geo referencing	10 control points (RTK)
Key Points	Median of 49869 key points per image
Tie Points	316108 points (median of 3137 points per photo)
Reprojection Errors (Median)	0.38 pixels
Reprojection Errors (RMS)	0.51 pixels
Distance to Rays (RMS)	0.644 metres

Table D.1-56: EX02 (Southwest) Position uncertainties (camera locations).

	X (metres)	**Y (metres)**	**Z (metres)**
Minimum	0.0017	0.0017	0.0008
Mean	0.0026	0.0027	0.0011
Maximum	0.0162	0.0128	0.0082

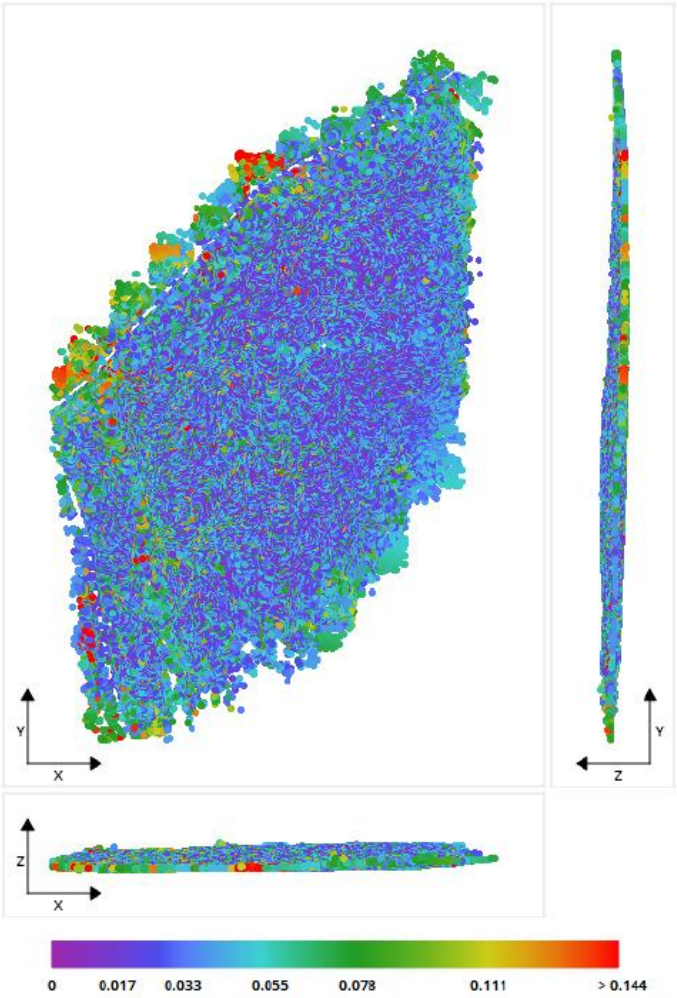

Figure D.1-55: Position uncertainties for EX02 (Southwest): Top view (XY plane), side view (ZY plane) and front view (XZ plane) displays of all tie points, with colours representing uncertainty in the individual point position. The values are in metres, with a minimum uncertainty of 0.0051 metres and a maximum of 0.6867 metres. The median position uncertainty equals 0.0335 metres.

Table D.1-57: EX02 (Southwest) control points.

Name	Accuracy (m)	Num of Photos	RMS of Reproject Error (pixels)	RMS of Dist to Rays (m)	3D Error (m)	Horizontal Errors (m)	Vertical Error (m)
uav01	H: 0.009 V: 0.019	14	0.57	0.0827	0.0064	X: -0.0021 Y: -0.0057	0.0019
uav02	H: 0.010 V: 0.019	24	0.48	0.0754	0.0038	X: 0.0008 Y: 0.0032	0.0018
uav03	H: 0.010 V: 0.017	29	0.47	0.0819	0.0022	X: 0.0014 Y: 0.0009	0.0015
uav04	H: 0.010 V: 0.016	14	0.51	0.0613	0.0042	X: 0.0030 Y: -0.0028	-0.0006
uav05	H: 0.011 V: 0.018	18	0.55	0.0783	0.0057	X: 0.0005 Y: 0.0027	-0.0049
uav06	H: 0.011 V: 0.017	21	0.46	0.0749	0.0064	X: 0.0002 Y: -0.0005	-0.0064
uav07	H: 0.009 V: 0.016	17	0.5	0.0654	0.0031	X: 0.0016 Y: -0.0018	-0.002
uav08	H: 0.016 V: 0.030	23	0.48	0.0697	0.0035	X: -0.0024 Y: 0.0021	-0.0015
uav09	H: 0.010 V: 0.021	28	0.52	0.0765	0.0038	X: -0.0036 Y: 0.0002	0.0011
uav10	H: 0.011 V: 0.028	25	0.42	0.0681	0.0034	X: 0.0019 Y: -0.0023	0.0017
Global RMS			0.5	0.0737	0.0045	X: 0.0020 Y: 0.0027	0.0029
Median			0.5	0.0754	0.0038	X: 0.0008 Y: 0.0002	0.0011

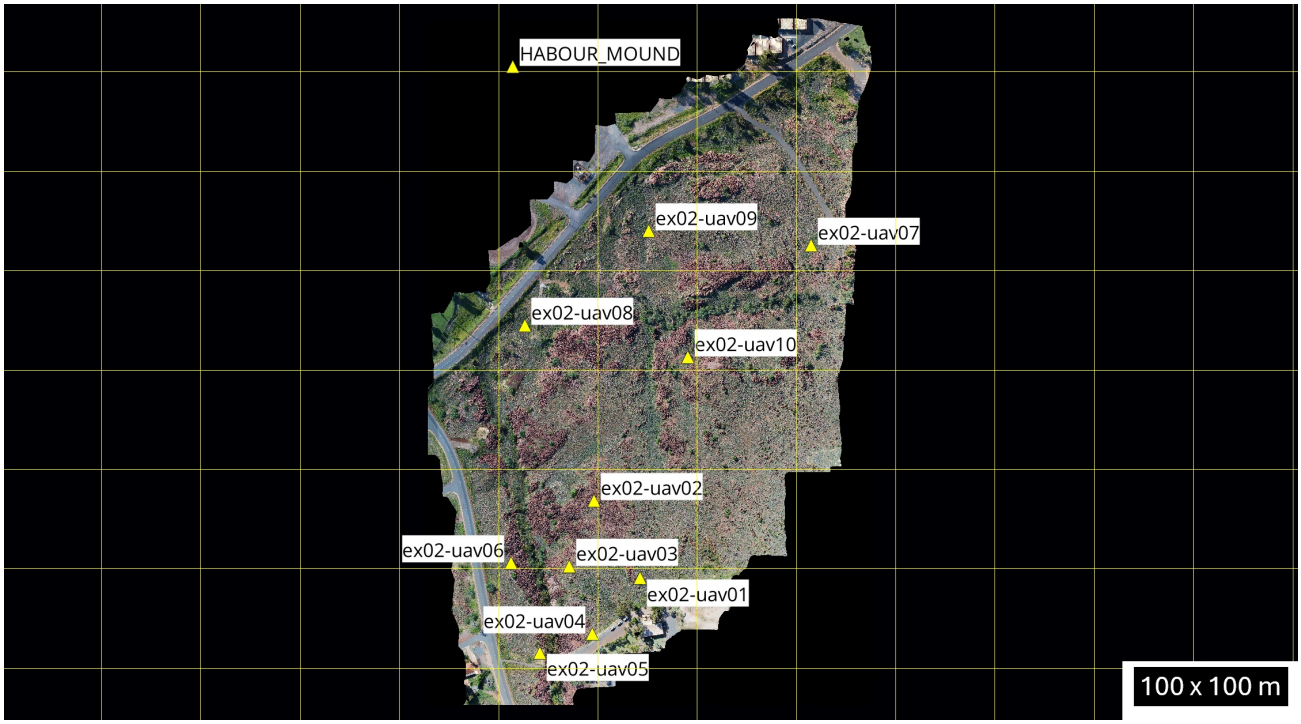

Figure D.1-56: Ortho-mosaic for EX02 (Southwest). Plotted with control points and 100 x 100 m grid spacing.

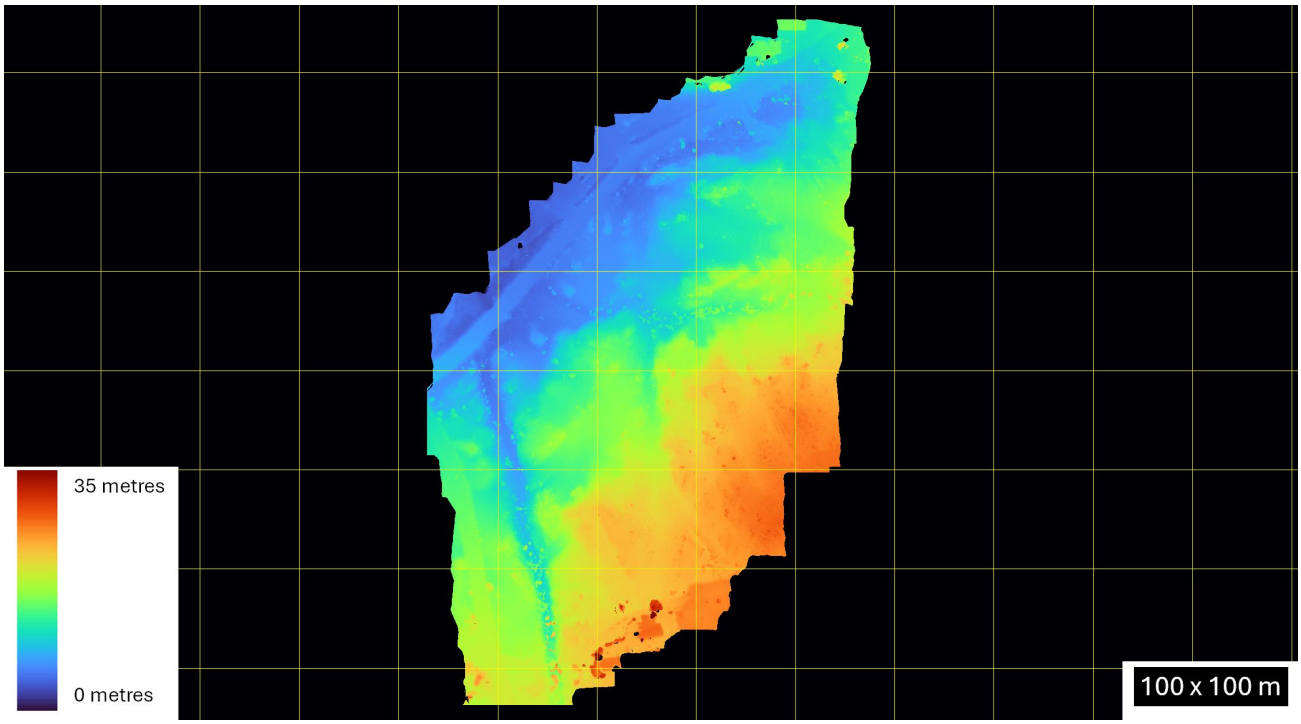

Figure D.1-57: DEM for EX02 (Southwest). Plotted with 100 x 100 m grid spacing.

EX03 site summary

Table D.1-58: EX03 site summary.

Drone	**Phantom 4 RTK**
Camera Model	DJI FC6310R
Images	651/651
Ground Coverage	0.326 km^2
Average ground resolution	19.5389 mm/pixel
Geo referencing	11 control points (RTK)
Key Points	Median of 31361 key points per image
Tie Points	320691 points (median of 3239 points per photo)
Reprojection Errors (Median)	0.40 pixels
Reprojection Errors (RMS)	0.55 pixels
Distance to Rays (RMS)	0.0256 metres

Table D.1-59: EX03 Position uncertainties (camera locations).

	X (metres)	**Y (metres)**	**Z (metres)**
Minimum	0.0013	0.0012	0.0006
Mean	0.0028	0.0023	0.001
Maximum	0.0059	0.0049	0.0027

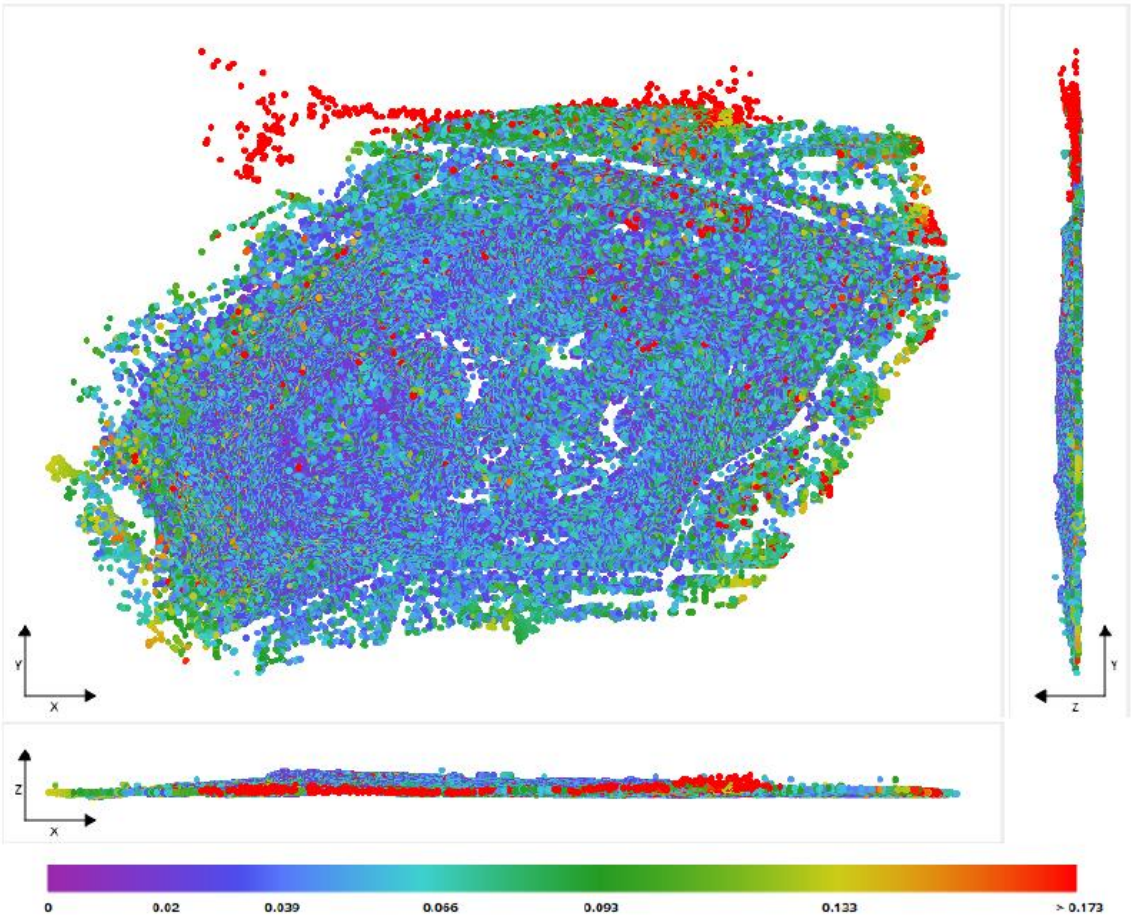

Figure D.1-58: Position uncertainties for EX03: Top view (XY plane), side view (ZY plane) and front view (XZ plane) displays of all tie points, with colours representing uncertainty in the individual point position. The values are in metres, with a minimum uncertainty of 0.0051 metres and a maximum of 0.6867 metres. The median position uncertainty equals 0.0335 metres.

Table D.1-60: EX03 control points.

Name	Accuracy (m)	Num of Photos	RMS of Reproject Error (pixels)	RMS of Dist to Rays (m)	3D Error (m)	Horizontal Errors (m)	Vertical Error (m)
uav01	H: 0.008 V: 0.016	63	0.78	0.0273	0.0134	X: 0.0058 Y: 0.0096	-0.0073
uav02	H: 0.008 V: 0.016	75	0.78	0.0266	0.0091	X: -0.0066 Y: 0.0025	-0.0054
uav05	H: 0.009 V: 0.016	81	0.82	0.0294	0.0114	X: -0.0111 Y: 0.0025	0.0012
uav07	H: 0.009 V: 0.018	64	0.67	0.0267	0.007	X: -0.0047 Y: -0.001	0.0052
uav09	H: 0.009 V: 0.018	71	0.82	0.0319	0.0098	X: 0.0076 Y: -0.006	-0.0015
uav10	H: 0.010 V: 0.020	79	0.79	0.0261	0.0107	X: 0.0101 Y: -0.0011	0.0035
uav11	H: 0.010 V: 0.020	64	0.61	0.0215	0.0046	X: 0.002; Y: 0.0039	0.0004
uav12	H: 0.006 V: 0.013	25	0.65	0.031	0.0062	X: 0.0013 Y: -0.0017	0.0058
uav13	H: 0.007 V: 0.014	26	0.72	0.0297	0.0134	X: 0.0004 Y: 0.0049	-0.0124
uav14	H: 0.007 V: 0.014	34	0.66	0.0487	0.011	X: -0.0032 Y: -0.0046	-0.0095
Global RMS			0.73	0.0307	0.0101	X: 0.0063 Y: 0.0046	0.0064
Median			0.78	0.0294	0.0107	X: 0.0013 Y: -0.0010	0.0004

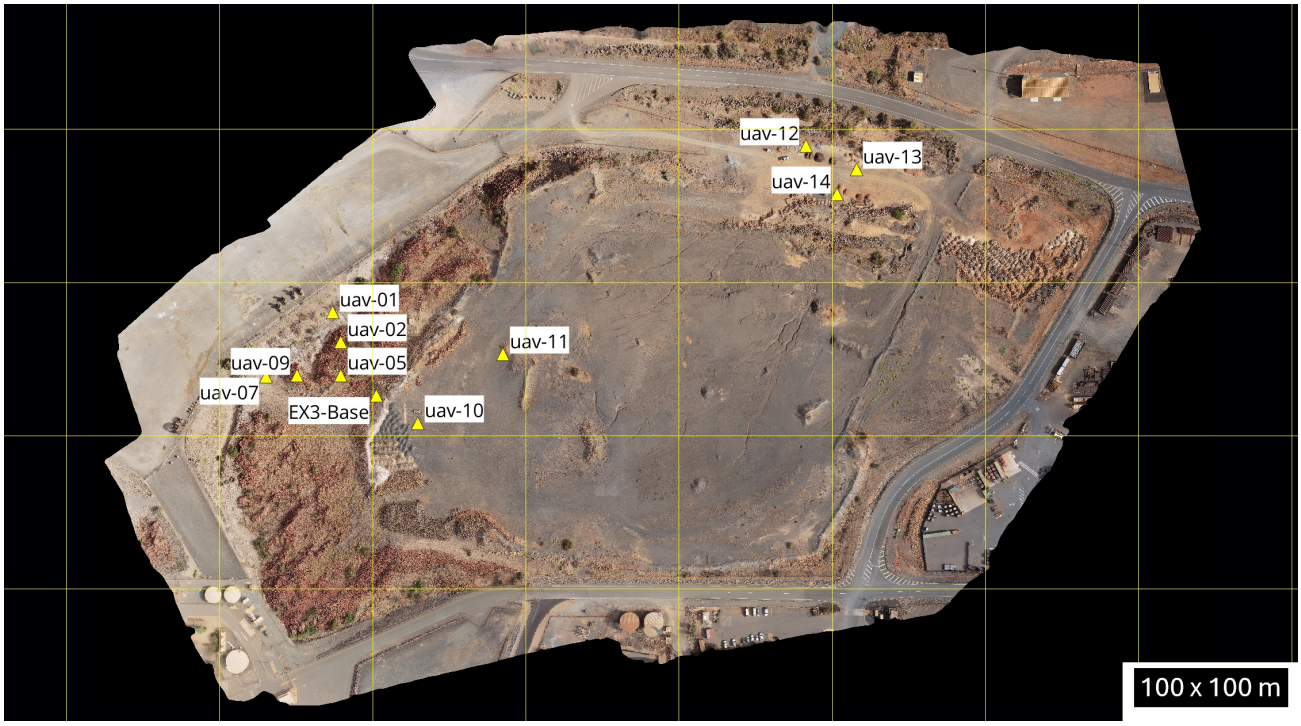

Figure D.1-59: Ortho-mosaic for EX03. Plotted with control points and 100 x 100 m grid spacing.

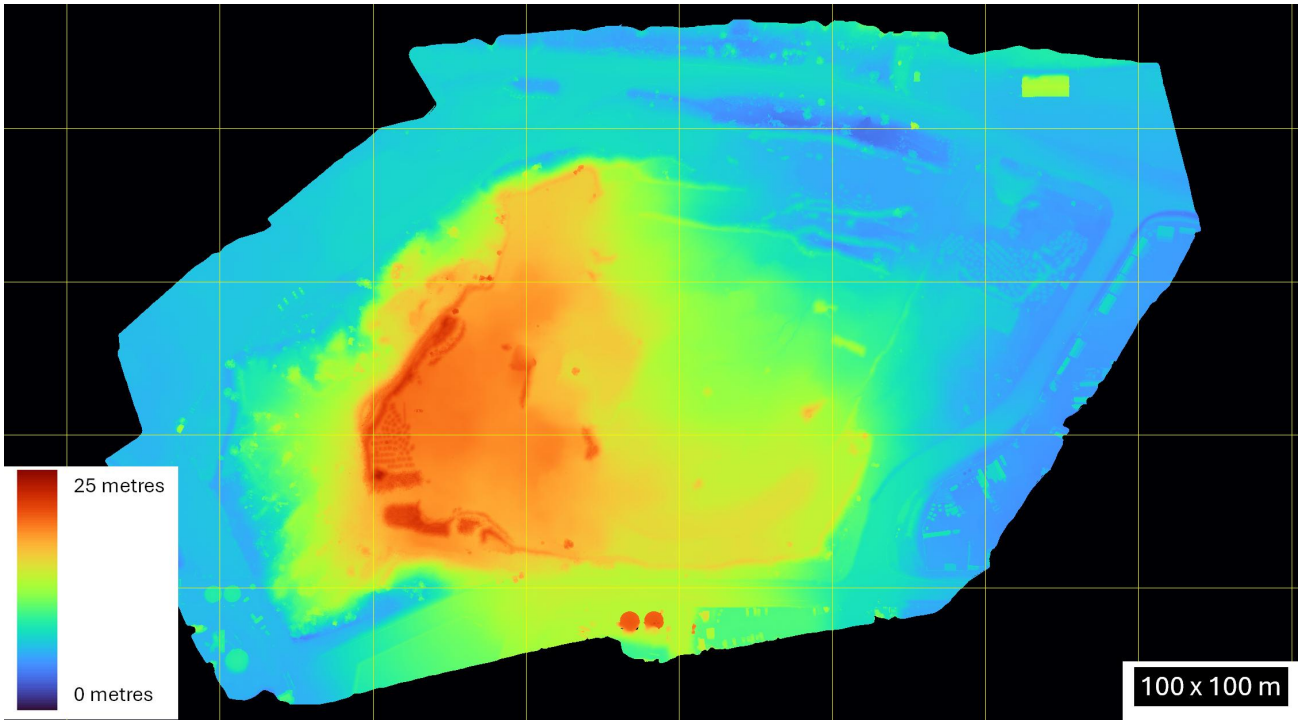

Figure D.1-60: DEM for EX03. Plotted with 100 x 100 m grid spacing.

EX04 site summary

Table D.1-61: EX04 site summary.

Drone	**Phantom 4 Pro**
Camera Model	DJI FC6310
Images	489/489
Ground Coverage	0.595 km^2
Average ground resolution	21.1398 mm/pixel
Geo referencing	6 control points (RTK)
Key Points	Median of 50655 key points per image
Tie Points	161987 points (median of 1294 points per photo)
Reprojection Errors (Median)	0.36 pixels
Reprojection Errors (RMS)	0.50 pixels
Distance to Rays (RMS)	0.0746 pixels

Table D.1-62: EX04 Position uncertainties (camera locations).

	X (metres)	**Y (metres)**	**Z (metres)**
Minimum	0.0027	0.0029	0.0012
Mean	0.0046	0.0052	0.0021
Maximum	0.0138	0.018	0.0096

Table D.1-63: EX04 control points.

Name	Accuracy (m)	Num of Photos	RMS of Reproject Error (pixels)	RMS of Dist to Rays (m)	3D Error (m)	Horizontal Errors (m)	Vertical Error (m)
uav01	H: 0.010 V: 0.006	7	0.52	0.0809	0.015	X: -0.0065 Y: -0.0007	-0.0135
uav05	H: 0.010 V: 0.008	21	0.83	0.0957	0.0133	X: -0.0132 Y: -0.0012	-0.0009
uav06	H: 0.010 V: 0.008	21	0.6	0.0892	0.0102	X: 0.0101 Y: 0.0004	0.0011
uav07	H: 0.010 V: 0.011	10	0.33	0.0581	0.0031	X: 0.0031 Y: 0.0003	-0.0002
uav08	H: 0.010 V: 0.008	6	0.57	0.0251	0.0072	X: 0.0031 Y: 0.0061	0.0022
uav09	H: 0.010 V: 0.010	9	0.43	0.0522	0.0044	X: -0.0007 Y: -0.0021	0.0039
Global RMS			0.57	0.0712	0.0099	X: 0.0075 Y: 0.0027	0.0058
Median			0.57	0.0809	0.0102	X: 0.0031 Y: 0.0003	0.0011

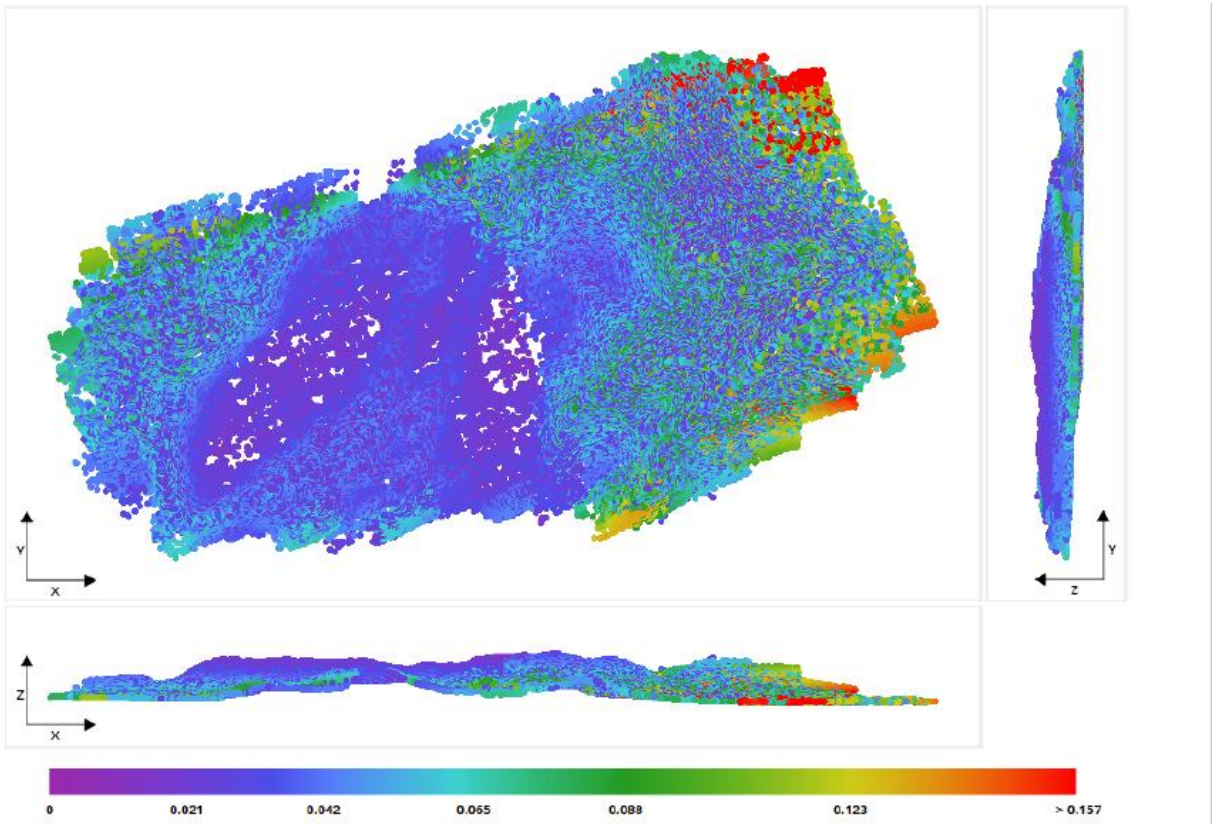

Figure D.1-61: Position uncertainties for EX04: Top view (XY plane), side view (ZY plane) and front view (XZ plane) displays of all tie points, with colours representing uncertainty in the individual point position. The values are in metres, with a minimum uncertainty of 0.0051 metres and a maximum of 0.6867 metres. The median position uncertainty equals 0.0335 metres.

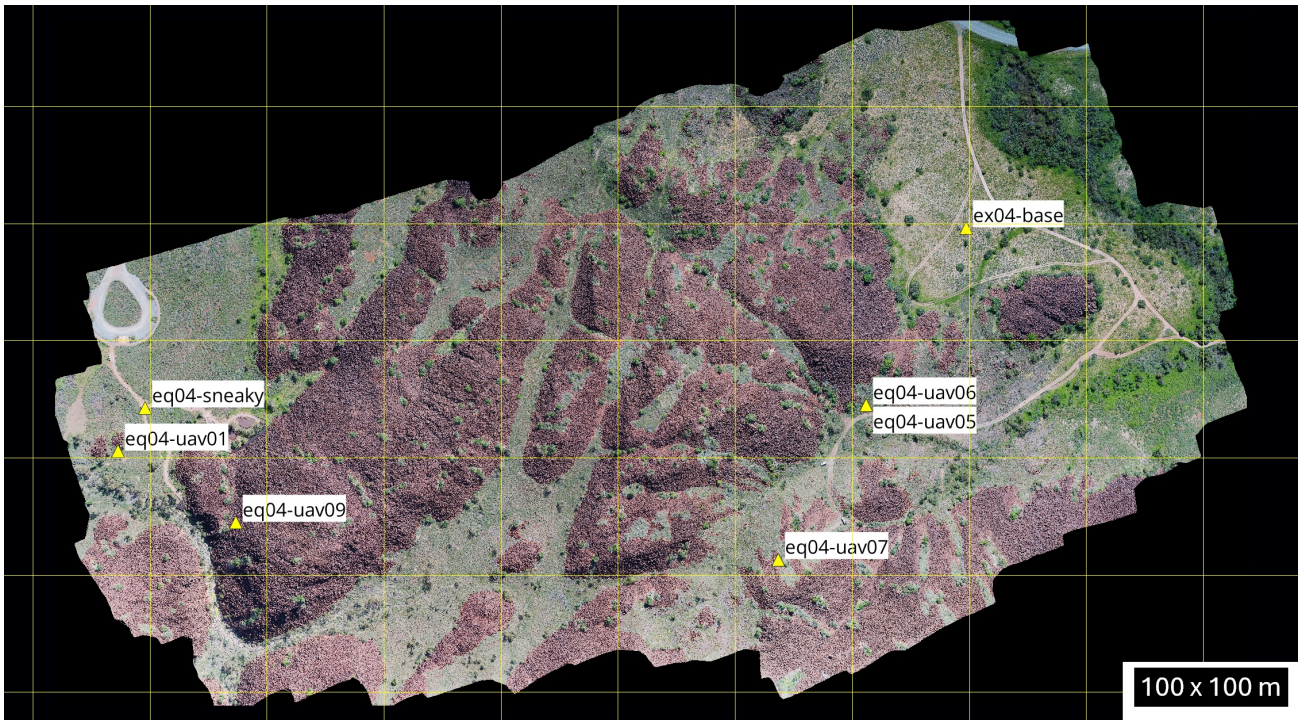

Figure D.1-62: Ortho-mosaic for EX04. Plotted with control points and 100 x 100 m grid spacing.

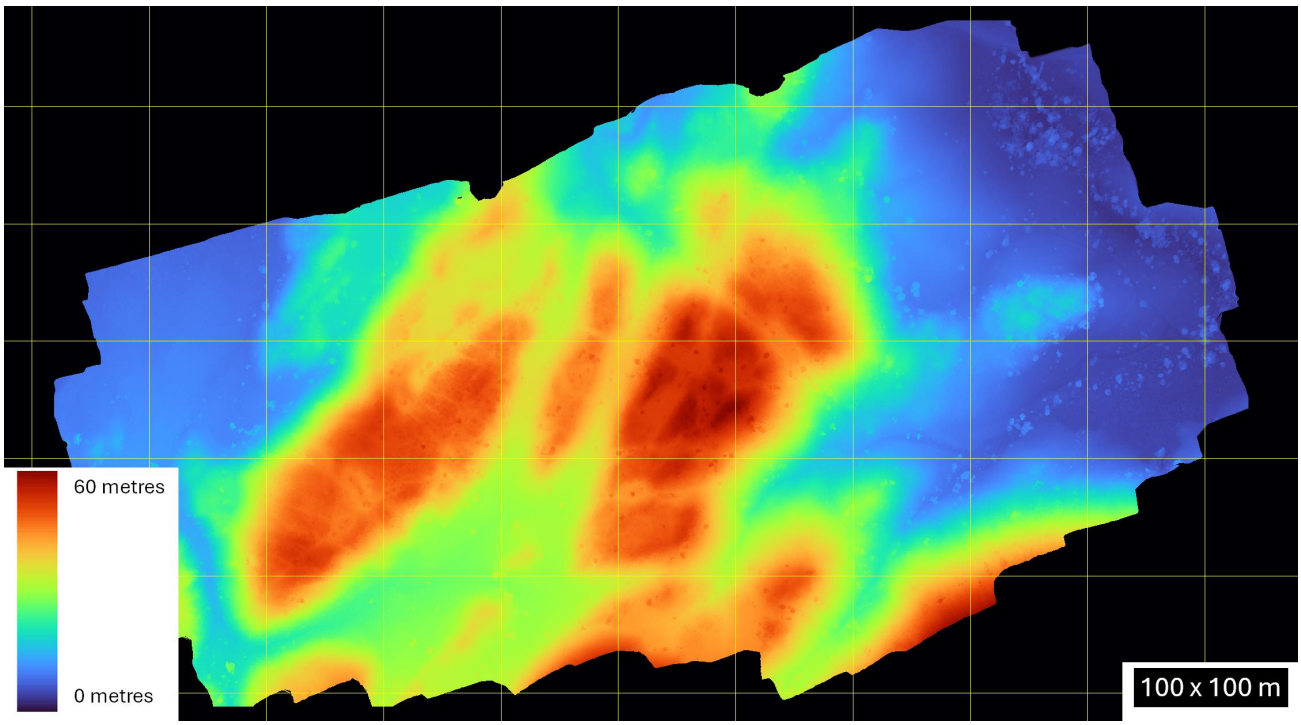

Figure D.1-63: DEM for EX04. Plotted with 100 x 100 m grid spacing.

EX05 site summary

Table D.1-64: EX05 site summary.

Drone	**Phantom 4 Pro**
Camera Model	DJI FC6310
Images	257/257
Ground Coverage	0.136 km^2
Average ground resolution	19.5331 mm/pixel
Geo referencing	6 control points (RTK)
Key Points	Median of 48015 key points per image
Tie Points	123414 points (median of 2800 points per photo)
Reprojection Errors (Median)	0.43 pixels
Reprojection Errors (RMS)	0.56 pixels
Distance to Rays (RMS)	0.0728 metres

Table D.1-65: EX05 Position uncertainties (camera locations).

	X (metres)	**Y (metres)**	**Z (metres)**
Minimum	0.0019	0.0017	0.0008
Mean	0.0028	0.0029	0.0013
Maximum	0.0128	0.0141	0.0109

Table D.1-66: EX05 control points.

Name	Accuracy (m)	Num of Photos	RMS of Reproject Error (pixels)	RMS of Dist to Rays (m)	3D Error (m)	Horizontal Errors (m)	Vertical Error (m)
uav06	H: 0.012 V: 0.031	26	0.84	0.0906	0.0123	X: 0.0013 Y: 0.0117	-0.0034
uav10	H: 0.009 V: 0.022	37	0.7	0.0846	0.0118	X: -0.0023 Y: -0.0098	0.006
uav12	H: 0.010 V: 0.022	23	0.61	0.0592	0.0076	X: -0.0061 Y: -0.0044	0
d141	H: 0.010 V: 0.023	15	0.65	0.0616	0.0067	X: 0.0025 Y: -0.0001	-0.0063
uav31	H: 0.009 V: 0.020	46	0.65	0.0984	0.0092	X: 0.0077 Y: 0.0037	0.0032
uav32	H: 0.009 V: 0.019	42	0.49	0.0854	0.005	X: -0.0041 Y: -0.0027	-0.0008
Global RMS			0.67	0.0813	0.0091	X: 0.0045 Y: 0.0068	0.004
Median			0.65	0.0854	0.0092	X: 0.0013 Y: -0.0001	0

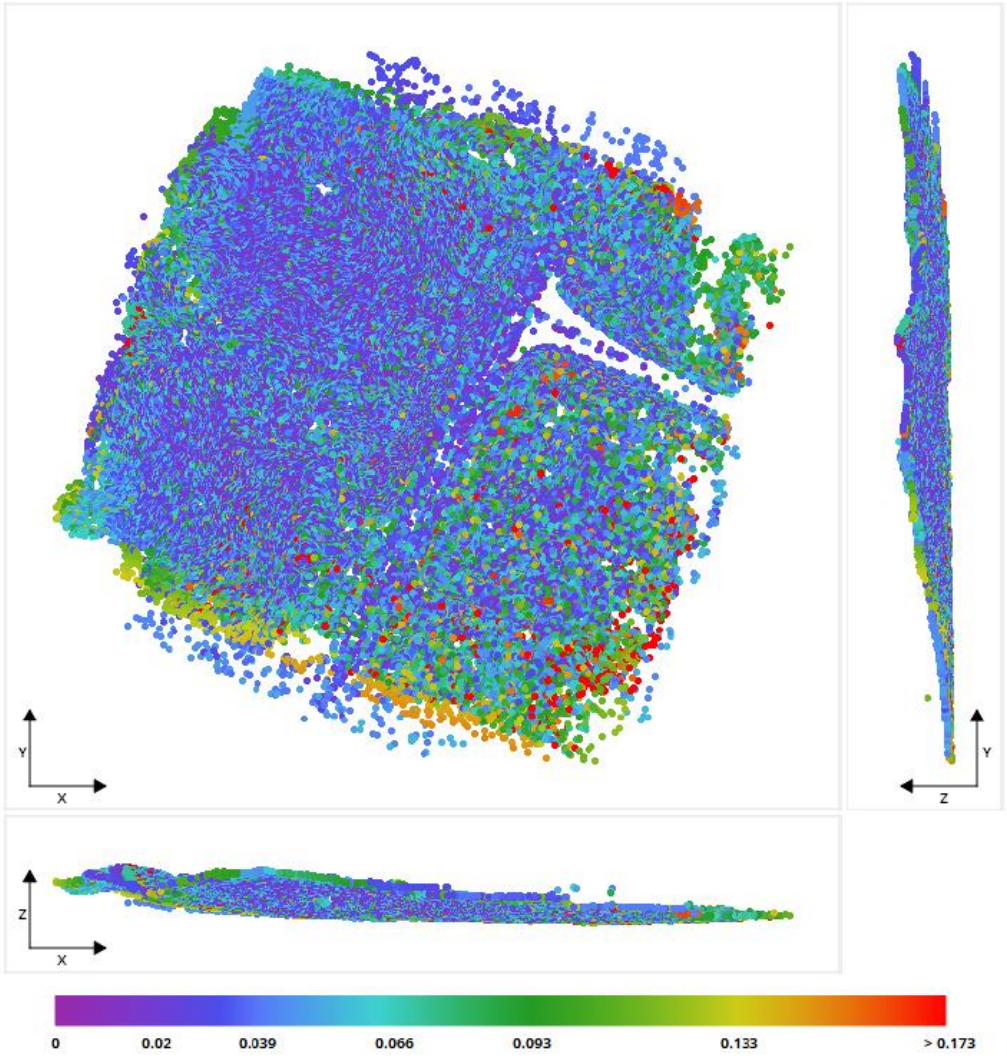

Figure D.1-64: Position uncertainties for EX05: Top view (XY plane), side view (ZY plane) and front view (XZ plane) displays of all tie points, with colours representing uncertainty in the individual point position. The values are in metres, with a minimum uncertainty of 0.0051 metres and a maximum of 0.6867 metres. The median position uncertainty equals 0.0335 metres.

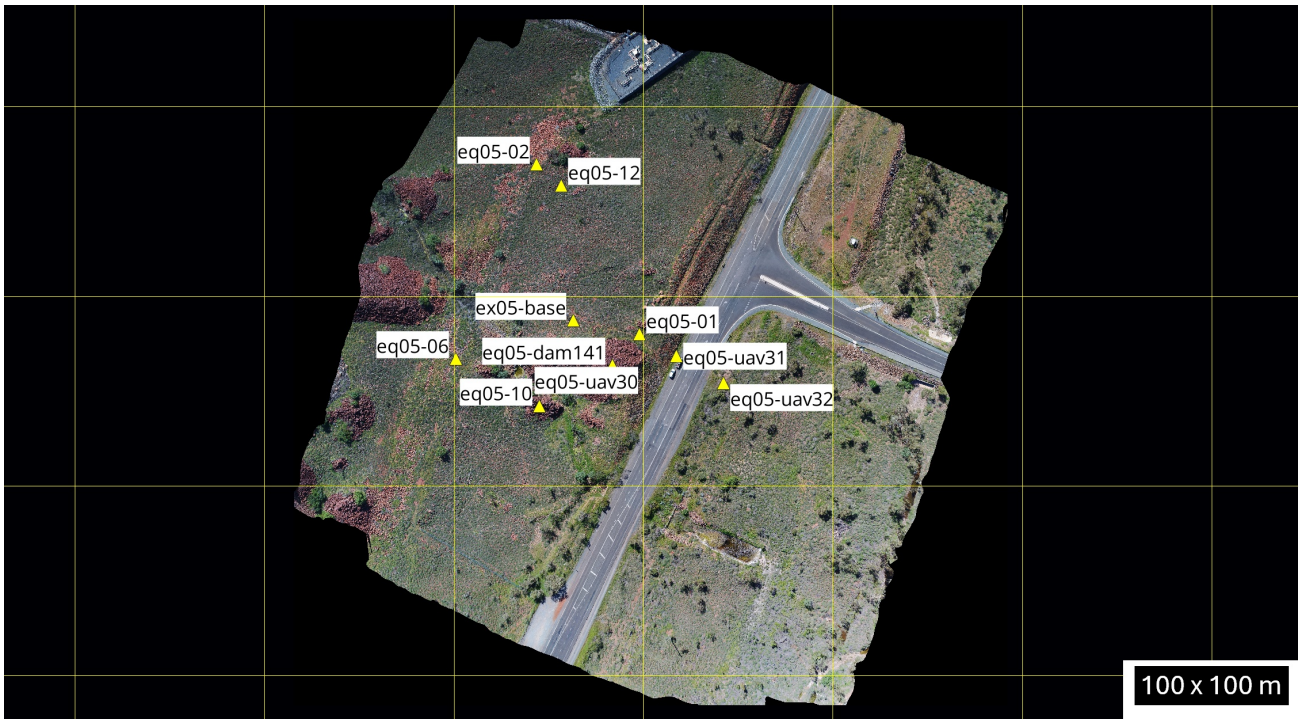

Figure D.1-65: Ortho-mosaic for EX05. Plotted with control points and 100 x 100 m grid spacing.

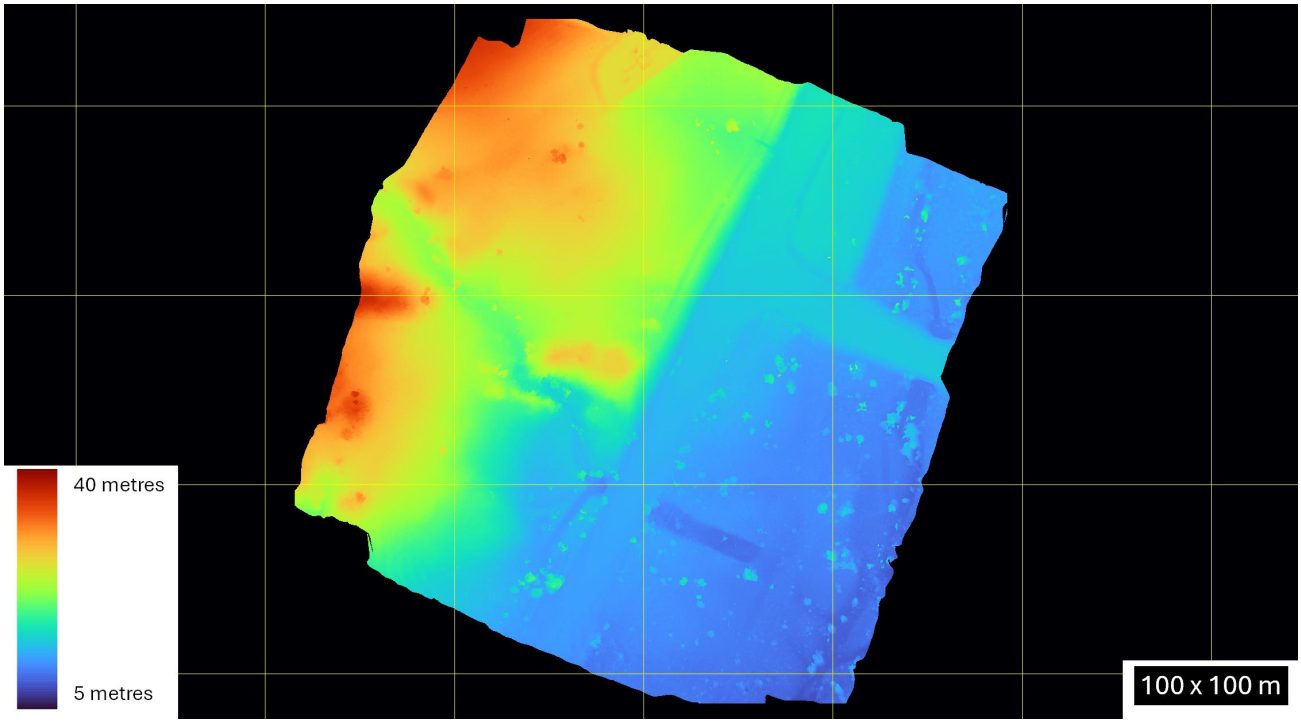

Figure D.1-66: DEM for EX05. Plotted with 100 x 100 m grid spacing.

EX06 site summary

Table D.1-67: EX06 site summary.

Drone	**Phantom 4 Pro**
Camera Model	DJI FC6310
Images	762/862
Ground Coverage	0.756 km^2
Average ground resolution	16.78875 mm/pixel
Geo referencing	8 control points (RTK)
Key Points	Median of 49740 key points per image
Tie Points	210933 points (median of 1255 points per photo)
Reprojection Errors (Median)	0.38 pixels
Reprojection Errors (RMS)	0.56 pixels
Distance to Rays (RMS)	0.06143 metres

Table D.1-68: EX06 Position uncertainties (camera locations).

	X (metres)	**Y (metres)**	**Z (metres)**
Minimum	0	0	0
Mean	0.0043	0.0045	0.002
Maximum	0.1816	0.171	0.0988

Table D.1-69: EX06 control points.

Name	Accuracy (m)	Num of Photos	RMS of Reproject Error (pixels)	RMS of Dist to Rays (m)	3D Error (m)	Horizontal Errors (m)	Vertical Error (m)
uav01	H: 0.015 V: 0.032	22	0.62	0.078	0.0066	X: -0.0013 Y: 0.0059	-0.0026
uav02	H: 0.013 V: 0.030	22	0.98	0.074	0.0186	X: 0.0185 Y: 0.0006	-0.0018
uav03	H: 0.019 V: 0.041	18	1.28	0.0824	0.0277	X: -0.0120 Y: -0.0109	0.0159
uav04	H: 0.014 V: 0.028	29	0.48	0.0918	0.0077	X: -0.0360 Y: -0.0019	0.0064
uav05	H: 0.014 V: 0.032	22	0.66	0.0852	0.0143	X: 0.0071 Y: -0.0044	-0.0116
uav06	H: 0.025 V: 0.056	13	0.56	0.0586	0.0033	X: -0.0023 Y: 0.0022	-0.0008
uav07	H: 0.018 V: 0.035	12	0.8	0.0683	0.017	X: -0.0070 Y: 0.0012	0.0154
uav08	H: 0.013 V: 0.023	24	0.8	0.08	0.0124	X: 0.0118 Y: 0.0026	-0.0028
Global RMS			0.81	0.0779	0.0153	X: 0.0112 Y: 0.0049	0.0092
Median			0.8	0.08	0.0143	X: -0.0013 Y: 0.0012	-0.0008

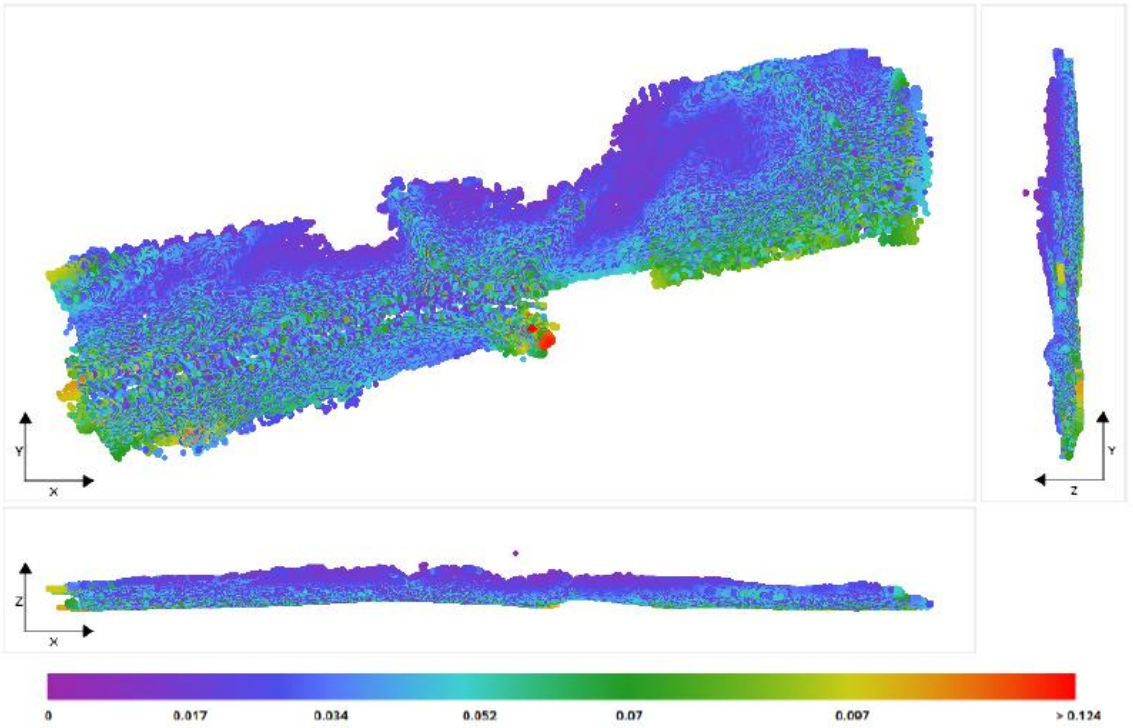

Figure D.1-67: Position uncertainties for EX06: Top view (XY plane), side view (ZY plane) and front view (XZ plane) displays of all tie points, with colours representing uncertainty in the individual point position. The values are in metres, with a minimum uncertainty of 0.0051 metres and a maximum of 0.6867 metres. The median position uncertainty equals 0.0335 metres.

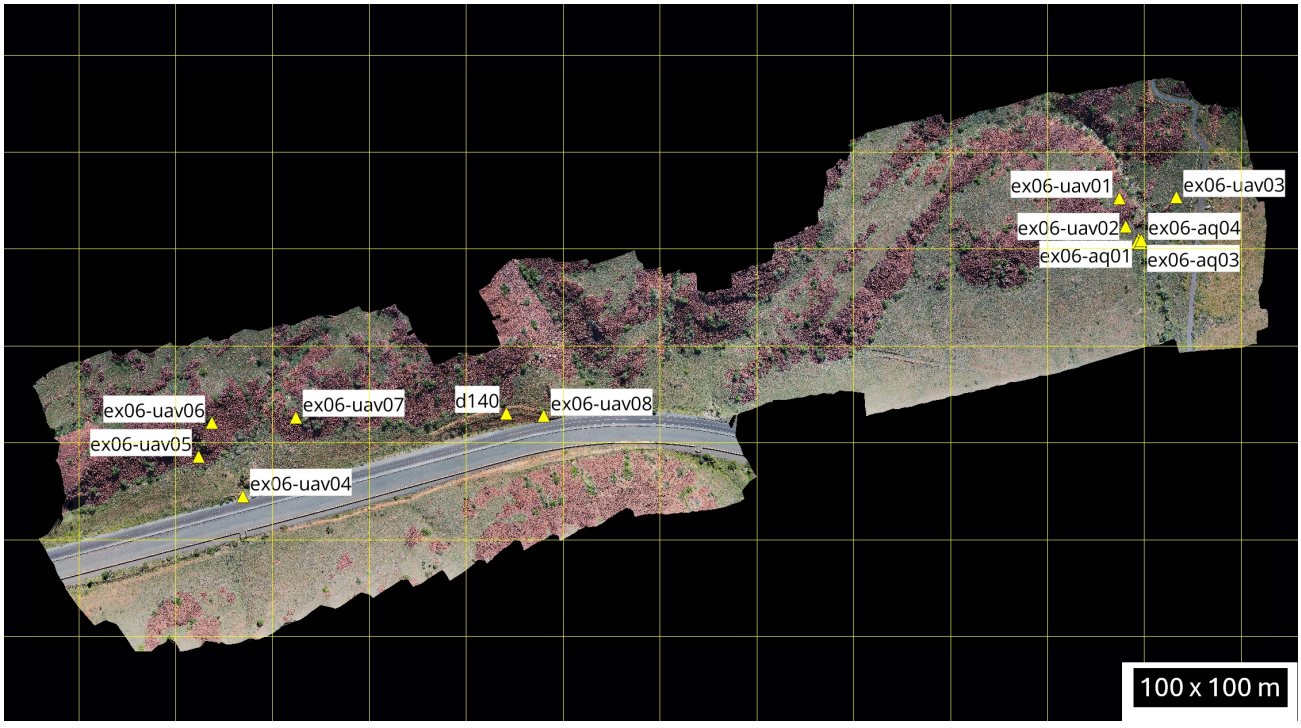

Figure D.1-68: Ortho-mosaic for EX06. Plotted with control points and 100 x 100 m grid spacing.

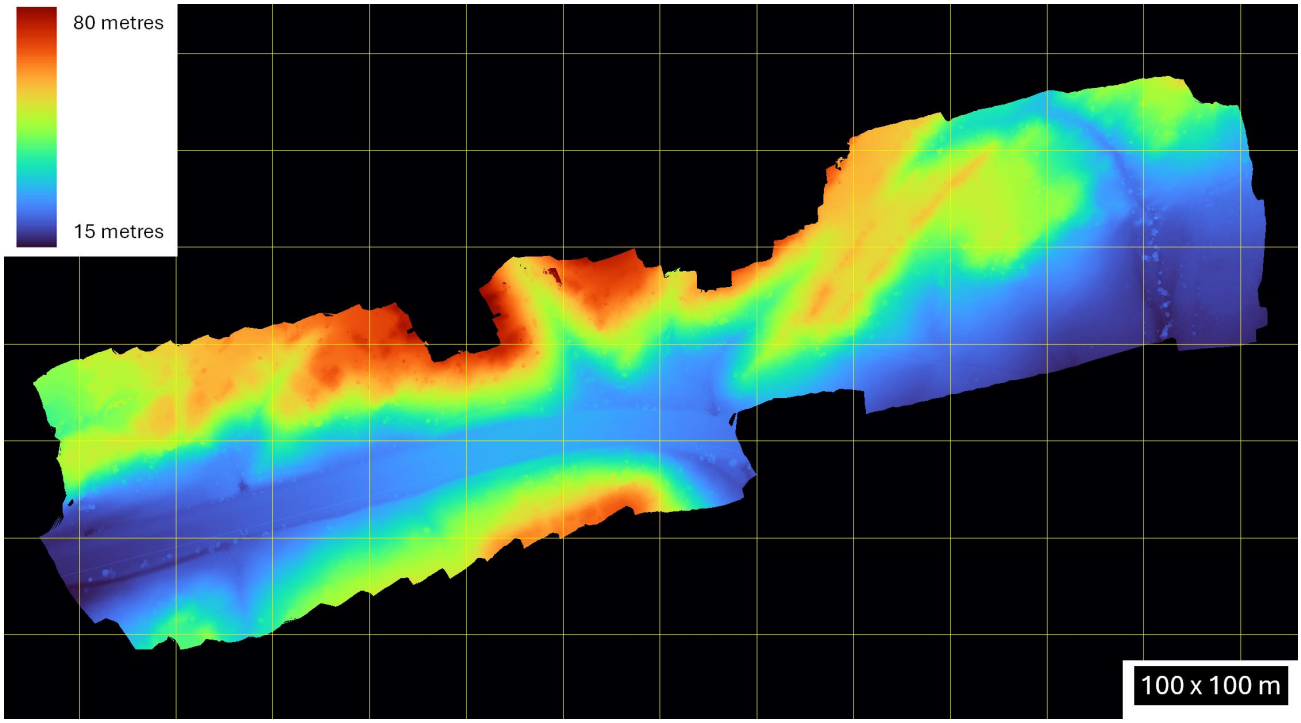

Figure D.1-69: DEM for EX06. Plotted with 100 x 100 m grid spacing.

EX07 site summary

Table D.1-70: EX07 site summary.

Drone	**Phantom 4 RTK**
Camera Model	DJI FC6310R
Images	408/408
Ground Coverage	0.182 km^2
Average ground resolution	20.0146 mm/pixel
Geo referencing	7 control points (RTK)
Key Points	Median of 44886 key points per image
Tie Points	168475 points (median of 2570 points per photo)
Reprojection Errors (Median)	0.43 pixels
Reprojection Errors (RMS)	0.56 pixels
Distance to Rays (RMS)	0.0275 metres

Table D.1-71: EX07 Position uncertainties (camera locations).

	X (metres)	**Y (metres)**	**Z (metres)**
Minimum	0.0016	0.0017	0.0009
Mean	0.0021	0.0022	0.0015
Maximum	0.0047	0.0042	0.0032

Table D.1-72: EX07 control points.

Name	Accuracy (m)	Num of Photos	RMS of Reproject Error (pixels)	RMS of Dist to Rays (m)	3D Error (m)	Horizontal Errors (m)	Vertical Error (m)
uav01	H: 0.009 V: 0.026	113	0.62	0.0239	0.0106	X: -0.0004 Y: -0.0080	0.007
uav02	H: 0.010 V: 0.027	91	0.43	0.0205	0.0053	X: -0.0022 Y: -0.0010	-0.0047
uav03	H: 0.010 V: 0.028	93	0.5	0.0295	0.0062	X: 0.0037 Y: 0.0043	-0.0027
uav04	H: 0.011 V: 0.030	83	0.58	0.0314	0.0095	X: -0.0088 Y: 0.0034	-0.0014
uav05	H: 0.012 V: 0.031	80	0.6	0.0297	0.0087	X: 0.0044 Y: 0.0019	-0.0073
uav06	H: 0.012 V: 0.033	97	0.63	0.0258	0.0086	X: 0.0059 Y: -0.0053	0.0033
uav07	H: 0.013 V: 0.034	81	0.48	0.0249	0.0056	X: -0.0028 Y: 0.0035	-0.0033
Global RMS			0.55	0.0268	0.008	X: 0.0047 Y: 0.0044	0.0047
Median			0.58	0.0258	0.0086	X: -0.0004 Y: 0.0019	-0.0027

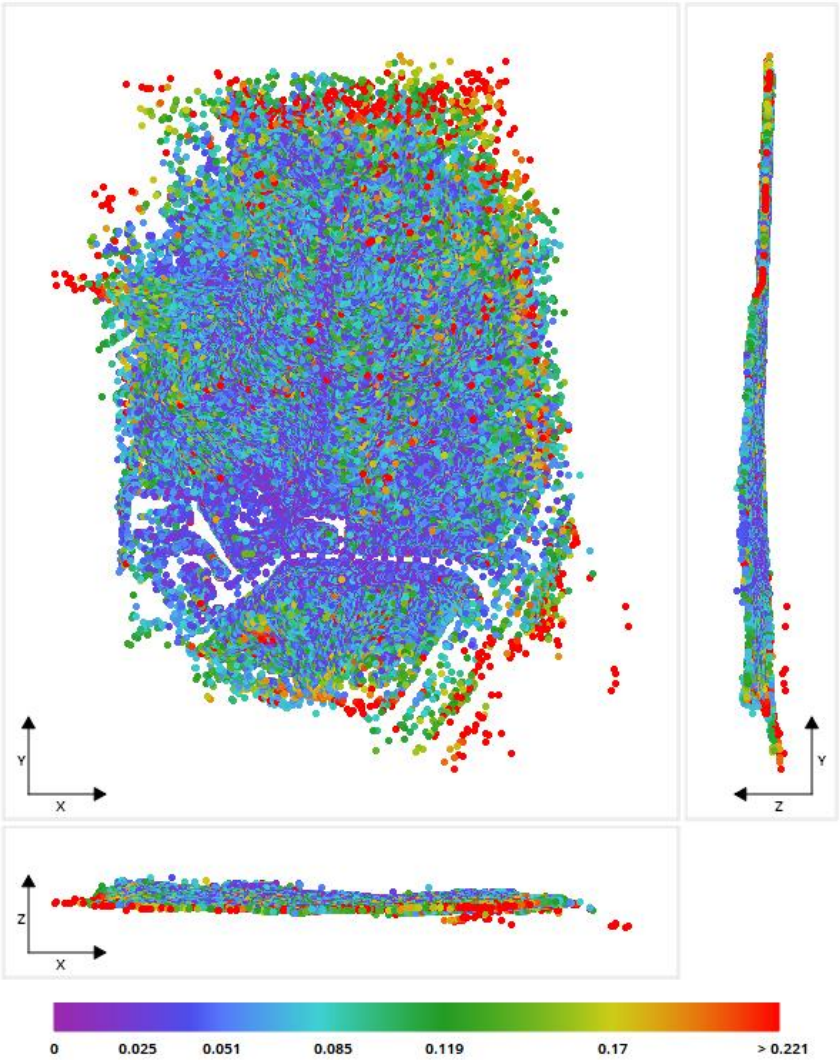

Figure D.1-70: Position uncertainties for EX07: Top view (XY plane), side view (ZY plane) and front view (XZ plane) displays of all tie points, with colours representing uncertainty in the individual point position. The values are in metres, with a minimum uncertainty of 0.0051 metres and a maximum of 0.6867 metres. The median position uncertainty equals 0.0335 metres.

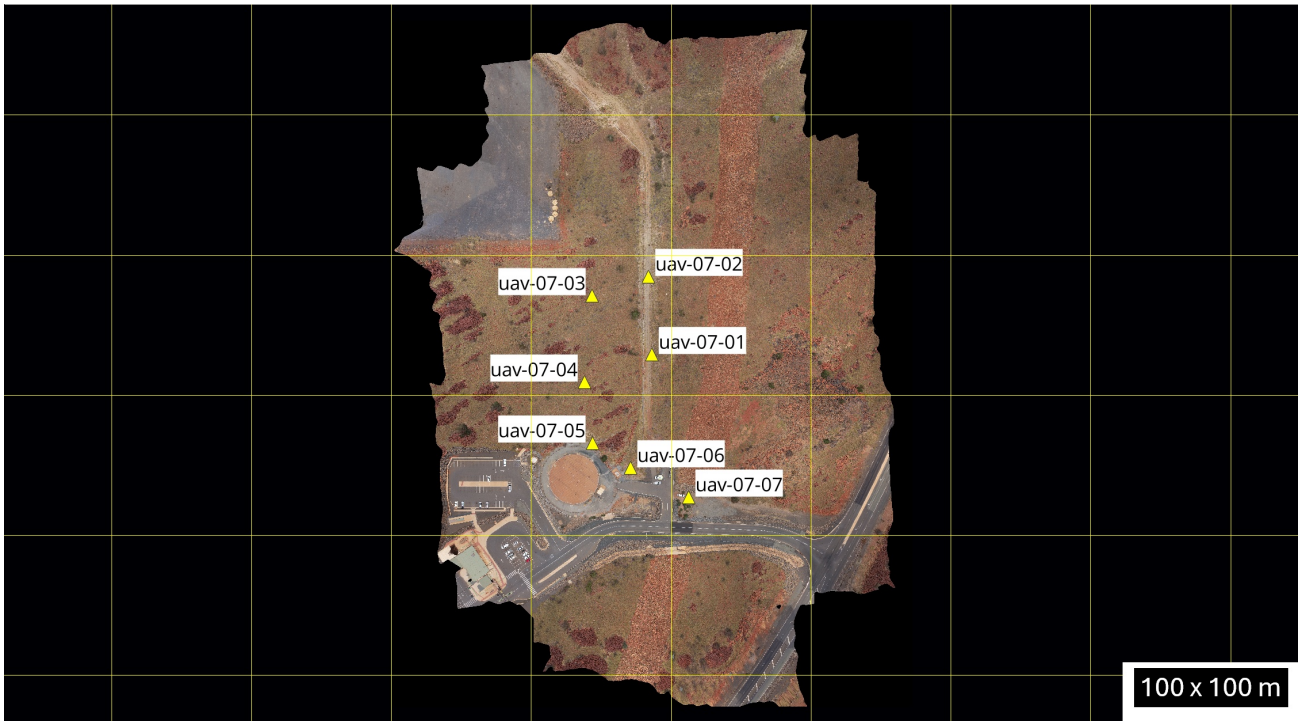

Figure D.1-71: Ortho-mosaic for EX07. Plotted with control points and 100 x 100 m grid spacing.

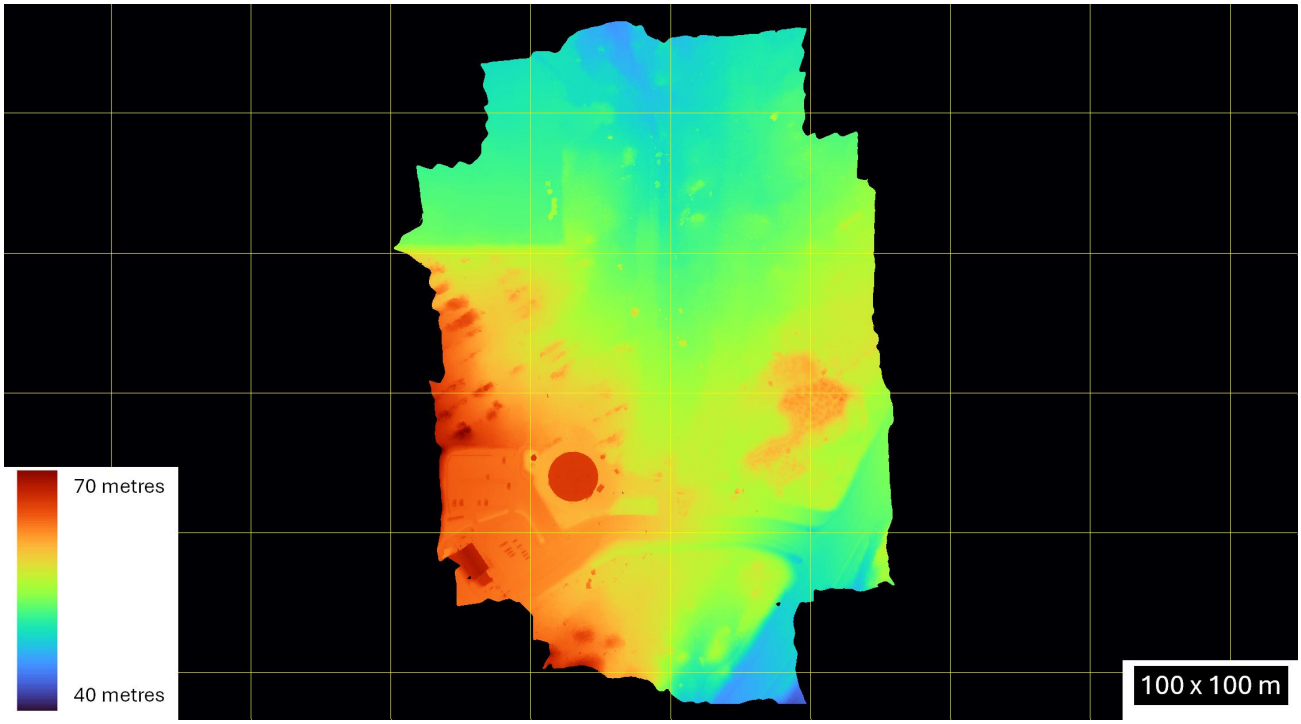

Figure D.1-72: DEM for EX07. Plotted with 100 x 100 m grid spacing.

EX08 site summary

Table D.1-73: EX08 site summary.

Drone	**Phantom 4 Pro, Phantom 4 RTK**
Camera Model	DJI FC6310, DJI FC6310R
Images	1088/1167
Ground Coverage	1.056 km^2
Average ground resolution	21.762 mm/pixel
Geo referencing	12 control points (RTK)
Key Points	Median of 47050 key points per image
Tie Points	409195 points (median of 1700 points per photo)
Reprojection Errors (Median)	0.36 pixels
Reprojection Errors (RMS)	0.50 pixels
Distance to Rays (RMS)	0.0575 metres

Table D.1-74: EX08 Position uncertainties (camera locations).

	X (metres)	**Y (metres)**	**Z (metres)**
Minimum	0.0015	0.0017	0.0009
Mean	0.0061	0.0047	0.0018
Maximum	1.8947	0.9225	0.2311

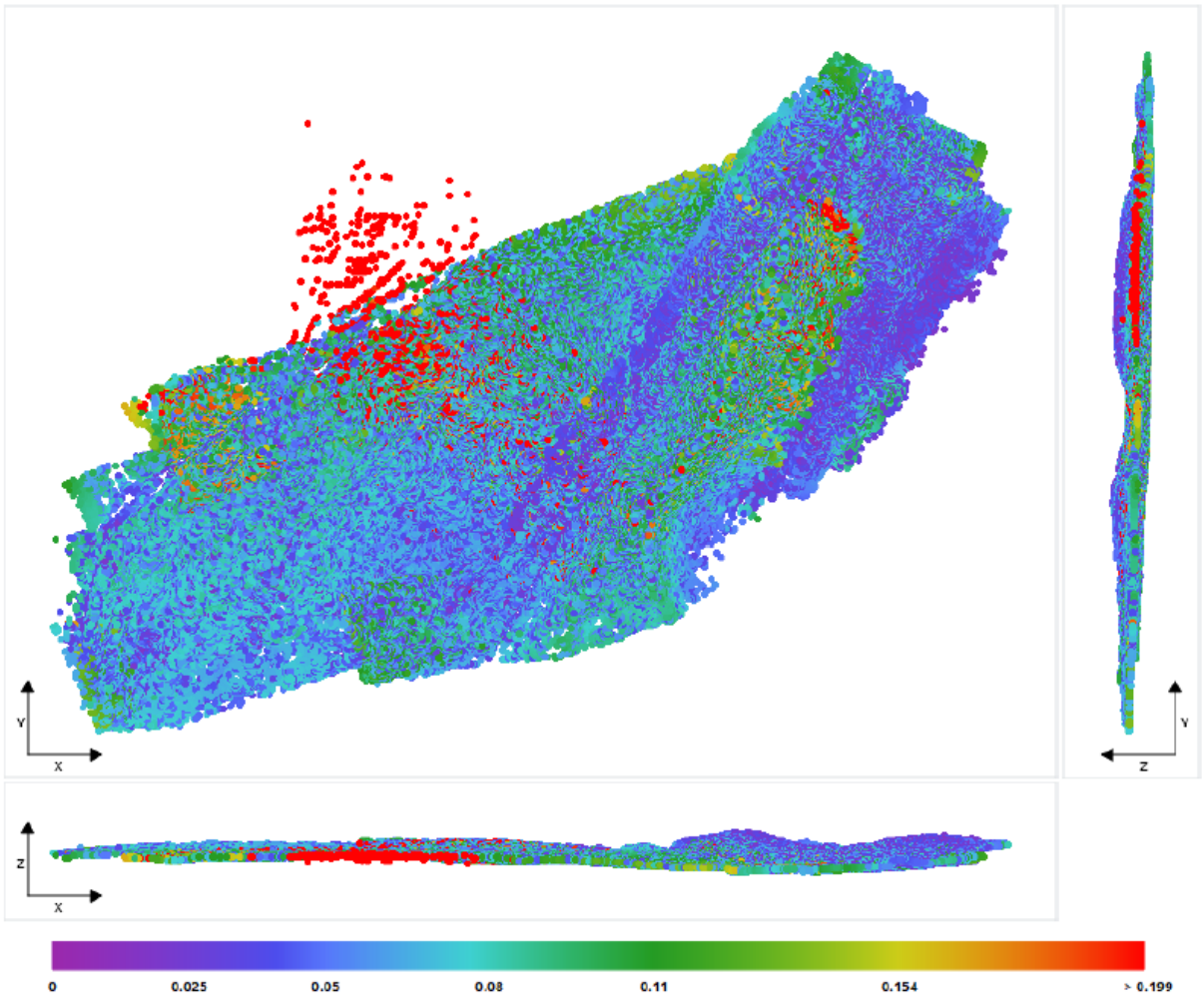

Figure D.1-73: Position uncertainties for EX08: Top view (XY plane), side view (ZY plane) and front view (XZ plane) displays of all tie points, with colours representing uncertainty in the individual point position. The values are in metres, with a minimum uncertainty of 0.0051 metres and a maximum of 0.6867 metres. The median position uncertainty equals 0.0335 metres.

Table D.1-75: EX08 control points.

Name	Accuracy (m)	Num of Photos	RMS of Reproject Error (pixels)	RMS of Dist to Rays (m)	3D Error (m)	Horizontal Errors (m)	Vertical Error (m)
uav11	H: 0.007 V: 0.013	26	0.61	0.0402	0.0017	X: 0.0012 Y: 0.0012	0.0003
uav13	H: 0.007 V: 0.012	13	0.42	0.0175	0.005	X: -0.0030 Y: -0.0005	-0.004
uav14	H: 0.010 V: 0.019	24	0.43	0.0202	0.0039	X: 0.0025 Y: -0.0020	0.0024
uav16	H: 0.008 V: 0.014	10	0.55	0.0343	0.0043	X: -0.0001 Y: 0.0012	-0.0041
uav02	H: 0.010 V: 0.024	29	0.46	0.0766	0.0087	X: 0.0030 Y: 0.0048	-0.0066
uav03	H: 0.012 V: 0.027	28	0.54	0.0729	0.0061	X: -0.0001 Y: -0.0057	0.0021
uav04	H: 0.012 V: 0.029	39	0.5	0.0807	0.0057	X: -0.0004 Y: -0.0017	0.0054
uav05	H: 0.012 V: 0.030	38	0.56	0.0862	0.0042	X: -0.0016 Y: 0.0034	-0.0019
uav06	H: 0.016 V: 0.041	21	0.52	0.0711	0.0073	X: -0.0005 Y: 0.0004	0.0073
uav07	H: 0.011 V: 0.030	14	0.83	0.0733	0.0083	X: -0.0044 Y: -0.0067	0.0021
uav08	H: 0.011 V: 0.030	35	0.51	0.0796	0.0049	X: -0.0034 Y: 0.0035	-0.0003
uav09	H: 0.013 V: 0.037	34	0.49	0.0964	0.0047	X: 0.0046 Y: -0.0001	-0.0005
Global RMS			0.55	0.0675	0.0057	X: 0.0026 Y: 0.0033	0.0038
Median			0.52	0.0733	0.005	X: -0.0001 Y: 0.0004	0.0003

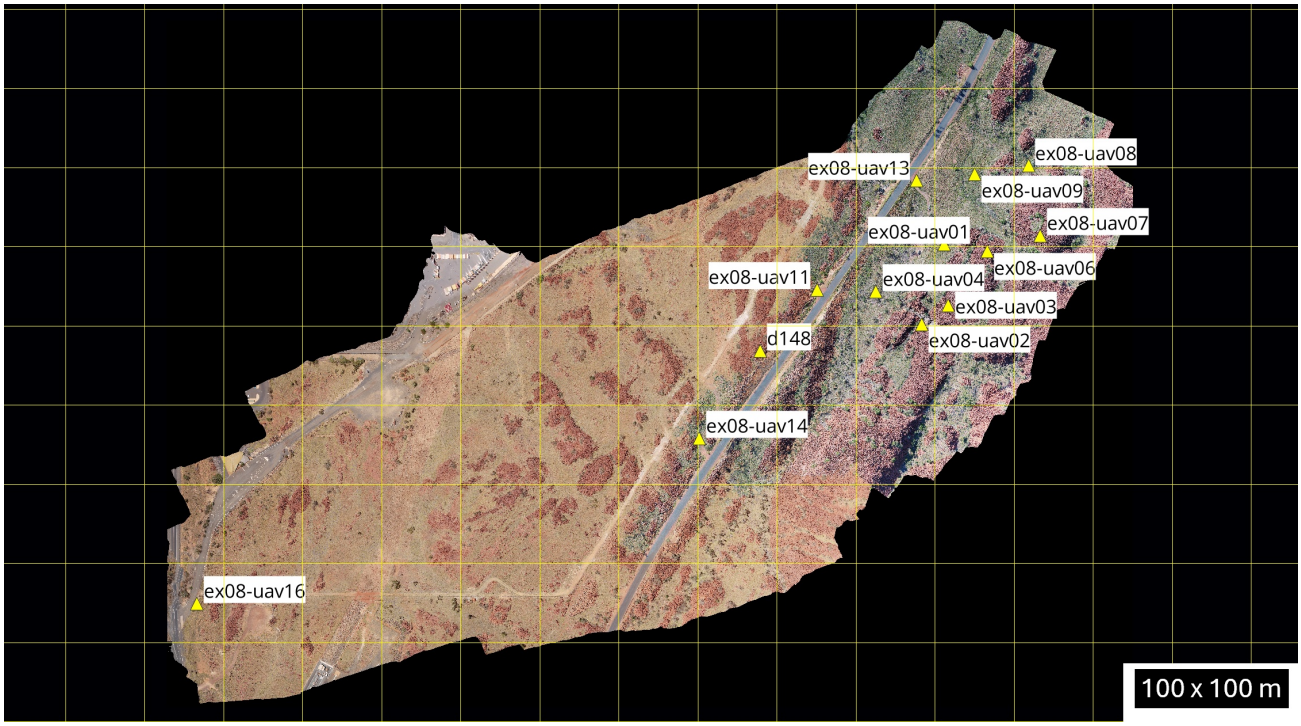

Figure D.1-74: Ortho-mosaic for EX08. Plotted with control points and 100 x 100 m grid spacing.

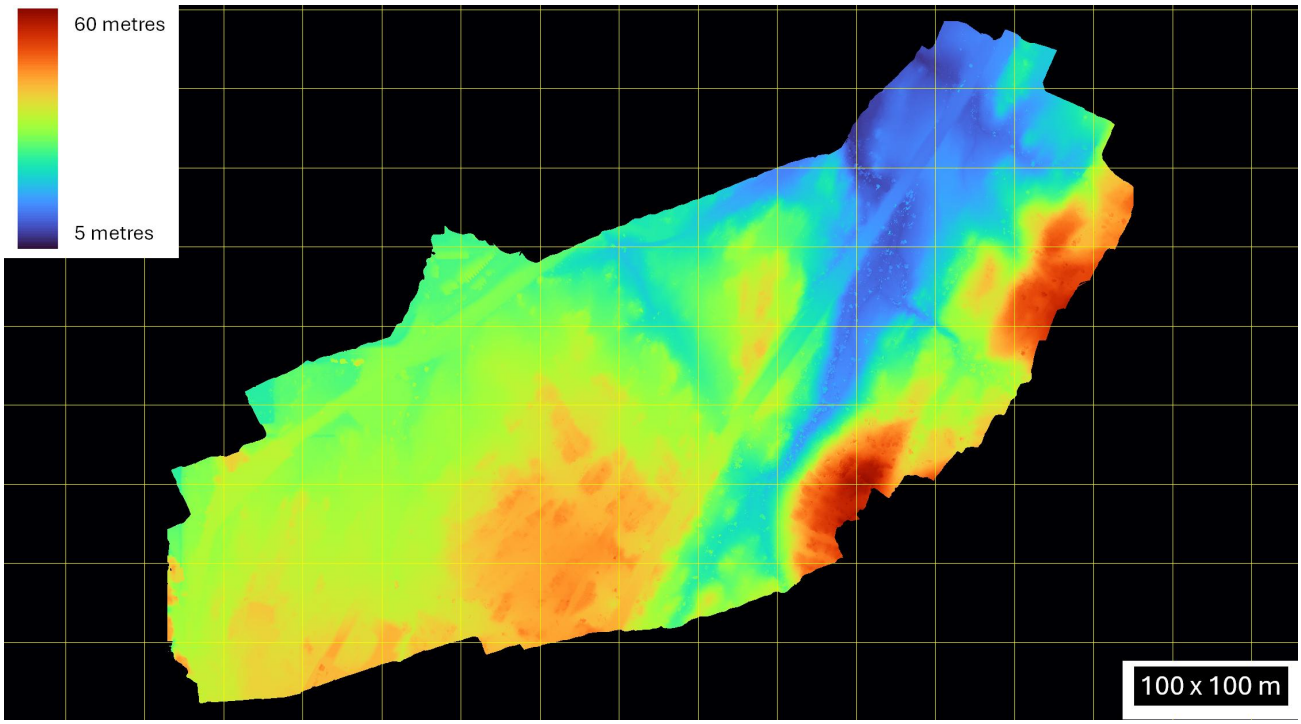

Figure D.1-75: DEM for EX08. Plotted with 100 x 100 m grid spacing.

EX09 site summary

Table D.1-76: EX09 site summary.

Drone	**Phantom 4 Pro, Phantom 4 RTK**
Camera Model	DJI FC6310, DJI FC6310R
Images	3180/3197
Ground Coverage	3.381 km^2
Average ground resolution	21.614 mm/pixel
Geo referencing	33 control points (RTK)
Key Points	Median of 50307 key points per image
Tie Points	1043943 points (median of 2351 points per photo)
Reprojection Errors (Median)	0.37 pixels
Reprojection Errors (RMS)	0.54 pixels
Distance to Rays (RMS)	0.0536 metres

Table D.1-77: EX09 Position uncertainties (camera locations).

	X (metres)	**Y (metres)**	**Z (metres)**
Minimum	0.0013	0.0012	0.0009
Mean	0.0051	0.0055	0.002
Maximum	0.9243	0.995	0.167

Table D.1-78: EX09 control points.

Name	Accuracy (m)	Num of Photos	RMS of Reproject Error (pixels)	RMS of Dist to Rays (m)	3D Error (m)	Horizontal Errors (m)	Vertical Error (m)
uav01	H: 0.008 V: 0.016	69	0.64	0.0697	0.00741	X: 0.0047 Y: -0.0054	-0.0018
uav02	H: 0.009 V: 0.021	70	0.67	0.0653	0.01036	X: -0.0091 Y: 0.0009	0.0048
uav10	H: 0.009 V: 0.020	46	0.61	0.075	0.01038	X: 0.0049 Y: 0.0082	0.004

Name	Accuracy (m)	Num of Photos	RMS of Reproject Error (pixels)	RMS of Dist to Rays (m)	3D Error (m)	Horizontal Errors (m)	Vertical Error (m)
uav11	H: 0.009 V: 0.020	63	0.6	0.08	0.00741	X: 0.0018 Y: -0.0072	-0.0007
uav12	H: 0.009 V: 0.020	62	1	0.0701	0.02108	X: -0.0161 Y: -0.0055	-0.0124
uav13	H: 0.010 V: 0.022	43	0.5	0.0792	0.00466	X: -0.0022 Y: 0.0026	0.0032
uav101	H: 0.012 V: 0.030	85	0.78	0.0687	0.01175	X: -0.0036 Y: 0.0048	0.0101
uav102	H: 0.011 V: 0.027	95	0.74	0.0685	0.0092	X: 0.0073 Y: -0.0045	0.0033
uav107	H: 0.010 V: 0.023	68	0.69	0.0733	0.01145	X: 0.0060 Y: 0.0090	0.0038
uav108	H: 0.012 V: 0.024	40	0.8	0.0981	0.01173	X: -0.0091 Y: 0.0070	0.0026
uav109	H: 0.011 V: 0.024	37	0.78	0.1016	0.01131	X: 0.0095 Y: -0.0022	0.0058
uav110	H: 0.012 V: 0.023	36	0.82	0.0832	0.01302	X: 0.0005 Y: -0.0126	-0.0034
uav112	H: 0.011 V: 0.023	42	0.63	0.0774	0.00423	X: 0.0035 Y: -0.0024	-0.0003
uav113	H: 0.011 V: 0.022	57	0.81	0.077	0.01604	X: 0.0127 Y: -0.0041	-0.0089
uav01	H: 0.010 V: 0.010	60	0.73	0.0732	0.01354	X: -0.0089 Y: 0.0072	-0.0072
uav02	H: 0.011 V: 0.021	63	0.77	0.0853	0.01378	X: 0.0136 Y: -0.0014	-0.0017
uav03	H: 0.012 V: 0.026	50	0.52	0.0549	0.0103	X: 0.0002 Y: -0.0031	0.0098
uav05	H: 0.013 V: 0.028	60	0.69	0.072	0.01187	X: 0.0017 Y: 0.0114	-0.003
uav06	H: 0.013 V: 0.026	43	0.75	0.0545	0.01107	X: -0.0018 Y: -0.0108	0.0016

Name	Accuracy (m)	Num of Photos	RMS of Reproject Error (pixels)	RMS of Dist to Rays (m)	3D Error (m)	Horizontal Errors (m)	Vertical Error (m)
uav07	H: 0.014 V: 0.028	52	0.74	0.062	0.01254	X: 0.0066 Y: -0.0081	0.0069
uav08	H: 0.013 V: 0.027	39	0.8	0.0586	0.00951	X: -0.0075 Y: 0.0055	0.0021
uav04	H: 0.021 V: 0.033	32	0.43	0.0495	0.00375	X: 0.0026 Y: 0.0024	-0.0012
uav07	H: 0.015 V: 0.023	20	0.47	0.0338	0.0074	X: -0.0053 Y: 0.0024	-0.0046
uav08	H: 0.013 V: 0.021	41	0.68	0.0376	0.01103	X: -0.0060 Y: 0.0073	0.0056
uav11	H: 0.012 V: 0.020	61	0.69	0.0436	0.0146	X: -0.0061 Y: -0.0012	-0.0132
uav13	H: 0.011 V: 0.019	58	0.74	0.0392	0.01335	X: 0.0018 Y: -0.0100	0.0086
uav14	H: 0.011 V: 0.019	48	0.75	0.0364	0.01008	X: 0.0073 Y: 0.0067	-0.0018
uav15	H: 0.011 V: 0.019	46	0.66	0.0389	0.00329	X: 0.0030 Y: -0.0010	0.001
uav16	H: 0.011 V: 0.019	40	0.67	0.03	0.00887	X: 0.0065 Y: 0.0037	-0.0047
uav17	H: 0.012 V: 0.020	57	0.74	0.0347	0.01299	X: -0.0121 Y: 0.0047	0.0003
uav19	H: 0.012 V: 0.020	75	0.75	0.0457	0.01472	X: 0.0127 Y: -0.0040	0.0062
uav21	H: 0.012 V: 0.020	87	0.7	0.0492	0.00969	X: -0.0088 Y: -0.0036	0.002
uav22	H: 0.012 V: 0.021	39	0.58	0.0459	0.00396	X: 0.0039 Y: -0.0007	0.0002
Global RMS			0.7	0.0644	0.01116	X: 0.0074 Y: 0.0061	0.0056
Median			0.7	0.0653	0.01103	X: 0.0018 Y: -0.0010	0.001

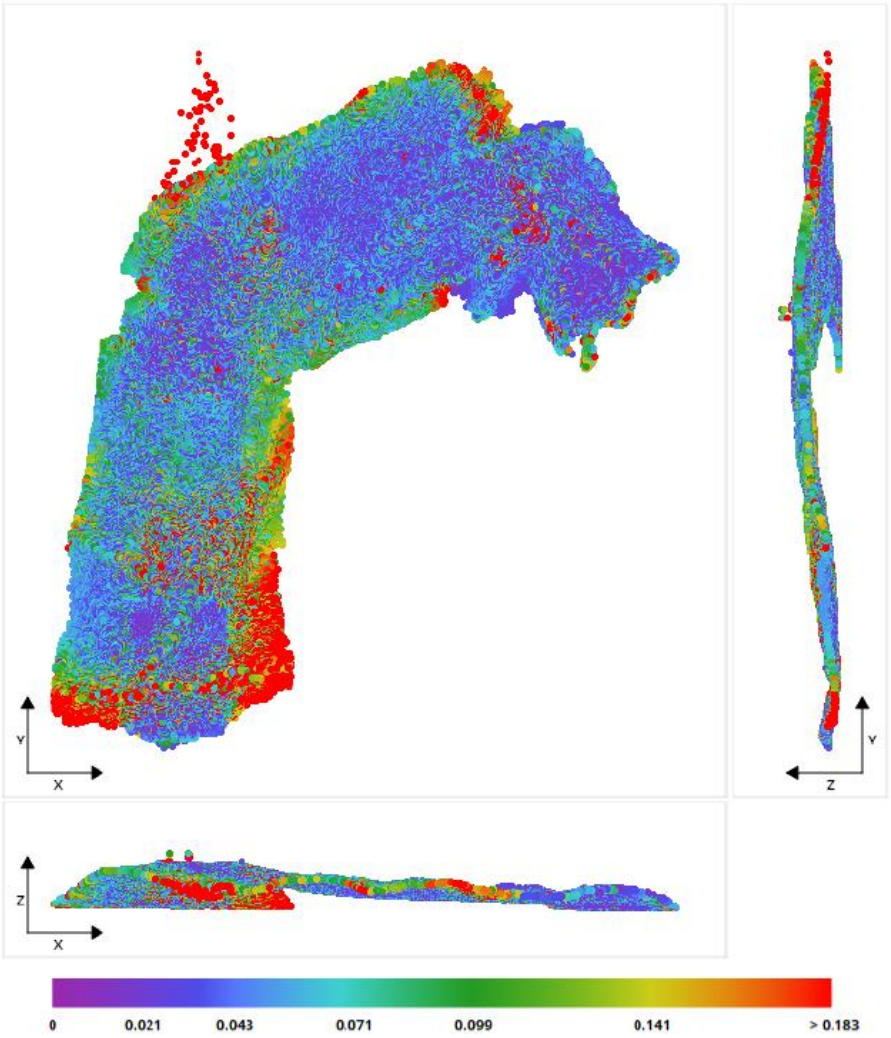

Figure D.1-76: Position uncertainties for EX09: Top view (XY plane), side view (ZY plane) and front view (XZ plane) displays of all tie points, with colours representing uncertainty in the individual point position. The values are in metres, with a minimum uncertainty of 0.0051 metres and a maximum of 0.6867 metres. The median position uncertainty equals 0.0335 metres.

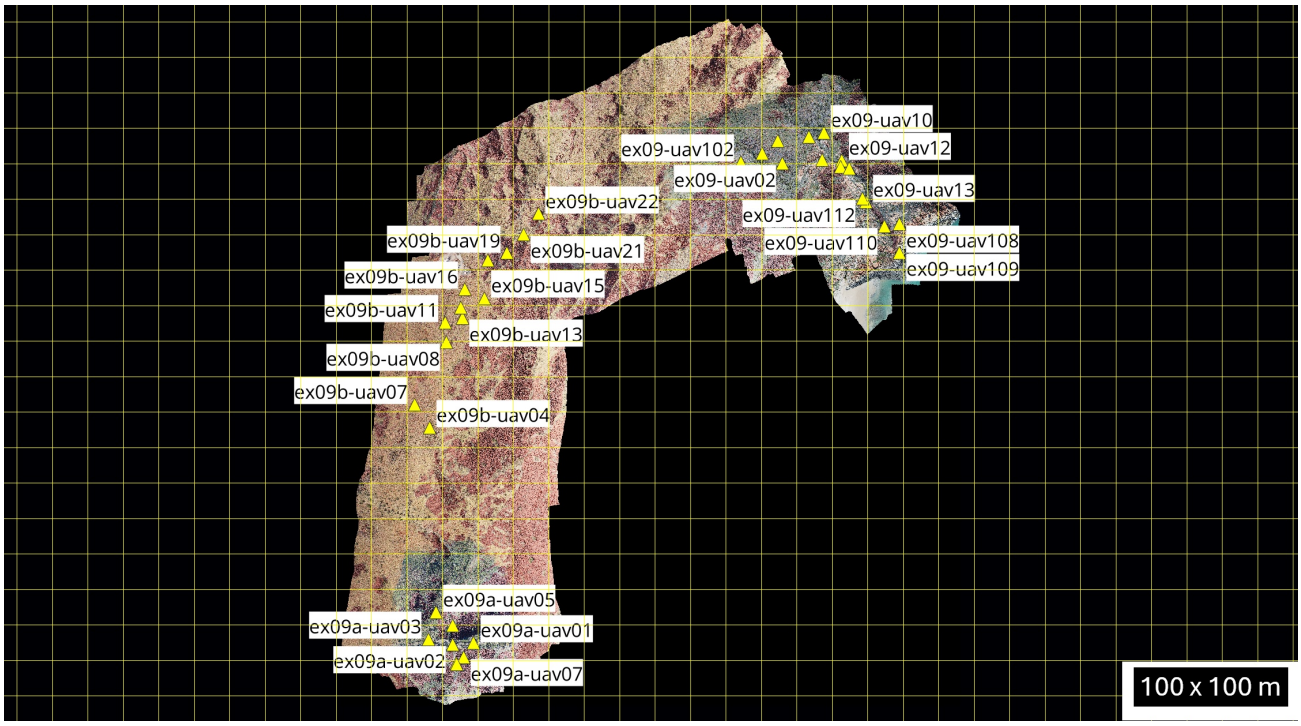

Figure D.1-77: Ortho-mosaic for EX09. Plotted with control points and 100 x 100 m grid spacing.

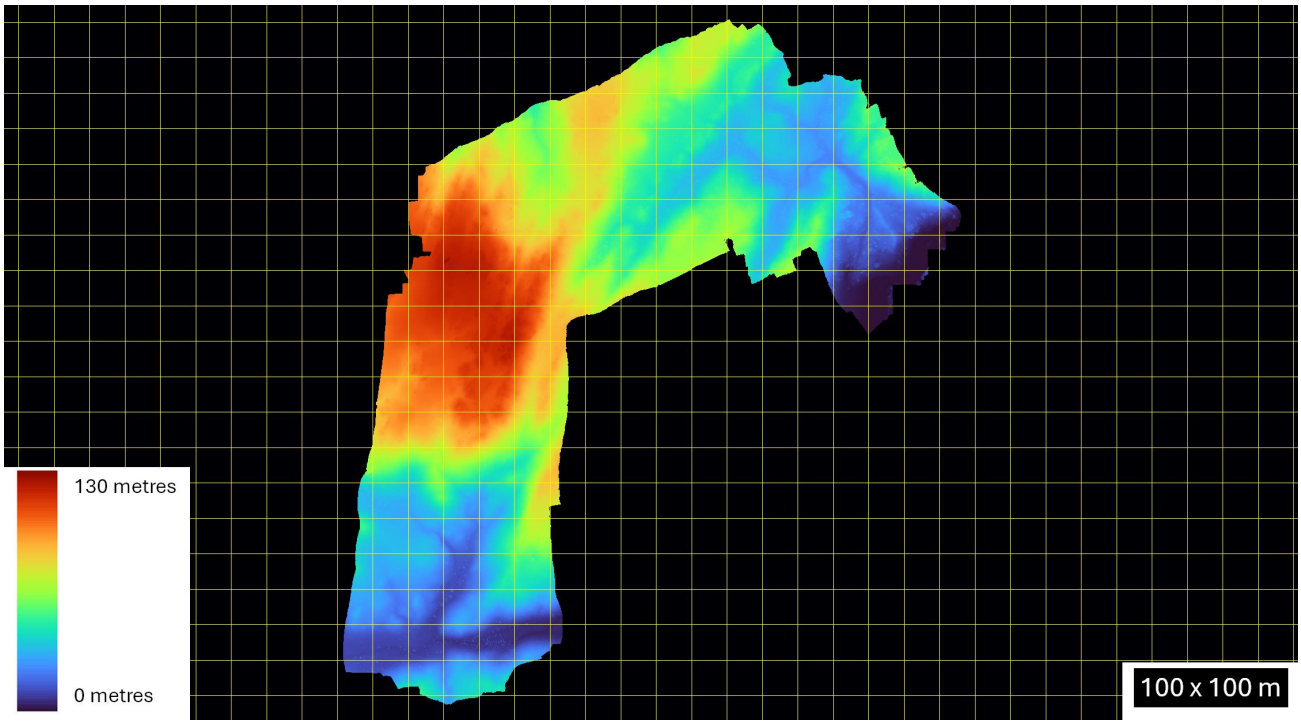

Figure D.1-78: DEM for EX09. Plotted with 100 x 100 m grid spacing.

D.2 CFD modelling process

This section provides technical detail on the process undertaken for the CFD simulations. OpenFOAM (Greenshields, 2022) was used for all CFD simulations, and reference to particular commands and files relates to this software.

D.3 Geometry, sources and locations

The surface elevation data were provided as digital elevation models (DEMs) as geo-referenced TIFF files with a scalar band containing elevation above sea level, and a NODATA value outside of the extents of the DEM.

The DEM files are interpreted using the MGA50 coordinate reference system with eastings/northings in meters. Raw easting/northing values can cause numerical issues when meshing (and post processing), so all data are offset to a local origin (478000E, 7720000N) for processing (the selection of this origin is immaterial).

Locations (AQMs, samples, emission sources) are similarly offset. 'Elevations' of these locations are taken as relative to sea level, however 'heights' are offset by the DEM elevation at the same point.

Converting the terrain data to be used as an input to the CFD model is required, particularly to take into account different DEM sources. Once the region of interest is identified a 2D flat grid is created (at an appropriate and adjustable resolution). For each point of the grid the elevation is sampled from the DEMs hierarchically. For a given grid point, the highest priority DEM is sampled, if the point is outside the data region, the next DEM in priority is sampled, until an elevation is determined. The priority is typically: MRAMP spatial scans (highest), Landgate 1m scan, SRTM topography (lowest). The SRTM topography data has complete coverage of the region, albeit at low spatial resolution (30m). The output of this process is a 3D OBJ file which is used as an input geometry to the OpenFOAM meshing tools.

The region to be sampled is indicated by a point indicating the centre of the domain, and its dimensions. For multiple wind directions around a sample region, the geometry is sampled once, encompassing the extent of all of the domains as the extraction process is (relatively) expensive.

D.4 Mesh creation

The region of interest is defined by a centre point, dimension, and orientation angle. These data are used to create a `blockMeshDict` for the domain, as a background mesh. The mesh generation tool `snappyHexMesh` was subsequently used to create the final mesh to be used in the CFD simulations, accounting for the final required mesh resolution.

D.5 Simulation set-up and running

Generally steady state simulations were undertaken, which allow the flow to be solved separately from the pollutant transport. For the flow simulations, two different solvers were used, depending on whether buoyant effects were required to be captured, i.e. industrial stack emissions are generally buoyant, and affect the airflow directly, whereas dust (PM10, etc) are released at ambient

temperature, and are passive with respect to the flow (isothermal). For isothermal simulations, the OpenFOAM solver `simpleFoam` was used, whereas for buoyant flows the solver `buoyantSimpleFoam` was used.

Once the flow was solved the scalar(/species) transport was solved using the solver `pollutantTransportFoam` (a modified version of `scalarTransportFoam` to solve multiple species at once).

Each simulation requires appropriate inputs as boundary conditions and sources. How these are determined are described below.

D.5.1 Source terms

Pollutant source terms are directly provided as explicit sources to the CFD domain. Each source are created using `topoSet` to create a `cellSet` identified by its (local) coordinate. Absolute emission rates are provided in <x>s^{-1} where <x> can depend on the pollutant.

Conditions at stack exits are also applied as constraints on the simulation in the cells coinciding with the exit location of the stack. This provides more flexibility than requiring the stack exit to exactly coincide with the domain boundary. The applied constraints for a typical stack exit are given in Table *D.5-1*. For momentum, both `meanVelocityForce` and `vectorFixedValueConstraint` were tested. The `meanVelocityForce` applies a body force to the fluid to maintain an average velocity in the region of constraint. This results in peak velocity higher compared with using the `vectorFixedValueConstraint` constraint. The more realistic constraint, however, is likely to be the `meanVelocityForce` constraint, where stack exits maintain a total flowrate based on process controls rather than maintaining a uniform velocity at the exit.

Table D.5-1: Conditions imposed on the simulation for emissions from stacks.

Variable	Equation	Source/Constraint
U	Momentum	`meanVelocityForce` or `vectorFixedValueConstraint`
k	k transport	`scalarFixedValueConstraint`
ε	ε transport	`scalarFixedValueConstraint`
T	Energy	`fixedTemperatureConstraint`
Pollutant Source	Scalar transport	`scalarSemiImplicitSource`

D.5.2 Boundary conditions

The typical boundary conditions used for the simulations are as follows, though these may be dependent on the specific case run.

Typical boundary conditions for the simulations are shown in Table *D.5-2* for steady state flow, for the buoyant flow, the p boundary condition was applied to p_rgh instead. For scalar/pollutant transport a `zeroGradient` boundary condition was applied for all species.

Table D.5-2: Boundary conditions for isothermal steady state flow (`simpleFoam`).

Boundary	Variable	Boundary condition
inlet	U	`atmBoundaryLayerInletVelocity`
	p	`zeroGradient`
	k	`atmBoundaryLayerInletK`
	$epsilon$	`atmBoundaryLayerInletEpsilon`
outlet	U	`inletOutlet`
	p	`uniformFixedValue`
	k	`inletOutlet`
	$epsilon$	`inletOutlet`
terrain/buildings	U	`uniformFixedValue`
	p	`zeroGradient`
	k	`kqRWallFunction`
	$epsilon$	`epsilonWallFunction`

D.5.3 Running the simulations

Simulations were generally run on the *Setonix* supercomputer at the Pawsey Supercomputing Centre. Convergence of the simulations were monitored to check completion, with a typical convergence result presented in Figure *D.5-1*.

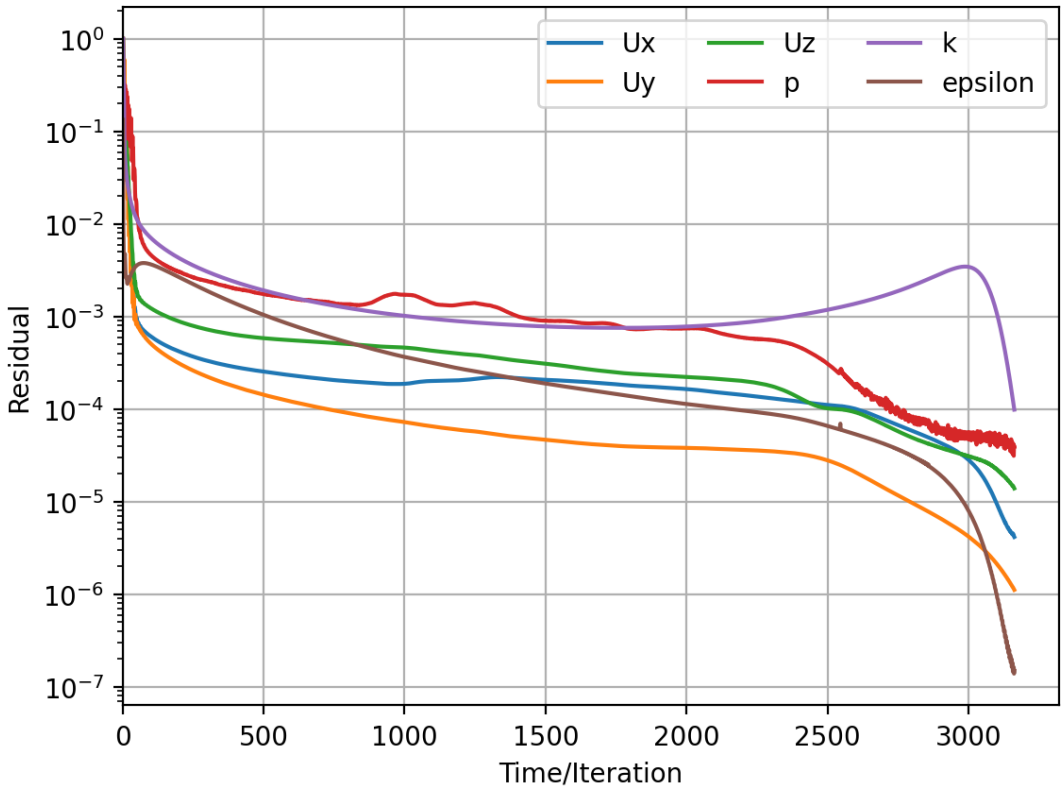

Figure D.5-1: Typical residual history for CFD simulation.

D.6 Post-processing

Post-processing the simulations was undertaken both interactively and with with a series of scripted (semi-automatic) processes. For each simulation, as a minimum, transects were made through the locations of AQMs and sample sites (rocks and petroglyphs) for the flow and scalar variables. These were also sampled at ground level and at vertical offsets from the ground for interpretation. The full 3D results were post-processed where additional interpretation was required.

D.7 Validation

Prior to conducting any CFD studies, the boundary conditions, solver settings, and approach were validated against suitable papers in the literature. Validation against field measurements is not viable due to large uncertainties in the actual conditions.

Shatzmann (1979) provides a range of experimental data for buoyant and non-buoyant plumes in flows with varying stratification. Additional experimental data is reported in Fan (1967), Chu and Goldberg (1974) and Slawson and Csanady (1971).

To validate that the flow and pollutant (scalar) transport is correctly modelled in the simulations a number of these cases were replicated with CFD and compared with the experimental data. The plume conditions in the experimental data are given in Table *D.7-1*, and comparisons with the CFD results in Figures *D.7-2*, *D.7-1* and *D.7-3*.

Table D.7-1: Conditions for validation.

Reference	**Froude No** Fr_r	**Velocity Ratio** $\frac{u_\infty}{u_j^*}$	**Temperature Ratio** $\frac{T_j - T_\infty}{T_\infty}$
Chu and Goldberg (1974)	15.3	0.0227	0
Fan (1967)	4.02	0.125	0.042
	24.1	0.0625	0.174
Slawson and Csanady (1971)	2.74	0.457	0.347

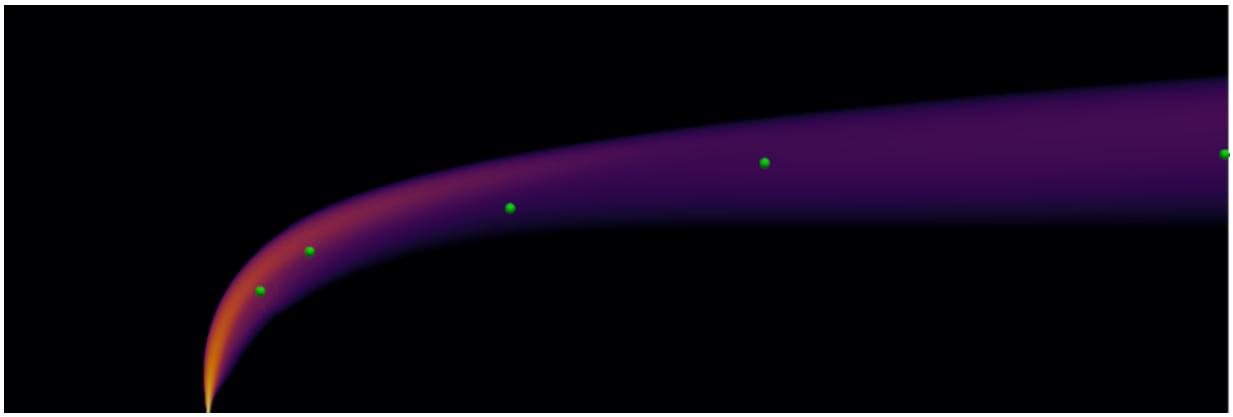

Figure D.7-1: Comparison of plume trajectories CFD and experiments of Chu and Goldberg (1974).

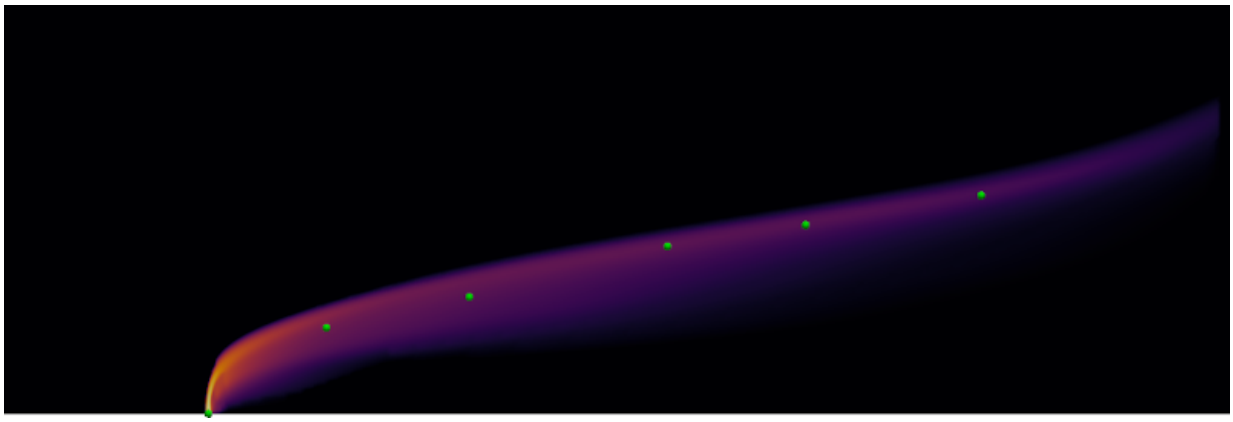

a) u_∞/u_j *= 0.125*

b) u_∞/u_j *= 0.0625*

Figure D.7-2: Comparison of plume trajectories CFD and experiments of Fan (1967).

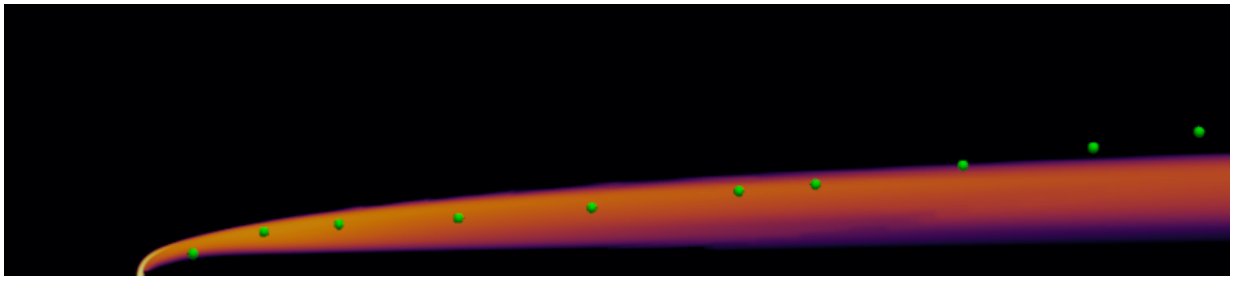

Figure D.7-3: Comparison of plume trajectories CFD and experiments of Slawson and Csanady (1971).

This page is intentionally blank.

E Estimation of major historic emissions (Dampier power station)

The Dampier power plant complex was operational from 1966 to c. 2010, consisting of a mixture of diesel (heavy oil) and gas driven engines (Hamersley News, 1969, 1970, 1971, 1972, 1973, 1975, 1978, 1979, 1984, 1985b,a). A timeline of the operations along with general fuel type and the ratings of the plants is shown in Figure *E-1*.

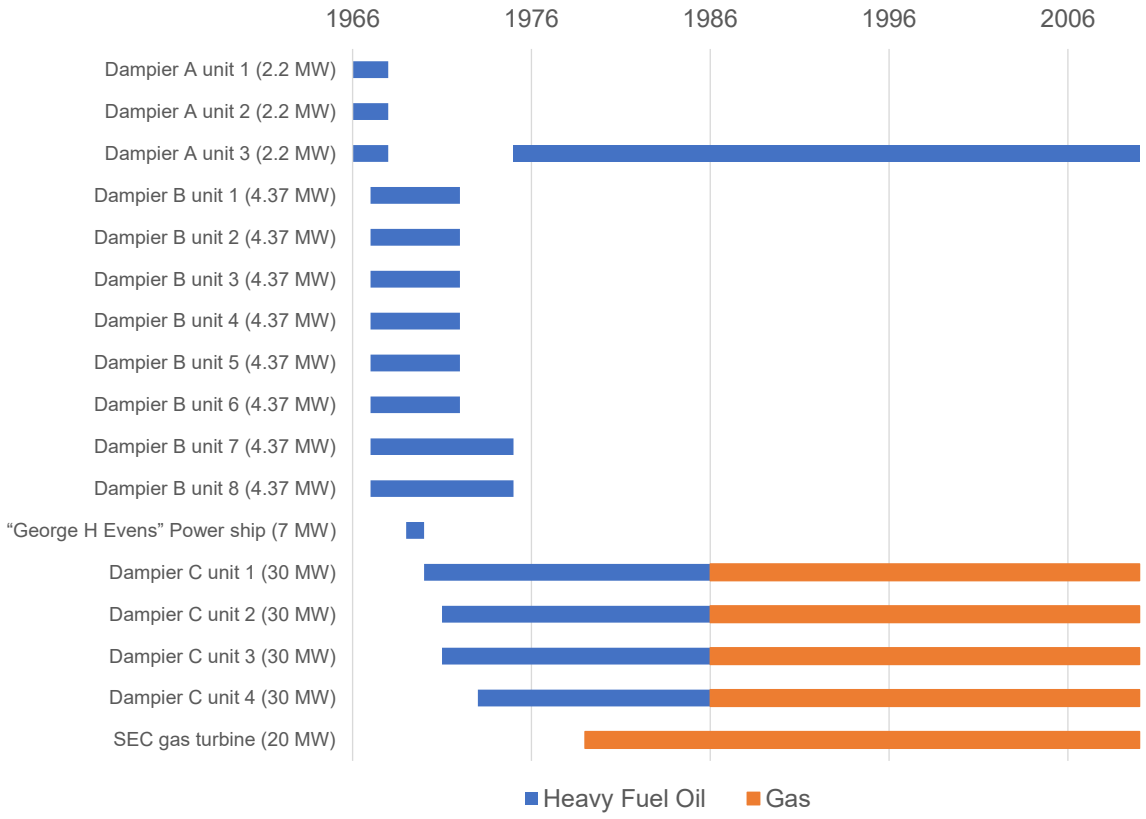

Figure E-1: Timeline of the Dampier power plant complex, categorised according to fuel type.

The NO_x emission rate of the heavy fuel oil based power plants was estimated to be 14 g/kWh. This was based on a survey of diesel and gas plants driven by internal combustion engines (Niemi, 1997), which found a typical range of NO_x emission rate of 6.7-19 g/kWh for diesel engine plants. The SO_2 emission rate was estimated on the basis of a fuel consumption rate of 200 g/kWh, with a typical heavy fuel oil Sulphur content of 1000 ppm. In 1986, the boilers in the “Dampier C” power stations were switched to natural gas. The NO_x emission rate in this case was estimated to have been

reduced to 2.1 g/kWh, based on emission figures published by Environmental Protection Agency (2019); Milligan et al. (1979). For the case of the S.E.C. gas-driven turbine, a NO_x emissions rate of 0.5 g/kWh was applied. Finally, the SO_2 emissions rate for the gas-driven plants were approximated to be 0.5 g/kWh.

Two bases were applied for the determination of the annual NO_x and SO_2 emissions rate from the Dampier power plant complex:

- "100% utilisation" assumed full utilisation of the available power infrastructure
- "Growth model" assumed a steady increase in electricity consumption within the Dampier region. According to Hamersley News (1975), there was an approximately linear growth of 15% in electricity usage in Dampier from 1970 to 1975, representing an average utilisation of 25% of the available infrastructure during the five year span. This linear trend was extrapolated to estimate electricity usage beyond 1975, from which the percentage of infrastructure utilisation was calculated. These percentages were assumed to be evenly distributed among the power stations within the complex.

The estimated NO_x annual emission rate from the Dampier power plant complex from 1966 to 2010 has been presented in Figures *E-2*a-b, alongside the total NO_x emission rates used in the Ramboll 2014 and 2030 models Ramboll Australia (2022). The mean and maximum values of NO_x emission rate under the 100% utilisation model were found to be 121% and 53% of the total NO_x emission rate in the Ramboll 2014 model, respectively, with a majority of the NO_x emissions resulting from the usage of heavy fuel oil prior to 1986. Under the growth model assumption, the NO_x emission rates were considerably lower in comparison to the 100% utilisation model, although still presenting a considerable proportion of the total NO_x production rate considered in the Ramboll 2014 model. Prior to 1986, the mean and maximum values of the NO_x emission (under the Growth model) were found to be 27% and 56% of the total NO_x emission rate in the Ramboll 2014 model, respectively. Post 1986, the switch to natural gas processes allowed for a significant reduction in NO_x emission rate, thus the mean NO_x emission rate out of the Dampier power plant complex was found to be 15% of the total NO_x emission rate in the Ramboll 2014 model.

The average SO_2 emissions rate of the Dampier power plant complex were found to be approximately 5.0% of the total SO_2 emission rate in the Ramboll 2014 model (based on the growth model assumption) (see Figure *E-3*a-b). Figure *E-3*b shows that a significant proportion of the SO_2 emission in the Ramboll 2014 model is due to shipping; a comparison of the average SO_2 emission value out of the Dampier power station complex (based on the Growth model) to the total SO_2 emissions due to industry sources of the Ramboll 2014 model shows that the average emission out of the Dampier power station is approximately 94.6% of the latter value.

This study shows that, while significant assumptions have been adopted in estimating the historical NO_x and SO_2 emission rates out of the Dampier power stations, both the lower and upper estimates (i.e. the growth model and 100% utilisation, respectively) indicate substantial emission rates in comparison to the current models of emissions. This is particularly the case in the years prior to 1986, where heavy fuel oil usage in the Dampier Power Station complex saw significant values of NO_x and SO_2 emission rates. As a result, it is expected that the cumulative NO_x and SO_2 values will be higher than those predicted by the Ramboll models. Further analysis into historical industrial activities in Dampier is required to characterise the cumulative exposure of the rocks to these pollutants.

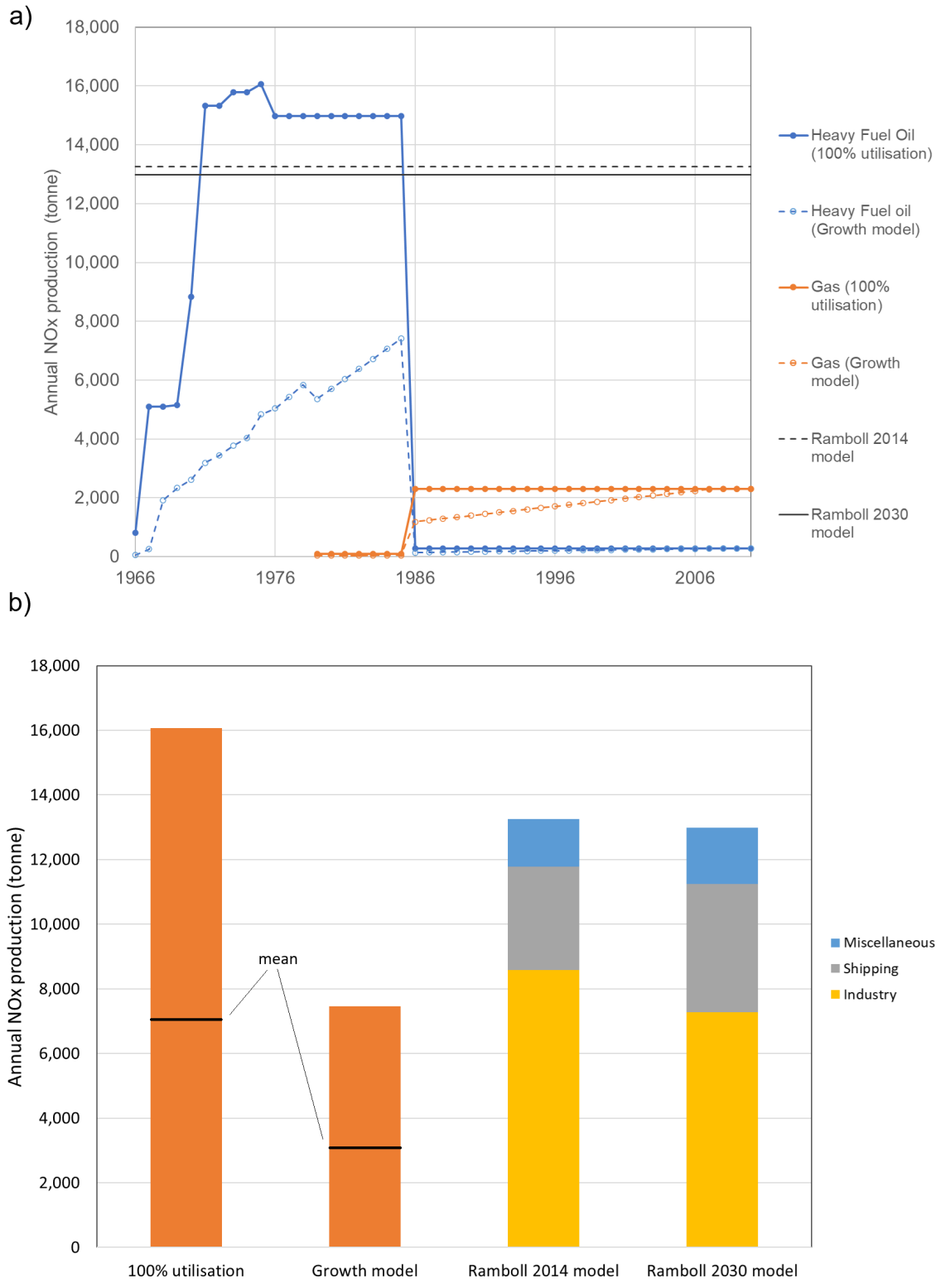

Figure E-2: Estimation of the NO_x emission rate out of the Dampier power plant complex: (a) Yearly emission rates, classified based on fuel usage; (b) maximum values of the NO_x emission rate using the 100% utilisation and growth models (mean values are indicated by black horizontal lines), compared against the Ramboll 2014 and 2030 models.

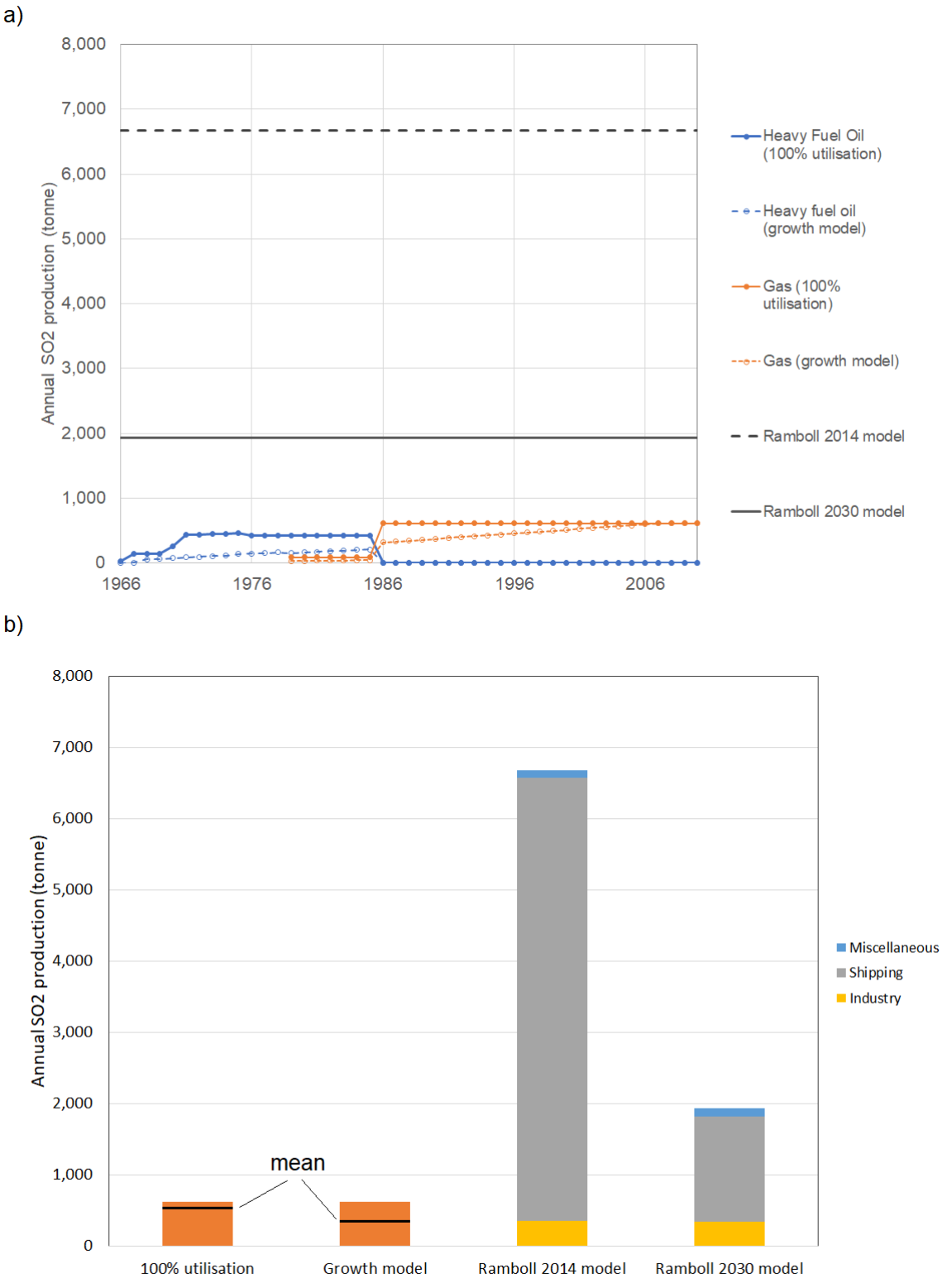

Figure E-3: Estimation of the SO_2 emission rate out of the Dampier power plant complex (see Figure E-2 for details on captions).

F Statistical methodology

This Appendix gives further details of statistical methodologies and techniques that were used to analyse data and produce graphics for this report.

Section *F*.1 describes the method for spatial smoothing of observations which is used frequently throughout this report. Section *F*.2 describes the new methodology for inferring rock porosity as a function of depth into the rock. Section *F*.3 describes Monte Carlo hypothesis tests used to assess statistical significance of the results.

F.1 Spatial smoothing

F.1.1 Executive summary

The statistical analyses reported in this report make frequent use of spatial smoothing. This Appendix provides details of the technique and explains its strengths and weaknesses.

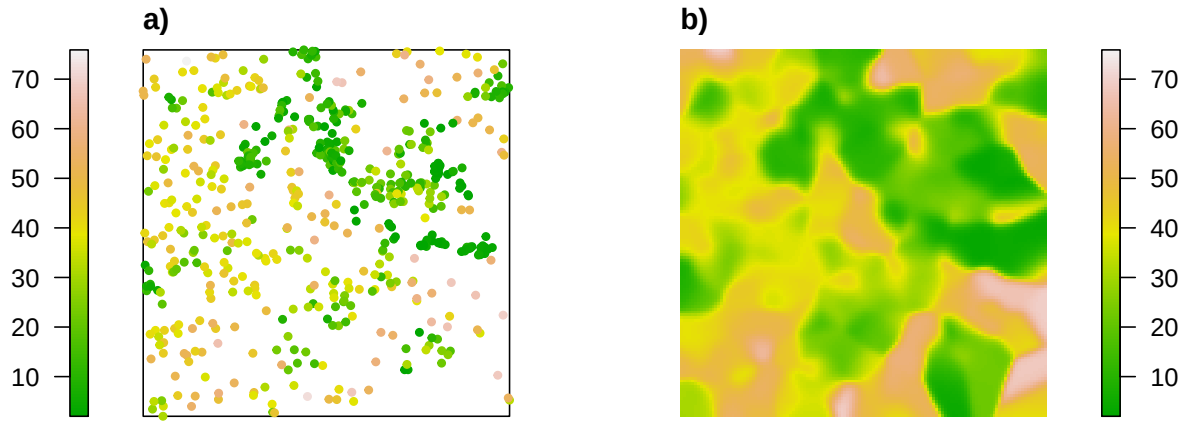

Figure F.1-1: Spatial smoothing: (a) input data consisting of observations at scattered locations in space; (b) output colour image obtained by spatially smoothing the observations. Colour ribbon shows the representation of numerical values as colours, used in both panels.

An illustrative example is depicted in Figure *F.1-1*. Panel (a) shows an example dataset, consisting of observations of some quantity recorded at different locations in space. The observed values are represented by colours according to the legend at left. The quantity appears to take lower values (more green colour) in an area at the upper right of the picture. The primary purpose of smoothing is to make this pattern more easily visible.

Figure *F.1-1*(b) shows a spatially smoothed image, obtained as a spatially-varying weighted average of the original data. Values are displayed using the same colour map. The pattern of lower values in the upper right of the picture is more clearly shown in this smoothed image. The image also draws attention to other areas which appear to have lower or higher values of the quantity.

The main role of spatial smoothing is to *simplify* the data, by a kind of averaging, to make it easier to discern any overall spatial trend or pattern. Apart from the spatial context, spatial smoothing is the same principle as the smoothing of a time series of economic data, which is often used to

discern trends over time. The smoothed values do not replace, interpolate, or represent the original observed data; rather, they can be interpreted as local averages of the data.

Spatial smoothing is used to discern a trend or overall tendency in the data. It needs to be complemented by other kinds of statistical analysis which measure the variability between observations.

Spatially smoothed images are also useful tools in many kinds of analysis including tests of statistical significance.

This Appendix describes the smoothing technique used in this report and explains its correct interpretation, its strengths and weaknesses.

F.1.2 Qualitative description of smoothing

F.1.2.1 Objectives

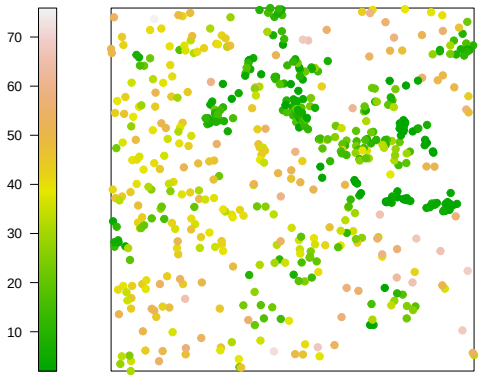

Figure F.1-2: Spatial data: values of a variable observed at scattered locations.

Figure *F.1-2* shows the example dataset used for demonstration purposes in this Appendix. It consists of observations of a variable at scattered locations in space. The observed values are depicted by colours according to the legend at left.

The overall objective of spatial smoothing is to discern any trend in the value of the variable across the spatial domain. For example, visual inspection of Figure *F.1-2* suggests that there is an area in the upper right of the spatial domain where the values are lower than they are elsewhere. Spatial smoothing is designed to highlight such patterns.

F.1.2.2 Smoothing technique

Variability or ‘noise’ in data can make it more difficult to discern the overall trend. The standard statistical technique for suppressing variability is to calculate an average. This suggests that a simple way to analyse the data in Figure *F.1-2* would be to divide the region into equal squares, and to calculate the average of the observed values in each square. This is shown in Figure *F.1-3*. The result in Figure *F.1-3*(b) corroborates the visual impression that there are lower values in the upper right of the spatial domain. These average values (represented by the colours in Figure *F.1-3*(b))

could be used for further statistical analysis, such as a hypothesis test to assess whether the difference in values is statistically significant.

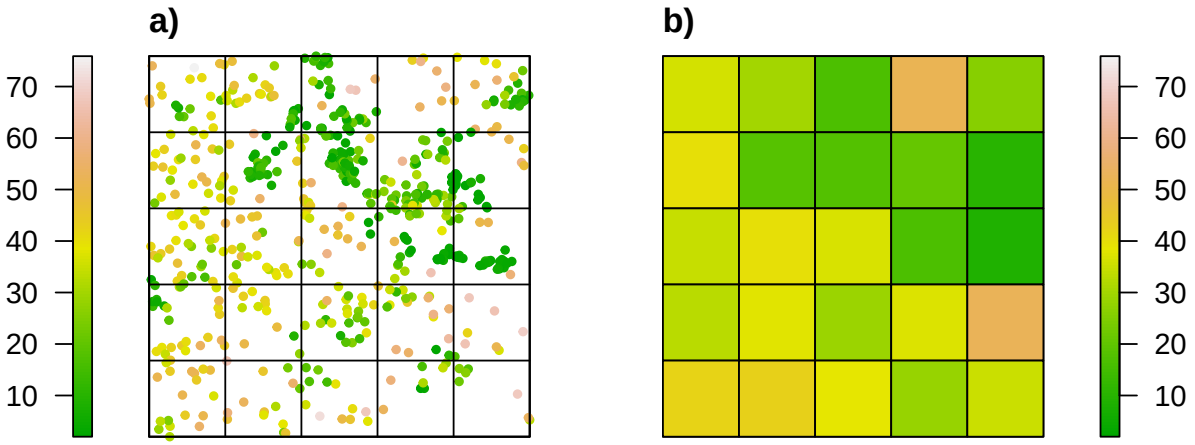

Figure F.1-3: Spatial smoothing by averaging within cells: (a) the spatial domain divided into a 5×5 *grid of cells; (b) average values in each square.*

The procedure sketched in Figure *F.1-3* has several disadvantages, including artefacts caused by the artificial boundaries between the squares. It can be improved by replacing the squares by a disc of fixed radius which is allowed to move freely across the spatial domain. This procedure is sketched in Figure *F.1-4*. In order to determine the spatially-smoothed value at a desired spatial 'query' location (indicated by "+" in the Figure) we draw a circle around this location, with a predetermined radius, and calculate the average of the observed values at all the data points lying within this circle. This average is taken as the smoothed value at the query location. Panels (a) and (b) of Figure *F.1-4* show this procedure applied at two different query locations. This procedure is repeated for all query locations across the spatial region, yielding a colour image of the smoothed values shown in Figure *F.1-4*(c).

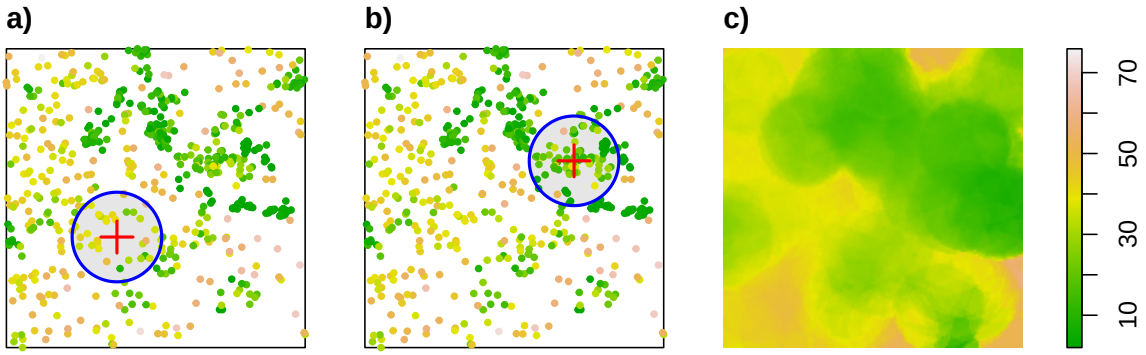

Figure F.1-4: Spatial smoothing using a moving disc of fixed radius. Panels (a) and (b) show different positions of the disc centre. Panel (c) shows the result of smoothing.

The discussion so far describes the smoothing procedure using a “circular uniform kernel”. This procedure avoids some of the artefacts that were seen in Figure *F.1-3*, but still exhibits some artefacts and poor properties.

The procedure used in this report uses the more standard Gaussian kernel, in which the disc of radius r is replaced by an isotropic Gaussian (Normal) probability density with standard deviation σ. In this procedure, data points which are closer to the query point are assigned a greater weight in the averaging process. The weighting is a smooth function of distance. Figure *F.1-1*(b) was produced using a Gaussian kernel.

F.1.2.3 Bandwidth

The circle radius r, or the standard deviation σ, used in the smoothing procedure is called the *smoothing bandwidth*, and it determines the extent of spatial smoothing.

Figure *F.1-5* shows the effect of choosing different values of the smoothing bandwidth in the standard Gaussian kernel. Larger values of bandwidth produce a flatter, smoother surface.

If σ is very large, the smoothing procedure effectively computes the average of all the observed values, and the spatially smoothed result is a flat image in a single colour. If σ is very small, the smoothed value at any given query location is simply the observed value at the data location nearest to the query location, and the spatially smoothed result is a busy patchwork of colours corresponding to the original observations. Intermediate values of bandwidth strike a compromise between bias and variability, that is, a tradeoff between the variability of the original data and the bias inherent in smoothing.

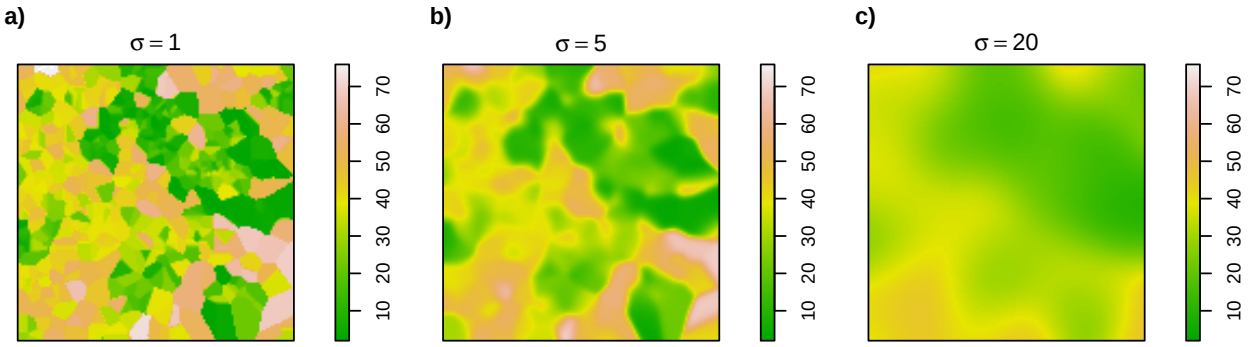

Figure F.1-5: Effect of smoothing bandwidth. Spatial smoothing with Gaussian kernel, with bandwidth (a) σ =1 metre, (b) σ = 5 metres and (c) σ = 20 metres. Spatial domain is 200 metres wide.

F.1.3 Mathematical definition

F.1.3.1 Notation and approach

Our task is to spatially smooth the values of some quantity, observed at several locations in space.

Many methods exist for this purpose, including Nadaraya-Watson smoothing, Kriging, thin-plate spline and 'soap film' smoothing, spatial copulas, diffusion smoothing and inverse-distance weighting. Our choice of technique is guided by the exigencies of the project.

We assume the study locations ('sites') are a fixed set of spatial locations $x_1, \ldots, x_n$ within a 'study region' W which is a bounded subset of two-dimensional space $\mathbf{R}^2$. The data consist of the observed values $y_1, \ldots, y_n$ of some quantity y, observed at the sites $x_1, \ldots, x_n$ respectively. The task is to compute a "spatially smoothed" value $\hat{y}(x)$ at every location $x \in W$.

We treat the data $y_1, \ldots, y_n$ as observations of a spatially-varying quantity plus error,

$$y_i = Y(x_i) + \epsilon_i \qquad (F.1.1)$$

where $Y(x), x \in \mathbf{R}^2$ is the "true surface", a smooth function that is the target of investigation, and $\epsilon_1, \ldots, \epsilon_n$ are random errors with mean zero. Two possible approaches are to:

- assume the surface $Y(x)$ is a fixed, non-random surface, representing the overall, large-scale spatial trend in the values of the quantity. The goal is to *estimate* $Y(x)$ from the data. Methods include Nadaraya-Watson smoothing and diffusion smoothing.
- assume $Y(x)$ is a random surface representing both the large-scale spatial trend and shorter-scale random variability. The goal is to *predict* $Y(x)$ from the data. Methods include Kriging and spatial copulas. These methods rely on assumptions about the mean and covariance of the observations, and involve modelling of the covariance.

At this stage of the investigation, many different quantities have been observed at the study sites, and the primary goal is to explore trends or connections between these quantities. This militates against the use of techniques that need to be validated and tuned carefully. The chosen technique should be an exploratory smoothing method which does not have elaborate assumptions or preconditions. A further challenge is that some of the data have heavy tails, extreme values, missing values and severe heteroscedasticity. The chosen technique should be able to cope with these "real data" features.

Accordingly, we judge that the best overall choice at this stage of the project is the nonparametric Nadaraya-Watson smoother, which is computationally efficient and whose weaknesses are well studied. Where necessary, we will make modifications to the Nadaraya-Watson smoother to handle extreme values. An important check on the validity of this approach is to inspect the residuals, as we discuss below.

F.1.3.2 Nadaraya-Watson smoother

The Nadaraya-Watson smoother (Nadaraya, 1964, 1989; Watson, 1964) is defined as

$$\widehat{y}(x) = \frac{\sum_i y_i \, \kappa(x - x_i)}{\sum_i \kappa(x - x_i)}, \qquad x \in W \tag{*F.1.2*}$$

where $\kappa(x)$ is the smoothing kernel, a probability density on the two-dimensional plane. The value of the smoother at any query location can be expressed as a weighted mean of the observations, with spatially-varying weights,

$$\widehat{y}(x) = \sum_i y_i \, a_i(x), \qquad x \in W \tag{*F.1.3*}$$

where

$$a_i(x) = \frac{\kappa(x - x_i)}{\sum_j \kappa(x - x_j)}, \qquad x \in W \tag{*F.1.4*}$$

is the weight ascribed to y_i for prediction at x, satisfying $a_i(x) \geq 0$ and $\sum_i a_i(x) = 1$. Since the same kernel function κ is used throughout, this technique is known as *fixed-bandwidth kernel smoothing*.

It is conventional to use the symbol σ only when the kernel κ is the Gaussian probability density with standard deviation σ. For a general kernel we use the symbol h to denote the bandwidth parameter, so that

$$\kappa(x) = \kappa_h(x) = h^{-2} K(h^{-1} x), \qquad x \in \mathbb{R}^2 \tag{*F.1.5*}$$

where K is the "template" kernel. We assume K is continuous at the origin, and is square-integrable.

F.1.3.3 Effect of bandwidth

If bandwidth $h \to \infty$, the N-W estimator converges pointwise to the overall mean $\overline{y} = \sum_i y_i / n$.

If $h \to 0$, and if the kernel is isotropic Gaussian, then the N-W estimator converges pointwise to the *nearest observation* $y_{I(x)}$, where $I(x)$ is the index of the data location closest to x,

$$I(x) = \text{argmin}_i \|x_i - x\|, \qquad x \in W. \tag{*F.1.6*}$$

If the kernel has bounded support, then for sufficiently small h, the numerator and denominator of (*F.1.2*) may both be zero, so that the N-W estimate is undefined. In this case the bandwidth h shall be constrained to be large enough that the denominator of (*F.1.2*) is positive for all locations $x \in W$.

F.1.3.4 Residuals

A residual is the difference between an observed value and the corresponding predicted or fitted value. Residuals contain information about the variability in the data. In spatial smoothing, the raw residuals are the values

$$r_i = y_i - \widehat{y}_h(x_i), \qquad i = 1, \ldots, n \tag{*F.1.7*}$$

This calculation can underestimate the amount of variability, especially when the data locations are sparse, because the estimate $\widehat{y}_h(x_i)$ is then strongly influenced by the value of y_i. It is usually preferable to calculate the "leave-one-out" residuals

$$r_i^{-i} = y_i - \widehat{y_h}^{-i}(x_i), \qquad i = 1, \ldots, n \tag{F.1.8}$$

where $\widehat{y_h}^{-i}(x_i)$ is the *leave-one-out smoother* at data location x_i,

$$\widehat{y_h}^{-i}(x_i) = \frac{\sum_{j \neq i} y_j \, \kappa(x_i - x_j)}{\sum_{j \neq i} \kappa(x_i - x_j)}, \qquad i = 1, \ldots, n \tag{F.1.9}$$

Again $\widehat{y_h}^{-i}(x_i) = \sum_j y_{j \neq i} \, a_j^{-i}(x_i)$ where

$$a_j^{-i}(x_i) = \frac{\kappa(x_i - x_j)}{\sum_{\ell \neq i} \kappa(x_i - x_\ell)}, \qquad i = 1, \ldots, n. \tag{F.1.10}$$

The interpretation of r_i^{-i} is that it is the discrepancy between the observed value y_i at x_i and a prediction of the value at x_i computed using all the other available data.

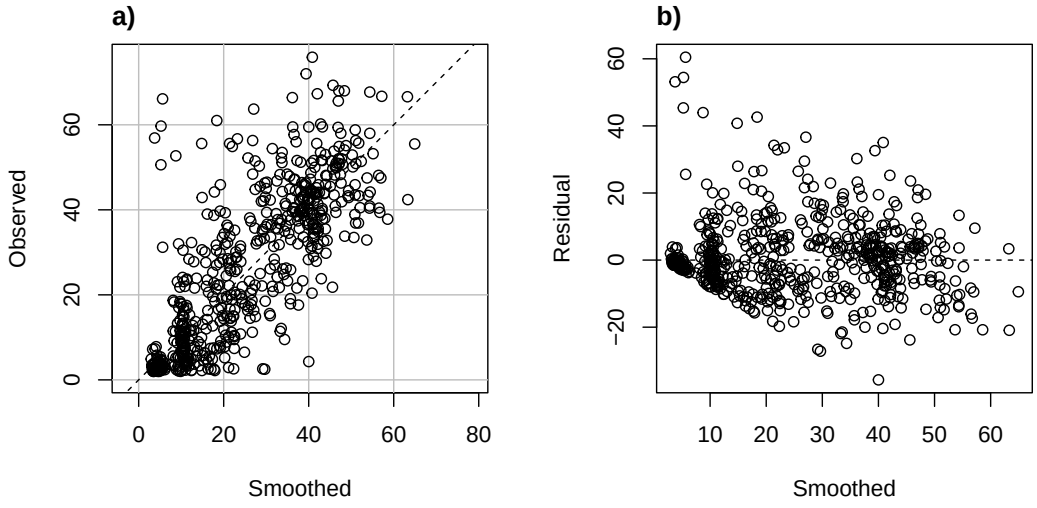

Figure F.1-6: Left: *observed versus predicted values.* Right: *leave-one-out residuals versus predicted values.*

In the context of spatial smoothing, it is important to inspect the residuals to decide whether any spatial structure remains, and to estimate the residual variability. In the simplest case, where there is no evidence of trend or spatial correlation in the residuals, the root-mean-squared residual provides an estimate of the standard deviation of the errors ϵ_i and it is possible to calculate a standard error for the N-W estimator $\widehat{y}(x)$.

Figure *F.1-7* shows the leave-one-out residuals for the data example, plotted at their spatial locations.

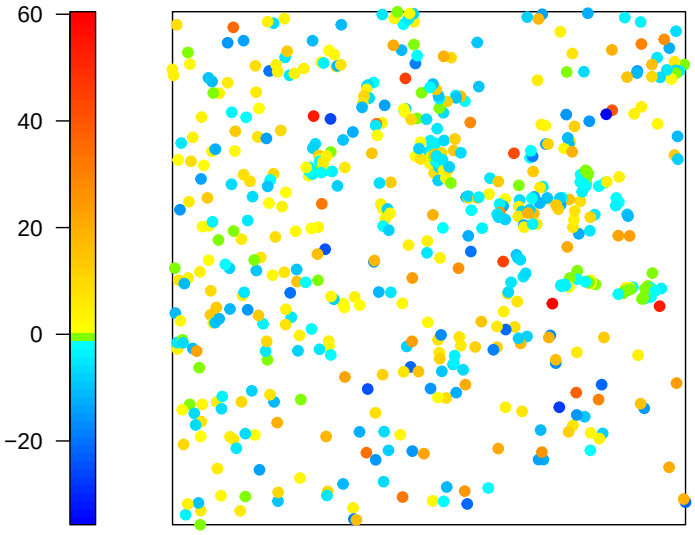

Figure F.1-7: Leave-one-out residuals plotted at their spatial locations

F.1.3.5 Bandwidth selection

The choice of smoothing bandwidth h for the Nadaraya-Watson estimator is important, as illustrated in Figure *F.1-5*.

The most common procedure for selecting the bandwidth is *least-squares cross-validation* which consists in choosing the value of h to minimise the mean squared residual

$$C(h) = \frac{1}{n}\sum_i (r_i^{-i})^2 = \frac{1}{n}\sum_i (y_i - \widehat{y_h}^{-i}(x_i))^2 \qquad (F.1.11)$$

where $\widehat{y_h}^{-i}(x_i)$ is the leave-one-out smoother (*F.1.9*). We set $C(h) = \infty$ if the denominator of (*F.1.9*) is zero.

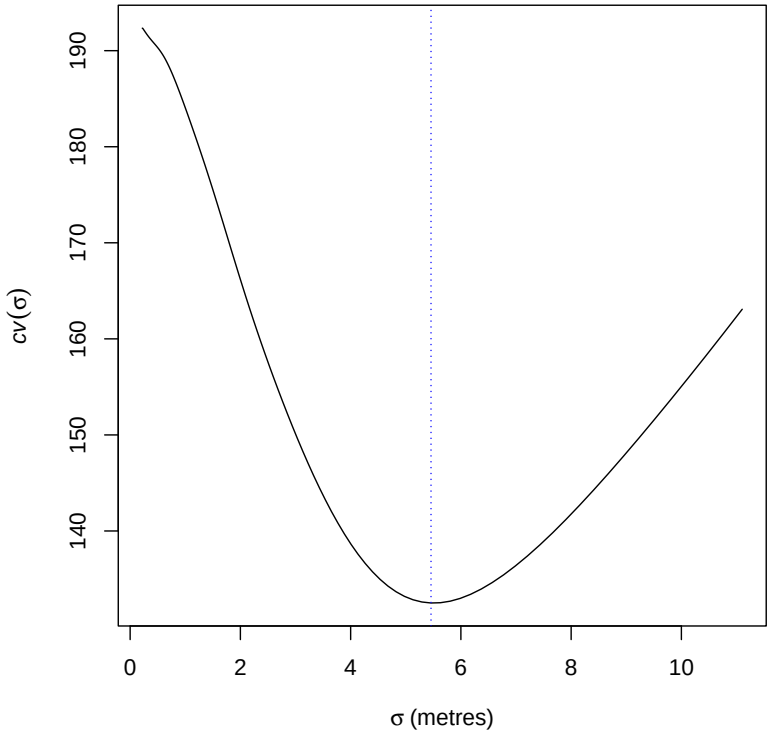

Figure F.1-8: Mean of squared residuals, as a function of smoothing bandwidth σ, for the data of Figure F.1-2. Optimal bandwidth value σ =5.46 metres indicated by dotted line.

Figure *F.1-8* shows a plot of the cross-validation criterion $C(\sigma)$ as a function of bandwidth σ for the Gaussian kernel, computed for the example data in Figure *F.1-2*. The optimal bandwidth value $\sigma = 5.46$ metres is indicated by the dotted line. The minimised value of $C(\sigma)$ is 132.5 so that the minimised root-mean-square residual is 11.5.

F.1.3.6 Critique of Nadaraya-Watson estimator

The Nadaraya-Watson (N-W) estimator has many practical advantages for the purposes of this project. It is relatively easy to explain to users; it is straightforward to compute; and it does not impose strict requirements or make detailed assumptions about the data.

The technique does have several weaknesses that should be understood:

1. The N-W estimator is a linear function of the original observations $\{y_i\}$ as shown in equation (*F.1.3*), and is therefore vulnerable to the effects of extreme values amongst the y_i, in the same way that the sample average of a data set is not robust or resistant to extremes.
2. Like all smoothing techniques, the N-W estimator tends to flatten peaks and fill valleys, that is, it is negatively biased around a local maximum and positively biased around a local minimum.
3. If the spatial locations x_i are unevenly distributed across the study region, then a given bandwidth h is likely to be inappropriately large for the areas where the sample locations are highly concentrated (causing over-smoothing) and also inappropriately small for the areas where the sample locations are sparse (causing under-smoothing).
4. There is no universally optimal way to select the bandwidth; automatic bandwidth selection procedures can sometimes choose poorly.
5. The kernel effectively ignores spatial discontinuity of the domain (e.g. it "leaps over water") which would be inappropriate for some applications (Barry and McIntyre, 2011; McIntyre and Barry, 2018; Baddeley et al., 2022)

Many options available in the literature to address these weaknesses. At this stage of the project, it is not our intention to pursue these improvements in the methodology, since they typically require substantially more attention and validation in each application.

In the MRAMP study, we have tried to prevent the problem described in item 3 above, by selecting sample sites that are uniformly positioned across the study region. However, this problem still occurs when we restrict attention to the data for a particular rock type, because of the non-uniform distribution of the different rock types.

F.1.4 Modifications

Several practical modifications of the N-W estimator will be used to ameliorate the weaknesses described above.

F.1.4.1 Weighting

The N-W estimator can be modified by introducing numerical weights $w_i \geq 0$ associated with the observations y_i:

$$\widehat{y}^w(x) = \frac{\sum_i w_i\, y_i\, \kappa(x - x_i)}{\sum_i w_i\, \kappa(x - x_i)} = \sum_i a_i^w(x) y_i \qquad (F.1.12)$$

where

$$a_i^w(x) = \frac{w_i\, \kappa(x - x_i)}{\sum_j w_j\, \kappa(x - x_j)}. \qquad (F.1.13)$$

The weights may represent sample sizes associated with each observation (for example if observation y_i was actually the average of m_i replicates, where the numbers m_i are not equal for all sites). Alternatively the weights w_i may be estimates of the reciprocal of the variance associated with the observations y_i.

F.1.4.2 Transformation

Smoothing on a different "scale" is appropriate if the observations y_i have a very skewed distribution or contain extreme values. This can be done by

1. transforming the data y_i to $z_i = g(y_i)$ where g is the chosen transformation
2. spatially smoothing the observations z_i
3. back-transforming to obtain $\widetilde{y}(x) = g^{-1}(x)$ where g^{-1} is the inverse function of g

Examples of useful transformations g include

- the logarithm $g(y) = \log y$, often used to symmetrise data which have a heavy right tail;
- the square root $g(y) = \sqrt{y}$ which is the variance stabilising transformation for the Poisson distribution, and is often applied to data which are integer counts;
- Fisher's transformation $g(y) = \sin^{-1}\sqrt{y}$ which is the variance stabilising transformation for proportions (fractions between zero and one).

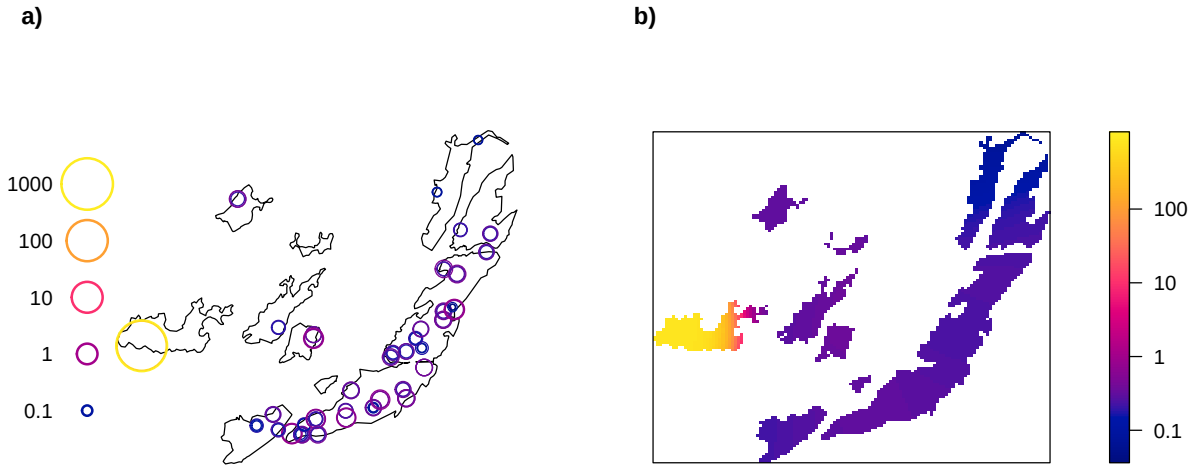

Figure F.1-9: Logarithmic smoothing: (a) ratio of iron (Fe) to silica (SiO2) assayed by pXRF instrument on 123 rocks at 41 sites across Murujuga. Values are displayed on a logarithmic scale; (b) spatially smoothed ratio, displayed on logarithmic scale.

Figure *F.1-9* shows an example with $g(y) = \log(y)$. Panel (a) shows the data giving the ratio of iron to silica assayed by the pXRF instrument on 123 rocks at 41 sites across Murujuga. The values

have an extremely skewed distribution. The sizes of symbols are proportional to the logarithm of the data values. Panel (b) shows the result of spatial smoothing using the logarithmic transformation. This example is equivalent to simply transforming the original data by applying the logarithmic transformation, and then computing the Nadaraya-Watson smoother, but labelling the resulting values on the original untransformed scale.

F.1.4.3 Probability Integral Transformation

Another useful transformation of data is the *probability integral transformation (PIT)*

$$g(y) = \widehat{F}(y)$$

where $\widehat{F}$ is an estimate of the cumulative probability distribution function of the y values. The transformed values are approximately uniformly distributed between zero and one. This principle can be applied to spatial data as follows:

1. estimate F from $\{y_i\}$ (either using the empirical CDF or by integrating a density estimate)
2. transform $z_i = \widehat{F}(y_i)$
3. perform spatial smoothing to obtain $\widehat{z}(x)$
4. back-transform to obtain $\widehat{y}(x) = \widehat{F}^{-1}(\widehat{z}(x))$.

Figure *F.1-10* shows an example.

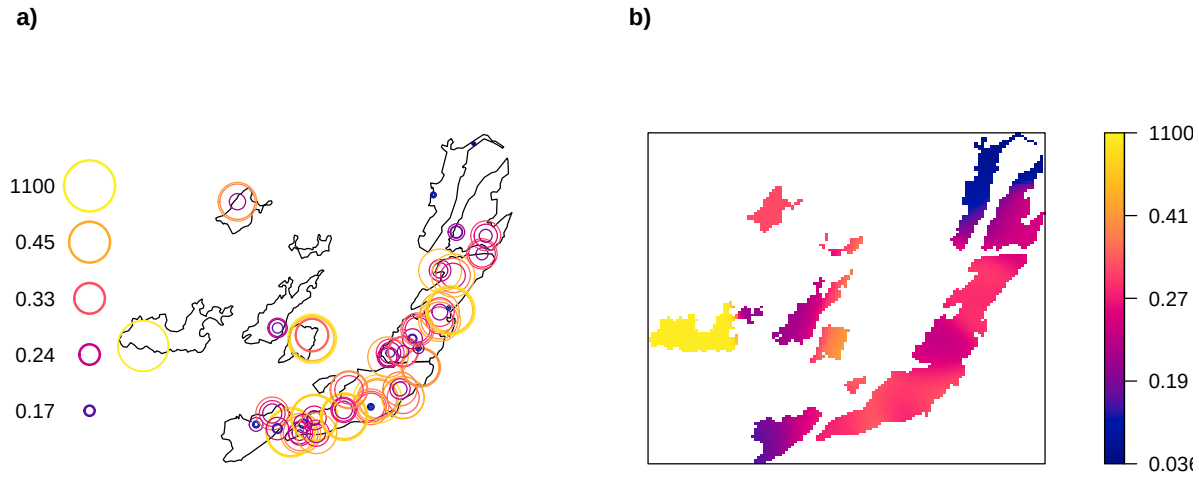

Figure F.1-10: Smoothing using the probability integral transformation. (a) ratio of iron (Fe) to silica (SiO2) assayed by pXRF instrument on 123 rocks at 41 sites across Murujuga. Values are displayed on the probability scale; (b) spatially smoothed ratio, displayed on probability scale.

F.1.4.4 Robustifying procedures — trimming and Winsorizing

The trimmed mean is a simple strategy for mitigating the effects of extreme values on the sample mean. To compute the trimmed mean of a set of numbers, the usual procedure is to delete a chosen fraction of the data, e.g. by removing the lower 5% and the upper 5% of the values. Then the sample mean of the remaining data is computed. The result is the "10% trimmed mean". Alternative, one-sided versions of trimming can also be used. The main disadvantage of trimming is the loss of information when the sample size is small.

For data y_i observed at spatial locations x_i, it may be appropriate to trim the observations by deleting a fixed fraction of the observations before computing the N-W smoother.

Winsorizing is a related procedure in which the extreme values, instead of being removed from the data, are replaced by less extreme values. For a set of numerical values y_i, the usual procedure is as follows.

1. Calculate first and third sample quartiles Q_1, Q_3 of data $\{y_i\}$ and hence calculate the inter-quartile range $IQR = Q_3 - Q_1$.
2. Calculate upper and lower thresholds

$$\begin{aligned} U &= Q_3 + c\,IQR \\ L &= Q_1 - c\,IQR \end{aligned}$$

   where $c \geq 0$ is a chosen coefficient. A typical value is $c = 1.5$.

3. Calculate the extreme values within $[L, U]$,

$$\begin{aligned} y_U &= \max\{y_i : L \leq y_i \leq U\} \\ y_L &= \min\{y_i : L \leq y_i \leq U\} \end{aligned}$$

4. Replace extreme values outside $[L, U]$ with the nearest extreme inside $[L, U]$:

$$y_i^* = \begin{cases} y_L & \text{if } y_i < L \\ y_i & \text{if } L \leq y_i \leq U \\ y_U & \text{if } y_i > U \end{cases}$$

Alternative, one-sided versions of this rule may also be chosen.

For data y_i observed at spatial locations x_i, it may be appropriate to Winsorize the observations before computing the N-W smoother.

F.1.5 Spatially weighted median

At each spatial location x, the Nadaraya-Watson estimate is a weighted average (*F.1.3*) of the individual observations y_i with weights $a_i(x)$. The weighted average has no resistance to extremes,

in the sense that if any single observation y_i diverges to $+\infty$ or $-\infty$, the weighted average also diverges.

An obvious remedy is to replace the weighted average by the weighted median, that is, the median of the observations y_i with weights $w_i = a_i(x)$.

There are at least 7 different definitions of the sample median of a set of numbers (Hyndman and Fan, 1996). Two of these definitions can easily be extended to the case of weighted numerical data. The **right-continuous** weighted median is

$$\widehat{m}(x) = \widehat{F}_x^{-1}(0.5) = \mathsf{inf}\{y : \widehat{F}_x(y) \geq 0.5\}$$

where $\widehat{F}_x$ is the weighted empirical CDF

$$\widehat{F}_x(y) = \sum_i a_i(x)\ 1\{y_i \leq y\}.$$

The **interpolated** weighted median is

$$\widetilde{m}(x) = \widetilde{F}_x^{-1}(0.5)$$

where $\widetilde{F}_x$ is the piecewise linear function that interpolates between the points $(y_j, \widehat{F}_x(y_j))$.

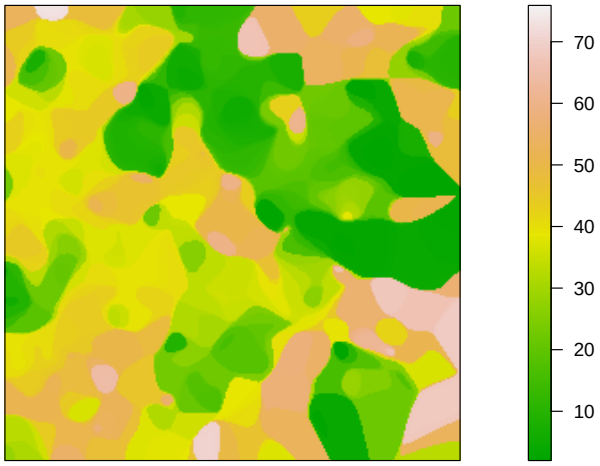

Figure F.1-11: Spatially weighted median with bandwidth $\sigma = 5$.

Figure *F.1-11* shows the spatially weighted median of 'interpolated' type, computed for the data in Figure *F.1-2* using a Gaussian kernel with bandwidth 5 km.

Spatially weighted quantiles can also be computed using the same principle.

F.1.6 Concordance between smoothed images

In this project, data are collected on a monthly basis at a network of monitoring stations. Spatially smoothed averages of the data from each month are computed. It is of interest to determine whether the smoothed images of a particular quantity exhibit a consistent spatial pattern across different months, while allowing for seasonal variation in the overall value of the quantity.

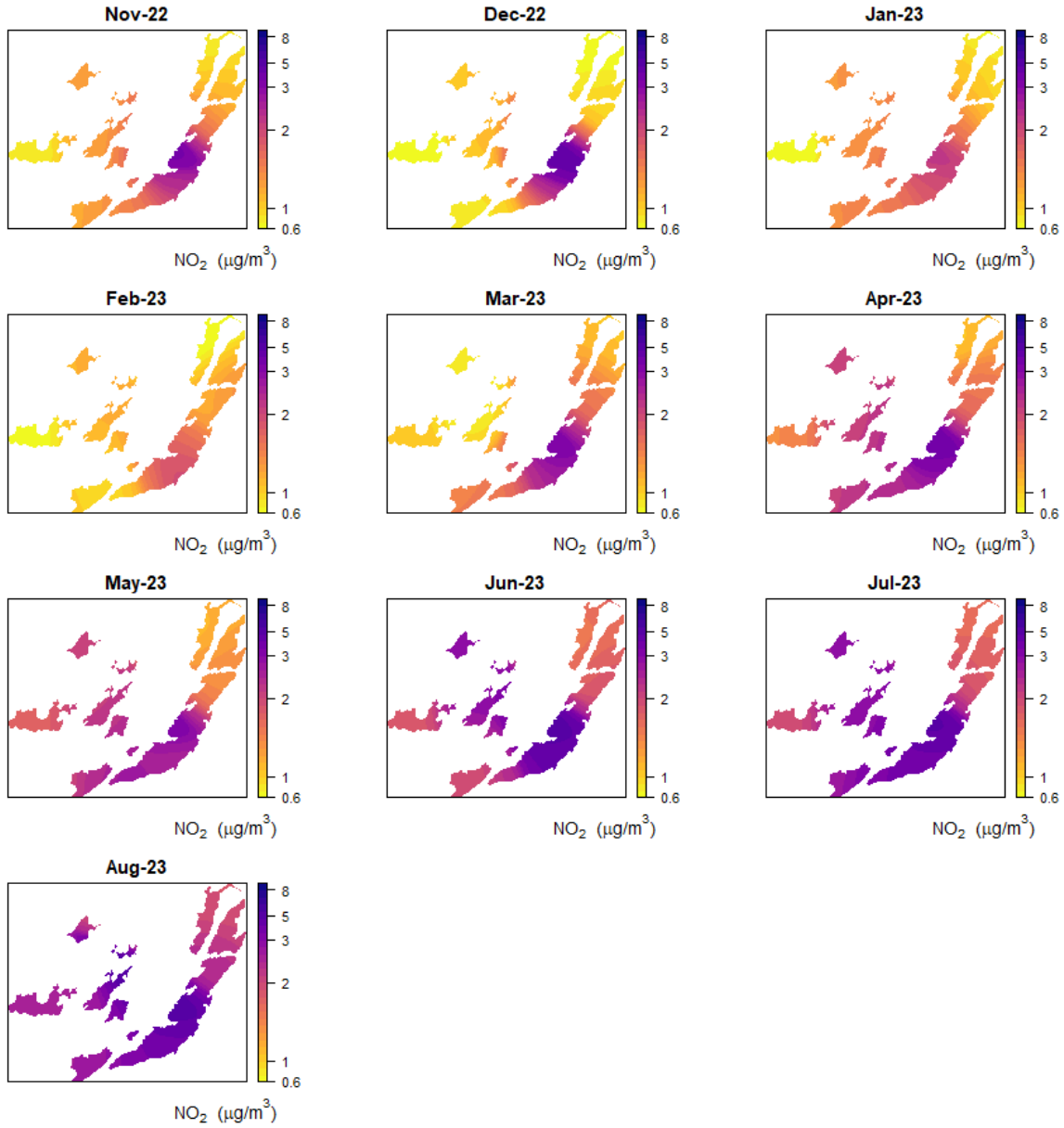

Figure F.1-12: Spatially smoothed monthly average concentration of NO_2 by sampling period. Common colour map based on percentiles.

For example, Figure *F.1-12*, shows spatially smoothed average estimates of NO_2 concentration from the passive samplers, for each month. (This figure is identical to Figure *7.11-14* on page 370). Images are plotted using the same colour map. It is immediately evident that the overall level of

NO_2 varies from month to month. However there is also a consistent spatial pattern in the sense that the locations having relatively high values of NO_2 concentration are the same for each month.

A tool for evaluating the concordance between images is:

1. For each image separately, apply the probability integral transformation. That is, for a given pixel, if the original image value is x, the transformed value at this pixel equals the fraction r of all pixels in the image which have values less than or equal to x. We shall call the values r the (fractional) "ranks". Fractional rank values range from 0 to 1. The pixel with the largest value is assigned fractional rank $r = 1$; the median pixel value corresponds to fractional rank $r = 0.5$.
2. Combine the rank images by computing their pixelwise average. That is, for a given pixel, compute the average of the fractional ranks assigned to that pixel in each of the images. The result will be called the "consensus rank"image. Consensus rank values range from 0 to 1 but may not attain these limits. A consensus rank equal to 1 implies that the pixel in question achieved the maximum pixel value in all of the original images.
3. Similarly combine the rank images by computing their pixelwise standard deviation. That is, for a given pixel, compute the sample standard deviation of the fractional ranks assigned to that pixel in each of the images. The result will be called the "disagreement" image. A disagreement value of 0 indicates that all images assigned exactly the same rank to the pixel in question.

Figure *F.1-13* shows the fractional rank images for the smoothed monthly NO_2 images of Figure *F.1-12*. These images effectively ignore the differences in overall level of NO_2 and retain only information about the comparative levels of NO_2 at different locations.

Figure *F.1-13* shows the fractional rank images computed from the smoothed monthly NO_2 images in Figure *F.1-12*. The fractional rank images effectively ignore the variation in the overall level of NO_2, and retain only information about the comparative levels of NO_2 at different locations at any given time. These images suggest that, at any given time, NO_2 values are usually higher near the Dampier port than elsewhere.

The consensus image is shown in Figure *F.1-14*. It indicates that the highest levels of NO_2 are consistently found near the Dampier port, while the lowest levels are consistently found at the extreme north and west of the Murujuga region.

The rank disagreement (standard deviation) image is shown in Figure *F.1-15*. Very low values of disagreement are seen in the region near Dampier port, indicating that in this region there is strong agreement between the rankings obtained in different months.

F.1.7 Software

The statistical calculations in this Appendix, and computations of spatially smoothed surfaces in the main report, were performed using the R statistical software system, available free from `cran.r-project.org`. The R package `spatstat` contains code for spatial smoothing, specifically the function `Smooth.ppp` for Nadaraya-Watson smoothing and `SpatialMedian.ppp` for the spatially-weighted median.

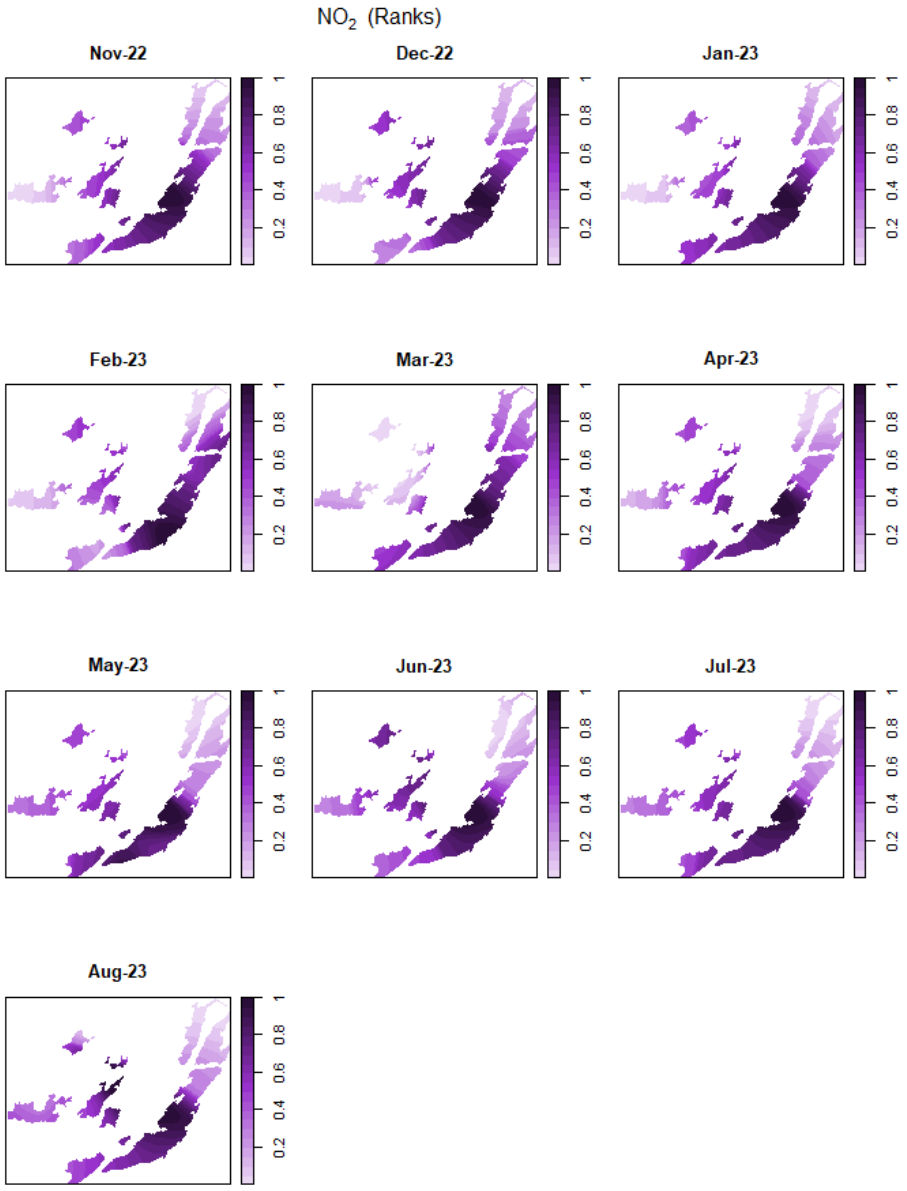

Figure F.1-13: Fractional rank of smoothed NO_2 concentration, for each month.

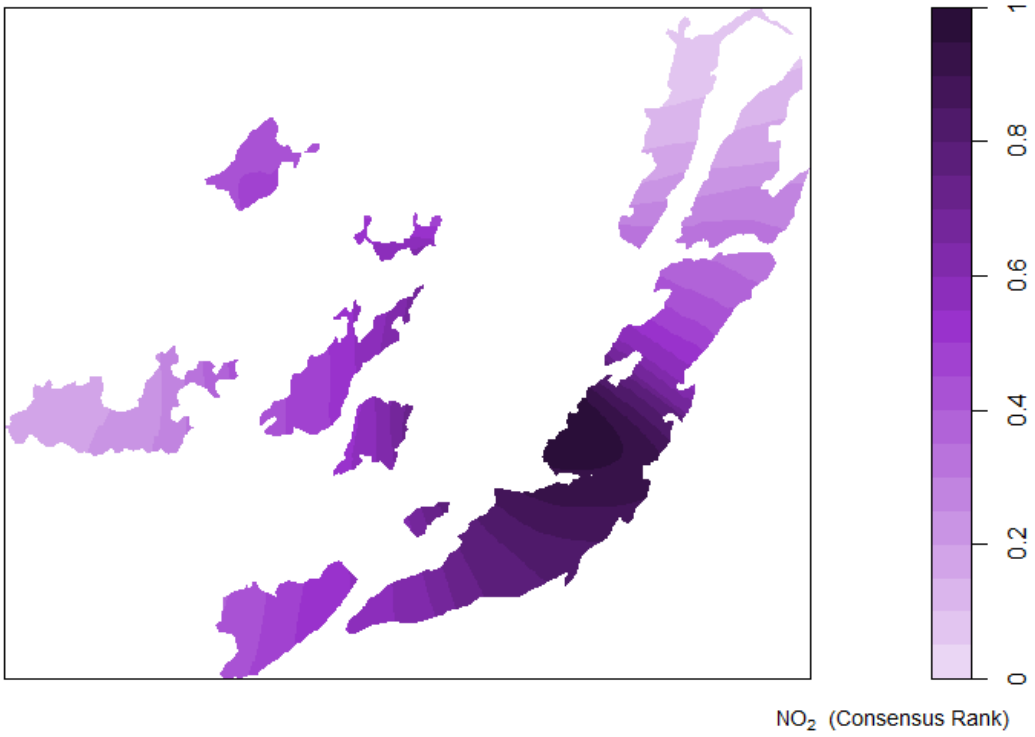

Figure F.1-14: Consensus rank for smoothed NO_2 concentration.

Figure F.1-15: Rank disagreement image for smoothed NO_2 concentration.

F.2 Porosity analysis

This section describes statistical methodology used in the report to measure rock porosity from grey scale images generated by a scanning electron microscope, and in particular, to measure how porosity changes with increasing depth below the rock surface.

New methodology was developed specifically for the MRAMP. It will be documented in detail in a peer-reviewed journal publication.

F.2.1 Problem statement

Figure *F.2-1* shows a scanning electron microscope image of a thin section of sample rock. Lighter areas in this greyscale image represent rock components of different kinds, while the very darkest areas are void space that is not occupied by rock. The large black area at the top of the image is empty space outside the rock sample; the macroscopic surface of the rock is the lighter area that is in contact with this black area.

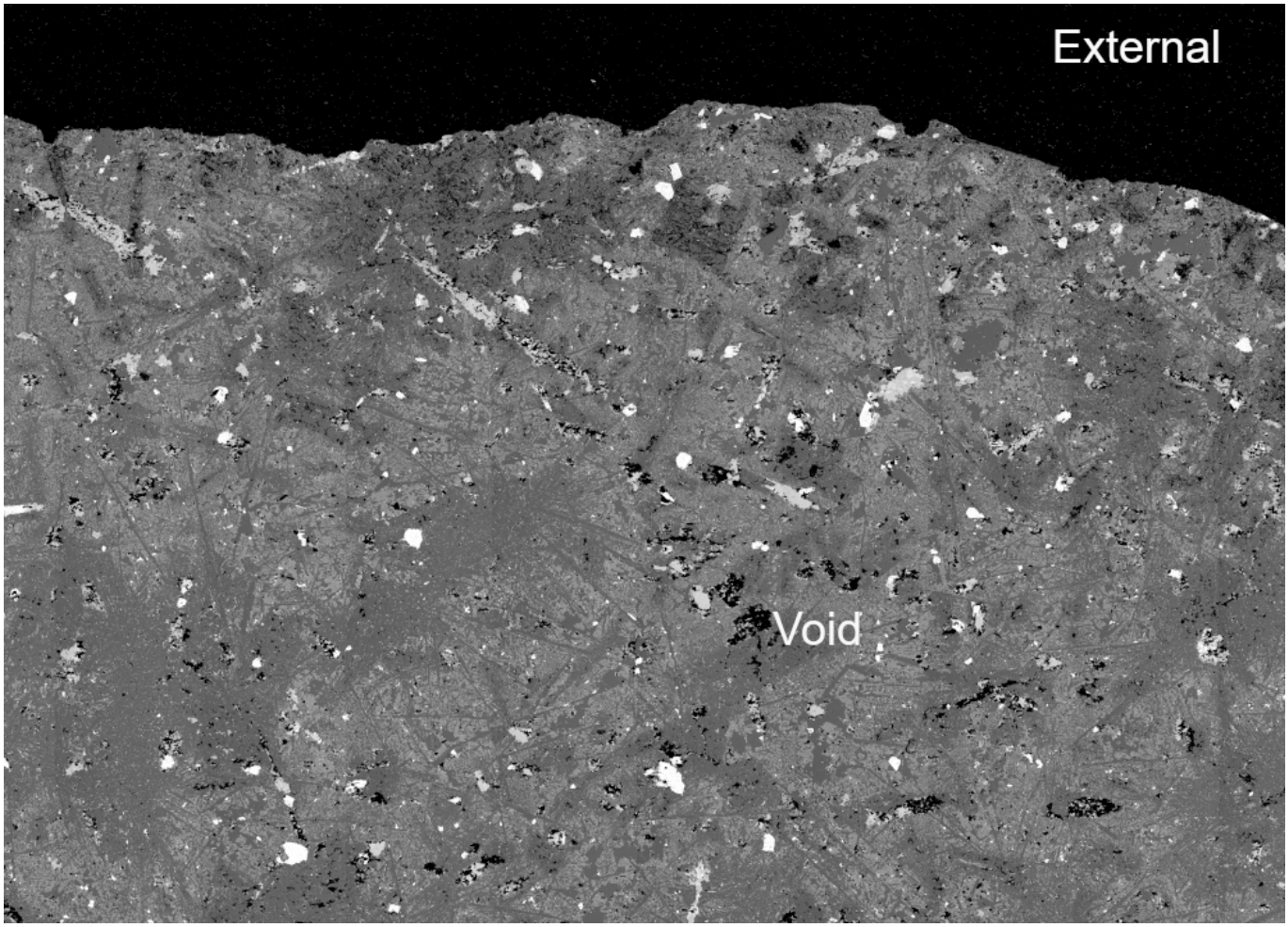

Figure F.2-1: Scanning electron microscope, backscattered electron image of thin section of sample rock - granophyre from site AQ03. Surface at top of image. Physical size of image is about 10 mm wide by 7.5 mm deep, image cut into four to provide multiple samples.

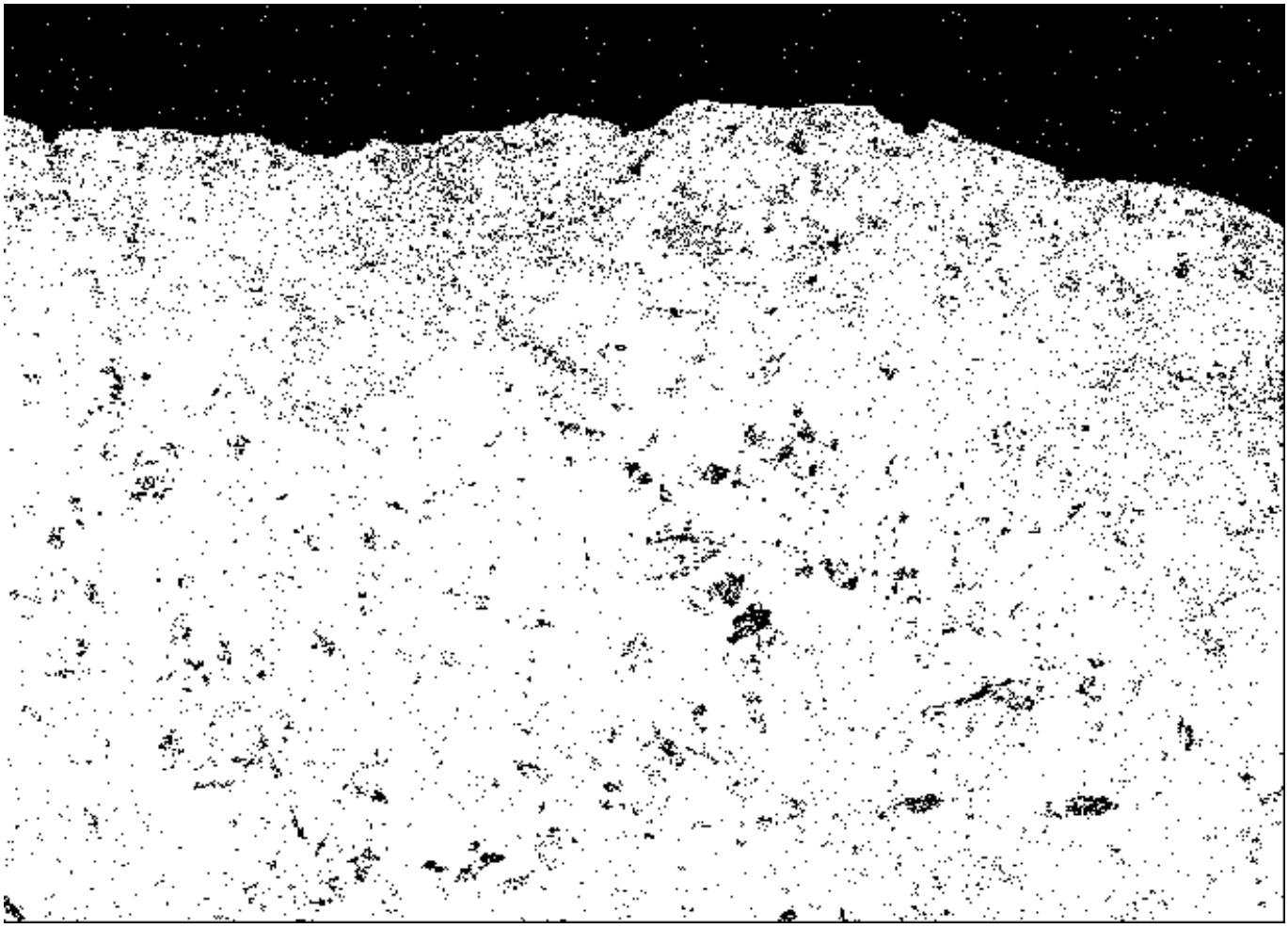

Figure F.2-2: Binary image obtained by thresholding Figure F.2-1. Binary value one (white) interpreted as rock; binary value zero (black) interpreted as void space.

Rock sample images provided were 39 mm to 44 mm wide and 4.5 mm to 13.2 mm deep with square pixels with side length of 2 μm to 2.5 μm. Figure *F.2-1* is approximately 10 mm by 7.5 mm. This is part of an original sample image that is 42.4 mm wide by approximately 8 mm wide with a pixel size of 2 μm by 2μm. Images needed to be cropped to remove any edges on the sides or bottom of the image. To help make processing times manageable and to allow multiple samples per site, the images were then cropped into four.

Our first step is to convert this grey-scale image to a binary image in which the value one (white) represents rock and the value zero (black) represents void space. This is done using a simple thresholding operation and the result is shown in Figure *F.2-2*. The result is of course sensitive to the choice of greyscale threshold.

The amount of void space appears to reduce progressively as we move from top to bottom in Figure *F.2-2*, that is, as we move deeper into the fresher rock and further away from the macroscopic surface. The objective of our analysis is to quantify this by inferring the porosity of the rock at different depths below the surface.

F.2.2 Definition of porosity

Volumetric porosity of rock is the average fraction of volume of three-dimensional space inside the rock which is occupied by voids. Delesse's Principle of petrography and quantitative microscopy (Delesse, 1847) states that the average observed fraction of *area* in a two-dimensional plane section of rock is equal to its volumetric porosity, under certain assumptions (DeHoff and Rhines, 1968; Underwood, 1970; Weibel, 1979, 1980; Elias and Hyde, 1983; Kurzydłowski and Ralph, 1995; Russ and DeHoff, 1999; Baddeley and Jensen, 2005). The area fraction of voids in a thin plane section is sometimes called the "optical porosity".

If the section plane is oriented vertically, that is, normal to the macroscopic surface of the rock, then the section image can be divided into bands of increasing depth below the rock surface. Delesse's Principle can then be applied separately to each band of depths, giving the researcher an estimate of the volumetric porosity in each band of depths below the surface. This is the essence of our approach.

F.2.3 Identification of macroscopic surface

This study investigates how porosity changes with increasing depth below the macroscopic surface of the rock. Measurement of depth requires identification of the profile of the macroscopic surface in the section image. The approach taken here is to first identify the region that is exterior to the rock.

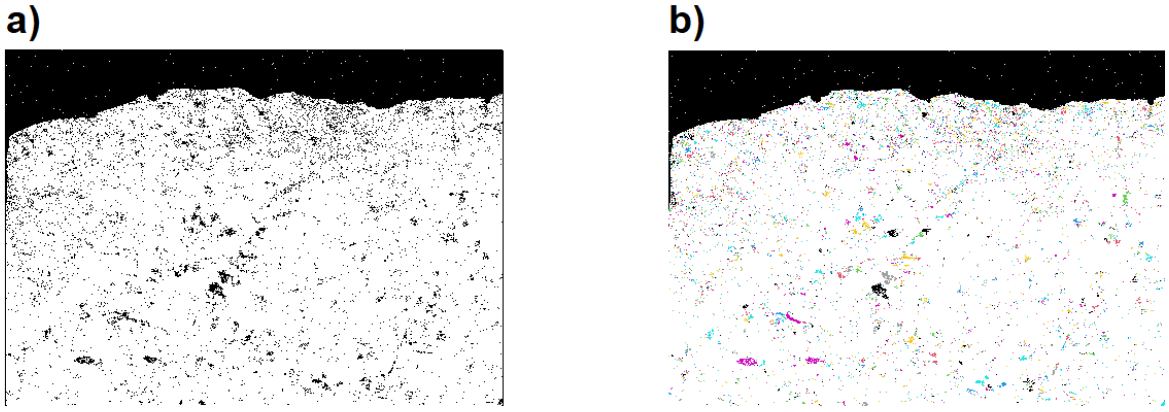

Figure F.2-3: Connected component transform for granophyre from site AQ03, field 4 of 4: (a) binary input image (white = rock, black = void). (b) connected component transform of void. Each connected component of the void space is labelled by a different integer value. The integer values are graphically depicted as colours.

We use the **connected component transform** (Rosenfeld and Pfalz, 1966). When applied to the black pixels in a binary image, this transform identifies the different 'islands' of black against the white background, and assigns each 'island' a different integer label. Any two void pixels which are connected to each other by a path lying entirely inside the void, and which therefore belong to the same 'island', are assigned the same label. The transform is illustrated in Figure *F.2-3* where

panel (a) shows the input binary image, and panel (b) the connected component transform, with labels represented as colours. (The large black area in panel (a) has been depicted as the colour black in panel (b)).

From the connected component transform, the region of space lying outside the (macroscopic surface of the) rock can be identified automatically by counting the frequency of each possible label in the connected component transform, and selecting the most frequent label value. This identifies the connected component with the largest area.

A problem occurs when the binary image includes a channel or crack that is inside the rock but is connected to the outer surface. The space occupied by a crack should be classified as “inside” the rock but the connected component transform will identify it as part of the “outside”. Our strategy for avoiding such artefacts is to pre-process the binary image using the operations of mathematical morphology (Serra, 1982; Soille, 2003), in particular, morphological opening of the black pixels. This effectively “smooths” the contour of the rock surface. Each island of black pixels is slightly reduced in area. Figure *F.2-4* shows the effect of a morphological opening of the black pixels followed by the connected component transform. In panels (a) and (b) the opening radius is 10 μm and we see in panel (b) that two channels into the rock have been coloured black, indicating that they are labelled as part of the “outside”. In panels (c) and (d) the opening radius is 40 μm and the channels are no longer labelled as part of the “outside”.

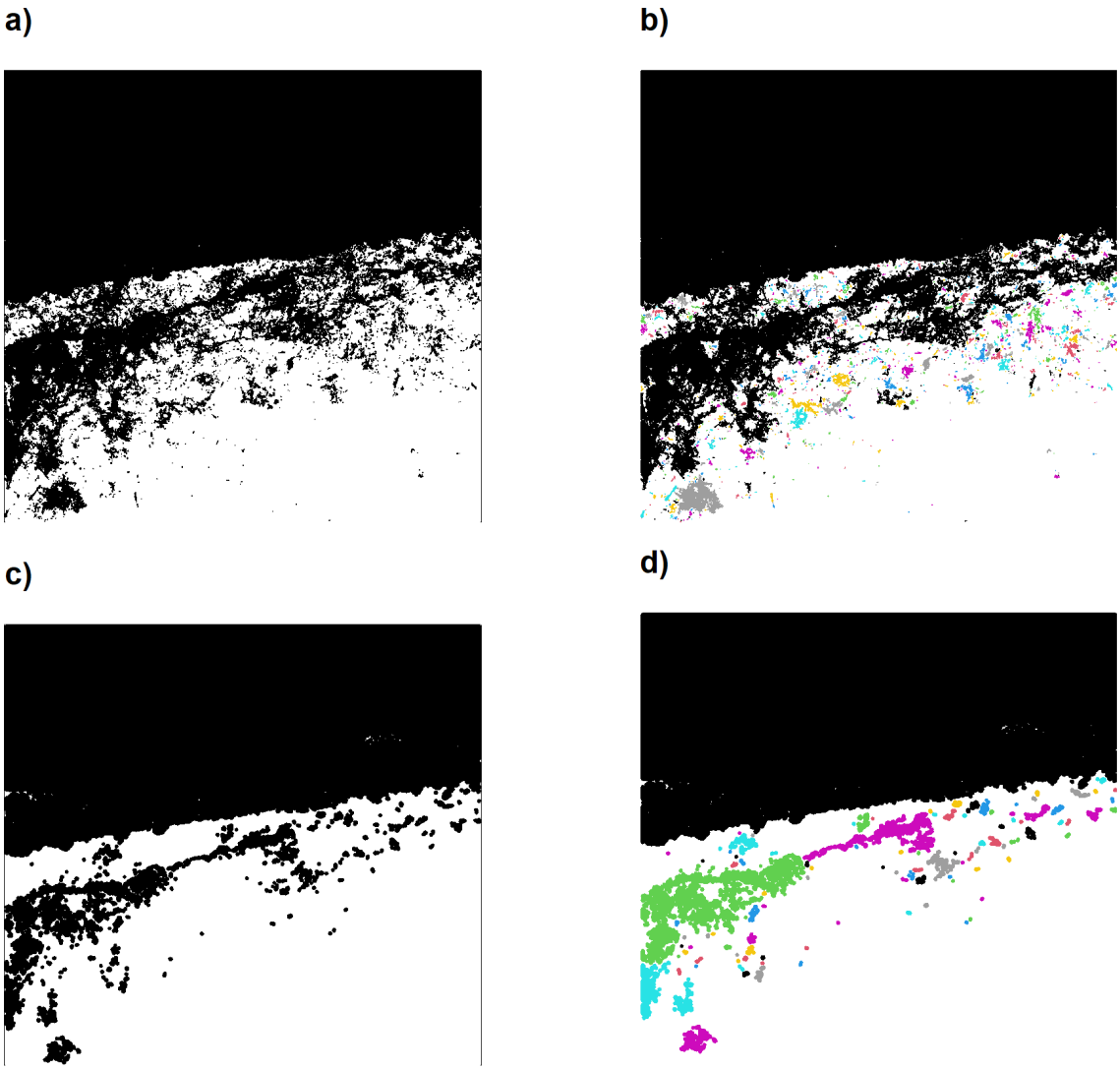

Figure F.2-4: Connected component transform applied to openings of different sizes for granophyre rock sample, site AQ09, field 4 of 4. (a) binary input image, opened by 10 μm, (b) connected component transform of void in (a). (c) binary input image, opened by 40 μm. (d) connected component transform of void in (c). Colours represent different connected sets (colours are repeated as needed).

F.2.4 Depth

The region identified as the largest connected component of the black pixels in the binary image is taken to be the “top” of the image. It determines the correct orientation of the images. The lower boundary of the “top” is our working definition of the macroscopic surface of the rock sample in the thin section.

The next task is to compute the “depth” (distance from the macroscopic surface) for each pixel inside the rock. Depth could be defined as either

1. the vertical distance from the pixel in question to the surface (measured using the vertical coordinate of pixel position); or
2. the shortest distance from the pixel to any point along the surface.

We follow the second approach and use the distance transform (Rosenfeld and Pfalz, 1968) applied to the “top” region. The value of the distance transform at a given pixel is the length of the shortest path, through a series of steps in the image raster, from the pixel in question to the “top”.

Figure *F.2-5* shows an example of application of the distance transform. In panel (b) the value at each pixel is equal to the distance from that pixel to the “top” region, expressed in μm. The deepest parts of the rock sample are approximately 6000 μm or 6 mm from the surface.

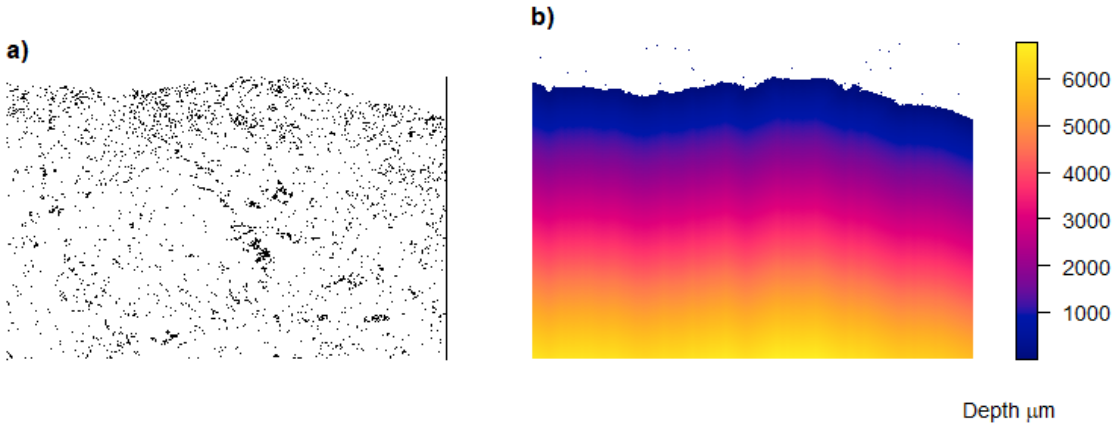

Figure F.2-5: Distance transform. (a) binary image; (b) distance transform of "top". Granophyre, site AQ03, field 4 of 4.

F.2.5 Estimating porosity as a function of depth

The foregoing calculations produce three digital images R, T and D where, for every pixel x in the image raster,

- $V(x) = 1$ if the pixel is in the void, and zero if it is in the rock;
- $T(x) = 1$ if the pixel is in the "top", and zero if not;
- $D(x)$ is the distance from pixel x to the "top".

Attention is now restricted to the complement of the "top". The algorithm collects the data as pairs of values (d_i, v_i) for all pixels x_i such that $T(x_i) = 0$. Figure *F.2-6* shows an illustrative dataset of this type, using a small sample of only 50 pixels.

The goal is to estimate $p(d) = \mathbb{P}\{v_i = 1 \mid d_i = d\} = \mathbb{E}[v_i \mid d_i = d]$ as a function of depth d. This is a straightforward task of nonparametric binary regression which has many practical solutions.

A simple approach would be to divide the range of possible distance values into bands, and to calculate the average value of v within each distance band. This is equivalent to applying Delesse's Principle to the three-dimensional slabs of rock defined by the bands. Figure *F.2-7* shows the result of this technique applied to the illustrative data of Figure *F.2-6*.

Alternatively, a one-dimensional version of the Nadaraya-Watson estimator can be used. The estimated value $\widehat{p}(d)$ is a weighted average of the values v_i with weights depending on $d_i - d$.

Other alternatives include smoothing splines and loess (locally weighted least squares) smoothers. Figure *F.2-8* shows the result of spline smoothing applied to the illustrative data of Figure *F.2-6*.

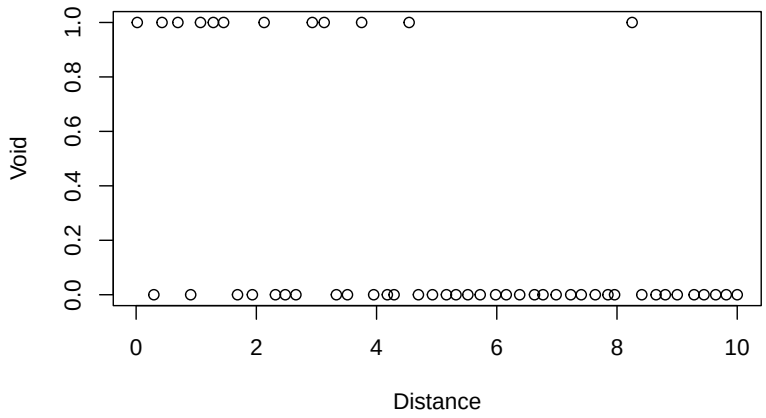

Figure F.2-6: Illustrative example data for estimation of porosity curve. Indicator of void (one = void, zero = rock) is plotted against distance from rock surface, for a small sample of 50 pixels.

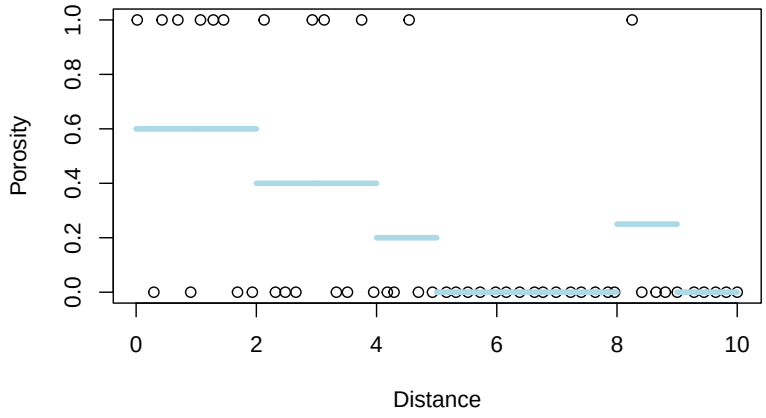

Figure F.2-7: Estimates of porosity calculated as the average void fraction in each band of distances, for the illustrative example in Figure F.2-6.

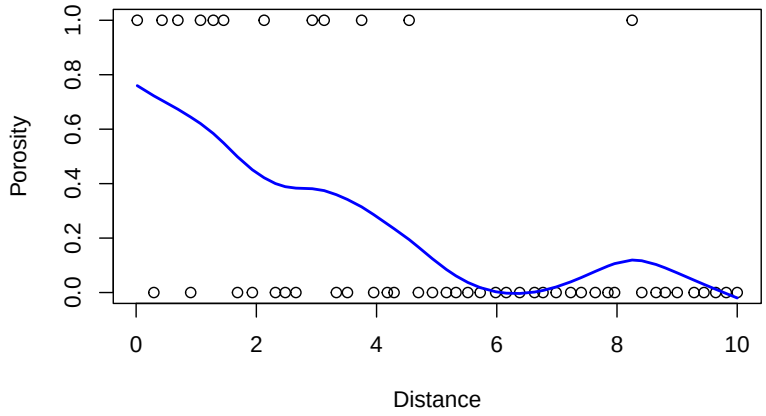

Figure F.2-8: Spline smoothing estimate of porosity as a function of depth, for the illustrative example in Figure F.2-6.

a)

b)

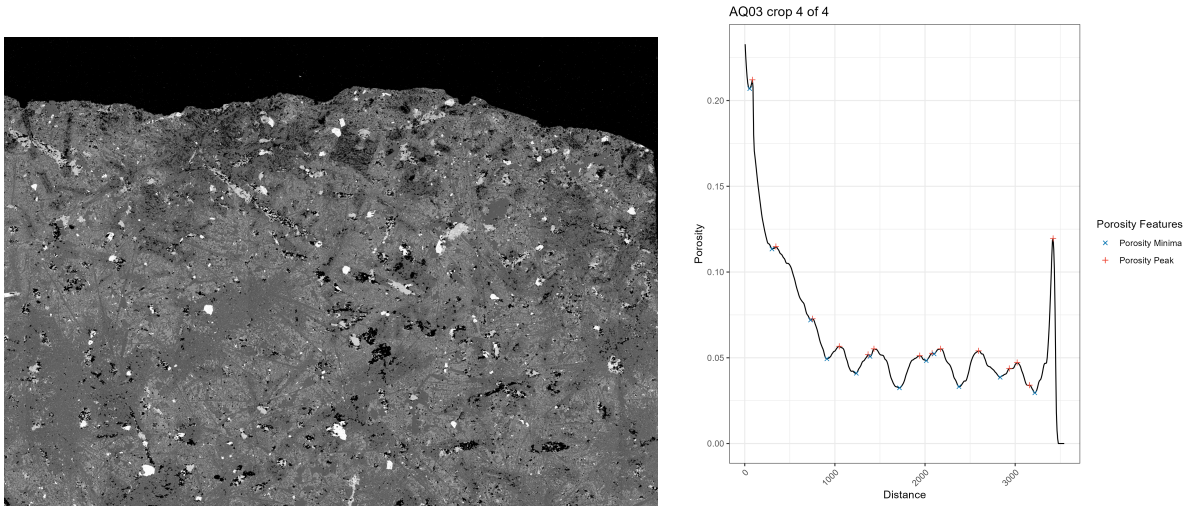

Figure F.2-9: Estimation of porosity as a function of depth. (a) grey scale back scattered electron image, scanning electron microscope. (b) smoothed estimate of porosity as a function of depth. Granophyre, site AQ03, field 3 of 4.

F.2.6 Summary indices of porosity

In order to facilitate comparison of the porosity of different rocks, it is useful to define a single numerical summary index of porosity. Bearing in mind that the estimates of porosity typically fall to a very small value as depth increases beyond 1.0 mm, the following measures were considered:

- the average porosity over $[0, D]$;
- the integral of $p(d)$ with respect to d;
- the maximum value of $p(d)$;
- the depth d at which porosity is maximised;
- the width of the range of depths associated with high porosity;
- indices of the flatness or variance of porosity.

The following indices were developed.

Average porosity was initially calculated by averaging the estimated smooth porosity curve values across the depth of the sample (for positive distances only). However, samples have a wide range of maximum depths: the shallowest sample had a depth of approximately 3.1 mm. Accordingly the index was redefined as the average of the smooth porosity curve values for the first 3.1 mm of the sample.

Maximum porosity was simply the maximum value of the porosity curve values (positive distance from the surface only). This measure follows similar patterns to both average values, but range tends to vary with the morphological opening: larger morphological openings tend to produce larger maximum values closer to the surface. This result is expected, as larger morphological openings mean that surface roughness contributes to the void areas boosting porosity.

Depth of first maximum porosity was the depth in micrometres at which the estimated porosity curve achieved its initial peak (its first local maximum). This measure was found to be excessively sensitive to, and inversely related to, the morphological opening radius. Depth of maximum porosity was also inversely related to maximum porosity, that is, rocks in which an initial peak of porosity occurs at a shallow depth tend to be rocks with high maximum porosity, as one might expect. In spatial studies, this measure provided inverse spatial patterns to those found with the maximum and average porosity indices, again consistent with interpretation. Patterns observed in the depth of first maximum porosity were unacceptably sensitive to the morphological opening radius, and were generally not found to be statistically significant.

Other measures, intended to summarise the range of porosity values and the variation in porosity values, tended to be difficult to construct without making arbitrary choices. Measures summarising the peaks and dips in the curves were also tried, but tended to be dominated by very small peaks and dips; also some initial high values were missed where the maximum values were on the surface. Trying to determine what qualified as a significant peak or dip again involved somewhat arbitrary choices.

F.3 Monte Carlo tests

F.3.1 Principle

Monte Carlo tests (Barnard, 1963; Dwass, 1957; Hope, 1968) are randomised procedures for testing statistical significance based on the principle of symmetry. A simplified summary is provided in Baddeley et al. (2015, Sec 10.6).

The most basic version of the Monte Carlo test applies when the null hypothesis H_0 is a simple hypothesis, i.e. the probability distribution of the data is completely specified by H_0 without any unknown parameters. First the researcher defines the test statistic T, which may be any function that returns a single numerical value when applied to the data. The researcher also chooses the number m of simulations to perform. Suppose the observed data are x_{obs}. Then the procedure is as follows.

1. Calculate the observed value of the test statistic $t_{\mathsf{obs}} = T(x_{\mathsf{obs}})$.
2. For $j = 1, \ldots, m$,
   (a) Generate a random dataset $x^{(j)}$ from the distribution specified by H_0.
   (b) Calculate the value of the test statistic for the simulated dataset, $t_j = T(x^{(j)})$.
3. Reject H_0 if the observed value of the test statistic t_{obs} is greater than the maximum of all the simulated values $t^{(1)}, \ldots, t^{(m)}$.

This test procedure has exact size (i.e. probability of type II error) equal to $1/(m+1)$ assuming there are no tied values. More generally one could calculate the Monte Carlo p-value $p = (k+1)/(m+1)$ where $k = \sum_{j=1}^{m} \mathbf{1}\{t_{\mathsf{obs}} <= t_j\}$ is the number of simulated values which exceed the observed value of the test statistic.

In more advanced versions of the Monte Carlo test, the random dataset generated in step 2a is obtained by randomising the observed data, or by any procedure which ensures that the observed and simulated datasets are probabilistically exchangeable under H_0.

F.3.2 Monte Carlo test of spatially constant mean

Returning to the context of Appendix *F*.1, we assume that numerical values $y_1, \ldots, y_n$ of some quantity have been observed at spatial locations $x_1, \ldots, x_n$ in a study region W. The objective is to assess whether the quantity is constant on average across the study region, or whether there are some areas where the quantity is elevated. Figure *F.3-1* shows an example dataset.

Figure *F.3-2* shows the spatially smoothed porosity obtained from Figure *F.3-1* using the Nadaraya-Watson smoother.

We may write $y_i = \mu_i + \epsilon_i$ where $\mu_i = \mathbb{E}[y_i]$ is the expected value of the quantity at location x_i, and ϵ_i is the measurement error. We shall assume that the errors $\epsilon_1, \ldots, \epsilon_n$ are exchangeable random variables. Consider the null hypothesis that the quantity has constant mean,

$$\mathsf{H}_0 : \mu_i \equiv \mu$$

where the mean μ is not specified in advance.

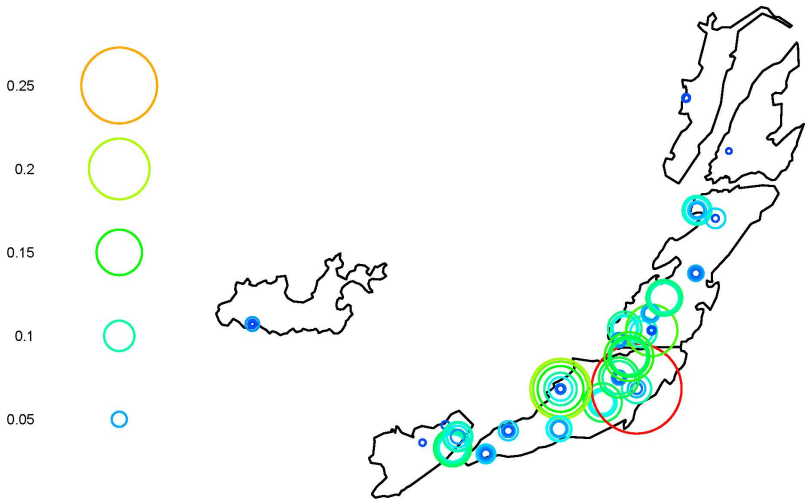

Figure F.3-1: Example data: values of porosity index obtained from rock samples at sites across Murujuga.

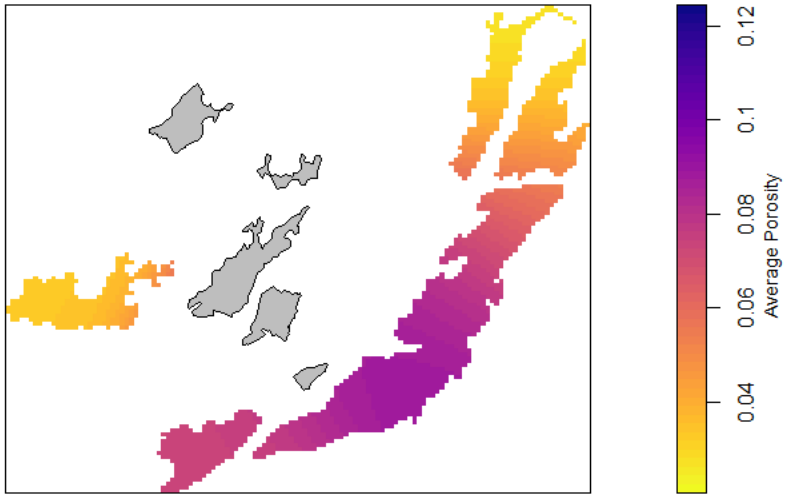

Figure F.3-2: Spatially smoothed (Nadaraya-Watson) porosity.

Figure F.3-3: Pointwise Monte Carlo p-values for the one-sided test of constant mean against the alternative of elevated local mean. Colour map for p-values is logarithmic.

The randomisation procedure is as follows.

1. Compute the spatially smoothed surface $\widehat{y}(x)$ at all $x \in W$ from the observed data.
2. For $j = 1, \ldots, m$
   (a) Randomly permute the values $\{y_i\}$ holding the locations $\{x_i\}$ fixed, to obtain a randomised dataset
   (b) Compute the spatially smoothed surface $\widehat{y}^{(j)}(x)$ at all $x \in W$ from the randomised data.

If H_0 is true, then the observations $\{y_i\}$ are exchangeable, and the permuted datasets are exchangeable realisations of the null hypothesis.

It remains to specify a test statistic T which, when applied to the smoothed surface $\widehat{y}(\cdot)$, yields a single numerical value.

For a "pointwise test" we fix a location x_0 and define $T(\widehat{y}) = \widehat{y}(x_0)$, the value of the smoothed surface at the specified location. The pointwise Monte Carlo test at location x_0 rejects H_0 at significance level $1/(m+1)$ if the value $\widehat{y}(x_0)$ of the smoothed data at x_0 exceeds all of the corresponding values $\widehat{y}^{(j)}(x_0)$ of the smoothed simulated data.

Figure *F.3-3* shows the Monte Carlo p-value of the pointwise Monte Carlo test at each spatial location.

Figure *F.3-4* identifies those locations in the study region where the pointwise Monte Carlo test would be significant at the level 0.05.

It is important to understand that the pointwise test requires the location x_0 to have been specified and fixed in advance of performing the test. Figures *F.3-3* and *F.3-4* can be used to read off the result that *would have been* obtained from a pointwise test at any chosen location x_0 if that location

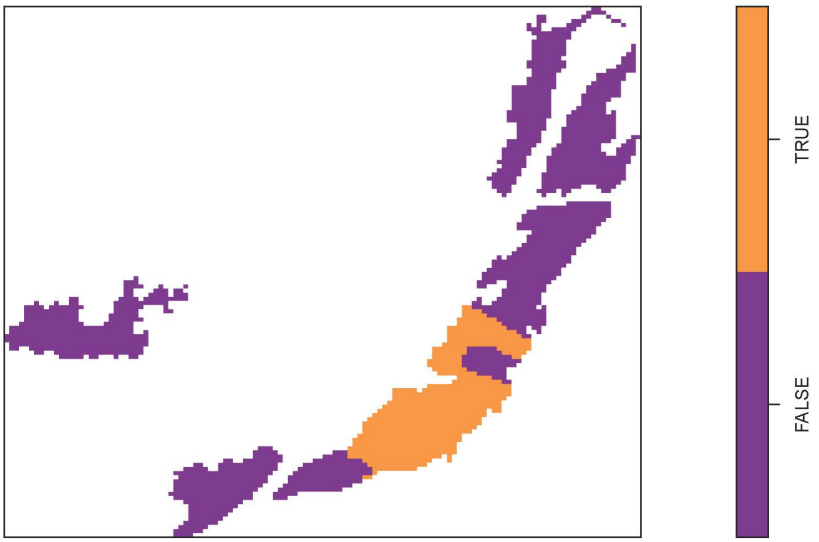

Figure F.3-4: Orange colour indicates locations where a pointwise Monte Carlo test would reject the null hypothesis of constant mean against the alternative of elevated mean.

had been specified in advance. For example, if we had chosen the location of Karratha airport, then reading Figure *F.3-4* shows that a pointwise Monte Carlo test at that location would have been significant at the 0.05 level; reading Figure *F.3-3* shows that the p-value would have been about 0.02. These figures can be used to assess the *sensitivity* of the pointwise test result to the choice of location x_0. For example, we can see from the figures that any choice of location in the Dampier-Karratha region would have yielded a statistically significant result for the pointwise test.

However, graphics which present the results of pointwise tests, like Figures *F.3-3* and *F.3-4*, are often misinterpreted. For example, a user who is hoping to find a statistically significant result, but who has no prior information about the location, might scan Figure *F.3-4* looking for regions where the result is significant; or worse, might scan Figure *F.3-3* looking for the most significant (smallest) p-value. This usage is invalid because it involves selecting the most favourable result from a battery of tests. This problem of "multiple testing" is further complicated in our context because the results of the pointwise test for two different locations are not probabilistically independent.

Our goal is to test the hypothesis of constant mean against the alternative of elevated mean at some locations. If the locations suspected of having elevated mean are not specified in advance, then a *global* rather than *pointwise* test is required. The test statistic T should measure the overall departure of the smoothed surface from a flat surface. While there are many options available, the most appropriate choice in this context is that $T(\widehat{y})$ should be the area of those locations where the pointwise test result is significant at (say) the 0.05 level. That is, for the data shown in Figure *F.3-1*, the test statistic value t_{obs} is the area of the orange region shown in Figure *F.3-4*. The "global" test rejects H_0 at level $1/(m+1)$ if the area of orange region computed for the data exceeds all of the values of the corresponding areas computed for the simulated data.

Figure *F.3-5* shows a histogram of the values of the test statistic computed for $m = 999$ simulated data sets. These values are the areas, in square kilometres, of the region where the pointwise test result is statistically significant at the 0.05 level. Approximately 70% of these values are equal to

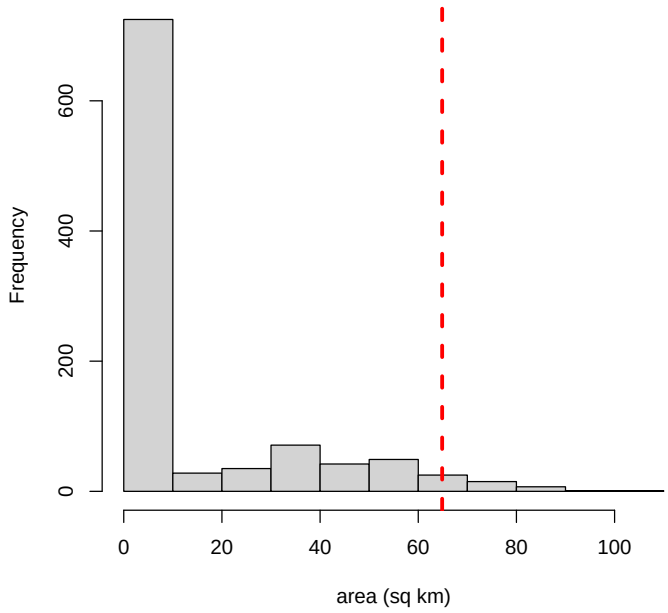

Figure F.3-5: Global test of uniformity. Histogram of test statistic values for the simulated data. Test statistic value for the observed data is shown as the red line.

zero, meaning that in 70% of simulated cases, there were no locations where the pointwise test result was significant. The vertical red line in the figure shows the value of the test statistic for the original data, approximately 65 square kilometres. Only 38 of the 999 simulated values exceed this value. The global p-value is $(1 + 38)/(1 + 999) = 0.039$, indicating significant evidence against the null hypothesis of constant mean, in favour of the alternative hypothesis of increased mean at some locations.

This page is intentionally blank.

G Statistical analysis: additional results

This Appendix reports further analysis of the data, including diagnostic checks on the validity of the data, diagnostics for assessing the appropriateness of the statistical methodology used, and re-analysis of the data using different choices of methodology.

Section *G*.1 revisits the analysis of rock surface porosity in Section 7.6 to investigate the sensitivity of the analysis to the tuning parameters of the algorithm. Section *G*.2 provides detail of the regression model of porosity index against rock height, used in Section 8.4. Section *G*.3 gives details of various anomalies detected in the colorimetry data, and of the procedure adopted for detecting anomalies, reported in Section 7.2. Section *G*.4 reports further analysis of the passive sampler data from Section 7.11. Section *G*.5 provides further exploration of the relationship between the Ramboll model predictions and the passive sampler observations, extending Section 8.3.

G.1 Porosity data

Analysis of rock porosity using back-scattered electron images from scanning electron microscopy of thin sections is described in Sections 7.6 and 8.4 of the main report. The supporting statistical methodology is documented in Appendix *F*.2.

Results of this analysis depend on the values of several tuning parameters, which control the image processing procedure, the estimation of porosity curves, the choice of a single numerical index of porosity, and the spatial smoothing of porosity index values. This section of the Appendix gives more detail about the effect of these tuning parameters and justification for the choices used in the main body of this report.

We shall explore the effect of the following parameters.

- Threshold: the value of grey-level intensity below which pixels are classified as void.
- Bandwidth: the smoothing bandwidth used in calculating porosity curves. Larger values of bandwidth produce smoother, flatter curves. Our algorithm first calculates the ‘optimal’ smoothing bandwidth according to the normal reference rule Silverman (1986, eq. (3.31), p. 48). This optimal bandwidth is then multiplied by an adjustment factor specified by the user. An adjustment value of 1.0 corresponds to using the automatically selected bandwidth.
- Morphological opening radius: the radius for the morphological opening used to define the rock surface. A radius of zero corresponds to skipping the morphological opening step. Larger values of opening radius cause larger pits and channels in the surface to be classified as part of the rock, increasing the estimated porosity at shallow depths.

G.1.1 Example outcomes for different rock samples

The method described in Appendix *F*.2.5, for determining porosity as a function of depth, was applied to all granophyre rock samples and also three gabbro rock samples. Granophyre is the most common rock type in Murujuga, but is not present at all sampling sites.

Figure *G.1-1* shows images from three granophyre rock samples. Each image has some different texture characteristics: panel (a) from site AQ08 shows a thick rind near the surface followed by an

area with many voids which seem to decrease further from the surface; panel (b) from AQ06 has a slightly coarser grain and has noticeable cracks running parallel to the surface; and panel (c) from AQ09 has extensive void areas that are linked to the surface.

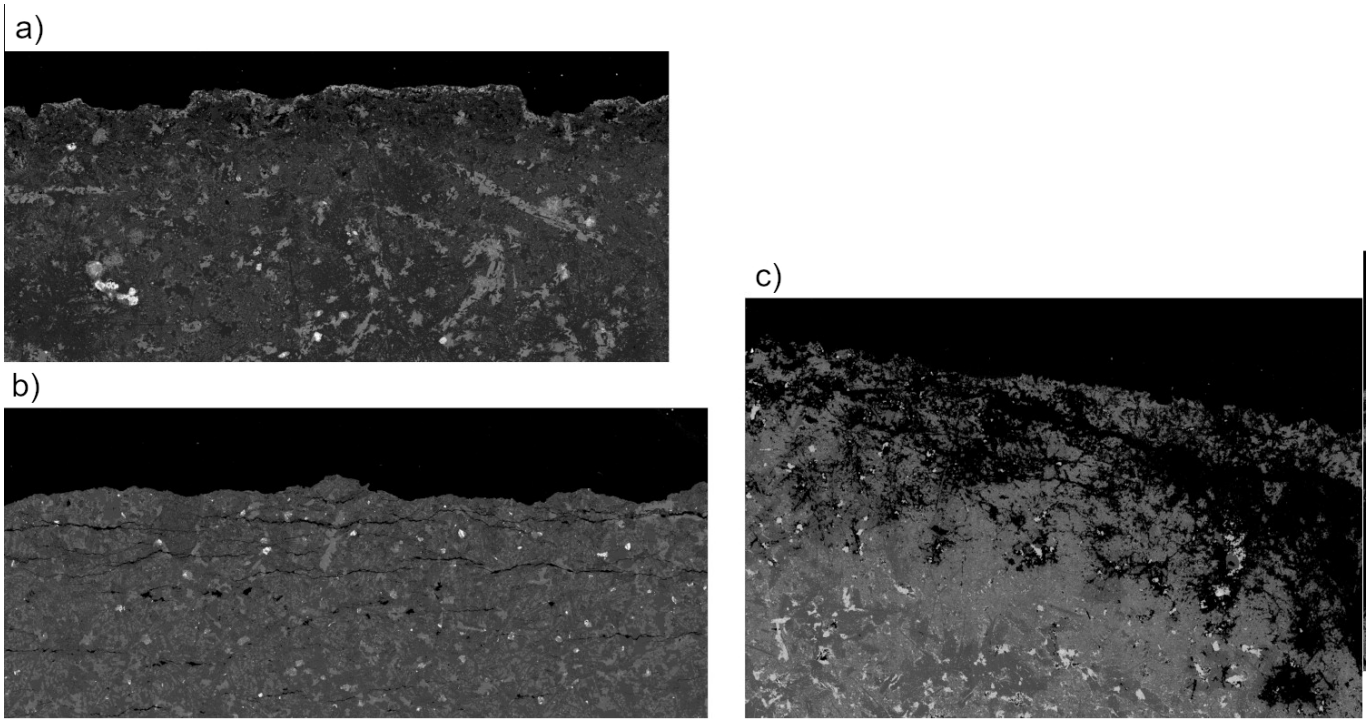

Figure G.1-1: Back scattered electron images from scanning electron microscopy of thin sections from three different granophyre rock samples. Sample images from left to right, top to bottom are: (a) AQ08 cropped image 3, (b) AQ06 cropped image 2, and (c) AQ09 cropped image 4.

Figure *G.1-2* shows the porosity curves calculated for each granophyre sample image in Figure *G.1-1* without using a morphological opening to define the surface. The expected effect is that any pits in the surface, or void channels connected to the surface, may not be counted as voids, reducing the calculated porosity.

Panel (a) in Figure *G.1-2* shows the porosity curve for the thin section image in Figure *G.1-2*(a) from AQ08. This curve has a prominent peak, at a shallow depth of approximately 250 μm, where the maximum porosity is 0.4, reflecting the presence of large voids near the surface. At depths greater than 1000 μm (1 mm) the estimated porosity decreases linearly toward zero. has the highest maximum porosity value of 0.4. Panel (b) in Figure *G.1-2* shows the porosity curve for Figure *G.1-2*(b) from AQ06. This curve also starts with a strong peak at shallow depth, although the maximum porosity is only 0.1. Unlike the previous example, this curve has a succession of relatively strong peaks at different depths, reflecting the observed presence of horizontal cracks in the image. Panel (c) in Figure *G.1-2* shows the porosity curve for Figure *G.1-2*(c) from AQ09. This curve is broadly similar to panel (a), although the maximum porosity is only 0.25. This does not reflect the striking presence of voids at shallow depths in Figure *G.1-2*(c).

For the first two sample images in panels (a) and (b), there is a satisfactory correspondence between the porosity curve and the observed features of the rock. However the image for panel (c)

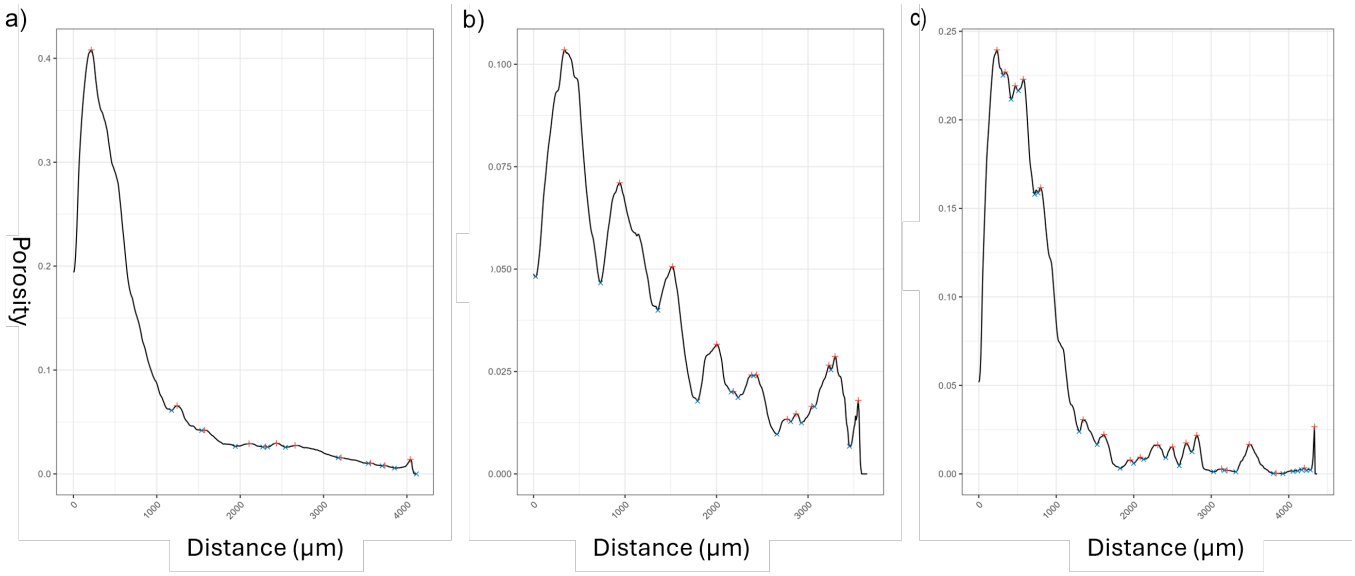

Figure G.1-2: Porosity curves for the three granophyre rock samples shown in Figure G.1-1. Curves computed using automatically selected bandwidth and without using morphological opening. Curves from left to right are for (a) AQ08 cropped image 3, (b) AQ06 cropped image 2, and (c) AQ09 cropped image 4 respectively.

is problematical: it appears that cavities connected to the surface may have been classified as external to the rock, and not included in porosity calculations. For automatic image processing, this issue is addressed by introducing morphological openings Serra (1988); Soille (2003) to define the surface. The effect of a morphological opening of radius r is that a pixel is classified as external to the rock when it is a void pixel and it lies inside a circle of radius r consisting entirely of void pixels. Thus, pits and cavities of diameter smaller than r are classified as lying inside the rock.

The images in Figure *G.1-1* were re-analysed using morphological openings with various values of the opening radius. Figure *G.1-3* shows the porosity curve for granophyre rock sample AQ09 cropped image 4 using an opening with radius 25 μm. The maximum estimated porosity increases to approximately 0.5 as a result of this morphological opening. This suggests that much more of the internal cavity is now included in the porosity calculation. The effects of morphological opening are discussed in greater detail below.

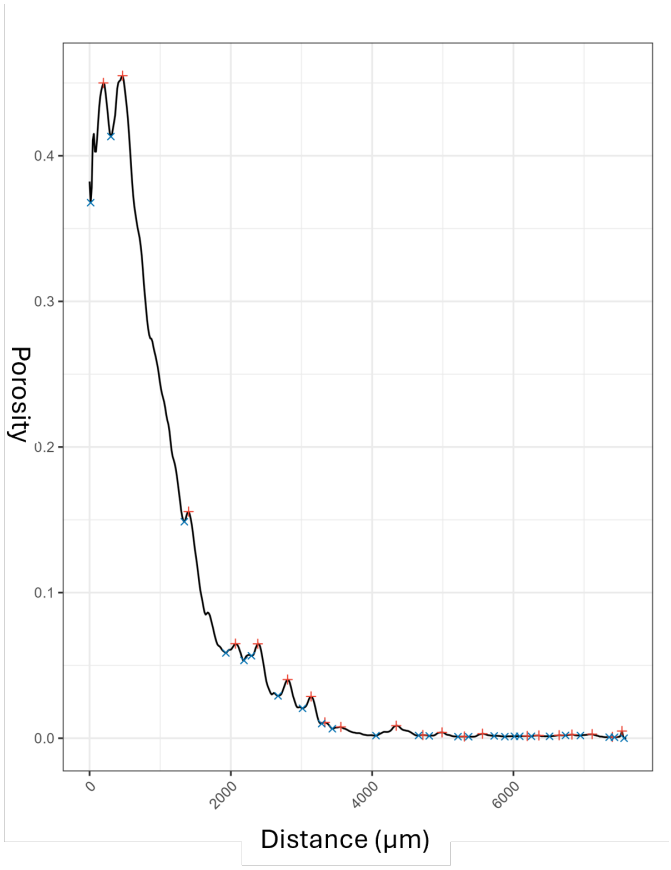

Figure G.1-3: Estimated porosity curve for granophyre rock sample in panel (c) of G.1-1, , using morphological opening with radius 25 μm, and automatically-selected smoothing bandwidth.

G.1.2 Effect of greyscale threshold

The greyscale images are converted to binary images by thresholding. The effect of the choice of threshold was investigated.

G.1.2.1 Initial test

An initial study looked at the impact of the greyscale intensity threshold on the calculated porosity curve for a single gabbro rock sample from AQ08. Figure *G.1-4* shows a lower resolution version of the original high-resolution image. It shows a surface rind, and a deeper area with many small void areas.

Greyscale values were first rescaled to the range between zero and one. Figure *G.1-5* shows the results of porosity curve estimation for six different threshold levels. These curves were produced by an earlier version of the software in which depth was measured in pixel units, where one pixel is approximately 2 μm. The curves were computed using the automatically-chosen bandwidth, and without using morphological opening. Panels (a) to (d), obtained using threshold intensities of 0.01, 0.02, 0.05 and 0.1 respectively, show remarkably little difference, with very similar maxima and width of peak. Panel (e), obtained with threshold intensity 0.2, shows an increase in maximum porosity value, and also higher porosity values, dropping less quickly after 500 pixel depth (a depth

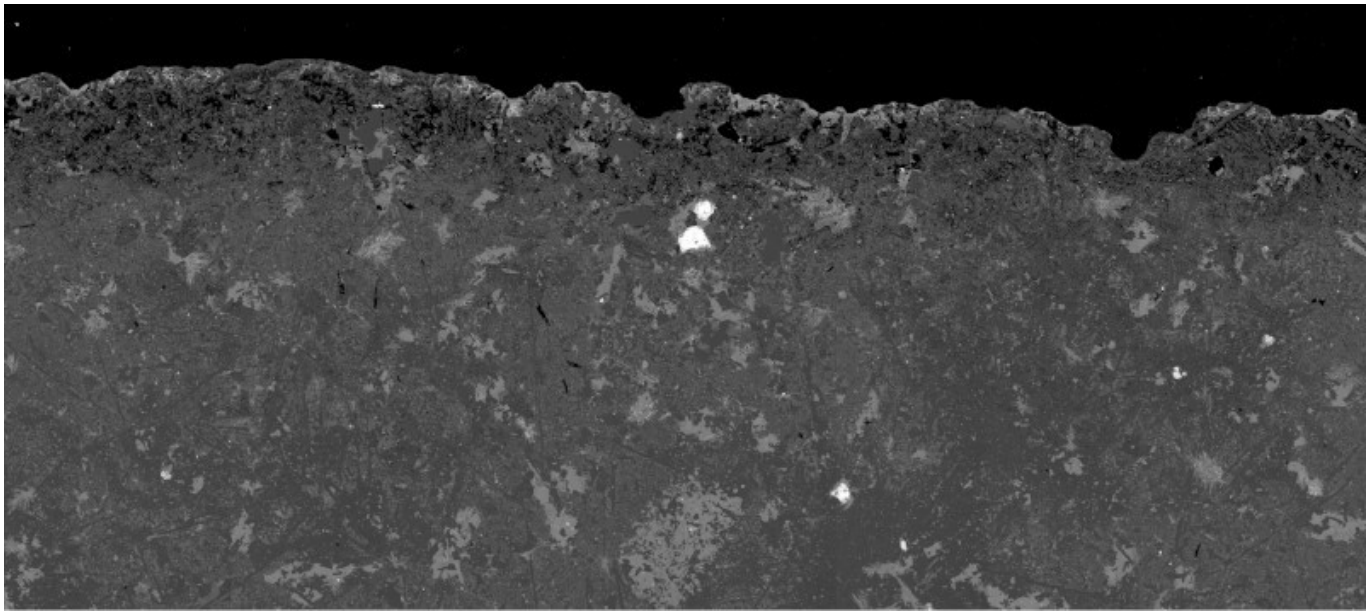

Figure G.1-4: Backscattered electron image from scanning electron microscope of thin section from gabbro rock sample, site AQ08. This sample was used for initial threshold testing.

of approximately 1 mm). However in panel (f), obtained using an intensity threshold of 0.5, the porosity curve changes shape drastically, and contains a numerical artefact, since porosity values cannot exceed 1. This analysis suggests that a threshold range up to 0.1 (for greyscale values scaled to the range from zero to one) should be considered.

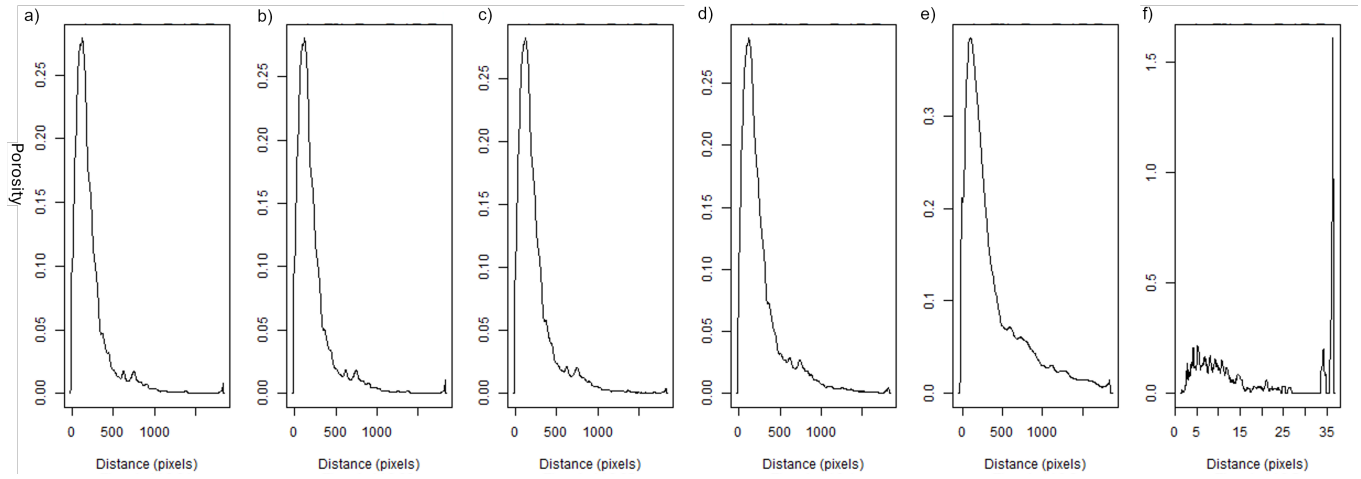

Figure G.1-5: Porosity curves for gabbro rock sample from site AQ08 (cropped image 1), showing the effects of different greyscale intensity thresholds. Thresholds (left to right) are: (a) 0.01, (b) 0.02, (c) 0.05, (d) 0.1, (e) 0.2, and (f) 0.5.

G.1.2.2 Comparing thresholds

The initial test was extended and explored using two different gabbro rock samples from sites AQ03 and RS10 showing a range of features; see Figure *G.1-6*. Panel (a) from RS10 shows large voids

which are connected to the surface and extend down to long cracks that run roughly parallel to the surface and prominent large grains. Panel (b) from AQ03 also shows some rind on the surface, with an area containing many void patches close to the surface. Threshold values 0.02, 0.05 and 0.1 were tried, in combination with bandwidth adjustments of 0.5, 1, and 2.

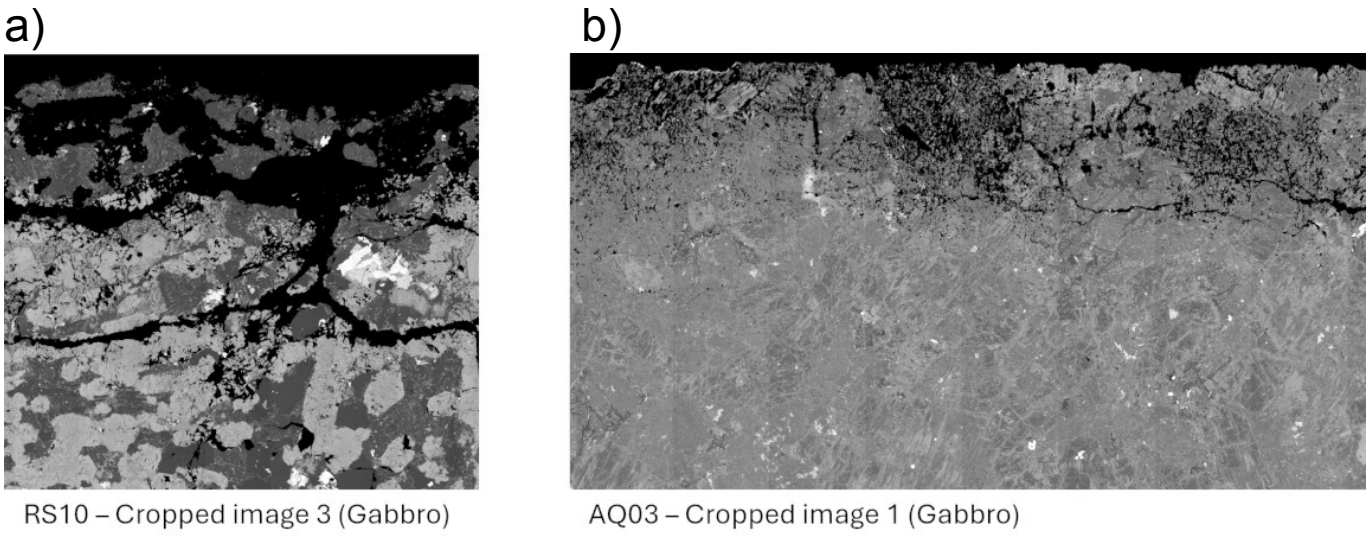

Figure G.1-6: Backscattered electron image from scanning electron microscope of thin sections from two gabbro rock sample images: (a) RS10 cropped image 3 (gabbro), and (b) AQ03 cropped image one (gabbro).

Figure *G.1-7* shows the estimated porosity curves obtained using different threshold levels. The top row, comprising plots (a)–(c), shows porosity curve estimates for sample image (a) in Figure *G.1-6*, while the bottom row, plots (d)–(f), shows estimates for sample image (b) in Figure *G.1-6*. In each row the threshold increases from 0.02 to 0.05 to 0.1 from left to right. Morphological opening was not used, and the curve smoothing bandwidth was chosen by the normal reference rule.

The porosity curves (a)–(c) in the top row of Figure *G.1-7* are broadly consistent with one another, so that the results are insensitive to the choice of threshold. The curves are consistent with the interpretation of the sample image (a) in Figure *G.1-6* as containing a layer of increased porosity close to the rock surface.

The porosity curves (d)–(f) in the bottom row of Figure *G.1-7* are again broadly consistent with one another, except that panels (d) and (e) have a peak, close to the maximum observed depth, which is missing from panel (f). These curves are consistent with the observed pattern of cracking and voids throughout the sample image (b) in Figure *G.1-6*, except that the porosity at very shallow depths is underestimated in the curves; the sample image contains large subsurface voids and cracks which are not reflected in the porosity estimate for depths $d \approx 0$. This is an artefact of the algorithm when morphological opening is not applied; most of the large voids at shallow depths are incorrectly classified as part of the exterior space.

These initial curve estimates were reviewed with the geology team, and a threshold of 0.05 was chosen for further porosity analysis.

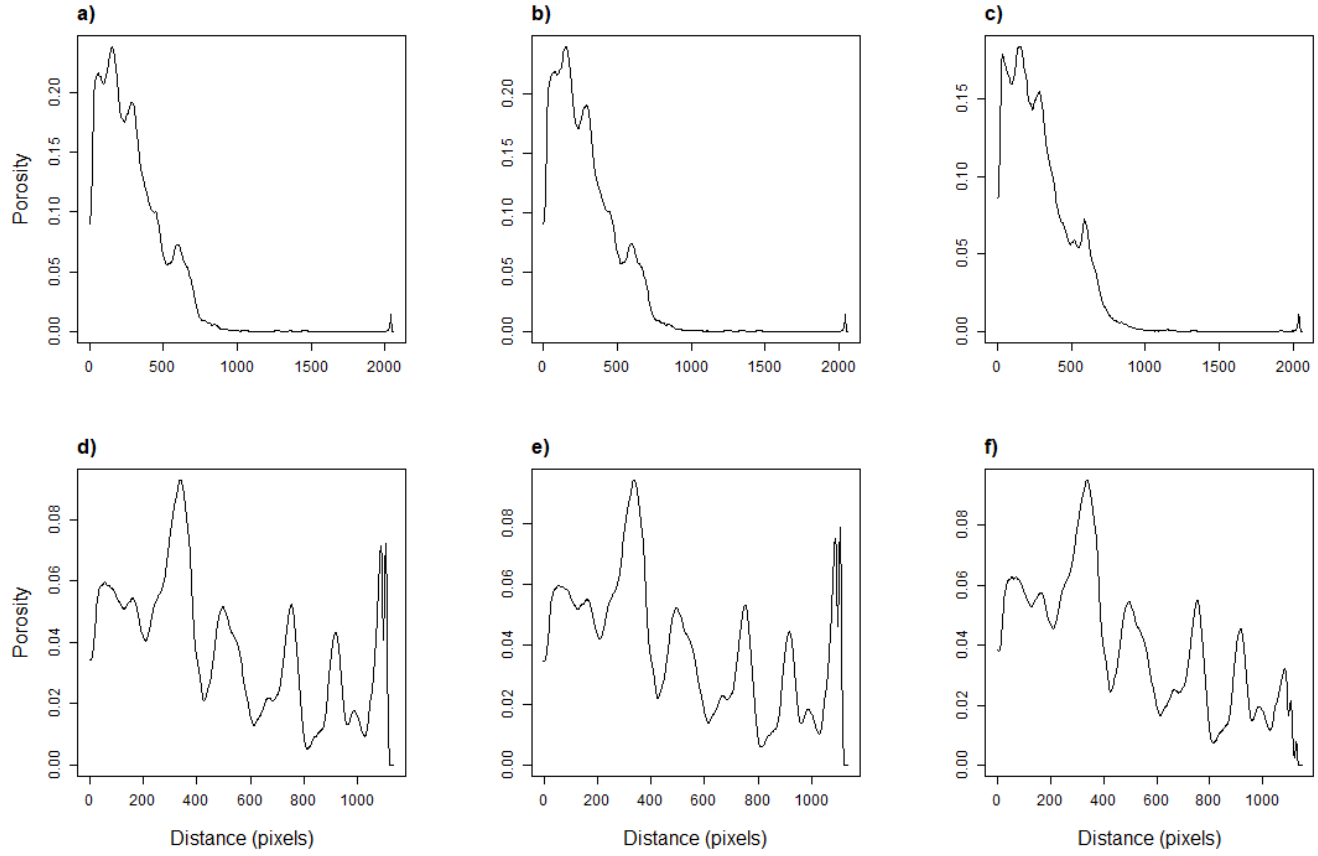

Figure G.1-7: Porosity curves computed from two sample images using different greyscale thresholds. Top and bottom rows are for the sample images (a) and (b) respectively in Figure G.1-6. Left column (a) and (d) uses threshold 0.02; middle column (b) and (e) uses threshold 0.05; right column (c) and (f) uses threshold 0.1.

G.1.2.3 Effects of morphological opening and smoothing bandwidth

The morphological opening radius and the curve smoothing bandwidth are smoothing parameters which have an effect on the calculated porosity curve.

Morphological opening (Serra, 1982; Soille, 2003) is used to automatically determine the rock surface in the thin section images. Morphological openings were computed using the `opening.owin` function in the `spatstat` package (Baddeley and Turner, 2005; Baddeley et al., 2015) which allows the radius to be specified as any numerical value expressed in physical units of length. For the following analysis, opening radii are expressed in micrometres (μm). A larger value of radius will have the effect that larger pits, voids and channels will be classified as interior to the rock, causing the estimated porosity at shallow depths to increase, and slightly changing the measurement of 'depth' below the surface. A radius of zero corresponds to skipping the morphological opening step.

Bandwidth refers to the smoothing bandwidth used to compute the smooth estimate of porosity as a function of depth. The porosity curves were computed using a one-dimensional version of the Nadaraya-Watson smoother (effectively equivalent to loess regression of order zero). Larger

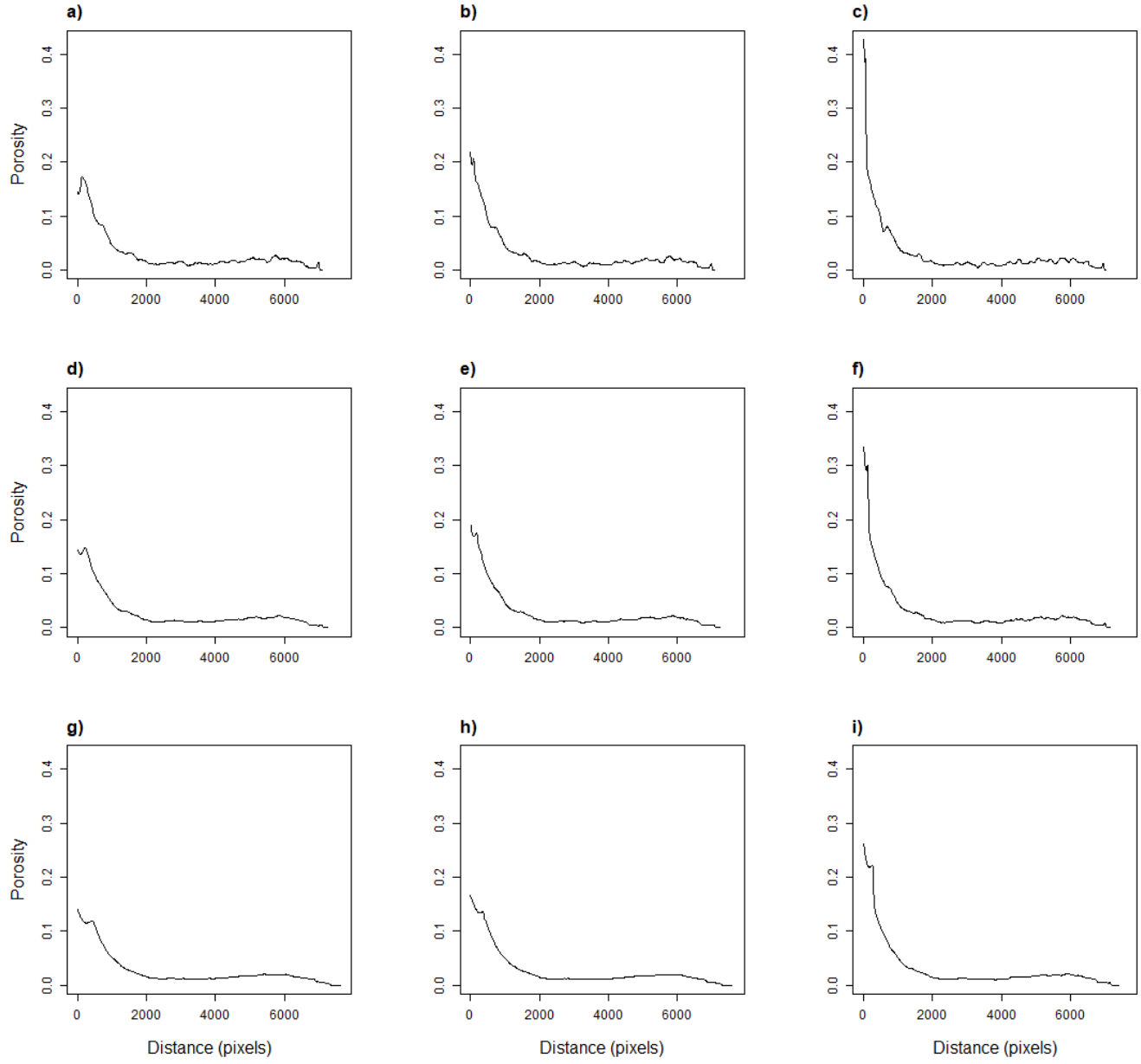

Figure G.1-8: Porosity curves showing the effects of different bandwidths and morphological opening radii for sample image (b) in Figure G.1-6. The top row (panels (a)–(c)) has bandwidth adjustment of 0.5; middle row (panels (d)–(f)) bandwidth adjustment 1.0; bottom row (panels (g)–(i)) bandwidth adjustment of 2.0. Left column (panels (a), (d), (g)) uses morphological opening radius of 0, i.e. opening is not used; middle column (panels (b), (e), (h)) uses morphological opening radius 20 μm; right column (panels (c), (f), (i)) uses morphological opening radius 40 μm.

values of bandwidth will produce smoother, flatter curves with fewer local minima and maxima. A reference bandwidth was computed automatically by applying the Normal reference rule of Silverman (1986, eq. (3.31), p. 48) to the depth values. We used the implementation `bw.nrd0` in the R package `stats`. The reference bandwidth is then multiplied by an 'adjustment' factor specified by the user. Adjustment value 1.0 corresponds to using the automatically selected bandwidth.

Porosity curves were calculated for morphological opening radii from 0 to 50 μm and bandwidth adjustment factors from 0.5 to 5. Figure *G.1-8* shows porosity curves for combinations of morphological opening radius (0, 20 and 40 μm) and for bandwidth adjustment factors of 0.5, 1 and 2.

Increasing the morphological opening radius tends to increase the maximum porosity in the porosity curve. Figure *G.1-8* shows that the maximum porosity for each bandwidth increases noticeably from radius zero to 20 μm and again from 20 to 40 μm. In the top row, maximum porosity increases from just over 0.15 for radius zero to just over 0.2 for radius 20μm, and just over 0.4 for radius 40μm.

Increasing morphological opening radius also changes the shape of the porosity curve closest to the surface. In Figure *G.1-8* the curve for opening radius of zero (first column of images) show a maximum peak at a short distance from the surface for bandwidth 0.5. For radius 20 μm and bandwidth adjustment 0.5, the maximum moves to the surface (depth zero) with a small secondary peak afterwards. For radius = 40μm, the maximum value stays at the surface and there is no immediate secondary peak.

Increasing the curve smoothing bandwidth makes the porosity curves smoother. Figure *G.1-8* shows that the curves become smoother with slightly lower peaks as bandwidth is increased. For the bandwidth adjustment factor of 2, the maximum is now at the surface with a smaller subsequent peak. In general the intermediate peaks are fewer and smaller. (This effect increases further for a bandwidth adjustment of 5, not shown.)

Increasing the curve smoothing bandwidth also tends to reduce the maximum porosity value. This is most prominent in the rightmost column of images (opening radius of 40μm) in Figure *G.1-8*, where the maximum porosity for bandwidth adjustment factor of 0.5 is just over 0.4, which decreases to just over 0.3 for bandwidth adjustment factor of 1, and decreases again to approximately 0.25 for bandwidth adjustment factor of 2. (This effect increases further for bandwidth adjustment factor of 5, where maximum porosity is approximately 0.18).

Voids are rarely observed in the deep interior of the rock. Accordingly the estimated porosity is expected to drop to a low value at a certain depth and to remain low at deeper depths. This general behaviour is observed in the porosity curves shown above. The curves in Figure *G.1-8* exhibit a slight rise and fall in porosity at the deepest depths, but this is likely to be an artefact of the smoothing procedure.

G.1.2.4 Porosity indices

In order to compare the porosity of different rock samples, it is useful to compute a single numerical summary index of porosity for each sample. Various options for such an index were proposed in Appendix *F*.2.6. This subsection considers three of those options:

- **Average porosity (unrestricted)**: the average of the estimated porosity $p(d)$ over the observed range of depths d in the sample.
- **Average porosity (to 3.1 mm)**: the average of the estimated porosity $p(d)$ over the range of depths d from 0 mm (the surface) to 3.1 mm (the depth of the narrowest sample).
- **Maximum porosity**: the maximum of the estimated porosity $p(d)$ over all observed depths d.

These indices were calculated for all granophyre rock samples for five different bandwidth adjustments. Granophyre samples were available for 29 sites, one of which (RS05) had 2 granophyre samples. Four cropped images were generated from each sample image. However, not all cropped images could be used; for instance, some images did not include a profile of the macroscopic surface across the full width of the image. For some images, a morphological opening with a large radius produced unrealistic discontinuities in the “top” region, so that the number of images accepted for analysis depended on the opening radius.

Table *G.1-1* provides a summary of the number of unique sites and sample images used for each morphological opening radius. Many results in subsequent analysis are reported for openings 0, 10, 20 and 40 μm only. (The radii 25 and 50 μm produced results in keeping with the results shown; they were used for cross-checking the algorithms).

Table G.1-1: Site and images used to calculate porosity indices for each morphology opening radius.

Opening radius (μm)	Number of images for indices	Unique associated sites	Mean number images per site
0	108	28	3.86
10	107	28	3.82
20	99	27	3.67
25	92	27	3.41
40	77	25	3.08
50	68	22	3.09

Figure *G.1-9* shows the three porosity indices computed for each cropped image, plotted against site name. Figure *G.1-9*(a) shows the unrestricted average porosity, Figure *G.1-9*(b) shows the maximum porosity; Figure *G.1-9*(c) shows the average porosity to depth 3.1 mm. Colours indicate the morphological opening radius of the indices. Shapes indicate which of the cropped images associated with the site the measure relates to.

The porosity index values are relatively insensitive to the choice of morphological opening radius, compared to the differences in porosity index between different sample images This may be seen, for example, by considering different cropped images obtained from the same site (e.g. AQ09, EX06 and RS05).

In general, porosity index values obtained using opening radius zero are lower than porosity indices for other opening radii. The opening radii of 40 and 50 μm generally result in the highest values of the porosity indices.

Values of the Average Porosity (0 to 3.1 mm) Index and the Average Porosity (unrestricted) Index are not identical, but they do show a similar pattern. Sites with relatively high values for one of these porosity indices tends to have relatively high values for the other. Sites with widely dispersed values for one index tend to be dispersed for the other. This probably reflects the fact that most

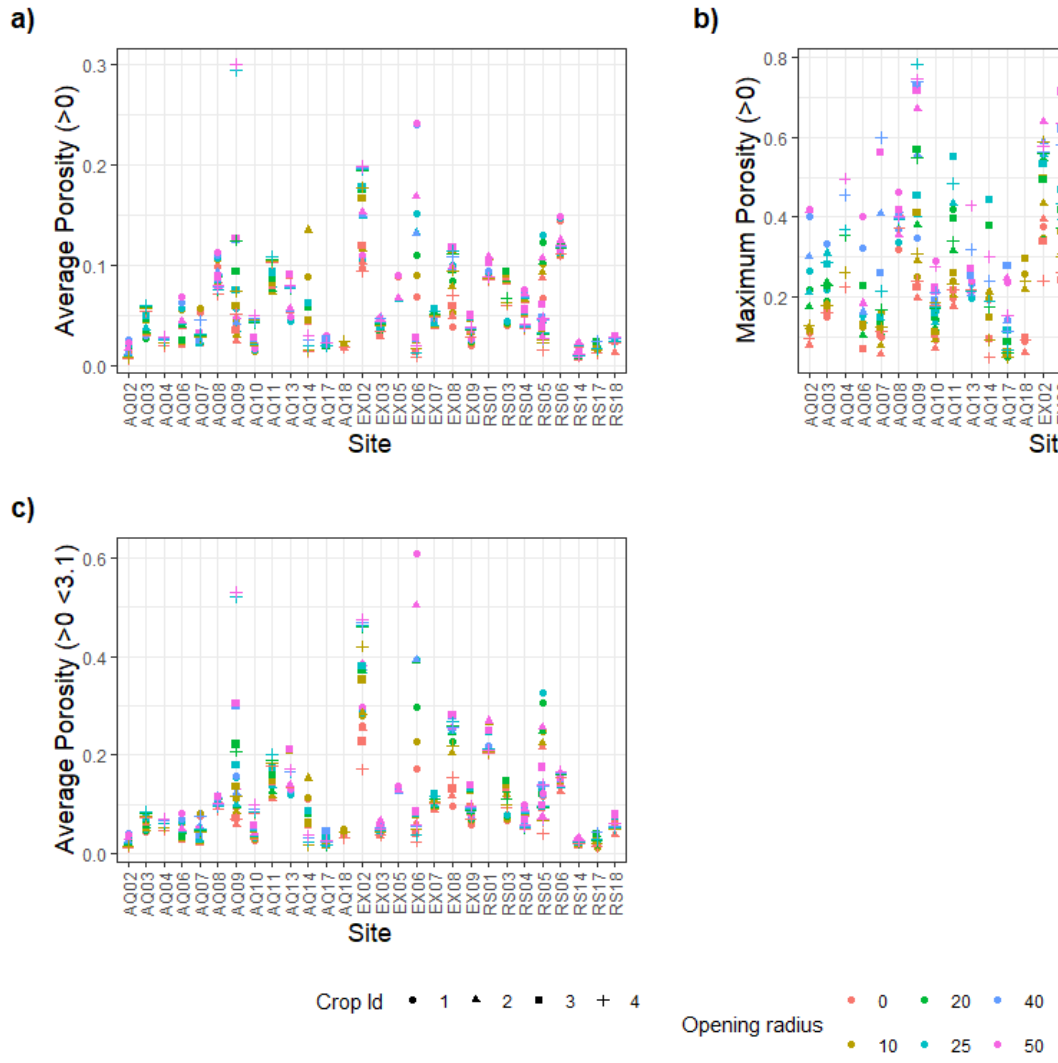

Figure G.1-9: Porosity indices by site. Indices shown are: (a) Average (depth $>$ 0), (b) Maximum (depth $>$ 0), and (c) Average (0 $<$ depth $<$ 3.1 mm).

voids lie close to the rock surface, often within the first millimetre (1000 μm).

Values of the Average Porosity (0 to 3.1 mm) Index tend to be higher than the Average Porosity (unrestricted) Index. Again this reflects the fact that the peak porosity tends to occur in the first millimetre.

Values of the Maximum Porosity Index are shown in Figure *G.1-9*(b). Compared to the other porosity indices, the Maximum Porosity Index exhibits greater variation between sites, and greater sensitivity to the choice of morphological opening radius. Generally speaking, the Maximum Porosity Index increases with increasing radius of the morphological opening.

Despite these differences, all three porosity indices seem to follow similar trends: sites with the highest average porosity values are usually the sites with the highest maximum porosity values. Further analysis in the main body of the report concentrates on the Average porosity over depths between 0 and 3.1 mm.

G.1.3 Spatial variation in porosity

Section 7.6.5 presented an exploratory analysis of spatial variation in porosity, and reported that there is statistically significant evidence of elevated porosity in a region of Murujuga.

It is important to assess whether this finding is sensitive to the choices made during the analysis. These choices include the selection of the porosity index and the algorithm parameters used to estimate the porosity curve, especially the morphological opening radius and (for maximum porosity) the curve smoothing bandwidth.

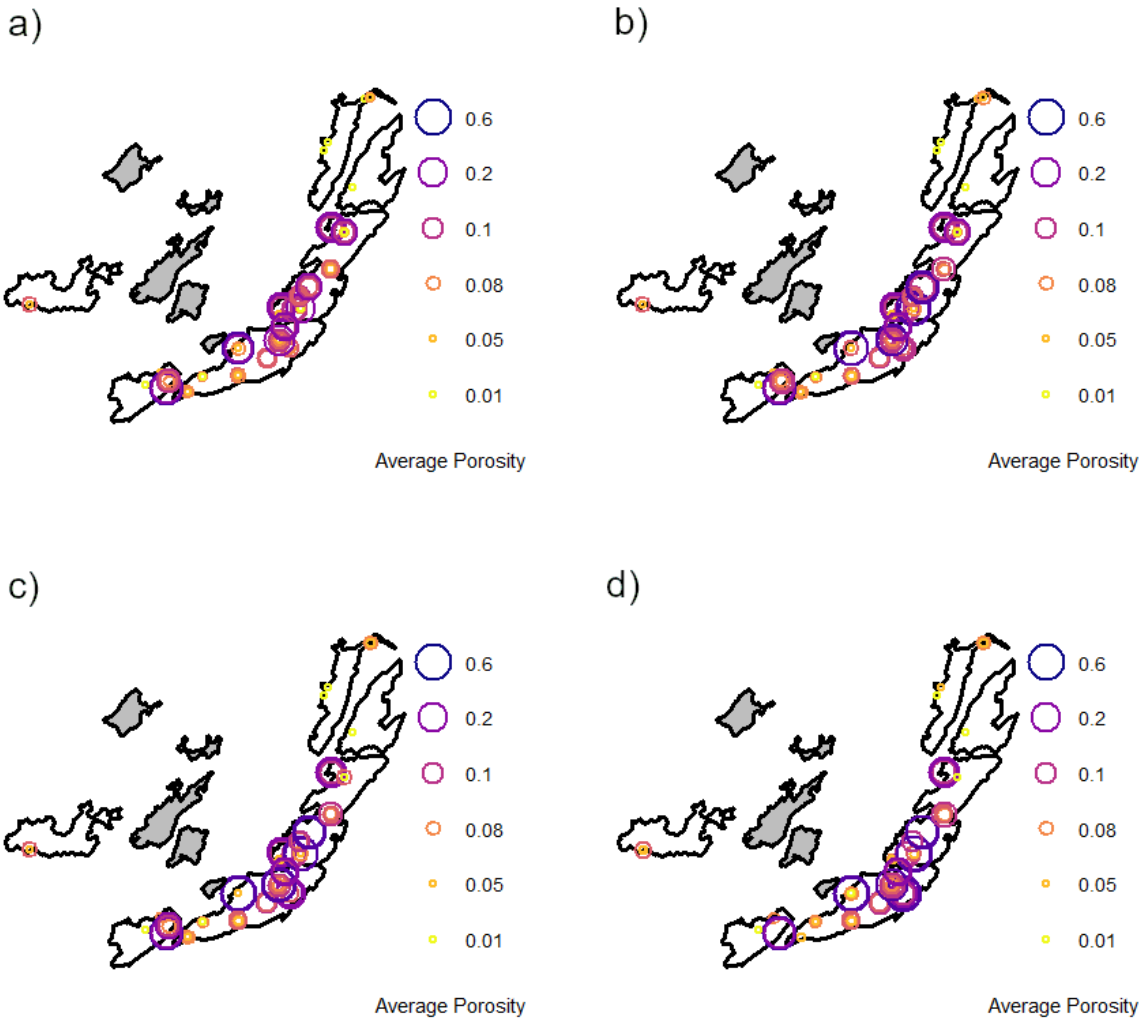

Figure G.1-10: Plots of the Average Porosity index (over depths from 0 to 3.1 mm) from granophyre rock samples at sites across Murujuga. Each panel shows results for a different morphological opening radius: (a) 0 μm, (b) 10 μm, (c) 20 μm, and (d) 40 μm.

Figure *G.1-10* shows spatial plots of values of the average porosity index (depths from 0 to 3.1 mm) using different values of the morphological opening radius. The symbol map is the same for each panel: the high values of porosity index are shown by purple circles while small values are shown by small yellow circles (dots). Most of the sites are on the main peninsula, with a few sites on the

northern and western islands. This reflects the distribution of granophyre. The average porosity values tend to be lower in the north and west. Many of the larger values are observed close to the port, industry and towns. This pattern is seen for all opening radii, but is more pronounced as the opening radius increases. Note that some of the smaller index values for sites on Dolphin Island are difficult to see in the two top panels.

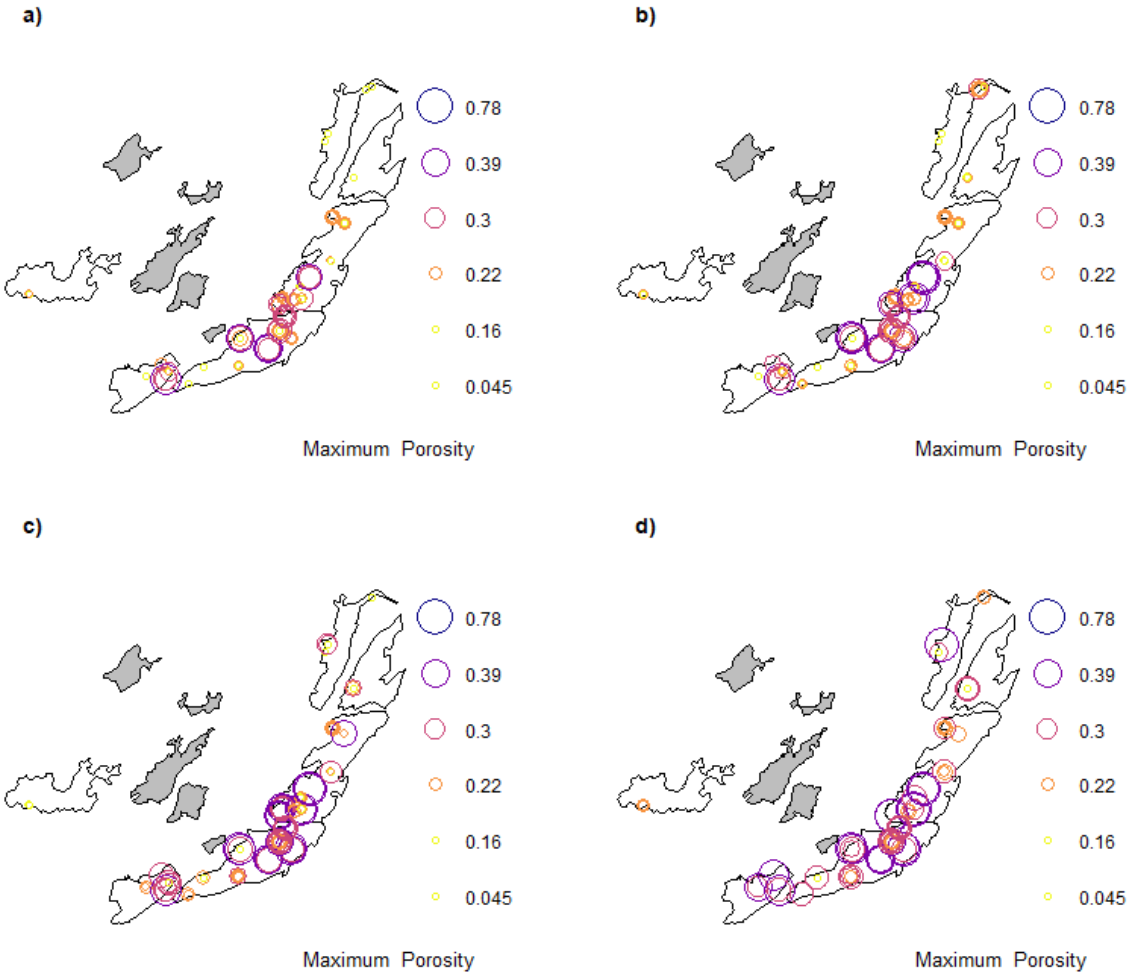

Figure G.1-11: Plots of the Maximum Porosity index (for all depths greater than 0 mm) from granophyre rock samples at sites across Murujuga. Each panel shows results for a different morphological opening radius: (a) radius = 0 μm, (b) radius = 10 μm, (c) radius = 20 μm, and (d) radius = 40 μm.

Figure *G.1-11* similarly plots the values of the maximum porosity index. The maximum values show stronger evidence of larger values around the port area and smaller values elsewhere. As the opening radius increases, the maximum porosity values increase, but the underlying pattern remains.

Figure *G.1-12* shows spatially smoothed surfaces of the average porosity index (depth 0 to 3.1 mm) calculated from the point data in Figure *G.1-10* using the Nadaraya-Watson smoother with least squares cross-validated spatial smoothing bandwidth. Each panel shows the result for a

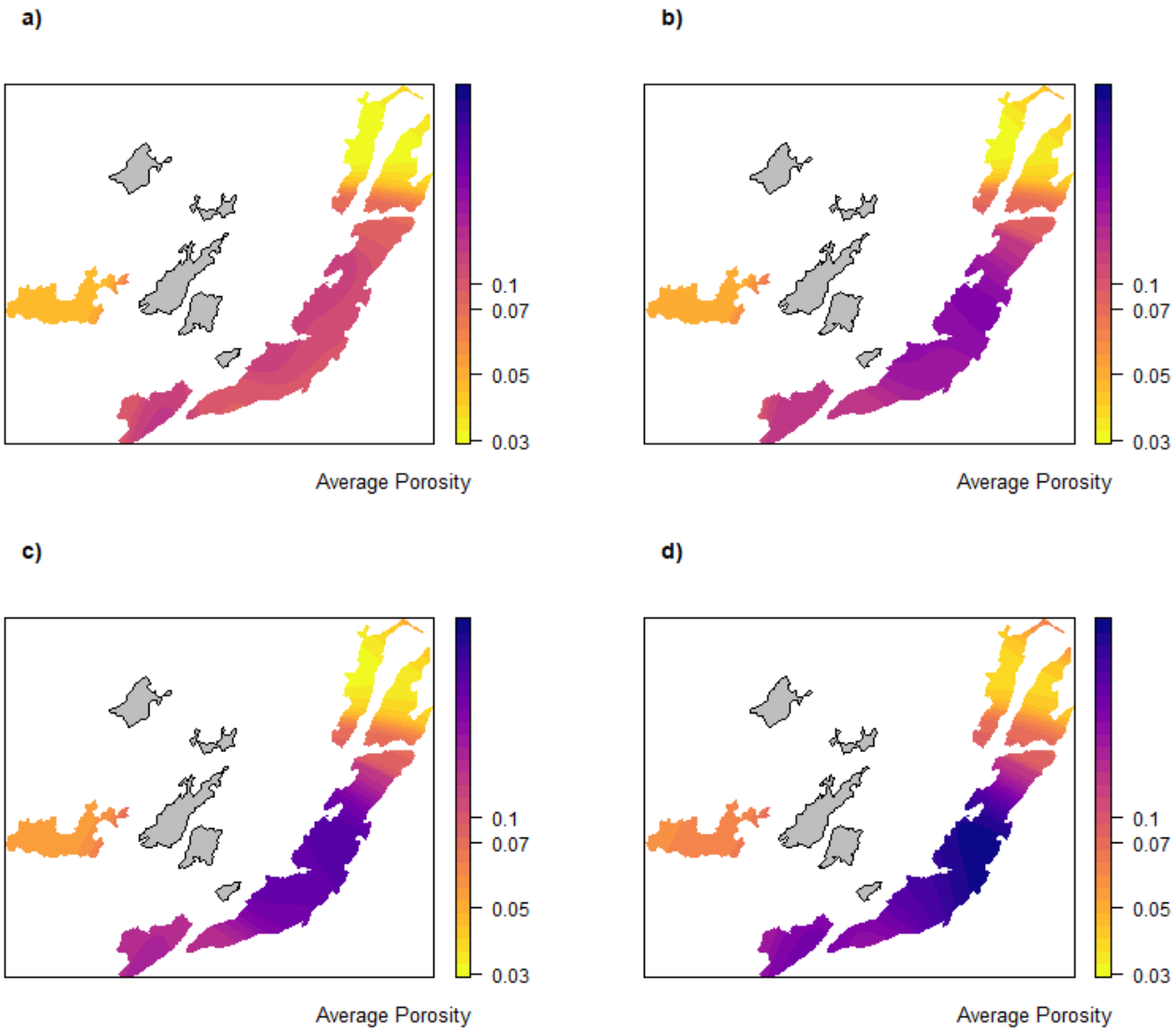

Figure G.1-12: Spatially smoothed (Nadaraya-Watson) average of the average porosity index (over depths from 0 to 3.1 mm). Each panel shows results for a different morphological opening radius: (a) radius = 0 μm, (b) radius = 10 μm, (c) radius = 20 μm, and (d) radius = 40 μm.

different value of the morphological opening radius. Panels share a common scale. The smoothed surface for opening radius zero (i.e. when no morphological opening is applied) has the smallest range in values and appears almost constant over the peninsula. The smoothed values tend to increase with increasing opening radius, as expected. There is a distinct area of higher estimated porosity close to the industrial and port area for all opening radii greater than zero.

The relatively flat surface obtained in Figure *G.1-12*(a) for opening radius zero does not indicate that the porosity index values themselves were approximately constant (since the spatial plot in Figure *G.1-10*(a) shows that these values vary widely). Rather, it is a consequence of the cross-validation procedure for selecting the spatial smoothing bandwidth. The procedure has selected a large bandwidth in this case, in order to suppress the relatively high variability between index values

obtained with radius zero. A very large bandwidth gives rise to a very flat surface.

As discussed in Section *G*.1.2.3 above, a morphological opening is considered necessary for correct identification of the rock surface, and we disregard the results for radius zero.

Figure *G.1-13* shows the spatially smoothed surfaces of the maximum porosity index, obtained from the data for each panel in Figure *G.1-11* using the Nadaraya-Watson smoother with the least squares cross-validated choice of the spatial smoothing bandwidth. Each panel shows the smoothing results from the maximum porosity (for all depths greater than zero) for a specific morphological opening radius. Each panel uses the same scale. Smoothed values of maximum porosity values are generally larger than the average values (as expected) with a range from 0.1 to 0.45. For this figure, each plot shows an area of higher values centred on the peninsula close to the port area.

G.1.3.1 Significance tests

Appendix *F*.3 describes the “pointwise” Monte Carlo test of the null hypothesis of constant mean porosity against the one-sided alternative hypothesis of elevated porosity, at a given location. It also describes the “global” test of the null hypothesis of constant mean against the alternative hypothesis of elevated porosity in some region (where the region of elevated porosity is not specified in advance).

These tests were demonstrated in one case in Section 7.6.6. This subsection provides the results of the same procedure using different porosity indices and different values of the morphological opening radius, in order to assess the sensitivity of the result to these parameters.

Figure *G.1-14* shows results of the pointwise Monte Carlo test applied to the average porosity index (depth 0 to 3.1 mm) computed using various values of the morphological opening radius. The panels on the top row show the p-value of the pointwise Monte Carlo test at each spatial location. Panels on the bottom row identify those locations in the study region where the pointwise Monte Carlo test would be significant at the level 0.05. Columns correspond to different values of the morphological opening radius. The region where the pointwise test result is statistically significant (labelled orange) does vary a little with the opening radius; it may decrease slightly with opening radius size. Nonetheless, these results are broadly consistent across the range of morphological opening radii.

Similarly, Figure *G.1-15* shows the results of the pointwise Monte Carlo test for the Maximum porosity computed using morphological opening radii from 0 to 40 μm. Again, there is an region where the pointwise test indicates there is statistically significant evidence that porosity is elevated. This region is slightly smaller than the region identified using the average porosity index. Again the result seems robust across the range of morphological opening radii.

Table *G.1-2* shows the p-values obtained for the global Monte Carlo test of elevated porosity, based on the Average porosity index (depth 0 to 3.1 mm) and the Maximum porosity index (depth greater than zero) for four different values of morphological opening radius. This global test outcome is significant for both indices for all morphological opening radius values.

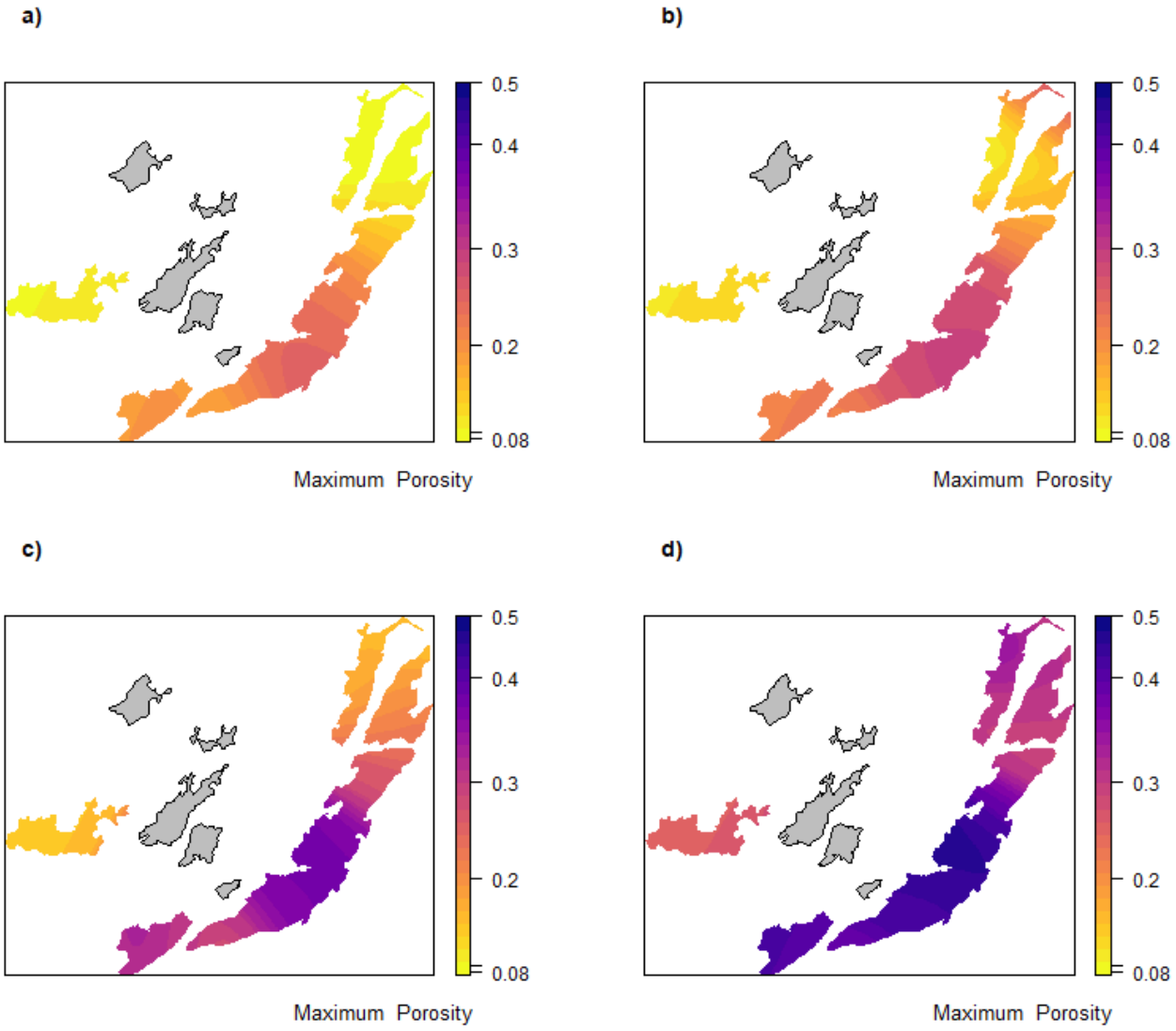

Figure G.1-13: Spatially smoothed surface of maximum porosity index. Each panel shows results for a different morphological opening radius: (a) radius = 0 μm, (b) radius = 10 μm, (c) radius = 20 μm, and (d) radius = 40 μm.

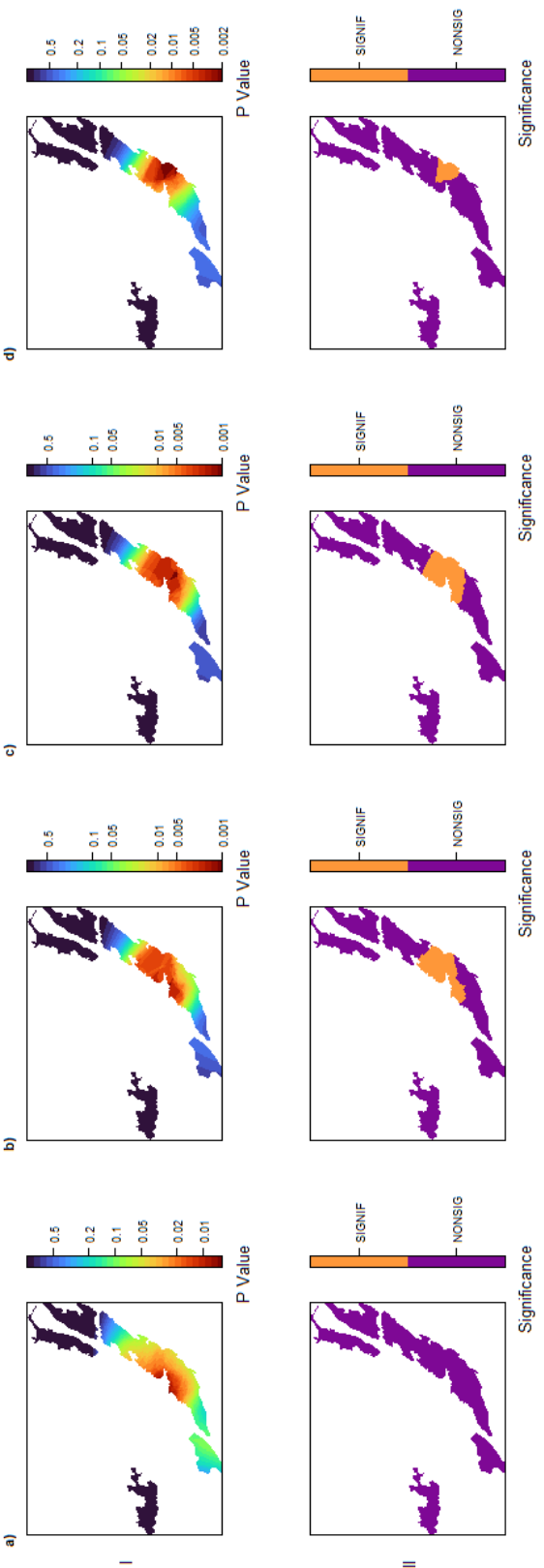

Figure G.1-14: Pointwise Monte Carlo test applied to the Average porosity (depth 0 to 3.1 mm) index data for morphology radius (a) 0 μm, (b) 10 μm, (c) 20 μm and (d) 40 μm. The top row shows the p-values calculated for the test. The bottom row shows points that are significant at the 0.05 level.

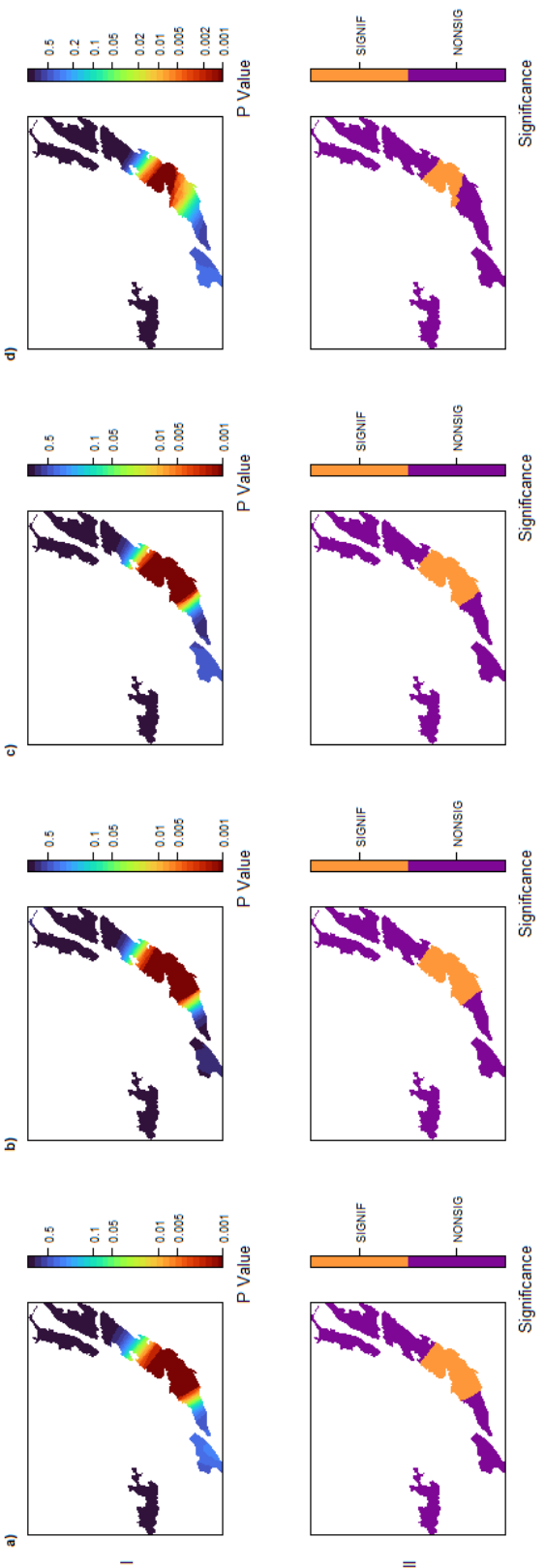

Figure G.1-15: Pointwise Monte Carlo test applied to the Maximum porosity (depth greater than 0) index data for morphology radius (a) 0 μm, (b) 10 μm, (c) 20 μm and (d) 40 μm. The top row shows the p-values calculated for the test. The bottom row shows points that are significant at the 0.05 level.

Table G.1-2: Results of global Monte Carlo test of elevated spatial porosity using different porosity indices and morphological opening radii. A p-value of less than or equal to 0.05 indicates statistical significance.

Porosity measure	**Opening radius (μm)**	**p-value**
Mean ($0 <$ depth $<$ 3.1 mm)	0	**0.02**
Mean ($0 <$ depth $<$ 3.1 mm)	10	**0.01**
Mean ($0 <$ depth $<$ 3.1 mm)	20	**0.01**
Mean ($0 <$ depth $<$ 3.1 mm)	40	**0.02**
Maximum ($0 <$ depth)	0	**0.01**
Maximum ($0 <$ depth)	10	**0.01**
Maximum ($0 <$ depth)	20	**0.01**
Maximum ($0 <$ depth)	40	**0.02**

G.2 Porosity and rock height: further results and diagnostics

This section gives further results from our analysis in Section 8.4 of spatial variation in porosity after accounting for the height of the rock above the surrounding terrain.

Since this choice of explanatory variable has several weaknesses (stated below and in Section 8.4), the material in this section is presented for demonstration purposes, and is not recommended as a basis for inference.

G.2.1 Assessing initial evidence for a relationship

The first objective is to formulate and fit a suitable model which predicts porosity as a function of height. Observational units are individual rock samples. The response variable is the average porosity index (depth 0 to 3.1 mm). The explanatory variable is the height of the rock above the surrounding terrain, in metres. In some graphics, 'height' is indicated as 'elevation', but the term 'height' is preferred in order to avoid confusion.

Figure *G.2-1* shows scatterplots of porosity index against height, computed using different values of the morphological opening radius. There is no clear evidence for a relationship between porosity and height. The height values are mostly in the range from 0 to 40 metres, but there are several values at approximately 80 and 120 meters. These relatively extreme values will have high leverage in the regression analysis. The porosity index values at these extreme heights are relatively low, so that these data points will also have large influence.

Table *G.2-1* shows numerical measures of the correlation between porosity and height. Sample estimates of Pearson correlation and Spearman rank correlation are reported in the table. Where the associated test of nonzero correlation was statistically significant, the correlation estimates are annotated with asterisks (one asterisk if $p < 0.05$, two asterisks if $p < 0.01$ and three if $p < 0.001$). The Pearson correlations are generally low, with the highest correlation 0.11. None of these correlations are significant at the 0.05 level. The Spearman rank correlation rho does indicate weak correlations between 0.1 and 0.4. The Spearman rank test is significant for opening radius values from 0 to 40 μm, but not significant for 50 μm.

Table G.2-1: Correlation between height and average porosity (to 3.1mm depth) by opening radius. The table shows the Pearson correlation and Spearman's rho with asterisks indicating statistical significance.

Porosity Index	Opening radius	Pearson correlation	Spearman correlation
Average (depth 0 to 3.1 mm)	0	0.0386	**0.2662****
Average (depth 0 to 3.1 mm)	10	0.0690	**0.3232****
Average (depth 0 to 3.1 mm)	20	0.0689	**0.2978****
Average (depth 0 to 3.1 mm)	25	0.0989	**0.2855****
Average (depth 0 to 3.1 mm)	40	0.1101	**0.2435***
Average (depth 0 to 3.1 mm)	50	0.0875	0.2122

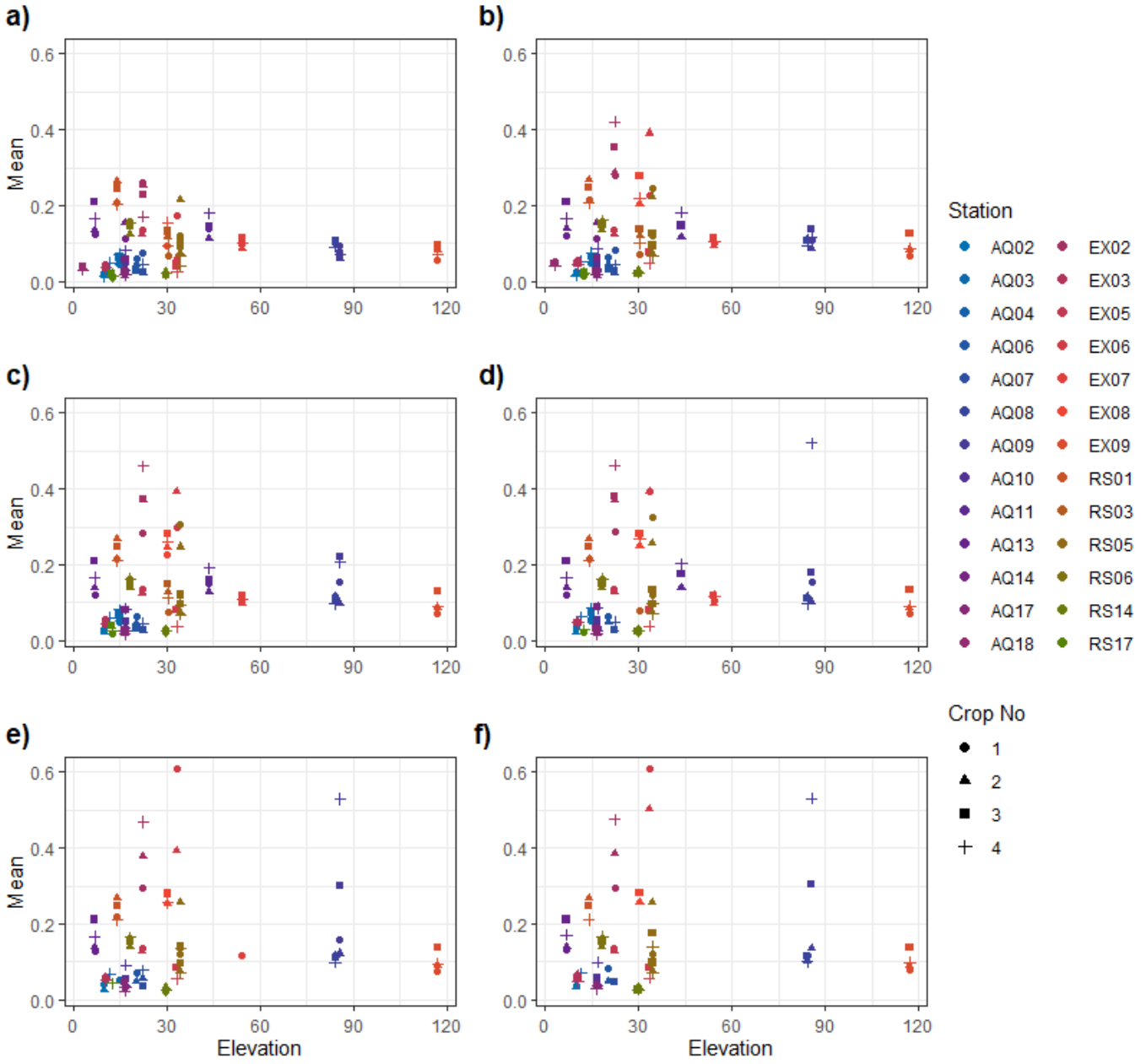

Figure G.2-1: Scatterplots of Average porosity index (depth 0 to 3.1 mm) versus rock height above surrounding terrain. Each panel shows the results for Average porosity calculated for a different opening radius as follows: (a) radius zero, (b) radius 10, (c) radius 20, (d) radius 25, (e) radius 40, and (f) radius 50.

G.2.2 Linear modelling

In order to explore the type of relationship between porosity and height, linear regression models were fitted to the data by Ordinary Least Squares. Using the standard model formula notation, these models were as follows:

```
Model 0: Porosity ~ 1
```

```
Model 1: Porosity ~ height
Model 2: Porosity ~ height + I(height^2)
```

Model 0 is the null model of constant mean porosity. Model 1 states that porosity depends linearly on height. Model 2 states that porosity depends quadratically on height. An analysis of variance (ANOVA) F-test of Model 1 against Model 0 was not significant. An ANOVA F-test of Model 2 against Model 0 was significant at level 0.05, for the morphological opening radius 10 μm, but with a very small adjusted R^2 value. This analysis is consistent with the null model of constant mean porosity.

G.2.3 Generalised linear modelling

Ordinary Least Squares implicitly assumes the responses are normally distributed with constant variance. This is inappropriate for the porosity index values, which are proportions (values between zero and one). Generalised linear models (McCullagh and Nelder, 1989) would be more appropriate, since they can accommodate various choices of the response distribution.

For exploratory purposes, a generalised linear model with quasi-binomial variance function and logit link function was fitted to the porosity data, using three model formulae given above. Again Models 1 and 2 were not significant, that is, the null model of constant mean porosity was accepted.

An appropriate choice of response distribution for the regression modelling can be found by inspecting the pooled histogram of the responses. This approach is valid only because there is weak evidence for any relationship between the response and explanatory variable.

Figure *G.2-2* shows (a) boxplots and (b) superimposed histograms of the porosity index values computed using different values of the morphological opening radius. As noted elsewhere, the range of porosity values increases as the opening radius increases. The histograms show that the porosity index values are strongly right skewed.

G.2.4 Beta regression modelling

Figure *G.2-2*, combined with the fact that the responses are fractions between 0 and 1, suggest that the responses could be modelled by beta distributions. The family of beta distributions has two parameters, and is not amenable to the standard approach to generalised linear models in which the response distribution has only one parameter. Methodology and software for beta regression is less well developed.

Beta regression models were fitted to the porosity/height data using the R package `betareg` (Cribari-Neto and Zeileis, 2010; Grün et al., 2012) with a logit link. This approach characterises the beta distribution by a mean and dispersion factor, where the mean is linked to a linear combination of the independent variables (Cribari-Neto and Zeileis, 2010; Grün et al., 2012). The dispersion factor can also be linked to a linear combination of the explanatory variables; but for this analysis a constant dispersion was assumed and estimated.

For each morphological opening radius 0, 10, 20, 30, 40 and 50 μm, beta regression models for porosity against height were fitted, assuming the mean relationship is either constant (Model 0), linear (Model 1) or quadratic (Model 2) on the logit scale. For example the quadratic model

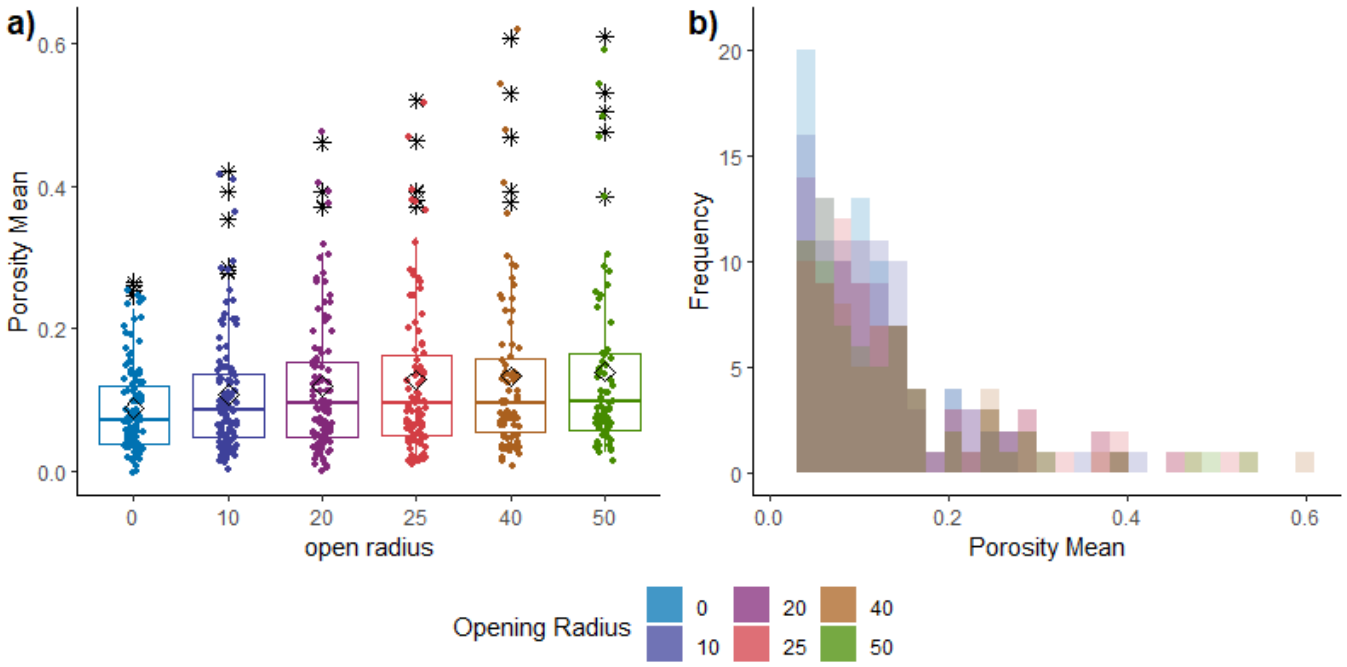

Figure G.2-2: Distribution of Average porosity (depth 0 to 3.1 mm): (a) shows boxplot of average values categorised by opening radius, while (b) shows a histogram of average values categorised by opening radius.

postulates that:

$$\log \frac{M}{1-M} = \beta_0 + \beta_1 \, H + \beta_2 \, H^2$$

where M is the mean value of the porosity index, H is rock height, and $\beta_0, \beta_1, \beta_2$ are model coefficients to be estimated.

Models 1 and 2 were tested against the null Model 0 (constant porosity) using the likelihood ratio test, implemented using the `lrtest` function from the R package `lmtest` (Zeileis and Hothorn, 2002). According to the likelihood ratio test, Model 1 was not statistically significant in any case, while Model 2 was significant for morphological opening radius values of 10, 20, and 25 μm.

Table *G.2-2* shows, for each value of the morphological opening radius, the fitted parameters for Model 2, the p-value of the likelihood ratio test against Model 0, the pseudo R squared value, the fitted model parameters β_1 and β_2, and the p-values for the likelihood ratio test of nonzero coefficient.

The variance of the beta distribution is governed by the inverse of the precision parameter, hence variance decreases for larger precision variables (Grün et al., 2012). The precision intercept parameter in the fitted models is quite large, Table *G.2-2*, which allows for relatively large variance.

Table G.2-2: Beta regression models of porosity for different morphological openings. Model was applied to Averaged porosity (0 to 3.1 mm). Table shows the likelihood ratio test (LR test) p-value, pseudo R square, the mean and precision intercepts, and estimates and p-values for each coefficient.

Opening radius	p-value LR Test	Pseudo R squared	Mean intercept	Precision intercept	Height coeff	p-value	Height sq coeff	p-value
0	0.0246	0.0754	-2.7729	20.9857	0.0231	0.0114	-0.0001	0.0341
10	0.0096	0.0991	-2.6357	15.6895	0.0274	0.0043	-0.0002	0.0162
20	0.0205	0.0897	-2.5413	13.4182	0.0280	0.0092	-0.0002	0.0274
25	0.0378	0.0846	-2.4333	11.2728	0.0270	0.0185	-0.0002	0.0478
40	0.1219	0.0676	-2.3068	10.3045	0.0246	0.0648	-0.0002	0.1215
50	0.2255	0.0565	-2.1982	9.3629	0.0234	0.1052	-0.0002	0.1599

The beta regression model summary for Average porosity (0 to 3.1 mm) versus height and height squared is shown by the code below:

```
    Call:
betareg(formula = a_function, data = cur_data_set)

Standardized weighted residuals 2:
    Min      1Q  Median      3Q     Max
-1.8273 -0.5311 -0.1183  0.6867  2.2206

Coefficients (mean model with logit link):
              Estimate Std. Error z value Pr(>|z|)
(Intercept)  -2.541e+00  2.247e-01 -11.310  < 2e-16 ***
height     2.796e-02  1.074e-02   2.604  0.00922 **
height_sq -2.024e-04  9.178e-05  -2.205  0.02743 *

Phi coefficients (precision model with identity link):
      Estimate Std. Error z value Pr(>|z|)
(phi)   13.418      2.001   6.705 2.01e-11 ***
---
Signif. codes:  0 '***' 0.001 '**' 0.01 '*' 0.05 '.' 0.1 ' ' 1

Type of estimator: ML (maximum likelihood)
Log-likelihood:   113 on 4 Df
Pseudo R-squared: 0.08965
```

The results of the likelihood ratio comparison of the above model to a null model `Porosity~1` is shown below: Likelihood ratio test

```
Model 1: min_max_Av ~ 1
Model 2: min_max_Av ~ height + height_sq
  #Df LogLik Df  Chisq Pr(>Chisq)
1   2 109.11
2   4 113.00  2 7.7739    0.02051 *
---
Signif. codes:  0 ‘***’ 0.001 ‘**’ 0.01 ‘*’ 0.05 ‘.’ 0.1 ‘ ’ 1
```

Figure *G.2-3* shows the residual diagnostic plots. These plots use standardised residuals from the `betareg` package (Cribari-Neto and Zeileis, 2010). Plots of residuals versus the observation index tend to be lower for indices 0 to 20 and greater than 80, which may relate to underlying spatial distribution of the observations. Residuals versus the linear predictor (the height and height squared combination) seem evenly distributed. The Cook's distance values and generalised leverage values are low, indicating no undue influence from extreme values.

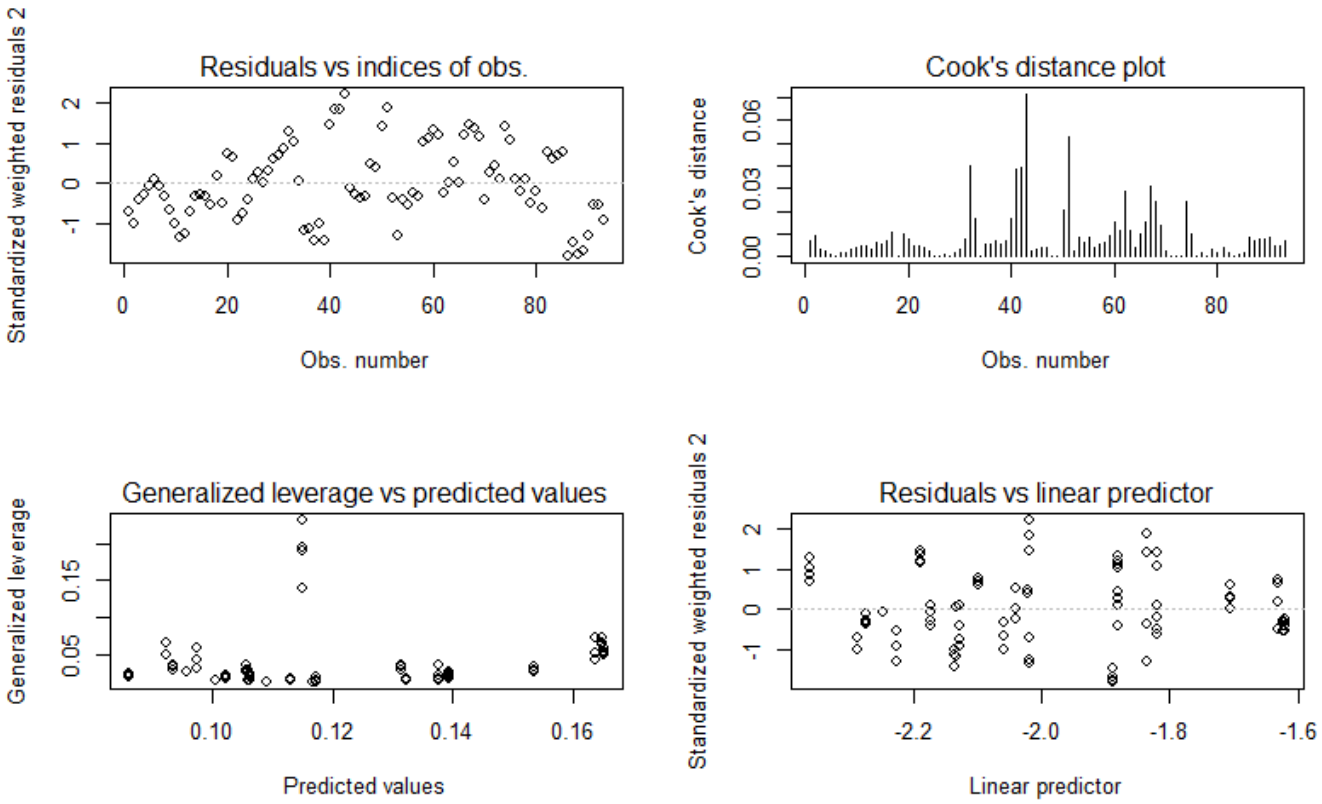

Figure G.2-3: Residual diagnostic plots for the beta regression for Average porosity (0 - 3.1 mm) for opening radius 20 μm

G.2.5 Significance tests

Table *G.2-3* shows results of the global Monte Carlo test based on the residuals, described in Section 8.4. That is, the null hypothesis is that the residuals from the regression have constant mean. The two-sided alternative is that the mean residual is nonzero at some unspecified locations. The global test is significant for all morphological opening radius values except radius zero. The result implies that, even after allowing for the (postulated) dependence of porosity on rock height, there remains significant evidence of a region of elevated porosity.

Table G.2-3: Results of global Monte Carlo test of constant mean residual, for each morphological opening radius.

Opening radius (μm)	p**-value**	**Alternative hypothesis**
0	0.01	greater
10	0.01	greater
20	0.02	greater
25	0.02	greater
40	0.02	greater
50	0.03	greater
0	0.06	two–sided
10	0.05	two–sided
20	0.02	two–sided
25	0.01	two–sided
40	0.03	two–sided
50	0.01	two–sided

G.3 Faulty field colour data

This section gives details of various anomalies detected in the data produced by the JAZ and HDX colorimeters, and describes our procedure for detecting anomalies.

G.3.1 Faults in JAZ data

Over the seven campaigns, a total of 334 rock art panels were measured by the JAZ instrument (Table *7.2-1*). In campaign 7, a total of nine rock art panels were measured by the HDX instrument.

Below are the criteria that define whether field colour measurements from the JAZ instrument for a particular target on a rock art panel are deemed faulty:

1. Calculated % reflectance was extremely large and/or small with values being less than -500% and/or greater than 500% at some wavelengths. This occurred in nine rock art panel measurements in campaigns 1, 2 and 3; see e.g. Figure *G.3-1* AQ09_GPH in campaign 2 (blue; this figure is also Figure 7-5a in Curtin University (2023)).
2. % reflectance was greater than 100%.
3. % reflectance was infinite (`Inf`) or not-a-number (`NaN`) indicating division by zero. This occurs when either $S - D$ or $R - D$ is equal to zero.
4. % reflectance was zero, this occurs when either S = D or R = D.
5. Negative % reflectance values, which arises when the dark current is higher than the colour measurement (S sample sensed photon count). There are two possible causes for this fault: 1) stray light entered during the dark current measurement; 2) the light probe was faulty or failed to activate during the colour measurement.
6. Dark current curve was not flat. The dark current should be approximately constant across the detector array, since it should measure thermal noise in the detector. If the dark current curve was not flat, then it is likely that either stray light entered during the dark current measurement or that the light probe was activated during the measurement. A non-constant dark current often results in a very “wiggly” curve of % reflectance. For example, in Figure *G.3-2* campaign 1 (orange) the dark current was not flat and the % reflectance was very “wiggly”.
7. The colour measurement (sample sensed photon count S) was flat. There are several causes for this flat curve, including the instrument failed to record the photon count; the light source in the probe was faulty or not switched on; stray light entered during the measurement because an uneven rock surface or difficulty holding the instrument steady against a vertical rock surface. At the beginning of campaign 4, the black-out cloth was modified to fully cover the whole box. Figure *G.3-3* shows RS13_GBR target 3 in campaign 7 measured by the JAZ instrument, replicates 9 and 10 (pink and light purple) were flat, which resulted in a flat % reflectance. These two replicates were removed from further analyses.
8. At 300 nm wavelength, the observed and predicted % reflectance was greater than 100%, there was a sharp decrease, at about 400 nm the % reflectance starts looking like a typical valid % reflectance curve. For example Figure *G.3-4*. This problem is still being investigated.

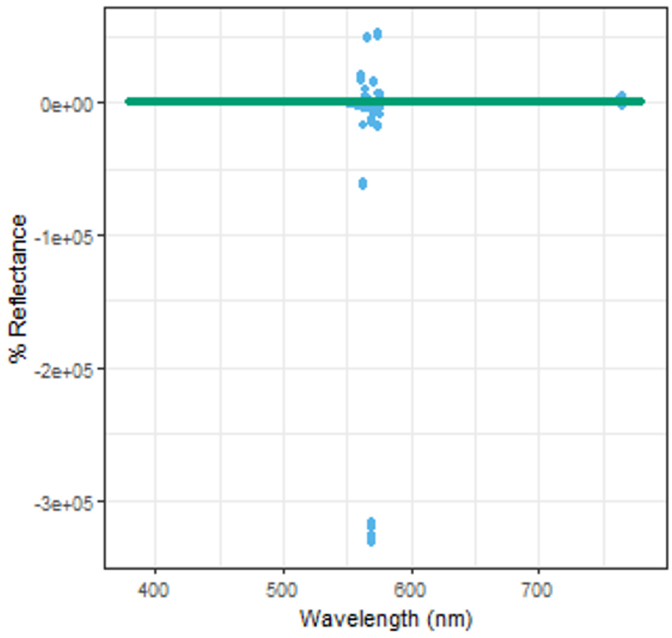

Figure G.3-1: AQ09_GPH predicted % reflectance vs wavelength (nm). Where orange is campaign 1, blue campaign 2, pink campaign 3 and green campaign 4.

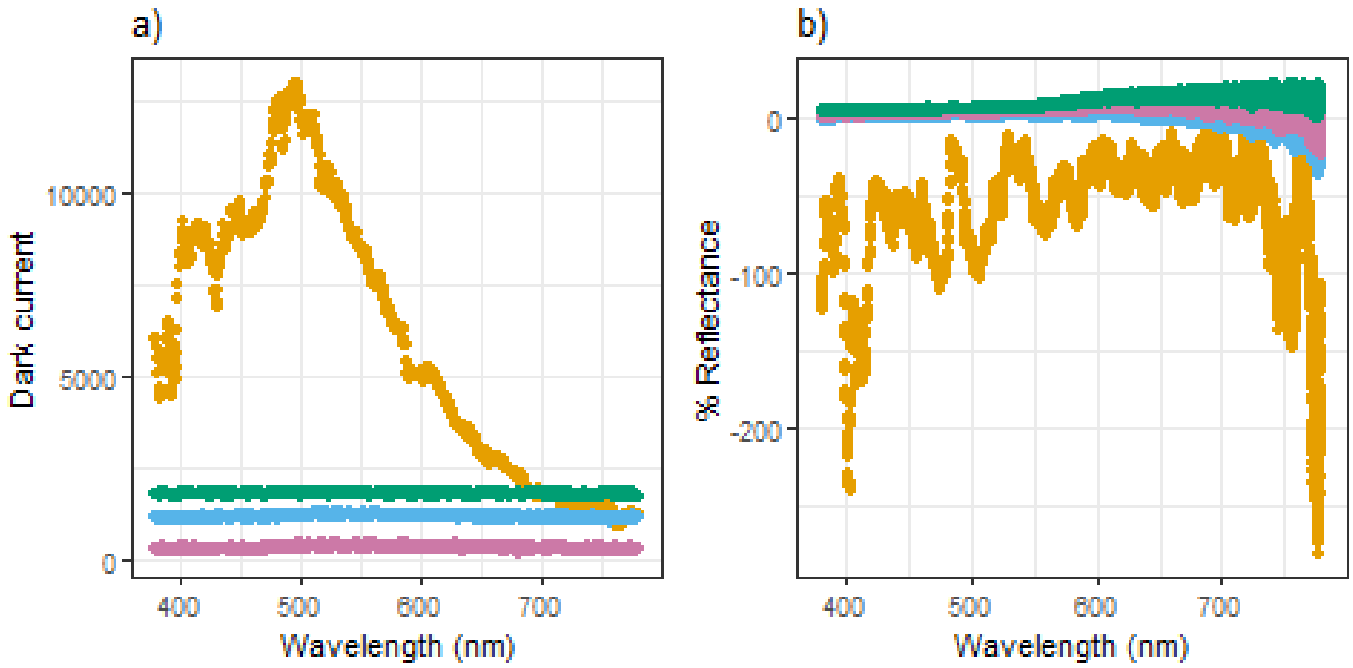

Figure G.3-2: AQ11_GPH predicted % reflectance vs wavelength (nm). Where orange is campaign 1, blue campaign 2, pink campaign 3 and green campaign 4.

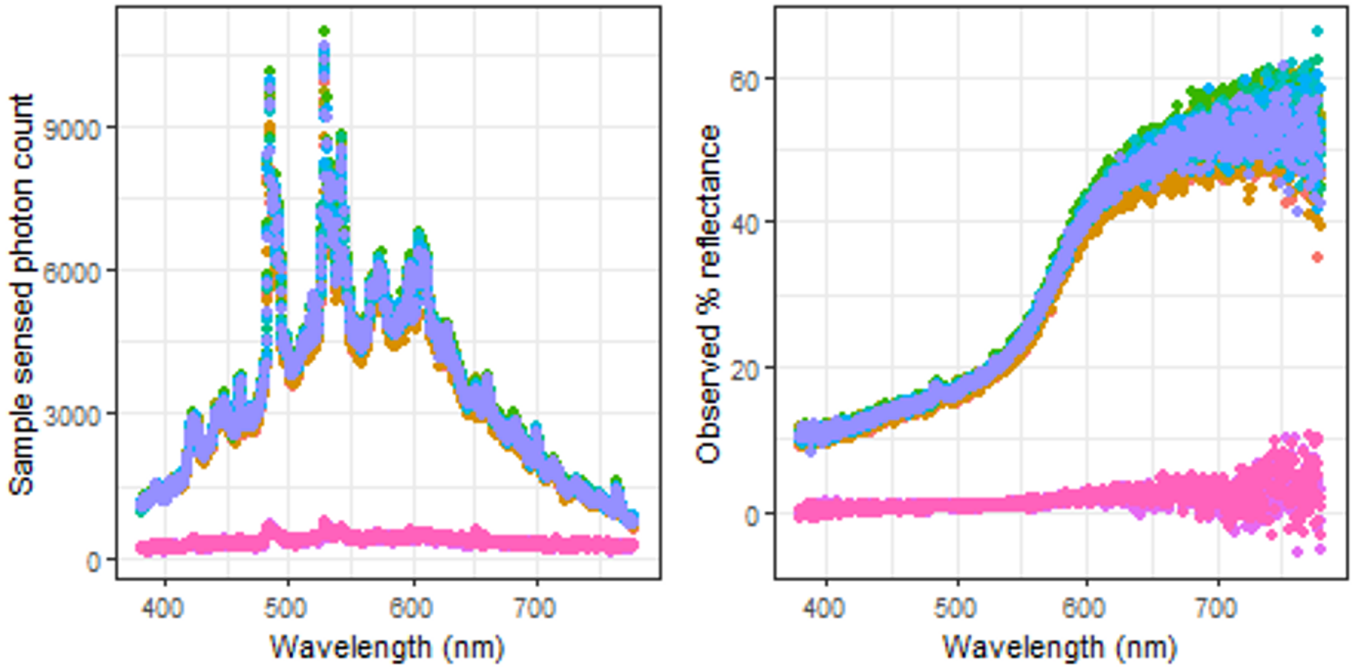

Figure G.3-3: RS13_GBR (a) colour measurement (sample sensed photon count) and (b) predicted % reflectance vs wavelength (nm). There is a different colour for each replicate number.

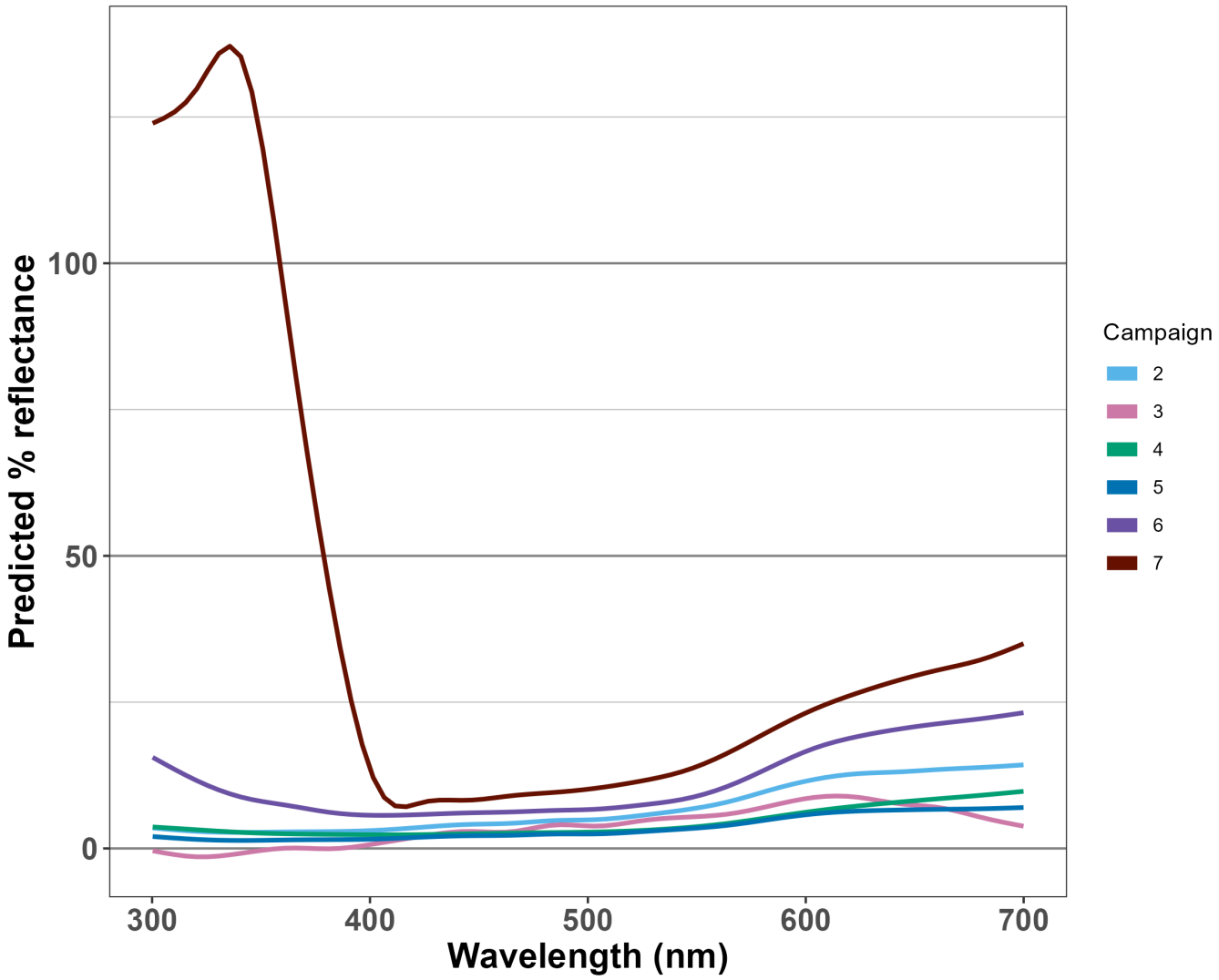

Figure G.3-4: AQ03_GPH predicted % reflectance vs wavelength (nm).

G.3.2 Faults in HDX data

The interactive software for the HDX instrument, developed by the statistical team, checks the data for the faults mentioned above.

During campaign 7, measurements of AQ03_GPH using the HDX instrument recorded a sample photon count (S column) of zero for all wavelengths on three targets. Figure *G.3-5*(a) shows the data for target 5, in which the sample sensed photon count had a value of zero for all wavelengths, resulting in a “wiggly” downward trend line for % reflectance. Figure *G.3-5*(b) shows data for target 10, in which the sample sensed photon count had a large variation in values, resulting in the observed % reflectance ranging from 8% to 75% reflectance. At the time of observation, these data were deemed valid by the HDX interactive software. Since then, faults of this kind have now been incorporated into the list of faults checked in the HDX interactive software.

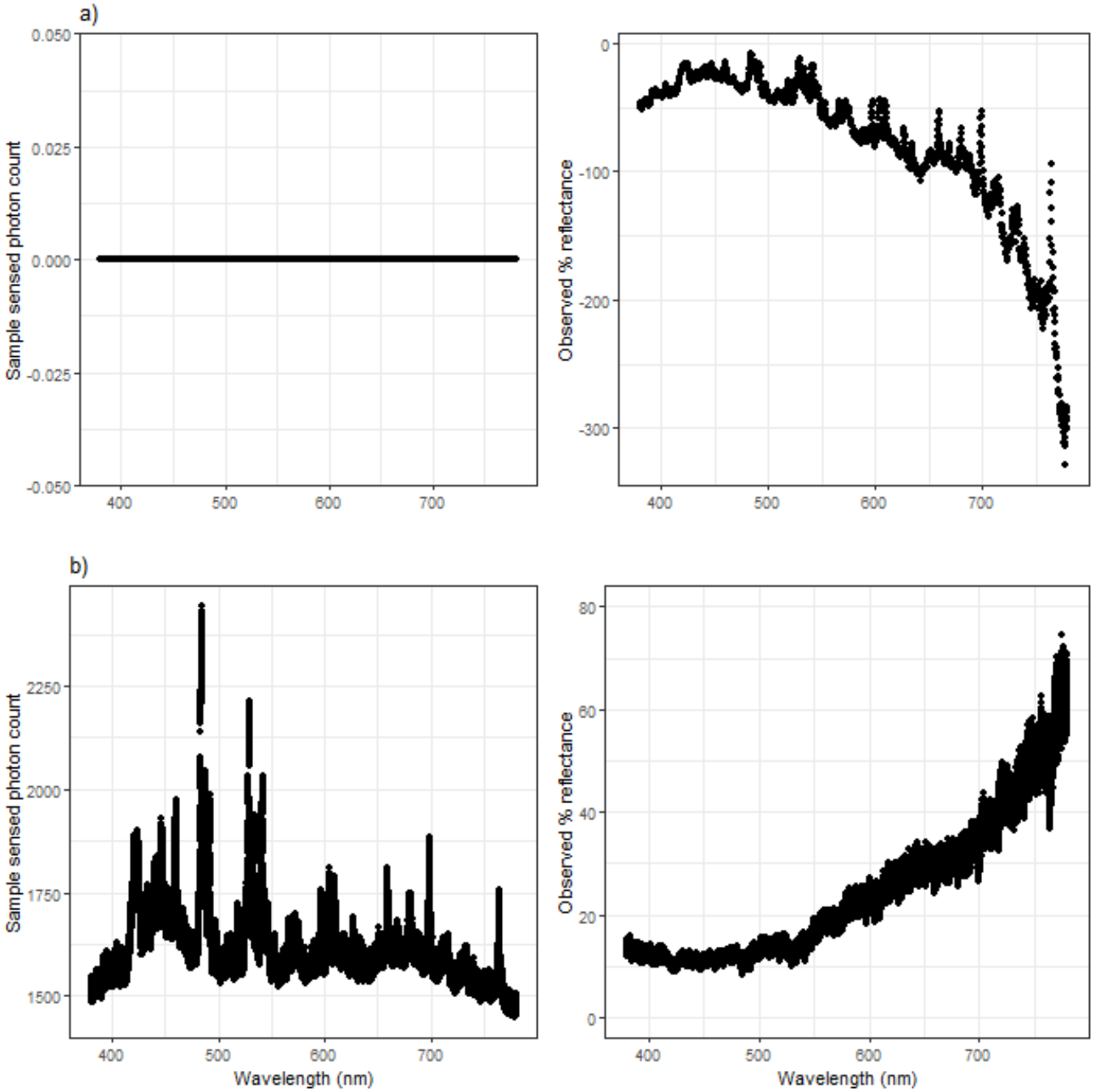

Figure G.3-5: AQ03_GPH (a) target 5 (top row) and (b) target 10 (bottom row). Left panel is sample sensed photon count versus wavelength (nm); and right panel is observed % reflectance versus wavelength (nm).

G.4 IVL passive samplers: further results and diagnostics

G.4.1 Passive samplers — concordance

Section 7.11.6 considered the spatial patterns of concentration of pollutant gases measured by the passive samplers. For the case of NO_2, it was determined that the spatial pattern of concentration is consistent between different months, although the overall level varies between months. Evidence for the consistent pattern was obtained using the concordance technique described in Appendix *F*.1.6.

In this section, the same concordance technique is applied to the data for the other gases. Figure *G.4-1* shows the consensus rank images for each gas.

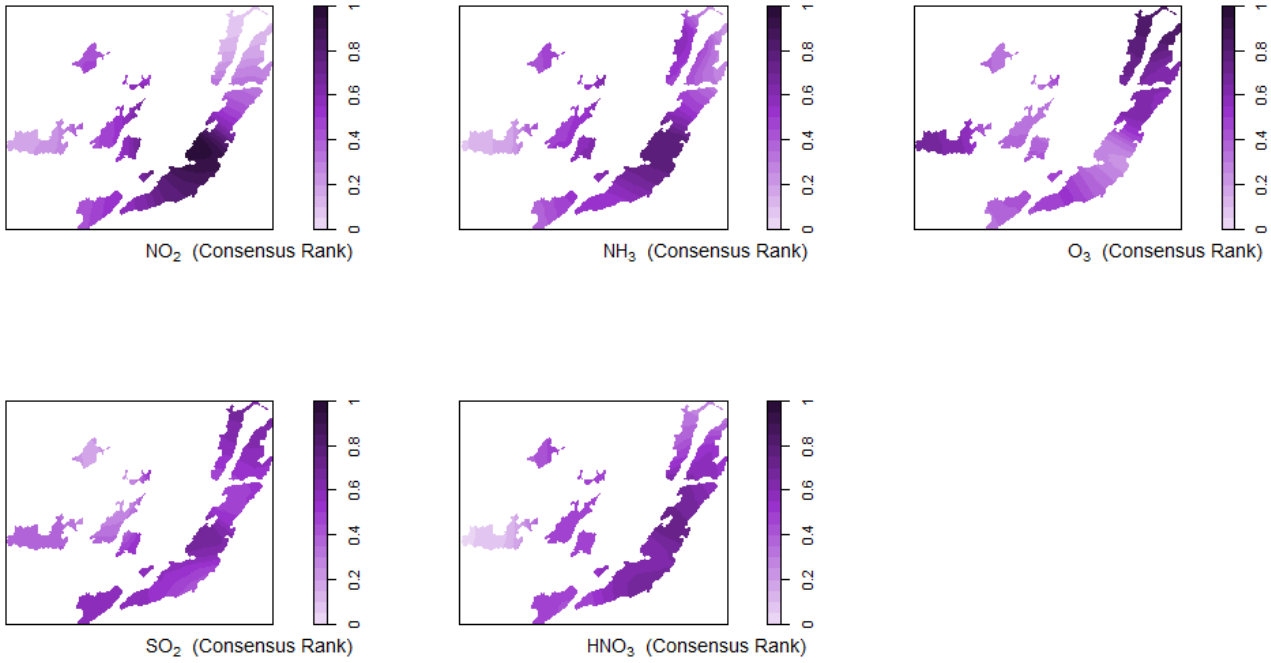

Figure G.4-1: Consensus rank images for each gas, for the spatially smoothed passive sampler data.

Figure *G.4-2* shows the rank disagreement (standard deviation) images for each gas.

As indicated in Section 7.11.6, there is a consistent spatial pattern in concentration of NO_2, and a moderately consistent pattern in the concentration of NH_3, and these two patterns are similar insofar as the highest concentrations tend to be observed close to Dampier port.

For O_3, there is a highly consistent pattern of high concentrations in the north and north-east of the peninsula, but in other areas the pattern is less consistent, with substantial variation in concentration on the outer islands. For other gases, there is less consistency between the patterns observed in different months.

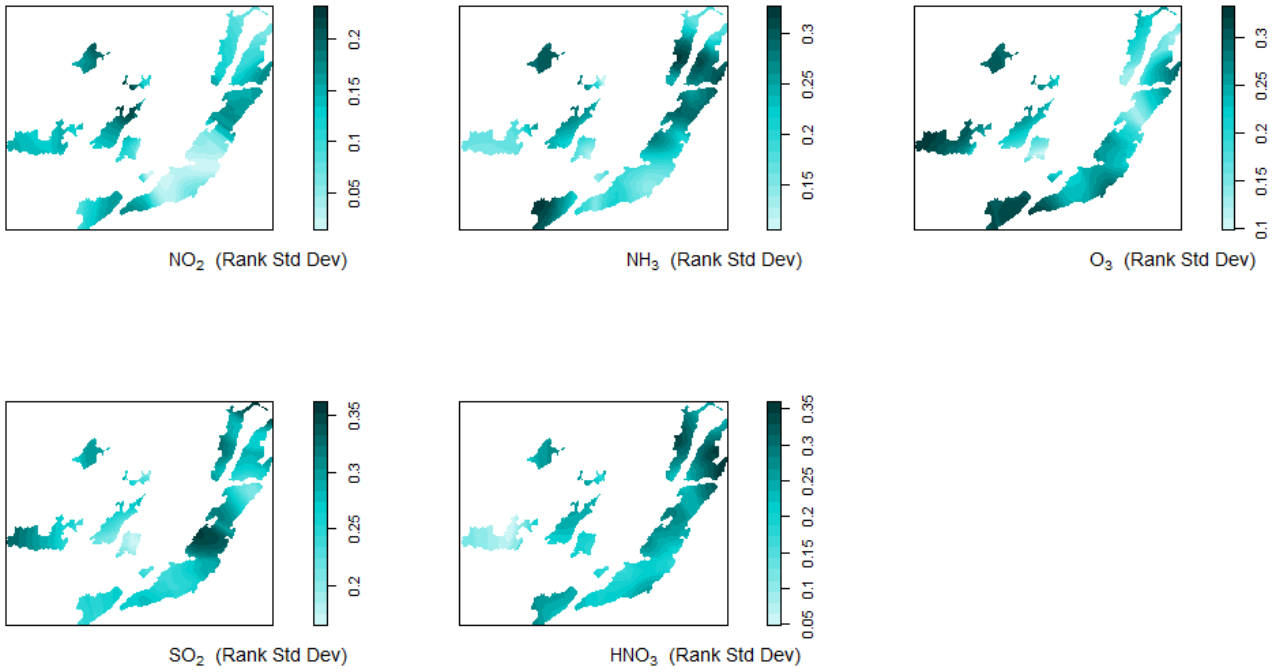

Figure G.4-2: Rank disagreement (standard deviation) images for each gas, for the spatially smoothed passive sampler data.

G.4.2 Correlations between different gases

Figure *G.4-3* shows an RDA biplot generated from the passive sampler estimates of gas concentration, the geographical coordinates of the monitoring sites, and elevation (height above sea level) of the monitoring sites. Northing and elevation explain approximately 24% of the variance in the data, which seems substantial but is less than the 38% explained by the sine and cosine of the month, as shown in Figure *7.11-5*. Both NO_2 and NH_3 seem to have a negative association with northing, while O_3 has a positive association. NO_2 and HNO_3 have a positive association with elevation, while SO_2 seems to have a negative relation. Note that easting is not included in this plot, as adding easting reduces the percentage of variance explained by the explanatory variables and only has a small effect. This may be a result of the strong north-south spread of most monitoring sites with only a small east-west range.

However, as shown in Figure *G.4-4* the strength of these associations is less than that obtained using the Month variables. The first two components (RDA1 and RDA2) explain the majority of the variance, a combined 36.64% of the total. The last two components explain a total of 0.98% of the variance, for a total of 37.63%.

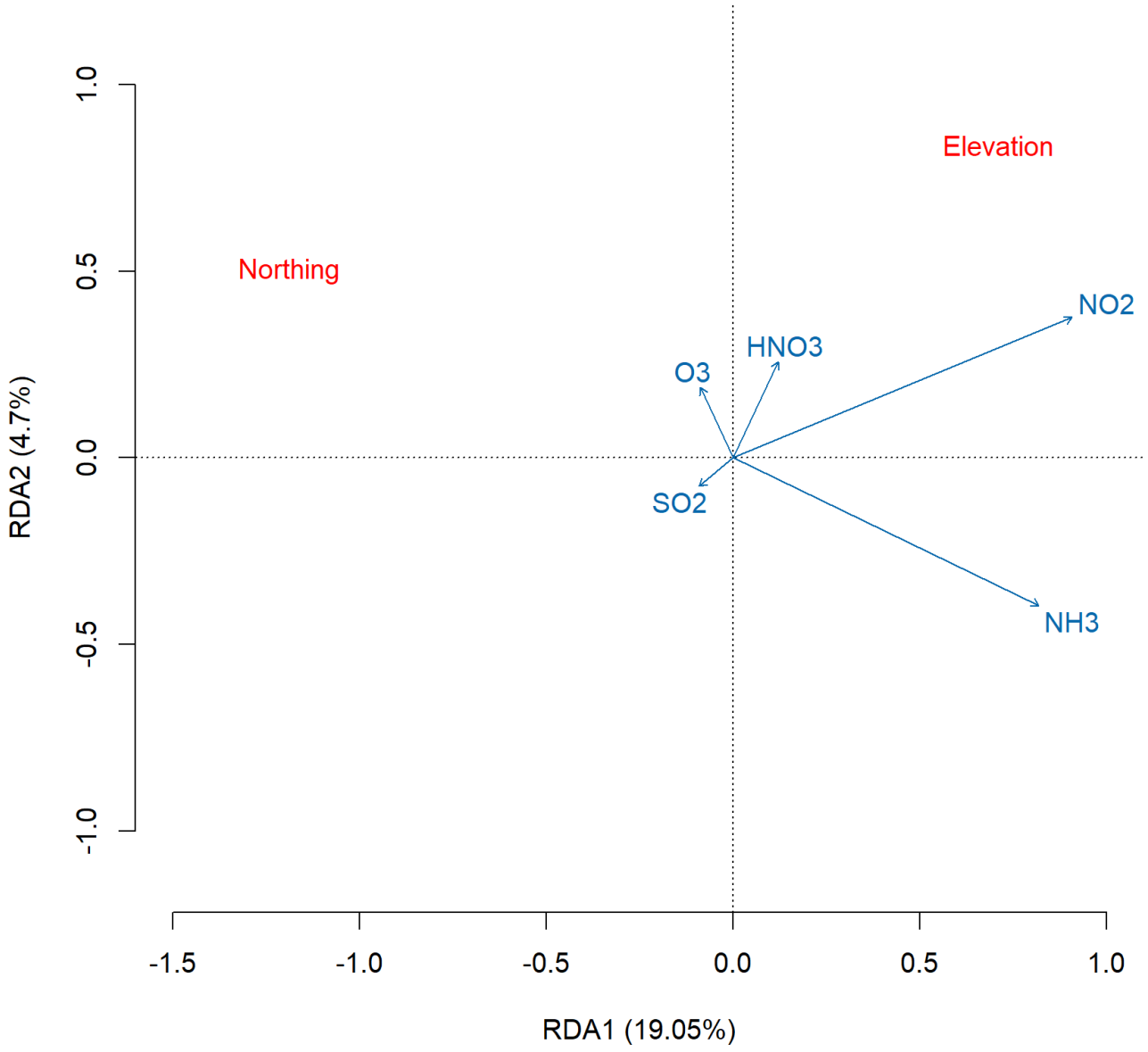

Figure G.4-3: RDA biplot of gas measurements (NO_2, NH_3, HNO_3, O_3) versus northing and elevation.

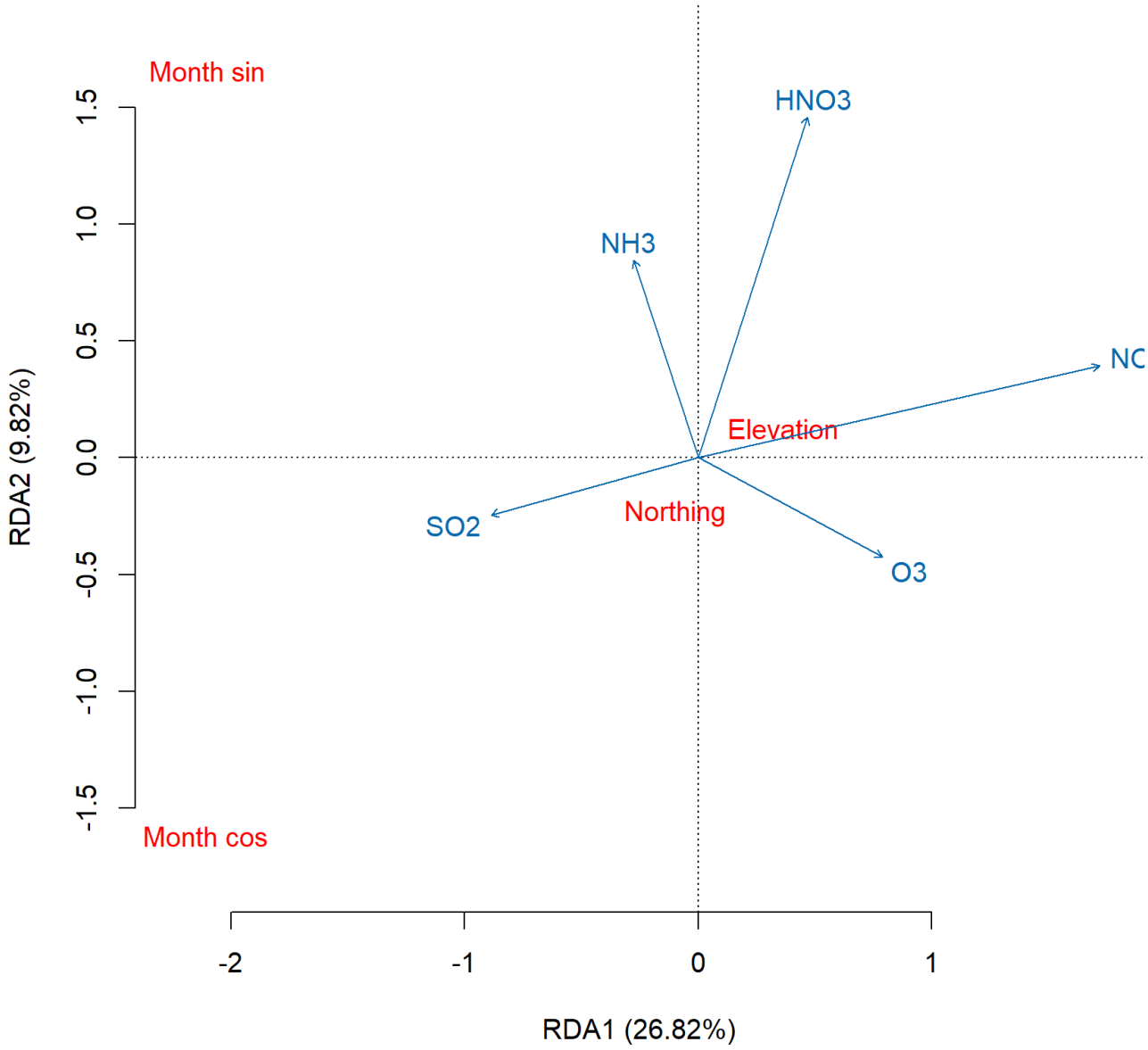

Figure G.4-4: RDA biplot of gas measurements (NO_2, NH_3, HNO_3, O_3) versus month sin, month cos, northing and elevation.

G.4.3 Residual variability

Section 7.11.4 estimated the residual variability in passive sampler observations, using the data from duplicate samplers deployed in the field. Additional figures are presented here.

Figures *G.4-5*–*G.4-10* show plots of the estimates of residual variance against the estimates of mean value, the month of observation, and the air quality station, for each analyte.

Plots of variance against mean are used to investigate the variance-mean relationship. There is little evidence that the residual variance depends on the mean, except in the case of toluene (Figure *G.4-10*).

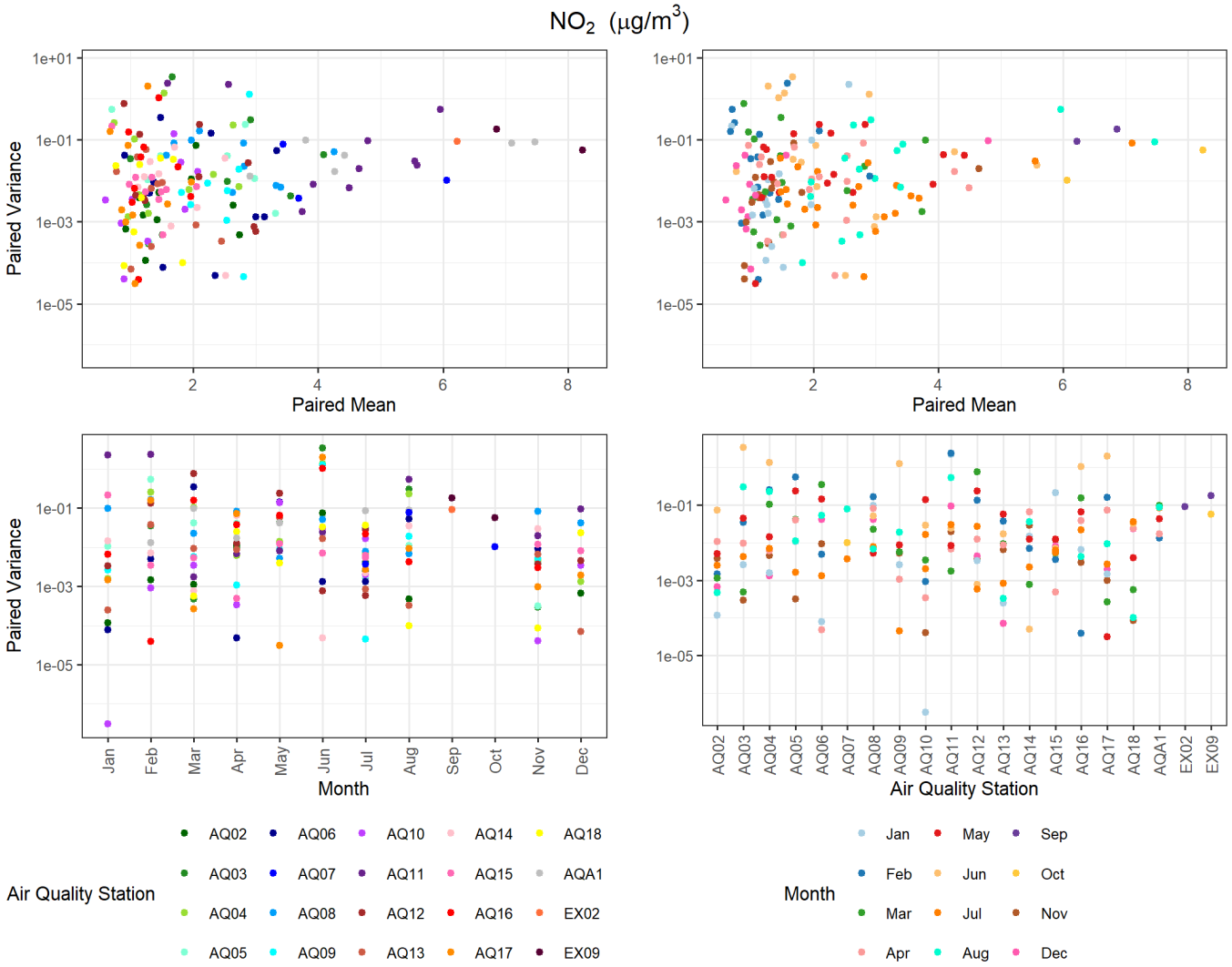

Figure G.4-5: Paired NO_2 variance by mean plots (top row) and paired NO_2 variance by month (left panels) and by station (right panels). Logarithmic scale for vertical axes. Where for example 1e-05 means 10^{-5}, or 0.00001.

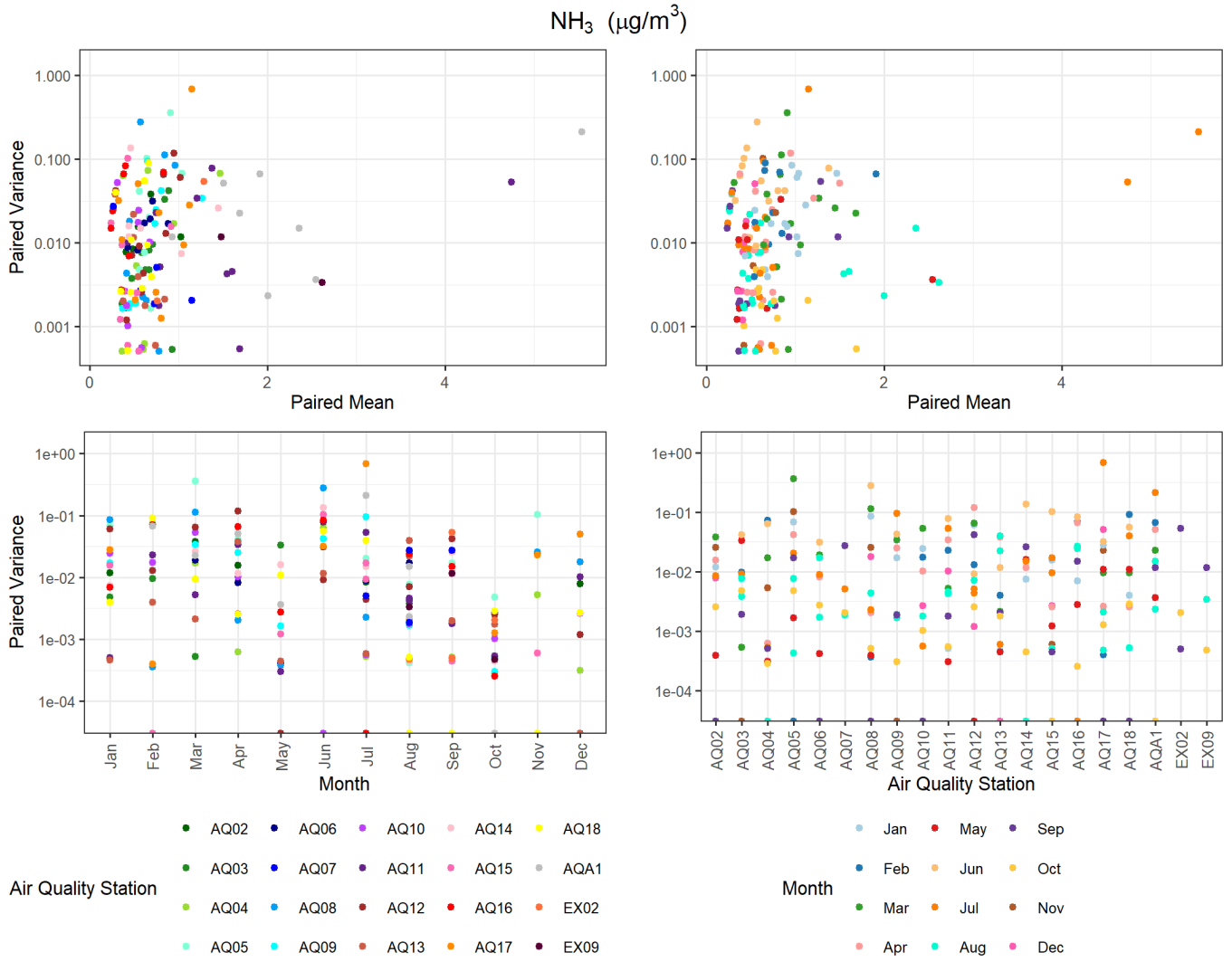

Figure G.4-6: Paired NH_3 variance by mean plots (top row) and paired NH_3 variance by month (left panels) and by station (right panels). Logarithmic scale for vertical axes.

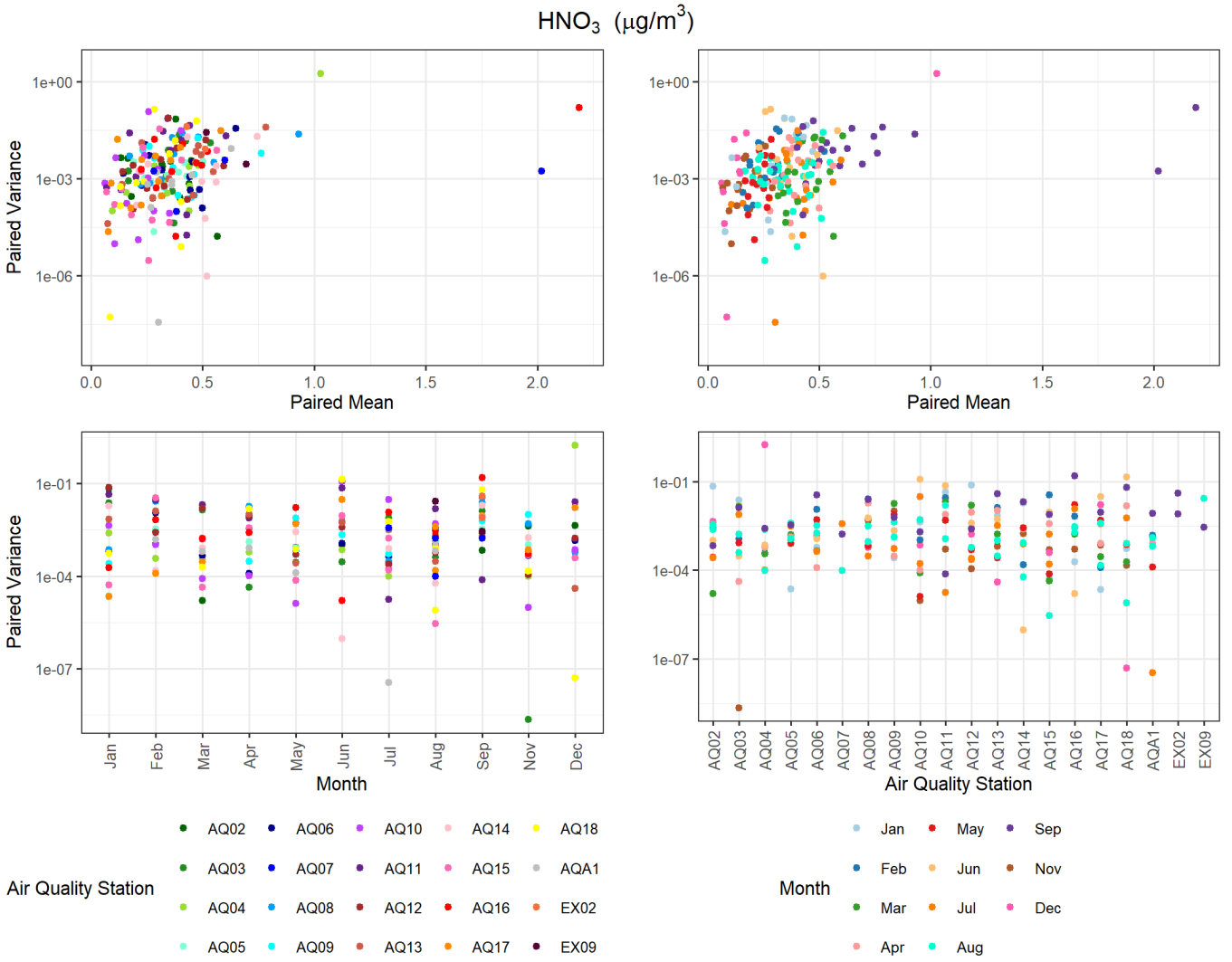

Figure G.4-7: Paired HNO_3 variance by mean plots (top row) and paired HNO_3 variance by month (left panels) and by station (right panels). Logarithmic scale for vertical axes.

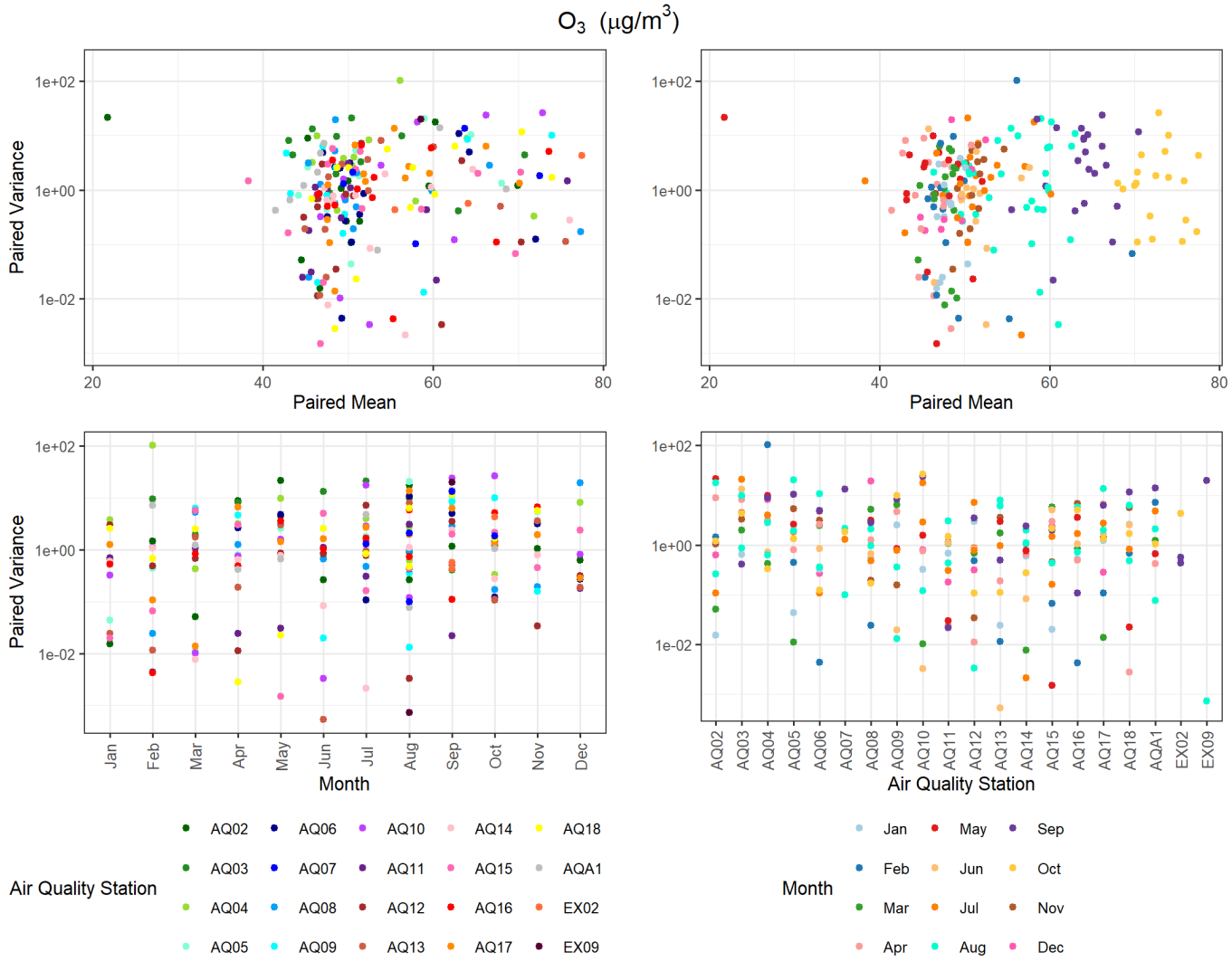

Figure G.4-8: Paired O_3 variance by mean plots (top row) and paired O_3 variance by month (left panels) and by station (right panels). Logarithmic scale for vertical axes.

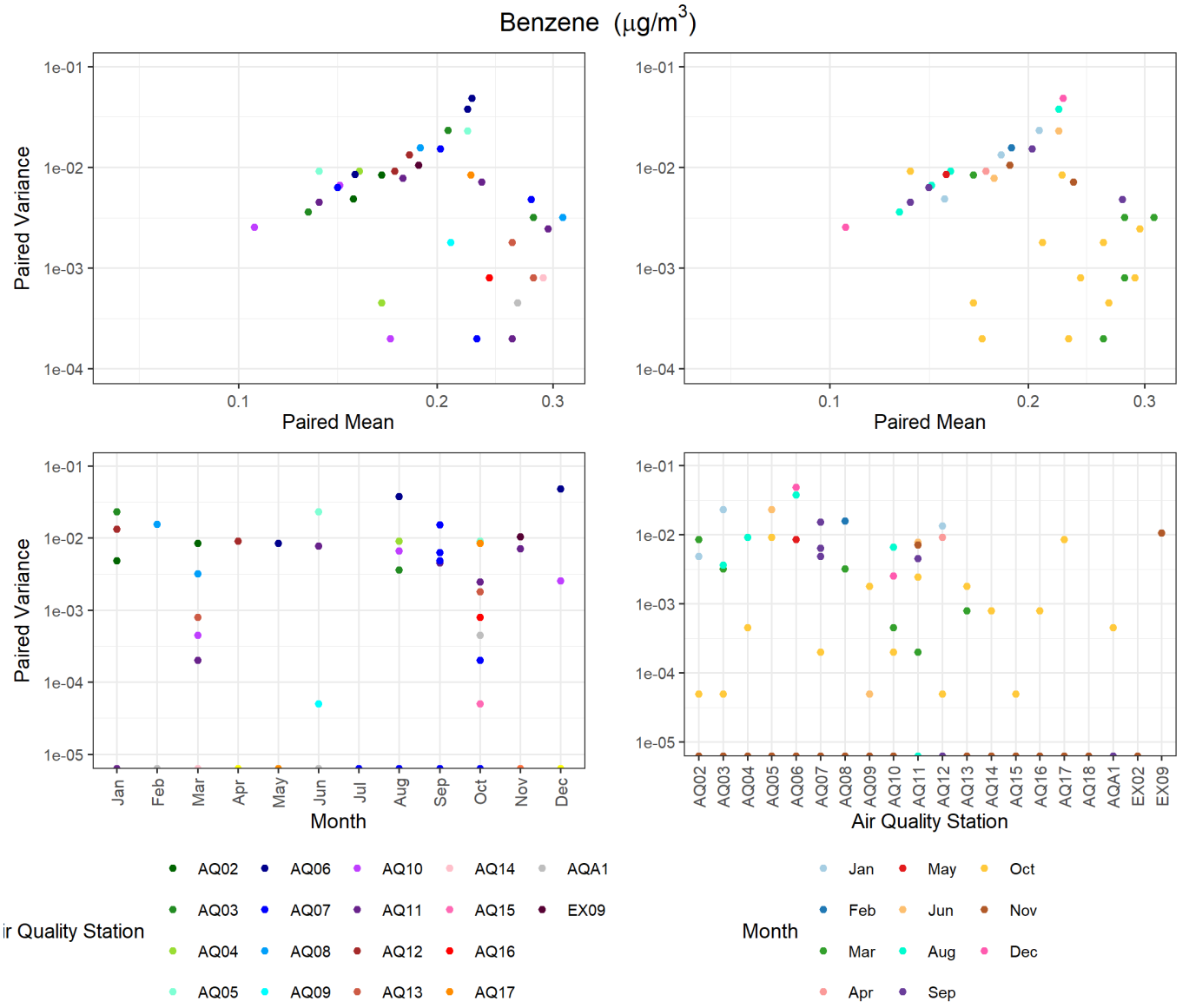

Figure G.4-9: Paired benzene variance by mean plots (top row) and paired benzene variance by month (left panels) and by station (right panels). Logarithmic scale for vertical axes and for mean value.

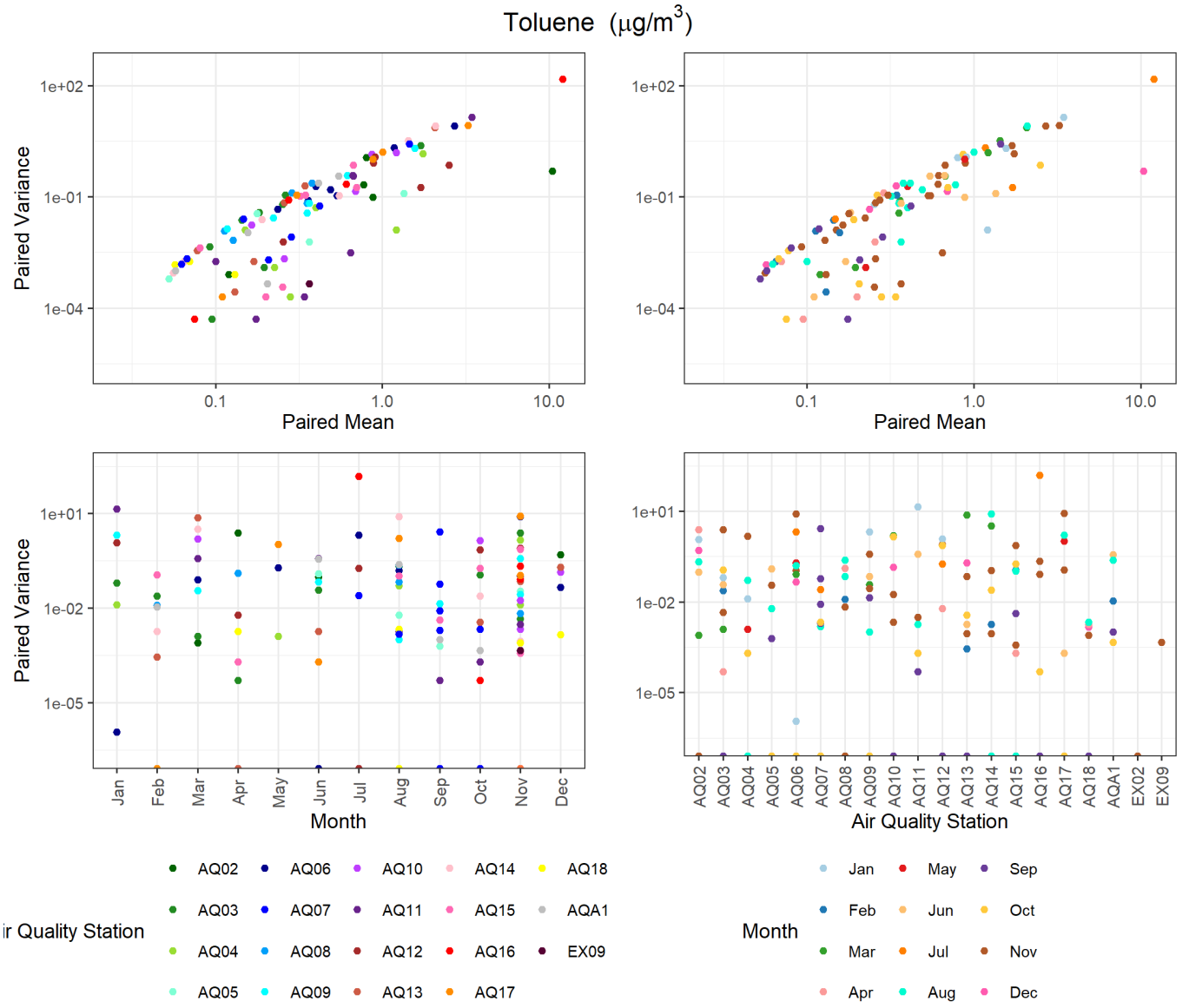

Figure G.4-10: Paired toluene variance by mean plots (top row) and paired toluene variance by month (left panels) and by station (right panels). Logarithmic scale for vertical axes and for mean value.

G.4.4 Analysis of co-located sites

Section 7.11.5 used the observations at the co-located sites AQ07 and AQ08 to investigate short-scale variability. As a complement to that analysis, this subsection performs an analysis of variance (ANOVA) and associated statistical tests which serve to determine whether systematic differences are present between the two stations.

Two-way ANOVA comparisons between stations

Two-way ANOVA of the passive sampler observations, grouped by station and by calendar month, was performed. For each analyte, the ANOVA F-test was applied to test for statistical significance of the Month effect, the station effect, and the interaction between month and station. For example, significance of the station effect would indicate evidence of a systematic difference between the two stations.

Table G.4-1: Significance tests based on two-way ANOVA for gas measurements by station and month for stations AQ07 and AQ08.

Gas	NO_2	NH_3	O_3	SO_2	HNO_3
Number Observations	8	20	20	16	16
Number unique periods	2	4	4	3	3
ANOVA p-value Station	0.141	0.1922	0.1759	0.5459	**0.0005**
ANOVA p-value Month	0.4356	**0.0004**	$<$ **0.0001**	**0.0003**	$<$ **0.0001**
ANOVA p-value Station:Month	0.2106	0.2641	0.8617	0.3306	$<$ **0.0001**
Levine test p-value	$<$ **0.0001**	**0.0068**	$<$ **0.0001**	$<$ **0.0002**	**0.0035**
Shapiro Wilk test (normality) p-value	0.7892	0.1657	0.8912	0.0888	0.9933

The resulting p-values for the ANOVA F-tests are given in Table *G.4-1*. For all gases except HNO_3, the results indicate no evidence of systematic difference between stations. For all gases except NO_2, the month effect is significant, suggesting seasonal variation in concentration of these gases.

Assumptions of the F-test include that the responses are normally distributed and homoscedastic (response variance is constant). To check these assumptions, the Shapiro-Wilk test of normality and the Levine test of homogeneity were performed. The resulting p-values are reported in Table *G.4-1*. Results for the Shapiro-Wilk test show no evidence against the normality assumption. Results for the Levine test constitute strong evidence against homogeneity of variance, violating one of the assumptions of the F-test. Consequently these results need to be considered with caution. Given the limited sample size, this analysis should be repeated when more data are available.

G.5 Ramboll predictions: further results and diagnostics

This section provides further graphs of the data analysed in Section 8.3 to compare the Ramboll model predictions with the passive sampler observations.

Figures *G.5-1– G.5-5* show monthly plots of the passive sampler observations and the Ramboll model predictions (monthly mean and monthly maximum) against air quality monitoring site. The AQM's are ordered by increasing value of average concentration of the gas.

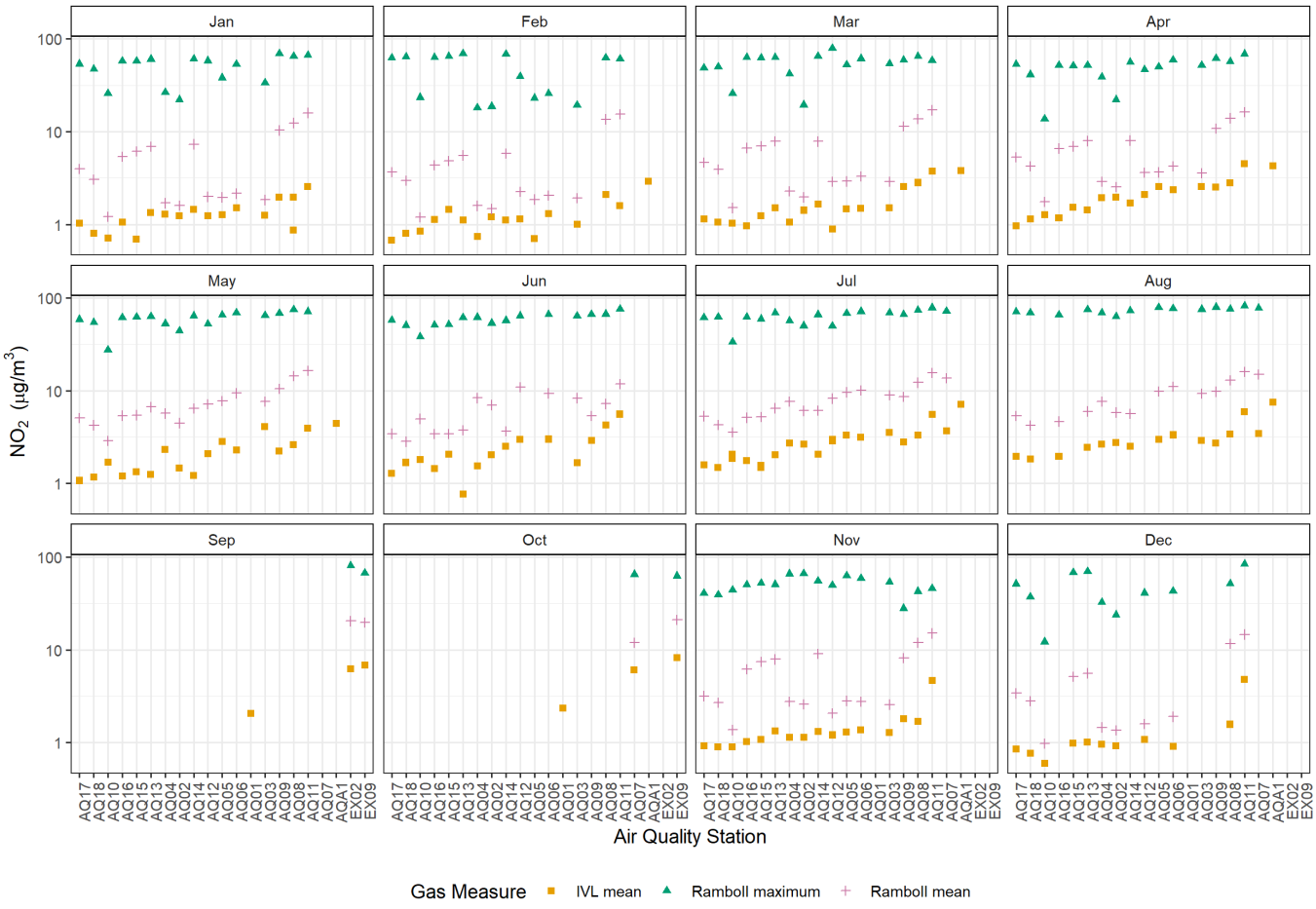

Figure G.5-1: Passive IVL Samplers and mean and maximum monthly Ramboll predictions for NO_2 showing each month.

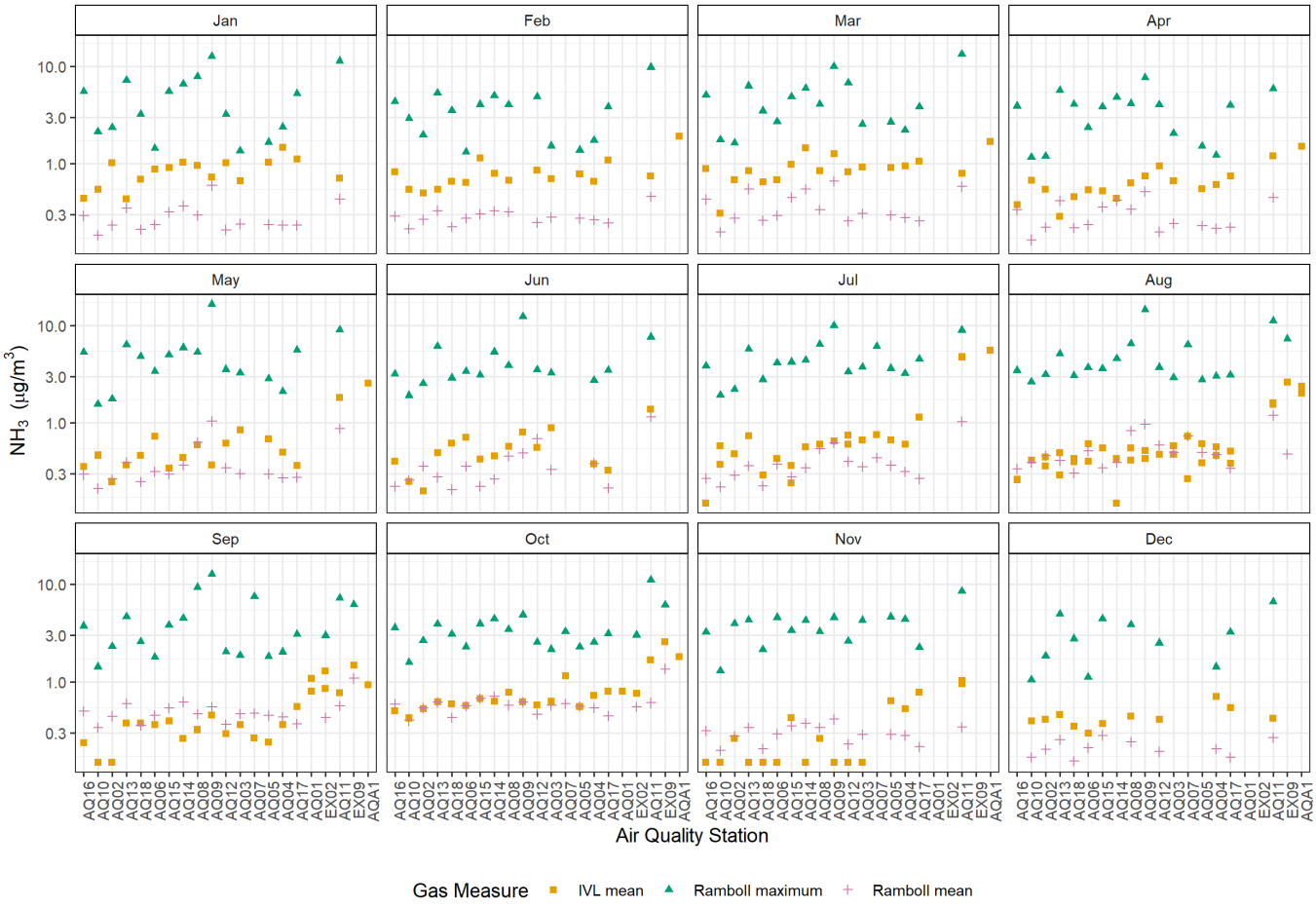

Figure G.5-2: Passive IVL Samplers and mean and maximum monthly Ramboll predictions for NH_3 showing each month.

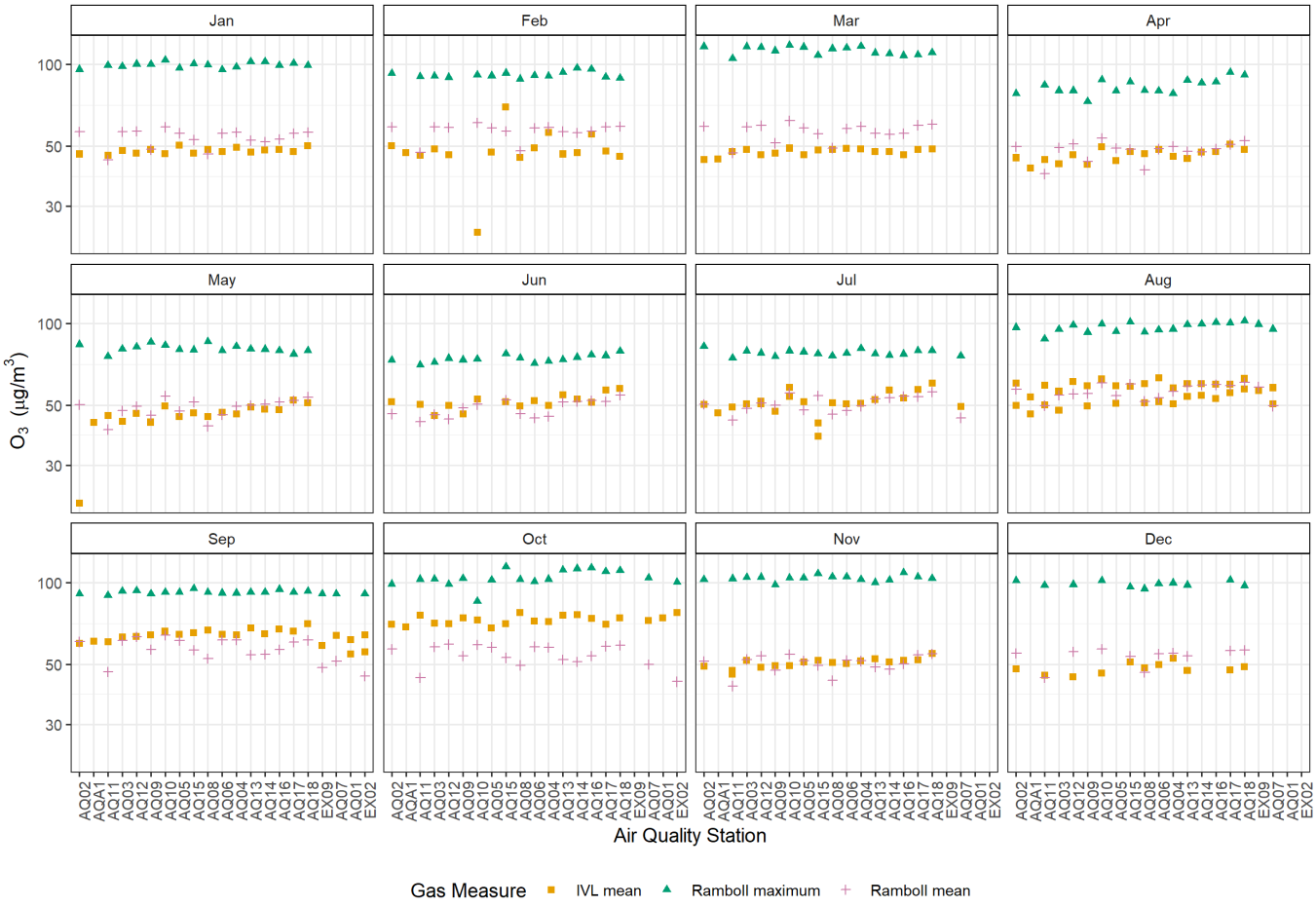

Figure G.5-3: Passive IVL Samplers and mean and maximum monthly Ramboll predictions for O_3 showing each month.

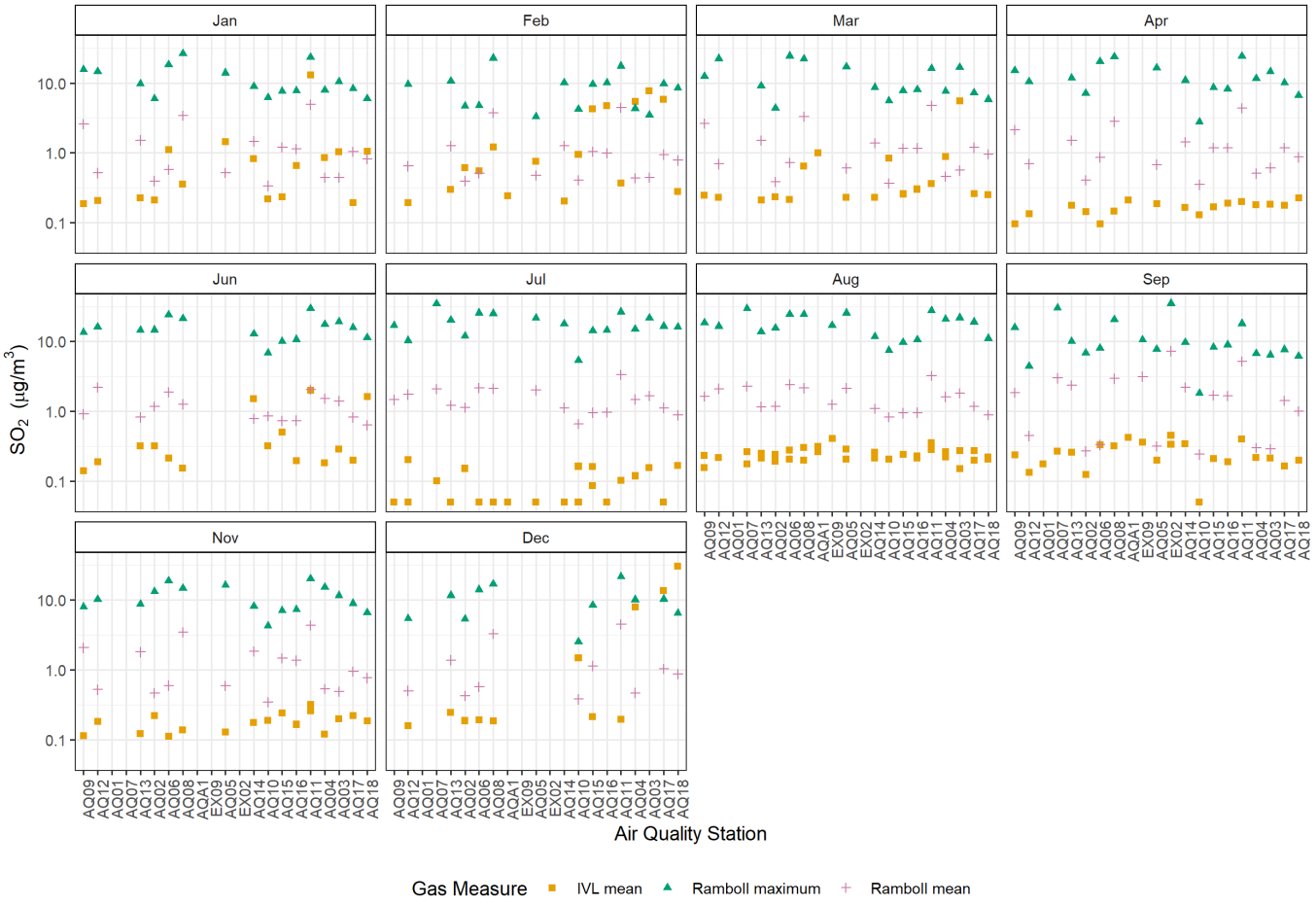

Figure G.5-4: Passive IVL Samplers and mean and maximum monthly Ramboll predictions for SO_2 showing each month.

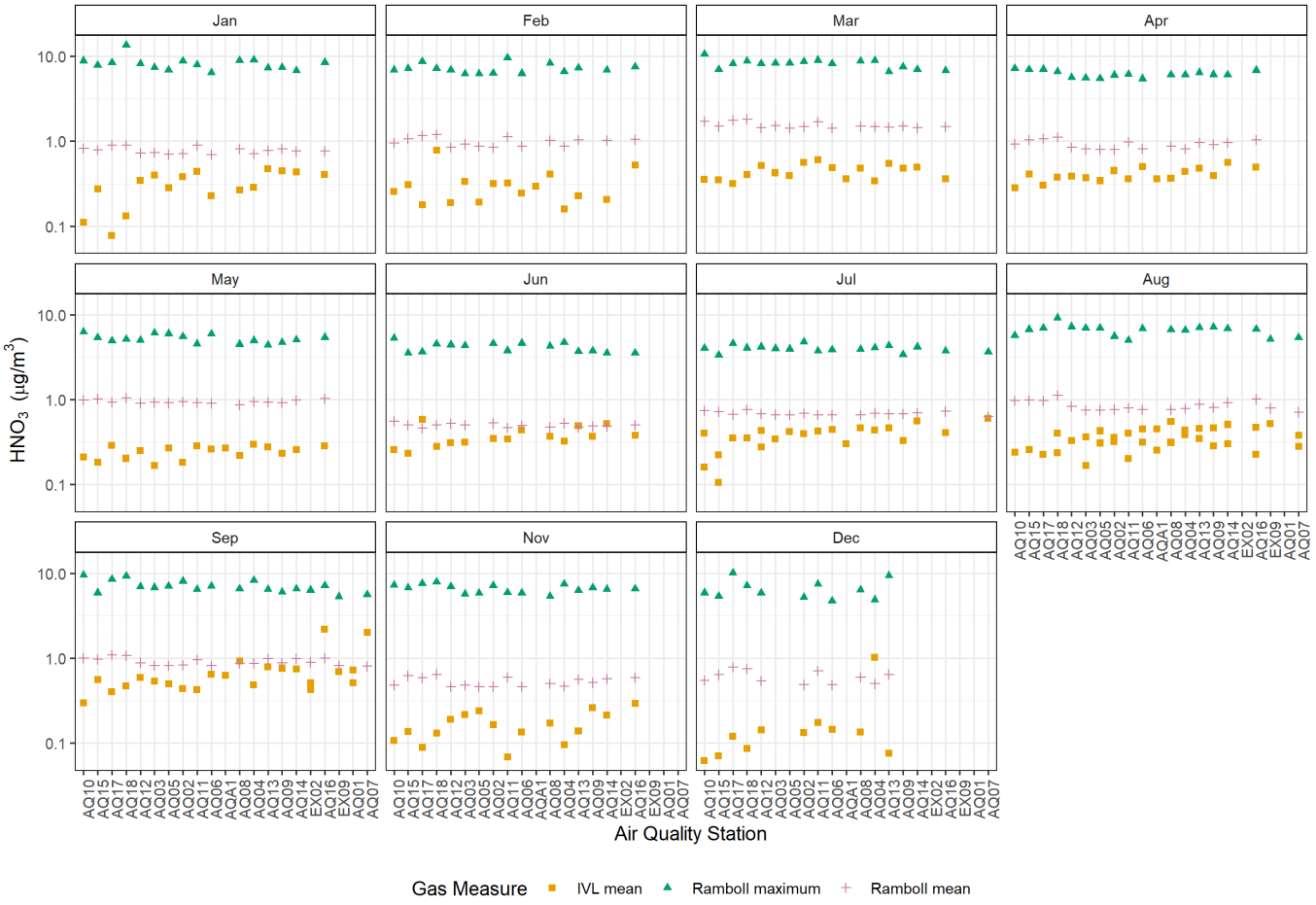

Figure G.5-5: Passive IVL Samplers and mean and maximum monthly Ramboll predictions for HNO_3 showing each month.

This page is intentionally blank.

H Micro-photogrammetry

Surface change to the rock surfaces at Murujuga can be monitored in a number of ways, with previous research focusing on colour change as a reasonable indicator. The current project has retained this metric but added surface *pH*, permeability and elemental change. Towards the end of the CSIRO research period, morphological change was trialled using stereometric imaging at a macro scale (Ramanaidou and Lau, 2015).

The term micro-photogrammetry refers to image acquisition through a microscope objective mounted to a 35mm DSLR camera. It can be argued that the imaging is macroscopic, given that the field of view is approximately 16 by 12 mm. The technique allows for closer imaging, subject to the limitations of the optical configuration, constrained by the objective employed and the resolving power of the digital camera. The CSIRO researchers recognised the value of morphological monitoring in 2015 (Ramanaidou and Lau, 2015) although the technique was only applied for that year. The approach is notable for taking stereo images only and capturing the whole surface at a distance of either 1.800 or 3.000 metres. It is doubtful such broad imaging would allow for fine-detailed analysis at that scale. The imaging configuration chosen was a Nikon D200 (10.2Mp) camera with an AF Micro Nikkor 60 mm 1:2.8 D lens. Despite the label Micro, this is simply a mid-range macro lens. At macro settings, a 60mm lens is no different from a 100 mm or longer lens, other than the focal distance to the object. At 60 mm and greater, the image will be more or less distortion-free.

To summarise the CSIRO approach, a 10.2 Mp sensor at 1.800 metres from the subject will provide an image 800 $\times$ 530 mm with a pixel density of 5 pixels per linear millimetre.

The configuration adopted for the current project has been in two formats. The first is using a 24Mp camera with a 5X Zeiss Planachromat objective attached. This provides a flat field of view of 16 $\times$ 12 mm with a pixel density of 377 pixels per linear millimetre. Through the focus stacking and photogrammetric processing described below, a particle of less than 30 μm (0.03 mm) can be discretely resolved. This compares to a sand grain that will be in the order of 0.2–1.0 mm in diameter and hence alterations at crystal dimensions can be observed, not just grain loss but deformation of a surface without loss. Other benefits of the applied system over a stereoscopic imaging process include the greater ability to resolve depth due to the multiple views of a particular point in the surface. In the described stereoscopic imaging each point is imaged twice. In the currently applied photogrammetric system each point is imaged at least four times. Both systems take perpendicular images although the current system can image at any offset to perpendicular desired. Indeed the second less precise method employed is takes a series of handheld images, ensuring that offsets are developed through imprecise camera angles.

H.1 Imaging method 1

Three sites were proposed in the study plan to demonstrate the value of morphological measurement as an adjunct to colour change, *pH* and gas permeability. Challenges of establishing the technique on site have led to just one site being imaged. This has provided very good resolution images, albeit without having achieved the objective of a full 100 $\times$ 100 mm study area being fully and consistently modelled in 3D.

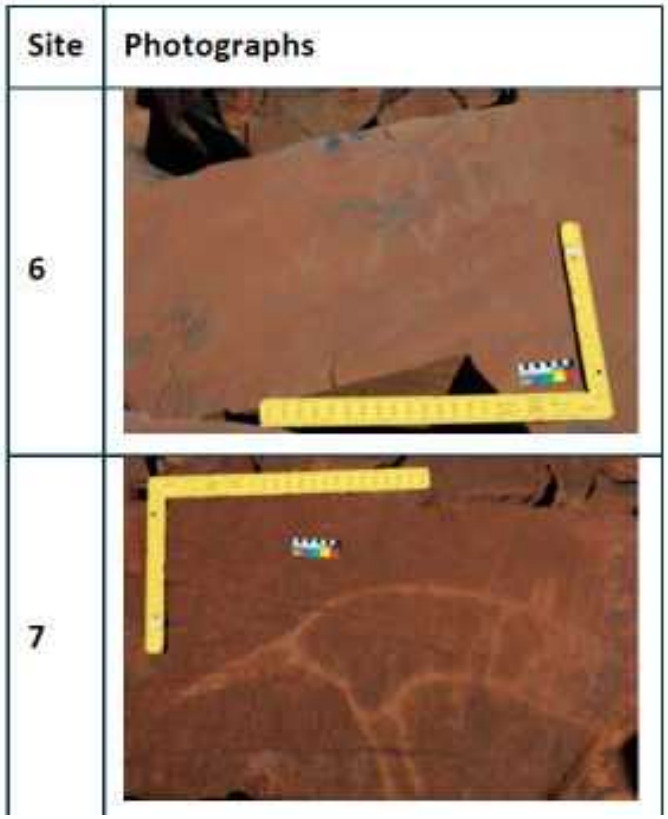

Figure H.0-1: Two sites in the current research EX06_GPH and EX04_GBR that have been studied by CSIRO in 2015. The imaging scale is apparent.

The system relies on a Zeiss 5X magnification objective attached to a 24Mp DSLR, in turn mounted to a programmable scanning frame.

The 5X Zeiss objective was arrived at with consideration to workable image size and focal distance from the surface. The image dimensions of 16 $\times$ 12 mm is an optimal balance between focal distance, depth of focus and image alignment in downstream processing. To create a 3D image an ideal 60% overlap between adjacent images becomes increasingly difficult to maintain with higher magnification. Focal distance of the Zeiss is approximately 80mm, ensuring that a 5 volt ring light can uniformly illuminate the scene, essential for removing shadows.

Objectives of greater magnification, even a 6X lens, prove too magnified and various other 5X objectives give very short focal distances. When mounted to the camera the objective becomes the front lens with no other glassware between it and the imaging sensor. The DSLR was chosen after trials with a stereo microscope proved too bulky and various digital imaging systems provided less resolution than the camera at greater expense. Field portability and affordability become significant in choosing the imaging system and in this case the only additional expenditure, assuming a DSLR is already available, is the objective and its camera mount.

The imaging system in Figure *H.1-1* is attached to a scanning frame whose movement is controlled by an Arduino control board driving Adafruit motor controllers that allow the camera to scan vertically and in the two planar axes. The Arduino is programmed to control the increments in each of the

Figure H.1-1: Camera configuration with objective partially obscured by ring light attached to the objective mount. When activated the ring light LED array provide a uniformly lit scene, removing all shadows created by the surface morphology.

three axes, which inevitably requires adjustment for the outward and return journeys for each motor controlling the movements. Naturally the vertical movement falls more readily than it rises, but this appears also to be the case for the two lateral motors. Slight out-of-horizontal mounting of the frame requires further programming to ensure uniform increments in each plane.

The mounting frame sits on rubber feet to ensure no impact on the surface. The feet are placed away from any engraved channels and can be further cushioned over sensitive surfaces.

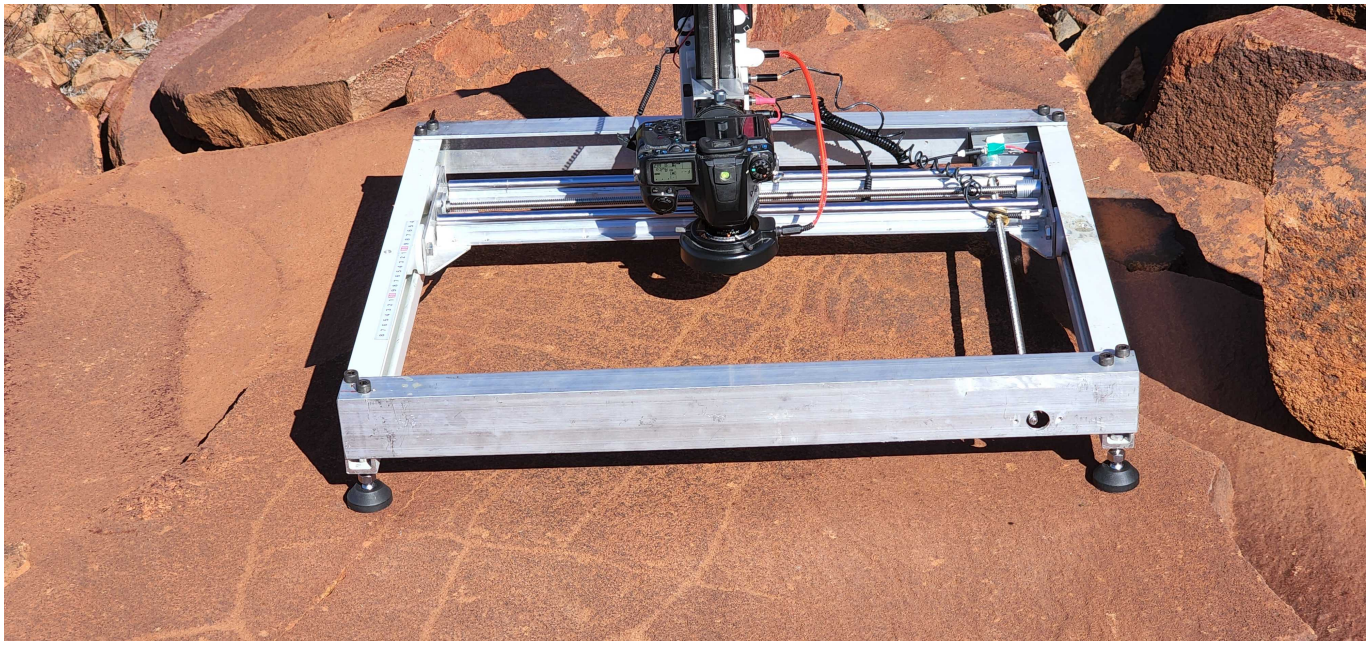

Figure H.1-2: Imaging system mounted onto scanning frame and set on engraved surface at AQ11.

Figure H.1-3: Scanning frame mounted vertically at EX08. This orientation required considerable reprogramming to achieve uniform movements.

One limitation, although in some respects an advantage, of the microscope objective is that the camera cannot self-focus. The advantage of non-focusing is that the objective captures exactly at the focal plane without attempting to guess what the scene is. The Zeiss objective has a depth of focus of 4 mm. Twenty frames are captured in the perpendicular axis at one-millimetre increments, meaning that any point is in focus for four frames. A location with a 3mm depth will have seven usable images out of the twenty captured.

It has proven difficult to maintain smooth movements at the operating magnification, however this is not a disadvantage but rather provides slightly offset capture angles for the four in-focus images, aiding the 3D interpretation of the surface in the photogrammetric processing. These movements are also within the aligning capabilities of the focus stacking software described below. Once a perpendicular run is completed the first of the lateral movements advances the camera 60% of the frame width before commencing to capture twenty more images in the reverse direction.

The scanned area is nominally 100 × 100 mm, although this is over-run by 20% to ensure a processed image of those dimensions. The target area is first registered with a general location shot for realignment in subsequent scans. A section of 4 mm square tube is inserted into the scene to provide scale.

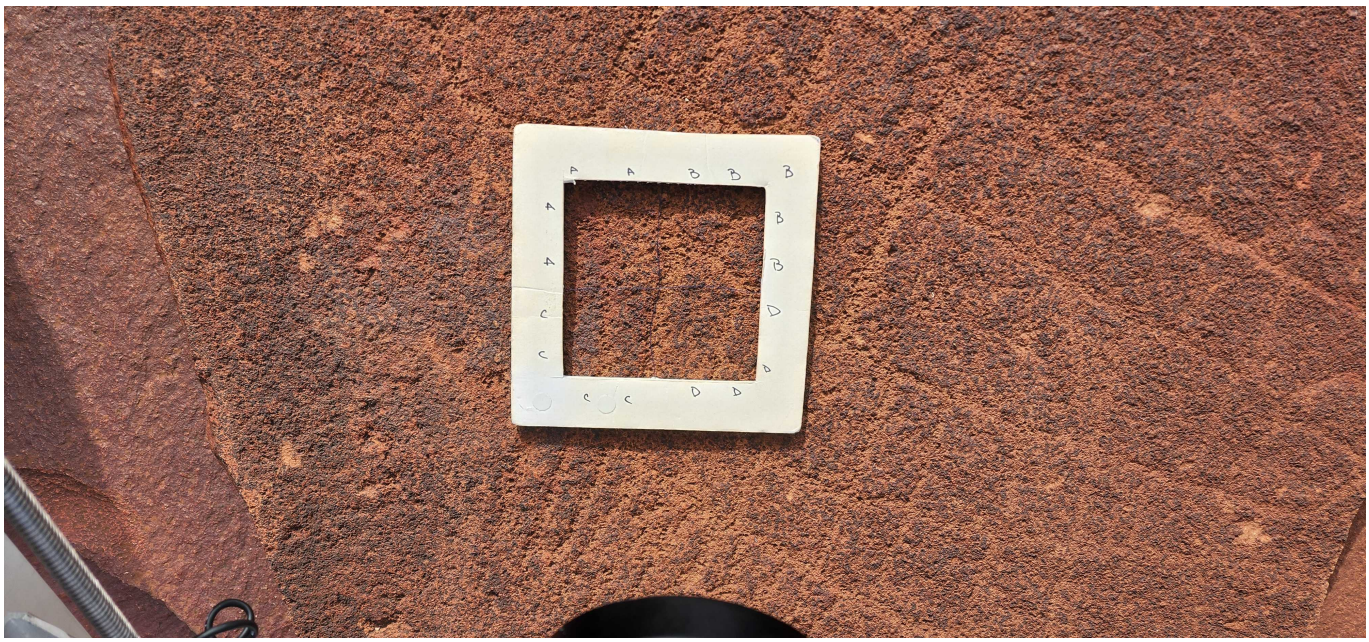

Figure H.1-4: The area to be scanned is defined by a 100 × 100 mm template that can be accurately realigned in subsequent scans.

Due to the stop start image gathering at 12 mm advances, the process is time consuming, taking over two hours to complete the 100 × 100 mm target area. Automation ensures that this time is not wasted, and the system is powered to complete a full run, although the camera battery needs to be changed at least once. This can be done without pausing the process. The ring light and scanning motors are all run from a multi voltage battery that remains above 50% at conclusion.

H.2 Imaging method 2

The scanning method described above has proven more complex than anticipated due to the harsh conditions leading to equipment irregularities. It has also been realised that the initial proposal of three sites does not provide a representative sample of the 54 study surfaces and is thus not compliant with the spatial statistical integrity required. To partially overcome this a second more time efficient method has been adopted. This method does not provide the resolution and hence the analytical strength of the scanning frame approach. It does however allow for the 3D

imaging of all 54 study surfaces at a resolution that allows for broad scale change. The method lies somewhere between the 30 micrometres resolution of the scanning frame and the very broad imaging advocated by CSIRO in 2015.

One of the documentation requirements has been to provide an image of the overall engraved study surface, primarily to study mass alterations such as spalling. To do this a photogrammetric approach has been adopted, imaging the surface at normal scale, typically in the order of 200–500 mm wide images. It is often difficult to gain a perpendicular image to capture a perfectly rectified image that is shadow free and that can capture all of a curved surface. By imaging as if for photogrammetric modelling, all parts of the surface are captured. While a photogrammetric model is constructed, its purpose is to produce a shadow free detailed image of the engraved surface.

The same approach has been adopted at a macroscopic scale over a target area of 100 $\times$ 100 mm. Early trials aimed to replicate the image dimensions of the scanning frame method. This required a high-quality macro attachment to a Samsung Galaxy phone camera, together with a dimmable ring light and a leg to ensure constant distance from the surface. While the resultant images were excellent, equal to those from the DSLR, alignment using free-form positioning proved far too difficult. This approach is currently being fitted to a robotic arm to match the scanning capabilities of the DSLR system. The more significant drawback is the time it takes to acquire a full set of images. Completing a whole scan in March cyclone conditions proved far too stressful and may be implemented with the robotic arm at another time.

The method being implemented is one where the surface is imaged at a broader scale through a magnifier app as used to re-register spectroscopy locations. The app is zoomed to set degree, providing images 50 $\times$ 24 mm. The app activates the camera light, this providing the same shadow free scene as the ring light.

A full scan takes seven minutes; however, a second run at 90° provided better photogrammetric resolution. The freehand nature of the imaging provides a more random orientation that aids in model production. The double run not only provides better imaging geometry but ensure there are no holes in the coverage. Of the twenty or more surfaces imaged in March 2024, none had holes in the final 3D model, a problem that has limited the progress of the scanning frame approach.

It is not necessary to focus stack as the camera is self-focusing. This has been described as a negative above but in this technique the camera is 200 mm above the surface.

Typically, sixty images are gathered and provide a very detailed perpendicular view of the surface. Where the model degrades in quality is on the sides of tall features where the perpendicular imaging has not been able to capture sufficient detail on the vertical walls of the feature. Give the purpose of this approach, to observe surface change, there is no change that is unique to the walls of a feature that would not manifest in the perpendicular view.

The aims of imaging at this scale are to observe macro alterations. These have already been observed under the spectroscopic re-registration imaging process. The spectroscopic survey gathers 540 pairs of macro images in each campaign. In at least twelve of these registration images substantial alterations have taken place. Apart from the obvious bird faeces deposition other features have been added or removed. Several of these are dark patina forms that were thought to be permanent. Such changes have substantial implications for spectroscopy but also add to the inventory of alteration, hence the expansion of this macro imaging.

H.3 Preliminary processing – focus stacking with Helicon Focus

With a successful run over 5,500 images are gathered from 275 locations, of which less than 35% are usable. The sets of twenty are processed through a focus stacking program, Helicon Focus (Helicon Soft Ltd., 2024)This program has proven better suited to the current project than several others commonly employed. It is possible to automate the 20-image sets and process them or select the in-focus images only. Processing is completed in less than five seconds with the final images being compiled from all the in-focus parts of the primary set.

The photogrammetry software Agisoft Metashape is used to process the images into a 3D form. It assumes that a camera is the imaging device, however by setting a nominal focal length for the focal stacked images, Metashape functions perfectly well.

a)

b)

Figure H.3-1: a) A focus stacked image from AQ11, b) compared to the most in-focus image from the primary set. Note how the left third of the primary image is now in focus on the stacked image. Image width 16 mm.

H.4 Photogrammetric model generation with Agisoft Metashape

In all acquisition systems discussed the final 3D model is developed with Agisoft Metashape (Agisoft LLC, 2024). This program comes in Professional and Standard versions with the latter sufficient for the current project. The Professional version allows for mensuration, among other tools, however this can equally be achieved by on-processing through additional software, required for the analysis of the model regardless of which Metashape version is used.

H.5 DSLR method

In the DSLR method a folder of (275) stacked images is processed whereas in the smartphone method the (60) primary images are used. 275 images is a very light workload for Metashape and hence the optimal settings can be used at all processing stages.

An example of the detail resolved using the DSLR method is provided in Figure *H.5-1*. This is not the complete model, a task that has yet to completely scan the entire surface due to environmental and equipment limitations. The result is still usable for further analysis.

Figures *H.5-1* to *H.5-3* illustrate the level of visual detail achievable using the scanning DSLR method. The final analysis is however conducted through various measuring systems including CloudCompare (CloudCompare Development Team, 2024) and conventional CAD software. CloudCompare can compare two versions of the same model at different epochs and reveal morphological changes in a heat map of difference. A comparison of the models will be presented over the course of this project. The heat map highlights areas of alteration that can then be relocated either in the model or in the primary images used to construct it.

CAD software can accept 3D models, albeit in less realistic appearance than the Metashape generated model. CAD provides a number of useful mensuration tools that can be used on a profile of the model. This is achieved by slicing the model through a given axis, much like a depth profile on a geological map. This profile can then be submitted to CAD where both linear and volume measurements can be applied. Cloud Compare also provide linear mensuration and both it and CAD are used to determine change.

H.6 Smartphone method

Cameras in smartphones have advanced to a point where they rival DSLR cameras for image gathering. Their main failing is the inherently excessive image manipulation they provide at default settings. These enhancements are almost exclusively tonal adjustments and thus do not compromise the resolution of the image in any way. If colour is not a factor, then the quality of the image comes down to sensor size and the number of pixels that gather the image. Smartphone sensors are smaller than DSLRs overall, however they make up for this in pixel density, with the cameras used in this project having up to 120 and 200 Mp capabilities in the Samsung phones and 48Mp in the Oppo. The Oppo produces an image using all pixels whereas the Samsung processes a cluster of nine pixels in the sensor into one pixel in the image.

The camera is triggered at prescribed intervals using an app, OP Auto Clicker, allowing the photographer to concentrate on camera position and coverage without having to operate the screen buttons. OP Auto Clicker has been chosen as it allows for multiple button presses at timed intervals.

a)

b)

c)

Figure H.5-1: A range of screen shots from the photogrammetric model.

Five button presses are used for the macro imaging; two to focus the screen and three to capture

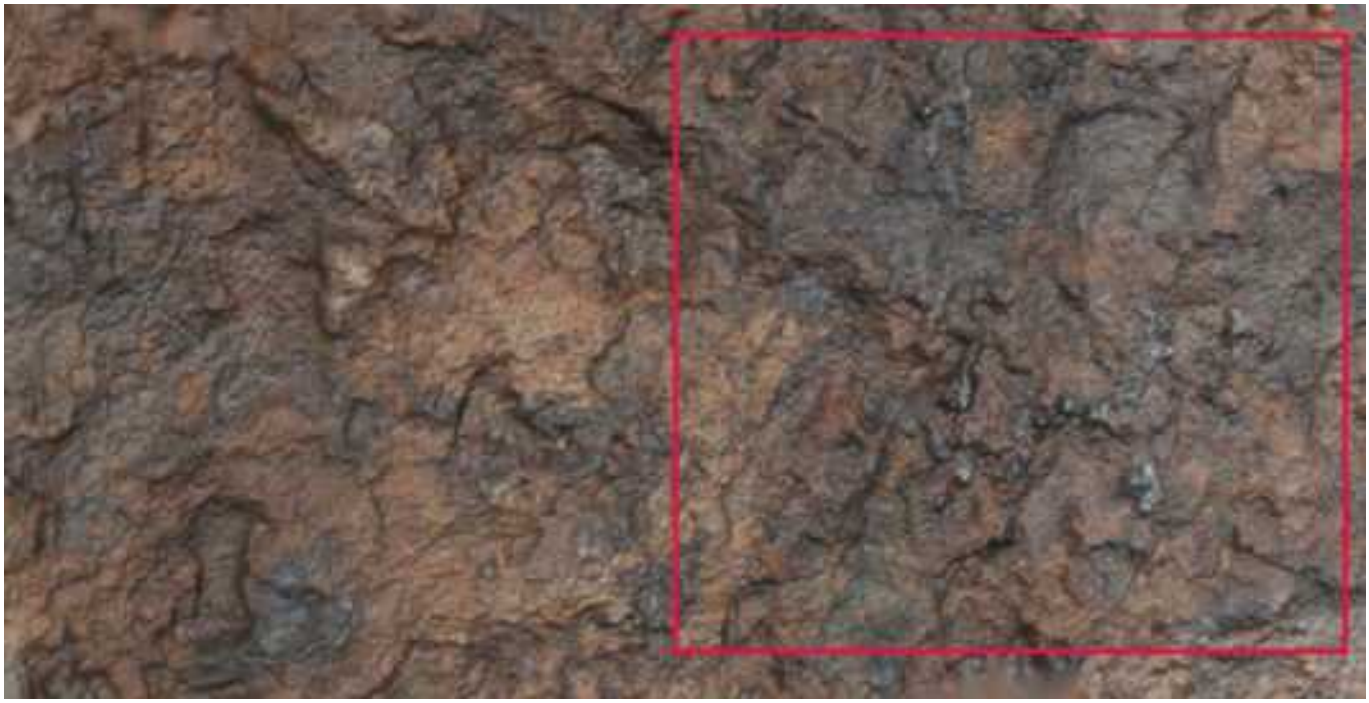

Figure H.5-2: Detail of the surface with a 4 × 4 mm reference grid.

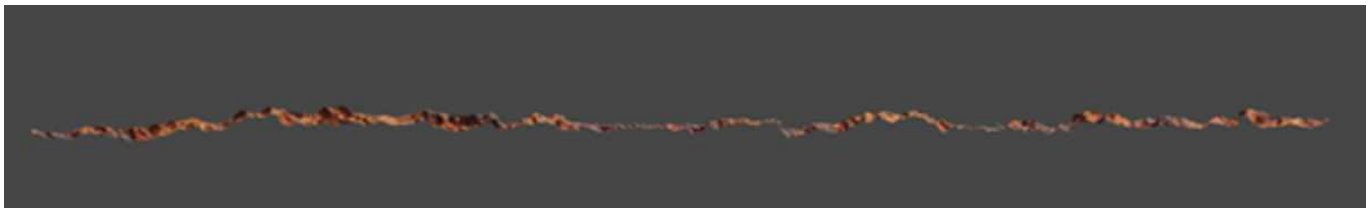

Figure H.5-3: This ribbon cross-section through the surface in Figure H.5-1. This view illustrates one way a detailed study of the surface profile can be made through appropriate mensuration software.

and store the image.

The smartphone imaging method does not attempt to provide the same level of detail as the DSLR method, despite being able to capture suitably sharp images of the same frame size. The main purpose of the smartphone approach is to provide a detailed view of one part of the engraved surface to act as a reference for observing visual alteration. The imaging configuration is the same as that used to re-image the surface during spectroscopy, in that case to confirm that the probe has been positioned precisely in the same location on each occasion. It has been noted that in at least 10 of the 540 spectroscopy reference images some form of alteration has occurred. This can be the sudden inclusion of bird faeces or its gradual dissipation over twelve months or more surprising alterations such as the increase or loss of patination features that had been considered permanent re-alignment reference features. The fact that some of the surfaces have undergone change at a very rapid rate, with substantial implications for the spectroscopic study, has prompted this more resolved approach to developing a reference area for ongoing study. Coupled with this is the need to ensure that any technique that provide evidence of change must do so across the

entire study suite to allow for statistically valid interpretation. Acknowledging this need does not however preclude the value of a single observation of a mechanism hitherto not documented.

A case in point is the potential for sulphurous pollutants to combine with oceanic sodium to form sodium sulphate, a highly mobile salt known for its mechanical destruction of stone. Sodium sulphate exists under normal atmospheric conditions in two forms – thenardite (H_2NaO_4S+) and mirabilite ($Na(SO_4).10\,H_2O$) with a 350% volume change between phases. These phase changes occur at 95% relative humidity but more pertinently at 32°C, ensuring that every time the temperature crosses the 32°C threshold the crystal expands or contracts by 350%. There is also a metastable $Na_2SO_4 \cdot 7\,H_2O$ with an equilibrium RH% of 82.9%, which may make a minor contribution to damage in the wet season at Murujuga.

Given the high potential for sodium sulphate formation to be increased with increased sulphur in the atmosphere it is reasonable to expect that spalling of the rock surface will increase. Apart from the manifestly visible large scale spalling present on many rocks, it is also possible that micro-spalling may increase. Observations of this type of spalling will not necessarily be apparent in normal viewing conditions or at the imaging scale employed by CSIRO in 2015.

This example of salt damage is not proven but illustrates the level of observation required to discern such impacts. These can be morphological and chromatic.

The smartphone imaging technique was introduced in March 2024 as part of the standard documentation of each of the 54 study surfaces, which also includes the rectified overall view of the surface using the same imaging techniques and photogrammetric processing. It is a quick method that takes 15 minutes to complete on-site and with a further 15 minutes of processing to achieve both the 3D model and consequent rectified 2D image. An example of the rectified image is presented in Figure *H.6-2*.

Figure *H.6-2* is a low-resolution representation of the image produced, which is most useful when studied in its 3D form. Nevertheless the 2D image provides a reasonable level of detail, as seen in Figure *H.6-3*.

Twenty-one study surfaces have been imaged with this technique in March 2024, and it is expected that all 54 will be completed by early to mid 2025. The imaging provides for observational change and by extending those observations from three sites to all 54 ensures a better understanding of morphological stability and a broader observational analysis of chromatic change in loss and gain to coloured features that lack form.

Chromatic change determined from digital images is possible but far less precise than the current spectroscopic techniques. It is noteworthy that one of the critiques of previous work relied on the use of hardcopy reproductions from which they determined colour values. This is not a satisfactory means of assessing colour as the lighting conditions under which the primary image was recorded has not been included in the image, in the form of a colour standard. Added to this is the unreliability of the printing process to render colours consistently. Thus, any use of printed images, images without colour reference, or images that have been duplicated cannot be used for scientific purposes. JPEG images are equally unreliable for colour comparison as the compression algorithm, relies entirely on reducing the full gamut of colour available to the imaging device to fewer colours that more or less accurately render the image true to colour at a substantially reduced file size. The implication for making colour judgements is that the compression will not always convert a pixel in

a)

b)

Figure H.6-1: An engraved rock showing gross spalling along the left side of the block. The engraved section on the right is also spalling but at a macro-scale that appears as lightening of the surface. It is this macro-spall area that is best studied with the macro-imaging technique. The area marked at right would make the ideal study area, having a deep groove that would reveal rounding and various surfaces including engraved channels.

TIFF or RAW format to the same JPG value every time.

The imaging presented here is not intended to be used for colour measurement. It is acquired under more or less uniform lighting conditions using the camera's light, but sunlight still contributes substantially. No colour scale has been used at this point as the resultant images have not been intended for colour analysis. A scale is included, and this could easily be substituted with a standard colour scale, assuming that future scales are printed with the same inks and remain true to colour over time. CIELAB colours can then be measured using the eyedropper tool in Photoshop, clicking in the colour swatch and reading the $L^*a^*b^*$ values from the screen.

This method is strengthened by taking readings in the standard colour card and defining a colour

a)

b)

Figure H.6-2: The rectified image of the reference area at AQ02.

as the difference between the target and each of the four reference colours. While this system can be applied to any photograph of reliable colour integrity it is time consuming and falls far short of the accuracy of a spectrometer.

For these reasons the field imaging has focused on restituted images and low-level 3D models that can provide a reasonably high degree of information about surface alterations at minimal expense in terms of field time.

Figure H.6-3: Detail of Figure H.6-2. Width of image 20 mm.

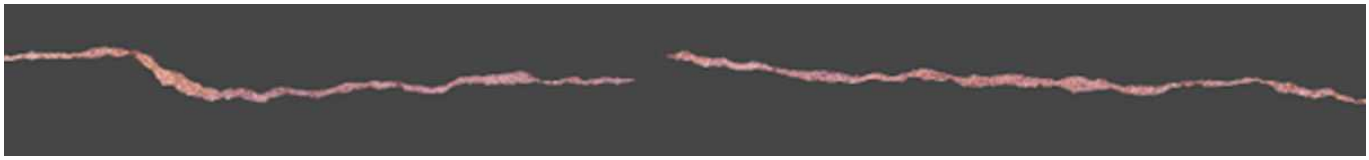

Figure H.6-4: Section view of the 3D model showing the well-developed contours achieved using the smartphone capturing 60 images in 15 minutes.

H.7 3D model analysis

The imaging techniques have not advanced in time to allow for any meaningful analysis. This will come in future reports.

Two forms of analysis are available to the 3D images. CloudCompare is a visualisation tool offering one very strong tool for analysis of 3D models. The technique requires the spatial alignment of

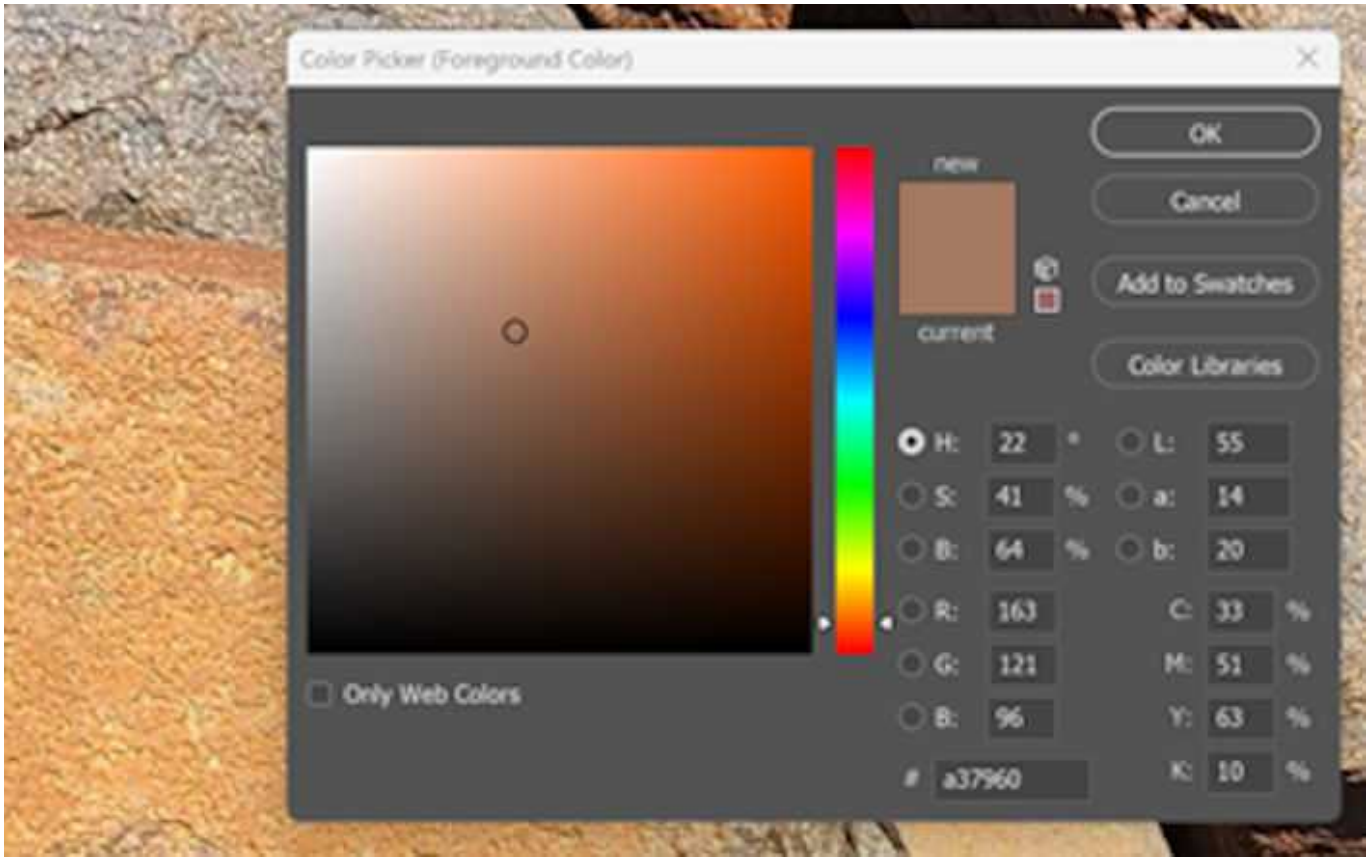

*Figure H.6-5: Screenshot of the Photoshop Color Picker tool with various measurement systems including L*a*b*.*

two models of the same subject, in this case any of the study surfaces using either the DSLR or smartphone imaging approaches. Several of the models developed from the March 2024 campaign will be compared in March 2025 to assess whether any morphological changes have developed.

H.8 Rectified images

All 54 study surfaces have been imaged since project commencement. More recently the need for more detailed images has emerged to allow for the long-term study of delamination and other gross surface alterations. One of the challenges of imaging the rocks is that most are in partial shadow for much of the day and attempting a perfectly perpendicular camera angle casts further shadows. With some surfaces extending to more than 3 metres and others curved such that the entire engraved surfaces cannot be captured in one image, the most appropriate imaging system is one of multiple images stitched together to form a single high-definition image.

Images have been captured using a Samsung smartphone at either 1X at 108Mp or 3X at 10Mpmagnification. The 1X is the obvious choice for sharpest detail regardless of the dimensions of the scene. OP Auto Clicker is also used as it allows the photographer to focus on the capture without looking at the screen, and more importantly, has a trigger aligned to the position of the camera button whether in portrait of landscape orientation. Capture time, for even the largest site, is under 5 minutes and processing time around 15 minutes to generate a 3D image. The

3D image development is necessary to produce a fully rectified image without requiring perfectly perpendicular camera angles. This is particularly beneficial where cast shadows are unavoidable, and the Metashape processing itself will remove shadows that do not occur in the same position in two images. There is thus an incentive for the photographer to stay on the move and capture the surface quickly.

The 3D model is saved in OBJ format and imported into CloudCompare where it can be oriented to any planar view and saved as a 2D image.

Two adjacent sites are presented here to illustrate the benefits of the 3D approach.

AQ09_GBR is a large, rounded block with engravings around the north-eastern surface, beyond the imaging range of a single photograph. Two images could be taken, however the 3D model exported to Cloud Compare allows for the composition of a perfectly perpendicular distortion-free view of any point on the surface without having to position the camera each time. This advantage can be applied to any site where a perfectly composed image of any part of the surface can be constructed at any time off-site. A side benefit of this approach, imaging for photogrammetric construction, is that the photographer is consciously imaging every part of the surface from every angle, resulting in a comprehensive catalogue of images. Instead of one or two images typically taken as routine documentation, this approach provides a folder of 60+ images covering all parts of the engraved surface and beyond.

Another strong feature of the 3D–2D pathway is that the background can be removed so that just the engraved block can be focused on. While this doesn't provide any greater detail it certainly makes the surface less busy.

The detail in Figure *H.8-2* is not exceptional, but it has been achieved from imaging that focused on the general rock form. Better close-up images can be achieved however the rock can be viewed in its entirety at this detail. The aim of these images has been to observe gross surface changes and the resolution certainly provides for that.

AQ09_GPH is a 4 $\times$ 3 metre inclined slab that cannot be imaged in its entirety at a suitably perpendicular angle. At most times of day the photographer's shadow dominates the scene. What is remarkable about Figure *H.8-3* is that it has been constructed from a series of photographs, almost all of which have compromising shadows. Figure *H.8-3* offers an almost shadow free view not physically attainable on site. The other benefit of the multi-image construction is that the resultant image is of a higher contrast than achievable with a single shot, such as that of Figure *H.8-4*.

H.9 Condition survey database

The project proposal included the observational study of up to 2,000 engravings, to give an overview of the general condition of the group. This was anticipated prior to the project starting and without knowing what logistical parameters would be available. With two dedicated MAC field officers assigned it is not possible to undertake general survey work beyond the commitments of spectrometry and other surface measurements at the 54 rocks under study.

To meet the objective and to allow for a broader understanding of conditions the survey has been confined to imaging with interpretation of conditions from the images. While face to face condition

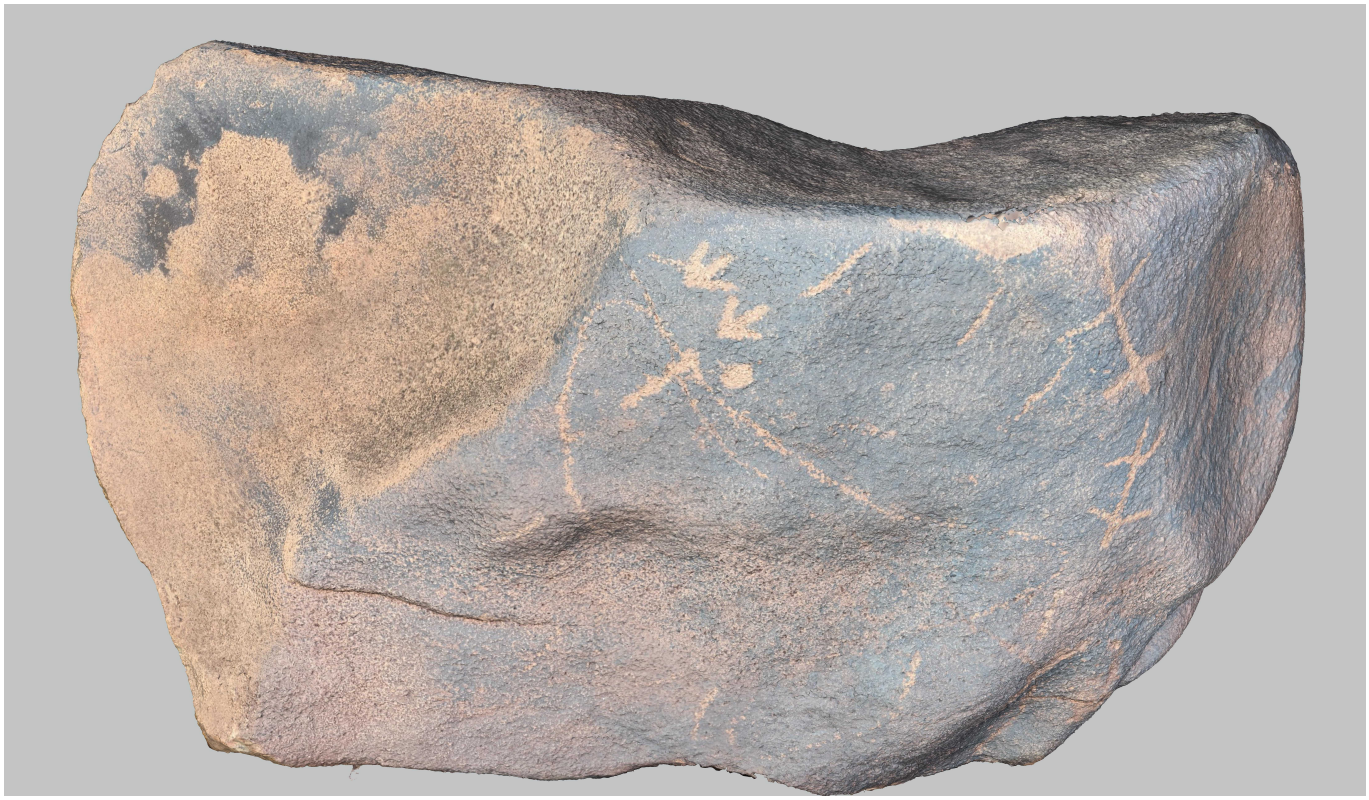

Figure H.8-1: AQ09: image oriented post-processing to provide the best view of the engravings. The background has been removed in Metashape.

Figure H.8-2: Detail of the image above zoomed up to just before pixelation. This is not an extraordinary level of detail but has been achieved through 60+ general shots of the rock.

Figure H.8-3: AQ09_GPH constructed from 60+ images and processed through Metashape and Cloud Compare to arrive at a shadow free perpendicular view. On close inspection some shadows do remain as slightly darker areas.

assessment provides far more vital information, there is enough in the images to build a reasonable picture of Murujuga. To date around 1,500 engravings have been imaged with geotagged location details, and a GIS mapping system partially developed to interpret conditions spatially and to show the representativeness of the rocks observed.

The imaging has been carried out without consideration for cultural meaning and it is expected that many of the images will need to be removed from the archive once the conditions have been catalogued. This issue has already been discussed with the appropriate MAC officer who will receive the completed archive and advise on what may remain. There is no need to keep any of

Figure H.8-4: A single shot view of AQ09_GPH shows strong shadows and very low contrast in the engraving.

the images as it is only the nature of the deterioration that is of interest.

Descriptors of rock surface condition that will emerge from the study will only be fully understood when the survey is almost completed, however they will include:

- Extent of delamination
- Granular erosion in terms of engraving faintness
- Extent and distribution of bird excreta

- Biological growth
- Vandalism.

Subsequent analysis will investigate spatial variation in rock condition using these descriptors.

I Transition to a second spectrometer

The project commenced using a JAZ spectrometer manufactured by Ocean Insight. This instrument has provided very reliable service in a range of cultural environments including hot deserts, high mountains and sub-temperate rainforests. The conditions at Murujuga have led to sub-optimal results in the form of unreliable returns. The spectrometer has run well until it suddenly returns corrupted readings for a period before regaining normal working order. The failures are sporadic but have a pattern. Ten spectra are recorded for each of the 10 targets at each study surface. The spectra will be viable for all 10 spectra at one target and then corrupted for all 10 spectra at the next.

Due to severe overheating in the first campaign, in March 2022, it was found that keeping the instrument running with only one calibration at the first target kept the instrument cooler than shutting down and recalibrating at each target. The JAZ has a thermal shutoff, so any overheating shut the instrument down rather than gathering data out of range. As the cooling system was optimised and the instrument could be operated with minimal overheating, recalibration was performed after each target. The benefit of regular recalibration is that it is to the temperature for the individual target rather than for the entire acquisition of all 10 targets.

One hundred spectra are gathered at each site and three sites or more may be recorded in a day. Running so many spectra at high temperatures may contribute to the erratic nature of viable spectra although this could not be replicated to confirm it as the cause.

In October 2023 software was developed by the statistical team that allowed for on site verification of the spectra. Any failed spectra could be repeated before departing the site and this led to higher yields. By March 2023 the JAZ spectrometer was able to provide a high percentage of viable spectra but only through the verification system and not through more reliable operation of the instrument itself.

The JAZ is a unique instrument in that it has been built to high performance criteria in a miniaturised set of modules including the processor, control panel, battery, and light source. These two latter components both generate heat as does opening the cooling case to operate the instrument. To further resolve the overheating problem a second spectrometer has been introduced, having stand-alone components and operated from a computer. By removing the battery light source and operating system form the cooling compartment, the spectrometer can be maintained at a consistent low temperature. The new spectrometer is an HDX by Ocean Insight, having essentially the same components but packed into individual housings. The Xenon light source also differs slightly; whereas the JAZ xenon produces energy in the range 180–1100 nm, the HDX is capped at 220–750 nm. There are logical reasons to do this, presumably by a low band pass filter that excludes all light above 750 nm as this is generally the upper limit for human visual perception. The limitations are that some characterising spectral features occur higher than 750 nm, but none

below 220 nm. Other than this one small difference the instruments are identical in their optical capabilities including resolution.

The HDX has also been programmed to run 100 spectra per target and appears to be able to complete 1,000 spectra per site without issue. The issue is that connections between the spectrometer, light source and computer were all very unreliable in the March 2024 campaign. This was not only while on site as the connections could not be reliably held in the air-conditioned accommodation for several days at a time. When it did run during early morning verifications it would run for two sites very well, then fail to connect for the third site. As for the JAZ there appears to be an element of fatigue in attempting to gather a day's worth of spectra. It has been noted however that the JAZ does not deteriorate with spectra run. On occasions it is the first site that is less reliable than any other. With the HDX failure begins later into the day. The instrument has been sent back to the supplier to fault check the connections but remains uncertain. In the March 2024 campaign around 75% of spectra were gathered on the JAZ and the balance on the HDX. As the HDX is to remain with MAC at the conclusion of the current project it is important to have it running reliably as soon as possible.

This page is intentionally blank.

References

Ageta, H., Iwata, K., and Natori, S. (1964). Fern constituents: Adianene, filicene, 7-fernene, isofernene and diploptene. Triterpenoid hydrocarbons isolated from adiantum monochlamys. *Tetrahedron Lett.*, 5:3413–3418.

Agisoft LLC (2024). Agisoft metashape. Photogrammetry software for 3D spatial data generation, including GIS, cultural heritage documentation, and visual effects. https://www.agisoft.com/.

Aho, K. and Weaver, T. (2006). Measuring water relations and pH of cryptogram rock-surface environments. *The Bryologist*, 109(3):348–357.

Albuquerque, L., Johnson, M. M., Schumann, P., Rainey, F. A., and da Costa, M. S. (2014). Description of two new thermophilic species of the genus Rubrobacter, Rubrobacter calidifluminis sp. nov. and Rubrobacter naiadicus sp. nov., and emended description of the genus Rubrobacter and the species Rubrobacter bracarensis. *Systematic and Applied Microbiology*, 37:235–243.

Antonelli, F., Esposito, A., Calvo, L., Licursi, V., Tisseyre, P., Ricci, S., Romagnoli, M., Piazza, S., and Guerrieri, F. (2020). Characterization of black patina from the Tiber River embankments using Next-Generation Sequencing. *PLoS One*, 15.

Aphalo, P. J. (2024). *rOmniDriver: Omni Driver R wrapper*. R package version 0.1.20.

Armstrong, G., Rahman, G., Martino, C., McDonald, D., Gonzalez, A., Mishne, G., and Knight, R. (2022). Applications and comparison of dimensionality reduction methods for microbiome data. *Front Bioinform*, 2:821–861.

Atahan, P., Grice, K., and Dodson, J. (2007). Agriculture and environmental change at Qingpu, Yangtze delta region, China: a biomarker, stable isotope and palynological approach. *The Holocene*, 17(4):507–515.

Aulinas, M., Garcia-Valles, M., Fernandez-Turiel, J. L., Gimeno, D., Saavedra, J., and Gisbert, G. (2014). Insights into the formation of rock varnish in prevailing dusty regions. *Earth Surface Processes and Landforms*, 40(4):447–458.

Baddeley, A., Davies, T., Rakshit, S., Nair, G., and McSwiggan, G. (2022). Diffusion smoothing for spatial point patterns. *Statistical Science*, 37(1):123–142.

Baddeley, A. and Jensen, E. V. (2005). *Stereology for Statisticians*. Chapman and Hall/CRC, Boca Raton.

Baddeley, A., Rubak, E., and Turner, R. (2015). *Spatial Point Patterns: Methodology and Applications with R*. Chapman and Hall/CRC, London.

Baddeley, A. and Turner, R. (2005). Spatstat: an R package for analyzing spatial point patterns. *Journal of Statistical Software*, 12(6):1–42. URL: www.jstatsoft.org, ISSN: 1548-7660.

Barnard, G. (1963). Contribution to discussion of “The spectral analysis of point processes” by M.S. Bartlett. *Journal of the Royal Statistical Society, Series B*, 25:294.

Barry, R. and McIntyre, J. (2011). Estimating animal densities and home range in regions with irregular boundaries and holes: a lattice-based alternative to the kernel density estimator. *Ecological Modelling*, 222:1666–1672.

Bednarik, R. (2012). The use of weathering indices in rock art science and archaeology. *Rock Art Research*, 29:59–84.

Bednarik, R. G. (2007). The science of Dampier rock art–Part 1. *Rock Art Research*, 24(2):209–246.

Berner, R. A., Sjöberg, E. L., Velbel, M. A., and Krom, M. D. (1980). Dissolution of pyroxenes and amphiboles during weathering. *Science*, 207(4436):1205–6.

Best, D. J. and Roberts, D. E. (1975). Algorithm AS 89: The upper tail probabilities of Spearman's Rho. *Journal of the Royal Statistical Society. Series C (Applied Statistics)*, 24(3):377–379.

Black, J. L., Box, I., and Diffey, S. (2017a). Inadequacies of research used to monitor change to rock art and regulate industry on Murujuga (Burrup Peninsula), Australia. *Rock Art Research*, 34(2):130–148.

Black, J. L., MacLeod, I. D., and Smith, B. W. (2017b). Theoretical effects of industrial emissions on colour change at rock art sites on Burrup Peninsula, Western Australia. *Journal of Archaeological Science: Reports*, 12:457–462.

Brooks, M. E., Kristensen, K., van Benthem, K. J., Magnusson, A., Berg, C. W., Nielsen, A., Skaug, H. J., Mächler, M., and Bolker, B. M. (2017). glmmTMB balances speed and flexibility among packages for zero-inflated generalized linear mixed modeling. *The R Journal*, 9(2):378–400.

Buckman, S., Morris, R. H., and Bourman, R. P. (2021). Fire-induced rock spalling as a mechanism of weathering responsible for flared slope and inselberg development. *Nature Communications*, 12(1):2150.

Bush, R. T. and McInerney, F. A. (2013). Leaf wax n-alkane distributions in and across modern plants: Implications for paleoecology and chemotaxonomy. *Geochimica et Cosmochimica Acta*, 117:161–179.

Callahan, B. J., McMurdie, P. J., Rosen, M. J., Han, A. W., Johnson, A. J. A., and Holmes, S. P. (2016). DADA2: High-resolution sample inference from illumina amplicon data. *Nature Methods*, 13:581–583.

Cameron, E. S., Schmidt, P. J., Tremblay, B. J., Emelko, M. B., and Müller, K. M. (2021). Enhancing diversity analysis by repeatedly rarefying next generation sequencing data describing microbial communities. *Scientific Reports*, 11(1):22302.

Chaddha, A. S., Sharma, A., Singh, N. K., Shamsad, A., and Banerjee, M. (2024). Biotic-abiotic mingle in rock varnish formation: A new perspective. *Chemical Geology*, 648.

Chang, W., Cheng, J., Allaire, J., Sievert, C., Schloerke, B., Xie, Y., Allen, J., McPherson, J., Dipert, A., and Borges, B. (2024). *shiny: Web Application Framework for R*. R package version 1.9.1.9000.

Chardon, E. S., Livens, F. R., and Vaughan, D. J. (2006). Reactions of feldspar surfaces with aqueous solutions. *Earth-Science Reviews*, 78(1-2):1–26.

Chen, R.-W., Li, C., He, Y.-Q., Cui, L.-Q., Long, L.-J., and Tian, X.-P. (2020). Rubrobacter tropicus sp. nov. and Rubrobacter marinus sp. nov., isolated from deep-sea sediment of the South China Sea. *International Journal of Systematic and Evolutionary Microbiology*, 70:5576–5585.

Chu, V. H. and Goldberg, M. B. (1974). Buoyant forced-plumes in cross-flow. *Journal of the Hydraulic Division ASCE*, 100:10805–10808.

Cleveland, W. (1979). Robust locally weighted regression and smoothing scatterplots. *Journal of the American Statistical Association*, 74:829–836.

CloudCompare Development Team (2024). Cloudcompare: 3d point cloud and mesh processing software. https://www.cloudcompare.org/. Version 2.13.2, Open Source under GNU General Public License (GPL). https://www.cloudcompare.org/.

Coplen, T. B., Brand, W. A., Gehre, M., Gröning, M., Meijer, H. A. J., Toman, B., and Verkouteren, R. M. (2006). New guidelines for $\delta^{13}C$ measurements. *Analytical Chemistry*, 78:2439–2441.

Corbin, J. C., Mensah, A. A., Pieber, S. M., Orasche, J., Michalke, B., Zanatta, M., Czech, H., Massabo, D., Buatier de Mongeot, F., Mennucci, C., El Haddad, I., Kumar, N. K., Stengel, B., Huang, Y., Zimmermann, R., Prevot, A. S. H., and Gysel, M. (2018). Trace metals in soot and PM(2.5) from heavy-fuel-oil combustion in a marine engine. *Environmental Science and Technology*, 52(11):6714–6722.

Corder, G. W. and Foreman, D. I. (2014). *Nonparametric statistics: a step-by-step approach*. Wiley, Hoboken, New Jersey, 2 edition.

Cox, D. and Snell, E. (1981). *Applied Statistics: Principles and Examples*. Chapman and Hall.

Cressie, N., Buxton, B. E., Calder, C. A., Craigmile, P. F., Dong, C., McMillan, N. J., Morara, M., Santner, T. J., Wang, K., Young, G., and Zhang, J. (2007). From sources to biomarkers: A Bayesian approach to human exposure modeling. *Journal of Statistical Planning and Inference*, 137:3361–3379.

Cribari-Neto, F. and Zeileis, A. (2010). Beta regression in R. *Journal of Statistical Software*, 34(2):1–24.

Currie, L. A., editor (1988). *Detection in Analytical Chemistry: Importance, Theory, and Practice*. American Chemical Societyr, Washington, DC.

Curtin University (2022). *Murujuga Rock Art Monitoring Program: Monitoring Studies Data Collection and Analysis Plan*. Technical report. Report prepared by Curtin University for the Murujuga Aboriginal Corporation and Department of Water and Environmental Regulation, Government of Western Australia (COPP21065-PLN-G-102_0). Government of Western Australia. https://www.wa.gov.au/government/publications/murujuga-rock-art-monitoring-program-monitoring-studies-data-collection-and-analysis-plan.

Curtin University (2023). *Murujuga Rock Art Monitoring Program: Monitoring Studies Report 2023*. Technical report. Report prepared by Curtin University for the Murujuga Aboriginal Corporation and Department of Water and Environmental Regulation, Government of Western Australia (COPP-21065-REP-G-101). Government of Western Australia. https://www.wa.gov.au/government/publications/murujuga-rock-art-monitoring-program-monitoring-studies-report-2023.

Curtin University (2025). Murujuga Rock Art Monitoring Program: Interim Environmental Quality Criteria. Technical Report COPP21065-REP-G-107. Report prepared by Curtin University for the Murujuga Aboriginal Corporation and the Department of Water and Environmental Regulation, Government of Western Australia.

Daly, M. J., Gaidamakova, E. K., Matrosova, V. Y., Vasilenko, A., Zhai, M., Venkateswaran, A., Hess, M., Omelchenko, M. V., Kostandarithes, H. M., Makarova, K. S., Wackett, L. P., Fredrickson, J. K., and Ghosal, D. (2004). Accumulation of Mn(II) in Deinococcus radiodurans facilitates gamma-radiation resistance. *Science*, 306:1025–1028.

Dawson, D., Grice, K., Alexander, R., and Edwards, D. (2007). The effect of source and maturity on the stable isotopic compositions of individual hydrocarbons in sediments and crude oils from the Vulcan Sub-basin, Timor Sea, Northern Australia. *Organic Geochemistry*, 38:1015–1038.

DeHoff, R. and Rhines, F., editors (1968). *Quantitative Microscopy*. McGraw-Hill, New York.

Delesse, A. (1847). Procédé mécanique pour déterminer la composition des roches. *Comptes Rendues de l'Académie des Sciences (Paris)*, 25:544–545.

Department of Water and Environmental Regulation (DWER) (2019). *Murujuga Rock Art Strategy: A monitoring, analysis and decision-making framework to protect Aboriginal rock art located on Murujuga (the Dampier Archipelago and Burrup Peninsula)*. Government of Western Australia. https://www.wa.gov.au/government/publications/murujuga-rock-art-strategy.

Department of Water and Environmental Regulation (DWER) (2021). *Murujuga Rock Art Monitoring Program: Conceptual Model* [Fact sheet]. Government of Western Australia. https://www.wa.gov.au/government/publications/murujuga-rock-art-monitoring-conceptual-model.

Department of Water and Environmental Regulation (DWER) (2024). *Air Quality Index — Western Australia*. https://www.der.wa.gov.au/your-environment/air/air-quality-index.

Dixon, P. (2003). VEGAN, a package of R functions for community ecology. *Journal of Vegetation Science*, 14:927–930.

Donaldson, M. (2011). Understanding the rocks: Rock art and the geology of Murujuga (Burrup 'Peninsula'). *Rock Art Research*, 28(1):1–9.

Dorn, R. (2007). *Rock Varnish*, pages 246–297. Wiley.

Dorn, R. and Krinsley, D. (2019). Nanoscale observations support the importance of chemical processes in rock decay and rock coating development in cold climates. *Geosciences*, 9(3).

Dorn, R. I. (1994). *Rock Varnish as Evidence of Climatic Change*, pages 539–552. Springer Netherlands, Dordrecht.

Dorn, R. I. (2013). Rock coatings. In Pope, G. A., editor, *Treatise on Geomorphology*, volume 4, chapter 4.5, pages 70–97. Academic Press.

Dorn, R. I. (2020). *Anthropogenic Interactions with Rock Varnish*, chapter 13, pages 267–283. American Geophysical Union (AGU).

Dorn, R. I. (2024). Rock varnish revisited. *Progress in Physical Geography: Earth and Environment*.

Dorn, R. I., Krinsley, D. H., Langworthy, K. A., Ditto, J., and Thompson, T. J. (2013). The influence of mineral detritus on rock varnish formation. *Aeolian Research*, 10:61–76.

Dorn, R. I., Mahaney, W. C., and Krinsley, D. H. (2017). Case hardening: Turning weathering rinds into protective shells. *Elements*, 13(3):165–169.

Dwass, M. (1957). Modified randomization tests for nonparametric hypotheses. *Annals of Mathematical Statistics*, 28:181–187.

Elias, H. and Hyde, D. (1983). *A guide to practical stereology*. Number 1 in Karger Continuing Education Series. Karger, Basel.

Environmental Protection Agency (2019). *Control Techniques for Nitrogen Oxides Emissions from Stationary Sources, Revised, 2nd Edition*.

Environmental Protection Authority (2016). *Technical Guidance: Protecting the Quality of Western Australia's Marine Environment.* Technical report, Environmental Protection Authority. https://www.epa.wa.gov.au/sites/default/files/Policies_and_Guidance/TechnicalGuidance_ProtectingTheQualityOfWAMarineEnvironment-131216_0.pdf.

Environmental Protection Authority (2017). *Environmental quality criteria reference document for Cockburn Sound*. Technical report, Environmental Protection Authority. https://www.epa.wa.gov.au/sites/default/files/Policies_and_Guidance/EQCRefDocforCockburnSoundFeb2017-2.pdf.

Etienne, S. (2002). The role of biological weathering in periglacial areas: a study of weathering rinds in south Iceland. *Geomorphology*, 47(1):75–86.

Ewels, P., Magnusson, M., Lundin, S., and Kaller, M. (2016). MultiQC: summarize analysis results for multiple tools and samples in a single report. *Bioinformatics 2016*, 32:3047–3048.

Fan, L. N. (1967). *Turbulent buoyant jets into stratified or flowing ambient fluids*. Technical Report KH-R-15, California Institute of Technology, Pasadena.

Feranchuk, S., Belkova, N., Potapova, U., Kuzmin, D., and Belikov, S. (2018). Evaluating the use of diversity indices to distinguish between microbial communities with different traits. *Research in Microbiology*, 169:254–261.

Finkelstein, M. M. and Verma, D. K. (2001). Exposure estimation in the presence of nondetectable values: Another look. *American Industrial Hygiene Association Journal*, 62:195–198.

Ganser, G. H. and Hewett, P. (2010). An accurate substitution method for analyzing censored data. *Journal of Occupational and Environmental Hygiene*, 7(4):233–244. PMID: 20169489.

Garvie, L. A. J., Burt, D. M., and Buseck, P. R. (2008). Nanometer-scale complexity, growth, and diagenesis in desert varnish. *Geology*, 36(3).

Goldich, S. S. (1938). A study in rock-weathering. *The Journal of Geology*, 46(1):17–58.

Goldsmith, Y., Stein, M., and Enzel, Y. (2014). From dust to varnish: Geochemical constraints on rock varnish formation in the Negev Desert, Israel. *Geochimica et Cosmochimica Acta*, 126:97–111.

Gorbushina, A. (2007). Life on rocks. *Environmental Microbiology*, 9:1613–1631.

Gordon, S. J. and Dorn, R. I. (2005). In situ weathering rind erosion. *Geomorphology*, 67(1-2):97–113.

Górecki, T. and Smaga, Ł. (2019). fdANOVA: an R software package for analysis of variance for univariate and multivariate functional data. *Computational Statistics*, 34(2):571–597.

Greenshields, C. (2022). *OpenFOAM v10 User Guide*. The OpenFOAM Foundation, London, UK.

Grice, K. and Brocks, J. J. (2011). Biomarkers (organic, compound-specific isotopes). In Reitner, J. and Thiel, V., editors, *Encyclopedia of Geobiology*, pages 167–182. Springer, Dordrecht, The Netherlands.

Grice, K. and Eiserbeck (2014). The analysis and application of biomarkers. In *Treatise on Geochemistry (second edition) Volume 12: Organic Geochemistry*, pages 47–78. Elsevier.

Grice, K., Lu, H., Atahan, P., Asif, M., Hallmann, C., Greenwood, P., Maslen, E., Tulipani, S., Williford, K., and Dodson, J. (2009). New insights into the origin of perylene in geological samples. *Geochimica et Cosmochimica Acta*, 73(21):6531–6543.

Grün, B., Kosmidis, I., and Zeileis, A. (2012). Extended beta regression in R: Shaken, stirred, mixed, and partitioned. *Journal of Statistical Software*, 48(11):1–25.

Gudbrandsson, S., Wolff-Boenisch, D., Gislason, S. R., and Oelkers, E. H. (2014). Experimental determination of plagioclase dissolution rates as a function of its composition and pH at 22°C. *Geochimica et Cosmochimica Acta*, 139:154–172.

Hamersley News (1969). Power ship arrives at Dampier. *Hamersley News*, 23 May 1969, p.1. Available online at: http://nla.gov.au/nla.news-article214791794. Last accessed 8/05/2024.

Hamersley News (1970). Dampier's new power station. *Hamersley News*, 1 October 1970, p.1. Available online at: http://nla.gov.au/nla.news-article214542029. Last accessed 8/05/2024.

Hamersley News (1971). Power ship goes to wreckers. *Hamersley News*, 1 January 1971, p.5. Available online at: http://nla.gov.au/nla.news-article214910973. Last accessed 8/05/2024.

Hamersley News (1972). The development of a power supply for Hamersley operations. *Hamersley News*, 21 December 1972, p.2. Available online at: http://nla.gov.au/nla.news-article214542371. Last accessed 8/05/2024.

Hamersley News (1973). Unusual power loss. *Hamersley News*, 29 March 1973, p.5. Available online at: http://nla.gov.au/nla.news-article214999340. Last accessed 8/05/2024.

Hamersley News (1975). Power - it's taken for granted. *Hamersley News*, 9 January 1972, p.2. Available online at: http://nla.gov.au/nla.news-article214549804. Last accessed 8/05/2024.

Hamersley News (1978). S.E.C. turbine to be installed at Dampier. *Hamersley News*, 26 January 1972, p.1. Available online at: http://nla.gov.au/nla.news-article214557687. Last accessed 8/05/2024.

Hamersley News (1979). News briefs. *Hamersley News*, 26 April 1972, p.8. Available online at: http://nla.gov.au/nla.news-article214548623. Last accessed 8/05/2024.

Hamersley News (1984). 'B' station an empty shell — but veterans still remember. *Hamersley News*, 1 June 1984, p.9. Available online at: http://nla.gov.au/nla.news-article234909501. Last accessed 8/05/2024.

Hamersley News (1985a). Gas gets rocky road to Dampier. *Hamersley News*, 1 December 1985, p.9. Available online at: http://nla.gov.au/nla.news-article234909828. Last accessed 8/05/2024.

Hamersley News (1985b). Pre-planning makes gas firing simple. *Hamersley News*, 1 December 1985, p.8. Available online at: http://nla.gov.au/nla.news-article234909832. Last accessed 8/05/2024.

Harrell Jr, F. E. (2023). *Hmisc: Harrell Miscellaneous*. R package version 5.1-1.

Helicon Soft Ltd. (2024). Helicon focus. Focus stacking software for extending depth of field in photographs, suitable for macro and other photography types. https://www.heliconsoft.com/heliconsoft-products/helicon-focus/.

Hezbri, K., Ghodhbane-Gtari, F., Montero-Calasanz, M. d. C., Nouioui, I., Rohde, M., Spröer, C., Schumann, P., Klenk, H.-P., and Gtari, M. (2016). *Geodermatophilus pulveris* sp. nov., a gamma-radiation-resistant actinobacterium isolated from the Sahara desert. *International Journal of Systematic and Evolutionary Microbiology*, 66:3828–3834.

Hezbri, K., Ghodhbane-Gtari, F., Montero-Calasanz, M. d. C., Sghaier, H., Rohde, M., Schumann, P., Klenk, H.-P., and Gtari, M. (2015). Geodermatophilus sabuli sp. nov., a γ-radiation-resistant actinobacterium isolated from desert limestone. *International Journal of Systematic and Evolutionary Microbiology*, 65:3365–3372.

Hezbri, K., Nouioui, I., Rohde, M., Spröer, C., Schumann, P., Gtari, M., Klenk, H.-P., Montero-Calasanz, M. d. C., and Ghodhbane-Gtari, F. (2018). Blastococcus xanthinilyticus sp. nov., isolated from monument. *International Journal of Systematic and Evolutionary Microbiology*, 68:1177–1183.

Ho, N. T., Li, F., Wang, S., and Kuhn, L. (2019). metamicrobiomeR: an R package for analysis of microbiome relative abundance data using zero-inflated beta GAMLSS and meta-analysis across studies using random effects models. *BMC Bioinformatics*, 20(1):188.

Holman, A. I., Grice, K., Jaraula, C. M. B., and Schimmelmann, A. (2014). Bitumen II from the Paleoproterozoic Here's Your Chance Pb/Zn/Ag deposit: Implications for the analysis of depositional environment and thermal maturity of hydrothermally-altered sediments. *Geochimica et Cosmochimica Acta*, 139(0):98–109.

Hong, J., Karaoz, U., de Valpine, P., and Fithian, W. (2022). To rarefy or not to rarefy: robustness and efficiency trade-offs of rarefying microbiome data. *Bioinformatics*, 38(9):2389–2396.

Hoover, R. B., Perry, R. S., Levin, G. V., Kolb, V. M., Lynne, B. Y., Rozanov, A. Y., Gladstone, G. R., Sephton, M. A., McLoughlin, N., Engel, M. H., Olendzenski, L., Brasier, M., and StaleyJr, J. T. (2005). How desert varnish forms? *Proceedings of SPIE - The International Society for Optical Engineering*, 5906:276–287.

Hope, A. (1968). A simplified Monte Carlo significance test procedure. *Journal of the Royal Statistical Society, Series B*, 30:582–598.

Hornung, R. and Reed, L. (1990). Estimation of average concentration in the presence of nondetectable values. *Applied Occupational and Environmental Hygiene*, 5(1):46–51.

Hoshino, Y. and George, S. (2015). Cyanobacterial inhabitation on Archean rock surfaces in the Pilbara Craton, Western Australia. *Astrobiology*, 15:559–574.

Hyndman, R. and Fan, Y. (1996). Sample quantiles in statistical packages. *The American Statistician*, 50(4):361–365.

Israeli, Y. and Emmanuel, S. (2018). Impact of grain size and rock composition on simulated rock weathering. *Earth Surface Dynamics*, 6(2):319–327.

IVL Swedish Environmental Research Institute (2024). https://www.ivl.se/.

Kaiser, J., Wasmund, N., Kahru, M., Wittenborn, A. K., Hansen, R., Häusler, K., Moros, M., Schulz-Bull, D., and Arz, H. W. (2020). Reconstructing N2-fixing cyanobacterial blooms in the Baltic Sea beyond observations using 6- and 7-methylheptadecane in sediments as specific biomarkers. *Biogeosciences*, 17:2579–2591.

Kammoun, I., Hezbri, K., Sbissi, I., del Carmen Montero-Calasanz, M., Klenk, H.-P., Gtari, M., and Ghodhbane-Gtari, F. (2023). Blastococcus carthaginiensis sp. nov., isolated from a monument sampled in Carthage, Tunisia. *International Journal of Systematic and Evolutionary Microbiology*, 73.

Kant, M. A., Rossi, E., Madonna, C., Höser, D., and Rudolf von Rohr, P. (2017). A theory on thermal spalling of rocks with a focus on thermal spallation drilling. *Journal of Geophysical Research: Solid Earth*, 122(3):1805–1815.

Koehn, D., Kelka, U., Toussaint, R., Siegel, C., Mullen, G., Boyce, A., and Piazolo, S. (2022). Outcrop scale mixing enhanced by permeability variations: the role of stationary and travelling waves of high saturation indices. *Geological Magazine*, 159(11-12):2279–2292.

Kolde, R. (2019). *pheatmap: Pretty Heatmaps*. R package version 1.0.12.

Krinsley, D. (1998). Models of rock varnish formation constrained by high resolution transmission electron microscopy. *Sedimentology*, 45(4):711–725.

Krinsley, D. H., DiGregorio, B., Dorn, R. I., Razink, J., and Fisher, R. (2017). Mn-Fe-enhancing budding bacteria in century-old rock varnish, Erie Barge Canal, New York. *The Journal of Geology*, 125(3):317–336.

Krissansen-Totton, J., Olson, S., and Catling, D. C. (2018). Disequilibrium biosignatures over Earth history and implications for detecting exoplanet life. *Science Advances*, 4(1).

Krklec, K., Domínguez-Villar, D., Carrasco, R. M., and Pedraza, J. (2016). Current denudation rates in dolostone karst from central Spain: Implications for the formation of unroofed caves. *Geomorphology*, 264:1–11.

Kurzydłowski, K. and Ralph, B. (1995). *The quantitative description of the microstructure of materials*. CRC Press, Boca Raton, FL.

Lambert, D., Peterson, B., and Terpenning, I. (1991). Nondetects, detection limits, and the probability of detection. *Journal of the American Statistical Association*, 86:266–277.

Landwehr, K. R., Hillas, J., Mead-Hunter, R., Brooks, P., King, A., O'Leary, R. A., Kicic, A., Mullins, B. J., and Larcombe, A. N. (2021). In vitro primary human airway epithelial whole exhaust exposure. *MethodsX*, 8:101561.

Lanza, N. L., Clegg, S. M., Wiens, R. C., McInroy, R. E., Newsom, H. E., and Deans, M. D. (2012). Examining natural rock varnish and weathering rinds with laser-induced breakdown spectroscopy for application to ChemCam on Mars. *Applied Optics*, 51(7):B74–82.

Legendre, P. and Gallagher, E. D. (2001). Ecologically meaningful transformations for ordination of species data. *Oecologia*, 129:271–280.

Legendre, P. and Legendre, L. (2012). *Numerical Ecology*. Elsevier, 3rd edition.

Lingappa, U. F., Yeager, C. M., Sharma, A., Lanza, N. L., Morales, D. P., Xie, G., Atencio, A. D., Chadwick, G. L., Monteverde, D. R., Magyar, J. S., Webb, S. M., Valentine, J. S., Hoffman, B. M., and Fischer, W. W. (2021). An ecophysiological explanation for manganese enrichment in rock varnish. *Proc Natl Acad Sci U S A*, 118.

Liu, B., Fu, R., Wu, B., Liu, X., and Xiang, M. (2022). Rock-inhabiting fungi: terminology, diversity, evolution and adaptation mechanisms. *Mycology*, 13:1–31.

Ljaljević-Grbić, M., Vukojević, J., Subakov-Simić, G., Krizmanić, J., and Stupar, M. (2010). Biofilm forming cyanobacteria, algae and fungi on two historic monuments in Belgrade, Serbia. *Archives of Biological Sciences*, 62:625–631.

Louati, M., Hezbri, K., Montero-Calasanz, M. d. C., Rohde, M., Göker, M., Ghodhbane-Gtari, F., Klenk, H.-P., Nouioui, I., and Gtari, M. (2022). Blastococcus tunisiensis sp. nov., isolated from limestone collected in Tunisia. *International Journal of Systematic and Evolutionary Microbiology*, 72.

Macholdt, D. S., Jochum, K. P., Pöhlker, C., Arangio, A., Förster, J. D., Stoll, B., Weis, U., Weber, B., Müller, M., Kappl, M., Shiraiwa, M., Kilcoyne, A. L. D., Weigand, M., Scholz, D., Haug, G. H., Al-Amri, A., and Andreae, M. O. (2017). Characterization and differentiation of rock varnish types from different environments by microanalytical techniques. *Chemical Geology*, 459:91–118.

Macholdt, D. S., Jochum, K. P., Pöhlker, C., Stoll, B., Weis, U., Weber, B., Müller, M., Kappl, M., Buhre, S., Kilcoyne, A. L. D., Weigand, M., Scholz, D., Al-Amri, A. M., and Andreae, M. O. (2015). Microanalytical methods for in-situ high-resolution analysis of rock varnish at the micrometer to nanometer scale. *Chemical Geology*, 411:57–68.

Masindi, V., Shabalala, A., and Foteinis, S. (2022). Passive co-treatment of phosphorus-depleted municipal wastewater with acid mine drainage: Towards sustainable wastewater management systems. *Journal of Environmental Management*, 324.

McCullagh, P. and Nelder, J. (1989). *Generalized Linear Models*. Chapman and Hall, second edition.

McIntyre, J. and Barry, R. (2018). A lattice-based smoother for regions with irregular boundaries and holes. *Journal of Computational and Graphical Statistics*, 27(2):360–367.

McKnight, D. T., Huerlimann, R., Bower, D. S., Schwarzkopf, L., Alford, R. A., and Zenger, K. R. (2019). microDecon: A highly accurate read□subtraction tool for the post□sequencing removal of contamination in metabarcoding studies. *Environmental DNA*, 1:14–25.

McMurdie, P. J. and Holmes, S. (2014). Waste not, want not: why rarefying microbiome data is inadmissible. *PLoS Computational Biology*, 10(4):e1003531.

McNaughton, C. S., Clarke, A. D., Freitag, S., Kapustin, V. N., Kondo, Y., Moteki, N., Sahu, L., Takegawa, N., Schwarz, J. P., Spackman, J. R., Watts, L., Diskin, G., Podolske, J., Holloway, J. S., Wisthaler, A., Mikoviny, T., de Gouw, J., Warneke, C., Jimenez, J., Cubison, M., Howell, S. G., Middlebrook, A., Bahreini, R., Anderson, B. E., Winstead, E., Thornhill, K. L., Lack, D., Cozic, J., and Brock, C. A. (2011). Absorbing aerosol in the troposphere of the Western Arctic during the 2008 ARCTAS/ARCPAC airborne field campaigns. *Atmospheric Chemistry and Physics*, 11(15):7561–7582.

McNaughton, C. S., Clarke, A. D., Kapustin, V., Shinozuka, Y., Howell, S. G., Anderson, B. E., Winstead, E., Dibb, J., Scheuer, E., Cohen, R. C., Wooldridge, P., Perring, A., Huey, L. G., Kim, S., Jimenez, J. L., Dunlea, E. J., DeCarlo, P. F., Wennberg, P. O., Crounse, J. D., Weinheimer, A. J., and Flocke, F. (2009). Observations of heterogeneous reactions between Asian pollution and mineral dust over the Eastern North Pacific during INTEX-B. *Atmospheric Chemistry and Physics*, 9(21):8283–8308.

Meunier, A. (2005). Clays. *Clays*, pages 1–472.

Milligan, R., Sailor, W., WasilewskI, J., and Kuby, W. (1979). Review of NOx emission factors for stationary fossil fuel combustion sources. Technical Report EPA-450/4-79-021, US Environmental Protection Agency, Research Triangle Park, North Carolina.

Montero-Calasanz, M. d. C., Göker, M., Pötter, G., Rohde, M., Spröer, C., Schumann, P., Klenk, H.-P., and Gorbushina, A. A. (2013). Geodermatophilus telluris sp. nov., an actinomycete isolated from Saharan desert sand. *International Journal of Systematic and Evolutionary Microbiology*, 63:2254–2259.

Mothetha, M., Kebede, K., Masindi, V., and Msagati, T. A. M. (2023). Effective treatment of real acid mine drainage using MgO-metakaolinite nanocomposite. *Journal of Water Process Engineering*, 51.

Nadaraya, E. (1964). On estimating regression. *Theory of Probability and its Applications*, 9:141–142.

Nadaraya, E. (1989). *Nonparametric Estimation of Probability Densities and Regression Curves*. Kluwer, Dordrecht.

Neumann, J. T., Black, J. L., Hœrlé, S., Smith, B. W., Watkins, R., Lagos, M., Ziegler, A., and Geisler, T. (2022). Artificial weathering of rock types bearing petroglyphs from Murujuga, Western Australia. *Heritage Science*, 10(1):77.

Niemi, S. (1997). *Survey of modern power plants driven by diesel and gas engines*. Technical Report 1860, Technical Research Centre of Finland, Espoo, Finland. ISBN 951–38–5155–9.

Ocean Insight (2024). Ocean hdx spectrometer product sheet. Technical report, Ocean Insight. https://www.oceanoptics.com/wp-content/uploads/2024/05/Ocean-HDX_Product-Sheet.pdf.

Oguchi, C. T. (2013). Weathering rinds: Formation Processes and Weathering Rates. In *Treatise on Geomorphology*, pages 98–110. Academic Press, San Diego.

Oguchi, C. T. and Yu, S. (2021). A review of theoretical salt weathering studies for stone heritage. *Progress in Earth and Planetary Science*, 8(1).

Otter, L. M., Macholdt, D. S., Jochum, K. P., Stoll, B., Weis, U., Weber, B., Scholz, D., Haug, G. H., Al-Amri, A. M., and Andreae, M. O. (2020). Geochemical insights into the relationship of rock varnish and adjacent mineral dust fractions. *Chemical Geology*, 551.

Parkhurst, D. and Appelo, C. (2013). Description of input and examples for PHREEQC version 3 – A computer program for speciation, batch-reaction, one-dimensional transport, and inverse geochemical calculations.

Parkhurst, D., Thorstenson, D., and Plummer, L. (1980). PHREEQC – A computer program for geochemical calculations. Technical report. Revised and reprinted August 1990. https: //digital.library.unt.edu/ark:/67531/metadc968363/.

Peters, K. E., Walters, C. C., and Moldowan, M. J. (2005). *The Biomarker Guide: Biomarkers and Isotopes in Petroleum Exploration and Earth History*, volume 2. New York, Cambridge University Press, 2 edition.

Pillans, B. and Fifield, L. K. (2013). Erosion rates and weathering history of rock surfaces associated with Aboriginal rock art engravings (petroglyphs) on Burrup Peninsula, Western Australia, from cosmogenic nuclide measurements. *Quaternary Science Reviews*, 69:98–106.

Potter, R. M. and Rossman, G. R. (1979). The manganese- and iron-oxide mineralogy of desert varnish. *Chemical Geology*, 25(1):79–94.

R Core Team (2023). *R: A Language and Environment for Statistical Computing*. R Foundation for Statistical Computing, Vienna, Austria.

R Development Core Team (2018). *R: A Language and Environment for Statistical Computing*. R Foundation for Statistical Computing, Vienna, Austria. ISBN 3-900051-07-0.

Rabbachin, L., Piñar, G., Nir, I., Kushmaro, A., Pavan, M. J., Eitenberger, E., Waldherr, M., Graf, A., and Sterflinger, K. (2022). A multi-analytical approach to infer mineral–microbial interactions applied to petroglyph sites in the Negev Desert of Israel. *Applied Sciences*, 12:6936.

Ramanaidou, E. and Lau, D. (2015). Heritage monitoring of 6 sites within 2km of the Yara Pilbara Nitrates Pty Ltd plant site (Western Australia). Report EP154895, CSIRO, Perth, Australia.

Ramanaidou, E. R. and Fonteneau, L. C. (2019). Rocky relationships: the petroglyphs of the Murujuga (Burrup Peninsula and Dampier Archipelago) in Western Australia. *Australian Journal of Earth Sciences*, 66(5):671–698.

Ramboll Australia (2022). *Study of the cumulative impacts of air emissions in the Murujuga airshed*. Technical report. Final Report prepared by Ramboll for the Department of Water and Environmental Regulation. Government of Western Australia (18000883-14 Rev B).

Ramsay, J. O. and Silverman, B. W. (2005). *Functional Data Analysis*. Springer-Verlag, New York, 2 edition.

Randall, S. P. and Vera, M. K. (2004). From Darwin to Mars: desert varnish as a model for preservation of complex (bio)chemical systems. In *Proceedings of SPIE - The International Society for Optical Engineering*, volume 5163, pages 136–144.

Reddy, S. M., Saxey, D. W., Rickard, W. D. A., Fougerouse, D., Montalvo, S. D., Verberne, R., and van Riessen, A. (2020). Atom Probe Tomography: Development and application to the geosciences. *Geostandards and Geoanalytical Research*, 44(1):5–50.

Rosado, T., Dias, L., Lança, M., Nogueira, C., Santos, R., Maria Rosário, M. Candeias, A., Mirão, J., and Caldeira, A. T. (2020). Assessment of microbiota present on a Portuguese historical stone convent using high□throughput sequencing approaches. *MicrobiologyOpen*, 9:1067–1084.

Rosenfeld, A. and Pfalz, J. L. (1966). Sequential operations in digital picture processing. *Journal of the Association for Computing Machinery*, 13:471.

Rosenfeld, A. and Pfalz, J. L. (1968). Distance functions on digital pictures. *Pattern Recognition*, 1:33–61.

Ruibal, C., Gueidan, C., Selbmann, L., Gorbushina, A. A., Crous, P. W., Groenewald, J. Z., Muggia, L., Grube, M., Isola, D., Schoch, C. L., Staley, J. T., Lutzoni, F., and de Hoog, G. S. (2009). Phylogeny of rock-inhabiting fungi related to Dothideomycetes. *Studies in Mycology*, 64:123–133.

Russ, J. and DeHoff, R. (1999). *Practical stereology*. Plenum Press, second edition.

Saeed, M. and Jadhawar, P. (2024). Modelling underground hydrogen storage: A state-of-the-art review of fundamental approaches and findings. *Gas Science and Engineering*, 121.

Serra, J. (1982). *Image Analysis and Mathematical Morphology*. Academic Press, London.

Serra, J., editor (1988). *Image analysis and mathematical morphology, volume 2: Theoretical advances*. Academic Press, London.

Shatzmann, M. (1979). An integral model of plume rise. *Atmospheric Environment*, 13:721–731.

Silverman, B. (1986). *Density Estimation for Statistics and Data Analysis*. Chapman and Hall, London.

Simpson, E. H. (1951). The interpretation of interaction in contingency tables. *Journal of the Royal Statistical Society, Series B*, 13:238–241.

Skeie, R. B., Hodnebrog, O., and Myhre, G. (2023). Trends in atmospheric methane concentrations since 1990 were driven and modified by anthropogenic emissions. *Communications Earth and Environment*, 4:317.

Skurtveit, E., Torabi, A., Sundal, A., and Braathen, A. (2021). The role of mechanical stratigraphy on co2 migration along faults — examples from Entrada Sandstone, Humbug Flats, Utah, USA. *International Journal of Greenhouse Gas Control*, 109:103376.

Slawson, P. R. and Csanady, G. T. (1971). The effect of atmospheric conditions on plume rise. *Journal of Fluid Mechanics*, 47:39–49.

Smith, B. W., Black, J. L., Hœrlé, S., Ferland, M. A., Diffey, S. M., Neumann, J. T., and Geisler, T. (2022). The impact of industrial pollution on the rock art of Murujuga, Western Australia. *Rock Art Research*, 39(1):3–14.

Soille, P. (2003). *Morphological Image Analysis: Principles and Applications*. Springer, New York.

Su, L., Guo, L., Hao, Y., Xiang, M., Cai, L., and Liu, X. (2015). Rupestriomyces and spissiomyces, two new genera of rock-inhabiting fungi from China. *Mycologia*, 107:831–844.

Thiagarajan, N. and Aeolus Lee, C.-T. (2004). Trace-element evidence for the origin of desert varnish by direct aqueous atmospheric deposition. *Earth and Planetary Science Letters*, 224(1-2):131–141.

Tripp, M., Schwark, L., Brocks, J. J., Mayer, P., Whiteside, J. H., Rickard, W., Greenwood, P. F., and Grice, K. (2023). Rapid encapsulation of true ferns and arborane/fernane compounds fossilised in siderite concretions supports analytical distinction of plant fossils. *Scientific Reports*, 13:19851.

Underwood, E. (1970). *Quantitative Stereology*. Addison-Wesley, Reading, Mass.

Vitzthum von Eckstaedt, C. D., Grice, K., Ioppolo-Armanios, M., Kelly, D., and Gibberd, M. (2012). Compound specific carbon and hydrogen stable isotope analyses of volatile organic compounds in various emissions of combustion processes. *Chemosphere*, 89:1407–1413.

Watson, G. (1964). Smooth regression analysis. *Sankhya A*, 26:359–372.

Weibel, E. (1979). *Stereological Methods, 1. Practical Methods for Biological Morphometry*. Academic Press, London.

Weibel, E. (1980). *Stereological Methods, 2. Theoretical Foundations*. Academic Press, London.

Weiss, S., Xu, Z. Z., Peddada, S., Amir, A., Bittinger, K., Gonzalez, A., Lozupone, C., Zaneveld, J. R., Vázquez-Baeza, Y., Birmingham, A., Hyde, E. R., and Knight, R. (2017). Normalization and microbial differential abundance strategies depend upon data characteristics. *Microbiome*, 5(1):27.

Welch, S. A. and Ullman, W. J. (1996). Feldspar dissolution in acidic and organic solutions: Compositional and ph dependence of dissolution rate. *Geochimica et Cosmochimica Acta*, 60(16):2939–2948.

Wickham, H. (2016). *ggplot2: Elegant Graphics for Data Analysis*. Springer-Verlag New York.

Yeager, C. M. (2019). Life on the edge: Microbes in rock varnish. Technical report, Los Alamos National Laoratory.

Yuan, G., Cao, Y., Schulz, H.-M., Hao, F., Gluyas, J., Liu, K., Yang, T., Wang, Y., Xi, K., and Li, F. (2019). A review of feldspar alteration and its geological significance in sedimentary basins: From shallow aquifers to deep hydrocarbon reservoirs. *Earth-Science Reviews*, 191:114–140.

Yule, G. H. (1903). Notes on the theory of association of attributes in Statistics. *Biometrika*, 2:121–134.

Zar, J. (1972). Significance testing of the Spearman rank correlation coefficient. *Journal of the American Statistical Association*, 67(339):578–580.

Zeileis, A. and Hothorn, T. (2002). Diagnostic checking in regression relationships. *R News*, 2(3):7–10.

Zhang, J. T. (2013). *Analysis of Variance for Functional Data*. Chapman and Hall/ CRC, 1 edition.

Zhang, X. and Yi, N. (2020). NBZIMM: negative binomial and zero-inflated mixed models, with application to microbiome/metagenomics data analysis. *BMC Bioinformatics*, 21(1):488.